



QA:QA

ANL-WIS-PA-000001 REV 03

October 2007

EBS Radionuclide Transport Abstraction

Prepared for:
U.S. Department of Energy
Office of Civilian Radioactive Waste Management
Office of Repository Development
1551 Hillshire Drive
Las Vegas, Nevada 89134-6321

Prepared by:
Sandia National Laboratories
OCRWM Lead Laboratory for Repository Systems
1180 Town Center Drive
Las Vegas, Nevada 89144

Under Contract Number
DE-AC04-94AL85000

DISCLAIMER

This report was prepared as an account of work sponsored by an agency of the United States Government. Neither the United States Government nor any agency thereof, nor any of their employees, nor any of their contractors, subcontractors or their employees, makes any warranty, express or implied, or assumes any legal liability or responsibility for the accuracy, completeness, or any third party's use or the results of such use of any information, apparatus, product, or process disclosed, or represents that its use would not infringe privately owned rights. Reference herein to any specific commercial product, process, or service by trade name, trademark, manufacturer, or otherwise, does not necessarily constitute or imply its endorsement, recommendation, or favoring by the United States Government or any agency thereof or its contractors or subcontractors. The views and opinions of authors expressed herein do not necessarily state or reflect those of the United States Government or any agency thereof.

QA: QA

EBS Radionuclide Transport Abstraction

ANL-WIS-PA-000001 REV 03

October 2007



Model Signature Page/Change History

Complete only applicable items.

1. Total Pages: 754

2. Type of Mathematical Model <input type="checkbox"/> Process Model <input checked="" type="checkbox"/> Abstraction Model <input type="checkbox"/> System Model Describe Intended Use of Model The abstraction for flow and transport of radionuclides in the Engineered Barrier System (EBS) will be incorporated into the GoldSim model for TSPA-LA.			
3. Title <i>EBS Radionuclide Transport Abstraction</i>			
4. DI (including Rev. No.): ANL-WIS-PA-000001 REV03			
	Printed Name	Signature	Date
5. Originator	James Schreiber	<i>James D. Schreiber</i>	10/2/2007
6. Independent Technical Reviewer	David Sassani	<i>David Sassani</i>	10/02/2007
7. Checker	Paul Mariner (Lead) <i>for</i>	<i>Paul Mariner</i>	10/2/07
8. QCS	John Devers	<i>John K Devers</i>	10/02/07
9. Responsible Manager/Lead	James Schreiber	<i>James D. Schreiber</i>	10/2/2007
10. Responsible Manager	Jerry McNeish	<i>Jerry A McNeish</i>	10/2/07
11. Remarks			
Change History			
12. Revision No.	13. Description of Change		
REV 00	Initial issue.		
REV 00, ICN 01	Changed functional dependence of diffusion coefficient on liquid saturation and porosity.		
REV 00, ICN 02	Modified EBS flow and transport abstraction to include an EBS design without backfill; modified thermal and mechanical response of drip shield to reflect new drip shield design and rockfall analyses.		

REV 01	<p>Complete revision. Revisions are too extensive to use change lines. Modified flux splitting model, incorporating experimental data; added model validation. Added in-package retardation and diffusion models, with validation. Modified invert diffusion properties model and added data qualification and validation. Included general mathematical description of EBS transport. Expanded treatment of colloid-facilitated transport. Updated YMRP Acceptance Criteria and FEPs list. Modified flow pathways and flow and transport abstractions. Added alternative conceptual models, including dual-continuum invert. Added DIRS numbers to references. Added summary of barrier capability. Added discussion of parameter and model uncertainty. Added list of nomenclature. Added appendices describing spreadsheets used to develop and validate models. Added output DTN. Added sorption in the invert. Revised and expanded discretization of EBS RT Abstraction. Added UZ input parameters for EBS-UZ boundary condition model. Addressed an error documented in CR 3980.</p>
REV 02	<p>This revision addresses CR-5141, CR-5293, and CR-5442. This is a complete revision; due to extensive changes, change bars were not used.</p>
REV 03	<p>Complete revision. Revisions are too extensive to use change bars. Extended temperature dependence of diffusion coefficient to entire EBS. Diffusion coefficients are now radionuclide-species dependent. Updated waste package and invert design. Revised in-package diffusion submodel water vapor adsorption isotherm. Added new adsorption isotherm for CSNF degradation rind to compute water saturation in the rind. Revised steel corrosion rates. Added new kinetic radionuclide sorption model for sorption onto corrosion products based on competitive surface complexation model. Revised output DTNs. Revised validation, including new critical review.</p> <p>This revision addresses the following CRs: 6509, 7197, 8656, 9293, 11204, 11233, and 11235.</p>

YMK
10/21/07

YMK
10/21/07

ACKNOWLEDGEMENTS

The following individuals contributed to the preparation of this document: Sunil Mehta, Patrick Brady, Paul Domski, Malcolm Siegel, Michael Lord, Joon Lee, James Houseworth, Ronald Iman, and Jason Groves.

Brady Hanson was the lead checker for all checking on this document prior to SCI-PRO-003 review. His team of checkers included Philip Meyer, Richard Wittman, and Signe Wurstner. His efforts and those of his checking team are gratefully acknowledged.

Following SCI-PRO-003 review, the document was final checked by Paul Mariner (lead), Robert Finch, Carlos Jove-Colon, Richard Wittman, Robert Zimmerman, and Philip Meyer.

INTENTIONALLY LEFT BLANK

CONTENTS

	Page
ACRONYMS AND ABBREVIATIONS	XVII
1. PURPOSE	1-1
2. QUALITY ASSURANCE	2-1
3. USE OF SOFTWARE	3-1
3.1 MICROSOFT EXCEL	3-1
3.2 GOLDSIM	3-1
3.3 PHREEQC	3-2
3.4 GRAB IT! TM DIGITIZING SOFTWARE	3-2
3.5 S-PLUS	3-2
3.6 JMP	3-2
4. INPUTS	4-1
4.1 DIRECT INPUT	4-1
4.1.1 Qualified Project Data and Parameters	4-1
4.1.2 Parameters and Other Technical Information	4-11
4.1.3 Design Information	4-46
4.2 CRITERIA	4-52
4.2.1 Applicable Acceptance Criteria from Section 2.2.1.3.3, “Quantity and Chemistry of Water Contacting Engineered Barriers and Waste Forms”	4-53
4.2.2 Applicable Acceptance Criteria from Section 2.2.1.3.4, “Radionuclide Release Rates and Solubility Limits”	4-57
4.3 CODES, STANDARDS, AND REGULATIONS	4-60
5. ASSUMPTIONS	5-1
5.1 ALL SEEPAGE FALLS ONTO DRIP SHIELD/WASTE PACKAGE	5-1
5.2 EVAPORATION FROM A DRIP SHIELD DOES NOT OCCUR	5-1
5.3 EVAPORATION FROM A WASTE PACKAGE DOES NOT OCCUR	5-2
5.4 PRODUCTION OR CONSUMPTION OF WATER BY CHEMICAL REACTIONS DOES NOT OCCUR	5-3
5.5 THIN WATER FILMS ALWAYS EXIST BELOW THE BOILING POINT OF WATER	5-4
5.6 NO CORROSION PRODUCTS EXIST IN THE INVERT	5-4
5.7 NO PHYSICAL FILTRATION OR GRAVITATIONAL SETTLING OF COLLOIDS	5-5
6. MODEL DISCUSSION	6-1
6.1 MODELING OBJECTIVE	6-1
6.1.1 Engineered Barrier System Components	6-1
6.1.2 Scenario Classes for the TSPA	6-2

CONTENTS (Continued)

	Page
6.2	FEATURES, EVENTS, AND PROCESSES INCLUDED IN THE MODEL..... 6-3
6.3	BASE CASE CONCEPTUAL MODEL 6-4
6.3.1	Introduction and Overview 6-4
6.3.2	Water Flux through the Drip Shield (F_2) 6-11
6.3.3	Water Flux through the Waste Package (F_4) 6-18
6.3.4	Transport through the EBS 6-31
6.4	CONSIDERATION OF ALTERNATIVE CONCEPTUAL MODELS 6-115
6.4.1	Bathtub Model for the Waste Package..... 6-117
6.4.2	Limited Water Vapor and Oxygen Diffusion Rate into Waste Package 6-118
6.4.3	Dual-Continuum Invert..... 6-118
6.4.4	Alternative Invert Diffusion Coefficient Models..... 6-119
6.4.5	Reversible Sorption of Radionuclides onto Waste Package Corrosion Products..... 6-119
6.4.6	Plutonium Sorption from Stationary Corrosion Products and Colloids 6-119
6.5	MODEL FORMULATION FOR BASE CASE MODEL..... 6-120
6.5.1	Mathematical Description of Base Case Conceptual Model 6-120
6.5.2	Summary of Computational Model 6-162
6.6	MODEL FORMULATION FOR ALTERNATIVE CONCEPTUAL MODELS.... 6-237
6.6.1	Bathtub Flow Model 6-237
6.6.2	Limited Water Vapor and Oxygen Diffusion Rate into Waste Package 6-249
6.6.3	Dual-Continuum Invert..... 6-257
6.6.4	Alternative Invert Diffusion Coefficient Models..... 6-275
6.6.5	Reversible Sorption of Radionuclides onto Waste Package Corrosion Products..... 6-283
6.6.6	Plutonium Sorption onto Stationary Corrosion Products and Colloids 6-287
6.7	DESCRIPTION OF BARRIER CAPABILITY 6-303
7.	VALIDATION..... 7-1
7.1	EBS FLOW MODEL..... 7-6
7.1.1	Flux-Splitting Submodel..... 7-6
7.1.2	Results of Critical Review of the EBS Flow Model..... 7-19
7.2	EBS TRANSPORT MODEL 7-19
7.2.1	In-Package Diffusion Submodel..... 7-21
7.2.2	Invert Diffusion Submodel—Temperature, Porosity, and Saturation Dependence..... 7-31
7.2.3	Competitive Surface Complexation Model 7-37
7.2.4	Results of Critical Review of the EBS Flow and Transport Models 7-42
7.3	EBS-UZ INTERFACE MODEL 7-43
7.3.1	Description of Drift-Scale Dual Continuum Flow and Transport Model 7-43
7.3.2	Results of Critical Review of the EBS-UZ Interface Model 7-57

CONTENTS (Continued)

	Page
7.4 VALIDATION SUMMARY	7-57
8. CONCLUSIONS.....	8-1
8.1 CONCEPTUAL MODEL SUMMARY	8-1
8.2 MODEL OUTPUTS	8-6
8.3 EVALUATION OF YUCCA MOUNTAIN REVIEW PLAN CRITERIA	8-37
8.4 RESTRICTIONS FOR SUBSEQUENT USE.....	8-50
9. INPUTS AND REFERENCES.....	9-1
9.1 DOCUMENTS CITED.....	9-1
9.2 CODES, STANDARDS, REGULATIONS, AND PROCEDURES.....	9-34
9.3 SOURCE DATA, LISTED BY DATA TRACKING NUMBER	9-35
9.4 OUTPUT DATA, LISTED BY DATA TRACKING NUMBER	9-38
9.5 SOFTWARE CODES.....	9-38
APPENDIX A — NOTATION	A-1
APPENDIX B — IMPLEMENTATION OF RADIONUCLIDE SORPTION ONTO COLLOIDAL AND STATIONARY PHASES WITH FINITE DIFFERENCE SOLUTION.....	B-1
APPENDIX C — MICROSOFT EXCEL SPREADSHEET “FLUX SPLIT DRIP SHIELD MODEL”.....	C-1
APPENDIX D — MICROSOFT EXCEL SPREADSHEET “FLUX SPLIT WASTE PACKAGE MODEL”.....	D-1
APPENDIX E — MICROSOFT EXCEL SPREADSHEET “FLUX SPLITTING VALIDATION”.....	E-1
APPENDIX F — ANALYSIS OF STAINLESS STEEL AND CARBON STEEL CORROSION RATES USING BAYESIAN UPDATING METHODOLOGY	F-1
APPENDIX G — MICROSOFT EXCEL SPREADSHEET “INVERT DIFFUSION COEFFICIENT”	G-1
APPENDIX H — QUALIFICATION OF DIFFUSION COEFFICIENT DATA	H-1
APPENDIX I — EBS-UZ VALIDATION TOUGH2 CALCULATIONS – SETUP, EXECUTION, AND POST-PROCESSING OF OUTPUT	I-1
APPENDIX J — QUALIFICATION OF THERMODYNAMIC DATA FOR GEOCHEMICAL MODELING OF ADSORPTION OF RADIONUCLIDES BY STATIONARY CORROSION PRODUCTS AND CORROSION PRODUCT COLLOIDS	J-1

CONTENTS (Continued)

	Page
APPENDIX K — SPECIFIC SURFACE AREA DISTRIBUTIONS FOR HFO AND GOETHITE.....	K-1
APPENDIX L — REPRESENTATION OF RADIAL DIFFUSIVE TRANSPORT USING CARTESIAN GRID GEOMETRY	L-1
APPENDIX M — CRITICAL REVIEW OF THE EBS FLOW MODEL, EBS TRANSPORT MODEL AND EBS-UZ INTERFACE MODEL	M-1

FIGURES

	Page
4.1-1. Dimensions of Drip Shield Mock-Up Used in Breached Drip Shield Experiments on Smooth Drip Shield Surface	4-8
6.1-1. Schematic Diagram of a Typical Emplacement Drift and the Major Components of the EBS	6-2
6.3-1. Schematic of the Potential Flow Pathways in the EBS	6-5
6.3-2. Illustration of Spreading of Rivulet Flow on the Drip Shield	6-16
6.3-3. (a) Actual SCC in Stainless Steel Plate, Cross-Sectional View of Transgranular Cracks; (b) Actual SCC in Stainless Steel Plate, Cross-Sectional View of Intergranular Cracks; (c) SCC Configuration as Modeled.	6-22
6.3-4. Uncertainty in the Statistical Fit for the Effective Diffusion Coefficient.....	6-42
6.3-5. Temperature Dependence of the Invert Diffusion Coefficient (Equation 6.3.4.1.2-4)	6-44
6.3-6. Water Adsorption Behavior of Seven Clay-Dominated Soils	6-63
6.3-7. Comparison of the Corrosion Products Water Adsorption Isotherm with Water Adsorption Behavior of Seven Clay-Dominated Soils	6-63
6.3-8. Isotherms for Water Vapor on α -Fe ₂ O ₃	6-64
6.3-9. Water Content versus Temperature at Four Constant Suction Values	6-67
6.3-10. Total Suction versus Temperature at Six Constant Water Contents.....	6-68
6.3-11. Water Content (Expressed as Fraction, or m ³ m ⁻³) versus Matric Potential at 20°C and 80°C Hysteresis Curves for a Sand and a Nonwelded Tuff.....	6-69
6.3-12. Water Content (Expressed as Fraction, or m ³ m ⁻³) versus Temperature at Constant Matric Potential for a Sand and a Nonwelded Tuff.....	6-70
6.3-13. Water Vapor Adsorption Isotherm for α -Fe ₂ O ₃	6-73
6.3-14. Water Vapor Adsorption Isotherm for α -Fe ₂ O ₃	6-74
6.3-15. Water Vapor Adsorption Isotherm for α -Fe ₂ O ₃	6-74
6.3-16. Water Vapor Adsorption Isotherm for α -Fe ₂ O ₃	6-74
6.3-17. Water Vapor Adsorption Isotherm for α -Fe ₂ O ₃	6-75
6.3-18. Water Vapor Adsorption Isotherm for γ -FeOOH	6-75
6.3-19. Water Vapor Adsorption Isotherm for α -Fe ₂ O ₃	6-76
6.3-20. Water Vapor Adsorption Isotherm for γ -FeOOH	6-76
6.3-21. Water Vapor Adsorption Isotherm for Goethite	6-77
6.3-22. Water Vapor Adsorption Isotherm for Goethite	6-77
6.3-23. Water Vapor Adsorption Isotherm for HFO.....	6-78
6.3-24. Water Vapor Adsorption Isotherm for Amorphous Ferric Oxide Hydroxide	6-78
6.3-25. Water Vapor Adsorption Isotherm for Cr ₂ O ₃	6-79
6.3-26. Water Vapor Adsorption Isotherm for Cr ₂ O ₃	6-79
6.3-27. Water Vapor Adsorption Isotherm for Cr ₂ O ₃	6-80
6.3-28. Water Vapor Adsorption Isotherm for Cr ₂ O ₃	6-80
6.3-29. Water Vapor Adsorption isotherm for α -HCrO ₂	6-81
6.3-30. Water Vapor Adsorption isotherm for α -HCrO ₂	6-81
6.3-31. Water Vapor Adsorption Isotherm for Chromium Oxide Gel.....	6-82

FIGURES (Continued)

	Page
6.3-32. Water Vapor Adsorption Isotherm for NiO.....	6-82
6.3-33. Water Vapor Adsorption Isotherm for Ni(OH) ₂	6-83
6.3-34. Composite Water Vapor Adsorption Isotherm for Steel Corrosion Products	6-83
6.3-35. Water Vapor Adsorption Isotherms for UO ₂ and CeO ₂ (ZrO ₂ and PuO ₂ data are not used).....	6-105
6.3-36. Water Vapor Adsorption Isotherm for ThO ₂	6-105
6.3-37. Water Vapor Adsorption Isotherm for ZrO ₂	6-106
6.3-38. Water Vapor Adsorption Isotherms for PuO ₂	6-106
6.3-39. Water Vapor Adsorption Isotherms for PuO ₂ at 50°C.....	6-107
6.3-40. Water Vapor Adsorption Isotherms for PuO ₂ at 75°C.....	6-107
6.3-41. Water Vapor Adsorption Isotherms for PuO ₂	6-108
6.3-42. Least Squares Fit of Adsorption Data to FHH Isotherm	6-109
6.3-43. Waste Form Rind Adsorption Isotherm Showing Uncertainty.....	6-111
6.3-44. Water Saturation Bounds in CSNF Waste Form Rind	6-114
6.5-1. Geometry and Nomenclature for a Centrally Located Breach with $\ell > x \tan \alpha$	6-127
6.5-2. Geometry and Nomenclature for a Centrally Located Breach with $\ell < x \tan \alpha$	6-131
6.5-3. Geometry and Nomenclature for an End-Located Breach with $\ell > x \tan \alpha$	6-133
6.5-4. Water Saturation in CSNF Corrosion Products Domain in Constant RH Sample Calculation.....	6-180
6.5-5. Water Saturation in CDSP Corrosion Products Domain in Constant RH Sample Calculation.....	6-181
6.5-6. Water Saturation in CSNF Waste Form Domain in Constant RH Sample Calculation.....	6-185
6.5-7. Water Saturation in HLWG Waste Form Domain in Constant RH Sample Calculation.....	6-188
6.5-8. Water Volume in Components of HLWG Waste Form Domain in Constant RH Sample Calculation	6-189
6.5-9. Water Saturation in DSNF Waste Form Domain in Constant RH Sample Calculation.....	6-190
6.5-10. Scatter Plot Matrix of First 5 Predictors Versus the pH Response.....	6-206
6.5-11. Scatter Plot Matrix of 6 Dissolved Concentration Predictors Versus the pH Response	6-207
6.5-12. Plot of R^2 Versus the Number of Model Terms for the logsU.CP Model	6-208
6.5-13. Diagnostic Plots for Regression Model of Response Variable pH.....	6-209
6.5-14. Diagnostic Plots for Regression Model of Response Variable logsU.CP	6-210
6.5-15. Diagnostic Plots for Regression Model of Response Variable logsPu.CP	6-211
6.5-16. Diagnostic Plots for Regression Model of Response Variable logsNp.CP	6-212
6.5-17. Diagnostic Plots for Regression Model of Response Variable logsAm.CP	6-213
6.5-18. Diagnostic Plots for Regression Model of Response Variable logsTh.CP.....	6-214
6.5-19. Diagnostic Plots for Regression Model of Response Variable logsNi.CP	6-215
6.5-20. Computational Grid in the EBS-UZ Interface Model.....	6-227
6.6-1. Schematic of the Bathtub Geometry for the Waste Package.....	6-239

FIGURES (Continued)

	Page
6.6-2. Water Vapor Diffusion Rate Dependence on Internal Surface Water Vapor Mole Fraction at Various Values of RH	6-256
6.6-3. Water Vapor Diffusion Rate Dependence on Drift Relative Humidity at Various Values of Internal Surface Water Vapor Mole Fraction, x_{As}	6-256
6.6-4. Schematic of the Potential Flow Pathways in the EBS	6-259
6.6-5. Computational Grid in the EBS-UZ Interface Model (Dual-Continuum Invert)	6-273
6.6-6. Relative Error of Mass-in-Place for Microsoft Excel Approximate Solution	6-276
6.6-7. Comparison of Microsoft Excel and GoldSim Flux Bifurcation Solutions.....	6-277
6.6-8. Range of the Bulk Diffusion Coefficients for Crushed Tuff	6-279
6.6-9. Desorption of Pu from (a) Hematite and (b) Goethite	6-293
6.6-10. Reinterpretation of Lu et al. Desorption Data for (a) Hematite and (b) Goethite.....	6-295
6.6-11. Two-Site Model of Painter et al., Fitted to Pu Sorption Data for Hematite and Goethite Using Two-Step Fitting Process.	6-299
6.6-12. Two-site Model of Painter et al., Applied to Pu Sorption Data for Hematite and Goethite, and Fitted in a Single Step	6-300
6.6-13. Kinetic Data for Pu Adsorption onto Hematite and Goethite at pH~8-8.5 Showing the Linear Fits to the Elovich Equation	6-303
7.1-1. Splash Radius Dependence on Number of Drips for Rough Drip Shield Tests	7-10
7.2-1. Water Vapor Adsorption Isotherm for (a) Goethite and (b) Hematite	7-23
7.2-2. Water Vapor Adsorption Isotherm for Cr ₂ O ₃	7-24
7.2-3. Water Vapor Adsorption Isotherm for NiO	7-24
7.2-4. Validation of Adsorption Isotherms for Water Vapor on Corrosion Products	7-25
7.2-5. Water Vapor Adsorption Isotherm for ThO ₂	7-26
7.2-6. Water Vapor Adsorption Isotherm for ZrO ₂ and PuO ₂	7-26
7.2-7. Water Vapor Adsorption Isotherm for PuO ₂	7-27
7.2-8. Validation of Adsorption Isotherms for Water Vapor on CSNF Degradation Rind.....	7-27
7.2-9. Comparison of Correlations for Self-Diffusion Coefficient of Water	7-33
7.2-10. Comparison of EBS Radionuclide Transport Abstraction Invert Diffusion Submodel (Equation 7.2.2.-1) with Measured Diffusion Coefficients for Tuff	7-34
7.2-11. EPA U Soil K_{ds} (EPA 1999 [DIRS 170376]) and C-SCM Iron Oxide K_{ds}	7-38
7.2-12. EPA Pu Soil K_{ds} (EPA 1999) and C-SCM Iron Oxide K_{ds}	7-39
7.2-13. EPA Np Soil Kds (EPA 1999 [DIRS 170376]) (Yellow Shaded Area) and C-SCM Iron Oxide Kds	7-40
7.2-14. EPA Am Soil K_{ds} and C-SCM Iron Oxide K_{ds}	7-41
7.2-15. EPA Th Soil K_{ds} and C-SCM Iron Oxide K_{ds}	7-42
7.3-1. Domain used for the RTA Validation Calculation a) Full Domain b) Detail of the Domain Near the Waste Emplacement Drift	7-45
7.3-2. Matrix/Intragranular Water Saturations a) Saturation Contours Over Entire Domain; b) Saturation Contours Near the Drift.....	7-50
7.3-3. Fracture/Intergranular Water Saturations a) Saturation Contours Over Entire Domain; b) Saturation Contours Near the Drift.....	7-51

FIGURES (Continued)

	Page
7.3-4. Matrix/Intragranular Water Flux a) Flux Contours Over Entire Domain; b) Flux Contours Near the Drift	7-51
7.3-5. Fracture/Intergranular Water Flux a) Flux Contours Over Entire Domain; b) Flux Contours Near the Drift	7-52
7.3-6. Matrix/Intragranular Solute Concentrations a) Concentration Contours Over Entire Domain; b) Concentration Contours Near the Drift.....	7-53
7.3-7. Fracture/Intergranular Solute Concentrations a) Concentration Contours Over Entire Domain. b) Concentration Contours Near the Drift.....	7-54
7.3-8. Matrix/Intragranular Solute Flux a) Solute Flux Contours Over Entire Domain; b) Solute Flux Contours Near the Drift	7-55
7.3-9. Fracture/Intergranular Solute Flux a) Solute Flux Contours Over Entire Domain; b) Solute Flux Contours Near the Drift	7-55
B-1. Concentrations with Respect to Water Volume, Advection Case	B-9
B-2. Concentrations with Respect to Water Volume, No Advection Case	B-9
B-3. Kinetic Sorption Reaction Rate as a Function of Colloid to Total Flux Out Ratio, Ω	B-13
C-1. Calculation of Experimental Breach Flow Fractions and Model Flow Fractions for Mean Minus One Standard Deviation Rivulet Spread Angle	C-1
C-2. Calculation of Model Flow Fractions for Mean Minus One Standard Deviation Rivulet Spread Angle.....	C-4
C-3. Calculation of Model Flow Fractions for Mean Rivulet Spread Angle.....	C-6
C-4. Calculation of Model Flow Fractions for Mean Plus One Standard Deviation Rivulet Spread Angle.....	C-8
C-5. Calculation of Rivulet Spread Angle	C-9
C-6. Dimensions and Locations of Breaches in Drip Shield Mockup Used in Breached Drip Shield Experiments.....	C-10
C-7. Summary of Drip Shield Flux-Splitting Submodel	C-11
C-8. Summary of Drip Shield Flux-Splitting Submodel	C-12
C-9. Summary of Drip Shield Flux-Splitting Submodel Comparing Measured and Calculated Breach Flows	C-13
C-10. Comparison of Calculated and Measured Breach Flow Fractions for Drip Shield Flux-Splitting Submodel for Minimum (8.87°), Mean (13.15°), and Maximum (17.29°) Rivulet Spread Angles	C-14
D-1. Calculation of Experimental Breach Flow Fractions and Model Flow Fractions for Mean Minus One Standard Deviation Rivulet Spread Angle	D-1
D-2. Calculation of Model Flow Fractions for Mean Minus One Standard Deviation Rivulet Spread Angle.....	D-4
D-3. Calculation of Model Flow Fractions for Mean Rivulet Spread Angle.....	D-6
D-4. Calculation of Model Flow Fractions for Mean Plus One Standard Deviation Rivulet Spread Angle.....	D-8

FIGURES (Continued)

	Page
D-5. Calculation of Rivulet Spread Angle	D-9
D-6. Dimensions and Locations of Breaches in Drip Shield Mockup Used in Breached Drip Shield Experiments.....	D-10
D-7. Calculation of Rivulet Spread Angles and Statistical Measures.....	D-11
D-8. Calculation of Rivulet Spread Angles	D-12
D-9. Summary of Waste Package Flux-Splitting Submodel.....	D-13
D-10. Summary of Waste Package Flux-Splitting Submodel.....	D-14
D-11. Summary of Waste Package Flux-Splitting Submodel Comparing Measured and Calculated Breach Flows	D-15
D-12. Comparison of Calculated and Measured Breach Flow Fractions for Waste Package Flux-Splitting Submodel for Minimum (5.50°), Mean (13.73°), and Maximum (21.96°) Rivulet Spread Angles	D-16
E-1. Effect of Number of Drips on Splash Radius	E-1
E-2. Effect of Number of Drips on Splash Radius; Data Organized by Type of Measurement	E-2
E-3. Effect of Number of Drips on Splash Radius; All Left and Right Measurements Are Consolidated	E-3
E-4. Splash Radius Determination.....	E-4
E-5. Worksheet Overview	E-5
E-6. Calculation of Experimental Breach Flow Fractions.....	E-6
E-7. Summary of Experimental Breach Flow Fractions.....	E-6
E-8. Rivulet Spread Distances	E-7
E-9. Rivulet Spread Data Reorganized.....	E-9
E-10. Calculation of Rivulet Spread Angles	E-10
E-11. Worksheet Overview	E-12
E-12. Calculation of Rivulet Spread Angles	E-13
E-13. Additional Calculations of Rivulet Spread Angles.....	E-14
E-14. Statistics of Rivulet Spread Angles	E-15
E-15. Calculation of Experimental Breach Flow Fractions.....	E-15
E-16. Summary of Experimental Breach Flow Fractions.....	E-16
F-1. Lilliefors Test for Normality for the 316 SS Data	F-3
F-2. Lilliefors Test for Normality for the A 516 CS Data.....	F-3
G-1. Invert Diffusion Coefficient Input Data (Water Content 1.50% to 6.93%).....	G-2
G-2. Invert Diffusion Coefficient Input Data (Water Content 7.30% to 11.60%).....	G-3
G-3. Invert Diffusion Coefficient Input Data (Water Content 11.60% to 17.50%).....	G-4
G-4. Invert Diffusion Coefficient Input Data (Water Content 17.50% to 66.30%).....	G-5
G-5. Plot of Fitted Invert Diffusion Coefficient Data	G-6
G-6. Plotted Results of Invert Diffusion Coefficient Data, Showing Uncertainty Range as Mean ± 3 Standard Deviations	G-7
G-7. Further Analysis of Invert Diffusion Coefficient Data.....	G-8

FIGURES (Continued)

	Page
G-8. Validation of Invert Diffusion Coefficient Data.....	G-9
H-1. Comparison of Diffusion Coefficients.....	H-4
H-2. Data Qualification Plan.....	H-5
K-1. Histogram of HFO Specific Surface Area Data.....	K-1
K-2. Normality Plot of HFO Specific Surface Area Data.....	K-2
K-3. Normality Plot of HFO Specific Surface Area Data with Extreme Outlier Removed	K-3
K-4. Lognormal Fitted Distribution of HFO Specific Surface Area Data	K-4
K-5. Lognormal Fitted Distribution of Goethite Specific Surface Area Data	K-5
L-1. Radial Diffusion.....	L-5

TABLES

	Page
4.1-1. Input Data for RTA.....	4-2
4.1-2. Atlas Breached Drip Shield Experiments on Smooth Drip Shield Surface – Dripping on Crown – Flow into Breaches.....	4-5
4.1-3. Atlas Breached Drip Shield Experiments on Smooth Drip Shield Surface – Dripping on Crown – Rivulet Spread Data – 33° from Crown.....	4-6
4.1-4. Atlas Breached Drip Shield Experiments on Smooth Drip Shield Surface – Dripping on Crown – Splash Radius Tests.....	4-6
4.1-5. Atlas Breached Drip Shield Experiments on Smooth Drip Shield Surface – Dripping at Off-Crown Locations – Flow into Breaches.....	4-7
4.1-6. Atlas Breached Drip Shield Experiments on Smooth Drip Shield Surface – Dripping off Crown – Rivulet Spread Data – 33° from Crown and at Transition.....	4-8
4.1-7. Species-Dependent Free Water Diffusion Coefficients at 25°C.....	4-9
4.1-8. J-13 Water Composition Used in PHREEQC Simulations.....	4-9
4.1-9. Sources of UZ Flow Field Data.....	4-10
4.1-10. Parameters for RTA (Established Fact).....	4-11
4.1-11. Parameters for RTA (Various Sources).....	4-12
4.1-12. Specific Surface Areas and Adsorption Site Densities for Goethite.....	4-17
4.1-13. Total Site Densities for HFO.....	4-22
4.1-14. Specific Surface Areas for HFO.....	4-22
4.1-15. Elemental Composition (Weight Percent) and Density of Waste Package Materials.....	4-25
4.1-16. Diffusion Coefficient for Granular Materials for Volumetric Moisture Content Between 1.5 Percent and 66.3 Percent.....	4-26
4.1-17. Surface Complexation Constants Used in PHREEQC Simulations.....	4-29
4.1-18. Water Vapor Adsorption Isotherms for SNF Waste Form Materials.....	4-31
4.1-19. Water Vapor Adsorption Isotherms for Steel Corrosion Products.....	4-34
4.1-20. Design Information for EBS Components.....	4-46
4.1-21. Component Dimensions in a 21-PWR Site-Specific Canister.....	4-48
4.1-22. Masses and Numbers of Components in Waste Packages.....	4-48
4.1-23. Component Masses Used in RTA Compared with Design Values.....	4-51
6.2-1. Included FEPs for This Report.....	6-3
6.3-1. Summary of Parameters for EBS Flow Pathways.....	6-8
6.3-2. Summary of Transport Modes and Parameters for the EBS Transport Pathways.....	6-10
6.3-3. Opening Area of a Single SCC in the Waste Package and Drip Shield.....	6-24
6.3-4. Site Densities Conversions for Goethite.....	6-55
6.3-5. Sample Ranges and Distributions Used for Sorption on Goethite Corrosion Products.....	6-57
6.3-6. Sample Ranges and Distributions Used for Sorption on HFO Corrosion Products.....	6-59
6.3-7. Specific Surface Area of Various Waste Package Corrosion Products.....	6-85

TABLES (Continued)

	Page
6.3-8. Estimated Masses (kg) of Steels and Equivalent Masses of Corrosion Products in 21-PWR TAD Waste Packages and Domains for Use in Modeling Water Adsorption and Retardation in the Waste Package.....	6-87
6.3-9. Estimated Masses (kg) of Steels and Equivalent Masses of Corrosion Products in 5- DHLW/DOE Long Waste Package Domains for Use in Modeling Water Adsorption and Retardation in the Waste Package.....	6-88
6.3-10. Initial Characteristics of Internal Components of a TAD Containing 21 PWR CSNF Assemblies.....	6-91
6.3-11. Internal Solids Volume in Degraded 21-PWR TAD Waste Package.....	6-92
6.3-12. Properties of Materials Used in Water Vapor Adsorption Measurements	6-104
6.4-1. Alternative Conceptual Models Considered.....	6-116
6.5-1. Dimensions Used in the Analysis of Breached Drip Shield Experiments, Based on Dimensions Shown in Figure 4.1-1	6-136
6.5-2. Comparison of Experimental Breach Inflow Fractions with Model Calculations from Appendix C	6-137
6.5-3. Additional Comparisons of Experimental Breach Inflow Fractions with Model Calculations from Appendix C	6-139
6.5-4. Water Collected in Drip Shield Experiment Q(film); Drip Location: Patch 4, 8 cm Right of Center, Crown.....	6-140
6.5-5. Domain Properties Used to Compute Corrosion Product Water Saturation and Volume.....	6-174
6.5-6. Constant Material Properties Used to Compute Corrosion Product Water Saturation and Volume.	6-175
6.5-7. Sampled Parameters Used to Compute Corrosion Product Water Saturation and Volume.....	6-176
6.5-8. Water Saturation in CSNF Corrosion Products Domain	6-180
6.5-9. Parameters Used to Compute Waste Form Water Saturation and Water Volume. ..	6-182
6.5-10. Data Used For Calculating Maximum Solubility Ratio	6-197
6.5-11. Solubility Controlling Phase.....	6-197
6.5-12. Surface Complexation Reactions and log <i>K</i> Values	6-199
6.5-13. List of Predictor and Response Variables.....	6-201
6.5-14. Coefficients for the Final Regression Models	6-203
6.6-1. Summary of Transport Modes and Parameters for the EBS Transport Pathways with Dual-Continuum Invert.....	6-260
6.6-2. Parameters Developed for Crushed Tuff.....	6-278
6.6-3. Tuff Matrix Properties for TSw35 and TSw36.....	6-282
6.6-4. Influences Over Radionuclide Sorption in Soils.....	6-285
6.6-5. Summary of Partition Coefficient (<i>K_d</i>) Ranges and Distributions for Retardation in the Waste Package Corrosion Products	6-287
6.6-6. Sorption of Pu(V) onto Hematite and Goethite Colloids.....	6-291
6.6-7. Lu Data for Desorption of Pu(V) from Hematite and Goethite Colloids	6-294
6.6-8. Reinterpretation of Lu et al. Data for Desorption of Pu(V) from Hematite and Goethite Colloids	6-296

TABLES (Continued)

	Page
6.6-9. Fitting Pu Sorption Data of Lu et al. with the Two-Site Model of Painter et al.; Two Steps	6-300
6.6-10. Fitting Pu Sorption Data of Lu et al. Using the Two-Site Model of Painter et al., One Step.....	6-301
7.1-1. Atlas Breached Drip Shield Experiments on Rough Drip Shield Surface – Dripping on Crown – Splash Radius Tests.....	7-9
7.1-2. Atlas Breached Drip Shield Experiments on Rough Drip Shield Surface – Dripping on Crown – Rivulet Spread Data – 33° from Crown	7-10
7.1-3. Atlas Breached Drip Shield Experiments on Rough Drip Shield Surface – Dripping on Crown – Flow into Breaches.....	7-11
7.1-4. Atlas Breached Drip Shield Experiments on Rough Drip Shield Surface – Dripping on Crown – Fraction of Dripping that Flowed into Breaches and Rivulet Spread Angle.....	7-11
7.1-5. Range of Estimates for F/f_{VD}	7-12
7.1-6. Comparison of f_{expt} Statistics for Smooth and Rough Drip Shield Surfaces.....	7-13
7.1-7. Summary of f_{DS} and f_{VD} Values.....	7-14
7.1-8. Atlas Breached Waste Package Experiments on Rough Mock-Up Surface – Dripping off Crown – Rivulet Spread Data	7-15
7.1-9. Atlas Breached Waste Package Experiments on Rough Mock-Up Surface – Dripping off Crown – Splash Radius Tests	7-16
7.1-10. Atlas Breached Waste Package Experiments on Rough Mock-Up Surface – Dripping off Crown – Flow into Breaches	7-17
7.1-11. Comparison of f_{expt} Statistics for Smooth and Rough Surfaces	7-18
7.1-12. Summary of f_{WP} and f_{VW} Values.....	7-18
7.2-1 Diffusion Coefficient of Crushed Tuff Invert Materials.....	7-35
7.3-1. Hydrological Properties	7-46
7.3-2. Tortuosity Coefficients for Diffusion in the Rock.....	7-47
8.1-1. Summary of EBS Flow Abstraction	8-3
8.1-2. Summary of EBS Transport Abstraction.....	8-5
8.2-1. Parameters for EBS Transport Abstraction	8-8
8.2-2. Sampled Parameter Ranges and Distributions Used for Kinetic Sorption on Stationary Corrosion Products.....	8-14
8.2-3. Surface Complexation Sorption Coefficients for the Final Regression Models.....	8-15
8.2-4. Sampled Model Inputs Used in the EBS Radionuclide Transport Abstraction.....	8-16
8.2-5. Unsaturated Zone Saturation and Flux Inputs Used in the EBS Radionuclide Transport Abstraction	8-18
8.2-5. Unsaturated Zone Saturation and Flux Inputs Used in the EBS Radionuclide Transport Abstraction (Continued).....	8-19
8.2-6. Fixed Model Inputs Used in the EBS Radionuclide Transport Abstraction.....	8-20

TABLES (Continued)

	Page
8.2-7. Impact Assessment of Using Preliminary Design Data and Preliminary Calculated Model Inputs Based on Design Data in the EBS Radionuclide Transport Abstraction	8-26
8.2-8. Model Equation Inputs Used in the EBS Radionuclide Transport Abstraction	8-30
8.2-9. Invert Diffusion Coefficient Alternative Conceptual Model Parameters	8-36
8.2-10. Model Equation Inputs Used in the EBS Radionuclide Transport Abstraction Invert Diffusion Coefficient Alternative Conceptual Model	8-36
B-1. Representative Parameter Values for Sample Calculation	B-8
F-1. Comparison of Two Simulations with Bayesian Analysis for 316 SS Corrosion Rates.....	F-4
F-2. Comparison of Two Simulations with Bayesian Analysis for A 516 CS Corrosion Rates.....	F-7
H-1. Diffusion Coefficient of Crushed Tuff Invert Materials.....	H-3
I.2-1. Hydrologic Conditions at F014Dh48 and M014Dh48	I-5
I.2-2. Flux Between Neighboring Vertical Elements	I-5
I.2-3. Connection Areas for Vertical Connections	I-5
J-1. Possible Effects on Calculated K_d s of Alternative Ways to Mix SCM Constants from Single-Site and 2-Site Models.....	J-12
J-2. Summary of Surface Complexation Constants.....	J-16
J-3. Summary of Surface Speciation Models Reviewed	J-18
K-1. HFO Specific Surface Area Statistical Parameters.....	K-2
K-2. HFO Specific Surface Area Statistical Parameters with Extreme Outlier Removed.....	K-3
K-3. Goethite Specific Surface Area Statistical Parameters	K-4

ACRONYMS AND ABBREVIATIONS

ASM	American Society for Metals
ASTM	American Society for Testing and Materials
BSC	Bechtel SAIC Company, LLC
BWR	boiling water reactor
CDSP	codisposal (waste package)
CFR	Code of Federal Regulations
CP	corrosion products
CR	condition report
CSNF	commercial spent nuclear fuel
DIRS	Document Input Reference System
DOE	U.S. Department of Energy
DSNF	defense spent nuclear fuel
DTN	data tracking number
EBS	Engineered Barrier System
ECDF	empirical cumulative distribution function
EPA	U.S. Environmental Protection Agency
EPRI	Electric Power Research Institute
FEP	features, events, and processes
FHH	Frenkel-Halsey-Hill adsorption isotherm equation
HFO	hydrous ferric oxide
HLW	high-level radioactive waste
IED	information exchange drawing
LA	license application
LA-ICP-MS	laser ablation coupled with inductively coupled plasma-mass spectrometry
LANL	Los Alamos National Laboratory
LFER	linear free energy relationship
LSC	liquid scintillation counting
NRC	U.S. Nuclear Regulatory Commission
RH	relative humidity
RT	radionuclide transport
RTA	Radionuclide Transport Abstraction
SCM	surface complexation model
SNF	spent nuclear fuel
SR	Site Recommendation

ACRONYMS AND ABBREVIATIONS (Continued)

TAD	transportation, aging, and disposal (canister)
TMI	Three Mile Island
TSPA	total system performance assessment
TWP	technical work plan
UZ	unsaturated zone
WE	Westinghouse Electric
YMP	Yucca Mountain Project

1. PURPOSE

The purpose of this report is to develop and analyze the Engineered Barrier System (EBS) Radionuclide Transport Abstraction Model, consistent with Level I and Level II model validation, as identified in *Technical Work Plan for: Near-Field Environment: Engineered Barrier System: Radionuclide Transport Abstraction Model Report* (BSC 2006 [DIRS 177739]). The EBS Radionuclide Transport Abstraction (or RTA) is the conceptual model used in the Total System Performance Assessment (TSPA) to determine the rate of radionuclide releases from the EBS to the unsaturated zone (UZ).

The RTA conceptual model consists of two main components: a flow model and a transport model. Both models are developed mathematically from first principles in order to show explicitly what assumptions, simplifications, and approximations are incorporated into the models used in the TSPA.

The flow model defines the pathways for water flow in the EBS and specifies how the flow rate is computed in each pathway. Input to this model includes the seepage flux into a drift. The seepage flux is potentially split by the drip shield, with some (or all) of the flux being diverted by the drip shield and some passing through breaches in the drip shield that might result from corrosion or seismic damage. The flux through drip shield breaches is potentially split by the waste package, with some (or all) of the flux being diverted by the waste package and some passing through waste package breaches that might result from corrosion or seismic damage. Neither the drip shield nor the waste package survives an igneous intrusion, so the flux splitting submodel is not used in the igneous scenario class. The flow model is validated in a critical review, as specified in SCI-PRO-006, *Models*. The drip shield and waste package flux splitting algorithms are developed and validated using experimental data.

The transport model considers advective transport and diffusive transport from a breached waste package. Advective transport occurs when radionuclides that are dissolved or sorbed onto colloids (or both) are carried from the waste package by the portion of the seepage flux that passes through drip shield and waste package breaches. Diffusive transport occurs as a result of a gradient in radionuclide concentration when a continuous film of water of sufficient thickness exists and may take place while advective transport is also occurring, as well as when no advective transport is occurring. Diffusive transport is addressed in detail because it is the sole means of transport when there is no flow through a waste package, which may dominate in a large portion of the repository during the regulatory compliance period. The advective transport rate, when it occurs, is generally greater than the diffusive transport rate. Colloid-facilitated advective and diffusive transport is also modeled and is presented in detail in this report.

Additional submodels and model parameters developed in this model report include:

- Diffusion inside a waste package. The time-dependent quantity of corrosion products inside a breached waste package is estimated; this enables the surface area available for adsorption of water to be approximated. Water saturation is determined from water vapor adsorption isotherms for corrosion products as a function of relative humidity, which in turn gives the water volume through which diffusion of radionuclides may occur.

- Diffusion in the invert, accounting for the dependence of diffusion on porosity, saturation, and temperature.
- Sorption in the invert.
- EBS-UZ interface model. Implementation in the TSPA includes this model to provide a realistic concentration boundary condition.

Parameter uncertainty associated with each model and submodel is discussed. The transport model and the EBS-UZ interface model are validated using corroborative data and models as well as a critical review, as specified in SCI-PRO-006, *Models*.

Alternative conceptual models considered, include:

- A “bathtub” flow model in which water must fill a breached waste package before any can flow out, as opposed to the flow-through model that is used
- A model that shows the effect of limitations on diffusion of water vapor and oxygen into a breached waste package and resulting delays in releases of radionuclides
- A dual-continuum invert flow and transport submodel
- Alternative invert diffusion coefficient submodels
- Reversible sorption of radionuclides onto waste package corrosion products
- Plutonium (Pu) sorption onto stationary corrosion products and colloids.

Output from the RTA includes:

- The flow model—the algorithms for computing the flow in each flow path within the EBS, with parameter values or sources for those parameters used in the model.
- The transport model—a model for advective and diffusive transport, specifying the computational procedure for both commercial spent nuclear fuel (CSNF) and codisposal waste packages in both the seep environment (where seepage into the drift and condensation on drift walls occur) and the no-seep environment (where no seepage into the drift or condensation on drift walls occurs), with parameter values or sources for those parameters used in the model.
- Ranges and distributions for parameters that are uncertain and are sampled in the TSPA implementation of the RTA.

Changes from the previous revision (REV 02) of the RTA:

- To estimate water saturation and water volume due to water vapor adsorption in a breached waste package, the corrosion products formed in the waste package are assumed to be a mixed assemblage of iron oxyhydroxides, namely hydrous ferric oxide

(HFO), goethite, and hematite, and the oxides of the two other major components of stainless steels (chromium and nickel), represented as Cr_2O_3 and NiO . These, and solid solutions of these end-members, are the solid phases most likely to form from the corrosion of all internal waste package components, except for fuel rods and spent nuclear fuel (SNF), under the anticipated moist and oxidizing repository conditions. Previous versions of the RTA used hematite properties for the corrosion products in this calculation.

- The method of calculating sorption of radionuclides onto stationary corrosion products and iron oxyhydroxide colloids has been modified. First, both equilibrium (reversible) adsorption and slow and fast desorption of radionuclides are now modeled. Second, competition for a finite number of sorption sites among various species whose concentration varies as a function of pH and P_{CO_2} is considered. Third, rapid, reversible desorption of uranium, neptunium, and thorium from stationary corrosion products is assumed when modeling radionuclide transport through the EBS. Plutonium and americium desorption is slower. Corrosion product properties used in radionuclide sorption calculations are the aggregate surface properties of goethite and HFO. These phases will likely be present along with hematite in the corrosion product assemblage in the waste package.
- The divisions between waste form and corrosion products domains have been redefined. Each waste form domain now includes a portion of the steel corrosion products that previously resided solely in the corrosion products domain.
- The dependence of diffusion coefficients in the waste form and waste package corrosion products on temperature has been included. The functional dependency is identical to that of the invert diffusion coefficient.
- Calculation of the waste form degradation rind water saturation as a function of relative humidity, analogous to the corrosion products water saturation calculation, has been added.
- The diffusion coefficient used in the transport model has been changed from a single bounding value (the self-diffusion coefficient of water) to radionuclide-specific values for each of the 15 radioelements that are considered in the TSPA.
- The diffusion coefficient for colloidal particles has been changed from a constant factor of 1/100th of the free-water diffusion coefficient to be dependent on a sampled colloid particle size using the Stokes-Einstein equation.
- The design of waste packages and the invert has been updated. In the new design, the depth of the invert has been increased, and CSNF waste packages now include a transportation, aging, and disposal (TAD) canister. Preliminary design updates were used to develop parameters that are model inputs for the TSPA; the impact of using these preliminary data is assessed in Sections 4.1.3 and 6.3.4, and is summarized in Table 8.2-8.

Deviations from work activities outlined in the TWP (BSC 2006 [DIRS 177739]) for the preparation of this report include the following:

- An alternative fine-scale multi-process model of in-package transport was planned for comparison with the two-cell representation currently used. This model was not developed.
- The drip shield and waste package flux splitting submodels were to be revised to broaden their range of applicability and to augment the limited experimental data on which the current uncertainty factors are based. These revisions were not carried out.
- An alternative conceptual model analyzing the flux of H₂O, O₂, and CO₂ into breached waste packages was to be developed, expanding on the current alternative conceptual model that evaluates the limitations on reactive gas fluxes through stress corrosion cracks. Although the existing model was revised, the revised model does not account for the more extensive list of processes that was planned in the TWP.
- An internal waste package heating submodel was to be developed to account for the effect of ongoing heat generation inside waste packages on the internal relative humidity and provide an adjustment that would affect the water content of corrosion products. This submodel was not developed.

This version of the RTA was prepared in 2007. By necessity, the RTA was built on technical bases that became well established in the technical literature substantially before that time. Many of the conceptual and numerical inputs that the RTA relies on come from fields that remain rich areas of science and engineering research. Consequently, the technical bases supporting the RTA may become more detailed as the technical literature expands and develops with time.

The scope of this abstraction and report is limited to flow and transport processes. Specifically, this report provides the algorithms that are implemented in the TSPA for transporting radionuclides using the flow geometry and radionuclide concentrations determined by other elements of the TSPA model. The RTA also identifies the important processes that are evaluated at the process level or component level using analytical or numerical solutions. Restrictions on the use of this abstraction are discussed in Section 8.4.

This report was prepared to comply with the U.S. Nuclear Regulatory Commission (NRC) regulation for high-level radioactive waste (HLW), 10 CFR Part 63 [DIRS 180319], which requires the U.S. Department of Energy (DOE) to conduct a performance assessment to demonstrate compliance with postclosure performance objectives. The results from this conceptual model allow portions of the acceptance criteria presented in *Yucca Mountain Review Plan, Final Report* (NRC 2003 [DIRS 163274]) to be addressed. This report also addresses the following CRs: 6509, 7197, 8656, 9293, 11204, 11233, and 11235 (see Section 4.2).

The following reports provide input to the RTA:

- *Multiscale Thermohydrologic Model* (SNL 2007 [DIRS 181383])

- *Thermal Conductivity of the Potential Repository Horizon* (BSC 2004 [DIRS 169854])
- *Calibrated Unsaturated Zone Properties* (SNL 2007 [DIRS 179545])
- *UZ Flow Models and Submodels* (SNL 2007 [DIRS 175177])
- *Waste Form and In-Drift Colloids-Associated Radionuclide Concentrations: Abstraction and Summary* (SNL 2007 [DIRS 177423])
- *Particle Tracking Model and Abstraction of Transport Processes* (SNL 2007 [DIRS 181006])
- *General Corrosion and Localized Corrosion of Waste Package Outer Barrier* (SNL 2007 [DIRS 180778])
- *DSNF and Other Waste Form Degradation Abstraction* (BSC 2004 [DIRS 172453])
- *Defense HLW Glass Degradation Model* (BSC 2004 [DIRS 169988])
- *CSNF Waste Form Degradation: Summary Abstraction* (BSC 2004 [DIRS 169987])
- *Cladding Degradation Summary for LA* (SNL 2007 [DIRS 180616]).

The following documents use output from the RTA as direct input:

- *In-Package Chemistry Abstraction* (SNL 2007 [DIRS 180506])
- *Total System Performance Assessment (TSPA) Model/Analysis for the License Application* (SNL 2007 [DIRS 178871]).

INTENTIONALLY LEFT BLANK

2. QUALITY ASSURANCE

Development of this model report and the supporting analyses have been determined to be subject to the Office of Civilian Radioactive Waste Management quality assurance program, as discussed in *Technical Work Plan for: Near-Field Environment: Engineered Barrier System: Radionuclide Transport Abstraction Model Report* (BSC 2006 [DIRS 177739], Section 8). Approved quality assurance procedures identified in Section 4 of the technical work plan have been used to conduct and document the activities described in this report. Section 8 of the technical work plan also identifies the methods used to control the electronic management of data during the analysis and documentation activities.

This report provides models for evaluating the performance of the Engineered Barrier System, including the drip shields, waste packages, and invert, which are classified in *Q-List* (BSC 2007 [DIRS 180109]) as Safety Category because they are important to waste isolation, as defined in AP-2.22Q, *Classification Analyses and Maintenance of the Q-List*. The results of this report are important to the demonstration of compliance with the postclosure performance objectives prescribed in 10 CFR Part 63 [DIRS 180319]. The report contributes to the analysis data used to support performance assessment; the conclusions do not directly impact engineered features important to safety, as defined in AP-2.22Q. This report was prepared in accordance with SCI-PRO-006, *Models*.

INTENTIONALLY LEFT BLANK

3. USE OF SOFTWARE

This section identifies all controlled and baselined software used in RTA model development, performance, and validation.

3.1 MICROSOFT EXCEL

Microsoft Excel 2003 “Add Trendline” capability was used to perform a statistical analysis of diffusion coefficient values reported in Section 6.3.4.1.1. Microsoft Excel 2003 was also used to analyze experimental data used to develop and validate the drip shield and waste package flux splitting submodels (Sections 6.5.1.1.2.4, 6.5.1.1.3, and 7.1.1). A calculation of the potential mass of corrosion products in fully degraded waste packages using Microsoft Excel 2003 is summarized in Table 6.3-4. A sample calculation to demonstrate the solution procedure used in the colloid transport model, described in Appendix B, was also carried out using Microsoft Excel 2003. A complete description of the formulas, inputs, and outputs used in the Microsoft Excel 2003 analysis of the drip shield experimental data is provided in Appendices C (the drip shield flux splitting submodel), D (the waste package flux splitting submodel), and E (validation of the flux splitting submodels). Distributions are developed using Microsoft Excel 2003 for the corrosion rates of stainless steel and carbon steel in Appendix F and for the specific surface areas of goethite and hydrous ferric oxide in Appendix K. The invert diffusion properties model analysis using Microsoft Excel 2003 is described in Appendix G. Data for water vapor adsorption onto steel corrosion products and CSNF waste form degradation rind were analyzed using Microsoft Excel 2003 in developing the in-package diffusion submodel, as described in Sections 6.3.4.3 and 6.3.4.6, respectively. Sample calculations using this submodel were carried out using Microsoft Excel 2003 and are described in Section 6.5.2.2. Validation of the in-package diffusion submodel (Section 7.2.1) involved additional analyses of water vapor adsorption using Microsoft Excel 2003. All of the analyses mentioned in this section used standard functions and capabilities of Microsoft Excel 2003.

3.2 GOLDSIM

GoldSim V. 8.02.500 (STN: 10344-8.02-05 [DIRS 174650]) and V. 9.60.100 (STN 10344-9.60-01 [DIRS 181903]) are run on Microsoft Windows 2000 on a Dell workstation with Intel Xeon processor and were developed to perform dynamic, probabilistic simulations. GoldSim V8.02.500 and V. 9.60.100 were used in accordance with IT-PRO-0011, *Software Management*. The Latin Hypercube Sampling capability of GoldSim V. 8.02.500 was used to generate sampling inputs for performing surface complexation calculations (Section 6.5.2.4). GoldSim V. 8.02.500 calculations were also run to verify an alternative conceptual model implementation in Section 6.6.3.4. GoldSim V. 9.60.100 calculations were done in support of validation of models developed in the RTA (see Sections 7.3.1) and to obtain finite difference solutions for radial diffusion for comparison with an analytical solution in Appendix L. This software was obtained from Configuration Management. The use of this software was consistent with the intended use and within the range of validation of the software. The range of validation is defined by the documented functionality (i.e., requirements) and the range of acceptable input. The requirements for these two versions of GoldSim are located in the *Requirements Document for: GoldSim V8.02, Rev. No. 00*, (DOE 2004 [DIRS 169875]) and *Requirements Document for: GoldSim V9.60* (DOE 2007 [DIRS 181106]). The range of

acceptable inputs is element-specific. The rules for the use of each type of element are discussed in *User's Guide, GoldSim Probabilistic Simulation Environment* (GoldSim Technology Group 2003 [DIRS 166226] and GoldSim Technology Group 2007 [DIRS 181727]).

3.3 PHREEQC

PHREEQC V. 2.11 (STN: 10068-2.11-00 [DIRS 175698]), a code for geochemical speciation, reaction path modeling, reactive transport, and surface-complexation modeling, was used to perform the competitive sorption calculations using single-site surface complexation reactions. PHREEQC was run on Microsoft Windows 2000 on a Dell Precision 670 PC with an Intel Xeon processor. PHREEQC was used in accordance with IT-PRO-0011, *Software Management*. The use of this software was consistent with the intended use and within the range of validation of the software. The range of validation is defined by the documented functionality (i.e., requirements) and the range of acceptable input, as described in the *User Manual (UM) for PHREEQC Version 2.3* (BSC 2001 [DIRS 154877]) and the *User's Guide to PHREEQC (Version 2)* (Parkhurst and Appelo 1999 [DIRS 159511]).

3.4 GRAB IT!TM DIGITIZING SOFTWARE

Grab It!TM Digitizing Software is Excel-based commercial off-the-shelf software from Datatrend Software that enables bitmap images of plots that have been captured from journal articles to be converted into (x, y) data in an Excel file for further processing. The software was used in Sections 6.3.4.3, 6.3.4.6, and 7.2.1 to convert the data in plots of adsorption isotherms into numerical values that are subsequently converted into analytical formulas with associated uncertainty. The results are verified by visual inspection; the captured direct input data are presented in Section 4.1, and the original plots are shown in Sections 6 and 7 where the data are used.

3.5 S-PLUS

S-PLUS V. 6.0 is commercial off-the-shelf support software used in conjunction with standard desktop software such as Excel. As defined in IT-PRO-0011 Rev. 3, *Software Management*, the usage is Level 2, and the software does not need to be qualified. S-PLUS was used for data analysis, statistical analysis, and graphics in the development of the competitive radionuclide sorption model.

3.6 JMP

JMP V. 5.1 is commercial off-the-shelf support statistical and data analysis software. The standard sorting and table-joining functions in JMP V. 5.1 were used to extract and sort data from UZ flow field calculations for use in the EBS-UZ interface model, described in Section 6.5.2.6 (output DTN: SN0703PAEBSRTA.001, file *Repository Values for Saturation and Flux.doc*).

4. INPUTS

4.1 DIRECT INPUT

4.1.1 Qualified Project Data and Parameters

Inputs in this section are used as direct input data for the models and analyses presented in Section 6. In order to provide complete transparency and traceability, data in this section are presented as found in the source documents; unit conversions and manipulation of data are not done in this section, but are performed as needed in Section 6. Data uncertainty is addressed in Section 6.

Tables in this section summarize qualified project data used in the RTA. These data are thus justified and appropriate for use in the RTA.

The rates of corrosion of carbon steel and stainless steel in Table 4.1-1 are taken from compilations of data in DTN: MO0409SPAACRWP.000 [DIRS 172059]; the particular data selected were obtained under conditions (e.g., freshwater, as opposed to saltwater) that are considered most likely to resemble those expected inside breached waste packages. Thus, these data are justified and appropriate for use in the RTA to estimate the mass of steel corrosion products in breached waste packages.

The breached drip shield experiments, carried out at the DOE North Las Vegas, Nevada, Atlas test facility, used a full-size mockup of a drip shield and were designed specifically to provide data for the RTA flux splitting submodels. These qualified project data, which are summarized in Tables 4.1-2 through 4.1-6 and Figure 4.1-1, are justified and appropriate for use in the RTA. The breached drip shield experimental test data are analyzed in Section 6.5.1, resulting in uncertain model input parameters.

Table 4.1-1. Input Data for RTA

Model Input	Value		Source
Rate of corrosion of A 516 carbon steels in simulated dilute well J-13 water at 60°C (4536 hr [0.52 yr] and 8670 hr [1.00 yr]) and 90°C (4632 hr [0.53 yr] and 8832 hr [1.01 yr])	Rate ($\mu\text{m yr}^{-1}$)	Temperature and Duration	DTN: MO0409SPAACRWP.000 [DIRS 172059], spreadsheet <i>aqueous-A516.xls</i> , worksheet "Freshwater," column D, rows 5 through 55
	101.01 108.43 105.33 88.15 101.95 117.92 87.80 88.29 78.71 112.46 103.18 99.73	60°C (4536 hr [0.52 yr])	
	80.00 66.75 77.31 69.84 83.74 79.29 71.25 65.77 70.00 72.64 72.89 106.93	60°C (8760 hr [1.00 yr])	
	89.41 68.90 84.02 87.65 107.46 130.02 76.96 70.45 74.29 58.08 66.27	90°C (4632 hr [0.53 yr])	
	43.65 45.19 48.30 55.97 63.58 50.17 42.42 45.91 29.53 65.04 65.73 88.68	90°C (8832 hr [1.01 yr])	

Table 4.1-1. Input Data for RTA (Continued)

Model Input	Value		Source
Rate of corrosion of 316L stainless steel in fresh water at 50°C–100°C	Rate ($\mu\text{m yr}^{-1}$)	Temperature	DTN: MO0409SPAACRWP.000 [DIRS 172059], spreadsheet <i>aqueous-316L.xls</i> , worksheet "freshwater," columns C through G, rows 59 through 64
	0.2286 0.1016 0.154	50°C	
	0.254 0.2286	70°C	
	0.2794 0.254 0.109	80°C	
	0.1524 0.254	90°C	
	0.1778 0.2032 0.037 0.51 0.51 0.51	100°C	
Mean colloid particle diameter generated from CSNF corrosion	300 nm		DTN: LL991109751021.094 [DIRS 142910], Scientific Notebook 1644, p. 34; figure on p. 34 is corrected in DTN: LL000905312241.018 [DIRS 152621], Scientific Notebook 1644, p. 74
Average (and standard deviation in units of nm) colloid particle diameter generated from HLW glass corrosion in tests of 14 days to 280 days duration	Test Length (days) <u>Avg. (Std Dev)</u> 14 116.9 nm (88.8) 30 155.5 nm (97.9) 70 118.0 nm (64.6) 140 118.8 nm (72.9) 280 1201.4 nm (1050.2)		DTN: LL991109751021.094 [DIRS 142910], RPC Pkg. ID MOY-000121-19-01, MOL.20000124.0207, p. 32
Density of HLW glass	2700 kg m ⁻³		DTN: MO0502ANLGAMR1.016 ECN1 [DIRS 172830], Table 8-1
Porosity of HLW glass alteration layer	0.17 (fraction)		DTN: MO0502ANLGAMR1.016 ECN1 [DIRS 172830], Table 8-1
Size of patches in Breached Drip Shield Experiments drip shield mock-up	0.27 m × 0.27 m		Howard 2002 [DIRS 161516], p. 13
Unsaturated zone fracture residual saturation	0.01 (fraction)		DTN: LB0207REVUZPRP.001 [DIRS 159526], file <i>faultprops_2002.xls</i> , worksheet "summary," Model Layer <i>tswf</i>
Unsaturated zone fracture interface area	9.68 m ² m ⁻³		DTN: LB0205REVUZPRP.001 [DIRS 159525], spreadsheet <i>FRACTURE_PROPERTY.xls</i> , worksheet "Table 1. Fracture Properties," row 20, column R
Unsaturated zone dry matrix density for TSw35 (stratigraphic unit Tptpl)	1,980 kg m ⁻³		DTN: SN0404T0503102.011 [DIRS 169129], file <i>ReadMe.doc</i> , Table 7-10

Table 4.1-1. Input Data for RTA (Continued)

Model Input	Value	Source
Invert moisture potential as a function of intergranular hydraulic conductivity	Lookup table: Hydraulic Conductivity (cm s^{-1}) Moisture Potential (bar) 1.54×10^{-17} 20. 1.22×10^{-16} 10. 9.63×10^{-16} 5.0 1.48×10^{-14} 2.0 1.18×10^{-13} 1.0 9.31×10^{-13} 0.50 1.43×10^{-11} 0.20 1.14×10^{-10} 0.01 8.97×10^{-10} 0.05 1.37×10^{-8} 0.02 1.07×10^{-7} 0.01 8.14×10^{-7} 0.005 1.07×10^{-5} 0.002 6.20×10^{-5} 0.001 2.65×10^{-4} 0.0005 1.00×10^{-3} 0.0002 1.88×10^{-3} 0.0001 2.83×10^{-3} 0.00005 3.98×10^{-3} 0.00002 4.71×10^{-3} 0.00001	MO0703PAHYTHRM.000 [DIRS 182093], file <i>Unsaturated Hydraulic Conductivity as a Function of Moisture Potential Rev01.xmcd</i>
Van Genuchten capillary pressure function parameter α for invert	1780.59 bar^{-1}	MO0703PAHYTHRM.000 [DIRS 182093], file <i>Van Genuchten Properties.xls</i> , worksheet "Summary Van Genuchten", Table 6-1
Van Genuchten capillary pressure function parameter n for invert	1.39 (dimensionless)	MO0703PAHYTHRM.000 [DIRS 182093], file <i>Van Genuchten Properties.xls</i> , worksheet "Summary Van Genuchten", Table 6-1
Van Genuchten capillary pressure function parameter m for invert	0.283 (dimensionless)	MO0703PAHYTHRM.000 [DIRS 182093], file <i>Van Genuchten Properties.xls</i> , worksheet "Summary Van Genuchten", Table 6-1
Intragranular porosity of crushed tuff invert ballast	0.111 m^3 pore vol. m^{-3} bulk vol.	MO0703PAHYTHRM.000 [DIRS 182093] Mathcad file: <i>Porosity Calculations.xmcd</i>
Intergranular porosity of crushed tuff invert ballast	0.224 m^3 pore vol. m^{-3} bulk vol.	MO0703PAHYTHRM.000 [DIRS 182093], file <i>arya_original_data interpretation 4.xls</i> , worksheet "LTBM-2, Average, revised"
Invert residual water content	0.0336 m^3 water vol. m^{-3} pore vol.	MO0703PAHYTHRM.000 [DIRS 182093], file <i>Van Genuchten Properties.xls</i> , worksheet "Summary Van Genuchten", Table 6-1
Invert bulk density	115 lb ft^{-3}	MO0703PAHYTHRM.000 [DIRS 182093], file <i>arya_original_data interpretation 4.xls</i> , worksheet "LTBM-2, Average, revised"

Table 4.1-1. Input Data for RTA (Continued)

Model Input	Value	Source
Yield strength of Alloy 22 (room temperature)	403 MPa	MO0702PASTRESS.002 [DIRS 180514], file <i>Model Output DTN.doc</i> , Table 8-1
Yield strength of Titanium Grade 7 (room temperature)	276 MPa	MO0702PASTRESS.002 [DIRS 180514], file <i>Model Output DTN.doc</i> , Table 8-1
Modulus of elasticity (Young's Modulus) of Alloy 22 (room temperature)	206 GPa	MO0702PASTRESS.002 [DIRS 180514], file <i>Model Output DTN.doc</i> , Table 8-1
Modulus of elasticity (Young's Modulus) of Titanium Grade 7 (at 21°C)	107 GPa	MO0702PASTRESS.002 [DIRS 180514], file <i>Model Output DTN.doc</i> , Table 8-1

Table 4.1-2. Atlas Breached Drip Shield Experiments on Smooth Drip Shield Surface – Dripping on Crown – Flow into Breaches

Drip Location	Water Input Mass (g)		Breach Where Water Was Collected	Water Collection Mass (g)	
	Tare	Final		Initial	Final
Single Patch Q(film) Tests (DTN: MO0207EBSATBWP.023 [DIRS 163402])					
8 cm right of Patch 4 centerline	-50.32	-228.52	B4	107.60	129.62
Patch 5 centerline	-12.66	-176.40	B5	109.40	130.52
4 cm left of Patch 5 centerline	-210.48	-344.27	B5	109.18	118.28
Patch 4 centerline	52.77	-135.86	B4	107.57	129.82
Multiple Patch Tests (DTN: MO0207EBSATBWP.024 [DIRS 163401])					
27 cm right of drip shield center	-0.51	-276.65	B5	109.10	113.59
27 cm left of drip shield center	710.10	433.27	B4	107.77	110.40
81 cm left of drip shield center	755.52	529.3	B4	107.18	110.63
81 cm right of drip shield center	768.79	547.67	B5	107.99	111.53
Bounding Flow Rate Tests (DTN: MO0207EBSATBWP.025 [DIRS 163403])					
54 cm left of drip shield center	853.83	516.11	B4	107.35	153.76
54 cm left of drip shield center	769.21	680.32	B4	107.73	115.61
27 cm left of drip shield center	857.57	524.88	B4	107.22	110.57
27 cm left of drip shield center	872.20	771.25	B4	107.00	107.65
27 cm right of drip shield center	907.84	529.11	B5	109.81	112.26
27 cm right of drip shield center ^a	782.29	644.57	B5	109.55	114.00

^a Drip location shown incorrectly as 7 cm in DTN: MO0207EBSATBWP.025 [DIRS 163403]; correct value of 27 cm obtained from Howard 2002 [DIRS 161522], p. 33.

Table 4.1-3. Atlas Breached Drip Shield Experiments on Smooth Drip Shield Surface – Dripping on Crown – Rivulet Spread Data – 33° from Crown

Drip Location	Left (cm)	Right (cm)	Relevant Patch ^b
Single Patch Q(film) Tests (DTN: MO0207EBSATBWP.023 [DIRS 163402])			
8 cm right of Patch 4 centerline	15.0	28.5	4
Patch 5 centerline	28.0	0	5
4 cm left of Patch 5 centerline	Not recorded	21	5
Patch 4 centerline	11.0	26.5	4
Multiple Patch Tests (DTN: MO0207EBSATBWP.024 [DIRS 163401])			
27 cm right of drip shield center	13.0	29.0	5
27 cm left of drip shield center	21.0	21.5	4
81 cm left of drip shield center	17.0	23.5	4
81 cm right of drip shield center	20.0	18.0	5
Bounding Flow Rate Tests (DTN: MO0207EBSATBWP.025 [DIRS 163403])			
54 cm left of drip shield center (High Flow Rate)	22.0	32.0	4
54 cm left of drip shield center (Low Flow Rate)	10.5	30.0	4
27 cm left of drip shield center (High Flow Rate)	24	19	4
27 cm left of drip shield center (Low Flow Rate)	10.0	8.0	4
27 cm right of drip shield center (High Flow Rate)	24.0	16.5	5
27 cm right of drip shield center (Low Flow Rate) ^a	20.0	13.5	5

^a Drip location shown incorrectly as 7 cm in DTN: MO0207EBSATBWP.025 [DIRS 163403]; correct value of 27 cm obtained from Howard 2002 [DIRS 161522], p. 33.

^b Refers to patch number shown in Figure 4.1-1.

Table 4.1-4. Atlas Breached Drip Shield Experiments on Smooth Drip Shield Surface – Dripping on Crown – Splash Radius Tests

No. Drips	Splash Radius (cm)		Comments ^a
	Left	Right	
Splash Radius Test #1 (DTN: MO0207EBSATBWP.022 [DIRS 163400])			
1	1.6	1.6	Measured at outer fringe
2	26.5	18.4	Measured outer fringe
5	37.5	18.4	Measured outer fringe
13	37.5	27.8	Measured outer fringe
21	37.5	31.5	Measured outer fringe
27	52.8	35.0	Measured outer fringe
38	59.9	54.2	Measured outer fringe
49	25.0	29.0	Measured inner cluster
49	72.0	63.2	Measured outer fringe
60	40.0	40.0	Measured inner cluster
60	72.5	54.2	Measured outer fringe
90	48.0	43.0	Measured inner cluster
Single Patch Q(film) Tests (DTN: MO0207EBSATBWP.023 [DIRS 163402])			
—	—	54.5	Patch 5, center, crown
—	—	82	Patch 4, center, crown
—	—	86	Patch 4, 8 cm right of center, crown

NOTE: “—” indicates that no measurements were made.

^a See Section 6.5.1.1.2 for explanation of terms “outer fringe” and “inner cluster.”

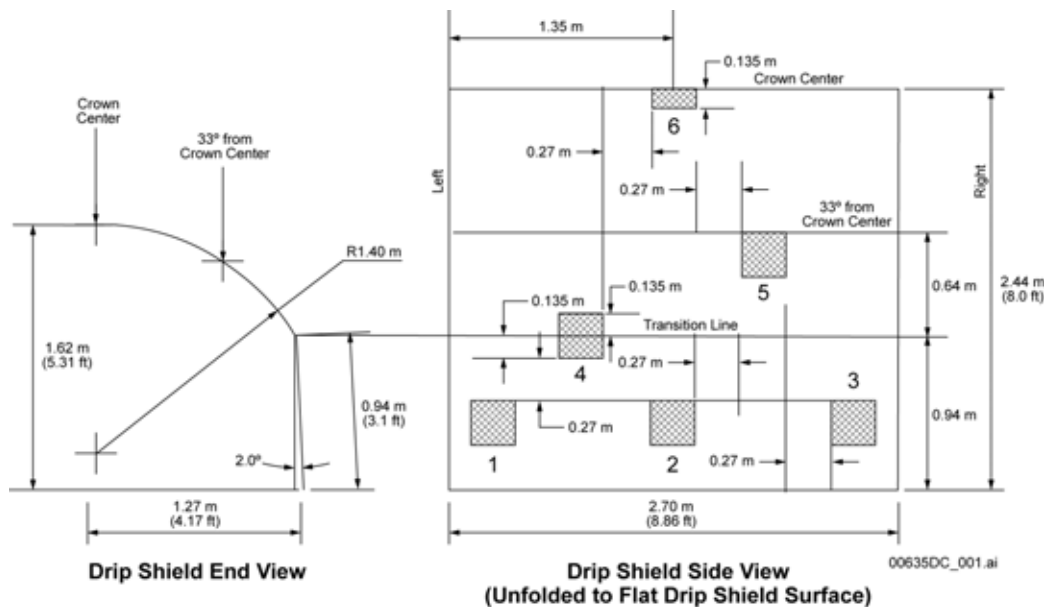
Table 4.1-5. Atlas Breached Drip Shield Experiments on Smooth Drip Shield Surface – Dripping at Off-Crown Locations – Flow into Breaches

Drip Location	Water Input Mass (g)		Breach Where Water Was Collected	Water Collection Mass (g)	
	Tare	Final		Initial	Final
Single Patch Q(splash) Tests (DTN: MO0207EBSATBWP.023 [DIRS 163402])					
Patch 5, 17.5 cm left of center, 33°	529.45	439.68	B5	108.57	108.86
Patch 4, center, 33°	685.41	548.20	B4	106.86	216.70
Patch 4, 17.5 cm right of center, 33°	670.30	538.88	B4	106.75	115.71
Patch 4, 17.5 cm right of center, 16.5°	667.12	516.36	B4	106.80	108.59
Patch 4, centerline, 16.5°	669.72	529.82	B4	106.98	191.33
Patch 5, 17.5 cm left of center, 16.5°	661.50	474.00	B5	109.13	111.79
Patch 6, 35.5 cm left of center, 16.5°	661.82	519.54	B4	107.31	108.90
Patch 5, centerline, 16.5°	676.13	551.39	B5	108.60	199.16
Patch 6, 36.5 cm left of center, between crown and 16.5°	660.40	531.13	B4	107.06	113.69
Single Patch Q(film) Tests (DTN: MO0207EBSATBWP.023 [DIRS 163402])					
Patch 4, 8 cm right of center, 16.5°	-0.90	-173.28	B4	107.16	199.69
Patch 2, 15 cm right of center, 16.5°	36.10	-141.12	B5	109.40	109.79
Patch 5, 4 cm left of center, 16.5°	-37.20	-210.37	B5	117.40	301.94
Patch 4, 8 cm right of center, 33°	53.74	-83.70	B4	114.89	222.27
Bounding Flow Rate Tests (DTN: MO0207EBSATBWP.025 [DIRS 163403])					
54 cm left of drip shield center, 16.5°	850.06	496.63	B4	107.44	277.21
54 cm left of drip shield center, 16.5°	822.71	715.70	B4	107.71	192.26
27 cm left of drip shield center, 16.5°	768.00	646.24	B5	109.21	109.79
27 cm left of drip shield center, 16.5°	868.59	498.18	B4	107.27	110.65
27 cm right of drip shield center, 16.5°	862.08	522.34	B5	109.33	113.57
27 cm right of drip shield center, 16.5°	808.93	713.52	B5	109.30	110.41
27 cm left of drip shield center, 33°	907.89	540.78	B4	107.17	108.13
27 cm right of drip shield center, 33°	835.68	518.08	B5	109.94	113.52
54 cm left of drip shield center, 33°	890.39	561.54	B4	107.28	294.13
54 cm left of drip shield center, 33°	685.39	584.26	B4	107.32	190.42
27 cm left of drip shield center, 33°	-1.99	-98.20	B4	109.88	111.06
27 cm right of drip shield center, 33°	-121.69	-217.44	B5	110.83	110.96

Table 4.1-6. Atlas Breached Drip Shield Experiments on Smooth Drip Shield Surface – Dripping off Crown – Rivulet Spread Data – 33° from Crown and at Transition

Drip Location	At 33°		At Transition	
	Right (cm)	Left (cm)	Right (cm)	Left (cm)
Q(film) Single Patch Tests (DTN: MO0207EBSATBWP.023 [DIRS 163402])				
Patch 4, 8 cm right of patch center, 16.5°	5.5	3.5	13.5	NA
Patch 2, patch center, 16.5°	7.5	4.5	19.5	22.0
Patch 2, 15 cm right of patch center, 16.5°	11.5	9.0	18.0	15.0
Patch 5, 4 cm left of patch center, 16.5°	8.5	8.5	NA	NA
Bounding Flow Rate Tests (DTN: MO0207EBSATBWP.025 [DIRS 163403])				
54 cm left of drip shield center, 16.5°	31.0	46.0	35.0	46.0
54 cm left of drip shield center, 16.5°	8.5	10.0	19.0	27.0
27 cm left of drip shield center, 16.5°	6.0	8.0	17.0	16.0
27 cm left of drip shield center, 16.5°	18.0	24.0	22.0	19.0
27 cm right of drip shield center, 16.5°	13.0	27.0	14.0	23.0
27 cm right of drip shield center, 16.5°	12.0	17.0	16.0	19.0
27 cm left of drip shield center, 33°	NA	NA	11.0	17.0
27 cm right of drip shield center, 33°	NA	NA	15.0	17.0
54 cm left of drip shield center, 33°	NA	NA	17.0	17.0
27 cm left of drip shield center, 33°	NA	NA	9.0	9.5
27 cm right of drip shield center, 33°	NA	NA	8.5	10.0

NOTE: NA indicates that rivulet spread measurements at drop location are not applicable to this analysis.



Source: Howard 2002 [DIRS 161516], p. 14.

NOTE: Figure modified from reference by labeling patches (1 through 6), adding labels for left and right (side view), and labeling crown center and transition lines (side view).

Figure 4.1-1. Dimensions of Drip Shield Mock-Up Used in Breached Drip Shield Experiments on Smooth Drip Shield Surface

Table 4.1-7 gives the species dependent free water diffusion coefficients for 15 radioelements of interest.

Table 4.1-7. Species-Dependent Free Water Diffusion Coefficients at 25°C

Radioelement	Diffusion Coefficient ($\text{m}^2 \text{s}^{-1}$)
Am	9.49×10^{-10}
C	1.18×10^{-9}
Cl	2.03×10^{-9}
Cs	2.06×10^{-9}
I	2.05×10^{-9}
Np	6.18×10^{-10}
Pa	6.04×10^{-10}
Pu	1.30×10^{-9}
Ra	8.89×10^{-10}
Se	1.04×10^{-9}
Sn	1.55×10^{-9}
Sr	7.91×10^{-10}
Tc	1.95×10^{-9}
Th	5.97×10^{-10}
U	6.64×10^{-10}

DTN: LB0702PAUZMTDF.001 [DIRS 180776], file *Readme.pdf*,
Table 2-8.

The J-13 water (DTN: MO0006J13WTRCM.000 [DIRS 151029]) was used in the PHREEQC simulations as the water in which the actinide solubility controlling phases dissolved to their specified saturation indices. The use of the J-13 composition (Table 4.1-8) is justified to maintain consistency with *Dissolved Concentration Limits of Radioactive Elements* (SNL 2007 [DIRS 177418]).

Table 4.1-8. J-13 Water Composition Used in PHREEQC Simulations

Constituent	Concentration (mg L^{-1})
Na^+	45.8
K^+	5.04
Ca^{2+}	13.
Mg^{2+}	2.01
Si	28.5
Cl^-	7.14
F^-	2.18
NO_3^-	8.78
SO_4^{--}	18.4
Alkalinity (HCO_3^-)	128.9
pH	7.41

DTN: MO0006J13WTRCM.000 [DIRS151029]

Database *phreeqcDATA025bdotCr3az.dat* (DTN: MO0609SPAINOUT.002 [DIRS 179645]) was the thermodynamic database used in the PHREEQC modeling. As stated in *phreeqcDATA025bdotCr3az.dat*:

This database is intended to match the R4 version of the EQ3/6 database data0.cr3 at 25[°]C. Corrections are made to log K values as listed in Table 6-37 of ANL-WIS-GS-000003 REV 00. Cr(VI), Cr(II), and Cr(V) reactions are commented out to allow only the Cr(III) oxidation state. Also, commented out are Cr(III) species Cr2(OH)2+4 and Cr3(OH)4+5. As in data0.cr3, eskolaite is defined in terms of Cr+3 and is given a log K of 8.52. Cr(OH)3(am) is added as in data0.cr3 with a log K of 9.35. These two log K values are originally from Ball and Nordstrom (1998, p. 910 [DIRS 163015]).

The above modifications allow the reaction path calculations to more closely predict the phases actually seen when Cr-containing steels corrode. Additional effort would be needed to model the formation of Cr-containing solid solutions that are observed in corrosion testing. Here they are modeled simply as physical mixtures of Fe(III) and Cr(III) oxyhydroxides. The database cites *Qualification of Thermodynamic Data for Geochemical Modeling of Mineral-Water Interactions in Dilute Systems* (SNL 2007 [DIRS 177409], Table 6-37). This is the most up-to-date thermochemical database available for PHREEQC; as such, its use in these calculations is justified.

Unsaturated zone fracture and matrix saturations and percolation fluxes for both glacial transition and post-10,000-year periods were extracted from UZ flow calculations reported in the DTNs listed in Table 4.1-9. Summaries of these data are used in the EBS-UZ interface model, described in Section 6.5.2.6 (output DTN: SN0703PAEBSRTA.001, file *Repository Values for Saturation and Flux.doc*).

Table 4.1-9. Sources of UZ Flow Field Data

Flow Field Data Used	Source DTN
UZ Grid	LB06123DPDUZFF.001 [DIRS 178587], mesh_la.2k1
Glacial Transition, 10th percentile flow field	LB07013DGTUZZFF.001 [DIRS 179066], gt_10.out
Glacial Transition, 30th percentile flow field	LB07013DGTUZZFF.001 [DIRS 179066], gt_30.out
Glacial Transition, 50th percentile flow field	LB07013DGTUZZFF.001 [DIRS 179066], gt_50.out
Glacial Transition, 90th percentile flow field	LB07013DGTUZZFF.001 [DIRS 179066], gt_90.out
Post-10K, 10th percentile flow field	LB0702UZP10KFF.002 [DIRS 179324], pk_10.out
Post-10K, 30th percentile flow field	LB0702UZP10KFF.002 [DIRS 179324], pk_30.out
Post-10K, 50th percentile flow field	LB0702UZP10KFF.002 [DIRS 179324], pk_50.out
Post-10K, 90th percentile flow field	LB0702UZP10KFF.002 [DIRS 179324], pk_90.out
Repository cells	LA0701PANS02BR.003 [DIRS 180497]
Percolation bin and repository column crosswalk	LA0701PANS02BR.003 [DIRS 180497]

4.1.2 Parameters and Other Technical Information

Parameters in Tables 4.1-10 through 4.1-17 are used as inputs for the analyses in Section 6. Uncertainty in parameters is discussed in Section 6.

Parameters in Table 4.1-10 are from various editions of the *CRC Handbook of Chemistry and Physics* (Weast 1985 [DIRS 111561]; Lide 2002 [DIRS 160832]); handbooks are established fact and are therefore justified for use in this report. Input parameters in Table 4.1-11 are from various outside sources, such as journals and textbooks. A description of each parameter is given following Table 4.1-11, together with the justification for its use. These inputs thus are considered qualified for their intended use within this report.

Table 4.1-10. Parameters for RTA (Established Fact)

Model Input	Value	Source
Avogadro's number, N_A	$6.0221419947 \times 10^{23} \text{ mol}^{-1}$	Lide 2002 [DIRS 160832], p. 1-7
Universal gas constant, R	$8.314472 \text{ J mol}^{-1} \text{ K}^{-1}$	Lide 2000 [DIRS 162229], p. 1-8
Boltzmann constant	$1.3806503 \times 10^{-23} \text{ J K}^{-1}$	Lide 2000 [DIRS 162229], p. 1-8
Water density at 25°C	$997.0449 \text{ kg m}^{-3}$	Weast 1985 [DIRS 111561], p. F-5
Water viscosity at 25°C	0.890 mPa-s	Lide 2000 [DIRS 162229], p. 6-180
Density of hematite ($\alpha\text{-Fe}_2\text{O}_3$)	5240 kg m^{-3}	Weast 1985 [DIRS 111561], p. B-104
Density of goethite (FeOOH)	4.26 g cm^{-3}	Lide 2000 [DIRS 162229], p. 4-66
Density of Cr_2O_3	5.22 g cm^{-3}	Lide 2000 [DIRS 162229], p. 4-54
Density of NiO	6.72 g cm^{-3}	Lide 2000 [DIRS 162229], p. 4-75
Density of UO_2	10.97 g cm^{-3}	Lide 2000 [DIRS 162229], p. 4-96
Density of PuO_2	11.5 g cm^{-3}	Lide 2000 [DIRS 162229], p. 4-79
Density of CeO_2	7.65 g cm^{-3}	Lide 2000 [DIRS 162229], p. 4-52
Density of ThO_2	10.0 g cm^{-3}	Lide 2000 [DIRS 162229], p. 4-93
Density of ZrO_2	5.68 g cm^{-3}	Lide 2000 [DIRS 162229], p. 4-100
Molecular weight of water (H_2O)	$0.01801528 \text{ kg mol}^{-1}$	Lide 2002 [DIRS 160832], p. 6-4
Molecular weight of hematite (Fe_2O_3)	$0.15969 \text{ kg mol}^{-1}$	Weast 1985 [DIRS 111561], p. B-104
Molecular weight of goethite (FeOOH)	$0.088852 \text{ kg mol}^{-1}$	Lide 2000 [DIRS 162229], p. 4-66
Molecular weight of NiO	$0.074692 \text{ kg mol}^{-1}$	Lide 2000 [DIRS 162229], p. 4-75
Molecular weight of Cr_2O_3	$0.151990 \text{ kg mol}^{-1}$	Lide 2000 [DIRS 162229], p. 4-54
Atomic weight of iron (Fe)	$0.055847 \text{ kg mol}^{-1}$	Weast 1985 [DIRS 111561], p. B-102
Atomic weight of chromium (Cr)	$0.051996 \text{ kg mol}^{-1}$	Weast 1985 [DIRS 111561], p. B-88
Atomic weight of nickel (Ni)	$0.05869 \text{ kg mol}^{-1}$	Weast 1985 [DIRS 111561], p. B-118

Table 4.1-11. Parameters for RTA (Various Sources)

Model Input	Value	Source
Water molecule cross-sectional area, A_w	10.6 Å ²	McCafferty and Zettlemoyer 1970 [DIRS 154382], p. 454
Cementation factor (exponent on porosity in Archie's law)	1.3 (dimensionless)	Bear 1988 [DIRS 101379], p. 116
Saturation exponent in Archie's law	2 (dimensionless)	Bear 1988 [DIRS 101379], p. 116
Density of HFO	3.96 g cm ⁻³	Towe and Bradley 1967 [DIRS 155334], p. 386
Parameter k in FHH water vapor adsorption isotherm for HLW glass	3.2 (dimensionless)	Ebert, Hoburg, and Bates 1991 [DIRS 111028], p. 134, Figure 1b
Parameter s in FHH water vapor adsorption isotherm for HLW glass	1.5 (dimensionless)	Ebert, Hoburg, and Bates 1991 [DIRS 111028], p. 134, Figure 1b
Specific surface area of kaolinite clay	10 – 38 m ² g ⁻¹	Langmuir 1997 [DIRS 100051], Table 10.2

FHH = Frenkel-Halsey-Hill adsorption isotherm equation

Water molecule cross-sectional area—The cross-sectional area of the water molecule is taken from the paper “Entropy of Adsorption and the Mobility of Water Vapor on α -Fe₂O₃” (McCafferty and Zettlemoyer 1970 [DIRS 154382]). The paper was published in *Discussions of the Faraday Society*, a publication started in 1947 and continuing to this day as the *Faraday Discussions* under the sponsorship of the Royal Society of Chemistry. The Royal Society of Chemistry is the largest organization in Europe for advancing the chemical sciences and is supported by a network of 45,000 members worldwide. The McCafferty and Zettlemoyer paper is directly relevant to the Yucca Mountain repository because hematite (Fe₂O₃) is expected to be part of a mixed assemblage of iron oxides that comprise the corrosion products in the waste package.

The value of 10.6 Å² per molecule reported by McCafferty and Zettlemoyer (1970 [DIRS 154382], p. 454) is corroborated by Holmes et al. (1974 [DIRS 154379], p. 368), who also use a value of 10.6 Å² for the cross-sectional area of a water molecule. Jurinak (1964 [DIRS 154381]) assumes a cross-sectional area of 10.8 Å² for a water molecule. Gregg and Sing (1982 [DIRS 153010], p. 188) state that a “close-packed” monolayer of water corresponds to a figure of 10.5 Å² for the cross-sectional area of a water molecule. Harju et al. (2005 [DIRS 178670], p. 122) assume a value of 10.5 Å² for the molecular area of a water molecule. Thus, the value of 10.6 Å² used in the RTA is representative of the range of values used by various researchers.

Cementation factor (exponent on porosity in Archie's law)—The value of 1.3 for the porosity exponent in Archie's law for unconsolidated sand is taken from the book *Dynamics of Fluids in Porous Media* (Bear 1988 [DIRS 101379], p. 116). The value 1.3 is corroborated by the *Handbook of Well Log Analysis for Oil and Gas Formation Evaluation* (Pirson 1963 [DIRS 111477]).

Saturation exponent in Archie's law—The value 2.0 for the saturation exponent in Archie's law for unconsolidated sand is taken from the book *Dynamics of Fluids in Porous Media* (Bear 1988 [DIRS 101379], p. 116). The value 2.0 is corroborated by *Electrical Methods in Geophysical Prospecting*, Volume 10 of *International Series in Electromagnetic Waves* (Keller and Frischknecht 1966 [DIRS 111470]).

Water vapor isotherm for HLW glass—The Frenkel-Halsey-Hill (FHH) adsorption isotherm parameters k and s for HLW glass are provided by Ebert et al. (1991 [DIRS 111028], p. 134, Figure 1b). These data were developed by the project and reported in *Defense HLW Glass Degradation Model* (BSC 2004 [DIRS 169988], Section 6.5.3.1). The use of these data is therefore justified and appropriate in the RTA.

Specific surface area of kaolinite clay—The degradation of HLW glass by water will result in transformation of glass into an alteration layer consisting of fine-grained clays (BSC 2004 [DIRS 169988], p. D-3). The composition of the clay is not specified, although the density of kaolinite, among others, is considered in estimating the density of the alteration layer (BSC 2004 [DIRS 169988], p. D-5). Kaolinite is therefore considered representative of the clay comprising the alteration layer. The source of specific surface area data is the widely used textbook on aqueous geochemistry by Langmuir (1997 [DIRS 100051], Table 10.2), a reputable, extensively published author and environmental chemistry researcher. The data and source are therefore appropriate for use in the RTA.

Sorption site density and specific surface area of goethite and ferrihydrite—The sorption density and specific surface area data for goethite listed in Table 4.1-12 were compiled from many laboratory studies mainly addressing the single metal sorption from aqueous solutions. The data for ferrihydrite (designated as amorphous hydrous ferric oxide [HFO] in this report), Table 4.1-13, were compiled from Dzombak and Morel (1990 [DIRS 105483]). The site densities for many ferric oxyhydroxide solids have been obtained mainly through the evaluation of sorption data using models such as the Surface Complexation Model (SCM) and other similar models. Given the difficulties in obtaining site density data, this parameter is usually constrained by either fitting the experimental sorption data or just using an accepted value for metal sorption models onto certain types of solids. Site density data have been obtained experimentally from acid-base surface titration measurements assuming complete surface saturation of ionic species that sorb to the oxyhydroxide surface (Villalobos et al. 2003 [DIRS 173017]). Other approaches include estimations of surface site densities on the basis of properties of the sorbent at distinct crystal planes (see Hiemstra and Van Riemsdijk 1996 [DIRS 173023]; Pivovarov 1997 [DIRS 173714]) and tritium exchange experiments.

Since most of the estimated site density values in these sources are obtained from single metal sorption and SCM studies, competitive effects are not taken into account. The assessment of competitive sorption in multi-component systems remains a subject of ongoing research and is restricted to a limited number of studies on few metal species. Therefore, it is reasonable to say that the range of largest values obtained from single metal sorption studies is close to upper bound values of the sorptive capacity of the solid. The validity of this argument still needs to be proven due to the specific behavior of some metals, as observed in some competitive sorption experiments. It is generally accepted that tritium exchange experiments yield the largest site densities, but these will not be considered here due to their large deviation from those estimated by SCMs and their scant adoption by researchers in the field. However, it is reasonable to say that the range of site density values based mainly on SCMs captures upper and lower bounds as delineated by their overall correspondence with those obtained from theoretical or crystallographic arguments.

For the purpose of this data qualification, the gathered data on sorption site density and specific surface area in iron oxyhydroxides is qualified on the grounds of prior uses of data and data corroboration (when possible) in accordance with Section 6.2.1(K) of SCI-PRO-006, *Models*. The use of data corroboration is exemplified by comparison of values from a large set of independent studies, thus establishing a valid range of site densities and specific surface areas. Therefore, this provides a valid range of values consistent with those reported for site densities and/or those often adopted in SCMs. The sorption data were obtained through extensive literature searches spanning about 20 years, and all these sorption studies were published in peer-reviewed journals. Most site density values considered were obtained experimentally in either surface titration or metal ion sorption experiments. Theoretically-determined values are based on crystal chemistry arguments. In general, all these approaches generate data that resulted in a well-defined range of values, thus establishing minimum and maximum bounds in the data. Given the overall consistency in the experimental and modeling approaches to evaluate surface site densities, the analytical methodologies used to examine specific surface areas, and the observed range of values, these data demonstrate the properties of interest for their intended use in this report.

The evaluation of Villalobos et al. (2003 [DIRS 173017]) outlines the range of reported site densities for goethite emphasizing the differences observed from various studies, suggesting that these are probably due to the formation of polynuclear species or solid precipitation on the surface, among other factors. Even with all these differences in the observed site densities, the authors advanced qualitative arguments to suggest trends that indicate some relationship between site density and surface area. For the case of goethite, the compilation of values for this parameter indicates that minimum and maximum bounds can be established in good agreement with the range used in the evaluation of experimental data using sorption models such as SCM.

As stated above, site densities can be measured or estimated through fitting in a SCM. Christl and Kretzschmar (1999 [DIRS 173811]) investigated the effect of varying hematite surface site densities on SCM predictions of metal sorption. These authors consider the range of 2.2-16.6 sites nm⁻² for the different model test cases. For acid-based titrations, they pointed out that complete surface saturation is not attained in surface titration experiments. Their modeling results indicate that full surface saturation is attained at low pH only for the case of low surface site density (2.2 sites nm⁻²). Overall, the range of site densities from 2.2-16.6 sites nm⁻² provides excellent model fits to their data for the cases of acid-base surface titration and of single and competitive metal sorption. For each adopted site density value in their model, there are other adjustable parameters corresponding to intrinsic stability constants for surface complexes. Again, this emphasizes the model dependency on these parameters but also outlines the range of surface site density values used for hematite. This range of values closely corresponds to or captures the value adopted for goethite and HFO in this model report. Christl and Kretzschmar (1999 [DIRS 173811]) observed that for competitive sorption between two metal species onto hematite, a surface site density range of 5 – 10 sites nm⁻² provides better fits to the data and conclude that modeling of competitive sorption could provide more helpful information to constrain surface site densities.

For the case of goethite and ferrihydrite/HFO, the same argument applies for the observed valid range of surface site densities for these phases. This is substantiated by the range of values (1 to 8.83 sites nm⁻²) adopted in many studies listed in Table 4.1-12, whether constrained by

model fitting, acid-base titration, or just metal sorption data. This surface site density range for goethite corresponds to that given by Villalobos et al. (2003 [DIRS 173017]), not including measurements based on tritium exchange experiments that yield much larger values.

Tritium exchange measurements yield site densities that are larger than those estimated from acid-base titration or metal sorption data (Sahai and Sverjensky, 1997 [DIRS 173812]). The use of metal sorption and acid-base titration data tends to underestimate site densities due to the inherent specificity of a certain ion to sorb onto particular sites of the sorbent or the inability to ionize all surface sites due to limitations on measurements at extreme pHs (Sahai and Sverjensky 1997 [DIRS 173812]). Tritium exchange is known to be the best method for estimating total site densities since it captures all exchangeable ^3H hydrogens coordinated with oxygens in the solid. Pivovarov (1997 [DIRS 173714]) suggested that tritium exchange data provide information on the total amount of protons on the surface but little information on those participating in the actual sorption process. For this reason, Pivovarov (1997 [DIRS 173714]) advanced a method of estimating site densities based on the crystallographic structure of the sorbent and suggested corrections to site densities derived from tritium exchange data. The result was a decrease (by an order of magnitude) relative to the experimentally determined tritium exchange values. The corrected values also fall within the range obtained from metal sorption data. Data based on this method were not considered, but the largest observed site density of between 15 and 16 sites nm^{-2} by Rustad et al. (1996 [DIRS 173766]) captures this upper limit corresponding to the consistent range of values observed for tritium exchange data.

Overall, the list of goethite site densities provided in Table 4.1-12 encompasses a widely adopted range of values for a broad set of specific surface areas. The observed consistency of these data values from numerous sources within the range adopted in this report and the results of the sensitivity studies by Christl and Kretzschmar (1999 [DIRS 173811], p. 2929) closely corresponding to this range render the data suitable for their intended use in the model.

Site densities for HFO are from Dzombak and Morel (1990 [DIRS 105483]), which has been referenced extensively in many sorption studies of this phase. The authors are recognized experts in the field, and, therefore, their data evaluation and resulting parameters are considered suitable for use in the YMP.

The total site densities for HFO from the evaluation of Dzombak and Morel (1990) are shown in Table 4.1-13. The study by Hofmann et al. (2005 [DIRS 173711], Table 2) obtained a site density of 4.00 sites nm^{-2} based on acid-base titrations and optimized parameters for Sr sorption in their SCM. These data appropriately demonstrate the parameters of interest, which are the result of a comprehensive evaluation of experimental data from multiple sources. The source from Dzombak and Morel (1990 [DIRS 105483]) is widely referenced in the sorption modeling literature and is accepted as a representative example of the application of SCM on HFO. Moreover, the two authors have published extensively on the subject of metal sorption and the use and application of SCM on metal sorption onto metal oxides.

Density of HFO—Eggleton and Fitzpatrick (1988 [DIRS 173878], p. 118) report the density of HFO as ranging from 3.3 g cm^{-3} (for natural samples) to 3.96 g cm^{-3} (for synthetic material, attributed to Towe and Bradley 1967 [DIRS 155334], p. 386). The density of 3.96 g cm^{-3} measured by Towe and Bradley is also cited by Clausen and Fabricius (2000 [DIRS 178655]),

Table 3), Cornell and Schwertmann (2003 [DIRS 173037]), and Hofmann et al. (2004 [DIRS 173783], p. 167). The repeated use of the value of Towe and Bradley in research reported in a variety of refereed journals indicates that it is considered to be a reliable value by a consensus of independent researchers and is therefore suitable for use in this report as the density of HFO.

Specific Surface Area of HFO—Specific surface area data for HFO, listed in Table 4.1-13, were compiled from numerous laboratory studies using a variety of measurement techniques. The specific surface area data were obtained through extensive literature searches covering a period of about 40 years, and all these studies were published in peer reviewed journals. The techniques used, particularly the Brunauer-Emmett Teller (BET) method, are considered to be standard procedures, as evidenced by the large number of studies reported using those techniques, both for HFO (Table 4.1-13) and for goethite (Table 4.1-12), so the data are suitable for their intended use in the model.

Table 4.1-12. Specific Surface Areas and Adsorption Site Densities for Goethite

Site Density	Site Density Units	Specific Surface Area ($\text{m}^2 \text{g}^{-1}$)	Source [†]	Comments
3.28×10^{-6}	mol m^{-2}	55*	Rodda et al. 1996 [DIRS 173710], Table 1 (SD), p. 365 (SSA)	Model fitting (2-site Langmuir adsorption model for Zn at 25°C). Tabulated site density denotes sum of low- and high-affinity sites: $2.90 \times 10^{-6} + 3.75 \times 10^{-7} = 3.28 \times 10^{-6} \text{ mol m}^{-2}$. Site density converted to 1.97 sites nm^{-2} in Table 6.3-4. Specific surface area by BET method.
1.43×10^{-5}	mol m^{-2}	55	Rodda et al. 1996 [DIRS 173710], Table 1 (SD), p. 365 (SSA)	Model fitting (2-site Langmuir adsorption model for Zn at 25°C). Tabulated site density denotes sum of low- and high-affinity sites: $1.30 \times 10^{-5} + 1.26 \times 10^{-6} = 1.43 \times 10^{-5} \text{ mol m}^{-2}$. Site density converted to 8.59 sites nm^{-2} in Table 6.3-4. Specific surface area by BET method.
2.2×10^{-6}	mol m^{-2}	55	Rodda et al. 1996 [DIRS 173710], Table 5 (SD), p. 365 (SSA)	Model fitting (BET adsorption model for Zn at 25°C). Site density converted to 1.32 sites nm^{-2} in Table 6.3-4. Specific surface area by BET method.
6.15	sites nm^{-2}	—	Hiemstra and Van Riemsdijk 1996 [DIRS 173023], p. 498	Total site density obtained from crystal plane structural relations for 021 and 110 goethite faces in corresponding proportions described by Hiemstra and Van Riemsdijk 1996 [DIRS 173023], p. 498. The listed value of 6.15 sites nm^{-2} is the total of low- and high-affinity sites given by the source: $3.45 + 2.7 = 6.15$ sites nm^{-2} .
8.0	sites nm^{-2}	52	Villalobos et al. 2003 [DIRS 173017], Table 2	Calculated from maximum sorption data for Pb^{2+} ; specific surface area from Hayes and Leckie 1987 [DIRS 173817], Table II
4.9	sites nm^{-2}	45*	Villalobos et al. 2003 [DIRS 173017], Table 2	Calculated from maximum sorption data for Pb^{2+}
7.4	sites nm^{-2}	28.5*	Villalobos et al. 2003 [DIRS 173017], Table 2	Calculated from maximum sorption data for F^- (assumed mononuclear complex)
4.6	sites nm^{-2}	32*	Villalobos et al. 2003 [DIRS 173017], Table 2	Calculated from maximum sorption data for F^- (assumed mononuclear complex)
7.2	sites nm^{-2}	30.8*	Villalobos et al. 2003 [DIRS 173017], Table 2	Calculated from maximum sorption data for F^- (assumed mononuclear complex)
3.4	sites nm^{-2}	32*	Villalobos et al. 2003 [DIRS 173017], Table 2	Calculated from maximum sorption data for phosphate (assumed binuclear complex)
4.0	sites nm^{-2}	38*	Villalobos et al. 2003 [DIRS 173017], Table 2	Calculated from maximum sorption data for phosphate (assumed binuclear complex)

Table 4.1-12. Specific Surface Areas and Adsorption Site Densities for Goethite (Continued)

Site Density	Site Density Units	Specific Surface Area ($\text{m}^2 \text{g}^{-1}$)	Source [†]	Comments
6.6	sites nm^{-2}	28.5	Villalobos et al. 2003 [DIRS 173017], Table 2	Calculated from maximum sorption data for phosphate (assumed binuclear)
2.6	sites nm^{-2}	66*	Villalobos et al. 2003 [DIRS 173017], Table 2	Calculated from maximum sorption data for oxalate (assumed binuclear)
2.9	sites nm^{-2}	66	Villalobos et al. 2003 [DIRS 173017], Table 2	Calculated from maximum sorption data for chromate (assumed binuclear complex)
4.2	sites nm^{-2}	105*	Villalobos et al. 2003 [DIRS 173017], Table 2	Calculated from maximum sorption data for F^- (assumed binuclear complex); specific surface area by BET method (Hiemstra and Van Riemsdijk 1996 [DIRS 173023], p. 497)
3.0	sites nm^{-2}	105	Villalobos et al. 2003 [DIRS 173017], Table 2	Calculated from maximum sorption data for phosphate (assumed binuclear complex); specific surface area by BET method (Hiemstra and Van Riemsdijk 1996 [DIRS 173023], p. 498)
2.9	sites nm^{-2}	80*	Villalobos et al. 2003 [DIRS 173017], Table 2	Calculated from maximum sorption data for phosphate (assumed binuclear complex)
2.7	sites nm^{-2}	80	Villalobos et al. 2003 [DIRS 173017], Table 2	Calculated from maximum sorption data for citrate (assumed trinuclear complex)
3.3	sites nm^{-2}	81*	Villalobos et al. 2003 [DIRS 173017], Table 2	Calculated from maximum sorption data for selenite (assumed binuclear complex)
3.3	sites nm^{-2}	81	Villalobos et al. 2003 [DIRS 173017], Table 2	Calculated from maximum sorption data for selenite (assumed binuclear complex)
2.6	sites nm^{-2}	81	Villalobos et al. 2003 [DIRS 173017], Table 2	Calculated from maximum sorption data for molybdate (assumed binuclear complex)
1.79×10^{-4}	mol g^{-1}	55.4*	Trivedi et al. 2001. [DIRS 173021], Table 3	Fe adsorption edges; site density converted to sites nm^{-2} in Table 6.3-4; specific surface area by BET method
4.22×10^{-5}	mol g^{-1}	21*	Trivedi et al. 2001 [DIRS 173021], Table 3	Ni/EDTA adsorption edges; site density converted to sites nm^{-2} in Table 6.3-4; specific surface area by BET method
3.54×10^{-5}	mol g^{-1}	21	Trivedi et al. 2001 [DIRS 173021], Table 3	Pb/EDTA adsorption edges; site density converted to sites nm^{-2} in Table 6.3-4; specific surface area by BET method
-	-	49.6	Trivedi et al. 2001 [DIRS 173021], Table 3	Cd adsorption edges; single-site Langmuir model
-	-	76	Trivedi et al. 2001 [DIRS 173021], Table 3	Cd adsorption edges; single-site Langmuir model; specific surface area by BET method

Table 4.1-12. Specific Surface Areas and Adsorption Site Densities for Goethite (Continued)

Site Density	Site Density Units	Specific Surface Area ($\text{m}^2 \text{g}^{-1}$)	Source [†]	Comments
1.87	sites nm^{-2}	20*	Naveau et al. 2005 [DIRS 173018], p. 6	Acid-base surface titration; specific surface area by BET method
7	sites nm^{-2}	47.5*	Coughlin and Stone 1995 [DIRS 173030], Table 1	Adopted from Hayes and Leckie 1986 [DIRS 173817]; specific surface area by BET method (N_2 gas)
2.3	sites nm^{-2}	50*	Grossl et al. 1997 [DIRS 173032], p. 322	Chromate and arsenate adsorption isotherms; specific surface area by BET method (N_2 gas)
2.3	sites nm^{-2}	54*	Fendorf et al. 1996 [DIRS 173034], p. 100	Assumed value
1.5	sites nm^{-2}	20*	Duc et al. 2003 [DIRS 173019], Table 2, (SD), Table 1 (SSA)	Acid-base surface titration; specific surface area by BET method
1.66	sites nm^{-2}	—	Pivovarov 1997 [DIRS 173714], Table 1	Average of calculated site density at (110) and (120) crystal planes (see Table 1 of the source): $(1.50 + 1.81)/2 = 1.66$; specific surface area by BET method
3.2	$\mu\text{mol m}^{-2}$	70*	Gräfe et al. 2004 [DIRS 173751], p. 6561 (SD), p. 6562 (SSA)	Arsenate isotherm (pH 4); site density converted to 1.93 sites nm^{-2} in Table 6.3-4; specific surface area by BET method (N_2 gas)
2.2	$\mu\text{mol m}^{-2}$	70	Gräfe et al. 2004 [DIRS 173751], p. 6561 (SD), p. 6562 (SSA)	Arsenate isotherm (pH 7); site density converted to 1.32 sites nm^{-2} in Table 6.3-4; specific surface area by BET method (N_2 gas)
2.20	sites nm^{-2}	35*	Missana et al. 2003 [DIRS 173759], p. 296 (SD), Table 3 (SSA)	Acid-base surface titration; specific surface area by BET method
6.3	sites nm^{-2}	—	Lützenkirchen et al. 2002 [DIRS 173757], p. 3394, Table 1	Acid-base surface titration; total site density for each crystal face {001} and {110} for two surface groups that represent a mixture of two crystallographic planes for one singly and one triply coordinated surface complex on goethite: $3.61 + 2.7 = 6.3$ sites nm^{-2}
9.18×10^{-6}	mol m^{-2}	14.7*	Müller and Sigg 1992 [DIRS 173760], p. 519	Acid-base surface titration; site density converted to 5.53 sites nm^{-2} in Table 6.3-4; specific surface area by BET method (N_2 gas)
1.68	sites nm^{-2}	33*	Randall et al. 1999 [DIRS 173709], Table 1	Assumed value adopted from Lövgren et al. 1990 [DIRS 173771]; specific surface area by BET method (N_2 gas)
2.89	sites nm^{-2}	86*	Felmy and Rustad 1998 [DIRS 173708], p. 26 (SD), p. 27 (SSA)	Total site density calculated from crystallographic dimensions assuming 90% for {110} (3.0 sites nm^{-2}) and 10% for {021} (1.86 sites nm^{-2}) planes: $(0.9 \times 3.0) + (0.1 \times 1.86) = 2.89$ sites nm^{-2}

Table 4.1-12. Specific Surface Areas and Adsorption Site Densities for Goethite (Continued)

Site Density	Site Density Units	Specific Surface Area ($\text{m}^2 \text{g}^{-1}$)	Source [†]	Comments
5.2	$\mu\text{mol m}^{-2}$	20*	Hongshao and Stanforth 2001 [DIRS 173754], p. 4754	Assumed value for site density; site density converted to 3.13 sites nm^{-2} in Table 6.3-4; specific surface area by BET method
2.3	sites nm^{-2}	21.4*	Buerge-Weirich et al. 2002 [DIRS 173752], p. 329	Estimated (no specific information given in the source); specific surface area by BET method (N_2 gas)
6.31	sites nm^{-2}	37*	Boily et al. 2001 [DIRS 173707], Table 3	Total site density estimated from crystallographic data at three different crystal planes: $2.7 + 2.7 + 0.91 = 6.31$ sites nm^{-2} ; specific surface area by BET method (N_2 gas)
6.31	sites nm^{-2}	85*	Boily et al. 2001 [DIRS 173707], Table 3	Total site density estimated from crystallographic data at three different crystal planes: $2.7 + 2.7 + 0.91 = 6.31$ sites nm^{-2} ; specific surface area by BET method (N_2 gas)
1.8	sites nm^{-2}	27.7*	Gao and Mucci 2001 [DIRS 173750], p. 2364 (SD), p. 2362 (SSA)	Acid-base surface titration; specific surface area by BET method (N_2 gas)
2.31	sites nm^{-2}	49*	Robertson and Leckie 1997 [DIRS 173763], Table 4 (SD), Table 3 (SSA)	Obtained by fits to potentiometric titration data
7.00	sites nm^{-2}	49	Robertson and Leckie 1997 [DIRS 173763], Table 4 (SD), Table 3 (SSA)	Obtained by fits to potentiometric titration data
8.38	sites nm^{-2}	49	Robertson and Leckie 1997 [DIRS 173763], Table 4 (SD), Table 3 (SSA)	Obtained by fits to potentiometric titration data
8.16	sites nm^{-2}	49	Robertson and Leckie 1997 [DIRS 173763], Table 4 (SD), Table 3 (SSA)	Obtained by fits to potentiometric titration data
1.68	sites nm^{-2}	39.9*	Lövgren et al. 1990 [DIRS 173771], p. 1303 (SD), p. 1301 (SSA)	Acid-base surface titration; specific surface area by BET method
210	$\mu\text{mol g}^{-1}$	81*	Machesky et al. 1991 [DIRS 173758], p. 771 (SD), p. 770 (SSA)	Estimated from maximum sorption data. Value is twice measured loading, because a bidentate surface complex is proposed by the authors. Site density converted to 3.12 sites nm^{-2} in Table 6.3-4; specific surface area by BET method (N_2 gas)
7.00	sites nm^{-2}	52*	Hayes and Leckie 1987 [DIRS 173817], Table II	Pb sorption data; specific surface area by BET method (N_2 gas)

Table 4.1-12. Specific Surface Areas and Adsorption Site Densities for Goethite (Continued)

Site Density	Site Density Units	Specific Surface Area ($\text{m}^2 \text{g}^{-1}$)	Source [†]	Comments
2.3	sites nm^{-2}	45*	van Geen et al. 1994 [DIRS 144702], Table 1	Adopted value is the same as that given by Davis and Kent (1990 [DIRS 143280]) and Dzombak and Morel 1990 [DIRS 105483]; specific surface area by BET method (N_2 gas)
1.7	sites nm^{-2}	43*	Persson et al. 1998 [DIRS 173762], p. 261, Table 1	Acid-base surface titration; specific surface area by BET method (N_2 gas)
5	sites nm^{-2}	110*	Davis and Upadhyaya 1996 [DIRS 173743], p. 1895	Assumed value based on Stumm 1992 [DIRS 141778]
4.84	sites nm^{-2}	64.3*	Xue and Traina 1996 [DIRS 173713], p. 3163 (SD), p. 3161 (SSA)	Calculated value from the smallest average for constant capacitance model (CCM); specific surface area by BET method (N_2 gas)
140	$\mu\text{mol g}^{-1}$	33*	Hansmann and Anderson 1985 [DIRS 173742], p. 547 (SD), p. 546 (SSA)	Maximum theoretical value estimated from crystal morphology; site density converted to 2.55 sites nm^{-2} in Table 6.3-4; specific surface area by BET method (N_2 gas)
80	$\mu\text{mol g}^{-1}$	33	Hansmann and Anderson 1985 [DIRS 173742], p. 547 (SD), p. 546 (SSA)	Estimated from maximum sorption data for selenite; site density converted to 1.46 sites nm^{-2} in Table 6.3-4; specific surface area by BET method (N_2 gas)
0.31	mmol g^{-1}	80.5*	Gabriel et al. 1998 [DIRS 130407], pp. 124, 126 (SD), p. 123 (SSA)	Uranyl adsorption SCM; site density converted to 2.32 sites nm^{-2} in Table 6.3-4; specific surface area by BET method
–	–	40.5	Christophi and Axe 2000 [DIRS 173020], Table 1	Site density not reported

Table 4.1-13. Total Site Densities for HFO

Total Site Density (mol sites/mol Fe)
0.2
0.1
0.2
0.2
0.18
0.23
0.24
0.14
0.2
0.15
0.2
0.5
0.15
0.16
0.05
0.18
0.1
0.13

Source: Dzombak and Morel 1990 [DIRS 105483], Table 5.3.

NOTE: Data compiled from various metal sorption isotherms; specific surface area = $600 \text{ m}^2 \text{ g}^{-1}$. These data were retrieved from metal sorption maxima obtained using various cations and anions under various pHs; see source for details.

Table 4.1-14. Specific Surface Areas for HFO

Specific Surface Area ($\text{m}^2 \text{ g}^{-1}$)	Method	Reference
109.0	BET-N ₂	Cornejo et al. 1984 [DIRS 178660], Table 1, Sample 1
137.0	BET-N ₂	Cornejo et al. 1984 [DIRS 178660], Table 1, Sample 2
235.5	BET-N ₂	Cornejo 1987 [DIRS 178659], Table I, heated at 25°C
218.3	BET-N ₂	Cornejo 1987 [DIRS 178659], Table I, heated at 100°C
246.0	α_s -plot	Cornejo 1987 [DIRS 178659], Table I, heated at 25°C
223.6	α_s -plot	Cornejo 1987 [DIRS 178659], Table I, heated at 100°C
239	BET-N ₂	Schwertmann et al. 2004 [DIRS 178734], Table 1, 16.7 $\mu\text{mol OH min}^{-1}$
276	BET-N ₂	Schwertmann et al. 2004 [DIRS 178734], Table 1, 33.3 $\mu\text{mol OH min}^{-1}$
227	BET-N ₂	Schwertmann et al. 2004 [DIRS 178734], Table 1, 66.7 $\mu\text{mol OH min}^{-1}$
214	BET-N ₂	Schwertmann et al. 2004 [DIRS 178734], Table 1, 333 $\mu\text{mol OH min}^{-1}$
160	BET	Mitov et al. 2002 [DIRS 178686], Table 5
215	BET-N ₂	Clausen and Fabricius 2000 [DIRS 178655], Table 2, 2-line ferrihydrite No. 1
229	BET-N ₂	Clausen and Fabricius 2000 [DIRS 178655], Table 2, 2-line ferrihydrite No. 2

Table 4.1-14. Specific Surface Areas for HFO (Continued)

Specific Surface Area (m ² g ⁻¹)	Method	Reference
193.3	BET-N ₂	O'Reilly and Hochella 2003 [DIRS 178704], Table 1
180	BET-N ₂	Sani et al. 2004 [DIRS 178727], p. 2640
378.6	BET-N ₂	Hofmann et al. 2004 [DIRS 173783], Table 1, 30°C
366.5	t-plot (N ₂ gas)	Hofmann et al. 2004 [DIRS 173783], Table 1, 30°C
320.1	BET-H ₂ O	Hofmann et al. 2004 [DIRS 173783], Table 1, 30°C
373.5	BET-N ₂	Hofmann et al. 2004 [DIRS 173783], Table 1, 50°C
366.4	t-plot (N ₂ gas)	Hofmann et al. 2004 [DIRS 173783], Table 1, 50°C
364.9	BET-N ₂	Hofmann et al. 2004 [DIRS 173783], Table 1, 80°C
352.4	t-plot (N ₂ gas)	Hofmann et al. 2004 [DIRS 173783], Table 1, 80°C
455.4	BET-H ₂ O	Hofmann et al. 2004 [DIRS 173783], Table 1, 80°C
170	BET-N ₂	Sauvé et al. 2000 [DIRS 178732], Table 1
277	BET-N ₂	Weidler 1997 [DIRS 178741], Table 1
266	BET-N ₂	Guzman et al. 1994 [DIRS 178669], Table 1
230	BET-N ₂	Larsen and Postma 2001 [DIRS 178683], Table 2, Sample 2Fer-1
250	BET-N ₂	Larsen and Postma 2001 [DIRS 178683], Table 2, Sample 2Fer-2
205	BET-N ₂	Larsen and Postma 2001 [DIRS 178683], Table 2, Sample 6Fer
277	BET-N ₂	Leone et al. 2001 [DIRS 178684], p. 1317
280	BET-H ₂ O	Leone et al. 2001 [DIRS 178684], p. 1317
182	BET-N ₂	Davis and Leckie 1978 [DIRS 125591], p. 95
300	negative adsorption	Davis and Leckie 1978 [DIRS 125591], p. 95
600	empirical estimate	Davis and Leckie 1978 [DIRS 125591], p. 95
260	BET-N ₂	Liaw et al. 1989 [DIRS 178685], Table 1
159	BET-N ₂	Crosby et al. 1983 [DIRS 178662], Table II, Fe ³⁺ source, 2-h age
234	BET-N ₂	Crosby et al. 1983 [DIRS 178662], Table II, Fe ³⁺ source, 2-day age
141	BET-N ₂	Crosby et al. 1983 [DIRS 178662], Table II, sediment water source, 2-day age
164	BET-N ₂	Crosby et al. 1983 [DIRS 178662], Table II, mine stream sediment source
36.6	BET-N ₂	Axe and Anderson 1995 [DIRS 178654], p. 159
265	BET-Ar	Van der Giessen 1966 [DIRS 178740], Table 1, 20°C, 1 month age
215	BET-Ar	Van der Giessen 1966 [DIRS 178740], Table 1, 20°C, 1 year age
270	BET-Ar	Van der Giessen 1966 [DIRS 178740], Table 1, 90°C, 1 month age
220	BET-Ar	Van der Giessen 1966 [DIRS 178740], Table 1, 90°C, 1 year age
300±50	BET-H ₂ O	Davies-Colley et al. 1984 [DIRS 178666], p. 492
250	TEM	Tipping 1981 [DIRS 178737], Table 1
398	BET-Ar	Carlson and Schwertmann 1981 [DIRS 142788], Table 1, Sample 6VT
425	BET-Ar	Carlson and Schwertmann 1981 [DIRS 142788], Table 1, Sample 6Y
236	BET-Ar	Carlson and Schwertmann 1981 [DIRS 142788], Table 1, Sample 27B
146	BET-Ar	Carlson and Schwertmann 1981 [DIRS 142788], Table 1, Sample 32F
172	BET-Ar	Carlson and Schwertmann 1981 [DIRS 142788], Table 1, Sample 40A

Table 4.1-14. Specific Surface Areas for HFO (Continued)

Specific Surface Area (m ² g ⁻¹)	Method	Reference
149	BET-Ar	Carlson and Schwertmann 1981 [DIRS 142788], Table 1, Sample 8A
274	BET-Ar	Carlson and Schwertmann 1981 [DIRS 142788], Table 1, Sample 5
200	BET-Ar	Carlson and Schwertmann 1981 [DIRS 142788], Table 1, Sample 4
154	BET-Ar	Carlson and Schwertmann 1981 [DIRS 142788], Table 1, Sample 3
68	BET-Ar	Carlson and Schwertmann 1981 [DIRS 142788], Table 1, Sample 2
502	EGME	Carlson and Schwertmann 1981 [DIRS 142788], Table 1, Sample 6VT
560	EGME	Carlson and Schwertmann 1981 [DIRS 142788], Table 1, Sample 6Y
326	EGME	Carlson and Schwertmann 1981 [DIRS 142788], Table 1, Sample 27B
304	EGME	Carlson and Schwertmann 1981 [DIRS 142788], Table 1, Sample 32F
513	EGME	Carlson and Schwertmann 1981 [DIRS 142788], Table 1, Sample 40A
418	EGME	Carlson and Schwertmann 1981 [DIRS 142788], Table 1, Sample 8A
489	EGME	Carlson and Schwertmann 1981 [DIRS 142788], Table 1, Sample 4
221	EGME	Carlson and Schwertmann 1981 [DIRS 142788], Table 1, Sample 3
318	EGME	Carlson and Schwertmann 1981 [DIRS 142788], Table 1, Sample 2
340	BET-N ₂	Eggleton and Fitzpatrick 1988 [DIRS 173878], Table 1, 2-line ferrihydrite
225	BET-N ₂	Eggleton and Fitzpatrick 1988 [DIRS 173878], Table 1, 6-line ferrihydrite
390±25	EGME	Eggleton and Fitzpatrick 1988 [DIRS 173878], Table 1, 2- and 6-line

NOTES: BET = Brunauer, Emmett, and Teller surface area measurement technique using the specified gas; EGME = ethylene glycol-monoethylether method; TEM = transmission electron micrographs; *t*-plot = plot of amount adsorbed vs. average film thickness; slope gives specific surface area; α_s -plot = similar to *t*-plot, providing specific surface area relative to that of a reference material (Gregg and Sing 1982 [DIRS 153010], p. 98).

The elemental composition of metals in a CSNF waste package is given in Table 4.1-15. The composition is used in Section 6.3.4.2.3.1 to calculate the mass of corrosion products in a waste package. The sources for these data are ASTM standard specifications for manufacturing the metals and the American Society for Metals (ASM) properties handbook. ASTM standards and the ASM handbook are established fact and are therefore justified for use in this report. The DTNs listed as sources are qualified project data whose original sources are ASTM standards and the ASM handbook.

Table 4.1-15. Elemental Composition (Weight Percent) and Density of Waste Package Materials

Element	316N Stainless Steel ^a	A 516 Carbon Steel ^b	304B4 Borated Stainless Steel ^c	Aluminum 6061 ^d	304L Stainless Steel ^e
Fe	Balance	Balance	Balance	0.7 (max)	Balance
Mo	2.00 to 3.00	—	—	—	—
Cr	16.00 to 18.00	—	18.00 to 20.00	0.04 to 0.35	18.0 to 20.0
Ni	10.00 to 14.00	—	12.00 to 15.00	—	8.0 to 12.0
Al	—	—	—	Remainder	—
Co	—	—	0.20 (max)	—	—
W	—	—	—	—	—
Mn	2.00 (max)	1.30 (max)	2.00 (max)	0.15 (max)	2.00 (max)
C	0.08 (max)	0.26 (max)	0.08 (max)	—	0.030 (max)
P	0.045 (max)	0.035 (max)	0.045 (max)	—	0.045 (max)
S	0.030 (max)	0.035 (max)	0.030 (max)	—	0.030 (max)
Si	0.75 (max)	0.45	0.75 (max)	0.40 to 0.8	0.75 (max)
N	0.10 to 0.16	—	0.10 (max)	—	0.10
Cu	—	—	—	0.15 to 0.40	—
Mg	—	—	—	0.8 to 1.2	—
Zn	—	—	—	0.25 (max)	—
Ti	—	—	—	0.15 (max)	—
V	—	—	—	—	—
Gd	—	—	—	—	—
B	—	—	1.1 to 1.2 ^g	—	—
Residuals	—	—	—	0.15 (max)	—
Density	7.98 g cm ^{-3f}	7,850 kg m ^{-3b}	7,810 kg m ⁻³	2,700 kg m ^{-3f}	7,940 kg m ⁻³

NOTES: “—” indicates that the alloy chemical composition specification does not include this element. Compositions listed are the maximum specified for each element in the data source. “Balance” and “Remainder” are specified in the data source for the principal component of the alloy.

^a DTN: MO0003RIB00076.000 [DIRS 153044], Column “ASTM, 1998.”

^b ASTM A 516/A 516M-90 1991 [DIRS 117138].

^c Carpenter Technology 2003 [DIRS 179642].

^d ASM 1979 [DIRS 154085], p. 115.

^e ASTM A 240/AA 240M 06c 2006 [DIRS 179346], Table 1, Type 304L

^f ASTM G 1-03 [DIRS 181437], Table X1.1.

^g SNL 2007 [DIRS 179394], Section 4.1.1.5. Density listed is for 1.2% boron (Carpenter Technology 2003 [DIRS 179642]).

Diffusion coefficient data for granular materials are shown in Table 4.1-16. These data are used to develop an effective diffusion coefficient for the invert in Section 6.3.4.1.1. The data are qualified for use in this report in Appendix H.

Table 4.1-16. Diffusion Coefficient for Granular Materials for Volumetric Moisture Content Between 1.5 Percent and 66.3 Percent

Sample	Volumetric Moisture Content (%)	Diffusion Coefficient (cm ² s ⁻¹)
1	1.50	1.39 × 10 ⁻⁸
2	1.70	6.60 × 10 ⁻⁹
3	1.90	8.60 × 10 ⁻⁹
4	2.17	2.77 × 10 ⁻⁸
5	2.20	3.63 × 10 ⁻⁸
6	2.29	1.09 × 10 ⁻⁸
7	2.50	2.50 × 10 ⁻⁸
8	3.10	3.30 × 10 ⁻⁸
9	3.14	3.06 × 10 ⁻⁸
10	3.20	1.35 × 10 ⁻⁸
11	3.27	2.79 × 10 ⁻⁸
12	3.33	6.35 × 10 ⁻⁸
13	3.34	2.60 × 10 ⁻⁸
14	3.57	3.37 × 10 ⁻⁸
15	3.70	3.70 × 10 ⁻⁸
16	3.70	6.60 × 10 ⁻⁸
17	4.00	5.22 × 10 ⁻⁸
18	4.20	5.94 × 10 ⁻⁸
19	4.60	6.21 × 10 ⁻⁸
20	4.90	7.20 × 10 ⁻⁸
21	5.10	1.32 × 10 ⁻⁷
22	5.30	2.40 × 10 ⁻⁸
23	5.40	7.60 × 10 ⁻⁸
24	5.51	7.68 × 10 ⁻⁸
25	5.83	1.23 × 10 ⁻⁷
26	5.90	9.30 × 10 ⁻⁸
27	6.00	8.92 × 10 ⁻⁸
28	6.30	1.06 × 10 ⁻⁷
29	6.90	6.00 × 10 ⁻⁸
30	6.93	1.50 × 10 ⁻⁷
31	7.30	1.60 × 10 ⁻⁷
32	7.40	2.50 × 10 ⁻⁷
33	7.60	2.60 × 10 ⁻⁷
34	7.60	1.10 × 10 ⁻⁷
35	7.60	2.69 × 10 ⁻⁷
36	7.70	1.10 × 10 ⁻⁷
37	8.00	1.98 × 10 ⁻⁷
38	8.10	1.70 × 10 ⁻⁷
39	8.32	4.10 × 10 ⁻⁷
40	8.35	2.15 × 10 ⁻⁷
41	8.60	3.20 × 10 ⁻⁷
42	8.80	2.30 × 10 ⁻⁷
43	9.24	2.55 × 10 ⁻⁷

Table 4.1-16. Diffusion Coefficient for Granular Materials for Volumetric Moisture Content Between 1.5 Percent and 66.3 Percent (Continued)

Sample	Volumetric Moisture Content (%)	Diffusion Coefficient (cm ² s ⁻¹)
44	9.24	2.55 × 10 ⁻⁷
45	9.56	3.00 × 10 ⁻⁷
46	9.64	3.07 × 10 ⁻⁷
47	9.75	3.20 × 10 ⁻⁷
48	10.1	3.51 × 10 ⁻⁷
49	10.1	3.62 × 10 ⁻⁷
50	10.2	3.54 × 10 ⁻⁷
51	10.2	3.30 × 10 ⁻⁷
52	10.3	3.34 × 10 ⁻⁷
53	10.3	2.10 × 10 ⁻⁷
54	10.4	3.40 × 10 ⁻⁷
55	10.9	3.62 × 10 ⁻⁷
56	11.1	3.72 × 10 ⁻⁷
57	11.1	4.22 × 10 ⁻⁷
58	11.1	4.27 × 10 ⁻⁷
59	11.2	4.19 × 10 ⁻⁷
60	11.2	5.48 × 10 ⁻⁷
61	11.4	4.27 × 10 ⁻⁷
62	11.4	4.12 × 10 ⁻⁷
63	11.6	5.40 × 10 ⁻⁷
64	11.7	2.60 × 10 ⁻⁷
65	11.8	4.80 × 10 ⁻⁷
66	12.0	2.40 × 10 ⁻⁷
67	12.0	4.47 × 10 ⁻⁷
68	12.2	4.09 × 10 ⁻⁷
69	12.3	5.05 × 10 ⁻⁷
70	12.3	4.40 × 10 ⁻⁷
71	12.3	3.60 × 10 ⁻⁷
72	12.3	4.50 × 10 ⁻⁷
73	12.5	2.90 × 10 ⁻⁷
74	12.7	4.37 × 10 ⁻⁷
75	12.7	4.90 × 10 ⁻⁷
76	12.7	5.32 × 10 ⁻⁷
77	13.1	4.77 × 10 ⁻⁷
78	13.9	5.39 × 10 ⁻⁷
79	13.9	7.80 × 10 ⁻⁷
80	14.1	5.12 × 10 ⁻⁷
81	14.2	5.52 × 10 ⁻⁷
82	14.4	4.50 × 10 ⁻⁷
83	14.4	5.20 × 10 ⁻⁷
84	14.4	4.50 × 10 ⁻⁷
85	14.6	6.82 × 10 ⁻⁷

Table 4.1-16. Diffusion Coefficient for Granular Materials for Volumetric Moisture Content Between 1.5 Percent and 66.3 Percent (Continued)

Sample	Volumetric Moisture Content (%)	Diffusion Coefficient ($\text{cm}^2 \text{s}^{-1}$)
86	14.7	9.00×10^{-7}
87	14.8	6.54×10^{-7}
88	16.0	1.47×10^{-6}
89	16.1	6.82×10^{-7}
90	16.5	5.45×10^{-7}
91	16.7	6.60×10^{-7}
92	17.0	1.20×10^{-6}
93	17.1	8.20×10^{-7}
94	17.3	1.76×10^{-6}
95	17.5	1.10×10^{-6}
96	18.8	1.60×10^{-6}
97	18.9	8.19×10^{-7}
98	19.4	9.89×10^{-7}
99*	20.4	4.19×10^{-6}
100	20.8	3.58×10^{-6}
101	21.0	2.34×10^{-6}
102	21.5	1.23×10^{-6}
103	21.6	1.29×10^{-6}
104	23.1	2.40×10^{-6}
105	23.1	1.90×10^{-6}
106	24.0	2.90×10^{-6}
107*	25.3	5.82×10^{-6}
108	25.4	2.50×10^{-6}
109*	25.7	9.26×10^{-6}
110	28.2	3.50×10^{-6}
111	28.5	1.00×10^{-6}
112	30.9	1.51×10^{-6}
113*	31.7	1.23×10^{-5}
114	32.3	4.60×10^{-6}
115*	33.8	1.34×10^{-5}
116*	35.8	1.57×10^{-5}
117	38.5	4.33×10^{-6}
118*	39.3	1.36×10^{-5}
119*	39.5	1.13×10^{-5}
120	40.0	6.90×10^{-6}
121	42.0	5.80×10^{-6}
122	42.5	3.22×10^{-6}
123*	43.4	1.02×10^{-5}
124	49.0	6.09×10^{-6}
125	66.3	1.83×10^{-5}

NOTE: All values are from Conca and Wright 1992 [DIRS 100436], Figure 2, except for those indicated by an asterisk, which are from Conca et al. 1993 [DIRS 170709], Figure 2.

Surface complexation reactions and constants are summarized in Table 4.1-17. A single self-consistent network for sorption of radionuclide species of interest onto either goethite or HFO does not exist. Therefore, the largest self-consistent network was identified and additional data were used to fill in the gaps. Based on the above considerations, the compilations of Wang et al. (2001 [DIRS 176816]) and Turner and Sassman (1996 [DIRS 179618]) are the best reaction networks upon which to base the set of surface complexation constants. These authors fit experimental data from several sources to a single site Double Layer Model using a standard set of acidity constants for goethite. Table 4.1-17 contains the recommended constants obtained from Wang et al. (2001 [DIRS 176816]) and Turner and Sassman (1996 [DIRS 179618]), with supplementary constants obtained from other sources. The surface complexation constant for PuO_2^{+2} from Dzombak and Morel (1990 [DIRS 105483]) was estimated using the linear free-energy relationships. The La^{+3} surface complexation constants were used as analog values for Am^{+3} as recommended by Pepper et al. (2006 [DIRS 179622]).

Table 4.1-17. Surface Complexation Constants Used in PHREEQC Simulations

Surface Complexation Reaction	Log ₁₀ K	Reference
$\text{HfssOH} + \text{H}^+ = \text{HfssOH}_2^+$	7.35	Turner and Sassman 1996 [DIRS 179618]
$\text{HfssOH} = \text{HfssO}^- + \text{H}^+$	-9.17	Turner and Sassman 1996 [DIRS 179618]
$\text{HfssOH} + \text{UO}_2^{+2} + 2\text{CO}_3^{2-} + \text{H}^+ = \text{HfssOH}_2\text{UO}_2(\text{CO}_3)_2^-$	29.15	Turner and Sassman 1996 [DIRS 179618]
$\text{HfssOH} + \text{UO}_2^{+2} + 3\text{CO}_3^{2-} + \text{H}^+ = \text{HfssOH}_2\text{UO}_2(\text{CO}_3)_3^{3-}$	36.28	Turner and Sassman 1996 [DIRS 179618]
$\text{HfssOH} + 2\text{UO}_2^{+2} + \text{CO}_3^{2-} + 3\text{H}_2\text{O} = \text{HfssOH}_2(\text{UO}_2)_2\text{CO}_3(\text{OH})_3 + 2\text{H}^+$	12.62	Turner and Sassman 1996 [DIRS 179618]
$\text{HfssOH} + \text{PuO}_2^+ = \text{HfssOPuO}_2^+$	5.14	Wang et al. 2001 [DIRS 176816]
$\text{HfssOH} + \text{PuO}_2^+ = \text{HfssOPuO}_2 + \text{H}^+$	-2.95	Wang et al. 2001 [DIRS 176816]
$\text{HfssOH} + \text{PuO}_2^+ + \text{H}_2\text{O} = \text{HfssOPuO}_2\text{OH}^- + 2\text{H}^+$	-11.35	Wang et al. 2001 [DIRS 176816]
$\text{HfssOH} + \text{Pu}^{+4} = \text{HfssOPu}^{+3} + \text{H}^+$	14.33	Wang et al. 2001 [DIRS 176816]
$\text{HfssOH} + \text{Pu}^{+4} + \text{H}_2\text{O} = \text{HfssOPuOH}_2^+ + 2\text{H}^+$	8.79	Wang et al. 2001 [DIRS 176816]
$\text{HfssOH} + \text{Pu}^{+4} + 3\text{H}_2\text{O} = \text{HfssOPu}(\text{OH})_3 + 4\text{H}^+$	-3.92	Wang et al. 2001 [DIRS 176816]
$\text{HfssOH} + \text{PuO}_2^{+2} = \text{HfssOPuO}_2^+ + \text{H}^+$	3.0	Dzombak and Morel 1990 [DIRS 105483]
$\text{HfssOH} + \text{NpO}_2^+ = \text{HfssOHNpO}_2^+$	6.03	Wang et al. 2001 [DIRS 176816]
$\text{HfssOH} + \text{NpO}_2^+ + \text{H}_2\text{O} = \text{HfssONpO}_2\text{OH}^- + 2\text{H}^+$	-12.0	Wang et al. 2001 [DIRS 176816]
$\text{HfssOH} + \text{Am}^{+3} + \text{H}_2\text{O} = \text{HfssOAmOH}^+ + 2\text{H}^+$	-6.27	Pepper et al. 2006 [DIRS 179622]
$\text{HfssOH} + \text{Th}^{+4} = \text{HfssOHTh}^{+4}$	18.7	Cromières et al. 1998 [DIRS 179616]
$\text{HfssOH} + \text{Th}^{+4} + 2\text{H}_2\text{O} = \text{HfssOTh}(\text{OH})_2^+ + 3\text{H}^+$	-2.0	Cromières et al. 1998 [DIRS 179616]
$\text{HfssOH} + \text{Th}^{+4} + 4\text{H}_2\text{O} = \text{HfssOTh}(\text{OH})_4^- + 5\text{H}^+$	-16.7	Cromières et al. 1998 [DIRS 179616]
$\text{HfssOH} + \text{Ni}^{+2} = \text{HfssONi}^+ + \text{H}^+$	-2.5	Dzombak and Morel 1990 [DIRS 105483]
$\text{HfssOH} + \text{CO}_3^{2-} = \text{HfssOHCO}_3^{2-}$	4.78	Appelo et al. 2002 [DIRS 168168]
$\text{HfssOH} + \text{CO}_3^{2-} + 2\text{H}^+ = \text{HfssHCO}_3 + \text{H}_2\text{O}$	20.3	Appelo et al. 2002 [DIRS 168168]

NOTE: Hfss represents the iron oxyhydroxide surface.

Table 4.1-18 lists water vapor adsorption data and specific surface areas for various waste form materials. These data are used in Section 6.3.4.6 to develop a model to estimate the water saturation in the CSNF waste form degradation rind as a function of relative humidity based on the physical adsorption of water. Data are unavailable for the bulk of SNF components or their degradation products, which consist of various forms of schoepite. However, the materials listed are considered representative of SNF, because, except for UO_2 , they are at least minor constituents of SNF. The data were obtained by reputable, widely-published researchers at Oak Ridge National Laboratory, Los Alamos National Laboratory, and Dow Chemical U.S.A. (Rocky Flats Division) and are reported in long-established refereed journals, including *The Journal of Physical Chemistry*, *Journal of Colloid and Interface Science*, and *Journal of Nuclear Materials*. Therefore, the data are considered reliable and suitable for use in this report. The data are presented on figures in the journal articles and were digitized using Grab It!TM Digitizing Software. Only the data points that are indicated in the original figures as being measured data values (as opposed to being smoothed or interpolated and shown as a smooth curve) are used and included in Table 4.1-18. Copies of the original figures are shown in Section 6.3.4.6. The number of digits, shown in the adsorption data in Table 4.1-18 reflects only the precision of the digitizing process and is not an indication of the precision of the data shown in the original figures, which is unknown.

Table 4.1-18. Water Vapor Adsorption Isotherms for SNF Waste Form Materials

Sample	Water Vapor Content	Water Adsorbed onto Solid	Specific Surface Area ($\text{m}^2 \text{g}^{-1}$)	Reference
UO ₂	RH (%)	Number of Water Layers	0.51	LaVerne and Tandon 2003 [DIRS 178303], Figure 1
	10.8	3.45		
	52.9	3.56		
	75.0	4.53		
	83.9	6.57		
	94.8	24.28		
ThO ₂	p/p_0	mg/g	11.20	Gammage et al. 1970 [DIRS 178304], Figure 2 (adsorption isotherm), p. 4277 (specific surface area)
	0.035	2.01		
	0.085	2.62		
	0.093	2.55		
	0.112	2.70		
	0.132	2.78		
	0.205	3.09		
	0.229	3.16		
	0.283	3.40		
	0.314	3.47		
	0.345	3.70		
	0.368	3.86		
	0.399	4.09		
	0.438	4.17		
	0.450	4.24		
	0.481	4.48		
	0.508	4.78		
	0.554	5.25		
	0.597	5.79		
	0.643	6.48		
	0.651	6.41		
	0.698	7.49		
	0.740	8.72		
	0.740	8.87		
	0.791	10.50		
	0.822	12.27		
0.837	12.81			
0.895	16.44			
0.903	17.36			
0.926	18.98			
0.957	21.38			
0.957	22.23			
0.981	25.62			
0.992	27.01			

Table 4.1-18. Water Vapor Adsorption Isotherms for SNF Waste Form Materials (Continued)

Sample	Water Vapor Content	Water Adsorbed onto Solid	Specific Surface Area (m ² g ⁻¹)	Reference
ZrO ₂	<u>p/p₀</u>	<u>mg/g</u>	14 to 15	Holmes et al. 1974 [DIRS 154379], Figure 3 (adsorption isotherm) p. 368 (specific surface area)
	0.007	5.08		
	0.010	5.66		
	0.021	6.39		
	0.048	7.11		
	0.074	7.55		
	0.100	7.84		
	0.126	8.28		
	0.164	8.87		
	0.205	9.31		
	0.250	9.89		
	0.291	10.33		
	0.332	10.91		
	0.378	11.35		
	0.419	11.79		
	0.464	12.38		
	0.505	12.96		
	0.550	13.55		
	0.591	14.42		
	0.629	15.30		
	0.670	16.46		
	0.692	17.33		
	0.714	18.35		
0.733	19.66			
0.755	21.26			
0.777	23.15			
0.796	25.76			
0.818	28.66			
0.840	32.44			
0.861	36.50			
0.883	41.15			
0.905	45.94			
0.926	50.44			
0.944	55.66			
CeO ₂	RH (%)	Number of Water Layers	4.18	LaVerne and Tandon 2003 [DIRS 178303], Figure. 1
	11.1	0.32		
	52.9	1.19		
	75.0	1.73		
	83.9	2.37		
	94.8	26.87		
PuO ₂ (Calcined at 350°)	RH (%)	g H₂O/g Sample × 10⁴	57	Stakebake 1971 [DIRS 178302], Figure 8 (adsorption isotherm), p. 253 (specific surface area)
	34.9	63.9		
	53.9	113.4		
	74.9	175.9		
	97.2	327.6		

Table 4.1-18. Water Vapor Adsorption Isotherms for SNF Waste Form Materials (Continued)

Sample	Water Vapor Content	Water Adsorbed onto Solid	Specific Surface Area ($\text{m}^2 \text{g}^{-1}$)	Reference
PuO ₂ (Calcined at 490°)	RH (%)	g H₂O/g Sample × 10⁴	53	Stakebake 1971 [DIRS 178302], Figure 8 (adsorption isotherm), p. 253 (specific surface area)
	34.9	71.3		
	53.9	85.5		
	74.9	116.4		
	97.6	225.3		
PuO ₂ (Calcined at 760°)	RH (%)	g H₂O/g Sample × 10⁴	9.9	Stakebake 1971 [DIRS 178302], Figure 8 (adsorption isotherm), p. 253 (specific surface area)
	34.9	9.9		
	53.9	11.1		
	74.9	29.0		
	97.2	150.9		
PuO ₂ (50 °C)	p (Torr)	mg H₂O/g Sample	16.9	Stakebake and Dringman 1968 [DIRS 178840], Figure 3 (adsorption isotherm), Table 1 (specific surface area)
	0.21	8.86		
	2.11	9.60		
	5.79	9.91		
	10.14	10.15		
	15.54	10.34		
	20.94	10.52		
25.84	10.83			
PuO ₂ (75 °C)	p (Torr)	mg H₂O/g Sample	16.9	Stakebake and Dringman 1968 [DIRS 178840], Figure 4 (adsorption isotherm), Table 1 (specific surface area)
	0.04	2.32		
	2.12	3.46		
	5.83	3.89		
	10.78	4.12		
	17.08	4.26		
	21.41	4.42		
25.63	4.68			
PuO ₂ (Dried in argon)	p/p₀	g water	0.8	Paffett et al. 2003 [DIRS 178712], Figure. 8 (adsorption isotherm), Table 1 (specific surface area)
	0.058	0.00105		
	0.113	0.00192		
	0.176	0.00279		
	0.278	0.00437		
	0.361	0.00576		
	0.435	0.00724		
	0.514	0.00890		
	0.574	0.01064		
	0.639	0.01281		
	0.688	0.01525		
	0.731	0.01803		
	0.771	0.02107		
0.803	0.02436			

NOTES: RH = relative humidity; p = water partial pressure; p₀ = water vapor pressure

Data on adsorption of water vapor on various steel corrosion product materials is presented in Table 4.1-19. Materials included are oxides of the major components of carbon steel and stainless steel, namely, various forms of iron oxide (hematite, goethite, and HFO), chromium oxide (Cr₃O₃ and HCrO₂), and nickel oxide and hydroxide [NiO and Ni(OH)₂]. The materials listed are representative of steel corrosion products expected when waste package internal components corrode. Therefore, the data are appropriate for use in the RTA. All of the data are

from reputable peer-reviewed journals. The data values were obtained by capturing data points from images of the referenced figures using Grab It!™ Digitizing Software (see Section 4.3.2). Only measured data points, as indicated by symbols in the cited figures, are included in Table 4.1-19 and in the analysis of the data (the one exception is the data of Hofmann et al. 2004 [DIRS 173783], Figure 8, in which individual data points were not shown). The number of digits shown in the adsorption data in the table reflects only the precision of the digitizing process and is not an indication of the precision of the data shown on the original figures, which is unknown.

Table 4.1-19. Water Vapor Adsorption Isotherms for Steel Corrosion Products

Sample	Water Vapor Content	Water Adsorbed onto Solid	Specific Surface Area (m ² g ⁻¹)	Reference
HFO	RH (fraction)	Number of Water Layers	320.1	Hofmann et al. 2004 [DIRS 173783], Figure 8; data in Figure 8 are presented as a smooth curve; data listed here were selected in digitizing the data in sufficient number to reproduce the smooth curve in Figure 8.
	0.0028	0.0138		
	0.0028	0.0227		
	0.0055	0.0277		
	0.0110	0.0326		
	0.0166	0.0375		
	0.0221	0.0415		
	0.0276	0.0455		
	0.0387	0.0514		
	0.0552	0.0583		
	0.0746	0.0652		
	0.0967	0.0721		
	0.1160	0.0771		
	0.1326	0.0820		
	0.1630	0.0889		
	0.2044	0.0988		
	0.2293	0.1038		
	0.2514	0.1107		
	0.2790	0.1176		
	0.3066	0.1245		
	0.3398	0.1334		
	0.3674	0.1413		
	0.4061	0.1522		
	0.4337	0.1591		
	0.4586	0.1670		
	0.5083	0.1798		
	0.5525	0.1907		
	0.5967	0.2016		
	0.6298	0.2075		
	0.6630	0.2134		
	0.6934	0.2164		
	0.7320	0.2194		
	0.7790	0.2223		
	0.8149	0.2223		
	0.8536	0.2243		
	0.8757	0.2253		
	0.9171	0.2253		
	0.9613	0.2273		
	0.9807	0.2263		

Table 4.1-19. Water Vapor Adsorption Isotherms for Steel Corrosion Products (Continued)

Sample	Water Vapor Content	Water Adsorbed onto Solid	Specific Surface Area ($\text{m}^2 \text{g}^{-1}$)	Reference
$\alpha\text{-Fe}_2\text{O}_3$	RH (fraction)	Number of Water Layers	(not reported)	McCafferty and Zettlemoyer 1970 [DIRS 154382], Figure 3
	0.0181	0.4311		
	0.0270	0.5475		
	0.0300	0.5707		
	0.0419	0.6288		
	0.0479	0.6869		
	0.0597	0.7100		
	0.0716	0.7797		
	0.0894	0.8492		
	0.1013	0.8956		
	0.1191	0.9419		
	0.1250	0.9534		
	0.1428	1.0113		
	0.1546	1.0343		
	0.1665	1.0807		
	0.1783	1.0338		
	0.1902	1.0802		
	0.1961	1.1383		
	0.2198	1.1494		
	0.2198	1.1961		
	0.2465	1.2421		
	0.2613	1.2651		
	0.2761	1.3114		
	0.2939	1.3343		
	0.3087	1.3690		
	0.3354	1.4267		
	0.3413	1.4382		
	0.3680	1.4842		
	0.3887	1.5421		
	0.3947	1.5769		
0.4095	1.5882			
0.4183	1.5764			
0.4213	1.6113			
0.4628	1.6686			
0.4865	1.7614			
0.5102	1.7608			
0.5191	1.7723			
0.5606	1.8996			
0.5694	1.8528			
0.6021	1.9570			
0.6229	2.0731			
0.6644	2.2121			
0.6762	2.1885			
0.7118	2.3626			
0.7534	2.4899			
0.7594	2.6181			

Table 4.1-19. Water Vapor Adsorption Isotherms for Steel Corrosion Products (Continued)

Sample	Water Vapor Content	Water Adsorbed onto Solid	Specific Surface Area ($\text{m}^2 \text{g}^{-1}$)	Reference
	0.7831	2.6642		
	0.8218	2.9548		
	0.8634	3.2454		
	0.8575	3.3272		
	0.8845	3.7114		
	0.8964	3.8044		
	0.9024	4.0258		
	0.9086	4.3989		
	0.9175	4.3753		
	0.9178	4.7835		
Amorphous Ferric Oxide Hydroxide	RH (fraction)	Adsorbed Amt. mg g^{-1}	77.0	Kandori and Ishikawa 1991 [DIRS 178680], Figure 2 (adsorption isotherm); Table I (specific surface area)
	0.0025	58.12		
	0.0074	62.55		
	0.0149	65.50		
	0.0198	68.45		
	0.0297	70.41		
	0.0396	73.36		
	0.0520	76.30		
	0.0743	80.22		
	0.0892	82.67		
	0.1115	85.60		
	0.1362	88.04		
	0.1659	90.48		
	0.1957	92.42		
	0.2279	93.86		
	0.2601	95.31		
	0.2947	96.26		
	0.3368	97.20		
	0.3765	98.15		
	0.4359	98.59		
	0.4780	99.04		
	0.5251	99.98		
	0.5672	101.41		
	0.5994	102.37		
	0.6192	103.82		
	0.6489	105.77		
	0.6687	107.72		
	0.6885	110.65		

Table 4.1-19. Water Vapor Adsorption Isotherms for Steel Corrosion Products (Continued)

Sample	Water Vapor Content	Water Adsorbed onto Solid	Specific Surface Area ($\text{m}^2 \text{g}^{-1}$)	Reference
Goethite	RH (fraction) 0.0035 0.0071 0.0220 0.0369 0.0593 0.0593 0.0930 0.1379 0.2090 0.2502 0.2952 0.3401 0.3925 0.4637 0.5385 0.6171 0.6806 0.7367 0.7703 0.8038 0.8298 0.8634 0.8670 0.8818 0.9003 0.9114 0.9187 0.9223	H₂O Adsorbed (mmol g^{-1}) 0.1992 0.2988 0.3983 0.4606 0.5228 0.5228 0.6100 0.6846 0.7593 0.8216 0.8714 0.9212 0.9834 1.0581 1.1701 1.3195 1.4689 1.6307 1.7676 1.9295 2.1037 2.2656 2.4025 2.5519 2.7012 2.8506 2.9751 3.1120	45±2.0 (293.13 K)	Koch and Møller 1987 [DIRS 173784], Figure 5 (adsorption isotherm); Table 1 (specific surface area)
Goethite	RH (fraction) 1.4×10^{-5} 0.0073 0.0431 0.2199 0.4355 0.6370 0.7079 0.7398 0.7753 0.8108 0.8428 0.8501 0.8644 0.8716 0.8789	H₂O Adsorbed (mmol g^{-1}) 0.0218 0.2480 0.5868 0.9108 1.1433 1.3988 1.6122 1.7472 1.9162 2.1078 2.3221 2.4691 2.6498 2.7855 2.9212	47.7 (298.41 K)	Koch and Møller 1987 [DIRS 173784], Figure 6 (adsorption isotherm); Table 1 (specific surface area)

Table 4.1-19. Water Vapor Adsorption Isotherms for Steel Corrosion Products (Continued)

Sample	Water Vapor Content	Water Adsorbed onto Solid	Specific Surface Area ($\text{m}^2 \text{g}^{-1}$)	Reference
Chromium Oxide Gel	RH (fraction) 0.0103 0.0359 0.0614 0.1080 0.1732 0.3247	Adsorbed Amt. $\mu\text{mol m}^{-2}$ 8.61 16.10 21.55 27.93 34.09 48.01	17.5	Carruthers et al. 1971 [DIRS 178656], Figure 7 (adsorption isotherm); Table IV (specific surface area); Sample C2(775)16
Chromium Oxide Gel	RH (fraction) 0.0175 0.0606 0.0979 0.1504 0.2030 0.2706 0.3197	Adsorbed Amt. $\mu\text{mol m}^{-2}$ 58.65 63.67 64.15 64.86 65.81 66.99 67.48	10.1	Carruthers et al. 1971 [DIRS 178656], Figure 7 (adsorption isotherm); Table IV (specific surface area); Sample C2(885)2
Chromium Oxide Gel	RH (fraction) 0.0105 0.0502 0.0852 0.1505 0.2229 0.3233	Adsorbed Amt. $\mu\text{mol m}^{-2}$ 1.37 2.07 2.55 2.83 3.33 3.86	10.1	Carruthers et al. 1971 [DIRS 178656], Figure 7 (adsorption isotherm); Table IV (specific surface area); Sample C2(910)20
$\alpha\text{-Fe}_2\text{O}_3$	Pressure (cm Hg) 0.0012 0.0015 0.0062 0.0153 0.0329 0.0810 0.1463 0.2332 0.3070 0.4242 0.5891 0.7541 0.9320	Vol. Adsorbed ml (STP) m^{-2} 0.0687 0.0842 0.1049 0.1269 0.1438 0.1762 0.2008 0.2241 0.2396 0.2642 0.2979 0.3316 0.3666	Monolayer Capacity: 0.242 ml (STP) m^{-2}	Morimoto et al. 1969 [DIRS 162877], Figure 3 (adsorption isotherm); Table I (monolayer capacity); Sample I
$\alpha\text{-Fe}_2\text{O}_3$	Pressure (cm Hg) 0.0031 0.0068 0.0583 0.1620 0.2877 0.4957 0.6822 0.8296	Vol. Adsorbed ml (STP) m^{-2} 0.0688 0.1039 0.1417 0.1757 0.2007 0.2362 0.2626 0.2863	Monolayer Capacity: 0.194 ml (STP) m^{-2}	Morimoto et al. 1969 [DIRS 162877], Figure 4 (adsorption isotherm); Table I (monolayer capacity); Sample II

Table 4.1-19. Water Vapor Adsorption Isotherms for Steel Corrosion Products (Continued)

Sample	Water Vapor Content	Water Adsorbed onto Solid	Specific Surface Area ($\text{m}^2 \text{g}^{-1}$)	Reference
Cr_2O_3	RH (fraction)	Vol. Adsorbed ml (STP) m^{-2}	Monolayer Volume: 0.32 ml (STP) m^{-2}	Harju et al. 2005 [DIRS 178670], Figure 4a (adsorption isotherm); Table 6 (monolayer volume)
	0.0095	0.0556		
	0.0167	0.0963		
	0.0333	0.1333		
	0.0738	0.2074		
	0.1048	0.2444		
	0.1571	0.2963		
	0.2524	0.3704		
	0.3286	0.4296		
	0.4000	0.4852		
	0.4619	0.5407		
	0.5143	0.5852		
	0.5524	0.6222		
	0.6000	0.6741		
0.6381	0.7222			
0.6690	0.7630			
0.7000	0.8074			
NiO	RH (fraction)	Number of Water Layers	(not reported)	Rice et al. 1980 [DIRS 178725], Figure 2; 15°C
	0.0448	0.0683		
	0.1495	0.2279		
	0.2453	0.5269		
	0.2571	0.3874		
	0.3469	0.6518		
	0.3470	0.7446		
	0.4517	1.0086		
	0.5505	1.2843		
	0.7514	2.2069		
0.8514	3.7587			
NiO	RH (fraction)	Number of Water Layers		Rice et al. 1980 [DIRS 178725], Figure. 2; 25°C
	0.4486	0.8810		
	0.5508	1.6323		
	0.6528	2.1632		
	0.7521	2.9493		
0.8522	4.5939			
NiO	RH (fraction)	Number of Water Layers		Rice et al. 1980 [DIRS 178725], Figure 2; 35°C
	0.2451	0.3645		
	0.3468	0.6054		
	0.4487	1.0202		
	0.5507	1.5279		
	0.6527	2.0472		
	0.7519	2.7289		
0.8516	4.0371			

Table 4.1-19. Water Vapor Adsorption Isotherms for Steel Corrosion Products (Continued)

Sample	Water Vapor Content	Water Adsorbed onto Solid	Specific Surface Area ($\text{m}^2 \text{g}^{-1}$)	Reference
Cr_2O_3	RH (fraction)	Vol. Adsorbed cm^3 (STP) m^{-2}	12.0	Nagao et al. 1995 [DIRS 162878], Figure 1b (adsorption isotherm); p. 222 (specific surface area)
	0.0014	0.0033		
	0.0016	0.0135		
	0.0019	0.0237		
	0.0024	0.0476		
	0.0028	0.0613		
	0.0031	0.0749		
	0.0038	0.1039		
	0.0137	0.1209		
	0.0268	0.1362		
	0.0367	0.1498		
	0.0404	0.1703		
	0.0439	0.1856		
	0.0538	0.2009		
	0.0574	0.2180		
	0.0706	0.2350		
	0.0900	0.2468		
	0.1158	0.2603		
	0.1416	0.2755		
	0.1769	0.2890		
0.2156	0.3076			
0.2574	0.3244			
0.2992	0.3429			
0.3475	0.3614			
0.3925	0.3800			
0.4471	0.4019			
0.4985	0.4203			
0.5436	0.4406			
$\alpha\text{-Fe}_2\text{O}_3$	RH (fraction)	Vol. Adsorbed cm^3 (STP) m^{-2}	15.14	Kuwabara et al. 1987 [DIRS 178682], Figure 1 (adsorption isotherm); p. 1060 (specific surface area)
	0.0023	0.0240		
	0.0046	0.0408		
	0.0070	0.0552		
	0.0141	0.0720		
	0.0330	0.0985		
	0.0471	0.1154		
	0.0708	0.1323		
	0.0968	0.1541		
	0.1276	0.1735		
	0.1702	0.1977		
	0.2199	0.2220		
	0.2648	0.2463		
	0.3193	0.2659		
	0.3690	0.2902		
	0.4234	0.3122		
	0.4637	0.3316		
0.5039	0.3487			
0.5607	0.3754			

Table 4.1-19. Water Vapor Adsorption Isotherms for Steel Corrosion Products (Continued)

Sample	Water Vapor Content	Water Adsorbed onto Solid	Specific Surface Area ($\text{m}^2 \text{g}^{-1}$)	Reference
	0.6176 0.6601 0.7051 0.7358 0.7713 0.8091 0.8422 0.8752	0.3998 0.4313 0.4603 0.4893 0.5231 0.5617 0.6051 0.6629		
$\alpha\text{-HCrO}_2$	RH (fraction) 0.0122 0.0669 0.0892 0.1236 0.1459 0.1642 0.1804 0.1966 0.2250 0.2980 0.3426 0.4034 0.4642 0.5250 0.5858	Vol. Adsorbed cm^3 (STP) m^{-2} 0.1267 0.1663 0.1723 0.1901 0.1980 0.2119 0.2238 0.2337 0.2535 0.2832 0.2931 0.3069 0.3208 0.3386 0.3564	20.1; Monolayer Coverage: 4.0 H_2O molecules nm^{-2}	Kittaka et al. 1984 [DIRS 178830], Figure 6a (adsorption isotherm); p. 459 (monolayer coverage); Table 1 (specific surface area)
Cr_2O_3	RH (fraction) 0.0032 0.0081 0.0145 0.0193 0.0241 0.0305 0.0322 0.0338 0.0354 0.0339 0.0355 0.0372 0.0468 0.0548 0.0612 0.0692 0.0772 0.0869 0.0981 0.1077 0.1189 0.1285	Vol. Adsorbed cm^3 (STP) m^{-2} 0.0099 0.0174 0.0273 0.0347 0.0397 0.0446 0.0521 0.0620 0.0745 0.0919 0.1168 0.1367 0.1466 0.1490 0.1565 0.1614 0.1663 0.1712 0.1761 0.1810 0.1884 0.1934	3.40; Monolayer Capacity: 7.01 H_2O molecules nm^{-2}	Kittaka et al. 1983 [DIRS 178681], Figure 6 (adsorption isotherm); Table I (specific surface area and monolayer capacity); Sample I

Table 4.1-19. Water Vapor Adsorption Isotherms for Steel Corrosion Products (Continued)

Sample	Water Vapor Content	Water Adsorbed onto Solid	Specific Surface Area ($\text{m}^2 \text{g}^{-1}$)	Reference
	0.1365	0.1983		
	0.1509	0.2057		
	0.1638	0.2106		
	0.1782	0.2154		
	0.1990	0.2253		
	0.2214	0.2301		
	0.2502	0.2424		
	0.2646	0.2448		
	0.2887	0.2496		
	0.2999	0.2545		
	0.3175	0.2594		
	0.3351	0.2667		
	0.3671	0.2765		
	0.3975	0.2837		
	0.4264	0.2910		
Cr ₂ O ₃	RH (fraction)	Vol. Adsorbed cm^3 (STP) m^{-2}	7.21; Monolayer Coverage: 7.22 H ₂ O molecules nm^{-2}	Kittaka et al. 1983 [DIRS 178681], Figure 7 (adsorption isotherm); Table I (specific surface area and monolayer capacity); Sample II
	0.0004	0.0173		
	0.0085	0.0370		
	0.0213	0.0541		
	0.0278	0.0689		
	0.0310	0.0812		
	0.0374	0.0935		
	0.0471	0.1057		
	0.0583	0.1155		
	0.0695	0.1203		
	0.0919	0.1349		
	0.1080	0.1447		
	0.1240	0.1568		
	0.1448	0.1690		
	0.1641	0.1762		
	0.1817	0.1909		
	0.2009	0.2055		
	0.2266	0.2201		
	0.2522	0.2371		
	0.2811	0.2516		
	0.3051	0.2638		
	0.3355	0.2758		
	0.3691	0.2878		
	0.4028	0.3023		
	0.4364	0.3193		

Table 4.1-19. Water Vapor Adsorption Isotherms for Steel Corrosion Products (Continued)

Sample	Water Vapor Content	Water Adsorbed onto Solid	Specific Surface Area ($\text{m}^2 \text{g}^{-1}$)	Reference
Ni(OH) ₂	Pressure (Pa$\times 10^{-3}$)	Water Coverage (molecule nm^{-2})	17; Statistical Monolayer: 9.52 H ₂ O molecules nm^{-2}	Micale et al. 1976 [DIRS 179136], Figure. 3 (adsorption isotherm); p. 541 (specific surface area); p. 542 (statistical monolayer); Sample A
	0.090	3.013		
	0.151	3.541		
	0.213	3.768		
	0.284	4.145		
	0.365	4.448		
	0.467	4.826		
	0.610	5.431		
	0.661	5.508		
	0.814	6.188		
	0.936	6.717		
	1.088	7.323		
	1.282	8.230		
	1.424	8.910		
	1.730	10.948		
	1.903	12.006		
	2.177	15.247		
2.410	19.166			
2.460	20.974			
2.591	24.439			
2.661	27.526			
Ni(OH) ₂	Pressure (Pa$\times 10^{-3}$)	Water Coverage (molecule nm^{-2})	33; Statistical Monolayer: 9.52 H ₂ O molecules nm^{-2}	Micale et al. 1976 [DIRS 179136], Figure 3 (adsorption isotherm); p. 542 (specific surface area and statistical monolayer); Sample B
	0.020	1.656		
	0.050	2.033		
	0.121	2.486		
	0.182	2.864		
	0.315	3.318		
	0.529	4.075		
	0.936	5.513		
	1.323	7.478		
	1.730	10.497		
	2.116	14.193		
2.430	18.564			
α -Fe ₂ O ₃	RH (fraction)	Adsorbed Water [molecules (100 \AA^{-1})⁻¹]	Monolayer Coverage: 7.8 molecules (100 \AA^2) ⁻¹	Micale et al. 1985 [DIRS 173785], Figure 2 (adsorption isotherm); Table I (monolayer coverage) (Figure 2 is erroneously shown as Figure 1 in the reference)
	0.0077	3.525		
	0.0442	6.075		
	0.0865	7.200		
	0.1346	7.950		
	0.2115	8.850		
	0.3058	10.275		
	0.4173	11.475		
	0.5038	12.450		
	0.6000	14.550		
0.7308	20.175			

Table 4.1-19. Water Vapor Adsorption Isotherms for Steel Corrosion Products (Continued)

Sample	Water Vapor Content	Water Adsorbed onto Solid	Specific Surface Area ($\text{m}^2 \text{g}^{-1}$)	Reference
$\gamma\text{-FeOOH}$	RH (fraction)	Adsorbed Water [molecules ($100 \text{ \AA}^2\text{-}^{-1}$)]	Monolayer Coverage: 10.0 molecules ($100 \text{ \AA}^2\text{-}^{-1}$)	Micale et al. 1985 [DIRS 173785], Figure 3 (adsorption isotherm); Table I (monolayer coverage)
	0.0087	3.918		
	0.0232	5.373		
	0.0609	6.604		
	0.1159	7.612		
	0.1855	8.507		
	0.2870	9.851		
	0.3855	10.970		
	0.4841	12.425		
	0.6145	15.112		
0.7449	20.261			
$\alpha\text{-Fe}_2\text{O}_3$	$-\log_{10}(\text{RH})$	Number of Water Layers	9.60 (N_2 area at 30°C activation temp.)	Jurinak 1964 [DIRS 154381], Figure 5 (adsorption isotherm); Table 1 (specific surface area)
	0.0198	5.420		
	0.0236	5.034		
	0.0236	4.888		
	0.0284	4.711		
	0.0284	4.441		
	0.0304	4.186		
	0.0313	4.280		
	0.0355	4.343		
	0.0374	3.888		
	0.0388	3.917		
	0.0397	3.831		
	0.0425	3.946		
	0.0482	3.506		
	0.0504	3.481		
	0.0504	3.430		
	0.0555	3.532		
	0.0580	3.162		
	0.0639	3.257		
	0.0644	3.162		
	0.0689	3.093		
	0.0742	2.769		
	0.0775	2.873		
	0.0848	2.852		
	0.0867	2.810		
	0.0873	2.894		
	0.0913	2.769		
0.0976	2.534			
0.0984	2.688			
0.1092	2.516			
0.1125	2.461			
0.1211	2.424			
0.1266	2.497			
0.1285	2.424			
0.1324	2.371			

Table 4.1-19. Water Vapor Adsorption Isotherms for Steel Corrosion Products (Continued)

Sample	Water Vapor Content	Water Adsorbed onto Solid	Specific Surface Area (m ² g ⁻¹)	Reference
	0.1437	2.203		
	0.1480	2.319		
	0.1492	2.203		
	0.1783	2.092		
	0.1878	2.031		
	0.2053	1.929		
	0.2053	1.886		
	0.2295	1.900		
	0.2365	1.845		
	0.2382	1.845		
	0.2491	1.818		
	0.3454	1.664		
	0.3532	1.604		
	0.3585	1.628		
	0.3949	1.523		
	0.4129	1.546		
	0.4190	1.557		
	0.4616	1.425		
	0.4972	1.373		
	0.5122	1.436		
	0.5642	1.314		
	0.6214	1.314		
	0.6594	1.285		
	0.6794	1.168		
	0.7824	1.168		
	0.8812	1.142		
	0.8812	1.109		
FeOOH	RH (fraction)	Number of Water Layers	16.2 (N ₂ area at 30°C activation temp.)	Jurinak 1964 [DIRS 154381], Figure 6 (adsorption isotherm); Table 1 (specific surface area)
	0.0254	3.759		
	0.0282	3.732		
	0.0299	3.518		
	0.0330	3.467		
	0.0340	3.269		
	0.0380	3.245		
	0.0398	3.128		
	0.0445	3.037		
	0.0491	2.971		
	0.0521	2.821		
	0.0574	2.700		
	0.0642	2.660		
	0.0740	2.508		
	0.0810	2.400		
	0.0906	2.313		
	0.0977	2.165		
	0.1076	2.118		
	0.1160	2.102		
	0.1222	2.026		

Table 4.1-19. Water Vapor Adsorption Isotherms for Steel Corrosion Products (Continued)

Sample	Water Vapor Content	Water Adsorbed onto Solid	Specific Surface Area ($\text{m}^2 \text{g}^{-1}$)	Reference
	0.1337	2.026		
	0.1378	1.953		
	0.1430	1.925		
	0.1636	1.842		
	0.1915	1.749		
	0.2017	1.736		
	0.2469	1.578		
	0.2741	1.637		
	0.2976	1.613		
	0.3697	1.521		
	0.3698	1.423		
	0.3984	1.488		
	0.4697	1.413		
	0.5374	1.342		
	0.5455	1.294		
	0.7358	1.211		
	0.7412	1.256		

4.1.3 Design Information

Some of the information necessary for the model presented in this document consists of parameters and other descriptions based on the license application (LA) conceptual design of the repository and waste packages. Included are dimensions, material amounts and properties, and physical configuration of the drifts and their contents, listed in Tables 4.1-20 through 4.1-22.

In the current conceptual design for CSNF waste packages, the CSNF is contained in a TAD canister, which in turn is placed inside an overpack container. In the RTA, the term “21-PWR waste package” refers to a TAD canister containing 21 PWR CSNF assemblies. The 21-PWR is the most common CSNF waste package so much of the discussion in this report refers to this waste package (see Section 6.3.3.1). Tables 4.1-20, 4.1-21, and 4.1-22 provide the design parameter values for the TAD and DHLW canisters and waste packages.

Table 4.1-20. Design Information for EBS Components

Model Input	Value	Source
Diameter of the drift	5.5 m	SNL 2007 [DIRS 179354], Table 4-1, Parameter Number 01-10
Length of drip shield with overlap	5,805 mm	SNL 2007 [DIRS 179354], Table 4-2, Parameter Number 07-01
Thickness of drip shield	15 mm	SNL 2007 [DIRS 179354], Table 4-2, Parameter Number 07-04
Maximum depth of invert	4 ft 4 in.	SNL 2007 [DIRS 179354], Table 4-1, Parameter Number 01-10

Table 4.1-20. Design Information for EBS Components (Continued)

Model Input	Value	Source
TAD Canister and Waste Package Characteristics		
Outer corrosion barrier outside diameter	74.08 in.	SNL 2007 [DIRS 179394], Table 4-3
Inner vessel outside diameter	71.70 in.	SNL 2007 [DIRS 179394], Table 4-3
Outer corrosion barrier length	224.07 in.	SNL 2007 [DIRS 179394], Table 4-3
Outer barrier thickness	1.00 in.	SNL 2007 [DIRS 179394], Table 4-3
Outer lid thickness	1.00 in.	SNL 2007 [DIRS 179394], Table 4-3
Inner vessel thickness	2.00 in.	SNL 2007 [DIRS 179394], Table 4-3
TAD canister outside diameter	66.50 in.	SNL 2007 [DIRS 179394], Section 4.1.1.1
TAD canister thickness	1.00 in.	SNL 2007 [DIRS 179394], Table 4-2
5 DHLW/DOE SNF – Long Codisposal Waste Package Characteristics		
Outer corrosion barrier thickness	1.00 in.	SNL 2007 [DIRS 179567], Table 4-9
Outer corrosion barrier outside diameter	80.5 in.	SNL 2007 [DIRS 179567], Table 4-9
Inner vessel outside diameter	78.13 in.	SNL 2007 [DIRS 179567], Table 4-9
Inner vessel thickness	2.00 in.	SNL 2007 [DIRS 179567], Table 4-9
Inner vessel length	192.38 in.	SNL 2007 [DIRS 179567], Table 4-9
Inner vessel cavity length	181.88 in.	BSC 2007 [DIRS 182365], Section A-A
Outer corrosion barrier length	202.57 in.	SNL 2007 [DIRS 179567], Table 4-9
Divider plate assembly tube thickness	1.25 in.	SNL 2007 [DIRS 179567], Table 4-9
HLW Glass Characteristics		
HLW glass canister length	4,500 mm	CRWMS M&O 2000 [DIRS 151743], Table 3
HLW glass canister outer diameter	610 mm	CRWMS M&O 2000 [DIRS 151743], Table 3
HLW glass canister wall thickness	10.5 mm	CRWMS M&O 2000 [DIRS 151743], Table 3
DSNF Characteristics		
SNF standard canister outside diameter	18 in.	DOE 2003 [DIRS 164970], Fig. 12
SNF standard canister length	15 ft.	DOE 2003 [DIRS 164970], Fig. 12
SNF standard canister wall thickness	0.375 in.	DOE 2003 [DIRS 164970], Fig. 13
SNF standard canister body weight	1,073 lb	DOE 2003 [DIRS 164970], Table 5
SNF canister sleeve weight	455 lb	DOE 2003 [DIRS 164970], Table 5
SNF canister impact plates weight	182 lb	DOE 2003 [DIRS 164970], Table 5
TMI canister length	149.75 in.	DOE 2003 [DIRS 164970], p. 25
TMI canister outside diameter	14 in.	DOE 2003 [DIRS 164970], p. 25
TMI canister wall thickness	0.25 in.	DOE 2003 [DIRS 164970], p. 25
TMI canister guide tube cross section width	9.0 in.	DOE 2003 [DIRS 164970], p. 25
TMI canister guide tube length	136-7/16 in.	DOE 2003 [DIRS 164970], p. 30
TMI canister top thickness	4 in.	DOE 2003 [DIRS 164970], p. 25
TMI canister bottom thickness	0.375 in.	DOE 2003 [DIRS 164970], p. 25

Table 4.1-20. Design Information for EBS Components (Continued)

Model Input	Value	Source
TMI fuel top nozzle weight	7.48 kg	DOE 2003 [DIRS 164970], Table B-1
TMI fuel bottom nozzle weight	8.16 kg	DOE 2003 [DIRS 164970], Table B-1
TMI fuel spring retainer weight	0.91 kg	DOE 2003 [DIRS 164970], Table B-1
TMI fuel upper end plug weight	0.06 kg	DOE 2003 [DIRS 164970], Table B-1
TMI fuel upper nut weight	0.51 kg	DOE 2003 [DIRS 164970], Table B-1
TMI fuel lower nut weight	0.15 kg	DOE 2003 [DIRS 164970], Table B-1

NOTES: DHLW=defense high-level (radioactive) waste; SNF=spent nuclear fuel; TMI = Three Mile Island

Table 4.1-21. Component Dimensions in a 21-PWR Site-Specific Canister

Component	Dimensions	Source
Basket Side Guide	0.375 in. thickness	SNL 2007 [DIRS 179394], Table 4-2
Basket End Side Guide	0.375 in. thickness	SNL 2007 [DIRS 179394], Table 4-2
Basket Corner Guide	0.375 in. thickness	SNL 2007 [DIRS 179394], Table 4-2
Fuel Basket Assembly A-Plate	0.4375 in. thickness	SNL 2007 [DIRS 179394], Table 4-2
Fuel Basket Assembly B-Plate	0.4375 in. thickness	SNL 2007 [DIRS 179394], Table 4-2
Fuel Basket Assembly C-Plate	0.4375 in. thickness	SNL 2007 [DIRS 179394], Table 4-2
Fuel Basket Assembly D-Plate	0.3125 in. thickness	SNL 2007 [DIRS 179394], Table 4-2
Fuel Basket Assembly E-Plate	0.3125 in. thickness	SNL 2007 [DIRS 179394], Table 4-2
Basket Tube	0.3125 in. thickness	SNL 2007 [DIRS 179394], Table 4-2
	191.00 in. length	BSC 2005 [DIRS 174152]

Table 4.1-22. Masses and Numbers of Components in Waste Packages

Material	Component (Quantity)	Total Mass (lbm)	Source
21-PWR TAD Waste Package and TAD Canister			
Originally A 516 Carbon Steel; currently Stainless Steel Type 316	Side Guide (16)	1.69×10^3	SNL 2007 [DIRS 179394], Table A-1
	End Side Guide (32)	2.52×10^3	SNL 2007 [DIRS 179394], Table A-1
	Corner Guide (16)	2.07×10^3	SNL 2007 [DIRS 179394], Table A-1
	Fuel Tube (21)	1.36×10^4	SNL 2007 [DIRS 179394], Table A-1

Table 4.1-22. Masses and Numbers of Components in Waste Packages (Continued)

Material	Component (Quantity)	Total Mass (lbm)	Source
Stainless Steel Type 316	Shield Plug (1)	1.22×10^4	SNL 2007 [DIRS 179394], Table A-3
	Inner Seal Plug (2)	5.30×10^{-1}	SNL 2007 [DIRS 179394], Table A-3
	Spread Ring (1)	9.38×10^1	SNL 2007 [DIRS 179394], Table A-3
	Spread Ring Filler Segment (1)	2.19×10^0	SNL 2007 [DIRS 179394], Table A-3
	Outer Seal Plate (1)	1.06×10^2	SNL 2007 [DIRS 179394], Table A-3
	Outer Seal Plug (1)	2.81×10^{-1}	SNL 2007 [DIRS 179394], Table A-3
	TAD Shell (1)	1.59×10^4	SNL 2007 [DIRS 179394], Table A-3
	Inner Vessel (1)	27,093.73	SNL 2007 [DIRS 179394], Table 4-3
	Inner Vessel Top Lid (1)	2,120.25	SNL 2007 [DIRS 179394], Table 4-3
	Inner Vessel Bottom Lid (1)	2,282.95	SNL 2007 [DIRS 179394], Table 4-3
	Interface Ring (1)	85.86	SNL 2007 [DIRS 179394], Table 4-3
	Spread Ring (1)	82.05	SNL 2007 [DIRS 179394], Table 4-3
	Total 316 SS Welds (-)	91.13	SNL 2007 [DIRS 179394], Table 4-3
Borated Stainless Steel Type 304B4	A Plate (8)	2.76×10^3	SNL 2007 [DIRS 179394], Table A-1
	B Plate (8)	2.76×10^3	SNL 2007 [DIRS 179394], Table A-1
	C Plate (16)	2.90×10^3	SNL 2007 [DIRS 179394], Table A-1
5 DHLW/DOE SNF – Long Co-Disposal Waste Package			
Carbon Steel Type A 516	Divider Plate Assembly Divider Plate (5)	1,107.51	SNL 2007 [DIRS 179567], Table 4-9
	Divider Plate Outer Assembly Bracket (5)	4,120.95	SNL 2007 [DIRS 179567], Table 4-9
	Divider Plate Assembly Inner Bracket (5)	3,291.61	SNL 2007 [DIRS 179567], Table 4-9
	Divider Plate Assembly Tube (1)	4,246.00	SNL 2007 [DIRS 179567], Table 4-9

Table 4.1-22. Masses and Numbers of Components in Waste Packages (Continued)

Material	Component (Quantity)	Total Mass (lbm)	Source
Stainless Steel Type 316	Inner Vessel (1)	25,884.44	SNL 2007 [DIRS 179567], Table 4-9
	Shield Plug (1)	11,604.30	SNL 2007 [DIRS 179567], Table 4-9
	Interface Ring (1)	93.65	SNL 2007 [DIRS 179567], Table 4-9
	Spread Ring (1)	90.03	SNL 2007 [DIRS 179567], Table 4-9
	Inner Vessel Bottom Lid (1)	2,714.86	SNL 2007 [DIRS 179567], Table 4-9
	Total 316 SS Welds (-)	100.88	SNL 2007 [DIRS 179567], Table 4-9

NOTE: “-” indicates that the number of welds is not specified in the source.

Impact Assessment – Use of Preliminary Design Values

The TSPA calculations were started before the direct confirming data were available in the design interface documents (SNL 2007 [DIRS 179394] and SNL 2007 [DIRS 179567]), so it was necessary to utilize preliminary values for the design of the EBS components to compute certain model inputs used in the TSPA. Specifically, the preliminary values for the masses and dimensions of several internal components used in the analyses described in Section 6 differ from those specified in Table 4.1-22. In Table 4.1-23, these preliminary parameter values are compared to the direct confirming design values.

In addition to changes in component masses, a preliminary value for the density of Stainless Steel Type 304B4 was used that differs from the value used in the TAD design interface document (SNL 2007 [DIRS 179394]). A value of $7,760 \text{ kg m}^{-3}$ (Kügler 1996 [DIRS 107760], p. 15) was used, based on the similar chemical composition of Neutronit with Stainless Steel Type 304B4. The TAD design interface document (SNL 2007 [DIRS 179394], Table A-8) uses a value of $0.282 \text{ lbm in}^{-3}$ ($7,810 \text{ kg m}^{-3}$), as shown in Table 4.1-15. The preliminary value for density was used to determine the mass of absorber plates A, B, and C as Stainless Steel Type 304B4 from a preliminary design that specified their composition as being Ni-Gd alloy.

As shown in Table 4.1-23, the preliminary values of component masses used in the RTA range from 2 percent lower to 21 percent higher than the design values. However, the components that comprise the bulk of the steel mass—fuel tubes, TAD shell, shield plug, and inner vessel—differ negligibly from the design values. These component masses are used to estimate the mass of corrosion products present in a breached waste package; specifically, the component masses are represented by a set of fixed model inputs used in the TSPA (see Table 8.2-6) for the mass of steel in waste package domains and for the fraction of total mass in waste package domains that is carbon steel or stainless steel. The preliminary values result in parameters that are within one percent of those obtained using final design values. Therefore, the use of preliminary values for component masses has negligible impact on the results presented in this report, and negligible impact on the TSPA results. Further details are presented in Section 6.3.4, and the impacts of using preliminary values on all parameters based on design data is summarized in Table 8.2-7.

In addition to component masses, preliminary values were used for the lengths of the inner vessel and outer corrosion barrier in a 5-DHLW/DOE SNF – Long Codisposal waste package. For the inner vessel, the design length is 192.38 in.; the preliminary length used was 192.57 in., or 0.1 percent less. For the outer corrosion barrier, the design length is 202.57 in.; the preliminary length was 202.56 in., or 0.005 percent less. The preliminary values were used in estimating the diffusive area, which are used in the TSPA to compute diffusive transport. Due to the small magnitude of these changes (smaller than the precision of parameters generated from these values), the use of these preliminary lengths has no impact on the results presented in this report, and therefore no impact on the TSPA results.

Table 4.1-23. Component Masses Used in RTA Compared with Design Values

Component	Design Value (Table 4.1-22) (lbm)	Preliminary Value, Used in RTA (lbm)	Impact Assessment
21-PWR TAD Waste Package and TAD Canister			
A Plate	2.76×10^3	3.10×10^3	RTA value 12% higher than Design value
B Plate	2.76×10^3	3.10×10^3	RTA value 12% higher than Design value
C Plate	2.90×10^3	3.25×10^3	RTA value 12% higher than Design value
Side Guide	1.69×10^3	1.66×10^3	RTA value 2% lower than Design value
End Side Guide	2.52×10^3	2.48×10^3	RTA value 2% lower than Design value
Corner Guide	2.07×10^3	2.04×10^3	RTA value 1% lower than Design value
Fuel Tube	1.36×10^4	1.34×10^4	RTA value 1% lower than Design value
TAD Shell	1.59×10^4	1.61×10^4	RTA value 1% higher than Design value
Inner Vessel	27,093.73	27,084	RTA value 0.04% lower than Design value
Inner Vessel Top Lid	2,120.25	2,180	RTA value 3% higher than Design value
Inner Vessel Bottom Lid	2,282.95	2,273	RTA value 0.4% lower than Design value
Interface Ring	85.86	86	RTA value 0.2% higher than Design value
Spread Ring	82.05	82	RTA value 0.06% lower than Design value
Total 316 SS Welds	91.13	110	RTA value 21% higher than Design value
5 DHLW/DOE SNF – Long Co-Disposal Waste Package			
Divider Plate Assembly Divider Plate	1,107.51	1,105	RTA value 0.2% lower than Design value
Divider Plate Outer Assembly Bracket	4,120.95	4,095	RTA value 0.6% lower than Design value
Divider Plate Assembly Inner Bracket	3,291.61	3,270	RTA value 0.7% lower than Design value
Divider Plate Assembly Tube	4,246.00	4,247	RTA value 0.02% higher than Design value
Inner Vessel	25,884.44	25,885	RTA value 0.002% higher than Design value
Shield Plug	11,604.30	11,658	RTA value 0.5% higher than Design value
Interface Ring	93.65	94	RTA value 0.4% higher than Design value

Table 4.1-23. Component Masses Used in RTA Compared with Design Values (Continued)

Component	Design Value (Table 4.1-22) (lbm)	Preliminary Value, Used in RTA (lbm)	Impact Assessment
5 DHLW/DOE SNF – Long Co-Disposal Waste Package (Continued)			
Spread Ring	90.03	91	RTA value 1% higher than Design value
Inner Vessel Bottom Lid	2,714.86	2,707	RTA value 0.3% lower than Design value
Total 316 SS Welds	100.88	118	RTA value 17% higher than Design value

Output DTN: SN0703PAEBSRTA.001, file *Preliminary Design Impact Assessment.doc*

4.2 CRITERIA

This report was prepared to comply with 10 CFR Part 63 [DIRS 178394]. Relevant requirements for performance assessment from Section 114 of that document are: “Any performance assessment used to demonstrate compliance with Sec. 113(b) shall: (a) Include data related to the geology, hydrology, and geochemistry used to define parameters and conceptual models used in the assessment. (b) Account for uncertainties and variabilities in parameter values and provide the technical basis for parameter ranges, probability distributions, or bounding values used in the performance assessment ... (g) Provide the technical basis for models used in the performance assessment such as comparisons made with outputs of detailed process-level models.”

Programmatic requirements for this document are listed in *Technical Work Plan for: Near-Field Environment: Engineered Barrier System: Radionuclide Transport Abstraction Model Report* (BSC 2006 [DIRS 177739]). This technical work plan (TWP) specifies that this document and all analyses described herein must adhere to the requirements of SCI-PRO-006, *Models*. The TWP also specifies that *Yucca Mountain Review Plan, Final Report* (NRC 2003 [DIRS 163274]) acceptance criteria must be addressed. In addition, the TWP specifies that the requirements of AP-16.1Q, *Condition Reporting and Resolution*, to enable closure of Condition Report (CR)-6509 and any other relevant CRs that may be generated by the Corrective Action Program, must be satisfied.

The following Condition Reports are addressed in this report:

CR-6509: No Temperature Modification in Corrosion Products Diffusion Coefficient

In a previous revision (REV 02) of this report, the diffusion coefficient for the corrosion products and waste form domains was not modified for temperature effects. In the current revision, the effects of temperature have been considered in the diffusion coefficients (see Section 6.3.4.1.2).

CR-7197: RIT Action Items Associated with AMR ANL-WIS-PA-000001, EBS Radionuclide Transport Abstraction

This CR tracks twenty-four Action Items associated with a previous revision of the report. These Action Items have been evaluated for incorporation into the current revision of the report. Where necessary, revisions were made.

CR-8656: Technical Product output sources listed in ATDT but not in DIRS

This CR concerns a disparity between the sources listed within DTNs of the parent report in the Automated Technical Data Tracking system and what is listed within the Document Input Reference System (DIRS). For those DTNs that are product output of this report, the source DTN information has been checked and is consistent with DIRS.

CR-9293: CR 6334 extent of condition review for ANL-WIS-PA-000001

A previous revision (REV 02) of this report was selected for extent of condition review for CR 6334. Four minor issues were found among a relatively large number of direct input values identified in REV 02 of the report. For these instances, the values from the report could not be readily traced to or did not match with the values from direct input sources. These issues were evaluated and it was found that none of the issues affected the results or conclusions of the report.

CR-11204: Non-Reproducibility of Matrix Diffusion Regression Correlation Coefficient

This CR questions the traceability and reproducibility in the source document for the regression relationship between matrix diffusion coefficient and permeability. This regression relationship is used Section 6.6.4.2 of the current report. However, its use in this report is limited to the Alternative Dual-Continuum Invert Diffusion Coefficient Model, which is an alternative conceptual model that is not a feed to, or used in, TSPA.

CR-11233: DTN MO0409SPAACRWP.000 Readme.doc

The Readme.doc for DTN: MO0409SPAACRWP.000 did not identify one of the files that is used as an input to ANL-WIS-PA-000001 REV 03G, and another was listed twice. This CR is addressed by correcting the readme file in DTN TDIF in TDMS. No changes to this report are required.

CR-11235: TDR-TDIP-ES-000006

There are two waste package input values that were used in ANL-WIS-PA-000001 REV 003G that are not included in TDR-TDIP-ES-000006 REV 00. These values were instead taken directly from the relevant IEDs. This information should be added to TDR-TDIP-ES-000006 during the next revision. No change to this report is required.

The acceptance criteria that concern flow and transport related to the EBS are presented in Section 2.2.1.3 of the *Yucca Mountain Review Plan, Final Report* (NRC 2003 [DIRS 163274]). Of the 14 model abstraction sections in the review plan, Sections 2.2.1.3.3 and 2.2.1.3.4 are applicable to this abstraction. The pertinent acceptance criteria from those two sections are listed in Sections 4.2.1 and 4.2.2, respectively.

4.2.1 Applicable Acceptance Criteria from Section 2.2.1.3.3, “Quantity and Chemistry of Water Contacting Engineered Barriers and Waste Forms”

The following acceptance criteria, listed in Section 2.2.1.3.3.3 of *Yucca Mountain Review Plan, Final Report* (NRC 2003 [DIRS 163274]), apply to this abstraction. These acceptance criteria are based on meeting the requirements of 10 CFR 63.114(a)–(c) and (e)–(g) [DIRS 178394], relating to the quantity and chemistry of water contacting engineered barriers and waste forms model abstraction.

Acceptance Criterion 1–System Description and Model Integration Are Adequate.

- (1) Total system performance assessment adequately incorporates important design features, physical phenomena, and couplings, and uses consistent and appropriate assumptions throughout the quantity and chemistry of water contacting engineered barriers and waste forms abstraction process.
- (2) The abstraction of the quantity and chemistry of water contacting engineered barriers and waste forms uses assumptions, technical bases, data, and models, that are appropriate and consistent with other related U.S. Department of Energy abstractions. For example, the assumptions used for the quantity and chemistry of water contacting engineered barriers and waste forms are consistent with the abstractions of “Degradation of Engineered Barriers” (NRC 2003 [DIRS 163274], Section 2.2.1.3.1); “Mechanical Disruption of Engineered Barriers” (NRC 2003 [DIRS 163274], Section 2.2.1.3.2); “Radionuclide Release Rates and Solubility Limits” (Section 2.2.1.3.4); “Climate and Infiltration” (NRC 2003 [DIRS 163274], Section 2.2.1.3.5); and “Flow Paths in the Unsaturated Zone” (NRC 2003 [DIRS 163274], Section 2.2.1.3.6). The descriptions and technical bases provide transparent and traceable support for the abstraction of quantity and chemistry of water contacting engineered barriers and waste forms.
- (3) Important design features, such as waste package design and material selection, backfill, drip shield, ground support, thermal loading strategy, and degradation processes, are adequate to determine the initial and boundary conditions for calculations of the quantity and chemistry of water contacting engineered barriers and waste forms.
- (4) Spatial and temporal abstractions appropriately address physical couplings (thermal-hydrologic-mechanical-chemical). For example, the U.S. Department of Energy evaluates the potential for focusing of water flow into drifts, caused by coupled thermal-hydrologic-mechanical-chemical processes.
- (5) Sufficient technical bases and justification are provided for total system performance assessment assumptions and approximations for modeling coupled thermal-hydrologic mechanical-chemical effects on seepage and flow, the waste package chemical environment, and the chemical environment for radionuclide release. The effects of distribution of flow on the amount of water contacting the engineered barriers and waste forms are consistently addressed, in all relevant abstractions.
- (6) The expected ranges of environmental conditions within the waste package emplacement drifts, inside of breached waste packages, and contacting the waste forms and their evolution with time, are identified. These ranges may be developed to include: (i) the effects of the drip shield and backfill on the quantity and chemistry of water (e.g., the potential for condensate formation and dripping from the underside of the shield); (ii) conditions that promote corrosion of engineered barriers and degradation of waste forms; (iii) irregular wet and dry cycles; (iv) gamma-radiolysis; and (v) size and distribution of penetrations of engineered barriers.

- (7) The model abstraction for quantity and chemistry of water contacting engineered barriers and waste forms is consistent with the detailed information on engineered barrier design and other engineered features. For example, consistency is demonstrated for: (i) dimensionality of the abstractions; (ii) various design features and site characteristics; and (iii) alternative conceptual approaches. Analyses are adequate to demonstrate that no deleterious effects are caused by design or site features that the U.S. Department of Energy does not take into account in this abstraction.
- (8) Adequate technical bases are provided, including activities such as independent modeling, laboratory or field data, or sensitivity studies, for inclusion of any thermal-hydrologic-mechanical-chemical couplings and features, events, and processes.
- (9) Performance-affecting processes that have been observed in thermal-hydrologic tests and experiments are included into the performance assessment. For example, the U.S. Department of Energy either demonstrates that liquid water will not reflux into the underground facility or incorporates refluxing water into the performance assessment calculation, and bounds the potential adverse effects of alteration of the hydraulic pathway that result from refluxing water.

Acceptance Criterion 2–Data Are Sufficient for Model Justification.

- (1) Geological, hydrological, and geochemical values used in the license application are adequately justified. Adequate description of how the data were used, interpreted, and appropriately synthesized into the parameters is provided.
- (2) Sufficient data were collected on the characteristics of the natural system and engineered materials to establish initial and boundary conditions for conceptual models of thermal-hydrologic-mechanical-chemical coupled processes, that affect seepage and flow and the engineered barrier chemical environment.
- (4) Sufficient information to formulate the conceptual approach(es) for analyzing water contact with the drip shield, engineered barriers, and waste forms is provided.

Acceptance Criterion 3–Data Uncertainty Is Characterized and Propagated Through the Model Abstraction.

- (1) Models use parameter values, assumed ranges, probability distributions, and bounding assumptions that are technically defensible, reasonably account for uncertainties and variabilities, and do not result in an under representation of the risk estimate.
- (2) Parameter values, assumed ranges, probability distributions, and bounding assumptions used in the total system performance assessment calculations of quantity and chemistry of water contacting engineered barriers and waste forms are technically defensible and reasonable, based on data from the Yucca Mountain region (e.g., results from large block and drift-scale heater and niche tests), and a combination of

techniques that may include laboratory experiments, field measurements, natural analog research, and process-level modeling studies.

- (3) Input values used in the total system performance assessment calculations of quantity and chemistry of water contacting engineered barriers (e.g., drip shield and waste package) are consistent with the initial and boundary conditions and the assumptions of the conceptual models and design concepts for the Yucca Mountain site. Correlations between input values are appropriately established in the U.S. Department of Energy total system performance assessment. Parameters used to define initial conditions, boundary conditions, and computational domain in sensitivity analyses involving coupled thermal-hydrologic-mechanical-chemical effects on seepage and flow, the waste package chemical environment, and the chemical environment for radionuclide release, are consistent with available data. Reasonable or conservative ranges of parameters or functional relations are established.
- (4) Adequate representation of uncertainties in the characteristics of the natural system and engineered materials is provided in parameter development for conceptual models, process-level models, and alternative conceptual models. The U.S. Department of Energy may constrain these uncertainties using sensitivity analyses or conservative limits. For example, the U.S. Department of Energy demonstrates how parameters used to describe flow through the Engineered Barrier System bound the effects of backfill and excavation-induced changes.

Acceptance Criterion 4—Model Uncertainty Is Characterized and Propagated Through the Model Abstraction.

- (1) Alternative modeling approaches of features, events, and processes are considered and are consistent with available data and current scientific understanding, and the results and limitations are appropriately considered in the abstraction.
- (2) Alternative modeling approaches are considered and the selected modeling approach is consistent with available data and current scientific understanding. A description that includes a discussion of alternative modeling approaches not considered in the final analysis and the limitations and uncertainties of the chosen model is provided.
- (3) Consideration of conceptual model uncertainty is consistent with available site characterization data, laboratory experiments, field measurements, natural analog information and process-level modeling studies; and the treatment of conceptual model uncertainty does not result in an under-representation of the risk estimate.
- (4) Adequate consideration is given to effects of thermal-hydrologic-mechanical-chemical coupled processes in the assessment of alternative conceptual models. These effects may include: (i) thermal-hydrologic effects on gas, water, and mineral chemistry; (ii) effects of microbial processes on the engineered barrier chemical environment and the chemical environment for radionuclide release; (iii) changes in water chemistry that may result from the release of corrosion products from the engineered barriers and interactions between engineered materials and groundwater; and (iv) changes in

boundary conditions (e.g., drift shape and size) and hydrologic properties, relating to the response of the geomechanical system to thermal loading.

Acceptance Criterion 5—Model Abstraction Output Is Supported by Objective Comparisons.

- (1) The models implemented in this total system performance assessment abstraction provide results consistent with output from detailed process-level models and/or empirical observations (laboratory and field testings and/or natural analogs).
- (2) Abstracted models for coupled thermal-hydrologic-mechanical-chemical effects on seepage and flow and the engineered barrier chemical environment, as well as on the chemical environment for radionuclide release, are based on the same assumptions and approximations demonstrated to be appropriate for process-level models or closely analogous natural or experimental systems. For example, abstractions of processes, such as thermally induced changes in hydrological properties, or estimated diversion of percolation away from the drifts, are adequately justified by comparison to results of process-level modeling, that are consistent with direct observations and field studies.
- (3) Accepted and well-documented procedures are used to construct and test the numerical models that simulate coupled thermal-hydrologic-mechanical-chemical effects on seepage and flow, engineered barrier chemical environment, and the chemical environment for radionuclide release. Analytical and numerical models are appropriately supported. Abstracted model results are compared with different mathematical models, to judge robustness of results.

4.2.2 Applicable Acceptance Criteria from Section 2.2.1.3.4, “Radionuclide Release Rates and Solubility Limits”

The following acceptance criteria, listed in Section 2.2.1.3.4.3 of *Yucca Mountain Review Plan, Final Report* (NRC 2003 [DIRS 163274]), apply to this abstraction. These acceptance criteria are based on meeting the relevant requirements of 10 CFR 63.114(a)–(c) and (e)–(g) [DIRS 178394], as they relate to the radionuclide release rates and solubility limits model abstraction.

Acceptance Criterion 1—System Description and Model Integration Are Adequate.

- (1) Total system performance assessment adequately incorporates important design features, physical phenomena, and couplings, and uses consistent and appropriate assumptions throughout the radionuclide release rates and solubility limits abstraction process.
- (2) The abstraction of radionuclide release rates uses assumptions, technical bases, data, and models that are appropriate and consistent with other related U.S. Department of Energy abstractions. For example, the assumptions used for this model abstraction are consistent with the abstractions of “Degradation of Engineered Barriers” (NRC 2003 [DIRS 163274], Section 2.2.1.3.1); “Mechanical Disruption of Engineered Barriers”

(NRC 2003 [DIRS 163274], Section 2.2.1.3.2); “Quantity and Chemistry of Water Contacting Engineered Barriers and Waste Forms” (NRC 2003 [DIRS 163274], Section 2.2.1.3.3); “Climate and Infiltration” (NRC 2003 [DIRS 163274], Section 2.2.1.3.5); and “Flow Paths in the Unsaturated Zone” (NRC 2003 [DIRS 163274], Section 2.2.1.3.6). The descriptions and technical bases provide transparent and traceable support for the abstraction of radionuclide release rates.

- (3) The abstraction of radionuclide release rates provides sufficient, consistent design information on waste packages and Engineered Barrier Systems. For example, inventory calculations and selected radionuclides are based on the detailed information provided on the distribution (both spatially and by compositional phase) of the radionuclide inventory, within the various types of high-level radioactive waste.
- (4) The U.S. Department of Energy reasonably accounts for the range of environmental conditions expected inside breached waste packages and in the engineered barrier environment surrounding the waste package. For example, the U.S. Department of Energy should provide a description and sufficient technical bases for its abstraction of changes in hydrologic properties in the near field, caused by coupled thermal-hydrologic-mechanical-chemical processes.
- (5) The description of process-level conceptual and mathematical models is sufficiently complete, with respect to thermal-hydrologic processes affecting radionuclide release from the emplacement drifts. For example, if the U.S. Department of Energy uncouples coupled processes, the demonstration that uncoupled model results bound predictions of fully coupled results is adequate.
- (6) Technical bases for inclusion of any thermal-hydrologic-mechanical-chemical couplings and features, events, and processes in the radionuclide release rates and solubility Review Plan for Safety Analysis Report limits model abstraction are adequate. For example, technical bases may include activities, such as independent modeling, laboratory or field data, or sensitivity studies.

Acceptance Criterion 2–Data Are Sufficient for Model Justification.

- (1) Geological, hydrological, and geochemical values used in the license application are adequately justified. Adequate description of how the data were used, interpreted, and appropriately synthesized into the parameters is provided.
- (2) Sufficient data have been collected on the characteristics of the natural system and engineered materials to establish initial and boundary conditions for conceptual models and simulations of thermal-hydrologic-chemical coupled processes. For example, sufficient data should be provided on design features, such as the type, quantity, and reactivity of materials, that may affect radionuclide release for this abstraction.
- (4) The corrosion and radionuclide release testing program for high-level radioactive waste forms intended for disposal provides consistent, sufficient, and suitable data for the in-package and in-drift chemistry used in the abstraction of radionuclide release

rates and solubility limits. For expected environmental conditions, the U.S. Department of Energy provides sufficient justification for the use of test results, not specifically collected from the Yucca Mountain site, for engineered barrier components, such as high-level radioactive waste forms, drip shield, and backfill.

Acceptance Criterion 3—Data Uncertainty Is Characterized and Propagated Through the Model Abstraction.

- (1) Models use parameter values, assumed ranges, probability distributions, and bounding assumptions that are technically defensible, reasonably account for uncertainties and variabilities, and do not result in an under representation of the risk estimate.
- (2) Parameter values, assumed ranges, probability distributions, and bounding assumptions used in the abstractions of radionuclide release rates and solubility limits in the total system performance assessment are technically defensible and reasonable based on data from the Yucca Mountain region, laboratory tests, and natural analogs. For example, parameter values, assumed ranges, probability distributions, and bounding assumptions adequately reflect the range of environmental conditions expected inside breached waste packages.
- (3) DOE uses reasonable or conservative ranges of parameters or functional relations to determine effects of coupled thermal-hydrologic-chemical processes on radionuclide release. These values are consistent with the initial and boundary conditions and the assumptions for the conceptual models and design concepts for natural and engineered barriers at the Yucca Mountain site. If any correlations between the input values exist, they are adequately established in the total system performance assessment. For example, estimations are based on a thermal loading and ventilation strategy; Engineered Barrier System design (including drift liner, backfill, and drip-shield); and natural system masses and fluxes that are consistent with those used in other abstractions.
- (4) Uncertainty is adequately represented in parameter development for conceptual models, process models, and alternative conceptual models considered in developing the abstraction of radionuclide release rates and solubility limits, either through sensitivity analyses or use of bounding analyses.
- (5) Parameters used to describe flow through and out of the engineered barrier, sufficiently bound the effects of backfill, excavation-induced changes, and thermally induced mechanical changes that affect flow.
- (8) DOE adequately considers the uncertainties, in the characteristics of the natural system and engineered materials, such as the type, quantity, and reactivity of material, in establishing initial and boundary conditions for conceptual models and simulations of thermal-hydrologic-chemical coupled processes that affect radionuclide release.

Acceptance Criterion 4—Model Uncertainty Is Characterized and Propagated Through the Model Abstraction.

- (1) Alternative modeling approaches of features, events, and processes are considered and are consistent with available data and current scientific understanding, and the results and limitations are appropriately considered in the abstraction.
- (2) In considering alternative conceptual models for radionuclide release rates and solubility limits, DOE uses appropriate models, tests, and analyses that are sensitive to the processes modeled for both natural and engineering systems. Conceptual model uncertainties are adequately defined and documented, and effects on conclusions regarding performance are properly assessed. For example, in modeling flow and radionuclide release from the drifts, DOE represents significant discrete features, such as fault zones, separately, or demonstrates that their inclusion in the equivalent continuum model produces a conservative effect on calculated performance.
- (3) Consideration of conceptual model uncertainty is consistent with available site characterization data, laboratory experiments, field measurements, natural analog information and process-level modeling studies; and the treatment of conceptual model uncertainty does not result in an under-representation of the risk estimate.
- (4) The effects of thermal-hydrologic-chemical coupled processes that may occur in the natural setting, or from interactions with engineered materials, or their alteration products, on radionuclide release, are appropriately considered.

Acceptance Criterion 5—Model Abstraction Output Is Supported by Objective Comparisons.

- (1) The models implemented in this total system performance assessment abstraction provide results consistent with output from detailed process-level models and/or empirical observations (laboratory and field testings and/or natural analogs);
- (3) DOE adopts well-documented procedures that have been accepted by the scientific community to construct and test the numerical models, used to simulate coupled thermal-hydrologic-chemical effects on radionuclide release. For example, DOE demonstrates that the numerical models used for high-level radioactive waste degradation and dissolution, and radionuclide release from the Engineered Barrier System, are adequate representations; include consideration of uncertainties; and are not likely to underestimate radiological exposures to the reasonably maximally exposed individual and releases of radionuclides into the accessible environment; and...[.]

4.3 CODES, STANDARDS, AND REGULATIONS

The relevant codes, standards, and regulations for the development of the RTA are listed in Section 9.2.

5. ASSUMPTIONS

5.1 ALL SEEPAGE FALLS ONTO DRIP SHIELD/WASTE PACKAGE

Assumption: It is assumed that the locations of seeps in the emplacement drifts are random with respect to waste package locations, but once a seep occurs, its location does not change over time. It is also assumed that fragments of the drip shield that may rest on the waste package, or fallen rock that may rest on the drip shield or waste package, do not divert any seepage flux. In addition, it is assumed that all seepage into the drift falls on the crown of the drip shield, and in the absence of a drip shield, all seepage falls on the crown of the waste package. In the event of a breach in the drip shield, all the seepage that penetrates the drip shield contacts the waste package.

Basis: Once seepage occurs during cooldown, the fracture characteristics that control the location of seepage are not expected to change. If such changes occur, they are likely to be limited in extent, or to occur in a random manner for many waste packages such that there is no overall, significant effect on the interaction of seepage water with waste forms. The mean seepage for the degraded drift is greater than for the non-degraded case, but the factors controlling seep locations are still likely to occur in a random manner for many waste packages. Seepage into the drift is more likely to flow down the sides of the drift the further away from the drift crown that it enters the drift, so dripping is more likely to occur from near the drift crown. Although seismic activity may move waste packages away from being centrally aligned along the drift, there is not room for significant movement away from the center. Thus, dripping from the crown of the drift will tend to fall primarily near the crown of the drip shield or waste package. Rock fall could also potentially shift the drift shield and waste package off center. However, rubble will fall randomly and on average tend to be distributed equally on both sides of the waste packages and maintain their alignment, so again, dripping from the crown of the drift is likely to fall in the proximity of the crown of the drip shield or waste package. If rubble covers the drift shield and waste package, it will tend to divert flow to the sides of the drift; in this case, this assumption would overestimate flow into breaches.

Confirmation Status: This assumption does not require confirmation because it reasonably maximizes the duration of seepage contact with drip shields and waste packages as represented in the TSPA, while simplifying the calculation. It also reasonably maximizes the flux of dripping water available to flow through breaches in the drip shield or waste package, once such flow is initiated as represented in the TSPA. Without a complex model that accounts for the possible distribution of dripping throughout the drift and for changes in the location or alignment of waste packages over time, any diversion from the crown location for drips, or modeling seepage as distributed over the entire surface of drip shields and waste packages, would reduce the flow through breached waste packages and potentially underestimate releases.

Use in the Model: This assumption is used throughout Sections 6 and 7.

5.2 EVAPORATION FROM A DRIP SHIELD DOES NOT OCCUR

Assumption: It is assumed that there is no evaporation of seepage water from the surface of the drip shield.

Basis: The heat output from the waste package will cause the drip shield generally to be hotter than the drift wall from which seepage water is dripping. Some seepage water that drips onto the drip shield may be evaporated, thereby reducing the flux of water through the drip shield. A reduction in the quantity of water flux through the drip shield reduces the potential for advective transfer and subsequent release and transport of radionuclides from the waste packages. Ignoring the process of evaporation in this analysis therefore reasonably bounds (maximizes) the impacts of the seepage flux on waste packages.

Although some splashing or splattering can occur as water droplets impinge on the drip shield, the splash distance would be limited, and the water would effectively be redistributed over the top of the drip shield. If water droplets were to fall near the edge of the top plate, some splashes could fall onto the invert or lower walls of the drift and drain directly into the invert. This situation would reduce the degrading effects of water dripping on the drip shield and therefore is eliminated from consideration in order reasonably to bound the impacts of the seepage flux on waste packages.

Confirmation Status: This assumption does not require confirmation because it provides for a reasonable upper bound on the flux available to interact with the drip shield and waste package, and reasonably bounds (maximizes) the potential degrading effects of seepage water on the drift environment.

Use in the Model: This assumption is used in Sections 6.3.2.4, 6.5.1.1, and 7.2.1.

5.3 EVAPORATION FROM A WASTE PACKAGE DOES NOT OCCUR

Assumption: It is assumed that evaporation of water from the surface or interior of a waste package does not occur.

Basis: Although heat released by spent nuclear fuel (SNF) will evaporate seepage water that drips onto the surface of or flows into breaches in a waste package, this process is not included in the analysis. Advective transport within the EBS is not possible if evaporation eliminates liquid fluxes. There is insufficient information to quantify the degree of water evaporation in a waste package, making modeling of internal waste package evaporation intractable, so no evaporation of water is considered. Therefore, evaporative processes are eliminated from this analysis, which reasonably maximizes the potential for advective transport of radionuclides. This assumption comes into play only after the thermal peak period of roughly 1,500 years (SNL 2007 [DIRS 181383], Figure 6.3-78[a]), since dripping onto a waste package will not occur until the drift has cooled sufficiently for liquid water to be present. Because the relative humidity in the drift is low during the thermal peak period, condensation on cooler waste packages is unlikely, precluding evaporation from those surfaces. By the time waste packages fail, they will have cooled off to the point where their temperature is close to the surroundings, and evaporation from a waste package is unlikely to have a significant effect.

Confirmation Status: This assumption does not require confirmation because it is used to ensure the maximum potential for advective transport of radionuclides.

Use in the Model: This assumption is used in Sections 6.3.3, 6.5.1.1.3, and 7.2.2.

5.4 PRODUCTION OR CONSUMPTION OF WATER BY CHEMICAL REACTIONS DOES NOT OCCUR

Assumption: It is assumed that chemical reactions in the EBS neither produce nor consume water and therefore do not affect the water mass balance in the EBS.

Basis: Chemical processes in the EBS will consume and, possibly, produce water. Conversion of CSNF to schoepite ($\text{UO}_3 \cdot 2\text{H}_2\text{O}$), goethite (FeOOH), and other hydrated corrosion products will likely remove large quantities of water from incoming fluids and the vapor phase. This might stabilize anhydrous CSNF degradation products, such as U_4O_9 and U_3O_8 as well as hematite over goethite or HFO. Hematite is likely to be a less effective sorber for radionuclides than goethite or HFO. Over time, hydrated phases will alter to less hydrated phases, and release water to the breached waste package in the process. While water uptake by waste form degradation should be relatively fast, the release of water from dehydration reactions should be slower. The overall uptake and release of water over time is certainly a complex function of water availability, temperature, and time, and is difficult to predict accurately. The assumption of no water uptake or release is a simplification of a complex process that will tend to over-predict the water saturation in a breached waste package.

However, consumption of water, particularly by corrosion reactions, is likely to occur. Anoxic corrosion of iron inside a waste package is a prime example of a water-consuming process that can consume enough water to impact flow through a waste package. Formation of hydrated corrosion products, particularly iron oxyhydroxides such as goethite, may also consume water. The amount of water potentially consumed by corrosion of steel inside a waste package can be estimated from the mass of corrosion products. Using a 21-PWR TAD waste package as an example, Table 6.3-8 lists the mass of goethite (FeOOH) that will be produced if all steel internal components except for the shield plug are fully corroded as 25,700 kg in the corrosion products domain. Using the corrosion stoichiometry given in Equation 6.6.2-5, the amount of water consumed to produce that quantity of goethite is approximately 2.6 m^3 . Since the lifetime of stainless steel components ranges from 49,800 yr to 5.08×10^6 yr (as estimated in Section 6.5.2.2.1), water is consumed at a miniscule rate. In Section 6.6.2, the rate of diffusion of water into a waste package through stress corrosion cracks alone is estimated and shown to be greater than the rate of consumption by corrosion of stainless steel. Therefore, water consumption by the primary reaction that occurs within a breached waste package is negligible. Corrosion of waste package internal components, as modeled in the TSPA, occurs at a constant rate and does not depend on how much water is present. So the same amount of corrosion products will be present regardless of whether water is consumed in the process.

Water absorption by hygroscopic salts deposited on the drip shield and waste package surfaces as dust or as precipitates would consume water as long as the relative humidity remains below the deliquescence point of the salts, although the quantity of water consumed is likely to be negligible. Neglecting consumption of water in the EBS radionuclide transport analysis is a reasonably bounding assumption, providing more water for dissolution and transport of radionuclides, and potentially greater releases, than would otherwise occur.

Confirmation Status: This assumption does not require confirmation because it reasonably bounds (maximizes) the amount of water potentially available for advective and diffusive transport and release of radionuclides.

Use in the Model: This assumption is used throughout Sections 6 and 7.

5.5 THIN WATER FILMS ALWAYS EXIST BELOW THE BOILING POINT OF WATER

Assumption: For the purpose of calculating the diffusive transport of radionuclides, a thin film of adsorbed water is assumed always to exist on the surfaces of internal waste package components and corrosion products in a breached waste package. This water film is assumed to be continuous and to behave as bulk liquid insofar as allowing radionuclides to diffuse through it. Colloids are also assumed to diffuse through this film. At and above the boiling point of water in the repository, the thin film is assumed not to exist, and no transport of radionuclides takes place.

Basis: All surfaces exposed to water vapor will adsorb water. The amount of adsorbed water vapor depends principally on the nature of the sorbing material and the ambient relative humidity.

The first layers of adsorbed water often do not contain ions from the sorbing solid (Lee and Staehle 1994 [DIRS 154380], p. 73). This indicates that multiple water layers are needed in order for solid species (such as radionuclides) to dissolve and diffuse. Thus, to assume that radionuclides will diffuse through the adsorbed water film regardless of its thickness will overestimate releases of radionuclides. It is also assumed that the water film is continuous, i.e., there are no gaps in the film from one particle or surface to the next, so that radionuclides can diffuse throughout the waste package interior and through corrosion products. In determining the amount of water adsorbed on surfaces inside the waste package, the relative humidity inside a degraded waste package is assumed to be the same as in the drift.

Above the boiling point of water, the thin films are assumed not to exist. Due to the lack of a continuous water film, transport cannot take place. The boiling point may vary due to the elevation of the repository or to dissolved salts in the water film. Temperatures above the boiling point will exist at least through the thermal peak period of roughly 1,500 years (SNL 2007 [DIRS 181383], Figure 6.3-78[a]), and may continue to exist on certain waste packages well beyond that time.

Confirmation Status: This assumption does not require confirmation because it allows for radionuclide transport due to the presence of a continuous thin film of water on the surfaces of internal waste package components and corrosion products.

Use in the Model: This assumption is used in Sections 6.3.4, 6.5.2, and 7.2.1.

5.6 NO CORROSION PRODUCTS EXIST IN THE INVERT

Assumption: It is assumed that no corrosion products exist in the invert.

Basis: Neglecting the corrosion products in the invert is an assumption that reasonably maximizes the potential transport of radionuclides through the invert. The invert consists of a carbon steel structural frame supported on the lower drift walls, and of crushed tuff ballast placed below and between the steel frame members. The invert steel structure consists of transverse beams anchored at each end on the drift wall, and of three longitudinal beams which directly support the waste package pallet. When the invert steel beams corrode, most of the iron oxide corrosion products will end up in the crushed tuff component of the invert. In addition, communication cables will eventually corrode, leaving copper oxide corrosion products in the invert. The crushed tuff has little radionuclide sorptive capacity compared to the metal oxide corrosion products, which are capable of sorbing large amounts of radionuclides, potentially enhancing the barrier capability of the invert. However, the corrosion products in the invert will tend to be localized and widely separated. For example, the transverse support beams in the invert are spaced 1.524 m (5 ft 0 in.) apart (BSC 2007 [DIRS 180181]). Thus, the corrosion products of the support beams will reside in a strip a few centimeters wide separated by 1.524 m of crushed tuff containing little or no corrosion products. Compared with the length of a waste package ranging from 3.54 m (5 DHLW/DOE SNF – Short, SNL 2007 [DIRS 179567], Table 4-8) to 5.69 m (Naval long, SNL 2007 [DIRS 179567], Table 4-6), the width of regions within the invert that would potentially contain corrosion products is small. Therefore, the chance of radionuclides being released from the waste package and passing through corrosion products in the invert is proportionately small. Although the invert will contain steel corrosion products, it is bounding in terms of radionuclide releases to neglect their presence.

Confirmation Status: This assumption does not require confirmation because it is a bounding assumption that reduces the potential effectiveness of the invert as a transport barrier; i.e., the potential for radionuclide sorption by steel corrosion products is ignored.

Use in the Model: This assumption is used in Section 6.3.4.2.

5.7 NO PHYSICAL FILTRATION OR GRAVITATIONAL SETTLING OF COLLOIDS

Assumption: It is assumed that physical filtration and gravitational settling of colloids will not occur within the waste package and the drift.

Basis: Filtration processes may affect transport of radionuclide-bearing colloids in the waste and EBS. Colloid filtration as discussed here refers to the physical removal of colloids from a flow system by pore clogging, sieving, and straining. Included in the definition of filtration is “film straining,” in which colloid movement is restricted by hydrodynamic forces when the water film in an unsaturated porous medium is thinner than the diameter of the colloid particle. Filtration of colloids generally means the retention of colloids moving with the suspending fluid in pores, channels, and fracture apertures that are too small or dry to allow passage of the colloids.

In the RTA, the assumption is made that all stable colloids formed within the waste package (the calculated colloid source term) exit the package and enter the invert without filtration. These colloids will then move through the invert material without being subjected to filtration until they reach the underlying UZ.

Filtration of colloids is excluded on the basis of low consequence (DTN: MO0706SPAFEPLA.001 [DIRS 181613], FEP Number 2.1.09.20.0A). Since filtration within the waste package and the invert will actually occur to some extent, the modeling approach of neglecting filtration overestimates the potential impact of colloid-facilitated transport of radionuclides in the TSPA dose calculations and is considered bounding.

In the RTA, it is assumed that all stable radionuclide-bearing colloids will not be subject to gravitational settling. Assuming that gravitational settling will not occur, results in an overestimation of the potential consequences of colloid-facilitated transport of radionuclides and is considered bounding.

Confirmation Status: This assumption does not require confirmation because it is a bounding assumption that reduces the potential effectiveness of the invert as a transport barrier.

Use in the Model: This assumption is used in Section 6.5.1.2.

6. MODEL DISCUSSION

6.1 MODELING OBJECTIVE

The objective of the Radionuclide Transport Abstraction (RTA) is to provide the conceptual model used to determine the time-dependent flux of radionuclides from the Engineered Barrier System (EBS) to the unsaturated zone (UZ) in the Total System Performance Assessment (TSPA). In particular, this model is used to quantify such releases from a failed waste package and the subsequent transport of those radionuclides through the EBS to the emplacement drift wall/UZ interface. The basic time-dependent inputs to the RTA in TSPA calculations consist of the drift seepage influx, the environmental conditions in the drift (temperature, relative humidity, and water chemistry), and the degradation state of the EBS components. Outputs consist of the rates of radionuclide fluxes to the UZ as a result of advective and diffusive transport, radionuclide solubility, retardation, the degree of liquid saturation of the waste form and invert materials, and the impact of colloids on potential radionuclide transport. The RTA is implemented directly into the TSPA GoldSim model to compute the release rates; details of the implementation are provided in Section 6.5.2.

6.1.1 Engineered Barrier System Components

The EBS consists of the emplacement drift, waste form, cladding, drip shield, the waste package on an emplacement pallet, and an invert constructed with steel supports and filled between the steel framework with crushed tuff (SNL 2007 [DIRS 179354], Section 4.1.1). The RTA focuses on the drip shield, waste package, and invert. Each of the components of the EBS is designed to prevent or delay the mobilization and release of radionuclides into the geologic environment (see Section 6.7 for a summary of barrier capabilities). For example, the drip shield is designed to redirect any seepage that flows into the drift away from the waste package. The invert supports the waste package and emplacement pallet. It resists diffusive transport of radionuclides in liquids if the liquid saturation in the crushed tuff is low. Figure 6.1-1 presents a typical cross-section of an emplacement drift and the major components of the EBS.

The drip shield is fabricated from titanium, a corrosion-resistant material to provide long-term effectiveness. The waste package outer corrosion barrier is comprised of Alloy 22 (UNS N06022). The major corrosive processes are stress corrosion cracking in the closure lid welds of the waste package, localized corrosion in the waste package outer corrosion barrier, and general corrosion for both the drip shield and waste package.

Once the drip shield fails (i.e., is initially breached), a portion of the total dripping flux can drip onto the waste package. It is possible for breaches to occur at the gap between adjacent waste packages. If breaches in the drip shield occur at the gap between two drip shield segments, which happens to be above a gap between waste packages, the dripping flux would fall directly to the invert, avoiding the waste package. The possibility that breaches in the drip shield can occur over a gap, allowing liquid to bypass the waste package, is not considered in the RTA.

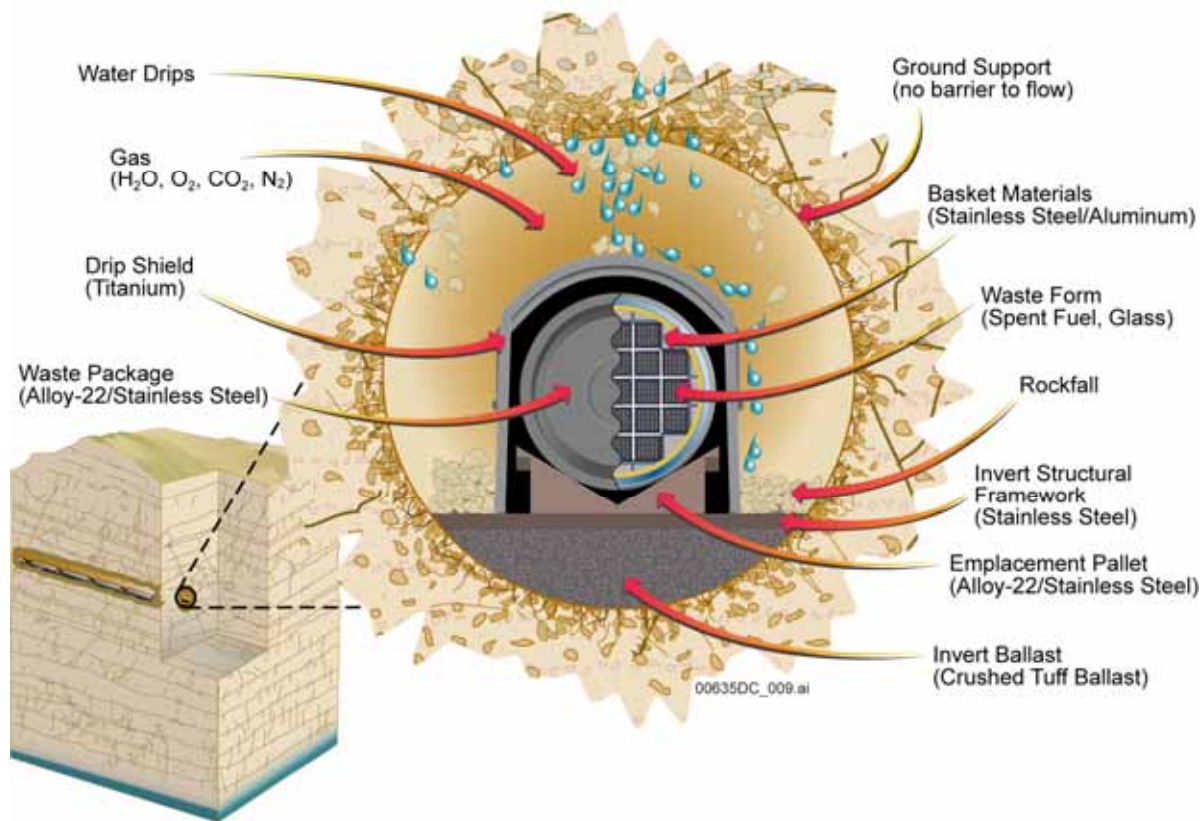


Figure 6.1-1. Schematic Diagram of a Typical Emplacement Drift and the Major Components of the EBS

After the waste package fails (breached by corrosion, seismic damage, or early failure mechanisms), a portion of the water that flows through the drip shield can enter the waste package, mobilizing radionuclides in any degraded waste form through cladding that has also failed, and transporting these radionuclides into the UZ. Diffusion is the primary transport mechanism when the flux into the waste package is small or zero, or if stress corrosion cracks are the only penetrations through the waste package. Advective transport is important when the dripping flux occurs. In this case, advective fluxes can pass through the breaches in the drip shield and waste package. In the case of an igneous intrusion, neither the drip shield nor the waste packages survives, so all of the dripping flux flows through the waste package.

6.1.2 Scenario Classes for the TSPA

A modeling case is a well-defined, connected sequence of features, events, and processes (FEPs) that can be thought of as an outline of a possible future condition in the repository system. Modeling cases can be designated as undisturbed, in which case the performance would be the expected or nominal performance of the system. Or, modeling cases can be designated as disturbed, if altered by disruptive events, such as human intrusion, or by natural phenomena,

such as volcanism or nuclear criticality. A scenario class is a set of related modeling cases that share sufficient similarities to aggregate them usefully for the purposes of screening or analysis. The scenario classes included in the TSPA are typically the Nominal Scenario Class, Igneous Scenario Class, and Seismic Scenario Class, although some stylized modeling cases are separately examined to evaluate the effect of early failure of waste packages and drip shields in terms of annual dose under nominal conditions (defined as an early failure waste package and early failure drip shield modeling case) and the effect of damage to a waste package from drilling by human activity (defined as the human intrusion modeling case). Each modeling case defines the waste package breach mechanisms, amount of breach, and the timing of the breaches besides defining other system perturbations such as changes in physical-chemical-thermal conditions in the EBS, UZ, and saturated zone (SZ) components of the TSPA Model. Based on the definition of the modeling case a set of processes is modeled in TSPA, which characterizes the nature of transport (whether primarily diffusive or advective) out of the waste package and EBS.

6.2 FEATURES, EVENTS, AND PROCESSES INCLUDED IN THE MODEL

A comprehensive list of FEPs potentially relevant to postclosure performance of the Yucca Mountain repository is presented in *FY 2007 LA FEP List and Screening* (DTN: MO0706SPAFEPLA.001 [DIRS 181613]). Table 6.2-1 provides a list of FEPs that are included in the TSPA Models described in this model document, summarizes the details of their implementation in TSPA, and provides specific references to sections within this document. Screening arguments for both included and excluded FEPs are summarized in DTN: MO0706SPAFEPLA.001 [DIRS 181613].

Table 6.2-1. Included FEPs for This Report

FEP No.	FEP Name/FEP Description	Section Where Disposition Is Described
2.1.06.06.0A	Effects of drip shield on flow	6.3.2.4 6.5.1.1
2.1.08.04.0A	Condensation forms on roofs of drifts (drift-scale cold traps)	6.3
2.1.08.04.0B	Condensation forms at repository edges (repository-scale cold traps)	6.3
2.1.08.05.0A	Flow through invert	6.3 6.5
2.1.08.06.0A	Capillary effects (wicking) in EBS	6.3 6.5
2.1.08.07.0A	Unsaturated flow in the EBS	6.3 6.5
2.1.09.05.0A	Sorption of dissolved radionuclides in EBS	6.3.4.2 6.5.1.2 6.5.2

Table 6.2-1. Included FEPs for This Report (Continued)

FEP No.	FEP Name/FEP Description	Section Where Disposition Is Described
2.1.09.08.0A	Diffusion of dissolved radionuclides in EBS	6.3.1.2 6.3.4.1 6.5.1.2 6.5.2.1
2.1.09.08.0B	Advection of dissolved radionuclides in EBS	6.3.1.2
2.1.09.19.0B	Advection of colloids in EBS	6.3.4.4 6.5.1.2 6.5.2
2.1.09.24.0A	Diffusion of colloids in EBS	6.3.4.4 6.5.1.2 6.5.2
2.1.11.09.0A	Thermal effects on flow in the EBS	6.3.1.1
2.2.07.06.0B	Long-term release of radionuclides from the repository	6

6.3 BASE CASE CONCEPTUAL MODEL

6.3.1 Introduction and Overview

6.3.1.1 EBS Flow Abstraction

The primary source of inflow to the EBS is the dripping flux from the crown (roof) of the drift and includes seepage flux and any condensation that may occur on the walls of the drift above the drip shield. The seepage flux is driven by downward infiltration through the existing fracture system at Yucca Mountain. The seepage flux is conceptualized to flow from discrete fractures above the roof of the drift, falling vertically downward, and is represented in the TSPA Model through *Abstraction of Drift Seepage* (SNL 2007 [DIRS 181244]). Condensation on the drift walls is represented in the TSPA Model through the *In-Drift Natural Convection and Condensation* model (SNL 2007 [DIRS 181648]). A secondary source of inflow to the EBS is imbibition into the invert crushed tuff particles from the surrounding UZ rock matrix. The inflow from these sources can flow through the EBS along eight pathways, as shown in Figure 6.3-1.

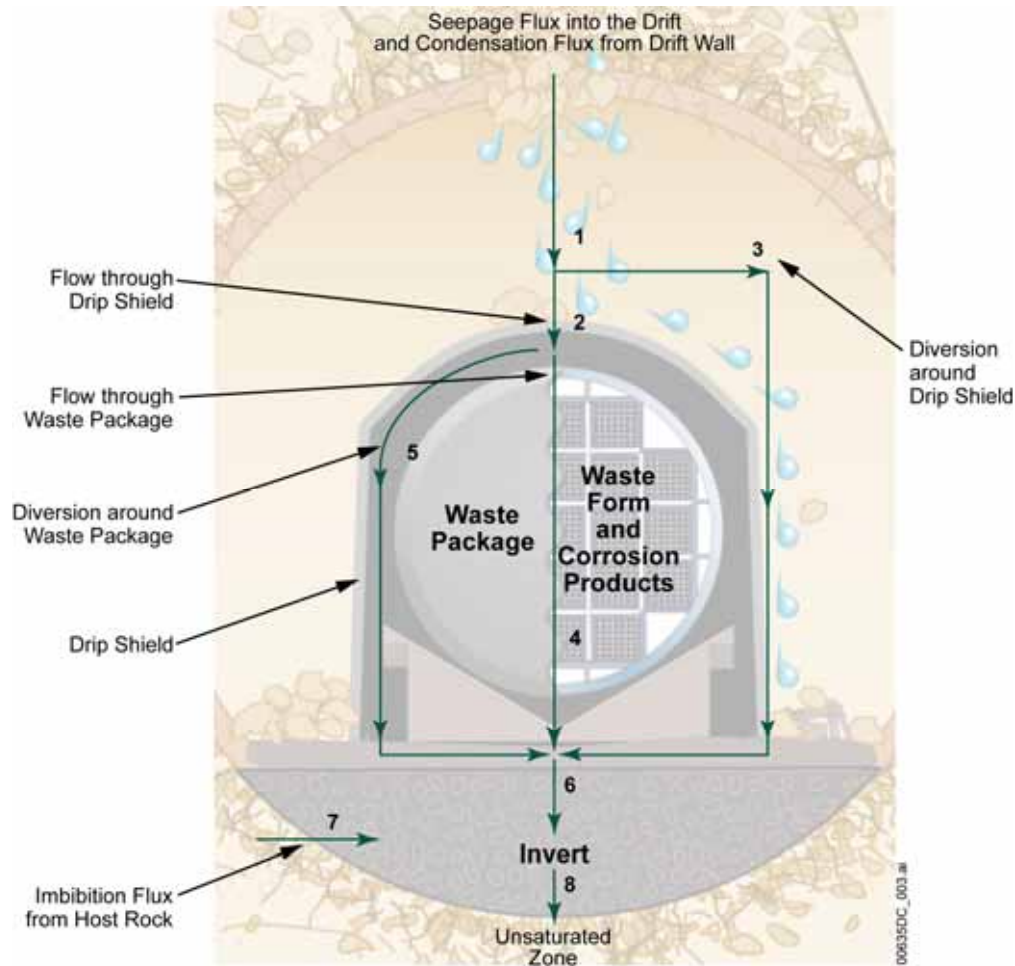


Figure 6.3-1. Schematic of the Potential Flow Pathways in the EBS

The eight pathways are (with the volumetric water flux through pathway j designated by F_j [$\text{m}^3 \text{s}^{-1}$]):

1. **Total dripping flux (F_1)**—This is the seepage inflow (dripping flux) from the crown (roof) of the drift plus any condensation that may occur on the walls of the drift above the drip shield.
2. **Flux through the drip shield (F_2)**—The flux through the drip shield is based on the presence of fully-penetrating patches due to general corrosion. Localized corrosion of the drip shield after closure of the repository has been screened out on the basis of low consequence (DTN: MO0706SPAFEPLA.001 [DIRS 181613], FEP Number 2.1.03.03.0B) and has been excluded from further consideration in the TSPA. Stress corrosion cracking of the drip shield has also been screened out on the basis of low consequence (DTN: MO0706SPAFEPLA.001 [DIRS 181613], FEP Number 2.1.03.10.0B). The liquid flux through corrosion patches is proportional to the ratio of the axial length of the penetration(s) in the drip shield to the total axial length of a drip shield section (see Section 6.3.2.4). This flux splitting submodel for the drip shield should only be applied when there is a time-varying failure of the drip shield.

3. **Diversion around the drip shield (F_3)**—The portion of the flux that does not flow through the drip shield is assumed to flow directly into the invert.
4. **Flux through the waste package (F_4)**—The flux through the waste package is based on the presence of patches due to general corrosion and localized corrosion in the waste package outer barrier. The number of patches in the waste package is calculated independently of the RTA by the WAPDEG code (SNL 2007 [DIRS 178871]). The flux through waste package corrosion patches is proportional to the ratio of the axial length of the penetration(s) in the waste package to the total axial length of a waste package (see Section 6.3.3.3).
5. **Diversion around the waste package (F_5)**—The portion of the flux that does not flow into the waste package bypasses the waste form and flows directly into the invert.
6. **Flux into the Invert (F_6)**—All water flux from the waste package is modeled as flowing directly into the invert, independent of patch location on the waste package. In addition, the fluxes that were diverted around the waste package (F_5) and around the drip shield (F_3) flow into the invert. Only a portion of the total flux to the invert (the flux through the waste package, F_4) will contain radionuclides.
7. **Imbibition Flux to the Invert (F_7)**—Water can be imbibed from the host rock matrix into the invert.
8. **Flux from the Invert to the Unsaturated Zone (F_8)**—A portion of the advective flux from the invert equal to the total dripping flux (F_1) flows directly into the UZ fractures. The portion of the advective flux from the invert equal to the imbibition flux to the invert (F_7) flows into the UZ matrix.

These pathways are time dependent, in the sense that total dripping flux, drip shield gaps, drip shield penetrations, and waste package penetrations will vary with time and local conditions in the repository.

The conceptual model for flow through the EBS includes three domains associated with radionuclides: the waste form domain, the waste package corrosion products domain, and the invert domain.

The waste form domain consists of fuel rods, high-level (radioactive) waste (HLW) glass, or DOE SNF (DSNF), along with steel components that are closely associated with the waste form. In commercial SNF (CSNF) waste packages, the waste form domain includes the stainless steel fuel basket tubes that contain the waste form and the neutron absorber plates that form the internal framework supporting the fuel tubes. Due to different degradation characteristics of the waste form and associated transport parameters, the waste form domain for the codisposal packages is divided into two subdomains: (1) HLW glass and the steel canisters containing the glass, and (2) DSNF, along with the steel canisters, sleeves, and components that are part of the DSNF. Fuel rods, glass logs, and DSNF undergo alteration to form a rind. The thickness of the rind changes as the degradation of the fuel rod or glass log continues; the DSNF degrades almost instantaneously and the rind thickness remains fixed. Flow is conceptualized as one-dimensional, from the waste package exterior, through the waste form domain, and into the

second domain. In codisposal waste packages, flow passes first through the HLW glass subdomain, then through the DSNF subdomain, and then into the second domain, as described in Section 6.5.2.1.2.

The second domain consists of corrosion products from degradation of steel internal components that are not part of the waste form domain. In CSNF waste packages, these steel components include the fuel basket guides, the TAD canister, and the inner vessel. In codisposal waste packages, the second domain steel components include the central support tube and divider assembly and the inner vessel. The TAD canister shield plug (15 in. thick) in CSNF waste packages and the inner lid (9 in. thick) in codisposal waste packages are not included as contributing to the second domain corrosion products because the large mass of these components is localized at one end of the waste package and will not appreciably affect transport throughout the rest of the waste package. The corrosion products domain fills the inside of a waste package within the Alloy 22 outer corrosion barrier, so its thickness is uncertain and can be as much as the radius of the waste package. In the one-dimensional flow conceptualization, flow enters from the first (waste form) domain and exits into the third (invert) domain.

The third domain, the invert, is modeled as being in intimate contact with the waste package and has a thickness of 0.934 m (see Section 6.5.2.3). This is the average thickness of the invert, and appropriate for the one-dimensional transport calculation. Because the presence of the emplacement pallet is ignored, water and radionuclides pass directly from the waste package to the invert.

The waste form domain represents the source term for the TSPA. Source term abstractions are defined in other model reports or design documents for radionuclide solubility (SNL 2007 [DIRS 177418]), HLW glass dissolution rate (BSC 2004 [DIRS 169988]), cladding response (SNL 2007 [DIRS 180616]), and inventory by waste package type (SNL 2007 [DIRS 180472], Table 6-2[a]). The source term represents input data or boundary conditions for the RTA and is not discussed in this document.

The final output from the RTA is the mass flux of radionuclides (kg yr^{-1}) from the EBS into the UZ. The parameters and formulas for calculating the water fluxes in the various pathways are summarized in Table 6.3-1.

Table 6.3-1. Summary of Parameters for EBS Flow Pathways

Flow Pathway, Pathway Flux F_i	Flow Parameters	Data Sources & Notes
1. Total dripping flux (seepage + wall condensation), F_1	Total dripping flux is a function of fracture properties, rock properties, air and water properties, and the percolation flux.	<i>Abstraction of Drift Seepage</i> (SNL 2007 [DIRS 181244]) and <i>In-Drift Natural Convection and Condensation</i> (SNL 2007 [DIRS 181648]) provide time- and location-dependent values of total dripping flux.
2. Flux through the drip shield, F_2	L_{DS_Patch} is the axial half-length of each patch due to general corrosion of titanium. L_{DS} is the axial length of the drip shield. N_{bDS} is the number of corrosion patches of length L_{DS_Patch} in the drip shield. f_{DS} is sampled uncertain parameter, DS_Flux_Uncertainty_a. $F_2 = \min[F_1 N_{bDS} L_{DS_Patch} f_{DS} / L_{DS}, F_1]$	This flux splitting submodel for the drip shield should only be applied when there is a time-varying failure of the drip shield. For the Seismic Scenario Class, the opening area is computed based on the drip shield damage fraction multiplied by the area of the drip shield.
3. Diversion around drip shield, F_3	$F_3 = F_1 - F_2$.	Continuity of liquid flux.
4. Flux into the WP, F_4	L_{WP_Patch} is the axial half-length of each patch due to general corrosion of Alloy 22. L_{WP} is the axial length of the WP. N_{bWP} is the number of corrosion patches in the waste package. f_{WP} is sampled uncertain parameter, WP_Flux_Uncertainty_a. $F_4 = \min[F_2 N_{bWP} L_{WP_Patch} f_{WP} / L_{WP}, F_2]$	WAPDEG (SNL 2007 [DIRS 178871]) provides the number of patches and stress corrosion cracks on the WP. No significant flow through stress corrosion cracks due to plugging (DTN: MO0706SPAFEPLA.001 [DIRS 181613], FEP Number 2.1.03.10.0A). Steady state flow through WP (outflow = inflow in steady state; this is bounding for release).
5. Diversion around the WP, F_5	$F_5 = F_2 - F_4$	Continuity of liquid flux.
6. Flux to the invert, F_6	$F_6 = F_5 + F_4 + F_3$ $= F_1$	All advective flux enters the invert. Only F_4 can transport radionuclides into the invert.
7. Imbibition flux from the host rock matrix into the invert, F_7	F_7 is an input to the EBS flow model.	Imbibition flux is provided by <i>Multiscale Thermohydrologic Model</i> calculations (SNL 2007 [DIRS 181383]).
8. Flux from the invert into the UZ, F_8	$F_8 = F_6 + F_7$ $= F_1 + F_7$	Total dripping flux portion (F_1) of advective flux from the invert flows into the UZ fractures, imbibition flux (F_7) flows into the UZ matrix.

NOTE:WP=waste package; UZ=unsaturated zone; WAPDEG=waste package degradation

6.3.1.2 EBS Transport Abstraction

The waste form is the source of all radionuclides considered for the EBS. Radionuclides can be transported downward, through the invert and into the UZ. Transport can occur through advection when there is a liquid flux through the waste package and invert and the waste form has been exposed to this flux, via pathways 4, 6, and 8 in Figure 6.3-1. Transport can also occur by diffusion in the waste form, in the waste package corrosion products, in stress corrosion cracks in the lid of the waste package, and in the invert, even in the absence of a liquid flux,

because it is assumed (Assumption 5.5) that there is a continuous liquid pathway via thin films. The pallet has the capability to provide some limitation to diffusion; however, this capability is not considered in the TSPA. Diffusive transport may occur via flow pathways 4, 6, and 8 even when no advection occurs on those pathways in the EBS flow model.

A detailed mathematical description of transport in the EBS is presented in Section 6.5.1.2. Retardation of radionuclides occurs in the waste package. Transport occurs by diffusion and by advection. Table 6.3-2 summarizes the modes and parameters for the transport pathways in the EBS.

Lateral and longitudinal dispersion are neglected in modeling radionuclide transport in the EBS. Because the EBS radionuclide transport model is a one-dimensional model, the lateral dispersion effects cannot be considered. Ignoring lateral dispersion results in an overestimation of the concentration in a given domain for greater mass flux. Longitudinal dispersion could potentially be considered in the invert, where advection is expected to occur due to imbibition flux, even when there is no drift seepage flux. However, the longitudinal dispersivity is uncertain, being dependent on the scale of transport (Anderson and Woessner 1992 [DIRS 123665], p. 326) and on porous media characteristics that are not well-defined. Since the thickness of the invert is less than one meter, longitudinal dispersion is expected to be small and to have negligible effect on the breakthrough times through the invert compared to the simulated time steps considered in the TSPA (tens of years). In addition, as shown in Section 6.3.4.1, the uncertainty in the invert diffusion coefficient ranges over a factor of 20 and essentially encompasses the variable breakthrough times that could occur from including the longitudinal dispersion. The dispersivity of the waste form and waste package corrosion product domains is also difficult to characterize; however, because the scale of these domains is comparable to that of the invert, and because the diffusion coefficients in these domains are similar (or larger) than those in the invert, it is reasonable to neglect dispersivity in these domains as well as in the invert.

There is no upward transport of radionuclides because there is no solid medium with a liquid pathway above the drip shield. After the drip shield is breached, upward diffusion is negligible in comparison to the downward advective flux through the drip shield. Gas transport in the EBS is excluded due to low consequence (DTN: MO0706SPA FEPLA.001 [DIRS 181613], FEP Number 2.1.12.06.0A).

Colloid-facilitated transport of radionuclides is included in the RTA. Radionuclide transport from the waste package occurs in a liquid containing colloids and dissolved radionuclides. There are three types of colloids in the EBS: (a) waste form colloids derived from degradation of HLW glass, DSNF, and CSNF, (b) iron oxyhydroxide colloids due to products from the corrosion of steel waste package components, and (c) groundwater or seepage water colloids. All three types of colloids may have radionuclides that are sorbed reversibly in what is modeled as an equilibrium process. The waste form colloids may also have radionuclides that are embedded within the colloid particle when it is formed and are not removable. The corrosion product colloids may have reversibly attached radionuclides (equilibrium sorption). However, some radionuclides, such as plutonium and americium, can be so strongly sorbed onto iron oxyhydroxide that for all practical purposes they do not desorb; for these radionuclides, sorption is modeled as a kinetic process, implemented using a sampled forward rate constant and zero backward rate constant. Colloids may be transported by diffusion as well as by advection. The

diffusion coefficient for colloids is a function of temperature and colloid particle size (see Section 6.3.4.4).

Table 6.3-2. Summary of Transport Modes and Parameters for the EBS Transport Pathways

Transport Pathway	Transport Modes	Transport Parameters and Data Sources
1. Waste form and corrosion products domains	<p>Diffusion through stress corrosion cracks (no advective transport through stress corrosion cracks).</p> <p>Diffusion and advection through corrosion products and corrosion patches.</p>	<p>No lateral or forward dispersion.</p> <p>Colloidal particles will transport radionuclides.</p> <p>Diffusive area for each stress corrosion crack is $7.7 \times 10^{-6} \text{ m}^2$ (see Table 6.3-3).</p> <p>Diffusive area for each patch is provided by WAPDEG (SNL 2007 [DIRS 178871]).</p> <p>Diffusion coefficient (all radionuclides):</p> <ul style="list-style-type: none"> • Species dependent free-water diffusion coefficients given in Table 4.1-7 • Modified for porosity and saturation (see Section 6.3.4.3.5) • Temperature modification defined in Section 6.3.4.1.2; waste form and corrosion product temperatures are provided by <i>Multiscale Thermohydrologic Model</i> calculations (SNL 2007 [DIRS 181383]) • Colloid diffusion coefficient computed as a function of waste form and corrosion product temperatures and sampled colloid particle diameter using Equation 6.3.4.4-1 (Section 6.3.4.4) <p>The flow cross-sectional area is given by the interface between the waste package corrosion products domain and the invert domain.</p> <p>See Section 6.5.2 for further details.</p>
2. Invert	<p>Diffusion and advection (F_6) from corrosion products domain through the invert.</p> <p>Advection from the UZ into the invert (F_7).</p>	<p>Liquid flux for advection = $F_6 = F_5$ (diverted by WP) + F_4 (flux through WP) + F_3 (diverted by drip shield).</p> <p>Diffusion coefficient (all radionuclides):</p> <ul style="list-style-type: none"> • Species dependent free-water diffusion coefficients given in Table 4.1-7 • Modified for porosity and saturation (see Section 6.3.4.1) • Temperature modification defined in Section 6.3.4.1.2; invert temperature is provided by <i>Multiscale Thermohydrologic Model</i> calculations (SNL 2007 [DIRS 181383]) • Colloid diffusion coefficient computed as a function of invert temperature and sampled colloid particle diameter using Equation 6.3.4.4-1 (Section 6.3.4.4) <p>The flow cross-sectional area is the surface area between the invert and the drift wall contacting the invert.</p> <p>See Section 6.5.2 for further details.</p>

Table 6.3-2. Summary of Transport Modes and Parameters for the EBS Transport Pathways (Continued)

Transport Pathway	Transport Modes	Transport Parameters and Data Sources
3. Invert-UZ interface	Advection from the invert to UZ fractures (F_6) and UZ matrix (F_7); total flux is F_8 . Diffusion from the invert to UZ fractures and matrix.	The invert diffusion calculation uses radionuclide concentrations in the WP corrosion products domain as the boundary condition at the top of the invert and a series of UZ computational cells below the invert that provide a gradient to a zero radionuclide concentration at some distance from the bottom of the invert (Section 6.5.2.6).

NOTE:WP=waste package; UZ=unsaturated zone

The species dependent free water diffusion coefficients in the invert are given in Table 4.1-7. The effects of variable porosity, liquid saturation, temperature, and uncertainty in the effect of these parameters are included in calculating the effective diffusion coefficients (Section 6.3.4.1). Sorption of radionuclides onto the crushed tuff is also included in the EBS transport abstraction (Section 6.3.4.2.2.1).

The corrosion products from the waste package and SNFs have the potential to be strong sorbers for the actinides. Including sorption in the waste package and invert is beneficial to performance because this process can retain radionuclides in the EBS and delay release to the UZ. Because the waste package corrosion products are in intimate contact with or directly in the flow or diffusion path of the radionuclide source inside the waste package, retardation by corrosion products inside the waste package will occur. However, because corrosion products in the invert are more localized and not necessarily in any flow path from the waste package, sorption onto corrosion products in the invert is ignored (Assumption 5.6).

6.3.2 Water Flux through the Drip Shield (F_2)

6.3.2.1 Water Movement into and through a Drift (F_1 and F_3)

Water movement from the land surface and down through the UZ at Yucca Mountain is conceptualized to occur through a dual continuum of the rock matrix and a system of fractures (Liu et al. 1998 [DIRS 105729]). Simulations of water movement through the mountain yield estimates of percolation fluxes in the vicinity of the emplacement drifts that are a function of drift location, the geologic unit in which the drift resides, and the climate, which varies over time (BSC 2004 [DIRS 167652]). Consideration of the interactions between water moving through the mountain and the EBS form the basis of this abstraction for performance assessment.

The basic EBS design concept is shown in Figure 6.1-1. The drifts are 5.5 m in diameter. The bottom of the drift, commonly referred to as the invert, is filled with a ballast material of crushed tuff. The waste packages are to be placed on emplacement pallets that hold them in place above the invert. A titanium drip shield surrounds the waste packages. The space between the waste package and the drip shield, which is referred to as the axial space, is designed to remain air filled. The current repository design does not include an engineered backfill material; all of the analyses in this report reflect the no-backfill design.

At early times, any water that enters the drift is vaporized and expelled due to the heat output from the waste packages. According to modeling of water movement through the EBS using *Multiscale Thermohydrologic Model* (SNL 2007 [DIRS 181383]), much of the water that enters the drift remains as liquid once thermal output has subsided after approximately 1,500 years (SNL 2007 [DIRS 181383], Figure 6.3-78[a]). Water that does seep into the drift can drip onto the drip shield and is diverted around the waste package, into the invert.

Water enters the drift by seepage from the roof of the drift. In this section, this mechanism is considered, followed by a discussion of water diversion around the drip shield.

6.3.2.1.1 Seepage and Condensation Flux (F_1)

Seepage Model for PA Including Drift Collapse (BSC 2004 [DIRS 167652]) presents results of drift-scale UZ flow modeling of the interaction between host rock containing a fracture continuum and a drift for a variety of percolation flux rates and several sets of representative host rock hydraulic parameters. The seepage flux was found to be related to the percolation flux. However, the air-filled space below the roof of the drift acts as a capillary barrier that diverts water around the drift and limits seepage. These findings are consistent with the theory for seepage exclusion around cylindrical cavities introduced by Philip et al. (1989 [DIRS 105743]). Philip et al. showed that for given capillary properties of the host rock and a given drift diameter, there exists a critical percolation flux beneath which water will not enter the drift. The drift-scale UZ flow modeling results, show a propensity for flow to diverge around the drifts.

Abstraction of Drift Seepage (SNL 2007 [DIRS 181244]) provides the rationale for calculating the seepage flux into the repository, accounting for thermal effects, spatial variability, and uncertainty of properties. The fractions of drifts that experience water seepage as a function of infiltration are given as a function of percolation rate. Across the range of percolation fluxes expected, a large majority of the drifts remain dry. *In-Drift Natural Convection and Condensation* (SNL 2007 [DIRS 181648], Section 8.3.1) provides the abstraction for determining the amount of condensation on the drift walls. This condensation is added to the seepage flux, resulting in the total dripping flux, F_1 . The effects of repository-scale condensation are captured within this model.

6.3.2.1.2 Diversion around the Drip Shield (F_3)

The drip shield has been designed to divert liquid water that may enter the drift away from the waste package. If the drip shield works as designed (this issue is discussed in detail below), it then acts as a no flow boundary. Any seepage that enters the drift moves downward under the force of gravity. As water migrates downward around the drip shield, it encounters the invert. The diversion around the drip shield occurs as droplets or rivulets, and any flow that enters the invert is concentrated at the sides of the drip shield while the drip shield is intact.

Once in the invert, water migrates quickly into the UZ host rock at the bottom of the drift.

The algorithm for calculating the flux diversion around a breached drip shield is discussed in Section 6.3.2.4.

6.3.2.2 Drip Shield Effectiveness

Design drawings for the drip shield are given in *D&E / PA/C IED Interlocking Drip Shield and Emplacement Pallet* (BSC 2005 [DIRS 173303]) with details in drawings 000-M00-SSE0-00102-000 REV 00C (BSC 2007 [DIRS 179838]), 000-M00-SSE0-02001-000-00A (BSC 2004 [DIRS 168326]), and other drawings cited on the information exchange drawing (IED). The drip shield has roughly the shape of the top of a mailbox with vertical sides and a top section that is curved for strength and to shed water. On one end, a drip shield connector guide is attached to the top of the curved section. The connector guide is a square rib, 50 mm wide (BSC 2004 [DIRS 168326]), that is attached to and extends across the curved top section. This connector guide provides extra stiffness to the end of the drip shield and can deflect seepage down the sides of the drip shield. On the other end of the drip shield, a connector plate is attached. The connector plate is 15 mm thick (BSC 2005 [DIRS 173303], Table 5) and also has a 50-mm-wide square connector guide (BSC 2004 [DIRS 168326]) that is attached to the underside of the connector plate.

Adjacent drip shields are interlocked with one another. This is accomplished during installation by lowering the connector plate of one drip shield over the upward extending connector guide of the previously emplaced drip shield. The minimum overlap is the width of two connector guides, 100 mm (BSC 2007 [DIRS 179838]), and the maximum overlap between adjacent drip shields is 320 mm (BSC 2007 [DIRS 179838], Section A-A).

The gaps that exist between drip shields in this interlocking design can, potentially, provide a pathway for water to penetrate the drip shield system. The potential for such leakage under design conditions is considered here, followed by consideration of the ways in which the integrity of the drip shield might become compromised. This discussion is limited to considering the top of the drip shield because any water entering the contact between drip shields from the side would simply flow down the vertical sides of the drip shields, never contacting the waste.

To evaluate the potential for seepage to leak through the interlocking overlap between drip shields, consider high seepage flux conditions, which must exist in order for flow to be driven into this overlap. First, the water must travel laterally up to 320 mm to get beyond the overlap between the drip shields. As this water travels, it must remain precisely along the crown of this gap between the drip shields. If there is any deviation, the sloping sides of the drip shield impose gravity forces that will cause the water to flow down the sides and into the invert. Second, the upward extending drip shield connector guide provides a barrier to flow along the crown. Sufficient water pressure must be provided to push water up and over this barrier. Furthermore, the connector guides provide surfaces of contact with the drip shield and the connector plate. These contact surfaces maintain continuity down along the sloping sides of the top portion of the drip shield. These contacting surfaces will act akin to fractures in the sense that they impart capillarity and are able to transmit water. Any water reaching this point would run down the contact between the drip shields. The air-filled voids (having no capillarity) in between and beyond the connector guides provide an additional barrier to flow.

6.3.2.3 Drip Shield Breaching

The advective flow of water into the EBS has been shown to bypass the waste packages as long as the integrity of the drip shield is maintained. Once corrosion patches form in the drip shield or adjacent drip shields separate, seepage can drip through the drip shield onto the waste package. The consequence of such drip shield failure is that a portion of the seepage water flux now migrates through the drip shield and comes into contact with the waste package. The thermal and mechanical response of the drip shield may produce gaps between adjacent sections of drip shield. These breaching mechanisms are screened out in *FY 2007 LA FEP List and Screening* (DTN: MO0706SPAFEPLA.001 [DIRS 181613], FEP Numbers 2.1.11.07.0A and 2.1.06.07.0B).

6.3.2.4 Water Flux through and around a Breached Drip Shield (F_2 and F_3)

Once the drip shield has been breached, a portion of the water flux (F_2) will pass through the drip shield and have access to the waste package. In this section, a flux splitting algorithm is developed to determine the fraction of the seepage flux that can pass through a degraded drip shield. A similar algorithm is developed in a later section to determine the fraction of the liquid flux through the drip shield that can enter a waste package. The flux splitting algorithm is important to TSPA because the liquid flux into the waste package determines in part the transport of radionuclides by advection, an important release mechanism from the waste package and from the repository.

Once the flux through the drip shield is known, the flux diverted around the drip shield, F_3 , is calculated using a quasi-static continuity of flow approach:

$$F_3 = F_1 - F_2. \quad (\text{Eq. 6.3.2.4-1})$$

Key features of the drip shield flux splitting algorithm include: (1) the dripping flux (seepage plus condensation) into the drift falls as droplets from the top of the drift onto the crown of the drip shield (Assumption 5.1); (2) droplets fall randomly along the length of the drip shield; (3) only flow through general corrosion patches is considered; (4) evaporation from the drip shield is neglected (Assumption 5.2); all of the seepage flux either flows through corrosion patches or drains down the sides of the drip shield; and (5) all water that flows through breaches in the drip shield flows onto or into the waste package.

Some aspects of the flux splitting algorithm have been defined or clarified by experiments. The breached drip shield experiments (BSC 2003 [DIRS 163406]) were performed to validate the drip shield flux splitting algorithm and to examine in more detail the real behavior of seepage water impinging on and flowing over a drip shield. The tests were conducted by dripping water onto a mock-up portion of a full-scale drip shield made of stainless steel. The mock-up section included slightly more than half of the shield from the top/center down the curvature to the side. The side was shortened along the longitudinal and vertical axes. Simulated corrosion patches-square holes 27 cm wide, the size of nodes in an earlier version of the WAPDEG corrosion model (CRWMS M&O 2000 [DIRS 151566], p. 36)–were cut into the drip shield at various locations to enable measurements of flow through breaches in the drip shield. Tests were performed with both smooth (machined stainless steel) and rough (silica anti-slip coating)

surfaces, the latter simulating the roughening expected due to general corrosion on the entire surface, not just in penetrating patches. While the rough surface is conceptually more realistic, the silica coating may not have the same hydrologic behavior as a corroded surface, so in practice the rough surface is not necessarily more realistic than the smooth surface. With two distinctively different surfaces, the two sets of tests were considered to be sufficiently different while still fundamentally alike that one set could be used for model development and the other to validate the first set, with no clear preference as to which set should be used for which purpose. Thus, data from the tests on the smooth surface were selected to develop parameter values for the flux splitting submodel, whereas the rough surface test data were used to validate the submodel. Tests were conducted in a test chamber in an environment that would minimize evaporation (i.e., relative humidity of at least 80 percent). Water was dripped at various rates intended to cover the expected range of seepage rates within the repository. The dripping distance was the full-scale distance from the top of the drift to the crown of the drip shield, 2.17 m (BSC 2003 [DIRS 163406], Figure 10), based on repository design.

The tests that were conducted included (BSC 2003 [DIRS 163406]): (1) splash radius tests to determine the distance from the point of impact and a rough distribution of splattered water when drops impinge on the surface of the drip shield; (2) spread factor tests to determine the lateral rivulet spread distance from the drip impact point; (3) single patch splash tests to determine the amount of water that enters targeted breaches as a result of splashing; (4) single patch flow tests to determine the amount of water that flows down the surface of the drip shield and into patches; (5) multiple patch tests to collect both splashed water and rivulet flows that entered all affected patches; and (6) bounding flow rate tests to provide data for extreme drift seepage conditions to compare with the nominal seepage rate.

Observations during the breached drip shield tests revealed that the primary mechanism for water to enter breaches is via rivulet flow that originates from an area around the point of drip impact. Following droplet impact at the crown, water splatters within some distance from the point of impact. The splattered water coalesces, forming beads that increase in size around the center of impact with each successive drop. After a time, the beads closest to the downhill curvature reach a critical mass and roll down the face of the drip shield in the form of a rivulet. The rivulet flow area spreads out in a delta formation (i.e., the maximum spread is located on the vertical section of the drip shield and the minimum spread is located at the point of impact). No film flow was observed during tests on the smooth or the rough drip shield surfaces.

Evaporation could occur in two forms during the test—from a freely falling drop and from a flow surface on the drip shield. The loss from a falling droplet is negligible; however, losses from the drip shield surface can be large. Experimental measurements included determination of evaporative losses. Although these data could be used to develop or validate a drip shield evaporation model, evaporation is not considered in the current model, which maximizes the potential for flow through breaches (Assumption 5.2).

For a given drip location onto the crown of the drip shield (see Assumption 5.1), the spreading of the rivulet flow is defined by a spread angle, α , which is half of the total spread angle, formed with the vertical plane through the impact point (Figure 6.3-2). The total lateral spread of the rivulet flow is given as $2x \tan \alpha$, where x is the arc length from the crown of the drip shield down to a location of interest (e.g., a corrosion patch). In the breached drip shield experiments

(BSC 2003 [DIRS 163406]), the lateral rivulet spread to each side of the vertical plane, or $x \tan \alpha$, was measured. For N_b breaches in the drip shield of length L_{DS} , with each patch having a width of 2ℓ (m), the flux through the drip shield is given by:

$$F_2 = F_1 \frac{N_b \ell}{L_{DS}} \left(1 + \frac{\tan \alpha}{2} \right) f_{DS} . \quad (\text{Eq. 6.3.2.4-2})$$

For details of the mathematical development of this expression, see Section 6.5.1.1.2.4.

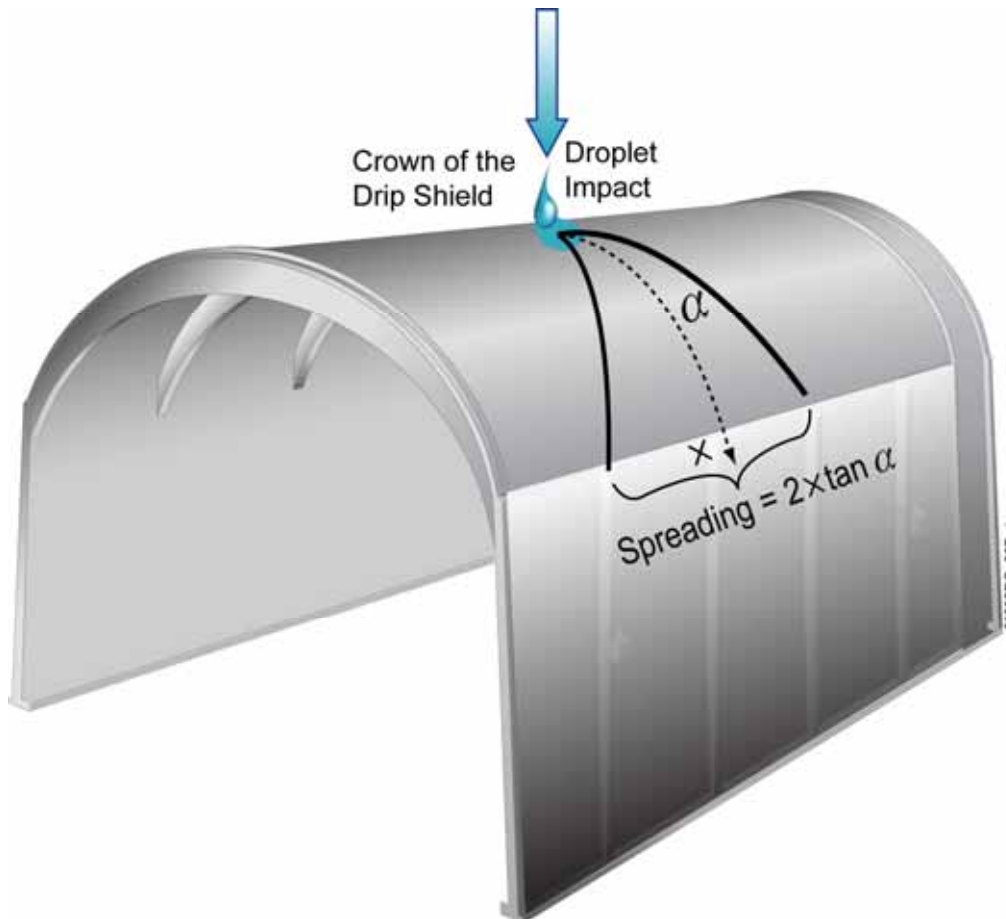


Figure 6.3-2. Illustration of Spreading of Rivulet Flow on the Drip Shield

The factor f_{DS} accounts for the uncertainty in the submodel and is a sampled parameter in TSPA simulations. Sources of uncertainty include:

1. **Drip location with respect to the crown of the drip shield**—Drops that fall to either side of the crown will not divide exactly in half, as assumed by this submodel.
2. **Patch location**—Patches located on the crown will allow the entire dripping flux to pass through, whereas Equation 6.3.2.4-2 considers all patches to be located off the crown. For a given value of f_{DS} , Equation 6.3.2.4-2 underestimates the flux into crown patches

because $f_{DS} < 1$, so $F_2 < F_1$, i.e., not all of the total dripping flux can flow through breaches. Since most of the randomly-located breaches occurring will not be located on the drip shield crown, this is a reasonable approximation, but not a bounding estimate of flow through drip shield breaches.

3. **Splattering distribution**—Although splattering of drops when they impinge on the drip shield is a random process, preferential directions or distributions could develop, for example, due to surface alteration as a result of corrosion or drift degradation (rockfall).
4. **Rivulet spread**—The breached drip shield experiments showed that a range of rivulet spread factors or spread angles can occur even on smooth surfaces. Surface roughness also affects the rivulet spread angle. Precipitation of salts or accumulation of dust on the drip shield surface could also affect rivulet flow.
5. **Interference among multiple patches**—Implicit in this submodel is that the patches do not interfere with each other, i.e., that no patch is lower on the drip shield surface than another patch. Patches located below another patch will see reduced or zero flux through the patch. By ignoring patch interference, water flux through the drip shield will be overestimated.
6. **Patches outside the footprint of the waste package**—Flux through these patches will pass directly to the invert. Since the conceptual model requires that all flow through the drip shield goes onto or into the waste package, Equation 6.3.2.4-2 will overestimate that flow.
7. **Evaporation from the surface of the drip shield**—Evaporation is neglected (Assumption 5.2); if it occurs, the flux through the drip shield is less than predicted by Equation 6.3.2.4-2.
8. **Size of corrosion patches**—The WAPDEG model assumes a fixed size and shape for all corrosion patches. In reality, the patches will vary widely in size and shape randomly as well as over time.

Bounds and a distribution for f_{DS} must be established for use in the TSPA calculations. Because, under some of these uncertain conditions, the flux through the drip shield may be zero even when breaches exist, an appropriate lower bound on f_{DS} is zero. Under some other circumstances mentioned above, the entire seepage flux could flow through the drip shield. Thus, an upper bound on f_{DS} cannot be specified *a priori*, but should be given by:

$$f_{DS} = \frac{1}{\frac{N_b \ell}{L_{DS}} \left(1 + \frac{\tan \alpha}{2} \right)}, \quad (\text{Eq. 6.3.2.4-3})$$

which makes $F_2 = F_1$. Since the number of patches, N_b , varies over time, f_{DS} should be a function of time, with a starting value of zero and potentially reaching a value equal to the total number of patches in the WAPDEG corrosion model of the drip shield (SNL 2007 [DIRS 178871]). A uniform distribution is appropriate given that the uncertainty is difficult to quantify. To ensure that the flux through the drip shield is not greater than the seepage flux, the flux through the drip shield is computed as:

$$F_2 = \min \left[F_1 \frac{N_b \ell}{L_{DS}} \left(1 + \frac{\tan \alpha}{2} \right) f_{DS}, F_1 \right]. \quad (\text{Eq. 6.3.2.4-4})$$

The uncertainty in spread angle α can be lumped in with f_{DS} since both would otherwise be sampled independently. A lumped uncertainty factor f'_{DS} is defined as:

$$f'_{DS} = \left(1 + \frac{\tan \alpha}{2} \right) f_{DS}, \quad (\text{Eq. 6.3.2.4-5})$$

with the flux through the drip shield to be computed as:

$$F_2 = \min \left[F_1 \frac{N_b \ell}{L_{DS}} f'_{DS}, F_1 \right]. \quad (\text{Eq. 6.3.2.4-6})$$

In Section 6.5.1.1.2.4, an upper bound on f'_{DS} is developed based on results of the breached drip shield experiments, and is used in the TSPA Model.

6.3.3 Water Flux through the Waste Package (F_4)

The conceptual model for the TSPA is based on the assumed presence of continuous flow paths through the patches that penetrate the waste package. More specifically, in the TSPA conceptual model, vertical flow of seepage into the waste package, through the waste form, and out of the waste package is not impeded by the location of patches on the surface of the waste package. Flow is modeled as steady state, so there is no change in the amount of liquid within the waste package for flow and transport when seepage occurs. Under no-seep conditions, the water content inside a waste package changes over time due to adsorption of water vapor onto corrosion products, but no flow takes place. (An alternative conceptual model (ACM) in which water fills the waste package before any water flows out—the “bathtub” model—is evaluated in Section 6.4.1). There is also no resistance to the flow through the waste form. The TSPA approach reasonably bounds the immediate release and mobilization of radionuclides, while retaining as much realism as justified by the data and understanding of the physical and chemical processes that take place.

As modeled, radionuclides cannot be released from the waste package if there is insufficient water or if there are no openings through either the wall or lid of the waste package. Section 6.3.3.1 describes the types and the general design features of the waste packages to be emplaced in the repository. Section 6.3.3.2 describes the types of openings that can form, how

and where they form, the timing of their formation, and the flow through these openings. The dimensions of these openings have implications for whether water is able to flow into and through the waste package or whether transport out of the waste package is by advection and/or diffusion. A model of advective flow of water through stress corrosion cracking (SCCs) is presented in Section 6.3.3.1. Section 6.3.3.3 describes the flux of liquid around or through the waste package. Section 6.3.3.4 describes the alternative pathway for liquid to reach the waste package; namely, evaporation from the invert and condensation on the inside of the drip shield can provide a source of liquid to the exterior of the waste package even when there are no openings in the drip shield. Section 6.3.3.5 describes the flux of liquid through the invert.

6.3.3.1 Waste Package Design

Twelve waste package configurations are planned for the waste to be emplaced in the repository, where the nominal quantity for LA is shown in parentheses (SNL 2007 [DIRS 180472], Table 6-2[a]):

1. 21-PWR TAD (4,586)
2. 12-PWR TAD (173)
3. 44-BWR TAD (3,037)
4. 5-DHLW/DOE SNF Long (1,940)
5. 5-DHLW/DOE SNF Short (1,257)
6. 2-MCO/2-DHLW (219)
7. Naval Short (94)
8. Naval Long (323)

Waste packages are broadly categorized as CSNF waste packages (21-PWR and 44-BWR are the most common, comprising about 65 percent of the waste packages listed above), codisposal waste packages (5-DHLW/DOE SNF Short and Long, and 2-MCO/2-DHLW), and Naval Short and Long waste packages. Although waste packages vary depending on the waste form they contain, the majority of designs have features in common. These commonalities are described here. The waste package consists of a cylindrical inner stainless steel vessel, which is sealed with a stainless steel lid. The inner vessel is placed into an Alloy 22 outer corrosion barrier, which is sealed with a middle and outer lid. The inner vessel has 2-in. (5.08-cm) thick walls and lid that provide structural integrity for the waste package. The Alloy 22 outer corrosion barrier has a wall 1 in. (2.54 cm) thick, a middle lid 0.5 in. (12.7 mm) thick, and a 1-in. (2.54-cm) thick outer lid, that provide resistance to corrosion. Inside a CSNF waste package inner vessel is a closely-fitting TAD canister consisting of a cylindrical stainless steel vessel having a 1-in. (2.54-cm) thick wall and a massive 15-in. (38.1-cm) thick lid referred to as a shield plug that is intended to provide radiation shielding during transportation and handling. Design information for waste packages is provided in *Total System Performance Assessment Data Input Package for Requirements Analysis for TAD Canister and Related Waste Package Overpack Physical Attributes Basis for Performance Assessment* (SNL 2007 [DIRS 179394]) and *Total System Performance Assessment Data Input Package for Requirements Analysis for DOE SNF/HLW and Navy SNF Waste Package Overpack Physical Attributes Basis for Performance Assessment* (SNL 2007 [DIRS 179567]), which identify detailed design drawings, including drawings of the 21-PWR, 44-BWR, the 5-DHLW/DOE Long, and the Naval Short and Long waste packages, among others. The TAD canister design has not been finalized; for purposes of estimating the

masses of internal components, the Site-Specific Canister design is used for the TAD canister design (see Table 4.1-21 for a complete list of drawings used in this report).

Codisposal waste packages have compartments that allow smaller containers of different waste types to be included in a single waste package. In a 5- DHLW/DOE Long, for instance, the waste package is divided into five compartments that accommodate one DHLW glass each. The five compartments surround a central tube that will contain a single DSNF canister.

The stainless steel inner vessel of the waste package is modeled as having no resistance to corrosion as reflected in the WAPDEG analysis of waste package and drip shield degradation (SNL 2007 [DIRS 178871]), forming an immediate flow pathway once the outer (Alloy 22) corrosion barrier has been breached. Similarly, as modeled, the closure weld on the inner stainless steel lid, as part of the stainless steel inner vessel, has no resistance to corrosion, and the inner lid fails once the outer lids have failed. In addition, the TAD canister radiation shield plug and the 5- DHLW/DOE Long inner top lid are not included as contributing to waste package corrosion products, because they are located at one end of the waste package, so the large masses of corrosion products that will eventually be produced there from those massive components, are unlikely to disperse effectively throughout the waste package interior.

In this report and in the TSPA, the 21-PWR and 5- DHLW/DOE Long are used to represent the two basic types of waste packages—CSNF and codisposal, respectively—because these are the most common of each of the two types of waste packages.

6.3.3.2 Breaching of the Waste Package

Three general types of openings can exist in the waste package due to corrosion. These are (1) stress corrosion cracks, (2) patches resulting from general corrosion, and (3) localized corrosion. The opening area of SCCs in the waste package as well as in the drip shield is calculated in Sections 6.3.3.2.2. The size and timing of patches resulting from general corrosion are predicted by the WAPDEG analysis (SNL 2007 [DIRS 178871]). The opening area from localized corrosion is described in *General Corrosion and Localized Corrosion of Waste Package Outer Barrier* (SNL 2007 [DIRS 178519], Section 8.3.1).

Heat generated by the waste form has the potential to evaporate water within the waste package. In this situation, water cannot collect inside the waste package and cannot support advective transport of radionuclides. Preliminary estimates using *Multiscale Thermohydrologic Model* (SNL 2007 [DIRS 181383], Section 6.3) indicate that the available heat can evaporate incoming water for several thousand years. However, although evaporation is expected to occur, complexities in the internal geometry of the waste packages (particularly the response of any water pooled at the bottom of the package and the potential presence of small conduits for water vapor to escape through stress corrosion cracks) make it difficult to say definitively that all incoming water is evaporated.

The expected evaporation in the waste package is ignored in the TSPA. This approach is reasonably bounding because evaporation might eliminate advection as a transport mechanism. In addition, by ignoring evaporation from a waste package, the approach used in TSPA of specifying a water saturation of 1.0 (fully saturated) inside a failed waste package whenever

dripping occurs is justified. If evaporation were accounted for, the water saturation inside a waste package would generally be less than 1.0, which would reduce the amount of radionuclides that could dissolve in the water and be advectively transported from the waste package. Lower water saturations would also reduce estimates of diffusive releases, since both the diffusion coefficient and the cross-sectional area for diffusion would be less. Thus, without these simplifying assumptions, the amount of radionuclides transported from a waste package would be expected to be less.

As a simplification, it is assumed that no radionuclide transport occurs when the temperature in the waste package is above the boiling point of water in the repository (Assumption 5.5), when a continuous film of water needed for transport is not expected to exist.

6.3.3.2.1 Drip Shield and Waste Package Through-Wall SCC Area

This section describes the model abstractions to estimate the opening areas of the through-wall cracks in the waste package and drip shield that could result from the SCC damage. In the repository, the source of the stresses that could cause the SCC damage in the waste package is the residual stress in the closure welds and damages due to rockfall and ground motion caused by seismic activity. The SCC damage in the drip shield could be the result of rockfall and seismic ground motion.

6.3.3.2.2 Opening Area of a Single Through-Wall SCC

SCCs in the waste package or drip shield can be treated as a semi-elliptical crack, as in *Stress Corrosion Cracking of Waste Package Outer Barrier and Drip Shield Materials* (SNL 2007 [DIRS 181953], Section 6.6.2). Figure 6.3-3 illustrates actual SCCs and the simplified conceptual image of a SCC as modeled.

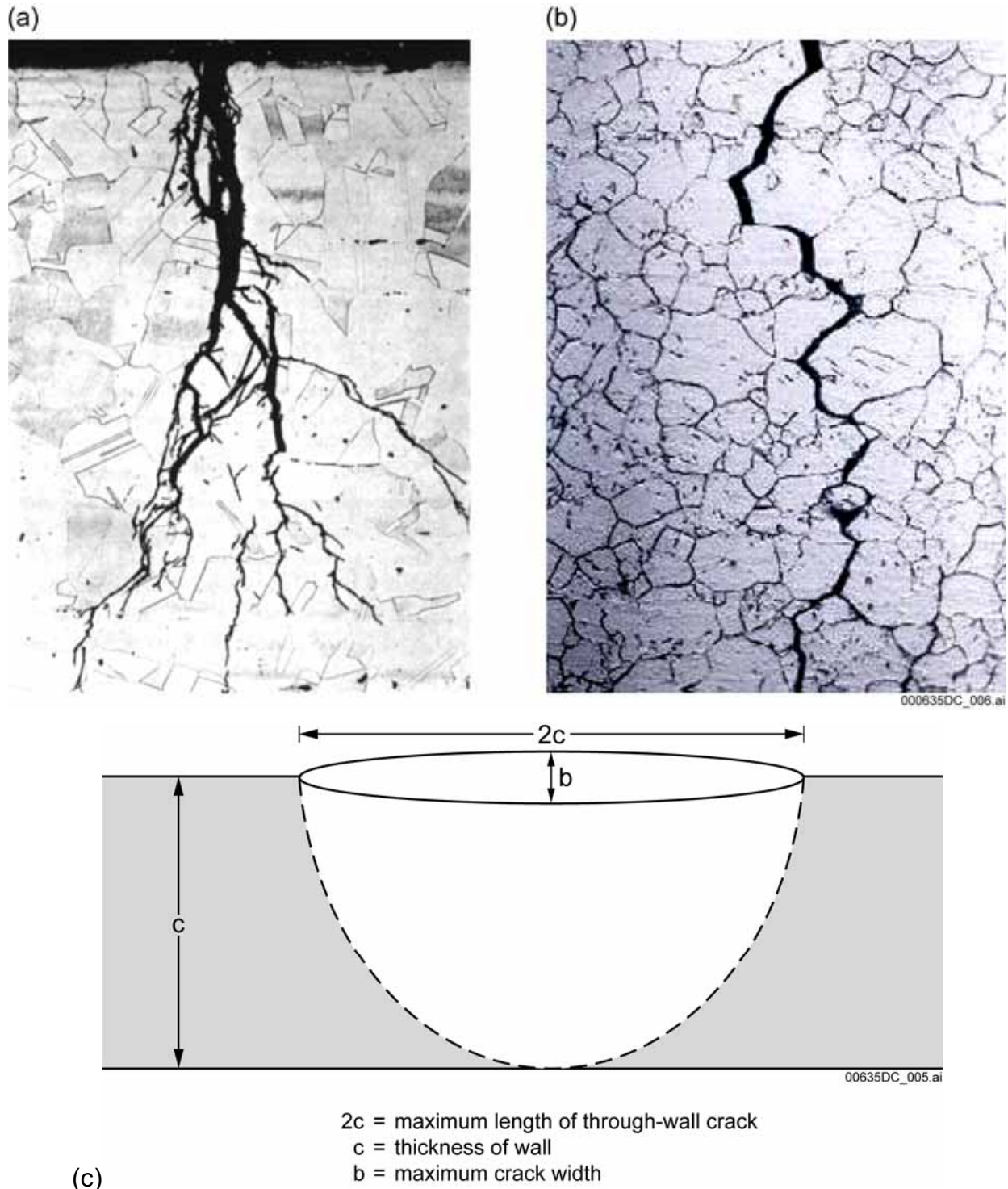


Figure 6.3-3. (a) Actual SCC in Stainless Steel Plate, Cross-Sectional View of Transgranular Cracks; (b) Actual SCC in Stainless Steel Plate, Cross-Sectional View of Intergranular Cracks; (c) SCC Configuration as Modeled.

The opening displacement of a crack in an infinite sheet for plane stress condition can be calculated using the equation given by Tada et al. (2000 [DIRS 167756], p. 125):

$$b = \frac{2(2c)\sigma}{E}, \quad (\text{Eq. 6.3.3.2.2-1})$$

where b = crack width (mm), $2c$ = crack length (mm), σ = residual tensile stress (Pa), and E = the modulus of elasticity (Pa). The opening area, A_{SCC} , for an elliptical crack can be estimated by:

$$\begin{aligned} A_{SCC} &= \pi \left(\frac{b}{2} \right) \left(\frac{2c}{2} \right) \\ &= \frac{(2\pi c^2)\sigma}{E}. \end{aligned} \quad (\text{Eq. 6.3.3.2.2-2})$$

When the above equations are used to estimate the width and opening area of a through-wall crack, σ is the maximum tensile stress across the wall thickness of the dominant stress plane (SNL 2007 [DIRS 181953], Section 6.6.2). Using the maximum tensile stress will overestimate the opening area on the inside surface where the crack fully penetrates the wall, which relieves the stress. The size of the penetration is unknown, so the outer surface opening area based on the maximum tensile stress is used as a reasonable bound on the opening area through the entire wall thickness.

For the TSPA implementation, the room temperature yield strength (σ_{YS}) of Alloy 22 and Titanium Grade 7 are used as bounding values for the residual stress, σ , in Equations 6.3.3.2.2-1 and 6.3.3.2.2-2. Values for σ_{YS} and E for Alloy 22 and Titanium Grade 7 at room temperature are found in DTN: MO0702PASTRESS.002 [DIRS 180514] (file *Model Output DTN.doc*, Table 8-1), and are listed in Table 4.1-1. Whereas material properties at 150°C or greater are specified in mechanical calculations and analysis for drip shield and waste package design (SNL 2007 [DIRS 179354], Table 4-2, Parameter Number 07-03; SNL 2007 [DIRS 179567], Table 4-1, Parameter Number 03-07), room temperature material properties are used in the RTA because the data are applied under conditions when SCCs are more likely to occur, namely, well after the thermal period, when temperatures have moderated and are closer to room temperature than to 150°C.

An initially semi-elliptical crack oriented into the material becomes a semi-circular crack as it grows to a through-wall crack (Figure 6.3-3). Therefore, the expected maximum length ($2c$) of the crack is twice the remaining wall thickness (SNL 2007 [DIRS 181953], Section 6.6.2). As a bounding approximation, the crack width and opening area are modeled to be constant through the wall thickness. For an actual SCC propagating through the wall thickness, the crack width and opening area are likely to decrease along the wall thickness because of the residual stress redistribution and relaxation at the crack tip as the crack grows through the wall thickness. Those effects can be amplified when neighboring cracks propagate in parallel through the wall thickness (SNL 2007 [DIRS 181953], Section 6.7.1.2 and Section 6.7.1.3).

For the TSPA implementation, the initial wall thickness is used for the waste package and drip shield, i.e., 25 mm for the waste package outer corrosion barrier (SNL 2007 [DIRS 179394], Table 4-3) and 15 mm for the drip shield (SNL 2007 [DIRS 179354], Table 4-2). The opening area of a single SCC in the waste package and drip shield calculated using Equation 6.3.3.2.2-2 is listed in Table 6.3-3.

Table 6.3-3. Opening Area of a Single SCC in the Waste Package and Drip Shield

Materials	Single Crack Opening Area (mm ²)
Alloy 22 (waste package outer barrier)	7.682
Titanium Grade 7 (drip shield)	3.647

Output DTN: SN0703PAEBSRTA.001

6.3.3.2.3 Waste Package Closure Weld SCC Damage

All of the residual stresses in a waste package that may result from the fabrication are fully annealed before being loaded with the waste. Residual stresses from the welding of the waste package closure lids are not fully annealed, except for the top surface layers that are annealed with a plasticity-burnishing technique. Detailed residual stress analyses for the waste package closure weld regions indicate that the hoop stress is the dominant stress component that could result in radially-oriented through-wall cracks (SNL 2007 [DIRS 181953], Section 6.5.3.4).

Because of the stress field interactions between closely spaced parallel cracks, the distance between two neighboring through-wall cracks in the closure weld region needs to be greater than the closure-lid thickness so that sufficient stress (and the resultant stress intensity factor) will be available to drive a crack through the wall. Therefore, the maximum number of through-wall radial cracks (N_{cw_SCC}) in the closure-weld region per waste package can be calculated as:

$$N_{cw_SCC} = \frac{2\pi R}{t}, \quad (\text{Eq. 6.3.3.2.3-1})$$

where R is the radius of waste package, and t is the remaining thickness of the closure-lid. The expected maximum length of these radial cracks is twice the remaining closure-lid thickness, and the opening area of an individual through-wall crack is calculated using Equation 6.3.3.2.2-2.

The room temperature yield strength (σ_{YS}) and modulus of elasticity (E) of Alloy 22 are used as bounding values in Equation 6.3.3.2.2-2 for the single crack opening area, and the initial wall thickness (25 mm), (SNL 2007 [DIRS 179394], Table 4-3) for the outer lid is used in Equation 6.3.3.2.3-1 to calculate the maximum number of through-wall radial cracks in the closure weld region per waste package. Values for σ_{YS} and E for Alloy 22 and Titanium Grade 7 at room temperature are found in DTN: MO0702PASTRESS.002 [DIRS 180514] and are listed in Table 4.1-1. Room temperature material properties are used in the RTA because the data are applied under conditions when SCCs are more likely to occur, namely, well after the thermal period, when temperatures have moderated and are closer to room temperature than to the 150°C specified in mechanical calculations and analysis for drip shield and waste package

design (SNL 2007 [DIRS 179354], Table 4-2, Parameter Number 07-03; SNL 2007 [DIRS 179567], Table 4-1, Parameter Number 03-07).

6.3.3.2.4 Waste Package and Drip Shield SCC Damage Induced by Seismic Events

The seismic consequence abstraction analysis provides the areas on the waste package and drip shield damaged by seismic ground motions (DTNs: MO0703PASDSTAT.001 [DIRS 183148] and MO0703PASEISDA.002 [DIRS 183156]). The damaged area on the waste package and drip shield is defined as the area in which the residual tensile stress exceeds 90 percent to 105 percent of the yield strength of the materials.

Damage to waste package and drip shield due to seismic ground motions is modeled as being distributed uniformly over the surface of waste package and drip shield. Two bounding arrangements for the through-wall cracks are considered to calculate the number of through-wall cracks and their opening areas:

1. A hexagonal array with side length $2t/\sqrt{3}$, where t is the remaining wall thickness. Each point of the hexagonal array is the center of a crack with length $2t/\sqrt{3}$, and this length allows for cracks, if they lie in the same plane, just to touch without overlapping.
2. A hexagonal array with side length t , where t is the remaining wall thickness. Each point of the hexagonal array is the center of a crack with length $2t$. This geometry allows for cracks, if they lie in the same plane, to overlap—each crack overlaps about half of each of its neighboring cracks.

Details of the above bounding crack arrangement and geometry are given in *Stress Corrosion Cracking of Waste Package Outer Barrier and Drip Shield Materials* (SNL 2007 [DIRS 181953]).

The SCC density (ρ_{SCC}) is defined as the number of through-wall cracks per unit seismically-damaged area. The bounding crack density estimates ($\rho_{SCC,\min}$ and $\rho_{SCC,\max}$) are:

$$\rho_{SCC,\min} = \frac{\sqrt{3}}{2t^2}, \quad (\text{Eq. 6.3.3.2.4-1})$$

$$\rho_{SCC,\max} = \frac{2}{\sqrt{3}t^2}. \quad (\text{Eq. 6.3.3.2.4-2})$$

Using the crack length, $2c = 2t/\sqrt{3}$, for the lower bound, and $2c = 2t$ for the upper bound, the corresponding crack opening area density (crack opening area per unit seismically damaged area) ($\rho_{SCCA,\min}$ and $\rho_{SCCA,\max}$) are estimated:

$$\begin{aligned}
\rho_{SCCA,\min} &= \rho_{SCC,\min} A_{SCC} \\
&= \frac{\sqrt{3} (2\pi c^2) \sigma_{YS}}{2t^2 E} \\
&= \frac{\pi \sigma_{YS}}{\sqrt{3} E},
\end{aligned}
\tag{Eq. 6.3.3.2.4-3}$$

$$\begin{aligned}
\rho_{SCCA,\max} &= \rho_{SCC,\max} A_{SCC} \\
&= \frac{2 (2\pi c^2) \sigma_{YS}}{\sqrt{3} t^2 E} \\
&= \frac{4\pi \sigma_{YS}}{\sqrt{3} E}.
\end{aligned}
\tag{Eq. 6.3.3.2.4-4}$$

Therefore, the crack opening area density is represented as:

$$\rho_{SCCA} = C_{SD} \frac{\pi \sigma_{YS}}{\sqrt{3} E}, \tag{Eq. 6.3.3.2.4-5}$$

$$C_{SD} = \text{uniform}(1,4), \tag{Eq. 6.3.3.2.4-6}$$

where C_{SD} is an epistemic uncertainty factor for seismic damage, given by an uniform distribution between one and four.

The total SCC opening area per waste package ($A_{SCC,WP}$) or drip shield ($A_{SCC,DS}$) that results from the seismic damage is calculated as follows:

$$A_{SCC,DS} = C_{SD} \frac{\pi \sigma_{YS-DS}}{\sqrt{3} E_{DS}} A_{SD,DS}, \tag{Eq. 6.3.3.2.4-7}$$

$$A_{SCC,WP} = C_{SD} \frac{\pi \sigma_{YS-WP}}{\sqrt{3} E_{WP}} A_{SD,WP}. \tag{Eq. 6.3.3.2.4-8}$$

$A_{SD,WP}$ and $A_{SD,DS}$ are the seismically damaged area in waste package and drip shield respectively, and are provided by the seismic consequence abstraction analysis (DTNs: MO0703PASDSTAT.001 [DIRS 183148] and MO0703PASEISDA.002 [DIRS 183156]). Because the seismic damage analysis input does not associate specific locations on the waste package and drip shield surface, the damage to waste package and drip shield due to seismic ground motions is modeled as being distributed uniformly over the waste package or drip shield surface (SNL 2007 [DIRS 176828]).

6.3.3.2.5 Water Flux through and around the Breached Waste Package (F_4 and F_5)

The flux through (into and out of) the waste package, F_4 , is conceptualized to be the flux through patches, which originates from the flux through the drip shield (F_2). Advective flux of water through stress corrosion cracks is unlikely and of low consequence and therefore is screened out (DTN: MO0706SPAFEPLA.001 [DIRS 181613], FEP Numbers 2.1.03.10.0A and 2.1.03.10.0B). A quasi-steady state approach is used. The presence of a gap between adjacent waste packages is neglected in the TSPA Model. Dripping onto the waste package from condensation on the underside of the drip shield is screened out (DTN: MO0706SPAFEPLA.001 [DIRS 181613], FEP Number 2.1.08.14.0A).

A flux splitting algorithm analogous to the drip shield flux splitting algorithm (Section 6.3.2.4) is developed here. The analogy is appropriate, based on similarities in geometry and assumptions regarding the source of liquid flux falling onto the waste package. The surface of the waste package is a horizontal cylinder, as is the top of the drip shield, the primary difference that impacts liquid flow on the curved surface being that the radius of curvature of the waste package is smaller than that of the drip shield. Thus, flow behavior on the surface of the waste package should be similar to that on the drip shield. In particular, if any water is available, it is expected to flow over the surface of the waste package in rivulets rather than as film flow, based on findings of the breached drip shield experiments (BSC 2003 [DIRS 163406]).

Whereas drip locations on the drip shield could reasonably be confined to the crown of the drip shield (because the drift seepage flux will most likely originate from the crown of the drift), the drip locations may be more widely dispersed on the waste package. This is the case for drips that fall from breaches in the drip shield, which are randomly located on the drip shield. Since breaches (mainly general corrosion patches) in the waste package are also randomly located, the fraction of dripping flux falling on the waste package that flows into the waste package might be expected to be proportional to the total area of waste package patches. However, since drips that fall onto an intact waste package surface will drain down the surface, the flux of water, if any, entering a waste package is proportional to the total length of patches. Again, the analogy to the drip shield applies. Rivulets flowing down the surface of the waste package are intercepted in proportion to the lengths of the patches (ignoring interference by multiple patches).

Two other considerations reinforce the comparison with the drip shield. First, any condensation on the underside of the drip shield that might fall onto the waste package, if it were considered, would fall from the crown of the drip shield. (Condensation on the underside of the drip shield has been excluded from consideration in TSPA on the basis of low consequence (DTN: MO0706SPAFEPLA.001 [DIRS 181613], FEP Numbers 2.1.08.14.0A).) Thus, for condensation at least, the geometry is completely analogous to that of the drip shield inside the drift. Second, the drip shield is modeled as a single entity and all drip shields in the repository fail by general corrosion at the same time in the model for a given realization (SNL 2007 [DIRS 178871]), with uncertainty in the corrosion rate of the drip shield resulting in different failure times in each realization. Once the drip shield is gone, the seepage flux will now fall directly from the drift crown onto the waste package crown, again completing the analogy with the drip shield under the drift crown. Since the corrosion rate of the titanium drip shield is higher than that of the Alloy 22 waste package outer corrosion barrier, the situation where a breached waste package lies unprotected under seepage from the drift crown should be more

likely than a breached waste package underneath a breached but still partially effective drip shield. Therefore, within the uncertainty of the model, it is an appropriate simplification to model the flux impinging on the waste package as falling entirely on the crown of the waste package. One implication of this simplification is that, as with the drip shield, half of this flux flows down each side of the waste package.

Based on these arguments, a flux splitting algorithm for the waste package can be given that is completely analogous to the drip shield flux splitting algorithm:

$$F_4 = \min \left[F_2 \left(\frac{N_{bWP} \ell_{WP}}{L_{WP}} \right) \left(1 + \frac{\tan \alpha}{2} \right) f_{WP}, F_2 \right], \quad (\text{Eq. 6.3.3.2.5-1})$$

where F_4 is the flux through the waste package, F_2 is the flux through the drip shield, and L_{WP} is the total axial length of the waste package. N_{bWP} patches each of length $2\ell_{WP}$ comprise the breaches in the waste package. Flow through stress corrosion cracks is neglected as being unlikely to occur (see Section 6.3.3.2.4).

The factor f_{WP} accounts for the uncertainty in this algorithm. As with the corresponding factor f_{DS} for the drip shield, bounds can be established for f_{WP} based on the dimensions of the patches, the waste package and the uncertain rivulet spread angle. A lower bound of zero is necessary to account for the possibility that seepage through the drip shield is completely diverted by an intact portion of the waste package outer corrosion barrier.

For an upper bound on f_{WP} , the drip shield experiments (BSC 2003 [DIRS 163406]) provide some guidance. Since the radius of curvature of the waste packages is smaller than that of the drip shield, the rivulet spread angle on the waste packages would be expected to differ from, and probably be smaller than, the spread angle on the drip shield. In some experiments, the drip location on the drip shield mock-up was well away from the crown on more steeply inclined regions of the drip shield. Rivulets flowing from those drip locations may simulate more closely the behavior on a surface having a smaller radius, such as a waste package. Because the waste package has a smaller radius and more curvature than the drip shield surface, more of the surface is sloped to such a degree that water will readily flow down from it by gravity. Only a larger cylindrical surface (the drip shield mock-up) was available on which to observe gravity flow behavior. Observations away from the crown, where the slope is steep enough to initiate flow as readily as on a more highly curved surface, are appropriate analogs to measurements on an actual smaller cylinder. An analysis of drip shield experimental data for off-crown drip locations (Section 6.5.1.1.3) gives a mean spread angle of 13.7° and a range from 5.5° to 22.0° . In analogy to f_{DS} , an upper bound on f_{WP} can be obtained using the minimum rivulet spread angle α of 5.5° and the known values for N_{bWP} (SNL 2007 [DIRS 178871]), $2\ell_{WP}$, and L_{WP} :

$$f_{WP} = \frac{1}{\frac{N_{bWP} \ell_{WP}}{L_{WP}} \left(1 + \frac{\tan \alpha}{2} \right)}. \quad (\text{Eq. 6.3.3.2.5-2})$$

As with the drip shield, the term $\left(1 + \frac{\tan \alpha}{2}\right)$, which is uncertain itself, can be factored in with f_{WP} to simplify the model, resulting in:

$$F_4 = \min \left[F_2 \left(\frac{N_{bWP} \ell_{WP}}{L_{WP}} \right) f'_{WP}, F_2 \right], \quad (\text{Eq. 6.3.3.2.5-3})$$

where

$$f'_{WP} = \left(1 + \frac{\tan \alpha}{2} \right) f_{WP} \quad (\text{Eq. 6.3.3.2.5-4})$$

is assigned a uniform distribution. In Section 6.5.1.1.3, an upper bound on f'_{WP} is developed based on results of the breached drip shield experiments. The range for f'_{WP} based entirely on experimental results is used in TSPA.

Finally, the flux that is diverted around the waste package, F_5 , is calculated using continuity of the quasi-static flow around and into the waste package:

$$F_5 = F_2 - F_4 \quad (\text{Eq. 6.3.3.2.5-5})$$

6.3.3.3 Condensation on the Drip Shield

Condensation of water on the underside of the drip shield may occur, as shown by a bounding analysis (SNL 2007 [DIRS 181648], Sections 6.3.7.2 and 6.1[a]). However, analysis of the amount of such condensation and its possible effects leads to a conclusion that condensation under drip shields will have limited occurrence and intensity, and that the overall effect on dose will be insignificant (DTN: MO0706SPAFEPLA.001 [DIRS 181613], FEP Number 2.1.08.14.0A).

Thermal-hydrologic simulations (SNL 2007 [DIRS 181648], Sections 6.3.3.2.1 and 8) show that condensation under any drip shield does not occur when the local water vapor partial pressure is controlled by the temperature at the bottom of the invert, which is always cooler than the top. Calculations in *Multiscale Thermohydrologic Model* (SNL 2007 [DIRS 181383], Section 6.3.11 and Table 6.3-45) show that for any given cross section, the coolest and most humid location is always at the bottom of the invert. These simulations also show that water vapor that is transported axially along the drift has a greater tendency to condense near the bottom of the invert, where it is coolest, than at the top of the invert or the underside of the drip shield. This occurs because the invert is permeable to gas movement and a poor conductor of heat.

The condensation model results show that condensation under a drip shield may occur if water vapor evaporates from the invert at one waste package location, then migrates under the connected drip shield segments and condenses on the underside of a cooler drip shield at another location (SNL 2007 [DIRS 181648], Section 6.3.7.2). This mode of formation is limited by the

efficiency of axial water vapor migration as compared with radial mixing. Also, the condensation model shows that the radial thermal gradient is much greater than the axial thermal gradient (SNL 2007 [DIRS 181648], Figure 6.3.5-13 and Figure J-1, typically). Such thermal gradients drive mixing, promoting condensation on cooler surfaces such as the drift wall, the bottom of the invert, or possibly the sides of the drip shield.

Experimental results reported in *In-Drift Natural Convection and Condensation* (SNL 2007 [DIRS 181648], Table 7.4.1-24) show that the drip shield sides are cooler than the top, because of proximity to the waste package surface and because of natural convection. Therefore, any condensation occurs preferentially on the sides, where it cannot contact the waste package.

The condensate will be a weak carbonic acid solution (pH approximately 5) (SNL 2007 [DIRS 177412]), with condensation occurring when the drip shield temperatures drop below about 96°C. These conditions do not initiate localized corrosion of Titanium Grade 7, and are within the range of validation for implementation of the corrosion models in TSPA for general corrosion (SNL 2007 [DIRS 178519], Sections 8.1 and 6.4.3.4, and Equation 6-29 which shows no chemistry dependence; SNL 2007 [DIRS 180778], Sections 8.3 and 6.9.1) and localized corrosion (SNL 2007 [DIRS 178519], Section 8.3; SNL 2007 [DIRS 180778], Section 8.4). Condensate mixed with dust is no more aggressive than the deliquescent dust without condensate. Condensate can interact with dust, yielding solutions more dilute than those resulting from dust deliquescence, which is addressed by excluded FEP Numbers 2.1.09.28.0A and 2.1.09.28.0B (DTN: MO0706SPA FEPLA.001 [DIRS 181613]). Therefore, the presence of any condensate on the underside of the drip shield does not impact the barrier capability of the drip shield.

Condensate waters present on the underside of the drip shield have a small potential to drip onto exposed waste packages. Analysis of advective flux through stress corrosion cracks (SNL 2007 [DIRS 181953], Section 6.3.7), an analogous situation that similarly accounts for water on the underside of the drip shield, excludes this process on the basis of low consequence (DTN: MO0706SPA FEPLA.001 [DIRS 181613], FEP Number 2.1.03.02.0B; DTN: MO0706SPA FEPLA.001 [DIRS 181613], FEP Number 2.1.03.10.0B).

6.3.3.4 Flux into and through the Invert (F_6 and F_7)

The flux leaving the waste package is equal to the flux entering the waste package, F_4 , by the quasi-steady-state flow assumption (the net effect of Assumptions 5.1 through 5.4 and 5.7). The total flux entering the invert from above is equal to the sum of the diversion around the waste package, F_5 , the flux leaving the waste package (equal to F_4), and the diversion around the drip shield, F_3 . The liquid flux leaving the invert, F_8 , is equal to the total flux entering the invert from above plus the imbibition flux from the UZ matrix into the invert. That is,

$$F_6 = F_5 + F_4 + F_3, \quad (\text{Eq. 6.3.3.4-1})$$

and

$$F_8 = F_6 + F_7. \quad (\text{Eq. 6.3.3.4-2})$$

Only the flux leaving the waste package, F_4 , can transport radionuclides to the invert.

Multiscale Thermohydrologic Model (SNL 2007 [DIRS 181383]) determines the imbibition flux from the UZ host rock matrix into the invert, F_7 , as well as the water saturation in the invert. The imbibition flux from the UZ matrix into the invert exits the invert back into the UZ matrix. The advective flux that flows into the invert from above, F_6 , exits the invert into the UZ fractures.

6.3.4 Transport through the EBS

The conceptual model for transport through the EBS consists of transport through three separate domains: (1) waste form, (2) waste package corrosion products, and (3) the invert. Transport through each of these domains occurs by advection and diffusion. Radionuclides travel in sequence through each of these domains. In other words, all radionuclides entering the corrosion products domain come from the waste form domain, and all radionuclides exiting the corrosion products domain enter the invert domain. Advection in each domain is modeled as steady state flow; i.e., the flow rate may vary over time, but no accumulation occurs. Diffusion through each domain is considered to be transient.

The rate of diffusive transport through each domain is dependent upon the following parameters: the effective diffusion coefficient, the cross-sectional area available for diffusive transport, and the diffusion path length across which a concentration gradient exists. For assumed transport through thin water films adsorbed onto materials, a reasonably bounding value for the effective diffusion coefficient for each radioelement is obtained using the free-water diffusion coefficient for each radioelement, modified to account for porosity, saturation, temperature, and the uncertainty associated with the dependence on these parameters. The cross-sectional area for transport in each domain is dependent upon the geometry of the domain, the relative humidity, and the specific surface area and adsorption isotherm for the given material. A range of diffusion path lengths is determined from the geometry of the domain.

The waste form is the source of all radionuclides in the repository system. If sufficient water is available, radionuclides mobilized from the waste form can be transported from the waste form, out of the waste package, downward through the invert, and into the UZ, as shown in Figure 6.3-1. Transport out of the waste package can occur by advection, when there is a liquid flux through the waste package, and by diffusion through assumed continuous liquid pathways in the waste package, including thin films of adsorbed water. These two transport processes (diffusion and advection) are each a function of the type of penetrations through the drip shield and waste package and the local seepage conditions. Diffusion can occur through stress corrosion cracks or through general corrosion patches in the waste package both with and without liquid flux through the waste package. Advection is not considered through stress corrosion cracks or through corrosion patches in the absence of seepage flux.

The free-water diffusion coefficient for each radioelement for radionuclide transport is given in Table 4.1-7. In addition to the radionuclides listed in Table 4.1-7, three other radionuclides—actinium, curium, and plutonium-241—are tracked in TSPA calculations, because they decay into other radionuclides that are tracked, but due to their short half-lives, their transport is not

modeled, based on the *Radionuclide Screening* analysis (SNL 2007 [DIRS 177424], Table 7-1); these are assigned diffusion coefficients of zero. The effects of temperature are accounted for using the formulation in Section 6.3.4.1.2. The effects of porosity, liquid saturation, and uncertainty on the invert diffusion coefficients are incorporated using the formulation in Section 6.3.4.1.1. For the waste form and corrosion product domains, the effects of porosity and water saturation on the diffusion coefficients are accounted for using the formulation in Section 6.3.4.3.5.

Advective transport is straightforward in the RTA. In particular, mobilized radionuclides are transported with the local liquid flux from the waste package (F_4) through the invert (F_6) to the UZ fractures (F_8). There are no modifications for dispersive effects (see Section 6.3.1.2); because the flow is modeled as one-dimensional vertically downward, lateral dispersion is not considered in the RTA. These effects are not considered important because lateral dispersion is directly proportional to the path length, and the path length through the invert is short compared to the entire path length to the accessible environment.

Diffusive transport depends on concentration gradients. The concentrations of radionuclides in the waste form domain are determined from the degree of waste form degradation and the solubility limit for each radionuclide. The concentrations in the waste package corrosion products domain take into account radionuclide solubility limits, sorption of radionuclides onto the corrosion products, sorption and desorption onto colloids, and colloid stability. The concentrations in the invert domain depend on the radionuclide solubility limits, colloid stability in the invert, the transfer of radionuclides between the corrosion products domain and the invert, and the boundary concentrations at the invert-UZ interface. The boundary condition at the UZ interface is implemented by defining multiple grid cells in the UZ that provide a diffusive path length that is sufficiently long such that the concentration at the outlet of the farthest cell from the drift wall can realistically be assigned a value of zero (Section 6.5.2.6).

The emphasis in this RTA is on transport of radionuclides through the EBS after the radionuclides are mobilized. This abstraction does not define related elements of the TSPA, such as corrosion processes, radionuclide solubility limits, waste form dissolution rates and concentrations of colloidal particles, which are generally represented as boundary conditions or input parameters for the RTA. This abstraction provides the algorithms for determining radionuclide transport in the EBS using the flow and radionuclide concentrations determined by other elements of the TSPA.

6.3.4.1 Invert Diffusion Submodel

The TSPA Model requires an abstraction for the effective diffusion coefficient in granular materials as a function of radionuclide, porosity, saturation, temperature, and concentration. This submodel is intended specifically to apply to the invert. The abstraction is as follows:

- Use the species dependent free water diffusion coefficients in Table 4.1-7.
- Modify the free water diffusion coefficient for the porosity and liquid saturation of the invert. The modification for porosity and saturation is based on Archie's law and experimental data for granular media, and is presented in Section 6.3.4.1.1.

- Further modify the diffusion coefficient for variation of the invert temperature using the formulation in Section 6.3.4.1.2. The invert temperature is provided by *Multiscale Thermohydrologic Model* (SNL 2007 [DIRS 181383]).
- Ignore the increase in the diffusion coefficient with increasing ionic strength of concentrated solutions (see Section 6.3.4.1.3). The maximum modification for a highly concentrated solution of potassium iodide is a factor of 1.27. This factor is well within the range of uncertainty of the invert diffusion coefficient (see Equations 6.3.4.1.1-22 and 6.3.4.1.1-27), and is neglected for the TSPA.

6.3.4.1.1 Modification of Diffusion Coefficient for Porosity and Saturation of the Invert

The modified diffusion coefficient for a partly saturated porous medium can be estimated from any of a number of empirical relationships developed in the soils and petroleum sciences, including the model of Penman (1940 [DIRS 109941]), the power law of Millington and Quirk (1961 [DIRS 139143]), and Archie's law (Archie 1942 [DIRS 154430]), among others (Jury 1991 [DIRS 102010], Section 6.3 and Table 6.1). All of these relationships yield similar values of the diffusion coefficient in unsaturated porous media, particularly at high water contents; each one is best suited to a particular soil structure and texture, such as undisturbed soil, compacted soil, consolidated sediments, etc. Archie's law was selected for use in the RTA in part because of its acceptance in the petroleum reservoir engineering literature (Bear 1988 [DIRS 101379], pp. 113 – 116), and in part because it is based on the same relationship between electrical conductance and diffusivity in a partially saturated porous rock that was used by Conca and Wright (1992 [DIRS 100436]), whose measurements of the diffusion coefficients in crushed tuff data are applied later in this section to diffusion in the invert. This relationship enables diffusion coefficients to be obtained from experimental measurements of the electrical conductivity of samples of the porous medium. From these measurements, an empirical function can be developed that relates the diffusion coefficient to the porosity and saturation of the porous medium. An alternative to the Archie's law approach for determination of the diffusion coefficient for the single-continuum invert is presented in Section 6.6.4.1.

Archie's law is an empirical function relating the electrical resistivity and porosity of a porous medium (Archie 1942 [DIRS 154430], p. 57; Keller and Frischknecht 1966 [DIRS 111470], p. 21):

$$\rho_s = a\rho_w^e\phi^{-m}, \quad (\text{Eq. 6.3.4.1.1-1})$$

where ρ_s is the bulk resistivity (or specific resistance) of the fully water-saturated porous medium (Ω m), ρ_w^e is the resistivity of liquid water (Ω m), ϕ is the porosity (m^3 pore volume m^{-3} total volume), m is a cementation factor (dimensionless), and a is an empirical parameter (dimensionless) that, to a first approximation, may be assumed to have a value of 1 (Keller and Frischknecht 1966 [DIRS 111470], p. 21).

For a partially saturated porous medium, the resistivity is given by Bear (1988 [DIRS 101379], p. 116); Keller and Frischknecht (1966 [DIRS 111470], p. 28); and Pirson (1963 [DIRS 111477], p. 24):

$$\rho_t = \rho_s S_w^{-n}, \quad (\text{Eq. 6.3.4.1.1-2})$$

where ρ_t is the bulk resistivity (or specific resistance) of the partially saturated porous medium ($\Omega \text{ m}$), S_w is the water saturation ($\text{m}^3 \text{ water m}^{-3} \text{ pore volume}$), and n is a saturation exponent (dimensionless).

The cementation factor m “is somewhat larger than 2 for cemented and well-sorted granular rocks and somewhat less than 2 for poorly sorted and poorly cemented granular rocks” (Keller and Frischknecht 1966 [DIRS 111470], p. 21). For unconsolidated sand, a value of 1.3 has been reported for the cementation factor (Bear 1988 [DIRS 101379], p. 116; Pirson 1963 [DIRS 111477], p. 24). The invert, being composed of well-graded crushed tuff (SNL 2007 [DIRS 179354], Table 4-1, Parameter Number 02-08B), should have cementation characteristics similar to unconsolidated sand and poorly cemented granular rock, with a cementation factor of 1.3 or slightly higher, but less than 2.

For unconsolidated sand, a value of 2 is accepted for the saturation exponent n (Bear 1988 [DIRS 101379], p. 116; Keller and Frischknecht 1966 [DIRS 111470], p. 28; Pirson 1963 [DIRS 111477], p. 24).

Combining and simplifying Equations 6.3.4.1.1-1 and 6.3.4.1.1-2 results in an Archie’s law formulation that gives the bulk resistivity of a partially saturated porous medium:

$$\rho_t = \rho_w^e \phi^{-m} S_w^{-n}. \quad (\text{Eq. 6.3.4.1.1-3})$$

The resistance, R_t (Ω), of a porous medium of length L and cross-sectional area A is given by:

$$R_t = \rho_t L / A. \quad (\text{Eq. 6.3.4.1.1-4})$$

Since the electrical conductance, G ($\text{S} = \Omega^{-1}$), is defined as the reciprocal of resistance (Atkins 1990 [DIRS 111464], p. 750), Archie’s law can be written for a partially saturated porous medium in terms of the conductance of the bulk porous medium, G_t (S) and the conductance of water, G_w (S):

$$G_t = G_w \phi^m S_w^n. \quad (\text{Eq. 6.3.4.1.1-5})$$

The last step is to rewrite Archie's law in terms of diffusion coefficients. The diffusion coefficient of an ion in solution is related to the conductivity through the Nernst-Haskell equation (Perry and Chilton 1973 [DIRS 104946], p. 3-235) for diffusion in a binary electrolyte mixture at infinite dilution:

$$D_w = \frac{RT}{F^2} \left(\frac{l_+^0 l_-^0}{\Lambda_0} \right) \left(\frac{z_+ + z_-}{z_+ z_-} \right). \quad (\text{Eq. 6.3.4.1.1-6})$$

where:

- D_w = diffusion coefficient ($\text{m}^2 \text{s}^{-1}$)
- R = molar gas constant = $8.314472 \text{ J mol}^{-1} \text{ K}^{-1}$ (Lide 2002 [DIRS 160832], p. 1-8)
- T = temperature (K)
- F = Faraday constant = $96485.3415 \text{ C mol}^{-1}$ (Lide 2002 [DIRS 160832], p. 1-7)
- l_+^0, l_-^0 = cationic and anionic molar conductivity, respectively, at infinite dilution ($\text{S m}^2 \text{ mol}^{-1}$)
- Λ_0 = equivalent electrolyte molar conductivity at infinite dilution ($\text{S m}^2 \text{ mol}^{-1}$)
- z_+, z_- = valence of cation and anion, respectively; magnitude only—no sign (dimensionless).

This equation can be simplified by making use of the average ionic molar conductivity at infinite dilution, \bar{l} , where

$$\bar{l} = \frac{\Lambda_0}{2} = \frac{l_+^0 + l_-^0}{2}. \quad (\text{Eq. 6.3.4.1.1-7})$$

Since the ionic molar conductivities l_+^0 and l_-^0 are non-negative numbers, $\bar{l}^2 \geq (l_+^0)(l_-^0)$, which can be seen as follows:

$$\begin{aligned}
 \bar{l}^2 &= \left(\frac{l_+^0 + l_-^0}{2} \right)^2 \\
 &= \frac{(l_+^0)^2 + 2(l_+^0)(l_-^0) + (l_-^0)^2}{4} \\
 &= \frac{(l_+^0)^2 + (l_-^0)^2}{4} + \frac{(l_+^0)(l_-^0)}{2} \\
 &= \frac{(l_+^0)^2 + (l_-^0)^2}{4} + \frac{(l_+^0)(l_-^0)}{2} + \frac{(l_+^0)(l_-^0)}{2} - \frac{(l_+^0)(l_-^0)}{2} \\
 &= \frac{(l_+^0)^2 + (l_-^0)^2}{4} - \frac{(l_+^0)(l_-^0)}{2} + (l_+^0)(l_-^0) \\
 &= \frac{1}{4}(l_+^0 - l_-^0)^2 + (l_+^0)(l_-^0) \\
 &\geq (l_+^0)(l_-^0).
 \end{aligned} \tag{Eq. 6.3.4.1.1-8}$$

Thus, the square of the average ionic molar conductivity can be substituted for the product of the individual conductivity. This substitution will generally overestimate the diffusion coefficient given by Equation 6.3.4.1.1-6. At the same time, the valence of the ions z_+ and z_- are given a value one, because this, too, maximizes the diffusion coefficient. With these substitutions, Equation 6.3.4.1.1-5 simplifies to give the maximum diffusivity in a binary electrolyte mixture at infinite dilution:

$$\begin{aligned}
 D_w &= \frac{RT}{F^2} \left(\frac{\bar{l}^2}{2\bar{l}} \right) (2) \\
 &= \frac{RT\bar{l}}{F^2} \\
 &= \frac{RT\Lambda_0}{2F^2}.
 \end{aligned} \tag{Eq. 6.3.4.1.1-9}$$

This shows that the diffusion coefficient for ions in an infinitely dilute binary mixture is proportional to the molar conductivity and therefore to the conductance of the electrolyte. For multicomponent solutions at other than infinite dilution, this equation represents an approximation with an associated uncertainty that can be estimated by comparison with experimental data, which is discussed later.

The relationship between diffusion coefficient and the measured conductivity of samples is dependent on the experimental method and apparatus used to obtain the conductivity of the porous medium. Conductivity is determined by measuring the electrical resistance of a sample in a conductivity cell. The cell is calibrated using a solution of known conductivity, and a cell constant. With no interfering porous medium, the conductance of water, G_w , is directly proportional to the equivalent electrolyte molar conductivity at infinite dilution (Λ_0), which in

turn, from Equation 6.3.4.1.1-9, is proportional to D_w . Due to the interference of the solid, the conductance of the bulk porous medium, G_i is more complicated and is proportional to the porosity, saturation, the diffusivity of the ion and the tortuosity, as explained in the following discussion of diffusion coefficient measurements.

Conca and Wright (1992 [DIRS 100436]) and Conca et al. (1993 [DIRS 170709]) measured the diffusion coefficient of unsaturated soil, gravel, bentonite, rock, and crushed tuff from Yucca Mountain over a broad range of water contents by measuring the electrical conductivity of samples. These measured data are qualified in Appendix H and have been used to analyze the dependence of the diffusion coefficient on volumetric moisture content for a variety of granular materials. Figure 6.3-4 presents a summary of the diffusivity data for various granular media at volumetric moisture contents ranging between 1.5 percent and 66.3 percent.

The measurements of Conca and Wright are based on the Nernst-Einstein relationship:

$$D_{wi} = \frac{RT}{F^2} \frac{\kappa_w t_i}{z_i C_i}, \quad (\text{Eq. 6.3.4.1.1-10})$$

where D_{wi} is the diffusion coefficient of the i^{th} ion in a dilute aqueous solution ($\text{m}^2 \text{s}^{-1}$), F is the Faraday constant (C mol^{-1}), R is the universal gas constant ($\text{J mol}^{-1} \text{K}^{-1}$), T is the absolute temperature (K), κ_w is the electrical conductivity (S m^{-1}) of the solution, t_i is the transport number for the i^{th} ion (which is the portion of the total electrical current carried by the i^{th} ion), z_i is the charge valence of the i^{th} ion, and C_i is the concentration of radionuclide species i (mol m^{-3}). Equation (2) in Conca and Wright (1992 [DIRS 100436]) shows that D_{wi} can be determined from the measured conductance (an extensive quantity dependent on the physical dimensions or mass of the sample equal to the reciprocal of resistance) of the soil or rock sample. In fact, what Conca and Wright measured and what the left-hand side of the equation should be is $\phi S_w D_i$, the effective or bulk diffusion coefficient in the porous medium. D_{wi} includes the effect of tortuous pathways, and is equal to D_{wi} multiplied by tortuosity.

There is much literature on how to measure the conductivity and/or salinity of soil water from bulk measurements of the sample conductance. For example, Rhoades and Oster (1986 [DIRS 173846]), Rhoades et al. (1976 [DIRS 173835]), and Shainberg et al. (1980 [DIRS 173836]) present a two parameter model for representing the bulk soil or rock conductivity, κ_a (S m^{-1}), in terms of the interstitial solution conductivity, κ_w , and the surface conductivity (conductivity of the double layer), κ_s . The quantity κ_a is the experimentally measured quantity, which is equal to the actual conductance measurement of the impedance bridge or electrode array, multiplied by the cell constant, which is the geometric factor that converts the extensive quantity, conductance, to the intensive quantity, conductivity. Conca and Wright incorrectly substitute κ_a directly into the Nernst-Einstein equation (Eq. 6.3.4.1.1-10). What needs to be substituted into the Nernst-Einstein equation is κ_w , which can be determined from κ_a with the linear, two-resistor model of Rhoades et al. (1976 [DIRS 173835]) and Rhoades and Oster (1986 [DIRS 173846]):

$$\kappa_a = \kappa_w \phi S_w T^* + \kappa_s, \quad (\text{Eq. 6.3.4.1.1-11})$$

where ϕS_w is the water content; T^* is the transmission coefficient, which incorporates tortuosity effects and varies as a function of water content. The transmission coefficient is related to formation factor, F_R (dimensionless), at high solution concentrations, through the relationship $F_R = (\phi S_w T^*)^{-1}$ (Shainberg et al. 1980 [DIRS 173836]). The quantity κ_s is the conductivity of the surface or solid (i.e., the double layer). Rhoades et al. (1976 [DIRS 173835]) have correctly shown in their Equation 11 the relationship between the measured κ_a and κ_w ($=1/R_b$ in their equation), if the conductivity of the surface or solid, κ_s , is ignored. In particular, consider the case where the κ_s electrical pathway is effectively an insulator (i.e., does not contribute to the overall bulk sample conductance). Then the above equation reduces to:

$$\kappa_a = \kappa_w \phi S_w T^*, \quad (\text{Eq. 6.3.4.1.1-12})$$

which can be solved for κ_w as $\kappa_w = \kappa_a / \phi S_w T^*$ and then substituted back into the Nernst-Einstein equation:

$$D_{wi} = \frac{RT}{F^2} \frac{\kappa_a}{\phi S_w T^*} \frac{t_i}{z_i C_i}. \quad (\text{Eq. 6.3.4.1.1-13})$$

The above equation solves for the ionic diffusion coefficient in terms of the measured conductivity, κ_a , of the rock sample. Replacing this conductivity with the corresponding extensive quantity, the conductance G , as designated by Conca and Wright, and the geometric factor or cell constant, Θ (m^{-1}), gives the following:

$$D_{wi} = \frac{RT}{F^2} \frac{G\Theta}{\phi S_w T^*} \frac{t_i}{z_i C_i}. \quad (\text{Eq. 6.3.4.1.1-14})$$

However, as is clear from the equation in Wright's report (CRWMS M&O 2000 [DIRS 156680], p. A-8) and the associated Table A-1, this was not what was done by these researchers, and the factor $\phi S_w T^*$ was left out of this equation by Wright. In fact, Wright tabulated the quantity:

$$\frac{RT}{F^2} \frac{G\Theta t_i}{z_i C_i}, \quad (\text{Eq. 6.3.4.1.1-15})$$

in Table A-1, which implies that they actually solved for $D_{wi} \phi S_w T^*$, the bulk diffusivity, not the ionic diffusivity, which can be seen by multiplying both sides of Equation 6.3.4.1.1-14 by $\phi S_w T^*$. Thus, the tabulated diffusion coefficients of Conca and Wright (1990 [DIRS 100436] and 1992 [DIRS 100436]) must be used as the quantity $\phi S_w D_i$ in the mass conservation equation (Equation 6.5.1.2-39), where D_i includes the effect of tortuous pathways, and is equal to D_{wi} multiplied by tortuosity; i.e., the Conca and Wright reported diffusion coefficients are in fact the

bulk diffusivity in the mass conservation equation. For the invert, the diffusion coefficient is denoted by D_{il} , where the subscript I refers to the invert.

Archie's law (Equation 6.3.4.1.1-5) can then be written in terms of the effective diffusivity of the bulk porous medium and the free water diffusivity of radioelement i , D_i :

$$\phi S_w D_{il} = D_{wi} \phi^m S_w^n. \quad (\text{Eq. 6.3.4.1.1-16})$$

This is the form of Archie's law that is generally applied for determination of the effective diffusion coefficient, D_{il} , as a function of porosity and saturation in a partly saturated, granular medium. The diffusion coefficient, D_{il} , as introduced here and used throughout this section, is an effective value for species i that implicitly includes the effects of tortuosity. With values of the cementation factor, m , of 1.3 and the saturation exponent, n , of 2 for unconsolidated sand, Archie's law becomes as:

$$\phi S_w D_{il} = D_{wi} \phi^{1.3} S_w^2. \quad (\text{Eq. 6.3.4.1.1-17})$$

Because the diffusion coefficients were measured by Conca and Wright as a function of volumetric water content, they have been analyzed using an alternative form of Archie's law in which the cementation factor and saturation exponent are equal (i.e., $n = m$). The effective diffusion coefficient is then a function of θ , the percent volumetric moisture content, defined as $\theta = 100\phi S_w$:

$$\begin{aligned} \phi S_w D_{il} &= D_{wi} \phi^m S_w^n \\ &= D_{wi} \left(\frac{\theta}{100} \right)^n \end{aligned} \quad (\text{Eq. 6.3.4.1.1-18})$$

A statistical analysis using Microsoft Excel (Appendix G) produces a fit to the diffusivity data (Conca and Wright 1992 [DIRS 100436], Figure 2; Conca et al. 1993 [DIRS 170709], Figure 2; listed in Table 4.1-16) using Equation 6.3.4.1.1-18 for moisture content in the range of 1.5 percent to 66.3 percent. The statistical fit to the effective diffusion coefficient, D_{il} , is based on a linearizing transformation to the variables X and Y , defined as:

$$\begin{aligned} Y &= \log_{10}(\phi S_w D_{il} / D_{wi}) \\ X &= \log_{10} \theta - 2, \end{aligned} \quad (\text{Eq. 6.3.4.1.1-19})$$

where

$$\begin{aligned} D_{il} &= \text{effective invert diffusion coefficient for species } i \text{ (m}^2 \text{ s}^{-1}\text{)} \\ D_{wi} &= \text{free water diffusivity for species } i \text{ (m}^2 \text{ s}^{-1}\text{)} \\ \phi &= \text{porosity (m}^3 \text{ void volume m}^{-3} \text{ bulk volume)} \end{aligned}$$

- S_w = water saturation (m^3 water volume m^{-3} void volume)
 θ = volumetric moisture content (percent, 100 m^3 water volume m^{-3} bulk volume).

The statistical fit uses the self-diffusion coefficient of water ($2.299 \times 10^{-9} \text{ m}^2 \text{ s}^{-1}$) (Mills 1973 [DIRS 133392], Table III) as a bounding value for the free water diffusivity for species i .

The slope of the X - Y relationship is found to be 1.863, leading to the following linear equation for Y as a function of X :

$$Y = 1.863X$$

$$\log_{10} \left(\frac{\phi S_w D_{il}}{D_{wi}} \right) = 1.863(\log_{10} \theta - 2), \quad (\text{Eq. 6.3.4.1.1-20})$$

or

$$\begin{aligned} \phi S_w D_{il} &= D_{wi} \phi^{1.863} S_w^{1.863} \\ &= D_{wi} \left(\frac{\theta}{100} \right)^{1.863}. \end{aligned} \quad (\text{Eq. 6.3.4.1.1-21})$$

The statistical fit for the effective invert diffusion coefficient has uncertainty, which is represented by the scatter of data points around the fit in Figure 6.3-4. This uncertainty is approximated by a normal distribution for the residuals (data–model) in log-log space. This normal distribution of residuals has a mean value of 0.033 and a standard deviation of 0.218. The uncertainty can be incorporated into the statistical fit as an additional factor on the full statistical fit.

$$\phi S_w D_{il} = D_{wi} \phi^{1.863} S_w^{1.863} 10^{ND(\mu=0.033, \sigma=0.218)}, \quad (\text{Eq. 6.3.4.1.1-22})$$

where ND represents a normal distribution with a mean, μ , of 0.033 and a standard deviation, σ , of 0.218. ND is in the exponent because the residuals are calculated in the log-log space of the statistical fit. This statistical fit is the submodel for the invert diffusion coefficient to be used for the TSPA. Since the normal distribution is theoretically unbounded, unrealistic values for the diffusion coefficient could potentially be obtained. To avoid this potential problem, the implementation in the TSPA will use a truncated normal distribution, limited to plus or minus three standard deviations from the mean.

Figure 6.3-4 presents the statistical fit (solid line) and the upper and lower bounds (dashed lines) at three standard deviations above and below the fit. The dashed lines encompass almost all the data points, because ± 3 standard deviations includes 99.7 percent of the area under a normal distribution. Equation 6.3.4.1.1-22, therefore, accurately represents the uncertainty in the diffusivity data for the TSPA calculations.

Because the saturation exponent (1.863) is less than the generally accepted value (2), the fit to the data provides less of a bounding estimate for the effective diffusion coefficient than if the accepted value were used. However, the estimate using Equation 6.3.4.1.1-22 is realistic instead of simply bounding the diffusion coefficient because it is developed from measured data rather than using the general behavior of unconsolidated sand as its basis. Furthermore, being based on a large number of measured data, the uncertainty in effective diffusion coefficient using Equation 6.3.4.1.1-22 is quantified, which provides additional support for use of this equation instead of a more bounding approach using the accepted value for saturation exponent.

One element of the uncertainty in the diffusion coefficient is the uncertainty in the porosity of the invert. The bulk porosity of the invert crushed tuff is expected to vary between 0.27 and 0.39, with an average of 0.31 (BSC 2004 [DIRS 168138], Table 5). From Equation 6.3.4.1.1-22, the diffusion coefficient would vary due to variations in porosity by a factor of:

$$\frac{(\phi S_w D_i)_{max}}{(\phi S_w D_i)_{min}} = \frac{\phi_{max}^{1.863}}{\phi_{min}^{1.863}} = \left(\frac{0.39}{0.27} \right)^{1.863} = 1.98. \quad (\text{Eq. 6.3.4.1.1-23})$$

The range about the mean diffusion coefficient, $(\overline{\phi S_w D})$, would be:

$$\frac{(\phi S_w D_i)_{min}}{(\overline{\phi S_w D_i})} = \left(\frac{0.27}{0.31} \right)^{1.863} = 0.77 \quad (\text{Eq. 6.3.4.1.1-24})$$

to

$$\frac{(\phi S_w D_i)_{max}}{(\overline{\phi S_w D_i})} = \left(\frac{0.39}{0.31} \right)^{1.863} = 1.53. \quad (\text{Eq. 6.3.4.1.1-25})$$

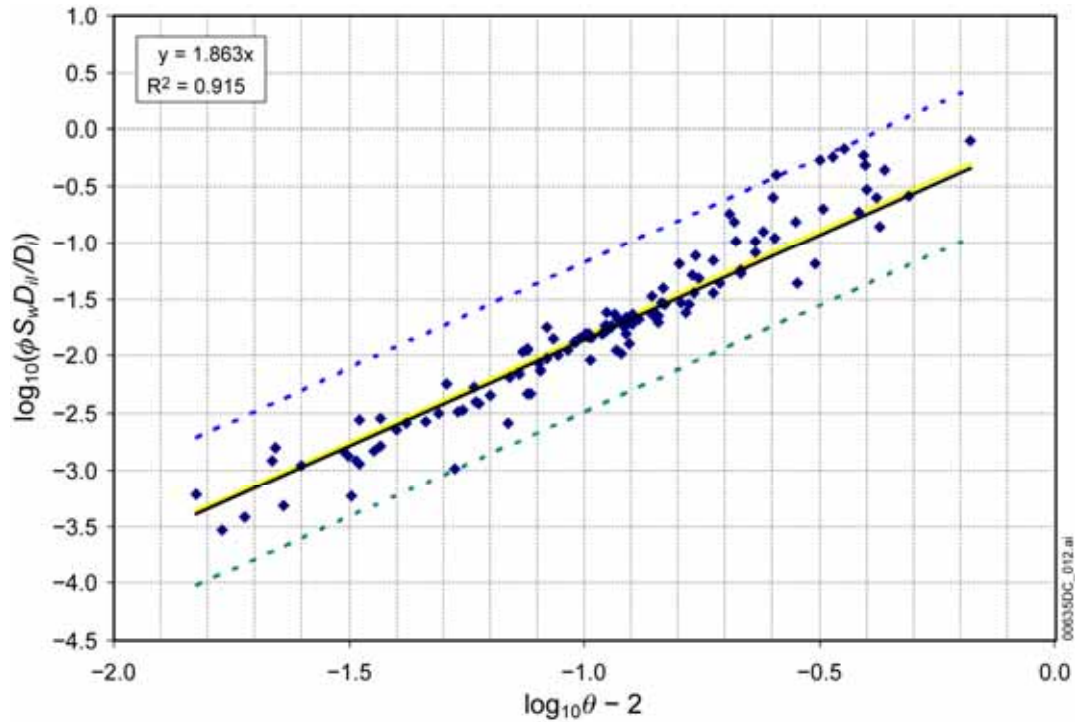
This range of uncertainty resulting from variation in the invert porosity is well within the range of the uncertain factor in Equation 6.3.4.1.1-22, which ranges from:

$$10^{0.033-3(0.218)} = 0.24 \quad (\text{Eq. 6.3.4.1.1-26})$$

to

$$10^{0.033+3(0.218)} = 4.86. \quad (\text{Eq. 6.3.4.1.1-27})$$

The uncertainty associated with the porosity of the invert is included in the uncertainty associated with the measurements of the diffusion coefficient, which were made on a variety of geologic materials having a range of porosities; thus the porosity uncertainty can be considered to be accounted for in the effective diffusion coefficient. The same conclusion is reached if the nominal value of intergranular porosity (0.224, as given in Tables 4.1-1 and 8.2-6) is substituted for the mean, with the same spread for the uncertainty range.



Source: Conca and Wright 1992 [DIRS 100436], Figure 2; Conca et al. 1993 [DIRS 170709], Figure 2.

NOTE: The dashed lines correspond to three standard deviations above and below the statistical fit to the data.

Figure 6.3-4. Uncertainty in the Statistical Fit for the Effective Diffusion Coefficient

For each realization of the TSPA calculations, the normal distribution is sampled, thereby incorporating the uncertainty of the experimental data into the diffusivity.

6.3.4.1.2 Modification for Temperature

The diffusivity D_T is proportional to absolute temperature and inversely proportional to viscosity η_T ; i.e., $D_T \propto T/\eta_T$ (Cussler 1997 [DIRS 111468], p. 114). It follows that if the diffusivity is known at some temperature T_0 , the diffusivity at temperature T can be found by:

$$\frac{D_T}{D_{T_0}} = \frac{\frac{T}{\eta_T}}{\frac{T_0}{\eta_{T_0}}}, \quad (\text{Eq. 6.3.4.1.2-1})$$

where D_T is the diffusion coefficient ($\text{m}^2 \text{s}^{-1}$) at temperature T (K), D_{T_0} is the diffusion coefficient ($\text{m}^2 \text{s}^{-1}$) at temperature T_0 (K), η_T is the viscosity of water (Pa s) at temperature T (K), and η_{T_0} is the viscosity of water (Pa s) at temperature T_0 . The dependence of viscosity on temperature T (K) ($293.15 \text{ K} \leq T \leq 373.15 \text{ K}$) is given by Weast and Astle (1981 [DIRS 100833], p. F-42):

$$\log_{10}\left(\frac{\eta_T}{\eta_{20}}\right) = \frac{1.3272(293.15 - T) - 0.001053(T - 293.15)^2}{T - 168.15}, \quad (\text{Eq. 6.3.4.1.2-2})$$

where η_{20} is the viscosity of water at 20°C (293.15 K). Then

$$\frac{\eta_T}{\eta_{T_0}} = \frac{10^{\left[\frac{1.3272(293.15 - T) - 0.001053(T - 293.15)^2}{T - 168.15}\right]}}{10^{\left[\frac{1.3272(293.15 - T_0) - 0.001053(T_0 - 293.15)^2}{T_0 - 168.15}\right]}}, \quad (\text{Eq. 6.3.4.1.2-3})$$

and the diffusion coefficient at temperature T is given by:

$$\begin{aligned} D_T &= D_{T_0} \frac{T}{T_0} \frac{\eta_{T_0}}{\eta_T} \\ &= D_{T_0} \frac{T}{T_0} 10^{\left[\frac{1.3272(293.15 - T_0) - 0.001053(T_0 - 293.15)^2}{T_0 - 168.15}\right] - \left[\frac{1.3272(293.15 - T) - 0.001053(T - 293.15)^2}{T - 168.15}\right]}. \end{aligned} \quad (\text{Eq. 6.3.4.1.2-4})$$

This equation is not valid above the boiling point of water (100°C, or 373.15 K; possibly lower at the elevation of the repository), where it is assumed that no transport occurs (Assumption 5.5). This temperature modification of the diffusion coefficient is applied to the invert, to waste package corrosion products, and to the waste form. The invert temperature is provided in *Multiscale Thermohydrologic Model* (SNL 2007 [DIRS 181383]). Figure 6.3-5 shows the temperature dependence of the invert diffusion coefficient relative to the diffusion coefficient at $T_0 = 25^\circ\text{C}$, the temperature at which the radionuclide-specific free water diffusion coefficients are specified (Table 4.1-7).

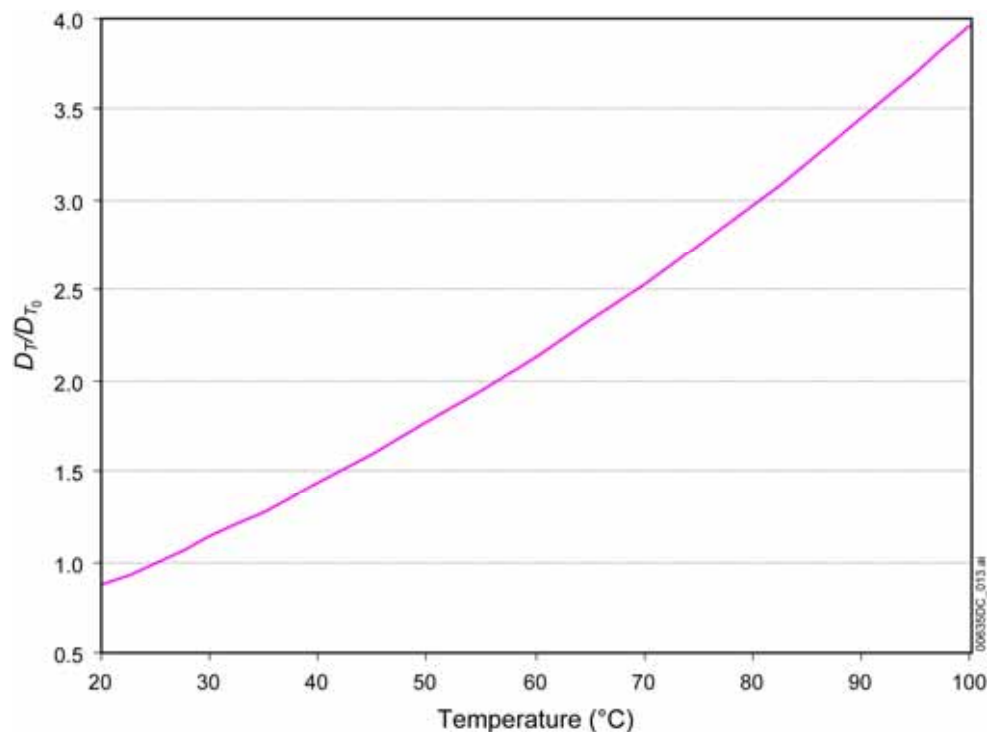


Figure 6.3-5. Temperature Dependence of the Invert Diffusion Coefficient (Equation 6.3.4.1.2-4)

6.3.4.1.3 Modification for Concentrated Aqueous Solutions

Data in *American Institute of Physics Handbook* (Gray 1972 [DIRS 138541], Table 2p-2) shows that the majority of the diffusion coefficients increase with increasing solution strength. For example, the diffusion coefficient of sodium iodide increases from $1.616 \times 10^{-9} \text{ m}^2 \text{ s}^{-1}$ in a dilute solution to $1.992 \times 10^{-9} \text{ m}^2 \text{ s}^{-1}$ for a 3 M solution and the coefficient for potassium iodide increases from $2.00 \times 10^{-9} \text{ m}^2 \text{ s}^{-1}$ in a dilute solution to $2.533 \times 10^{-9} \text{ m}^2 \text{ s}^{-1}$ at 3.5 M. The percent increase for potassium iodide, 26.7 percent, is the greatest of any in Gray's table (Gray 1972 [DIRS 138541], Table 2p-2) excluding HCl. HCl has been excluded from consideration because, being volatile, it is not representative of the type of radionuclides released from the waste package.

The free water diffusion coefficient for each species i in water is used for all concentrations of radionuclides at a given temperature (DTN: LB0702PAUZMTDF.001 [DIRS 180776]). The modification for concentrated aqueous solutions is neglected in the TSPA. However, the variability due to ionic strength is captured by the uncertainty in the effective diffusion coefficient. For the invert, this uncertainty is shown explicitly in Equations 6.3.4.1.1-22 and 6.3.4.1.1-27. For the waste form and corrosion products, this uncertainty in the effective diffusion coefficient results from uncertainty in the water saturation resulting from adsorption of water (see Sections 6.3.4.3 and 6.3.4.6).

6.3.4.2 Retardation in the Engineered Barrier System

In this section, parameters are developed to enable the impact of sorption processes on radionuclide transport through the EBS to be quantified. Transport through the EBS is affected

by the adsorption and desorption of radionuclides on the stationary materials in the waste package (steel corrosion products) and invert (crushed tuff) as well as on colloid particles. The degree of sorption and desorption of the aqueous complex at the surface of the sorbent depends on the type and strength of the bond formed under the prescribed transport conditions. Based on the transport conditions, the sorption processes can be grouped into two end members, namely, those described by equilibrium sorption and those described by non-equilibrium (kinetic) sorption. If the sorptive process is rapid compared to the residence time of the fluid, the solute will reach an equilibrium condition with the sorbed phase and can be considered to undergo equilibrium sorption. On the other hand, if the time scale of the sorptive process (both adsorption and desorption) is slow compared to the residence time (or the rate of fluid flow through porous medium) the solute may not come to equilibrium with the sorbed phase and can be considered to undergo non-equilibrium (kinetic) sorption. These are insufficiently fast, heterogeneous surface reactions. Depending on the nature of the surface complexes formed with the sorbent and their binding energies, some radionuclides may form strong bonds and be best modeled using the kinetic sorption models (by forward and backward reaction rates) while others may be modeled by linear equilibrium sorption models using distribution coefficients (K_d).

6.3.4.2.1 Conceptual Model for the In-Drift Sorption Environment

In this section, the conceptual model of the in-drift environment as it affects sorption onto stationary materials is described. Although sorption will take place on crushed tuff, the focus in this section is on corrosion products (metal oxides), because these materials have the greatest potential for sorption in the EBS. Sorption onto colloidal materials is discussed separately in Section 6.3.4.4.

The mild steel and stainless steel in the waste package and invert are expected to degrade to iron oxyhydroxides more rapidly than the corrosion-resistant materials in the EBS (e.g., Alloy 22 and titanium). The sorption capability of corrosion products in the invert is not considered in the TSPA. The time sequence for corrosion of iron-based components in the EBS is:

- Steel in the invert (e.g., support beams, cap plate, and gantry rails) will begin to degrade after closure of the repository because the invert is directly exposed to the relative humidity and temperature environment within the drifts. Corrosion begins when the relative humidity becomes great enough to produce aqueous conditions on the metal surface, although the presence of deliquescent salts can result in aqueous conditions at lower humidity (if the in-drift humidity is higher than the minimum deliquescent point of the salts; Campbell and Smith 1951 [DIRS 163817], p. 237).

The steel and copper are in the top portion of the invert. More specifically, the longitudinal and transverse support beams are in the top half of the invert (BSC 2007 [DIRS 180181], Typical Invert Elevation). The transverse support beams are spaced at 5-ft (1.524-m) intervals (BSC 2007 [DIRS 180181]), so the corrosion products from the beam will not always be directly beneath the emplacement pallet or stress corrosion cracks. Below and on either side of these beams, the invert is filled to depth with granular ballast that does not contain any steel.

- Stainless steel tubes in the emplacement pallet will corrode more slowly than mild steel (for mild carbon steel and stainless steel corrosion rates, see Section 6.3.4.3.4 and Appendix F). Again, the tubes are directly exposed to the in-drift temperature and relative humidity after closure. The tubes in the emplacement pallet are located directly beneath the waste package, close to, if not directly in, the anticipated flow path from the waste package.
- Mild steel (i.e., Carbon Steel Type A 516) inside the codisposal waste package can begin to degrade after the waste package is breached by stress corrosion cracks, localized corrosion, or general corrosion. Water vapor can enter the waste package once it is breached, and this vapor will be adsorbed on the steel surfaces, providing an environment for corrosion within the waste package.
- Stainless steel inside the waste package can also corrode, albeit more slowly than mild steel, after the waste package is breached.

Aluminum thermal shunts in CSNF waste packages comprise less than two percent of the total mass of the waste package. Because the amount of aluminum is small, it is ignored in the RTA.

Because the corrosion rates of the carbon steel and stainless steel used for invert components is greater than that of the Alloy 22 waste package outer corrosion barrier, all steel components in the invert will degrade to iron oxyhydroxides by the time the waste package is breached by general corrosion. In other words, iron oxyhydroxides will be present in the invert before any radionuclides are transported from the waste package. After the waste package outer corrosion barrier is breached, the stainless steel inner vessel is expected to breach quickly due to localized corrosion, and any mild steel internal components in the waste package will degrade rapidly, adding iron oxyhydroxides to the in-package environment. The inner vessel will degrade to corrosion products by 95,000 years, based on a thickness of the inner vessel of stainless steel of 50.8 mm (SNL 2007 [DIRS 179567], Tables 4-6 to 4-10; SNL 2007 [DIRS 179394], Table 4-3), corrosion occurring from both inside and outside, and a mean corrosion rate of $0.267 \mu\text{m yr}^{-1}$ (see Section 6.3.4.3.4 and Appendix F).

The degradation products in the waste package will include hydrous metal oxides from corrosion of steel and aluminum materials (YMP 1998 [DIRS 104441], p. C-23; BSC 2005 [DIRS 180506]) and clays and schoepite from degradation of HLW glass and CSNF, respectively (SNL 2007 [DIRS 180506]). Because they comprise the great majority of the corrosion products, and because of their strong sorptive characteristics, the iron oxyhydroxides will dominate the sorptive properties of the corrosion products, although the aluminum oxides and manganese oxides are also highly sorptive, depending on pH and the zero point of charge. Together, nickel and chromium comprise about 30 percent of the mass of stainless steel, and although much of this will form solid solutions with the iron oxyhydroxides, the water sorptive characteristics of the individual metal oxides must be considered as well. In the EBS RTA, pure iron oxide surface properties are used to model sorption onto what will in reality be a solid solution of Fe(III), Cr(III), and Ni(II).

The degradation products in the invert will include iron oxyhydroxides and other hydrous metal oxides from the corrosion of steels and copper-based materials, and minerals from the granular

invert backfill. The invert corrosion products occur in the top portion of the invert because all steel and copper is located in the top half of the invert (BSC 2007 [DIRS 180181], Typical Invert Elevation).

The in-package degradation products are envisioned to be composed of unconsolidated particulates and larger agglomerations of clays, iron oxyhydroxides, and other mineral assemblages that slump to the bottom of the waste package. Any seepage through the waste package is expected to flow through the sludge at the bottom of the waste package. The invert degradation products are initially located near the top of the invert, but may move into the mass of granular invert backfill during thermal changes or seismic events.

Corrosion products in the waste package are represented as a single porosity medium, a reasonable approach given the granularity of the corrosion products and the randomness of the slumping process. Channelized flow paths with no sorption, as in the discrete fractures of a dual porosity medium, are not anticipated to occur in this unconsolidated material. One conceptual model is for the radionuclides to have access to the mass of corrosion products in the waste package. An ACM, with corrosion products that form a contiguous mass that has a low permeability and tight pore structure, would limit access to the full sorptive capacity of the corrosion products.

The bulk of the mass of materials in a CSNF waste package, excluding the SNF and the outer corrosion barrier, consists of three types of steel. The iron content of these steels (Table 4.1-15) ranges from about 63.1 weight percent (Borated Stainless Steel Type 304B4, used in the neutron absorber plates; ASTM A 887-89 2004 [DIRS 178058], Table 1)), to about 65.5 weight percent (Stainless Steel Type 316, used in the inner vessel and internal components in CSNF waste packages; DTN: MO0003RIB00076.000 [DIRS 153044]), to 97.9 weight percent (Carbon Steel Type A 516, used in codisposal waste package divider assembly components; ASTM A 516/A 516M-90 1991 [DIRS 117138]).

In the RTA, the products of the corrosion of all internal waste package components except for fuel rods, HLW glass, and spent nuclear fuel (SNF), are modeled as a mixed assemblage, primarily of iron oxides, specifically FeOOH (goethite), and ferrihydrite (HFO), along with oxides of the two major components of stainless steels (chromium and nickel), specifically Cr₂O₃ and NiO. Establishing the mineralogical type of corrosion products enables the amount of water adsorbed onto surfaces to be estimated. In addition, specifying the mineralogical composition of the corrosion products allows the surface charge (or site) density for adsorption of certain radionuclides that undergo sorption to be determined, which provides a basis for calculating the mass of radionuclides that are sorbed. Again, Cr in steels is modeled as corroding to Cr(III) oxyhydroxides and minerals as seen in corrosion testing (SNL 2007 [DIRS 181165], Section 6.3.16); appreciable substitution of Cr(III) in Fe(III)-containing minerals will occur as well.

Geochemical analyses of the basket degradation process (YMP 1998 [DIRS 104441], p. C-23) have demonstrated that the iron oxide produced from corrosion of carbon steel and borated stainless steels will remain in the waste package as insoluble hematite. A more recent analysis of Carbon Steel A 516 corrosion (SNL 2007 [DIRS 180506], p. 6-21) states:

Although the formation of large masses of ferric (hydr) oxide corrosion products is inevitable, it is difficult to predict which one will dominate the mineralogy of the whole. Goethite and hematite are expected to eventually be the most abundant iron oxides in corrosion products (Schwertmann and Cornell 1991 [DIRS 144629], Section 4.2.2). Poorly crystalline solids such as ferrihydrite ($\text{Fe}_3\text{HO}_8 \cdot 4\text{H}_2\text{O}$) and $\text{Fe}(\text{OH})_3$ that form during rapid oxidation of Fe(II) and hydrolysis of Fe(III), will probably be present throughout the period of steel degradation in the waste package (Schwertmann and Cornell 1991 [DIRS 144629], Sections 1.3 and 8.1). These poorly crystalline iron oxides are unstable with respect to hematite and goethite, but their transformation is significantly inhibited or retarded by their adsorption or structural substitution, or both, of silicate, phosphate, and Cr(III), which are common components of the waste package solution. To summarize, the corrosion product assemblage is likely to be made up of some mixture of hematite, goethite, and ferrihydrite.

The RTA uses properties of the oxides of the major components of steel for determining the degree of water adsorption and water saturation in corrosion products, including hematite, goethite, HFO, Cr_2O_3 , and NiO. Goethite and HFO properties are used for modeling corrosion product surface chemistry (specifically, competitive and kinetic sorption). Because the water vapor adsorption isotherms (expressed as water layer thickness) for these five oxides are all similar, a composite isotherm obtained by combining adsorption data for these oxides is used to compute the water content in the corrosion products.

6.3.4.2.2 Sorption Parameters for the Invert

In the invert, radionuclide sorption can potentially take place on the crushed tuff ballast material and on products of corrosion of the metallic components such as steel support beams and copper conductor bars. In the RTA, sorption onto the crushed tuff is included so as to be consistent with the model for sorption onto tuff in UZ transport (SNL 2007[DIRS 177396], Section 6.1.2.3). Sorption of radionuclides on corrosion products in the invert is ignored (Assumption 5.6) because contact with radionuclides with corrosion products in the invert cannot be guaranteed due to the localized deposition of corrosion products.

6.3.4.2.2.1 Sorption onto Crushed Tuff in the Invert

Sorption onto the crushed tuff is included in the EBS transport abstraction. K_d values on crushed tuff in the invert are given by the ranges and distributions of radionuclide sorption distribution coefficients for sorption on devitrified UZ tuff given in DTNs: LA0408AM831341.001 [DIRS 171584] (file *UZ Kds.doc*, for all radionuclides of interest except for Se and Sn) and LB0701PAKDSESN.001 [DIRS 179299] (file *ReadMe.doc*, for Se and Sn). Correlations are assigned to invert crushed tuff for sampling sorption distribution coefficient probability distributions using correlations for devitrified UZ tuff given in DTN: LB0701PAKDSESN.001 [DIRS 179299] (file *Sorption Correlation Table.xls*). The ranges of K_d values for sorption onto devitrified tuff are used because the crushed tuff in the invert will be the same tuff that is removed when the drifts are bored; most of the repository will be developed in the TSw33 through TSw36 stratigraphic units, which are composed of devitrified tuff.

6.3.4.2.2 Sorption onto Corrosion Products in the Invert

Invert corrosion products will be localized and widely spaced, with the possibility being that seepage from the waste package could completely miss corrosion products in the invert. In this case, even small K_d values could overestimate the amount of retardation of radionuclides in the invert. Steel longitudinal beams in the invert are spaced 2.5 ft (0.762 m) from the centerline of the drift (BSC 2007 [DIRS 180030]), where the bulk of releases would be expected from a horizontal cylindrical waste package. Thus, their corrosion products are unlikely to interact with releases from a waste package. Steel transverse beams 12-in. (0.3048-m) wide are spaced 5 ft (1.524 m) apart (BSC 2007 [DIRS 180181]). Thus, on average, transverse beams underlie 20 percent of the centerline of a waste package, with a correspondingly small 20 percent chance of their corrosion products interacting with releases from a waste package.

Although steel corrosion products have the potential to retard both iodine and technetium (in the case of the latter particularly where reduced iron is present), no credit is taken for radionuclide sorption onto these materials that are likely to be present locally in the invert (Assumption 5.6), through which radionuclides must be transported to reach the accessible environment. By ignoring sorption in the invert, there is added confidence that the radionuclide inventory actually transported is less than the calculated value used in assessing dose to the individual.

6.3.4.2.3 Sorption onto Waste Package Corrosion Products

Possible sorption of radionuclides on the large expected mass of corrosion products could have significant impact on the release of radionuclides out of the waste package. The degree of sorption for a given radionuclide depends on a number of factors, such as its dissolved concentration, chemistry of the solution, type of sorbent, etc. Based on the understanding of sorption characteristics under chemical conditions similar to what would be encountered inside the waste package, the sorption process can be modeled with a high degree of confidence. Whether the sorption is best modeled as an equilibrium process, non-equilibrium (kinetic) process with both sorption and desorption, or as an irreversible process (no desorption) depends on the understanding of the sorption characteristics of the sorbate under the expected chemical conditions and observation timeframes. Sometimes the exact sorption process may not be known with greater degree of confidence or may not be appropriate for the timescales over which the behavior is to be predicted. For example, effectively irreversible uptake may be the dominant control over contaminant transport in soils and there is evidence for soil sequestering of bomb-pulse plutonium and americium and of uranium, iodine, technetium, cesium, and strontium from ore processing and reactor operations (Coughtrey et al. 1983 [DIRS 132164]) but such studies although informative are not conclusive enough to predict or quantify sorption behavior under different chemical conditions and over longer timescales.

There is significant literature on the sorption characteristics of plutonium in the natural environments but there are also conflicting views on the applicability of the data over the repository time scales for the purpose of performance assessment calculations. Recent reviews of field and laboratory measurements indicate that the fraction of sorbed plutonium that is available for desorption rarely exceeds 1 percent (Brady et al. 1999 [DIRS 154421], Appendix F, pp. 141 to 142; Davis and Kent 1990 [DIRS 143280] and from a modeling point of view, the sorption process could be considered as partly irreversible for the observed timescales.

However, the National Research Council (2000 [DIRS 174394]) states that irreversible sorption models should not be applied to quantitative models of environmental contamination. With regard to the report on contaminant attenuation of Brady et al. (1999 [DIRS 154421]), the National Research Council (2000 [DIRS 174394], p. 224) states: “irreversible sorption...is not understood for either organic or inorganic contaminants; much more scientific research is needed before this process can be quantified.” In addition, the National Research Council (2000 [DIRS 174394], Table ES-1, p. 9) judged the likelihood of success of long-term plutonium immobilization as low, at the current level of knowledge. The National Research Council (2000 [DIRS 174394], p. 13) refers to Brady et al. (1999 [DIRS 154421]) as follows: “Furthermore, although the DOE document [Brady et al. 1999] proposes a method for assessing natural attenuation processes for inorganic contaminants, such processes are extremely complex, and the DOE document does not adequately reflect this complexity. The DOE document has to be peer reviewed and substantially revised before it is used as a decision-making tool.”

At the Rocky Flats site in Colorado, soil plutonium is largely associated with the negatively charged organic macromolecular fraction and not with the more abundant iron oxides and clays (Santschi et al. 2002 [DIRS 170923]; Ibrahim and Salazar 2000 [DIRS 170882]). Litaor and Ibrahim (1996 [DIRS 161667]) used 0.01 M CaCl₂ as an extractant and measured plutonium in Rocky Flats soil to be 0.04 to 0.08 percent exchangeable. Transport of minute quantities of colloidal plutonium (10⁻¹⁴ M) over hundreds of meters was observed at the Nevada Test Site (Kersting et al. 1999 [DIRS 103282]), although the presence of organics may limit the relevance of these data to Yucca Mountain. Laboratory experiments of plutonium sorption onto iron oxide colloids have shown that approximately 1 percent of the initially sorbed plutonium can be desorbed into solution over a period of several months (Lu et al. 2000 [DIRS 166315]; BSC 2005 [DIRS 177423], Section 6.3.3.2), which is broadly consistent with field observations, although much shorter in time scale compared to the timescales needed to simulate the performance of the repository.

Based on the above discussion, it is clear that a sorption model is needed that is valid over the various physical and chemical conditions expected inside the waste package and over the simulation timescales needed for the performance assessment calculations. The sorption model should also account for the uncertainty in the available sorption sites and for competition among various aqueous complexes for the finite number of sorption sites. The sorption model should also be consistent with the conceptual model for transport through the waste package.

Transport through the waste package is conceptualized to occur in two spatially separated transport domains—the upstream waste form domain and the downstream corrosion products domain. The waste form domain (also referred to as Cell 1) acts as the source of radionuclides that are generated as the waste form degrades and the radionuclides are released, either as dissolved in the water or as sorbed onto the colloids. The released mass of radionuclides then passes (via advection and/or diffusion) through the downstream corrosion products domain (also referred to as Cell 2), where the sorption-desorption reactions occur. Cell 1 is composed primarily of SNF elements and glass; although some steel is included in it, the bulk of the steel resides in Cell 2, so sorption of radionuclides onto corrosion products is modeled as occurring only in Cell 2. Excluding sorption of radionuclides in Cell 1 is further justified because sorption onto corrosion products is not going to change the concentrations of radionuclides in Cell 1 as long as the waste form is present, since the concentrations will be at their solubility limits.

Transport inside the waste package is considered analogous to transport through host rock that contains a disseminated ore body, where the ore body is the source of contamination, and the host rock is the porous medium through which the contaminant moves. As the contaminant plume moves through the host rock, the concentration changes due to dilution, dispersion, and sorption reactions, which could also influence the local chemistry and redox conditions. Unlike a reactive transport code, in the RTA, none of the various chemical and physical changes calculated by other models is linked such that changes in one cell affect another cell, and changes in Cell 2 do not affect conditions in Cell 1. In the waste package, Cell 1 is conceptualized to be composed of disseminated waste form with some steel corrosion products, while Cell 2, composed of corrosion products, forms the porous medium analogous to the host rock. It is possible to consider transport along discrete flow paths rather than through a porous material, but it is reasonable to assume that over time more and more corrosion products will form and coat the surfaces along which radionuclide transport occurs and possibly plug up the discrete flow paths. Modeling the interior of the waste package as a porous material is a reasonable simplification. The local chemistry will dictate the waste form degradation rates and the dissolved radionuclide concentration.

In order to model the radionuclide sorption under varying physical and chemical conditions, where the water volumes, mass of corrosion products, waste form degradation rates, dissolved concentration limits, and aqueous speciation of various actinides, all vary spatially and temporally, the modeling approach based on surface complexation was deemed most appropriate. The surface complexation (or electrostatic adsorption) models have distinct advantages over other methods such as simple adsorption isotherms and ion-exchange models when the sorbents (iron oxyhydroxide surfaces) themselves exhibit amphoteric behavior of pH-dependent surface charge by offering hydrogen ions or hydroxyl ions for cation or anion exchange respectively. The number of sorption sites and type of charge on the sorption sites determines which aqueous ionic species can undergo surface complexation and also determine the strength of the bond when the competition among various aqueous ionic species is being considered. In the surface complexation model (SCM), it is assumed that the sorbing surface is composed of specific functional groups that react with sorbing solutes to form surface complexes (inner sphere or true complexes, or ion pairs) in a manner analogous to the formation of aqueous complexes in the bulk solution. The surface charge results from chemical reactions involving the surface functional groups, while the binding constants determined for the mass-law adsorption equations are empirical parameters related to thermodynamic constants via activity coefficients of the surface species.

In the surface complexation based modeling, the aqueous species of uranium, neptunium, plutonium, americium, thorium, and nickel are considered. The first five elements are considered because they are the primary contributors to the waste form inventory, while nickel is considered because it is derived from corrosion of steel and has a strong affinity to form surface complexes. The other major components of the stainless steel, such as chromium and molybdenum, were not included in the SCM because these metals are expected to be present in low concentrations due to rapid precipitation. Other divalent ions, such as Ca^{2+} , Mg^{2+} , and SO_4^{2-} were not included in the SCM because they have a low affinity to form surface complexes compared to Ni.

A single-site diffuse layer model has been used rather than a more complex generalized (2-site) diffuse-layer model (Dzombak and Morel 1990 [DIRS 105483]) or triple-layer model. In doing so, the recommendations of Turner and Sassman (1996 [DIRS 179618]) and Wang et al. (2001 [DIRS 176816]) are adopted, to use the single site model even though the PHREEQC model allows for use of a 2-site model. The choice of a single-site versus 2-site model is based on the following: The corrosion products in the waste package will likely be a mixture of different iron oxyhydroxide mineralogy (i.e., goethite, hematite, and HFO), but it is difficult to predict accurately the exact proportions of the various iron oxide phases over time. A one-site generic iron oxide sorption model is therefore used instead. Surface complexation constants were developed from data for a number of iron oxides, including HFO, goethite, and hematite. The bulk of the data were developed from HFO and goethite data. Hematite was used to fill in gaps. This assumption relies on the general similarity in surface properties of iron oxides. Appendix J outlines the specific steps that were taken to develop the database. Because of uncertainties in oxide mineralogy, site densities, and solution composition, the competitive surface complexation model is built by sampling over a wide range of potential conditions.

A single self-consistent set of sorption reactions and log K values (where K is the solubility constant) for sorption of uranium, plutonium, neptunium, americium, and thorium species onto either goethite or HFO do not exist. Therefore, the largest self-consistent network was identified, and additional data were used to fill in the gaps. Based on the above considerations, the compilations of Wang et al. (2001 [DIRS 176816]) and Turner and Sassman (1996 [DIRS 179618]) are the best reaction networks upon which to base the set of surface complexation constants. These authors fit experimental data from several sources to a single site Double Layer Model using a standard set of acidity constants for goethite.

Since the results of the surface complexation modeling will be used in the EBS transport model of the TSPA, the calculations need to cover the expected range of concentrations of various radionuclides in the TSPA simulated time frames over varying water volume and sorption sites in a system with varying P_{CO_2} and pH. The calculated sorbed masses from the SCM need to be implemented such that both equilibrium and kinetic sorption-desorption processes can be considered on both stationary corrosion products and on the iron oxyhydroxide colloids.

Besides the uncertainty in the degree of sorption of various radionuclides there is uncertainty in the properties of the sorbent itself under varying physical-chemical-thermal environments. The sorption processes can be modeled only after the mineralogy of the corrosion products is understood with some degree of confidence along with the understanding of the number of and type of sorption sites available. These are discussed in the following section.

6.3.4.2.3.1 Properties of Waste Package Corrosion Products

Ferrihydrite will convert to the more stable phase goethite under repository conditions so the latter will most likely be the dominant phase after long periods of time. Under controlled laboratory conditions, this conversion occurs rapidly, with time frames on the order of days to even months depending on temperatures and solution composition. A study by Hamzaoui et al. (2002 [DIRS 173866]), for example, on the transformation of ferrihydrite to goethite at alkaline conditions for a given range of temperatures indicates that full conversion will occur in a period of about 80 hours at pH 11 and about 20 hours at pH 12.2 and a temperature of 40°C. A similar

result at pH 12.2 was obtained by Cornell and Giovanoli (1988 [DIRS 173864]) but at a temperature of 70°C, where full conversion to goethite was obtained in about 24 hours. Hamzaoui et al. (2002 [DIRS 173866]) also show that transformation rates increases with increasing pH. The studies by Cornell and Giovanoli (1988 [DIRS 173864]), and Cornell et al. (1989 [DIRS 173865]) indicate that the presence of some metals in solution and organics tends to retard the transformation of HFO to more crystalline phases. Slower rates are expected at ambient temperatures and near-neutral pH conditions. Schwertmann et al. (2000 [DIRS 173863]), studied long-term transformation of ferrihydrite to more crystalline oxyhydroxides at pH 4-7 and 25°C. Their results show that the presence of other metals in soils, such as aluminum, can slow down the conversion process. Even at low metal concentration, the full transformation process can be on the order of many months. However, whereas laboratory data show fast conversion rates from ferrihydrite to goethite, field-type corrosion experiments under atmospheric conditions indicate the consistent presence of amorphous ferric oxyhydroxide material for long periods of time (Misawa et al. 1974 [DIRS 159327]). The field experiments of Misawa et al. (1974) exposed mild and low-alloy steels to a semi-rural environment for 2.5 years. Phase identification analyses of the generated rusted material showed a larger proportion of amorphous ferric oxyhydroxide compared to goethite. Still, the former will transform to the latter with further aging. Dillmann et al. (2004 [DIRS 171480]) studied the corrosion products in ancient artifacts open to indoor atmospheric environments. Even for time periods on the order of a few to tens of years, the proportion of the ferric amorphous phase observed in the corrosion products can be roughly in the range of 20 – 70 percent (Dillmann et al. (2004 [DIRS 171480], Table 1, p. 1405). Therefore, field evidence indicates that conversion of amorphous ferric oxyhydroxide to goethite can be slower than observed under laboratory conditions due to various factors inherent to local corrosion environments, such as the presence of additional metals in solution, pH, wet and dry cycles, and temperature. Given these large differences observed for the apparent speed of conversion between laboratory and field experiments, it is difficult to constrain transformation rates with a high level of confidence, and the range of compositions advanced above (45 to 80 percent goethite, the rest being HFO; see Section 6.3.4.2.1) is reasonable in capturing this variability.

The lack of data for both corrosion and phase transformation kinetics to reflect the inherent complexities of the in-package chemical environment precludes any attempts at estimating a well-constrained fraction of corrosion products with time. For model details on the in-package chemical environment and justification for the use of goethite and ferrihydrite as the metal sorbing corrosion product phases see Section 6.3.2 of *In-Package Chemistry Abstraction* (SNL 2007 [DIRS 180506]). This in-package chemistry abstraction model assumes a mixture of sorbing ferric Fe oxyhydroxide corrosion products consistent with the sorption submodel considered in the current report. For these reasons, the adopted range is a reasonable representation that captures the presence of these two phases at any given time. The limited data available are still useful to support the argument for a rapid transformation as represented by the selected bounds for goethite fraction, considering the expected environmental repository conditions. However, the data also indicate that retardation of this conversion may be a result of other metals present in solution as it would be expected during waste package degradation.

The composition of HFO is not well defined given the variable content of H₂O adsorbed, yielding a range of Fe:O:H ratios with respect to the phase structural properties (Cornell and Schwertmann 2003 [DIRS 173037]). Due to the arbitrary designation of ferrihydrite as

amorphous hydrous ferric oxide with the formula $\text{Fe}(\text{OH})_3$, as often found in the literature, a more accurate representation of its composition should be considered based on chemical and structural analyses. Cornell and Schwertmann (2003 [DIRS 173037]) suggested that the chemical formula representation of ferrihydrite should be expressed as $\text{FeO}_{1.07}(\text{OH})_{0.86}$ and $\text{FeO}_{0.89}(\text{OH})_{1.22}$ for 6-line ferrihydrite and 2-line ferrihydrite, respectively. The work of Towe and Bradley (1967 [DIRS 155334]) advanced a ferrihydrite composition ($4\text{Fe}_2\text{O}_3 \cdot 6\text{H}_2\text{O}$) with larger amounts of H_2O . As discussed by Eggleton and Fitzpatrick (1988 [DIRS 173878]), many of the structural models for ferrihydrite do not conform to the reported bulk compositions, probably due to added adsorption effects caused by the aggregation of small particles, thus generating the emplacement of additional OH onto the surface. Eggleton and Fitzpatrick (1988 [DIRS 173878]) also concluded that any relations assessed from the structural analysis of ferrihydrite should be associated to a structural formula of $\text{FeO}(\text{OH})$. This chemical formula is consistent with that adopted for HFO ($\text{Fe}_2\text{O}_3 \cdot \text{H}_2\text{O}$) along with the conversion factor of 89 g HFO/mol Fe by Dzombak and Morel (1990 [DIRS 105483]). Therefore, the adopted chemical formula for ferrihydrite/HFO in this analysis is $\text{FeO}(\text{OH})$, which is equivalent to that of goethite. Adoption of this chemical composition is consistent with that used in the HFO sorption analysis presented by Dzombak and Morel (1990 [DIRS 105483]). The close correspondence of the adopted chemical formula for ferrihydrite/HFO when compared to the range of reported compositions given above for ferrihydrite (Cornell and Schwertmann 2003) supports the use of this chemical formula in this report.

For performing sorption calculations in the TSPA, the composition of the iron oxyhydroxide corrosion products is modeled as a mixture of goethite, ranging from 45 – 80 percent, with the balance being HFO (Section 6.3.4.2.1).

Kinetic sorption of radionuclides occurs only on specific sites on the surface of corrosion product particles. The number of sites per unit area of surface, or site density (typically in units of sites nm^{-2}), determines the total quantity of radionuclides that can be adsorbed. Site density data for goethite and HFO are compiled in Tables 4.1-12 and 4.1-13, respectively, and qualified for use in TSPA in Section 4.1.2. Site density data for goethite in Table 4.1-12 in units other than sites nm^{-2} are converted to sites nm^{-2} in Table 6.3-4. These data provide a range of values to be sampled in TSPA for both goethite and HFO. The data in Tables 4.1-12 and 4.1-13 are used to develop discrete distributions, shown in Table 6.3-5 and Table 6.3-6. To calculate the discrete probability distribution, the data in Tables 4.1-12 and 4.1-13 were first sorted into ascending order. Multiple occurrences of the same number were removed from the sorted data list, but their occurrence frequency was assigned for probability calculation. The probability levels were calculated by dividing the frequency of the each data number by the total number of original data points in the data list.

The sorptive capacity of the corrosion products is directly proportional to the surface area of the solids. Data for the specific surface area of goethite and HFO are compiled in Tables 4.1-12 and 4.1-14 and qualified for use in TSPA in Section 4.1.2. These data provide a range of values to be sampled in TSPA for both goethite and HFO. The data in Tables 4.1-12 and 4.1-14 are used to develop the distributions described in Appendix K (see Section 6.3.4.3.3).

Table 6.3-4. Site Densities Conversions for Goethite

Site Density (Various Units)	Source	Conversion	Site Density (sites nm ⁻²)
3.28×10^{-6} mol m ⁻²	Rodda et al. 1996 [DIRS 173710], Table 1	Model fitting (2-site Langmuir adsorption model for Zn and Pb). Site density value represents the summation of low- and high-affinity sites: $2.90 \times 10^{-6} + 3.75 \times 10^{-7} = 3.28 \times 10^{-6}$ mol m ⁻² . Value converted to sites nm ⁻² using the following relation: $3.28 \times 10^{-6} \text{ mol/m}^2 \left(\frac{6.022 \times 10^{23}}{\text{mol}} \right) \left(\frac{1 \times 10^{-18} \text{ m}^2}{\text{nm}^2} \right)$	1.97
1.43×10^{-5} mol m ⁻²	Rodda et al. 1996 [DIRS 173710], Table 1	Model fitting (2-site Langmuir adsorption model for Zn and Pb). Site density value represent the summation of low- and high-affinity sites: $1.30 \times 10^{-5} + 1.26 \times 10^{-6} = 1.43 \times 10^{-5}$ mol m ⁻² . Value converted to sites nm ⁻² using the following relation: $1.43 \times 10^{-5} \text{ mol/m}^2 \left(\frac{6.022 \times 10^{23}}{\text{mol}} \right) \left(\frac{1 \times 10^{-18} \text{ m}^2}{\text{nm}^2} \right)$	8.59
2.2×10^{-6} mol m ⁻²	Rodda et al. 1996 [DIRS 173710], Table 5	Model fitting (BET adsorption model for Zn). Value converted to sites nm ⁻² using the following relation: $2.2 \times 10^{-6} \text{ mol/m}^2 \left(\frac{6.022 \times 10^{23}}{\text{mol}} \right) \left(\frac{1 \times 10^{-18} \text{ m}^2}{\text{nm}^2} \right)$	1.32
1.79×10^{-5} mol g ⁻¹	Trivedi et al. 2001 [DIRS 173021], Table 3	Fe adsorption edges. Value converted to sites nm ⁻² using the following relation: $1.79 \times 10^{-4} \text{ mol/g} \left(\frac{6.022 \times 10^{23}}{\text{mol}} \right) \left(\frac{\text{g}}{55.4 \text{ m}^2} \right) \left(\frac{1 \times 10^{-18} \text{ m}^2}{\text{nm}^2} \right)$	1.95
4.22×10^{-5} mol g ⁻¹	Trivedi et al. 2001 [DIRS 173021], Table 3	NIEDTA adsorption edges. Value converted to sites nm ⁻² using the following relation: $4.22 \times 10^{-5} \text{ mol/g} \left(\frac{6.022 \times 10^{23}}{\text{mol}} \right) \left(\frac{\text{g}}{21 \text{ m}^2} \right) \left(\frac{1 \times 10^{-18} \text{ m}^2}{\text{nm}^2} \right)$	1.21
3.54×10^{-5} mol g ⁻¹	Trivedi et al. 2001 [DIRS 173021], Table 3	PbEDTA adsorption edges. Value converted to sites nm ⁻² using the following relation: $3.54 \times 10^{-5} \text{ mol/g} \left(\frac{6.022 \times 10^{23}}{\text{mol}} \right) \left(\frac{\text{g}}{21 \text{ m}^2} \right) \left(\frac{1 \times 10^{-18} \text{ m}^2}{\text{nm}^2} \right)$	1.02
140 μmol g ⁻¹	Hansmann and Anderson 1985 [DIRS 173742], p. 547	Maximum theoretical value estimated from crystal morphology. Value converted to sites nm ⁻² using the following relation: $140 \frac{\mu\text{mol}}{\text{g}} \left(\frac{1 \times 10^{-6} \text{ mol}}{\mu\text{mol}} \right) \left(\frac{6.022 \times 10^{23}}{\text{mol}} \right) \left(\frac{\text{g}}{33 \text{ m}^2} \right) \left(\frac{1 \times 10^{-18} \text{ m}^2}{\text{nm}^2} \right)$	2.55

Table 6.3-4. Site Densities Conversions for Goethite (Continued)

Site Density (Various Units)	Source	Conversion	Site Density (sites nm ⁻²)
80 μmol g ⁻¹	Hansmann and Anderson 1985 [DIRS 173742], p. 547	Estimated from maximum sorption data for selenite. Value converted to sites nm ⁻² using the following relation: $80 \frac{\mu\text{mol}}{\text{g}} \left(\frac{1 \times 10^{-6} \text{ mol}}{\mu\text{mol}} \right) \left(\frac{6.022 \times 10^{23}}{\text{mol}} \right) \left(\frac{\text{g}}{33 \text{ m}^2} \right) \left(\frac{1 \times 10^{-18} \text{ m}^2}{\text{nm}^2} \right)$	1.46
0.31 mmol g ⁻¹	Gabriel et al. 1998 [DIRS 130407], pp. 124, 126	Uranyl adsorption SCM. Value converted to sites nm ⁻² using the following relation: $0.31 \frac{\text{mmol}}{\text{g}} \left(\frac{1 \times 10^{-3} \text{ mol}}{\text{mmol}} \right) \left(\frac{6.022 \times 10^{23}}{\text{mol}} \right) \left(\frac{\text{g}}{80.5 \text{ m}^2} \right) \left(\frac{1 \times 10^{-18} \text{ m}^2}{\text{nm}^2} \right)$	2.32
9.18 × 10 ⁻⁶ mol m ⁻²	Müller and Sigg 1992 [DIRS 173760], p. 519	Acid-base surface titration. Value converted to sites nm ⁻² using the following relation: $9.18 \times 10^{-6} \frac{\text{mol}}{\text{m}^2} \left(\frac{6.022 \times 10^{23}}{\text{mol}} \right) \left(\frac{1 \times 10^{-18} \text{ m}^2}{\text{nm}^2} \right)$	5.53
3.2 μmol m ⁻²	Gräfe et al. 2004 [DIRS 173751], p. 6561	Arsenate isotherm (pH 4). Value converted to sites nm ⁻² using the following relation: $3.2 \frac{\mu\text{mol}}{\text{m}^2} \left(\frac{1 \times 10^{-6} \text{ mol}}{\mu\text{mol}} \right) \left(\frac{6.022 \times 10^{23}}{\text{mol}} \right) \left(\frac{1 \times 10^{-18} \text{ m}^2}{\text{nm}^2} \right)$	1.93
2.2 μmol m ⁻²	Gräfe et al. 2004 [DIRS 173751], p. 6561	Arsenate isotherm (pH 7). Value converted to sites nm ⁻² using the following relation: $2.2 \frac{\mu\text{mol}}{\text{m}^2} \left(\frac{1 \times 10^{-6} \text{ mol}}{\mu\text{mol}} \right) \left(\frac{6.022 \times 10^{23}}{\text{mol}} \right) \left(\frac{1 \times 10^{-18} \text{ m}^2}{\text{nm}^2} \right)$	1.32
5.2 μmol m ⁻²	Hongshao and Stanforth 2001 [DIRS 173754], p. 4754	Assumed value; converted to sites nm ⁻² using the following relation: $5.2 \frac{\mu\text{mol}}{\text{m}^2} \left(\frac{1 \times 10^{-6} \text{ mol}}{\mu\text{mol}} \right) \left(\frac{6.022 \times 10^{23}}{\text{mol}} \right) \left(\frac{1 \times 10^{-18} \text{ m}^2}{\text{nm}^2} \right)$	3.13
210 μmol g ⁻¹	Machesky et al. 1991 [DIRS 173758], p. 771	Estimated from maximum sorption data. Value is twice measured loading, because a bidentate surface complex is proposed by the authors. Value converted to sites nm ⁻² using the following relation: $(2) \left(210 \frac{\mu\text{mol}}{\text{g}} \right) \left(\frac{1 \times 10^{-6} \text{ mol}}{\mu\text{mol}} \right) \left(\frac{6.022 \times 10^{23}}{\text{mol}} \right) \left(\frac{\text{g}}{81 \text{ m}^2} \right) \left(\frac{1 \times 10^{-18} \text{ m}^2}{\text{nm}^2} \right)$	3.12

The capacity (in moles of sites per gram of corrosion products) for sorption on stationary corrosion products is computed based on these four parameters (specific surface area and sorption site density of goethite and HFO), combining the capacity of goethite and HFO:

$$\frac{10^{18}}{N_A} [\omega_G \bar{s}_G + (1 - \omega_G) \bar{s}_{HFO}] [\omega_G N_{S,G} + (1 - \omega_G) N_{S,HFO}] \quad (\text{Eq. 6.3.4.2.3.1-1})$$

where:

- ω_G = mass fraction of corrosion products as goethite (dimensionless)
- \bar{s}_G = specific surface area of goethite ($\text{m}^2 \text{g}^{-1}$)
- \bar{s}_{HFO} = specific surface area of HFO ($\text{m}^2 \text{g}^{-1}$)
- $N_{S,G}$ = sorption site density for goethite (sites nm^{-2})
- $N_{S,HFO}$ = sorption site density for HFO (sites nm^{-2})
- N_A = Avogadro's number (sites mol^{-1}).

The factor of 10^{18} converts the result from nm^{-2} to m^{-2} .

Table 6.3-5 and Table 6.3-6 show discrete probabilities for various values of several parameters. The sum of these parameters is 1.0, and the cumulative sum at any parameter value is the cumulative (probability) distribution function.

Table 6.3-5. Sample Ranges and Distributions Used for Sorption on Goethite Corrosion Products

Input Name	Input Description	Range	Distribution
Relative_Abundance_Goethite_a	Fraction of total iron oxide that is goethite	0.45 – 0.8	Uniform
Goethite_Site_Density_a	Goethite site density; discrete distribution	<u>Density (sites nm^{-2})</u>	<u>Probability Level</u>
		1.02	0.01786
		1.21	0.01786
		1.32	0.03571
		1.46	0.01786
		1.50	0.01786
		1.66	0.01786
		1.68	0.03571
		1.70	0.01786
		1.80	0.01786
		1.87	0.01786
		1.93	0.01786
		1.95	0.01786
		1.97	0.01786
2.20	0.01786		

Table 6.3-5. Sample Ranges and Distributions Used for Sorption on Goethite Corrosion Products (Continued)

Input Name	Input Description	Range	Distribution
Goethite_Site_Density_a (continued)		2.30	0.07143
		2.31	0.01786
		2.32	0.01786
		2.55	0.01786
		2.60	0.03571
		2.70	0.01786
		2.89	0.01786
		2.90	0.03571
		3.00	0.01786
		3.12	0.01786
		3.13	0.01786
		3.30	0.03571
		3.40	0.01786
		4.00	0.01786
		4.20	0.01786
		4.60	0.01786
		4.84	0.01786
		4.90	0.01786
		5.00	0.01786
		5.53	0.01786
		6.15	0.01786
		6.30	0.01786
		6.31	0.03571
		6.60	0.01786
		7.00	0.05357
		7.20	0.01786
		7.40	0.01786
8.00	0.01786		
8.16	0.01786		
8.38	0.01786		
8.59	0.01778		

Output DTN: SN0703PAEBSRTA.001.

Table 6.3-6. Sample Ranges and Distributions Used for Sorption on HFO Corrosion Products

Input Name	Input Description	Range	Distribution
HFO_Site_Density_a	HFO site density; discrete distribution	Density (sites nm ⁻²)	Probability Level
		0.56	0.05263
		1.13	0.10526
		1.47	0.05263
		1.58	0.05263
		1.69	0.10526
		1.81	0.05263
		2.03	0.10526
		2.26	0.26316
		2.60	0.05263
		2.71	0.05263
		4.00	0.05263
		5.65	0.05265

Output DTN:SN0703PAEBSRTA.001.

6.3.4.3 In-Package Diffusion Submodel for Commercial Spent Nuclear Fuel Waste Packages

The objective of this submodel is to compute the effective diffusion coefficient, cross-sectional area for diffusion, and the path length for diffusion of radionuclides in a breached waste package. From these output parameters, the rate of diffusion of radionuclides from the waste package to the invert can be determined.

The focus in this submodel is on diffusive releases from CSNF waste packages in no-seep regions of the repository (where no seepage into the drift or condensation on drift walls occurs). In a no-seep environment, the water saturation inside the CSNF waste package is computed as a function of relative humidity using a water vapor adsorption isotherm. In a seep environment (where seepage into the drift and condensation on drift walls occur), the water saturation in a CSNF waste package is set to 1.0, and is not dependent on the relative humidity in the waste package. For HLW packages, the water saturation is also set to 1.0 in seep environments independently of the relative humidity in the waste package. Under no-seep conditions, separate water vapor adsorption isotherms are used for CSNF and HLW packages, so the water saturation is computed separately for each type of waste package as a function of relative humidity.

The fundamental basis of this submodel is that the only liquid water present is the thin film of adsorbed water that uniformly covers all surfaces exposed to humid air (Assumption 5.5). The relative humidity inside a breached waste package is assumed to be the same as the relative humidity in the drift (Assumption 5.5). In this submodel, all dissolution and diffusion of radionuclides occur in this thin film.

As the steel internal components corrode, porous corrosion products accumulate in the interior of the waste package. Diffusion will occur on the thin water films coating the surfaces of particles of corrosion products. The extent of corrosion will determine the amount of corrosion products

and, in turn, the amount of adsorbed water that is present, from which the water saturation is computed. Together with estimates of the porosity, the effective diffusion coefficient is calculated using Archie's law. A bulk cross sectional area for diffusion is estimated for each domain, and the length of the diffusion path is a sampled parameter for each leg of the path from the waste form domain to the corrosion products domain to the invert domain. The extent of corrosion is taken to vary linearly over the lifetime of the waste package steels. The amount of water adsorbed is a function of the relative humidity. Consequently, the rate of diffusive releases varies over time.

A number of uncertain parameters are associated with this submodel. The surface area available for adsorption of water is uncertain because the condition of the corrosion products cannot be determined—they may be finely powdered with a high specific surface, or agglomerated into an impermeable mass with low specific surface area, all depending on unpredictable circumstances and material behaviors. The water vapor adsorption isotherm used to calculate water saturation also contains uncertain parameters. The lengths of diffusive pathways could conceivably be considered uncertain because the location of the failed fuel rods and therefore the distance from the points of failure to the openings in the waste package outer corrosion barrier cannot be known. However, no credit is taken for the cladding—it is modeled as not providing any isolation capability once a waste package is breached—so the diffusive path length is fixed (see Section 6.5.2.1.1.1).

6.3.4.3.1 Adsorption of Water Vapor in Commercial Spent Nuclear Fuel Waste Packages

All surfaces exposed to water vapor will adsorb water. The amount of adsorbed water vapor depends principally on the nature of the material and the relative humidity. On clean metal surfaces, formation of hydrogen-bonded clusters of water molecules is common, because hydrogen bonding between two or more water molecules is often energetically competitive with the molecule-substrate bond (Thiel and Madey 1987 [DIRS 120496], p. 230). In contrast, on oxidized surfaces, water generally does not form hydrogen-bonded clusters at low coverage (Thiel and Madey 1987 [DIRS 120496], p. 337); the tendency to cluster is overridden by the oxide substrate-water interaction. On this basis, water adsorption is conceptualized in this submodel as forming uniform layers.

In many cases, the first layer of water adsorbed is chemically bound to the surface (McCafferty and Zettlemoyer 1971 [DIRS 154378], p. 239) and is difficult to remove except at high temperatures, higher than will exist in the repository. Subsequent layers are less tightly bound, being attracted simply by van der Waals forces to lower water layers. The first few layers of water often form an ice-like structure with little mobility. As the relative humidity approaches 100 percent, the outer layers of water begin to behave more like bulk liquid. At 100 percent relative humidity, bulk condensation of water occurs, forming a liquid phase.

Most metals, except for inert metals such as gold and platinum, form an oxide or oxyhydroxide surface layer when exposed to oxygen or water. Thus, all metals in a waste package contain a surface oxide layer on which water adsorption takes place. In the case of Alloy 22, stainless steel, Zircaloy, and aluminum—metals found in the waste package or waste form—the surface oxide layer is passivating, where the resistance to oxygen diffusion protects the metal underneath.

Adsorption isotherms define the amount of water adsorbed as a function of relative humidity or relative pressure, provided sufficient time is allowed for equilibrium to be achieved. Isotherms have been measured for powdered samples of some metal oxides found in waste packages, including hematite (Fe_2O_3), goethite (FeOOH), HFO (FeOOH), nickel and chromium (hydr)oxides (oxidized components of stainless steel and carbon steel), ZrO_2 (oxidized surface of Zircaloy fuel rods and assembly components), UO_2 , PuO_2 , ThO_2 , (components and fission products of SNF), and HLW glass. The amount of water adsorbed is represented as the statistical number of monolayers of water present if it uniformly covers the entire surface area of the sample.

Water at solid surfaces varies in nature from a highly structured form on hydrophilic substrates to a loose, entropic form on more hydrophobic substrates possessing hydrophilic sites (Lee and Staehle 1994 [DIRS 154380], p. 74). The adsorption of water on solids depends on the capacity of the surface to orient the water dipoles, usually with the proton outward. Near polar surfaces of solids such as metal and oxides, the cause of the orientation of water molecules at the interface could be either hydrogen bonding or dipole-dipole interactions, depending on the chemical nature of the solid. Depending on the dissimilarity between the ordered (dipole-dipole), induced structure near the interface and the bulk structure, various thicknesses of the ordered layers are possible (Lee and Staehle 1994 [DIRS 154380], p. 75).

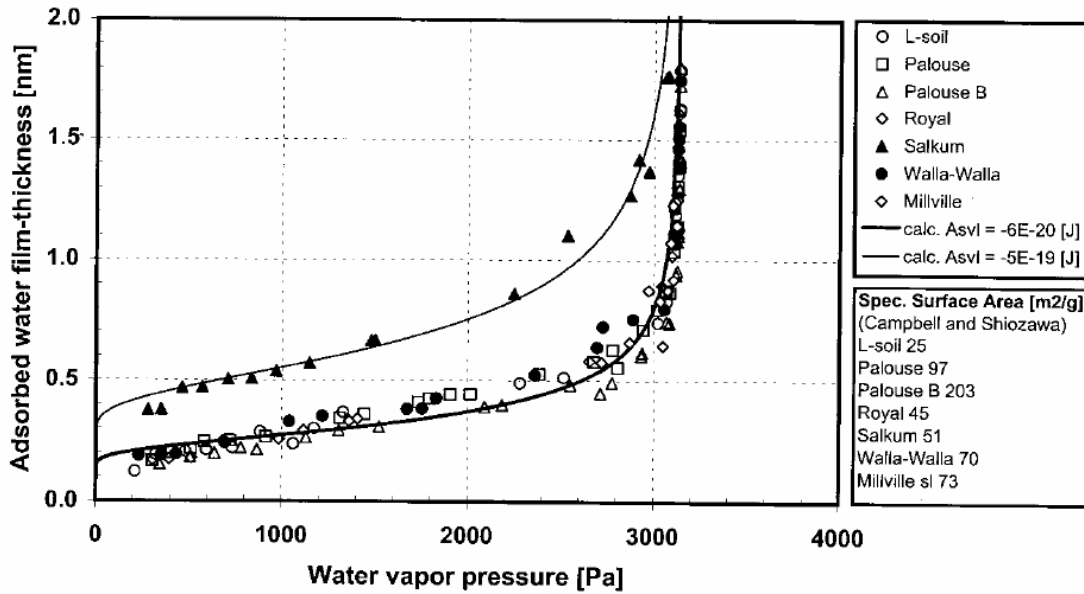
The structure of liquid water is considered to consist of unbonded molecules and of molecules hydrogen-bonded in clusters that have a mean size of about 90 molecules at 0°C (Lee and Staehle 1994 [DIRS 154380], p. 79). At hydrophilic surfaces, such as most metal oxides, the structure of water resembles that of ice (McCafferty and Zettlemoyer 1971 [DIRS 154378], p. 239). This behavior is attributed to the existence of a monolayer in which the adsorbed water is held rigidly to the solid surface at fixed sites. The first layer is localized by double hydrogen bonding of a single water molecule to two surface hydroxyls. This highly constrained first layer relaxes in the next layers, where the water molecules start to possess a rotational degree of freedom, being singly hydrogen-bonded. The second layer becomes more ordered when hydrogen bonds to a third layer, and so on, until the ordering effect of the surface is overcome and bulk liquid layers form farther from the surface. On a hydrophobic surface, such as silica, different behavior is observed. When half of the surface hydroxyls on silica are occupied by water, the water starts to agglomerate into clusters instead of adsorbing uniformly over the surface.

Layers of water adsorbed on an oxide surface can promote lateral ion movement, which sets up localized electrochemical cells due to inhomogeneities in the underlying metal (Lee and Staehle 1994, [DIRS 154380] p. 141). Such cells promote localized corrosion. Surface water dipoles may act to shield oxygen ions from an internal field that promotes ion movement. On the other hand, the gel-like structure of a metal oxyhydroxide may not support the charge separation that normally accounts for the field-driven process. Instead, ion movement may take place under the influence of a concentration gradient. The first layers of adsorbed water often do not contain ions from the solid (Lee and Staehle 1994 [DIRS 154380], p. 73), which indicates that multiple water layers are needed in order for solid species (such as radionuclides) to dissolve and diffuse.

As a bounding assumption in the RTA, it is assumed (Assumption 5.5) that the adsorbed water film behaves as a bulk liquid in that radionuclides dissolve in this film and that colloids as well as radionuclides diffuse through it.

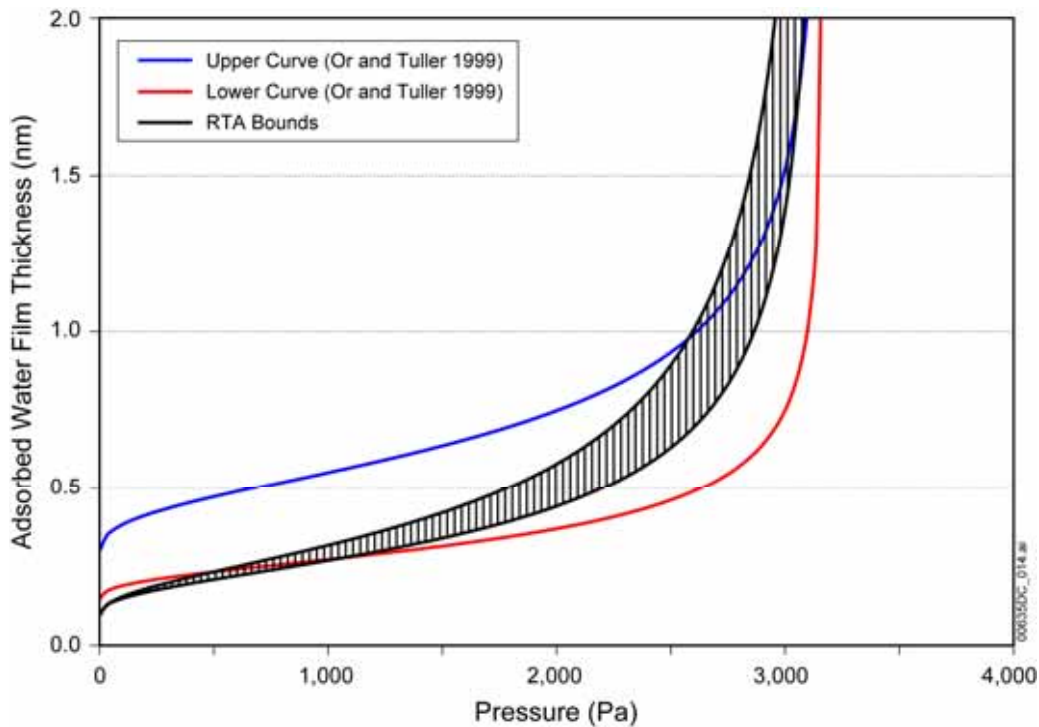
Waste package corrosion products are considered to be a mixed assemblage of iron, chromium, and nickel oxides (see Section 6.3.4.2.1). The properties of hematite (Fe_2O_3), goethite (FeOOH), hydrous ferric oxide (HFO), Cr_2O_3 , and NiO are used for calculating the amount of water adsorbed onto stationary corrosion product surfaces. The adsorptive behavior of the iron, nickel, and chromium oxides is similar insofar as water vapor adsorption is concerned, so a single adsorption isotherm is used to represent all corrosion products (see Section 6.3.4.3.2).

While it is difficult to predict the precise nature of corrosion products in terms of texture and grain size, it is reasonable that corrosion products will accumulate within the waste package as fine-grained masses of material. The in-package degradation products described in Section 6.3.4.2.1 are envisioned to be composed of unconsolidated particulates and larger agglomerations of clays, iron oxyhydroxides, and other mineral assemblages in unknown proportions that slump to the bottom of the waste package over time. Any seepage through the waste package is expected to flow through the sludge at the bottom of the waste package. The water adsorption isotherm developed for corrosion products in Section 6.3.4.3.2 is compared here with the water retention characteristics of fine-grained soils. This comparison shows that corrosion products exhibit similar water retention behavior as a fine-grained geologic porous medium and can thus be described in terms of the behavior of porous media such as soils. Figure 6.3-6 (adapted from Or and Tuller 1999 [DIRS 173799], Figure 5) presents data for clay-dominated soils plotted as water film thickness as a function of water vapor partial pressure. Water film thickness is a function of the number of adsorbed water layers. Water vapor partial pressure is proportional to RH; as the partial pressure approaches the vapor pressure of 3169 Pa at 25°C; (Lide 1981 [DIRS 162229], p. 6-10), RH approaches 1.0, and the adsorbed water film thickness increases rapidly, with bulk condensation occurring when $\text{RH} = 1.0$.



Source: Or and Tuller 1999 [DIRS 173799], Figure 5.

Figure 6.3-6. Water Adsorption Behavior of Seven Clay-Dominated Soils

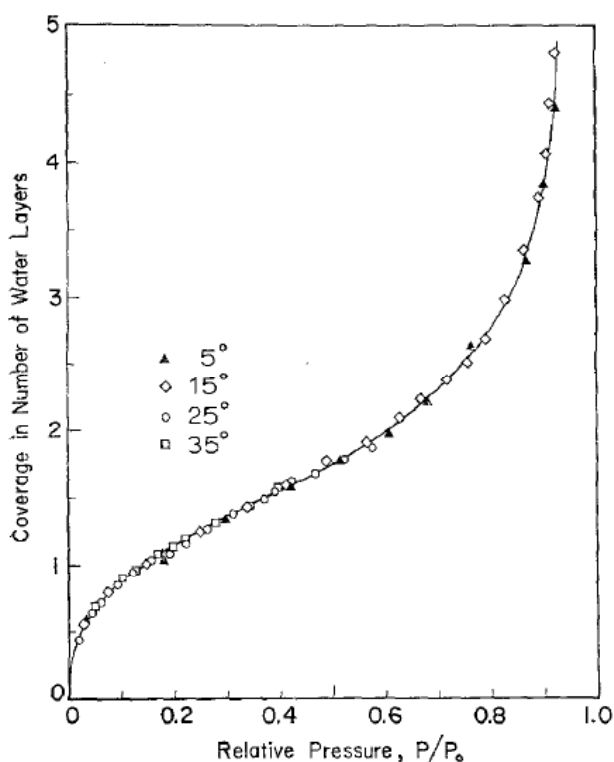


NOTE: The "RTA Bounds" curves are the isotherms from Figure 6.3-34. The upper and lower curves are from Or and Tuller 1999 [DIRS 173799], Figure 5.

Figure 6.3-7. Comparison of the Corrosion Products Water Adsorption Isotherm with Water Adsorption Behavior of Seven Clay-Dominated Soils

The data points in Figure 6.3-6 represent measured water retention data for seven soils with varying mixtures of clays (montmorillonite and kaolinite); the upper and lower curves are functions calculated in "Liquid Retention and Interfacial Area in Variability Saturated Porous Media: Upscaling from Single-Pore To Sample-Scale Model" (Or and Tuller 1999 [DIRS 173799]). The functions calculated by Or and Tuller are compared with the corrosion products water adsorption isotherm in Figure 6.3-7. The band shows the bounds of the corrosion products water adsorption isotherms from Figure 6.3-34 plotted as a function of water partial pressure. The water adsorption isotherm for corrosion products, agree well with empirical water retention data for clays having a range of compositions. This indicates that the porous media characteristics of fine-grained hematite and clay are similar.

The waste package corrosion products will begin to adsorb water after the temperature falls below the boiling point and the RH begins to rise. Information on water adsorption isotherms is scarce at temperatures above 25°C, although sources indicate that at some higher temperatures the water sorption isotherm for hematite shows no significant dependence on temperature at a given RH, and that an adsorption isotherm for 25°C is a good approximation for isotherms for higher temperatures. For example, McCafferty and Zettlemoyer (1970 [DIRS 154382]) experimentally determined the entropy of adsorption for water on hematite ($\alpha\text{-Fe}_2\text{O}_3$) at several temperatures and up to RH of about 0.7 at 25°C and 0.5 and at 35°C. Figure 6.3-8 presents the data of McCafferty and Zettlemoyer (1970 [DIRS 154382]) in terms of relative pressure (i.e., RH) and number of water layers.



Source: McCafferty and Zettlemoyer 1970 [DIRS 154382], Figure 3.

Figure 6.3-8. Isotherms for Water Vapor on $\alpha\text{-Fe}_2\text{O}_3$

Lee and Staehle (1997 [DIRS 104943]) investigated the adsorption of water on iron at RH values up to about 0.95 under humidified air and temperatures ranging from 7°C to 85°C. They determined that under the experimental conditions an oxide layer formed on the surface of the iron (Lee and Staehle 1997 [DIRS 104943], pp. 34-5, p. 41). The authors experimentally determined the increased mass of the samples due to water adsorption using the quartz-crystal microbalance technique (Lee and Staehle 1997 [DIRS 104943]). They showed that the measurements of mass increase due to water adsorption were similar for the five temperatures used, within the scatter of the data; scatter increased with increasing temperature (Lee and Staehle 1997 [DIRS 104943], Figure 9). The authors concluded that water coverage of one monolayer thickness was exhibited at 10 percent RH at 25°C, 10 percent RH at 45°C, and 6 percent RH at 85°C. Furthermore, multilayer adsorption and capillary condensation occurred as RH increased. Based on the shapes of the isotherms, they concluded that capillary condensation and filling of pores occurred at all temperatures and RH ranges investigated (Lee and Staehle 1997 [DIRS 104943]).

The temperature dependence of water retention curves has not been extensively studied but in recent years has been receiving more attention. The most important physical factors affecting the capillary pressure (also called matric suction) for a given water content, are probably pore space topology, interfacial tension, and temperature (Bachmann and van der Ploeg 2002 [DIRS 174739], p. 468). In general, an increase in temperature results in a decrease in liquid surface tension, which causes a decrease of the contact angle and capillary pressure (i.e., less negative values) at a given degree of saturation. Further, in most cases, surface tension of a soil solution is somewhat lower than that of pure water (Bachmann and van der Ploeg 2002 [DIRS 174739], p. 473), and the temperature effect on the surface tension of soil solutions is larger than for pure water (Bachmann and van der Ploeg 2002 [DIRS 174739], p. 474; Nimmo and Miller 1986 [DIRS 174124], p. 1112).

Capillary pressure is generally thought to decrease linearly as a function of temperature at a given volumetric water content. A detailed treatment of this relationship is beyond the scope of this report, but the following relationships are pertinent to this discussion. The dependence on temperature and volumetric water content of the capillary pressure due to liquid surface tension effect may be expressed as (Bachmann and van der Ploeg 2002 [DIRS 174739], p. 474):

$$\psi(T, \theta)_{\theta} \approx a(\theta) + b(\theta)T, \quad (\text{Eq. 6.3.4.3.1-1})$$

where:

- θ = volumetric water content (percent)
- $\psi(T, \theta)_{\theta}$ = capillary pressure as function of temperature and volumetric water content (Pa)
- T = temperature (K)
- a = fitting parameter (Pa)
- b = fitting parameter (Pa K⁻¹).

This leads to a generalized expression for the temperature dependence of capillary pressure (Bachmann and van der Ploeg 2002 [DIRS 174739], p. 475; Grant and Salehzadeh 1996 [DIRS 174738], p. 266):

$$\psi(T) = \psi_{T_r} \left(\frac{\beta_0 + T}{\beta_0 + T_r} \right) \quad (\text{Eq. 6.3.4.3.1-2})$$

where:

$$\begin{aligned} \psi_{T_r} &= \text{capillary pressure at reference temperature, } T_r \text{ (Pa)} \\ T_r &= \text{reference temperature (K)} \\ \beta_0 &= a/b. \end{aligned}$$

Equation 6.3.4.3.1-2 may be incorporated into any empirical capillary pressure function (Grant and Salehzadeh 1996 [DIRS 174738], p. 266). Incorporation into the closed-form equation of van Genuchten 1980 [DIRS 100610] yields (Bachmann et al. 2002 [DIRS 173887], Equation 7):

$$\theta(\psi, T) = \theta_r + \frac{\theta_s - \theta_r}{\left\{ [1 + \alpha \psi(T)]^n \right\}^m} \quad (\text{Eq. 6.3.4.3.1-3})$$

where:

$$\begin{aligned} \psi(T) &= \text{capillary pressure (Pa)} \\ \theta(\psi, T) &= \text{volumetric water content as a function of capillary pressure and temperature (percent)} \\ \theta_r &= \text{residual water content (percent)} \\ \theta_s &= \text{saturated water content (percent)} \\ \alpha &= \text{fitting parameter (Pa}^{-1}\text{)} \\ m &= \text{fitting parameter (dimensionless)} \\ n &= \text{fitting parameter (dimensionless)} \end{aligned}$$

The results of several investigations of temperature dependence of capillary pressure are presented below.

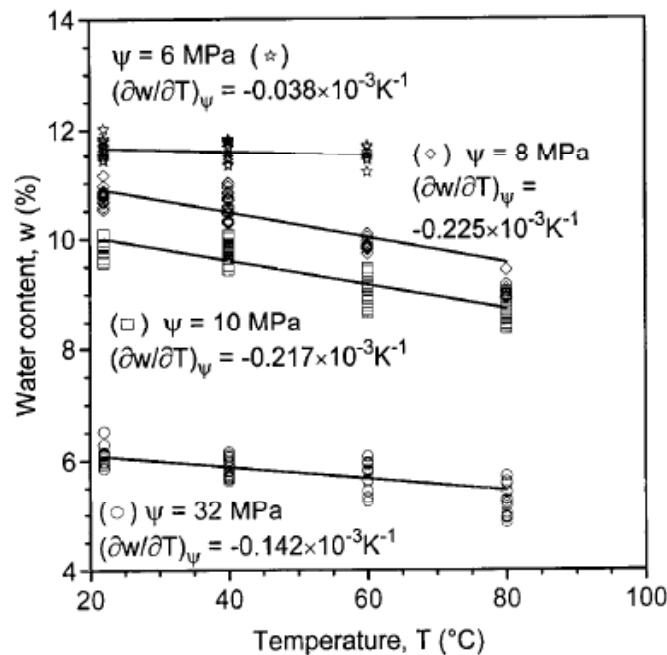
Bachmann et al. (2002 [DIRS 173887]), in the course of investigating the effects of temperature on capillary pressure and angle of contact, studied drying and wetting of three soil types and determined maximum and minimum saturations as a function of temperature up to 38°C. The particle sizes were in the sand and silt ranges, in contrast to the soil data from Or and Tuller (1999 [DIRS 173799]) shown in Figure 6.3-6, which are clay mixtures.

The samples of Bachmann et al. (2002 [DIRS 173887]) included a sand and a silt. The sand exhibited a temperature dependence of water content at saturation ($\Delta\theta_s / \Delta T$) (percent°C⁻¹)

of -0.173 , and the $\Delta\theta_s/\Delta T$ for silt was -0.140 . While the data represent only two samples, the two values for $\Delta\theta_s/\Delta T$ are in close agreement. These indicate that maximum saturation from wetting decreases with temperature.

Romero et al. (2001 [DIRS 174022]) conducted a series of experiments with clay samples to investigate the influence of temperature on the hydraulic properties of fine-grained soils. The authors adapted vapor equilibrium and axis translation techniques to the measurement of hydraulic properties of prepared clayey samples at temperatures to 80°C for a range of matric suctions and water contents.

Samples of clay powder were prepared from natural Boom clay (from Mol, Belgium). Results from the vapor equilibrium technique at four different temperatures are presented in Figure 6.3-9. The figure presents the data at total constant suction, ψ (MPa), in terms of water content (for which Romero et al. use the symbol w), and temperature, T ($^\circ\text{C}$). Suction values of 32 MPa to 6 MPa correspond to RH values of roughly 80 to 97 percent. The changes in water content as a function of temperature are small; for $\psi = 6$ MPa and w approximately 12 percent, $\Delta w/\Delta T$ was only $-0.038 \times 10^{-3} \text{ K}^{-1}$.



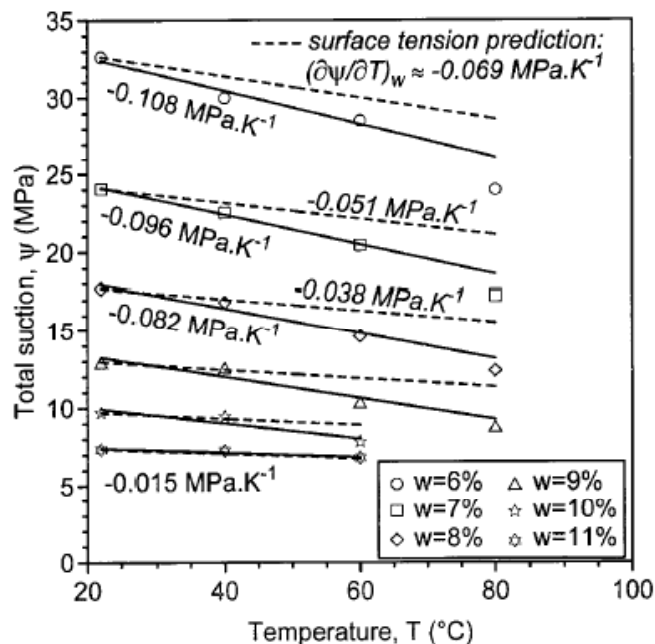
Source: Romero et al. 2001 [DIRS 174022], Figure 4.

NOTE: Samples are clay powder prepared from natural Boom clay, Mol, Belgium.

Figure 6.3-9. Water Content versus Temperature at Four Constant Suction Values

Figure 6.3-10 presents the same data at constant water content, w (percent), in terms of total suction, ψ (MPa), and temperature, T ($^\circ\text{C}$). Changes in suction with respect to temperature at constant water content are also relatively small. For $w = 11$ percent and ψ approximately 7 MPa, $\Delta\psi/\Delta T$ is only $-0.015 \text{ MPa K}^{-1}$. The figure also presents the slopes of $\Delta\psi/\Delta T$ for constant water

content as predicted by surface tension theory. The effect of temperature is greater than surface tension theory alone would predict. Other investigators of unsaturated soil properties have reached the same conclusion (Nimmo and Miller 1986 [DIRS 174124]; Hopmans and Dane 1986 [DIRS 174122]; Haridasan and Jensen 1972 [DIRS 174125]).



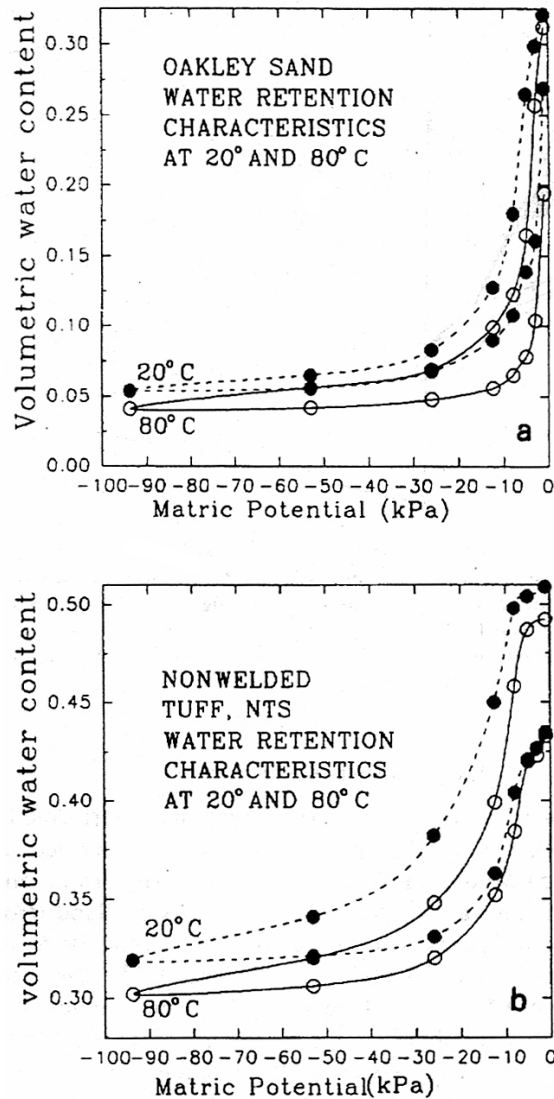
Source: Romero et al. 2001 [DIRS 174022], Figure 4.

NOTE: Samples are clay powder prepared from natural Boom clay, Mol, Belgium. Dashed curves represent values as predicted by surface tension theory.

Figure 6.3-10. Total Suction versus Temperature at Six Constant Water Contents

Constantz (1991 [DIRS 174120]) investigated isothermal and isobaric water retention in two different porous materials, a sand (the Oakley Sand, from Contra Costa County, California, bulk density 1.77 g cm^{-3} , porosity 0.34) and a nonwelded tuff core sample (part of the Paint Brush Tuff, Yucca Mountain, Nevada, bulk density 1.30 g cm^{-3} , porosity 0.52).

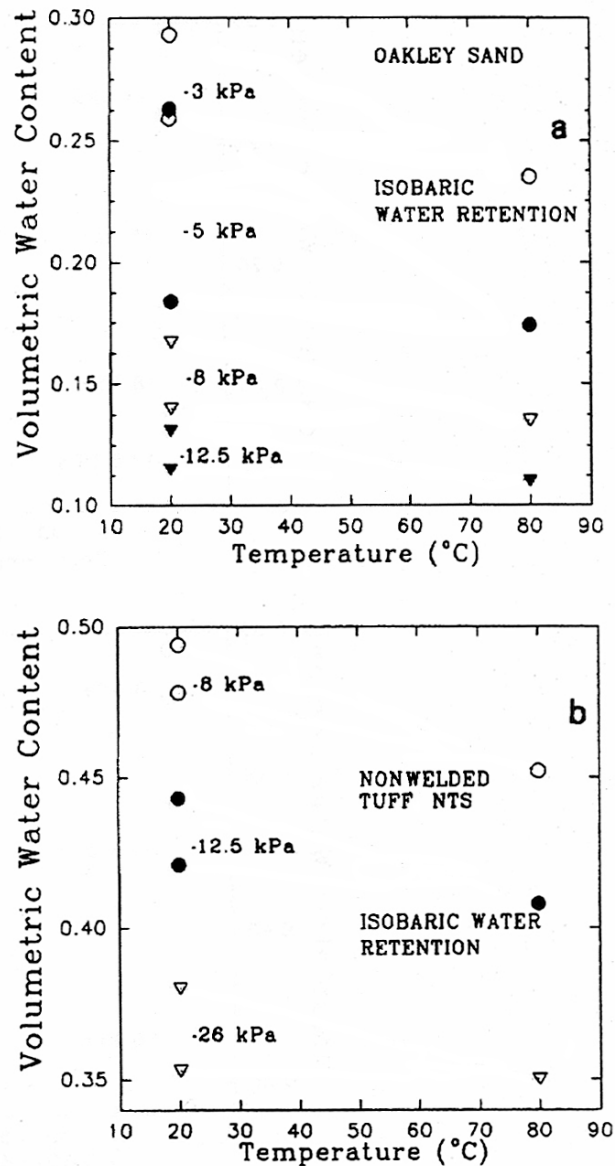
Isothermal water retention tests were conducted at 20°C and 80°C . The author states, “[a]s expected, measurably less water was held within each matrix at 80°C compared to 20°C , except near saturation” (Constantz 1991 [DIRS 174120], p. 3167). Figure 6.3-11 shows hysteresis loops for the two samples generated by cycling the pressure on the samples up and then down at constant temperature; this procedure was followed at each temperature. The curves illustrate the small response to temperature at near saturation conditions.



Source: Constantz 1991 [DIRS 174120], Figure 3.

Figure 6.3-11. Water Content (Expressed as Fraction, or $m^3 m^{-3}$) versus Matric Potential at 20°C and 80°C Hysteresis Curves for a Sand and a Nonwelded Tuff

The isobaric tests were conducted by determining water content at 20°C, then 80°C, and then back to 20°C at constant pressure to effect a drying-wetting cycle. Figure 6.3-12 shows the results of these tests at four pressures (-3 kPa, -5 kPa, -8 kPa, and -12.5 kPa) for the sand, and three pressures (-8 kPa, -12.5 kPa, and -26 kPa) for the tuff. The drying part of the cycle, i.e., from 20°C to 80°C, results in a significant reduction in water content, particularly at the lower pressures. However, for the wetting part of the cycle, i.e., from 80°C to 20°C, results indicate that little water was reincorporated into the samples. This is as expected; the gain in water content from 80°C to 20°C represents only a few percent.



Source: Constantz 1991 [DIRS 174120], Figure 4.

NOTE: For each matric potential, water content was determined at 20°C, then 80°C, then again at 20°C.

Figure 6.3-12. Water Content (Expressed as Fraction, or $\text{m}^3 \text{m}^{-3}$) versus Temperature at Constant Matric Potential for a Sand and a Nonwelded Tuff

During cooldown after the thermal period, humidity will rise and water will adsorb onto surfaces. The results of Constantz (1991 [DIRS 174120]) support the thesis that temperature has a small effect on water content near saturation, i.e., at low suction, high RH conditions.

Experimental studies of water adsorption and soil water retention have been limited to RH values below about 98 percent. This is due at least in some cases to difficulties with condensation in the experimental apparatus. For example, McCafferty and Zettlemoyer (1970 [DIRS 154382]) noted that their 25°C runs were limited to relative pressures (RH) of about 0.7 due to condensation of

water vapor in the dosing bulbs. The soils data from Or and Tuller (1999 [DIRS 173799]) presented in Figure 6.3-6 have a maximum RH of about 98 percent. The Lee and Staehle (1997 [DIRS 104943]) data described above were obtained at maximum RH of about 95 percent.

The transition from “water layer behavior” to “bulk liquid behavior” begins in the vicinity of the high RH values at which experimental difficulties with condensation begin to occur. However, the RH values at which porous media approach saturation are higher, well above 99 percent. Two arguments support extrapolation of film thickness-scale water adsorption isotherms to high RH, with concomitant high saturation and bulk water behavior. First, the goodness of fit shown by the steel corrosion products water adsorption isotherm and the calculated soils isotherms (which are based on empirical retention curve data), shown in Figure 6.3-7, indicate that water behavior in corrosion products may be approximated by the water retention behavior of clays. Second, the goodness of fit of all cited data to similarly shaped isotherms adds confidence to the extrapolation of those isotherms to the high RH values where more generic porous medium behavior is exhibited.

6.3.4.3.2 Corrosion Products Water Vapor Adsorption Isotherm

The isotherms for adsorption of water onto metal oxides have been extensively measured and reported in the literature. A relationship for the coverage (i.e., number of monolayers of water adsorbed) as a function of relative humidity is often based on the Frenkel-Halsey-Hill (FHH) Equation for multilayer adsorption:

$$\ln(p_w / p_w^o) = \frac{-k}{(V / V_m)^s}, \quad (\text{Eq. 6.3.4.3.2-1})$$

where

- p_w = partial pressure of water (Pa)
- p_w^o = vapor pressure of water (Pa)
- k = FHH adsorption isotherm fitting parameter (dimensionless)
- s = FHH adsorption isotherm fitting parameter (dimensionless)
- V = volume of water vapor adsorbed at relative pressure p_w / p_w^o ($\text{m}^3 \text{H}_2\text{O kg}^{-1}$ sorbent)
- V_m = volume of adsorbed water vapor that provides a one-monolayer coverage on the surface ($\text{m}^3 \text{H}_2\text{O kg}^{-1}$ sorbent).

The ratio of water vapor partial pressure to vapor pressure, sometimes referred to as the relative pressure, is the relative humidity (RH). The ratio of V to V_m is the statistical number of monolayers of water (i.e., the number of layers of individual water molecules) adsorbed on the surface, assuming complete and uniform coverage. Letting $\theta_a = V/V_m$ and $RH = p_w/p_w^o$, the FHH correlation may be written in general terms with parameters k and s :

$$\ln(RH) = \frac{-k}{\theta_a^s}, \quad (\text{Eq. 6.3.4.3.2-2})$$

or

$$\theta_a = \left[\frac{-k}{\ln(RH)} \right]^{\frac{1}{s}}. \quad (\text{Eq. 6.3.4.3.2-3})$$

Water vapor adsorption isotherms for products of stainless steel corrosion—oxides of iron, chromium, and nickel—are shown in Figures 6.3-13 – 6.3-33. Although smooth curves are shown in each plot, only the measured data points, as indicated by symbols in the plots, were used to develop the representative isotherm for generic corrosion products. These data points were obtained by digitizing each plot using Grab It!™ Excel based digitizing software, and are listed in Table 4.1-19. All data points extracted from the original plots are used, although statistical analyses might suggest some data points to be outliers. Since there is no basis for eliminating any data in the literature sources, none was deleted.

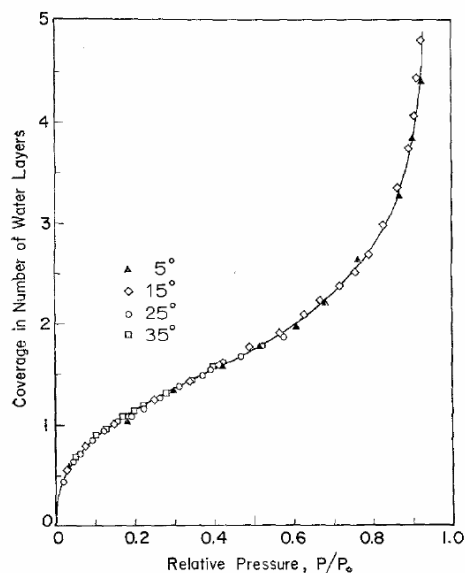
The data for all the iron, nickel, and chromium oxyhydroxides in Table 4.1-19 were combined, and a single composite FHH adsorption isotherm was fit to the combined data in Figure 6.3-34. The justification for combining the data for different materials is that the variability in the measured amount of water adsorbed, even for a single substance, tends to be large due to variations in how a sample was prepared, pretreated, and tested. Various techniques were used to measure the amount of water adsorbed; the precision of the techniques is seldom reported. The humidity during measurements is maintained using a variety of techniques, also of uncertain precision. The result of all this variability and uncertainty is that adsorption isotherms for many substances overlap, as seen in Figure 6.3-34. In addition to uncertainty due to measurements of adsorption isotherms, the mineralogical composition and morphology of corrosion products and SNF degradation products is uncertain. To account for this uncertainty, the parameters in the adsorption isotherm used for corrosion products are assigned ranges based on three standard deviation variations about the mean values of the FHH fitting parameters s and k (1.632 and 1.155, respectively). Both parameters are assigned uniform distributions, although a joint normal distribution is also justified on the basis of assumptions implicit in the statistical analysis from which the ranges were calculated. The 95 percent prediction interval is also shown in Figure 6.3-34; this measure of uncertainty was considered to be too broad, resulting in excessively high or low estimates of water saturation in corrosion products. The corrosion products adsorption data are analyzed in output DTN: SN0703PAEBSRTA.001, Excel file *Corrosion Products Composite Isotherm 7-19-2007.xls*. In the TSPA, the FHH parameters s and k are sampled independently in each realization and the resulting adsorption isotherm is then

fixed for the entire realization. The functional dependence on s and k is such that (s_{min}, k_{max}) and (s_{max}, k_{min}) bound the isotherms; these are the bounds shown in Figures 6.3-7 and 6.3-34.

Range for corrosion products FHH parameter s : 1.493 – 1.799 (dimensionless).

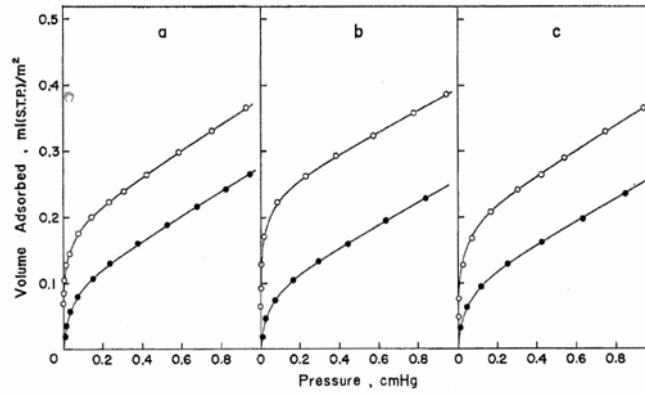
Range for corrosion products FHH parameter k : 1.030 – 1.326 (dimensionless).

The FHH isotherm function causes curves with a range of s and k values to converge as RH approaches zero, resulting in a narrow band of uncertainty at low RH. The FHH isotherm was developed for multilayer adsorption (Gregg and Sing 1982 [DIRS 153010], pp. 89 – 90), so it fits data best at $RH > 0.7$ or so, where there is more than one water layer adsorbed. There, the uncertainty band in Figure 6.3-34 captures a good portion of measured data. Most adsorption data are taken at low RH, since the objective is typically to reveal surface properties that become obscured by multiple water layers. At low RH, much of the measured data fall outside the band of uncertainty. However, since multiple layers of water are needed for diffusive transport to take place, the high-RH range behavior is of greatest importance for use in the TSPA. Thus, the goodness of the model fits to the measured data at low RH is not as important as at high RH. The uncertainty in adsorptive behavior at low RH contributes to the overall uncertainty, but low-RH behavior has no impact in the TSPA calculations because insufficient water is present for transport to occur.



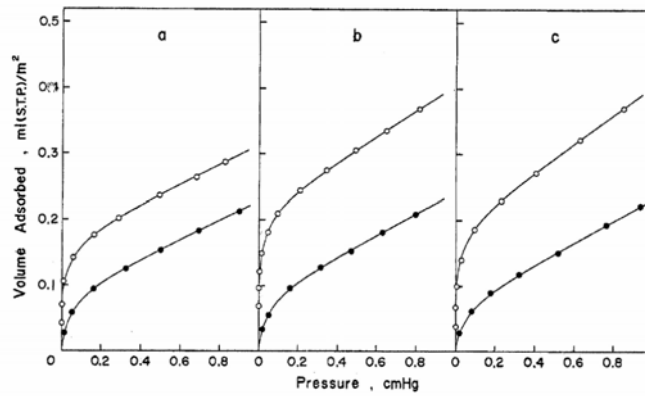
Source: McCafferty and Zettlemoyer 1970 [DIRS 154382], Fig. 3

Figure 6.3-13. Water Vapor Adsorption Isotherm for $\alpha\text{-Fe}_2\text{O}_3$



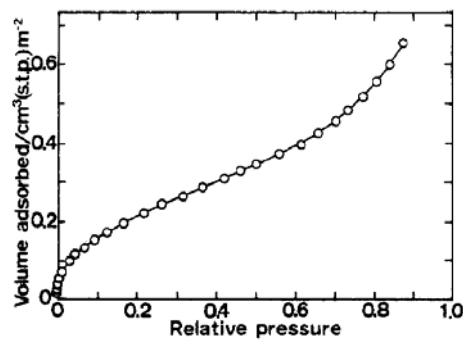
Source: Morimoto et al. 1969 [DIRS 162877], Fig. 3

Figure 6.3-14. Water Vapor Adsorption Isotherm for $\alpha\text{-Fe}_2\text{O}_3$



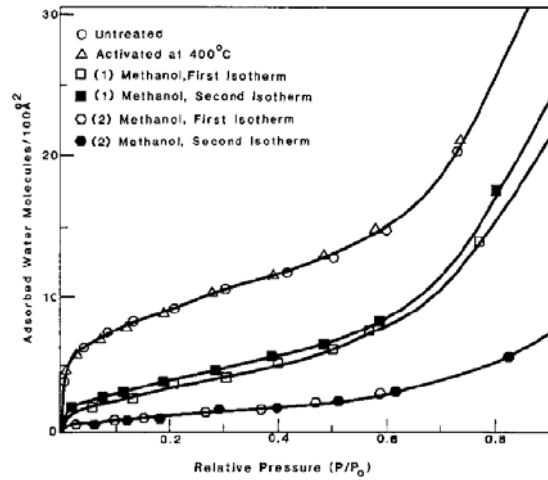
Source: Morimoto et al. 1969 [DIRS 162877], Fig. 4

Figure 6.3-15. Water Vapor Adsorption Isotherm for $\alpha\text{-Fe}_2\text{O}_3$



Source: Kuwabara et al. 1987 [DIRS 178682], Fig. 1

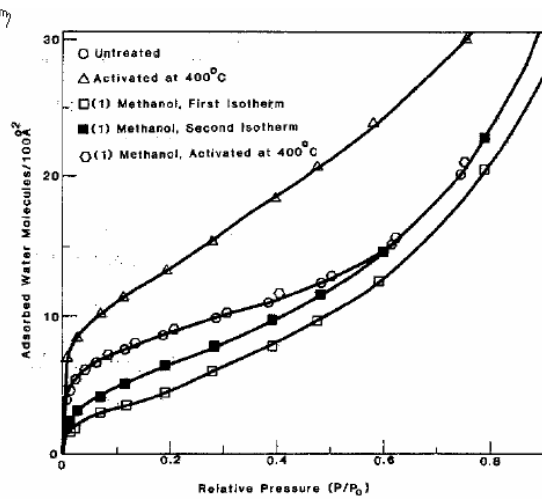
Figure 6.3-16. Water Vapor Adsorption Isotherm for $\alpha\text{-Fe}_2\text{O}_3$



Source: Micale et al. 1985 [DIRS 173785], Fig. 1

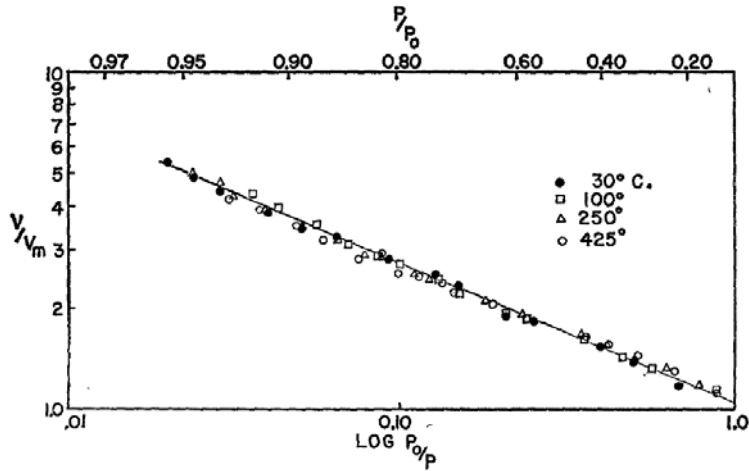
NOTE: Reference erroneously shows this as Fig. 1 (methanol isotherms), but the text and figure captions indicate that this is meant to be Fig. 2 (α - Fe_2O_3 isotherms).

Figure 6.3-17. Water Vapor Adsorption Isotherm for α - Fe_2O_3



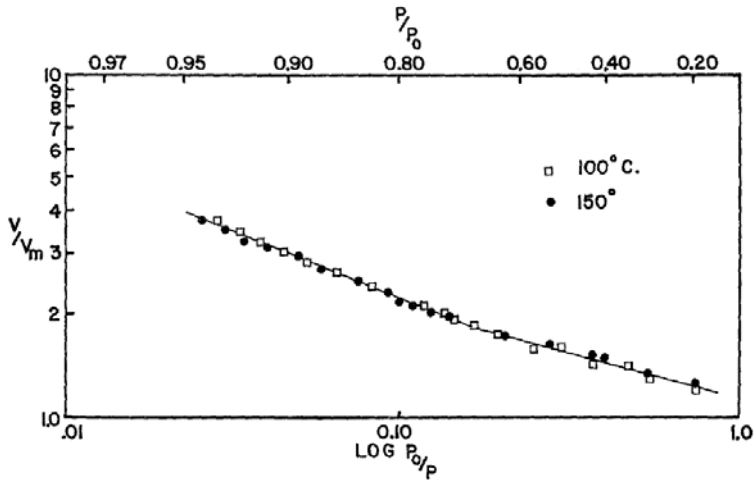
Source: Micale et al. 1985 [DIRS 173785], Fig. 3

Figure 6.3-18. Water Vapor Adsorption Isotherm for γ - FeOOH



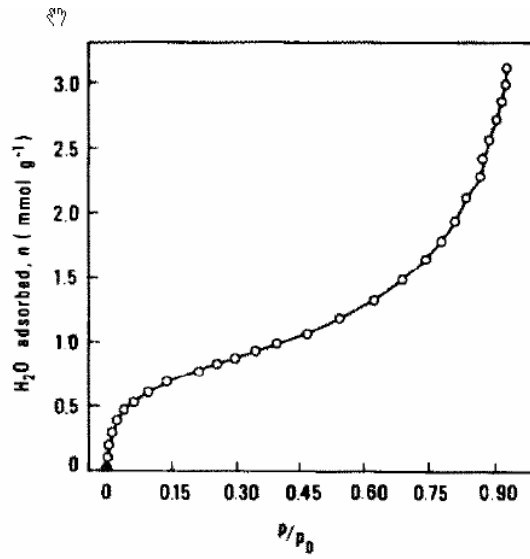
Source: Jurinak 1964 [DIRS 154381], Fig. 5

Figure 6.3-19. Water Vapor Adsorption Isotherm for $\alpha\text{-Fe}_2\text{O}_3$



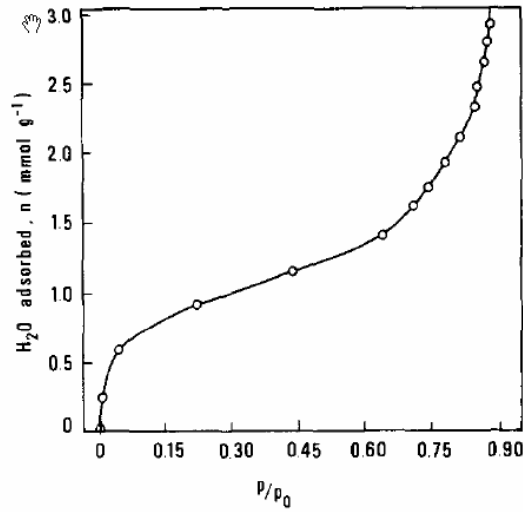
Source: Jurinak 1964 [DIRS 154381], Fig. 6

Figure 6.3-20. Water Vapor Adsorption Isotherm for $\gamma\text{-FeOOH}$



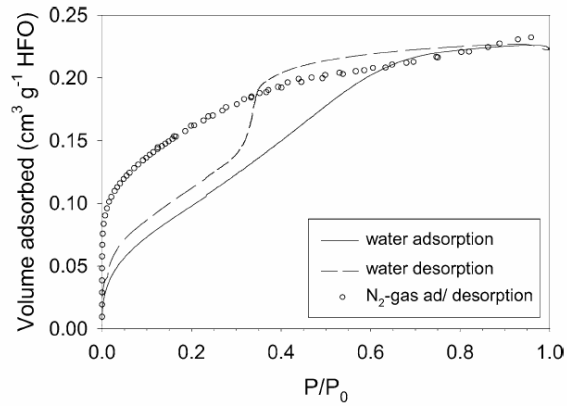
Source: Koch and Møller 1987 [DIRS 173784], Fig. 5

Figure 6.3-21. Water Vapor Adsorption Isotherm for Goethite



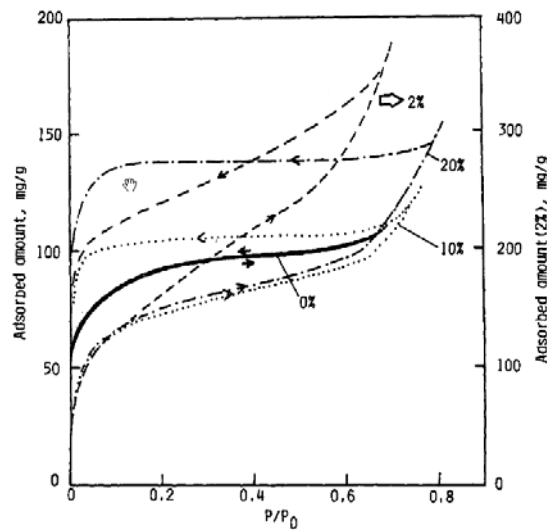
Source: Koch and Møller 1987 [DIRS 173784], Fig. 6

Figure 6.3-22. Water Vapor Adsorption Isotherm for Goethite



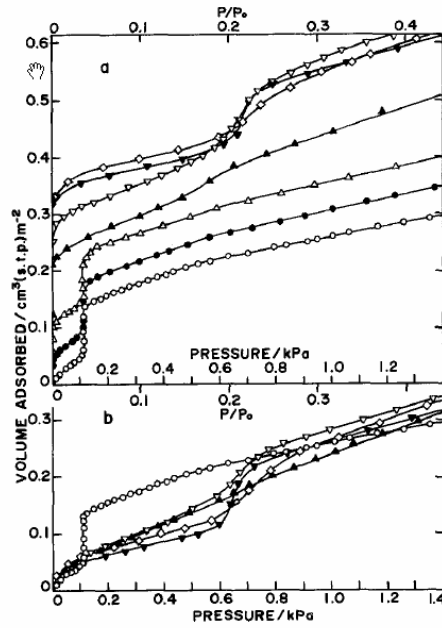
Source: Hofmann et al. 2004 [DIRS 173783], Fig. 8

Figure 6.3-23. Water Vapor Adsorption Isotherm for HFO



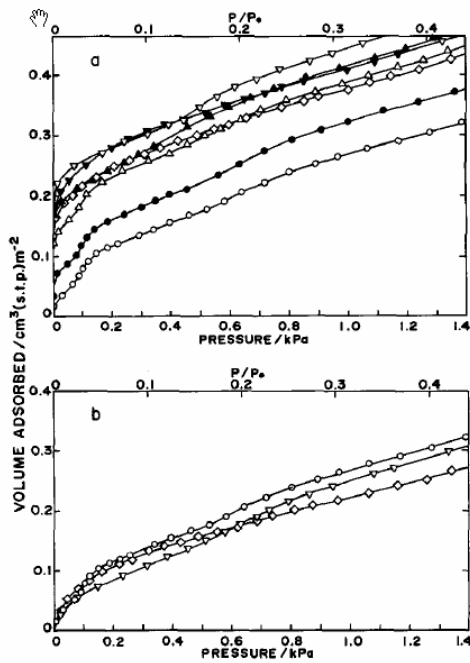
Source: Kandori and Ishikawa 1991 [DIRS 178680], Fig. 2

Figure 6.3-24. Water Vapor Adsorption Isotherm for Amorphous Ferric Oxide Hydroxide



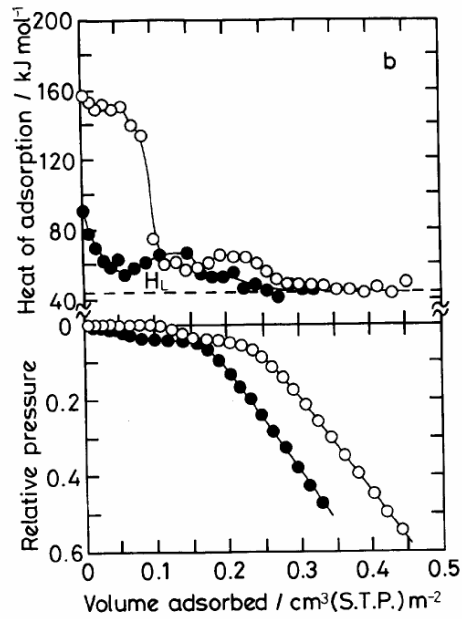
Source: Kittaka et al. 1983 [DIRS 178681], Fig. 6

Figure 6.3-25. Water Vapor Adsorption Isotherm for Cr_2O_3



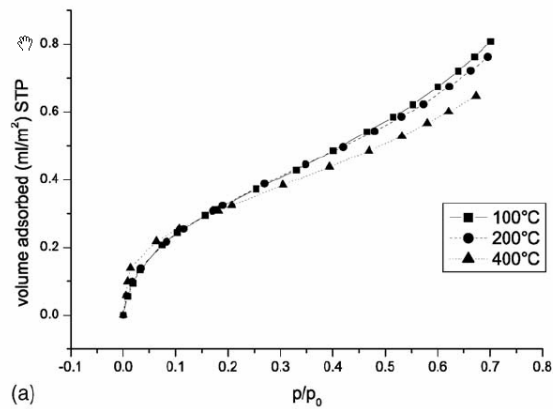
Source: Kittaka et al. 1983 [DIRS 178681], Fig. 7

Figure 6.3-26. Water Vapor Adsorption Isotherm for Cr_2O_3



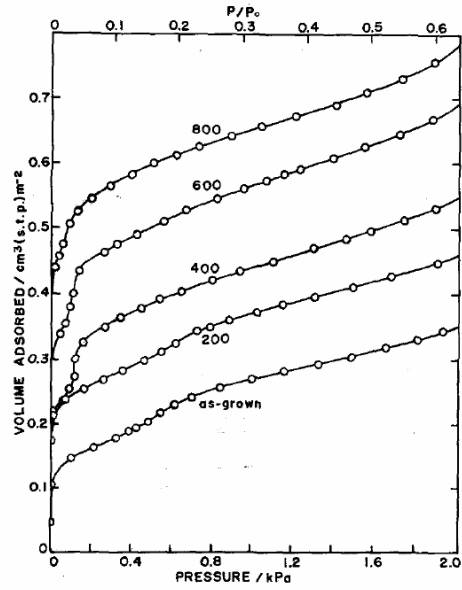
Source: Nagao et al. 1995 [DIRS 162878], Fig. 1b

Figure 6.3-27. Water Vapor Adsorption Isotherm for Cr_2O_3



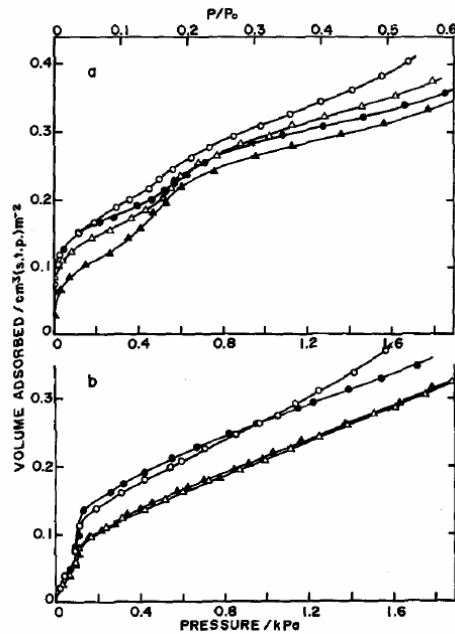
Source: Harju et al. 2005 [DIRS 178670], Fig. 4a

Figure 6.3-28. Water Vapor Adsorption Isotherm for Cr_2O_3



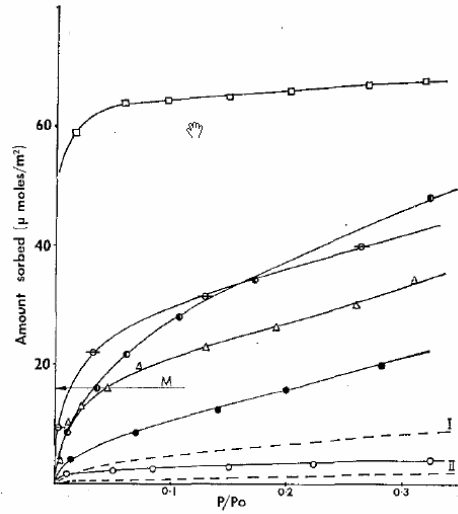
Source: Kittaka et al. 1984 [DIRS 178830], Fig. 5

Figure 6.3-29. Water Vapor Adsorption isotherm for α -HCrO₂



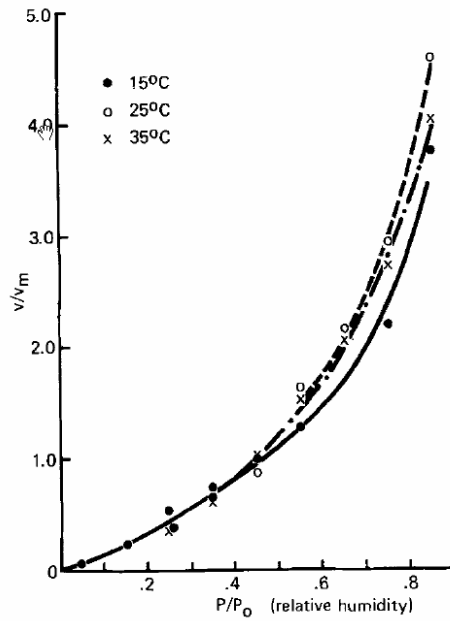
Source: Kittaka et al. 1984 [DIRS 178830], Fig. 6

Figure 6.3-30. Water Vapor Adsorption isotherm for α -HCrO₂



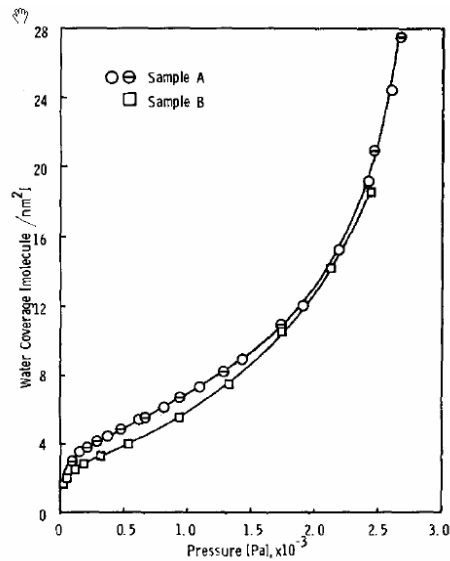
Source: Carruthers et al. 1971 [DIRS 178656], Fig. 7

Figure 6.3-31. Water Vapor Adsorption Isotherm for Chromium Oxide Gel



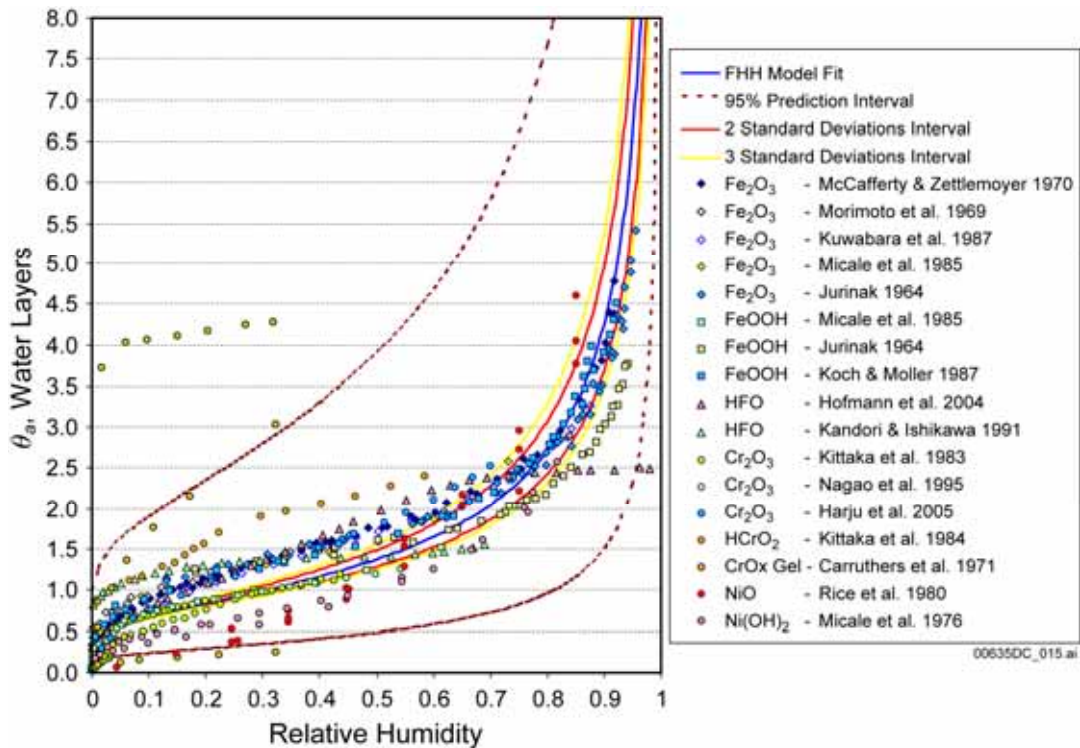
Source: Rice et al. 1980 [DIRS 178725], Fig. 2

Figure 6.3-32. Water Vapor Adsorption Isotherm for NiO



Source: Micale et al. 1976 [DIRS 179136], Fig. 3

Figure 6.3-33. Water Vapor Adsorption Isotherm for Ni(OH)₂



Source: Output DTN: SN0703PAEBSRTA.001.

Figure 6.3-34. Composite Water Vapor Adsorption Isotherm for Steel Corrosion Products

The average thickness of a monolayer of water can be computed from the cross-sectional area of a water molecule. Values reported in the literature for the cross-sectional area of a water molecule range from about 10.5 \AA^2 (Gregg and Sing 1982 [DIRS 153010], p. 188),

corresponding to a “close-packed” monolayer of water, to 10.8 \AA^2 (Jurinak 1964 [DIRS 154381]). Holmes et al. (1974 [DIRS 154379], p. 368) and McCafferty and Zettlemoyer (1970 [DIRS 154382], p. 453) assume a cross-sectional area of the water molecule of 10.6 \AA^2 . In this report, a value for the cross-sectional area of a water molecule of $A_w = 10.6 \text{ \AA}^2$ per molecule (McCafferty and Zettlemoyer 1970 [DIRS 154382], p. 454) is used. Using a water density at 25°C of $\rho_w = 997.0449 \text{ kg m}^{-3}$ (Weast 1985 [DIRS 111561], p. F-5), the thickness of a water monolayer film, t_f , is:

$$\begin{aligned}
 t_f &= \frac{M_w}{A_w \rho_w N_A} \\
 &= \frac{18.01528 \times 10^{-3} \frac{\text{kg}}{\text{mol}}}{\left(10.6 \times 10^{-20} \frac{\text{m}^2}{\text{molec}}\right) \left(997.0449 \frac{\text{kg}}{\text{m}^3}\right) \left(6.02214199 \times 10^{23} \frac{\text{molec}}{\text{mol}}\right)} \quad (\text{Eq. 6.3.4.3.2-4}) \\
 &= 2.83 \times 10^{-10} \text{ m},
 \end{aligned}$$

where N_A is Avogadro’s number (Lide 2002 [DIRS 160832], p. 1-7), and M_w is the molecular weight of water (kg mol^{-1}). Using a water molecule cross-sectional area of 10.8 \AA^2 instead of 10.6 \AA^2 would have a negligible effect, giving a monolayer thickness of $2.78 \times 10^{-10} \text{ m}$.

At 50°C , the density of water is $988.0363 \text{ kg m}^{-3}$ (Weast 1985 [DIRS 111561], p. F-5) and the adsorbed water monolayer thickness is $2.86 \times 10^{-10} \text{ m}$, which shows that the monolayer thickness sensitivity to temperature is small.

6.3.4.3.3 Specific Surface Area of Metal Oxides

The specific surface areas of waste package component corrosion products are shown in Table 6.3-7. Most measurements of specific surface area listed in Table 6.3-7 were made using the BET nitrogen method. Water is sometimes used (Harju et al. 2005 [DIRS 178670], Table 6). However, measurement of surface area as well as the water adsorption isotherm itself is problematical due to chemisorption of water. Jurinak (1964 [DIRS 154381], p. 480) measured surface area of Fe_2O_3 by nitrogen adsorption ranging from 9.60 to $9.70 \text{ m}^2 \text{ g}^{-1}$, whereas water adsorption surface areas ranged from 6.52 to $9.10 \text{ m}^2 \text{ g}^{-1}$. It was concluded that about one-third of the Fe_2O_3 is covered with chemisorbed water that, unless removed by activation (i.e., heating to at least 425°C), blocks water adsorption sites on the surface. Heat treatment of the sample to sufficiently high temperature to drive off all of the chemisorbed water can, however, alter the pore structure of material and affect the adsorptive properties. For example, Carruthers et al. (1971 [DIRS 178656], p. 214), found that heating chromium oxide gels caused micropores to be enlarged and the specific surface area to be reduced, which reduced the amount of water adsorbed and resulted in water uptake becoming reversible when it had been irreversible prior to heat treatment.

Specific surface areas for goethite (\bar{s}_G) and HFO (\bar{s}_{HFO}) are used for the competitive radionuclide sorption model (Section 6.3.4.2.3) as well as for the water sorption and saturation model in this section. Due to the comparatively greater impact on radionuclide transport, as well as the greater availability of data, the specific surface areas of these species have been analyzed in greater detail than other corrosion products. As described in Appendix K, the extensive specific surface area data presented in Tables 4.1-12 (goethite) and 4.1-14 (HFO) have been found to fit the following truncated lognormal distributions:

Goethite: Range = 14.7 – 110 m² g⁻¹
 Mean = 51.42 m² g⁻¹
 Mean of $\ln(\bar{s}_G)$ = 3.793
 Standard deviation = 30.09 m² g⁻¹
 Standard deviation of $\ln(\bar{s}_G)$ = 0.543.

HFO: Range = 68 – 600 m² g⁻¹
 Mean = 275.6 m² g⁻¹
 Mean of $\ln(\bar{s}_{HFO})$ = 5.541
 Standard deviation = 113.4 m² g⁻¹
 Standard deviation of $\ln(\bar{s}_{HFO})$ = 0.396.

Ranges and distributions for nickel and chromium oxyhydroxides are based on the data shown in Table 4.1-19 and summarized in Table 6.3-7. Distributions for both parameters are uniform.

NiO: Range = 1.0 – 30 m² g⁻¹.

Cr₂O₃: Range = 1.0 – 20 m² g⁻¹.

Table 6.3-7. Specific Surface Area of Various Waste Package Corrosion Products

Corrosion Product	Specific Surface Area (m ² g ⁻¹)	Source
Goethite	14.7 – 110	See Table 4.1-12
HFO	68 – 600	See Table 4.1-14
Fe ₂ O ₃	1.8	Langmuir 1997 [DIRS 100051], Table 10.2 (natural hematite)
	3.1	Langmuir 1997 [DIRS 100051], Table 10.2 (synthetic hematite)
	5.60	Tamura et al. 1999 [DIRS 161625], Table 1 (Grignard method)
	9.1	Jurinak 1964 [DIRS 154381], p. 480
	10	McCafferty and Zettlemoyer 1970 [DIRS 154382], p. 453
	13.3 – 14.3	Gregg and Sing 1982 [DIRS 153010], Table 3.17
	14.5	Morimoto et al. 1969 [DIRS 162877], Table I (from calcinations of FeSO ₄ ·7H ₂ O)

Table 6.3-7. Specific Surface Area of Various Waste Package Corrosion Products (Continued)

Corrosion Product	Specific Surface Area ($\text{m}^2 \text{g}^{-1}$)	Source
	15.9	Tamura et al. 1999 [DIRS 161625], Table 1 (NaOH method)
	21.2	Morimoto et al. 1969 [DIRS 162877], Table I (from calcinations of α -FeOOH)
	21.4	Briand et al. 2001 [DIRS 161617], Table 4
Cr ₂ O ₃	3.0	Briand et al. 2001 [DIRS 161617], Table 4
	17.5	Carruthers et al. 1971 [DIRS 178656], Table IV; chromium oxide gel, Sample C2(775)16
	10.1	Carruthers et al. 1971 [DIRS 178656], Table IV; chromium oxide gel, Sample C2(885)2
	10.1	Carruthers et al. 1971 [DIRS 178656], Table IV; chromium oxide gel, Sample C2(910)20
	5.24	Harju et al. 2005 [DIRS 178670], Table 6
	3.40	Kittaka et al. 1983 [DIRS 178681], Table 1
	20.1	Kittaka et al. 1984 [DIRS 178830], Table 1; α -HCrO ₂
	1.09	Tamura et al. 1999 [DIRS 161625], Table 1
	12.0	Nagao et al. 1995 [DIRS 162878], p. 222
NiO	1.1	Briand et al. 2001 [DIRS 161617], Table 4
	12.0	Nagao et al. 1995 [DIRS 162878], p. 222
	17	Micale et al. 1976 [DIRS 179136], p. 541
	33	Micale et al. 1976 [DIRS 179136], p. 542
	22.4	Matsuda et al. 1992 [DIRS 154383], p. 1839 [for NiO(II)]
CoO	0.4	Briand et al. 2001 [DIRS 161617], Table 4
MoO ₃	5.0	Briand et al. 2001 [DIRS 161617], Table 4
UO ₂ (SNF)	0.4	BSC 2004 [DIRS 172453], Table 6-9 (Group 8b)
TiO ₂	9.94	Morimoto et al. 1969 [DIRS 162877], Table I
ZrO ₂	14.5	Holmes et al. 1974 [DIRS 154379], p. 368; average of 2 values
	39.0	Briand et al. 2001 [DIRS 161617], Table 4

6.3.4.3.4 Waste Package and Corrosion Product Mass, Surface Area, and Porosity

6.3.4.3.4.1 Waste Package Corrosion Product Mass

The maximum potential mass of sorbing material in the waste package has been estimated using compositional information from Table 4.1-15 and numbers and masses of components listed in design drawings listed in Tables 4.1-20 and 4.1-22. The mass of sorbing material in the waste package is based on the corrodible contents of Stainless Steel Type 304B4, Stainless Steel Type 316, Carbon Steel Type A 516, and aluminum Type 6061, and the masses of these alloys in the 21-PWR and 5-DHLW/DOE Long waste package types. As pointed out in

Section 6.3.3.1.1, all waste packages in the repository are represented by these two waste packages, because they are the most common of the two basic types—CSNF and codisposal. The estimated masses of corrosion products are in output DTN: SN0703PAEBSRTA.001, file 5-DHLW-SNF DOE Long + TMI SNF + 21-PWR TAD 7-10-2007.xls, and shown in Tables 6.3-8 and 6.3-9. For purposes of estimating the mass of corrosion products, the corrosion products are modeled as FeOOH, Cr₂O₃, and NiO (Section 6.3.4.2.1), and the mass of corrosion products is calculated based on the ratio of molecular weights of FeOOH, Cr₂O₃, and NiO to the atomic weight of iron, chromium, and nickel, respectively, accounting for stoichiometry. In Section 6.5.2.2, the procedure for computing the time-dependent corrosion product mass is developed. That calculation makes use of the masses of each type of steel (stainless steel or carbon steel) and the total steel mass in each waste package domain, as summarized in Tables 6.3-8 and 6.3-9.

Because the TSPA calculations were started before the direct confirming data were available in the design interface documents (SNL 2007 [DIRS 179394], and SNL 2007 [DIRS 179567]), it was necessary to utilize preliminary values for the design of the EBS components to compute certain model inputs used in the TSPA. The component masses and equivalent masses of corrosion products listed in Tables 6.3-8 and 6.3-9 are developed from component masses specified in the design documents. Tables 6.3-8 and 6.3-9 show the results obtained using both the preliminary design data as well as the final design data from SNL 2007 [DIRS 179394], and SNL 2007 [DIRS 179567]. The TSPA uses the parameters from the preliminary design data. Parameters from Tables 6.3-8 and 6.3-9 that are used as model inputs in the TSPA are compared in Table 6.5-5, where it is shown that the impact of using the preliminary data is negligible. The model inputs are summarized in Table 8.2-6, and the impact of using the preliminary design data is summarized in Table 8.2-7.

Table 6.3-8. Estimated Masses (kg) of Steels and Equivalent Masses of Corrosion Products in 21-PWR TAD Waste Packages and Domains for Use in Modeling Water Adsorption and Retardation in the Waste Package

	TAD Canister	TAD Overpack	CSNF Waste Form Domain ^a	CSNF Corrosion Products Domain ^b
Basis: Preliminary design values for component masses[#]				
Total 316 SS	22,000	14,400	6,180	30,200
316 SS Shield Plug	5,530	–	–	5,530
316 SS w/o Shield Plug	16,400	14,400	6,180	24,700
304B4 SS	3,800	–	3,800	0
Total A 516 Carbon Steel	0	0	0	0
Total All Steels w/o Plug	20,200	14,400	9,980	24,700
Fraction CS in WP Steel	0	0	0	0
Fe Mass w/o Shield Plug	13,200	9,450	6,450	16,200
Cr Mass w/o Shield Plug	3,510	2,450	1,770	4,190
Ni Mass w/o Shield Plug	2,480	1,730	1,250	2,960
FeOOH Mass w/o Plug	20,900	15,000	10,300	25,700
Cr ₂ O ₃ Mass w/o Plug	5,140	3,590	2,590	6,130
NiO Mass w/o Plug	3,160	2,200	1,600	3,770
Total Corrosion Products Mass w/o Shield Plug	29,200	20,800	14,400	35,600

Table 6.3-8. Estimated Masses (kg) of Steels and Equivalent Masses of Corrosion Products in 21-PWR TAD Waste Packages and Domains for Use in Modeling Water Adsorption and Retardation in the Waste Package (Continued)

	TAD Canister	TAD Overpack	CSNF Waste Form Domain ^a	CSNF Corrosion Products Domain ^b
Basis: Final design values for component masses^{##}				
Total 316 SS	21,900	14,400	6,170	30,100
316 SS Shield Plug	5,530	–	–	5,530
316 SS w/o Shield Plug	16,300	14,400	6,170	24,600
304B4 SS	3,820	–	3,820	0
Total A 516 Carbon Steel	0	0	0	0
Total All Steels w/o Plug	20,100	14,400	9,990	24,600
Fraction CS in WP Steel	0	0	0	0
Fe Mass w/o Shield Plug	13,100	9,430	6,460	16,100
Cr Mass w/o Shield Plug	3,500	2,450	1,780	4,170
Ni Mass w/o Shield Plug	2,470	1,730	1,260	2,950
FeOOH Mass w/o Plug	20,900	15,000	10,300	25,600
Cr ₂ O ₃ Mass w/o Plug	5,120	3,580	2,600	6,100
NiO Mass w/o Plug	3,150	2,200	1,600	3,750
Total Corrosion Products Mass w/o Shield Plug	29,100	20,800	14,500	35,400

Output DTN: SN0703PAEBSRTA.001, file 5-DHLW-SNF DOE Long + TMI SNF + 21-PWR TAD 7-10-2007.xls, worksheet "21-PWR - 304B4 SS Plates".

Output DTN: SN0703PAEBSRTA.001, file 5-DHLW-SNF DOE Long + TMI SNF + 21-PWR TAD 9-19-2007 Final TDIP.xls, worksheet "21-PWR - 304B4 SS Plates".

NOTE: All values shown are rounded from the values in the spreadsheets to 3 digits in this table. Values in **bold** are model inputs summarized in Tables 6.5-5 and 8.2-6.

^a Includes: Absorber Plates (304B4 SS), Fuel Basket Tubes (316 SS), Aluminum Plates (Fe content only).

^b Includes: Canister Shell, Side Guides, End Side Guides, Corner Guides, Inner Seal Plug, Spread Ring, Spread Ring Filler Segment, Outer Seal Plate, Outer Seal Plug, Inner Vessel, Inner Top Lid, Inner Bottom Lid, Interface Ring, 316 SS Welds (all 316 SS).

CS = carbon steel; SS = stainless steel; TAD = transportation, aging, and disposal (canister); CSNF = commercial spent nuclear fuel; WP = waste package.

Table 6.3-9. Estimated Masses (kg) of Steels and Equivalent Masses of Corrosion Products in 5- DHLW/DOE Long Waste Package Domains for Use in Modeling Water Adsorption and Retardation in the Waste Package

	5-DHLW/DOE Long Corrosion Products Domain ^a	HLWG Subdomain ^b	DSNF (TMI) Subdomain ^c
Basis: Preliminary design values for component masses[#]			
Total 316 SS	18,400	3,780	487
316 SS Inner Top Lid	5,290	–	–
Net 316 SS w/o Inner Top Lid	13,100	3,780	487
Total 304 SS	0	0	473
Total A 516 Carbon Steel	5,770	0	319
Total All Steels w/o Inner Top Lid	18,900	3,800	1,270
Fraction CS in WP Steel	0.31	0	0.25

Table 6.3-9. Estimated Masses (kg) of Steels and Equivalent Masses of Corrosion Products in 5- DHLW/DOE Long Waste Package Domains for Use in Modeling Water Adsorption and Retardation in the Waste Package (Continued)

	5-DHLW/DOE Long Corrosion Products Domain ^a	HLWG Subdomain ^b	DSNF (TMI) Subdomain ^c
Fe Mass	14,200	2,570	953
Cr Mass	2,230	718	173
Ni Mass	1,570	378	106
FeOOH Mass	22,600	4,090	1,520
Cr ₂ O ₃ Mass	3,260	1,050	252
NiO Mass	2,000	481	135
Total Corrosion Products Mass w/o Inner Top Lid	27,900	5,620	1,900
Basis: Final design values for component masses^{###}			
Total 316 SS	18,400	3,780	487
316 SS Inner Top Lid	5,260	–	–
Net 316 SS w/o Inner Top Lid	13,100	3,780	487
Total 304 SS	0	0	473
Total A 516 Carbon Steel	5,790	0	319
Total All Steels w/o Inner Top Lid	18,900	3,780	1,280
Fraction CS in WP Steel	0.31	0	0.25
Fe Mass	14,200	2,570	953
Cr Mass	2,230	718	173
Ni Mass	1,570	378	106
FeOOH Mass	22,700	4,090	1,520
Cr ₂ O ₃ Mass	3,260	1,050	252
NiO Mass	2,000	481	135
Total Corrosion Products Mass w/o Inner Top Lid	27,900	5,620	1,900

[#] Output DTN: SN0703PAEBSRTA.001, file 5-DHLW-SNF DOE Long + TMI SNF + 21-PWR TAD 7-10-2007.xls, worksheet "5-DHLW-DOE Long + TMI SNF".

^{###} Output DTN: SN0703PAEBSRTA.001, file 5-DHLW-SNF DOE Long + TMI SNF + 21-PWR TAD 9-19-2007 Final TDIP.xls, worksheet "5-DHLW-DOE Long + TMI SNF".

NOTE: All values shown are rounded from the values in the spreadsheets to 3 digits in this table. Values in **bold** are model inputs summarized in Tables 6.5-5 and 8.2-6.

^a Includes: Inner Vessel, Inner Bottom Lid, Interface Ring, Spread Ring, 316 SS Welds (all 316 SS), Divider Plate, Inner Bracket, Outer Bracket, Support Tube (all A 516 Carbon Steel).

^b Includes: Five HLWG Canisters (316 SS).

^c Includes: SNF Canister (316 SS), SNF Canister Impact Plates, Sleeve, and Standoffs (all Carbon Steel), TMI Canister, TMI Canister Guide Tube, TMI Canister Top, TMI Canister Bottom, TMI Fuel Top Nozzle, TMI Fuel Bottom Nozzle, TMI Fuel Spring Retainer, TMI Fuel Upper End Plug, TMI Fuel Upper Nut, TMI Fuel Lower Nut (all 304 SS). Initial estimate of Standoffs mass resulted in Total All Steels value of 1,270 kg, the value used in the TSPA; correcting the mass of Standoffs increased the Total of All Steels mass to 1,280 kg.

CS = carbon steel; SS = stainless steel; DHLW = defense high-level (radioactive) waste; SNF = spent nuclear fuel; DOE = U.S. Department of Energy; TMI = Three Mile Island (nuclear power plant); WP = waste package.

6.3.4.3.4.2 Interior Surface Area, Volume, and Porosity of 21-PWR TAD Waste Package

The internal surface area of a waste package in an undegraded state containing CSNF can be approximated given the dimensions and numbers of fuel rods, baskets, side guides, and other support components. Since the surface area will increase by orders of magnitudes as the waste package components degrade, the initial surface area is useful only as a bounding value, but one that can be estimated accurately (unlike the surface area of corrosion products). Typical measurements for a 21-PWR TAD waste package are used (SNL 2007 [DIRS 179394], Table A-1). The surface areas of fuel assembly spacer grids and end connections are ignored. The total initial internal surface area of a 21-PWR TAD waste package is approximately 1196 m².

The initial void volume of a 21-PWR TAD waste package is computed using the data in Table 6.3-10. The volume inside the 21-PWR TAD waste package overpack outer corrosion barrier is calculated from dimensional data given in SNL 2007 [DIRS 179394], Table 4-3: The outer corrosion barrier outside diameter is 1.8816 m and thickness is 0.0254 m. The inside length is estimated from the inner vessel length of 5.4991 m and total outer corrosion barrier-inner vessel end-to-end gaps of 0.1128 m, which give an inside volume of 14.77 m³ for the overpack. Then the initial void volume is 7.99 m³, and the initial average porosity is 0.54. An estimate of the waste package porosity when all steel internal components are fully degraded but the outer corrosion barrier is essentially intact can be obtained using the total potential equivalent mass of FeOOH, Cr₂O₃, and NiO in a 21-PWR TAD waste package from the corrosion of non-SNF components. Solids volumes are calculated in Table 6.3-11 for intact and degraded fuel rods and for intact and degraded shield plug. For intact fuel rods and shield plug, the void volume is 1.66 m³, resulting in a porosity of 0.11. For intact fuel rods and degraded shield plug, the void volume is 0.60 m³, resulting in a porosity of 0.04. For degraded fuel rods and shield plug, the solids volume is greater than the capacity of the outer corrosion barrier, which must rupture if all steel and CSNF internal components fully degrade.

Table 6.3-10. Initial Characteristics of Internal Components of a TAD Containing 21 PWR CSNF Assemblies

Component	Total Mass ^a (kg)	Total Surface Area ^b (m ²)	Total Volume ^c (m ³)
Fuel Rods ^d	—	636.93	1.513
Basket Side Guide ^f	753	20.1	0.094
Basket End Side Guide ^f	1,125	30.1	0.141
Basket Corner Guide ^f	925	24.8	0.116
Fuel Basket A-Plate ^f	1,406	28.9	0.180
Fuel Basket B-Plate ^f	1,406	28.9	0.180
Fuel Basket C-Plate ^f	1,474	30.3	0.189
Aluminum A-Plate	310	29.0	0.115
Aluminum B-Plate	310	29.0	0.115
Fuel Basket Tube ^f	6,078	195.	0.762
Inner Vessel	12,285	61.2	1.539
Inner Top Lid	989	4.75	0.124
Inner Bottom Lid	1,031	5.21	0.129
Interface ring	39	0.665	0.005
Spread Ring and Filler Segment	38	0.341	0.005
Shield Plug	5,530	5.74	0.693
Outer Seal Plate and Plug	48	4.12	0.006
TAD Shell	7,300	60.3	0.915
Total	41,047 ^e	1195.	6.820

NOTE: "—" indicates value not used.

^a SNL 2007 [DIRS 179394], Tables 4-3 and A-1, except for preliminary values listed in Table 4.1-23.

^b SNL 2007 [DIRS 179394], Tables A-1 and A-3.

^c Computed from (Total Mass, kg)/(Density, kg m⁻³) (except for fuel rods).

^d Surface area and volume computed from 0.94996 cm outside diameter, 384.962 cm length, 264 rods/assembly, 5,544 fuel rods total (DOE 1992 [DIRS 102588], Volume 1, p. 2A-30. W1717W used as representative assembly).

^e Total mass of internal components, excluding CSNF.

^f Preliminary value used for Total Mass, as listed in Table 4.1-23.

Table 6.3-11. Internal Solids Volume in Degraded 21-PWR TAD Waste Package

Solid Component	Total Mass ^a (kg)	Grain Density ^b (kg m ⁻³)	Solids Volume (m ³)
Intact Fuel Rods and Shield Plug			
Fuel Rods ^c	—	—	1.513
FeOOH	36,000	4,260	8.451
Cr ₂ O ₃	8,990	5,220	1.722
NiO	5,540	6,720	0.824
Shield Plug (316 SS)	5,530	7,980	0.693
Total			13.20
Intact Fuel Rods and Degraded Shield Plug			
Fuel Rods ^c	—	—	1.513
FeOOH	41,400	4,260	9.718
Cr ₂ O ₃	10,400	5,220	1.992
NiO	6,380	6,720	0.949
Total			14.17
Degraded Fuel Rods and Shield Plug			
Fuel Rods ^{c,d}	—	—	2.161
FeOOH	41,400	4,260	9.718
Cr ₂ O ₃	10,400	5,220	1.992
NiO	6,380	6,720	0.949
Total			14.82

^a Output DTN: SN0703PAEBSRTA.001, file 5-DHLW-SNF DOE Long + TMI SNF + 21-PWR TAD 7-10-2007.xls, worksheet "21-PWR - 304B4 SS Plates".

^b FeOOH: Lide 2000 [DIRS 162229], p. 4-66.
 Cr₂O₃: Lide 2000 [DIRS 162229], p. 4-54.
 NiO: Lide 2000 [DIRS 162229], p. 4-75.
 316 SS: ASTM G 1-03 [DIRS 181437], Table X1.1.

^c DOE 1992 [DIRS 102588], Volume 1, p. 2A-30; W1717W used as representative assembly.

^d Effective "solids" volume increased by $1/(1-\phi_{rind})$ due to expansion of CSNF degradation rind having maximum porosity of $\phi_{rind} = 0.30$ (DTN: MO0411SPACLDDG.003 [DIRS 180755], Table 7-1).

The morphology of corrosion products resulting from extensive corrosion of stainless steel is not well characterized, simply because stainless steel corrodes so slowly that no samples have corroded extensively under low-temperature atmospheric conditions since stainless steel was invented, less than a century ago. Lamination and flaking of corrosion products is expected to occur due to seismic activity and rock fall that will jar the waste packages and knock loose any corrosion products that would normally adhere to internal component surfaces. Over time, these movements will redistribute this material within the waste package pore space. If the oxide settles to the bottom of a waste package, the physical geometry of the granular iron oxide that has settled can be represented by that of tightly packed sand, which has a solid content of 58 percent (Brown and Richards 1970 [DIRS 131479], Table 2.2), or a porosity of 0.42 (CRWMS M&O 1997 [DIRS 102824], p. 29). This value (0.42) for corrosion products porosity within a waste package has been used in criticality studies (CRWMS M&O 1997 [DIRS 102824], p. 29) and in an independent performance assessment of the Yucca Mountain repository (EPRI 2000 [DIRS 154149], p. 6-21 to 6-22). A porosity of 0.4 has been used in other criticality studies (YMP 1998 [DIRS 104441], p. C-23 to C-25) and in a model of diffusive releases from breached waste packages (Lee et al. 1996 [DIRS 100913], p. 5-67). For comparison, the porosity of

unconsolidated geologic materials ranges from 0.25 to 0.70 (Freeze and Cherry 1979 [DIRS 101173], Table 2.4). Although some uncertainty exists and small-scale variability is likely, for the waste package as a whole, a fixed value of 0.4 is reasonable for the porosity of corrosion products in TSPA. A single fixed value is adequate because it is representative of the corrosion products porosity over all degraded waste packages that are at various states of degradation. Based on the concept of central tendency theorem, as the number of waste packages increase, the variability in porosity should be reduced.

The surface area inside a waste package can be computed as a function of time, if the degradation rates of the basket components and the stainless steel inner vessel are known. The calculation is complicated by the different compositions of each component of the waste package. Spatial variability in degradation rates due to variations in accessibility to water vapor further complicate the picture. However, an average corrosion rate for a 21-PWR TAD waste package provides a reasonable approximation from which surface areas and quantities of adsorbed water can be computed.

The complete degradation of a 21-PWR TAD waste package gives an estimated upper bound on the surface area available for adsorption. The total amount of FeOOH in a 21-PWR TAD waste package (from Table 6.3-8), neglecting the contribution from the shield plug, is 36,000 kg FeOOH. Using a specific surface area that ranges from $14.7 \text{ m}^2 \text{ g}^{-1}$ to $110 \text{ m}^2 \text{ g}^{-1}$ (Section 6.3.4.3.3), the estimated upper bound for total surface area for adsorption in a 21-PWR TAD waste package is $3.9 \times 10^9 \text{ m}^2/\text{package}$, an increase over the initial steel surface area of a factor of 3.3×10^6 .

6.3.4.3.4.3 Steel Corrosion Rates

The corrosion rates for Carbon Steel A 516 are known with some uncertainty, as shown by the data presented in Table 4.1-1 (DTN: MO0409SPAACRWP.000 [DIRS 172059], data for steel type "A516 Grade 55" only in worksheet 'Freshwater' in spreadsheet '*aqueous-A516.xls*'). Carbon Steel A 516 corrosion is considered because codisposal waste packages have carbon steel internal components (divider plate, brackets, and support tube; see Table 4.1-22). The corrosion rates used are for simulated dilute J-13 well water (10 times the normal concentration of J-13 water) at 60°C and 90°C in tests of 0.5 yr and 1.0 yr in duration. Freshwater data were used, as opposed to saltwater data, because the species in saltwater most responsible for corrosion of steel, namely chloride ion, is unlikely to be present inside waste packages at concentrations found in saltwater. The 10-times concentration in the simulated dilute J-13 well water is considered representative of the small potential degree of concentration that might occur inside a breached waste package. Both the 60°C and 90°C data were used, to be consistent with the data used for stainless steel corrosion rates (described in the next paragraph). Because general corrosion rates of metals and alloys tend to decrease over time (SNL 2007 [DIRS 178519], Section 6.4.3.5.1), the 1.0-yr data are more representative of rates that will occur during most of the regulatory period; however, again to be consistent with the stainless steel corrosion rate data, both the 0.5-yr and 1.0-yr data are used. In view of the tendency of corrosion rates to decrease over time, the use of data from corrosion tests lasting no more than one year may overestimate corrosion rates. Consequently, retardation of radionuclides by sorption onto corrosion products (Section 6.3.4.2.3) may be overestimated, thereby underestimating releases. However, water saturation and diffusion coefficients (Section 6.3.4.3.5), and hence diffusive transport, may also

be overestimated if corrosion rates are overestimated. Thus, even if corrosion rates are overestimated, diffusive releases of radionuclides are not necessarily underestimated. Although on average the rates are lower at 90°C than at 60°C, with data available at only two temperatures, a defensible temperature dependent distribution for carbon steel corrosion rates cannot be developed. One data point at 90°C (0.53 yr, 180.42 $\mu\text{m yr}^{-1}$) is considered to be an outlier, because it is 50 $\mu\text{m yr}^{-1}$ greater than the next highest measured rate, and is neglected. The data were fit to a truncated lognormal distribution using Bayesian updating (see Appendix F), with lower and upper bounds of 25 $\mu\text{m yr}^{-1}$ and 135 $\mu\text{m yr}^{-1}$ specified at approximately 5 $\mu\text{m yr}^{-1}$ beyond the measured minimum and maximum rates in order to capture all of the measurements (except for the one outlier) reported in DTN: MO0409SPAACRWP.000 [DIRS 172059]. The cumulative distribution function has a true mean rate of 78.5 $\mu\text{m yr}^{-1}$ and a true standard deviation of 25.0 $\mu\text{m yr}^{-1}$.

The corrosion rate for Stainless Steel Type 316L is based on data summarized in DTN: MO0409SPAACRWP.000 [DIRS 172059] (worksheet 'freshwater' in spreadsheet '*aqueous-316L.xls*'). The data set used is for corrosion rates in fresh water (J-13 well water, and tuff conditioned water and steam) for the temperature range of 50°C to 100°C; these corrosion tests ranged in duration from 41.67 days (0.11 yr) to 479.67 days (1.31 yr). These rates are believed to be higher than will actually occur during much of the regulatory period because they were measured at early times. General corrosion rates of metals and alloys tend to decrease over time (SNL 2007 [DIRS 178519], Section 6.4.3.5.1) as corrosion products build up on the surfaces and inhibit diffusion of water and oxygen to the metal surface. Longer term (up to 16 yr) data in DTN: MO0409SPAACRWP.000 [DIRS 172059] are not used because, as reported in the original reference (Southwell et al. 1976 [DIRS 100927], Tables 4, 5, and 6), no weight loss was measured, so the actual measured corrosion rates were zero. As with carbon steel, the use of data from corrosion tests lasting little more than one year may overestimate corrosion rates. However, even if corrosion rates are overestimated, the resulting higher diffusive releases due to higher water saturations and diffusion coefficients caused by more corrosion products being present tend to offset the overestimated retardation of radionuclides by sorption onto corrosion products. Thus, diffusive releases of radionuclides are not necessarily underestimated if corrosion rates are overestimated. To characterize the uncertainty in stainless steel corrosion rates, a truncated lognormal distribution was developed applying Bayesian updating (see Appendix F) to the data listed in Table 4.1-1, over a range from 0.01 $\mu\text{m yr}^{-1}$ to 0.51 $\mu\text{m yr}^{-1}$. The cumulative distribution function has a true mean rate of 0.267 $\mu\text{m yr}^{-1}$ and a true standard deviation of 0.209 $\mu\text{m yr}^{-1}$. The lower bound was chosen to be the approximate mean general corrosion rate of Alloy 22 (SNL 2007 [DIRS 178519], Fig. 6-26) at 75°C, the midpoint of the temperature range of the data used from DTN: MO0409SPAACRWP.000 [DIRS 172059], on the basis that Stainless Steel Type 316 is recognized to corrode faster than Alloy 22 (SNL 2007 [DIRS 178519], p. 1-1). The upper bound is chosen as the largest measured rate.

From these rates and the thicknesses of the steel components, the lifetime of each type of steel is computed. The extent of corrosion, specifically, the mass of corrosion products, is interpolated over the lifetime of each type of steel. The implementation of this interpolation scheme in TSPA is presented in Section 6.5.2.2.

Although this interpolation provides a reasonable means for approximating the mass of corrosion product in the interior of a waste package over time as it degrades, there is still uncertainty as to the actual mass of corrosion product. The corrosion rates themselves are uncertain. In addition, many factors affect the mass of the corrosion products. The chemical and physical conditions under which corrosion takes place, impacts the morphology of the corrosion products. Seismic occurrences and collapse of the internal components as they degrade will affect the surface area. The samples used in adsorption isotherm measurements are typically finely ground and highly purified, and have a higher specific surface area than typical corrosion products. At the same time, the morphology of corrosion products inside a waste package over the course of thousands of years is uncertain, so specific surface areas higher than purified samples are possible.

6.3.4.3.5 Diffusion Coefficient in Corrosion Products

The rate of diffusion of radionuclide species i , q_i ($\text{kg } i \text{ s}^{-1}$), through corrosion products to the exterior of a waste package is given by:

$$\begin{aligned} q_i &= -\phi S_w D_{si} A \frac{\partial C_i}{\partial x} \\ &\approx -\phi S_w D_{si} A \frac{\Delta C_i}{\Delta x} \end{aligned} \quad (\text{Eq. 6.3.4.3.5-1})$$

where

- D_{si} = effective diffusion coefficient of species i ($\text{m}^2 \text{ s}^{-1}$)
- ϕ = porosity (m^3 void volume m^{-3} bulk volume)
- S_w = water saturation (m^3 water volume m^{-3} void volume)
- A = cross-sectional area of the diffusive pathway (m^2)
- C_i = concentration of the radionuclide of species i ($\text{kg } \text{m}^{-3}$)
- x = length of the diffusive pathway (m).

The effective diffusion coefficient, D_{si} , as defined and used in this section, implicitly includes the effects of tortuosity. The area used for TSPA calculations depends on the scenario class and is presented in Section 6.5.2.1. The length of the diffusive path is fixed (see Section 6.5.2.1.1.2). Fixed path length is appropriate for the current spatial discretization in the EBS. The path length would actually vary depending on the actual transport pathway considered inside the waste package. Multiple pathways could exist at any given time, and considerable variability could exist in the path lengths depending on where the waste form is degrading relative to the breach location. The current model does not consider the spatial variability inside the waste package, since it is a one-dimensional transport model. Thus, a constant average transport distance over all degradation states is applied.

The effective diffusion coefficient itself depends on the complex interactions of source term composition, water chemistry, porosity, water saturation, and temperature, none of which can be characterized in a deterministic fashion. Thus, each term in the above equation— A and parameters affecting D_{si} and S_w —needs to be sampled or specified for each modeling case, and a reasonable range and distribution for each has to be determined. All terms are interrelated through the geometry used for the waste package interior, and all are effectively a function of relative humidity and time.

In a seep environment, the water saturation in the corrosion products is set to 1.0, a reasonably bounding approach when there is flow through the waste package since the effective diffusion coefficient computed under this condition will be higher. In a no-seep environment, the effective water saturation in the corrosion products results from adsorbed water, as described in the rest of this section.

Archie's law, discussed in Section 6.3.4.1.1, gives the diffusion coefficient as a function of porosity and saturation in a partly saturated, granular medium as:

$$\phi S_w D_{si} = D_{wi} \phi^{1.3} S_w^2 \quad (\text{Eq. 6.3.4.3.5-2})$$

where D_{wi} is the free water diffusion coefficient of species i ($\text{m}^2 \text{s}^{-1}$). The diffusion coefficient D_{si} again is an effective value that implicitly includes the effect of tortuosity in a porous medium. The exponents are the values originally proposed by Archie (1942 [DIRS 154430], p. 57) for unconsolidated sands, and will vary for different materials (Bear 1988 [DIRS 101379], p. 116). Whereas exponents of 1.863 are used for invert materials, based on experimental measurements of diffusion coefficients for crushed rock, Archie's values (1.3 on porosity and 2 on water saturation) are used throughout this section to estimate in-package diffusion coefficients for corrosion products.

The effective water saturation within the corrosion products, $S_{we,CP}$, can be obtained as a function of RH by dividing the water volume by the pore volume of the corrosion products. The water volume is given by the adsorbed water film thickness multiplied by the surface area covered by water. The film thickness is $t_f \theta_a$, where t_f is the thickness of a water monolayer (Equation 6.3.4.3.2-4), and θ_a is the number of monolayers of coverage, a function of RH .

The surface area of the corrosion products is given by:

$$\begin{aligned} s_{CP} &= m_{CP} \bar{s}_{CP} \\ &= \rho_{CP} V_{CP} \bar{s}_{CP} \left(\frac{1 - \phi_{CP}}{\phi_{CP}} \right). \end{aligned} \quad (\text{Eq. 6.3.4.3.5-3})$$

In this equation, m_{CP} is the mass of corrosion products (kg), \bar{s}_{CP} is the specific surface area ($\text{m}^2 \text{kg}^{-1}$), ρ_{CP} is the solid density of corrosion products (kg m^{-3}), V_{CP} is the pore volume of the corrosion products (m^3), and the porosity of corrosion products is ϕ_{CP} . The factor $(1 - \phi_{CP}) / \phi_{CP}$

is the ratio of solids volume to void volume within the bulk volume of corrosion products, which is multiplied by $\rho_{CP}V_{CP}$ to give the mass of solids, m_{CP} . The ratio of surface area to pore volume of the corrosion products can be expressed as:

$$\frac{s_{CP}}{V_{CP}} = \rho_{CP}\bar{s}_{CP}\left(\frac{1-\phi_{CP}}{\phi_{CP}}\right). \quad (\text{Eq. 6.3.4.3.5-4})$$

Then the effective water saturation of the corrosion products is given by:

$$\begin{aligned} S_{we,CP} &= \frac{s_{CP}}{V_{CP}}t_f\theta_a \\ &= \rho_{CP}\bar{s}_{CP}t_f\left(\frac{1-\phi_{CP}}{\phi_{CP}}\right)\theta_a. \end{aligned} \quad (\text{Eq. 6.3.4.3.5-5})$$

Equation 6.3.4.3.5-5 shows that water saturation is not dependent on the mass of corrosion products. However, it does depend on material properties (solid density and specific surface area) that, for a heterogeneous or composite material, are computed based on the relative amounts or mass fractions of each material comprising the bulk. This comment applies specifically to the calculation of domain water saturations, in which the domain is comprised of several different materials. For example, the CSNF waste form domain consists of both CSNF degradation rind and corrosion products, each with its own density, porosity, specific surface area, and adsorption isotherm. Furthermore, the corrosion products, as modeled in the RTA, consist of up to four metal oxides, each with different physical properties; although a single adsorption isotherm applies to all steel corrosion products, the properties are combined in proportion to the mass fraction of each metal comprising the steel. Implementation of the calculation of domain water saturations and water volumes is described in Section 6.5.2.2.

The diffusion coefficients for the corrosion products and waste form domains are modified for temperature as for the invert diffusion coefficient (Section 6.3.4.1.2). As shown in Figure 6.3-5, the diffusion coefficient can increase by a factor of 4 from 25°C to 100°C.

6.3.4.4 Colloidal Transport

Radionuclide transport from the waste package occurs as dissolved species at the appropriate solubility or dissolution rate limit and as colloidal particles. Three types of colloids are anticipated to exist in the EBS (SNL 2007 [DIRS 177423], Section 6.3.1): (a) waste form colloids from degradation of HLW glass and CSNF, (b) iron oxyhydroxide colloids due to products from the corrosion of steel waste packages, and (c) groundwater or seepage water colloids. On all three types of colloids, radionuclides may undergo reversible, or equilibrium, sorption. The waste form colloids may also contain embedded radionuclides that are not removable. Plutonium and americium can be strongly sorbed onto iron oxyhydroxide; for these radionuclides, sorption is modeled as a kinetic process. The stability and mass concentrations of colloids are functions of the ionic strength and pH of the groundwater or local liquid chemistry in the waste package and invert. Both groundwater and waste form colloids are modeled using smectite mineralogy (SNL 2007 [DIRS 177423], Section 6.3.1), and therefore sorption

distribution coefficients (K_d) values associated with radionuclide sorption onto smectite colloids are used in the TSPA Model (SNL 2007 [DIRS 177423], Table 6-6). The K_d values for colloids used in the TSPA calculations are presented in DTNs: MO0701PASORPTN.000 [DIRS 180391], Table 1-3; MO0701PAKDSUNP.000 [DIRS 180392], Table 1-2; and MO0701PACSNFCP.000 [DIRS 180439], Table 6-1.

The potential mass of radionuclides embedded in the waste form colloids (SNL 2007 [DIRS 177423], Section 6.3.3.3) is determined from reactions within the waste package. The mass of radionuclides reversibly attached to all three types of colloids is determined primarily by three parameters:

- Mass concentration of dissolved (aqueous) radionuclide in the liquid
- Mass concentration of colloid material in the liquid
- Radionuclide distribution coefficient (K_d) of a specific radionuclide on a specific colloid mineralogical type.

The potential concentrations of colloids in the drifts and EBS have also been assessed (SNL 2007 [DIRS 177423]). In a DOE-funded research project at the University of Nevada at Las Vegas to evaluate the corrosion of scaled-down miniature waste packages, the data indicate a preponderance of amorphous corrosion products released as colloids, including magnetite (Fe_3O_4), lepidocrocite (FeOOH), and goethite (FeOOH) (Zarrabi et al. 2003 [DIRS 171238], Table 10 and Section 5; DTN: MO0302UCC034JC.003 [DIRS 162871]; BSC 2005 [DIRS 177423], Section 6.3.1.3).

Colloidal transport of radionuclides occurs by advective and diffusive processes. Advective transport moves colloids (and the associated radionuclides) at approximately the same velocity as the liquid flux through the EBS. Longitudinal dispersion, which could potentially enable colloids to travel faster than the bulk average liquid velocity, is ignored because of the short travel distance through the EBS (see Section 6.3.1.2). Diffusive transport moves colloids due to the concentration gradient and the medium diffusive properties. The diffusivity is given by the Stokes-Einstein equation (Bird et al. 1960 [DIRS 103524], p. 514, Equation 16.5-4):

$$D_{coll} = \frac{kT}{3\pi\mu_w d_{coll}} \quad (\text{Eq. 6.3.4.4-1})$$

where

D_{coll} = diffusion coefficient for a colloid particle of diameter d_{coll} ($\text{m}^2 \text{s}^{-1}$)

k = Boltzmann constant ($1.3806503 \times 10^{-23} \text{ J K}^{-1}$; Lide 2000 [DIRS 162229], p. 1-8)

T = absolute temperature (K)

μ_w = viscosity of water at temperature T (Pa s)

d_{coll} = diameter of colloid particle (m).

Equation 6.3.4.4-1 applies to diffusion of spherical colloid particles in bulk liquid, in which the particle is subject solely to hydrodynamic forces. In a saturated medium, the particle is also subject to sorption onto solid surfaces, agglomeration, and filtration. In an unsaturated medium, other considerations also come into play, including the thickness of the water film in which the colloid is being transported, sorption of the colloid to the gas-liquid interface as well as to the solid surface, nonuniformity of the liquid layer in a three-dimensional pore space, and non-Fickian diffusion when motion is constrained to fewer than three dimensions. In addition, the shape of a colloid particle may impact its transport behavior—elongated particles may have a greater tendency to clog pores than other types of colloids. Colloid size distribution is an important characteristic in both saturated and unsaturated media, since smaller particles may be more mobile (based on Equation 6.3.4.4-1) and less susceptible to filtration. Other than particle size, these effects are neglected in the EBS transport model, as explained below.

Colloids are defined as ranging in size (diameter) from 1 nm to 1,000 nm (BSC 2005 [DIRS 177423], p. 1-2). A range of values for diffusion coefficients of colloids can be estimated for this range of sizes using Equation 6.3.4.4-1 at any given temperature. For example, at 25°C, where the viscosity of water is 0.890 mPa s (Lide 2000 [DIRS 162229], p. 6-180), Equation 6.3.4.4-1 gives a range of colloid diffusion coefficients of $4.9 \times 10^{-10} \text{ m}^2 \text{ s}^{-1}$ to $4.9 \times 10^{-13} \text{ m}^2 \text{ s}^{-1}$. As seen in Equation 6.3.4.4-1, the diffusion coefficient decreases as the particle size increases. Since colloid particles are typically larger than dissolved actinide ions, the diffusivity of colloids is expected to be smaller than that of radionuclides. This is confirmed by comparing the range of colloid diffusion coefficients computed using Equation 6.3.4.4-1 with the free water diffusion coefficients of dissolved radionuclides (see Table 4.1-7). The colloid diffusion coefficient is seen to be a factor of 1.2 (for Th) to 4,200 (for Cs) smaller than the free water diffusion coefficient of dissolved radionuclides.

The effect of colloid particle size, and thus the colloid diffusion coefficient, on releases of radionuclides from the EBS can be evaluated by sampling on the colloid particle size in TSPA. Because of the low concentration of colloid particles and the low diffusivity compared to the free water diffusivity of dissolved radionuclide species, a representative value of the colloid size chosen from the population of colloid particles is considered suitable for modeling colloid transport in the TSPA. This representative value is expected to be uncertain and can be represented by an epistemic uncertainty distribution that will be sampled in TSPA. The uncertainty range in the representative value is going to be narrower than the size range in the colloid population. At the same time, the representative value must be representative of all three types of colloids that are considered in the EBS transport model.

The size distribution of radionuclide-bearing colloids generated from the corrosion of HLW glass and CSNF has been measured using dynamic light scattering and filtration (CRWMS M&O 2001 [DIRS 154071], Section 6.3). Measurements on leachates from glass corrosion tests (450-nm filtrate minus the 6-nm filtrate) varied widely and depended on the length of the tests (CRWMS M&O 2001 [DIRS 154071], pp. 38 to 39). For up to 140 days of reaction time, a wide, monomodal distribution of sizes was observed, with a mean diameter of about 120 nm (116.9 –

118.8 nm, with standard deviations of 64.9 – 88.8 nm) for the 14-, 70-, and 140-day samples and a larger mean diameter for the 30-day sample of 155.5 nm (standard deviation of 97.9 nm) (DTN: LL991109751021.094 [DIRS 142910], p. 32). The 280-day leachate inexplicably “showed a dramatic increase in the particle size” (CRWMS M&O 2001 [DIRS 154071], p. 39) to about 1,200 nm (standard deviation of 1050.2 nm) (DTN: LL991109751021.094 [DIRS 142910], p. 32); these measurements are ignored because they appear to be inconsistent in that such large particles should not exist in the 450-nm filtrate (minus the 6-nm filtrate) that was used.

Fewer data are available on the size distribution of colloids from CSNF corrosion—dynamic light scattering measurements indicated the presence of colloids above the detection limits on only one of twelve samples (CRWMS M&O 2001 [DIRS 154071], p. 42). This one sample of leachate from the 56-month sampling of the vapor test showed a wide particle distribution with a mean diameter of 300 nm (DTNs: LL000905312241.018 [DIRS 152621], Scientific Notebook 1644, p. 74; LL991109751021.094 [DIRS 142910], Scientific Notebook 1644, p. 34).

Groundwater colloid particle sizes are discussed in *Waste Form and In-Drift Colloids-Associated Radionuclide Concentrations: Abstraction and Summary* (BSC 2005 [DIRS 177423], Section 6.3.2.4 and Appendix I). The groundwater colloid samples analyzed represent colloid particle size distributions from 50 nm to 200 nm in diameter (SNL 2007 [DIRS 177423], Table I-2; DTN: LA0002SK831352.001 [DIRS 149232]). Evaluation of the colloid populations in the various size fraction classes for each groundwater sample did not reveal a systematic increase in the number of particles with decreasing particle-size class (SNL 2007 [DIRS 177423], pp. 6-30 to 6-31). Therefore, inclusion of particle-size classes smaller than 50 nm should not result in a substantially greater mass concentration in the water sample, especially since the smaller particles would have exponentially lower mass—therefore, omission of the less than 50-nm particle-sized fraction in the mass concentration calculations is reasonable.

Corrosion product colloid sizes are documented in two reports. In *Waste Form and In-Drift Colloids-Associated Radionuclide Concentrations: Abstraction and Summary* (BSC 2005 [DIRS 177423], Appendix II, Table II-2), measurements by Roden and Zachara (1996 [DIRS 171518], p. 1621, Table 1) are reported. Particle sizes range from 2 nm to 6 nm for amorphous Fe(III) gel particles, 15 nm to 200 nm for goethite particles, and 100 nm to 200 nm for hematite particles. In *Corrosion and Mass Transport Processes in Carbon Steel Miniature Waste Packages* (Zarrabi et al. 2003 [DIRS 171238], pp. 31 to 43), solids in the effluent stream from miniature waste package corrosion tests carried out under a variety of conditions were examined; experiments where J-13 well water was used as inflow are considered to be most representative of conditions expected in the repository and are discussed here. No differentiation was made between solids with average diameters smaller than 0.1 μm and “dissolved” components in the effluent. On average, 99 percent by mass of the transported solids in the miniature waste package effluent were particles with average diameters greater than 0.1 μm (Zarrabi et al. 2003 [DIRS 171238], p. 31). Particle sizes were characterized by measuring the mass of solids collected on three filter sizes. For the J-13 well water experiments, 84 percent of the solids were collected on the 450 nm filter, 11 percent on the 220 nm filter, and 5 percent on the 100 nm filter (Zarrabi et al. 2003 [DIRS 171238], Figure 18). The corrosion products consisted of goethite, lepidocrocite, magnetite, maghemite, and amorphous iron oxyhydroxides (Zarrabi et al. 2003 [DIRS 171238], Table 10 and Section 5). The observed particle sizes are

consistent with the goethite particle sizes measured by Roden and Zachara (1996 [DIRS 171518], p. 1621, Table 1).

The range of colloid particle diameters to be sampled in TSPA includes the mean particle sizes measured for HLW glass and CSNF: 120 – 300 nm. The lower end of the range is extended to 50 nm to include groundwater and corrosion product colloids, for which smaller particle sizes have been repeatedly observed. Still smaller particle sizes, as measured for some corrosion product colloids, are not considered representative, since waste form and groundwater colloid mean particle sizes smaller than 50 nm are not reported. To capture just a narrow representative range of sizes from the middle of a wide range of actual potential sizes, and considering the wide disparities among different types of colloids and the lack of precise size data to define a distribution for any one type of colloid, a uniform distribution is appropriate for the sampled range of 50 nm to 300 nm. For each TSPA realization, a single size (diameter) is sampled from this distribution. This size is used only for calculation of the colloid diffusion coefficient in Equation 6.3.4.4-1 and does not apply to any other aspects of colloid models in TSPA.

Per Assumption 5.7, filtration and gravitational settling are assumed not to occur in the EBS. Filtration, as defined here, refers to the permanent removal of colloids from suspension in a flowing fluid by clogging, sieving, or straining in pores, channels, and fracture apertures that are too small or dry to allow passage of the colloids. Colloid removal, by physical or electrochemical interactions with surfaces, is considered to be accounted for by reversible or irreversible sorption, as mentioned in the preceding paragraph. In particular, a type of filtration referred to as film straining (Wan and Tokunaga 1997 [DIRS 108285]) is neglected. In film straining, a colloid particle is restrained from moving due to capillary forces that hold the particle to a surface when the water film thickness is less than the diameter of a colloid particle. Depending on the strength of forces holding a particle to a surface, two-dimensional non-Fickian diffusion may occur when the water film thickness is less than the diameter of a colloid particle. Film straining can be neglected because the effect of low water saturation alone causes diffusion of both colloids and dissolved species to be negligible, as shown by Equations 6.3.4.1.1-22 and 6.3.4.3.5-2, which give the dissolved species effective diffusion coefficient for the invert and corrosion products, respectively, as a function of water saturation.

Neglecting filtration and gravitational settling in the EBS is consistent with the treatment of colloids in the SZ transport abstraction (SNL 2007 [DIRS 181650], p. 5-1), which also ignores permanent filtration and gravitational settling as a bounding assumption that maximizes colloid-facilitated transport of radionuclides. The UZ transport abstraction (SNL 2007 [DIRS 181006], p. 6-22) neglects colloid filtration for reversible colloids. For irreversible colloids, the UZ transport abstraction models filtration of colloids at various rock unit interfaces when transport occurs in the rock matrix (SNL 2007 [DIRS 181006], Section 6.5.9) and between fractures and matrix (SNL 2007 [DIRS 181006], Section 6.5.10). The treatment of colloid size in TSPA differs between the EBS and the UZ. In the EBS, the sampled colloid size is applied to all the colloids (to the entire population—given by colloid concentration) without considering filtration, and hence a single representative value is appropriate. In the UZ, each colloid particle is tracked separately; hence, each particle is assigned a size for computing filtration. The colloid transport methodologies are different among the EBS, the UZ, and the SZ, and appropriate in their respective domains.

6.3.4.5 Transport through Stress Corrosion Cracks

Transport through stress corrosion cracks in the waste package is limited to diffusion. Once stress corrosion cracks form in the lid of the waste package, all surfaces inside the waste package are assumed to be coated with a thin film of water (per Assumption 5.5). This thin film provides the medium for diffusion from the waste form, through the stress corrosion crack, and out of the waste package. The diffusive area is calculated as the product of the area and number of cracks. The area of each crack is estimated from the data in Table 6.3-3 using the maximum tensile stress across the wall thickness of the dominant stress plane (SNL 2007 [DIRS 181953], Section 6.6.2), which provides a reasonable bound on the opening area through the entire wall thickness.

6.3.4.6 Transport through Waste Form Rind

The waste form contains fuel rods or glass logs and DSNF, which undergo degradation to form an alteration rind when the waste form is breached and exposed to humid air. Transport of radionuclides occurs through the water contained in the pore space in the rind. The amount of water present depends on the environment (seep or no-seep), the volume of rind, the pore volume, and the physicochemical and hydrodynamic properties of the rind. In the seep case, the rind is modeled as being fully saturated with water, and transport is predominately by advection. In the no-seep case, the only water present is the result of adsorption and capillary condensation from the humidity inside the waste package onto the porous rind surfaces. The water saturation in this case is a function of waste form temperature, RH, and properties of the waste form rind materials. This functional dependency is developed in this section.

The rind volume depends on the thickness of the rind, which changes as the degradation of the fuel rod or glass log continues. The DSNF is modeled as degrading instantaneously (BSC 2004 [DIRS 172453], Section 8.1), so the DSNF rind thickness remains fixed. The volume of the rind determines in part the volume of water contained in the rind, which in turn gives the mass of radionuclides that are potentially dissolved in the rind, as determined by the temperature and solubility of the radionuclides contained in the waste form. The other parameters that determine rind water volume are porosity, given in *Cladding Degradation Summary for LA* (SNL 2007 [DIRS 180616]), and water saturation.

The makeup of the rind differs, depending on the type of waste. For CSNF, the rind is expected to be composed of various oxides of uranium, particularly metaschoepite ($\text{UO}_3 \cdot 1-2\text{H}_2\text{O}$). Other oxides and hydrated oxides of uranium may also be present, including U_3O_7 , U_3O_8 , U_4O_9 , dehydrated schoepite ($\text{UO}_3 \cdot 0.8\text{H}_2\text{O}$), and schoepite ($\text{UO}_3 \cdot 2\text{H}_2\text{O}$). The behavior of UO_2 , which is the primary component of CSNF, in humid air is complex and difficult to predict. For steel corrosion products, the water vapor adsorption behavior of iron oxyhydroxides (goethite and HFO) was found to be indistinguishable from that of iron oxide (hematite), with the uncertainty of the available data (Section 6.3.4.3.2). Furthermore, other transition metal (nickel and chromium) oxides and hydroxides were found to behave similarly. Thus, it is reasonable to treat CSNF rind as a mixture of uranium oxides and other actinide rather than as an oxyhydroxide of uranium (metaschoepite) for purposes of estimating the amount of water that is adsorbed on surfaces. In addition to spent fuel, the rind may also contain cladding corrosion products, primarily ZrO_2 .

For CDSP waste packages, the waste form consists of HLW glass and DSNF. Although the composition of DSNF varies widely, for purposes of computing the water saturation, it is treated as CSNF, specifically, as Three Mile Island spent fuel. The DSNF is grouped into 11 categories (BSC 2004 [DIRS 172453], Section 6.1); however, Category 1 is representative of Naval SNF and is modeled as CSNF in the TSPA. Ignoring the mass associated with DSNF Category 7, which is included in only 6 percent of the CDSP WPs (only in the 2-MCO/2-DHLW configuration) (SNL 2007 [DIRS 180472], Table 6-2[a]), the U-Oxide/Mixed-Oxide fuel group (represented by DSNF Categories 4, 6, and 8) is found to contain the majority of the total DSNF mass for the remaining categories. Within this group, the TMI fuel has the highest number of waste packages (DOE 2004 [DIRS 169354] Appendix D), and thus is deemed to be the most representative of the DSNF fuel for the TSPA model. The predominant waste package configuration for the TMI fuel is the Long waste package (the 1L/5L configuration). The carbide fuel group (DSNF Categories 3 and 5) has the next highest DSNF mass (about 7 percent), followed by the aluminum-based fuel (DSNF Category 9) which has about 6 percent of the mass.

HLW glass degradation rind consists of clay-like substances (BSC 2004 [DIRS 169988], Appendix D). The adsorptive behavior of HLW glass in humid air has been examined in the *Defense HLW Glass Degradation Model* (BSC 2004 [DIRS 169988], Section 6.5.3.1), and is well-characterized compared with CSNF and DSNF rind.

The approach that is used for the no-seep case is to compute an effective diffusion coefficient using Archie's law, in which the diffusivity of a radionuclide is modified by the porosity and water saturation of the porous rind. The effective diffusion coefficient is used in Fick's law to determine the rate of diffusive transport. The water saturation is determined as a function of relative humidity using water vapor adsorption isotherms for spent fuel materials or analogs.

6.3.4.6.1 CSNF Waste Form Rind Water Saturation

CSNF rind water saturation in a humid air environment is predicted in the same manner as that of waste package corrosion products, namely, from the amount of water adsorbed, given by a water vapor adsorption isotherm. Because of the complex behavior of uranium oxides in humid air, reactions with water are usually investigated in terms of reaction rates and mechanisms (Ritchie 1981 [DIRS 179308]; Senanayake et al. 2005 [DIRS 179307]; McEachern and Taylor 1998 [DIRS 113270], pp. 91 to 92; Leenaers et al. 2003 [DIRS 168991]) as UO_2 is further oxidized to schoepite or dehydrated schoepite. Water vapor adsorption isotherms are seldom measured, the one known exception being LaVerne and Tandon (2003 [DIRS 178303], Fig 1) on UO_2 . Icenhour et al. (2004 [DIRS 179309], p. 260), attempted measurement of water sorption on UO_2 , but found no weight gain on their sample after one month at 97.5 percent relative humidity, although other oxides (UO_3 and U_3O_8) that might be present in degraded SNF showed weight gains of up to 33 percent (Icenhour et al. 2004 [DIRS 179309], Table 1). Due to this lack of water vapor adsorption isotherms for the stable oxides of uranium, isotherms for ThO_2 , PuO_2 , ZrO_2 , and CeO_2 will be used to supplement the UO_2 isotherm of LaVerne and Tandon (2003 [DIRS 178303]). The use of these substances as surrogates for UO_2 is justified by analogy to steel corrosion products, wherein a variety of oxides and oxyhydroxides of iron and other transition metals (nickel and chromium) have been observed to display similar water vapor adsorption behavior (Section 6.3.4.3.2). In addition, all are present to some extent in CSNF as fuel (thorium), fission products (plutonium, thorium, cerium, and zirconium), or cladding

materials (zirconium). As the data show, the isotherms show a large amount of variability that can be attributed to uncertainty in measurements as well as differences in material properties, particularly in the specific surface area of the samples measured and how the samples were prepared and processed prior to measurements.

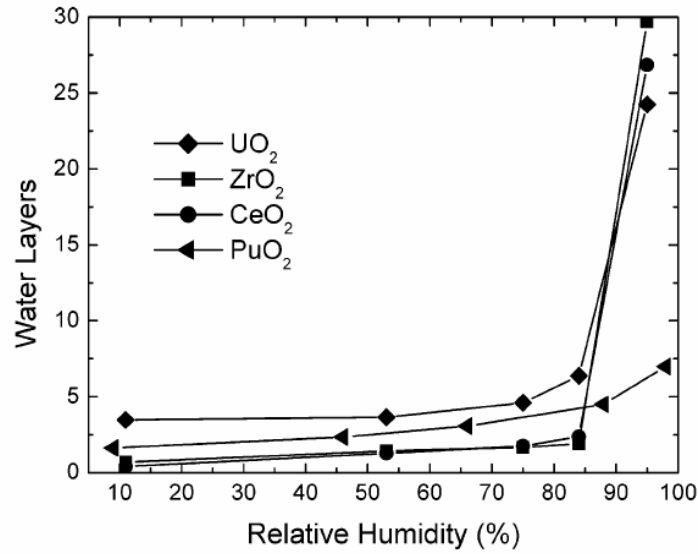
Water adsorption data are sparse even for the four surrogate materials. Earlier measurements are more extensive and are used to develop this model; more recent measurements that are less extensive are used in Section 7.2.1 to validate the model.

Table 6.3-12 summarizes the specific surface areas and pretreatment of samples for which the adsorption isotherms were measured.

Table 6.3-12. Properties of Materials Used in Water Vapor Adsorption Measurements

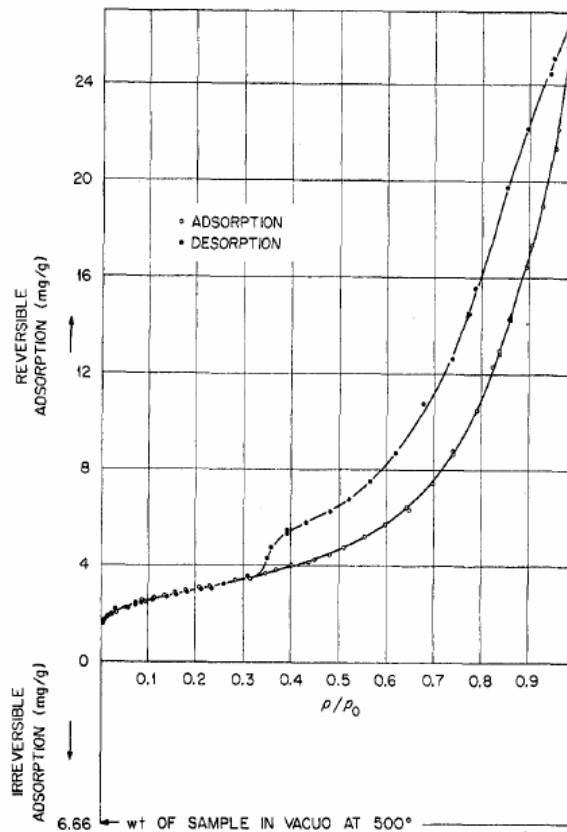
Material	Specific Surface Area (m ² g ⁻¹)	Pretreatment	Reference
UO ₂	0.51	Dried at 100°C for 48 hr under vacuum	LaVerne and Tandon 2003 [DIRS 178303], p. 13624
ThO ₂	11.2	Outgassed <i>in vacuo</i> (10 ⁻⁶ to 10 ⁻⁷ Torr) at 500°C, then treated with O ₂ at 500°C	Gammage et al. 1970 [DIRS 178304], p. 4277
ZrO ₂	14 to 15	Outgassed at 500°C	Holmes et al. 1974 [DIRS 154379], p. 368
CeO ₂	4.18	Baked at 500°C for 48 hr	LaVerne and Tandon 2003 [DIRS 178303], p. 13624
PuO ₂	57	Calcined at 350°C	Stakebake 1971 [DIRS 178302], p. 253
PuO ₂	53	Calcined at 490°C	Stakebake 1971 [DIRS 178302], p. 253
PuO ₂	9.9	Calcined at 760°C	Stakebake 1971 [DIRS 178302], p. 253
PuO ₂	16.9	Heated 20 – 60 hr under vacuum at 50°C	Stakebake and Dringman 1968 [DIRS 178840], Table I
PuO ₂	16.9	Heated 20 – 60 hr under vacuum at 75°C	Stakebake and Dringman 1968 [DIRS 178840], Table I
PuO ₂	0.8	Dried by thermal cycling in dry argon atmosphere	Paffett et al. 2003 [DIRS 178712], Table 1

The original adsorption isotherms from the literature for each of the ten samples listed in Table 6.3-12 are shown in Figures 6.3-35 to 6.3-41. Although smooth curves were drawn in each plot, only the measured data points, as indicated by symbols in the plots, are used to develop the representative isotherm for the rind saturation submodel. These data points were obtained by digitizing each plot using Grab It!TM Excel based digitizing software, and are listed in Table 4.1-18.



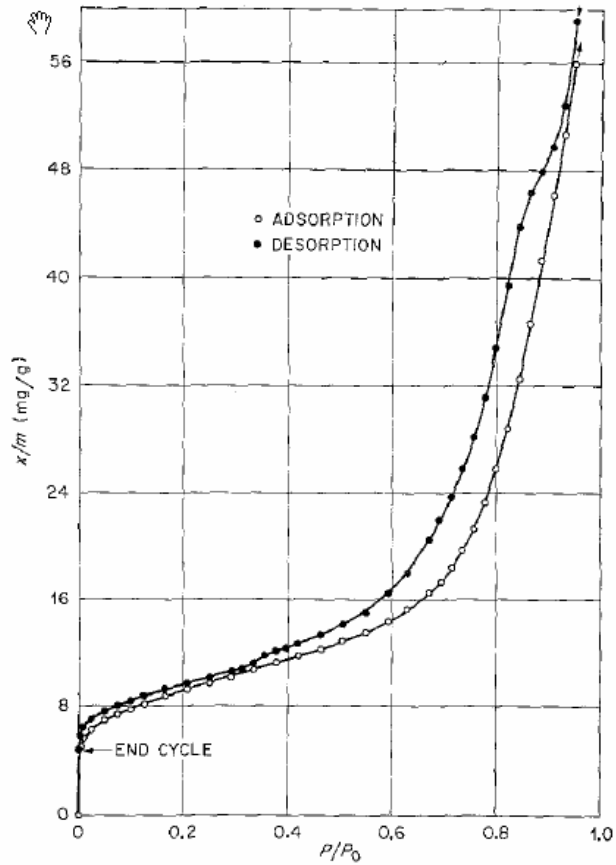
Source: Laverne and Tandon 2003 [DIRS 178303], Fig. 1

Figure 6.3-35. Water Vapor Adsorption Isotherms for UO₂ and CeO₂ (ZrO₂ and PuO₂ data are not used)



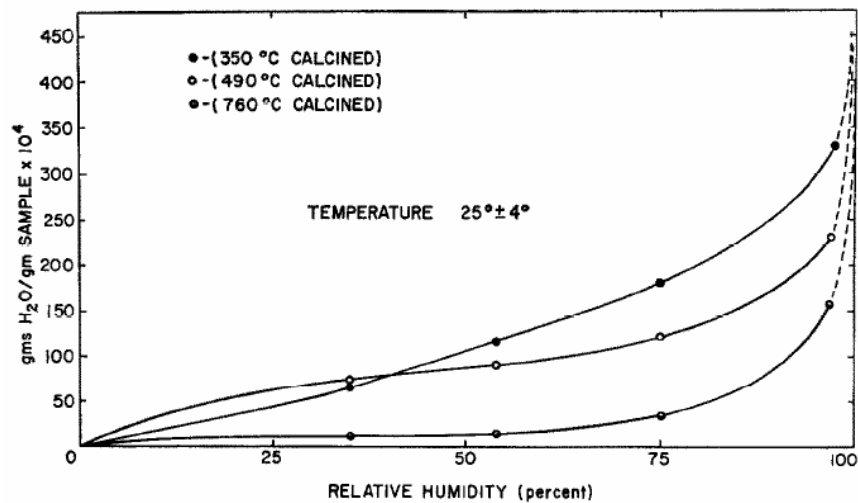
Source: Gammage et al. 1970 [DIRS 178304], Fig. 2

Figure 6.3-36. Water Vapor Adsorption Isotherm for ThO₂



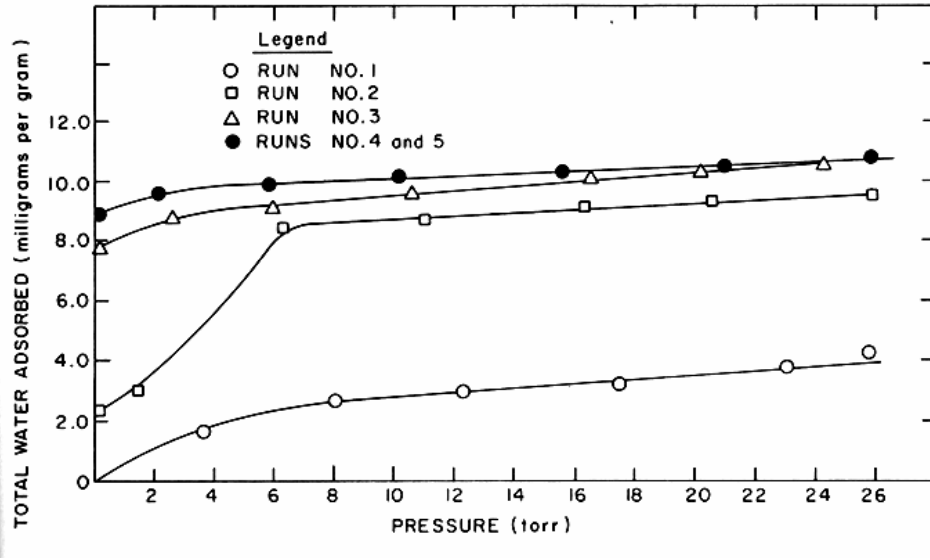
Source: Holmes et al. 1974 [DIRS 154379], Fig. 3

Figure 6.3-37. Water Vapor Adsorption Isotherm for ZrO_2



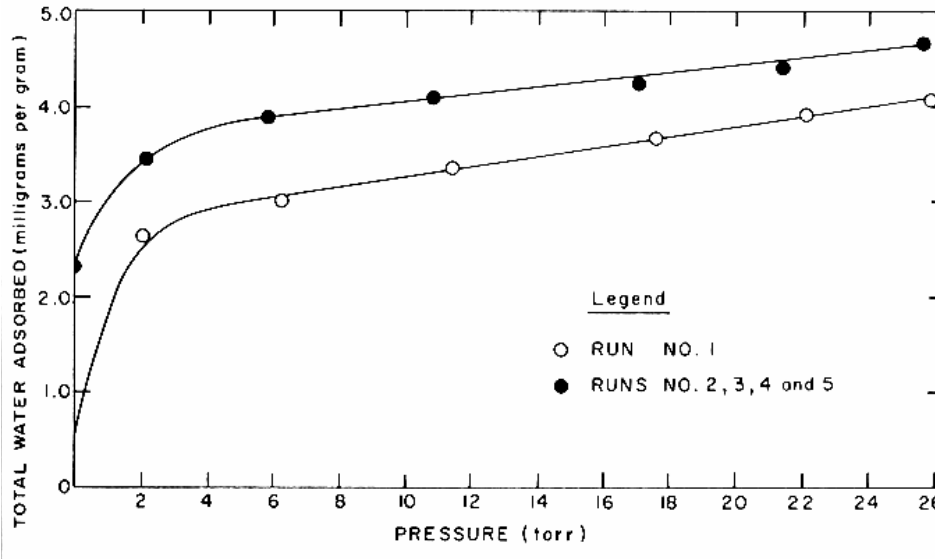
Source: Stakebake 1971 [DIRS 178302], Fig. 8

Figure 6.3-38. Water Vapor Adsorption Isotherms for PuO_2



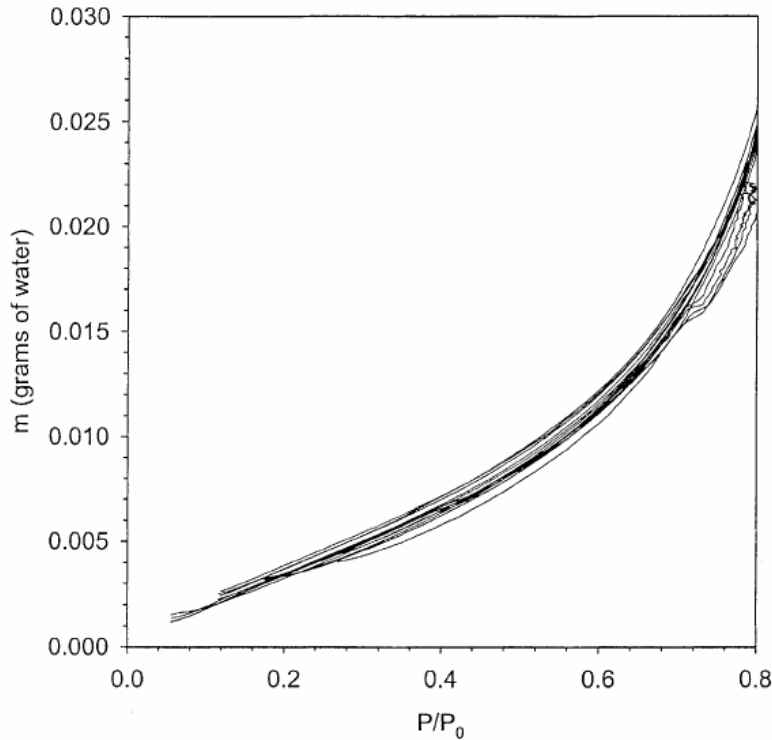
Source: Stakebake and Dringman1968 [DIRS 178840], Fig. 3

Figure 6.3-39. Water Vapor Adsorption Isotherms for PuO₂ at 50°C



Source: Stakebake and Dringman1968 [DIRS 178840], Fig. 4

Figure 6.3-40. Water Vapor Adsorption Isotherms for PuO₂ at 75°C



Source: Paffett et al. 2003 [DIRS 178712], Fig. 8

Figure 6.3-41. Water Vapor Adsorption Isotherms for PuO_2

Using the same approach as for corrosion products in Section 6.3.4.2, all of the data for the several surrogate materials are combined and fit to a Frenkel-Halsey-Hill (FHH) multilayer adsorption isotherm. The adsorption isotherm has the functional form (see Equation 6.3.4.3.2-1):

$$\ln(RH) = \frac{-k_{rind}}{\theta_{rind}^{s_{rind}}}, \quad (\text{Eq. 6.3.4.6.1-1})$$

or

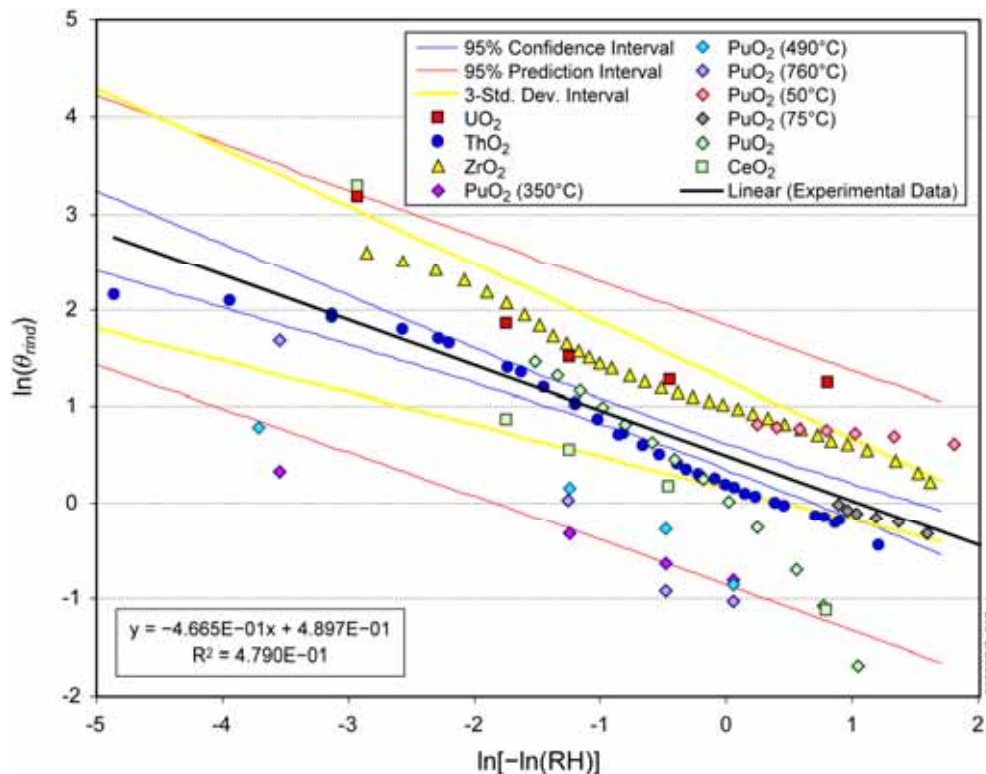
$$\theta_{rind} = \left(\frac{-k_{rind}}{\ln(RH)} \right)^{1/s_{rind}}, \quad (\text{Eq. 6.3.4.6.1-2})$$

where θ_{rind} is the number of monolayers of water adsorbed onto the rind solid surface, RH is the relative humidity (fraction), and k_{rind} and s_{rind} are adjustable parameters. Equation 6.3.4.6.1-2 can be rewritten as:

$$\ln(\theta_{rind}) = \left(\frac{-1}{s_{rind}} \right) \ln[\ln(RH)] + \left(\frac{\ln k_{rind}}{s_{rind}} \right), \quad (\text{Eq. 6.3.4.6.1-3})$$

which is linear of the form $y = ax + b$, with slope $a = -1/s_{rind}$ and intercept $b = (\ln k_{rind})/s_{rind}$. The data listed in Table 4.1-18 are fit to Equation 6.3.4.6.1-3 using the Excel Trendline least squares functionality as shown in Figure 6.3-42, and the parameters k_{rind} and s_{rind} are evaluated as $s_{rind} = -1/a$ and $k_{rind} = \exp(-b/a)$. From Figure 6.3-42, $a = -0.4665$ and $b = 0.4897$, which translates into mean values for the FHH isotherm parameters of $s_{rind} = 2.144$ and $k_{rind} = 2.857$.

With a correlation coefficient of $R^2 = 0.479$, the data fit is not good. The quality of the fit is affected by several factors: (1) The data are sparse and include five different materials. (2) The FHH isotherm is not universally applicable to all materials, but is used as a compromise; whereas the ThO_2 and ZrO_2 data appear to fit well (as indicated by a linear trend in the data in Figure 6.3-42), the other materials are likely to be represented better by a different isotherm function. (3) Some of the materials tested, particularly UO_2 and PuO_2 , are difficult to handle, resulting in large experimental uncertainty. (4) With the exception of ZrO_2 , these materials tend to react readily with water, further reducing the reproducibility and increasing the scatter in the measurements. (5) Preparation and pretreatment of the samples affects the adsorptive behavior, as shown by the PuO_2 data in Figure 6.3-42. All data points extracted from the original plots are used, although statistical analyses might suggest some data points to be outliers. Since there is no basis for eliminating any data in the literature sources, none was deleted.

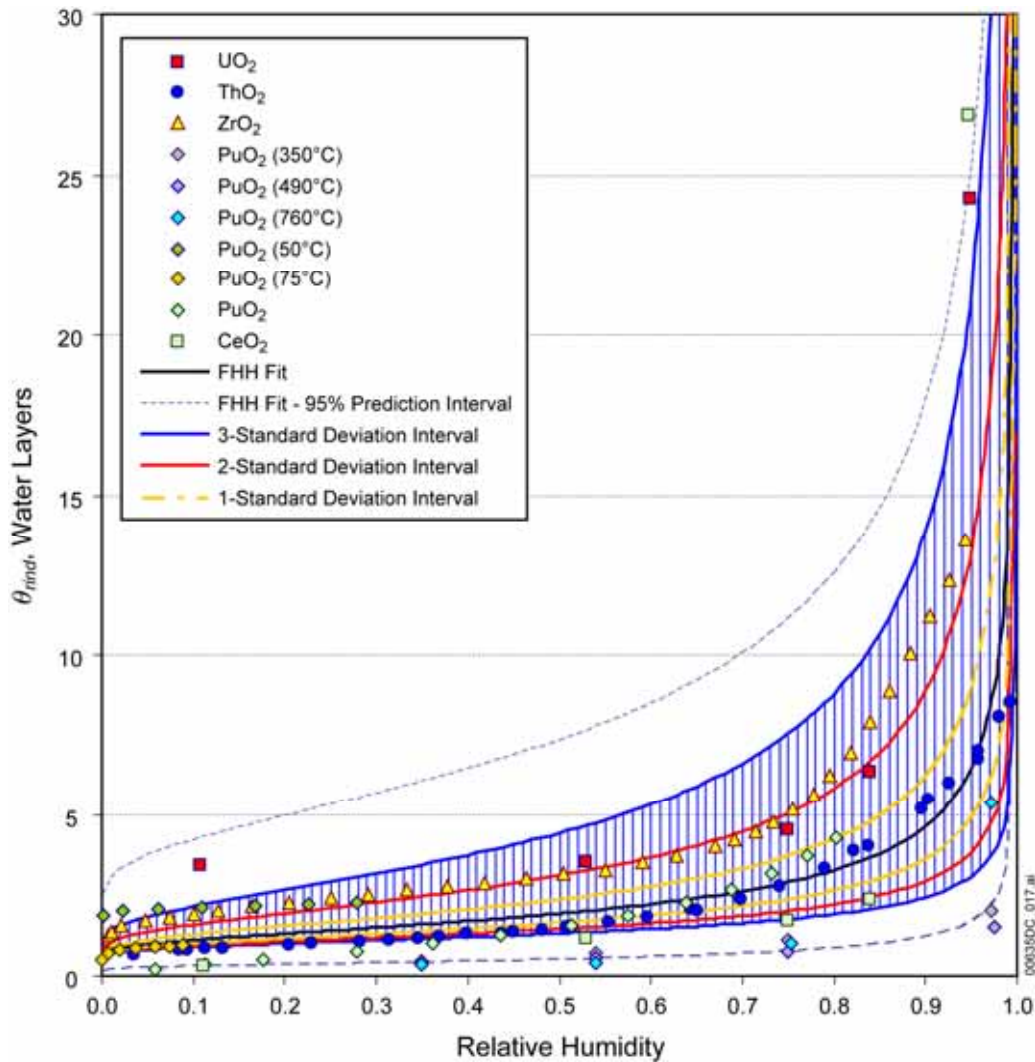


Source: Output DTN: SN0703PAEBSRTA.001

Figure 6.3-42. Least Squares Fit of Adsorption Data to FHH Isotherm

It is desirable to incorporate uncertainty in the rind saturation model, since the data demonstrate high uncertainty in the adsorptive behavior of waste form degradation products. In addition to showing the least squares fit to the data, Figure 6.3-42 also shows two commonly used measures of uncertainty in the data and the linear fit to the data. The 95 percent confidence interval encloses the region in which the true best-fit linear least squares fit is 95 percent certain to lie. The 95 percent prediction interval is the area in which data are 95 percent certain to fall, based on the data used to generate the least squares fit.

Figure 6.3-43 shows the fitted FHH adsorption isotherm for the waste form rind along with the data on which it is based. Also shown are various measures of uncertainty associated with the fitted isotherm, including the 95 percent prediction interval from Figure 6.3-42. As this figure shows, the prediction interval does not provide a suitable indication of uncertainty in the model. The prediction interval does encompass the experimental data, but is so broad that the predictions will result in unrealistically high water saturation in the rind in so many instances that sensitivity to RH is lost. The confidence interval shown in Figure 6.3-42 is not shown in Figure 6.3-43, since it is a measure of uncertainty in the mean, or fitted curve, and is not an appropriate indicator of the spread of the data.



Source: Output DTN: SN0703PAEBSRTA.001

Figure 6.3-43. Waste Form Rind Adsorption Isotherm Showing Uncertainty

Another approach to expressing uncertainty is also shown in the form of standard deviation intervals; these are computed from the standard deviation in the linear least squares parameters, a and b : $\sigma_a = 0.0458$ and $\sigma_b = 0.0679$. The FHH parameters, s_{rind} and k_{rind} , are then calculated for $\pm n\sigma_a$ and $\pm n\sigma_b$, for $n = 1, 2$, and 3 , and the FHH isotherm for combinations of s and k that give the bounds for each value of n are plotted in Figure 6.3-43. To be consistent with the calculation of the effective diffusion coefficient (Section 6.3.4.1.1) and with the corrosion products adsorption isotherm (Section 6.3.4.3.2), the three standard deviation bounds is used. The one and two standard deviation bounds are too narrow, failing to encompass experimentally observed behavior. The three standard deviation bounds appear to be most suitable in terms of providing a range of adsorption estimates that will allow the sensitivity to this model to be shown in the TSPA calculations, while encompassing much of the experimental data.

For the waste form rind saturation model, Equation 6.3.4.6.1-2 will be used with the following ranges for parameters: s_{rind} : 1.656 to 3.038; k_{rind} : 1.606 to 8.215. Due to the sparseness of the data on which these parameters are based, a uniform distribution is recommended, although a joint normal distribution is also justified on the basis of assumptions implicit in the statistical analysis from which the ranges were calculated.

The effective water saturation of the rind is computed in the same manner as for corrosion products (Equation 6.3.4.3.5-5):

$$S_{we,rind} = \min \left[\rho_{rind} \bar{s}_{rind} t_f \left(\frac{1 - \phi_{rind}}{\phi_{rind}} \right) \theta_{rind}(RH), 1.0 \right], \quad (\text{Eq. 6.3.4.6.1-4})$$

In addition to the adsorption isotherm, the density of rind solids, ρ_{rind} [kg m^{-3}], the rind specific surface area, \bar{s}_{rind} [$\text{m}^2 \text{kg}^{-1}$], and the rind porosity, ϕ_{rind} [$\text{m}^3 \text{void m}^{-3} \text{total volume}$], are needed to evaluate the water saturation. The thickness of a monolayer of water (Equation 6.3.4.3.2-4) is treated as a constant, $t_f = 2.83 \times 10^{-10} \text{ m}$. The minimum of the calculated saturation and 1.0 is used in Equation 6.3.4.6.1-4 because the amount of water adsorbed using the FHH isotherm is unbounded as RH approaches 1.0, which may result in an unrealistic effective water saturation greater than 1.0.

Each of the individual material properties that make up Equation 6.3.4.6.1-4 varies, depending on the composition of the rind. Whereas steel corrosion products are treated as a mixture of four distinct substances representing the most prominent materials present in corroded steel, the rind is represented as a single substance having composite properties of the surrogate rind materials. This approach is used because the rind will actually contain little of the surrogate materials, yet, to be consistent with the uncertainty resulting from the use of these surrogates in developing the adsorption isotherm, the ranges of physical properties of the surrogates must also be considered.

The solid density of these materials, listed in Table 4.1-10, varies from $5,680 \text{ kg m}^{-3}$ (ZrO_2) to $11,500 \text{ kg m}^{-3}$ (PuO_2). The theoretical density of schoepite is $4,830 \text{ kg m}^{-3}$ (SNL 2007 [DIRS 180616], Table 7-1), so use of the higher surrogate material densities will overestimate the water saturation in the rind (see Equation 6.3.4.5-5) and consequently overestimate releases of radionuclides.

The specific surface area of the surrogate rind materials, as listed in Table 6.3-12, varies widely, from $0.51 \text{ m}^2 \text{g}^{-1}$ to $57 \text{ m}^2 \text{g}^{-1}$. The materials used in the cited adsorption studies have a greater specific surface area than CSNF. *CSNF Waste Form Degradation: Summary Abstraction* (BSC 2004 [DIRS 169987], Tables 8-2 and 8-3) specifies an effective specific surface area of CSNF ranging from $5 \times 10^{-5} \text{ m}^2 \text{g}^{-1}$ to $4 \times 10^{-3} \text{ m}^2 \text{g}^{-1}$, or a factor of 10,000 to 15,000 smaller than the specific surface areas of the surrogate rind materials. The specific surface area of degraded CSNF (schoepite) is unknown. While the specific surface area does not necessarily affect the adsorption isotherm, the water saturation is directly proportional to specific surface area (Equation 6.3.4.5-5). Thus, the estimated saturation using Equation 6.3.4.6.1-4 and the effective specific surface area of CSNF from *CSNF Waste Form Degradation: Summary Abstraction* will be negligible at any RH less than 1.0. The use of surrogate material properties, where both

specific surface area and density are higher than the values estimated for schoepite and CSNF, will result in overestimating water saturation in and releases of radionuclides from the CSNF rind. Sampling from the range and distribution for rind specific surface area given above will enable TSPA to evaluate the sensitivity of estimates for releases of radionuclides to this parameter.

The rind porosity is specified as being uniformly distributed between 0.05 and 0.3 (DTN: MO0411SPACLDDG.003 [DIRS 180755], Table 7-1). The product of material properties that appears in the equation for water saturation (Equation 6.3.4.5-5),

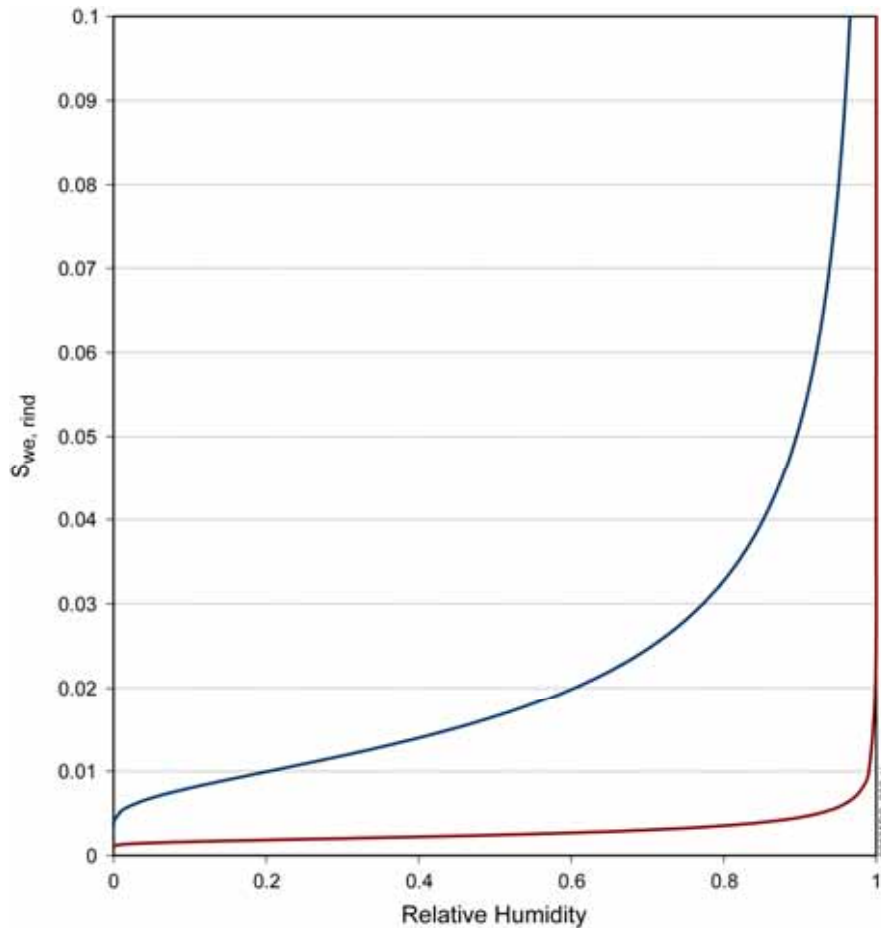
$\rho_{rind} \bar{s}_{rind} t_f \left(\frac{1 - \phi_{rind}}{\phi_{rind}} \right)$, therefore ranges over nearly three orders of magnitude, from 3.7×10^{-3} to

3.5, for the surrogate rind materials. To capture this large uncertainty, the specific surface area and density of the rind materials, as well as the porosity, will be sampled from uniform distributions over the ranges of the surrogate material properties:

Specific surface area:	0.5 to 60 m ² g ⁻¹
Solid density:	5,600 to 11,500 kg m ⁻³

Alternatively, the product, $\rho_{rind} \bar{s}_{rind} t_f$, could be sampled from a uniform distribution ranging from 7.92×10^{-4} to 0.195 [dimensionless]. This product can be viewed as the volume of a monolayer of water per unit volume of rind. Although the range of rind porosity could be subsumed in this parameter range, it is more transparent to factor it in separately, since rind porosity is already a separate sampled parameter.

The range of CSNF rind water saturations that can be obtained given the range of input parameters is now considered. The rind saturation is maximized using the maximum values for k_{rind} , \bar{s}_{rind} , and ρ_{rind} , and the minimum values for s_{rind} and ϕ_{rind} . $S_{we,rind}$ will reach a value of 1.0 at RH \approx 0.9992. The rind saturation is minimized using the minimum values for k_{rind} , \bar{s}_{rind} , and ρ_{rind} , and the maximum values for s_{rind} and ϕ_{rind} . $S_{we,rind}$ reaches a value of 1.0 at an RH of nearly 1.0 (8×10^{-9} less than 1.0). Figure 6.3-44 shows the bounding values of rind saturation as a function of RH. Since the CSNF waste form domain contains both CSNF rind as well as corrosion products (which use a different adsorption isotherm, described in Sections 6.3.4.3.2 to 6.3.4.3.5), the domain saturation is obtained by combining the water saturation of each material, as discussed in Section 6.5.2.2.2.



Source: Output DTN: SN0703PAEBSRTA.001

Figure 6.3-44. Water Saturation Bounds in CSNF Waste Form Rind

The effective diffusion coefficient in the rind is computed analogously to the diffusion coefficient in the waste package corrosion products (Equation 6.3.4.3.5-2) using Archie's law:

$$\phi S_{we,rind} D_{s,rind} = \phi_{rind}^{1.3} S_{we,rind}^2 D_0. \quad (\text{Eq. 6.3.4.6.1-5})$$

The implementation of the rind water saturation and water volume in TSPA is described in Section 6.5.2. Briefly, the EBS is modeled in TSPA as a series of three domains—waste form with associated steel components, waste package corrosion products, and invert. For the waste form water saturation and volume calculation, the water associated with the rind is combined with water adsorbed onto corrosion products of the waste form steel components, which is obtained from the corrosion product water adsorption submodel developed in Section 6.3.4.3.5.

6.3.4.6.2 HLW Glass Rind Water Saturation

The interaction of humid air with HLW glass is discussed in *Defense HLW Glass Degradation Model* (BSC 2004 [DIRS 169988], Section 6.5.3.1). When glass is exposed to humid air, water molecules will adsorb onto specific sites on the glass surface, primarily silanol and alkali metal

sites. The amount of water that sorbs on the glass will depend on the relative humidity of the air, the temperature of the glass surface, and how fast the water reacts with the glass. The sorption isotherm for water on a reference waste glass made with SRL 165 frit has been measured at room temperature (Ebert et al. 1991 [DIRS 111028], p. 134, Figure 1b). The measured isotherm was fit using the following FHH isotherm equation:

$$\theta_{HLWG} = \left(\frac{-k_{HLWG}}{\ln RH} \right)^{\frac{1}{s_{HLWG}}}, \quad (\text{Eq. 6.3.4.6.2-1})$$

where θ_{HLWG} is the number of statistical monolayers of adsorbed water, RH is the relative humidity, k_{HLWG} and s_{HLWG} are constants with values of $k_{HLWG} = 3.2$ and $s_{HLWG} = 1.5$ for SRL 165 glass.

The density of HLW glass is $\rho_{HLWG} = 2,700 \text{ kg m}^{-3}$, the porosity of HLWG rind is $\phi_{HLWG} = 0.17$ (all data from DTN: MO0502ANLGAMR1.016 ECN1 [DIRS 172830], Table 8-1). The specific surface area of HLWG, $2.70 \times 10^{-6} \text{ m}^2 \text{ g}^{-1}$, as given in the DTN, is calculated by dividing the geometric surface area of a glass log by its mass. This is not an appropriate measure of specific surface area of the finely-divided clay-like rind material. For the rind, the specific surface area of kaolinite is used; to characterize the uncertainty in rind specific surface area, it is assigned a range (that of kaolinite) of $\bar{s}_{HLWG} = 10$ to $38 \text{ m}^2 \text{ g}^{-1}$ (Langmuir 1997 [DIRS 100051], Table 10.2). The water saturation is then given by:

$$S_{we,rind,HLWG} = \min \left[\rho_{HLWG} \bar{s}_{HLWG} t_f \left(\frac{1 - \phi_{HLWG}}{\phi_{HLWG}} \right) \theta_{HLWG}(RH), 1.0 \right]. \quad (\text{Eq. 6.3.4.6.2-2})$$

HLW glass rind volume, $V_{rind,HLWG}$, is given in DTN: MO0502ANLGAMR1.016 ECN1 [DIRS 172830], Equation 54, as a function of time. For fully water saturated conditions, Equation 55 in the DTN also gives the water volume in the HLW glass rind. The implementation in TSPA of the HLW glass rind water saturation and water volume under unsaturated conditions is described in Section 6.5.2.2.2.2.

6.4 CONSIDERATION OF ALTERNATIVE CONCEPTUAL MODELS

Alternative conceptual models considered in the RTA are discussed in this section. A summary of models that are analyzed is presented in Table 6.4-1.

In a deviation from the TWP (BSC 2006 [DIRS 177739]), the following additional alternative conceptual models that were planned have not been developed:

- Fine-scale multi-process simulation of in-package transport, intended to justify the coarser-scale, two-cell waste package model implemented in TSPA (BSC 2006 [DIRS 177739], Section 1.2.3)

- Bounding analysis for flux of H₂O, O₂, and CO₂ into breached waste packages (BSC 2006 [DIRS 177739], Section 1.2.10), a more detailed, complex version of the alternative conceptual model described in Section 6.4.2.

Table 6.4-1. Alternative Conceptual Models Considered

Alternative Conceptual Models	Key Assumptions	Screening Assessment and Basis
Bathtub flow model (alternative to flow-through model)	Seepage water flowing into breached waste package accumulates until void volume is filled before water containing dissolved radionuclides flows out. Various cases, such as changing inflow rates and effect of solubility and dissolution rate limits, are evaluated.	Screened out in analysis in Section 6.6.1. For several of the most pertinent cases, the flow-through model is bounding with respect to releases of radionuclides.
Water vapor and oxygen diffusion limitations through stress corrosion cracks (alternative to unlimited access to water vapor and oxygen)	If the rate of corrosion of steel components inside waste package is greater than the rate of diffusion of water vapor and oxygen into waste package, a film of adsorbed water cannot form, which delays diffusive releases until all steel is fully corroded. Water vapor concentration inside and outside waste package varied to determine conditions where rate of consumption of water and oxygen by corrosion might be greater than diffusion rate through stagnant air.	Screened out. Potentially delays releases for hundreds to thousands of years. To model the concept defensibly requires a far more complex, detailed model. Unpredictable spatial variations in extent of corrosion, for example, may cause releases to be underestimated. The assumption that no water is physically adsorbed until all steel is corroded is questionable, since adsorption is typically a fast process. On the other hand, if water consumption by corrosion keeps the relative humidity inside the waste package low, the effective water saturation, as computed in the in-package diffusion submodel, will be so low that bulk liquid phase behavior allowing dissolution and diffusion of dissolved radionuclides will not exist until corrosion is complete. If cracks are filled with porous solids such as corrosion products, adsorption of water may partially or largely seal cracks from vapor diffusion, and other mass transfer mechanisms may dominate.
Dual-continuum invert model	Crushed tuff invert ballast is modeled as a dual-continuum material consisting of intergranular pore space and intragranular pore space. All seepage flow into the drift flows through the intergranular pore space and into the UZ fractures. Imbibition from UZ host rock into the invert flows through the intragranular pore space. Diffusion of radionuclides also occurs in both the intergranular and intragranular pore spaces, from the waste package corrosion products into UZ fractures and matrix, as well as between the two invert continua.	Screened out. Insufficient data to validate diffusion coefficients in individual continua. Insufficient data to confirm whether this is a bounding approach with respect to chemical behavior in the invert.

Table 6.4-1. Alternative Conceptual Models Considered (Continued)

Alternative Conceptual Models	Key Assumptions	Screening Assessment and Basis
Invert diffusion coefficient model with lower limit on water content	As the water content of the crushed tuff ballast decreases, the water films that connect pore spaces become disconnected, and the effective diffusion coefficient drops more rapidly than predicted by Archie's law. Below some critical water content, the diffusion coefficient becomes zero. Based on models of diffusion in soils.	Screened out. Insufficient data to validate diffusive behavior at very low water contents. Does not provide upper bounds on diffusion coefficients.
Reversible (equilibrium) sorption of radionuclides onto waste package corrosion products	Iron oxyhydroxide corrosion products sorb many radionuclide species. Sorption is assumed to be reversible and not compete with other radionuclides nor compete for kinetic sorption sites.	Screened out. Does not account for limitations on total number of sorption sites. Does not account for competition with other radionuclides for sorption sites. Does not account for competition with kinetic sorption for sorption sites.
Pu sorption from stationary corrosion products and colloids	Plutonium sorbs strongly to iron oxyhydroxide corrosion product colloids and stationary corrosion products. Sorption may be considered "slowly reversible" (as opposed to kinetic). The model is applicable to the range of pH values expected in the repository environment.	Experiment durations are short (hours to weeks) compared to the repository time scale. The mechanisms of plutonium sorption are not well-enough understood to fully interpret the data. Plutonium sorption and desorption data are not available for the highest pH ranges expected in the repository environment.

6.4.1 Bathtub Model for the Waste Package

The bathtub model is an alternative conceptual EBS flow model in which seepage collects within the waste package before being released to the EBS. This is an alternative to the "flow-through" geometry, and is analyzed in Section 6.6.1. It is concluded that, with respect to releases of radionuclides, the flow-through model increases releases relative to the bathtub model and is therefore bounding for the following cases:

1. Primary case, in which the water inflow rate is constant, the rate of radionuclide dissolution is limited, and the radionuclide concentration is solubility-limited. Unlike the bathtub model, there is no delay in release of radionuclides in the flow-through model.
2. Secondary case 1, in which the inflow rate undergoes a step change. The response of the bathtub model is identical to the flow-through model for solubility-limited radionuclides. For dissolution-rate-limited radionuclides, the flow-through model overestimates releases of radionuclides for the case of decreasing inflow, or increasing concentration, which is of primary interest from a performance or regulatory standpoint.
3. Secondary case 2, a step change in groundwater chemistry. The flow-through model overestimates releases of radionuclides relative to the bathtub model when the solubility or dissolution rate increases because it has an instantaneous change to the higher

equilibrium value, whereas the bathtub geometry delays the change. For decreasing solubility or dissolution rate, the bathtub overestimates the fractional releases of radionuclides, but this case is of no interest from a performance or regulatory point of view, because the overall rate decreases.

- Secondary case 3, wherein a second corrosion patch opens instantaneously beneath the water level in the waste package in the bathtub model. The impact of this alternative flow path was screened out because of the potential mitigation from sorption and because the variability of corrosion rates provides large uncertainty in radionuclide release rates from the waste package. The existence of a second corrosion patch through the Alloy 22 outer corrosion barrier (which has a lower corrosion rate than that of the stainless steel internal components), implies that corrosion of steel internal components is already extensive, so there should be a high potential for sorption.

As a result of this analysis, the bathtub model has been screened out as an ACM in order to overestimate radionuclide transport.

6.4.2 Limited Water Vapor and Oxygen Diffusion Rate into Waste Package

This ACM accounts for the resistance to diffusion of water vapor and oxygen *into* a waste package through SCCs. In the base model, there is no limit to the amount of water vapor available to adsorb onto surfaces within a waste package, which creates a pathway for diffusive transport of radionuclides out of the waste package. (This applies to the in-package diffusion submodel, Section 6.3.4.3.) However, the base model currently used for the TSPA to calculate dose overestimates releases of radionuclides, particularly at early times when the only breaches in a waste package are small SCCs. If the diffusion rate is limited, the rate of steel corrosion is limited by the rate of diffusion of water vapor and oxygen. The potential result is that no water is available to adsorb and form a thin liquid film on corrosion products, and no water would be available for radionuclide transport, because all water is consumed by the corrosion process as quickly as it diffuses into the waste package. This prevents formation of a diffusive path until all of the internal steel components are fully corroded, which in turn delays diffusive releases until that time. Since this may take hundreds to thousands of years, the delay in releases of radionuclides from breached waste packages could be extensive. During this delay, radioactive decay will decrease the quantity of radionuclides in the waste package, ultimately reducing releases to the environment.

A mathematical description of this model is presented in Section 6.6.2, where sample calculations show that the corrosion rate is so slow that the small cross-sectional area of SCCs for diffusion does not limit diffusion of water vapor and oxygen relative to the rate of consumption by corrosion, so ample water vapor is available for adsorption.

6.4.3 Dual-Continuum Invert

This ACM treats the crushed tuff in the invert as a dual continuum comprised of two pore spaces – intragranular pore space (tuff particle matrix) and intergranular pore space. Although radionuclide transport by both advection and diffusion can occur in both pore spaces, the dominant flow and transport processes in each of these two pore spaces is generally different. In

order to simulate flow and transport through the invert accurately, the invert is conceptualized in this ACM as overlapping dual continua using a dual-permeability approach, wherein flow and transport occur in both pore spaces, and mass transfer takes place between the two pore spaces.

A mathematical description of this model is presented in Section 6.6.3.

6.4.4 Alternative Invert Diffusion Coefficient Models

The following two alternative models for determining the diffusion coefficient in the invert are assessed: the single-continuum invert diffusion coefficient model and the dual-continuum invert diffusion coefficient model. In the single-continuum invert diffusion coefficient model, an alternative to the Archie's law approach for determination of the diffusion coefficient for the single-continuum crushed tuff invert ballast (Section 6.3.4.1) is modeled using an approach that has been applied to diffusion in soils. In the dual-continuum invert diffusion coefficient model, the bulk diffusion coefficient is dominated by the intergranular diffusion coefficient above the critical bulk moisture content, while below this critical value, the intragranular diffusion coefficient dominates.

Mathematical descriptions of these models are presented in Section 6.6.4.

6.4.5 Reversible Sorption of Radionuclides onto Waste Package Corrosion Products

In this ACM, reversible sorption of radionuclides takes place on waste package corrosion products. Iron oxyhydroxides are generated through corrosion of mild steel and stainless steels within the waste package. The iron oxyhydroxides are known to be excellent sorbers (as indicated by their high K_d values) of many radionuclide species. In this ACM, sorption is modeled as being completely reversible for all radionuclides and represented by linear adsorption isotherms in the form of K_d values. The K_d values allow retardation factors to be computed for transport through the EBS.

K_d values for 13 radionuclides are discussed in Section 6.6.5.

6.4.6 Plutonium Sorption from Stationary Corrosion Products and Colloids

The TSPA Model accounts for limited plutonium desorption from iron oxyhydroxides by incorporating a kinetic sorption component developed from the results of surface complexation based modeling. In contrast, this ACM accounts for the slow desorption of plutonium observed in experiments investigating adsorption and desorption of plutonium from iron oxyhydroxide. Postulated mechanisms of plutonium sorption are described and the experimentally observed desorption is interpreted in the context of these mechanisms. K_d values are calculated for application to plutonium transport in the EBS and for comparison with the TSPA Model base case. This ACM is not incorporated into the base-case model because the durations of sorption-desorption experiments, upon which the parameters are developed, are short relative to the repository time scale. Furthermore, sorption experiments are performed without considering competition with other actinides, and data on plutonium sorption and desorption are not available for high pH ranges.

This model is described in detail in Section 6.6.6.

6.5 MODEL FORMULATION FOR BASE CASE MODEL

6.5.1 Mathematical Description of Base Case Conceptual Model

A solute transport model typically consists of two component models: a model to solve the flow equation and another to solve the transport equation (Anderson and Woessner 1992 [DIRS 123665], p. 327). The solution of the flow equation yields the flow velocities or flow rates. These flow rates are input to the transport model, which predicts the concentration distribution in time and space. Development of the EBS flow model and the EBS transport model are discussed separately in the next two subsections.

6.5.1.1 EBS Flow Model

The EBS flow model is essentially a mass balance on water in the EBS. Because the microscopic details of processes that occur in the EBS are not important on a drift or waste package scale, an appropriate starting point for developing the EBS flow model is a general macroscopic balance on water within a drift (Bird et al. 1960 [DIRS 103524], p. 686):

$$\frac{dm_w}{dt} = -\Delta w_w + w_w^m + r_w. \quad (\text{Eq. 6.5.1.1-1})$$

Here, m_w (kg) is the instantaneous total mass of water within the walls of a drift, which encompass the EBS. This equation states that the rate of change of water mass in the EBS is equal to the mass rate of flow out of minus the mass rate of flow into the EBS (Δw_w [kg s^{-1}]), plus w_w^m (kg s^{-1}), the net mass flow rate of water across bounding surfaces into the EBS by mass transfer (e.g., condensation or evaporation transfer water across a liquid surface, which is a boundary between gas-phase flow and transport and liquid-phase flow and transport), plus the rate of production of water by chemical reactions, r_w (kg s^{-1}). Per Assumption 5.4, production or consumption of water by chemical reactions is assumed to be zero, resulting in:

$$\frac{dm_w}{dt} = -\Delta w_w + w_w^m. \quad (\text{Eq. 6.5.1.1-2})$$

At steady state or when the mass of water in the EBS changes slowly, the time derivative can be set to zero:

$$-\Delta w_w + w_w^m = 0. \quad (\text{Eq. 6.5.1.1-3})$$

The alternative bathtub conceptual model, using Equation 6.5.1.1-2 for the waste package, is screened out as an ACM in Section 6.6.1. By neglecting changes in the density of the water within a drift as it passes through the EBS, Equation 6.5.1.1-3 can be divided by the density of water, ρ_w (kg m^{-3}), to transform it into a volume balance involving volumetric flow rates:

$$-\Delta F_w + F_w^m = 0, \quad (\text{Eq. 6.5.1.1-4})$$

where $F_w = w_w / \rho_w$ is the volumetric flow rate ($\text{m}^3 \text{s}^{-1}$), and the superscript m still refers to mass transfer processes. Since both $-\Delta F_w$ and F_w^m represent a net inflow minus outflow, Equation 6.5.1.1-4 simply states that outflow is equal to inflow. This is the general form of the water mass balance that is used for individual flow paths in the EBS in the RTA. It is applicable to the EBS as a whole as well as to individual components of the EBS. In particular, the terms Δw_w and w_w^m can be broken down into the separate and distinct flow paths listed in Section 6.3.1.1.

The volumetric flow rate of water into the top of the EBS is referred to as the total dripping flux, designated F_1 in Table 6.3-1, and is comprised of seepage flux into the top of the drift and condensation on walls of the drift. The seepage flux is computed in the GoldSim TSPA Model using *Abstraction of Drift Seepage* (SNL 2007 [DIRS 181244]), and condensation on the drift walls is represented in the TSPA Model through the *In-Drift Natural Convection and Condensation* model (SNL 2007 [DIRS 181648]); these are inputs or sources of inflow into the EBS flow model.

Over the entire EBS, Equation 6.5.1.1-4 becomes

$$F_1 + F_7 = F_8, \quad (\text{Eq. 6.5.1.1-5})$$

where F_1 is the total dripping flux into the top of the drift and F_7 is the imbibition flux into the invert; see Figure 6.3-1. F_8 is the flow rate of water leaving the invert and entering the UZ.

For the drip shield, the flux through corrosion breaches in the drip shield is F_2 , and the flux of water diverted by the drip shield is F_3 , so the water balance on the drip shield is:

$$F_1 = F_2 + F_3. \quad (\text{Eq. 6.5.1.1-6})$$

For the waste package, the water mass balance is:

$$F_2 = F_4 + F_5. \quad (\text{Eq. 6.5.1.1-7})$$

As modeled at steady state, there is no change in water storage in the waste package. Therefore, the flow rate of water from the waste package to the invert is equal to the flow into the waste package, F_4 . The water balance over the invert includes this influx of water that has flowed through the waste package as well as water diverted around the waste package and water diverted around the drip shield. The total flow into the invert that originates from seepage flux and condensation (F_1), is:

$$\begin{aligned} F_6 &= F_3 + F_4 + F_5 \\ &= F_1. \end{aligned} \quad (\text{Eq. 6.5.1.1-8})$$

A water mass balance over the invert indicates that the sum of the seepage flux (F_1) and imbibition flux (F_7) flows out of the invert (Equation 6.5.1.1-5):

$$\begin{aligned} F_8 &= F_6 + F_7 \\ &= F_1 + F_7. \end{aligned} \quad (\text{Eq. 6.5.1.1-9})$$

6.5.1.1.1 Water Flux through a Breached Drip Shield

Key features of the drip shield flux splitting algorithm include: (1) the seepage flux into the drift falls as droplets from the top of the drift onto the crown of the drip shield (Assumption 5.1), (2) droplets fall randomly along the length of the drip shield, (3) only flow through general corrosion patches is considered, (4) evaporation from the drip shield is neglected (Assumption 5.2); all of the seepage flux either flows through corrosion patches or drains down the sides of the drip shield, (5) all water that flows through breaches in the drip shield flows onto the waste package.

In the conceptual model of the breached drip shield, corrosion patches are represented by square holes, with dimensions specified in an earlier version of the WAPDEG corrosion model as approximately 27 cm in width (CRWMS M&O 2000 [DIRS 151566], p. 36), where, the patch area is specified to be $7.214 \times 10^4 \text{ mm}^2$. The breached drip shield experiments (BSC 2003 [DIRS 163406]) were designed using holes of this size.

Consider first some simple cases with idealized behavior, in which drops falling onto the drip shield either fall straight through corrosion patches or, after impacting the drip shield surface, flow straight down the sides of the drip shield. These will provide bounding cases for comparison as more realism is added to the flux splitting submodel. Let 2ℓ be the width (m) of a square corrosion patch, L_{DS} the axial length (m) of the drip shield, and N_b the number of patches on the drip shield, assumed to not overlap each other.

In the simplest case, N_c patches are located on the crown of the drip shield, none off the crown. Since all of the seepage flux F_1 falls on the crown of the drip shield, the amount that passes straight through breaches in the drip shield (F_2) is simply the ratio of the total length of the $N_b = N_c$ patches to the total length of the drip shield multiplied by the seepage flux:

$$F_2 = F_1 \frac{2\ell N_c}{L_{DS}}. \quad (\text{Eq. 6.5.1.1.1-1})$$

Next, suppose a single patch exists, randomly located on the top of the drip shield, but fully off the crown so that none of the seepage flux falls directly through the patch, but instead lands on the drip shield crown and then flows straight down the surface. Ideally, exactly half of the seepage flux drains down one side of the drip shield, and half down the other side. The reality is not far removed from the ideal: when drops strike the drip shield, they splatter in a random pattern; the region where splattered droplets fall is roughly circular. After a large number of drops have fallen, on average half of the droplets will have landed on each of the two sides of the drip shield. Since only half of the seepage flux drains down one side of the drip shield, a single

patch can only capture $2\ell/L_{DS}$ of the flow down one side ($F_1/2$), so the flux through a single patch in the drip shield is:

$$F_2 = F_1 \frac{\ell}{L_{DS}}. \quad (\text{Eq. 6.5.1.1.1-2})$$

If two patches exist, with one patch on each side of the drip shield, the total flux will clearly be twice what flows through a single patch:

$$F_2 = F_1 \frac{2\ell}{L_{DS}}. \quad (\text{Eq. 6.5.1.1.1-3})$$

If two patches are located on one side of the drip shield, away from the crown, and located randomly except that they do not interfere with each other (i.e., one patch is not upstream from another where it would intercept flow that would be captured by a lower patch), then a fraction $2\ell/L_{DS}$ of the flow down one side ($F_1/2$) will enter each patch. The total flux through the drip shield in this case is:

$$F_2 = 2 \left(\frac{F_1}{2} \right) \frac{2\ell}{L_{DS}} = F_1 \frac{2\ell}{L_{DS}}. \quad (\text{Eq. 6.5.1.1.1-4})$$

In the general case where N_c patches are randomly distributed on the drip shield, off the crown and not interfering with each other, Equation 6.5.1.1.1-4 becomes:

$$F_2 = F_1 \frac{N_c \ell}{L_{DS}}. \quad (\text{Eq. 6.5.1.1.1-5})$$

Different behavior is clearly seen depending on whether the patch is located directly on the crown such that drops fall straight through it, or whether the seepage is split by falling on the drip shield first, causing half of the dripping flux to flow down each side of the drip shield. If N_c patches are located on the crown ($N_c \leq N_b$), the most general form of the flux splitting algorithm for this idealization is:

$$\begin{aligned} F_2 &= F_1 \frac{\ell}{L_{DS}} [2N_c + (N_b - N_c)] \\ &= F_1 \frac{(N_b + N_c)\ell}{L_{DS}}. \end{aligned} \quad (\text{Eq. 6.5.1.1.1-6})$$

Although this equation is general, it requires a distinction between patches on the crown and off the crown. However, the location of patches is completely random, so the location cannot be specified *a priori*. To account for the different flux through crown patches, note that crown patches occur within a distance $\pm 2\ell$ from the crown, or over an area $4\ell L_{DS}$. The total surface area of a drip shield is $W_{DS} L_{DS}$, where W_{DS} is the total unfolded width of the drip shield (m) as

measured from the bottom edge of one side, over the top, and down to the bottom of the other side. Then the probability of a patch occurring on the crown is:

$$\frac{4\ell L_{DS}}{W_{DS} L_{DS}} = \frac{4\ell}{W_{DS}}. \quad (\text{Eq. 6.5.1.1.1-7})$$

Equation 6.5.1.1.1-6 can be rewritten to account for the probability of seepage flux falling into a crown patch or onto intact drip shield, and for the flux through a single crown patch being twice the flux through an off-crown patch for a given seepage flux:

$$\begin{aligned} F_2 &= F_1 \left(\frac{2N_b \ell}{L_{DS}} \right) \left(\frac{4\ell}{W_{DS}} \right) + F_1 \left(\frac{N_b \ell}{L_{DS}} \right) \left(1 - \frac{4\ell}{W_{DS}} \right) \\ &= F_1 \frac{N_b \ell}{L_{DS} W_{DS}} (4\ell + W_{DS}) \\ &= F_1 \frac{N_b \ell}{L_{DS}} \left(\frac{4\ell}{W_{DS}} + 1 \right). \end{aligned} \quad (\text{Eq. 6.5.1.1.1-8})$$

For a patch size of $2\ell = 27$ cm and a total drip shield width of $W_{DS} = 6.94$ m, the term $4\ell/W_{DS} = 0.078$. To a good approximation, the term $4\ell/W_{DS}$ can be neglected, yielding:

$$F_2 = F_1 \frac{N_b \ell}{L_{DS}}, \quad (\text{Eq. 6.5.1.1.1-9})$$

which is identical to Equation 6.5.1.1.1-5. This result indicates that, although the flux is higher through crown patches, the probability of patches occurring on the crown is small ($4\ell/W_{DS}$, or 7.8 percent) and may be ignored in light of the uncertainties discussed in Section 6.3.2.4.

The simple model presented thus far assumes ideal drops that do not splatter and that run down the drip shield in straight, nondiverging paths. Next, realism is added to the flux splitting submodel by taking into account observations and data from breached drip shield experiments, which account for drop splattering and the nature of rivulet flow along the surface of the drip shield.

6.5.1.1.2 Breached Drip Shield Experiments

The breached drip shield experiments (BSC 2003 [DIRS 163406]) are described in Section 6.3.2.4. The tests were performed at three different drip rates, which represent the range of expected liquid water influx rates over a single drip shield. The bulk of the tests were performed at a drip rate of $2 \text{ m}^3 \text{ yr}^{-1}$. Additional bounding flow rate tests were performed at a lower rate of $0.2 \text{ m}^3 \text{ yr}^{-1}$ and a higher rate of $20 \text{ m}^3 \text{ yr}^{-1}$. The tests were performed by dripping water at specified drip locations, one location at a time for a period that allowed a measurable amount of liquid to be collected through breaches in the drip shield (typically 30 min to 60 min at $2 \text{ m}^3 \text{ yr}^{-1}$, 10 min at $20 \text{ m}^3 \text{ yr}^{-1}$, and 5-5½ hr at $0.2 \text{ m}^3 \text{ yr}^{-1}$).

Four basic types of tests were performed: (1) “q(splash)” test, in which the splash distance was measured when a drop falls onto the drip shield surface; (2) “q(film)” tests, where the primary goals were to measure rivulet spread and the amount of flow into a single breach in the drip shield; (3) multiple breach tests, which were similar to the q(film) tests, except that multiple breaches existed in the drip shield mock-up; and (4) bounding flow rate tests, which repeated the q(film) and multiple breach tests using different drip rates. Most of the tests were performed on both a smooth drip shield and a rough drip shield.

The dripping distance was based on design parameters and carried out at full scale. Thus the dripping distance used for dripping onto the crown of the drip shield was 2.173 m (BSC 2003 [DIRS 163406]). The splash radius on the drip shield was measured for both the smooth surface (DTN: MO0207EBSATBWP.022 [DIRS 163400]) and the rough surface (DTN: MO0207EBSATBWP.021 [DIRS 163399]). The maximum lateral splash radius observed in Splash Radius Test #1 on the smooth surface was 72.5 cm after 60 drops; in Test #2, the maximum splash radius was 53.0 cm after 66 drops. On the rough surface, the maximum lateral splash radius in the five tests that were conducted was 106.5 cm after 203 drops. In addition to the splash radius tests, splash distances were recorded for some of the single patch q(film) rivulet flow tests; a maximum splash distance of 86 cm (DTN: M0207EBSATBWP.023 [DIRS 163402]) was observed for drip location Patch 4, 8 cm right of center, onto the crown of the drip shield. The distribution of droplet formation on the surface as a function of distance from the impact location was not measured, although an approximate determination was made to distinguish an “inner cluster” of droplets from an “outer fringe,” where the droplets were noticeably smaller (Table 4.1-4). It was observed that the outer splashes on the fringe tended to be smaller and less frequent on the rough surface than on the smooth surface.

Observations during the breached drip shield tests revealed that the primary mechanism for water to enter breaches is via rivulet flow that originates from an area around the point of drip impact. Following droplet impact at the crown, beads formed and increased in size around the center of impact with each successive drop. After a time, the beads closest to the downhill curvature would reach a critical mass and roll down the face of the drip shield in the form of a rivulet. The rivulet flow area spreads out in a delta formation (i.e., the maximum spread was located on the vertical section of the drip shield and the minimum spread was located at the point of impact). No film flow was observed during tests on the smooth or the rough drip shield surfaces.

For a given drip location onto the crown of the drip shield (Assumption 5.1), the spreading of the rivulet flow is defined by a spread angle, α , which is half of the total spread angle, formed with the vertical plane through the impact point. The total lateral spread of the rivulet flow is given by $2x \tan \alpha$, where x is the arc length from the crown of the drip shield down to a location of interest. In the breached drip shield experiments (BSC 2003 [DIRS 163406]), the lateral rivulet spread to one side of the vertical plane, or $x \tan \alpha$, was measured. These definitions are illustrated in Figure 6.3-2. The curvature/shape of the drip shield is not shown in Figure 6.3-2 for simplicity and clarity.

The spread of rivulets from drips onto the crown of the experimental drip shield is reported in DTNs: MO0207EBSATBWP.023 [DIRS 163402], MO0207EBSATBWP.024 [DIRS 163401], and MO0207EBSATBWP.025 [DIRS 163403] and summarized in Table 4.1-6. The data are analyzed in Microsoft Excel spreadsheet: Flux Split Drip Shield Model, Worksheet: Spread

angles, which is documented in Appendix C. The average spread at 33° from the crown in 26 measurements was 20.1 cm, corresponding to an average spread angle of about 13.2° . The range of spread angles, from one standard deviation smaller and greater than the mean, was about 8.9° to 17.3° . The distribution for spread angle is not clearly defined by the experimental data, and therefore a uniform distribution is considered appropriate.

The initial simple model wherein drips flow straight down the curved top of the drip shield is made more realistic by incorporating the random spread of rivulets over an angle α as they flow down the drip shield surface. The spreading of rivulets increases the probability that they will flow into a breach (corrosion patch). Three cases are considered, two for a centrally located breach at different distances from the crown such that different proportions of the rivulet spread will encounter a breach, and one for a breach at the end of the drip shield.

6.5.1.1.2.1 Drip Shield Flux for a Centrally Located Breach, Case 1

Consider a breach that is centrally located on the drip shield. The breach is centrally located if Points A and B (defined below) are located on the same segment of the drip shield as the breach itself. In other words, the ends of the drip shield lie beyond Point A and Point B. Figure 6.5-1 illustrates the location and geometry for potential rivulet flows into a breach with length 2ℓ and whose top edge is located a curved distance of x from the crown. For simplicity in evaluating coordinates, the zero point of the y -axis is coincident with the center of the breach.

In Case 1, $\ell > x \tan \alpha$; in other words, the breach is wider than the rivulet spread at the top of the breach.

Points A through D are defined as follows:

- Point A corresponds to the leftmost point from which the edge of the fan from the rivulet can enter the left side of the breach.
- Point B corresponds to the leftmost point from which all rivulets will enter the top edge of the breach. Point B lies between $-\ell$ (left side of the breach) and the origin, $y = 0$.
- Point C corresponds to the rightmost point from which all rivulets will enter the top edge of the breach. Point C lies between the origin and $+\ell$ (right side of the breach).
- Point D corresponds to the rightmost point at which the edge of the fan from the rivulet can enter the right side of the breach.

Rivulets originating between Point A and Point $-\ell$ can (all or partially) flow into the left side or the top of the breach. Symmetrically, rivulets originating between Point $+\ell$ and Point D can (all or partially) flow into the right side or the top of the breach. All rivulets originating between Point $-\ell$ and $+\ell$ completely flow only into the top of the breach, not into the sides. The y -coordinates of Points A through D are:

$$\begin{aligned} y_A &= -\ell - (x + 2\ell)\tan\alpha \\ y_B &= -\ell + x\tan\alpha \\ y_C &= \ell - x\tan\alpha \\ y_D &= \ell + (x + 2\ell)\tan\alpha. \end{aligned} \tag{Eq. 6.5.1.1.2.1-1}$$

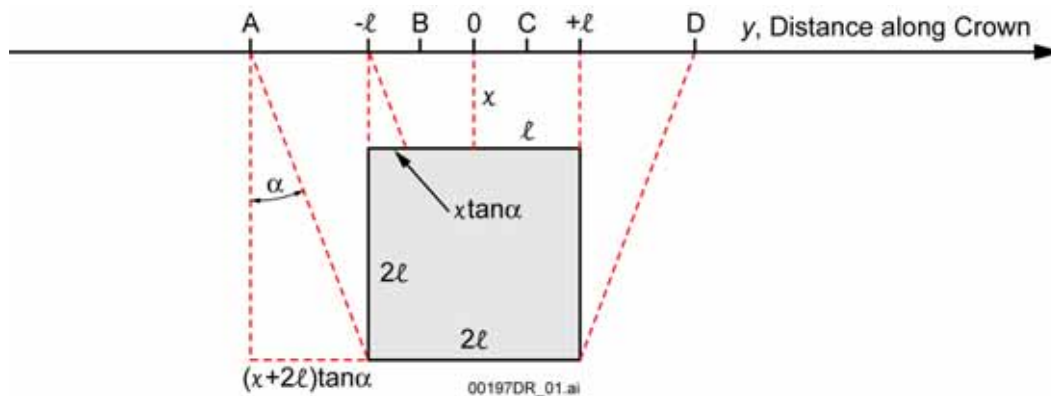


Figure 6.5-1. Geometry and Nomenclature for a Centrally Located Breach with $\ell > x \tan \alpha$

For a uniform distribution of rivulet flow between $-\alpha$ and $+\alpha$, the fraction f of the random rivulet flow that enters the breach depends on the origin y of the rivulet:

- For $y \leq y_A$ $f_{A-} = 0$
- For $y_A < y \leq -\ell$,

$$f_{A\ell} = \frac{y + \ell + (x + 2\ell)\tan\alpha}{2(x + 2\ell)\tan\alpha} \tag{Eq. 6.5.1.1.2.1-2}$$

- For $-\ell < y < y_B$,

$$f_{\ell B} = \frac{y + \ell + x\tan\alpha}{2x\tan\alpha} \tag{Eq. 6.5.1.1.2.1-3}$$

- For $y_B \leq y \leq y_C$,

$$f_0 = 1 \tag{Eq. 6.5.1.1.2.1-4}$$

- For $y_C < y < \ell$,

$$f_{C\ell} = \frac{-y + \ell + x\tan\alpha}{2x\tan\alpha} \tag{Eq. 6.5.1.1.2.1-5}$$

- For $\ell \leq y < y_D$,

$$f_{\ell D} = \frac{-y + \ell + (x + 2\ell) \tan \alpha}{2(x + 2\ell) \tan \alpha} \quad (\text{Eq. 6.5.1.1.2.1-6})$$

- For $y \geq y_D$, $f_{D+} = 0$

In this context, f is essentially a probability distribution function (i.e., the probability that a rivulet will intersect the square corrosion patch). Integrating f over the full length of the drip shield (from $-L_{DS}/2$ to $+L_{DS}/2$) gives the total water flux through a breach of width 2ℓ . Then the fraction F ($= F_2 / F_1$) of seepage flux passing through the breach is:

$$F = \frac{1}{2L_{DS}} \int_{-L_{DS}/2}^{L_{DS}/2} f(y) dy \quad (\text{Eq. 6.5.1.1.2.1-7})$$

$$= \frac{1}{2L_{DS}} \left[\int_{y_A}^{\ell} f_{A\ell}(y) dy + \int_{\ell}^{y_B} f_{\ell B}(y) dy + \int_{y_B}^{y_C} f_0 dy + \int_{y_C}^{\ell} f_{C\ell}(y) dy + \int_{\ell}^{y_D} f_{\ell D}(y) dy \right] \quad (\text{Eq. 6.5.1.1.2.1-8})$$

$$= \frac{\ell}{L_{DS}} + \frac{\ell \tan \alpha}{2L_{DS}}. \quad (\text{Eq. 6.5.1.1.2.1-9})$$

The factor of 2 in the denominator starting in Equation 6.5.1.1.2.1-7 accounts for the seepage flux being split in two when it drips onto the crown of the drip shield, and half of the flux flows down each side.

The result is independent of x , the distance from the crown. The amount of seepage flux that flows into a breach is, however, dependent on the rivulet spread angle α . This is reasonable because a wider spread angle allows rivulets from a wider span of the crown to access the breach. In effect, the width of the drip shield crown from which rivulets can flow into a breach is expanded from 2ℓ to $2\ell + \ell \tan \alpha$. Flow into the sides of the breach contributes only a small amount to the total if the spread angle is small. If, for example, $\alpha = 13.2^\circ$ (the mean spread angle from the drip shield experiments), the total flow into a breach, from Equation 6.5.1.1.2.1-9, is $(\ell / L_{DS})(1 + 0.117)$, so only about $0.117 / 1.117 \approx 1/10$ of the total breach flow enters through the sides of the breach.

As a check on this result, consider the case where the rivulets do not spread out over an angle α , but instead flow straight down (i.e., $\alpha = 0 = \tan \alpha$). Then Equation 6.5.1.1.2.1-9 becomes:

$$F = \frac{\ell}{L_{DS}}, \quad (\text{Eq. 6.5.1.1.2.1-10})$$

or

$$F_2 = F_1 \frac{\ell}{L_{DS}}. \quad (\text{Eq. 6.5.1.1.2.1-11})$$

Equation 6.5.1.1.2.1-11 is identical to Equation 6.5.1.1.1.1-2, which was obtained from simple logic arguments.

As a further check on the validity of Equation 6.5.1.1.2.1-9, consider a single patch located adjacent to the crown, just far enough away from the crown that the dripping seepage flux can impinge on the crown and flow down both sides (i.e., $x \approx 0$, about the width of a drop). Water flowing from the crown toward the patch will immediately enter the patch, since the spread over the angle α is negligible. Seepage flux dripping onto the drip shield crown to the left and right of the patch will flow down the drip shield in rivulets, fanning out over the angle α . In this case, $y_A = -\ell - 2\ell \tan \alpha$, $y_B = -\ell$, $y_C = +\ell$, and $y_D = \ell + 2\ell \tan \alpha$. The fractions of the rivulet flow down one side of the drip shield into the patch are:

- For $y \leq y_A$, $f_{A-} = 0$

- For $y \leq y_A$, $f_{A-} = 0$,

$$f_{A\ell} = \frac{y + \ell + 2\ell \tan \alpha}{4\ell \tan \alpha} \quad (\text{Eq. 6.5.1.1.2.1-12})$$

- For $-\ell \leq y \leq \ell$,

$$f_0 = 1 \quad (\text{Eq. 6.5.1.1.2.1-13})$$

- For $y_C = \ell < y < y_D$,

$$f_{\ell D} = \frac{-y + \ell + 2\ell \tan \alpha}{4\ell \tan \alpha} \quad (\text{Eq. 6.5.1.1.2.1-14})$$

- For $y \geq y_D$, $f_{D+} = 0$.

Moving right from $y = y_A$, where $f = 0$, f increases linearly until $y = -\ell^-$ (on the left side of $-\ell$), where $f = 1/2$; because half of the rivulet fan is directed away from the patch at that point, at most half of the rivulet will enter the patch. Between $-\ell$ and $+\ell$, all of the rivulets flow directly into the patch, so $f = 1$. As on the left side of the patch, to the right of the patch, from $y = \ell$ to $y = y_D = \ell + 2\ell \tan \alpha$, f decreases linearly from $1/2$ to 0. Performing the same integration as in Equations 6.5.1.1.2.1-7 and 6.5.1.1.2.1-8 results in:

$$F = \frac{\ell}{L_{DS}} + \frac{\ell \tan \alpha}{2L_{DS}}, \quad (\text{Eq. 6.5.1.1.2.1-15})$$

which is again identical to Equation 6.5.1.1.2.1-9. Since, as seen earlier, the flow into the top edge of the patch is ℓ/L_{DS} , the term $\ell \tan \alpha/(2L_{DS})$ accounts for rivulet flow into the sides of the patch for this bounding example.

Multiple patches increase the flow into patches in direct proportion to the number of patches, assuming that patches do not interfere:

$$F = N_b \left[\frac{\ell}{L_{DS}} + \frac{\ell \tan \alpha}{2L_{DS}} \right], \quad (\text{Eq. 6.5.1.1.2.1-16})$$

or

$$F_2 = F_1 N_b \left[\frac{\ell}{L_{DS}} + \frac{\ell \tan \alpha}{2L_{DS}} \right]. \quad (\text{Eq. 6.5.1.1.2.1-17})$$

If patches are located below other patches, the rivulets are intercepted by the higher patches, and none or less flows into lower patches. In that case, the flux through the drip shield, F_2 , is less than predicted by Equation 6.5.1.1.2.1-17. That is, neglecting interference among multiple patches and using Equation 6.5.1.1.2.1-17 overestimates releases of radionuclides.

6.5.1.1.2.2 Drip Shield Flux for a Centrally Located Breach, Case 2

In Case 2, $\ell < x \tan \alpha$; in other words, the breach is narrower than the rivulet spread at the top of the breach (see Figure 6.5-2). In Case 1, over some range of y centered at $y = 0$, all of the rivulet flow enters the top edge of the breach ($f_0 = 1$). In contrast, in Case 2, the rivulet spread is too wide for all of the rivulet flow to enter the breach at any point ($f_0 < 1$).

Points A through D are defined as follows:

- Point A corresponds to the leftmost point from which the edge of the fan from the rivulet can enter the left side and top of the breach.
- Point B corresponds to the rightmost point from which rivulets cannot spread beyond the upper right corner of the breach. Point B lies between $-\ell$ (left side of the breach) and the origin, $y = 0$. Rivulets originating between $-\ell$ and Point B enter only a portion of the top edge of the breach.
- Point C corresponds to the leftmost point from which rivulets cannot spread beyond the upper left corner of the breach. Point C lies between the origin and $+\ell$ (right side of the breach). Rivulets originating between Point C and $+\ell$ enter only a portion of the top edge of the breach. Rivulets originating between Point B and Point C can enter the entire top edge of the breach.
- Point D corresponds to the rightmost point at which the edge of the fan from the rivulet can enter the right side and top of the breach.

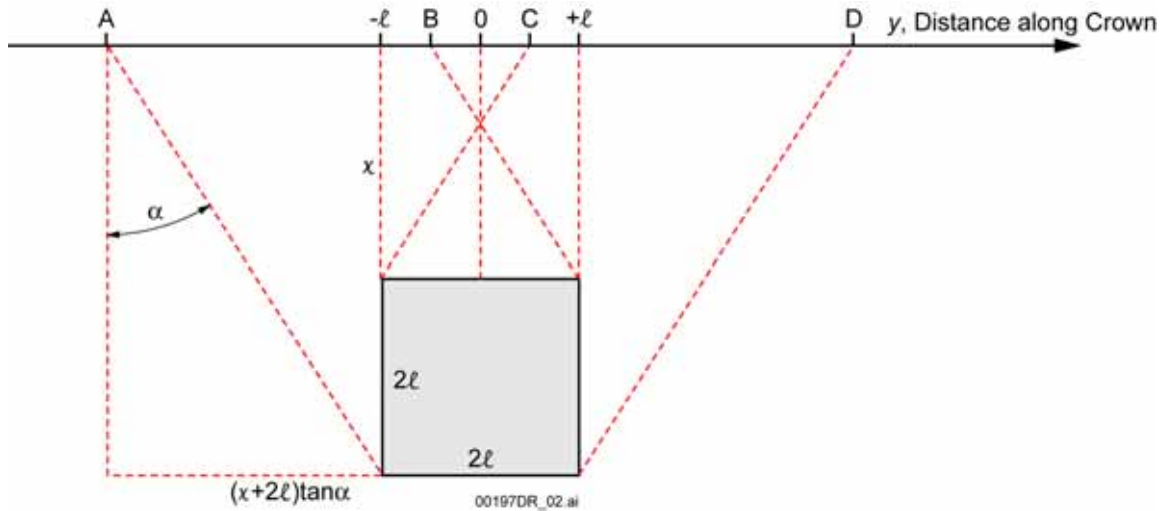


Figure 6.5-2. Geometry and Nomenclature for a Centrally Located Breach with $\ell < x \tan \alpha$

As in Case 1, rivulets originating between Point A and Point $-\ell$ can flow into the left side or the top of the breach. Symmetrically, rivulets originating between Point $+\ell$ and Point D can flow into the right side or the top of the breach. All rivulets originating between Point $-\ell$ and $+\ell$ flow only into the top of the breach, not into the sides. The y -coordinates of Points A through D are:

$$\begin{aligned}
 y_A &= -\ell - (x + 2\ell) \tan \alpha \\
 y_B &= \ell - x \tan \alpha \\
 y_C &= -\ell + x \tan \alpha \\
 y_D &= \ell + (x + 2\ell) \tan \alpha.
 \end{aligned}
 \tag{Eq. 6.5.1.1.2.2-1}$$

The central region boundaries, y_B and y_C , are different for Case 2 than for Case 1.

For a uniform distribution of rivulet flow between $-\alpha$ and $+\alpha$, the fraction f of the random rivulet flow that enters the breach depends on the origin y of the rivulet. These fractions are identical for corresponding regions to those in Case 1 except for the region $y_B \leq y \leq y_C$, where now $f_0 < 1$ instead of $f_0 = 1$.

- For $y \leq y_A$, $f_{A-} = 0$
- For $y_A < y \leq -\ell$,

$$f_{A\ell} = \frac{y + \ell + (x + 2\ell) \tan \alpha}{2(x + 2\ell) \tan \alpha}
 \tag{Eq. 6.5.1.1.2.2-2}$$

- For $-\ell < y < y_B$,

$$f_{\ell B} = \frac{y + \ell + x \tan \alpha}{2x \tan \alpha}
 \tag{Eq. 6.5.1.1.2.2-3}$$

- For $y_B \leq y \leq y_C$,

$$f_0 = \frac{2\ell}{2x \tan \alpha} \quad (\text{Eq. 6.5.1.1.2.2-4})$$

- For $y_C < y < \ell$,

$$f_{Cl} = \frac{-y + \ell + x \tan \alpha}{2x \tan \alpha} \quad (\text{Eq. 6.5.1.1.2.2-5})$$

- For $\ell \leq y < y_D$,

$$f_{lD} = \frac{-y + \ell + (x + 2\ell) \tan \alpha}{2(x + 2\ell) \tan \alpha} \quad (\text{Eq. 6.5.1.1.2.2-6})$$

- For $y \geq y_D$, $f_{D+} = 0$.

Integrating f over the full length of the drip shield (from $-L_{DS}/2$ to $+L_{DS}/2$), as in Case 1, gives the total water flux through a breach of width 2ℓ . The fraction F ($= F_2 / F_1$) of seepage flux passing through the breach is:

$$F = \frac{1}{2L_{DS}} \int_{-L_{DS}/2}^{+L_{DS}/2} f(y) dy \quad (\text{Eq. 6.5.1.1.2.2-7})$$

$$= \frac{1}{2L_{DS}} \left[\int_{y_A}^{\ell} f_{A\ell}(y) dy + \int_{\ell}^{y_B} f_{\ell B}(y) dy + \int_{y_B}^{y_C} f_0 dy + \int_{y_C}^{+\ell} f_{Cl}(y) dy + \int_{+\ell}^{y_D} f_{lD}(y) dy \right] \quad (\text{Eq. 6.5.1.1.2.2-8})$$

$$= \frac{\ell}{L_{DS}} + \frac{\ell \tan \alpha}{2L_{DS}}. \quad (\text{Eq. 6.5.1.1.2.2-9})$$

For Case 2, the seepage flux passing through the breach is identical to Case 1 (Equation 6.5.1.1.2.1-9). This is reasonable considering that F is independent of x . In other words, the breach can be located at any distance from the crown, and the same fraction of seepage flux will flow into it. The two cases are really a single case where the breach in Case 2 is simply located further from the crown than in Case 1.

6.5.1.1.2.3 Drip Shield Flux for an End-Located Patch

The drip shield design (BSC 2007 [DIRS 179843]) includes a connector guide at one end and a connector plate at the other end that, being thicker than the plates comprising the top and sides of the drip shield, should survive intact longer than the plates. These components will prevent any rivulets from flowing off the ends of the drip shield. This will alter the fraction of rivulet flow that enters patches that are located at the ends of the drip shield. If the patch is located a short distance from the end, the space between the patch and the connector guide will allow water diverted by the guide to flow down the drip shield instead of into the patch. This distance is unknown, but for simplicity is chosen to be zero (i.e., if the patch is not coincident with the connector guide, it behaves as a centrally located patch).

Consider a breach that is located at one end of the drip shield. Figure 6.5-3 illustrates the location and geometry for potential rivulet flows into a breach with length 2ℓ and whose top edge is located a distance of x from the crown. For simplicity in evaluating coordinates, the zero point of the y -axis is again coincident with the center of the patch, and the end of the patch as well as the drip shield are at $y = -\ell$.

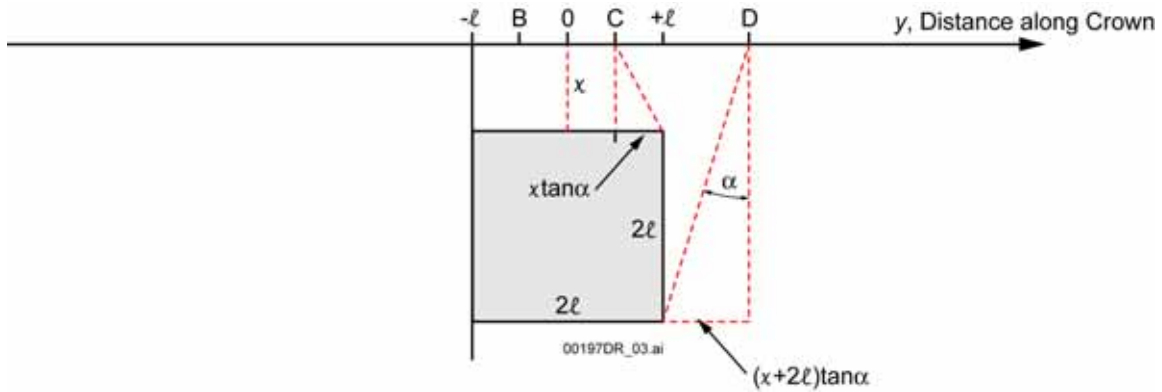


Figure 6.5-3. Geometry and Nomenclature for an End-Located Breach with $\ell > x \tan \alpha$

The Points C and D are defined as above for Case 1. Point A is beyond the end of the drip shield, and distinguishing Point B is unimportant because all rivulets originating to the left of Point C flow completely into the breach.

$$\begin{aligned}
 y_B &= -\ell + x \tan \alpha \\
 y_C &= \ell - x \tan \alpha \\
 y_D &= \ell + (x + 2\ell) \tan \alpha.
 \end{aligned}
 \tag{Eq. 6.5.1.1.2.3-1}$$

It is shown above that the result is independent of x for the centrally located breach. Therefore, either case is adequate for analysis. For the case where $\ell > x \tan \alpha$, corresponding to Case 1 above, the fraction f of rivulet flow into the patch over ranges of y are:

- For $y \leq -\ell$, $f = 0$
- For $-\ell \leq y \leq y_C$,

$$f_0 = 1 \tag{Eq. 6.5.1.1.2.3-2}$$

- For $y_C < y < \ell$,

$$f_{cl} = \frac{-y + \ell + x \tan \alpha}{2x \tan \alpha} \tag{Eq. 6.5.1.1.2.3-3}$$

- For $\ell \leq y < y_D$,

$$f_{\ell D} = \frac{-y + \ell + (x + 2\ell) \tan \alpha}{2(x + 2\ell) \tan \alpha} \quad (\text{Eq. 6.5.1.1.2.3-4})$$

- For $y \geq y_D$, $f_{D+} = 0$.

Integrating f over the full length of the drip shield (from $-L_{DS}/2$ to $+L_{DS}/2$) gives the total water flux through a breach of width 2ℓ . The fraction F ($= F_2 / F_1$) of seepage flux passing through the breach is:

$$F = \frac{1}{2L_{DS}} \int_{-L_{DS}/2}^{+L_{DS}/2} f(y) dy \quad (\text{Eq. 6.5.1.1.2.3-5})$$

$$= \frac{1}{2L_{DS}} \left[\int_{-\ell}^{y_C} f_0 dy + \int_{y_C}^{+\ell} f_{C\ell}(y) dy + \int_{+\ell}^{y_D} f_{\ell D}(y) dy \right] \quad (\text{Eq. 6.5.1.1.2.3-6})$$

$$= \frac{\ell}{L_{DS}} + \frac{\ell \tan \alpha}{4L_{DS}}. \quad (\text{Eq. 6.5.1.1.2.3-7})$$

Thus, the seepage flux fraction F for breaches at the end of the drip shield is independent of the distance x from the crown. The only difference from centrally located breaches is the term that accounts for flow into the side of a breach $[\ell \tan \alpha / (4L_{DS})]$. Since only one side of the breach is accessible to rivulet flow, the flow through the one side of the breach at the end of the drip shield is just half of the flow through two sides in a centrally located breach.

As seen above, for a small rivulet spread angle, the portion of the flow into a breach that enters through the side is small. For an end breach, that fraction is even smaller. In the example given in Section 6.5.1.1.2.1, for a mean spread angle of $\alpha = 13.2^\circ$, flow through the sides of the breach accounts for only about 1/10 of the total. For an end breach, based on Equation 6.5.1.1.2.3-7, side flow will account for only 6 percent in this example. In Section 6.5.1.1.2, experimental results are discussed that show the spread angle is approximately 13.2° and that the amount of seepage flux that actually enters a breach varies widely. Differences of 6 percent are negligible. Since the end-located breach model (Equation 6.5.1.1.2.3-7) applies only to breaches that are exactly at the ends of the drip shield, which will be an infrequent occurrence, it is reasonable to ignore the distinction between end breaches and centrally located breaches.

Then the flux through one patch in the drip shield is:

$$F_2 = F_1 \frac{\ell}{L_{DS}} \left(1 + \frac{\tan \alpha}{2} \right). \quad (\text{Eq. 6.5.1.1.2.3-8})$$

6.5.1.1.2.4 Analysis of Breached Drip Shield Experiments

The breached drip shield experiments (BSC 2002 [DIRS 158193]; BSC 2003 [DIRS 163406]) provide estimates of the rivulet spread factor from which the spread angle α can be determined (DTN: MO0207EBSATBWP.022 [DIRS 163400]), the splash radius from drops falling from the roof of the drift to the crown of the drip shield (DTN: MO0207EBSATBWP.022 [DIRS 163400]), and the flow into breaches from a number of discrete drip locations (DTN: MO0207EBSATBWP.023 [DIRS 163402]). In addition, the tests characterized the flow behavior on the drip shield surface, determining that flow occurs as rivulets rather than as film flow.

In Splash Radius Test #1 (DTN: MO0207EBSATBWP.022 [DIRS 163400]), water was dripped onto the drip shield crown, and the distance that the water splattered was measured. In 12 separate sets of measurements (Table 4.1-4), using from 1 to 90 drips, splash distances to the right ranged from 1.6 cm (single drip) to 63.2 cm (49 drips); splash distances to the left ranged from 1.6 cm (single drip) to 72.5 cm (60 drips). Tests using larger numbers of drips tended to result in larger maximum splash distances. “Outer fringe” measurements using more than 20 drips ranged from 31.5 cm to 72.5 cm, whereas “inner cluster” measurements using more than 20 drips ranged from 25.0 cm to 48.0 cm. The definition of the grouping as “outer fringe” and “inner cluster” was not specified, but the results indicate a distribution of splashed water heavily weighted to a median radius of about 40 cm.

The splash radius is useful for providing a distribution of rivulet origins based on limited experimental data. In the flow tests, water was dripped onto the drip shield in only a few discrete locations. In order to make greater use of the data to determine the uncertainty in applying the drip shield flux splitting submodel (Equation 6.5.1.1.2.3-8), the distribution of splattered water can be treated as multiple drip locations in comparing Equation 6.5.1.1.2.3-8 to the experimental data.

Rivulet spread was measured in single patch $q(\text{film})$ tests (DTN: MO0207EBSATBWP.023 [DIRS 163402]), multiple patch tests (DTN: MO0207EBSATBWP.024 [DIRS 163401]), and in bounding flow rate tests (DTN: MO0207EBSATBWP.025 [DIRS 163403]). Table 4.1-3 summarizes the maximum rivulet spread to the left and right of a straight line down the drip shield from the drip impact point. The rivulet spread data are analyzed in Microsoft Excel spreadsheet: Flux Split Drip Shield Model, Worksheet: Spread angles, which is documented in Appendix C. The results—the mean and range of spread angles—are reported in Section 6.5.1.1.2.

Rivulet spread measurements at the top edge of patches in the drip shield mock-up are used. The distance x from the drip location on the crown of the drip shield to the point of measurement is determined from the drawing of the drip shield mock-up shown in Figure 4.1-1, which is reproduced from Howard (2002 [DIRS 161516], p. 14). Various dimensions used in the Microsoft Excel spreadsheet analysis of the data are listed in Table 6.5-1. Because the drip shield top surface is a circular arc (Figure 4.1-1), the 16.5° line is at half the distance from the crown to the 33° line, or 0.43 m from the crown.

Table 6.5-1. Dimensions Used in the Analysis of Breached Drip Shield Experiments, Based on Dimensions Shown in Figure 4.1-1

Dimension	Calculation	Distance (m)
Crown to 33° line	2.44 m – 0.94 m – 0.64 m	0.86
Crown to 16.5° line	½ distance from Crown to 33° line	0.43
Crown to top edge of Patch 4	2.44 m – 0.94 m – 0.135 m	1.365
Crown to top edge of Patch 5	2.44 m – 0.94 m – 0.64 m	0.86
Crown to transition line	2.44 m – 0.94 m	1.50
16.5° line to transition line	0.43 m (Crown to 16.5° line)+ 0.64 m	1.07
16.5° line to 33° line	½ distance from Crown to 33° line	0.43
16.5° line to Patch 4	0.43 m (Crown to 16.5° line)+ 0.64 m – 0.135 m	0.935
16.5° line to Patch 5	½ distance from Crown to 33° line	0.43
33° line to Patch 4	0.64 m – 0.135 m	0.505
33° line to transition line	0.64 m	0.64
½ distance between Crown and 16.5° line to Patch 4	½(0.43 m [Crown to 16.5° line]) + 0.43 m (16.5° line to 33° line) + 0.64 m -0.135 m	1.15

Source: Howard 2002 [DIRS 161516], p. 14.

Since the experiments involved dripping at a few discrete locations, it is not possible to calculate the flux through the drip shield as given by Equation 6.5.1.1.2.3-8 using experimental data. Instead, the fraction f of dripping flux at an individual drip location that flows into a given breach can be computed for the tests and compared with the fraction expected using one of the Equations 6.5.1.1.2.1-1 to 6.5.1.1.2.1-6 (Case 1) or 6.5.1.1.2.1-18 to 6.5.1.1.2.1-23 (Case 2). The appropriate equation to be used depends on the drip location relative to the breach. The variability in the experimental values (f_{expt}) and comparisons with calculated values (f_{calc}) show the range of uncertainty in the drip shield flux ratio $F = F_2 / F_1$. The values of f_{expt} and f_{calc} are calculated in Microsoft Excel spreadsheet: Flux Split Drip Shield Model, Worksheet: f calculations, which is documented in Appendix C.

Experimental data from two breaches are pertinent to this analysis—Breach 4 and Breach 5. Breach 4 straddled the transition line between the top of the drip shield and the vertical side, with the top edge 136.5 cm from the crown. Breach 5 was located on the top of the drip shield, about half way between the crown and the transition line, with the top edge 86 cm from the crown.

Table 6.5-2 shows the fraction of the total dripping flux that entered a breach in each of 14 tests. The data sources are single patch q(film) test results (DTN: MO0207EBSATBWP.023 [DIRS 163402]), multiple patch test results (DTN: MO0207EBSATBWP.024 [DIRS 163401]), and bounding flow rate test results (DTN: MO0207EBSATBWP.025 [DIRS 163403]), and are given in Table 4.1-2. The results are compared with calculated fractions for the mean spread angle as well as for the spread angles corresponding to plus or minus one standard deviation from the mean rivulet spread angle. The experimentally observed fractions, f_{expt} , were calculated assuming that one-half of the measured total dripping flux flowed down the side of the drip shield where the breaches were located. This is necessary for f_{expt} to be consistent with the fractions in Sections 6.5.1.1.2.1 and 6.5.1.1.2.2, which are the fractions of flow down one side of the drip shield that enters a breach.

Table 6.5-2. Comparison of Experimental Breach Inflow Fractions with Model Calculations from Appendix C

Drip Location (Test Description)	Breach No.	y, Drip Location Relative to Breach Center (cm)	x, Vertical Distance from Crown (drip) to Top of Breach ^a (cm)	f_{expt}	f_{calc}		
					$\alpha=8.9^\circ$	$\alpha=13.2^\circ$	$\alpha=17.3^\circ$
8 cm right of Patch 4 centerline (Q[film] Test)	4	8	136.5	0.247	0.629	0.423	0.318
Patch 5 centerline (Q[film] Test)	5	0	86.0	0.258	1.000	0.672	0.504
4 cm left of Patch 5 centerline (Q[film] Test)	5	-4	86.0	0.136	0.854	0.680	0.504
Patch 4 centerline (Q[film] Test)	4	0	136.5	0.236	0.634	0.423	0.318
27 cm right of drip shield center (Multiple Patch Test)	5	-27	86.0	0.033	0.117	0.244	0.504
27 cm left of drip shield center (Multiple patch test)	4	27	136.5	0.019	0.236	0.323	0.318
81 cm left of drip shield center (Multiple Patch Test)	4	-27	136.5	0.031	0.236	0.323	0.318
81 cm right of drip shield center (Multiple Patch Test)	5	27	86.0	0.032	0.117	0.244	0.504
54 cm left of drip shield center (High Flow Rate Test)	4	0	136.5	0.275	0.634	0.423	0.318
54 cm left of drip shield center (Low Flow Rate Test)	4	0	136.5	0.177	0.634	0.423	0.318
27 cm left of drip shield center (High Flow Rate Test)	4	27	136.5	0.020	0.236	0.323	0.318
27 cm left of drip shield center (Low Flow Rate Test)	4	27	136.5	0.013	0.236	0.323	0.318
27 cm right of drip shield center (High Flow Rate Test)	5	-27	86.0	0.013	0.117	0.244	0.504
Mean				0.111	0.414	0.380	0.398
Std. Dev.				0.106	0.305	0.144	0.096

Table 6.5-2. Comparison of Experimental Breach Inflow Fractions with Model Calculations from Appendix C (Continued)

Drip Location (Test Description)	Breach No.	y, Drip Location Relative to Breach Center (cm)	x, Vertical Distance from Crown (drip) to Top of Breach ^a (cm)	f_{expt}	f_{calc}		
					$\alpha=8.9^\circ$	$\alpha=13.2^\circ$	$\alpha=17.3^\circ$
Std. Dev.				0.106	0.305	0.144	0.096
Median				0.049	0.236	0.323	0.318
Minimum				0.013	0.117	0.244	0.318
Maximum				0.275	1.000	0.680	0.504

^a Vertical distance from crown to top of breach is calculated in Table 6.5-1.

DTNs: MO0207EBSATBWP.023 [DIRS 163402]; MO0207EBSATBWP.024 [DIRS 163401];
MO0207EBSATBWP.025 [DIRS 163403].

The experimentally observed fraction of drip seepage flowing into a breach varies widely. This variability is primarily due to the drip location—when the drip location is centered over the breach, much of the flow enters the breach, and when the drip is far off to the side of a breach, little of it enters the breach. However, the variability also includes differences in drip rate, the distance from the crown to the breach, evaporation from the drip shield surface, and random variability in drop splashing and rivulet flow behavior.

The fraction of drip seepage flowing into a breach calculated from the model is found always to be higher than observed experimentally, particularly when the drip location is far from the breach. When the drip location is well away from the patch center, and little water flows into the breaches (f_{expt} less than about 0.1), the model overestimates the experimental fraction increasingly as the estimated spread angle increases (see Table 6.5-3). In contrast, the model predicts that ever-increasing amounts of water flow into a breach as the spread angle increases. This can be seen in Equation 6.5.1.1.2.3-8, which shows that the flow into breaches is proportional to $(1 + \frac{1}{2} \tan \alpha)$, so as the spread angle α increases, so does the flow into breaches. Evaporation also plays a part. The model assumes no evaporative losses (Assumption 5.2), whereas evaporation from the drip shield occurred in the experiments because the relative humidity was less than 100 percent. Using a larger spread angle in the model results in increased predicted flow into a breach, whereas evaporation consistently reduces the experimentally measured inflow. Thus, ignoring the observed occurrence of evaporation in the development of the drip shield flux splitting submodel will overestimate the transport of radionuclides.

When the drip location is directly above the breach, the model agrees more closely with experiments as the spread angle increases. Again, the model generally overestimates the flow into breaches. In this case, as the estimated spread angle increases, less flow into breaches is predicted, so the model agrees more closely with experiments.

A major reason for the differences between the flux splitting submodel calculations and the experimental results is that splashing of the drops when they impinged on the drip shield resulted in a dispersed source of rivulets. In contrast, the model supposes that the entire dripping flux flows down the drip shield from the point of impact. Splattering spreads the dripping flux over a

wide span of the drip shield crown. The splash radius tests recorded splashes that extended up to 72.5 cm from the drip location, with an “inner cluster” radius of 25 cm to 48 cm (DTN: MO0207EBSATBWP.022 [DIRS 163400]). In three of the q(film) rivulet flow tests, lateral splash distances ranging from 54.5 cm to 86 cm from the drip point on the crown were observed (DTN: MO0207EBSATBWP.023 [DIRS 163402], Drip Location: Patch 5, center, crown; Patch 4, center, crown; and Patch 4, 8 cm right of center, crown). Since a large portion of the dripping flux in the tests splattered beyond the range of rivulet flow into individual breaches, the flow into breaches was much less than predicted by the model. Thus, ignoring the observed occurrence of splattering in the development of the drip shield flux splitting submodel will overestimate the transport of radionuclides.

Table 6.5-3. Additional Comparisons of Experimental Breach Inflow Fractions with Model Calculations from Appendix C

Drip Location (Test Description)	f_{expt}	$f_{calc} - f_{expt}$			f_{calc} / f_{expt}		
		$\alpha=8.9^\circ$	$\alpha=13.2^\circ$	$\alpha=17.3^\circ$	$\alpha=8.9^\circ$	$\alpha=13.2^\circ$	$\alpha=17.3^\circ$
8 cm right of Patch 4 centerline (Q[film] Test)	0.247	0.382	0.176	0.071	2.545	1.713	1.286
Patch 5 centerline (Q[film] Test)	0.258	0.742	0.414	0.246	3.876	2.604	1.955
4 cm left of Patch 5 centerline (Q[film] Test)	0.136	0.718	0.544	0.368	6.277	4.998	3.707
Patch 4 centerline (Q[film] Test)	0.236	0.398	0.187	0.082	2.686	1.794	1.347
27 cm right of drip shield center (Multiple Patch Test)	0.033	0.085	0.212	0.472	3.606	7.515	15.507
27 cm left of drip shield center (Multiple patch test)	0.019	0.217	0.304	0.299	12.393	17.016	16.722
81 cm left of drip shield center (Multiple Patch Test)	0.031	0.205	0.293	0.287	7.720	10.600	10.417
81 cm right of drip shield center (Multiple Patch Test)	0.032	0.085	0.212	0.472	3.662	7.632	15.750
54 cm left of drip shield center (High Flow Rate Test)	0.275	0.359	0.148	0.043	2.306	1.540	1.156
54 cm left of drip shield center (Low Flow Rate Test)	0.177	0.456	0.246	0.140	3.574	2.387	1.792
27 cm left of drip shield center (High Flow Rate Test)	0.020	0.215	0.303	0.298	11.693	16.055	15.777
27 cm left of drip shield center (Low Flow Rate Test)	0.013	0.223	0.310	0.305	18.286	25.108	24.673
27 cm right of drip shield center (High Flow Rate Test)	0.013	0.104	0.231	0.491	9.064	18.888	38.978
27 cm right of drip shield center (Low Flow Rate Test)	0.065	0.053	0.180	0.440	1.815	3.781	7.804

Table 6.5-3. Additional Comparisons of Experimental Breach Inflow Fractions with Model Calculations from Appendix C (Continued)

Drip Location (Test Description)	f_{expt}	$f_{calc} - f_{expt}$			f_{calc} / f_{expt}		
		$\alpha=8.9^\circ$	$\alpha=13.2^\circ$	$\alpha=17.3^\circ$	$\alpha=8.9^\circ$	$\alpha=13.2^\circ$	$\alpha=17.3^\circ$
Mean	0.111	0.303	0.269	0.287	6.393	8.688	11.205
Std. Dev.	0.106	0.221	0.107	0.155	4.885	7.672	11.033
Median	0.049	0.220	0.239	0.298	3.769	6.256	9.110
Minimum	0.013	0.053	0.1484	0.043	1.8145	1.540	1.156
Maximum	0.275	0.742	0.5439	0.491	18.286	25.108	38.978

Table 6.5-4. Water Collected in Drip Shield Experiment Q(film); Drip Location: Patch 4, 8 cm Right of Center, Crown

Collection Station	Initial Mass (g)	Final Mass (g)	Net Water Mass (g)	Water Collected in Each Group of Collection Stations (g)
Input Water	-50.32	-228.52	-178.20	178.20
Gutter 1-1	7.652	16.434	8.782	36.351
Gutter 3-1	7.611	8.677	1.066	
Gutter 3-2	7.600	23.213	15.613	
Gutter 3-3	7.612	8.899	1.287	
Gutter 3-4	7.521	17.124	9.603	
Breach 2	107.02	109.00	1.98	24.00
Breach 4	107.60	129.62	22.02	
Drip Shield OUT 1	7.634	8.738	1.104	72.685
Drip Shield OUT 2	7.578	19.681	12.103	
Drip Shield OUT 3	7.574	34.446	26.872	
Drip Shield OUT 4	7.702	40.308	32.606	

DTN: MO0207EBSATBWP.023 [DIRS 163402].

One other cause for the discrepancies between experimental and predicted flow fractions is that, in the model, all dripping flux flows down the drip shield surface. In the experiments, a large amount of water remained on the drip shield as splattered drops that had not yet grown large enough to flow down the surface. For example, Table 6.5-4 shows the amount of water collected in the first experiment listed in Table 6.5-2. Of the 178.2 g of water that was dripped onto the surface, only 60.35 g was collected from the breaches or drainage gutters, whereas 72.685 g, or 41 percent, remained on the surface (“Drip Shield OUT” entries). This is a source of uncertainty in the experimental results that could be reduced by increasing the duration of the experiment far beyond the one-hour length of the test, but is inherent in the experiment and cannot be eliminated. The result is that less of the dripping flux actually flowed down the drip shield surface than is predicted by the model. This also causes the model to overestimate the fraction that flows into breaches, and, therefore, overestimates the transport of radionuclides.

Results presented in Table 6.5-2 and Table 6.5-3 show a large uncertainty in the fraction of rivulet flow that enters breaches. The integrated fraction of flow into breaches, which is the desired result, is not readily discerned from the uncertainty in the inflow fractions, even though the flows obtained experimentally are more clearly quantified.

Another approach, which is used to develop an uncertainty factor for use in TSPA, is to apply the integrated flow fraction approach to a drip shield whose length is about as wide as the splash diameter. If the rivulet source is dispersed along the crown, the integrated flow into a breach, Equation 6.5.1.1.2.3-8, can be applied. However, instead of the full drip shield length, the splash diameter is used for L_{DS} . Thus, for the breached drip shield experiments, L_{DS} has a range that is double the measured range for “inner cluster” splash radius (25 to 48 cm, as discussed at the beginning of this section, Section 6.5.1.1.2.4), or 50 to 96 cm.

The uncertainty in the effective drip shield length and in the spread angle is accounted for in a parameter f_{DS} , and the fraction of seepage flux that enters a breach, F_2/F_1 , is written as in Equation 6.3.2.4-2:

$$F_2/F_1 = \frac{N_b \ell}{L_{DS}} \left(1 + \frac{\tan \alpha}{2} \right) f_{DS}. \quad (\text{Eq. 6.5.1.1.2.4-1})$$

In this approach, the uncertainty factor f_{DS} is obtained by replacing F_2/F_1 with f_{expt} , the experimental fraction of drip flow that enters a breach:

$$\begin{aligned} f_{DS} &= \frac{F_2/F_1}{\frac{\ell}{L_{DS}} \left(1 + \frac{\tan \alpha}{2} \right)} \\ &= \frac{f_{expt}}{\frac{\ell}{L_{DS}} \left(1 + \frac{\tan \alpha}{2} \right)}. \end{aligned} \quad (\text{Eq. 6.5.1.1.2.4-2})$$

The range of values for f_{DS} is obtained by evaluating it with the appropriate minimum and maximum values of L_{DS} and α so as to minimize and maximize f_{DS} . The minimum value of f_{DS} , using $L_{DS} = 50$ cm and $\alpha = 17.3^\circ$, is $f_{DS} = 3.205 f_{expt} = 0.356$ using the mean value of 0.111 for f_{expt} . The maximum value of f_{DS} , using $L_{DS} = 96$ cm and $\alpha = 8.9^\circ$, is $f_{DS} = 6.5947 f_{expt} = 0.732$ using the mean value of 0.111 for f_{expt} . Because zero must be the low end of the range of f_{DS} , these estimates are regarded as a range for the maximum value of f_{DS} . By treating the experimental drip shield as a segment whose length is the splash diameter, a maximum value of 0.36 to 0.73 for the flux splitting uncertainty factor f_{DS} is obtained.

It is also reasonable to use the median value for f_{expt} (0.0486) instead of the mean to define the range for f_{DS} . In this case, f_{DS} would range from 0.16 to 0.32, a factor of 2.3 lower than when

the mean is used, which gives some indication of the degree of uncertainty in the experimental measurements and the resulting flux splitting submodel.

The drip shield flux splitting submodel, Equation 6.3.2.4-4, includes the rivulet spread angle, α . As discussed in Section 6.3.2.4, this equation can be simplified by lumping the uncertainty in α with the range in f_{DS} . In Section 6.5.1.1.2, α was found based on experiments to range from about 8.9° to 17.3° . The uncertainty in α appears as a factor $(1 + \tan \alpha / 2)$, ranging from 1.08 to 1.16, which multiplies f_{DS} , resulting in a range for the product $f'_{DS} = (1 + \tan \alpha / 2)f_{DS}$. The maximum for f'_{DS} based on experimental results is $(1.16)(0.73) = 0.85$ (using the maximum spread angle of 17.3° in the factor $(1 + \tan \alpha / 2)$ and the minimum spread angle of 8.9° to define f_{DS}). This “maximum” is based on the mean of the f_{expt} . The proper way to obtain f_{DS} would be to use a complete set of values for f_{expt} , L_{DS} , and α for each experiment, and then determine the minimum and maximum of f_{DS} . However, the data were not obtained that way; i.e., these were measured in separate experiments, so a consistent set of $(f_{expt}, L_{DS}, \alpha)$ data does not exist. f_{expt} and L_{DS} would not both be expected to be large in a single experiment—if splashing is widespread (L_{DS} is large), not so much will flow into a single breach (f_{expt} will be small), which will not necessarily maximize f_{DS} . So pairing each f_{expt} with extremes of L_{DS} and α is not appropriate, and use of composite measurements (means, standard deviations) is preferred, especially for f_{expt} . Whereas L_{DS} and α for any one experiment can be considered something of a composite measure (L_{DS} because it represents many drops; α because it is the maximum observed during transient behavior), f_{expt} is a single measurement. Due to the sparseness and wide scatter of the experimental data, an individual measurement of f_{expt} is not considered to be an appropriate indicator of the behavior of flow on the drip shield, so the mean of f_{expt} is used.

The sampled parameter is then f'_{DS} , and the drip shield flux splitting algorithm is:

$$F_2 = \min \left[F_1 \frac{N_b \ell}{L_{DS}} f'_{DS}, F_1 \right], \quad (\text{Eq. 6.5.1.1.2.4-3})$$

which is identical to Equation 6.3.2.4-6. Using the higher value of maximum for f'_{DS} of 0.85 is both more reliable, being based on experimental data, and overestimates releases of radionuclides by predicting a higher water flow rate through the drip shield. The range for f'_{DS} to be used in TSPA is 0 to 0.85. A uniform distribution is appropriate for f'_{DS} because insufficient data are available to define any other distribution.

6.5.1.1.3 Water Flux through a Breached Waste Package

The submodel for flow through a breached waste package is conceptually identical to the submodel for flow through a breached drip shield. Key features listed at the start of Section 6.5.1.1.1 apply to both the drip shield and waste package cases. The waste package and drip shield flow submodels differ in two important respects: (1) the radius of curvature of the waste package is less than that of the drip shield; and (2) the nominal corrosion patch size as modeled by WAPDEG (SNL 2007 [DIRS 178871]) is smaller for a waste package than for the drip shield. These differences have no effect on the formulation of the waste package flow model. However, they have an effect on the values of uncertainty parameters that are part of the model. Because experiments were performed on a breached drip shield mock-up but not on a breached waste package mock-up, application of drip shield data to the waste package flow model introduces additional uncertainty in development of the model; however, these uncertainties cannot be quantified.

The water flux through a breached waste package, F_4 , as developed in Section 6.3.3.3, is given by:

$$F_4 = \min \left[F_2 \frac{N_{bWP} \ell_{WP}}{L_{WP}} f'_{WP}, F_2 \right], \quad (\text{Eq. 6.5.1.1.3-1})$$

where F_2 is the flux through the breached drip shield. This is a simplification of a more rigorous expression:

$$F_4 = \min \left[F_2 \frac{N_{bWP} \ell_{WP}}{L_{WP}} \left(1 + \frac{\tan \alpha}{2} \right) f_{WP}, F_2 \right], \quad (\text{Eq. 6.5.1.1.3-2})$$

which explicitly accounts for the rivulet spread angle α . Because α is an uncertainty parameter itself, it can be lumped in with the parameter f_{WP} to give f'_{WP} . Equation 6.5.1.1.3-2 is considered first in order to examine the dependence on α .

As with the drip shield model, the primary mechanism for water to enter breaches is via rivulet flow that originates from an area around the point of drip impact. The rivulets spread out in a delta formation from the point of impact defined by a half-angle, α , and the lateral spread of the rivulet flow is given by $2x \tan \alpha$, where x is the distance along the surface from the crown to the top edge of the breach. The smaller radius of curvature of the waste package would be expected to result in a smaller spread angle, although the difference may be lost in the variability and uncertainty of rivulet flow. The radius of curvature of the drip shield is 1.40 m, whereas waste package radii range from 0.941 m for a 21-PWR (SNL 2007 [DIRS 179394]) to 1.022 m –or a 5-DHLW/DOE Long (SNL 2007 [DIRS 179567]).

Rivulet spread measurements (DTNs: MO0207EBSATBWP.023 [DIRS 163402] and MO0207EBSATBWP.025 [DIRS 163403]) at the 16.5° line, at the 33° line, and at the transition line between the curved top surface and the vertical side of the drip shield mock-up are used. The distance x from the drip location to the point of measurement is determined from the

drawing of the drip shield mock-up shown in Figure 4.1-1, which is reproduced from Howard (2002 [DIRS 161516], p. 14); various dimensions used in analyzing the data are listed in Table 6.5-1. The rivulet spread angle data are analyzed in Microsoft Excel spreadsheet: Flux Split Waste Package Model, Worksheet: Spread angles, which is documented in Appendix D.

To capture some of the effect of the smaller radius, namely the steeper incline closer to the crown, the data from drip locations that are off the crown of the smooth drip shield surface experiments are used to develop parameters for the waste package model. Additionally, the drop distance to drip locations that are off the crown was greater than for drips on the crown (2.17 m to the crown, 2.22 m to the 16.5° line, and 2.31 m to the 33° line; BSC 2003 [DIRS 163406], p. 6), which more closely mimics the greater drop distance from the drift to the waste package compared with the drip shield surface. The results varied widely. In 20 measurements at the 33° line with drips at the 16.5° line, the mean spread angle was 17.0° ($\pm 11.2^\circ$ = one standard deviation). In 17 measurements at the transition line with drips at the 16.5° line, the mean spread angle was 11.1° ($\pm 4.1^\circ$). In 10 measurements at the transition line with drips at the 33° line, the mean spread angle was 11.5° ($\pm 3.3^\circ$). For all 47 measurements the mean spread angle was 13.7° ($\pm 8.2^\circ$), which is just slightly larger than the spread angle measured for drips on the crown of the drip shield mock-up, although the variability is greater (standard deviation of 8.2°, compared with 4.1° for drips from the crown). Utilizing all of the data available, the spread angle for rivulet flow on the waste package can be assigned a mean value of about 13.7° and a range (\pm one standard deviation) from 5.5° to 22.0°.

The splash distance is uncertain for drip locations off the crown. In four of the q(film) rivulet flow tests, maximum lateral splash distances ranging from 56 cm to 122 cm from the drip point were observed (DTN: MO0207EBSATBWP.023 [DIRS 163402]) for drip locations at the 16.5° line. However, no further observations indicated any change in the “inner cluster” splash distance range of 50 cm to 96 cm from Splash Radius Test #1 (DTN: MO0207EBSATBWP.022 [DIRS 163400]).

The parameter f'_{WP} is obtained from an analysis of experimental data for flow into breaches in the drip shield mock-up from DTNs: MO0207EBSATBWP.023 [DIRS 163402] and MO0207EBSATBWP.025 [DIRS 163403]. Analogous to the analysis of data for the drip shield flux splitting model in Section 6.5.1.1.2, values of f'_{expt} are computed. The flow data are analyzed in Microsoft Excel spreadsheet: Flux Split Waste Package Model, Worksheet: f calculations, which is documented in Appendix D. In Microsoft Excel spreadsheet: Flux Split Waste Package Model, Worksheet: Summary, documented in Appendix D, tables analogous to Tables 6.5-2 and 6.5-3 are presented.

An uncertainty factor f_{WP} that can be obtained by replacing the fraction F_4 / F_2 with f_{expt} :

$$f_{WP} = \frac{F_4 / F_2}{\frac{\ell}{L_{WP}} \left(1 + \frac{\tan \alpha}{2} \right)} \quad (\text{Eq. 6.5.1.1.3-3})$$

$$= \frac{f_{expt}}{\frac{\ell}{L_{WP}} \left(1 + \frac{\tan \alpha}{2} \right)}.$$

The range of values for f_{WP} is obtained by evaluating it with the appropriate minimum and maximum values of L_{WP} and α so as to minimize and maximize f_{WP} . The half-width of the patch used in the experiments ($\ell = 13.5$ cm) is used to evaluate f_{WP} . The minimum value of f_{WP} , using $L_{WP} = 50$ cm and $\alpha = 22.0^\circ$, is $f_{WP} = 3.081 f_{expt} = 0.909$ using the mean value of 0.295 for f_{expt} . The maximum value of f_{WP} , using $L_{WP} = 96$ cm and $\alpha = 5.5^\circ$, is $f_{WP} = 6.784 f_{expt} = 2.001$ using the mean value of 0.295 for f_{expt} .

A much lower range could also be justified by using the median inflow fraction of 0.014 instead of the mean (0.295) to define f_{WP} . In this case, f_{WP} would range from 0.043 to 0.095, which demonstrates the large degree of uncertainty in the experimental measurements and the resulting flux splitting submodel.

The values for f_{WP} discussed in this section actually represent a range for the maximum value of f_{WP} , since the minimum must be zero. If the factor $(1 + \frac{1}{2} \tan \alpha)$ that accounts for the rivulet spread angle is lumped in with f_{WP} , the sampled uncertain factor f'_{WP} has an upper bound (using the maximum rivulet spread angle, $\alpha = 22^\circ$) of 2.41. The range for f'_{WP} to be used in TSPA is 0 to 2.41. The parameter f'_{WP} is assigned a uniform distribution.

6.5.1.2 EBS Transport Model

The EBS transport model consists of a system of coupled mass balance equations for each radionuclide species. Some species occur as embedded mass on the waste form colloids and kinetic sorption mass on iron oxyhydroxide colloids and corrosion products. The waste form embedded mass and kinetic sorption mass on the iron products are treated as distinct species with their own mass balance equations. Coupling of mass balance equations occurs in the spatial sense due to advective/diffusive transport. Coupling occurs between parent and daughter species due to radioactive decay and coupling of mass balance equations occur due to the processes which generate the embedded and kinetic sorption masses. The transport model is more complex than the flow model for several reasons. The transport model is necessarily transient because the mass of each radionuclide at any particular location is dependent on its history (i.e., how far it has traveled, the quantity remaining at the source, and the extent of radioactive decay or ingrowth). Further, several complex interacting processes occur in transport, including

dissolution and precipitation, sorption, advective transport, diffusion, and colloid-facilitated transport. The term “colloid-facilitated transport” includes numerous phenomena, including adsorption and desorption of radionuclides onto mobile and immobile colloids, capture of colloids by solid surfaces and the air-water interface, filtering, dispersion, and diffusion. Transport can take place at any degree of water saturation greater than zero, so the model has to account for water saturation. Dissolution and precipitation may occur at finite rates or sufficiently fast to reach equilibrium. Solubility limits that determine whether, or to what extent, these processes occur are dependent on the chemical environment of the EBS. The EBS transport model applies to the waste package, the invert, and the invert/UZ interface.

Transport of rind mass and corrosion products out of the waste package is not explicitly accounted as the depletion inside the waste package is likely to be insignificant compared to the available mass. For example, the CSNF rind mass that is predominantly made up of schoepite would not be depleted even though uranium transport is modeled. Assuming uranium solubility of 10^{-5} mol L⁻¹ (a constant high value) and multiplying it by the constant advective flux through the waste package of 100 L yr⁻¹ over a time period of one million years results in the transport of 1000 mol of uranium, which is about 3 percent of the ²³⁸U mass per CSNF waste package. The relative mass of corrosion products that would get depleted would be even less because the solubility of ferrihydrite is smaller than that of the uranium, and there is much more corrosion products mass than the rind mass.

Mass Balance for Dissolved and Reversibly Sorbed Radionuclides

As with the flow model, the details of pore structure within the EBS are not important, and macroscopic mass balances using phenomenological rate expressions are appropriate. The starting point is the equation of continuity, or mass balance equation, for each dissolved radionuclide species i (Bird et al. 1960 [DIRS 103524], p. 561):

$$\frac{\partial \rho_i}{\partial t} = -\nabla \cdot \mathbf{J}_i + Q_i^m + \Lambda_i. \quad (\text{Eq. 6.5.1.2-1})$$

Here, ρ_i is the mass concentration of dissolved radionuclide species i (kg i m⁻³ bulk volume), \mathbf{J}_i is the mass flux vector (or mass specific discharge) (kg m⁻² s⁻¹) of dissolved radionuclide species i in the mobile water phase and accounts for advection, hydrodynamic dispersion, and diffusion of the dissolved radionuclide species i . The term Q_i^m is the net rate on a bulk volume basis (kg m⁻³ s⁻¹) of the various mass transfer processes, including reversible and kinetic sorption onto solid stationary materials in the EBS, dissolution and precipitation, and the various colloid-facilitated transport processes. The reaction term, Λ_i , accounts for radioactive decay and ingrowth on a bulk volume basis (i.e., production by decay of the parent of i) (kg m⁻³ s⁻¹). Each of these terms is expanded and described in more detail below, then simplified as appropriate for application in the TSPA Model.

It is convenient to develop the transport model following the approach normally taken in the literature (Corapcioglu and Jiang 1993 [DIRS 105761], pp. 2217 to 2219; Choi and Corapcioglu 1997 [DIRS 161621], p. 306), with particular attention to colloid-facilitated transport, since the complexity of those processes tends to dominate the mathematical

formulation. First, Equation 6.5.1.2-1 is rewritten in terms of concentrations of radionuclides in an unsaturated porous medium. The density, or mass concentration, of dissolved radionuclide species i is given by:

$$\begin{aligned}\rho_i &= \phi S_w C_i \\ &= \theta_w C_i,\end{aligned}\tag{Eq. 6.5.1.2-2}$$

where C_i is the concentration on a water volume basis of radionuclide species i (kg m^{-3}), ϕ is the porosity (m^3 void m^{-3} bulk volume) of a representative elemental volume of EBS, and S_w is the water saturation (m^3 water m^{-3} void), and θ_w is the water content (m^3 water m^{-3} bulk volume), expressed as a fraction, as distinguished from θ , which is expressed as a percentage. The expression for ρ_i is inserted into Equation 6.5.1.2-1, resulting in:

$$\frac{\partial(\theta_w C_i)}{\partial t} = -\nabla \cdot \mathbf{J}_i + Q_i^m + \Lambda_i.\tag{Eq. 6.5.1.2-3}$$

The concentration C_i may be constrained by the solubility limit, C_{si} , which is evaluated in *Dissolved Concentration Limits of Elements with Radioactive Isotopes* (SNL 2007 [DIRS 177418], Section 6.1) for each of 17 elements (actinium, americium, carbon, cesium, chlorine, iodine, neptunium, protactinium, lead, plutonium, radium, selenium, strontium, technetium, thorium, tin, and uranium). Dissolved concentration limits for plutonium, neptunium, uranium, thorium, americium, protactinium, and tin are presented as tabulated functions of environmental conditions (namely, pH and CO_2 fugacity) with one or more uncertainty terms or distributions. Fixed solubility limits are given for the other elements in the list (SNL 2007 [DIRS 177418], Table 8-1), except for actinium and lead, for which transport is not modeled in the TSPA because of their short half-life (about 22 years). To account for actinium dose, secular equilibrium with ^{231}Pa is assumed (SNL 2007 [DIRS 177418], Section 6.1). Lead dose effects are calculated in the TSPA by assuming secular equilibrium with ^{226}Ra (SNL 2007 [DIRS 177418], Section 6.1).

The mass flux vector is expressed as

$$\mathbf{J}_i = -\theta_w \mathbf{D}_i \cdot \nabla C_i + \mathbf{q}_w C_i,\tag{Eq. 6.5.1.2-4}$$

where \mathbf{D}_i is the hydrodynamic dispersion tensor of species i ($\text{m}^2 \text{s}^{-1}$), and \mathbf{q}_w is the specific discharge vector, or Darcy velocity, of water (m s^{-1}). The specific discharge vector is related to the water flow rates F_j ($\text{m}^3 \text{s}^{-1}$) in each pathway j of the EBS flow model (Section 6.5.1.1) by:

$$\mathbf{q}_w = \frac{F_j}{A} \mathbf{n},\tag{Eq. 6.5.1.2-5}$$

where A is the spatially dependent cross sectional flow area within the pathway j (m^2), and \mathbf{n} is a unit vector in the direction of the flow path. Because of the complex flow geometry in the EBS, assigning a value to A is not always straightforward; for example, for pathway 4

(Section 6.5.1.1), flow through the waste package, A can be the cross sectional area of corrosion patches or some fraction of the cross sectional area of a waste package.

The hydrodynamic dispersion, \mathbf{D}_i , can be expressed in terms of two components:

$$\mathbf{D}_i = \mathbf{D}_{di} + D_{mi} \mathbf{I}, \quad (\text{Eq. 6.5.1.2-6})$$

where \mathbf{D}_{di} is the mechanical dispersivity associated with the interstitial water velocity, D_{mi} is the effective molecular diffusion coefficient ($\text{m}^2 \text{s}^{-1}$), which implicitly includes the effects of tortuosity, and \mathbf{I} is the identity tensor. The dispersivity can be broken down into lateral and longitudinal dispersivities. However, the dispersivity in the EBS is ignored (see Section 6.3.1.2). Consequently, the hydrodynamic dispersion is accounted for solely by molecular diffusion. The free water diffusion coefficients for all radionuclides in the EBS are given in Table 4.1-7. Modifications to the diffusion coefficient for the porosity, saturation, and temperature within the waste package are described in Section 6.3.4.3. The effects of concentrated solutions are ignored. Throughout the mathematical description of the radionuclide transport, $D_i = D_{mi}$ represents the effective diffusion coefficient for species i . Since $D_{mi} \mathbf{I} \cdot \nabla C_i = D_i \nabla C_i$, the mass flux vector in Equation 6.5.1.2-4 is:

$$\mathbf{J}_i = -\theta_w D_i \nabla C_i + \mathbf{q}_w C_i. \quad (\text{Eq. 6.5.1.2-7})$$

The term Q_i^m ($\text{kg m}^{-3} \text{s}^{-1}$) in Equation 6.5.1.2-3 is expanded to account for individual contributions of different processes to radionuclide transport:

$$Q_i^m = Q_{idp} - Q_{is}^{rev} - Q_{is}^{kinetic} + Q_{iaq}^{kinetic} - Q_{icm}^{rev} - Q_{icm}^{kinetic} - Q_{icc} - Q_{icc}^{int} \pm Q_{imt} - Q_{icm}^{embed}. \quad (\text{Eq. 6.5.1.2-8})$$

The first term is the source term, Q_{idp} , accounting for the rate of dissolution or precipitation of species i . If the mass balance equation calculates a concentration below the solubility limit, then dissolution occurs, and mass is moved from precipitate to solution ($Q_{idp} > 0$). If a concentration above the solubility limit is calculated, then precipitation occurs, and mass is moved from solution to precipitate ($Q_{idp} < 0$).

The next seven terms in Equation 6.5.1.2-8 account for sorption-related processes. Q_{is}^{rev} is the net rate of reversible sorption of radionuclide species i onto the stationary solid matrix (internal waste package corrosion products and inert matrix). $Q_{is}^{kinetic}$ is the rate of kinetic sorption of radionuclide species i onto the stationary solid matrix (internal waste package corrosion products). $Q_{iaq}^{kinetic}$ is the rate of desorption from the stationary iron oxyhydroxide corrosion product material to solution. No desorption is modeled for the iron oxyhydroxide mobile colloids. This maximizes the transport of colloidal Plutonium and Americium and is not inconsistent with the limited desorption data that is available. Q_{icm}^{rev} is the net rate of reversible sorption of radionuclide species i onto mobile colloid surfaces. Development of this term requires assumptions regarding the reversibility of radionuclide sorption onto colloids and is

discussed below. $Q_{icm}^{kinetic}$ is the rate of kinetic sorption of radionuclide species i onto mobile colloid surfaces.

The terms Q_{icc} and Q_{icc}^{int} are the net rates of sorption of radionuclide species i onto immobile colloid surfaces captured by the stationary solid matrix and by the air-water interface, respectively. Wan and Wilson (1994 [DIRS 124994]) found that “particle transport was tremendously retarded by the air-water interface acting as a strong sorption phase” (Choi and Corapcioglu 1997 [DIRS 161621], p. 301). However, as a bounding assumption (BSC 2005 [DIRS 177423], Assumption 5.4), sorption by the air-water interface is assumed not to occur ($Q_{icc}^{int} = 0$). Distribution coefficients for sorption onto the stationary solid matrix and onto immobile colloid surfaces will generally be different. However, it is difficult to distinguish among various types of matrixes and immobile colloids. Therefore, no distinction is made, and the term Q_{icc} (sorption onto immobile colloids) is lumped in with Q_{is}^{rev} or $Q_{is}^{kinetic}$ (sorption onto the stationary solid matrix). Sorption and retardation in the waste package are discussed in more detail in Section 6.3.4.2.

The term Q_{imt} is the net rate of interface transfer of dissolved mass between the continua in a dual continuum. The sign of this transfer term is determined by the sign of the concentration difference between the media and which medium is associated with the mass balance equation. This term is included even though it is zero in the single-continuum domains that represent the EBS in the RTA in order to keep the mass balance equations as generally applicable as possible. In particular, the equations apply in the dual-continuum invert model presented as an ACM in Section 6.6.3.

The term Q_{icm}^{embed} is the rate of mass conversion from dissolved state to embedded state onto waste form colloids for radionuclide species i . Radionuclides become embedded only in waste form colloids, not in iron oxyhydroxide or groundwater colloids. The conversion rate to embedded species is represented by a first order conversion of the species in solution:

$$Q_{icm}^{embed} = \theta_w \lambda_i^{embed} C_i, \quad (\text{Eq. 6.5.1.2-9})$$

where λ_i^{embed} is the first order rate constant (s^{-1}) for mass conversion from the dissolved state to the embedded state onto waste form colloids for radionuclide species i .

Ingrowth and decay are expressed as:

$$\Lambda_i = \lambda_i^p r_{Mi}^p \theta_w C_i^p - \lambda_i \theta_w C_i. \quad (\text{Eq. 6.5.1.2-10})$$

Ingrowth is the production of radionuclide species i mass by the decay of its parent species and occurs at a rate proportional to the concentration of the parent, C_i^p (kg m^{-3}), and the parent species decay constant, λ_i^p (s^{-1}). The decay constant is related to the half-life, $t_{1/2,i}^p$ (s), of the radionuclide by:

$$\lambda_i^p = \frac{\ln(2)}{t_{1/2,i}^p}. \quad (\text{Eq. 6.5.1.2-11})$$

The term r_{Mi}^p in the production rate is the dimensionless ratio of the mass (kg) of species i produced by decay of the parent species to the mass (kg) of the parent species lost by decay. This is equal to the ratio of the atomic weight of species i to that of its parent. Similarly, mass of species i is lost by decay at a rate $\lambda_i \theta_w C_i$ ($\text{kg m}^{-3} \text{ s}^{-1}$), where λ_i is the decay constant for species i (s^{-1}), defined analogously to λ_i^p .

Mass transport of dissolved and reversibly sorbed radionuclide species i in the aqueous phase is then given by:

$$\begin{aligned} \frac{\partial(\theta_w C_i)}{\partial t} = & \nabla \cdot (\theta_w D_i \nabla C_i) - \nabla \cdot \mathbf{q}_w C_i \\ & + Q_{idp} - Q_{is}^{rev} - Q_{is}^{irrev} - Q_{icm}^{rev} - Q_{icm}^{irrev} \\ & \pm Q_{imt} - Q_{icm}^{embed} + \theta_w (\lambda_i^p r_{Mi}^p C_i^p - \lambda_i C_i), \end{aligned} \quad (\text{Eq. 6.5.1.2-12})$$

which is essentially identical to Equations 19 and 20 by Choi and Corapcioglu (1997 [DIRS 161621], p. 306), with the addition of decay and ingrowth terms and a dissolution/precipitation source term, Q_{idp} . A further modification of the equations by Choi and Corapcioglu involves the diffusive term, $\nabla \cdot (\theta_w D_i \nabla C_i)$, which Choi and Corapcioglu write as $\nabla \cdot [D_i \nabla(\theta_w C_i)]$. This form of the term incorrectly models diffusive flux based on the species concentration gradient with respect to bulk volume. Instead, the diffusive flux is determined by the concentration gradient with respect to the water volume. The incorrect form allows diffusion to occur in the absence of a concentration gradient as long as the water content, θ_w , varies.

The source term for radionuclide species i reversibly sorbed onto the stationary solid matrix (corrosion products or invert matrix) is given by:

$$Q_{is}^{rev} = \frac{\partial(\rho_b K_{dis} C_i)}{\partial t} - \rho_b (\lambda_i^p r_{Mi}^p K_{dis}^p C_i^p - \lambda_i K_{dis} C_i), \quad (\text{Eq. 6.5.1.2-13})$$

where ρ_b is the dry bulk density of the stationary solid matrix (kg m^{-3} bulk volume). A linear sorption isotherm is used for the relationship between the aqueous and solid phase equilibrium concentration, expressed in terms of a sorption distribution coefficient of the dissolved species i , K_{dis} ($\text{m}^3 \text{ water kg}^{-1} \text{ solid}$ [customary units of mL g^{-1}]). K_{dis} depends both on the radionuclide

species i being sorbed and on the solid substrate, either stationary iron oxyhydroxide corrosion products or invert material or both, in this case.

The source term for radionuclide species i kinetically sorbed onto the stationary solid iron oxyhydroxide corrosion products is given by:

$$Q_{is}^{kinetic} = \rho_b \bar{s}_{CP} k_{if} C_i \quad (\text{Eq. 6.5.1.2-14})$$

where \bar{s}_{CP} is the specific surface area of iron oxyhydroxide corrosion products [$\text{m}^2 \text{CP kg}^{-1} \text{CP}$], and k_{if} is the kinetic forward rate constant for species i ($\text{m}^3 \text{water m}^{-2} \text{CP s}^{-1}$). The reaction is modeled as first order in the solution concentration. The kinetic sorption to the iron oxyhydroxide corrosion products is modeled as experiencing a slow desorption. This is a mass transfer from the corrosion product material to solution. The source term representing this process is:

$$Q_{iaq}^{kinetic} = \rho_b \bar{s}_{CP} k_{ir} \hat{C}_{iCP} \quad (\text{Eq. 6.5.1.2-15})$$

where k_{ir} is the reverse sorption (or desorption) rate and \hat{C}_{iCP} is the concentration of species i on the iron oxyhydroxide corrosion products on a water volume basis.

The source term for radionuclide species i reversibly sorbed onto the mobile colloids is given by:

$$Q_{icm}^{rev} = \frac{\partial [\theta_w (K_{dicWF} C_{cWF} + K_{dicFeO} C_{cFeO} + K_{dicGW} C_{cGW}) C_i]}{\partial t} + \nabla \cdot (\mathbf{J}_{icWF} + \mathbf{J}_{icFeO} + \mathbf{J}_{icGW}) - \theta_w [\lambda_i^p r_{Mi}^p (C_{icWF}^p + C_{icFeO}^p + C_{icGW}^p) - \lambda_i (C_{icWF} + C_{icFeO} + C_{icGW})], \quad (\text{Eq. 6.5.1.2-16})$$

where C_{icWF} , C_{icFeO} , and C_{icGW} are the concentrations on a water volume basis of radionuclide species i reversibly sorbed onto the mobile waste form (WF) colloids, iron oxyhydroxide (FeO) colloids originating from corrosion products, and groundwater (GW) colloids, respectively ($\text{kg } i \text{ m}^{-3} \text{ water}$). The superscript p refers to the parent of radionuclide species i . The terms C_{cWF} , C_{cFeO} , and C_{cGW} are the concentrations on a water volume basis of mobile waste form, iron oxyhydroxide, and groundwater colloids, respectively ($\text{kg colloid m}^{-3} \text{ water}$). The K_d values of radionuclide species i for the respective colloids are K_{dicWF} , K_{dicFeO} , and K_{dicGW} (customary units: mL g^{-1}). The first term on the right side of Equation 6.5.1.2-16 accounts for the accumulation of mass of radionuclide species i reversibly sorbed to colloids. The second term on the right hand side of Equation 6.5.1.2-16 accounts for mass transport by advection and diffusion of radionuclide species i reversibly sorbed to colloids. The third line of Equation 6.5.1.2-16 accounts for production or loss of mass of radionuclide species i reversibly sorbed to colloids by ingrowth and decay.

The vectors for mass fluxes of mobile colloids, \mathbf{J}_{icWF} , \mathbf{J}_{icFeO} , and \mathbf{J}_{icGW} , are:

$$\mathbf{J}_{icWF} = -\theta_w D_c \nabla (K_{dicWF} C_{cWF} C_i) + \mathbf{q}_w K_{dicWF} C_{cWF} C_i \quad (\text{Eq. 6.5.1.2-17})$$

$$\mathbf{J}_{icFeO} = -\theta_w D_c \nabla (K_{dicFeO} C_{cFeO} C_i) + \mathbf{q}_w K_{dicFeO} C_{cFeO} C_i \quad (\text{Eq. 6.5.1.2-18})$$

$$\mathbf{J}_{icGW} = -\theta_w D_c \nabla (K_{dicGW} C_{cGW} C_i) + \mathbf{q}_w K_{dicGW} C_{cGW} C_i \quad (\text{Eq. 6.5.1.2-19})$$

The source term for radionuclide species i kinetically sorbed onto the mobile iron oxyhydroxide colloids is given by:

$$Q_{icm}^{kinetic} = \theta_w C_{cFeO} \bar{s}_{cFeO} k_{if} C_i, \quad (\text{Eq. 6.5.1.2-20})$$

where \bar{s}_{cFeO} is the specific surface area of mobile iron oxyhydroxide colloids (m^2 colloids kg^{-1} colloids), and k_{if} is the forward rate constant for kinetic sorption (m^3 water m^{-2} FeO colloids s^{-1}). The rate constant k_{if} for mobile iron oxyhydroxide colloids is the same as for stationary iron oxyhydroxide corrosion products. The reaction is modeled as first order in the solution concentration. Kinetic sorption onto mobile colloids occurs only onto mobile iron oxyhydroxide colloids, not onto mobile waste form or mobile groundwater colloids. As discussed earlier, radionuclides may become embedded in waste form colloids, which has a similar net effect as kinetic sorption but is modeled as a distinctly separate process.

The term Q_{imt} is the net rate of interface transfer of dissolved and reversibly sorbed mass between the continua in a dual continuum material (as in the dual continuum invert ACM; see Section 6.6.3) on a bulk volume basis ($\text{kg m}^{-3} \text{s}^{-1}$). The dual-continuum invert model conceptualizes the invert as crushed in-situ material with inter-pore space as the pore space between solid particles. The intra-pore space is the pore space within the solid particles. Q_{imt} is given by Corapcioglu and Wang (1999 [DIRS 167464], p. 3265); Gerke and van Genuchten (1996 [DIRS 167466], p. 345):

$$\begin{aligned} Q_{imt} = & \gamma_d [(C_i)_{intra} - (C_i)_{inter}] \\ & + \gamma_c [(C_{icWF})_{intra} - (C_{icWF})_{inter} + (C_{icFeO})_{intra} - (C_{icFeO})_{inter} \\ & + (C_{icGW})_{intra} - (C_{icGW})_{inter}] \end{aligned} \quad (\text{Eq. 6.5.1.2-21})$$

In a single-continuum material, $Q_{imt} = 0$. The dissolved and colloid mass transfer coefficients, γ_d and γ_c , respectively, depend on which continuum the mass balance represents. For the dissolved mass transfer term applied to the intragranular mass balance:

$$\gamma_d = \alpha \phi_{intra} S_{w_intra}, \quad (\text{Eq. 6.5.1.2-22})$$

and applied to the intergranular mass balance:

$$\gamma_d = \alpha \phi_{intra} S_{w_intra} \left(\frac{1 - w_{inter}}{w_{inter}} \right), \quad (\text{Eq. 6.5.1.2-23})$$

where w_{inter} is the ratio of the intergranular continua volume to the total bulk volume, and α is the first-order mass transfer coefficient (s^{-1}) of the form:

$$\alpha = \frac{\beta}{d^2} D_{ie}, \quad (\text{Eq. 6.5.1.2-24})$$

β is a dimensionless geometry-dependent coefficient, d is a characteristic length (m) of the matrix structure (e.g., half the aggregate width or half the fracture spacing), and D_{ie} is an effective diffusion coefficient ($m^2 s^{-1}$) that represents the diffusion properties of the interface between the two continua for radionuclide species i . Because the intergranular continuum is open pore space, diffusion is expected to be controlled by the diffusive properties of the intragranular continuum. Thus, D_{ie} is taken to be the effective diffusion coefficient in the intragranular continuum. The colloid coefficient γ_c is evaluated similarly to the dissolved coefficient, but uses an effective colloid diffusion coefficient to evaluate α in Equation 6.5.1.2-24. The mass transfer function between the two invert continua is described in Section 6.6.3.1 in connection with a dual-continuum invert ACM. Since the EBS is modeled as a single continuum in the EBS transport model, the interface transfer term Q_{imt} is zero and is not included in the mass balance equations that follow.

In a dual-continuum material, the intergranular porosity ϕ_{inter} and intragranular porosity ϕ_{intra} are defined as follows. Let V_p be the total volume of pore space in the bulk material, which has a total volume of V_t . The intergranular pore space has a total volume designated by V_{t_inter} and a pore volume of V_{p_inter} . Similarly, the intragranular pore space has a total volume designated by V_{t_intra} and a pore volume of V_{p_intra} . $V_p = V_{p_intra} + V_{p_inter}$ and $V_t = V_{t_intra} + V_{t_inter}$. The porosities are defined as:

$$\phi_{inter} = \frac{V_{p_inter}}{V_t} \quad (\text{Eq. 6.5.1.2-25})$$

and

$$\phi_{intra} = \frac{V_{p_intra}}{V_t}. \quad (\text{Eq. 6.5.1.2-26})$$

The total bulk porosity of the material is:

$$\phi_t = \frac{V_p}{V_t} = \phi_{inter} + \phi_{intra}. \quad (\text{Eq. 6.5.1.2-27})$$

The parameter w_{inter} is the ratio of the intergranular continuum volume to the total bulk volume:

$$w_{inter} = \frac{V_{t_inter}}{V_t}. \quad (\text{Eq. 6.5.1.2-28})$$

Then $\left(\frac{1-w_{inter}}{w_{inter}}\right)$ is the ratio of intragranular continuum volume to intergranular continuum volume:

$$\frac{1-w_{inter}}{w_{inter}} = \frac{1-\frac{V_{t_inter}}{V_t}}{\frac{V_{t_inter}}{V_t}} = \frac{V_t - V_{t_inter}}{V_{t_inter}} = \frac{V_{t_intra}}{V_{t_inter}}. \quad (\text{Eq. 6.5.1.2-29})$$

Mass Balance for Radionuclides Kinetically Sorbed onto Iron Oxyhydroxide Mobile Colloids and Stationary Corrosion Products

The mass balance for kinetically sorbed radionuclides on mobile iron oxyhydroxide colloids, which originate in the corrosion products, accounts for advection, diffusion, and decay and is given by:

$$\frac{\partial(\theta_w \hat{C}_{icFeO})}{\partial t} = -\nabla \cdot (\mathbf{J}_{icFeO}^{kinetic}) + Q_{icm}^{kinetic} + \theta_w (\lambda_i^p r_{Mi}^p \hat{C}_{icFeO}^p - \lambda_i \hat{C}_{icFeO}), \quad (\text{Eq. 6.5.1.2-30})$$

where

$$\mathbf{J}_{icFeO}^{kinetic} = -\theta_w D_c \nabla (\hat{C}_{icFeO}) + \mathbf{q}_w \hat{C}_{icFeO}. \quad (\text{Eq. 6.5.1.2-31})$$

The quantity \hat{C}_{icFeO} is the concentration of radionuclide species i kinetically sorbed onto mobile iron oxyhydroxide colloids on a water volume basis ($\text{kg } i \text{ m}^{-3} \text{ water}$). The source term for radionuclide species i kinetically sorbed onto the mobile corrosion products colloids, $Q_{icm}^{kinetic}$, is given by Equation 6.5.1.2-20.

The mass balance for kinetically adsorbed radionuclides onto stationary iron oxyhydroxide corrosion products accounts for decay and is given by:

$$\frac{\partial(\theta_w \hat{C}_{iCP})}{\partial t} = Q_{is}^{kinetic} - Q_{iaq}^{kinetic} + \theta_w (\lambda_i^p r_{Mi}^p \hat{C}_{iCP}^p - \lambda_i \hat{C}_{iCP}), \quad (\text{Eq. 6.5.1.2-32})$$

where \hat{C}_{iCP} is the concentration of radionuclide species i kinetically adsorbed onto stationary iron oxyhydroxide corrosion products on a water volume basis ($\text{kg } i \text{ m}^{-3}$). The source term for radionuclide species i kinetically sorbed onto the solid stationary iron oxyhydroxide corrosion

products, $Q_{is}^{kinetic}$, is given by Equation 6.5.1.2-14. The source term for the radionuclide species i kinetically desorbing from the solid stationary iron oxyhydroxide corrosion products, $Q_{iaq}^{kinetic}$, is given by Equation 6.5.1.2-15.

Mass Balance for Waste Form Colloid Particles

The waste form colloids are generated in the waste form domain and are transported in accordance with an advective/diffusive mass balance. The waste form colloid concentration is subject to stability constraints based on the local domain chemistry. The iron oxyhydroxide and groundwater colloids both exist in the corrosion products and invert domains; their stability and concentrations are dependent on the local domain chemistry (BSC 2005 [DIRS 177423]). Because seepage brings the groundwater colloids into the EBS, the groundwater colloids are modeled as having the same concentration in both the waste package and invert. Similarly, due to the presence of steel in both waste package and invert, it is reasonable for iron oxyhydroxide colloids to have the same concentrations in both domains as well, if the colloids are stable under the local conditions. Hence, no transport mass balance equations are required for iron oxyhydroxide and groundwater colloids. Since waste form colloids can only be generated in the waste form domain, it is necessary to know how much of the waste form colloid mass has moved by advection and diffusion into the corrosion product and invert domains. Thus, an advective/diffusive mass balance must be applied to compute the waste form colloid mass in each of the downstream domains. The stability for waste form colloids is checked in each domain, since they may be stable in the corrosion product domain but precipitate in the invert domain.

The mass balance for waste form colloidal particles suspended in the aqueous phase can be expressed as (Choi and Corapcioglu 1997 [DIRS 161621], p. 302):

$$\frac{\partial(\theta_w C_{cWF})}{\partial t} = -\nabla \cdot \mathbf{J}_{cWF} - Q_{cWF} - Q_{cWF}^{int} - Q_{cWFfg} + Q_{cWFs} \pm Q_{cWFmt}. \quad (\text{Eq. 6.5.1.2-33})$$

The quantity C_{cWF} is the concentration of suspended waste form colloids in the aqueous phase ($\text{kg waste form colloids m}^{-3} \text{ water}$), and \mathbf{J}_{cWF} is the mass flux vector of waste form colloids ($\text{kg m}^{-2} \text{ s}^{-1}$). The term Q_{cWFfg} is the net rate of waste form colloid removal from suspension ($\text{kg m}^{-3} \text{ s}^{-1}$) by means of physical filtering (pore clogging, sieving, and straining) and by gravitational settling. Physical filtering and gravitational settling are assumed not to occur (Assumption 5.7). Thus, the term Q_{cWFfg} is neglected. The term Q_{cWF} ($\text{kg m}^{-3} \text{ s}^{-1}$) is the net rate of waste form colloid capture on the solid surface. Although colloid capture on the solid surface is akin to sorption and a different process from physical filtration, the net effect is indistinguishable from physical filtration, and it is also neglected ($Q_{cWF} = 0$). The term Q_{cWF}^{int} ($\text{kg m}^{-3} \text{ s}^{-1}$) represents capture at the air-water interface; as mentioned earlier, this term is neglected as a bounding assumption (BSC 2005 [DIRS 177423], Assumption 5.4).

With these assumptions, Equation 6.5.1.2-33 simplifies to:

$$\frac{\partial(\phi S_w C_{cWF})}{\partial t} = -\nabla \cdot \mathbf{J}_{cWF} + Q_{cWFs} \pm Q_{cWFmt} \quad (\text{Eq. 6.5.1.2-34})$$

The source term, Q_{cWFs} ($\text{kg m}^{-3} \text{s}^{-1}$), in Equation 6.5.1.2-34 represents the formation or degradation of waste form colloids. Colloid formation may be rate limited, or it may be instantaneous, with equilibrium between the colloids and their dissolved components. In either case, colloid stability is strongly dependent on the chemical environment, specifically on the pH and ionic strength of the aqueous phase. The colloid source term is the subject of *Waste Form and In-Drift Colloids-Associated Radionuclide Concentrations: Abstraction and Summary* (BSC 2005 [DIRS 177423]), and is discussed further below.

The term Q_{cWFmt} is the net rate of interface transfer of waste form colloidal mass between the intergranular and intragranular continua in a dual continuum model, such as the dual continuum invert ACM (Section 6.6.3). For a single continuum, $Q_{cWFmt} = 0$. The sign of this transfer term is determined by the sign of the waste form colloid concentration difference between the media and which medium is associated with the mass balance equation. This is analogous to the colloid transfer term in Equation 6.5.1.2-21:

$$Q_{cWFmt} = \gamma_c [(C_{cWF})_{intra} - (C_{cWF})_{inter}]. \quad (\text{Eq. 6.5.1.2-35})$$

Since Equation 6.5.1.2-34 is for the waste form colloid particles themselves, as opposed to radionuclides sorbed onto the particles, there are no decay or ingrowth terms.

The mass flux vector for waste form colloids is expressed as (Choi and Corapcioglu 1997 [DIRS 161621], p. 303, Equation 4):

$$\begin{aligned} \mathbf{J}_{cWF} &= \mathbf{J}_{cB} + \mathbf{J}_{cMD} + \mathbf{q}_w C_{cWF} \\ &= -\theta_w D_B \nabla C_{cWF} - \theta_w D_{MD} \nabla C_{cWF} + \mathbf{q}_w C_{cWF} \\ &= -\theta_w D_c \nabla C_{cWF} + \mathbf{q}_w C_{cWF}, \end{aligned} \quad (\text{Eq. 6.5.1.2-36})$$

where subscript B refers to Brownian diffusion, and MD refers to mechanical dispersion. The mechanical dispersion and Brownian diffusion terms can be lumped together in a colloid hydrodynamic dispersion term with a colloid dispersion or diffusion coefficient D_c ($\text{m}^2 \text{s}^{-1}$). The colloid diffusion coefficient is given by the Stokes-Einstein equation (Equation 6.3.4.4-1). The mass balance on waste form colloid particles, Equation 6.5.1.2-34, then becomes (with the term Q_{cWFmt} , Equation 6.5.1.2-35, no longer included, since it is zero for the EBS as currently modeled):

$$\frac{\partial(\theta_w C_{cWF})}{\partial t} = \nabla \cdot (\theta_w D_c \nabla C_{cWF}) - \nabla \cdot (\mathbf{q}_w C_{cWF}) + Q_{cWFs} \quad (\text{Eq. 6.5.1.2-37})$$

Mass Balance for Embedded Mass on Waste Form Colloids

The mass balance for the radionuclide species i embedded on waste form colloids is:

$$\frac{\partial(\theta_w C_i^{embedded})}{\partial t} = \nabla \cdot (\theta_w D_c \nabla C_i^{embedded}) - \nabla \cdot (q_w C_i^{embedded}) + \theta_w (\lambda_i^p r_{Mi}^p C_i^{p,embedded} - \lambda_i C_i^{embedded}) + Q_{icm}^{embedded}, \quad (\text{Eq. 6.5.1.2-38})$$

where $C_i^{embedded}$ and $C_i^{p,embedded}$ are the concentrations of species i and the parent of species i , respectively, embedded on waste form colloids.

Summary of Mass Balances

Inserting the source terms into Equation 6.5.1.2-12, and neglecting the dual continuum interface transport, gives the equation for the transport of radionuclides dissolved in the aqueous phase and reversibly sorbed:

$$\begin{aligned} \frac{\partial}{\partial t} [\theta_w R_{fi} C_i] = & \nabla \cdot (\theta_w D_i \nabla C_i) \\ & + \nabla \cdot \{ \theta_w D_c \nabla [(K_{dicWF} C_{cWF} + K_{dicFeO} C_{cFeO} + K_{dicGW} C_{cGW}) C_i] \} \\ & - \nabla \cdot [q_w (1 + K_{dicWF} C_{cWF} + K_{dicFeO} C_{cFeO} + K_{dicGW} C_{cGW}) C_i] \\ & \pm Q_{idp} - (\rho_b \bar{s}_{CP} + \theta_w C_{cFeO} \bar{s}_{cFeO}) k_{if} C_i + \rho_b \bar{s}_{CP} k_{ir} \hat{C}_{iCP} - \theta_w \lambda_i^{embedded} C_i \\ & + \theta_w [\lambda_i^p r_{Mi}^p R_{fi}^p C_i^p - \lambda_i R_{fi} C_i], \end{aligned} \quad (\text{Eq. 6.5.1.2-39})$$

where the retardation factor for species i is defined by:

$$R_{fi} = 1 + \frac{\rho_b K_{dis}}{\theta_w} + K_{dicWF} C_{cWF} + K_{dicCP} C_{cFeO} + K_{dicGW} C_{cGW}, \quad (\text{Eq. 6.5.1.2-40})$$

and R_{fi}^p is the corresponding retardation factor for the parent of radionuclide species i :

$$R_{fi}^p = 1 + \frac{\rho_b K_{dis}^p}{\theta_w} + K_{dicWF}^p C_{cWF} + K_{dicCP}^p C_{cFeO} + K_{dicGW}^p C_{cGW}. \quad (\text{Eq. 6.5.1.2-41})$$

In Equation 6.5.1.2-39, the left side of the equation represents the accumulation of dissolved and reversibly sorbed radionuclide species i . The term in brackets is the mass of species i present in a unit bulk volume of EBS material, so the equation units are mass of species i per unit bulk volume of EBS per time. The first term on the right side represents the rate of diffusion of dissolved species i in the aqueous phase. The second term accounts for diffusion of mobile colloids on which species i is sorbed. The third term is the rate at which species i dissolved mass and mass reversibly sorbed to mobile colloids is transported by advection. The fourth term represents the net rate of dissolution or precipitation of species i . The fifth term is the conversion rate due to kinetic sorption on both iron oxyhydroxide stationary corrosion products and mobile

colloids. The sixth term is the conversion rate due to desorption from the iron oxyhydroxide corrosion products. The seventh term is the rate of capture of species i by embedding in waste form colloids. The last (eighth) term accounts for ingrowth, or production of species i by decay of the parent of i , and decay of species i , as dissolved species and as sorbed onto colloids.

Inserting the source terms into Equation 6.5.1.2-30, the mass balance for kinetically sorbed radionuclides on iron oxyhydroxide corrosion product colloids becomes:

$$\frac{\partial(\theta_w \hat{C}_{icFeO})}{\partial t} = \nabla \cdot (\theta_w D_c \nabla \hat{C}_{icFeO}) - \nabla \cdot (\mathbf{q}_w \hat{C}_{icFeO}) + \theta_w C_{cFeO} \bar{s}_{cFeO} k_{if} C_i + \theta_w (\lambda_i^p r_{Mi}^p \hat{C}_{icFeO}^p - \lambda_i \hat{C}_{icFeO}). \quad (\text{Eq. 6.5.1.2-42})$$

The term $\theta_w C_{cFeO} \bar{s}_{cFeO} k_{if} C_i$ in Equation 6.5.1.2-42 couples this equation to Equation 6.5.1.2-39.

The mass balance for kinetically sorbed radionuclides onto stationary iron oxyhydroxide corrosion products, Equation 6.5.1.2-32, accounts for sorption/desorption reactions and decay and is given by:

$$\frac{\partial(\theta_w \hat{C}_{iCP})}{\partial t} = \rho_b \bar{s}_{CP} k_{if} C_i - \rho_b \bar{s}_{CP} k_{ir} \hat{C}_{iCP} + \theta_w (\lambda_i^p r_{Mi}^p \hat{C}_{iCP}^p - \lambda_i \hat{C}_{iCP}). \quad (\text{Eq. 6.5.1.2-43})$$

The source term in Equation 6.5.1.2-43, $\rho_b \bar{s}_{CP} k_{if} C_i$, couples this equation to Equation 6.5.1.2-39.

For a single continuum medium with no colloids or corrosion products present, Equation 6.5.1.2-39 reduces to the conventional advection/diffusion transport equation (with source and sink terms):

$$\frac{\partial(\theta_w R_{fi} C_i)}{\partial t} = \nabla \cdot (\theta_w D_i \nabla C_i) - \nabla \cdot (\mathbf{q}_w C_i) \pm Q_{idp} + \theta_w (\lambda_i^p r_{Mi}^p C_i R_{fi}^p - \lambda_i C_i R_{fi}), \quad (\text{Eq. 6.5.1.2-44})$$

with the conventional retardation factors for radionuclide species i and parent of species i , respectively:

$$R_{fi} = 1 + \frac{\rho_b K_{dis}}{\theta_w} \quad (\text{Eq. 6.5.1.2-45})$$

and

$$R_{fi}^p = 1 + \frac{\rho_b K_{dis}^p}{\theta_w}. \quad (\text{Eq. 6.5.1.2-46})$$

Equations 6.5.1.2-39 (mass balance for dissolved and reversibly sorbed radionuclide species i), 6.5.1.2-42 (mass balance for radionuclide species i kinetically sorbed onto iron oxyhydroxide colloids) and 6.5.1.2-43 (mass balance radionuclide species i kinetically sorbed onto stationary iron oxyhydroxide corrosion products) are solved simultaneously for all radionuclides to obtain the dependent variables, C_i , \hat{C}_{iCP} , and \hat{C}_{iFeO} , the concentration of dissolved radionuclide species i , the concentration of species i kinetically sorbed onto iron oxyhydroxide colloids, and species i kinetically sorbed onto stationary iron oxyhydroxide corrosion products, respectively. The solution is a finite difference approximation to the continuum equations with discretization of time and space (Section 6.5.2.5).

The initial conditions are $C_i = \hat{C}_{iCP} = \hat{C}_{iFeO} = 0$ for all species i . Upstream of the waste form domain, all radionuclide concentrations are zero. Consequently, the upstream boundary maintains a zero flux condition. Radionuclide concentrations will remain zero until a waste package failure occurs. A treatment of the zero downstream concentration boundaries within the UZ is provided in Section 6.5.2.6. The radionuclides are released or mobilized within the waste form domain. Flow is expected to be predominately downward. Then the resulting transport will be in a downward direction from the waste form to the corrosion products, which will accumulate in the bottom of the waste container. From the corrosion products, the radionuclides will migrate down to the invert, and from there they will enter the UZ. The representation for the radionuclide transport is consequently a one-dimensional mass balance equation for radionuclide species. For the one-dimensional EBS radionuclide transport model, the positive z -direction is oriented downward. The specific discharge (Darcy velocity) vector, \mathbf{q}_w , is always in the downward positive z -direction and is denoted by $\mathbf{q}_w = q_{wz} \mathbf{i}$, where \mathbf{i} is a unit vector in the positive z -direction, and q_{wz} is the scalar specific discharge in the z -direction (zero in the other two directions). In one dimension, the mass balance equations can be written as scalar equations and are summarized as follows.

The one-dimensional mass balance equation describing transport of dissolved and reversibly sorbed radionuclide species i (Equation 6.5.1.2-39) is:

$$\begin{aligned} \frac{\partial}{\partial t} [\theta_w R_{fi} C_i] &= \frac{\partial}{\partial z} \left(\theta_w D_i \frac{\partial C_i}{\partial z} \right) \\ &+ \frac{\partial}{\partial z} \left(\theta_w D_c \frac{\partial}{\partial z} [(K_{dicWF} C_{cWF} + K_{dicFeO} C_{cFeO} + K_{dicGW} C_{cGW}) C_i] \right) \\ &- \frac{\partial}{\partial z} [q_{wz} (1 + K_{dicWF} C_{cWF} + K_{dicFeO} C_{cFeO} + K_{dicGW} C_{cGW}) C_i] \quad (\text{Eq. 6.5.1.2-47}) \\ &\pm Q_{idp} - (\rho_b \bar{s}_{CP} + \theta_w C_{cFeO} \bar{s}_c) k_{if} C_i + \rho_b \bar{s}_{CP} k_{ir} \hat{C}_{iCP} - \lambda_i^{embed} C_i \\ &+ \theta_w [\lambda_i^p r_{Mi}^p R_{fi}^p C_i^p - \lambda_i R_{fi} C_i]. \end{aligned}$$

Within the corrosion products domain, the concentrations will remain below the solubility limit, and the term $Q_{idp} = 0$ in Equation 6.5.1.2-47. Also, within the corrosion products domain there is no source term for the waste form colloids, and $\lambda_i^{embed} = 0$. Within the waste form domain,

there are no groundwater or iron oxyhydroxide colloids and no immobile corrosion product material, which imply the terms in Equation 6.5.1.2-47 associated with these processes will be zero.

Similarly, the one-dimensional mass balance equation for kinetically sorbed radionuclide species i on mobile iron oxyhydroxide colloids (Equation 6.5.1.2-42) is:

$$\frac{\partial(\theta_w \hat{C}_{icFeO})}{\partial t} = \frac{\partial}{\partial z} \left(\theta_w D_c \frac{\partial \hat{C}_{icFeO}}{\partial z} \right) - \frac{\partial}{\partial z} (q_{wz} \hat{C}_{icFeO}) + \theta_w C_{cFeO} \bar{s}_{cCP} k_{if} C_i + \theta_w (\lambda_i^p r_{Mi}^p \hat{C}_{icFeO}^p - \lambda_i \hat{C}_{icFeO}). \quad (\text{Eq. 6.5.1.2-48})$$

This equation is not required within the waste form domain.

The one-dimensional mass balance equation for kinetically sorbed radionuclide species i on stationary iron oxyhydroxide corrosion products is the same as Equation 6.5.1.2-43, since there is no advection or diffusion of corrosion products:

$$\frac{\partial(\theta_w \hat{C}_{iCP})}{\partial t} = \rho_b \bar{s}_{CP} k_{if} C_i - \rho_b \bar{s}_{CP} k_{ir} \hat{C}_{iCP} + \theta_w (\lambda_i^p r_{Mi}^p \hat{C}_{iCP}^p - \lambda_i \hat{C}_{iCP}). \quad (\text{Eq. 6.5.1.2-49})$$

This equation only applies to the corrosion product domain.

In one dimension, the mass balance equation for waste form colloid transport (Equation 6.5.1.2-37) is:

$$\frac{\partial(\theta_w C_{cWF})}{\partial t} = \frac{\partial}{\partial z} \left(\theta_w D_c \frac{\partial C_{cWF}}{\partial z} \right) - \frac{\partial}{\partial z} (q_w C_{cWF}) + Q_{cWFs}. \quad (\text{Eq. 6.5.1.2-50})$$

Within the waste package, the media supporting transport are represented as single continua. In the UZ, however, the bulk medium is conceptualized as a dual continuum, characterized by two sets of local-scale properties unique to each continuum. Transport in the dual continuum media is represented by a mass balance equation for each continuum. The single invert continuum interfaces a dual continuum (fracture/matrix) UZ medium. Advective transport from the invert enters both the UZ fracture and matrix continua.

The diffusive transport between the single invert continuum and the dual UZ continua is determined from the continuity of mass transport across the interface. This requirement states that the diffusive rate exiting or entering the invert domain is equal to the sum of the diffusive rates fluxes entering or exiting the two UZ continua. The diffusive rate split at the interface will depend on the diffusive properties in the invert domain and both UZ continua together with the concentration gradients across the interface.

For discussion of the diffusive transport treatment at the invert/UZ interface, consider a diffusive rate term, either aqueous or colloid, within the transport mass balance equation. Let $z_{interface}$

denote the spatial location of the invert/UZ interface. Then for $z < z_{interface}$, the diffusive rate for radionuclide species i at a location within the invert domain is:

$$\theta_{wl} A_I D_{il} \frac{\partial C_{il}}{\partial z}, \quad (\text{Eq. 6.5.1.2-51})$$

where subscript I denotes the single-continuum invert domain.

For $z > z_{interface}$, the diffusive rates within the UZ matrix and UZ fracture continua are, respectively,

$$\theta_{wm} A_{mf} D_{im} \frac{\partial C_{im}}{\partial z}, \quad (\text{Eq. 6.5.1.2-52})$$

$$\theta_{wf} A_{mf} D_{if} \frac{\partial C_{if}}{\partial z}. \quad (\text{Eq. 6.5.1.2-53})$$

where A_{mf} denotes the area normal to transport in the matrix/fracture domain.

The mass transport rate via diffusion across this interface is modeled as continuous at the interface:

$$\theta_{wl} A_I D_{il} \frac{\partial C_{il}}{\partial z^-} = \theta_{wm} A_{mf} D_{im} \frac{\partial C_{im}}{\partial z^+} + \theta_{wf} A_{mf} D_{if} \frac{\partial C_{if}}{\partial z^+}, \quad (\text{Eq. 6.5.1.2-54})$$

where

$$\frac{\partial}{\partial z^-} \quad \text{and} \quad \frac{\partial}{\partial z^+}$$

are the derivative from the left (backward) and the derivative from the right (forward), respectively, at the interface. The spatial direction from the invert to the UZ domain is in the positive z -direction.

The waste form colloids are generated in the waste form domain and are transported in accordance with an advective/diffusive mass balance. The waste form colloid concentration is subject to stability constraints based on the local domain chemistry. The waste form colloids transport both reversibly sorbed radionuclide mass and embedded radionuclide mass. The iron oxyhydroxide colloids exist in the corrosion products and invert domains, and the colloid concentrations are dependent on the local domain chemistry. The iron oxyhydroxide colloids transport both reversibly sorbed and kinetically sorbed radionuclide mass. The kinetically sorbed radionuclides are sorbed onto the surface of these colloids, rather than being embedded within the colloid matrix, as are the radionuclides associated with the waste form colloids. The groundwater colloids exist in the corrosion products and invert domains, and their concentrations are dependent on the local domain chemistry. The groundwater colloids transport only

reversibly sorbed radionuclide mass. The iron oxyhydroxide corrosion products are immobile and found only in the corrosion products domain. These corrosion products support both reversibly sorbed and kinetically sorbed radionuclide mass with the kinetic sorbed mass desorbing to solution.

All of the features of the EBS radionuclide transport abstraction are accounted for in Equations 6.5.1.2-39, 6.5.1.2-37, 6.5.1.2-42, and 6.5.1.2-43 (or the one-dimensional versions of these equations, Equations 6.5.1.2-47, 6.5.1.2-50, 6.5.1.2-48, and 6.5.1.2-49, respectively), including invert diffusion, retardation in the waste package, in-package diffusion, and transport facilitated by reversible and irreversible colloids. Implementation of these equations into TSPA involves additional simplifications and restrictions that are discussed in Section 6.5.2.

6.5.2 Summary of Computational Model

The object of the EBS radionuclide transport abstraction is to determine the rate of radionuclide releases from the EBS to the UZ. In the EBS transport model, the EBS is spatially partitioned into the following domains: (1) waste form, consisting of, for example, fuel rods, HLW glass, and DSNF; (2) waste package corrosion products; and (3) invert. In addition, the UZ immediately underlying the invert is conceptualized as a dual continuum consisting of (4) UZ matrix continuum and (5) UZ fracture continuum. The inclusion of a portion of the UZ is needed for an accurate calculation of the invert-to-UZ interface fluxes by providing a diffusive path length that is sufficiently long such that the concentration at the outlet of the UZ can realistically be assigned a value of zero.

In the waste form domain, degradation processes occur, including breaching and axial splitting of fuel rods, dissolution of SNF and HLW glass, and formation of waste form colloids wherever applicable. Dissolved species are transported by advection and/or diffusion to the waste package corrosion products domain. The primary interactions in the corrosion products domain involving radionuclide species are competitive reversible and kinetic sorption onto stationary corrosion products, reversible and kinetic sorption of dissolved species onto iron oxyhydroxide colloids, and reversible sorption onto groundwater colloids and waste form colloids (when present). In the invert domain, radionuclides released from the corrosion products domain are transported by advection and diffusion, and interact with the crushed tuff by adsorption processes. The properties of each domain, including the volume, porosity, water saturation, diffusion cross-sectional area, and diffusive path length, affect the rate of advective and diffusive transport of radionuclides through the domain. The invert domain interfaces with both continua of the UZ. The properties of the domains are defined in the following sections.

6.5.2.1 Waste Form and Waste Package Diffusion Properties

This section summarizes the general approach, major assumptions, main steps in the computational algorithm, and the stochastic parameters for the in-package diffusion submodel for the TSPA. The mathematical equations for the in-package diffusion submodel are described in Section 6.3.4.3.

The general approach for the commercial SNF waste packages is to consider two pathways for diffusion: (1) through porous waste form products inside the package, and (2) through porous

corrosion products filling the bottom of the waste package. Starting from the time when a package is first breached, the extent of degradation is determined. This parameter is the basis for estimating the amount of corrosion products present inside a package, and allows the water saturation and effective diffusion coefficient to be computed.

Implementation of the three-domain EBS abstraction requires that properties be specified for each domain, including the volume, diffusive cross-sectional area, the diffusive path length, porosity, water saturation, and the procedure for calculating the diffusion coefficient. These properties must be specified for each type of waste package (CSNF and codisposal waste packages) and for the drip and no-seep environments.

CSNF Waste Packages Properties

This section discusses the CSNF waste package properties in the following two domains: CSNF waste form and CSNF corrosion products.

6.5.2.1.1.1 CSNF Waste Form Domain

In CSNF waste packages, the waste form domain consists of fuel rods and the corrosion products of stainless steel basket tubes and the fuel basket tube assembly, which is constructed of borated stainless steel neutron absorber plates and aluminum thermal shunt plates. Except for ^{14}C , which is released from fuel hardware at the time of waste package breach (DTN: SN0310T0505503.004 [DIRS 168761]), radionuclides are released only from failed rods. However, no credit is taken for the fuel rod cladding—the initial rod failure, i.e., the distribution of failed cladding, as-received, is specified to be constant at 100 percent (SNL 2007 [DIRS 180616], Table 7-2[a]). The SNF begins to react with the oxygen and moisture inside the waste package, forming metaschoepite, the instant that the waste package is breached.

The reacted SNF constitutes a porous “rind,” both in a seep and no-seep environment. The volume of the rind as a function of time, $V_{rind}(t)$, and the rind porosity, ϕ_{rind} , are provided by *Cladding Degradation Summary for LA* (SNL 2007 [DIRS 180616]). Radionuclides dissolve in the water that accumulates in the pore volume of the rind. The water volume in the rind is dependent on the water saturation in the rind, $S_{we,rind}$:

$$V_{w,rind} = \phi_{rind} S_{we,rind} V_{rind}. \quad (\text{Eq. 6.5.2.1.1.1-1})$$

In a seep environment, the rind is modeled as saturating quickly and completely with water, so the rind saturation is $S_{we,rind} = 1$. In a no-seep environment, the water saturation is determined in Section 6.5.2.2.2.1 as a function of RH and depends on the specific surface area, density, and water adsorption behavior of the rind.

The water volume in the domain includes water contained in products from the corrosion of steel components in the domain—the fuel basket tubes and the absorber plates. The domain water volume calculation is described in Section 6.5.2.2.2.1.

The area through which radionuclides may diffuse after being released from fuel rods depends on the state of the waste form. No credit is taken for the effectiveness of fuel rod cladding as a barrier, so once a waste package is breached, all of the SNF is modeled as exposed to the environment inside the waste package. The waste form and steel components will begin to degrade immediately. On the scale of an entire waste package, the waste form domain can be pictured conceptually as a homogeneous mixture within the confines of the TAD canister. A further conceptual picture is that the outer corrosion barrier is covered with numerous randomly located breaches (SCCs or general corrosion) that penetrate the inner vessel and TAD canister, so that radionuclides inside the waste package will tend to diffuse radially outward from the waste form. Then the maximum diffusive path length is the inside radius of the TAD canister, which defines parameter `Diff_Path_Length_CSNF_1`. This parameter is assigned a constant value equal to the inside radius of the TAD canister (0.819 m; from outside diameter of 66.5 in. (SNL 2007 [DIRS 179394], Section 4.1.1.1); and 1.00 in. thickness, (SNL 2007 [DIRS 179394], Table 4-2)). In the cell-centered finite difference methodology adopted in TSPA for solving the transport equation, the diffusive distance from the cell center node defining the waste form domain (Cell 1) to the interface of the adjoining downstream domain (Cell 2) will be half the maximum diffusive length (i.e., $\frac{1}{2} \times \text{Diff_Path_Length_CSNF_1} = 0.41$ m). This constant distance is deemed appropriate as it represents an average diffusive distance to the interface of the adjoining cell for the simulated timeframes in the TSPA and is consistent with the level of discretization of the waste form modeled as a single computational cell.

The diffusive area for the waste form domain (parameter `Diff_Area_CSNF_1`) is taken to be the area of the cylinder having a radius equal to that at the cell center ($\frac{1}{2} \times \text{Diff_Path_Length_CSNF_1} = 0.410$ m) and the length of the CSNF waste form, which is approximately equal to the length of the fuel basket tubes (191.00 in. = 4.8514 m length (BSC 2005 [DIRS 174152])). Thus, `Diff_Area_CSNF_1` has a constant value of 12.5 m². The ends of the TAD canister are neglected, consistent with the radial diffusion conceptualization. Furthermore, diffusion is unlikely ever to occur through the thick shield plug at one end (15.0 in. thick Stainless Steel Type 316 (SNL 2007 [DIRS 179394], Table 4-2)), and the end opposite the shield plug would only contribute marginally (less than 4 percent) to the total surface area if it were included. The lateral area itself can be considered to be the bounding surface area for diffusion as it ignores the area reduction from un-degraded steel components. The diffusive area is not expected to vary significantly over time, so a representative constant value is used. The fixed average diffusive area is consistent with the fixed value for the diffusive path length and with the level of discretization of the waste form modeled as a single computational cell.

The diffusion coefficient is computed using Archie's law (Equation 6.3.4.3.5-2), with the porosity of the rind and the water saturation as determined in Section 6.3.4.6. As discussed in Section 6.5.2.5, the discretized mass balance equations use a diffusive conductance, which is a harmonic average of diffusion coefficient terms (including diffusivity, porosity, saturation, diffusive path length, and cross-sectional area for diffusion; see Equation 6.5.2.5-7), in this case, for the waste form and corrosion products domains. Since the TSPA Model computes the diffusive conductance, only the diffusion coefficients need to be input, rather than the diffusive conductances themselves. The CSNF waste form domain diffusion coefficient is modified for temperature effects using Equation 6.3.4.1.2-4. The waste form temperature is provided in *Multiscale Thermohydrologic Model* calculations (SNL 2007 [DIRS 181383]).

6.5.2.1.1.2 CSNF Corrosion Products Domain

The second domain consists of the corrosion products inside the waste package from corrosion of the stainless steel guide assembly (side guides, end side guides, and corner guides), the stainless steel TAD canister shell, the stainless steel inner vessel, and stainless steel lids. The stainless steel shield plug in the TAD canister is not included. The shield plug is thick and massive (15 in. thick, 12,200 lb = 5,530 kg (SNL 2007 [DIRS 179394], Table 4-2)), and located at one end of the waste package. Since there is no ready mechanism for the potentially large mass of corrosion products from the shield plug to be dispersed throughout the waste package and thereby contribute to water saturation and diffusion in the diffusive pathway for radionuclide transport, the shield plug is ignored for purposes of computing water saturation, diffusion, and sorption. The mass of corrosion products (m_{CP}) is given as a function of time in Section 6.5.2.2. In Section 6.3.4.3.4, a porosity (ϕ_{CP}) of 0.4 for corrosion products is shown to be appropriate. For purposes of calculating the water content of a breached waste package, the corrosion products are assumed to be a porous medium composed of a mixture of goethite and HFO (the representative products of oxidation of iron in both carbon steel and stainless steel) and, for stainless steel corrosion, Cr_2O_3 and NiO, representing the products of oxidation of the chromium and nickel in the stainless steel.

In a seep environment, the water saturation (S_w) is assigned a value of 1.0. In a no-seep environment, the only water present is adsorbed water, and the saturation is the effective saturation of corrosion products given by Equation 6.3.4.3.5-5. Uncertainty in the water saturation of the corrosion products is provided for in the sampled specific surface area of the corrosion products components, in the relative proportions of goethite and HFO in the iron corrosion products, and in the sampled FHH adsorption isotherm parameters for generic corrosion products (Section 6.3.4.3.2).

In a seep environment, the effective diffusion coefficient for corrosion products is given by Archie's law (Equation 6.3.4.3.5-2), with the porosity $\phi_{CP} = 0.4$ and the assigned water saturation of 1.0.

In a non-seep environment, the effective diffusion coefficient is given by Equation 6.3.4.3.5-5. The diffusive area of the corrosion products domain for diffusion to the invert domain is the total area of all waste package breaches, including corrosion patches and stress corrosion cracks. The breached area is determined differently for each scenario class, since different breach mechanisms predominate in each class, ranging from SCC in the Seismic Scenario Class to general corrosion at late times in the Nominal Scenario Class. Consistent with the picture of the waste form domain, radionuclides will tend to diffuse radially outward from the waste form through the products from the corrosion of the guide assembly, TAD canister, and inner vessel. Then the maximum diffusive path length excluding the outer barrier, consistent with the level of discretization of the waste form modeled as a single computational cell, is the distance from the inside of the TAD canister (outside diameter of 66.5 in. = 1.689 m (SNL 2007 [DIRS 179394], Section 4.1.1.1); and 1.00 in. = 0.0254 m thickness, (SNL 2007 [DIRS 179394], Table 4-2)) to the outside of the inner vessel (outside diameter of 71.70 in. = 1.821 m (SNL 2007 [DIRS 179394], Table 4-3)). This distance, parameter Diff_Path_Length_CSNF_2, is 0.0914 m. The dimensions show that there is a gap of 0.60 in. = 0.015 m between the TAD and the inner

vessel, which is treated as radially symmetric and is included in Diff_Path_Length_CSNF_2. In the cell-centered finite difference methodology adopted in the TSPA for solving the transport equation, the actual diffusive distance from the cell center node defining the CSNF corrosion products domain (excluding the outer barrier) to the interface of the adjoining downstream outer barrier will be half the diffusive length (i.e., $\frac{1}{2} \times \text{Diff_Path_Length_CSNF_2} = 0.0457 \text{ m}$).

The diffusive path length through the outer barrier, Diff_Thick_OB_CSNF, is the radial distance from the outside of the inner vessel (outside diameter of 71.70 in. = 1.821 m (SNL 2007 [DIRS 179394], Table 4-3)) to the outside of the outer barrier (outside diameter of 74.08 in. = 1.882 m (SNL 2007 [DIRS 179394], Table 4-3)), which includes a small gap (0.19 in. = 0.0048 m) that is treated as radially symmetric. This distance, Diff_Thick_OB_CSNF, is 0.0302 m. The distance from the cell center to the interface with the adjoining invert cell will be half this distance (0.0151 m). These constant distances (Diff_Path_Length_CSNF_2 and Diff_Thick_OB_CSNF) are deemed appropriate as they represent an average diffusive distance to the interface of the adjoining cell for the simulated timeframes in the TSPA.

The diffusive areas are calculated at the cell centers. So the diffusive area for the path excluding the outer barrier is given by the surface area of a cylinder halfway between the inside surface of the TAD canister (radius of 0.819 m, from Section 2.4.2.1) and the outside surface of the inner vessel (radius of 0.911 m, or half the outside diameter of 71.70 in. = 1.821 m (SNL 2007 [DIRS 179394], Table 4-3)). The radius of this cylindrical surface is $(0.819 \text{ m} + 0.911 \text{ m})/2 = 0.865 \text{ m}$. The length of the CSNF corrosion products domain excluding the outer barrier is the inner vessel length of 216.50 in. = 5.499 m (SNL 2007 [DIRS 179394], Table 4-3). Therefore, the diffusive area for the path excluding the outer barrier, parameter Diff_Area_CSNF_2, is 29.9 m². The diffusive area is not expected to vary significantly over time, so a representative constant value is used, consistent with the fixed value for the diffusive path length. The ends of the inner vessel are neglected for the same reasons as in CSNF waste form domain.

The diffusive area for the path through the outer barrier of the waste package is taken to be the smaller of either (a) the total area of all waste package breaches (scenario class dependent) or (b) the surface area of a cylinder at the midpoint between the inner vessel outer surface and the outer surface of the CSNF waste package outer barrier. This cylinder has a diameter equal to the average of the outside diameter of the outer barrier (74.08 in. = 1.882 m (SNL 2007 [DIRS 179394], Table 4-3)) and the outside diameter of the inner vessel (71.70 in. = 1.821 m (SNL 2007 [DIRS 179394], Table 4-3)), or 1.852 m. The length of the outer barrier, parameter WP_Total_Length_CSNF, is 224.07 in. = 5.691 m (SNL 2007 [DIRS 179394], Table 4-3). Therefore, the cylindrical surface area, parameter Diff_Area_CSNF_2_Max, is 33.1 m². The diffusive area is not expected to vary significantly over time, so a representative constant value is used. As with the waste form and corrosion products area treatment, this estimate for the path through the outer barrier of the waste package neglects the areas of the ends of the inner vessel, consistent with the conceptualization of radial diffusion, the presence of the shield plug, and the minor contribution of the end opposite the shield plug.

The corrosion products domain diffusion coefficient is modified for temperature effects using Equation 6.3.4.1.2-4. The corrosion products temperature is provided by the calculations given in *Multiscale Thermohydrologic Model* (SNL 2007 [DIRS 181383]).

6.5.2.1.2 Codisposal Waste Packages Properties

Codisposal waste packages consist of five cylindrical canisters containing HLW glass (glass “logs”) surrounding a central canister of defense spent nuclear fuel (DSNF). After the codisposal waste package is breached, the HLW glass canister is also immediately breached, and the HLW glass slowly degrades to a clay-like alteration product. The stainless steel HLW glass canisters corrode at the same rate as other stainless steel internal waste package components. The degraded HLW glass and stainless steel corrosion products comprise one subdomain of the codisposal waste form domain. As the steel support framework inside the waste package gradually corrodes, the HLW glass logs collapse onto each other such that the general cylindrical shape of the logs is retained.

The DSNF is modeled as being breached and degrading instantaneously (within a single TSPA time step) once the waste package is breached (BSC 2004 [DIRS 172453], Section 8.1). The stainless steel and carbon steel components of the DSNF gradually corrode. Since the DSNF is centrally located within the codisposal waste package, surrounded by HLW glass logs and contained in a stainless steel canister, it will tend to remain localized within the waste package even as all of the components of the waste package degrade. Thus, the DSNF is modeled as a separate subdomain of the codisposal waste form domain.

Analogous to the treatment of CSNF waste packages, a second codisposal domain consists of corrosion products from steel internal components, including the carbon steel divider plate assembly (divider plates, inner and outer brackets, and support tube), the stainless steel inner vessel, and the stainless steel inner bottom lid, interface ring, and spread ring. The thick, massive inner top lid shield plug (9.00 in. thick, 11,604 lb = 5,264 kg (SNL 2007 [DIRS 179567], Table 4-9)) is not included as part of the codisposal corrosion products domain for the same reasons that the shield plug is excluded from the CSNF corrosion products domain.

Since the EBS transport model is a one-dimensional model, the two waste form subdomains are modeled sequentially, such that the HLW glass subdomain is upstream of the DSNF subdomain. The mass released from the degradation of HLW glass moves to the DSNF subdomain by advection and/or diffusion and is then transported to the corrosion product domain. This sequential representation is consistent with the conceptualization that the DSNF will degrade quickly, while the HLW glass logs will retain their cylindrical geometry and remain up-gradient of the corrosion products. The seepage flux through the waste package is also conceptualized to pass in series so that each waste form subdomain and the corrosion product domain have the same seepage flux.

Consistent with the treatment for the CSNF waste form domain, radionuclides will tend to diffuse radially outward from the HLWG waste form subdomain. Then the maximum diffusive path length is the inside radius of the inner vessel of a codisposal waste package. This parameter, `Diff_Path_Length_CDSP_1a`, is assigned a constant value of 0.941 m (based on inner vessel outside diameter of 78.13 in. and thickness of 2.00 in. (SNL 2007 [DIRS 179567],

Table 4-9)). The fixed value for the diffusive path length is consistent with the level of discretization of the waste form modeled as a single computational cell. In the cell-centered finite difference methodology used in TSPA for solving the transport equation, the actual diffusive distance from the cell center node defining the HLWG waste form subdomain (Cell 1a) to the interface of the adjoining downstream domain (Cell 2) is half the maximum diffusive length ($\frac{1}{2} \times \text{Diff_Path_Length_CDSP_1a} = 0.471 \text{ m}$). This constant distance is deemed appropriate as it represents an average diffusive distance to the interface of the adjoining cell for the simulated timeframes in TSPA.

The diffusive area (parameter Diff_Area_CDSP_1a) is the surface area of a cylinder with a radius at the cell center of $\frac{1}{2} \times \text{Diff_Path_Length_CDSP_1a} = 0.471 \text{ m}$ and the inner vessel cavity length of the 5-DHLW/DOE Long waste package (181.88 in. = 4.620 m (BSC 2007 [DIRS 182365], Section A-A)). Thus, Diff_Area_CDSP_1a has a constant value of 13.7 m^2 . The diffusive area is not expected to vary significantly over time, so a representative constant value is used, consistent with the fixed value for the diffusive path length. The ends of the inner vessel are neglected for the same reasons as in CSNF domains.

The volume of the HLW glass waste form subdomain is set equal to the volume of the degraded glass, which is determined in *Defense HLW Glass Degradation Model* (BSC 2004 [DIRS 169988], Section 8.1). The volume of the DSNF waste form subdomain is set equal to the initial volume of DSNF in a codisposal waste package, which is equal to 1.0 m^3 (BSC 2004 [DIRS 172453], Section 8.1). Unlike the volume increase in the HLW glass subdomain as degradation continues, the volume of DSNF is modeled as constant.

DSNF is modeled as degrading instantaneously upon exposure to groundwater (BSC 2004 [DIRS 172453], Section 8.1). Since the carbon steel support tube, divider plates, and brackets that support the HLWG canisters surrounding the DSNF also degrade rapidly (compared to the degradation rates of HLWG and stainless steel inner vessel), the DSNF is not expected to retain its initial cylindrical shape, but rather will settle to the bottom of the inner vessel. Because of the one-dimensional modeling approach, the diffusive area (parameter Diff_Area_CDSP_1b) is set to be the same as for the HLWG waste form subdomain ($\text{Diff_Area_CDSP_1b} = \text{Diff_Area_CDSP_1a} = 13.7 \text{ m}^2$). The effective diffusive path length, parameter $\text{Diff_Path_Length_CDSP_1b}$, is calculated by dividing the initial volume of DSNF 1 m^3 (BSC 2004 [DIRS 172453], Section 8.1) by the diffusive area (Diff_Area_CDSP_1b), leading to total diffusive length of 0.0730 m . Representative constant values are used, consistent with the discretization of the DSNF waste form modeled as a single computational cell, and the ends of the DSNF standard canister are reasonably neglected due to the predominately radial direction of diffusion and the small area of the long, narrow cylinder.

The diffusion coefficient for the HLW glass subdomain is computed using Archie's law (Equation 6.3.4.3.5-2). For the DSNF subdomain the effective diffusion coefficient is computed by multiplying the free water diffusion coefficient with porosity and saturation. The exponents on porosity and saturation used in Archie's Law, are set to unity in order to maximize the diffusion coefficient without taking credit for tortuosity, as the powdered mass of DSNF is conceptualized to be mixed in with the DSNF subdomain stationary corrosion products. The diffusion coefficients for both the HLW and DSNF subdomains are modified for temperature

effects using Equation 6.3.4.1.2-4. The codisposal waste form temperature, is provided by the calculations given in *Multiscale Thermohydrologic Model* (SNL 2007 [DIRS 181383]).

The porosity of the HLW glass degradation products (rind) is given as 17 percent in *Defense HLW Glass Degradation Model* (BSC 2004 [DIRS 169988], Table 8-1), and the water saturation is computed as a function of the temperature and RH in the waste package. A porosity of 0.2 is used for DSNF, as degraded DSNF waste form and corrosion products are conceptualized to be in a powdered form. The porosity is based on the porosity of unconsolidated sand, which ranges from 0.25 to 0.50 (Freeze and Cherry 1979 [DIRS 101173], Table 2.4). A value lower than this range is used to account for some consolidation; the porosity of sandstone, for example, ranges from 0.05 to 0.30 (Freeze and Cherry 1979 [DIRS 101173], Table 2.4). This value is adequate for ^{99}Tc and ^{129}I , whose concentrations are rate-controlled, as smaller water volume results in higher radionuclide concentrations for such species and hence overestimates releases. Nevertheless, very high concentrations of ^{99}Tc and ^{129}I might also trigger formation of a solubility-limiting phase. ^{14}C releases may be limited by formation of calcite, in which case smaller volumes would likewise have no effect on releases.

The diffusive area and path lengths in the corrosion products domain in a codisposal waste package are treated identically to those in the CSNF corrosion products domain.

The maximum diffusive path length excluding the outer barrier is the thickness of the inner vessel (parameter Diff_Path_Length_CDSP_2), a constant value of 0.0508 m (2.00 in. = 0.0508 m inner vessel thickness (SNL 2007 [DIRS 179567], Table 4-9)). In the cell-centered finite difference methodology adopted in the TSPA for solving the transport equation, the diffusive distance from the cell center node defining the CDSP corrosion products domain (excluding the outer barrier) to the interface of the adjoining downstream outer barrier is half the diffusive length ($\frac{1}{2} \times \text{Diff_Path_Length_CDSP_2} = 0.0254 \text{ m}$).

The diffusive path length through the outer barrier, Diff_Thick_OB_CDSP, is the distance from the outside of the inner vessel (outside diameter 78.13 in. = 1.985 m (SNL 2007 [DIRS 179567], Table 4-9)) to the outside of the outer barrier (outside diameter 80.50 in. = 2.045 m (SNL 2007 [DIRS 179567], Table 4-9)), or 0.0301 m. The distance from the cell center to the interface with the adjoining invert cell will be half the outer barrier thickness ($\frac{1}{2} \times \text{Diff_Thick_OB_CDSP} = 0.0150 \text{ m}$). These constant distances are deemed appropriate as they represent an average diffusive distance to the interface of the adjoining cell for the simulated timeframes in the TSPA.

The diffusive area for the path excluding the outer barrier is given by the surface area of a cylinder halfway between the inside surface and the outside surface of the inner vessel. The outside diameter of the inner vessel is 78.13 in. = 1.985 m, and its thickness is 2.00 in. = 0.0508 m (SNL 2007 [DIRS 179567], Table 4-9), so the radius of the cylindrical surface is $(1.985 \text{ m})/2 - 0.0508 \text{ m} = 0.941 \text{ m}$. The length of the CDSP corrosion products domain excluding the outer barrier is the inner vessel length of 192.38 in. = 4.886 m (SNL 2007 [DIRS 179567], Table 4-9). Therefore, the diffusive area for the path excluding the outer barrier, parameter Diff_Area_CDSP_2, is 28.9 m^2 . The diffusive area is not expected to vary significantly over time, so a representative constant value is used, consistent with the fixed value for the diffusive path length. The ends of the inner vessel are neglected for the same reasons as in CSNF waste form domain (see Section 2.4.2.1). A preliminary calculation erroneously

resulted in a radius of the cylindrical surface of 0.967 m, giving a diffusive area for the path excluding the outer barrier of 29.7 m²; this is the value used in the TSPA. The incorrect diffusive area is 2.8 percent higher than the correct value, which overestimates diffusive releases by a negligibly small amount.

The diffusive area for the path through the outer barrier of the waste package is taken to be the smaller of either (a) the total area of all waste package breaches (scenario class dependent) or (b) the surface area of a cylinder at the midpoint between the inner vessel outer surface and the outer surface of the CDSP waste package outer barrier. This cylinder has a diameter equal to the average of the outside diameter of the outer barrier, 80.50 in. = 2.045 m (SNL 2007 [DIRS 179567], Table 4-9), and the outside diameter of the inner vessel (78.13 in. = 1.985 m (SNL 2007 [DIRS 179567], Table 4-9)), or 2.015 m. The length of the outer barrier, parameter WP_Total_Length_CDSP, is 202.57 in. = 5.145 m (SNL 2007 [DIRS 179567], Table 4-9). Therefore, the cylindrical surface area, parameter Diff_Area_CDSP_2_Max, is 32.6 m². The diffusive area is not expected to vary significantly over time, so a representative constant value is used. As with the waste form and corrosion products area treatment, this estimate neglects the areas of the ends of the inner vessel, consistent with the conceptualization of radial diffusion, the presence of the shield plug, and the minor contribution of the end opposite the shield plug.

The diffusion coefficient in the codisposal waste package corrosion products domain is computed the same as for the CSNF corrosion products domain using Archie's law (Equation 6.3.4.3.5-2), with the porosity of the corrosion products ($\phi_{CP}=0.4$) and the assigned water saturation of 1.0. The diffusion coefficient is modified for temperature effects using Equation 6.3.4.1.2-4. The CDSP waste package corrosion products temperature is provided by *Multiscale Thermohydrologic Model* calculations (SNL 2007 [DIRS 181383]).

6.5.2.2 Calculation of Domain Water Saturation and Water Volume

The water content of each domain determines its transport behavior. The water saturation affects the diffusive characteristics of the domain. The water volume is used to determine the amount of dissolved radionuclides that can be contained in the domain. In this section, the time-dependent water saturation and water volume are calculated for no-seep environments (a saturation of 1.0 is used in seep environments) using parameters developed in Section 6.3.4. The FHH water vapor adsorption isotherm parameters s and k are sampled in each realization for the waste form degradation rind and for corrosion products, and the resulting adsorption isotherms (functions of time-dependent relative humidity) are then fixed for the entire realization. For both waste package types, the second domain contains only steel corrosion products; the saturation and water volume for these domains are calculated in Section 6.5.2.2.1. The first (waste form) domain in both waste package types contains both steel corrosion products as well as degraded waste form, which also contributes to the time-varying water content of the domain. The water saturation and water volume for the waste form domains are calculated in Section 6.5.2.2.2.

6.5.2.2.1 Corrosion Products Water Saturation and Water Volume

The mass of corrosion products in a breached waste package varies over time, from zero when the waste package is first breached to a maximum amount given in Tables 6.3-8 and 6.3-9 that depends on the type of waste package and the particular domain within the waste package. The

mass is computed by linearly interpolating over the lifetime of each of the two major types of steel comprising the internal components of a waste package—carbon steel and stainless steel.

The following parameters are used in the calculation of water saturation and water volume in corrosion products:

$f_{CS,n}$	=	fraction of carbon steel in steel mass in domain n (remainder is stainless steel) [dimensionless]
$m_{s,n}$	=	total mass of steel in domain n [kg]
$t_{LCS,n}$	=	lifetime of carbon steel in domain n [yr]
$t_{LSS,n}$	=	lifetime of stainless steel in domain n [yr]
ω_G	=	mass fraction of goethite in iron corrosion products [dimensionless];
f_{GHFO}	=	$\begin{cases} \omega_G, & \text{for goethite} \\ (1 - \omega_G), & \text{for HFO} \\ 1.0, & \text{for NiO and Cr}_2\text{O}_3 \end{cases}$
$\omega_{CS,Fe}$	=	mass fraction of iron in carbon steel [dimensionless]
$\omega_{CS,Ni}$	=	mass fraction of nickel in carbon steel [dimensionless]
$\omega_{CS,Cr}$	=	mass fraction of chromium in carbon steel [dimensionless]
$\omega_{SS,Fe}$	=	mass fraction of iron in stainless steel [dimensionless]
$\omega_{SS,Ni}$	=	mass fraction of nickel in stainless steel [dimensionless]
$\omega_{SS,Cr}$	=	mass fraction of chromium in stainless steel [dimensionless]
M_{Fe}	=	atomic weight of iron [kg mol ⁻¹]
M_{Ni}	=	atomic weight of nickel [kg mol ⁻¹]
M_{Cr}	=	atomic weight of chromium [kg mol ⁻¹]
M_G	=	molecular weight of goethite [kg mol ⁻¹]
M_{HFO}	=	molecular weight of HFO [kg mol ⁻¹]
M_{NiO}	=	molecular weight of NiO [kg mol ⁻¹]
M_{CrOx}	=	molecular weight of Cr ₂ O ₃ [kg mol ⁻¹]
$m_{G,n,CS}$	=	mass of goethite in domain n from corrosion of carbon steel [kg]
$m_{HFO,n,CS}$	=	mass of HFO in domain n from corrosion of carbon steel [kg]
$m_{NiO,n,CS}$	=	mass of NiO in domain n from corrosion of carbon steel [kg]
$m_{CrOx,n,CS}$	=	mass of Cr ₂ O ₃ in domain n from corrosion of carbon steel [kg]
$m_{G,n,SS}$	=	mass of goethite in domain n from corrosion of stainless steel [kg]
$m_{HFO,n,SS}$	=	mass of HFO in domain n from corrosion of stainless steel [kg]

$m_{NiO,n,SS}$	=	mass of NiO in domain n from corrosion of stainless steel [kg]
$m_{CrOx,n,SS}$	=	mass of Cr ₂ O ₃ in domain n from corrosion of stainless steel [kg]
k_{CP}	=	FHH parameter k for corrosion products [dimensionless]
s_{CP}	=	FHH parameter s for corrosion products [dimensionless]
r_{CS}	=	rate of corrosion of carbon steel [$\mu\text{m yr}^{-1}$]
r_{SS}	=	rate of corrosion of stainless steel [$\mu\text{m yr}^{-1}$]
$t_{max,CS,n}$	=	maximum thickness of carbon steel in domain n [m]
$t_{max,SS,n}$	=	maximum thickness of stainless steel in domain n [m]
ρ_G	=	grain density of goethite [kg m^{-3}]
ρ_{HFO}	=	grain density of HFO [kg m^{-3}]
ρ_{NiO}	=	grain density of NiO [kg m^{-3}]
ρ_{CrOx}	=	grain density of Cr ₂ O ₃ [kg m^{-3}]
\bar{s}_G	=	specific surface area of goethite [$\text{m}^2 \text{kg}^{-1}$]
\bar{s}_{HFO}	=	specific surface area of HFO [$\text{m}^2 \text{kg}^{-1}$]
\bar{s}_{NiO}	=	specific surface area of NiO [$\text{m}^2 \text{kg}^{-1}$]
\bar{s}_{CrOx}	=	specific surface area of Cr ₂ O ₃ [$\text{m}^2 \text{kg}^{-1}$]
α_G	=	stoichiometric coefficient for conversion of Fe to goethite [mol Fe mol ⁻¹ goethite].
α_{HFO}	=	stoichiometric coefficient for conversion of Fe to HFO [mol Fe mol ⁻¹ HFO]
α_{NiO}	=	stoichiometric coefficient for conversion of Ni to NiO [mol Ni mol ⁻¹ NiO]
$\alpha_{Cr_2O_3}$	=	stoichiometric coefficient for conversion of Cr to Cr ₂ O ₃ [mol Cr mol ⁻¹ Cr ₂ O ₃].

Although parameters $\omega_{CS,Ni}$ and $\omega_{CS,Cr}$ are zero (because there is no nickel or chromium in carbon steel), the parameters are retained because the equations for calculating corrosion product mass are then all uniformly defined for both carbon steel and stainless steel. Parameter values for this model are listed in Table 6.5-5 for each domain. The mass of steel in each domain and the fraction of that mass that is carbon steel are developed in Tables 6.3-8 and 6.3-9. The maximum thickness of each type of steel in each domain is obtained by inspection of design data presented in Tables 4.1-20 through 4.1-22. Material property parameters used in this model are shown in Table 6.5-6. Parameters with associated uncertainty represented by a range and distribution are listed in Table 6.5-7.

Because the TSPA calculations were started before the direct confirming data were available in the design interface documents (SNL 2007 [DIRS 179394], and SNL 2007 [DIRS 179567]), it was necessary to utilize preliminary values for the design of the EBS components. The

parameters listed in Table 6.5-5 are developed in Tables 6.3-8 and 6.3-9 from component masses specified in the design documents. Table 6.5-5 shows the parameter values obtained using both the preliminary design data as well as the final design data from SNL 2007 [DIRS 179394], and SNL 2007 [DIRS 179567]. The TSPA uses the parameters from the preliminary design data. Table 6.5-5 also compares preliminary and final design data, showing that the differences are negligible, so that the impact of using the preliminary design data on TSPA results should also be negligible. The dimensional parameters, $t_{max,CS,n}$ and $t_{max,SS,n}$, based on preliminary design data are identical to the parameters based on the final design data.

Table 6.5-5. Domain Properties Used to Compute Corrosion Product Water Saturation and Volume.

	Basis: Preliminary Design	Basis: Final Design	Difference: Final - Preliminary Final
Domain, <i>n</i>	$m_{s,n}$ (kg)^a	$m_{s,n}$ (kg)^a	%
CSNF-1	9,980	9,990	-0.1
CSNF-2	24,700	24,600	0.4
CDSP-1a	3,800	3,780	0.0
CDSP-1b	1,270	1,280	-0.8
CDSP-2	18,900	18,900	0.0
Domain, <i>n</i>	$f_{CS,n}$^a	$f_{CS,n}$^a	%
CSNF-1	0	0	0.0
CSNF-2	0	0	0.0
CDSP-1a	0	0	0.0
CDSP-1b	0.25	0.25	0.0
CDSP-2	0.31	0.31	0.0
Domain, <i>n</i>	$t_{max,CS,n}$ (mm)	Component and Source	
CSNF-1	0	–	
CSNF-2	0	–	
CDSP-1a	0	–	
CDSP-1b	6.35	TMI canister wall thickness (0.25 in.) (DOE 2003 [DIRS 164970], p. 25)	
CDSP-2	31.75	Divider plate assembly tube thickness (1.25 in.) (SNL 2007 [DIRS 179567], Table 4-9)	
Domain, <i>n</i>	$t_{max,SS,n}$ (mm)	Component and Source	
CSNF-1	11.11	Fuel Basket Assembly A-, B- & C-Plates (0.4375 in.) (SNL 2007 [DIRS 179394], Table 4-2)	
CSNF-2	50.8	Inner vessel thickness (2.00 in.) (SNL 2007 [DIRS 179394], Table 4-3)	
CDSP-1a	10.5	HLW glass canister wall thickness (CRWMS M&O 2000 [DIRS 151743], Table 3)	
CDSP-1b	9.525	SNF standard canister wall thickness (0.375 in.) (DOE 2003 [DIRS 164970], Fig. 13)	
CDSP-2	50.8	Inner vessel thickness (2.00 in.) (SNL 2007 [DIRS 179567], Table 4-9)	

^a Source: Tables 6.3-8 and 6.3-9.

Table 6.5-6. Constant Material Properties Used to Compute Corrosion Product Water Saturation and Volume.

Property	Value	Source
Density of goethite (FeOOH)	4,260 kg m ⁻³	Lide 2000 [DIRS 162229], p. 4-66
Density of HFO	3,960 kg m ⁻³	Towe and Bradley 1967 [DIRS 155334], p. 386
Density of Cr ₂ O ₃	5,220 kg m ⁻³	Lide 2000 [DIRS 162229], p. 4-54
Density of NiO	6,720 kg m ⁻³	Lide 2000 [DIRS 162229], p. 4-75
Mass fraction of iron in carbon steel	0.98 kg kg ⁻¹	ASTM A 516/A 516M-90 1991 [DIRS 117138]
Mass fraction of nickel in carbon steel	0 kg kg ⁻¹	ASTM A 516/A 516M-90 1991 [DIRS 117138]
Mass fraction of chromium in carbon steel	0 kg kg ⁻¹	ASTM A 516/A 516M-90 1991 [DIRS 117138]
Mass fraction of iron in stainless steel	0.65 kg kg ⁻¹	DTN: MO0003RIB00076.000 [DIRS 153044]; balance*
Mass fraction of nickel in stainless steel	0.12 kg kg ⁻¹	DTN: MO0003RIB00076.000 [DIRS 153044]; average*
Mass fraction of chromium in stainless steel	0.17 kg kg ⁻¹	DTN: MO0003RIB00076.000 [DIRS 153044]; average*
Atomic weight of iron	0.055847 kg mol ⁻¹	Weast 1985 [DIRS 111561], p. B-102
Atomic weight of nickel	0.05869 kg mol ⁻¹	Weast 1985 [DIRS 111561], p. B-118
Atomic weight of chromium	0.051996 kg mol ⁻¹	Weast 1985 [DIRS 111561], p. B-88
Molecular weight of goethite	0.088852 kg mol ⁻¹	Lide 2000 [DIRS 162229], p. 4-66
Molecular weight of HFO	0.088852 kg mol ⁻¹	See Section 6.3.4.2.3.1
Molecular weight of NiO	0.074692 kg mol ⁻¹	Lide 2000 [DIRS 162229], p. 4-75
Molecular weight of Cr ₂ O ₃	0.151990 kg mol ⁻¹	Lide 2000 [DIRS 162229], p. 4-54
Stoichiometric coefficient for conversion of Fe to goethite	1.0 mol Fe mol ⁻¹ goethite	From stoichiometry
Stoichiometric coefficient for conversion of Fe to HFO	1.0 mol Fe mol ⁻¹ HFO	From stoichiometry
Stoichiometric coefficient for conversion of Ni to NiO	1.0 mol Ni mol ⁻¹ NiO	From stoichiometry
Stoichiometric coefficient for conversion of Cr to Cr ₂ O ₃	2.0 mol Cr mol ⁻¹ Cr ₂ O ₃	From stoichiometry

* Elemental composition, as shown in Table 4.1-15; average value is used when a range is specified; Fe content is balance when average values used for non-Fe components

Table 6.5-7. Sampled Parameters Used to Compute Corrosion Product Water Saturation and Volume.

Property	Range and Distribution	Comments
Specific surface area of goethite (FeOOH)	14.7 – 110 m ² g ⁻¹ Log-Normal (Truncated)	See Section 6.3.4.3.3; Mean = 57.6 m ² g ⁻¹ Std. Dev. = 34.5 m ² g ⁻¹
Specific surface area of HFO	68 – 600 m ² g ⁻¹ Log-Normal (Truncated)	See Section 6.3.4.3.3 Mean = 275.6 m ² g ⁻¹ Std. Dev. = 113.4 m ² g ⁻¹
Specific surface area of NiO	1 – 30 m ² g ⁻¹ Uniform	Based on data in Table 6.3-10
Specific surface area of Cr ₂ O ₃	1 – 20 m ² g ⁻¹ Log-Uniform	Based on data in Table 6.3-10; log-uniform distribution emphasizes lower values that are more frequently observed, with less emphasis on high values for Cr oxide gel
Mass fraction of iron oxides (goethite and HFO) that is goethite	0.45 – 0.80 (fraction) Uniform	See Section 6.3.4.2.3.1
Rate of corrosion of carbon steel	25 – 135 μm yr ⁻¹ Log-Normal (Truncated)	See Section 6.3.4.3.4.3
Rate of corrosion of stainless steel	0.01 – 0.51 μm yr ⁻¹ Log-Normal (Truncated)	See Section 6.3.4.3.4.3
FHH adsorption isotherm parameter <i>k</i> for corrosion products	1.048 – 1.370 (dimensionless) Uniform	See Section 6.3.4.3.2
FHH adsorption isotherm parameter <i>s</i> for corrosion products	1.525 – 1.852 (dimensionless) Uniform	See Section 6.3.4.3.2

The lifetime of internal components in a waste package is based on the time required for the thickest component to corrode completely. Since corrosion can occur on both sides of a component, the maximum thickness is halved to obtain the lifetime for carbon steel and stainless steel components:

$$t_{LCS,n} = \frac{1000 t_{max,CS,n}}{2r_{CS}}, \quad (\text{Eq. 6.5.2.2.1-1})$$

$$t_{LSS,n} = \frac{1000 t_{max,SS,n}}{2r_{SS}}, \quad (\text{Eq. 6.5.2.2.1-2})$$

where the factor of 1000 converts the thickness (mm) to μm, since the corrosion rate is expressed in units of μm yr⁻¹.

For each type of corrosion product (*CPm* = goethite, HFO, NiO, and Cr₂O₃) in each domain *n*, the mass of corrosion product is obtained as a function of time by linearly interpolating from the time of waste package breach at *t*₀ to time *t* over the lifetime of carbon steel and stainless steel

components; the maximum amount of corrosion product is reached at the lifetime of the components, after which time the corrosion product mass remains constant:

$$m_{CPm,CS,n}(t) = \begin{cases} \left(\frac{t-t_0}{t_{LCS,n}} \right) f_{CS,n} f_{GHFO} \omega_{CS,m} \frac{M_{CPm}}{\alpha_{CPm} M_m} m_{s,n}, & t-t_0 \leq t_{LCS,n} \\ f_{CS,n} f_{GHFO} \omega_{CS,m} \frac{M_{CPm}}{\alpha_{CPm} M_m} m_{s,n}, & t-t_0 > t_{LCS,n} \end{cases}, \text{(Eq. 6.5.2.2.1-3)}$$

$$m_{CPm,SS,n}(t) = \begin{cases} \left(\frac{t-t_0}{t_{LSS,n}} \right) (1-f_{CS,n}) f_{GHFO} \omega_{SS,m} \frac{M_{CPm}}{\alpha_{CPm} M_m} m_{s,n}, & t-t_0 \leq t_{LSS,n} \\ (1-f_{CS,n}) f_{GHFO} \omega_{SS,m} \frac{M_{CPm}}{\alpha_{CPm} M_m} m_{s,n}, & t-t_0 > t_{LSS,n} \end{cases}, \text{(Eq. 6.5.2.2.1-4)}$$

where subscript m refers to the metal (Fe that becomes goethite, Fe that becomes HFO, Ni, or Cr) associated with CPm , and f_{GHFO} is a dimensionless parameter whose meaning and value depends on each type of corrosion product; for goethite, $f_{GHFO} = \omega_G$, the sampled mass fraction of goethite in iron-based corrosion products; for HFO, $f_{GHFO} = (1 - \omega_G)$; and for NiO and Cr_2O_3 , f_{GHFO} is a placeholder with a value of 1.0. $f_{CS,n}$ is the fraction of carbon steel in steel mass in domain n . $\omega_{CS,m}$ is the mass fraction of metal m in carbon steel, and $\omega_{SS,m}$ is the mass fraction of metal m in stainless steel. Atomic weights of metals, M_m , and molecular weights of corrosion products, M_{CPm} , are listed in Table 6.5-8. The mass of steel in domain n , $m_{s,n}$, is developed in Tables 6.3-8 and 6.3-9. The stoichiometric coefficient, α_{CPm} , is the number of moles of metal m in a mole of corrosion product CPm , when the corrosion products are represented as FeOOH, Cr_2O_3 , and NiO.

The total mass of corrosion products in domain n is the mass of corrosion products from carbon steel and stainless steel summed over the four types of corrosion products:

$$m_{CP,n} = \sum_{CPm} (m_{CPm,CS,n} + m_{CPm,SS,n}). \quad \text{(Eq. 6.5.2.2.1-5)}$$

The water saturation in corrosion product CPm in domain n , $S_{we,CPm,n}$, is dependent on the relative humidity (RH), which varies over time, on the specific surface area, $\bar{s}_{CPm,n}$, and on the corrosion product grain density, ρ_{CPm} :

$$S_{we,CPm,n}(RH) = \min \left[t_f \rho_{CPm} \bar{s}_{CPm,n} \left(\frac{1 - \phi_{CP}}{\phi_{CP}} \right) \theta_{CP,n}(RH), 1.0 \right], \quad \text{(Eq. 6.5.2.2.1-6)}$$

where t_f is the thickness (m) of a monolayer of water, ϕ_{CP} is the porosity of corrosion products as well as the porosity of corrosion products domains (0.4; the same constant value is used for all corrosion products), and $\theta_{CP,n}(RH)$ is the number of monolayers of water adsorbed on the surface of corrosion products, a function of RH , as given in Section 6.3.4.3.5. A single adsorption isotherm is used for all corrosion products, so a single RH -dependent value of $\theta_{CP,n}(RH)$ is used for all corrosion products in domain n . The water saturation for the entire domain n (summed over all four CP types and any waste form degradation rind) is computed once the domain water volume is obtained, following Equation 6.5.2.2-10. The min function is needed because the adsorption isotherm function $\theta_{CP,n}(RH)$ is unbounded as RH approaches 1.0.

The pore volume in each type of corrosion product in each domain is:

$$V_{\phi,CPm,n}(t) = \frac{[m_{CPm,CS,n}(t) + m_{CPm,SS,n}(t)] \left(\frac{\phi_{CP}}{1 - \phi_{CP}} \right)}{\rho_{CPm}} \quad (\text{Eq. 6.5.2.2.1-7})$$

Since the corrosion products are commingled, the saturation and water volume of all of the individual components of the corrosion products are summed to provide the characteristics of the entire domain. The total pore volume in domain n steel corrosion products is given by Equation 6.5.2.2.1-7 summed over the four corrosion product types:

$$V_{\phi,CP,n}(t) = \left(\frac{\phi_{CP}}{1 - \phi_{CP}} \right) \sum_{CPm} \left[\frac{[m_{CPm,CS,n}(t) + m_{CPm,SS,n}(t)]}{\rho_{CPm}} \right], \quad (\text{Eq. 6.5.2.2.1-8})$$

where the porosity factor can be taken outside the summation because the porosity is identical for all corrosion product types.

The bulk volume of corrosion products in domain n is:

$$V_{CP,n}(t) = \left(\frac{1}{1 - \phi_{CP}} \right) \sum_{CPm} \left[\frac{[m_{CPm,CS,n}(t) + m_{CPm,SS,n}(t)]}{\rho_{CPm}} \right]. \quad (\text{Eq. 6.5.2.2.1-9})$$

The water volume in each type of corrosion product in each domain that contains only steel corrosion products is:

$$\begin{aligned} V_{w,CPm,n}(RH, t) &= V_{\phi,CPm,n}(t) S_{we,CPm,n}(RH) \\ &= \frac{[m_{CPm,CS,n}(t) + m_{CPm,SS,n}(t)] \left(\frac{\phi_{CP}}{1 - \phi_{CP}} \right)}{\rho_{CPm}} S_{we,CPm,n}(RH) \quad (\text{Eq. 6.5.2.2.1-10}) \\ &= [m_{CPm,CS,n}(t) + m_{CPm,SS,n}(t)] t_f \bar{s}_{CPm,n} \theta_{CP,n}(RH), \end{aligned}$$

and the water volume in these domains is:

$$\begin{aligned}
 V_{w,CP,n}(RH,t) &= \sum_{CPm} [V_{w,CPm,n}(RH,t)] \\
 &= \sum_{CPm} \left[\frac{[m_{CPm,CS,n}(t) + m_{CPm,SS,n}(t)]}{\rho_{CPm}} \left(\frac{\phi_{CP}}{1 - \phi_{CP}} \right) S_{we,CPm,n}(RH) \right] \text{ (Eq. 6.5.2.2.1-11)} \\
 &= t_f \theta_{CP,n}(RH) \sum_{CPm} (\bar{s}_{CPm,n} [m_{CPm,CS,n}(t) + m_{CPm,SS,n}(t)]).
 \end{aligned}$$

The adsorption isotherm function is taken outside the summation because it is identical for all corrosion product types.

The water saturation for domains that contain only steel corrosion products is given by:

$$S_{we,CP,n}(RH) = \min \left[\frac{V_{w,CP,n}(RH,t)}{V_{\phi,CP,n}(t)}, 1.0 \right]. \quad \text{(Eq. 6.5.2.2.1-12)}$$

Until the end of the lifetime of the shorter-lived carbon steel ($t - t_0 < t_{LCS,n}$), the water saturation is not explicitly time-dependent, varying only with RH , which may vary with time. In this case, the water saturation is given by:

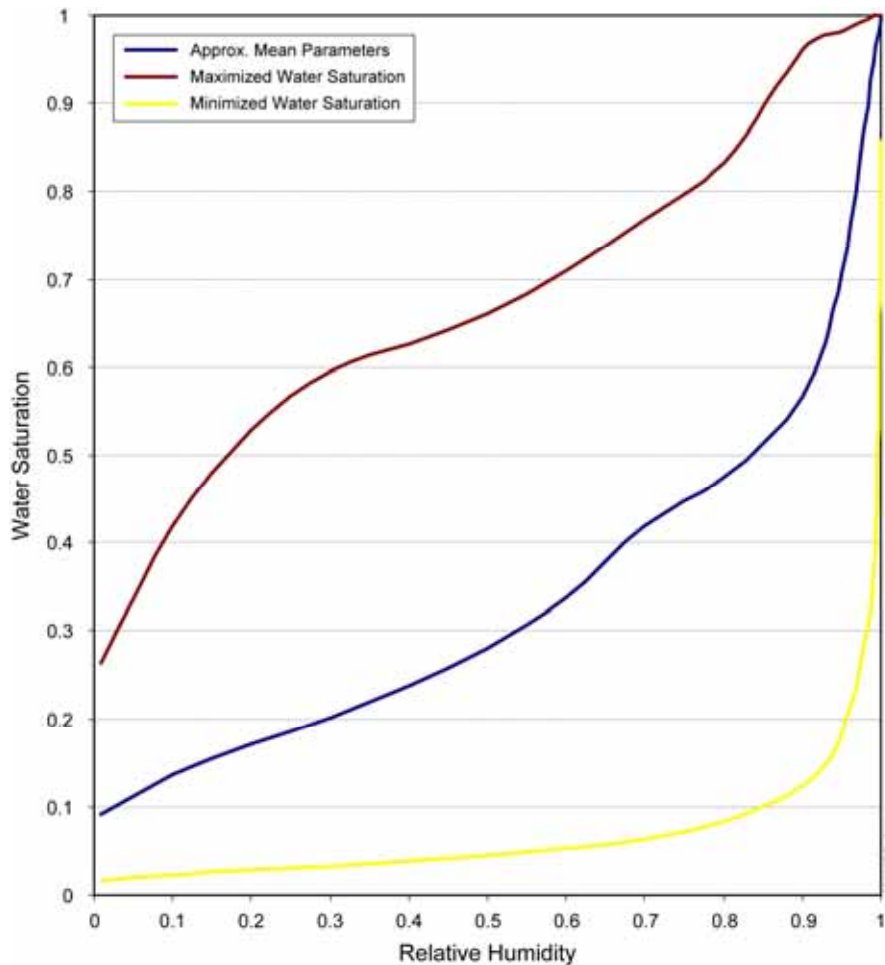
$$S_{we,CP,n}(RH) = \min \left[t_f \left(\frac{1 - \phi_{CP}}{\phi_{CP}} \right) \theta_{CP,n}(RH) \frac{\sum_{CPm} \left(\bar{s}_{CPm,n} f_{GHFO} \frac{M_{CPm}}{M_m} [f_{CS,n} \omega_{CS,m} + (1 - f_{CS,n}) \omega_{SS,m}] \right)}{\sum_{CPm} \left(\frac{1}{\rho_{CPm}} f_{GHFO} \frac{M_{CPm}}{M_m} [f_{CS,n} \omega_{CS,m} + (1 - f_{CS,n}) \omega_{SS,m}] \right)}, 1.0 \right] \quad \text{(Eq. 6.5.2.2.1-13)}$$

Figure 6.5-4 shows the results of a sample calculation of water saturation in the CSNF corrosion products domain for constant RH using values of uncertain parameters from Table 6.5-7 that minimize and maximize the saturation. Included in this figure is a curve showing water saturation using approximate mean values for the uncertain parameters. Since the CSNF corrosion products domain contains only stainless steel, and since the RH is constant in this example, the water saturation does not vary over time. Table 6.5-8 lists numerical results at selected values of RH .

Table 6.5-8. Water Saturation in CSNF Corrosion Products Domain

RH	Water Saturation Minimized		Water Saturation Maximized	
	Monolayers of Water	Water Saturation	Monolayers of Water	Water Saturation
0.1	0.6	0.023	0.7	0.406
0.2	0.8	0.028	0.9	0.516
0.5	1.2	0.046	1.5	0.659
0.8	2.3	0.084	3.3	0.833
0.9	3.6	0.127	5.6	0.963
0.95	5.3	0.189	8.8	0.983
0.99	13.1	0.386	26.3	1.000

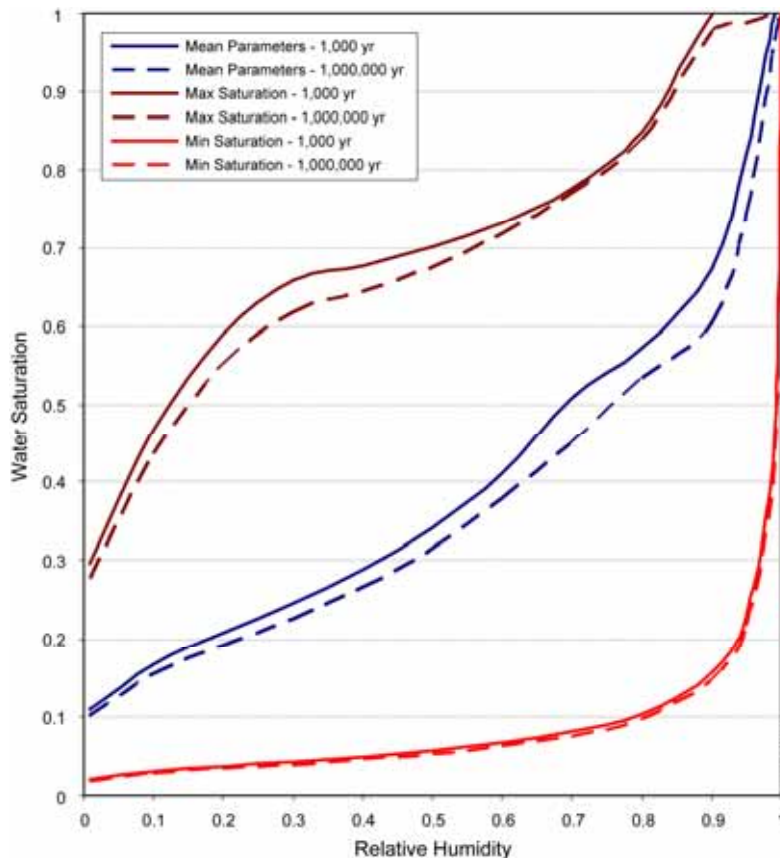
Output DTN: SN0703PAEBSRTA.001, file *CP Sample Calcs 7-19-2007.xls*, worksheet "CSNF-2 (CPs) Min&Max"



Source: Output DTN: SN0703PAEBSRTA.001, file *CP Sample Calcs 7-19-2007.xls*, worksheet "CSNF-2 (CPs) Min&Max"

Figure 6.5-4. Water Saturation in CSNF Corrosion Products Domain in Constant RH Sample Calculation

In a second example calculation, this time for the corrosion products domain in a codisposal waste package, the domain contains both carbon steel and stainless steel; results are shown in Figure 6.5-5. As in Figure 6.5-4, this figure shows the water saturation in the CDSP corrosion products domain for constant RH using values of uncertain parameters from Table 6.5-7 that minimize and maximize the saturation, as well as approximately mean parameter values. Results are shown at 1,000 yr and at 10^6 yr. For a constant RH , the water saturation is constant until the end of the carbon steel lifetime, which is shorter than that of the stainless steel. Water saturation is maximized when the steel lifetime is minimized by using the maximum corrosion rates; the saturation is minimized by using the minimum corrosion rates. For carbon steel, the lifetime ranges from 118 yr to 1,270 yr in the codisposal waste package corrosion products domain, in which the maximum thickness of carbon steel is 31.75 mm (Table 6.5-5). For stainless steel, the lifetime ranges from 49,800 yr to 5.08×10^6 yr in the codisposal waste package corrosion products domain, in which the maximum thickness of stainless steel is 50.8 mm (Table 6.5-5). After the end of the carbon steel lifetime, the domain water saturation varies over time, although the change is small, as seen in Figure 6.5-5; in this example, at $RH = 0.95$, the maximum water saturation is 0.9994 at 1,000 yr and 0.9887 at 10^6 yr, while the minimum water saturation is 0.239 at 1,000 yr and 0.226 at 10^6 yr.



Source: Output DTN: SN0703PAEBSRTA.001, file *CP Sample Calcs 7-19-2007.xls*, worksheet "CDSP-2 (CPs) Min&Max"

Figure 6.5-5. Water Saturation in CDSP Corrosion Products Domain in Constant RH Sample Calculation

The effective diffusion coefficient for steel corrosion products in domain n is obtained using Archie's law (see Section 6.3.4.3.5, Equation 6.3.4.3.5-2) with a fixed corrosion products porosity of 0.4 (see Section 6.3.4.3.4) and the water saturation $S_{we,CP,n}$ obtained from Equation 6.5.2.2.1-12 in a no-seep environment; in a seep environment, a water saturation of 1.0 is used.

6.5.2.2.2 Waste Form Domains Water Saturation and Water Volume

The calculation of waste form degradation rind water content is completely analogous to that of steel corrosion products and includes the calculation of steel corrosion products water content, since the waste form domain includes steel associated with the waste form. Parameter values used in this calculation are summarized in Table 6.5-9.

Table 6.5-9. Parameters Used to Compute Waste Form Water Saturation and Water Volume.

Property	Range and Distribution	Comments
Specific surface area of CSNF rind	0.5 – 60 m ² g ⁻¹ Uniform	See Section 6.3.4.6.1
Grain density of CSNF rind	5,600 – 11,500 kg m ⁻³ Uniform	See Section 6.3.4.6.1
FHH adsorption isotherm parameter k for CSNF rind	1.606 – 8.215 (dimensionless) Uniform	See Section 6.3.4.6.1
FHH adsorption isotherm parameter s for CSNF rind	1.656 – 3.038 (dimensionless) Uniform	See Section 6.3.4.6.1
Porosity of CSNF rind	0.05 – 0.3 (fraction) Uniform	DTN: MO0411SPACLDDG.003 [DIRS 180755], Table 7-1
Specific surface area of HLW glass	10 – 38 m ² g ⁻¹ Uniform	Langmuir 1997 [DIRS 100051], Table 10.2
Grain density of HLW glass rind	2,700 kg m ⁻³ Constant	DTN: MO0502ANLGAMR1.016 ECN1 [DIRS 172830], Table 8-1
FHH adsorption isotherm parameter k for HLW glass	13.2 (dimensionless) Constant	Ebert et al. 1991 [DIRS 111028], p. 134, Figure 1b
FHH adsorption isotherm parameter s for HLW glass	1.5 (dimensionless) Constant	Ebert et al. 1991 [DIRS 111028], p. 134, Figure 1b
Porosity of HLW glass rind	0.17 (fraction) Constant	DTN: MO0502ANLGAMR1.016 ECN1 [DIRS 172830], Table 8-1

6.5.2.2.1 CSNF Waste Form Domain

As in Equation 6.5.2.2.1-6, the water saturation in waste form rind r in domain n is dependent on the relative humidity (RH), which varies over time, on the rind specific surface area, $\bar{s}_{rind,n}$, and on the rind grain density, ρ_r :

$$S_{we,rind,n}(RH) = \min \left[t_f \rho_r \bar{s}_{rind,n} \left(\frac{1 - \phi_{rind}}{\phi_{rind}} \right) \theta_{r,n}(RH), 1.0 \right]. \quad (\text{Eq. 6.5.2.2.2.1-1})$$

The adsorption isotherm for CSNF rind is developed in Section 6.3.4.6.1 and for HLW glass rind in Section 6.3.4.6.2. For DSNF, the rind is modeled as identical to that of CSNF rind.

The water volume in the CSNF rind in domain n is given by:

$$V_{w,rind,n}(RH, t) = \phi_{rind} S_{we,rind,n}(RH) V_{rind,n}(t), \quad (\text{Eq. 6.5.2.2.2.1-2})$$

where the rind bulk volume, $V_{rind,n}$, is provided by *Cladding Degradation Summary for LA* (SNL 2007 [DIRS 180616], Eq. 6-7 in Table 6-4). The CSNF actually contains the solid UO₂ fuel pellets, cladding, and open space between fuel rods. However, for purposes of this model, the CSNF rind in this model domain includes only the porous rind, whose volume increases over time; the open space and impermeable solids are not included, since they contain no pathway for transport of radionuclides. (Unreacted UO₂ fuel pellets have a small amount of porosity that is neglected, consistent with the treatment in *Cladding Degradation Summary for LA*, (SNL 2007 [DIRS 180616], pp. 6 to 11)). The total bulk volume of the CSNF domain is the sum of the rind bulk volume and the bulk volume of basket tube and absorber plate corrosion products, which also increase over time:

$$V_{CSNF}(t) = V_{rind,CSNF}(t) + V_{CP,CSNF}(t). \quad (\text{Eq. 6.5.2.2.2.1-3})$$

The bulk volume of CSNF domain corrosion products is (Equation 6.5.2.2.1-9 for $n = \text{CSNF}$):

$$V_{CP,CSNF}(t) = \left(\frac{1}{1 - \phi_{CP}} \right) \sum_{CPm} \left[\frac{m_{CPm,CS,CSNF}(t) + m_{CPm,SS,CSNF}(t)}{\rho_{CPm}} \right]. \quad (\text{Eq. 6.5.2.2.2.1-4})$$

The pore volume in the CSNF waste form domain is the sum of CSNF rind pore volume and steel corrosion products pore volume:

$$V_{\phi,CSNF}(t) = \phi_{rind} V_{rind,CSNF}(t) + V_{\phi,CP,CSNF}(t), \quad (\text{Eq. 6.5.2.2.2.1-5})$$

where the CSNF rind porosity, ϕ_{rind} , is a sampled parameter ranging from 0.05 to 0.30 with a uniform distribution. The corrosion products pore volume is computed as in Equation 6.5.2.2.1-8 using the steel corrosion products porosity, ϕ_{CP} , which has a constant value of 0.4, and the mass of steel shown in Table 6.5-5.

The effective porosity of the CSNF waste form domain, which is needed for computing the diffusion coefficient using Archie's law, is time dependent because the pore volume and bulk volume of the domain are time dependent:

$$\phi_{CSNF}(t) = \frac{V_{\phi,CSNF}(t)}{V_{CSNF}(t)}. \quad (\text{Eq. 6.5.2.2.2.1-6})$$

The water volume in the CSNF waste form domain is the sum of CSNF rind water volume (from Equation 6.5.2.2.2.1-2) and steel corrosion products pore volume (from Equation 6.5.2.2.1-11):

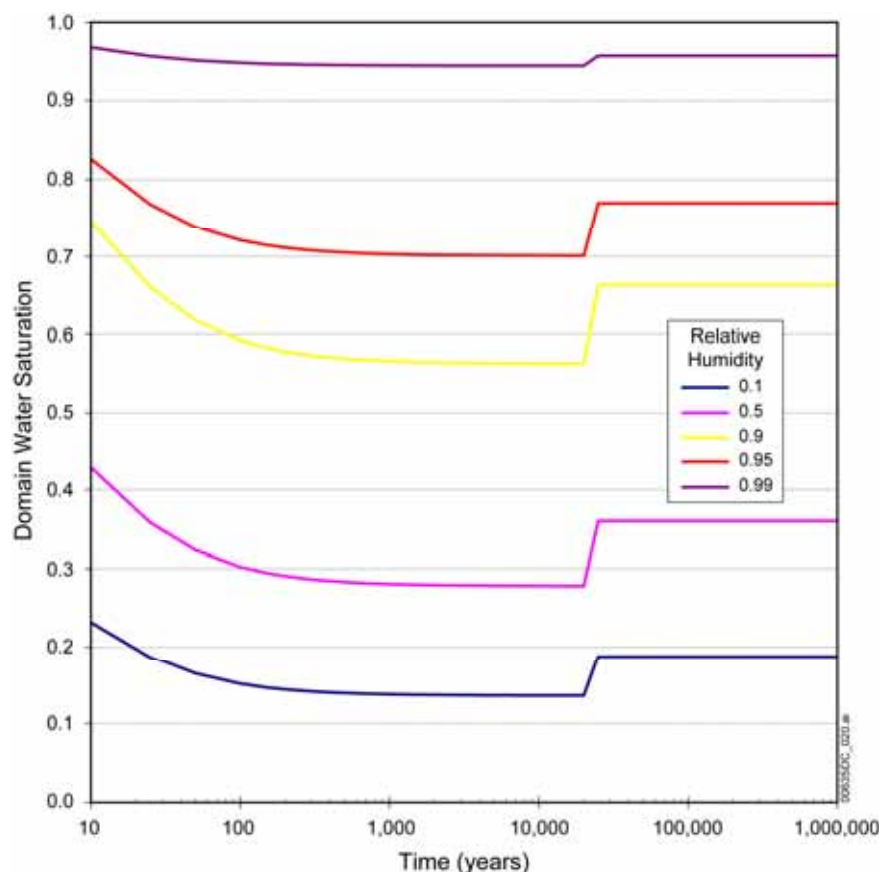
$$V_{w,CSNF}(RH, t) = V_{w,rind,CSNF}(RH, t) + V_{w,CP,CSNF}(RH, t). \quad (\text{Eq. 6.5.2.2.2.1-7})$$

The water saturation in the CSNF waste form domain is given by:

$$S_{we,CSNF}(RH) = \min \left[\frac{V_{w,CSNF}(RH, t)}{V_{\phi,CSNF}(t)}, 1.0 \right]. \quad (\text{Eq. 6.5.2.2.2.1-8})$$

Since the FHH isotherm function that provides the water volume in both the CSNF rind and the steel corrosion products in the waste form domain is unbounded as RH approaches 1.0, the saturation must be limited to a value of 1.0.

Results of a sample calculation for CSNF waste form domain water saturation are shown in Figure 6.5-6. In this calculation, the RH is held constant for 10^6 yr. In this sample calculation, all fuel rods are assumed to be intact except for 0.1 percent that have prematurely failed. The TSPA compliance case takes no credit for CSNF cladding as a barrier to flow, as explained in *Cladding Degradation Summary for LA* (SNL 2007 [DIRS 180616], Section 6.2[a]). A seismic event occurs at 25,000 yr in which all fuel rods are assumed to fail and all waste form instantaneously degrades to the CSNF rind. This immediate increase in the water adsorption capacity of the waste form causes the step increase in the pore volume and water volume in the waste form domain that appears at 25,000 yr. Since coincidentally all steel in this example has finished corroding at 24,258 yr, the water saturation remains constant following the seismic event. Unlike the corrosion product domain, the water saturation in this example decreases over time (until the seismic event), instead of remaining constant. This occurs because, in this example, even though the CSNF rind results from only 0.1 percent of the fuel rods having prematurely failed, the water volume in the rind is of the same order of magnitude as the water volume in the corrosion products in this domain, since the mass of steel is small compared to that of the corrosion products domain. However, until the seismic event, this water volume remains constant, while the pore volume of corrosion products increases (up to the lifetime of the stainless steel). Thus, the total domain water saturation decreases, even though the saturation of the corrosion products remains constant.



Source: Output DTN: SN0703PAEBSRTA.001, file *CP Sample Calcs 7-19-2007.xls*, worksheet “CSNF-1 (WF+CPs)”

Figure 6.5-6. Water Saturation in CSNF Waste Form Domain in Constant RH Sample Calculation

6.5.2.2.2.2 HLWG and DSNF Waste Form Subdomains

The HLW glass subdomain includes the porous glass degradation rind and the porous products of the corrosion of the stainless steel HLW glass canisters. The volume of both the HLW glass rind and the steel corrosion products increase over time until all of the glass is degraded and the steel is fully corroded. HLW glass rind bulk volume, V_{HLWG} , and the water volume, $V_{w,HLWG}$, for fully water saturated conditions are given as a function of time in DTN: MO0502ANLGAMR1.016 ECN1 [DIRS 172830], Equations 54 and 55, respectively. For partially saturated conditions, the water volume in HLW glass rind is given by:

$$V_{w,HLWG} = \phi_{HLWG} S_{we,HLWG} V_{HLWG} \quad (\text{Eq. 6.5.2.2.2.2-1})$$

The effective water saturation of the HLW glass rind is given the following equation (identical to Equation 6.3.4.6.2-2):

$$S_{we,HLWG} = \min \left[\rho_{HLWG} \bar{s}_{HLWG} t_f \left(\frac{1 - \phi_{HLWG}}{\phi_{HLWG}} \right) \theta_{HLWG}(RH), 1.0 \right], \quad (\text{Eq. 6.5.2.2.2.2-2})$$

using the FHH water vapor adsorption isotherm (also shown as Equation 6.3.4.6.2-1):

$$\theta_{HLWG} = \left(\frac{-k_{HLWG}}{\ln RH} \right)^{\frac{1}{s_{HLWG}}}. \quad (\text{Eq. 6.5.2.2.2.2-3})$$

The rind porosity is modeled as constant at 0.17 (DTN: MO0502ANLGAMR1.016 ECN1 [DIRS 172830], Table 8-1).

The pore volume in the HLW glass waste form subdomain is the sum of HLW glass rind pore volume and steel corrosion products pore volume:

$$V_{\phi,HLWG}(t) = \phi_{HLWG} V_{rind,HLWG}(t) + V_{\phi,CP,HLWG}(t). \quad (\text{Eq. 6.5.2.2.2.2-4})$$

The corrosion products pore volume is computed as in Equation 6.5.2.2.1-8.

The total bulk volume of the HLW glass waste form subdomain is the sum of the HLW glass bulk rind volume and the volume of HLW glass steel canister corrosion products, both of which increase over time:

$$V_{HLWG}(t) = V_{rind,HLWG}(t) + V_{CP,HLWG}(t). \quad (\text{Eq. 6.5.2.2.2.2-5})$$

The effective porosity of the entire HLW glass waste form domain, $\phi_{T,HLWG}$, is needed for computing the diffusion coefficient using Archie's law. This porosity is time dependent because the pore volume and bulk volume of the domain are time dependent:

$$\phi_{T,HLWG}(t) = \frac{V_{\phi,HLWG}(t)}{V_{HLWG}(t)}. \quad (\text{Eq. 6.5.2.2.2.2-6})$$

The water volume in the HLW glass waste form subdomain is the sum of HLW glass rind water volume (from Equation 6.5.2.2.2.1-9) and steel corrosion products water volume (from Equation 6.5.2.2.1-11):

$$V_{w,HLWG}(RH, t) = V_{w,rind,HLWG}(RH, t) + V_{w,CP,HLWG}(RH, t). \quad (\text{Eq. 6.5.2.2.2.2-7})$$

The water saturation in the HLW glass waste form subdomain is given by:

$$S_{we,HLWG}(RH) = \min \left[\frac{V_{w,HLWG}(RH, t)}{V_{\phi,HLWG}(t)}, 1.0 \right]. \quad (\text{Eq. 6.5.2.2.2.2-8})$$

Since the FHH isotherm function that provides the water volume in both the HLW glass rind and the steel corrosion products is unbounded as RH approaches 1.0, the saturation must be limited to a value of 1.0.

The DSNF waste form subdomain includes the Three Mile Island (TMI) SNF as the representative SNF along with the corrosion products from the corrosion of the steel SNF canister, the sleeve and standoffs, and the TMI canister and steel components associated with the TMI SNF. DSNF is modeled as fully degraded as soon as the codisposal waste package is breached. The porosity of DSNF is set at a constant value of 0.20 (see Section 6.5.2.1.2).

The pore volume in the DSNF waste form subdomain is the sum of DSNF rind pore volume and steel corrosion products pore volume:

$$V_{\phi,DSNF}(t) = \phi_{DSNF}V_{rind,DSNF}(t) + V_{\phi,CP,DSNF}(t). \quad (\text{Eq. 6.5.2.2.2.2-9})$$

The corrosion products pore volume is computed as in Equation 6.5.2.2.1-8.

The total bulk volume of the DSNF waste form subdomain is the sum of the DSNF rind bulk volume and the volume of DSNF steel canister corrosion products; both increase over time:

$$V_{DSNF}(t) = V_{rind,DSNF}(t) + V_{CP,DSNF}(t). \quad (\text{Eq. 6.5.2.2.2.2-10})$$

The effective porosity of the DSNF waste form domain, $\phi_{T,DSNF}$, as distinguished from the porosity of the DSNF waste form, ϕ_{DSNF} , is needed for computing the diffusion coefficient using Archie's law. The porosity is time dependent because the pore volume and bulk volume of the domain are time dependent:

$$\phi_{T,DSNF}(t) = \frac{V_{\phi,DSNF}(t)}{V_{DSNF}(t)}. \quad (\text{Eq. 6.5.2.2.2.2-11})$$

The water volume in the DSNF waste form subdomain is the sum of DSNF rind water volume and steel corrosion products pore volume (from Equation 6.5.2.2.1-11):

$$V_{w,DSNF}(RH,t) = \phi_{DSNF}S_{we,rind,DSNF}(RH)V_{w,rind,DSNF} + V_{w,CP,DSNF}(RH,t), (\text{Eq. 6.5.2.2.2.2-12})$$

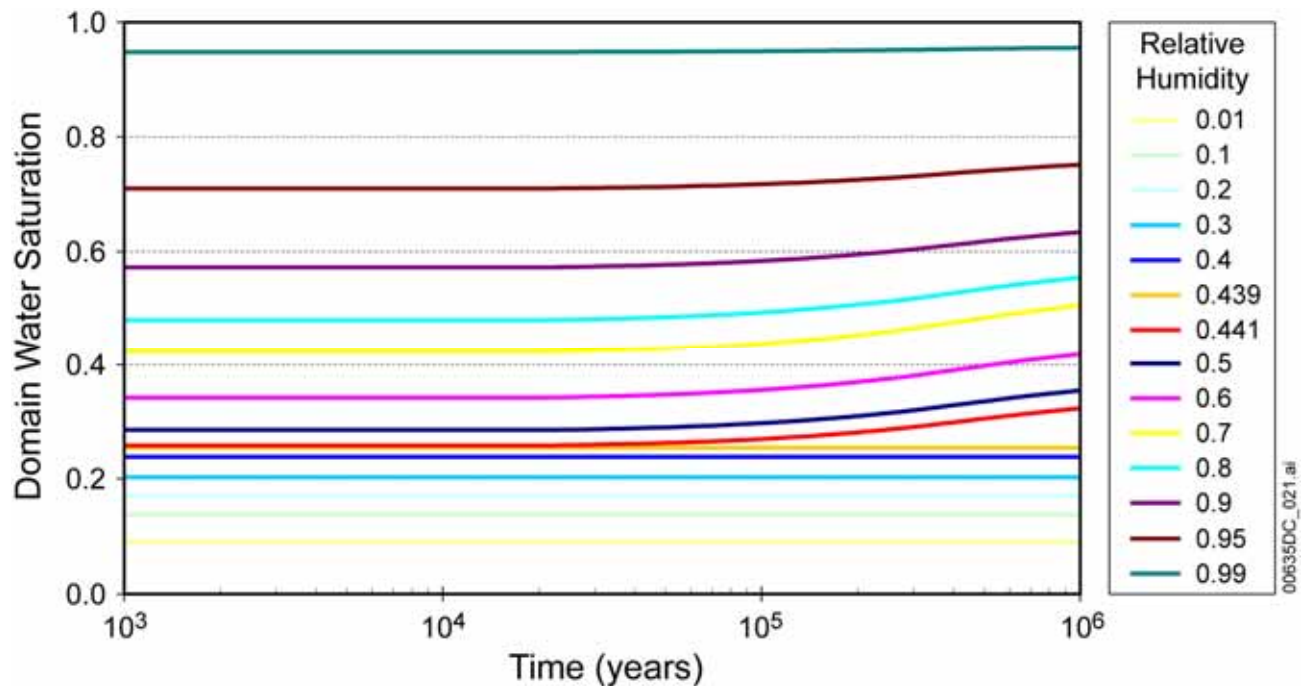
where the water saturation in DSNF waste form degradation rind is computed the same as for CSNF degradation rind (Equation 6.5.2.2.2.1-1). The water saturation in the DSNF waste form subdomain is given by:

$$S_{we,DSNF}(RH) = \min \left[\frac{V_{w,DSNF}(RH,t)}{V_{\phi,DSNF}(t)}, 1.0 \right]. \quad (\text{Eq. 6.5.2.2.2.2-13})$$

Since the FHH isotherm function that provides the water volume in the steel corrosion products is unbounded as RH approaches 1.0, the saturation must be limited to a value of 1.0.

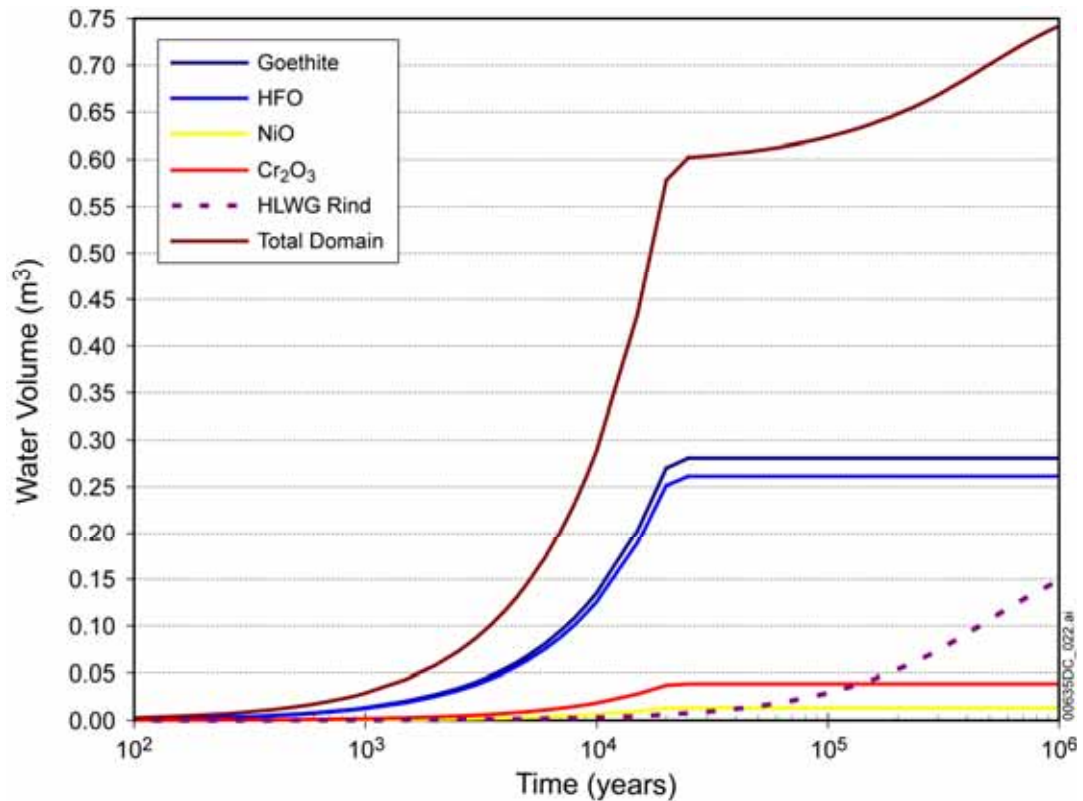
Figures 6.5-7 and 6.5-8 show the results of a sample calculation for the codisposal HLWG waste form domain in which RH is held constant for 10^6 yr. This example uses approximate mean or median values for uncertain parameters in Tables 6.5-7 and 6.5-9. The only steel present in this domain is in the stainless steel HLWG canisters. In this example, stainless steel has a lifetime of

20,800 yr. The mass of HLWG degradation products increases over time, but degradation only occurs when the *RH* is above 44 percent, as described in *Defense HLW Glass Degradation Model* (BSC 2004 [DIRS 169988], Section 6.7). Prior to the end of the stainless steel lifetime, the water volume and resulting water saturation in the domain is dominated by the stainless steel corrosion products. As seen above for CSNF corrosion products, when only one type of steel is present and the *RH* is constant, the water saturation in the domain is constant. Here, because the HLWG rind water saturation contributes little to the domain water volume before the steel is fully consumed (see Figure 6.5-8), the domain water saturation is nearly constant until the steel is consumed. After 20,800 yr, as HLW glass continues to degrade, the water saturation continues to increase. In this example, some HLW glass remains undegraded after 10^6 yr.



Source: Output DTN: SN0703PAEBSRTA.001, file *CP Sample Calcs 7-19-2007.xls*, worksheet "CDSP-1a (HLWG+CPs)"

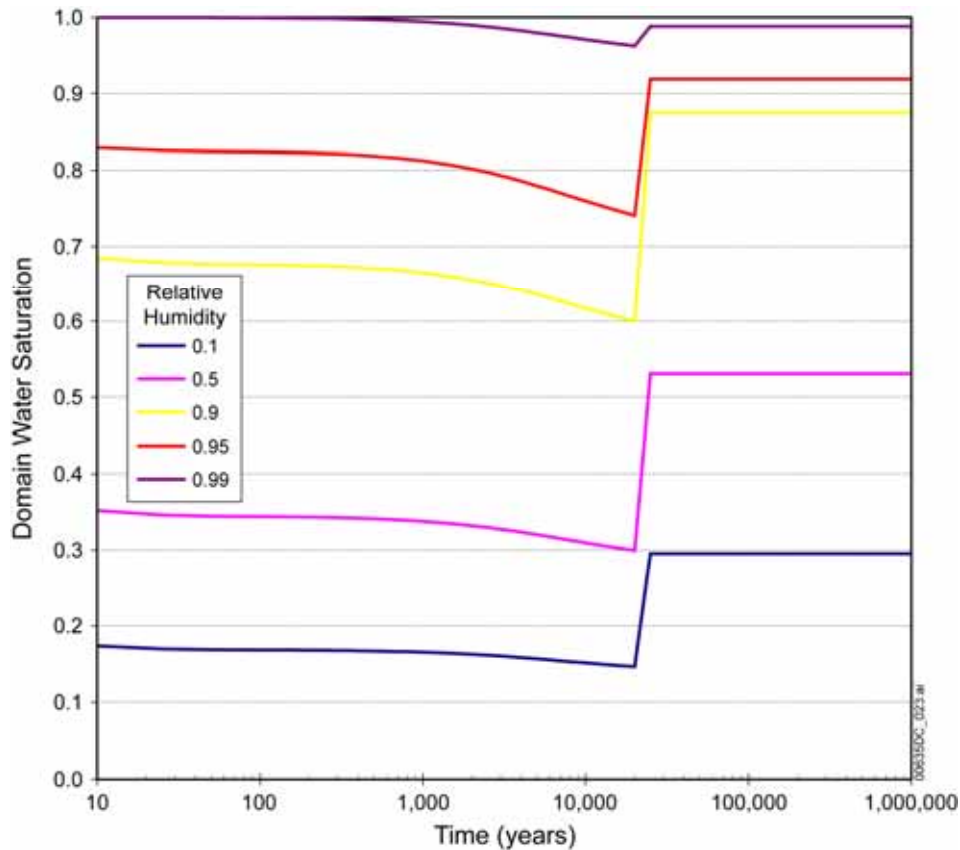
Figure 6.5-7. Water Saturation in HLWG Waste Form Domain in Constant RH Sample Calculation



Source: Output DTN: SN0703PAEBSRTA.001, file *CP Sample Calcs 7-19-2007.xls*, worksheet "CDSP-1a (HLWG+CPs)"

Figure 6.5-8. Water Volume in Components of HLWG Waste Form Domain in Constant RH Sample Calculation

Results of a sample calculation for DSNF waste form domain water saturation are shown in Figure 6.5-9. Again, the *RH* is held constant for 10^6 yr. A seismic event occurs at 25,000 yr, at which time all of the DSNF fuel is assumed to be instantly breached and degraded. This step increase in water adsorption capacity causes the increase in domain water saturation seen in Figure 6.5-9 at 25,000 yr. As in the CSNF waste form domain sample calculation (Figure 6.5-6), the domain water saturation decreases until the seismic event occurs, because the domain pore volume continually increases as steel corrodes, while the contribution of the DSNF degradation rind to the domain water volume remains constant.



Source: Output DTN: SN0703PAEBSRTA.001, file *CP Sample Calcs 7-19-2007.xls*, worksheet "CDSP-1b (DSNF+CPs)"

Figure 6.5-9. Water Saturation in DSNF Waste Form Domain in Constant RH Sample Calculation

6.5.2.3 Invert Domain Properties

The volume of the invert is equal to its cross sectional area (i.e., the area of a segment of a circle) times the axial length. Based on the drift diameter of 5.5 m (SNL 2007 [DIRS 179354], Table 4-1, Parameter Number 01-10) (or drift radius $r_D = 2.75$ m) and maximum invert thickness of $t_{I,max} = 4$ ft 4 in. = 1.321 m (SNL 2007 [DIRS 179354], Table 4-1, Parameter Number 01-10), the width of the top surface of the invert is (Perry et al. 1963 [DIRS 119529], p. 2-6):

$$w_I = 2\sqrt{r_D^2 - (r_D - t_{I,max})^2} = 4.70 \text{ m.} \quad (\text{Eq. 6.5.2.3-1})$$

The frontal cross sectional area of the invert is (Perry et al. 1963 [DIRS 119529], p. 2-6):

$$\begin{aligned} A_I &= r_D^2 \cos^{-1}\left(\frac{r_D t_{I,max}}{r_D}\right) - (r_D - t_{I,max}) \sqrt{2r_D t_{I,max} - t_{I,max}^2} \\ &= 4.39 \text{ m}^2. \end{aligned} \quad (\text{Eq. 6.5.2.3-2})$$

The invert volume is this area (A_I) multiplied by the length of interest, for example, the length of a waste package, L_{WP} . The volume of water in the invert beneath a waste package of length L_{WP} is:

$$V_{wI} = \phi S_w A_I L_{WP}, \quad (\text{Eq. 6.5.2.3-3})$$

where ϕ is the porosity of the invert, and S_w is the water saturation of the invert.

For purposes of modeling flow and diffusion through the invert, the invert is regarded as having a rectangular cross section with a top surface being the actual top surface of the invert. The cross sectional area for flow or diffusion between the invert and the UZ is:

$$A_{I/UZ} = w_I L_{WP}. \quad (\text{Eq. 6.5.2.3-4})$$

The average thickness of the invert is given by:

$$\bar{t}_I = \frac{A_I}{w_I} = 0.934 \text{ m}. \quad (\text{Eq. 6.5.2.3-5})$$

Using this value preserves the top surface area and volume of the invert.

Sorption of radionuclides to the invert crushed tuff is modeled by applying the devitrified tuff K_d values from the UZ submodel to the invert. Ranges and distributions for these K_d values are given in DTNs: LA0408AM831341.001 [DIRS 171584] (file *UZ Kds.doc*, for all radionuclides of interest except for Se and Sn) and LB0701PAKDSESN.001 [DIRS 179299] (file *ReadMe.doc*, for Se and Sn). Correlations for sampling sorption distribution coefficient probability distributions for devitrified UZ tuff given in DTN: LB0701PAKDSESN.001 [DIRS 179299] (file *Sorption Correlation Table.xls*) are assigned to invert crushed tuff.

A single-continuum invert model is used in the TSPA. The reason for this is that diffusion coefficients (Section 6.3.4.1.1) are applicable only to a bulk porous medium, i.e., a single continuum medium. Insufficient data exist to validate diffusion coefficients in the individual continua in a dual-continuum model. There are also insufficient data to confirm whether a dual-continuum model is a bounding approach with respect to chemical behavior in the invert. (See Section 6.6.3 for the development of a dual-continuum ACM.)

The bulk water content in the invert, θ (percent), is used to compute the diffusion coefficient in the invert, Equation 6.3.4.1.1-22 (in which $\phi^{1.863} S_w^{1.863} = (\theta/100)^{1.863}$). The bulk water content in the invert is determined from the intragranular water saturation provided in *Multiscale Thermohydrologic Model* (SNL 2007 [DIRS 181383], Appendix X) and the seepage flux provided in *Seepage Model for PA Including Drift Collapse* (BSC 2004 [DIRS 167652]).

The relationship between the bulk water content and the intergranular and intragranular water contents is based on the definitions of water content using the volumes of water, solids, and pore spaces:

$$\begin{aligned}\theta &= 100 \frac{V_{w_inter} + V_{w_intra}}{V_t} = 100 \frac{V_{w_inter}}{V_t} + 100 \frac{V_{w_intra}}{V_t} \\ &= \theta_{inter} + 100 \frac{V_{w_intra}}{V_t},\end{aligned}\quad (\text{Eq. 6.5.2.3-6})$$

where V_{w_inter} is the volume of water in the intergranular pore space (m^3), V_{w_intra} is the volume of water in the intragranular (matrix) pore space (m^3), V_t is the total bulk invert volume (m^3), and θ_{inter} is the intergranular water content (percent).

The ratio of intragranular water volume to total invert bulk volume, V_{w_intra}/V_t , is related to the porosity of the of the intragranular (tuff matrix) pore space, ϕ_{intra} (m^3 pore volume m^{-3} matrix volume):

$$\frac{V_{w_intra}}{V_t} = \frac{V_{t_intra} S_{w_intra}}{V_t} = \frac{\phi_{intra} (V_t - V_{t_inter}) S_{w_intra}}{V_t}, \quad (\text{Eq. 6.5.2.3-7})$$

where S_{w_intra} is the water saturation of the matrix (m^3 water m^{-3} pore volume), V_{t_intra} is the total pore volume of the matrix (m^3), and V_{t_inter} is the total pore volume of the intergranular pore space (m^3). This expression makes use of the definition of matrix porosity, ϕ_{intra} , as the ratio of matrix pore volume to total matrix volume, where the latter is the difference between the bulk invert volume, V_t , and the intergranular pore volume, V_{t_inter} :

$$\phi_{intra} = \frac{V_{t_intra}}{V_t - V_{t_inter}}, \quad (\text{Eq. 6.5.2.3-8})$$

which can be rearranged to give:

$$V_{t_intra} = \phi_{intra} (V_t - V_{t_inter}). \quad (\text{Eq. 6.5.2.3-9})$$

Substituting the definitions of percent water content ($\theta_{intra} = 100 \phi_{intra} S_{w_intra}$) and porosity (fraction) of the intergranular pore space, ($\phi_{inter} = V_{t_inter}/V_t$), the ratio V_{w_intra}/V_t in Equation 6.5.2.3-6 can be written:

$$100 \frac{V_{w_intra}}{V_t} = \theta_{intra} (1 - \phi_{inter}). \quad (\text{Eq. 6.5.2.3-10})$$

Inserting this into Equation 6.5.2.3-6 results in the expression for the bulk water content of the invert:

$$\theta = \theta_{inter} + (1 - \phi_{inter})\theta_{intra}. \quad (\text{Eq. 6.5.2.3-11})$$

The intragranular water content, θ_{intra} , is calculated by multiplying the intragranular water saturation provided in *Multiscale Thermohydrologic Model* (SNL 2007 [DIRS 181383]) with the intragranular porosity of $\phi_{intra} = 0.111$ (DTN: MO0703PAHYTHRM.000 [DIRS 182093] Mathcad file: *Porosity Calculations.xmcd*).

The intergranular water content, θ_{inter} , is evaluated indirectly from the total dripping flux into the drift. The volumetric discharge into the invert, Q_I ($\text{m}^3 \text{ water s}^{-1}$), is equal to the total dripping flux (seepage plus condensation) into the drift (see Equation 6.5.1.1-8, where $F_6 = F_1$); the imbibition flux, F_7 , does not enter the intergranular continuum and is not included in Q_I , which is given by:

$$Q_I = K_{us} I_s A_{Is} \quad (\text{Eq. 6.5.2.3-12})$$

where K_{us} is the unsaturated hydraulic conductivity of the invert (m s^{-1}), I_s is the hydraulic head gradient in the invert (m m^{-1}), and A_{Is} is the intercepted flow area of a drift over the length of one waste package, having a value of 28.05 m^2 (BSC 2004 [DIRS 167652], Section 6.3.1). For vertical one-dimensional flow, a hydraulic head gradient of unity ($I_s = 1 \text{ m/m}$) is a bounding value for saturated rock with a free surface exposed to the open drift. Unsaturated crushed rock in the invert will have a lower head gradient, but by using a gradient of unity, Equation 6.5.2.3-12 simplifies and allows the unsaturated hydraulic conductivity of the invert to be evaluated given the seepage flux into the drift:

$$K_{us} = \frac{Q_I}{A_{Is}}. \quad (\text{Eq. 6.5.2.3-13})$$

The moisture potential, ψ (bar), of the invert has been evaluated as a function of unsaturated hydraulic conductivity in *Multiscale Thermohydrologic Model* (SNL 2007 [DIRS 181383], Appendix X, Table X-6) for various particle sizes. The determination of intergranular water content uses a particle size of 3 mm (SNL 2007 [DIRS 181383], Section 6.3.11). Interpolating in Table X-6 of *Multiscale Thermohydrologic Model* (SNL 2007 [DIRS 181383]) for the unsaturated hydraulic conductivity of the invert, K_{us} , as given by Equation 6.5.2.3-13, results in a value for the moisture potential, ψ , which is inserted into a van Genuchten fitting function (SNL 2007 [DIRS 181383], Equation X.4) to give the intergranular water content:

$$\theta_{inter} = \theta_r + \frac{(\theta_s - \theta_r)}{\left[1 + (\psi\alpha)^n\right]^m}, \quad (\text{Eq. 6.5.2.3-14})$$

Parameters in Equation 6.5.2.3-14 are (DTN: MO0703PAHYTHRM.000 [DIRS 182093], file *Van Genuchten Properties.xls*, worksheet “Summary Van Genuchten”, Table 6-1, Column “LTBM minus 2 inch, Average”):

θ_r = residual volumetric water content in the invert (percent)
= 3.36

θ_s = saturated volumetric water content in the invert (percent)
= 22.4

α = van Genuchten air-entry parameter (bar^{-1})
= 1780.59 bar^{-1}

n = van Genuchten n value (dimensionless)
= 1.39

m = van Genuchten m value (dimensionless)
= 0.283.

With the algorithm and parameters described in this section, the bulk volumetric water content in the invert is obtained.

6.5.2.4 Sorption onto Iron Oxyhydroxide Colloids and Stationary Corrosion Products

As stated earlier (Section 6.3.4.2.3), the sorption processes in transport calculations are applied to the isotopes of uranium, neptunium, plutonium, americium, and thorium. Transport of nickel is not considered in the TSPA even though it is included in the surface complexation based model in order to account for competition among various elements for sorption on a finite number of sites. The equilibrium sorption is modeled for uranium, neptunium, and thorium, while kinetic sorption/desorption on the corrosion products is modeled for plutonium and americium, because they also get transported while irreversibly sorbed onto iron oxyhydroxide colloids.

6.5.2.4.1 Sampling Methodology

In order to perform calculations based on surface complexation, the input concentrations of various elements expected in the TSPA over the course of simulated timescale, need to be determined. This is difficult to predict because waste form degradation rates, transport processes, water volumes, chemical conditions, decay and in-growth rates, etc., vary with time and space. There are virtually an infinite number of combinations for the set of concentrations of various elements that could be considered in the sorption calculations. Each combination of concentration could lead to different sorption amounts.

Even though the concentrations for various elements considered, cannot be determined *a priori*, the range over which they could vary can be estimated. The maximum value cannot be greater than the solubility of the controlling mineral phase, and the minimum value could be nearly zero. Once the maximum and minimum values for each element are determined, the concentration space can be sampled randomly using the Latin Hypercube Sampling methodology. This

provides various combinations of elemental concentrations for which the surface complexation calculations can be performed to determine sorbed mass.

The maximum value or the dissolved concentration limit for the controlling mineral phase for a given pH and P_{CO_2} is determined by *Dissolved Concentration Limits of Elements with Radioactive Isotopes* (SNL 2007 [DIRS 177418]). The methodology outlined in DTN: MO0702PADISCON.001 [DIRS 179358] is to compute the mean value of the solubility controlling mineral phase for a given pH and P_{CO_2} to which two uncertainties are added as shown below:

$$\text{Solubility}[\text{Pu, Np, U, Am, \&Th}] = 10^S 10^{\varepsilon_1} + \varepsilon_2 N, \quad (\text{Eq. 6.5.2.4.1-1})$$

where 10^S is the mean actinide solubility provided in a series of 2-D look up tables provided in DTN: MO0702PADISCON.001 [DIRS 179358], ε_1 is the uncertainty term associated with uncertainty in $\log K$ (\log of the solubility product) values described by a normal distribution truncated at 2σ , and ε_2 is the uncertainty term associated with variations in fluoride concentration that varies by the type of waste package being considered and by the pH. The fluoride uncertainty for the various actinides is perfectly correlated during sampling and is defined by a right-sided triangular distribution. N is the factor by which the maximum fluoride uncertainty (ε_2) is normalized for pH.

Due to the complexity involved in calculating the range of solubility for various combinations of pH and P_{CO_2} and incorporating the uncertainties, the methodology was simplified by determining the maximum possible value of solubility. This approach is reasonable and sufficient, because ultimately the dissolved concentration space will have to be sampled between the maximum and minimum values. The minimum value is arbitrarily chosen to be 10^{-8} times the maximum value, to cover the range of expected concentrations in the TSPA Model. The maximum solubility of an element at a given pH and P_{CO_2} is calculated by placing the maximum of ε_1 (from DTN: MO0702PADISCON.001 [DIRS 179358]) and the maximum of ε_2 (from DTN: MO0702PAFLUORI.000 [DIRS 181219]) values in Equation 6.5.2.4.1-1 for that element (see Table 6.5-10):

$$\text{Solubility}^{\max} = 10^S 10^{\varepsilon_1^{\max}} + \varepsilon_2^{\max} N. \quad (\text{Eq. 6.5.2.4.1-2})$$

Since the surface complexation based calculations have been done using PHREEQC (V. 2.11 2006 [DIRS 175698]), the pre-sampled combination of dissolved concentrations would have to be first generated in PHREEQC. This can be achieved by simply adjusting the saturation index of the solubility controlling phase in PHREEQC such that the adjusted amount is either an additive or subtractive term in the log space, which translates into a multiplicative ratio in the linear space whose value varies from greater than one to less than one. The multiplicative ratio is equal to the ratio of the dissolved concentration to the mean solubility, and thus the log of the ratio is equivalent to the adjusted saturation index of the controlling phase—a value that can be directly used as input in the PHREEQC simulations. The maximum value of the ratio, R^{\max} , is calculated by dividing the maximum solubility (that includes the two uncertainty terms; Equation 6.5.2.4.1-2) by the mean solubility as shown below:

$$R^{\max} = 10^{\varepsilon_1^{\max}} + \varepsilon_2^{\max} (N/10^S)^{\max}. \quad (\text{Eq. 6.5.2.4.1-3})$$

The maximum value of this ratio is shown in Table 6.5-10 for the actinides of interest. For Ni, the maximum value of the ratio is set to 1.0, indicating that there is no uncertainty in the solubility.

The maximum ratio value for a given element is then multiplied by an uncertainty distribution that varies log-uniformly from 1 to 10^{-8} in order to sample the range of concentrations expected in TSPA. The uncertainty distribution for each element is defined by a separate stochastic that is sampled using the Latin Hypercube Sampling methodology using GoldSim V. 8.02.500 (2005 [DIRS 174650]) (file: *Sampling_Surface_Complexation_Calc_v8.02.500*, output DTN: SN0703PAEBSRTA.002). A total of 100 realizations are generated, where each realization represents a unique combination of concentrations of actinides (via the adjustment of the saturation index of the solubility controlling phase). In addition, the log of the drift P_{CO_2} is also sampled uniformly, over 100 realizations, from $\log_{10}(10^{-2} \text{ bar})$ to $\log_{10}(10^{-4} \text{ bar})$, since it affects the pH and aqueous speciation. The sampled values are listed in output DTN: SN0703PAEBSRTA.002 (file: *Final_Calc_Results_Surf_Complx_Data_1.xls*).

Besides the varying dissolved concentrations of the competing species, the surface properties would also vary in the EBS transport model implemented in the TSPA. The available surface area for sorption per unit water volume varies as a function of water saturation, corrosion rate, sampled specific surface area, and site density. The relative abundance of goethite and HFO is also uncertain and affects the sorption sites per unit water volume for both the stationary corrosion products and iron oxyhydroxide colloids. The number of sites available for sorption, in units of moles per liter of water, is calculated from the uncertain surface properties, considering the stationary corrosion products concentration to vary uniformly from 1 kg L^{-1} to 50 kg L^{-1} and iron oxyhydroxide colloid concentrations to vary log-uniformly from 0.001 mg L^{-1} to 30 mg L^{-1} . The uncertainty distributions are sampled using the Latin Hypercube Sampling methodology using GoldSim V. 8.02.500 (2005 [DIRS 174650]) (file: *Sampling_Surface_Complexation_Calc_v8.02.500*, output DTN: SN0703PAEBSRTA.002). A total of 50 realizations are generated to compute the total available sites for sorption per liter of water (output DTN: SN0703PAEBSRTA.002, file: *Final_Calc_Results_Surf_Complx_Data_1.xls*). The number of realizations chosen was deemed adequate since larger number of realizations did not change the shape of the output distribution appreciably.

For each realization of the surface property, 100 realizations of the dissolved concentrations and P_{CO_2} are considered in the SCM. In effect, the surface property realizations represents the outer loop while the dissolved concentration realizations represents the inner loop over which the SCM is exercised. A total of $50 \times 100 = 5,000$ combinations of surface property and dissolved concentrations are analyzed using the SCM.

Table 6.5-10. Data Used For Calculating Maximum Solubility Ratio

Element	ϵ_1^{\max}	$10^{\epsilon_1^{\max}}$	ϵ_2^{\max}	$\epsilon_2^{\max} (N/10^{\epsilon_1^{\max}})^{\max}$	Max Ratio
U	1.2	15.8	5385	216.6	232.4
Np	1.7	50.1	853	0.87	51
Pu	1.52	33.1	5460	0.249	33.3
Th	1.52	33.1	23723	3542	3575
Am	2.08	120.2	688.6	6.88	127

Output DTN: SN0703PAEBSRTA.002

6.5.2.4.2 Surface Complexation Modeling

A two-step modeling approach is adopted in PHREEQC. In the first step, equilibrium chemical modeling is performed to generate the dissolved concentrations for all six elements corresponding to the sampled saturation indices (sampled ratios) and P_{CO_2} for the 100 realizations. This step encompasses equilibrium speciation of the J-13 water composition (DTN: MO0006J13WTRCM.000 [DIRS 151029]) with dissolved actinides at concentrations calculated as a function of the saturation index of their solubility controlling phase. The J-13 composition was chosen to be consistent with *Dissolved Concentration Limits of Elements with Radioactive Isotopes* (SNL 2007 [DIRS 177418]).

In the second step, surface complexation reactions are modeled for the given surface property of stationary corrosion products and iron oxyhydroxide colloids (out of 50 realizations) by equilibrating the solution from the first step with both stationary corrosion products and iron oxyhydroxide colloid surfaces. In this step the dissolved concentrations are held at the values generated in the first step.

The first step contains additional sub-steps to account for the adjusted Eh model used for plutonium. The output of the surface complexation modeling includes the total aqueous concentration and the total sorbed concentration for each of the six elements, as well as the equilibrium pH.

The solubility controlling phases were the same as those used in *Dissolved Concentration Limits of Elements with Radioactive Isotopes* (SNL 2007 [DIRS 177418]). The actinides and their solubility controlling phases are listed in Table 6.5-11.

Table 6.5-11. Solubility Controlling Phase

Element	Solubility Controlling Phase
Uranium	Schoepite
Plutonium	PuO ₂ (hyd,aged)
Neptunium	NpO ₂
Americium	AmOHCO ₃
Thorium	ThO ₂ (am)

Output DTN: SN0703PAEBSRTA.002

The thermodynamic database “*phreeqcDATA025bdotCr3az.dat*” (DTN: MO0609SPAINOUT.002 [DIRS 179645]) was used in both steps of the PHREEQC modeling, with the surface complexation reactions and log K values entered directly in each input file. This is the most up to date thermo-chemical database available for PHREEQC; as such, its use in these calculations is justified.

The 100 realizations of the multiplication ratios generated are analogous to the ratio of dissolved concentration to the mean saturated concentration at a given P_{CO_2} . Thus, the log of the ratio yields the saturation index of the solubility controlling phase for any particular actinide element for a given P_{CO_2} . The nickel concentration is sampled directly, from 3×10^{-8} mg L⁻¹ to 3 mg L⁻¹. This range was chosen based on possible variability in the steel corrosion rates. In PHREEQC, it is possible to specify the concentration of an element in terms of the degree of saturation of a mineral phase containing that element, thus making it possible to combine elemental concentrations, i.e., the J-13 composition, with the sampled actinide solubility ratios and P_{CO_2} , while allowing PHREEQC to calculate the equilibrium actinide concentrations and pH of the solution.

The solution pH and aqueous solution concentration for all of the actinides, with the exception of plutonium, were calculated first where the P_{CO_2} , actinide phase saturation, J-13 composition, and P_{O_2} were specified. In *Dissolved Concentration Limits of Elements with Radioactive Isotopes* (SNL 2007 [DIRS 177418]), the Eh is calculated as a function of oxygen fugacity, where the fugacity is set to the atmospheric partial pressure of oxygen ($10^{-0.7}$ bar). Likewise, this same redox constraint was used in the present model for all of the actinides with the exception of plutonium.

Plutonium was excluded from the initial solution calculation because its solubility is redox sensitive, and the modified Eh relationship from *Dissolved Concentration Limits of Elements with Radioactive Isotopes* (SNL 2007 [DIRS 177418]) was implemented. This relationship calculates an Eh value based on the solutions pH via

$$Eh = 1.10 - 0.0592 \text{ pH.} \quad (\text{Eq. 6.5.2.4.2-1})$$

Thus, the solution pH from initial PHREEQC calculation was used to calculate the Eh condition under which PuO₂ (phase hyd,aged) would dissolve. The output concentrations (J-13 water plus actinide) from the initial PHREEQC run were used as input for the Pu calculation step.

Of the 100 realizations for the fluid composition, 96 converged in PHREEQC. Four realizations did not converge due to very high values of schoepite saturation (>100×), or high values of schoepite saturation combined with high saturation of another controlling phase. In these extreme circumstances, the PHREEQC convergence criteria could not be met, and the realization had to be dropped from further consideration. The non-convergence of four realizations (out of 100) is simply an artifact of pre-sampling the uncertainty in the solubility for various elements and P_{CO_2} independently of each other for input into PHREEQC. It is manifested by adjusting the saturation indices of the mineral phases. Because the uncertainties are pre-sampled randomly,

some of the inputs to PHREEQC become non-physical in that the saturation indices for schoepite and other mineral phases had to be set to extreme values.

The results of the solution calculation Step 1, which were passed to the corrosion product equilibration Step 2, included the J-13 composition with the sampled P_{CO_2} , and the PHREEQC calculated pH and actinide concentration values. In Step 2, each of the 96 aqueous solutions from Step 1 was equilibrated with the 50 sets of corrosion product and colloid surface properties while the P_{CO_2} , P_{O_2} , and actinide solubility controlling phases were maintained at their Step 1 values. The actinide phase solubility control was maintained for the purpose of loading the adsorption sites on the iron corrosion products and colloids such that surface loading could be accounted for in the K_d abstractions.

The surface complexation reactions and their accompanying log K values used in the analyses are listed in Table 6.5-12. These reactions and log K values were entered directly in each of the PHREEQC input files (*stat_col_ZPC.pqi*) included in output DTN: SN0703PAEBSRTA.002 and were not contained in the thermodynamic database "*phreeqcDATA025bdotCr3az.dat*". The surface complexes in Table 6.5-12 were identified and chosen for inclusion in the model because they represented the most comprehensive and best available internally consistent set of single-site complexes for the actinides of interest (a literature search and selection details for surface complexation reactions and their accompanying log K values are described in Appendix J). The output of Step 2 included the sorbed actinide concentrations for the corrosion products and colloids, the aqueous actinide concentrations, and the pH. These output data were reduced in Excel using the surface properties of the corrosion products and colloids to yield the distribution coefficients for each of the actinide elements. Uncertainty in the surface complexation constants (Table 6.5-12) was not considered at this stage; instead, uncertainty in the mineral and aqueous species thermochemical data was propagated through the SCM.

Table 6.5-12. Surface Complexation Reactions and log K Values

Surface Complexation Reaction*	Log K
HfssOH + H+ = HfssOH2+	7.35
HfssOH = HfssO- + H+	-9.17
HfssOH + UO2+2 + 2CO3-2 + H+ = HfssOH2UO2(CO3)2-	29.15
HfssOH + UO2+2 + 3CO3-2 + H+ = HfssOH2UO2(CO3)3-3	36.28
HfssOH + 2UO2+2 + CO3-2 + 3H2O = HfssOH2(UO2)2CO3(OH)3 + 2H+	12.62
HfssOH + PuO2+ = HfssOPuO2+	5.14
HfssOH + PuO2+ = HfssOPuO2 + H+	-2.95
HfssOH + PuO2+ + H2O = HfssOPuO2OH- + 2H+	-11.35
HfssOH + Pu+4 = HfssOPu+3 + H+	14.33
HfssOH + Pu+4 + H2O = HfssOPuOH+2 + 2H+	8.79
HfssOH + Pu+4 + 3H2O = HfssOPu(OH)3 + 4H+	-3.92
HfssOH + PuO2+2 = HfssOPuO2+ + H+	3.0
HfssOH + NpO2+ = HfssOHNpO2+	6.03
HfssOH + NpO2+ + H2O = HfssONpO2OH- + 2H+	-12.0
HfssOH + Am+3 + H2O = HfssOAmOH+ + 2H+	-6.27
HfssOH + Th+4 = HfssOHTh+4	18.7

Table 6.5-12. Surface Complexation Reactions and log K Values (Continued)

Surface Complexation Reaction*	Log K
HfssOH + Th+4 + 2H2O= HfssOTh(OH)2+ + 3H+	-2.0
HfssOH + Th+4 + 4H2O= HfssOTh(OH)4- + 5H+	-16.7
HfssOH + Ni+2 = HfssONi+ + H+	-2.5
HfssOH + CO3-2 = HfssOHCO3-2	4.78
HfssOH + CO3-2 + 2H+ = HfssHCO3 + H2O	20.3

*Hfss represents the iron oxy-hydroxide surface.

Output DTN: SN0703PAEBSRTA.002

6.5.2.4.3 Abstraction and Multiple Linear Regression

The output of the surface complexation based competitive sorption modeling included a total of 4,800 simulated realizations (= 50 surface property × 96 dissolved concentration combinations) of sorbed masses. These results are abstracted in order to develop a response surface to predict the sorbed amounts for each of the elements for implementation in the TSPA Model.

Since the total available sites for sorption (spl), in mole per liter of water, are computed from the specific surface area (ssa), in $\text{m}^2 \text{g}^{-1}$, and the concentrations, in $\text{g L}^{-1} \text{H}_2\text{O}$, of corrosion products (mass) and iron oxyhydroxide colloids, these two parameters were also considered in computing the response surface. It was noted that the sorbed masses on the stationary corrosion products and iron oxyhydroxide colloids, when normalized (per sorbate mass), gave the same values. Thus, the response surface for sorption need not be computed separately for the corrosion products and iron oxyhydroxide colloids, but rather the response surface developed for sorption on the corrosion products could be directly applied to the iron oxyhydroxide colloids.

For computing the response surface of the sorbed masses, the three corrosion product properties, $\text{pCO}_2 = -\log_{10}(P_{\text{CO}_2})$, and the dissolved concentration of the six elements were considered as predictors. This made a total of ten possible variables to be considered as predictors for the six regression models (one each for the element of interest). In addition, a regression model is developed for predicting the pH, since it is also an output of the SCM. Table 6.5-13 shows the predictors, response variables and their corresponding abbreviations as used in this section.

Table 6.5-13. List of Predictor and Response Variables

Predictor Variables	Abbreviation
$-\log_{10}(P_{CO_2})$	pCO2
Corrosion product sites per volume of water	spl
Corrosion product specific surface area	ssa
Corrosion product mass concentration	mass
U dissolved concentration	U
Pu dissolved concentration	Pu
Np dissolved concentration	Np
Am dissolved concentration	Am
Th dissolved concentration	Th
Ni dissolved concentration	Ni
$\log_{10}(X)$, where X is the nuclide concentration abbreviation	logX
Response Variables	Abbreviation
pH	pH
U sorbed concentration	sU.CP
Pu sorbed concentration	sPu.CP
Np sorbed concentration	sNp.CP
Am sorbed concentration	sAm.CP
Th sorbed concentration	sTh.CP
Ni sorbed concentration	sNi.CP
$\log_{10}(X)$, where X is the nuclide concentration abbreviation	logX

The most important criterion in abstracting the results from the competitive sorption modeling was that the regression model had to provide good predictive capability over the anticipated parameter space. In this section, the term “model” is used to refer to the abstracted (regression) model. Another important consideration was that the model had to be implemented for prediction in GoldSim, so a simple closed-form analytical expression was desirable.

Several regression approaches were considered in developing the model using the statistical software S-PLUS. The simplest approach would be multiple regressions with a linear model. Other forms of the linear model could involve transformations of the parameters or polynomial terms. Nonparametric regression approaches were also considered, such as alternating conditional expectations and projection pursuit regression, which includes predictor interactions. Because these nonparametric approaches did not yield results that were substantially better than the simpler linear models, and since the nonparametric approaches could be more difficult to implement as predictive models in GoldSim, the preference was given to a form of multiple regression.

6.5.2.4.4 Analysis

In any regression analysis, a prudent first step is examining scatter plot matrices of the predictor and response variables, to see if any obvious correlations exist among the variables. Figure 6.5-10 shows an example of a scatter plot matrix for pCO₂, and the corrosion product

properties, along with the response variable, pH. Concentrations for both the predictor (and response variables, not shown in this plot) are log-transformed, since they range over many orders of magnitude. Scatter plot matrices are useful in showing both predictor-predictor relationships and predictor-response relationships. For example, Figure 6.5-10 shows the strong correlation between pH and pCO₂, with little correlation with any of the other predictors. Figure 6.5-11 shows the dissolved nuclide concentration predictors plotted with the same response variable, pH. There is no strong, monotonic trend between pH and any of these predictors. However, for some ranges of pH, there is a trend. For example, for high values of pH, logAm has a good positive correlation with pH. Thus, some of these predictors may appear in the pH regression model, but will not be the dominant predictors. Plots such as these give an early indication of what variables may be important in the regression models.

The initial multiple regression models explored log transformations of the corrosion product predictors. It was determined, through trial and error, that log transformation of spl improved the regression fit. It was also determined that adding second order polynomial terms improved the regression models. Therefore, the initial model was a model with all 10 predictors and corresponding second order terms for the 10 predictors.

To increase the simplicity and robustness of the models, the first and second order terms were evaluated by stepwise regression. In stepwise regression, each term is added or removed from the model to judge its effect on a particular model selection criteria. In this case, the model selection criterion is the Akaike Information Criteria, or AIC (Venables and Ripley 2001 [DIRS 159088]). The AIC is calculated as follows:

$$AIC = 2k - 2 \log_{10}(L). \quad (\text{Eq. 6.5.2.4.4-1})$$

Here, k is the number of model parameters, and L is the likelihood function. The AIC is a measure of the goodness of fit of the model balanced against the complexity of the model.

The stepwise regression started with a full model, with all predictors as second order polynomials. The stepwise regression process then drops terms, refits the model, and evaluates the AIC to see whether the model is better without a particular term. A penalty parameter (penalizing model complexity) can be adjusted by the analyst to force the stepwise regression to produce a simpler model, with fewer terms. Figure 6.5-12 shows an example of the coefficient of variation (R^2) increase with increasing number of predictors, for the logsU.CP model. The figure shows that the fit does not improve significantly after the inclusion of about five predictors.

6.5.2.4.5 Results

The stepwise regression for all of the response variables was performed. The primary predictors for all of the sorbed concentration models followed a similar trend. First, spl and pCO₂ were included. In addition, the dissolved concentration of the nuclide corresponding to the response variable and the dissolved concentration of U were included. Table 6.5-14, below, shows the coefficients for each of the predictors, for each of the response variables.

Table 6.5-14. Coefficients for the Final Regression Models

	pH	logsU.CP	logsPu.CP	logsNp.CP	logsAm.CP	logsTh.CP	logsNi.CP
(Intercept)	4.5342	0.9727	-2.0371	0.1561	-3.2250	-0.3107	-5.0808
pCO2	0.6132		0.6036		1.0190		0.8026
pCO2^2		-0.0837				0.0838	
log(spl)		1.0027	0.9972	0.9789	0.9754	1.0151	0.9144
log(U)	-0.3805	-0.3489	-0.9172	-1.1643	-1.4669	-0.7201	-1.6646
log(U)^2	-0.0254	-0.0922	-0.0516	-0.0671	-0.0887	-0.0379	-0.1019
logPu			0.9500				
logNp				0.9784			
logAm					0.9423		
logTh						0.8942	
logNi							0.9478
R ²	0.6281	0.9509	0.9460	0.9539	0.9606	0.9574	0.9584

Output DTNs: SN0703PAEBSRTA.001, SN0703PAEBSRTA.002

Also shown in Table 6.5-14 is the coefficient of variation (R^2) for each model. For the sorbed concentration responses, the coefficient of variation is close to unity in each case, indicating a good model fit. For pH, the R^2 value is 0.63, which still indicates a decent predictive capability for the model, however, with some unexplained variance. This unexplained variance can be accounted by adding an error term to the regression model. The error term is computed by considering the plot of the residuals (Figure 6.5-13), which indicates that the residuals (unexplained variance) follow a normal distribution with mean of zero and standard deviation of 0.32. As a result, the error term is defined by the same distribution but truncated at ± 2 standard deviations.

Figure 6.5-13 shows the diagnostic plots for the regression model of pH. The plot in the upper left shows the observed versus predicted points in the data set. Although the general trend of the points follows the 1:1 line, there is some scatter, which is expected given the R^2 value of 0.63. This is contrasted with the logsU.CP diagnostics in Figure 6.5-14, where the observed versus predicted plot shows points more tightly clustered around the 1:1 line, with the higher R^2 value of 0.95. In Figure 6.5-13, the plot in the upper right shows fitted versus residuals. Most of the residuals are evenly distributed around zero over the data range, which indicates minimal bias in the model. Most of the residuals lie between -0.5 and 0.5 pH unit. Finally, the plot in the lower left shows the normal q-q diagnostic plot. The points fall on the line from approximately -2 to 2, indicating a close-to-normal distribution of residuals from -2 to +2 standard deviations. This normal distribution of residuals helps confirm the lack of bias in the model.

Figures 6.5-14 through 6.5-19 show the diagnostic plots for the sorbed concentration regression models. These are mostly unremarkable; that is, the fitted versus response plots show tight clustering around the 1:1 line, and the residual versus fitted plots show most of the points clustered around the origin, with the occasional small group of outliers. There is some indication of non-normality for the quantiles <-1.0 , for some of the models.

6.5.2.4.6 Model Implementation

Based on the results presented in Table 6.5-14, the sorbed mass on stationary corrosion products and iron oxyhydroxide colloids for a given element is computed in terms of sorbed moles per liter of water. This amount is then converted to an effective K_d value by dividing first by the mass concentration of stationary corrosion products (kg L^{-1}) and then dividing it by the dissolved concentration that is computed at the beginning of the time step. The effective K_d calculated for the stationary corrosion products is the same as that for the iron oxyhydroxide colloids. Although the model calculations are performed by varying the P_{CO_2} over two orders of magnitude (ranging from 10^{-2} to 10^{-4} bars) and by varying the stationary corrosion products concentrations over an order of magnitude (ranging from 1.0 to 50 kg L^{-1}), the regression results can be extrapolated with a reasonable degree of confidence over a broader range of P_{CO_2} ranging from less than 10^{-4} bars to 2×10^{-2} bars. Extrapolating the regression equation over this range is reasonable as the extrapolated values would fall within the uncertainty band of the dataset reflected in the coefficient of variation of the regression model. Furthermore the in-drift P_{CO_2} values less than 10^{-4} bars and greater than 10^{-2} bars are expected to be possible only during the early phase of the thermal cooling down period and to last for only a short time period compared to the simulation time.

The computed effective K_d value is directly applicable in the transport equation for U, Np, and Th that are modeled to undergo equilibrium sorption. The transport for these elements is described by Equation 6.5.1.2-47. For plutonium and americium, that undergo kinetic sorption-desorption reactions, Equations 6.5.1.2-48 and 6.5.1.2-49 are applied. The forward reaction rate is calculated by Equations 6.5.1.2-14 and 6.5.1.2-20, while the reverse (desorption) rate is calculated from Equation 6.5.1.2-15. The forward rate constant is a sampled parameter that is an output from DTN: MO0701PAIRONCO.000 [DIRS 180440]. It ranges from 0.002 to $0.05 \text{ m}^3 \text{ m}^{-2} \text{ yr}^{-1}$ with a log-uniform distribution. The same forward rate constant value is applied to both Pu and Am. The reverse rate constant is computed by dividing the forward rate constant by the K_d value derived from surface complexation based modeling. A kinetic approach is taken for plutonium and Am as there is information that suggests the desorption from iron oxyhydroxide colloids is much slower than the sorption processes (Lu et al. 1998 [DIRS 174714], Lu et al. 2000 [DIRS 166315]) and thus best modeled with a non-equilibrium (kinetic) based approach.

Results from experiments performed to study sorption of plutonium and americium on colloidal hematite and montmorillonite (Lu et al. 2000 [DIRS 166315]) indicate that almost all of the plutonium and americium mass is strongly sorbed on the colloids and negligibly small fraction remains in dissolved state or desorbs over the observation timeframes. Thus, it can be considered that plutonium and americium are so strongly bound to colloids that they are considered practically irreversibly sorbed during the residence time of the colloids in the EBS. Observations in nature, such as the transport of plutonium from the Benham test site (Kersting et al. 1999 [DIRS 103282]) indicate that >99 percent of the total plutonium mass being transported is on the colloids. In an attempt to match the field and experimental observations, a target flux out ratio (Ω) is set, which is described as the target ratio of radionuclide flux exiting the corrosion product domain that is transported by colloids (both reversibly and irreversibly

sorbed) to the total radionuclide flux exiting the corrosion product domain carrying plutonium and americium in both dissolved state and sorbed onto colloids):

$$\Omega = \frac{\text{colloid mass flux out}}{\text{total mass flux out}} \quad (\text{Eq. 6.5.2.4.6-1})$$

The target flux out ratio rather than being set as a fixed number is given a range of 0.9 to 0.99 (uniform distribution) (BSC 2005 [DIRS 177423], Section 6.3.3.2) to indicate epistemic uncertainty in this value. The mass of radionuclides in the fluid exiting the corrosion products domain is expected to be proportioned such that the mass of radionuclide species i both reversibly and irreversibly sorbed onto all colloids is some fraction of the total mass of radionuclide species i exiting the system in all forms—aqueous, reversibly sorbed, and irreversibly sorbed.

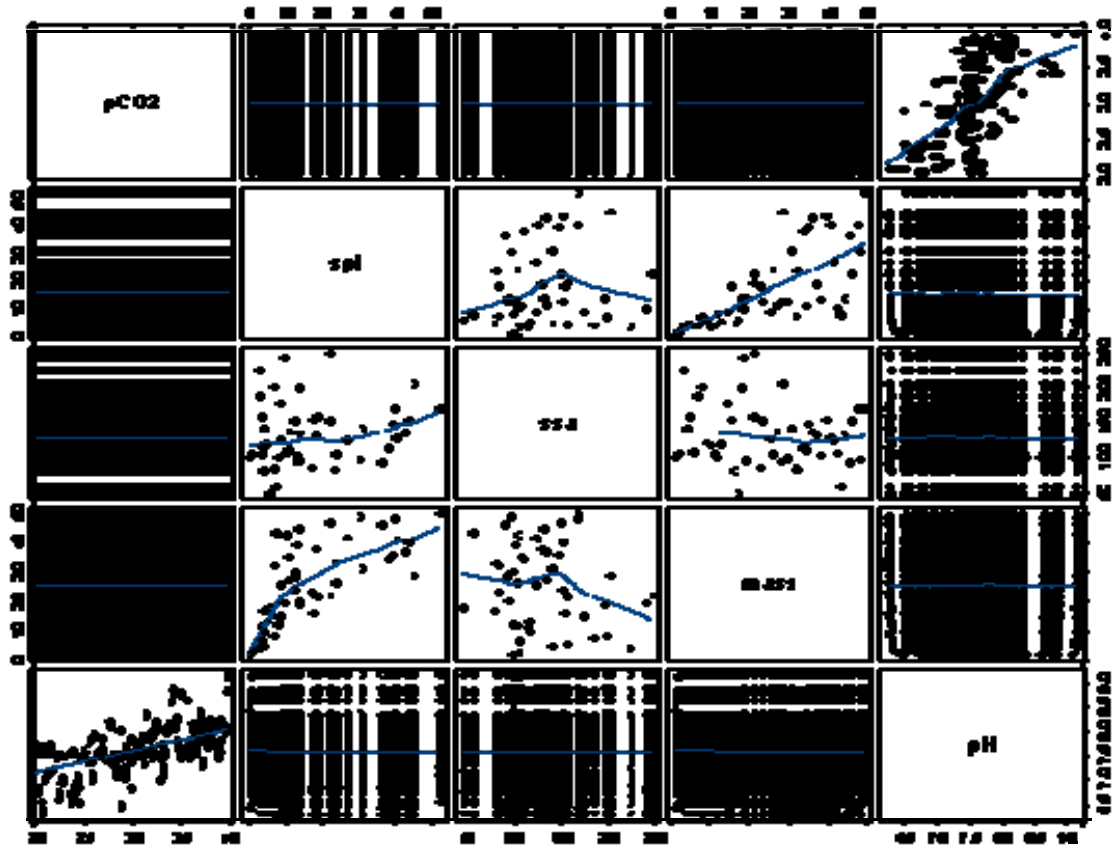
The concept of target flux out ratio is purely theoretical based on the observations and expert judgment used in predicting the general transport behavior of plutonium and americium such that most of the mass is transported on colloids as compared to the dissolved state. Thus an attempt is made to reach the target flux out ratio whenever possible during the transport calculations but if this is not attainable under given physical-chemical-thermal conditions or by remaining within the valid range of transport parameters then the target flux out ratio is not honored. In other words, there is no attempt made to force the transport parameters such as forward rate constant or dissolved concentrations or colloid concentrations to go outside their valid range in order to meet the target flux out ratio. The methodology used (an inverse analytical solution) in computing the forward rate constant to match the target flux out ratio is described in detail in Appendix B. The application of the inverse solution has limitations in that it is not practical to apply when the colloids are unstable or when there is no advective transport due to long times needed to reach steady-state concentrations compared to the simulation time. The computed forward rate constant (from inverse solution) is further checked by comparing it to the physically acceptable range. If the value is outside the physical range then it is set to maximum (or minimum) value of the range.

The pH for the corrosion products domain (Cell 2) is computed by applying the following equation:

$$\text{pH} = 4.5342 + 0.6132(\text{pCO}_2) - 0.3805 \log_{10}[U] - 0.0254(\log_{10}[U])^2 + E, (\text{Eq. 6.5.2.4.6-2})$$

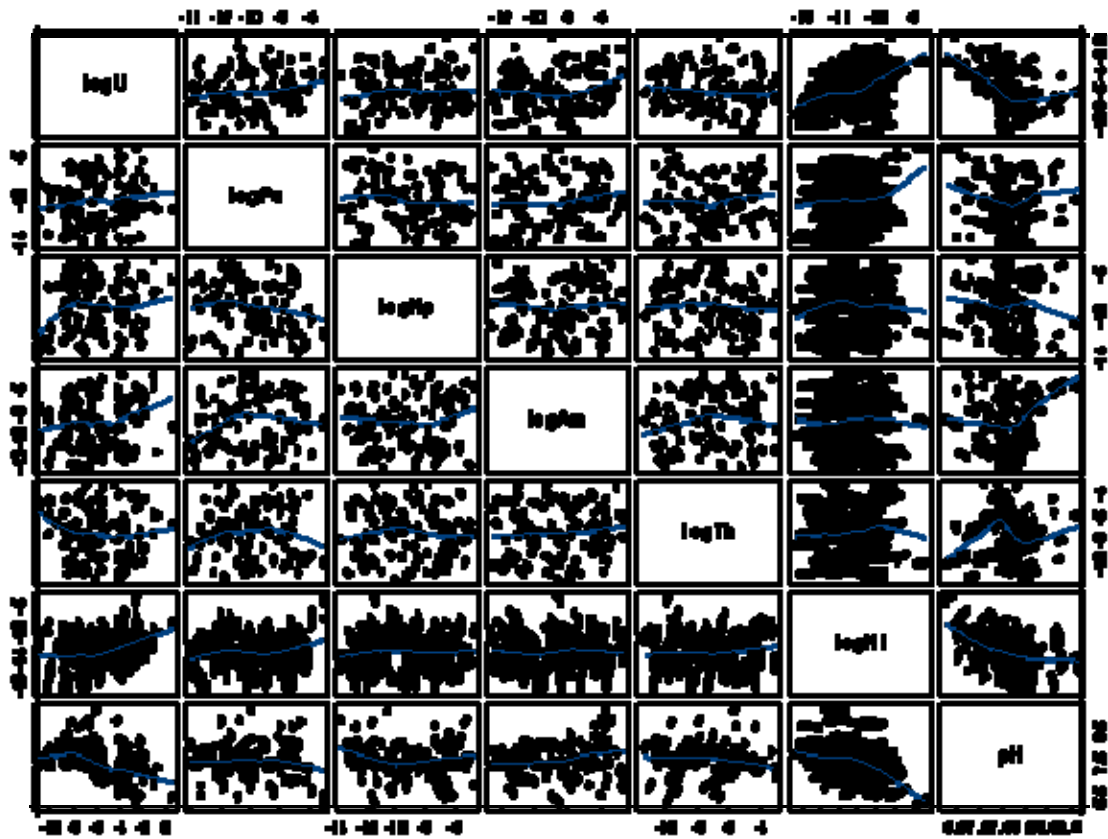
where, pCO₂ is the negative log of the in-drift CO₂ partial pressure (bars), [U] is the dissolved concentration of U in mol L⁻¹, and E is the error term (pH_Cell_2_Regression_Error) defined by a normal distribution with mean of zero and standard deviation of 0.32 truncated at ± 2 standard deviations.

The ionic strength for the corrosion products domain is assumed to be the same as that computed for the upstream domain by the in-package chemistry model.



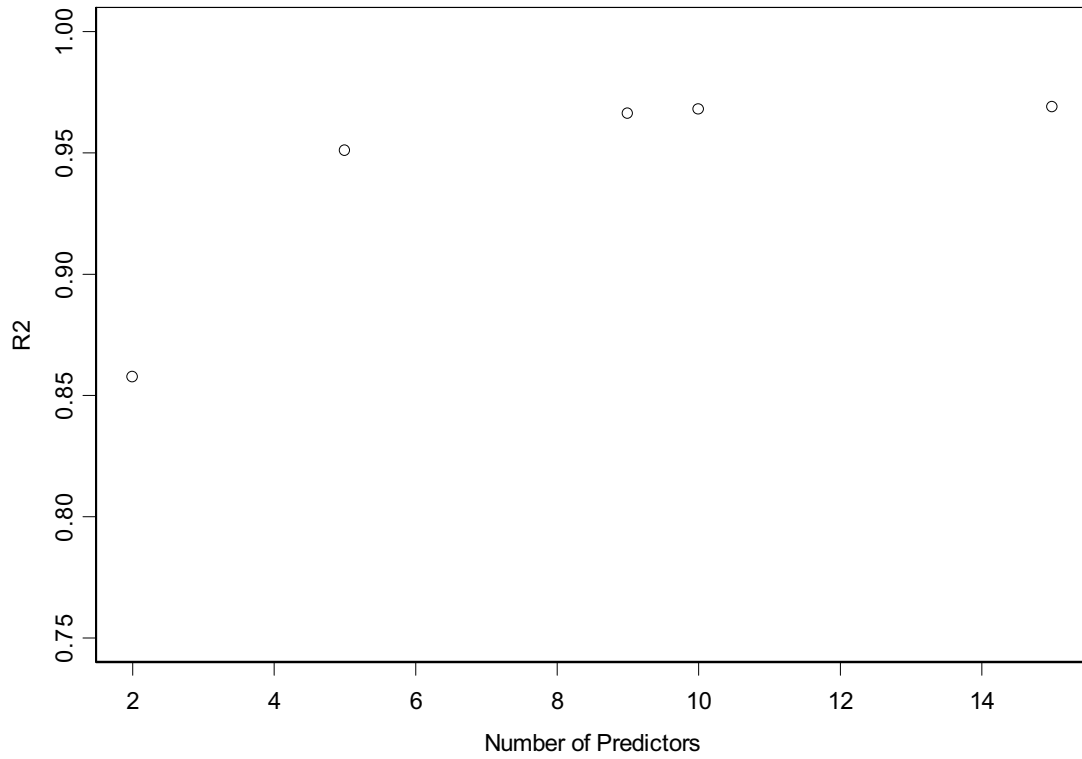
S-PLUS plot of data in output DTN: SN0703PAEBSRTA.002

Figure 6.5-10. Scatter Plot Matrix of First 5 Predictors Versus the pH Response



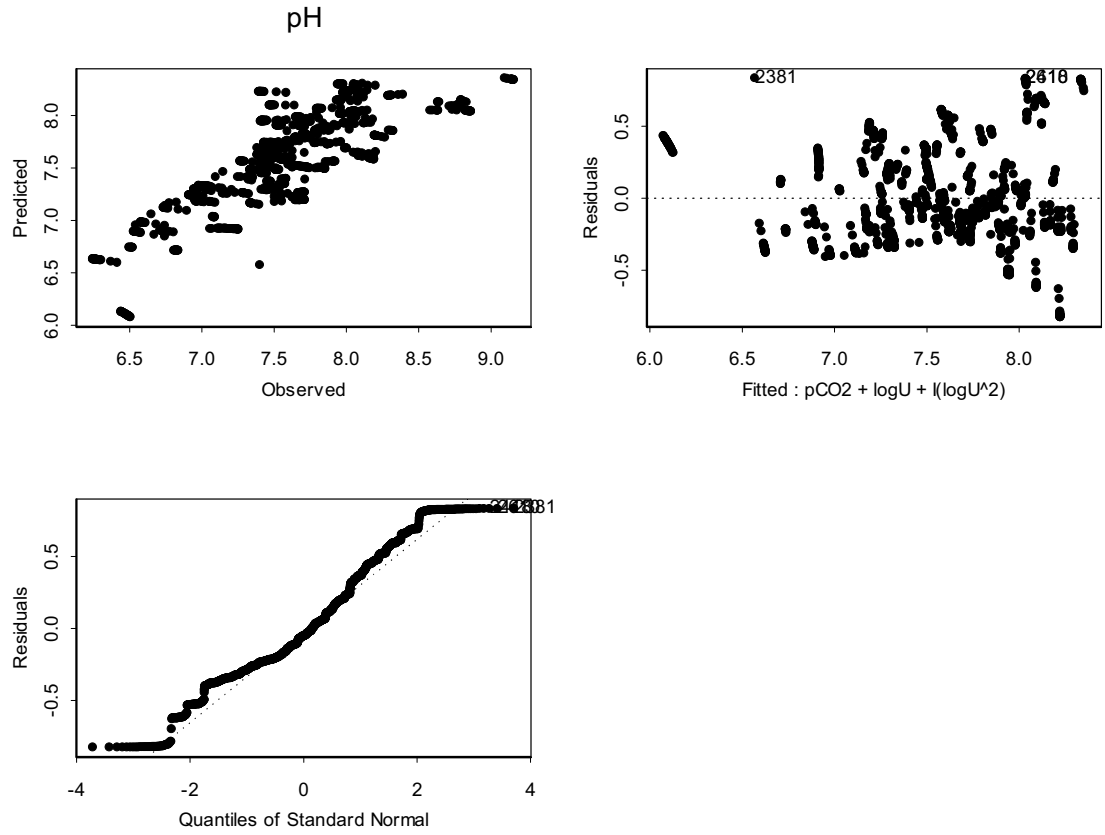
S-PLUS plot of data in output DTN: SN0703PAEBSRTA.002

Figure 6.5-11. Scatter Plot Matrix of 6 Dissolved Concentration Predictors Versus the pH Response



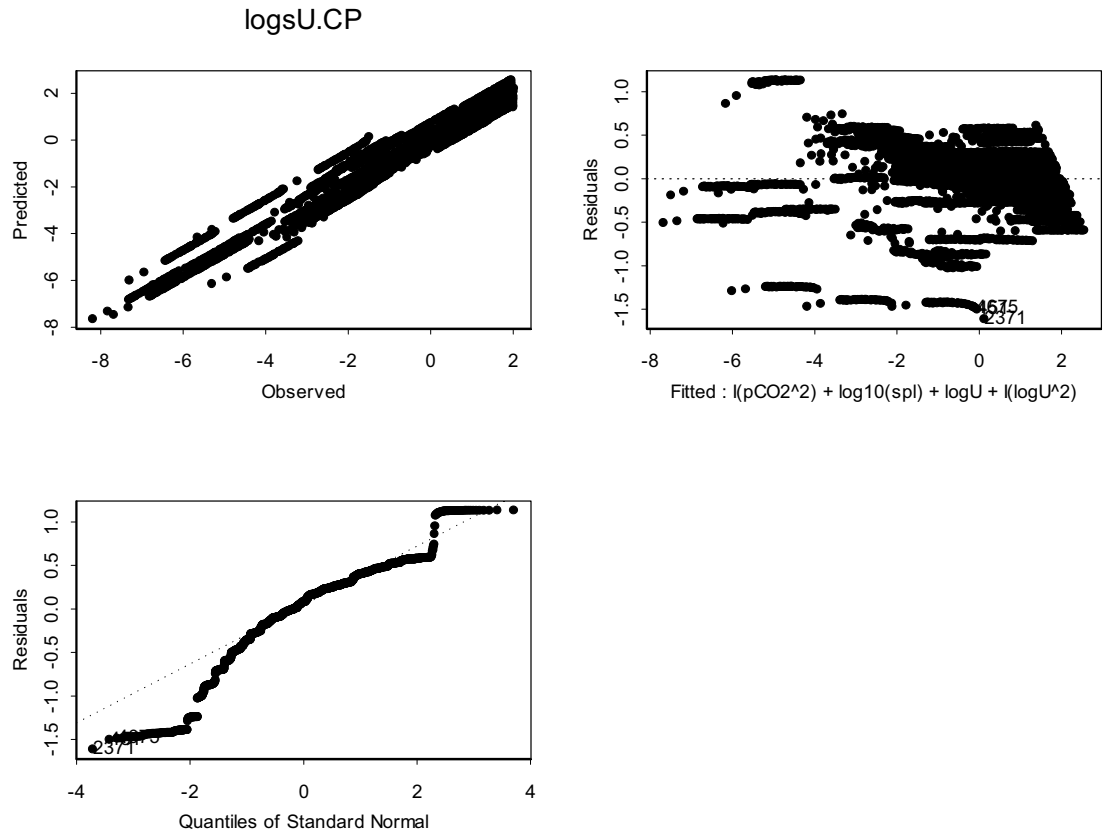
S-PLUS plot of data in output DTN: SN0703PAEBSRTA.002

Figure 6.5-12. Plot of R^2 Versus the Number of Model Terms for the logsU.CP Model



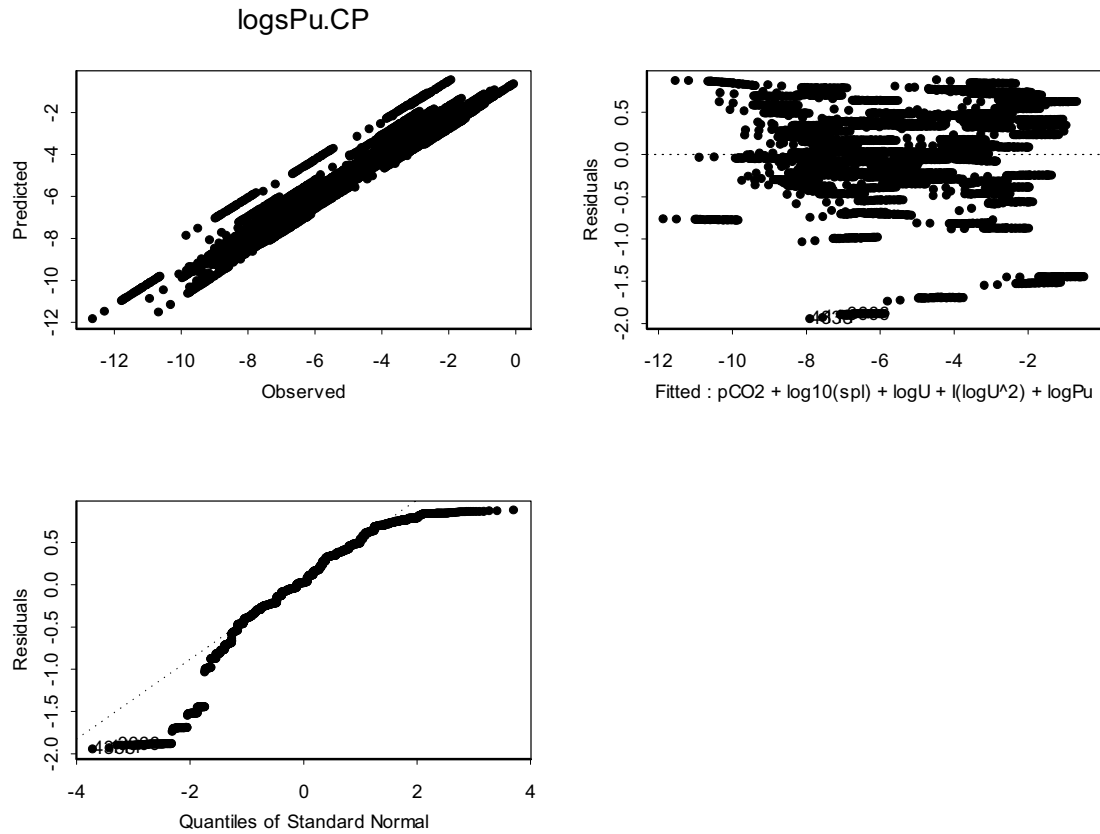
S-PLUS plot of data in output DTN: SN0703PAEBSRTA.002

Figure 6.5-13. Diagnostic Plots for Regression Model of Response Variable pH



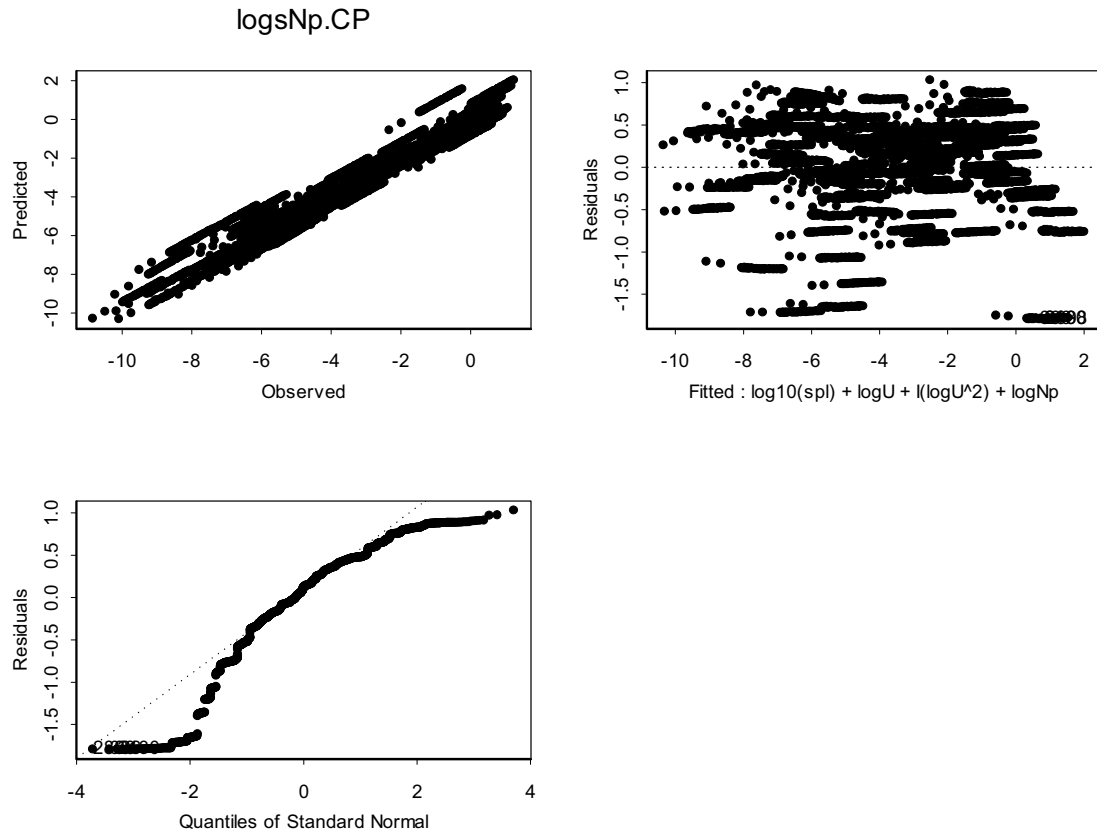
S-PLUS plot of data in output DTN: SN0703PAEBSRTA.002

Figure 6.5-14. Diagnostic Plots for Regression Model of Response Variable logsU.CP



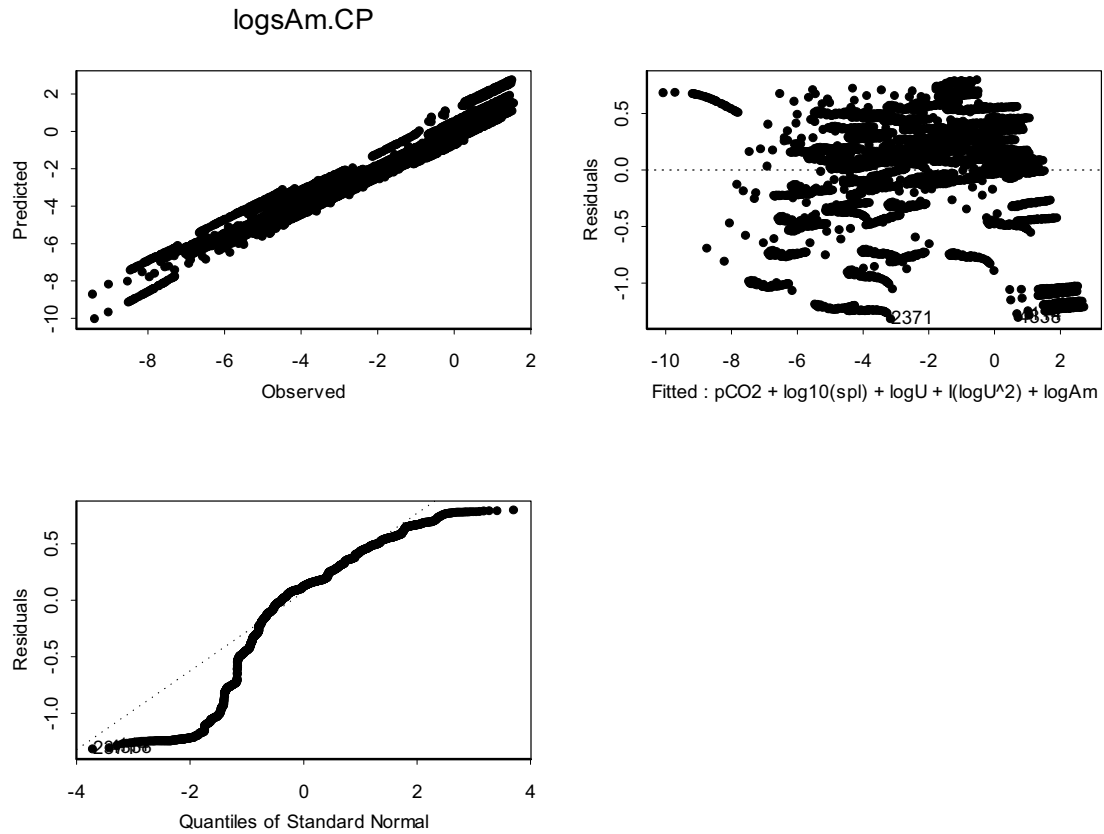
S-PLUS plot of data in output DTN: SN0703PAEBSRTA.002

Figure 6.5-15. Diagnostic Plots for Regression Model of Response Variable $\log_{10}(\text{Pu.CP})$



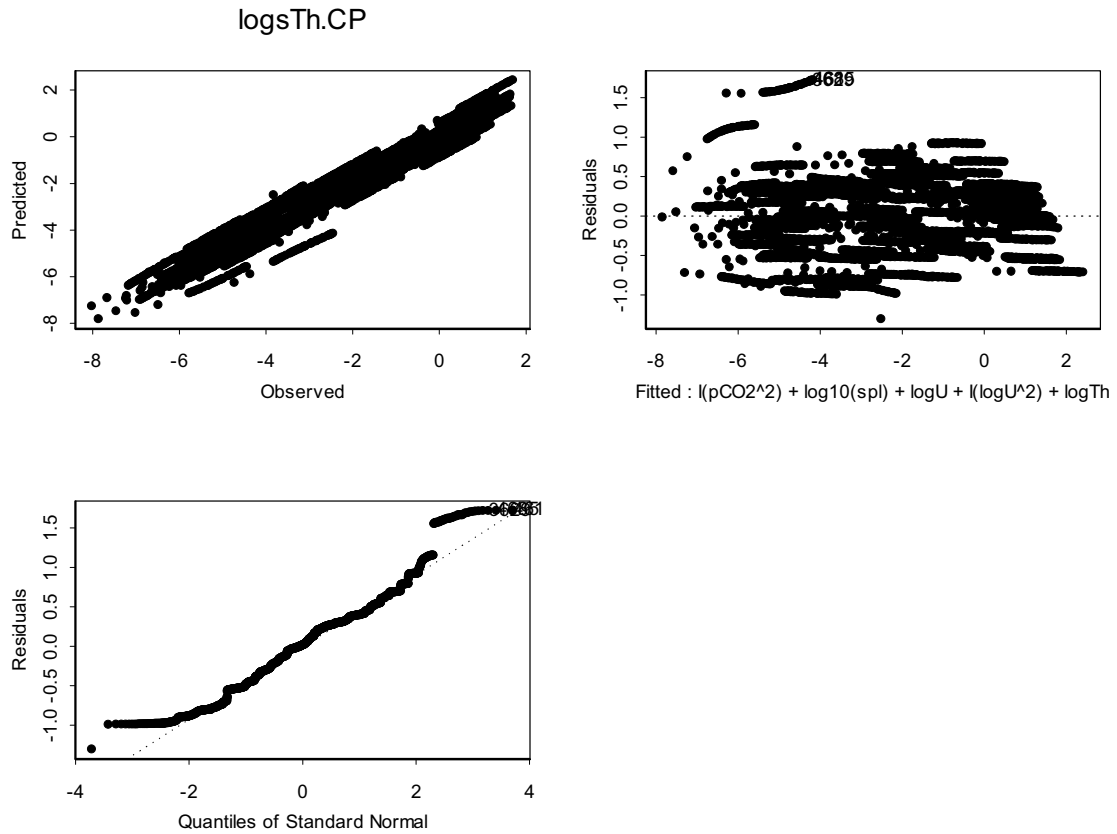
S-PLUS plot of data in output DTN: SN0703PAEBSRTA.002

Figure 6.5-16. Diagnostic Plots for Regression Model of Response Variable logsNp.CP



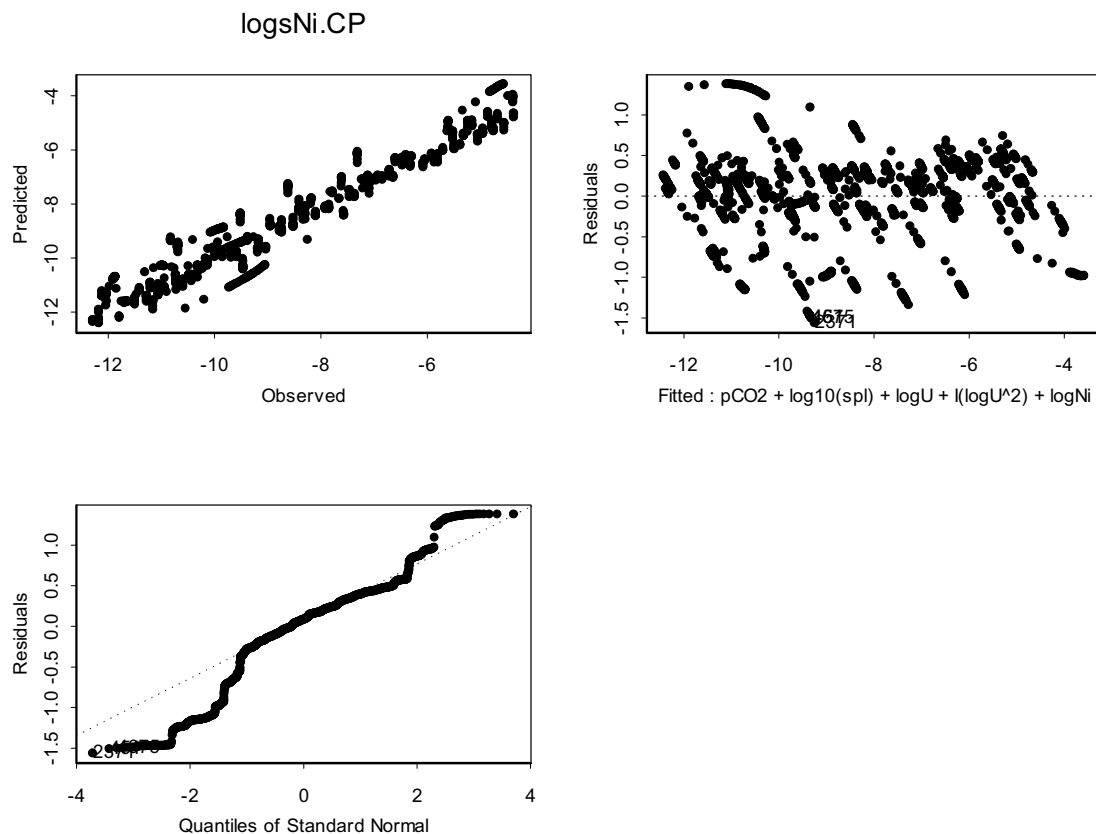
S-PLUS plot of data in output DTN: SN0703PAEBSRTA.002

Figure 6.5-17. Diagnostic Plots for Regression Model of Response Variable logsAm.CP



S-PLUS plot of data in output DTN: SN0703PAEBSRTA.002

Figure 6.5-18. Diagnostic Plots for Regression Model of Response Variable logsTh.CP



S-PLUS plot of data in output DTN: SN0703PAEBSRTA.002

Figure 6.5-19. Diagnostic Plots for Regression Model of Response Variable logsNi.CP

6.5.2.5 Discretization and Development of Computational Model for the TSPA

The continuum mass balance equations for EBS transport model are described and developed in Section 6.5.1.2. The one-dimensional mass balance equation describing transport of dissolved and reversibly sorbed radionuclide species i is provided by Equation 6.5.1.2-48. The one-dimensional mass balance equations for kinetically sorbed radionuclide species i on iron oxyhydroxide colloids and corrosion products are given by Equations 6.5.1.2-49 and 6.5.1.2-50, respectively. The solution of these continuum-form mass balance equations is approximated for the purpose of numerical modeling by the solution of discrete forms of these equations using a finite-difference approach. This requires the discretization of the time derivative (or mass accumulation term) and the advective and diffusive terms for both dissolved and colloidal transport. All other source terms and decay terms do not require discretization in either time or space.

Numerical modeling of the EBS radionuclide transport is performed using the GoldSim software (GoldSim Technology Group 2007 [DIRS 181727]) cell pathway capability, available in the GoldSim Contaminant Transport Module. The cell pathway acts as a batch reactor, where radionuclide mass is assumed to be instantaneously and completely mixed and partitioned among all media (fluid or solid) within the cell. Both advective and diffusive transport mechanisms can

be explicitly represented using the cell pathways. When multiple cells are linked together via advective and diffusive mechanisms, the behavior of the cell network is mathematically described using a coupled system of differential equations, and is mathematically equivalent to a finite difference network. GoldSim numerically solves the coupled system of equations to compute the radionuclide mass present in each cell and the mass fluxes between cells as a function of time. Both initial and boundary conditions for a cell can be defined explicitly, and systems of varying geometry can be modeled.

Within a computational cell network, each cell is allowed to communicate by advection and/or diffusion with any other cell. This concept is crucial in implementing the bifurcation of diffusive fluxes across an interface between a single continuum domain and a dual continuum domain, such as at the interface between the invert domain and the UZ. Each computational cell is provided with parameters describing water volumes, diffusive properties, and advective and diffusive flux links to other cells. Between any two cells, the diffusive flux can be bidirectional, depending on the concentration gradient, while the advective flux is unidirectional. The output of a cell is given in terms of the advective and diffusive mass fluxes for radionuclide species i and its concentration at the cell center.

The number of cells in the finite-difference network and the discretization of the cells is chosen in such a way as to capture the unique physical and chemical properties of the EBS components with respect to radionuclide transport. The abstractions are in the form of logic statements and stochastic distributions that provide a method for linking various cells in the network. Implementation of the EBS flow and transport model for the TSPA uses the output of the drift seepage model (SNL 2007 [DIRS 181244]), the models for drip shield and waste package degradation (SNL 2007 [DIRS 178871]), the EBS physical and chemical environment model (SNL 2007 [DIRS 177412]), the thermal-hydrologic environment model (SNL 2007 [DIRS 181383]), and the waste form degradation and mobilization model (BSC 2004 [DIRS 172453]); *Defense HLW Glass Degradation Model* (BSC 2004 [DIRS 169988]); and *CSNF Waste Form Degradation: Summary Abstraction* (BSC 2004 [DIRS 169987]). The flow through various cells is based on the continuity equations and conservation of mass, as discussed in Section 6.3. An overview of the computational model for TSPA, as implemented using GoldSim, is provided below.

Radionuclide transport through the waste package is modeled by spatially discretizing the waste package into two domains: an upstream waste form domain and a downstream corrosion products domain. This discretization although simplistic is reasonable and adequate for the spatial and temporal resolution at which the flow and transport processes are understood and modeled. When the degradation of the waste-form starts, the waste package internals (the basket material and the inner vessel), will also start to corrode due to the presence of water vapor and oxygen. The exact geometry and transport pathway inside the waste package cannot be predicted *a priori*, but it is reasonable and realistic to assume that some corrosion products will be present along the transport pathway since the radionuclide mass would have to eventually pass through the corroding inner vessel and some basket material in order to get out of the waste package. The transport domains are illustrated in Figure 6.5-20 by the EBS portion of the cell network – waste form cell, corrosion products cell, and invert cell. More specifically,

the waste form and corrosion products computational domains contain mass from the degradation of following components:

CSNF Waste Package:

- | | |
|---------------------------|---|
| CSNF Waste Form Domain | —Waste form (CSNF rods), basket tubes (Stainless Steel Type 316), absorber plates (Borated Stainless Steel Type 304B4) |
| Corrosion Products Domain | —Transportation, aging and disposal (TAD) canister (Stainless Steel Type 316), guide assembly (Stainless Steel Type 316), inner vessel (Stainless Steel Type 316) |

CDSP Waste Package:

- | | |
|---------------------------|---|
| HLWG Waste Form Subdomain | —HLW glass, HLWG canisters (Stainless Steel Type 316) |
| DSNF Waste Form Subdomain | —DSNF (SNF and Stainless Steel Type 304), DSNF canister (Carbon Steel Type A 516, Borated Stainless Steel Type 304, and Stainless Steel Type 316) |
| Corrosion Products Domain | —Divider plate (Carbon Steel Type A 516), inner brackets (Carbon Steel Type A 516), outer brackets (Carbon Steel Type A 516), support tube (Carbon Steel Type A 516), inner vessel (Stainless Steel Type 316) |

In order to model transport through each domain on a macro scale, consistent with the in-package chemistry model and waste form and waste package degradation models, the transport pathways are predominantly based on geometry of the intact waste package. As such the waste form domains include some steel degradation products besides the waste form while corrosion products domain contain remaining steel degradation products that are not included in the waste form domain. The cylindrical geometry of the waste package is approximated using Cartesian grid geometry. The suitability of this representation for radial diffusive transport is discussed in Appendix L.

The waste form cell receives mass from a specialized GoldSim “Source” cell, which models the waste package failure, degradation of the waste form, and release of the inventory for possible transport through the EBS. The “Source” cell provides the specified flux boundary condition for solving the mass transport equations. Both advective and diffusive transport can occur from the waste form cell to the corrosion products cell. Both equilibrium and kinetic sorption of radionuclides to the corrosion products along with colloid facilitated transport of radionuclides is modeled. Three types of colloids, namely, waste form colloids, iron oxyhydroxide colloids, and groundwater colloids, are considered that can facilitate the transport of radionuclides by reversible and/or kinetic sorption. The waste form colloids are generated in the waste form cell (from degradation of CSNF, HLW, and DSNF), the iron oxyhydroxide colloids are modeled in the corrosion products cell (even though they could also be potentially generated in the waste

form cell), and groundwater colloids are modeled in both waste form cell and the corrosion products cell. All three types of colloids can be transported to the downstream cells by diffusion and advection.

The discretization of the invert domain, using GoldSim, consists of one cell. Both advective and diffusive flux communication exist between the corrosion product and invert cells. Advective flux due to imbibition from the host rock to the invert may enter the invert cell.

Below the invert, part of the near-field UZ is modeled by an array of cells. The inclusion of the UZ portion in the model serves to establish a far field zero-concentration boundary and an accurate representation of the radionuclide flux at the invert-to-UZ interface. The EBS-UZ interface model is described in more detail in Section 6.5.2.6. The dual continuum approach for modeling the UZ is achieved by creating UZ matrix and fracture cells. The invert cell communicates with the UZ matrix and fracture cells directly below it in the UZ cell array (see Section 6.5.2.6).

The following description focuses on discretization of the mass balance equation for the dissolved and reversibly sorbed mass (Equation 6.5.1.2-48). Similar treatments apply to the mass balance transport equations for the irreversibly sorbed radionuclide species. In order to describe the time discretization, let the superscript n represent a solution at the n^{th} time. The n^{th} time step assumes the radionuclide concentrations are known at time step n , and the solution provides the concentrations at time step $n+1$. Over this time step, the accumulation term uses a first order backward-in-time discretization:

$$\frac{\partial}{\partial t} [\theta_w R_{fi} C_i] \approx \frac{\theta_w R_{fi}^n (C_i^{n+1} - C_i^n)}{\Delta t}, \quad (\text{Eq. 6.5.2.5-1})$$

where the adsorption retardation factor,

$$R_{fi} = 1 + \frac{\rho_b K_{dis}}{\theta_w} + \bar{K}_{dic}, \quad (\text{Eq. 6.5.2.5-2})$$

and the cell water content are evaluated at the beginning of the time step, and Δt is the time step size from the n^{th} to the $(n+1)^{\text{th}}$ time. $\bar{K}_{dic} = C_{ic} K_{dic}$ is the dimensionless distribution coefficient for equilibrium sorption onto colloids, with C_{ic} the concentration of species i in the colloidal state ($\text{kg } i \text{ m}^{-3}$) and K_{dic} the distribution coefficient for equilibrium sorption onto colloids ($\text{m}^3 \text{ kg}^{-1}$).

The advective transport is discretized with a first order backward (with respect to the flow direction) difference approximation. If the mass balance is applied to cell B , and the advective flux is from cell A to cell B with magnitude q_{wz} ($\text{m}^3 \text{ water m}^{-2} \text{ yr}^{-1}$), then

$$\frac{\partial}{\partial z} [q_{wz} (1 + \bar{K}_{dic}) C_i] \approx [Q_{wz}^n (1 + \bar{K}_{dic})^n C_i^{n+1}]_A - [Q_{wz}^n (1 + \bar{K}_{dic})^n C_i^{n+1}]_B, \quad (\text{Eq. 6.5.2.5-3})$$

where Q_{wz} ($\text{m}^3 \text{ water m}^{-3} \text{ cell B yr}^{-1}$) is the advective water volumetric flow rate per unit bulk volume. The advective volumetric flow rate and colloid concentrations are evaluated at the beginning of the time step. The concentration of radionuclide species i is evaluated at the end of time step. The first term in the difference approximation is the advective mass flow rate entering cell B from cell A . The second term is the advective mass flow rate exiting cell B .

Consider the accumulation of solute mass in cell B due to diffusion. Suppose there are diffusive flux links from cell A to cell B and from cell B to cell C . The dissolved mass diffusive flux accumulation in cell B is approximated by:

$$\frac{\partial}{\partial x} \left(\theta_w D_i \frac{\partial C_i}{\partial x} \right) \approx \frac{F_{A/B} - F_{B/C}}{V_B}, \quad (\text{Eq. 6.5.2.5-4})$$

where $F_{A/B}$ is the diffusion rate (mass/time) across the cell A and B interface. Similarly, $F_{B/C}$ is the diffusion rate (mass/time) across the cell B and C interface.

Consider the discretization of the diffusive flux at the A/B interface. A similar representation occurs at the B/C interface. Apply Fick's First Law and continuity of flux at the interface. Then the flux entering the A/B interface from cell A must equal the flux exiting the A/B interface to cell B . This interface flux continuity condition is expressed as:

$$\begin{aligned} F_{A/B} &= \left(\frac{\theta_w D_i A}{L} \right)_A \left([C_i^{n+1}]_A - [C_i^{n+1}]_{A/B} \right) \\ &= \left(\frac{\theta_w D_i A}{L} \right)_B \left([C_i^{n+1}]_{A/B} - [C_i^{n+1}]_B \right), \end{aligned} \quad (\text{Eq. 6.5.2.5-5})$$

where $[C_i^{n+1}]_{A/B}$ is the concentration at time step $n+1$ at the interface, as indicated by the subscript A/B , and D_i , A , and L are the cell effective diffusion coefficient, diffusive area, and diffusive length, respectively. If the A/B interface diffusion rate is expressed as an interface diffusive conductance times the concentration difference between cells A and B :

$$F_{A/B} D_{ic_A/B} (C_{iA} - C_{iB}), \quad (\text{Eq. 6.5.2.5-6})$$

then the flux continuity condition provided by Equation 6.5.2.5-5 gives the interface diffusive conductance as:

$$D_{ic_A/B} = \frac{1}{\left(\frac{L}{\theta_w D_i A} \right)_A + \left(\frac{L}{\theta_w D_i A} \right)_B}. \quad (\text{Eq. 6.5.2.5-7})$$

The diffusive conductance is the harmonic average of $\frac{\theta_w D_i A}{2L}$ between the two cells. At the B/C interface a similar expression gives:

$$D_{ic_B/C} = \frac{1}{\left(\frac{L}{\theta_w D_i A}\right)_B + \left(\frac{L}{\theta_w D_i A}\right)_C}. \quad (\text{Eq. 6.5.2.5-8})$$

The discretization of the accumulation of solute mass in cell B due to diffusive transport is:

$$\frac{\partial}{\partial x} \left(\theta_w D_i \frac{\partial c}{\partial x} \right) \approx \frac{D_{ic_B/C} ([C_i^{n+1}]_C - [C_i^{n+1}]_B) - D_{ic_A/B} ([C_i^{n+1}]_B - [C_i^{n+1}]_A)}{V_B}. \quad (\text{Eq. 6.5.2.5-9})$$

The mass balance equations are discretized with the dependent concentration variable for the spatially dependent terms evaluated at the end of time step, C_i^{n+1} . This is stated explicitly in the discretization of the advective/diffusive terms. For other source terms, such as radionuclide decay, kinetic sorption reaction onto iron oxyhydroxide material and so forth, the concentration is also evaluated at the end of the time step. In this sense, the mass balance equations are fully implicit and the discretization provides numerical stability. However, coefficient terms such as the moisture content are evaluated at the beginning of the time step. This formulation results in a linear system of equations that is solved for concentrations. If the coefficients depending on concentration were evaluated at the end of time step, then the resulting discretized algebraic equations would be nonlinear. The nonlinear system would require much more computational effort. Furthermore, the computational modeling tool (GoldSim) only solves linear systems. For this reason, all concentration-dependent coefficient terms are evaluated explicitly at time step n .

Within the waste form domain, some part of the dissolved mass of plutonium and americium made available from the degradation of HLW glass and CSNF is converted to “embedded” mass on the waste form colloids. This conversion is required to satisfy the condition that some mass of plutonium and americium is “embedded” as an intrinsic part of the colloid and is not in equilibrium with the aqueous system, when generated from the degradation of HLW glass and CSNF. This mass is thus transported separately as a distinct species [*Waste Form and In-Drift Colloids-Associated Radionuclide Concentrations: Abstraction and Summary* (BSC 2005 [DIRS 177423], Sections 6.3.1 & 6.3.3.3)]. The mass rate of conversion per unit volume of water is modeled as a first order reaction given by $\lambda_i^{embed} C_i$, where λ_i^{embed} is the linear rate constant, and concentration C_i is the dissolved concentration of plutonium and americium species in the waste form domain. The conversion rate λ_i^{embed} is calculated at each time step in the waste form domain. Its calculation is discussed below.

The concentration of the embedded radionuclide mass with respect to the water volume in the waste form domain, C_i^{embed} , and the concentration of waste form colloids, C_{cWF} , are determined at each time step based on the logic given in the *Waste Form and In-Drift Colloids-Associated Radionuclide Concentrations: Abstraction and Summary* (BSC 2005 [DIRS 177423], Section 6.5.1.1). Taking the ratio of embedded radionuclide concentration to the waste form

colloid concentration, $\frac{C_i^{embed}}{C_{cWF}}$, gives the embedded radionuclide mass per unit mass of the waste form colloid.

Suppose that the solution for embedded radionuclide concentration $(C_i^{embed})^n$ and colloid concentration $(C_{cWF})^n$ has been determined at time step n and the solution at current time step $n+1$ is required. Furthermore, suppose that the total mass flux (combined advective and diffusive mass flux) of waste form colloids per unit bulk volume, $(Q_{adv/diff}^{wfc})^n$, is available from the solution at time step n from the waste form colloid mass balance equation (Eq. 6.5.1.2-38). Then the quantity, $\left(Q_{adv/diff}^{wfc} \frac{C_i^{embed}}{C_{cWF}}\right)^n$, represents the mass flux at time level n of embedded radionuclide species i from the waste form subdomain containing the HLW or CSNF glass logs to the downstream domain. A continuum mass balance for embedded radionuclide mass within the waste form domain is:

$$\frac{\partial(\theta_w C_i^{embed})}{\partial t} = -Q_{adv/diff}^{wfc} \frac{C_i^{embed}}{C_{cWF}} + \lambda_i^{embed} \theta_w C_i. \quad (\text{Eq. 6.5.2.5-10})$$

Discretization of this equation gives:

$$\frac{(\theta_w C_i^{embed})^{n+1} - (\theta_w C_i^{embed})^n}{t^{n+1} - t^n} = -\left(Q_{adv/diff}^{wfc} \frac{C_i^{embed}}{C_{cWF}}\right)^n + \lambda_i^{embed} (\theta_w C_i)^n. \quad (\text{Eq. 6.5.2.5-11})$$

This equation is solved for the conversion rate:

$$\lambda_i^{embed} = \frac{\frac{(\theta_w C_i^{embed})^{n+1} - (\theta_w C_i^{embed})^n}{\Delta t} + \left(Q_{adv/diff}^{wfc} \frac{C_i^{embed}}{C_{cWF}}\right)^n}{(\theta_w C_i)^n}. \quad (\text{Eq. 6.5.2.5-12})$$

$(C_i^{embed})^{n+1}$ is calculated from the logic provided in the *Waste Form and In-Drift Colloids-Associated Radionuclide Concentrations: Abstraction and Summary* (BSC 2005 [DIRS 177423], Section 6.5.1.1). The concentration $(C_i^{embed})^{n+1}$ in the waste form domain is a function of the ionic strength and pH. This waste form domain conversion rate is applied to the i species mass balance equation for the solution mass, Eq. 6.5.1.2-39, and for the embedded mass, Eq. 6.5.1.2-38.

The above diffusive flux discussion considers the diffusive flux communication from cells within a single continuum. For transport from the invert domain (single continuum) to the UZ (dual continuum), the flux continuity condition at the interface provides the diffusive flux bifurcation between the single continuum and the dual continuum.

The diffusive fluxes of radionuclide species i within the invert cell, the UZ fracture cell, and the UZ matrix cell are, respectively,

$$\begin{aligned} F_{il} &= \frac{\theta_w D_{il} A_{I/UZ}}{L_I} (C_{il} - C_{il/UZ}) \\ &= \hat{D}_{il} (C_{il} - C_{il/UZ}), \end{aligned} \quad (\text{Eq. 6.5.2.5-13})$$

$$\begin{aligned} F_{if} &= \frac{\theta_w D_{if} A_{I/UZ}}{L_f} (C_{il/UZ} - C_{if}) \\ &= \hat{D}_{if} (C_{il/UZ} - C_{if}), \end{aligned} \quad (\text{Eq. 6.5.2.5-14})$$

$$\begin{aligned} F_{im} &= \frac{\theta_w D_{im} A_{I/UZ}}{L_m} (C_{il/UZ} - C_{im}) \\ &= \hat{D}_{im} (C_{il/UZ} - C_{im}), \end{aligned} \quad (\text{Eq. 6.5.2.5-15})$$

where

- D_{il} = effective diffusion coefficient within the invert cell ($\text{m}^2 \text{s}^{-1}$),
- D_{if} = effective diffusion coefficient within the UZ fracture cell ($\text{m}^2 \text{s}^{-1}$),
- D_{im} = effective diffusion coefficient within the UZ matrix cell ($\text{m}^2 \text{s}^{-1}$),
- $A_{I/UZ}$ = diffusive area between the invert and UZ cells (m^2),
- L_I = diffusive length within the invert cell (m),
- L_f = diffusive length within the UZ fracture cell (m),
- L_m = diffusive length within the UZ matrix cell (m) = L_f ,
- C_{il} = concentration of radionuclide species i in the invert cell ($\text{kg } i \text{ m}^{-3}$),
- C_{if} = concentration of radionuclide species i in the UZ fracture cell ($\text{kg } i \text{ m}^{-3}$),
- C_{im} = concentration of radionuclide species i in the UZ matrix cell ($\text{kg } i \text{ m}^{-3}$),
- $C_{il/UZ}$ = concentration of radionuclide species i at the interface between the invert and UZ cells ($\text{kg } i \text{ m}^{-3}$),

and the $\hat{D}_i = \frac{\theta_w D_i A}{L}$ are respective diffusive conductances ($\text{m}^3 \text{s}^{-1}$) of radionuclide species i .

The flux continuity at the interface requires:

$$F_{il} = F_{if} + F_{im}. \quad (\text{Eq. 6.5.2.5-16})$$

From the flux continuity, the interface concentration of radionuclide species i is determined as a function of the diffusive parameters and the cell concentrations as:

$$C_{il/UZ} = \frac{\hat{D}_{il}C_{il} + \hat{D}_{if}C_{if} + \hat{D}_{im}C_{im}}{\hat{D}_{il} + \hat{D}_{if} + \hat{D}_{im}}. \quad (\text{Eq. 6.5.2.5-17})$$

This provides the diffusive fluxes of radionuclide species i in UZ fracture and matrix cells, respectively, as:

$$F_{if} = \frac{\hat{D}_{il}\hat{D}_{if}}{\hat{D}_{il} + \hat{D}_{if} + \hat{D}_{im}}(C_{il} - C_{if}) + \frac{\hat{D}_{if}\hat{D}_{im}}{\hat{D}_{il} + \hat{D}_{if} + \hat{D}_{im}}(C_{im} - C_{if}) \quad (\text{Eq. 6.5.2.5-18})$$

$$F_{im} = \frac{\hat{D}_{il}\hat{D}_{im}}{\hat{D}_{il} + \hat{D}_{if} + \hat{D}_{im}}(C_{il} - C_{im}) + \frac{\hat{D}_{if}\hat{D}_{im}}{\hat{D}_{il} + \hat{D}_{if} + \hat{D}_{im}}(C_{im} - C_{if}). \quad (\text{Eq. 6.5.2.5-19})$$

The expression for the diffusive flux of radionuclide species i from the invert cell to the UZ fracture cell can be expressed as a diffusive conductance multiplied by a concentration difference of radionuclide species i between the invert cell and the UZ fracture cell plus a corrective flux between the UZ fracture and matrix cells. Similarly, the expression for the diffusive flux from the invert to the UZ matrix cell is expressed as a diffusive flux between the invert and the UZ matrix cell minus the same corrective flux between the UZ cells. The corrective flux term accounts for coupling among the invert cell, UZ fracture and matrix cells, as the following explains. The flux to both UZ cells should depend on the diffusive properties in the invert cell and the two UZ cells, together with the concentrations in these three cells. Therefore, the flux to the UZ fracture cell cannot be expressed only in terms of the concentration drawdown between the invert cell and the UZ fracture cell. The corrective term includes the dependence of the UZ fracture flux on the concentration of radionuclide species i in the UZ matrix cell due to the requirement that the sum of the two UZ continua receive exactly the flux leaving the invert. The corrective flux term is not a true flux expression between the two UZ cells, since the diffusive conductance coefficient is dependent on the diffusive area between the invert and the UZ, and the diffusive lengths are the lengths with respect to flow from the invert cell to the UZ cells. The model also explicitly includes diffusion between the UZ fracture and matrix continua, as shown in Figure 6.5-20.

The UZ fluxes result in defining three diffusive conductances from the flux expressions:

$$\hat{D}_{ilf}(C_{il} - C_{if}) = \frac{\hat{D}_{il}\hat{D}_{if}}{\hat{D}_{il} + \hat{D}_{if} + \hat{D}_{im}}(C_{il} - C_{if}), \quad (\text{Eq. 6.5.2.5-20})$$

$$\hat{D}_{ilm}(C_{il} - C_{im}) = \frac{\hat{D}_{il}\hat{D}_{im}}{\hat{D}_{il} + \hat{D}_{if} + \hat{D}_{im}}(C_{il} - C_{im}), \quad (\text{Eq. 6.5.2.5-21})$$

$$\hat{D}_{imf}(C_{im} - C_{if}) = \frac{\hat{D}_{im}\hat{D}_{if}}{\hat{D}_{il} + \hat{D}_{if} + \hat{D}_{im}}(C_{im} - C_{if}), \quad (\text{Eq. 6.5.2.5-22})$$

where

- \hat{D}_{ilf} = effective diffusive conductance between invert cell and UZ fracture cell ($\text{m}^3 \text{s}^{-1}$);
- \hat{D}_{ilm} = effective diffusive conductance between invert cell and UZ matrix cell ($\text{m}^3 \text{s}^{-1}$);
- \hat{D}_{if} = effective diffusive conductance between UZ fracture and matrix cells ($\text{m}^3 \text{s}^{-1}$).

In order to accommodate the GoldSim representation of diffusive conductance as a two-term expression, the diffusive conductances of radionuclide species i are written as:

$$\hat{D}_{ilf} = \frac{1}{\frac{L_I}{(\theta_w D_i A)_I \left[\frac{(\theta_w D_i)_f}{(\theta_w D_i)_f + (\theta_w D_i)_m} \right]} + \frac{L_f}{(\theta_w D_i A)_f}}, \quad (\text{Eq. 6.5.2.5-23})$$

$$\hat{D}_{ilm} = \frac{1}{\frac{L_I}{(\theta_w D_i A)_I \left[\frac{(\theta_w D_i)_m}{(\theta_w D_i)_f + (\theta_w D_i)_m} \right]} + \frac{L_m}{(\theta_w D_i A)_m}}, \quad (\text{Eq. 6.5.2.5-24})$$

$$\hat{D}_{imf} = \frac{1}{\frac{L_f}{(\theta_w D_i A)_f \left[\frac{L_I (\theta_w D_i)_m}{L_I (\theta_w D_i)_m + L_m (\theta_w D_i)_I} \right]} + \frac{L_m}{(\theta_w D_i A)_m}}. \quad (\text{Eq. 6.5.2.5-25})$$

Although the above approach is rigorous, it is complex and difficult to implement in the TSPA Model. A second approach that is easier to understand and simpler to implement, while providing the same results as the above approach, is presented here and is implemented in TSPA. This approach requires introduction of an interface cell, located between the invert cell and the UZ cells. This interface cell provides an approximate interface concentration and the resulting flux split at the invert-to-UZ cell interface. The interface cell is conceptualized as a very thin slice of the invert cell. This implies the interface cell takes on the invert diffusive properties, with the exception of diffusive length. Let the diffusive length within the interface cell be some small fraction (a scale factor) of the invert diffusive length, say, `Interface_Scale_Factor` = 10^{-6} :

$$L_{I-int} = 10^{-6} L_I. \quad (\text{Eq. 6.5.2.5-26})$$

As in Equation 6.5.2.5-7, the diffusive conductance between the invert cell and the invert interface cell is calculated as the harmonic average:

$$\hat{D}_{il/I-int} = \frac{1}{\frac{L_I}{(\theta_w D_i A)_I} + \frac{L_{I-int}}{(\theta_w D_i A)_{I-int}}}. \quad (\text{Eq. 6.5.2.5-27})$$

For diffusion between the interface cell and the UZ fracture and matrix cells, the diffusive conductances of radionuclide species i are, respectively,

$$\hat{D}_{il-int/f} = \frac{1}{\frac{L_{I-int}}{(\theta_w D_i A)_{I-int}} + \frac{L_{UZ}}{(\theta_w D_i A)_f}}, \quad (\text{Eq. 6.5.2.5-28})$$

$$\hat{D}_{il-int/m} = \frac{1}{\frac{L_{I-int}}{(\theta_w D_i A)_{I-int}} + \frac{L_{UZ}}{(\theta_w D_i A)_m}}. \quad (\text{Eq. 6.5.2.5-29})$$

The interface cell concentration of radionuclide species i is computed as part of the cell network solution. Because the transport mass balance equations conserve mass, the mass flux leaving the interface cell must equal the sum of the mass fluxes entering the two UZ cells. The solution provides the flux continuity across the interface between the invert interface cell and UZ cells. This formulation expects the flux exiting the invert cell (or entering the interface cell) is approximately equal to the flux exiting the interface cell. This approximation is dependent on the diffusive length within the interface cell. The error in this approximate solution approaches zero as the diffusive length of the interface cell approaches zero.

6.5.2.6 EBS-UZ Boundary Condition Implementation in the TSPA

For TSPA, a semi-infinite zero-concentration boundary condition is used for the EBS-UZ interface. This is approximated by applying an effective zero-concentration boundary at approximately three drift diameters below the invert-UZ boundary into the UZ. In an alternative approach, a zero-concentration boundary condition can be used at the interface between the invert and the UZ, which will result in an unrealistically high diffusive gradient through the invert. By moving the zero-concentration boundary some distance below the invert, a more realistic diffusive gradient through the invert is achieved.

In the EBS-UZ interface model, the near-field UZ is modeled as a dual continuum of overlapping UZ-matrix and UZ-fracture media. This approach is consistent with the dual-permeability modeling approach used by the UZ transport model, as described in *Particle Tracking Model and Abstraction of Transport Processes* (SNL 2007 [DIRS 181006]). The matrix and fracture continua are represented in the RTA by a two-dimensional vertical array of cells oriented parallel to a cross section of a drift and located immediately beneath a drift (Figure 6.5-20). This array

consists of three columns or vertical zones, with each zone containing both a fracture cell and a matrix cell. The invert is in direct communication with the second or center zone of UZ matrix/fracture cells. Each zone is four layers deep in the vertical direction. Thus, the array consists of twelve pairs of matrix and fracture cells within the UZ. Laterally, each zone is one drift diameter wide (5.5 m; SNL 2007 [DIRS 179354, Table 4-1), with the middle zone centered beneath the drift, so that each layer of the array extends one drift diameter on either side of the drift. In the longitudinal direction of a drift, the length of the array is equal to the length of the waste package being modeled.

The thickness of the first (top) layer of cells is 10 percent greater than the average invert thickness (0.934 m; see Equation 6.5.2.3-5), or 1.0274 m. The thickness of the second layer is double that of the first layer, or 2.0548 m. The third and fourth layers are given an arbitrary thickness of 5 m and 10 m, respectively. A “collector cell” is placed beneath the fourth layer and is given a very large, numerically infinite, water volume (10^{10} m^3) to simulate an effective zero-concentration boundary. This collector cell acts as a sink for all the mass flow from the invert and UZ cells.

As depicted in Figure 6.5-20, each fracture cell interacts, via diffusive connection only, with the matrix cell of the same zone. The fracture cell also interacts via diffusive connection vertically with the fracture cell of underlying and overlying layers of the same zone. The matrix cell of each zone interacts via diffusive connection laterally with the matrix cells of adjacent zones and vertically with the matrix cell of underlying and overlying layers of the same zone. Radionuclides diffuse based on the concentration gradient between cells. Advection occurs downward only, from the fracture cell of one layer to the fracture cell of the underlying layer in the same zone, and from the matrix cell of one layer to the matrix cell of the underlying layer in the same zone; advection does not occur across zones. Each zone is spatially distinct. Each is one drift diameter in width. The only connection possible between left and right adjacent zones is by diffusion through the middle zone.

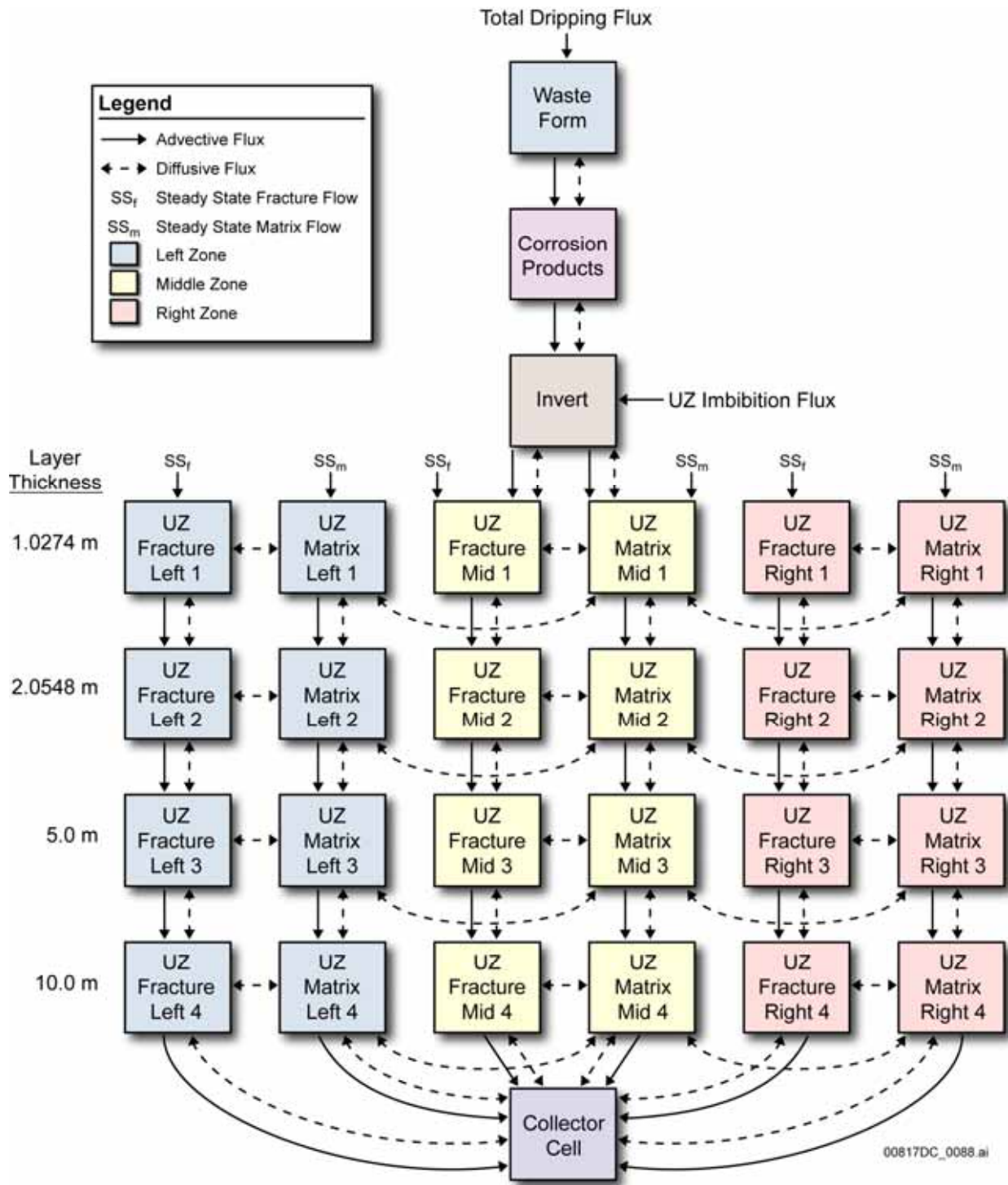


Figure 6.5-20. Computational Grid in the EBS-UZ Interface Model

The mass flux from the invert flows into the top layer of the middle zone in the UZ. The portion of the advective flux from the invert that is attributable to the total dripping flux (F_1) flows into the UZ fractures. The imbibition flux into the invert (F_7) flows out of the invert into the UZ matrix. The diffusive flux from the invert can go into both UZ continua based on the concentration gradient and effective diffusion coefficient. The advective flux flowing through the UZ fracture cells in the middle zone is given by the greater of the advective flux out of the invert (F_1) and the steady state UZ fracture flux. The advective flux in the two outer zones is given by the steady state UZ flow in each continuum at the repository horizon; the drift shadow effects are ignored in the transport calculation.

For the advective mass transport calculation shown in Equation 6.5.2.5-3, volumetric discharges for the fracture and matrix continua are needed. Since fracture and matrix percolation fluxes are given as specific discharge, the volumetric flux is calculated by multiplying the percolation flux for each continuum by the projected bulk area normal to the flux, where the projected area A_{UZ} is calculated as:

$$A_{UZ} = d_D L_{WP}, \quad (\text{Eq. 6.5.2.6-1})$$

where d_D is the drift diameter (m) and L_{WP} is the length of a waste package (m). This area is used for the diffusive and advective flux calculations between UZ cells. For the calculation between the invert and UZ, the area $A_{I/UZ}$ given by Equation 6.5.2.3-4 ($A_{I/UZ} = w_I L_{WP}$) is used.

The void volume for each continuum is computed by multiplying the bulk volume for each discretized zone in each layer (based on the geometry) by either the fracture porosity or matrix porosity. The average fraction of the UZ that is occupied by fractures (also referred to as fracture porosity) is given for TSw35 as a beta distribution in DTN: LA0701PANS02BR.003 [DIRS 180497]. Similarly, the water volume is calculated by multiplying the void volume of each continuum by its respective saturation.

For diffusive mass transport, in the calculation shown in Equation 6.5.2.5-5, the effective diffusion coefficient for the matrix continuum is calculated using a method developed in *Radionuclide Transport Models under Ambient Conditions* (SNL 2007 [DIRS 177396]), wherein the tortuosity of the rock type is determined based on experimental work (Reimus et al. 2007 [DIRS 179246], Equation 2) while the free water diffusion coefficient is species dependent. Multiplying the tortuosity with the free water diffusion coefficient gives the effective diffusion coefficient.

The effects of climate variations on the matrix diffusion coefficient in the UZ were considered in *Particle Tracking Model and Abstraction of Transport Processes* (SNL 2007 [DIRS 181006]). Because of the lower sensitivity to climate, the effects of climate variations on matrix diffusion were combined so that the diffusion coefficient was a function only of the rock type. Tortuosities were first computed for individual rock units in the UZ model and then the rock units are combined into three rock groups based on similar characteristics for tortuosity. Almost all of the rock units that comprise the repository host rock belong to Rock Group 3. The mean tortuosity for the Rock Group 3 is computed on a volume-weighted basis (from each unit) to be about 1.45×10^{-2} represented by a normal distribution (DTN: LB0702PAUZMTDF.001

[DIRS 180776]). The value obtained for the effective UZ matrix diffusion coefficient is applied to the fracture diffusion coefficient as well for lack of other information.

The diffusive area between the fracture and matrix continua is computed by multiplying the bulk volume by the fracture interface area, which provides the connection area per unit bulk volume. This diffusive area is further reduced by the fracture-matrix interface reduction factor, given as $S_{ef}^{1+\gamma}$, where S_{ef} is the effective fracture saturation, and γ is the active fracture parameter (SNL 2007 [DIRS 175177]). The effective fracture saturation (S_{ef}) is computed as:

$$S_{ef} = \frac{S_{wf} - S_{wfr}}{1 - S_{wfr}}, \quad (\text{Eq. 6.5.2.6-2})$$

where S_{wf} is the fracture water saturation, and S_{wfr} is the fracture residual saturation.

The mass flux of radionuclides from the invert domain to the dual continuum UZ, computed at the boundary of the EBS-UZ interface (between the invert cell and the adjacent UZ matrix and fracture cells), is passed to the UZ transport model for TSPA calculations as described in *Particle Tracking Model and Abstraction of Transport Processes* (SNL 2007 [DIRS 181006]). In addition to the total mass flux, the relative fraction of the mass going into each of the fracture and the matrix cells at the EBS-UZ boundary is required by the UZ transport model. This fracture-matrix partitioning of mass is calculated on the basis of the mass fraction going into the fracture continuum (compared to the matrix continuum) from the invert domain in the EBS-UZ interface model. This partitioning is time dependent and captures the temporal processes active in the EBS, such as varying radionuclide concentrations in the waste form, corrosion products, and invert domains, and the changing water flux through various subcomponents of the EBS. Furthermore, this partitioning is computed by solving the mass transport equations for the EBS and part of the UZ as a coupled system with appropriate boundary conditions and adopting a modeling approach using the dual continuum invert model saturation results presented in *Multiscale Thermohydrologic Model* (SNL 2007 [DIRS 181006]), and the dual continuum transport model for the UZ (SNL 2007 [DIRS 181006]).

Sorption of radionuclides to the UZ matrix continuum is modeled by applying the devitrified tuff K_d values from the UZ submodel. For sorption calculations, the mass of UZ matrix continuum is calculated as: $V_b \rho_b (1 - \phi_f)$, where V_b is the bulk volume of the matrix cell considered (m^3), ϕ_f is the fracture porosity, and ρ_b is the dry bulk density of TSw35 matrix (kg m^{-3}).

All three types of colloids are transported from the invert to the UZ cells. Groundwater colloids are present in all four layers. The iron oxyhydroxide and waste form colloids with reversibly sorbed radionuclides are modeled to be present in only the first two layers of the middle column, making the groundwater colloid the only type of colloid available for far-field transport, consistent with colloid-facilitated transport modeled in the UZ as described in *Particle Tracking Model and Abstraction of Transport Processes* (SNL 2007 [DIRS 181006]).

Most of the input hydrologic parameters used for the EBS-UZ boundary condition implementation are taken from *Particle Tracking Model and Abstraction of Transport Processes*

(SNL 2007 [DIRS 181006]), in which specification of the ranges and distributions for the parameters is discussed. The fracture and matrix saturation and water fluxes are developed from the UZ flow model output at 560 repository cells for eight climate cases: glacial-transition 10th percentile, glacial-transition 30th percentile, glacial-transition 50th percentile, glacial-transition 90th percentile, post-10k 10th percentile, post-10k 30th percentile, post-10k 50th percentile, and post-10k 90th percentile. For each case, updated fracture and matrix saturation, water content, and percolation flux values at 560 repository cells have been extracted from the UZ flow model output. The 560 repository cells are grouped into five percolation subregions (bins) for TSPA use. The saturation and flux for the repository cells within a given percolation subregion is averaged for each of the eight climate cases. Standard sorting and table-joining functions in statistical and data analysis software JMP V. 5.1 were used to extract and sort data from UZ flow field calculations for use in the EBS-UZ interface model. The extracted data are presented in output DTN: SN0703PAEBSRТА.001, in eight *bin splits* Excel files, and described in file *Repository Values for Saturation and Flux.doc*.

Fracture frequency, fracture aperture, and fracture porosity corresponding to Rock Group 8, as described in *Particle Tracking Model and Abstraction of Transport Processes* (SNL 2007 [DIRS 181006]) and given in DTN: LA0701PANS02BR.003 [DIRS 180497], is used in the EBS-UZ boundary condition implementation as Rock Group 8 comprise most of the repository host rock and rock type below the repository. Fracture aperture is calculated by taking the ratio of fracture frequency to fracture porosity, both of which are treated as epistemically uncertain parameters. The fracture residual saturation is fixed at 0.01 (DTN: LB0207REVUZPRP.001 [DIRS 159526], file *faultprops_2002.xls*, worksheet “summary,” Model Layer *tswf*). The matrix porosity is fixed at 0.149. The currently accepted value for TSw35 matrix porosity is 0.131 (DTN: LB0207REVUZPRP.002 [DIRS 159672], file *hydroprops_fin.xls*, worksheet “Summary,” Column J). The value used (0.149) is nonetheless considered representative and suitable for use in the EBS-UZ interface model for the following reasons. First, the currently accepted value of 0.131 is uncertain, with a standard deviation of 0.031 (DTN: LB0207REVUZPRP.002 [DIRS 159672], file *hydroprops_fin.xls*, worksheet “Summary,” Column K). The fixed value used is within one standard deviation of the current value and can therefore be considered to agree with the current value within its range of uncertainty. Second, the matrix porosity used is within the range of matrix porosities of the geological units in which the repository will reside: for TSw33, TSw34, TSw35, and TSw36 (BSC 2007 [DIRS 180938], Table 1), the matrix porosity reported in DTN: LB0207REVUZPRP.002 [DIRS 159672], file *hydroprops_fin.xls*, worksheet “Summary,” Column J, ranges from 0.103 (TSw36) to 0.155 (TSw33), further justifying the use of 0.149 for the UZ matrix porosity.. The active fracture parameter γ is sampled uniformly between 0.2 and 0.6 as given in DTN: LA0701PANS02BR.003 [DIRS 180497] for all climate states consistent with the implementation in the *Particle Tracking Model and Abstraction of Transport Processes* (SNL 2007 [DIRS 181006]).

6.5.2.7 Stoichiometry for Conversion of Radionuclide Mass to Kinetically Sorbed Mass onto Iron Oxyhydroxide Colloids, Stationary Corrosion Products, and Waste Form Colloids

6.5.2.7.1 Conceptual Model

The EBS Transport Submodel is implemented using the cell pathway capability of GoldSim (GoldSim Technology Group 2007 [DIRS 181727]). The cell pathways act as a batch reactor, where radionuclide mass is modeled as instantaneously and completely mixed, and partitioned among all media, fluid or solid, within the cell. The following five reactions for converting radionuclide mass to other species mass are considered at each time step:

- Simple radioactive decay reaction of a parent species to a daughter species for the entire mass in the cell pathway in all domains
- Reaction of dissolved mass to form radionuclide species embedded in waste form colloids within the waste form domain
- Reaction of dissolved mass to form kinetic sorption species to the iron oxyhydroxide colloids within the corrosion products domain
- Reaction of dissolved mass to form kinetic sorption species to the iron oxyhydroxide corrosion products within the corrosion products domain
- Reverse kinetic reaction of sorption species from the iron oxyhydroxide corrosion products to dissolved mass within the corrosion products domain.

Within GoldSim, the total of all appropriate reactions is modeled by combining the individual reaction rate constants into a single effective reaction rate constant. After the reaction is completed, the relative masses formed from each reaction are determined by applying appropriate stoichiometry to the effective daughter products. Because all reaction rate constants are of first order, they can be summed together into an effective reaction rate constant. The mass of a given species in the cell pathway is thus converted into the different daughter species and tracked separately in GoldSim. The radionuclides that are specifically modeled for kinetic sorption are the plutonium and americium isotopes that are mobilized inside the waste package after the waste form has degraded. Americium and plutonium species that undergo these reactions will form embedded mass on the waste form colloids and kinetically sorbed mass on the iron oxyhydroxide colloids and corrosion products in addition to true radioactive decay and equilibrium sorption to waste form and groundwater colloids. Further, a reverse kinetic sorption reaction accounts for a slow desorption from the corrosion products sorbed mass to solution mass. For other radionuclide species with only true radioactive decay, stoichiometry for the daughter species is set to unity. Radiolysis is not considered here. Instead the impacts of radiolysis on in-package chemistry and transport are shown to be limited in FEP Number 2.1.13.01A (DTN: MO0706SPAFEPLA.001 [DIRS 181613]).

6.5.2.7.2 Stoichiometry Calculations

The discussion regarding the stoichiometry associated with all reactions is presented with respect to ²⁴³Am, though similar treatment holds for other americium and plutonium species. The ²⁴³Am

species will experience radioactive decay to ^{239}Pu for both dissolved mass and the mass in equilibrium sorption with the waste form and groundwater colloids. The ^{243}Am species will require conversion to embedded mass on the waste form colloids within the waste form domain, and will require conversion to kinetically sorbed mass on the iron oxyhydroxide colloids and corrosion products within the corrosion products domain. In order to account for these four conversion processes, ^{243}Am is assigned four daughters:

- ^{239}Pu : radioactive daughter of ^{243}Am
- $Ic^{243}\text{Am}$: ^{243}Am species embedded on waste form colloids
- $If^{243}\text{Am}$: ^{243}Am species kinetically sorbed to iron oxyhydroxide colloids
- $Ifcp^{243}\text{Am}$: ^{243}Am species kinetically sorbed to iron oxyhydroxide corrosion products.

Also, a reverse (desorption) kinetic reaction converts $Ifcp^{243}\text{Am}$ mass to solution mass, ^{243}Am , and to $Ifcp^{243}\text{Am}$ radioactive daughter $Ifcp^{239}\text{Pu}$ (^{239}Pu kinetically sorbed to corrosion products). In the subsequent discussion, the above reactions as applied to ^{243}Am within the corrosion product domain are considered first, followed by the application of the above reactions to ^{243}Am species within the waste form cell. Finally, the stoichiometry for the kinetically sorbed species $Ifcp^{243}\text{Am}$ is considered within the corrosion product cell.

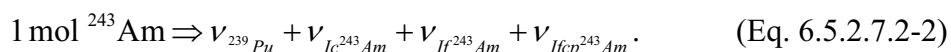
The ^{243}Am conversion rates (yr^{-1}) for each of the above four reaction processes are denoted respectively:

- $\lambda_{243\text{Am}}$
- $\lambda_{243\text{Am}}^{embed}$
- R_{fc}
- R_{fcp} .

However, within the waste form domain the conversion rates for kinetic sorption to corrosion materials, R_{fc} and R_{fcp} , will be zero as there are no corrosion products. Similarly, within the corrosion products domain, the conversion rate to embedded waste form colloids, $\lambda_{243\text{Am}}^{embed}$, is zero as the waste form is not present. With this understanding of the domain dependence of the reactions, the general form for the total or effective ^{243}Am conversion rate is written as:

$$\rho_{243\text{Am}} = \lambda_{243\text{Am}} + \lambda_{243\text{Am}}^{embed} + R_{fc} + R_{fcp}. \quad (\text{Eq. 6.5.2.7.2-1})$$

The following stoichiometric coefficients for species i , ν_i , illustrate how a unit mole of ^{243}Am is partitioned among the four daughters:



This states that one mole of ^{243}Am converts to $\nu_{^{239}\text{Pu}}$ (mol) of ^{239}Pu , $\nu_{\text{Ic}^{243}\text{Am}}$ (mol) of Ic^{243}Am , $\nu_{\text{If}^{243}\text{Am}}$ (mol) of If^{243}Am , and $\nu_{\text{Ifcp}^{243}\text{Am}}$ (mol) of $\text{Ifcp}^{243}\text{Am}$. Specification of the total effective conversion rate (Equation 6.5.2.7.2-1), the daughter species formed from the reaction, and the stoichiometric coefficients of each daughter species (Equation 6.5.2.7.2-2) completely describes all reactions.

The effective conversion rate within the corrosion products domain will include a total of three reactions, the two kinetic reactions of the ^{243}Am onto iron oxyhydroxide colloids and corrosion products, respectively, and the radioactive decay of ^{243}Am . There is no conversion to embedded waste form colloids in the corrosion product domain. The total effective conversion rate (based on the formulation of Equation 6.5.1.2-39) which accounts for both the dissolved mass and the equilibrium sorbed mass can be written as:

$$\Lambda_{^{243}\text{Am}} = R_{fc} + R_{fcp} + \lambda_{^{243}\text{Am}} \left(1 + \bar{K}_{dcWF} + \bar{K}_{dcGW}\right), \quad (\text{Eq. 6.5.2.7.2-3})$$

or

$$\Lambda_{^{243}\text{Am}} = R_{fc} + R_{fcp} + \lambda_{^{243}\text{Am}} \left(1 + \sum \bar{K}_d\right), \quad (\text{Eq. 6.5.2.7.2-4})$$

where the equilibrium sorbed mass to the waste form and ground water colloids are included.

The stoichiometric coefficient for the radioactive decay to species ^{239}Pu is the ratio of the radioactive conversion rate of ^{243}Am to the total effective conversion rate. This is given by:

$$\nu_{^{239}\text{Pu}} = \frac{\lambda_{^{243}\text{Am}} \left(1 + \sum \bar{K}_d\right)}{R_{fc} + R_{fcp} + \lambda_{^{243}\text{Am}} \left(1 + \sum \bar{K}_d\right)}. \quad (\text{Eq. 6.5.2.7.2-5})$$

Similarly, the stoichiometric coefficient for the conversion of ^{243}Am to daughter If^{243}Am is:

$$\nu_{\text{If}^{243}\text{Am}} = \frac{R_{fc}}{R_{fc} + R_{fcp} + \lambda_{^{243}\text{Am}} \left(1 + \sum \bar{K}_d\right)}, \quad (\text{Eq. 6.5.2.7.2-6})$$

and the stoichiometric coefficient for the conversion of ^{243}Am to daughter $\text{Ifcp}^{243}\text{Am}$ is:

$$v_{\text{Ifcp}^{243}\text{Am}} = \frac{R_{\text{fcp}}}{R_{\text{fc}} + R_{\text{fcp}} + \lambda_{^{243}\text{Am}} \left(1 + \sum \bar{K}_d\right)}. \quad (\text{Eq. 6.5.2.7.2-7})$$

As noted above, within the corrosion products domain, the stoichiometric coefficient for the embedded waste form colloids is zero:

$$v_{\text{Ic}^{243}\text{Am}} = 0. \quad (\text{Eq. 6.5.2.7.2-8})$$

In order to implement the above stoichiometric coefficients in GoldSim, a modification is needed because Equation 6.5.2.7-1 is formulated with respect to dissolved concentrations while the material balance equations in GoldSim are formulated with respect to the total mass in the cell pathway (dissolved mass plus equilibrium sorbed mass). As a result, the radioactive decay rate constant that is applied in GoldSim is just λ_i (or $\lambda_{^{243}\text{Am}}$ in this example) without the term $\left(1 + \sum \bar{K}_d\right)$. In other words, the conversion of $\left(1 + \sum \bar{K}_d\right)$ is not needed in GoldSim because the radioactive decay is applied to the entire mass in the cell pathway and not just to the dissolved mass. However, the kinetic reaction rate constants, R_{fc} and R_{fcp} , require modification in GoldSim, as these reactions only apply to the dissolved mass rather than to the entire mass in the cell pathway (Equation 6.5.2.7-1). Thus, these rate constants must be multiplied by a conversion factor, which is equivalent to the ratio of mass in solution to mass in pathway. The conversion factor for americium species, as applied in GoldSim, is given as:

$$f_{\text{Am}} = \frac{V_w}{V_w + m_{\text{cWF}} K_{\text{dc,Am,WF}} + m_{\text{cGW}} K_{\text{dc,Am,GW}}} \quad (\text{Eq. 6.5.2.7.2-9})$$

where

- V_w = volume of water in the corrosion products cell [m^3]
- m_{cWF} = mass of waste form colloids in the corrosion products cell [kg]
- m_{cGW} = mass of ground water colloids in the corrosion products [kg]
- $K_{\text{dc,Am,WF}}$ = americium distribution coefficient for waste form colloids [$\text{m}^3 \text{kg}^{-1}$]
- $K_{\text{dc,Am,GW}}$ = americium distribution coefficient for ground water colloids [$\text{m}^3 \text{kg}^{-1}$].

Then the total or effective rate in a given domain (Equation 6.5.2.7-1) for ^{243}Am , as applied in GoldSim, can be written as:

$$\Lambda_{^{243}\text{Am,GS}} = \lambda_{^{243}\text{Am}} + \lambda_{^{243}\text{Am}}^{\text{embed}} + f_{\text{Am}} (R_{\text{fc}} + R_{\text{fcp}}). \quad (\text{Eq. 6.5.2.7.2-10})$$

Note that the second term in the above equation is zero in the corrosion products domain, while the third term is zero in the waste form domain.

The total kinetic reaction rate in the corrosion products domain, or kinetic conversion rate is:

$$\lambda_{T,Am} = f_{Am} (R_{fc} + R_{fcp}). \quad (\text{Eq. 6.5.2.7.2-11})$$

Denote:

$$f_c = \frac{R_{fc}}{R_{fc} + R_{fcp}}. \quad (\text{Eq. 6.5.2.7.2-12})$$

Then stoichiometric coefficient in the corrosion products domain, as applied in GoldSim, for kinetic sorption to the corrosion products colloids is calculated as:

$$V_{Ifc^{243}Am} = \frac{f_c \lambda_{T,Am}}{\lambda_{T,Am} + \lambda_{243Am}}, \quad (\text{Eq. 6.5.2.7.2-13})$$

and the stoichiometric coefficient for corrosion products is calculated as:

$$V_{Ifcp^{243}Am} = \frac{(1 - f_c) \lambda_{T,Am}}{\lambda_{T,Am} + \lambda_{243Am}}. \quad (\text{Eq. 6.5.2.7.2-14})$$

It can be shown that Equations 6.5.2.7-13 and 6.5.2.7-14, as implemented in GoldSim, are equivalent to Equations 6.5.2.7-6 and 6.5.2.7-7.

If both the numerator and denominator of Equation 6.5.2.7.2-9 are divided by V_w , the conversion factor for americium species can be written as:

$$\begin{aligned} f_{Am} &= \frac{1}{1 + \bar{K}_{dc,Am,WF} + \bar{K}_{dc,Am,GW}} \\ &= \frac{1}{1 + \sum \bar{K}_d}. \end{aligned} \quad (\text{Eq. 6.5.2.7.2-15})$$

As a result, Equation 6.5.2.7.2-11 can be expressed as:

$$\lambda_{T,Am} = \frac{R_{fc} + R_{fcp}}{1 + \sum \bar{K}_d}, \quad (\text{Eq. 6.5.2.7.2-16})$$

Substitution of Equations 6.5.2.7.2-12 and 6.5.2.7.2-16 in Equations 6.5.2.7.2-13 and 6.5.2.7.2-14 yield:

$$V_{If^{243}Am} = \frac{\left(\frac{R_{fc}}{R_{fc} + R_{fcp}} \right) \left(\frac{R_{fc} + R_{fcp}}{1 + \sum \bar{K}_d} \right)}{\left(\frac{R_{fc} + R_{fcp}}{1 + \sum \bar{K}_d} \right) + \lambda_{243} Am}, \quad (\text{Eq. 6.5.2.7.2-17})$$

$$V_{Ifcp^{243}Am} = \frac{\left(1 - \frac{R_{fc}}{R_{fc} + R_{fcp}} \right) \left(\frac{R_{fc} + R_{fcp}}{1 + \sum \bar{K}_d} \right)}{\left(\frac{R_{fc} + R_{fcp}}{1 + \sum \bar{K}_d} \right) + \lambda_{243} Am}. \quad (\text{Eq. 6.5.2.7.2-18})$$

The above expressions simplify to:

$$V_{If^{243}Am} = \frac{R_{fc}}{R_{fc} + R_{fcp} + \lambda_{243} Am (1 + \sum \bar{K}_d)}, \quad (\text{Eq. 6.5.2.7.2-19})$$

$$V_{Ifcp^{243}Am} = \frac{R_{fcp}}{R_{fc} + R_{fcp} + \lambda_{243} Am (1 + \sum \bar{K}_d)}, \quad (\text{Eq. 6.5.2.7.2-20})$$

which is the expression for these stoichiometric coefficients given in Equations 6.5.2.7.2-6 and 6.5.2.7.2-7.

The stoichiometric coefficient for the radioactive decay to species ^{239}Pu in GoldSim is computed as:

$$V_{I^{239}Pu} = \frac{\lambda_{243} Am}{\lambda_{T,Am} + \lambda_{243} Am}. \quad (\text{Eq. 6.5.2.7.2-21})$$

Substituting Equation 6.5.2.7.2-16 in the above equation gives:

$$\begin{aligned} V_{I^{239}Pu} &= \frac{\lambda_{243} Am}{\left(\frac{R_{fc} + R_{fcp}}{1 + \sum \bar{K}_d} \right) + \lambda_{243} Am}, \\ &= \frac{\lambda_{243} Am (1 + \sum \bar{K}_d)}{R_{fc} + R_{fcp} + \lambda_{243} Am (1 + \sum \bar{K}_d)} \end{aligned}, \quad (\text{Eq. 6.5.2.7.2-22})$$

which is the same as Equation 6.5.2.7.2-5.

The reaction rate constant for conversion of embedded mass on the waste form colloids, $\lambda_{243 Am}^{embed}$, as shown in Equation 6.5.2.7.2-1, remains unchanged in GoldSim, as the conversion is applied to the entire mass in the waste form cell pathway (solution and reversibly sorbed mass). The two nonzero stoichiometric coefficients within the waste form domain are:

$$V_{239 Pu} = \frac{\lambda_{243 Am}}{\lambda_{243 Am}^{embed} + \lambda_{243 Am}} \quad (\text{Eq. 6.5.2.7.2-23})$$

$$V_{Ic^{243 Am}} = \frac{\lambda_{243 Am}^{embed}}{\lambda_{243 Am}^{embed} + \lambda_{243 Am}}. \quad (\text{Eq. 6.5.2.7.2-24})$$

Within the corrosion product domain the mass species $I_{fcp}^{243 Am}$, kinetically sorbed mass to the corrosion products, experiences reactions from radioactive decay and kinetic desorption. Since the radioactive daughter of ^{243}Am is ^{239}Pu , the radioactive daughter of $I_{fcp}^{243 Am}$ is $I_{fcp}^{239 Pu}$. This implies that any ^{243}Am mass kinetically sorbed to the corrosion products decays to ^{239}Pu kinetically sorbed to the corrosion products. The effective conversion rate for the $I_{fcp}^{243 Am}$ species is:

$$\rho_{I_{fcp}^{243 Am}} = \lambda_{243 Am} + R_{rcp}, \quad (\text{Eq. 6.5.2.7.2-25})$$

where R_{rcp} is the reverse (desorption) rate for the $I_{fcp}^{243 Am}$ species. For the $I_{fcp}^{243 Am}$ species, the effective conversion rate is applied to the entire mass in the corrosion product cell pathway. That is to say, there is no equilibrium sorption of the $I_{fcp}^{243 Am}$ species. Therefore, the stoichiometric coefficients are:

$$V_{I_{fcp}^{239 Pu}} = \frac{\lambda_{243 Am}}{\lambda_{243 Am} + R_{rcp}} \quad (\text{Eq. 6.5.2.7.2-26})$$

$$V_{239 Pu} = \frac{R_{rcp}}{\lambda_{243 Am} + R_{rcp}}. \quad (\text{Eq. 6.5.2.7.2-27})$$

6.6 MODEL FORMULATION FOR ALTERNATIVE CONCEPTUAL MODELS

6.6.1 Bathtub Flow Model

The conceptual model for the TSPA is based on the presence of continuous flow paths through the patches and stress corrosion cracks that penetrate the waste package. More specifically, the TSPA Model conceptualizes that vertical flow of seepage into the waste package, through the waste form and out of the waste package is not impeded by the location of patches and stress corrosion cracks on the surface of the waste package. There is no long-term build-up and retention of liquid within the waste package for flow and transport. There is also no resistance to the flow through the waste form. The TSPA approach attempts to maximize the immediate

release and mobilization of radionuclides into the local groundwater environment. This approach is referred to as the “flow through” geometry.

An ACM to the “flow through” geometry is the “bathtub” geometry (Mohanty et al. 1996 [DIRS 130419]). The bathtub geometry allows seepage to collect within the waste package before being released to the EBS. In theory, “bathtub” geometry could result in the release of a large pulse of radionuclides when a second patch appears beneath the water line, initiating gravity drainage; such a release would be “sudden” relative to time steps used in the TSPA, typically thousands of years long at late times when corrosion patches appear.

The “bathtub” effect would be most important during the period when only a few patches or cracks have penetrated the drip shield and waste package. In this situation, there may be penetrations through the top of the waste package while the bottom surface remains intact, leading to retention of liquid. At later times, the presence of multiple penetrations makes “flow-through” geometry the more likely configuration.

The response of the bathtub geometry is evaluated for a primary case and for three secondary cases. The primary case includes consideration of two limiting conditions on radionuclide releases: dissolution rate limited and solubility limited. Tc is typical of dissolution rate limited radionuclides. The Tc released due to waste dissolution can always be dissolved in the available water because the solubility limit of Tc is high (SNL 2007 [DIRS 177418], Section 6.14). This is particularly true when the time step size in the TSPA model is small compared to the dissolution rate. However, if the time step size in the TSPA model is large enough such that the dissolution of the entire waste occurs in a single time step, then the rate limitation effects will not be seen. Np is typical of the solubility limited type of radionuclide, where the release of Np from dissolution is limited by its low solubility (SNL 2007 [DIRS 177418], Section 6.6).

The results for the primary case are based on a closed form analytic solution with constant values of inflow rate, dissolution rate, and solubility. The three secondary cases consider a step change in inflow rate, such as would occur from a climatic change, a step change in water chemistry, or a step change in flow geometry, as would occur if a patch suddenly appeared beneath the waterline. The basic geometry and flow pattern for the primary bathtub model is shown in Figure 6.6-1 (from Mohanty et al. 1996 [DIRS 130419], Figure 2-7); q_{in} is identical to F_4 and in Section 6.3.1.1.

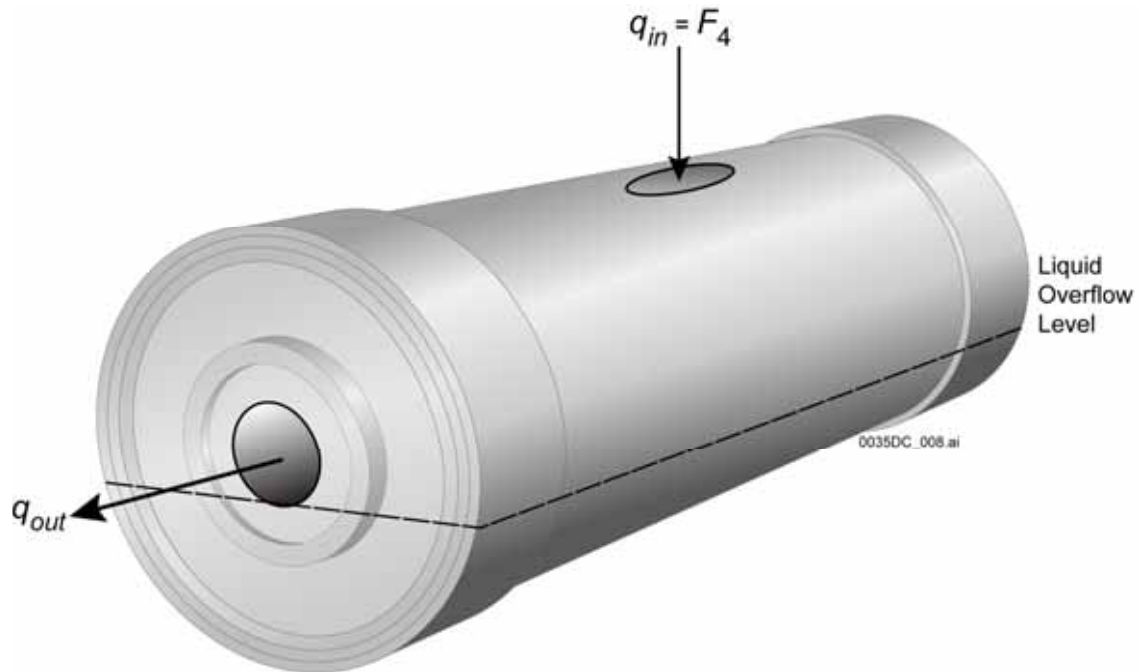


Figure 6.6-1. Schematic of the Bathtub Geometry for the Waste Package

6.6.1.1 Primary Case

6.6.1.1.1 Dissolution-Rate-Limited Radionuclide

In this case, the concentration of radionuclides is limited by the rate of dissolution. Consider the system shown in Figure 6.6-1, with a constant inflow rate, q_{in} , and let V_{tub} be the total volume of liquid that can be retained within the waste package before it overflows. The response of the waste package is a two step process. During Step 1, the package is filling with liquid and the outflow rate, q_{out} , is zero. This condition continues until the waste package fills with liquid at a time, t_{fill} , given by V_{tub} / q_{in} . Step 2 occurs after time t_{fill} ; the amount of liquid inside the waste package remains constant, and $q_{out} = q_{in}$. This is a steady state condition, consistent with the assumption that q_{in} is constant and that liquid does not continue to accumulate within the package. The following analysis also supposes there is complete contact between the liquid and the waste form within the waste package, and that the dissolution rate is constant.

During Step 1, for time t such that $0 < t < t_{fill}$, the dissolution of a radioisotope into the water inside the waste package can be represented as:

$$\dot{m}_i = r_s \omega_i, \quad (\text{Eq. 6.6.1.1.1-1})$$

where

\dot{m}_i = the rate of release of radionuclide into the liquid (kg s^{-1})

r_s = the dissolution rate of the waste form (kg s^{-1})

ω_i = the mass fraction of radioisotope i released per unit mass of waste form (dimensionless); ω_i is less than one for a waste form with multiple radionuclides.

During the fill period q_{out} is zero, so the mass, $m_i(t)$, of radioisotope dissolved (assuming it is under-saturated with respect to the solubility controlling mineral phase) within the liquid in the waste package at time t is given by:

$$m_i(t) = r_s \omega_i t, \quad (\text{Eq. 6.6.1.1.1-2})$$

because r_s and ω_i are constant. Similarly, the volume of liquid in the waste package at time t , $V(t)$, is given by:

$$V(t) = q_{in} t, \quad (\text{Eq. 6.6.1.1.1-3})$$

so the concentration of dissolved isotope i in the waste package, $C_i(t)$, is

$$C_i(t) = \frac{m_i(t)}{V(t)} = \frac{r_s \omega_i t}{q_{in} t} = \frac{r_s \omega_i}{q_{in}}. \quad (\text{Eq. 6.6.1.1.1-4})$$

The concentration, $C_i(t)$, is constant during the fill phase because the values of r_s , ω_i , and q_{in} are chosen to be constant. This condition is appropriate because the dissolved mass, m_i , and the volume of liquid, V , are linear functions of the time (and initially both are zero), so their ratio remains constant.

The result in Equation 6.6.1.1.1-4 holds for each dissolution-rate-limited radioisotope i in the waste form, although the numerical value of $C_i(t)$ differs because the mass fraction, ω_i , is different for each isotope.

During Step 2, when $t > t_{fill}$, the radioisotope mass within the waste package is a balance between the dissolution of radioisotope into the groundwater within the waste package and the loss of radioisotope due to outflow from the waste package:

$$\dot{m}_i = r_s \omega_i - q_{out} C_i(t). \quad (\text{Eq. 6.6.1.1.1-5})$$

Because the water inflow rate, waste form solubility, and mass fraction of radioisotope i all remain constant, the concentration $C_i(t)$ remains constant even when the solution is removed at a rate q_{out} . Therefore, at $t > t_{fill}$, the *net* rate of radionuclide release into the water inside the waste package is zero (i.e., the dissolution rate is exactly offset by the outflow rate):

$$\dot{m}_i = r_s \omega_i - q_{out} C_i(t) = 0. \quad (\text{Eq. 6.6.1.1.1-6})$$

For constant q_{in} , with $q_{out} = q_{in}$,

$$C_i(t) = \frac{r_s \omega_i}{q_{in}}. \quad (\text{Eq. 6.6.1.1.1-7})$$

The dissolved mass in the waste package is constant for $t > t_{fill}$. In addition, the concentration of dissolved radionuclide is constant for all time $t > 0$ (until all of the waste form is dissolved), as shown by Equations 6.6.1.1.1-4 and 6.6.1.1.1-7. These results are reasonable because the waste package is in steady state for $t > t_{fill}$. This means that the inflow rate equals the outflow rate and that any loss of dissolved radionuclide mass in the outflow from the waste package is exactly balanced by the addition of dissolved radionuclide mass from dissolution of the waste form.

The response for the comparable flow-through model has the same radionuclide concentration, $C_i(t)$, and the same release flux, given by $C_i(t)q_{out}$, as the bathtub geometry. The sole difference between the flow-through and bathtub models is that the flux from the flow-through model starts from $t = 0$ while the flux from the bathtub model is zero until time t_{fill} . The bathtub model introduces a delay in the response but does not change the concentration in the package or the mass flux out of the package.

Therefore, for the dissolution-rate-limited case, the flow-through model is bounding relative to the bathtub model for radionuclide releases from the waste package. The bathtub analysis considers advective transport with no sorption of radionuclides, whereas the current EBS transport model includes sorption onto stationary corrosion products (retardation in the waste package) as well as colloid-facilitated transport. In this bathtub analysis of alternative conceptual models, sorption onto stationary corrosion products inside the waste package would effectively reduce the dissolution rate. Since that rate is still constant and the same for both the flow-through and bathtub models, sorption would affect the concentrations of radionuclides in the outflow, but would have no impact on the conclusion that the bathtub model introduces a delay in releases compared to the flow-through model. Sorption onto colloids would have the opposite net effect of increasing the effective solubility and again would have no impact on the conclusions regarding release delay.

6.6.1.1.2 Solubility-Limited Radionuclide

The response for a solubility-limited radionuclide, in which the solubility limit of the radionuclide is instantaneously achieved, is similar to that for a dissolution-rate-limited radionuclide, in the sense that the bathtub model delays the release from the waste package but does not change the release rate.

During Step 1, $0 < t < t_{fill}$, the amount of radionuclide dissolved in the groundwater in the waste package can be represented as:

$$\dot{m}_i = C_{si} q_{in}, \quad (\text{Eq. 6.6.1.1.2-1})$$

where C_{si} is the solubility limit of the radionuclide. If the groundwater chemistry is constant, the solubility is constant and the mass, m_i , of radioisotope retained in the waste package at time t is:

$$m_i(t) = C_{si}q_{in}t. \quad (\text{Eq. 6.6.1.1.2-2})$$

The volume of liquid in the waste package at time t , $V(t)$, is given by:

$$V(t) = q_{in}t, \quad (\text{Eq. 6.6.1.1.2-3})$$

so that the concentration of dissolved isotope in the waste package is:

$$C_i(t) = \frac{m_i(t)}{V(t)} = \frac{C_{si}q_{in}t}{q_{in}t} = C_{si}. \quad (\text{Eq. 6.6.1.1.2-4})$$

The concentration is constant during the fill phase and equal to the solubility limit, as would be expected. This is true for each radionuclide in the system, although the numerical values of the solubility limit vary.

For $t > t_{fill}$, the mass balance within the waste package is a steady state condition given by:

$$\dot{m}_i = C_{si}q_{in} - C_i(t)q_{out} = C_{si}q_{in} - \frac{m_i(t)}{V_{tub}}q_{out} = 0. \quad (\text{Eq. 6.6.1.1.2-5})$$

The solution to Equation 6.6.1.1.2-5 with $q_{out} = q_{in}$ is:

$$m_i(t) = C_{si}V_{tub}, \quad (\text{Eq. 6.6.1.1.2-6})$$

with

$$C_i(t) = C_{si}. \quad (\text{Eq. 6.6.1.1.2-7})$$

Again the dissolved mass in the waste package is constant for $t > t_{fill}$ (until all of the waste form is dissolved) and the concentration of dissolved radionuclide is constant at the solubility limit for all times $t > 0$.

The comparable flow-through model has the same radionuclide concentration, C_{si} , and the same release flux, given by $C_{si}q_{out}$, as the bathtub geometry. The sole difference is that the flux from the flow-through model starts from $t = 0$ while the flux from the bathtub model is zero until time t_{fill} . The bathtub model introduces a delay in the response but does not change the dose rate. Therefore, the flow-through model is again bounding relative to the bathtub model because radionuclides are released with no delay time to the EBS.

6.6.1.2 Secondary Cases

The secondary cases evaluate the response of the bathtub model when changes occur in the groundwater inflow rate, in inflow chemistry, or in the flow geometry.

6.6.1.2.1 Change in Inflow Rate

The response of a bathtub model to a change in inflow rate differs for a solubility-limited or a dissolution-rate-limited radionuclide. The solubility-limited case is simpler because of chemical equilibrium and is discussed first.

Consider a step change in inflow rate after the bathtub has filled for a *solubility-limited* radionuclide. Since kinetic effects are ignored, the chemical system is always at equilibrium and the concentration within the waste package remains unchanged at the solubility limit. The only change in the system is that the radionuclide mass flux out of the waste package changes instantaneously from $C_i q_{out}$ to $C_i q_{out,new}$. This response is exactly the same as it would be for the flow-through model, so the response of the bathtub model is identical to that for the flow-through model.

Now consider a step change in inflow rate after the bathtub has filled for a *dissolution-rate-limited* radionuclide. In this case, the mass released per unit time remains constant because the dissolution rate remains constant, but the radionuclide concentration comes to a new equilibrium value. This new equilibrium value can be determined by Equation 6.6.1.1.1-7, with the product of concentration and liquid inflow remaining constant:

$$C_{i,new} q_{in,new} = C_{i,old} q_{in,old} = r_s \omega_i \quad (\text{Eq. 6.6.1.2.1-1})$$

If the inflow rate decreases, the final concentration increases because the product of concentration and liquid inflow remains constant. A flow-through model has an instantaneous increase in concentration, whereas the bathtub model shows an exponential growth to the new concentration. Thus, the flow-through model is bounding for concentration released into the EBS because there is no delay in changing to the new increased radionuclide concentration.

The exponential growth to the new concentration can be seen as follows. The replacement of “old” inflow with concentration $C_{i,old}$ with “new” inflow with concentration $C_{i,new}$ is represented through a parameter, β , the volume fraction of old inflow to V_{tub} , the total liquid volume in the bathtub. The rate of change of the volume of old inflow, V_{old} , is given by:

$$\frac{dV_{old}}{dt} = -\beta q_{out,new} = -\beta q_{in,new} \quad (\text{Eq. 6.6.1.2.1-2})$$

Equation 6.6.1.2.1-2 represents the loss of old inflow through outflow, with the factor β representing the (decreasing) volume fraction of old inflow that is lost. By definition,

$$\beta \equiv \frac{V_{old}}{V_{tub}}. \quad (\text{Eq. 6.6.1.2.1-3})$$

Substituting this definition into the left-hand side of Equation 6.6.1.2.1-2 gives:

$$\frac{d\beta}{dt} = -\frac{q_{in,new}}{V_{tub}} \beta. \quad (\text{Eq. 6.6.1.2.1-4})$$

The solution to Equation 6.6.1.2.1-4 with initial condition $\beta = 1$ at $t = 0$ is:

$$\beta = \exp\left(-\frac{q_{in,new}}{V_{tub}} t\right), \quad (\text{Eq. 6.6.1.2.1-5})$$

which corresponds to an exponential decay of C_i from $C_{i,old}$ to $C_{i,new}$.

If the inflow rate were to increase, the concentration would decrease. In a flow-through model, the concentration would instantaneously decrease, whereas in the bathtub model, the concentration would exponentially relax to the new concentration. The flow-through model is then not bounding for concentration released into the EBS. The mass of radionuclide mobilized is identical, as implied by Equation 6.6.1.2.1-1, but the dissolved concentration varies with the amount of fluid flowing through the system. However, the TSPA Model passes mass to the UZ, rather than concentration, so the difference between the flow through model and the bathtub model for this case is not critical to performance.

Finally, a change in inflow rate during the initial period, when the bathtub is filling, only affects the value of t_{fill} and hence the delay until the bathtub fills, after which it behaves as described in Section 6.6.1.1.

In summary, the response of the bathtub model to a change in inflow rate is identical to that of the flow-through model for solubility-limited radionuclides. For dissolution-rate-limited radionuclides, the response of the bathtub model is less bounding than the flow-through model when the inflow rate decreases (and concentration increases). If the inflow rate increases (resulting in a decrease in the outflow concentration of radionuclides), the bathtub model is more bounding than the flow-through model for dissolution-rate-limited radionuclides.

6.6.1.2.2 Change in Inflow Chemistry

Consider a step change in inflow chemistry after the bathtub has filled. Initially, there will be minor changes in concentration within the bathtub because the bulk of the water retains the original inflow composition. Eventually the “old” groundwater is flushed out and replaced with the “new” inflow, resulting in new concentrations within the bathtub.

As in the preceding section where a change in inflow rate was examined, the replacement of old with new inflow can be represented through a parameter β , representing the volume fraction of old inflow in V_{tub} , the total liquid volume in the bathtub. The rates of change of the volumes of old and new inflow are given by:

$$\frac{dV_{old}}{dt} = -\beta q_{out}, \quad (\text{Eq. 6.6.1.2.2-1})$$

and

$$\frac{dV_{new}}{dt} = q_{in} - (1 - \beta)q_{out}, \quad (\text{Eq. 6.6.1.2.2-2})$$

where V_{old} and V_{new} represent the volumes of inflow with the old and new chemistries, respectively. Equation 6.6.1.2.2-1 represents the loss of old inflow through outflow, with the factor β representing the volume fraction of old inflow that is lost. Equation 6.6.1.2.2-2 represents the addition of new inflow and its partial loss through outflow. Remembering that $q_{out} = q_{in}$ because of the steady state assumption, it follows that:

$$\frac{dV_{old}}{dt} = -\beta q_{in}; \quad \frac{dV_{new}}{dt} = +\beta q_{in}. \quad (\text{Eq. 6.6.1.2.2-3})$$

By definition:

$$\beta \equiv \frac{V_{old}}{V_{tub}}. \quad (\text{Eq. 6.6.1.2.2-4})$$

Substituting this definition into the left-hand equation in 6.6.1.2.2-3, it follows that:

$$\frac{d\beta}{dt} = -\frac{q_{in}}{V_{tub}} \beta = -\frac{1}{t_{fill}} \beta. \quad (\text{Eq. 6.6.1.2.2-5})$$

The solution to Equation 6.6.1.2.2-5 with the initial condition $\beta(0) = 1$ is given by:

$$\beta(t) = e^{-\frac{t}{t_{fill}}}. \quad (\text{Eq. 6.6.1.2.2-6})$$

It follows that the old and new volumes of inflow are given by:

$$V_{old} = V_{tub} e^{-\frac{t}{t_{fill}}} \quad (\text{Eq. 6.6.1.2.2-7})$$

and:

$$V_{new} = V_{tub} \left(1 - e^{-\frac{t}{t_{fill}}} \right). \quad (\text{Eq. 6.6.1.2.2-8})$$

These equations say that the volume fraction of inflow with the old chemistry decays exponentially with the characteristic time t_{fill} . Alternatively, the volume fraction of new inflow increases to 1.0 with a characteristic time of t_{fill} for the exponential growth given by Equation 6.6.1.2.2-8.

The impact of changing inflow chemistry on dissolution rate or solubility is much more difficult to predict analytically because chemical interactions are nonlinear. More specifically, the pH of mixtures of inflows is not proportional to β because the pH scale is proportional to the log of the hydrogen ion concentration and inherently nonlinear and because potential chemical interactions in mixtures, such as buffering, produce a nonlinear response. In addition, solubility and dissolution rate are often complex nonlinear functions of the pH.

Nonlinear response makes it particularly difficult to predict the time-dependent response for solubility; however, because the starting state and the ending state, for $t \gg t_{fill}$, are well defined, the evolution can be approximated to first order by:

$$C_{si}(t) \approx C_{si,old} e^{-\left(\frac{t}{t_{fill}}\right)} + C_{si,new} \left(1 - e^{-\left(\frac{t}{t_{fill}}\right)} \right). \quad (\text{Eq. 6.6.1.2.2-9})$$

Consider the response when $C_{si,new} \gg C_{si,old}$. This condition can easily occur for the actinides, where solubility increases by several orders of magnitude as pH changes from between 7 and 8 to a value below 6 or above 10. In the limit of large $C_{si,new}$, Equation 6.6.1.2.2-9 becomes:

$$(C_{si,new} \gg C_{si,old}): \quad C_{si}(t) \approx C_{si,new} \left(1 - e^{-\left(\frac{t}{t_{fill}}\right)} \right). \quad (\text{Eq. 6.6.1.2.2-10})$$

In effect the initial solubility is negligible compared to $C_{si,new}$, and solubility at late times increases to $C_{si,new}$ from below. Alternatively, if $C_{si,new} \ll C_{si,old}$,

$$(C_{si,new} \ll C_{si,old}): \quad C_{si}(t) \approx C_{si,old} e^{-\left(\frac{t}{t_{fill}}\right)} + C_{si,new}. \quad (\text{Eq. 6.6.1.2.2-11})$$

Here the solubility decays towards a much smaller value in the new inflow mixture.

While the details of the time-dependent behavior are only approximated, the starting and ending states must be accurate and Equations 6.6.1.2.2-10 and 6.6.1.2.2-11 provide a simplified

transition from one chemical regime to another. The dissolution rate could replace solubility in Equations 6.6.1.2.2-9 through 6.6.1.2.2-11, and the same general conclusions would hold.

In summary, the response of the bathtub model to a change in inflow chemistry is slower than that of a flow-through model, where the solubility or dissolution rate changes abruptly with a step change in inflow chemistry. The bathtub dampens or delays the response to a change in inflow chemistry over a time scale on the order of t_{fill} to $7t_{fill}$. The upper estimate of $7t_{fill}$ corresponds to an exponential factor of e^{-7} or 0.0009, at which point Equation 6.6.1.2.2-11 has reached an asymptote of $C_{si,new}$. The analytic models cannot predict the precise time dependence because of the nonlinear effects of mixing on pH and of pH on solubility and dissolution rate.

The flow-through model overestimates radionuclide releases compared to the bathtub model when solubility increases because the bathtub geometry delays the increase in radionuclide concentrations and mass fluxes from the waste package to the EBS. The case of increasing solubility or increasing dissolution rate is important because it will increase the peak dose rate. The fact that the flow-through model is not bounding when solubility or dissolution rate decreases is therefore of less importance for performance assessment and is of secondary importance in selecting the conceptual model for flow through the waste package.

6.6.1.2.3 Change in Patch Geometry

The geometry for the bathtub model allows seepage to collect within the waste package before being released to the EBS. In the primary model (Figure 6.6-1), the patch is positioned such that release is governed by the condition $q_{out} = q_{in}$ after the package fills with liquid.

As an alternative to the primary patch model, consider a waste package that does not have an existing (outflow) patch on the side of the package, but instead has a second patch open abruptly beneath the water line. While the radionuclide concentration within the waste package is unchanged by the alternative location, failure results in the sudden release of a larger pulse of radionuclide mass at the time the second patch opens. Mathematically, the flux of radionuclides leaving the waste package in the primary model, F_{pri} , is given by:

$$F_{pri} = C_i q_{out} = C_i q_{in} = C_i \frac{V_{tub}}{t_{fill}}, \quad (\text{Eq. 6.6.1.2.3-1})$$

and the flux of radionuclides leaving the waste package in the alternative model, F_{alt} , is given by:

$$F_{alt} = C_i \frac{V_{tub}}{\Delta t}, \quad (\text{Eq. 6.6.1.2.3-2})$$

where Δt is the time to empty the retained liquid through the second patch. In theory, it is possible that $\Delta t \ll t_{fill}$, so that $F_{alt} \gg F_{pri}$.

Equations 6.6.1.2.3-1 and 6.6.1.2.3-2 have the same value for radionuclide concentration, C_i , in the retained liquid because the chemistry of the groundwater is independent of patch location. Implicit in Equations 6.6.1.2.3-1 and 6.6.1.2.3-2 is that the second patch in the ACM occurs after the volume of liquid in the waste package in the primary model has reached steady state.

The flow-through model produces an average release continuously, while the bathtub model with the alternative flow path produces zero release initially, followed by a high pulse that soon returns to the same flux as the flow-through model. In other words, the flow-through model represents a time average of the response of the bathtub model. From this viewpoint, the potential difference between F_{alt} and F_{pri} is partly mitigated by the sorption and diffusion processes in the unsaturated and saturated zones. The potential difference between F_{alt} and F_{pri} is also small if the second patch appears shortly after the first penetration because there is less retained liquid.

This alternative can also be thought of as being equivalent to the appearance of additional penetrations in the waste package. This analogy is appropriate because additional penetrations in the waste package increase the inflow flux into the waste form, resulting in higher releases to the EBS. The main effect of the alternative patch geometry model is to generate the increase earlier. This is not considered a major difference because there is a wide range of variability in corrosion rates for the TSPA WAPDEG model (SNL 2007 [DIRS 178871]). The effect of the alternative patch geometry model can then be reasonably considered to be captured within this variability.

The results and observations in this section (6.6.1.2.3) and throughout Section 6.6.1 are appropriate for the general boundary conditions considered here. In other words, this comparison is based on the full fluid flux into the waste package having access to all radioisotopes in the waste. The model implemented in TSPA, in which radionuclides are mobilized in a mass of corrosion products around the fuel pellets, partly mitigates the differences discussed here. This mitigation occurs because a large fluid flux will not transport radionuclides at the solubility limit if the mass in solution is limited by the pore volume in a mass of corrosion products. The situation is then similar to that mentioned at the end of Section 6.6.1.2.1, where mass transfer to the UZ is the dominant issue, rather than dissolved concentration.

6.6.1.3 Summary

The response of the bathtub geometry has been evaluated for a primary case, with constant boundary conditions and material properties, and for three secondary cases. Analyses for the three secondary cases consider a step change in inflow rate, a step change in inflow chemistry, and a change in flow geometry as would occur if a patch suddenly appeared beneath the waterline. All cases include consideration of two types of radionuclide release mechanisms: dissolution-rate-limited and solubility-limited. The comparisons are based on closed form analytic solutions.

The key conclusions from the evaluation follow:

- The bathtub model introduces a time delay in the release of radionuclides from the waste package to the EBS in comparison to the flow-through model for the primary case. The

base case flow-through model overestimates releases of radionuclides in relation to the bathtub geometry for the primary case because there is no delay in release of radionuclides to the EBS.

- The response of the bathtub model to a step change in inflow rate (secondary case 1) is identical to the flow-through model for solubility-limited radionuclides. The response of the bathtub model for dissolution-rate-limited radionuclides is to delay the change in concentration and mass flux associated with the new inflow rate. The base case flow-through model overestimates releases of radionuclides with respect to the bathtub geometry for the case of decreasing inflow, when the concentration of radionuclide increases. The case of increasing radionuclide concentration is of primary interest from a performance or regulatory viewpoint since this case will result in greater releases.
- The response of the bathtub model to a step change in inflow chemistry (secondary case 2) is to delay the change in concentration and mass flux associated with the new inflow chemistry. Analytical models cannot define the exact time delay, which is sensitive to nonlinear chemical effects when inflows mix. Limiting cases, when solubility increases or decreases by several orders of magnitude, have been examined to define a first order approximation to the response of the chemical system.

The base case flow-through model overestimates releases of radionuclides relative to the bathtub geometry when solubility or dissolution rate increase with changing inflow chemistry. The flow-through model has an instantaneous change to the higher equilibrium value while the bathtub geometry delays the change as the initial inflow is flushed out of the waste package. Increases in radionuclide concentrations and fluxes are of primary interest from a performance or regulatory viewpoint, so the underestimation of releases of radionuclides in the flow-through model for decreasing solubility or dissolution rate can reasonably be excluded from the TSPA.

- The response of the bathtub model when a second patch opens instantaneously beneath the water level in the waste package (secondary case 3) has also been analyzed. The impact of the instantaneous opening is to release a pulse of radionuclides in comparison to the base case flow-through model. The impact of this ACM is mitigated by the time delays introduced through sorption and diffusion in the unsaturated and saturated zones. In addition, the higher mass flux from the alternative flow path is similar to the impact from additional patches opening in the waste package. There is a wide range of variability in corrosion rates for the TSPA Model, and the impact from the instantaneous opening is encompassed in the uncertainty in corrosion rates. The impact of this alternative flow model has therefore been screened out of the TSPA analyses because of the potential mitigation from sorption and diffusion and because the variability of corrosion rates provides large uncertainty in radionuclide release rates from the waste package.

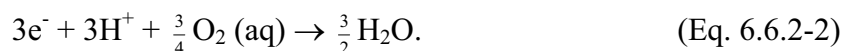
6.6.2 Limited Water Vapor and Oxygen Diffusion Rate into Waste Package

In this ACM, a film of adsorbed water does not form on the surface of corrosion products if the rate of water consumption by corrosion reactions is greater than the rate of diffusion of water

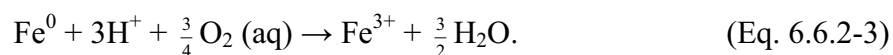
vapor into the waste package. Until a film of water forms on internal corrosion products surfaces, diffusive releases of radionuclides through the adsorbed water cannot occur (according to the in-package diffusion submodel). In addition, corrosion of iron requires oxygen (dissolved in water). Thus, the resistance to diffusion of water vapor and oxygen through stress corrosion cracks can potentially delay releases until all of the corrodible materials inside a waste package are fully degraded. It is implicit in this ACM that stress corrosion cracks appear before general corrosion patches form; this will not necessarily be the outcome of TSPA calculations. Other simplifications are made to make this ACM tractable; for example, the resistance of a water film to diffusion of oxygen through the film to the steel surface is neglected, as are the effects of water adsorption or condensation on vapor diffusion through the porous solids that might fill the SCCs.

The objective is to determine the rate of consumption of water vapor and oxygen by corrosion of steel internal components and compare this with the diffusive influx through SCCs. If corrosion consumes water vapor and oxygen more rapidly than these gases can diffuse into the waste package, then the length of time required to complete the corrosion of steel internal components can be computed, which is equivalent to the delay from the time a waste package is first breached by stress corrosion cracks until diffusive releases can first take place. This delay can potentially be important since it provides additional time for decay to reduce the concentration of radionuclides before they are released from a waste package.

The rate of consumption of water vapor and oxygen depends on the rate of steel corrosion (when not limited by availability of reactants) and on the stoichiometry of the corrosion reactions. For oxidation of iron to goethite (FeOOH), the following electrochemical half-cell reactions occur for oxidation of zero-valent iron to Fe⁺³, where the intermediate steps of oxidation to Fe(II) and its subsequent oxidation to Fe(III) are not shown since oxidation of Fe(II) is comparatively rapid:



The sum of these reactions is the total redox reaction:



Conversion to goethite involves the reaction:



The net corrosion reaction is the sum of the redox reaction and the conversion to goethite:



An example calculation is presented for a typical set of conditions in the drift and waste package to estimate the time lag between appearance of stress corrosion cracks and the earliest times when an adsorbed water film can first form through which radionuclides can diffuse. In this

example, the temperature of the waste package and drift air is 50°C, the relative humidity in the drift is 95 percent, and the relative humidity is zero inside the waste package. Using a relative humidity of zero inside the waste package maximizes the water vapor concentration gradient between the exterior and interior of the waste package and thereby maximizes the water vapor influx rate.

The diffusion distance used is the thickness of the waste package outer lid, 0.0254 m (SNL 2007 [DIRS 179394], Table 4-3). This is the outer closure lid, made of Alloy 22, with a circumferential weld in which stress corrosion cracks may develop. The average diffusive distance within a TAD canister is greater—half the length of the canister shell, or about 270 cm (TAD shell length = 212.0 in. = 5.385 m; SNL 2007 [DIRS 179394], Table A-5)—but the cross-sectional area is less in the stress corrosion cracks than in the TAD canister, so diffusion through the cracks is the limiting segment of the path.

To calculate the diffusion rate, the concentration (mole fraction) of water vapor in humid air is calculated. At relative humidity RH (fraction) and temperature T (°C), the partial pressure of water p_w (Pa) is:

$$p_w = RH \cdot p_w^{\circ}, \quad (\text{Eq. 6.6.2-6})$$

where p_w° (Pa) is the vapor pressure of water at T (°C), given by Singh et al. (2002 [DIRS 161624], Eqs. 1a and 1b):

$$p_w^{\circ} = \begin{cases} 610.78 \exp\left[\frac{17.269T}{237.3 + T}\right] & (0^{\circ}\text{C} < T < 63.0^{\circ}\text{C}) \\ 610.78 \exp\left[\frac{17.269T}{236.3 + 1.01585T}\right] & (63.0^{\circ}\text{C} < T < 110^{\circ}\text{C}). \end{cases} \quad (\text{Eq. 6.6.2-7})$$

The mole fraction of water vapor in air obtained from:

$$x_A = \frac{p_w}{p} = \frac{RH \cdot p_w^{\circ}}{p}, \quad (\text{Eq. 6.6.2-8})$$

where p is the total pressure. As an example, at 50°C and RH in the drift of 95 percent, the vapor pressure of water, from Equation 6.6.2-7, is $p_w^{\circ} = 12,334$ Pa, so the partial pressure at $RH = 0.95$ is $p_w = 11,717$ Pa; if the total pressure is 1.0 atm (101,325 Pa), the water vapor mole fraction is 0.1156.

To calculate the binary diffusion coefficient, the following equation is used (Bird et al. 1960 [DIRS 103524], Equation 16.3-1):

$$D_{AB} = a \left(\frac{T}{\sqrt{T_{cA} T_{cB}}} \right)^b (p_{cA} p_{cB})^{1/3} (T_{cA} T_{cB})^{5/12} \left(\frac{1}{M_A} + \frac{1}{M_B} \right)^{1/2} p^{-1}, \quad (\text{Eq. 6.6.2-9})$$

where:

D_{AB}	=	diffusion coefficient ($\text{m}^2 \text{s}^{-1}$) for water or oxygen (A) in air (B)
T	=	absolute temperature (K)
p	=	pressure (atm)
M	=	molecular weight (g mol^{-1})
a	=	3.640×10^{-8} for H_2O with a nonpolar gas (air) 2.745×10^{-8} for nonpolar gas pairs (O_2 in air)
b	=	2.334 for H_2O with a nonpolar gas (air) 1.823 for nonpolar gas pairs (O_2 in air)

subscript c refers to critical properties.

For water (A):

$$T_{cA} = 373.99^\circ = 647.14 \text{ K (Lide 2000 [DIRS 162229], p. 6-4)}$$

$$p_{cA} = 22.064 \text{ MPa} = 217.72 \text{ atm (Lide 2000 [DIRS 162229], p. 6-4)}$$

$$M_A = 18.01528 \text{ g mol}^{-1} \text{ (Lide 2000 [DIRS 162229], p. 6-4)}$$

For oxygen (A):

$$T_{cA} = 154.59 \text{ K (Lide 2000 [DIRS 162229], p. 6-50)}$$

$$p_{cA} = 5.043 \text{ MPa} = 49.77 \text{ atm (Lide 2000 [DIRS 162229], p. 6-50)}$$

$$M_A = 31.99 \text{ g mol}^{-1} \text{ (Lide 2000 [DIRS 162229], p. 4-77)}$$

For air (B):

$$T_{cB} = 132 \text{ K (Lide 2000 [DIRS 162229], p. 6-50)}$$

$$p_{cB} = 36.4 \text{ atm (Lide 2000 [DIRS 162229], p. 6-50)}$$

$$M_B = 28.964 \text{ g mol}^{-1} \text{ (Lide 2000 [DIRS 162229], p. 4-76).}$$

Substituting these values into the above equation, the binary diffusion coefficient for water vapor in air is $3.12 \times 10^{-5} \text{ m}^2 \text{ s}^{-1}$. The binary diffusion coefficient for oxygen in air is $2.37 \times 10^{-5} \text{ m}^2 \text{ s}^{-1}$. For the mixture diffusion coefficient for water vapor and oxygen diffusing through air, the average of the binary diffusion coefficients for water vapor and oxygen will be used: $D_m = 2.75 \times 10^{-5} \text{ m}^2 \text{ s}^{-1}$. For steady state diffusion of water vapor (A) and oxygen (C) through stagnant air in the stress corrosion cracks, the molar diffusive flux of water vapor, N_A ($\text{mol m}^{-2} \text{ s}^{-1}$), is given by Fick's first law (Bird et al. 1960 [DIRS 103524], p. 502):

$$N_A = x_A(N_A + N_C) - cD_m \frac{dx_A}{dz} \quad (\text{Eq. 6.6.2-10})$$

where N_c is the molar diffusive flux of oxygen, x_A is the mole fraction of water vapor, c is the molar density (mol m^{-3}), and z is the distance (m) through the SCC ($z = 0$ at the outside surface of the waste package, and $z = \Delta z$, the thickness of the outer corrosion barrier wall or closure lid, at the inside surface).

Since diffusion results solely from consumption of water and oxygen due to the corrosion reaction, Equation 6.6.2-5, the flux of water vapor relative to that of oxygen is proportional to the stoichiometry of the corrosion reaction. Thus, $N_c = \frac{3}{2}N_A$, and Equation 6.6.2-10 can be rewritten as:

$$N_A = \frac{-cD_m}{\left(1 - \frac{5}{2}x_A\right)} \frac{dx_A}{dz}. \quad (\text{Eq. 6.6.2-11})$$

At steady state, the flux is constant:

$$\frac{dN_A}{dz} = 0 = \frac{d}{dz} \left(\frac{-cD_m}{\left(1 - \frac{5}{2}x_A\right)} \frac{dx_A}{dz} \right). \quad (\text{Eq. 6.6.2-12})$$

This equation is solved with boundary conditions:

$$\begin{aligned} \text{at } z = 0, \quad x_A &= x_{Ab} \\ \text{at } z = \Delta z, \quad x_A &= x_{As}, \end{aligned} \quad (\text{Eq. 6.6.2-13})$$

where x_{Ab} is the mole fraction of water vapor in the bulk drift air (e.g., 0.1156 at 95 percent RH), and x_{As} is the mole fraction of water vapor at the inside surface of the outer corrosion barrier wall or closure lid. Both x_{Ab} and x_{As} are treated as constant in this model. The value of x_{As} is unknown; however, the maximum flux through SCCs will occur when $x_{As} = 0$. The diffusive path length, Δz , is conceptualized to be the wall thickness, since it is the cross-sectional area of through-wall SCCs that potentially limits the diffusive mass flow of water vapor and oxygen and hence the corrosion rate. However, as will be seen, the *flux*, as opposed to the mass flow rate, is not dependent on the cross-sectional area, so Δz could also be considered to be the distance from the outside surface to an internal corroding surface, with a maximum value equal to the length of a waste package.

Integration of Equation 6.6.2-12 results in:

$$-\frac{2}{5} \ln \left(1 - \frac{5}{2}x_A \right) = C_1 z + C_2, \quad (\text{Eq. 6.6.2-14})$$

where C_1 and C_2 are the integration constants to be determined by applying the boundary conditions. The boundary condition at $z = 0$ gives the value of C_2 :

$$C_2 = -\frac{2}{5} \ln \left(1 - \frac{5}{2} x_{Ab} \right). \quad (\text{Eq. 6.6.2-15})$$

From the boundary condition at $z = \Delta z$, the value of C_1 is:

$$C_1 = -\frac{2}{5\Delta z} \ln \left(\frac{1 - \frac{5}{2} x_{As}}{1 - \frac{5}{2} x_{Ab}} \right). \quad (\text{Eq. 6.6.2-16})$$

The solution to Equation 6.6.2-12 is then:

$$\left(\frac{1 - \frac{5}{2} x_A}{1 - \frac{5}{2} x_{Ab}} \right) = \left(\frac{1 - \frac{5}{2} x_{As}}{1 - \frac{5}{2} x_{Ab}} \right)^{\frac{z}{\Delta z}}, \quad (\text{Eq. 6.6.2-17})$$

or

$$x_A = \frac{2}{5} \left[1 - \left(1 - \frac{5}{2} x_{Ab} \right) \left(\frac{1 - \frac{5}{2} x_{As}}{1 - \frac{5}{2} x_{Ab}} \right)^{\frac{z}{\Delta z}} \right]. \quad (\text{Eq. 6.6.2-18})$$

The diffusive flux is obtain using Equation 6.6.2-11:

$$N_A = -\frac{2cD_m}{5\Delta z} \ln \left(\frac{1 - \frac{5}{2} x_{As}}{1 - \frac{5}{2} x_{Ab}} \right). \quad (\text{Eq. 6.6.2-19})$$

As expected, the diffusive flux is constant, i.e., it does not depend on either z or x_A . It does, however, depend on temperature and pressure (both constant in this model), which impact the molar density, c , the mole fraction of water vapor in the bulk drift air, x_{Ab} (which is directly related to the RH), and, to a lesser extent, the diffusion coefficient. For a given value of the inside surface water vapor mole fraction, x_{As} , the diffusive flux decreases in proportion to the diffusive path length, although these two parameters would not be expected to be independent—a longer path length might result in a lower x_{As} , so the diffusive flux may not be as strongly dependent on path length as Equation 6.6.2-19 suggests.

For a given path length and drift RH , an upper bound on diffusive flux is obtained when x_{As} is zero, and is maximized when $RH = 1.0$. At 50°C , the molar density, c , for an ideal gas is $3.77 \times 10^{-5} \text{ mol m}^{-3}$ (from the molar volume of $0.022414 \text{ m}^3 \text{ mol}^{-1}$ at 0°C and 1 atm pressure; (Lide 2000 [DIRS 162229], p. 1-8). At $RH = 1.0$ and 50°C , the water vapor mole fraction is 0.1217 (from Equation 6.6.2-8). Using the average value for the mixture diffusion coefficient and a path length of 0.0254 m, the maximum diffusive flux of water vapor is $5.93 \times 10^{-3} \text{ mol m}^{-2} \text{ s}^{-1}$, or $1.87 \times 10^5 \text{ mol m}^{-2} \text{ yr}^{-1}$. The molar flow rate (mol yr^{-1}) through SCCs is obtained by multiplying the diffusive flux by the total cross-sectional area of all SCCs, A_{scc} . The typical cross-sectional area of a SCC in the waste package outer barrier is $7.68 \times 10^{-6} \text{ m}^2$ per stress corrosion crack (Table 6.3-3), using the maximum tensile stress across the wall thickness of the dominant stress plane (SNL 2007 [DIRS 181953], Section 6.6.2), which provides a reasonable bound on the opening area through the entire wall thickness. Using the maximum expected number of through-wall radial SCCs in the closure lid weld of 233 SCCs per waste package (Equation 6.3.3.2.1.2-1), $A_{scc} = 1.79 \times 10^{-3} \text{ m}^2$, and the maximum rate of diffusion of water vapor through SCCs is $335 \text{ mol H}_2\text{O yr}^{-1}$.

The maximum diffusion rate of water vapor through SCCs is compared with the rate of consumption by corrosion of stainless steel, which ranges from 0.01 to $0.51 \mu\text{m yr}^{-1}$. To compute the mass rate of corrosion, the surface area directly exposed to SCCs could be used, or, neglecting the additional diffusive path length to internal waste package components, the total surface area of steel can be used to provide an upper bound on water consumption. The total surface area inside a waste package is 1196 m^2 (from Table 6.3-11). Then the corrosion rate of steel ranges from $1.20 \times 10^{-5} \text{ m}^3 \text{ yr}^{-1}$ to $6.10 \times 10^{-4} \text{ m}^3 \text{ yr}^{-1}$. Using a density of $7,980 \text{ kg m}^{-3}$ (ASTM G 1-03 [DIRS 181437], Table X1.1), considering only the iron content of 316 SS (65.5 percent; DTN: MO0003RIB00076.000 [DIRS 153044], Column "ASTM, 1998"), the atomic weight of iron of $0.055847 \text{ kg mol}^{-1}$ (Weast 1985 [DIRS 111561], p. B-102), corrosion of stainless steel occurs at a rate ranging from $1.71 \text{ mol Fe yr}^{-1}$ to $87.2 \text{ mol Fe yr}^{-1}$. From the stoichiometry, the rate of water consumption by corrosion ranges from $0.854 \text{ mol H}_2\text{O yr}^{-1}$ to $43.6 \text{ mol H}_2\text{O yr}^{-1}$. Thus, the rate of water consumption is less than the maximum rate of diffusion through SCCs by a factor ranging from 7.6 to 391.

Next, consider circumstances that might reduce this surplus of diffusive influx and potentially delay corrosion of internal components. The two most important effects are the RH in the drift and the mole fraction of water at the inside boundary. Equation 6.6.2-19 confirms that if the drift RH is zero or if x_{As} is equal to the mole fraction of water vapor in the drift, the diffusive flux is zero, since there is no driving force. Figure 6.6-2, in which the water vapor diffusion rate is plotted as a function of x_{As} for various RH values, shows that diffusion rates will be less than the consumption rate (horizontal lines indicating minimum and maximum corrosion rates) when the RH or x_{As} is low. In Figure 6.6-3, water vapor diffusion rate is plotted as a function of RH for various x_{As} values. Increasing the diffusive path length would shift all curves to the right, provided that path length and x_{As} can be considered independent of each other. To resolve the question whether diffusion limitations can delay releases, a means of estimating x_{As} is needed.

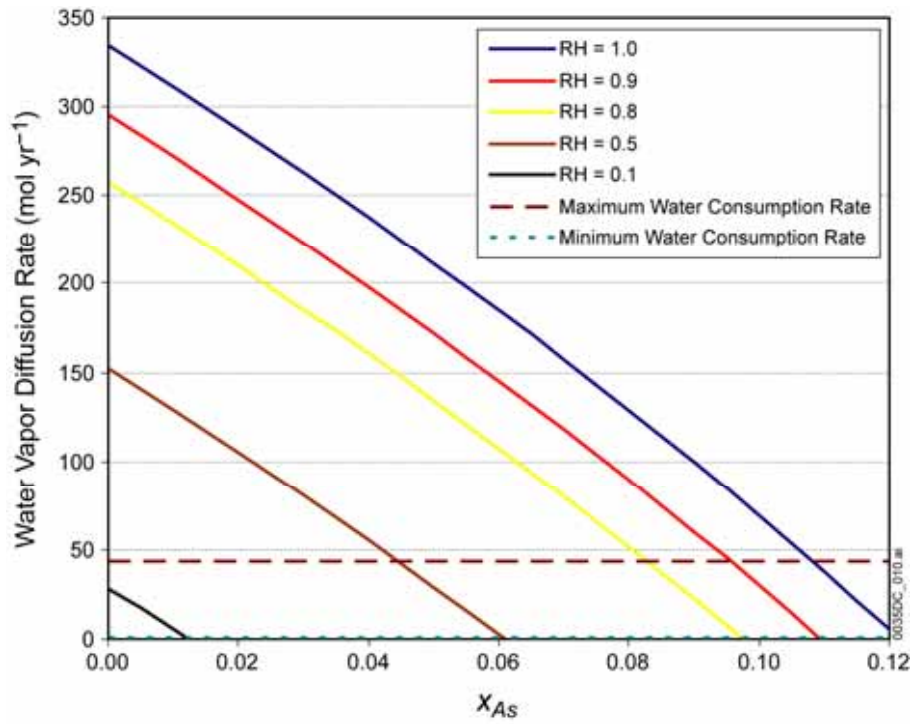


Figure 6.6-2. Water Vapor Diffusion Rate Dependence on Internal Surface Water Vapor Mole Fraction at Various Values of RH

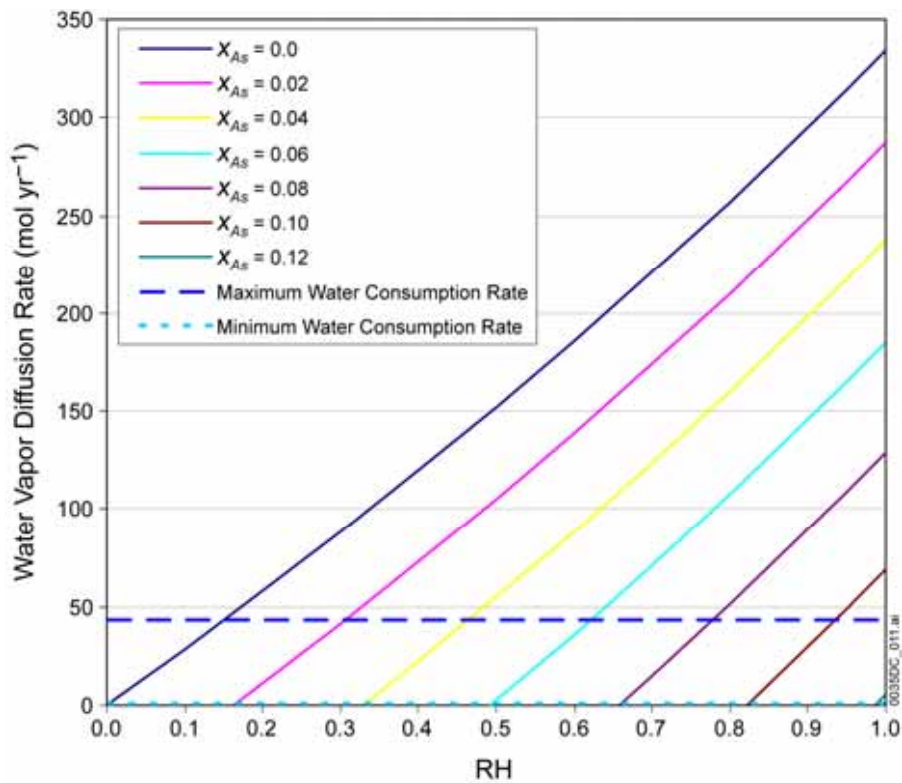


Figure 6.6-3. Water Vapor Diffusion Rate Dependence on Drift Relative Humidity at Various Values of Internal Surface Water Vapor Mole Fraction, x_{As}

If the SCCs are filled with porous corrosion products, the cross-sectional area for diffusion is less, and the water vapor diffusion rate is proportionately less. For a porosity ϕ_{sc} of the SCC, the effective cross sectional area is $A_{sc,eff} = \phi_{sc} A_{sc}$. The tortuosity (defined as the ratio of the diffusivity in the porous medium to the diffusivity in bulk fluid medium) of the corrosion products can also reduce the diffusivity significantly. For example, the volume-average tortuosity of UZ Rock Group 3 is about 1.45×10^{-2} (DTN: LB0702PAUZMTDF.001 [DIRS 180776], file *Tortuosities by Model Unit.xls*, worksheet ‘Averages for Rock Groups’). If the corrosion products have a similar tortuosity, the water vapor diffusion rate would be reduced by about two orders of magnitude.

This ACM provides additional realism compared to the base model by accounting for the potential delay in formation of a diffusive pathway for transport of radionuclides due to water consumption by corrosion reactions. However, data and analyses are not available to support certain assumptions used in this alternative model. For example, it is not known whether water will in fact be consumed by corrosion reactions so preferentially that none will adsorb anywhere inside a breached waste package. In addition, this ACM does not account for possible spatial variations in the extent of corrosion. As an example, if the steel near the breaches in the outer corrosion barrier is completely corroded before the steel far from a breach has even begun to corrode, then water adsorption could occur there, forming a diffusive release pathway before all of the steel in the waste package has been consumed. In that case, this model would predict a longer delay in releases than would actually occur, thereby underestimating releases. Because of the lack of data and potential to underestimate releases, this ACM has not been implemented in the TSPA Model.

6.6.3 Dual-Continuum Invert

The LA invert design (SNL 2007 [DIRS 179354], Section 4.1.1) uses crushed tuff as the invert ballast material. This material is actually comprised of two pore spaces – intragranular pore space (tuff particle matrix) and intergranular pore space. Although radionuclide transport by both advection and diffusion can occur in both pore spaces, the dominant flow and transport processes in each of these two pore spaces is generally different. In order to simulate flow and transport through the invert accurately, the invert may be conceptualized as overlapping dual continua and modeled using a dual-permeability approach (Šimůnek et al. 2003 [DIRS 167469], p. 22), wherein flow and transport occur in both pore spaces, and mass transfer takes place between the two pore spaces.

Transport through the drift invert can occur either through the intergranular porosity of the invert ballast material or through the intragranular porosity. Advective transport depends upon the liquid flux through each of these porosities. Diffusive transport through each of these porosities depends upon the diffusive properties associated with each pathway. For this ACM, the invert is modeled as overlapping dual continua in which one continuum is represented by the intergranular porosity and the other continuum is represented by the intragranular porosity, as shown in Figure 6.6-4.

Whereas the single-continuum invert model, as shown in Figure 6.3-1, has a single advective flow path (Pathway 8) from the invert to the UZ, the dual-continuum invert has two potential advective flow pathways, as shown in Figure 6.6-4:

- Pathway 8 **Flux from the Intragranular Invert Continuum to the Unsaturated Zone**—
Advective flux from the invert intragranular continuum flows directly into the UZ matrix.
- Pathway 9 **Flux from the Intergranular Invert Continuum to the Unsaturated Zone**—
All advective flux from the invert intergranular continuum flows directly into the UZ fractures.

In this model, no advective flux occurs between the two invert continua. Thus, the flux through pathway 8 is identical to the imbibition flux, pathway 7: $F_8 = F_7$.

Ignoring three-dimensional effects (e.g., flow along the axis of the drift), the quasi-steady state flux through the intergranular invert continuum is equal to the seepage flux: $F_9 = F_1$.

This ACM for flow and transport through the EBS includes five domains: the waste form (e.g., fuel rods or HLW glass), waste package corrosion products, the intergranular invert continuum, the intragranular invert continuum, and the invert/UZ interface domain. The first two domains are the same as in the base case model. The third domain (the intergranular invert continuum) is modeled as being in intimate contact with the waste package and has an average thickness of 0.934 m (Section 6.5.2.3). The fourth domain (the intragranular invert continuum) is also modeled as being in intimate contact with the waste package and has the same average thickness, 0.934 m, as the intergranular invert continuum.

Table 6.6-2 summarizes the transport modes and transport parameters for the transport pathways in the EBS when the invert is modeled as a dual continuum.

The diffusive fluxes to the dual invert continua are determined from the flux continuity at the interface between the corrosion products domain and the invert continua. This requirement states that the diffusive flux exiting the corrosion products domain is equal to the sum of the diffusive fluxes entering the two-invert continua. The diffusive flux split will depend on the diffusive properties in the corrosion products domain and both invert continua together with the concentration gradients across the corrosion products domain/invert interface.

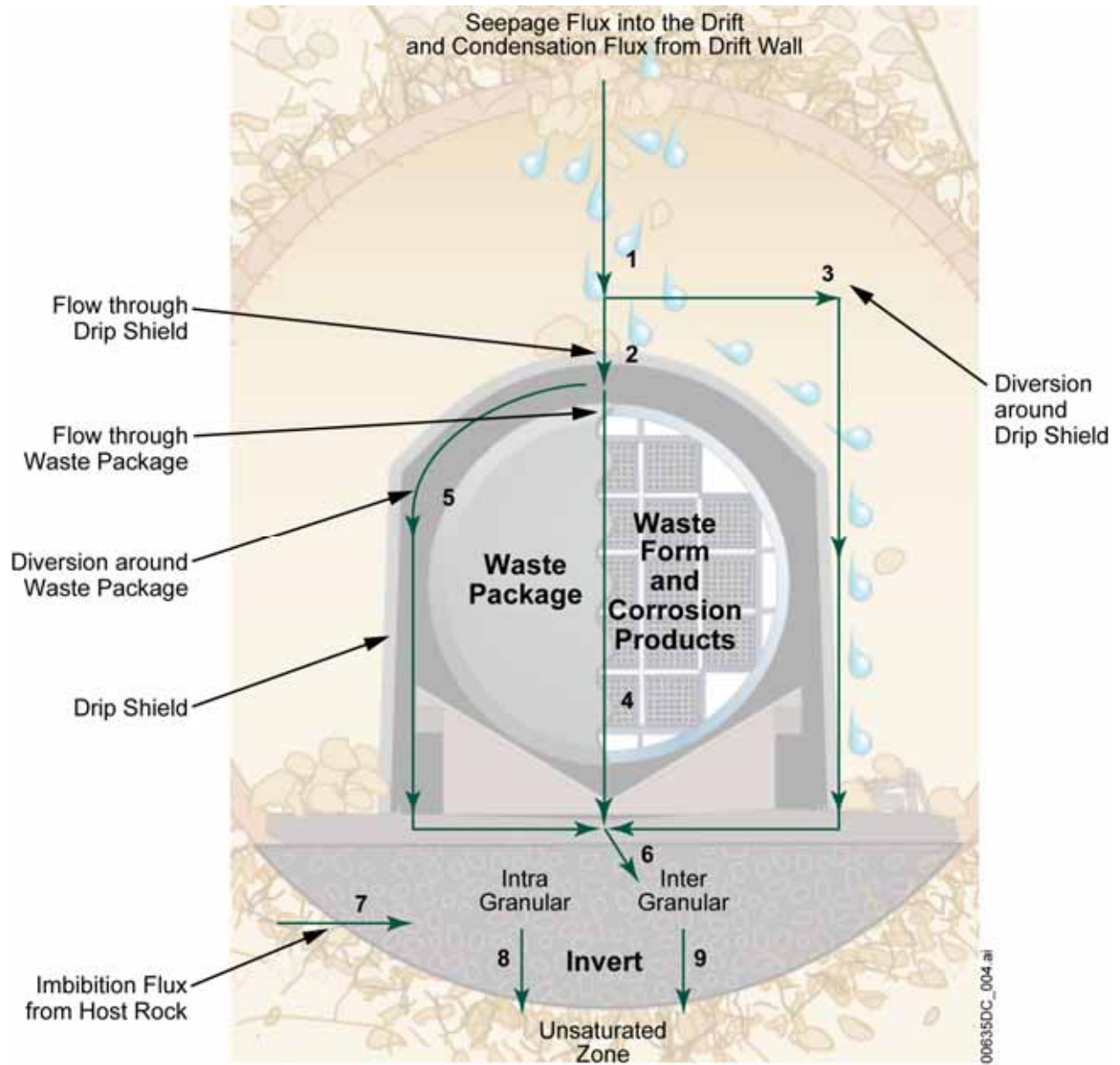


Figure 6.6-4. Schematic of the Potential Flow Pathways in the EBS

Table 6.6-1. Summary of Transport Modes and Parameters for the EBS Transport Pathways with Dual-Continuum Invert

Transport Pathway	Transport Modes	Transport Parameters and Data Sources
1. Waste form and corrosion products domains	Diffusion through stress corrosion cracks (no advective transport through stress corrosion cracks). Diffusion and advection through corrosion products and patches.	<p>No lateral or forward dispersion.</p> <p>Colloidal particles will transport radionuclides.</p> <p>Diffusive area for each stress corrosion crack is $7.7 \times 10^{-6} \text{ m}^2$ (see Table 6.3-3).</p> <p>Diffusive area for each patch is provided by WAPDEG (SNL 2007 [DIRS 178871]).</p> <p>Diffusion coefficient (all radionuclides):</p> <ul style="list-style-type: none"> • Species dependent free-water diffusion coefficients given in Table 4.1-7 • Modified for porosity and saturation (see Section 6.3.4.3.5) • Temperature modification defined in Section 6.3.4.1.2; waste form temperature is provided by <i>Multiscale Thermohydrologic Model</i> calculations (SNL 2007 [DIRS 181383]) • Colloid diffusion coefficient computed as a function of waste form and corrosion product temperatures and sampled colloid particle diameter using Equation 6.3.4.4-1 (see Section 6.3.4.4). <p>The cross-sectional area $A_{CP/invert}$ for radionuclide transport is given by the interface between the waste package corrosion products domain and the invert domain.</p> <p>See Section 6.5.2 for further details.</p>
2. Intragranular invert continuum	Diffusion from corrosion products domain through the invert intragranular continuum.	<p>No advection from corrosion products domain into invert intragranular continuum. Advection UZ into invert intragranular continuum (F_7).</p> <p>Diffusion coefficient (all radionuclides):</p> <ul style="list-style-type: none"> • Species dependent free-water diffusion coefficients given in Table 4.1-7 • Modified for porosity and saturation (see Section 6.3.4.1) • Temperature modification defined in Section 6.3.4.1.2; invert temperature is provided by <i>Multiscale Thermohydrologic Model</i> calculations (SNL 2007 [DIRS 181383]) • Colloid diffusion coefficient computed as a function of invert temperature and sampled colloid particle diameter using Equation 6.3.4.4-1 (see Section 6.3.4.4). <p>Flow cross-sectional areas given by the top surface area of the invert, $A_{I/UZ}$ (Equation 6.5.2.3-4).</p>

Table 6.6-1. Summary of Transport Modes and Parameters for the EBS Transport Pathways with Dual-Continuum Invert (Continued)

Transport Pathway	Transport Modes	Transport Parameters and Data Sources
3. Intergranular invert continuum	Diffusion and advection (F_6) from corrosion products domain through the invert intergranular continuum.	Liquid flux for advection = $F_6 = F_5$ (diverted by WP) + F_4 (flux through WP) + F_3 (diverted by drip shield). Diffusion coefficient (all radionuclides): <ul style="list-style-type: none"> • Species dependent free-water diffusion coefficients given in Table 4.1-7 • Modified for porosity and saturation (see Section 6.3.4.1) • Temperature modification defined in Section 6.3.4.1.2; invert temperature is provided by <i>Multiscale Thermohydrologic Model</i> calculations (SNL 2007 [DIRS 181383]) • Colloid diffusion coefficient computed as a function of invert temperature and sampled colloid particle diameter using Equation 6.3.4.4-1. The cross-sectional area $A_{I/UZ}$ for radionuclide transport is the top surface area of the invert (Equation 6.5.2.3-4).
4. Invert intragranular – intergranular interface	Diffusion between the invert intergranular continuum and the intragranular continuum.	Mass transfer coefficient uses (see Section 6.6.3.1): <ul style="list-style-type: none"> • Diffusion coefficient of the intragranular continuum • Sampled geometry-dependent factor, β (Invert_Geometry_Coef) • Diffusive path length equal to mean invert tuff particle radius, 5 mm. Parameters are dependent on discretization of the invert model; see Section 6.5.2.5 for discretization and implementation details.
5. Invert-UZ interface	Advection from the invert intragranular continuum to UZ matrix (F_8). Advection from the invert intergranular continuum to UZ fractures (F_9). Diffusion from the invert intragranular continuum to UZ fractures and matrix. Diffusion from the invert intergranular continuum to UZ fractures and matrix.	The invert diffusion calculation uses radionuclide concentrations in the WP corrosion products domain as the boundary condition at the top of the invert and a series of UZ computational cells below the invert that provide a gradient to a zero radionuclide concentration at some distance from the bottom of the invert. See Section 6.5.2.6.

NOTE: WP = waste package

For discussion of the diffusive flux treatment at the corrosion products domain/invert interface consider a diffusive flux term, either aqueous or colloid flux, within the transport mass balance equation. Let $z_{interface}$ denote the spatial location of the corrosion products domain/invert interface. Then for $z < z_{interface}$, the diffusive flux for radionuclide species i at a location within the corrosion products domain is:

$$\phi_{CP} S_{w_CP} D_{iCP} \frac{\partial C_{iCP}}{\partial z}, \quad (\text{Eq. 6.6.3-1})$$

where ϕ_{CP} is the porosity of the single-continuum corrosion products domain.

For $z > z_{interface}$, the diffusive fluxes within the intergranular invert and intragranular invert media are, respectively,

$$\phi_{inter} S_{w_inter} D_{iinter} \frac{\partial C_{iinter}}{\partial z}, \quad (\text{Eq. 6.6.3-2})$$

$$\phi_{intra} S_{w_intra} D_{iintra} \frac{\partial C_{iintra}}{\partial z}. \quad (\text{Eq. 6.6.3-3})$$

The mass transport across this interface is coupled by the flux continuity condition at the interface:

$$\begin{aligned} \phi_{CP} S_{w_CP} D_{iCP} \frac{\partial C_{iCP}}{\partial z^-} &= \phi_{inter} S_{w_inter} D_{iinter} \frac{\partial C_{iinter}}{\partial z^+} \\ &+ \phi_{intra} S_{w_intra} D_{iintra} \frac{\partial C_{iintra}}{\partial z^+}, \end{aligned} \quad (\text{Eq. 6.6.3-4})$$

where

$$\frac{\partial}{\partial z^-} \quad \text{and} \quad \frac{\partial}{\partial z^+}$$

are the derivative from above and the derivative from below, respectively, at the interface.

A similar flux continuity condition for each invert continuum is applied at the invert/UZ interface.

6.6.3.1 Invert Dual Continuum Interface Transfer

If a gradient exists in the concentration of dissolved radionuclide species i , or of colloids that contain radionuclide species i , mass will be transferred across the interface between the two continua. The mass transfer coefficients for dissolved species and colloids, α (s^{-1} , given by Equation 6.5.1.2-24), are dependent on the geometry and diffusivity in the neighborhood of the interface.

Mass will also be transferred with advective flow across the interface as a result of head or pressure gradients between the two continua, for example, when imbibition into the tuff matrix (i.e., intragranular continuum) occurs. This effect is ignored in the invert since it should be a short term and infrequent occurrence.

When advective interface mass transfer is neglected, the mass transfer coefficient has the form (Gerke and van Genuchten 1996 [DIRS 167466], p. 345; Corapcioglu and Wang 1999 [DIRS 167464], p. 3263; Šimůnek et al. 2003 [DIRS 167469], pp. 28 and 30):

$$\alpha = \frac{\beta}{d^2 D_{ie}}, \quad (\text{Eq. 6.6.3.1-1})$$

where β is a dimensionless geometry-dependent coefficient, d is a characteristic length (m) of the matrix structure (e.g., half the aggregate width or half the fracture spacing), and D_{ie} is an effective diffusion coefficient ($\text{m}^2 \text{s}^{-1}$) that represents the diffusion properties of dissolved species at the interface between the two continua for radionuclide species i . For colloids containing sorbed radionuclides, D_{ie} represents the diffusion properties of those colloids at the interface between the two continua. The subscript i on the diffusion coefficient in Equation 6.5.1.2-24 has been dropped in Equation 6.6.3.1-1.

Mass transfer coefficients obtained analytically using Laplace transform comparisons derived values for β of 3 for rectangular slabs, 8 for solid cylinders, and 15 for spheres (Gerke and van Genuchten 1996 [DIRS 167466], p. 345). Values of β have also been obtained (Gerke and van Genuchten 1996 [DIRS 167466]) by directly matching analytical solutions of the diffusion models to results obtained with the first-order model such as Equation 6.5.1.2-20. Gerke and van Genuchten (1996 [DIRS 167466]) derived an empirical expression to estimate β for complex and mixed types of structural geometry. A dimensionless surface-area-to-volume ratio of a particle, $\zeta = \frac{A_g}{V_g} a_g$, is defined, where a_g is the effective length of the matrix pore system; for example, for a solid cylinder, a_g is the radius; for a cube, a_g is half the length of a side; for a sphere, a_g is the radius. Thus, for a solid cylinder, $\zeta = 2$, and for a sphere and a cube, $\zeta = 3$. For values $2 < \zeta \leq 10$, Gerke and van Genuchten (1996 [DIRS 167466], p. 354) give the following fitted empirical expression:

$$\beta = 11.4275 - 7.4438\zeta + 3.5473\zeta^2. \quad (\text{Eq. 6.6.3.1-2})$$

For cubes and spheres, Equation 6.6.3.1-2 gives a value for β of 21.0 (compared to 15 for a sphere using the analytical method), and for a solid cylinder, $\beta = 10.7$ (compared to 8 from the analytical method). Since the geometry of crushed tuff invert particles is uncertain, these estimates of β help to establish a range of values over which β can be sampled.

The crushed tuff invert material will be produced by a tunnel boring machine that will excavate the drifts for the repository. The cuttings from tunnel boring machines can be characterized as

generally well graded material containing large flat and elongated chips and moderate excess of fines (Gertsch et al. 1993 [DIRS 107880], p. 20). Tests done on samples of TSw2 tuff using a linear cutting machine produced cuttings that, in the plus inch fraction, were elongated and flat, while the finer particles were more cubic (Gertsch et al. 1993 [DIRS 107880], p. 42-43). The operating parameters expected to be utilized in the Yucca Mountain Project tunnel boring machine will reduce the maximum particle size and result in the particles being more cubic (Gertsch et al. 1993 [DIRS 107880], p. 44). Particle sizes for the invert material will range from 0.075 mm (No. 200 sieve) to 50 mm, with 50 percent of the particles passing a 10-mm sieve (SNL 2007 [DIRS 179354], Table 4-1, Parameter Number 02-08B). Therefore, the average diameter for invert crushed tuff particles (spherical or cylindrical) is 10 mm; and if the particles are treated as cubes, the average length of a side is 10 mm. The characteristic length d (Diff_Length_Inv_Inter_Intra) is the radius or half the distance through a cube, or 5 mm.

The invert material will be composed of particles that are roughly spherical or cubic, along with elongated particles that can be considered roughly cylindrical. For cylinders, cubes, and spheres, estimates of β (Invert_Geometry_Coef) range from 8 to 21. A particle shape distribution is not available; therefore, a uniform distribution for β is appropriate.

The model for the mass transfer between overlapping continua is represented by the diffusion of solute on a macroscopic control volume scale, i.e., between two entire domains or computational cells, rather than on the elemental volume scale used to formulate the mass balance equations in Section 6.5.1.2. Consequently, the mass transfer between the two invert continua is not written as a gradient of diffusive mass flux with respect to the coordinate dimensions. In the discrete formulation, this flux is modeled as a diffusive flux between two invert cells. For the discrete realization of the invert continua mass transfer, the diffusive length within the intergranular continuum is taken to be zero. This is a result of the water within the intergranular continuum consisting of a film of negligible thickness on the surface of the intragranular materials. The diffusive length within the intragranular continuum depends on some mean diffusive length within the crushed tuff material. This diffusive length is taken as a mean radius of spherical particles, 5 mm. The diffusive area is estimated as the surface area of all spherical particles necessary to fill the invert volume. Therefore, the characteristic length parameter, d , is identified as the diffusive length (5 mm) within the intragranular continuum.

6.6.3.2 Discretization of Dual-Continuum Invert Alternative Computational Model

Discretization of the continuum mass balance equations for EBS transport model is described in Section 6.5.2.5 for a single-continuum invert. Numerical modeling of the EBS radionuclide transport is performed using the GoldSim software (GoldSim Technology Group 2007 [DIRS 181727]) cell pathway capability. The cell pathway acts as a batch reactor, where radionuclide mass is assumed to be instantaneously and completely mixed and partitioned among all media (fluid or solid) within the cell. When multiple cells are linked together in a cell network via advective and diffusive mechanisms, GoldSim numerically solves the coupled system of equations to compute the radionuclide mass present in each cell and the mass fluxes between cells as a function of time.

Within a computational cell network, each cell is allowed to communicate by advection and/or diffusion with any other cell. This concept is crucial in implementing the bifurcation of diffusive

fluxes across an interface between a single continuum domain and a dual continuum domain, such as at the interface between the corrosion products domain and the dual continuum invert domains. Each computational cell is provided with parameters describing water volumes, diffusive properties, and advective and diffusive flux links to other cells. Between any two cells, the diffusive flux can be bidirectional, depending on the concentration gradient, while the advective flux is unidirectional. The output of a cell is given in terms of the advective and diffusive mass fluxes for radionuclide species i and its concentration at the cell center.

In this ACM, the invert is conceptualized as a dual continuum domain of intergranular and intragranular continua. The discretization of the invert domain, using GoldSim, consists of two cells—one representing the invert intergranular continuum and the other representing the invert intragranular continuum.

Between the corrosion products and invert domains, an advective flux communication exists from the corrosion products cell to the invert intergranular cell only; none enters the intragranular invert cell. Any advective flux due to imbibition from the host rock to the invert enters the intragranular cell only. The advective exchange from the intergranular continuum to the intragranular continuum is excluded by capillary pressure differences. Diffusive flux communication exists between the single-continuum corrosion products and dual-continuum invert. It is shown subsequently in this section how the diffusive flux bifurcation at this interface satisfies the flux continuity condition (Equation 6.5.1.2-54). The mass balance transport equations for the dual-continuum invert cells are coupled by the radionuclide mass transfer flux (Section 6.6.3.1), which is represented within GoldSim as a diffusive flux link between the intergranular and intragranular invert cells.

Below the invert, part of the near-field UZ is modeled by an array of cells, which serves to establish a far field zero-concentration boundary and an accurate representation of the flux at the invert-to-UZ interface. The EBS-UZ interface model is described in more detail in Section 6.5.2.6. The dual-continuum approach for modeling the UZ is considered by creating UZ matrix and fracture cells. The two invert cells communicate with the UZ matrix and fracture cells directly below them in the UZ cell array (Section 6.5.2.6).

For transport from the corrosion products domain (single-continuum) to the invert domain (dual-continuum), the flux continuity condition at the interface provides the diffusive flux bifurcation between the single-continuum and the dual-continuum.

The diffusive fluxes of radionuclide species i within the corrosion products cell, the invert intergranular cell, and the invert intragranular cell are, respectively,

$$\begin{aligned}
 F_{iCP} &= \frac{(\theta_w D_i A)_{CP}}{L_{CP}} (C_{iCP} - C_{iCP/invert}) \\
 &= \hat{D}_{iCP} (C_{iCP} - C_{iCP/invert}),
 \end{aligned}
 \tag{Eq. 6.6.3.2-1}$$

$$\begin{aligned}
 F_{iinter} &= \frac{(\theta_w D_i A)_{inter}}{L_{inter}} (C_{iCP/invint} - C_{iinter}) \\
 &= \hat{D}_{iinter} (C_{iCP/invint} - C_{iinter}),
 \end{aligned}
 \tag{Eq. 6.6.3.2-2}$$

$$\begin{aligned}
 F_{iintra} &= \frac{(\theta_w D_i A)_{intra}}{L_{intra}} (C_{iCP/invint} - C_{iintra}) \\
 &= \hat{D}_{iintra} (C_{iCP/invint} - C_{iintra}),
 \end{aligned}
 \tag{Eq. 6.6.3.2-3}$$

where

- D_{CP} = effective diffusion coefficient of radionuclide species i within the corrosion products cell ($\text{m}^2 \text{s}^{-1}$)
 D_{iinter} = effective diffusion coefficient of radionuclide species i within the invert intergranular cell ($\text{m}^2 \text{s}^{-1}$)
 D_{iintra} = effective diffusion coefficient of radionuclide species i within the invert intragranular cell ($\text{m}^2 \text{s}^{-1}$)
 L_{CP} = diffusive length within the corrosion products cell (m)
 L_{iinter} = diffusive length within the invert intergranular cell (m)
 L_{iintra} = diffusive length within the invert intragranular cell (m)
 $\phantom{L_{iintra}}$ = L_{iinter}
 C_{iCP} = concentration of radionuclide species i in the corrosion products cell ($\text{kg } i \text{ m}^{-3}$)
 C_{iinter} = concentration of radionuclide species i in the invert intergranular cell ($\text{kg } i \text{ m}^{-3}$)
 C_{iintra} = concentration of radionuclide species i in the invert intragranular cell ($\text{kg } i \text{ m}^{-3}$)
 $C_{iCP/invint}$ = concentration of radionuclide species i at the interface between the corrosion products and invert cells ($\text{kg } i \text{ m}^{-3}$)

and the $\hat{D}_i = \frac{\theta_w D_i A}{L}$ are respective diffusive conductances ($\text{m}^3 \text{s}^{-1}$).

The flux continuity at the interface requires:

$$F_{iCP} = F_{iinter} + F_{iintra}. \tag{Eq. 6.6.3.2-4}$$

From the flux continuity, the interface concentration of radionuclide species i is determined as a function of the diffusive parameters and the cell concentrations as:

$$C_{iCP/invert} = \frac{\hat{D}_{iCP} C_{iCP} + \hat{D}_{iinter} C_{iinter} + \hat{D}_{iintra} C_{iintra}}{\hat{D}_{iCP} + \hat{D}_{iinter} + \hat{D}_{iintra}}. \quad (\text{Eq. 6.6.3.2-5})$$

This provides the invert intergranular and intragranular diffusive fluxes of radionuclide species i , respectively, as:

$$F_{iinter} = \frac{\hat{D}_{iCP} \hat{D}_{iinter}}{\hat{D}_{iCP} + \hat{D}_{iinter} + \hat{D}_{iintra}} (C_{iCP} - C_{iinter}) + \frac{\hat{D}_{iinter} \hat{D}_{iintra}}{\hat{D}_{iCP} + \hat{D}_{iinter} + \hat{D}_{iintra}} (C_{iintra} - C_{iinter}) \quad (\text{Eq. 6.6.3.2-6})$$

$$F_{iintra} = \frac{\hat{D}_{iCP} \hat{D}_{iintra}}{\hat{D}_{iCP} + \hat{D}_{iinter} + \hat{D}_{iintra}} (C_{iCP} - C_{iintra}) - \frac{\hat{D}_{iinter} \hat{D}_{iintra}}{\hat{D}_{iCP} + \hat{D}_{iinter} + \hat{D}_{iintra}} (C_{iintra} - C_{iinter}). \quad (\text{Eq. 6.6.3.2-7})$$

The expression for the diffusive flux of radionuclide species i from the corrosion products cell to the invert intergranular cell can be expressed as a diffusive conductance multiplied by a concentration difference of radionuclide species i between the corrosion products cell and the invert intergranular cell plus a corrective flux between the invert intergranular and intragranular cells. Similarly, the expression for the diffusive flux from the corrosion products to the invert intragranular cell is expressed as a diffusive flux between the corrosion products and the invert intragranular cell minus the same corrective flux between the invert cells. The inclusion of the corrective flux term is explained as follows. The flux to both invert cells should depend on the diffusive properties in the corrosion products cell and the two invert cells, together with the concentrations in these three cells. Therefore, the flux to the invert intergranular cell cannot be expressed only in terms of the concentration drawdown between the corrosion products cell and the invert intergranular cell. The corrective term includes the dependence of the invert intergranular flux on the concentration of radionuclide species i in the invert intragranular cell. Further, the corrective flux term is not a true flux expression between the two invert cells, since the diffusive conductance coefficient is dependent on the diffusive area between the corrosion products and the invert, and the diffusive lengths are the lengths with respect to flow from the corrosion products cell to the invert cells.

The invert fluxes result in defining three diffusive conductances from the flux expressions:

$$\hat{D}_{iCP/inter} (C_{iCP} - C_{iinter}) = \frac{\hat{D}_{iCP} \hat{D}_{iinter}}{\hat{D}_{iCP} + \hat{D}_{iinter} + \hat{D}_{iintra}} (C_{iCP} - C_{iinter}), \quad (\text{Eq. 6.6.3.2-8})$$

$$\hat{D}_{iCP/intra} (C_{iCP} - C_{iintra}) = \frac{\hat{D}_{iCP} \hat{D}_{iintra}}{\hat{D}_{iCP} + \hat{D}_{iinter} + \hat{D}_{iintra}} (C_{iCP} - C_{iintra}), \quad (\text{Eq. 6.6.3.2-9})$$

$$\hat{D}_{i\text{intra}/\text{inter}}(C_{i\text{intra}} - C_{i\text{inter}}) = \frac{\hat{D}_{i\text{intra}}\hat{D}_{i\text{inter}}}{\hat{D}_{i\text{CP}} + \hat{D}_{i\text{inter}} + \hat{D}_{i\text{intra}}}(C_{i\text{intra}} - C_{i\text{inter}}), \quad (\text{Eq. 6.6.3.2-10})$$

where

- $\hat{D}_{i\text{CP}/\text{inter}}$ = effective diffusive conductance between corrosion products cell and invert intergranular cell ($\text{m}^3 \text{s}^{-1}$)
- $\hat{D}_{i\text{CP}/\text{intra}}$ = effective diffusive conductance between corrosion products cell and invert intragranular cell ($\text{m}^3 \text{s}^{-1}$)
- $\hat{D}_{i\text{intra}/\text{inter}}$ = effective diffusive conductance between invert intragranular and intergranular cells ($\text{m}^3 \text{s}^{-1}$).

In order to accommodate the GoldSim representation of diffusive conductance as a two-term expression, the diffusive conductances of radionuclide species i are written as:

$$\hat{D}_{i\text{CP}/\text{inter}} = \frac{1}{\frac{L_{\text{CP}}}{(\theta_w D_i A)_{\text{CP}} \left[\frac{(\theta_w D_i A)_{\text{inter}}}{(\theta_w D_i A)_{\text{inter}} + (\theta_w D_i A)_{\text{intra}}} \right]} + \frac{L_{\text{inter}}}{(\theta_w D_i A)_{\text{inter}}}}, \quad (\text{Eq. 6.6.3.2-11})$$

$$\hat{D}_{i\text{CP}/\text{intra}} = \frac{1}{\frac{L_{\text{CP}}}{(\theta_w D_i A)_{\text{CP}} \left[\frac{(\theta_w D_i A)_{\text{intra}}}{(\theta_w D_i A)_{\text{inter}} + (\theta_w D_i A)_{\text{intra}}} \right]} + \frac{L_{\text{intra}}}{(\theta_w D_i A)_{\text{intra}}}}, \quad (\text{Eq. 6.6.3.2-12})$$

$$\hat{D}_{i\text{intra}/\text{inter}} = \frac{1}{\frac{L_{\text{inter}}}{(\theta_w D_i A)_{\text{inter}} \left[\frac{L_{\text{CP}}(\theta_w D_i A)_{\text{intra}}}{L_{\text{CP}}(\theta_w D_i A)_{\text{intra}} + L_{\text{intra}}(\theta_w D_i A)_{\text{CP}}} \right]} + \frac{L_{\text{intra}}}{(\theta_w D_i A)_{\text{intra}}}}. \quad (\text{Eq. 6.6.3.2-13})$$

Another approach to discretizing the dual-continuum invert requires introduction of an interface cell, located between the corrosion products cell and the invert cells. This approach is used for this alternative invert model. The interface cell provides an approximate interface concentration and the resulting flux split at the corrosion products to invert cell interface. The interface cell is conceptualized as a very thin slice of the corrosion products cell.

This implies the interface cell takes on the corrosion products diffusive properties, with the exception of diffusive length. Let the diffusive length within the interface cell be some small fraction (an `Interface_Scale_Factor`) of the corrosion products diffusive length, say, `Interface_Scale_Factor` = 10^{-6} :

$$L_{\text{CP-int}} = 10^{-6} L_{\text{CP}}. \quad (\text{Eq. 6.6.3.2-14})$$

The use of an `Interface_Scale_Factor` of 10^{-6} is examined in Section 6.6.3.4.

The diffusive conductance between the corrosion products cell and the corrosion products interface cell is calculated as the harmonic average:

$$\hat{D}_{iCP/CP-int} = \frac{1}{\frac{L_{CP}}{(\theta_w D_i A)_{CP}} + \frac{L_{CP-int}}{(\theta_w D_i A)_{CP}}}. \quad (\text{Eq. 6.6.3.2-15})$$

For diffusion between the interface cell and the invert intergranular and intragranular cells, the diffusive conductances are, respectively,

$$\hat{D}_{iCP-int/inter} = \frac{1}{\frac{L_{CP-int}}{(\theta_w D_i A)_{CP}} + \frac{L_{invert}}{(\theta_w D_i A)_{inter}}}, \quad (\text{Eq. 6.6.3.2-16})$$

$$\hat{D}_{iCP-int/intra} = \frac{1}{\frac{L_{CP-int}}{(\theta_w D_i A)_{CP}} + \frac{L_{invert}}{(\theta_w D_i A)_{intra}}}. \quad (\text{Eq. 6.6.3.2-17})$$

The interface cell concentration of radionuclide species i is computed as part of the cell network solution. Because the transport mass balance equations conserve mass, the mass flux leaving the interface cell must equal the sum of the mass fluxes entering the two invert cells. The solution provides the flux continuity across the interface between the corrosion products interface cell and invert cells. This formulation expects the flux exiting the corrosion products cell (or entering the interface cell) to be approximately equal to the flux exiting the interface cell. This approximation is dependent on the diffusive length within the interface cell. The error in this approximate solution will approach zero as the diffusive length of the interface cell approaches zero.

At the invert-to-UZ interface, there is diffusive transport between both the invert cells and the UZ matrix and fracture cells. This implies four connections: from invert intergranular to UZ matrix, from invert intergranular to UZ fracture, invert intragranular to UZ matrix, and from invert intragranular to UZ fracture. An analysis similar to that for the diffusive conductances between the corrosion products cell and the dual invert cells (Equations 6.6.3.25-11 through 6.6.3.2-13) would provide expressions for diffusive conductances for each of the four diffusive flux links. However, for the TSPA, the approximation provided by introducing an interface cell when diffusing from a single to a dual continuum exits is used. An approximate solution is obtained by the introduction of two interface cells at the invert-UZ interface. This approach is identical to that used above for the interface between the corrosion products cell and the invert dual continuum cells. One interface cell represents a thin slice of the invert intergranular cell, and the other represents a thin slice of the invert intragranular cell. Let the length of both invert interface cells be a fraction (an `Interface_Scale_Factor`) of the invert diffusive length, say, `Interface_Scale_Factor` = 10^{-6} :

$$L_{I_int} = 10^{-6} L_{invert} . \quad (\text{Eq. 6.6.3.2-18})$$

The use of an Interface_Scale_Factor of 10^{-6} is examined in Section 6.6.3.4.

The diffusive conductance between the invert intergranular cell and the invert intergranular interface cell is:

$$\hat{D}_{iinter/inter-int} = \frac{1}{\frac{L_{invert}}{(\theta_w D_i A)_{inter}} + \frac{L_{I_int}}{(\theta_w D_i A)_{inter}}} , \quad (\text{Eq. 6.6.3.2-19})$$

while the diffusive conductance between the invert intragranular cell and the invert intragranular interface cell is:

$$\hat{D}_{iintra/intra-int} = \frac{1}{\frac{L_{invert}}{(\theta_w D_i A)_{intra}} + \frac{L_{invert_int}}{(\theta_w D_i A)_{intra}}} . \quad (\text{Eq. 6.6.3.2-20})$$

The fluxes of radionuclide species i from the invert intergranular interface cell to the matrix-fracture UZ cells are computed with diffusive conductances:

$$\hat{D}_{iinter-int/UZm} = \frac{1}{\frac{L_{invert_int}}{(\theta_w D_i A)_{inter}} + \frac{L_{UZ}}{(\theta_w D_i A)_{UZm}}} , \quad (\text{Eq. 6.6.3.2-21})$$

$$\hat{D}_{iinter-int/UZf} = \frac{1}{\frac{L_{invert_int}}{(\theta_w D_i A)_{inter}} + \frac{L_{UZ}}{(\theta_w D_i A)_{UZf}}} . \quad (\text{Eq. 6.6.3.2-22})$$

Similarly, the fluxes of radionuclide species i from the invert intragranular interface cell to the matrix-fracture UZ cells are computed with diffusive conductances:

$$\hat{D}_{iintra-int/UZm} = \frac{1}{\frac{L_{invert_int}}{(\theta_w D_i A)_{intra}} + \frac{L_{UZ}}{(\theta_w D_i A)_{UZm}}} , \quad (\text{Eq. 6.6.3.2-23})$$

$$\hat{D}_{iintra-int/UZf} = \frac{1}{\frac{L_{invert_int}}{(\theta_w D_i A)_{intra}} + \frac{L_{UZ}}{(\theta_w D_i A)_{UZf}}} . \quad (\text{Eq. 6.6.3.2-24})$$

One last term to be discussed is the mass transfer term, Q_{imt} , between the two invert continua given by Equation 6.5.1.2-21. This term appears in the mass balance for the transport of radionuclides dissolved in the aqueous phase and reversibly sorbed (Equation 6.5.1.2-40, or, for

the one-dimensional case, Equation 6.5.1.2-48), and in the mass balance for kinetically adsorbed radionuclides on iron oxyhydroxide colloids (Equation 6.5.1.2-43, or Equation 6.5.1.2-49 in one dimension). In these equations, the mass transfer between overlapping continua is represented by the diffusion of solute on a macroscopic control volume scale. Consequently, the mass transfer between the two invert continua is not written as a gradient of diffusive mass flux with respect to the coordinate dimensions, and the treatment described above for diffusive conductances does not directly apply. For the discrete realization of the invert continua mass transfer, the diffusive length within the intergranular continuum is taken to be zero. This is a result of the water within the intergranular continuum consisting of a thin film on the surface of the intragranular materials. The diffusive length within the intragranular continuum depends on some mean diffusive length within the crushed tuff material. This diffusive length is taken as a mean radius of spherical particles. The effective diffusive area is estimated as the surface area of all spherical particles necessary to fill the invert volume. Therefore, the characteristic length parameter, d (m), is identified as the diffusive length within the intragranular continuum, and the diffusive area to length ratio is:

$$\left(\frac{A}{L}\right)_{inter/intra} = \frac{\beta\theta_{intra}V_{t_intra}}{100d^2}, \quad (\text{Eq. 6.6.3.2-25})$$

where V_{t_intra} is the volume of the invert intragranular continuum (m^3), θ_{intra} is the water content in the invert intragranular continuum (percent), and β is the sampled geometry-dependent factor, Invert_Geometry_Coef (dimensionless). The effective diffusive conductance is:

$$\hat{D}_{ic} = D_{iintra} \left(\frac{A}{L}\right)_{inter/intra}. \quad (\text{Eq. 6.6.3.2-26})$$

6.6.3.3 Dual-Continuum EBS-UZ Boundary Condition

The EBS-UZ boundary condition implementation described in Section 6.5.2.6 is used to obtain a realistic concentration boundary condition at the invert-UZ interface. For the dual-continuum invert alternative model, the boundary condition implementation is modified to account for diffusive fluxes from each invert continuum to both UZ fractures and matrix. This implementation is represented in Figure 6.6-5.

The mass flux from either invert continuum flows into the top layer of the middle zone in the UZ. The intergranular invert advective flux flows into the top middle UZ fracture cell, while the intragranular invert advective flux flows into the top middle UZ matrix cell. Advective transfer of water between the two continua is ignored. The diffusive flux from each of the invert continua can go into both UZ continua based on the concentration gradient and effective diffusion coefficient. The advective flux flowing through the UZ fracture cells in the middle zone is given by the greater of the advective flux out of the invert and the steady state UZ fracture flux. The advective flux in the two outer zones is given by the steady state UZ flow in each continuum at the repository horizon; the drift shadow effects are ignored in the transport calculations as a bounding approximation.

The mass flux from the dual continuum invert domain to the dual continuum UZ, computed at the boundary of the EBS-UZ interface, would be passed to the UZ transport model, which is described in *Particle Tracking Model and Abstraction of Transport Processes* (SNL 2007 [DIRS 181006]). In addition to the total mass flux, the relative fraction of the mass going into each of the fracture and the matrix cells at the EBS-UZ boundary is required by the UZ transport model. This fracture-matrix partitioning of mass is calculated on the basis of the mass fraction going into the fracture continuum (compared to the matrix continuum) from the dual continuum invert domain in the EBS-UZ interface model. This partitioning is time dependent and captures the temporal processes active in the EBS, such as varying radionuclide concentrations in the waste form, corrosion products, and invert domains and changing water flux through various subcomponents of the EBS.

6.6.3.4 Verification of Dual Invert/Dual UZ Diffusive Flux Bifurcation

In this section, calculation of the diffusive flux from a single cell (corrosion products) to dual invert cells (intergranular invert and intragranular invert) and then to two UZ cells (UZ matrix and UZ fracture) is tested. These tests show that the approximations in the GoldSim implementation using an `Interface_Scale_Factor` of 1.0×10^{-6} are correct and that the implementation in GoldSim agrees with Microsoft Excel calculations.

In this verification test calculation, there is no diffusive communication between the dual continuum invert cells, and there is no diffusive communication between the UZ matrix/fracture cells. The corrosion products cell provides a diffusive flux to the dual continuum invert cells. Each invert cell provides a diffusive flux to both the UZ matrix and fracture cells. For this verification, at time zero, an initial mass of one gram is released in the corrosion products cell, while all other cells have initial mass of zero. Parameters controlling diffusion through this test network were not determined strictly from TSPA data, but were set so that measurable mass transport to all cells within the network occurs in a reasonable time frame. No parameters were assigned a value of one (other than the initial mass in the waste form cell), because any mistake in multiplication or division by a unit parameter would not be readily detectable.

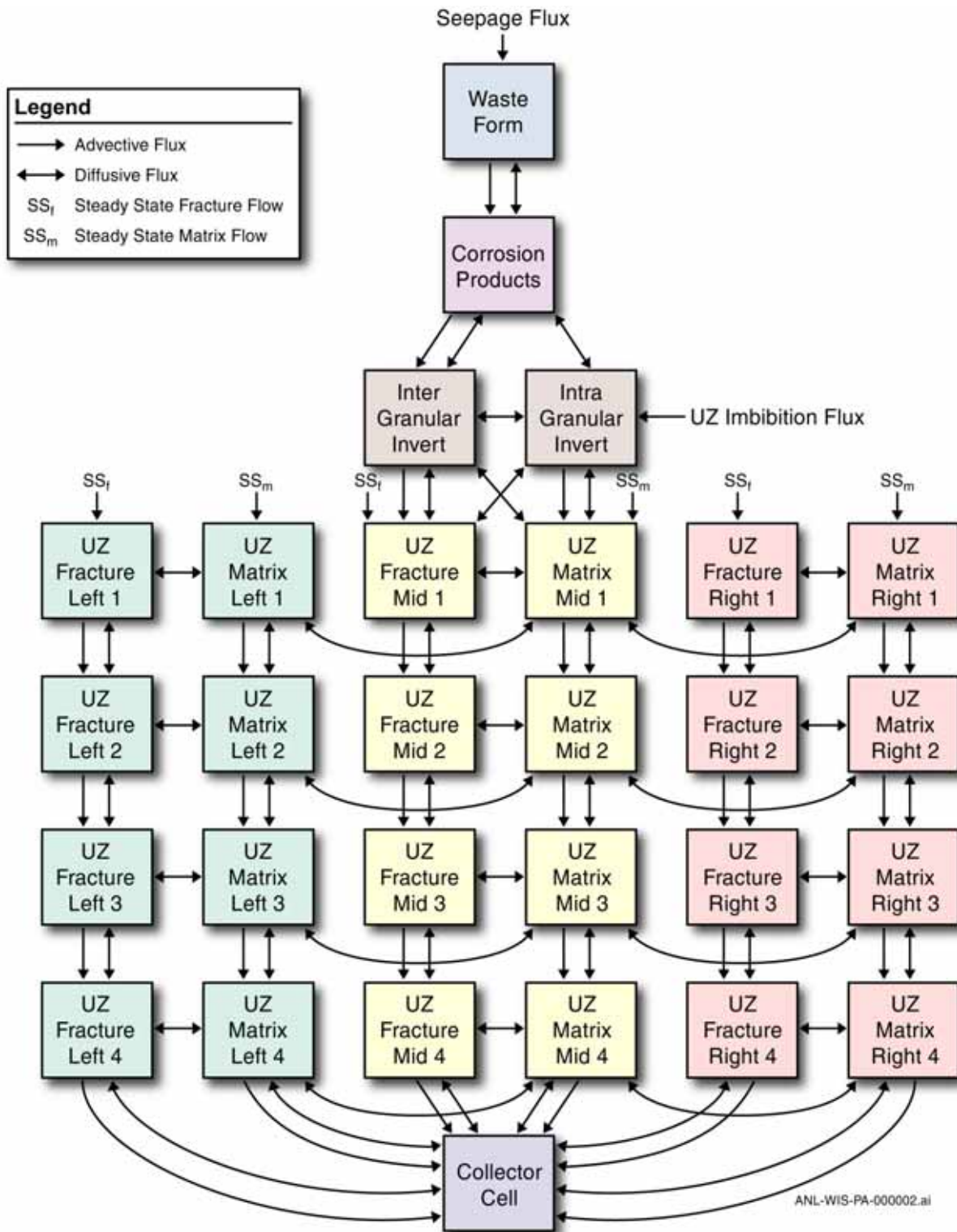


Figure 6.6-5. Computational Grid in the EBS-UZ Interface Model (Dual-Continuum Invert)

Two analytical approaches (**A1** and **A2**) to the flux bifurcation can be taken when diffusion occurs from a single cell to dual cells:

A1: The first approach computes diffusive conductances between the single cell and each dual continuum cell; an auxiliary conductance is required between the dual continuum cells. This formulation presents the appearance of a diffusive flux communication between the dual continuum cells, when physically there is no such flux. This approach requires a five-cell network (corrosion products, invert intergranular, invert intragranular, UZ matrix, and UZ fracture) and provides an exact representation of the fluxes.

A2: The second approach incorporates an interface cell between cells where diffusion bifurcates from a single continuum cell to dual continuum cells. The interface cell provides an approximate concentration at the flux bifurcation interface. For diffusion from a single continuum cell to dual continuum cells, the interface cell is conceptualized as a thin slice of the single continuum cell. This implies that, for the proposed cell network, an interface cell is located between the corrosion products cell and the dual invert continuum cells. This cell is assigned representative properties of the corrosion products cell, with the exception of the diffusive length. The diffusive length for the interface cell is taken to be an `Interface_Scale_Factor` times the diffusive length of the corrosion products cell. Between the intergranular invert cell and the dual UZ cells, an intergranular invert interface cell is introduced with diffusive properties of the intergranular invert and a diffusive length of the `Interface_Scale_Factor` times the diffusive length of the invert. Similarly, between the intragranular invert cell and the dual UZ cells, an intragranular invert interface cell is introduced. This conceptualization requires an eight-cell network (five cells of **A1** plus three interface cells) and provides an approximate solution.

Three solutions to the diffusion problem are presented:

S1: The first solution is an Excel calculation using the **A1** approach. This provides an exact solution for the transport network.

S2: The second solution is an Excel calculation using the **A2** approach. This provides an approximate solution dependent on the `Interface_Scale_Factor` parameter. A successive refinement of the `Interface_Scale_Factor` demonstrates the convergence of the approximate solution (**S2**) to the exact solution (**S1**).

S3: The third solution is a GoldSim stand-alone calculation using the **A2** approach. This solution is compared with solution **S2** to verify the GoldSim implementation of the model within the EBS transport abstraction.

The convergence of the approximate solution **S2** to the exact solution **S1** with refinement of the `Interface_Scale_Factor` is shown in Figure 6.6-6, where the relative error $[(S1 - S2)/S1]$ of the mass in place for each network cell is plotted as a function of the `Interface_Scale_Factor`. Figure 6.6-6 shows that the solution **S2** converges to the exact solution **S1** (i.e., a relative error of zero) with first order convergence rate with respect to the `Interface_Scale_Factor`. The error in the UZ matrix cell is not observed in Figure 6.6-6, since it is overlain by the error in the UZ fracture cell.

Figure 6.6-7 presents the GoldSim V. 8.02.500 (2005 [DIRS 174650]) solution **S3** and the Microsoft Excel solution **S2**. The Microsoft Excel solution **S2** and GoldSim solution **S3** use an `Interface_Scale_Factor` of 1.0×10^{-6} . Figure 6.6-7 shows the mass in place for each of the five cells and demonstrates the excellent agreement between the Microsoft Excel solution and GoldSim solution. After 2 years, the maximum relative error for the corrosion products cell and the two invert cells is 0.2 percent, and the maximum relative error for the two UZ cells is 1.5 percent.

These results confirm that the bifurcation of diffusive flux from a single continuum (corrosion products domain) to a dual continuum (invert domain) and then to another dual continuum (UZ) is accurate and properly implemented in GoldSim.

6.6.3.5 Summary of Dual-Continuum Invert Alternative Conceptual Model

This ACM treats the crushed tuff in the invert as a dual continuum comprised of two pore spaces – intragranular pore space (tuff particle matrix) and intergranular pore space. Although radionuclide transport by both advection and diffusion can occur in both pore spaces, the dominant flow and transport processes in each of these two pore spaces is generally different. The invert is conceptualized in this ACM as overlapping dual continua using a dual-permeability approach, wherein flow and transport occur in both pore spaces, and mass transfer takes place between the two pore spaces. Despite the potential for increased accuracy compared to the base case, single-continuum model, insufficient data exist to validate diffusion coefficients in the individual continua. There are also insufficient data to confirm whether this is a bounding approach with respect to chemical behavior in the invert. Therefore, the single-continuum model is used in the TSPA.

6.6.4 Alternative Invert Diffusion Coefficient Models

The following two alternative models for determining the diffusion coefficient in the invert are assessed in this section: the single-continuum invert diffusion coefficient model and the dual-continuum invert diffusion coefficient model.

6.6.4.1 Alternative Single-Continuum Invert Diffusion Coefficient Model

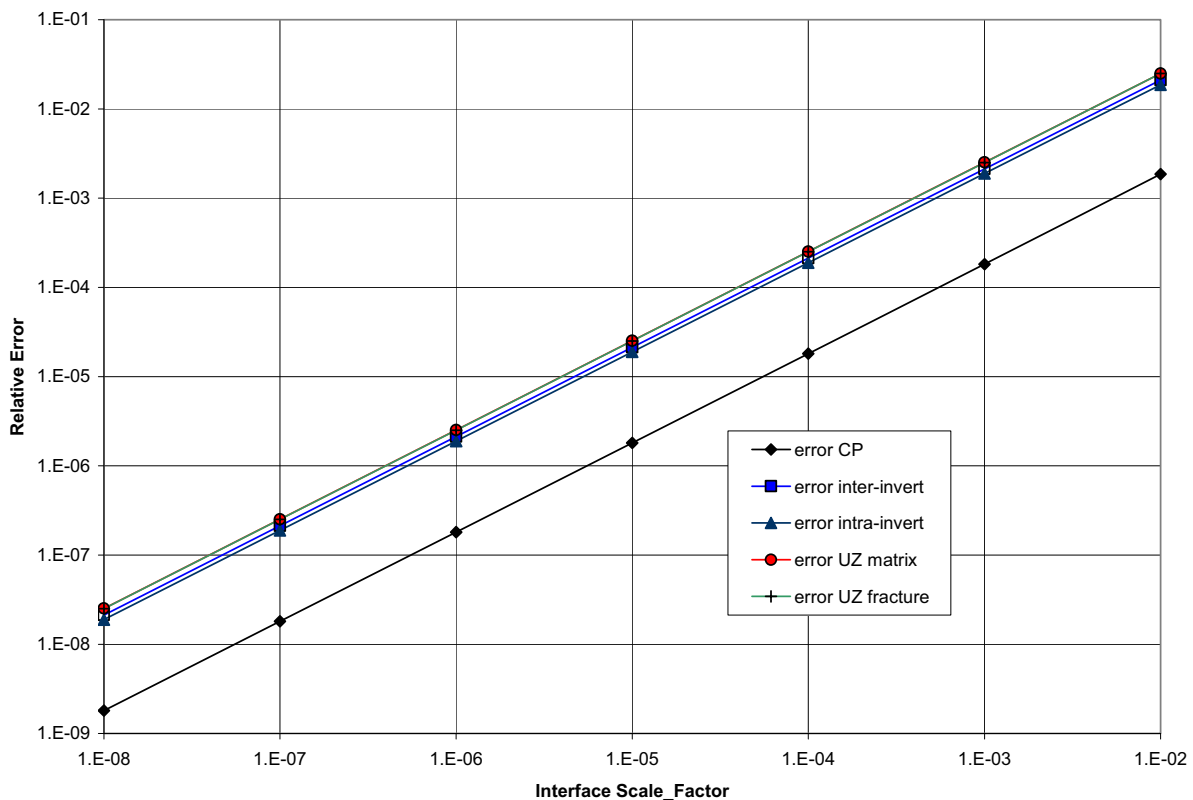
As an alternative to the Archie's law approach for determination of the diffusion coefficient for the single-continuum invert (Section 6.3.4.1), diffusion through the crushed tuff invert ballast is modeled using an approach that has been applied to diffusion in soils. Studies generally show that the bulk diffusion coefficients of soils at high water content decline with the moisture content and that a Millington-Quirk power law developed for high moisture content overpredicts the diffusion coefficient at low moisture content (Nye 1979 [DIRS 167377]; Olesen et al. 1999 [DIRS 154588]). The studies also show that, below a critical moisture content, the diffusion coefficient for granular materials becomes negligible (So and Nye 1989 [DIRS 170588]).

Olesen et al. (1996 [DIRS 155700]) found the best description of the bulk diffusion coefficient of granular soils is the following:

$$D = 0.0045D_i \theta \frac{(\theta - 2.2b)}{(100\phi - 2.2b)}, \quad \theta \geq 2.2b$$

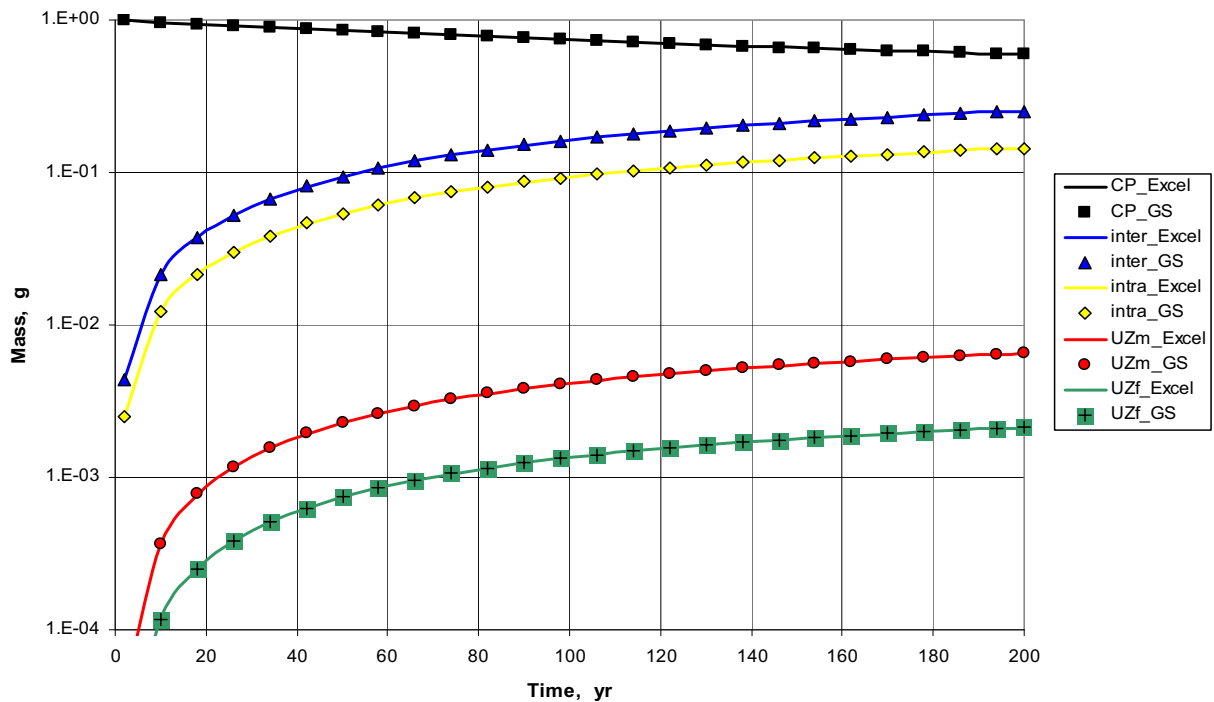
$$D = 0, \quad \theta < 2.2b,$$
(Eq. 6.6.4.1-1)

where D , θ , and ϕ are the bulk diffusion coefficient ($\text{m}^2 \text{s}^{-1}$), moisture content (percent), and bulk porosity of the soil (fraction), respectively; D_i is the free water diffusion coefficient for species i ; in this calculation, the self-diffusion of water, $2.299 \times 10^{-9} \text{m}^2 \text{s}^{-1}$ at 25°C (Mills 1973 [DIRS 133392], Table III), is used as representative of a free water diffusion coefficient for a radioelement. The term $2.2b$ (percent) corresponds to the critical moisture content for these soils. In this expression, the parameter b corresponds to the dimensionless slope of the Campbell moisture retention curve on a log-log plot that varies with the pore and grain size distribution of the soil (Olesen et al. 1996 [DIRS 155700]).



Source:DTN: MO0508SPAUZDIF.000 [DIRS 182278].

Figure 6.6-6. Relative Error of Mass-in-Place for Microsoft Excel Approximate Solution



Source: DTN: MO0508SPAUZDIF.000 [DIRS 182278].

Figure 6.6-7. Comparison of Microsoft Excel and GoldSim Flux Bifurcation Solutions

This behavior for granular materials is generally explained (Olesen et al. 1999 [DIRS 154588]) in terms of a picture in which:

- Above the critical moisture content, the bulk diffusion coefficient of granular materials is dominated by diffusion coefficient in films of moisture on the grain surfaces.
- The diffusion coefficient declines as the moisture content decreases and the tortuosity associated with these films increases.
- Below the critical moisture content, diffusion by the surface films cannot be supported and the diffusion coefficient is reduced to a very low value.

Conca and Wright (1990 [DIRS 101582]) have concluded that this picture is consistent with their measurements of crushed tuff.

A moisture retention relation proposed by Campbell (1985 [DIRS 100565], pp. 45 to 47) is used to develop the moisture potential relation for the crushed tuff invert. The relationship between moisture potential, ψ (J kg^{-1}), and volumetric moisture content, θ (percent), is the soil moisture retention curve, described by the function (Campbell 1985 [DIRS 100565], p. 43):

$$\psi = \psi_e (\theta / \theta_s)^{-b}, \quad (\text{Eq. 6.6.4.1-2})$$

where ψ_e is the air-entry moisture potential (i.e., water potential at which the largest water-filled pore in the soil will drain) (J kg^{-1}), θ_s is the saturated moisture content (percent), and b is the slope (dimensionless) of the $\ln\psi$ versus $\ln\theta$ curve. As the mean pore diameter becomes smaller, the air-entry moisture potential decreases (becomes more negative). The b parameter increases as the standard deviation σ_g (mm) of the pore size increases. Campbell studied the relationships between geometric particle diameter, d_g (mm), geometric standard deviation, σ_g (mm), and air entry potential, ψ_e (J kg^{-1}). By fitting Equation 6.6.4.1-2 to measured data, he obtained the following approximate relationships for soils (Campbell 1985 [DIRS 100565], p. 45) having a bulk density of $1,300 \text{ kg m}^{-3}$:

$$\psi_{es} = -0.5d_g^{-1/2}, \quad (\text{Eq. 6.6.4.1-3})$$

$$b = -2\psi_{es} + 0.2\sigma_g, \quad (\text{Eq. 6.6.4.1-4})$$

where ψ_{es} is the air-entry moisture potential (J kg^{-1}); the subscript *es* refers to the bulk density of $1,300 \text{ kg m}^{-3}$. The geometric standard deviation depends on the soil texture. The geometric standard deviation can be estimated from a soil texture diagram as equal to 1 for coarse sand particles and 5 for fine-grained material (Campbell 1985 [DIRS 100565], Figure 2.1).

The results for the Campbell retention relation for crushed tuff of 0.31 bulk porosity and calculations at various grain sizes ranging from 0.317 mm to 20 mm, which encompass the majority of the expected crushed tuff grain sizes for the invert (SNL 2007 [DIRS 181383], Appendix X), are shown in Table 6.6-2. Table 6.6-2 also shows the associated range of the critical bulk moisture content in Equation 6.6.4.1-1.

Table 6.6-2. Parameters Developed for Crushed Tuff

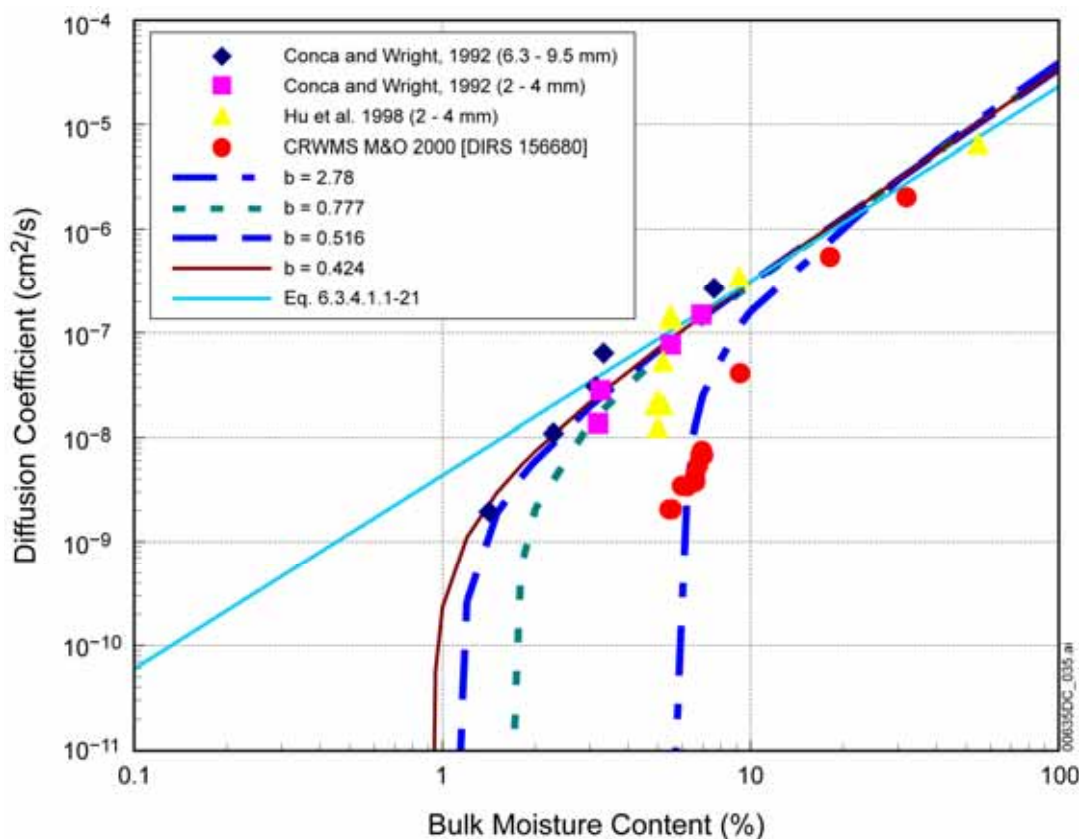
Parameter				
Grain Size (mm) ^a	0.317	3	10	20
Bulk Porosity ^b	0.31	0.31	0.31	0.31
Standard Deviation, σ_g (mm) ^c	5	1	1	1
Slope of the Campbell retention curve, b	2.78	0.777	0.516	0.424
Critical bulk moisture content, $2.2b$ (%)	6.12	1.71	1.14	0.932

^a SNL 2007 [DIRS 181383], Appendix X, Section X.4.

^b SNL 2007 [DIRS 181383], Appendix X, Section X.3.

^c Campbell 1985 [DIRS 100565], Figure 2.1.

Figure 6.6-8 shows the corresponding range in the diffusion coefficient evaluated according to Equation 6.6.4.1-1. In general, the invert will include a distribution of tuff grain sizes. Therefore, the determination of the critical bulk moisture content is made by sampling from a uniform distribution between 0.932 percent and 6.12 percent. This corresponds to the range of tuff grain sizes from 20 mm to 0.317 mm, as shown in Table 6.6-3; a uniform distribution is appropriate for covering the range for an initial analysis of an ACM. The corresponding diffusion coefficient would then be evaluated for this sampled moisture content according to Equation 6.6.4.1-1.



Source: Conca and Wright 1992 [DIRS 100436]; CRWMS M&O 2000 [DIRS 156680]; Hu et al. 2001 [DIRS 161623].

Figure 6.6-8. Range of the Bulk Diffusion Coefficients for Crushed Tuff

For conditions in which advective flow does not occur in the crushed tuff, observations indicate that the intergranular moisture content will generally be negligible. Conca and Wright (1990 [DIRS 101582]) observed that tuff gravel samples allowed to stand for several hours in the presence of 100 percent relative humidity reached moisture contents between 0.5 and 1.5 percent and negligible surface moisture. The measured diffusion coefficients were found in these cases to be below their measurement limit of $1.03 \times 10^{-15} \text{ m}^2 \text{ s}^{-1}$. Therefore, in the portion of the invert in which there is no flow, the diffusion coefficient is expected to be negligible.

For conditions in which flow does occur in the crushed tuff, the bulk diffusion coefficient can be directly evaluated from Equation 6.6.4.1-1 as described above. The uncertainty is accounted for by expressing the threshold in terms of the critical bulk moisture content:

$$D = 0.0045D_i \theta \frac{(\theta - \theta_c)}{(100\phi - \theta_c)}, \quad \theta \geq \theta_c \quad (\text{Eq. 6.6.4.1-5})$$

$$D = 0, \quad \theta < \theta_c,$$

where θ is the bulk moisture content (percent), given by Equation 6.5.2.3-11, and θ_c is the critical value of the bulk moisture content, $2.2b$ (percent). The critical bulk moisture content is

selected by sampling a uniform distribution between 0.932 percent and 6.12 percent, as discussed earlier in this section.

Diffusion coefficients of crushed tuff have been estimated using the ultracentrifuge technique and measurements of electrical resistivity. Conca and Wright (1992 [DIRS 100436]) and Conca et al. (1993 [DIRS 170709]) measured the bulk diffusion coefficients for a variety of granular materials, including crushed tuff, as a function of moisture content. Figure 6.6-8 shows the results of their measurements of crushed tuff samples with tuff grain sizes between 6.3 mm and 9.5 mm, and between 2 mm and 4 mm. Diffusion coefficients for crushed tuff with grain sizes between 2 mm and 4 mm have also been measured by Hu et al. (2001 [DIRS 161623]); these results are also shown in Figure 6.6-8. Finally, the diffusion coefficient measured for samples of crushed tuff with an unspecified distribution of grain sizes (CRWMS M&O 2000 [DIRS 156680]) are also shown in Figure 6.6-8. Comparison of all of these measurements for crushed tuff indicates that the model provides a reasonable representation of the diffusion coefficient for these measured moisture contents (1.4 to 55 percent).

6.6.4.2 Alternative Dual-Continuum Invert Diffusion Coefficient Model

In general, the literature supports a dual continuum picture of the diffusive conductance by the invert granular material. For example, Roberts and Lin (1997 [DIRS 101710]) observed multiple conduction pathways in their measurements of the electrical conductance of unsaturated tuff samples. Their measurements indicated conduction by adsorbed water on the solid surfaces of the tuff samples and conduction by water within the tuff rock. These measurements support a dual continuum picture of the tuff samples in which the water on the surface of the samples corresponds to the intergranular continuum and the water within the samples corresponds to the intragranular continuum.

Other observations also support this picture. Porter et al. (1960 [DIRS 123115]) studied the way in which chloride ions move through soil and the effect of the moisture content of the soil on this movement. These characteristics were interpreted in terms of diffusion within the soil grains and diffusion on the solid surfaces of those grains. Nye (1979 [DIRS 167377]) concluded that, to a first approximation at least, diffusion can be considered to occur through two independent pathways in soil: through moisture between the soil grains and through the grains themselves. In this picture, the bulk diffusion coefficient, D , is represented by:

$$D_i = D_{iinter} \phi_{inter} + D_{iintra} (1 - \phi_{inter}), \quad (\text{Eq. 6.6.4.2-1})$$

where D_{iinter} is the diffusion coefficient for the intergranular continuum determined by the moisture films on the surfaces of the grains, D_{iintra} is the diffusion coefficient for the intragranular continuum determined by the moisture within the grains, and ϕ_{inter} is the intergranular porosity of the material.

In this picture, the bulk diffusion coefficient is dominated by the saturation-dependent intergranular diffusion coefficient above the critical bulk moisture content, while below this critical value, the intragranular diffusion coefficient dominates. That is, Equation 6.6.4.2-1 becomes:

$$\begin{aligned} D_i &\approx D_{iinter}(\theta)\phi_{inter}, & \theta &\geq \theta_c \\ D_i &= D_{iintra}(1-\phi_{inter}), & \theta &< \theta_c, \end{aligned} \quad (\text{Eq. 6.6.4.2-2})$$

where θ_c is the critical moisture content (percent). In this picture, the intergranular diffusion coefficient is represented by the bulk diffusion coefficient model in Equation 6.6.4.1-1, divided by the intergranular porosity:

$$\begin{aligned} D_{iinter} &= 0.45D_i \left(\frac{\theta}{100\phi_{inter}} \right) \left(\frac{\theta - \theta_c}{100\phi_I - \theta_c} \right), & \theta &\geq \theta_c \\ D_{iinter} &= D_{limit}, & \theta &< \theta_c. \end{aligned} \quad (\text{Eq. 6.6.4.2-3})$$

D_{limit} is the measurement limit, $10^{-16} \text{ m}^2 \text{ s}^{-1}$, ϕ_I is the bulk porosity of the invert, $\phi_I = \phi_{inter} + (1 - \phi_{inter})\phi_{intra}$ (fraction), and θ_c (percent) corresponds to 2.2*b* in Equation 6.6.4.1-1.

The intragranular diffusion coefficient is determined by the following considerations.

Reimus et al. (2002 [DIRS 163008]) measured diffusion coefficients for saturated whole rock samples of tuff. The measured values for the samples ranged from $1.5 \times 10^{-11} \text{ m}^2 \text{ s}^{-1}$ to $2 \times 10^{-9} \text{ m}^2 \text{ s}^{-1}$. From these measurements, Reimus et al. (2002 [DIRS 163008], p. 2.25, Equation 2.5) developed a correlation between the saturated diffusion coefficient, D_{ms} , and the porosity, ϕ_m , and intrinsic permeability, k_m , of the tuff rock matrix:

$$\log_{10} D_{ms} = -3.49 + 1.38\phi_m + 0.165 \log_{10} k_m. \quad (\text{Eq. 6.6.4.2-4})$$

The tuff samples were from Pahute Mesa, Nevada, but many of them are similar to tuff rocks at Yucca Mountain. To evaluate the flow characteristics of the drift invert, matrix porosity and intrinsic permeability for tuff from two different Topopah Spring welded tuff units, TSw35 and TSw36, were identified (DTN: LB0207REVUZPRP.002 [DIRS 159672]; Spreadsheet: *Matrix_Props.xls*, Row 20, Column C). These properties are summarized in Table 6.6-3. Using the correlation in Equation 6.6.4.2-4, the diffusion coefficient for saturated tuff whole rock with a saturated moisture content of 10.3 percent is $3.69 \times 10^{-11} \text{ m}^2 \text{ s}^{-1}$, and the diffusion coefficient for a saturated moisture content of 13.1 percent is $6.73 \times 10^{-11} \text{ m}^2 \text{ s}^{-1}$.

Table 6.6-3. Tuff Matrix Properties for TSw35 and TSw36

Parameter	TSw36	TSw35
Porosity of the rock matrix in an individual granule, ϕ_m	0.103	0.131
Intrinsic permeability, k_m (m ²)	2.00×10^{-19}	4.48×10^{-18}
Saturated diffusion coefficient (from Equation 6.6.4.2-4), D_{ms} (m ² s ⁻¹)	3.69×10^{-11}	6.73×10^{-11}

DTN:LB0208UZDSCPMI.002 [DIRS 161243]; Spreadsheet “*drift-scale calibrated properties for mean infiltration2.xls*,” Rows 17-18, Columns B-C.

A laser ablation microprofiling technique has been used to estimate the diffusion characteristics for an unsaturated whole tuff rock sample (Hu et al. 2001 [DIRS 161623]). Hu et al. (2001 [DIRS 161623], p. 25) found that, for a measured moisture content of the sample of 8.9 percent, the internal diffusion coefficients were on the order of 10^{-16} m² s⁻¹ (Hu et al. 2001 [DIRS 161623], p. 25). This result indicates a very low intragranular diffusion coefficient for tuff at intragranular saturations below about 80 percent.

The model developed for the intragranular diffusion coefficient considering this information is the following. For intragranular moisture content, θ_{intra} , below 8.9 percent, a value of 10^{-16} m² s⁻¹ is used to represent the diffusion coefficient. For saturated conditions ($\frac{\theta_{intra}}{100} = \phi_{intra}$, the intragranular porosity), the diffusion coefficient is set to a value corresponding to Equation 6.6.4.2-4. For unsaturated grains with moisture content above 8.9 percent, a power-law extrapolation from the saturated value is used. The overall model proposed for the intragranular diffusion coefficient is the following power law model:

$$D_{iintra} = D_{ms} \left(\frac{\left(\frac{\theta_{intra}}{100} \right)}{\phi_{intra}} \right)^p, \quad \theta_{intra} \geq \theta_{min} \quad (\text{Eq. 6.6.4.2-5})$$

$$D_{iintra} = D_{limit}, \quad \theta_{intra} < \theta_{min},$$

where θ_{intra} is the intragranular moisture content (percent), ϕ_{intra} is the intragranular porosity (fraction), D_{limit} is the measurement limit, 10^{-16} m² s⁻¹, and θ_{min} is equal to 8.9 percent. The exponent p is the slope of Equation 6.6.4.2-5 in a plot of $\log_{10}(D_{iintra})$ versus $\log_{10}(\theta_{intra})$. This plot is a straight line (in log-log space) between points $\left(\frac{\theta_{min}}{100}, D_{limit} \right)$ and (ϕ_{intra}, D_{ms}) . Thus, p is given by:

$$p = \frac{\log_{10}(D_{limit}) - \log_{10}(D_{ms})}{\log_{10}\left(\frac{\theta_{min}}{100}\right) - \log_{10}(\phi_{intra})}. \quad (\text{Eq. 6.6.4.2-6})$$

The dual porosity model for the invert diffusion coefficient follows by specifying values for the intergranular and intragranular diffusion coefficients. The intergranular diffusion coefficient is evaluated from Equation 6.6.4.1-5 and dividing by the intergranular porosity (i.e., Equation 6.6.4.2-3). The intragranular diffusion coefficient is evaluated from Equation 6.6.4.2-5. The effective bulk diffusion coefficient is determined from Equation 6.6.4.2-2.

6.6.4.3 Summary of Alternative Invert Diffusion Coefficient Conceptual Models

These conceptual models consider alternatives to Archie's law for determining the diffusion coefficient in the crushed tuff invert. One variation treats the invert as a single continuum, as in the base model; the second variation models the invert as a dual continuum comprised of two pore spaces—intragranular pore space (tuff particle matrix) and intergranular pore space. Despite the potential for increased accuracy compared to the base case single-continuum model using Archie's law, insufficient data exist to validate diffusion behavior at very low water contents. In addition, these alternative conceptual models do not provide upper bounds on diffusion coefficients, as the Archie's law approach does. Therefore, invert diffusion coefficients are computed in TSPA using Archie's law.

6.6.5 Reversible Sorption of Radionuclides onto Waste Package Corrosion Products

The conceptual model in this section describes the alternative approach of allowing for reversible sorption onto stationary corrosion products by using K_d values.

Descriptions of sorption based on a K_d are approximate because this approach is empirical, with little information about underlying mechanisms, and is therefore not easily extendable to different chemical environments and physical substrates (sorptive media). The use of a linear isotherm is also approximate because it does not predict saturation of the sorption sites with sorbed species that may include natural components of the groundwater. The mass of iron oxyhydroxides from waste package corrosion is large (Tables 6.3-8 and 6.3-9), so each waste package provides many sites for sorption. For these reasons, the K_d approach is an order of magnitude measure of contaminant uptake in geologic environments (Davis and Kent 1990 [DIRS 143280]).

The use of the linear isotherm (K_d) approach to represent the subsequent release of radionuclides into fresh recharge (i.e., the desorption process) can be inconsistent with observations in geologic media. Typically, contaminants become more closely attached to a mineral surface after sorption, either adsorbed at high energy sites on the surface or absorbed through overcoating and buried due to other mineral surface reactions. The net result is that only a fraction of the original sorbed population remains available at the surface and able to react with adjacent solutions or be accessed by microorganisms. A linear isotherm (K_d) approach, on the other hand, assumes that all sorbed radionuclides are freely able to desorb from the substrate.

Sorption distribution coefficients are typically measured for groundwaters and substrates at ambient or near ambient temperatures. There are few experimental data for sorption distribution coefficients at the elevated temperatures that may occur in the EBS with either the repository design and operating mode described in *Yucca Mountain Science and Engineering Report*

(DOE 2001 [DIRS 153849]) or an alternative thermal operating mode. In this situation, the available data for sorption distribution coefficients were used to define the ranges of K_d values for the earlier TSPA analyses, but it is not possible to distinguish alternative thermal operating modes. The effect of temperature on sorption coefficients was reviewed by Meijer (1990 [DIRS 100780], p. 17). Measured sorption coefficients onto tuffs were higher at elevated temperatures for all elements studied: americium, barium, cerium, cesium, europium, plutonium, strontium, and uranium. The conclusion was drawn that sorption coefficients measured at ambient temperatures should be applicable and generally bounding when applied to describing aqueous transport from a repository at elevated temperatures. This conclusion must be tempered by the possibility that elevated temperatures could result in changes in the near-field mineralogy and water chemistry that are not predictable by short-term laboratory and field experiments.

As discussed previously, the use of a linear isotherm is an empirical, order-of-magnitude description of mineral surface processes because it is not based on underlying physical or chemical mechanisms. In essence, a K_d value is valid only for the specific substrate and chemical conditions under which it is measured. More defensible models of contaminant uptake by mineral surfaces require a more comprehensive mechanistic understanding of the chemical reactions involved (Davis et al. 1998 [DIRS 154436]). In lieu of a more involved mechanistic treatment based on surface complexation that includes a provision for kinetic sorption, K_d values can provide a first-order picture of the sorption process, using generic ranges based on soils and iron oxyhydroxides. The rationale for this approach is described below.

Based on previous TSPA calculations, the pH of waste package fluids is expected to fall within the range observed in soils and groundwaters, with pH values between 5 and 10 (SNL 2007 [DIRS 180506], Section 6.10.1[a]). Although the composition of in-package fluids will vary with time due to degradation of the waste package components (primarily steels, Zircaloy cladding, SNF, and waste glass), major characteristics (such as alkalinity and system redox state) will be controlled by equilibrium with atmospheric carbon dioxide and free oxygen. The primary reactive components in the degraded waste package environment are iron hydroxides, the same mineral phases that tend to dominate trace element sorption in soils. The only major element species that will be present in waste package fluids, but that tend to be scarcer in natural soils and groundwaters, are those containing uranium.

The trace element composition of waste package fluids will differ due to the presence of metal components and various radiogenic isotopes. On the other hand, the waste package environment is expected to contain greater volumes of iron hydroxides than all but the most iron-rich soils. Consequently, sorption calculations using ranges of K_d values measured on iron-containing soils or iron hydroxides provide a reasonable measure of sorption inside the waste package.

Sorption distribution coefficients often vary by at least an order of magnitude. Each range of K_d represents the compilation of many experimental measurements with wide variations in sorbent composition and characteristics, contaminant level, solution composition and temperature, and method of measurement.

Sorption distribution coefficient values for a linear, reversible isotherm can be interpreted physically (Stumm 1992 [DIRS 141778], Section 4.12) in terms of retarding the movement of a contaminant relative to the velocity of the water carrying it. If the average water velocity is \bar{v}

(m s^{-1}) and the front of the contaminant concentration profile has an average velocity v_c , the retardation of the front relative to the bulk mass of water is described by the relation:

$$R_f = \frac{\bar{v}}{v_c} = 1 + \frac{\rho_b}{\phi} K_d, \quad (\text{Eq. 6.6.5-1})$$

where R_f is the retardation factor (dimensionless ratio of water velocity to the concentration front velocity), ρ_b is the bulk density of the rock (kg m^{-3}) having a porosity ϕ (fraction). For example, a contaminant with a K_d of $1,000 \text{ mL g}^{-1}$ will move at one ten-thousandth the rate of the carrier water for a rock porosity of 20 percent and a rock density of $2,000 \text{ kg m}^{-3}$. A contaminant with a K_d of 1 mL g^{-1} will move at one-eleventh the velocity of the carrier water, and a contaminant with a K_d of 0 moves at the velocity of the water, both for the same values of rock porosity and rock density. These effective transport velocities provide an estimate of the delay for first breakthrough of the contaminant; after the sorption sites are completely saturated, changes in mass flow rate will be delayed only by the water transport time through the system.

The corrosion product assemblage is predicted by the in-package chemistry model reaction path calculations to be made up primarily of iron oxyhydroxides (e.g., goethite, hematite, ferrihydrite) and aluminum oxides. Lesser amounts of manganese oxides, metal phosphates and clay minerals are anticipated. The integrated sorptive properties of the assemblage might therefore be approximated as being that of iron oxyhydroxides with some aluminum oxides. The latter possess high specific surface areas and a strong chemical affinity for many radionuclides. Cesium primarily exchanges onto clay minerals. Strontium and radium tend to exchange onto clay lattices in soils, although strontium does sorb onto iron oxyhydroxides, particularly above pH 7. The fact that strontium and radium behave similarly in soils indicates that limited radium uptake by iron oxyhydroxides can be expected as well. Under oxidizing conditions technetium and iodide sorb negligibly to most soil components. However, reduction of technetium on solid surfaces containing reduced elements (e.g., iron metal) can cause strong retardation.

Table 6.6-4 summarizes the observations above by listing the components of soils that tend to control sorption. Iron oxyhydroxides are an important sorbing component of soils for all radioelements except iodine and technetium.

Table 6.6-4. Influences Over Radionuclide Sorption in Soils

Element	Important Solid Phase and Aqueous-Phase Parameters Influencing Contaminant Sorption*
Americium	[Clay Minerals], [Iron/Aluminum Oxide Minerals], pH
Cesium	[Aluminum/Iron Oxide Minerals], [Ammonium], Cation Exchange Capacity, [Clay Mineral], [Mica-like Clays], pH, [Potassium]
Iodine	[Dissolved Halides], [Organic Matter], Redox, Volatilization, pH
Neptunium	[Clay Minerals], [Iron/Aluminum Oxide Minerals], pH
Radium	BaSO ₄ Coprecipitation, [Dissolved Alkaline Earth Elements], Cation Exchange Capacity, [Clay Minerals], Ionic Strength, [Iron-/Aluminum-Oxide Minerals], [Organic Matter], pH
Technetium	[Organic Matter], Redox

Table 6.6-4. Influences Over Radionuclide Sorption in Soils (Continued)

Element	Important Solid Phase and Aqueous-Phase Parameters Influencing Contaminant Sorption*
Plutonium	[Aluminum/Iron Oxide Minerals], [Carbonate, Fluoride, Sulfate, Phosphate], [Clay Mineral], [Organic Matter], pH, Redox
Strontium	Cation Exchange Capacity, [Calcium], [Carbonate], pH, [Stable Strontium]
Thorium	[Aluminum/Iron Oxide Minerals], [Carbonate], [Organic Matter], pH
Uranium	[Aluminum/Iron-Oxide Minerals], [Carbonate, Fluoride, Sulfate, Phosphate], [Clay Mineral], [Organic Matter], pH, Redox, [U]

Source: EPA (2004 [DIRS 172215]), Table 5.35.
EPA (1999 [DIRS 170376]), Table 5.20.

*Parameters listed in alphabetical order. Square brackets represent concentration.

Corrosion product K_d ranges have been compiled by the Electric Power Research Institute (EPRI) (2000 [DIRS 154149], Table 6-9) from a literature review of iron oxyhydroxide sorption measurements. The U.S. Environmental Protection Agency (EPA) has compiled K_d values for soils for many of the same radionuclides (EPA 1999 [DIRS 170376]; EPA 2004 [DIRS 172215]).

The large role of iron and aluminum oxyhydroxides minerals in controlling overall soil K_d values is explicitly recognized in the EPA documents. For this reason, one would expect EPA soil K_d values and EPRI iron oxyhydroxides K_d values to be similar and both to provide a reasonable approximation of retardation in the waste package corrosion products. There are some caveats, however, the most important one being that K_d values for a given material and radionuclide are approximate values that can vary widely depending on the specifics of the measurement (solid/solution ratio, radionuclide level, time allowed for equilibration). General coherence in an order-of-magnitude sense is the best that can be expected as the K_d approach does a poor job of reproducing actual transport profiles; see, for example, Bethke and Brady (2000 [DIRS 154437]) and Reardon (1981 [DIRS 154434]).

Table 6.6-5 gives K_d ranges describing retardation in the waste package corrosion products for 13 radionuclides, with the minimum K_d and maximum K_d being the ranges used in this ACM. Distributions for K_d values in Table 6.6-5 are log-uniform for all elements except for iodine, for which the range is small, justifying a uniform distribution. All the other elements in Table 6.6-5 have K_d values that range over more than an order of magnitude. A log-uniform distribution is specified to avoid the high-end bias that results from sampling from a uniform distribution that has a large range. The upper range for technetium is valid only under reducing conditions.

Table 6.6-5. Summary of Partition Coefficient (K_d) Ranges and Distributions for Retardation in the Waste Package Corrosion Products

Element	K_d Range (ml g ⁻¹)	K_d Range Source
Ac	1,000–20,000	EPRI 2000 [DIRS 154149], Table 6-9
Am	1,000–>100,000 1,000–20,000	EPA 2004 [DIRS 172215], Section 5.2.5.1; EPRI 2000 [DIRS 154149], Table 6-9
C	0–100	EPRI 2000 [DIRS 154149], Table 6-9
Cs	10–3,500 1–200	EPA 1999 [DIRS 170376], Table D.10 (low clay soils); EPRI 2000 [DIRS 154149], Table 6-9
I	0–1	EPRI 2000 [DIRS 154149], Table 6-9
Np	0.16–929 10–1,000 (0.1–1,000)	EPA 2004 [DIRS 172215], Section 5.6.5.4; EPRI 2000 [DIRS 154149], Table 6-9 (reduced by factor of 100 for U site saturation)
Pa	100–10,000	EPRI 2000 [DIRS 154149], Table 6-9
Pu	60–15,000 1,000–20,000	EPA 1999 [DIRS 170376], p. G-4 EPRI 2000 [DIRS 154149], Table 6-9
Ra	1–120 50–1,000	EPA 2004 [DIRS 172215] (Section 5.7.5.1: use Sr values) EPRI 2000 [DIRS 154149], Table 6-9
Sr	1–120 10–100	EPA 1999 [DIRS 170376], Table 5.13 EPRI 2000 [DIRS 154149], Table 6-9
Tc	0–1,000	EPRI 2000 [DIRS 154149], Table 6-9
Th	20–300,000 1,000–20,000	EPA 1999 [DIRS 170376], Table 5.15 EPRI 2000 [DIRS 154149], Table 6-9
U	0–630,000 50–10,000	EPA 1999 [DIRS 170376], Table 5.17 EPRI 2000 [DIRS 154149], Table 6-9

This ACM is not used as the base model in TSPA for several reasons. First, it does not account for limitations on the number of sites available for sorption. Second, it does not account for competition for sorption sites among the radionuclides that can sorb. Third, it does not account for sorption when the pH and P_{CO_2} is changing.

6.6.6 Plutonium Sorption onto Stationary Corrosion Products and Colloids

Iron oxides and hydroxides are a primary sorptive sink for many metal ions and metal oxyion complexes in natural systems. Desorption studies have been done with ferrihydrite and goethite using Mn(II), Co(II), Ni(II), Cu(II), Pb(II), Zn(II), Cd(II), Cr(III), and the metal complexes arsenate, chromate, selenate, selenite, and uranyl; Pu(IV) and Pu(V) have also been examined (Barney 1984 [DIRS 174702]; Schultz et al. 1987 [DIRS 173028]; Ainsworth et al. 1994 [DIRS 173033]; Payne et al., 1994 [DIRS 174707]; Coughlin and Stone 1995 [DIRS 173030]; Manning and Bureau 1995 [DIRS 174725]; Davis and Upadhyaya 1996 [DIRS 173743]; Eick

et al. 1999 [DIRS 174704]; Fendorf et al. 1996 [DIRS 173034]; Fendorf et al. 1997 [DIRS 173031]; Ford et al. 1997 [DIRS 174727]; Grossl et al. 1997 [DIRS 173032]; Sanchez et al. 1985 [DIRS 107213]; Lu et al. 1998 [DIRS 100946]; and Lu et al 1998 [DIRS 174714]). Adsorption of these metal species onto iron oxyhydroxides is initially very rapid, reaching a steady-state concentration within minutes to hours; however, slow uptake commonly continues indefinitely. Desorption is also initially rapid, though generally slower than adsorption. It is often incomplete, with the fraction of readily desorbed metal a function of the metal/oxide contact (pre-equilibration) time, the time allowed for desorption, and, in some cases, the pre-equilibration pH (Schultz et al. 1987 [DIRS 173028]). Continued slower desorption is commonly observed for the duration of the experiment. For this reason, Schultz et al. (1987 [DIRS 173028]) have stated that the term “slowly reversible sorption” should be preferred over “irreversible sorption” when discussing metals that remain bound to the sorbent during desorption re-equilibration. In many cases, though, a fraction of the metal does appear to be irreversibly sequestered by the iron oxyhydroxide. As a result, there is a decrease in the labile, or readily available, fraction of metal ions in the system and a drop in the net metal toxicity.

Many mechanisms have been proposed for slowly reversible sorption; most would result in the observed continued slow uptake of metal from solution as well. Possible mechanisms include:

- Incorporation of metal ions into the FeOOH structure by isomorphic substitution. This mechanism has been suggested to occur during recrystallization of ferrihydrite as goethite, but may also be effective during growth or coarsening (Ostwald ripening) of goethite in suspension. Irreversible adsorption of divalent metal ions, of similar size to Fe^{+3} , has been attributed to this process (Schultz et al. (1987 [DIRS 173028]); Ainsworth et al. 1994 [DIRS 173033]; Ford et al. 1997 [DIRS 174727]; Coughlin and Stone 1995 [DIRS 173030]). Watson (1996 [DIRS 173035]) has shown that entrapment of adsorbed contaminant ions by crystal growth permanently sequesters such ions from the environment, as solid-state diffusion of ions out of mineral structures is too slow at near-surface temperatures to allow for re-equilibration.

A related mechanism, potentially important during recrystallization of ferrihydrite as goethite, is overgrowth and encapsulation of sorbed or precipitated phases during goethite formation and growth.

- Formation of slowly dissolving metal hydroxide surface precipitates (Fendorf et al. 1996 [DIRS 173034]). However, such precipitates are unlikely to form at concentrations much lower than the solubility of the contaminant.
- Sorption of ions onto high-energy sites on the FeOOH surface. If such sites are numerous relative to the concentration of the sorbent, then with time, an increasing number of sorbent ions will become bound in the more stable high-energy sites relative to the lower energy sites, and the proportion of slowly reversible or irreversibly bound metal will increase.
- A time-dependent change in the metal-surface site stoichiometry, resulting in a higher energy bond. Fendorf et al. (1997 [DIRS 173031]) and Grossl et al. (1997 [DIRS 173032]) demonstrated that arsenate and chromate initially formed monodentate

surface complexes on goethite, but with time these transformed into more stable bidentate complexes, resulting in progressively larger fractions of slowly desorbing adsorbate. Adsorption of ions to the FeOOH surface in two or more distinct stoichiometries will yield a progressive increase in the amount of adsorbed metal, and an increase in the fraction of slowly desorbing metal, if the formation rate constant for the more stable surface complex is considerably slower than that of the less stable complex. The degree of adsorption would level out with time, as secular equilibrium is reached.

- Creation of and adsorption to sites higher in binding energy than those initially available, e.g., changes in the surface properties of the substrate with aging. Such changes occur during the transformation of ferrihydrite to goethite. However, Schultz et al. (1987 [DIRS 173028]) performed experiments with nickel, zinc, and chromium and showed that the relative proportion of quickly and slowly desorbed adsorbate did not vary with the age of the ferrihydrite used (goethite progressively ingrows as the material ages), indicating that goethite and ferrihydrite do not “irreversibly adsorb” differing amounts of adsorbate. (This is consistent with the sorption model implemented in the base case [Section 6.5.2.4]; there are fewer sites per unit surface area on HFO relative to goethite, but HFO has a higher surface area. The net number of high energy sites is nearly the same on both materials.)
- Slow diffusion of ions into and out of the crystal structure. Coughlin and Stone (1995 [DIRS 173030]) have suggested that divalent metal ions first adsorb onto the mineral surface, and then slowly diffuse into internal binding sites; hence, the slow continued uptake of metals by iron oxyhydroxides. The slow desorption would presumably be the result of diffusion out of the internal sites. However, as stated earlier, solid-state diffusion rates are too slow under natural conditions for this mechanism to be effective (Watson, 1996 [DIRS 173035]).
- Slow diffusion of ions into and out of micropores and microfractures on the mineral surface, or into and out of mineral aggregates (e.g., ferrihydrite floc). Ainsworth et al. (1994 [DIRS 173033]) suggest that the observed variations in metal ion behavior indicate that this mechanism is not an important cause of slowly reversible adsorption. The degree to which a metal ion is strongly adsorbed is dependent upon its coordination chemistry (Coughlin and Stone, 1995 [DIRS 173030]); if diffusion into micropores were the causal mechanism, then all metal ions should be similarly affected.
- For plutonium, a special mechanism has been proposed (Keeney-Kennicutt and Morse 1985 [DIRS 106313]); Sanchez et al. 1985 [DIRS 107213]; Morse and Choppin 1986 [DIRS 174703]; Runde et al. 2002 [DIRS 168432]; Powell et al. 2005 [DIRS 174726]). Pu(V) reduces to a more stable Pu (IV) on the goethite surface, which is both stabilized in the reduced oxidation state and more strongly sorbed, and thus, less sensitive to changes in solution chemistry such as pH or ionic strength. For instance, the Pu(V) sorption edge occurs in the pH range 5 to 7, while the Pu(IV) sorption edge occurs at pH 3 to 5. The mechanisms for Pu(V) reduction to Pu(IV) during sorption are not known, and Sanchez et al. (1985 [DIRS 107213]) hypothesized that it could either happen upon adsorption onto the surface or in the adsorbed layer near solid-solution interface. Sanchez et al. (1985 [DIRS 107213]) suggested a few possible causes for

Pu(V) reduction, including reducing impurities in the sorbent material or, as proposed earlier by Keeney-Kennicutt and Morse (1985 [DIRS 106313]) a heterogeneous Pu(V) disproportionation reaction to produce Pu(IV) and Pu(VI). Sanchez et al. (1985 [DIRS 107213]) confirmed the presence of Pu(IV) in the solid and solution through solvent extraction and also noticed that Pu(V) was stable in solution whereas Pu(IV) was stable on the goethite solid. Runde et al. (2002 [DIRS 168432]) offer supporting data; they evaluated redox thermodynamic data for Pu and concluded that Pu(IV) solids are likely to control Pu solubilities under water chemistries typical of natural environments.

The degree to which these processes permanently sequester the contaminant varies. Incorporation into the iron oxyhydroxide crystal structure or sequestration by overgrowth is effectively permanent, as release is limited by dissolution of the iron oxide. Release from surface precipitates is limited to the solubility of the precipitated species. Migration into higher affinity sites, or changes in the stoichiometry of the sorbed phase, raises the K_d and stabilizes the sorbed species with respect to changes in water chemistry. Even reversible sorption effectively immobilizes a contaminant, if sufficient iron oxyhydroxide is present, the K_d is large enough, and the water chemistry is restricted to the range at which sorption is high. Because many metals and metal-oxyanions sorb so strongly to Fe-oxyhydroxides at near-neutral pH, desorption experiments commonly require either adjusting the pH to values too low to represent natural conditions or adding chelating agents which would not be present in natural environments.

Because the mechanism by which plutonium and americium are strongly sorbed on Fe-oxyhydroxide surfaces is not well known, it is difficult to evaluate the degree to which sorption is truly irreversible, and the sensitivity of that assumption to changes in chemical conditions. Therefore, alternative conceptual models to non-equilibrium sorption are considered here. To determine the appropriate form for that ACM, we evaluate project data for sorption of plutonium onto goethite and hematite from DTN: LA0004NL831352.001 [DIRS 150272]; development of this data is described by Lu et al. (1998 [DIRS 100946]) and Lu et al. (1998 [DIRS 174714]).

Yucca Mountain Project Experimental Sorption-Desorption Data for Plutonium

The Yucca Mountain Project has performed sorption and desorption experiments with Pu(V) in natural and synthetic J-13 waters, using hematite and goethite colloids. The experimental procedures used in these experiments are documented by Lu et al. (1998 [DIRS 100946]); however, the sorption data presented there contains errors; the actual sorption data used is from DTN: LA0004NL831352.001 [DIRS 150272], and is described by Lu et al. (1998 [DIRS 174714]). The desorption data from Lu et al. (1998 [DIRS 100946]) is used, however, as there is no project DTN containing this information.

In this model report, corrosion products are assumed to be a mixture of goethite and HFO, and in this ACM, K_d s derived from goethite experiments are used as the basis for a model involving reversible sorption. The hematite data are presented for comparison.

Sorption experiments—The sorption experiments are described by Lu et al. (1998 [DIRS 100946], pp. 10 to 12; Sorption #2 experiments). They were performed at room temperature using air-equilibrated natural and synthetic J-13 waters, with pH values of 8.2 and 8.5, respectively. In these experiments, 1 mL of 2.74×10^{-7} M ^{239}Pu solution was added to

20 mL of colloid solution containing approximately 1 g L^{-1} colloids (Lu et al 1998 [DIRS 174714], Table 1), resulting in a sample containing 0.02 g (nominal) colloid in 21 mL of $1.3 \times 10^{-8} \text{ M}$ Pu(V) solution. Samples were collected over a period of 5,760 minutes (4 days). The remaining plutonium in solution was determined by liquid scintillation counting (LSC), a standard analytical technique for measuring radiation from α - and β -emitting radionuclides by detecting small flashes of light emitted by radionuclides placed in an organic solution. The results of these experiments are presented in Table 6.6-6. For both hematite and goethite, in both natural and synthetic J-13 water, sorption is initially very rapid, reaching a high value within minutes to hours; however, slow uptake continues until the end of the experiment. Behavior is slightly different in natural and synthetic water, but in three of the four cases examined, sorption exceeded 99 percent, resulting in K_d values of 10^5 to 10^6 (DTN: LA0004NL831352.001 [DIRS 150272]). In the fourth case, goethite in natural J-13 water, sorption continued to increase through the experiment, but had only reached 90 percent after 4 days; the final K_d value was about $8.7 \times 10^3 \text{ mL g}^{-1}$ (DTN: LA0004NL831352.001 [DIRS 150272]).

In each of these cases, the measured K_d value is considered to be a minimum value. Either concentrations in solution decreased below the detection limit, or concentrations were continuing to drop when the experiment was terminated.

Table 6.6-6. Sorption of Pu(V) onto Hematite and Goethite Colloids

Minerals	Time (min.)	Fraction of Pu Sorbed		K_d (mL g^{-1})	
		J-13	SYN.J-13	J-13	SYN.J-13
Hematite	10	0.539	0.933	1.20×10^3	1.67×10^4
	30	0.565	0.966	1.32×10^3	3.39×10^4
	60	0.594	0.957	1.51×10^3	2.78×10^4
	240	0.674	0.996	2.22×10^3	3.66×10^5
	360	0.740	0.998	3.03×10^3	5.91×10^5
	1,440	0.907	0.999	9.98×10^3	2.08×10^6
	2,880	0.948	1.000	1.87×10^4	NC
	5,760	0.994	0.999	1.96×10^5	NC
Goethite	10	0.303	0.831	3.97×10^2	5.06×10^3
	30	0.328	0.831	4.40×10^2	4.98×10^3
	60	0.360	0.837	5.18×10^2	5.36×10^3
	240	0.515	0.911	1.01×10^3	1.03×10^4
	360	0.595	0.932	1.39×10^3	1.40×10^4
	1,440	0.793	0.987	3.45×10^3	7.65×10^4
	2,880	0.869	0.997	6.00×10^3	7.63×10^5
	5,760	0.902	0.991	8.72×10^3	1.39×10^5

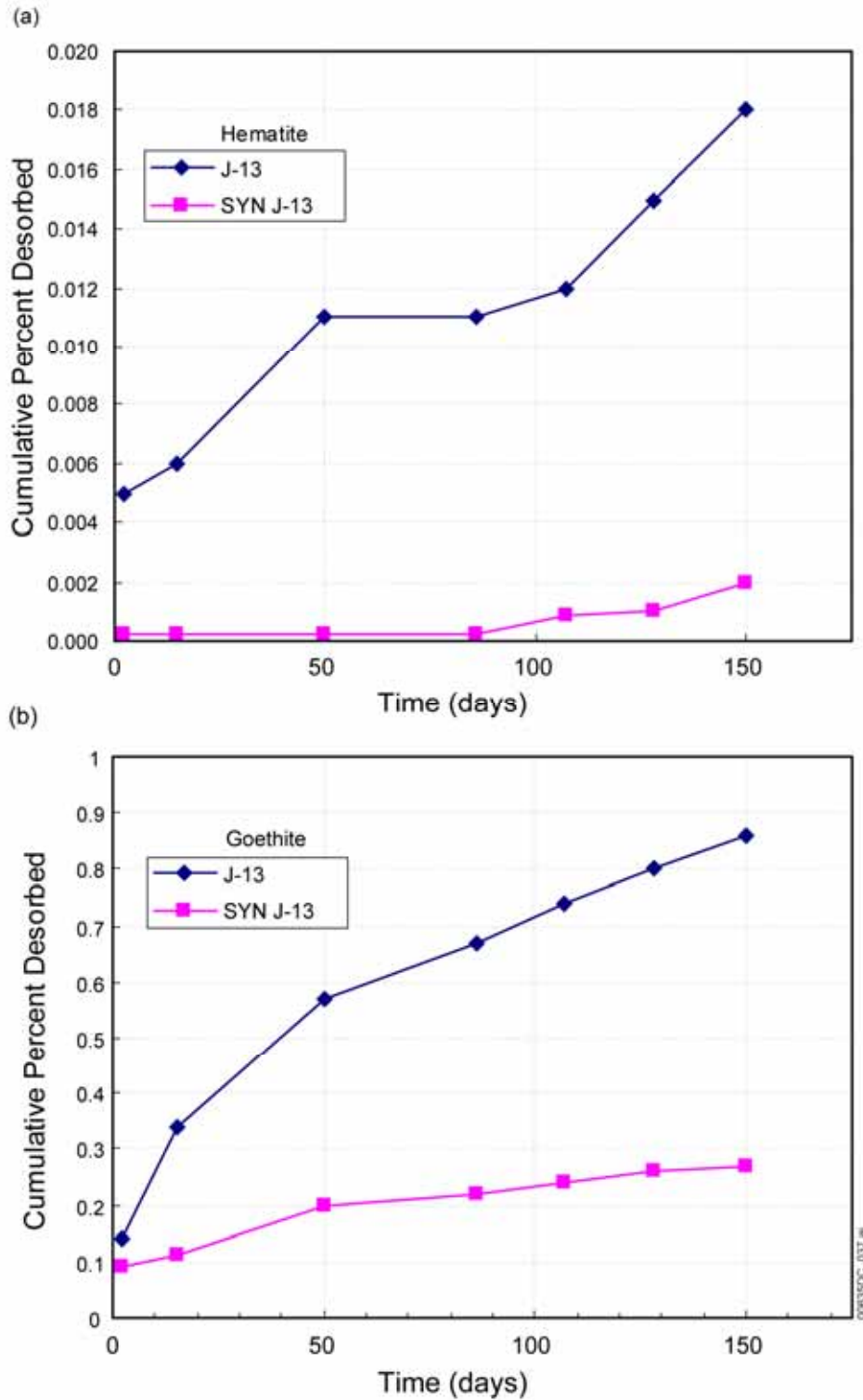
Source: LA0004NL831352.001 [DIRS 150272].

Desorption experiments—Procedures for the plutonium desorption experiments are described by Lu et al. (1998 [DIRS 100946]). Substrate for the desorption experiments was produced by equilibrating 0.5 g of colloids with 20 mL of J-13 or synthetic J-13 water, with a Pu(V) concentration of $2.74 \times 10^{-7} \text{ M}$. Following equilibration, the samples were centrifuged, and the

colloids resuspended in 5 mL of unspiked electrolyte. Periodically over a period of 150 days, these samples were centrifuged and the electrolyte extracted and replaced with fresh solution. The extracted liquid was filtered and analyzed by LSC. The results of this analysis are listed in Table 6.6-7, as presented by Lu et al. (1998 [DIRS 100946], Tables 10 and 11), and are plotted in Figure 6.6-9. Lu et al. (1998 [DIRS 100946]; 1998 [DIRS 174714]) and Runde et al. (2002 [DIRS 168432]) interpreted the small amounts of desorbed plutonium to indicate that kinetics of plutonium desorption from Fe-oxides/oxyhydroxides are much slower than the kinetics of sorption, a conclusion at odds with the calculated “desorption K_d values,” which are smaller than those for sorption, and decrease with time. The change in “desorption K_d values” would imply that the affinity of plutonium for the surface of the substrate actually decreases with time. However, these data have been misinterpreted, and the calculated “desorption K_d values” are incorrect.

Lu et al. (1998 [DIRS 100946]) misinterpreted the data in assuming that low concentrations of plutonium in the desorption experiments do not necessarily imply slow desorption. When the goethite and hematite colloids were equilibrated with plutonium-spiked groundwater, 97 percent to 100 percent of the plutonium was adsorbed. Hence, K_d values were high. Extracting the nearly radionuclide-depleted water and replacing it with unspiked water provided no significant driving force for desorption. Even if the plutonium were instantly exchangeable, concentrations in the solution would remain low because of the high K_d value; anything that desorbed would immediately re-sorb. Thus, the low degree of desorption may only indicate a high K_d value. In addition, because desorption was viewed as an irreversible process, the cumulative percentage of plutonium sorbed was used to calculate the “desorption K_d value.” Hence, the “desorption K_d value” was observed to decrease with time. To evaluate the desorption data properly, each successive equilibration and extraction must be viewed as a separate desorption experiment, in which the total amount of plutonium in the system is nearly constant (a total of less than 1 percent of the plutonium was extracted in the worst case), and the applicable K_d value can be calculated from the plutonium concentrations in solution and on the solid.

The results of this new analysis are presented in Table 6.6-8 and in Figure 6.6-10. For hematite, sorption is so complete that the tiny amount of plutonium in solution represents values near the detection limit for the analysis. There is no significant trend with time, and predicted K_d values are consistent with, or higher than, those measured in the sorption experiments (Table 6.6-7), on the scale of 10^5 to 10^6 mL g⁻¹. Sorption was less complete on goethite, but K_d values continued to increase with time; the final few extractions yielded K_d values of 10^4 to 10^5 mL g⁻¹.



Source: DTN: SN0508T0507703.020 [DIRS 182215], spreadsheet *Pu sorption-desorption.xls*, worksheet "Desorp data."

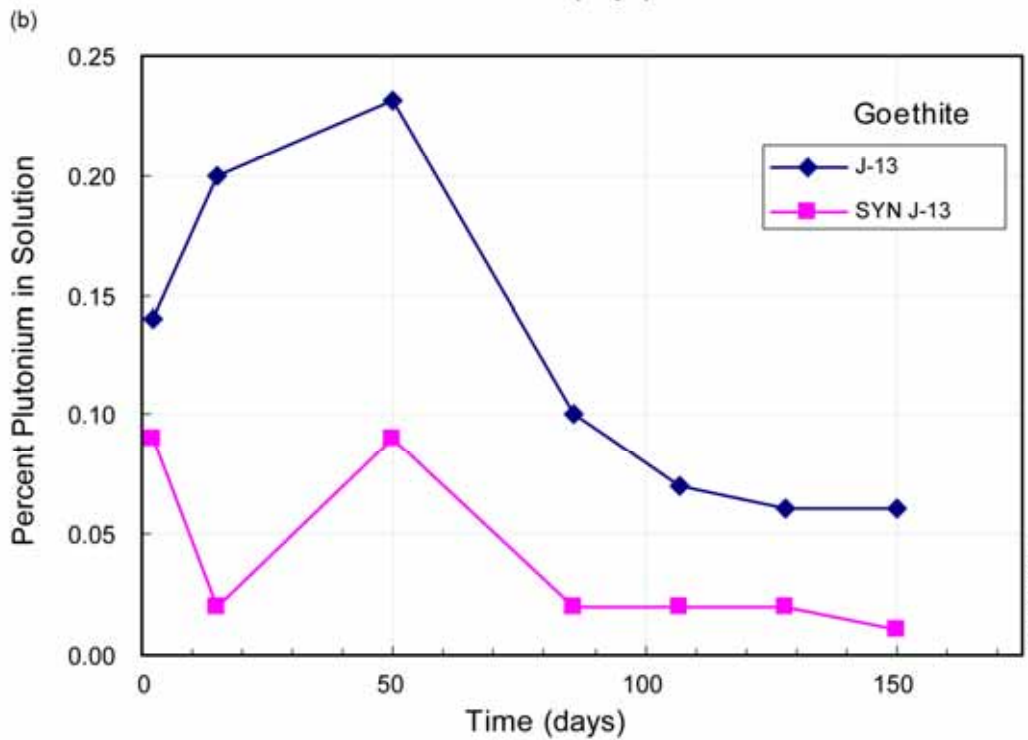
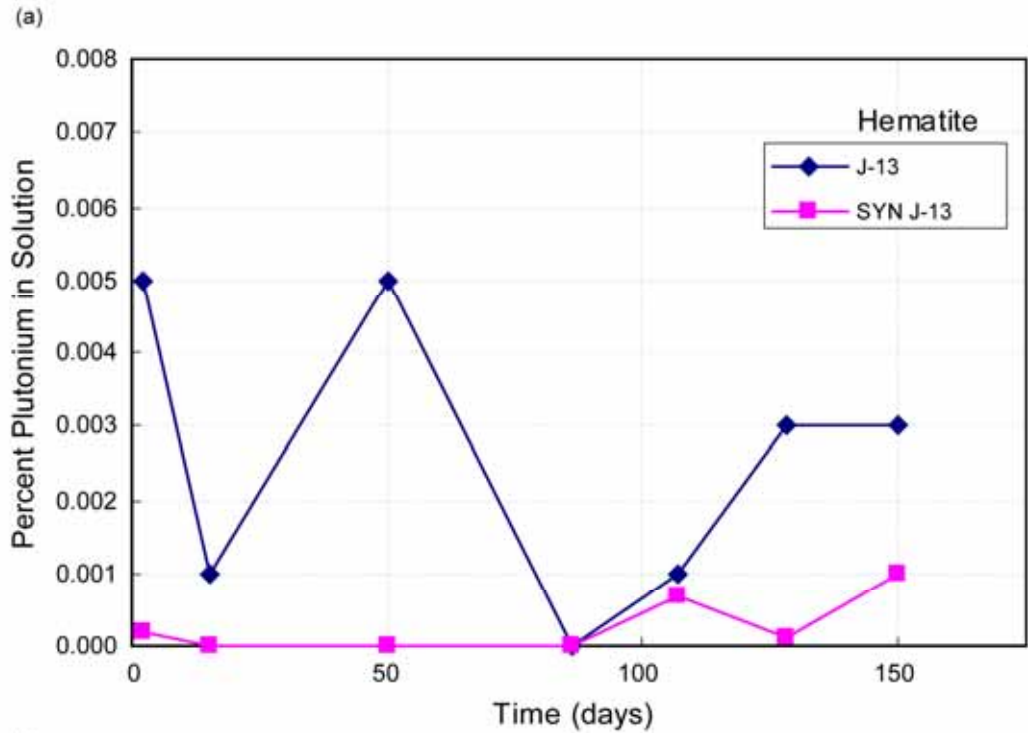
NOTE: The cumulative Pu desorbed was measured by successive extractions with J-13 or synthetic J-13 water.

Figure 6.6-9. Desorption of Pu from (a) Hematite and (b) Goethite

Table 6.6-7. Lu Data for Desorption of Pu(V) from Hematite and Goethite Colloids

Minerals	Time (days)	Cumulative % of Pu desorbed		Desorption K_d (mL g ⁻¹)	
		J-13	SYN.J-13	J-13	SYN.J-13
Hematite	2	0.005	0.0002	1.33×10^5	2.88×10^6
	15	0.006	0.0002	1.12×10^5	2.88×10^6
	50	0.011	0.0002	6.61×10^4	2.88×10^6
	86	0.011	0.0002	6.61×10^4	2.88×10^6
	107	0.012	0.0009	5.96×10^4	7.83×10^5
	128	0.015	0.0010	4.83×10^4	7.53×10^5
	150	0.018	0.0020	4.33×10^4	4.95×10^5
Goethite	2	0.14	0.09	5.18×10^4	8.12×10^3
	15	0.34	0.11	2.08×10^3	6.11×10^3
	50	0.57	0.20	1.24×10^3	3.32×10^3
	86	0.67	0.22	1.04×10^3	3.09×10^3
	107	0.74	0.24	9.49×10^2	2.81×10^3
	128	0.80	0.26	8.87×10^2	2.67×10^3
	150	0.86	0.27	8.41×10^2	2.60×10^3

Source: Lu et al. 1998 [DIRS 100946], Tables 10 and 11.



Source: DTN: SN0508T0507703.020 [DIRS 182215], spreadsheet *Pu sorption-desorption.xls*, worksheet "Desorp data, reinterpreted."

NOTE: Desorption data for hematite are near detection limits for the method, and are scattered. Data for goethite show an overall decrease in the amount in solution with time.

Figure 6.6-10. Reinterpretation of Lu et al. Desorption Data for (a) Hematite and (b) Goethite

Table 6.6-8. Reinterpretation of Lu et al. Data for Desorption of Pu(V) from Hematite and Goethite Colloids

Minerals	Time (days)	% of Pu in aqueous phase		Desorption K_d (mL g ⁻¹)	
		J-13	SYN.J-13	J-13	SYN.J-13
Hematite	2	0.005	0.0002	2.0×10^5	5.0×10^6
	15	0.001	0.0000	1.0×10^6	
	50	0.005	0.0000	2.0×10^5	
	86	0.000	0.0000		
	107	0.001	0.0007	1.0×10^6	1.4×10^6
	128	0.003	0.0001	3.3×10^5	1.0×10^7
	150	0.003	0.0010	3.3×10^5	1.0×10^6
Goethite	2	0.14	0.09	7.1×10^3	1.1×10^4
	15	0.20	0.02	5.0×10^3	5.0×10^4
	50	0.23	0.09	4.3×10^3	1.1×10^4
	86	0.10	0.02	9.9×10^3	5.0×10^4
	107	0.07	0.02	1.4×10^4	5.0×10^4
	128	0.06	0.02	1.7×10^4	5.0×10^4
	150	0.06	0.01	1.7×10^4	1.0×10^5

Source: DTN: SN0508T0507703.020 [DIRS 182215], spreadsheet *Pu sorption-desorption.xls*, worksheet "Desorp data, reinterpreted."

The long term increase in the proportion of Pu adsorbed in the goethite "desorption" experiments may be inconsistent with the single site K_d model, which would predict equilibrium, based on the rapid short term sorption data, in much shorter time intervals. However, desorption data cannot be uniquely interpreted. Each point represents the concentration in solution after 20 to 30 days of re-equilibration; however, it is not clear whether, during that particular extraction step, the concentration was still increasing, or decreasing, when the sample was taken. However, regardless of whether the sampled concentration represents a point on the "up" or the "down" part of the desorption curve, the measured value gets progressively smaller with time, and the rate at which this change occurs indicates that the plutonium is somehow being converted to a more stable form on the surface of the mineral.

Thus, both the sorption and desorption data suggest that two reactions or processes are occurring, leading to rapid uptake followed by slower stabilization of plutonium on the mineral surface, although no information on the form, or the resistance to remobilization, of the "stabilized" plutonium is available. If we assume that sorption is occurring onto two sites on the mineral surface, then this would imply some kinetic inhibition of sorption onto the higher affinity site. Eventually, however, most of the plutonium would transfer to the high affinity site.

Painter et al. (2002 [DIRS 174071]) fitted the LANL sorption data for plutonium using a two-site sorption model. Their model is a K_d model—forward and backward rate coefficients for sorption onto both sites are derived by fitting the experimental data, and the rate of mass transfer to and from the surface is only a function of the concentrations in solution and on the solid. The K_d value for each of the two sites can be calculated from the forward and backward rate coefficients. Therefore, the Painter et al. (2002 [DIRS 174071]) approach can be used to fit the goethite

sorption data from DTN: LA0004NL831352.001 [DIRS 150272], and the forward and backward rate constants for the fast and slow sorbing sites determined. These can be used to estimate the long-term equilibrium K_d value for plutonium sorption onto goethite.

The model assumes that there are two sorption sites available on the solid, and that the total amount of plutonium is small relative to the number of sites—that is, sorption is not site-limited. It is assumed that one site is a “fast” site, a lower affinity site that reaches equilibrium with the solution quickly and controls sorption in the short term. The other site is a “slow” site, a higher affinity site that only gradually reaches equilibrium with the solution. Different forward and backward rate constants are associated with mass transfer to and from the two sorption sites, and the rate constants are related by the K_d value that applies to each site. For the fast site:

$$k_f = k_r K_c C_c \quad (\text{Eq. 6.6.6.1-1})$$

where k_f (hr^{-1}) is the forward rate constant for the fast site, k_r (hr^{-1}) the reverse rate constant for the fast site, K_c (L g^{-1}), the partitioning coefficient for the fast site, and C_c (g L^{-1}), the substrate load in solution.

For the slow site:

$$\alpha = \beta K'_c C_c \quad (\text{Eq. 6.6.6.1-2})$$

where α (hr^{-1}) is the forward rate constant for the slow site, β (hr^{-1}) the reverse rate constant for the slow site, K'_c (L g^{-1}) the partitioning coefficient for the slow site, and C_c (g L^{-1}), is, again, the substrate load in solution.

The analytical solution describing the concentration in solution over time is as follows (Painter et al. 2002 [DIRS 174071], Equation 7):

$$X(t) = f(t) + \beta F(t) \quad (\text{Eq. 6.6.6.1-3})$$

where

$$f(t) = \frac{1}{2} e^{(b-a/2)t} + \frac{1}{2} e^{-(b+a/2)t} + \frac{1}{2b} \left(k_r - \frac{a}{2} \right) \left[e^{(b-a/2)t} - e^{-(b+a/2)t} \right]$$

$$F(t) = \frac{1}{2(b-a/2)} \left[e^{(b-a/2)t} - 1 \right] + \frac{1}{2(b+a/2)} \left[1 - e^{-(b+a/2)t} \right] + \frac{1}{2b} \left(k_r - \frac{a}{2} \right) \left\{ \frac{1}{b-a/2} \left[e^{(b-a/2)t} - 1 \right] - \frac{1}{b+a/2} \left[1 - e^{-(b+a/2)t} \right] \right\}$$

and

$$a \equiv k_f + k_r + \alpha + \beta$$

$$b^2 \equiv \frac{a^2}{4} - k_r \alpha - k_r \beta - k_f \beta$$

Note that the definition of b^2 given by Painter et al. (2002 [DIRS 174071]) is missing the final term; it has been corrected here. To solve the analytical solution, Painter et al. (2002 [DIRS 174071]) first make a simplifying assumption, that the fast sites have reached steady state once the sorption curves level out, and that the slow increase beyond that point is due to uptake by the slow sites. This allows the complex analytical solution (Equation 6.6.6.1-3) to be reduced to a simpler form (Painter et al. (2002 [DIRS 174071], equation 10) for the fraction of Pu adsorbed (ϕ), which only depends on two parameters, α and K_c :

$$\phi = \frac{K_c C_c}{1 + K_c C_c} + \frac{\alpha t}{(1 + K_c C_c)^2}. \quad (\text{Eq. 6.6.6.1-4})$$

In the Painter et al. (2002 [DIRS 174071]) approach, the last few data points in the sorption dataset are fitted using Equation 6.6.6.1-4 to estimate values for α and K_c . This was done using the Excel Solver add-in to optimize the fit to the data (see DTN: SN0508T0507703.020 [DIRS 182215], spreadsheet *Pu sorption-desorption.xls*, worksheet “2-site fit”). Then, the full analytical solution is fit, using the estimates for α and K_c from the longer-term data, and optimizing the fit on k_r and β , while holding $k_f = k_r K_c C_c$, and constraining $\alpha \geq \beta$, and all forward and backward rate constants greater than or equal to 0.

Once this has been done, K_c represents the short-term K_d , and K'_c , representing the slow site partitioning coefficient, can be calculated using:

$$K'_c = \frac{\alpha}{\beta C_c} \quad (\text{Eq. 6.6.6.1-5})$$

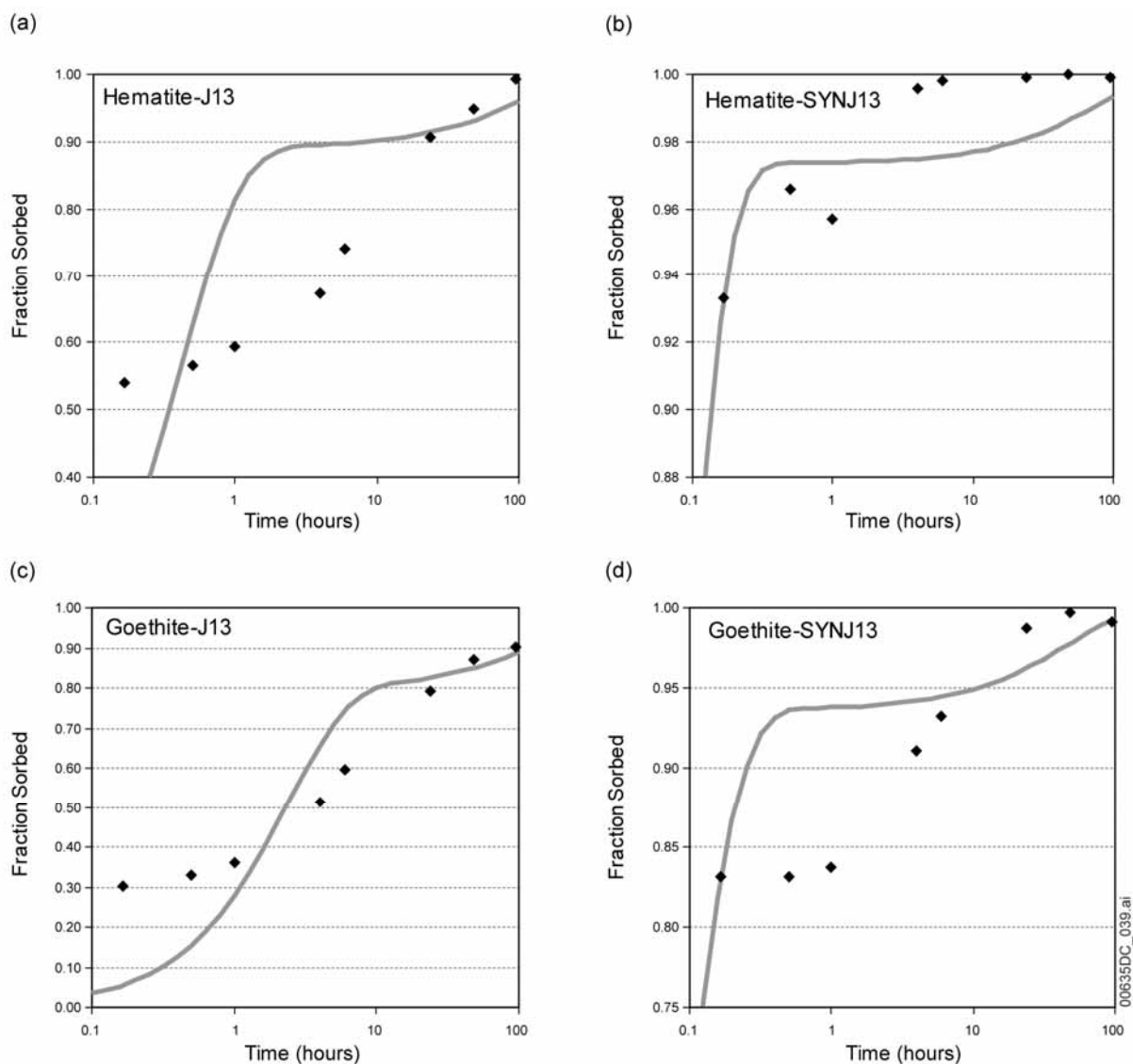
The long-term K_d value for plutonium sorption onto the substrate of interest is equal to the sum of K_c and K'_c . For the cases examined here, K'_c is much larger than K_c , and dominates the sorption behavior at long time intervals.

The Painter et al. (2002 [DIRS 174071]) method was used to evaluate the project data for plutonium sorption onto goethite and hematite in DTN: LA0004NL831352.001 [DIRS 150272]. The results are presented in Figure 6.6-11 and Table 6.6-9. The fits are poor, especially for the short-term data. They are also highly sensitive to the number of data points used in the first step, in which the longer-term data are fitted to determine α and K_c . The sorption data only extend out to 100 hours, and the few long-term points are insufficient to accurately constrain the values for α and K_c .

Because the long-term data are insufficient to constrain any of the fitting parameters, the Painter et al. (2002 [DIRS 174071]) method was applied a second time, using only Equation 6.6.6.1-3, and finding the best fit by adjusting all four rate parameters at once, subject only to the constraints that all rates are positive, and that forward rates must be larger than reverse rates (Table 6.6-10 and Figure 6.6-12). The data fits are much better using this method. There is considerable variability in the data, with hematite sorbing more rapidly and more completely than goethite, and both minerals sorbing more completely in the synthetic water relative to the natural J-13 water. The calculated K_c and K'_c values show these variations. The $(K_c + K'_c)$ values for

goethite are 1.1×10^4 and 1.3×10^5 mL g⁻¹, for J-13 and synthetic J-13, respectively. These are consistent with the K_d values determined from the desorption experiments of 1.7×10^4 and 1.0×10^5 mL g⁻¹, respectively (Table 6.6-8).

The reason for the variability in sorption K_d values between the J-13 and synthetic J-13 water is not known. Synthetic J-13 water was made by dissolving sodium carbonate and sodium bicarbonate in deionized water, and had a pH of 8.5, an ionic strength of 0.005 M, and an alkalinity of 22.5 meq L⁻¹. The natural J-13 water had a pH of 8.2, an ionic strength of 0.005 M, and an alkalinity of 22.5 meq L⁻¹, but also contained many other components, most notably 13 ppm Ca and 30 ppm silica. These differences in chemistry may account for the differences in plutonium sorption, and offer some indication of the sensitivity of sorption to water composition.



Source: Painter et al. 2002 [DIRS 174071].

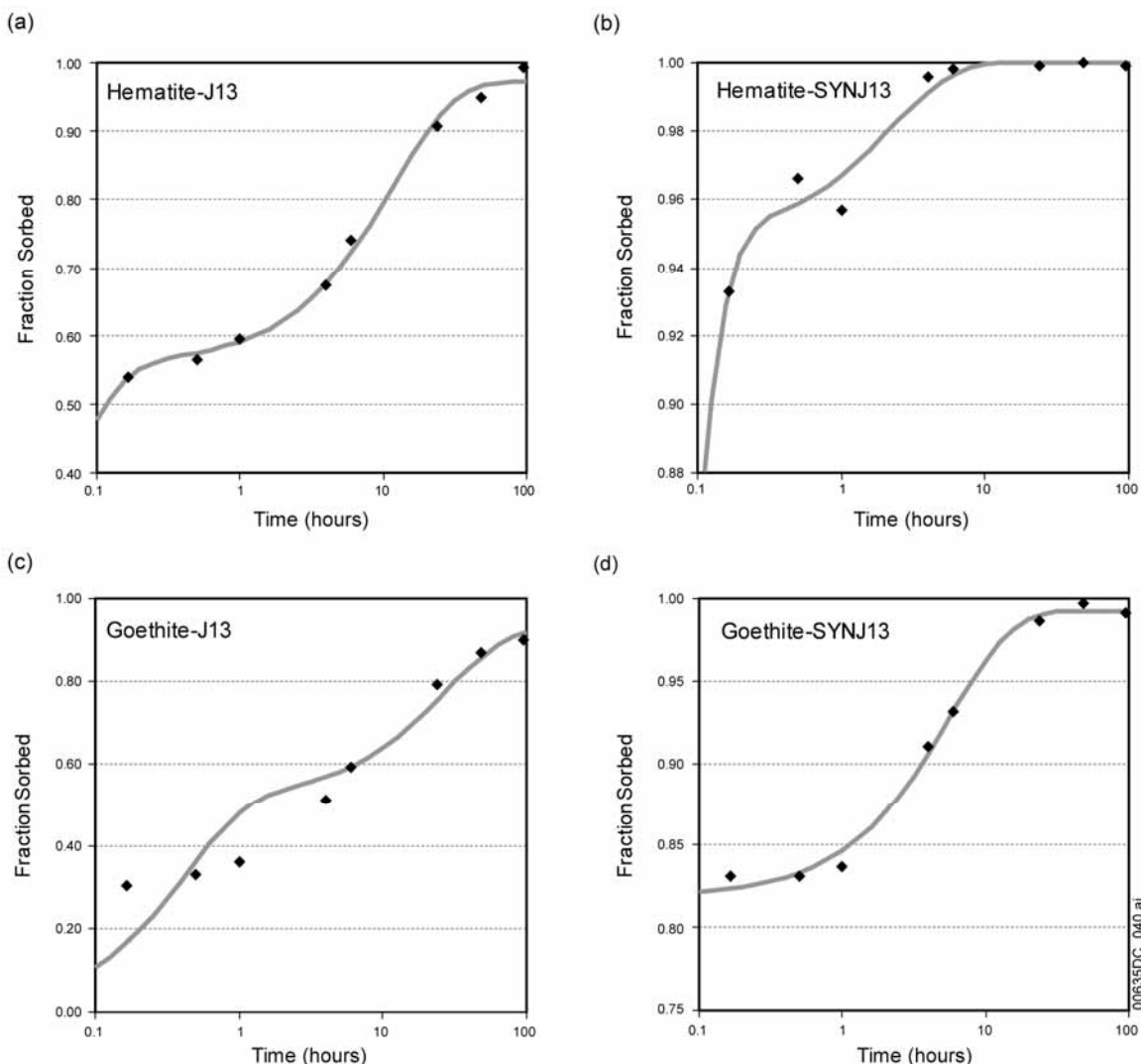
Figure 6.6-11. Two-Site Model of Painter et al. Fitted to Pu Sorption Data for Hematite and Goethite Using Two-Step Fitting Process.

Table 6.6-9. Fitting Pu Sorption Data of Lu et al. with the Two-Site Model of Painter et al.; Two Steps

Mineral	Water	C_c (g L ⁻¹)	k_f (hr ⁻¹)	k_r (hr ⁻¹)	α (hr ⁻¹)	β (hr ⁻¹)	K_c (mL/g)	K'_c (mL/g)
Hematite	J-13	0.99	2.08	0.272	0.0871	0.0	7.69×10^3	9.48×10^4
	Syn. J-13	0.85	18.0	0.515	0.508	0.0	4.12×10^4	∞
Goethite	J-13	1.11	0.313	0.0900	0.0279	0.0	3.12×10^3	4.02×10^4
	Syn. J-13	0.98	11.9	0.847	0.335	0.0	1.43×10^4	∞

Source: DTN: SN0508T0507703.020 [DIRS 182215], spreadsheet *Pu sorption-desorption.xls*, worksheet "2-site fit, best fit 2 par."

NOTE: Values of C_c are corrected from Lu et al. (1998 [DIRS 174714], Table 1) by multiplying by a factor of 20/21 to account for dilution when Pu-spiked water was added.



Source: Painter et al. 2002 [DIRS 174071].

Figure 6.6-12. Two-site Model of Painter et al. Applied to Pu Sorption Data for Hematite and Goethite, and Fitted in a Single Step

Table 6.6-10. Fitting Pu Sorption Data of Lu et al. Using the Two-Site Model of Painter et al., One Step

Mineral	Water	C_c (g L ⁻¹)	k_f (hr ⁻¹)	k_r (hr ⁻¹)	α (hr ⁻¹)	β (hr ⁻¹)	K_c (mL g ⁻¹)	K'_c (mL g ⁻¹)
Hematite	J-13	0.99	10.4	8.41	0.186	5.28×10^{-3}	1.25×10^3	3.43×10^4
	Syn. J-13	0.85	15.7	1.62	6.43	0.0	1.14×10^4	∞
Goethite	J-13	1.11	5.64	1.14	0.136	1.95×10^{-2}	8.97×10^2	1.10×10^4
	Syn. J-13	0.98	71.0	16.1	0.954	6.93×10^{-3}	4.49×10^3	1.36×10^5

Source: DTN: SN0508T0507703.020 [DIRS 182215], spreadsheet *Pu sorption-desorption.xls*, worksheet "2-site fit, best fit 4 par."

NOTE: Values of C_c are corrected from Lu et al. (1998 [DIRS 174714], Table 1) by multiplying by a factor of 20/21 to account for dilution when Pu-spiked water was added.

In three of the four cases, the two-site model fits the data very well; in the fourth, sorption onto goethite in J-13 water, the fit is poorer. In most of the cases, sorption onto the fast site appears to have reached, or nearly reached, steady state prior to collection of the first data point, 10 minutes after initiation of the experiment. However, the data still offer constraints on the sorption/desorption rate constants for the fast site, because the ratio of these values (divided by the mass of goethite in the system in g L⁻¹) is equal to the value of K_c , the fast site distribution coefficient (Equation 6.6.6.1-1). The value of K_c determines the concentration of the plateau in the first three data points for most of the data sets.

Given the small number of data points in each system (8) and the use of four fitting parameters the goodness of fit does not prove that a two-site model is correct; however, it does indicate that a model able to capture the complexities of multiple, heterogeneous processes at the mineral-solution interface is necessary to describe the behavior of plutonium sorption onto goethite and hematite. The data do not show the smoothly decaying exponential curve that sorption onto a single site would produce; instead, there appear to be at least two processes involved—rapid sorption followed by slow conversion into a less exchangeable form. In the case of the two-site model, this would be transfer into the higher-affinity site, but other processes, such as the Pu(V) reduction step described earlier, would yield the same results. These results, based on analysis of the sorption data, are entirely consistent with the experimental desorption results discussed earlier. Another method of evaluating the sorption rate data, and useful for checking against the model described above, is through use of the 'Elovich' rate formulation (Low 1960 [DIRS 174812]) which has been widely adopted in soil sciences (Sposito 1984 [DIRS 127253]; Chien and Clayton 1980 [DIRS 174705]; and Havlin et al. 1985 [DIRS 174706]). This equation has also been applied extensively to data relevant to chemisorption and is known for its accurate representation of rate data whether fast and slow kinetics are present (Low 1960 [DIRS 174812]). The Elovich equation as applied to sorption has the following form (Low 1960 [DIRS 174812]):

$$\frac{d\Gamma}{dt} = ae^{-\alpha\Gamma} \quad (\text{Eq. 6.6.6.1-6})$$

where Γ delineates the amount sorbed per unit area at time t , and α and a are constants. Integration of Equation 6.6.6.1-6 assuming $\Gamma = 0$ and $t = 0$ yields (Low 1960 [DIRS 174812]):

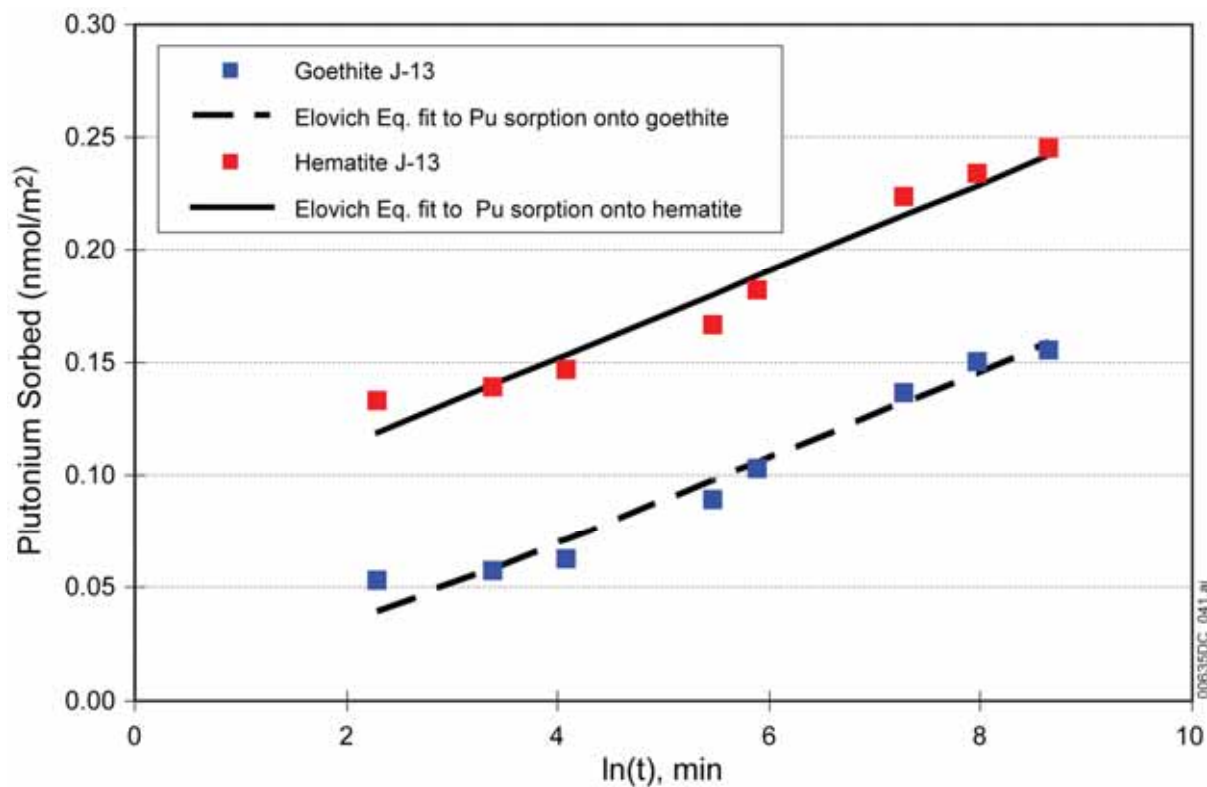
$$\Gamma = \frac{1}{\alpha} \ln(1 + a\alpha t) \quad (\text{Eq. 6.6.6.1-7})$$

Equation 6.6.6.1-7 can also be expressed as:

$$\Gamma = \frac{1}{\alpha} \ln(t + t_0) - \frac{1}{\alpha} \ln t_0 \quad (\text{Eq. 6.6.6.1-8})$$

where $t_0 = \frac{1}{(a\alpha)}$.

Fitting the plutonium sorption data for goethite and hematite (J-13 water only) from DTN: LA0004NL831352.001 [DIRS 150272] using the Elovich equation rate law (Figure 6.6-13) indicates very similar values for the α rate parameter. These rate data are only valid at pH~8. Overall, the model fit to the data is very good; both goethite and hematite have similar trends, and generate very similar rates. The values obtained for a and α for hematite are 0.88 and 51.5, respectively, while for goethite, the values are 0.01 and 51.78. It is assumed that the rate data extracted from these sources is taken as representative of forward rates for the formation of the predominant surface complex at this pH, $\text{SO}^- \text{-Pu}(\text{OH})_4$, as proposed by Sanchez et al. (1985 [DIRS 107213]). The equation was fitted only to the 'J-13' data; the 'SYN J-13' could not be fit because the early stage of sorption was not captured—83 to 93 percent sorbed in the first time step.



Source: DTN:LA0004NL831352.001 [DIRS 150272].

Figure 6.6-13. Kinetic Data for Pu Adsorption onto Hematite and Goethite at pH~8-8.5 Showing the Linear Fits to the Elovich Equation

Therefore, analysis of the LANL sorption-desorption experiments shows, using two approaches for the sorption and desorption data, that the long-term K_d values for plutonium sorption onto goethite, assuming that sorption is completely reversible, are on the range of 8,700 to 140,000 mL g⁻¹, for the chemical conditions examined. In some cases, these are minimum values, limited by the detection limits of the analysis.

6.7 DESCRIPTION OF BARRIER CAPABILITY

This section discusses the ability of barriers to prevent or delay the movement of water or radioactive materials and deals specifically with the features comprising the engineered barrier that are addressed in this report—the drip shield, the waste package, and the invert. In assessing these features, a number of assumptions are made (see Section 5).

The engineered barrier addressed in this report is subject to disruption under conditions assumed for the Seismic and Igneous Scenario Classes. Analyses and discussions presented in this report are confined to the Nominal Scenario Class. Disruption of barrier capability from volcanic processes may be found in *Atmospheric Dispersal and Deposition of Tephra from a Potential Volcanic Eruption at Yucca Mountain, Nevada* (SNL 2007 [DIRS 177431]), *Dike/Drift Interactions* (SNL 2007 [DIRS 177430]), and *Number of Waste Packages Hit by Igneous Intrusion* (SNL 2007 [DIRS 177432]). Disruption of barrier capability from seismic events may be found in *Seismic Consequence Abstraction* (SNL 2007 [DIRS 176828]) and *Characterize*

Framework for Seismicity and Structural Deformation at Yucca Mountain, Nevada (BSC 2004 [DIRS 168030]).

The drip shield prevents groundwater seepage that enters the drift from dripping onto the waste package. It will be completely effective until it is breached, and it is partially effective thereafter. Condensation on the underside of the drip shield has been screened out due to low consequence (DTN: MO0706SPAFEPLA.001 [DIRS 181613], FEP Number 2.1.08.11.0A). In this case, the presence of the drip shield can potentially increase the amount of water that contacts the waste package, but the effect is negligible. The RTA presents an algorithm to determine the fraction of seepage entering the drift that passes through a breached drip shield, based on the number and size of breaches (Section 6.3.2.4). In the case where no groundwater seepage or dripping of drift-wall condensation into the drift occurs, there will be no water flux through the drip shield. The flux of water into the waste package is equal to the groundwater and dripping condensation flux passing through the drip shield, less the fraction that is diverted by intact portions of the waste package. In this way, the effectiveness of the drip shield as a feature of the engineered barrier can be quantified.

The waste package outer corrosion barrier consists of corrosion-resistant material that will prevent and delay water from entering the waste package. Once breaches occur, water may enter the waste package, dissolve radionuclides, and flow out, thereby generating advective releases of radionuclides. (Although the waste package stainless steel inner vessel provides structural stability to the Alloy 22 outer barrier, no other performance credit is taken for the waste package inner vessel, and it is modeled as breaching quickly after the outer barrier is breached; (SNL 2007 [DIRS 178871]). The RTA presents an algorithm to determine the fraction of the water flux impinging on the waste package (having passed through drip shield breaches) that enters the waste package, depending on the size and number of breaches, as well as the total water flux through the waste package (Section 6.3.3.3). Flow is modeled as steady state and passing through the waste package with no change in the amount of water hold-up inside the waste package. Submodels not detailed in this report provide the concentration of radionuclides that are dissolved in the water flowing through the waste package (SNL 2007 [DIRS 177418]) and the behavior of colloids (BSC 2005 [DIRS 177423]). Advective and diffusive transport of radionuclides from breached waste packages is limited by sorption of radionuclides onto steel internal component corrosion products; sorption and retardation characteristics of radionuclides inside the waste package are discussed in this report (Section 6.3.4.2). When there is no advective transport, diffusive releases may still occur; a submodel for diffusion inside the waste package is presented (Section 6.3.4.3). With these models implemented in the TSPA, the effectiveness of the waste package as a feature of the engineered barrier can be quantified with respect to radionuclide transport.

The invert consists of crushed tuff that can delay releases of radionuclides to the UZ. The invert limits diffusive transport of radionuclides out of the engineered barriers by maintaining unsaturated conditions under the waste package. The invert limits advective and diffusive transport of radionuclides by sorbing radionuclides onto crushed tuff. A simple model for computing the diffusion coefficient of the invert as a function of the porosity and water saturation is presented in this report (Section 6.3.4.1). This enables the effectiveness of the invert as a feature of the engineered barrier to be quantified when implemented in TSPA.

7. VALIDATION

Model validation for the *EBS Radionuclide Transport Abstraction* was performed in accordance with SCI-PRO-002, *Planning for Science Activities*, and SCI-PRO-006, *Models*, and follows the validation guidelines in the *Technical Work Plan for: Near-Field Environment: Engineered Barrier System: Radionuclide Transport Abstraction Model Report* (BSC 2006 [DIRS 177739]). References in the TWP to Bechtel-SAIC Company procedures (LP-2.29Q-BSC, *Planning for Science Activities*, and LP-SIII.10Q-BSC, *Models*) have been updated to their corresponding Lead Lab procedures (SCI-PRO-002 and SCI-PRO-006, respectively) in this section.

SCI-PRO-006, *Models*, requires that TSPA model components be validated for their intended purpose and stated limitations, and to the level of confidence required by the relative importance of the component to the potential performance of the repository system. Two levels of model validation are defined in SCI-PRO-002, *Planning for Science Activities*, Attachment 3. Level I validation is for models of lower relative importance and Level II for models of higher relative importance to the estimated performance of the repository system.

The levels of confidence required for the models of the RTA, as stated in Section 2.2.2 of the TWP, are given as follows:

- The required level of confidence for the EBS flow model is Level I, based on the low level of importance to the estimate of mean annual dose in *Risk Information to Support Prioritization of Performance Assessment Models* (BSC 2003 [DIRS 168796], Section 4.6).
- The required level of confidence for radionuclide transport from the waste package to the drift wall through the invert is Level I, based on the low level of importance to the estimate of mean annual dose (BSC 2003 [DIRS 168796], Section 4.6). However, this is overridden by the required level of confidence for the overall EBS transport model being Level II (BSC 2005 [DIRS 174695], p. 6), due to the potentially high impact on total probability-weighted system dose of sorption onto corrosion products with the waste package.
- The EBS-UZ interface model of the RTA provides input to the unsaturated zone radionuclide transport model as described in *Particle Tracking Model and Abstraction of Transport Processes* (SNL 2007 [DIRS 181006]). The appropriate level of confidence identified for unsaturated zone radionuclide transport is Level II (BSC 2003 [DIRS 168796], Section 4.7). Therefore, Level II also represents the appropriate level of confidence for the EBS-UZ interface model of the RTA.

The following submodels were modified in the current version (REV 03) of the RTA, requiring revision of their validation:

- Water vapor adsorption isotherms, developed in Sections 6.3.4.3.2 and 6.3.4.6, used in the in-package diffusion submodel to estimate water saturation under no-seep conditions as a function of relative humidity for corrosion products and CSNF degradation rind

- Temperature dependence of diffusion coefficient, now applied to the entire EBS, rather than to the invert alone
- Radionuclide competitive surface complexation model used to compute the amount of sorption onto stationary corrosion products inside a breached waste package as a function pH and P_{CO_2} .

Although the EBS-UZ interface model was not revised in RTA REV 03, the UZ transport model with which it interfaces, *Particle Tracking Model and Abstraction of Transport Processes* (SNL 2007 [DIRS 181006]), along with the input hydrologic parameters used in the model, have been revised. Therefore, the model is revalidated in RTA REV 03 to be consistent with the revised UZ transport model.

Confidence Building During Model Development to Establish Scientific Basis and Accuracy for Intended Use

For Level I validation, SCI-PRO-002, Attachment 3, provides guidance for documenting a discussion of decisions and activities for confidence building during model development. Additionally, the development of the model will be documented in accordance with the requirements of Section 6.3.1(E) of SCI-PRO-006. The development of the RTA model has been conducted according to these requirements, and the requisite criteria have been met as discussed below:

1. *Selection of input parameters and/or input data, and a discussion of how the selection process builds confidence in the model [SCI-PRO-006, Attachment 2 (6)].*

The inputs to the RTA have been obtained from appropriate sources as described in Section 4.1. All the data are qualified project data developed by or for the Yucca Mountain Project. Tables 4.1-1 through 4.1-23 describe the input parameters, values of the parameters, and source of the information. Inputs were selected because they are expected to represent conditions at the repository and therefore build confidence in the model. Thus, this requirement can be considered satisfied.

2. *Description of calibration activities, initial boundary condition runs, run convergences, simulation conditions set up to span the range of intended use and avoid inconsistent outputs, and a discussion of how the activity or activities build confidence in the model. Inclusion of a discussion of impacts of any non-convergence runs [SCI-PRO-006, Attachment 2 (6)].*

A detailed discussion of the computational implementation of the RTA is described in Section 6.5.2. The discretization and development of the computational cell network of the sub-model domains is described in Section 6.5.2.5. Section 6.5.2.6 provides special emphasis and a discussion of the EBS-UZ boundary condition. Simulation conditions account for both seepage or no seepage boundary conditions, and the flux-splitting algorithm accounts for the eight key flow pathways in the engineered barrier system. Discussion about non-convergence runs is not relevant for this model report. Thus, this requirement can also be considered satisfied.

3. *Discussion of the impacts of uncertainties to the model results including how the model results represent the range of possible outcomes consistent with important uncertainties [SCI-PRO-006, Attachment 2 (6)].*

Data uncertainty and parameter uncertainty are addressed in Section 6. In particular, corrosion rates of carbon and stainless steels are listed as model input with ranges and distributions determined from the data in Table 4.1-1. Sorption coefficient distribution ranges and sampling correlations are described in Section 6.5.2.4. Tables 4.1-1 and 4.1-9 provide uncertainty for unsaturated zone parameters. The breached drip shield experimental test data in Tables 4.1-2 through 4.1-6 and Figure 4.1-1 are evaluated in Section 6.5.1, resulting in uncertain model input parameters (Flux_Split_DS_Uncert and Flux_Split_WP_Uncert).

Model uncertainty is addressed through the evaluation of alternative conceptual models. In considering alternative conceptual models for radionuclide release rates and solubility limits (Sections 6.4. and 6.6), the EBS radionuclide transport abstraction uses models and analyses that are sensitive to the processes modeled for both natural and engineered systems.

Conceptual model uncertainties are defined and documented, and effects on conclusions regarding performance are assessed. The fundamental relationships, (e.g., mass balance and flow equations) upon which the RTA is based are well-established with a long history of use in the scientific community and, as such, are not subject to significant uncertainty. In addition, the alternative conceptual models have been screened out (Section 6.4), thereby increasing confidence in the selected conceptual model. Other sources of uncertainty involve modeling choices (e.g., assumptions, geometry) that effectively bound uncertainty. Therefore, this requirement can be considered satisfied.

4. *Formulation of defensible assumptions and simplifications [SCI-PRO-002, Attachment 3, Level I (2)].*

A discussion of assumptions is provided in Section 5. The conceptual model for RTA is documented in Section 6.3.1, and the simplifications necessary for implementation based on EBS design details and failure mechanisms are presented in Sections 6.3.3 and 6.3.4. Thus, this requirement can also be considered satisfied.

5. *Consistency with physical principles, such as conservation of mass, energy, and momentum [SCI-PRO-002, Attachment 3, Level I (3)].*

Consistency with physical principles is demonstrated by the development of the mass balance mathematical formulations in Section 6.5.1. Thus, this requirement can also be considered satisfied.

Confidence Building after Model Development to Support the Scientific Basis of the Model

Level II validation includes the above Level I criteria and two post-development model validation methods described in Section 6.3.2 of SCI-PRO-006, *Models*, consistent with a model of higher relative importance to the estimated performance of the repository system.

Although the TWP specifies Level I validation for the EBS flow model, the flux splitting submodel is validated to Level II by means of corroboration of model results with data acquired from the laboratory not previously used to develop or calibrate the model in Section 7.1.1. The EBS transport model is corroborated with information published in refereed journals and literature. The EBS-UZ interface model is corroborated with other model results developed for similar use.

To build further confidence in the RTA, a critical review was conducted as specified by the TWP (BSC 2006 [DIRS 177739], Sections 2.2.3 and 2.2.4) for the EBS flow model, EBS transport model, and EBS-UZ interface model. This approach is based on requirements of SCI-PRO-006, Section 6.3.2), where critical review is listed as an appropriate method for model validation. Validation is achieved if the review determines that the questions/criteria for this model, listed in Section 2.2.4 of the TWP, are met. Qualifications of and review tasks to be completed by the critical reviewer are described in Section 2.2.4 of the TWP. The model validation criteria are described in the following paragraphs (BSC 2006 [DIRS 177739], Section 2.2.4).

EBS Flow Model Validation Criteria

Criteria that the validation of the EBS flow model is met are as follows. Each shall be confirmed by the critical reviewer.

- a. The approach and algorithms described in the document and provided to the TSPA capture all known flow pathways into and from EBS components.
- b. Modeling assumptions are clearly defined, discussed, and justified as appropriate for the intended use of the model.
- c. Uncertainties in parameters, processes, and assumptions are sufficiently described, and impacts of these uncertainties are discussed.
- d. The overall technical credibility of the approach, including assumptions, parameters, equations, and the TSPA implementation, are sufficient for the model's intended use.

EBS Transport Model Validation Criteria

Criteria that the validation of the EBS transport model is met are as follows. Each shall be confirmed by the critical reviewer.

- a. The approach and algorithms described in the document and provided to TSPA address all known modes of radionuclide transport within and from the EBS components.

- b. Modeling assumptions are clearly defined, discussed, and justified as appropriate for the intended use of the model.
- c. Uncertainties in parameters, processes, and assumptions are sufficiently described, and impacts of these uncertainties are discussed.
- d. The overall technical credibility of the approach, including assumptions, parameters, equations, and the TSPA implementation, are sufficient for the model's intended use.
- e. The data used for and the results of the corrosion product sorption model are consistent with, and corroborated by information published in refereed journals and literature.

EBS-UZ Interface Model Validation Criteria

The criterion that the validation of the EBS-UZ interface model is met shall consist of concurrence by a critical reviewer that the results obtained using this model compare favorably with the results of dual continuum near field UZ flow modeling using TOUGH2 V1.6 (2003 [DIRS 161491]) and transport modeling using T2R3D V1.4 (1999 [DIRS 146654]). Results of the comparison shall show qualitative agreement between the two methods and also demonstrate that the EBS-UZ interface model provided to the TSPA does not underestimate radionuclide transport from the EBS to the UZ.

The results of the critical review for the flow and transport models demonstrate that the appropriate criteria from above have been met and are presented in Section 7.2.4. The results of the EBS-UZ interface model review demonstrate that the appropriate criteria listed above have been met and are presented in Section 7.3.2.

The validation guidelines in the TWP (BSC 2006 [DIRS 177739]) also state that the Subject Matter Expert (author) may elect, as deemed appropriate, to provide additional validation in accordance with Section 6.3.2 of SCI-PRO-006, *Models*, in the form of:

- Corroboration of model results with data previously acquired from laboratory experiments or other relevant observations
- Corroboration of model results with results of alternative models
- Corroboration with information published in refereed journals or literature.

In addition to the critical review, the post development model validation for the EBS-UZ interface model, as delineated in the TWP, includes corroboration by comparison to an alternative mathematical model developed for a closely comparable description of the relevant EBS-UZ features. This validation approach is consistent with Section 6.3.2 of SCI-PRO-006, *Models*, which lists corroboration of results with alternative mathematical models as one of the validation methods for Level II validation. This comparison is documented in Section 7.3.1.

Additional validation of the flux-splitting portion of the flow model was performed through corroboration of model results of experimental data. The results of that validation exercise are presented in Section 7.1.1.

Additional validation of the in-package diffusion portion of the transport model was performed through corroboration with alternative models. The results of that validation exercise are presented in Section 7.2.

7.1 EBS FLOW MODEL

The EBS flow is modeled as a one-dimensional, steady advective flow through the components of the EBS. The sources of flow to the model include a seepage flux from the roof of the drift, condensation on the walls of the drift above the drift shield, and an imbibition flux from the unsaturated zone into the crushed tuff invert. The output of the flow model includes an advective flux from the invert into the unsaturated zone.

The conceptual model divides the EBS components into three domains: waste form, waste package corrosion products, and the invert. Flow and transport in these domains are treated separately. The output of the waste form domain feeds into the corrosion products domain. The output of the corrosion products domain in turn feeds the invert.

The flow through the EBS may occur along eight pathways: (1) total dripping flux (seepage inflow from the crown of the drift plus any condensation that may occur on the walls of the drift above the drift shield), (2) flux through the drip shield, (3) diversion around the drip shield, (4) flux through the waste package, (5) diversion around the waste package, (6) total flux into the invert, (7) imbibition flux from the unsaturated zone matrix to the invert, and (8) flux from the invert to the unsaturated zone fractures.

The magnitude of seepage fluid passing through the drip shield and waste package is accounted for using the flux-splitting submodel. This submodel determines how much water flows through the drip shield or waste package and how much is diverted around these components. Below is the validation of the submodel and validation criteria for both the drip shield and waste package applications. Further discussions relevant to the validation of the flow model can be found in Sections 5, 6.3.2, 6.3.3, 6.5.1.1.1, 6.5.1.1.2, and 6.5.1.1.3.

7.1.1 Flux-Splitting Submodel

The EBS flux-splitting submodel, which is part of the RTA flow model, determines the fraction of total dripping flux that will flow through the drip shield and/or waste package. This submodel is directly related to the waste isolation attribute (i.e., the limited release of radionuclides from engineered barriers). The amount of water flowing through engineered barriers, when combined with radionuclide solubility limits and diffusive transport, defines the mass flux of radionuclides that is mobilized for transport through the EBS to the unsaturated zone.

Level I validation is appropriate for the flux-splitting submodel because it is part of the process for radionuclide transport from waste package to the drift wall through the invert (Section 7). In addition, the flux-splitting submodel has the following features:

- The submodel is not extrapolated over large distances, spaces, or time.
- The submodel has large uncertainties because of the chaotic nature of the flow of droplets or rivulets on corroded, roughened surfaces.
- Sensitivity analyses in the prioritization report, *Risk Information to Support Prioritization of Performance Assessment Models* (BSC 2003 [DIRS 168796], Sections 3.3.6 through 3.3.11) show that the flux-splitting abstraction will not have a large impact on dose in the first 10,000 years.
- The flux-splitting submodel is used in TSPA-LA for those modeling cases where the waste packages breach by general corrosion over a period of time. The general corrosion patches typically appear after 10,000 years, and thus, only the long-term (million year) simulations are likely to incorporate the effects of flux-splitting submodel. More specifically, only the Nominal Scenario Class modeling case and the Seismic Scenario Class ground motion modeling case, with simulated duration of million years, would use the results from the flux-splitting submodel as the waste packages breach by general corrosion patches. In other modeling cases, where early failure of waste package or drip shield is considered or where the igneous intrusion is modeled, the damage to the drip shields and waste packages are stylized to damage the entire area. The flux-splitting submodel is not used for the drip shields in TSPA-LA because the drip shields are modeled either to be all intact or all failed, either from general corrosion or by the disruptive events. For the waste packages, the breach by general corrosion patches typically occurs much later than the appearance of the stress corrosion cracks, and most of the initial mass may be depleted via diffusion through the cracks.

This flux-splitting submodel is validated through comparison to experimental data. A work plan entitled *Test Plan for: Atlas Breached Waste Package Test and Drip Shield Experiments* (BSC 2002 [DIRS 158193]) defines the experiments used for validation of this flux-splitting submodel.

The flux-splitting submodel is applied to two components of the EBS—the drip shield and the waste package—and is validated for each. Validation is achieved through comparison of the models developed in this document (based in part on the qualified experimental data) to other qualified data collected during associated testing. This comparison is limited because the validation experiments are based on flow measurements from a single fixed source for dripping, whereas the abstraction is based on randomly located drips relative to multiple patches on the drip shield. In this situation, the appropriate criterion for model validation is that the ranges of predictions of the abstraction, based on smooth drip shield mock-up surface data, overlap the ranges of experimental measurements made on the rough drip shield mock-up surface. This criterion is appropriate because of the large spread of the experimental data.

The rough drip shield surface experiments replicate the smooth drip shield surface experiments and constitute a consistent set of data that can be compared with and serve as validation for the smooth drip shield surface data. The rough surface would be expected to yield results (specifically, the flux splitting uncertainty factors) that differ from those obtained for the smooth surface. However, because the only difference in the experiments is the surface texture, the

trends in the data and values obtained for the uncertainty factors should be similar, which validates the flux-splitting submodel.

Experimental data used to develop the flux-splitting submodel include the splash radius, rivulet spread distance or angle, and fraction of dripping flux that flowed into breaches. For the drip shield and waste package flux-splitting submodels, data from smooth drip shield experiments were used (DTNs: MO0207EBSATBWP.022 [DIRS 163400]; MO0207EBSATBWP.023 [DIRS 163402]; MO0207EBSATBWP.024 [DIRS 163401]; MO0207EBSATBWP.025 [DIRS 163403]). For validation of the models, data from the rough drip shield experiments are used (DTNs: MO0207EBSATBWP.021 [DIRS 163399]; MO0208EBSATBWP.027 [DIRS 163404]; and MO0208EBSATBWP.028 [DIRS 163405]). Each of the types of data used is discussed below, first for the drip shield submodel validation and then for the waste package flux-splitting submodel validation.

7.1.1.1 Drip Shield Flux Splitting Submodel

Splash radius data for dripping onto the crown of the rough drip shield surface are listed in Table 7.1-1. The data are analyzed in the Microsoft Excel spreadsheet: Flux Splitting Validation, Worksheet: Splash Rad vs Number, which is documented in Appendix E. As shown in Figure 7.1-1, the splash radius tends to increase as the number of drips increases. The inner cluster radius is of interest because it is used to define the effective length of the drip shield in developing the flux-splitting submodel (Section 6.5.1.1.2). While the data do not indicate that a maximum splash radius was achieved, it stands to reason that a maximum must exist, simply because the distance a splashed droplet can travel is finite, limited by the kinetic energy of a falling drop. The uncertain parameter in the drip shield flux-splitting submodel, f'_{DS} , was based on the maximum splash distance observed for the inner cluster of droplets on a smooth drip shield, 48 cm (see Section 6.5.1.1.2.4 for a discussion of the development of f'_{DS} based on the 48-cm maximum inner cluster splash radius). For the rough drip shield tests, the maximum inner cluster splash radius for dripping onto the crown was again 48 cm. Another approach is to use the splash radius at which rivulets begin to flow from coalesced droplets. In Splash Radius Test #1, rivulet flow began after 143 drips; in Test #2, after 145 drips; and in Test #3, after 133 drips (DTN: MO0207EBSATBWP.021 [DIRS 163399]), for an average of 140 drips. Using the Microsoft Excel Trendline application (least squares fitting routine) for the inner cluster data in Figure 7.1-1, the splash radius when rivulets began to flow was 31 cm. The minimum splash radius was about 3.5 cm for more than 20 drips (Table 7.1-1). The range of uncertainty is bounded using the extreme values of splash radius (3.5 cm to 48 cm). Since the value of splash radius at which rivulets begin to flow (31 cm) is between those extremes, an estimate of uncertainty based on that value will not affect the estimated bounds on uncertainty.

The flux-splitting submodel also depends on the rivulet spread angle. These data are analyzed in the Microsoft Excel spreadsheet: Flux Splitting Validation, Worksheet: Rough DS, which is documented in Appendix E. For the smooth drip shield, the spread angle from crown drip locations ranged from 8.9° to 17.3° (\pm one standard deviation from the mean of 13.2°; Section 6.5.1.1.2.4). For drip locations on the crown, the rough drip shield surface had a mean rivulet spread angle of 7.3°, with a range of 0° to 14.4° (\pm one standard deviation from the

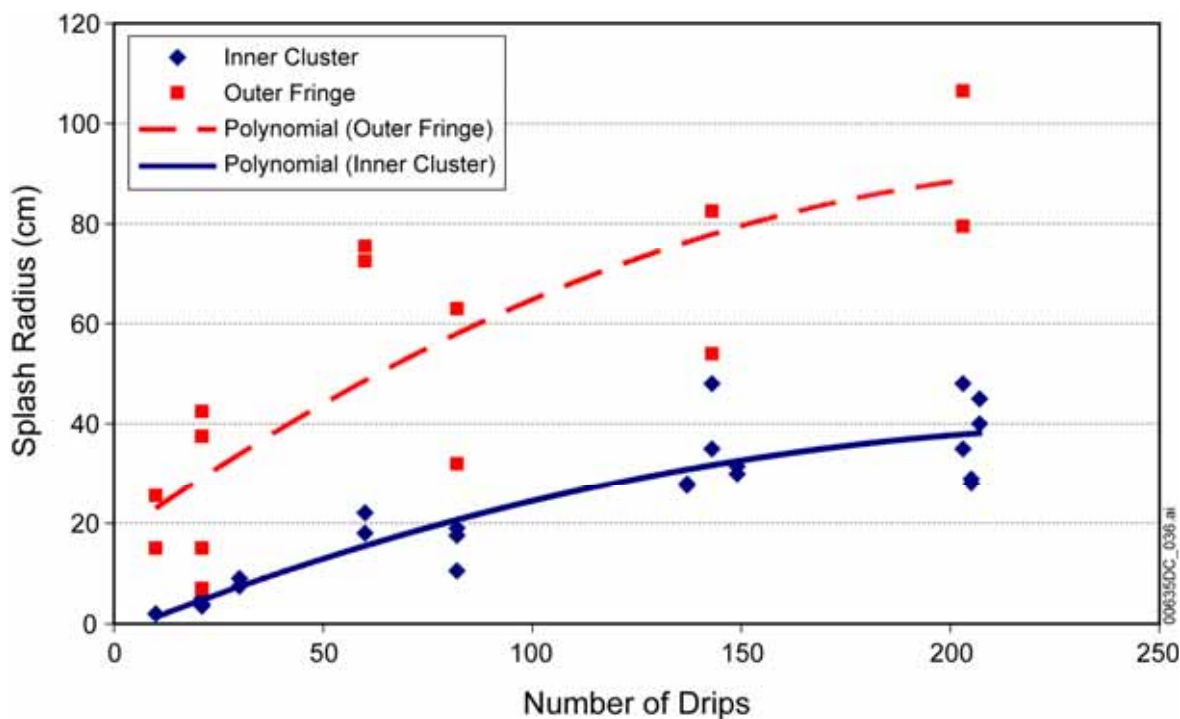
mean). Rivulet spread data for the rough surface are shown in Table 7.1-2. In Table 7.1-4, the spread angle calculation results are shown.

The amount of water dripped onto the crown and the water flow into breaches on the rough drip shield surface are listed in Table 7.1-3. The fraction of the dripping flux that flowed into the pertinent breach, f_{expt} , is shown along with the rivulet spread angle for each particular test in Table 7.1-4.

Table 7.1-1. Atlas Breached Drip Shield Experiments on Rough Drip Shield Surface – Dripping on Crown – Splash Radius Tests

No. Drips	Splash Radius (cm)		Comments
	Left	Right	
Splash Radius Test #1			
10	2.0	2.0	Measured inner cluster (bulk)
10	15.0	25.5	Measured outer fringe
21	5.0	4.0	Measured inner cluster (bulk)
21	15.0	42.5	Measured outer fringe
60	18.0	22.0	Measured inner cluster (bulk)
60	72.5	75.5	Measured outer fringe
143	35.0	48.0	Measured inner cluster (bulk)
143	54.0	82.5	Measured outer fringe
203	35.0	48.0	Measured inner cluster (bulk)
203	79.5	106.5	Measured outer fringe
Splash Radius Test #2			
21	3.5	4.0	Measured inner cluster (bulk)
21	37.5	7.0	Measured outer fringe
82	10.5	19.0	Measured inner cluster (bulk)
82	63.0	32.0	Measured outer fringe
149	31.5	30.0	Measured inner cluster (bulk)
207	45.0	40.0	Measured inner cluster (bulk)
Splash Radius Test #3			
30	7.5	9.0	Measured inner cluster (bulk)
82	19.0	17.5	Measured inner cluster (bulk)
137	28.0	27.5	Measured inner cluster (bulk)
205	29.0	28.0	Measured inner cluster (bulk)

Source: DTN: MO0207EBSATBWP.021 [DIRS 163399].



Source: Output DTN: SN0703PAEBSRTA.001, file *Flux Splitting Validation - 09-03-2004.xls*, worksheet "Splash Rad vs Number"

Figure 7.1-1. Splash Radius Dependence on Number of Drips for Rough Drip Shield Tests

Table 7.1-2. Atlas Breached Drip Shield Experiments on Rough Drip Shield Surface – Dripping on Crown – Rivulet Spread Data – 33° from Crown

Drip Location	Left (cm)	Right (cm)	Relevant Patch
Multiple Patch Tests (DTN: MO0208EBSATBWP.027 [DIRS 163404])			
81 cm left of drip shield center	32.5	17.5	4
27 cm left of drip shield center	21.5	18.0	4
27 cm right of drip shield center	10.0	10.0	5
27 cm right of drip shield center	1.0	0	5
81 cm right of drip shield center	17.0	34.0	5
Bounding Flow Rate Tests (DTN: MO0208EBSATBWP.028 [DIRS 163405])			
54 cm left of drip shield center (High Flow Rate)	2	0	4
27 cm left of drip shield center (High Flow Rate)	15	15	4
27 cm right of drip shield center (High Flow Rate)	6	6	5
27 cm right of drip shield center (Low Flow Rate)	50.0	16.0	5
27 cm right of drip shield center (Low Flow Rate)	—	1.0	5
27 cm left of drip shield center (Low Flow Rate)	25.5	12.0	4
54 cm left of drip shield center (Low Flow Rate)	0	0	4

Table 7.1-3. Atlas Breached Drip Shield Experiments on Rough Drip Shield Surface – Dripping on Crown – Flow into Breaches

Drip Location	Drip Location Relative to:		Water Input (g)	Water Collected in:	
	Breach B4 (cm)	Breach B5 (cm)		Breach B4 (g)	Breach B5 (g)
Multiple Patch Tests (DTN: MO0208EBSATBWP.027 [DIRS 163404])					
81 cm left of drip shield center	-27	-135	292.35	0.27	0.00
27 cm left of drip shield center	27	-81	288.45	5.27	0.00
27 cm right of drip shield center	81	-27	291.62	0.00	0.08
27 cm right of drip shield center	81	-27	294.13	0.00	0.27
81 cm right of drip shield center	135	27	290.10	0.00	1.01
Bounding Flow Rate Tests (DTN: MO0208EBSATBWP.028 [DIRS 163405])					
54 cm left of drip shield center (High Flow Rate)	0	-108	330.74	193.87	0.00
27 cm left of drip shield center (High Flow Rate)	27	-81	328.65	0.63	0.00
27 cm right of drip shield center (High Flow Rate)	81	-27	306.65	0.00	0.35
27 cm right of drip shield center (Low Flow Rate)	81	-27	545.14	0.00	11.11
27 cm right of drip shield center (Low Flow Rate)	81	-27	70.80	0.00	0.39
27 cm left of drip shield center (Low Flow Rate)	27	-81	113.32	1.36	0.00
54 cm left of drip shield center (Low Flow Rate)	0	-108	118.10	0.00	0.00

Table 7.1-4. Atlas Breached Drip Shield Experiments on Rough Drip Shield Surface – Dripping on Crown – Fraction of Dripping that Flowed into Breaches and Rivulet Spread Angle

Drip Location	Breach Collecting Flow	f_{expt}	Spread Angle (degree)	
			Left	Right
81 cm left of drip shield center	4	0.0018	13.4	7.3
27 cm left of drip shield center	4	0.0365	9.0	7.5
27 cm right of drip shield center	5	0.0005	6.6	6.6
27 cm right of drip shield center	5	0.0018	0	0.7
81 cm right of drip shield center	5	0.0070	11.2	21.6
54 cm left of drip shield center (High Flow Rate)	4	1.1723	0.8	0
27 cm left of drip shield center (High Flow Rate)	4	0.0038	6.3	6.3
27 cm right of drip shield center (High Flow Rate)	5	0.0023	4.0	4.0
27 cm right of drip shield center (Low Flow Rate)	5	0.0408	30.2	10.5
27 cm right of drip shield center (Low Flow Rate)	5	0.0110	—	0.7

Table 7.1-4. Atlas Breached Drip Shield Experiments on Rough Drip Shield Surface – Dripping on Crown – Fraction of Dripping that Flowed into Breaches and Rivulet Spread Angle (Continued)

Drip Location	Breach Collecting Flow	f_{expt}	Spread Angle (degree)	
			Left	Right
27 cm left of drip shield center (Low Flow Rate)	4	0.0240	10.6	5.0
54 cm left of drip shield center (Low Flow Rate)	4	0.0	0	0
Mean	—	0.108	7.25	
Standard Deviation	—	0.335	7.18	
Median	—	0.005	6.29	

Source: Microsoft Excel spreadsheet: Flux Splitting Validation, Worksheet: Rough DS, documented in Appendix E

NOTES: — = no measurement

Mean, standard deviation, and median for spread angle are for all (left and right) measurements.

Following the approach used in Section 6.5.1.1.2.4, the “inner cluster” splash diameter is used for the effective length of the drip shield in the validation of the flux-splitting algorithm, which is given by Equations 6.3.2.4-4 and 6.3.2.4-6 (or 6.5.1.1.2-35). The form of the equation is:

$$F = \frac{N_b \ell}{L_{DS}} \left(1 + \frac{\tan \alpha}{2} \right) f_{VD}, \quad (\text{Eq. 7.1.1.1-1})$$

where F is the fraction of dripping flux that flows through breaches, ℓ is one-half the width of a breach or patch, L_{DS} is the effective length of the drip shield (i.e., the length over which dripping or splattering occurs), α is the rivulet spread angle, and f_{VD} is the uncertainty factor for the drip shield developed for validation, corresponding to the drip shield uncertainty factor, f_{DS} . For the validation tests, the number of breaches, N_b , is one.

The splash diameter is used for the effective length, L_{DS} . As shown in Table 7.1-1, the “inner cluster” splash radius on the rough drip shield surface ranged from 3.5 cm to 48 cm (for more than 20 drops), giving a range for L_{DS} of 7 cm to 96 cm. The spread angle ranged (one standard deviation from the mean) from zero to 14.4°. For a drip shield patch width of 27 cm, $\ell = 13.5$ cm. Then, as shown in Table 7.1-5, $F / f_{VD} = \frac{N_b \ell}{L_{DS}} \left(1 + \frac{\tan \alpha}{2} \right)$ ranges from 0.141 to 2.17.

Table 7.1-5. Range of Estimates for F/f_{VD}

L_{DS} (cm)	Drip Shield F/f_{VD}	
	$\alpha = 0^\circ$	$\alpha = 14.4^\circ$
7	1.93	2.17
96	0.141	0.158

The fraction of dripping flux, f_{expt} , that entered breaches in 12 rough drip shield experiments ranged from zero to 1.17, with a mean of 0.108 and median of 0.0054. The wide range of uncertainty and randomness in the experiments is demonstrated in two of the tests having the same drip location (54 cm to the left of the drip shield center). The high drip rate test yielded the highest flow into a breach with a negligible spread, which is the expected result. What appears to be an unphysical result for this test, $f_{expt} = 1.17$, is obtained from the assumption that half of the dripping flux onto the crown flows down each side of the drip shield. This was evidently not the case in this particular test, since more than half of the dripping flux flowed into the breach. However, since there are no data available to determine what fraction of the dripping flux flowed down the side with the breach, the procedure for calculating f_{expt} is followed without limiting the values that are obtained (e.g., by limiting f_{expt} to a maximum of 1.0). The low drip rate test at the same drip location, which had zero rivulet spread, unexpectedly resulted in no flow into the breach. Statistics for f_{expt} are compared in Table 7.1-6 between the smooth drip shield surface experimental results (Table 6.5-2) and rough surface results discussed in this section.

Table 7.1-6. Comparison of f_{expt} Statistics for Smooth and Rough Drip Shield Surfaces

Experiments	Mean f_{expt}	Minimum f_{expt}	Maximum f_{expt}	Median f_{expt}
Drip Shield (Smooth Surface)	0.111	0.013	0.275	0.049
Drip Shield Validation (Rough Surface)	0.108	0.0	1.17	0.0054

The rough surface experimental results are now used to calibrate the drip shield flux-splitting submodel that is developed for validation purposes, yielding the uncertainty factor f_{VD} :

$$f_{VD} = \frac{f_{expt}}{\frac{\ell}{L_{DS}} \left(1 + \frac{\tan \alpha}{2} \right)} \quad (\text{Eq. 7.1.1.1-2})$$

f_{VD} is at a minimum using the minimum value for L_{DS} (7 cm) and the maximum value for α (14.4°), resulting in $f_{VD} = 0.46f_{expt}$. The maximum for f_{VD} is obtained using the maximum value for L_{DS} (96 cm) and minimum value for α (0°), resulting in $f_{VD} = 7.1f_{expt}$. Using the mean value for f_{expt} (0.108) results in a range for f_{VD} of 0.050 to 0.77. The drip shield flux-splitting algorithm developed in Section 6.5.1.1.2.4 produced the corresponding factor f_{DS} ranging from about 0.36 to 0.73. These factors (f_{VD} and f_{DS}) actually represent the estimates of the upper bound on the uncertainty, since a lower bound is necessarily zero (i.e., no flow through a breach). Using the actual measured range of f_{expt} (0.0 to 1.17) instead of the mean increases the range estimated for f_{VD} to 0.0 to $(7.1)(1.17) = 8.3$. The corresponding range for f_{DS} , using the measured range of f_{expt} (0.013 to 0.275) (Table 6.5-2) for the smooth surface tests instead of the mean (0.111), is $0.013/0.31 = 0.041$ (for $L_{DS} = 50$ cm, $\alpha = 17.3^\circ$) to $0.275/0.152 = 1.8$ (for $L_{DS} = 96$ cm, $\alpha = 8.9^\circ$). Thus, using the extreme values of f_{expt} for estimating f_{DS} and f_{VD} , the

upper bound on f_{VD} actually spans the uncertainty in the upper bound estimate of f_{DS} , as summarized in Table 7.1-7.

Table 7.1-7. Summary of f_{DS} and f_{VD} Values

	Based on Mean f_{expt}		Based on Minimum f_{expt}	Based on Maximum f_{expt}
	Minimum	Maximum	Minimum	Maximum
f_{DS}	0.36	0.73	0.041	1.8
f_{VD}	0.050	0.77	0	8.3

Based on mean values for the experimentally measured fraction of the dripping flux that flows through a breach, the rough drip shield surface factor shows that less of the dripping flux will flow through a breach, compared with the smooth surface results used to develop the drip shield flux-splitting submodel. The rough surface data validate the drip shield submodel by confirming an estimate of the upper bound on the uncertainty of 0.77, based on mean values for f_{expt} . The range on the estimate for f_{VD} is also about 0.7, which is comparable (about a factor of 2) to the uncertainty in f_{DS} . While the upper bound on the uncertainty factor is about the same for both the smooth and rough surfaces (0.73 vs. 0.77), the lower bound is much higher for the smooth surface (0.36 vs. 0.05). A random sampling from these ranges will give a mean value of about 0.54 for the smooth surface versus about 0.42 for the rough surface. So the smooth surface range will, on average, overestimate the flux through the drip shield compared to the rough surface range. Both the smooth surface and the rough surface results include a wide range of variability that is incorporated in the sampled uncertainty parameter f_{DS} for the drip shield flux-splitting submodel. The rough drip shield surface data provide confirmation that the drip shield submodel will generally overestimate the flux through that barrier.

A final comparison is made between f'_{DS} , which lumps the uncertainty in the rivulet spread angle into f_{DS} , and a corresponding parameter for the rough drip shield surface, f'_{VD} , is derived, where

$$f'_{VD} = \left(1 + \frac{\tan \alpha}{2}\right) f_{VD}. \quad (\text{Eq. 7.1.1.1-3})$$

Since α ranges from 0° to 14.4° , applying the maximum value for α will result in the range for f'_{VD} of 0 to 0.87, based on the mean value of f_{expt} (0.108) that gives a range of 0.050 to 0.77 for f_{VD} . For comparison, f'_{DS} was estimated to range from 0 to 0.85. The nearly identical ranges for f'_{DS} and f'_{VD} validate the drip shield flux-splitting submodel.

7.1.1.2 Waste Package Flux-Splitting Submodel

Whereas the drip shield flux-splitting submodel is based on data from dripping on the crown of the smooth drip shield mock-up surface, the waste package flux-splitting submodel is based on data from off-crown drip locations on the smooth drip shield mock-up surface. Off-crown drip

locations are used because the steeper slope on the mock-up surface at those locations simulates more closely the higher radius of curvature of the waste package compared with the drip shield (Section 6.5.1.1.3). Additionally, the drop distance to drip locations that are off the crown was greater than for drips on the crown (2.17 m to the crown, 2.22 m to the 16.5° line, and 2.31 m to the 33° line (BSC 2003 [DIRS 163406], p. 6), which more closely mimics the greater drop distance from the drift to the waste package compared with the drip shield surface. Consistent with the validation of the drip shield flux-splitting submodel, the validation of the waste package flux-splitting submodel is based on data from the rough drip shield mock-up surface, but for off-crown drip locations, to be consistent with the waste package flux-splitting submodel. Using off-crown drip location data for the rough waste package surface (Table 7.1-8), the rivulet spread angle was found to depend strongly on the drip rate. These data are analyzed in the Microsoft Excel spreadsheet: Flux Splitting Validation, Worksheet: Rough off crown WP model, which is documented in Appendix E. The high drip rate resulted in an average spread angle of 27.1°; the nominal drip rate had a mean spread angle of 20.6°; and the low drip rate had a mean spread angle of 3.1°. However, to be consistent with the development of the spread angle for the waste package submodel, and to incorporate the real possibility of widely varying drip rates, all 50 data points are combined. The mean spread angle for the rough waste package surface with off-crown drip locations is therefore 9.4°, with a range (\pm one standard deviation of 9.6°) of 0° to 19.0°.

In the off-crown splash radius tests #4 and #5 (Table 7.1-9) (Microsoft Excel spreadsheet: Flux Splitting Validation, Worksheet: Splash Radius, which is documented in Appendix E), the drip location was 33° and 16.5° off the crown. The mean splash radius was 8.9 cm, with a measured range of 3.0 cm to 15.0 cm. This gives an effective waste package length of about 6 cm to 30 cm for the tests.

Table 7.1-8. Atlas Breached Waste Package Experiments on Rough Mock-Up Surface – Dripping off Crown – Rivulet Spread Data

Drip Location on Mock-Up	Spread at 33°		Spread at Transition		Relevant Patch
	Left (cm)	Right (cm)	Left (cm)	Right (cm)	
Multiple Patch Tests (DTN: MO0208EBSATBWP.027 [DIRS 163404])					
81 cm right of center, 16.5°	— ^a	—	—	—	5
27 cm right of center, 16.5°	8	12	6	8	5
27 cm left of center, 16.5°	21	19	12	13	4
81 cm left of center, 16.5°	16	22	14	12	4
81 cm right of center, 33°	—	—	2	2	5
27 cm right of center, 33°	—	—	3	1	5
27 cm left of center, 33°	—	—	2	1	4
81 cm left of center, 33°	—	—	3	4	4
Bounding Flow Rate Tests (DTN: MO0208EBSATBWP.028 [DIRS 163405])					
54 cm left of center, 33° (Low Flow Rate)	—	—	—	—	4
54 cm left of center, 33° (High Flow Rate)	—	—	—	—	4
27 cm left of center, 33° (High Flow Rate)	6 ^b	9 ^b	8	14	4
27 cm right of center, 33° (High Flow Rate)	5 ^b	3 ^b	12	11	5
27 cm right of center, 33° (Low Flow Rate)	—	—	2.5	2.5	5
27 cm right of center, 16.5° (High Flow Rate)	16	15	17	10	5

Table 7.1-8. Atlas Breached Waste Package Experiments on Rough Mock-Up Surface – Dripping off Crown – Rivulet Spread Data (Continued)

Drip Location on Mock-Up	Spread at 33°		Spread at Transition		Relevant Patch
27 cm left of center, 16.5° (High Flow Rate)	26	32	13	34	4
54 cm left of center, 16.5° (High Flow Rate)	25	20	26	19	4
54 cm left of center, 16.5° (Low Flow Rate)	3	6	—	—	4
27 cm left of center, 16.5° (Low Flow Rate)	3	2	1	0	4
27 cm right of center, 16.5° (Low Flow Rate)	0	0	0	0	5
27 cm left of center, 33° (Low Flow Rate)	—	—	6	4.5	4

^a — = rivulet spread not measured

^b These data are ignored due to inconsistent behavior – rivulet spread should not occur at the drip location.

Table 7.1-9. Atlas Breached Waste Package Experiments on Rough Mock-Up Surface – Dripping off Crown – Splash Radius Tests

No. Drips	Splash Radius (cm)		Comments
	Left	Right	
Splash Radius Test #4 (33°) (DTN: MO0207EBSATBWP.021 [DIRS 163399])			
31	3.0	3.5	Measured inner cluster (bulk)
82	5.5	6.0	Measured inner cluster (bulk)
158	6.5	6.5	Measured inner cluster (bulk)
Splash Radius Test #5 (16.5°) (DTN: MO0207EBSATBWP.021 [DIRS 163399])			
22	9.0	10.0	Measured inner cluster (bulk)
82	13.0	14.5	Measured inner cluster (bulk)
156	14.0	15.0	Measured inner cluster (bulk)

The experimentally measured fraction of the drip flux that flowed into all breaches (f_{expt}) from off-crown drip locations is given in Table 7.1-10. The breaches that were the focus of a particular test or into which flow was expected have f_{expt} values shown in bold. For f_{expt} values in bold, f_{expt} had a mean of 0.12, with a standard deviation of 0.23. The measured minimum fraction was 0.0 and maximum was 0.621.

Following the approach used in Section 6.5.1.1.3, the “inner cluster” splash diameter is used for the effective length of the waste package in the validation of the flux-splitting algorithm, which is given by Equations 6.3.3.2.5-1 (or 6.5.1.1.3-2) and 6.3.3.2.5-3 (or 6.5.1.1.3-1). The form of the equation is:

$$F = \frac{N_b \ell}{L_{WP}} \left(1 + \frac{\tan \alpha}{2} \right) f_{vw}, \quad (\text{Eq. 7.1.1.2-1})$$

where F is the fraction of dripping flux that flows through breaches, ℓ is one-half the width of a breach or patch, L_{WP} is the effective length of the waste package (i.e., the length over which dripping or splattering occurs), α is the rivulet spread angle, and f_{vw} is the uncertainty factor

for the waste package developed for validation, corresponding to the waste package uncertainty factor, f_{WP} . For the validation tests, the number of breaches, N_b , is one. f_{VW} is obtained by inserting f_{expt} , the measured fraction of the dripping flux that flowed into breaches, for F in Equation 7.1.1.2-1:

$$f_{VW} = \frac{f_{expt}}{\frac{N_b \ell}{L_{WP}} \left(1 + \frac{\tan \alpha}{2} \right)}. \quad (\text{Eq. 7.1.1.2-2})$$

Table 7.1-10. Atlas Breached Waste Package Experiments on Rough Mock-Up Surface – Dripping off Crown – Flow into Breaches

Drip Location on Mock-Up	Water Input (g)	Breach 4 Inflow (g)	Breach 4 f_{expt}	Breach 5 Inflow (g)	Breach 5 f_{expt}
81 cm right of center, 16.5°	282.96	0	0	0.76	0.0027
27 cm right of center, 16.5°	316.74	0	0	0.35	0.0011
27 cm left of center, 16.5°	309.57	0.48	0.0016	0.44	0.0014
81 cm left of center, 16.5°	242.56	0.94	0.0039	0	0
81 cm right of center, 33°	109.4	0	0	0.22	0.0020
27 cm right of center, 33°	108.44	0	0	0.30	0.0028
27 cm left of center, 33°	107.33	0.33	0.0031	0	0
81 cm left of center, 33°	106.75	0.01	0.0001	0	0
54 cm left of center, 33° (Low Flow Rate)	123.13	53.27	0.4326	0	0
54 cm left of center, 33° (High Flow Rate)	330.03	204.99	0.6211	0	0
27 cm left of center, 33° (High Flow Rate)	339.24	0.06	0.0002	0	0
27 cm right of center, 33° (High Flow Rate)	330.22	0.10	0.0003	1.23	0.0037
27 cm right of center, 33° (Low Flow Rate)	112.36	0	0	0.80	0.0071
27 cm right of center, 16.5° (High Flow Rate)	313.82	0	0	1.14	0.0036
27 cm left of center, 16.5° (High Flow Rate)	322.07	1.34	0.0042	0.19	0.00059
54 cm left of center, 16.5° (High Flow Rate)	328.27	197.92	0.6029	0	0
54 cm left of center, 16.5° (Low Flow Rate)	94.41	57.18	0.6056	0	0
27 cm left of center, 16.5° (Low Flow Rate)	115.97	0.34	0.0029	0.45	0.0039
27 cm right of center, 16.5° (Low Flow Rate)	119.76	0	0	0.09	0.0008
27 cm left of center, 33° (Low Flow Rate)	115.81	0.36	0.0031	0	0

Sources: DTNs: MO0208EBSATBWP.027 [DIRS 163404]; MO0208EBSATBWP.028 [DIRS 163405]

NOTE: For all f_{expt} values in bold: mean = 0.115; standard deviation = 0.234; median = 0.0031; minimum = 0.00014; maximum = 0.621.

Statistics for f_{expt} are compared in Table 7.1-11 between the smooth surface experimental results used for the waste package flux-splitting submodel (Appendix D) and rough surface results discussed in this section (Table 7.1-10).

Table 7.1-11. Comparison of f_{expt} Statistics for Smooth and Rough Surfaces

Experiments	Mean f_{expt}	Minimum f_{expt}	Maximum f_{expt}	Median f_{expt}
Waste Package (Smooth Surface)	0.295	0.0	1.066	0.0142
WP Validation (Rough Surface)	0.115	0.0001	0.621	0.0031

WP = waste package

With the values for the breach flow fraction (f_{expt}), the effective waste package length (L_{WP}), and the spread angle (α) as determined above, using off-crown rough surface test data, the range for f_{VW} is determined. The half-width of the patch used in the experiments ($\ell = 13.5$ cm) is used to evaluate f_{VW} . The minimum for f_{VW} is obtained using the minimum effective waste package length ($L_{WP} = 6.0$ cm) and the maximum spread angle ($\alpha = 19.0^\circ$), resulting in $f_{VW} = 0.379f_{expt}$. The maximum for f_{VW} is obtained using the maximum effective waste package length ($L_{WP} = 30$ cm) and the minimum spread angle ($\alpha = 0^\circ$), resulting in $f_{VW} = 2.22f_{expt}$. Using the mean value of f_{expt} (0.115), f_{VW} for the waste package ranges from 0.044 to 0.26. Over the measured range of f_{expt} (0 to 0.621), f_{VW} ranges from 0.0 to $(2.22)(0.621) = 1.38$. The range obtained for f_{WP} (0.909 to 2.00), based on the mean smooth surface value of f_{expt} (0.295), is higher. When the measured range of smooth surface f_{expt} values (0.0 to 1.066; Figure D-10) for the waste package flux-splitting analysis is used instead of the mean, f_{WP} ranges from 0.0 to 3.28. The waste package flux-splitting submodel (based on smooth surface data) overestimates flow through breaches compared to the model validation estimates (based on rough surface data), which in turn overestimates the advective releases of radionuclides compared to the model validation estimates. The estimated values for f_{WP} and f_{VW} are summarized in Table 7.1-12.

Table 7.1-12. Summary of f_{WP} and f_{VW} Values

	Based on Mean f_{expt}		Based on Minimum f_{expt}	Based on Maximum f_{expt}
	Minimum	Maximum	Minimum	Maximum
f_{WP}	0.909	2.001	0.0	3.28
f_{VW}	0.044	0.26	0.0	1.38

As with the drip shield flux-splitting submodel, a final comparison is between f'_{WP} , which lumps the uncertainty in the rivulet spread angle into f_{WP} , and a corresponding parameter for the rough waste package surface, f'_{VW} , where

$$f'_{VW} = \left(1 + \frac{\tan \alpha}{2}\right) f_{VW}. \quad (\text{Eq. 7.1.1.2-3})$$

For the rough surface, α ranges from 0° to 19.0° . Applying the maximum value for α results in the range for f'_{VW} of 0 to 0.30, based on the mean value of f_{expt} . For comparison, f'_{WP} was estimated to range from 0 to 2.41. The wider range for f'_{WP} means that the waste package flux-splitting submodel tends to overestimate the flow through breaches in the waste package compared to the rough surface validation tests. The overlapping ranges for f'_{WP} and f'_{VW} validate the waste package flux-splitting submodel.

Sections 7.1.1.1 and 7.1.1.2 have demonstrated that the drip shield and waste package flux-splitting submodels based on experiments using smooth drip shield mock-up surfaces overestimate fluxes when compared to the experimental data using rough drip shield mock-up surfaces. The validations discussed uncertainties in relevant parameters. Based on these validation results, the EBS flow model is adequate for its intended use.

7.1.2 Results of Critical Review of the EBS Flow Model

A critical review of the EBS flow model was conducted as specified in the TWP (BSC 2006 [DIRS 177739], Section 2.2.3). This model validation approach is justified based on requirements of SCI-PRO-006, Section 6.3.2, where the critical review is listed as an appropriate method for model validation. The results of the critical review are presented in Appendix M.

7.2 EBS TRANSPORT MODEL

The transport of radionuclides through the EBS is modeled, using assumptions in Section 5, as a combination of advective and diffusive transport, including retardation between a series of three domains:

- Waste form domain
- Corrosion products domain
- Invert domain.

Advective transport is considered when water enters the waste form domain and is able to flow through the EBS and enter the UZ. The EBS flow model (Section 7.1) calculates the water flux between each domain and a separate model provides radionuclide concentrations.

Diffusive transport between each of the domains occurs regardless of whether water is flowing through the EBS, since, by Assumption 5.5, a continuous film of water is always present on all surfaces of internal waste package components and corrosion products in a breached waste package when the temperature is below the boiling point of water in the repository. Diffusive

transport between each domain is modeled in one dimension and, therefore, is dependent upon the following parameters that can vary as a function of time and according to the specific transport pathway:

- Effective diffusion coefficient
- Diffusive area
- Diffusion length.

The effective diffusion coefficient is calculated from Archie's law and is dependent upon the free water diffusion coefficient, porosity, and saturation in each domain. Additionally a temperature correction is made for diffusion in the invert domain. Porosity is either assumed to be constant or is provided by a separate model (e.g., SNL 2007 [DIRS 180616]). Saturation varies with relative humidity. The diffusive area is calculated differently for each domain but is either a function of the number of breaches in the waste package (corrosion patches or stress corrosion cracks) or it is calculated from the geometry of the different components of the EBS. The diffusive area of breaches also depends on the scenario class being modeled. The diffusion length is either calculated from EBS geometry or is sampled, depending upon the domain.

As stated in Section 7, the level of confidence required for the EBS transport model is Level II, which is described in Section 7. In Sections 6.3 and 6.5, a detailed explanation and justification is presented on the formulation of the transport model. These sections include a great amount of information that is relevant to Level II validation. In addition, the following sections include auxiliary information aimed to validate further certain components of the transport model.

Section 7.2.1 develops water vapor adsorption isotherms for corrosion products and CSNF degradation rind from laboratory measurements reported in refereed journals; these data had not been used to develop the adsorption submodels described in Sections 6.3.4.3.2 and 6.3.4.6. Comparison with the model isotherms shows that the bands of uncertainty overlap, thereby validating the isotherms used in the in-package diffusion submodel. Section 7.2.1 also describes a comparison between the in-package diffusion submodel and two similar, independently developed models of transport from a waste package to the invert. The comparison shows that although each model uses a different set of assumptions, the assumptions used and the final diffusion coefficients calculated by each model generally agree and, thus, the transport model is valid for its intended purpose.

Section 7.2.2 compares the invert diffusion coefficient temperature, porosity, and saturation dependence with other published data. The temperature dependence of the diffusion coefficient applies throughout the EBS, not just to the invert, and is validated by close agreement with independent measurements of diffusion coefficient temperature dependence reported in refereed journals.

Section 7.2.3 compares the K_d values obtained using the radionuclide competitive surface complexation model with recent tabulations of K_{ds} measured in the laboratory.

7.2.1 In-Package Diffusion Submodel

Diffusive transport within the waste package will limit the release of radionuclides for those waste packages in a no-seep environment. The in-package diffusion submodel is directly related to the waste isolation attribute (limited release of radionuclides from the engineered barriers) because the model predicts delays in the release of mass from the waste package in comparison to the TSPA-SR model, which immediately mobilized radionuclides at the external surface of the waste package.

Level II validation is appropriate for the in-package diffusion submodel as it is part of the EBS radionuclide transport model (Section 7). In addition, the in-package diffusion submodel has the following features:

- The in-package diffusion submodel is not extrapolated over large distances or spaces. There is an inherent time extrapolation in the model.
- The in-package diffusion submodel bounds the uncertainties by considering two bounding states. In the first state, the waste package internal components are considered to be in their intact, as-emplaced condition. For the second state, the iron-based waste package internal components are considered to be completely degraded to a porous material. Although these are two bounding end states, uncertainties exist in the time- and spatially-dependent intermediate conditions.
- The in-package diffusion submodel has a minor impact on dose time history in the first 10,000 years, based on sensitivity calculations performed for the prioritization report, *Risk Information to Support Prioritization of Performance Assessment Models* (BSC 2003 [DIRS 168796], Sections 3.3.6 through 3.3.11). Those studies indicate that the estimate of mean annual dose in the first 10,000 years has only a minor dependence on in-package conditions that impact diffusion.

The in-package diffusion submodel addresses radionuclide transport under no-drip conditions, where the only water present is water vapor and adsorbed water on internal waste package surfaces. This submodel is based on the assumption that all surfaces exposed to humid air have a thin film of water adsorbed onto the surface in which radionuclides may dissolve and through which diffusion may occur. The objective of the in-package diffusion submodel is to calculate the water saturation resulting from water vapor adsorption on porous steel and waste form degradation products and estimate the saturation-dependent diffusion coefficients in the porous material. The in-package diffusion submodel is applied to two distinct materials inside a breached waste package: (1) waste form degradation rind, and (2) steel corrosion products. The form and application of the submodel is identical for the two materials; only the material properties are different, specifically, the water vapor adsorption isotherms, the specific surface areas, the densities, and the porosities.

The in-package diffusion submodel is validated by comparison to two other models:

- Electric Power Research Institute (EPRI) *Phase 5* (EPRI 2000 [DIRS 154149])

- A model by Lee et al. (1996 [DIRS 100913]) for diffusive releases from waste package containers with multiple perforations.

The in-package diffusion submodel is based on the one-dimensional diffusion equation, Fick's first law of diffusion (Bird et al. 1960 [DIRS 103524], p. 503):

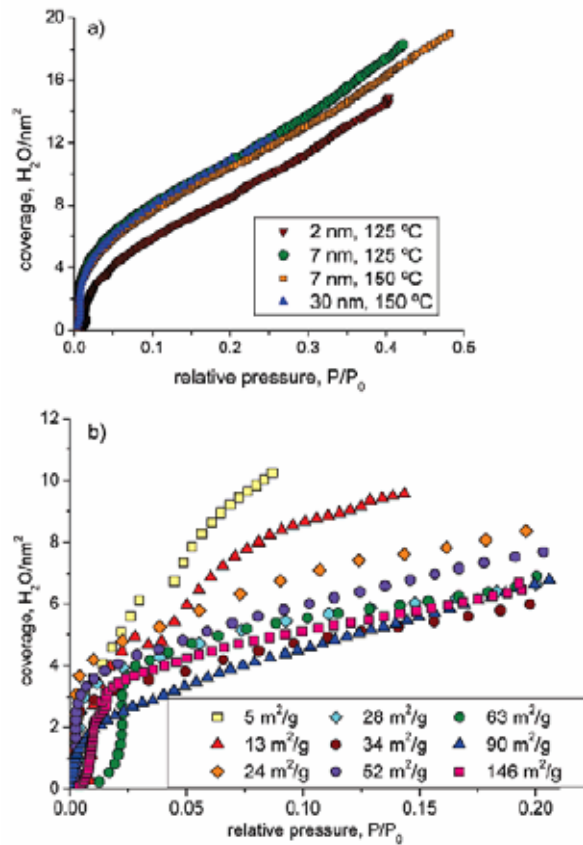
$$\frac{q_i}{A} = -D \frac{\partial C_i}{\partial x}. \quad (\text{Eq. 7.2.1-1})$$

That is, the fundamental process being modeled is diffusion through a porous medium, a process that is well understood and fully accepted throughout the scientific and engineering community.

Certain underlying assumptions need to be addressed. It is assumed that the bulk of the corrosion products inside a waste package are a mixture of goethite, HFO, Cr₂O₃, and NiO, based on the composition of steels in the internal non-waste form components.

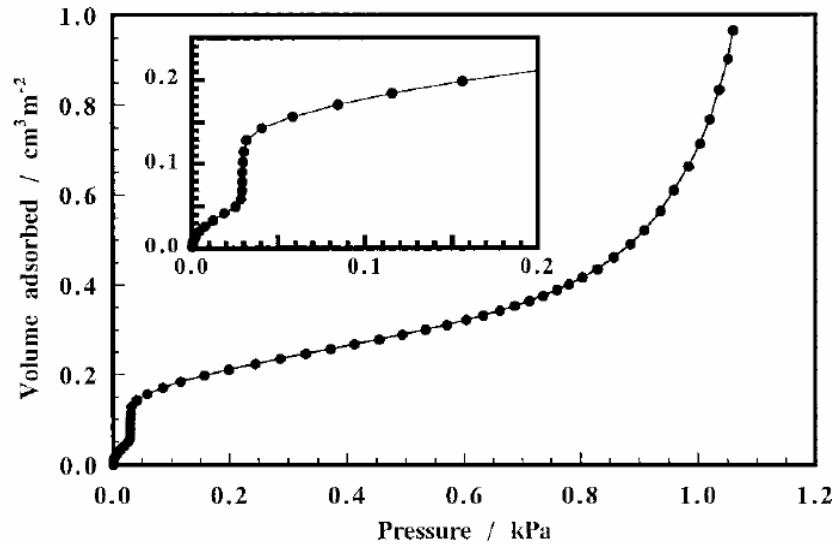
In the RTA, for purposes of estimating water saturation, the waste form is treated as a mixture of surrogate actinide oxides to represent the schoepite and various other oxidized fission products. The most important physical properties affecting water saturation—water vapor adsorption isotherm and specific surface area—are sampled parameters that allow the uncertainty in their values to be assessed in TSPA.

The composite corrosion products water vapor adsorption isotherm used for the in-package diffusion submodel is compared with other measured isotherms for goethite, hematite, Cr₂O₃, and NiO, shown in Figures 7.2-1, 7.2-2, and 7.2-3, respectively. Data from these figures were captured using Grab It!TM Excel based digitizing software. Only measured data points were used when individual data points were discernible in the plots (Figures 7.2-1b, 7.2-2, and 7.2-3). In Figure 7.2-1a, sufficient points were captured to allow the shape of the original plot to reproduced faithfully. Except for the Cr₂O₃ isotherm, the data cover only a narrow range of *RH*, to less than 0.50. A composite isotherm was created using these few data. This isotherm is shown in Figure 7.2-4, along with its three-standard-deviation bounds, and is compared with the model composite isotherm with its three-standard-deviation bounds. The regions overlap for *RH* values greater than about 0.42, which is the region that is most important in TSPA calculations, since this is where water saturation is high enough to allow diffusion of radionuclides to occur. For the most part, the validation isotherm predicts a greater amount of adsorbed water than the model isotherm. This is due in part to the sparseness of validating data, most of which show a larger amount of water adsorbed at a given *RH*. In addition, the validation isotherm is unduly weighted by the one isotherm that extends to high *RH* values. This isotherm is for Cr₂O₃, which, as seen in Figure 6.3-34, tends to adsorb more water at a given *RH* than the other corrosion product components, causing the validation isotherm to be high compared to the model isotherm. The validation isotherm is also shifted to higher amounts of adsorbed water due to the isotherms for hematite from Mazeina and Navrotsky (2007 [DIRS 181235]) using a new calorimetric technique. The amount of adsorbed water they measured is higher by at least a factor of two than has been reported for hematite by any other researcher. Considering the limitations in the data available for validation, these data support validation of the model isotherm.



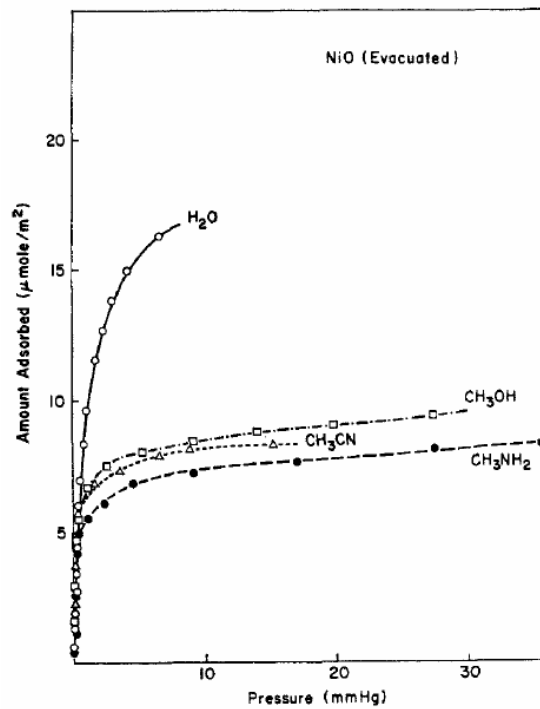
Source: Mazeina and Navrotsky 2007 [DIRS 181235], Figure 3

Figure 7.2-1. Water Vapor Adsorption Isotherm for (a) Goethite and (b) Hematite



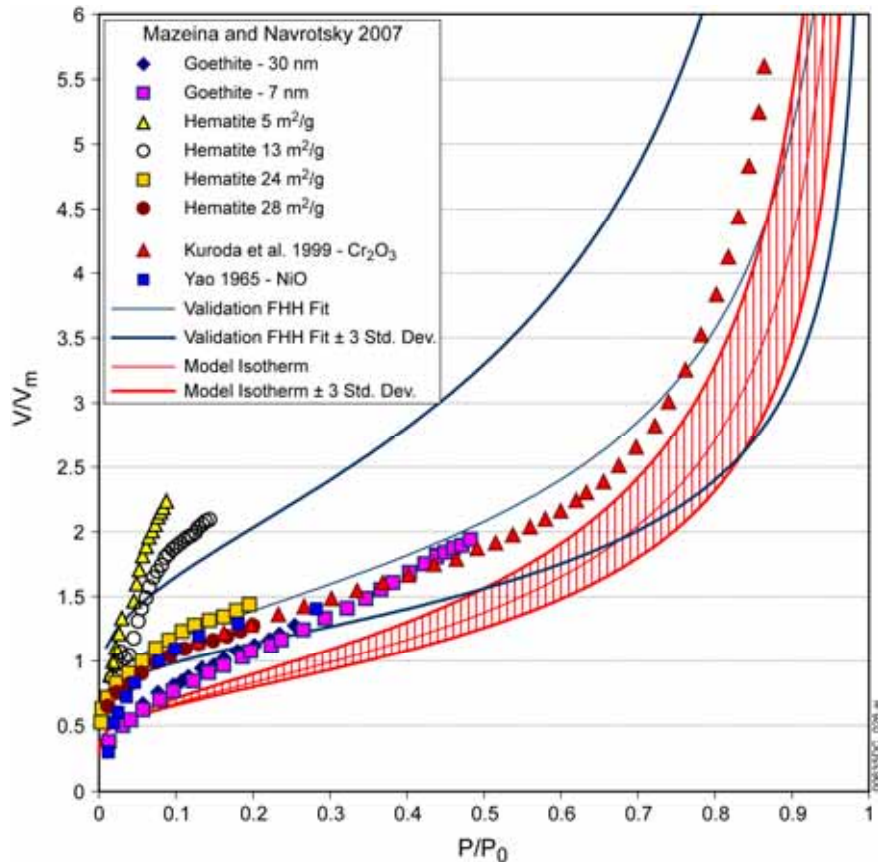
Source: Kuroda et al. 1999 [DIRS 181246], Figure 1

Figure 7.2-2. Water Vapor Adsorption Isotherm for Cr_2O_3



Source: Yao 1965 [DIRS 181240], Figure 3

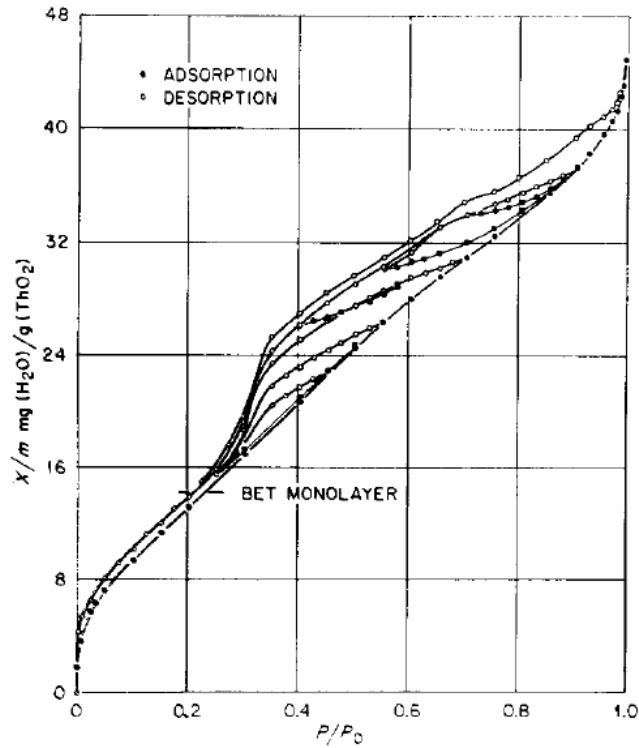
Figure 7.2-3. Water Vapor Adsorption Isotherm for NiO



Source: Mazeina and Navrotsky 2007 [DIRS 181235]; Kuroda et al. 1999 [DIRS 181246] and Yao 1965 [DIRS 181240]

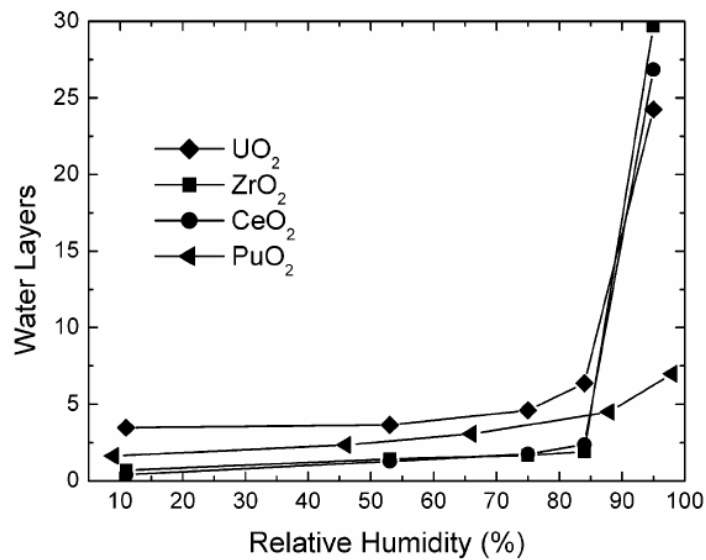
Figure 7.2-4. Validation of Adsorption Isotherms for Water Vapor on Corrosion Products

The composite CSNF rind degradation products water vapor adsorption isotherm, based on surrogate waste form materials, is validated in the same manner as the steel corrosion products, namely, by comparing separate measurements of water vapor adsorption isotherms for other, similar materials, with the model CSNF rind isotherm. Isotherms for adsorption onto ThO₂, Figure 7.2-5 (Fuller and Agron 1976 [DIRS 178306]), ZrO₂, Figure 7.2-6 (LaVerne and Tandon 2003 [DIRS 178303]), and PuO₂, Figures 7.2-6 and 7.2-7 (LaVerne and Tandon 2003 [DIRS 178303] and Stakebake and Steward 1973 [DIRS 178305]) are included in a composite adsorption isotherm for waste form materials for validation of the CSNF model isotherm. This isotherm is shown in Figure 7.2-8, along with its three-standard-deviation interval, and compared with the model isotherm and its three-standard-deviation interval, from Figure 6.3-43. The validation isotherm lies with the three-standard-deviation interval of the model isotherm, and the three-standard-deviation interval of the model isotherm is fully bounded by that of the validation isotherm, which supports validation of the model isotherm.



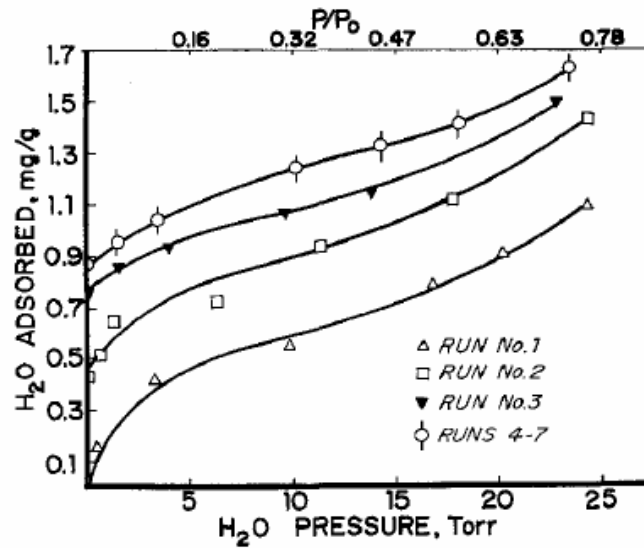
Source: Fuller and Agron 1976 [DIRS 178306], Figure 1

Figure 7.2-5. Water Vapor Adsorption Isotherm for ThO₂



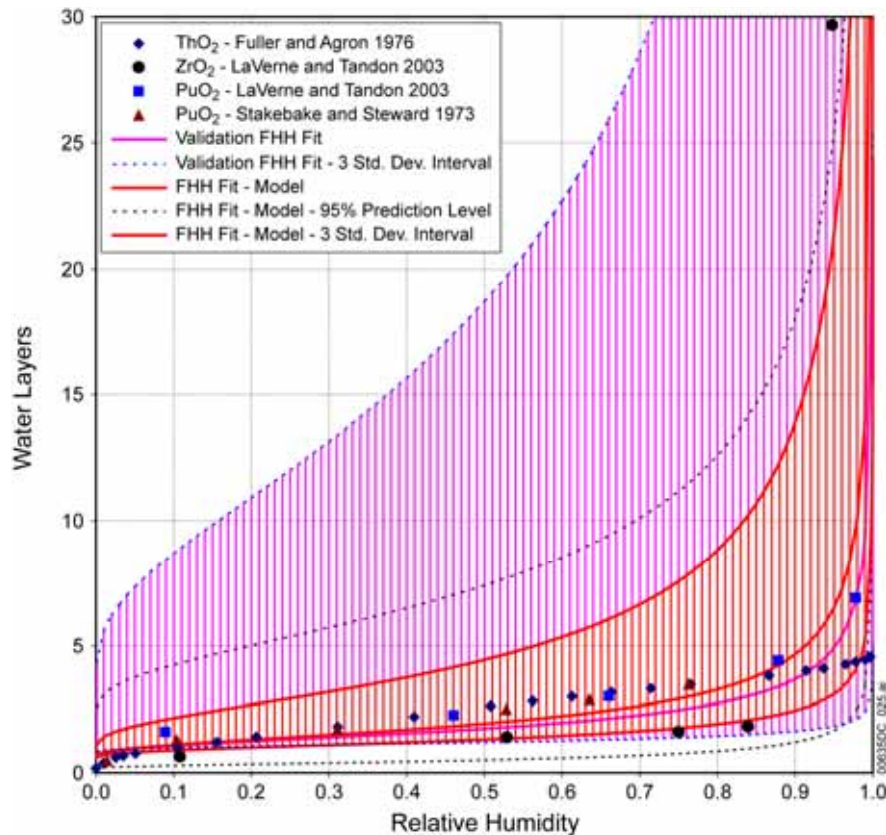
Source: LaVerne and Tandon 2003 [DIRS 178303], Figure 1

Figure 7.2-6. Water Vapor Adsorption Isotherm for ZrO₂ and PuO₂



Source: Stakebake and Steward 1973 [DIRS 178305], Figure 2

Figure 7.2-7. Water Vapor Adsorption Isotherm for PuO₂



Source: DTN: SN0703PAEBSRTA.001, file CSNF Isotherm Compilation.xls, worksheet "Validation & FHH Fit"

Figure 7.2-8. Validation of Adsorption Isotherms for Water Vapor on CSNF Degradation Rind

7.2.1.1 Comparison with Electric Power Research Institute 2000

Validation of the diffusion coefficient calculation in the in-package diffusion submodel is provided in part by comparison with a similar model developed independently by a reputable performance assessment program (EPRI 2000 [DIRS 154149]). The specific criteria to be met are that the EPRI model diffusion coefficient agrees with the diffusion coefficient calculated in the in-package diffusion submodel within an order of magnitude or that the EPRI model value is reasonably bounded by the in-package diffusion submodel value in the pertinent range of relative humidity (>90 percent). The wide range of acceptance for the diffusion coefficient calculation is justified considering that while the EPRI model specifies a fixed set of conditions, it is intended to be applied under all expected repository conditions, yet uncertainty is not characterized.

The EPRI source-term model, COMPASS2000, implements five compartments—Waste, Corrosion Products, Canister, Invert, Near-Field Rock—of which two (Corrosion Products and Canister) are analogous to portions of the in-package diffusion submodel. The Corrosion Products compartment represents the porous material that is formed after the basket materials are corroded. The Canister compartment represents the failed metal canisters. As with the GoldSim TSPA model, each compartment is treated as a mixing cell in which radionuclide concentrations are assumed to be uniform. Mass balances in each compartment account for the various processes that comprise the model, including transport by diffusion and advection, radioactive decay and ingrowth, sorption, dissolution, and precipitation.

In the EPRI model, EBS transport parameters are assigned fixed values. Both the Corrosion Products and corroded Canister compartments have a porosity of 0.42 (EPRI 2000 [DIRS 154149], p. 6-21), comparable to the porosity of 0.40 used for corrosion products in the RTA. A lower value for porosity overestimates releases of radionuclides.

The EPRI report (EPRI 2000 [DIRS 154149], p. 6-22) assumes corrosion products are Fe_2O_3 , based on cited studies (EPRI 2000 [DIRS 154149], p. 6-31) of corrosion products of carbon steel in humid, oxidizing environments that indicate that in the presence of an abundant supply of oxygen, iron would be expected to exist as Fe_2O_3 , or FeOOH or $\text{Fe}(\text{OH})_3$. However, the EPRI report (EPRI 2000 [DIRS 154149], p. 6-31) acknowledges that goethite may well be the dominant phase due to the slow kinetics of the transition from goethite to hematite, which supports the use in the RTA of goethite and HFO as the iron oxide phases.

The EPRI model assumes a fixed water saturation of 0.35 in both the Corrosion Products and corroded Canister compartments (EPRI 2000 [DIRS 154149], p. 6-21). This value is appropriate for modeling cases involving advective transport but overestimates releases of radionuclides for the expected large fraction of the repository that has no seepage flux, where the only water present is adsorbed water. The in-package diffusion submodel specifically applies to those regions and provides a more realistic estimate of saturation as a function of relative humidity.

In the EPRI report, water saturation in the waste form is an assumed constant value (20 percent) “that is likely to be very conservative... that is likely to cause the release rate of potentially solubility-limited species... to be overestimated” (EPRI 2000 [DIRS 154149], pp. 6-21 to 6-22). The RTA diffusion submodel reduces that excessive conservatism by letting the water saturation

depend on the relative humidity and the extent of degradation of the waste form, both of which vary over time.

The EPRI model uses a fixed value for effective diffusion coefficient of $4.645 \times 10^{-4} \text{ m}^2 \text{ yr}^{-1}$ ($1.472 \times 10^{-11} \text{ m}^2 \text{ s}^{-1}$) in both the Corrosion Products and corroded Canister compartments (EPRI 2000 [DIRS 154149], p. 6-22). Using the fixed values of porosity and saturation used in the EPRI model, 0.42 and 0.35, respectively, the only variation in computing the effective diffusion coefficient using Archie's law (Equation 6.3.4.3.5-2) is the radionuclide molecular diffusion coefficient, which ranges from $5.97 \times 10^{-10} \text{ m}^2 \text{ s}^{-1}$ (for Th) to $2.06 \times 10^{-9} \text{ m}^2 \text{ s}^{-1}$ (for Cs) (see Table 4.1-7). Then the effective diffusion coefficient ranges from $2.4 \times 10^{-11} \text{ m}^2 \text{ s}^{-1}$ to $8.2 \times 10^{-11} \text{ m}^2 \text{ s}^{-1}$, or a factor of 1.6 to 5.6 higher than the EPRI effective diffusion coefficient. This shows that the use of Archie's law in the RTA results in slightly overestimating the effective diffusion coefficient relative to the value used in the EPRI model.

The value used for water saturation in the EPRI model appears too high for no-drip conditions, where the only source of water is humidity in the air. A comparison can be made with the RTA water saturation calculation, which depends on porosity, density, specific surface area, relative humidity, and FHH adsorption isotherm parameters s and k . Except for porosity, which is fixed, and relative humidity, which varies with time and environmental conditions in the TSPA calculation, these are uncertain parameters represented by a range and distribution. Consider a representative value for specific surface area of $100 \text{ m}^2 \text{ g}^{-1}$ (at the high end of the range for goethite and the low end for HFO), a density of $4,000 \text{ kg m}^{-3}$ (approximate average for goethite and HFO), and the porosity of 0.4 used for corrosion products in the RTA. A water saturation of 0.35 (the EPRI value) is achieved in the RTA model at nearly 100 percent relative humidity (the actual range being 0.99985 to 0.999989, for the range of FHH parameters). In effect, the EPRI model, based on RTA estimates, assumes nearly bulk water condensation conditions. Thus, when the humidity is high, the EPRI model and in-package diffusion submodel, agree. In contrast, the in-package diffusion submodel provides diffusion coefficient values that depend on humidity, composition of the domain (various waste forms and steels), as well as radionuclide species.

The EPRI model also specifies fixed diffusive lengths, which are defined as the distance from the center of the compartment to the interface of the two contacting compartments. For the Corrosion Products compartment, the diffusion length is 0.046 m; for the Canister compartment, the diffusion length is 0.025 m (EPRI 2000 [DIRS 154149], p. 6-22). In a well-degraded waste package, these are reasonable values, comparable to those used in the in-package diffusion submodel.

For the conditions assumed in the EPRI model, namely, at later times when the waste package is extensively corroded, the in-package diffusion submodel agrees well with the EPRI model in terms of conceptual models and approximate values for important parameters. The primary differences are that the in-package diffusion submodel accounts for a wider range of conditions, including times just after breaches first appear in the waste package. In addition, the in-package diffusion submodel accounts explicitly for the relative humidity, which realistically is the only source of water when seepage does not occur, and for differences in diffusion coefficients among radionuclides. Thus, there is agreement between the models, and where differences occur, it is

primarily to increase the realism of the diffusive release calculation in the RTA and to account for uncertainty.

7.2.1.2 Comparison with Lee et al. 1996

Validation of the in-package diffusion submodel is provided in part by comparison with a similar model developed independently and published in technical literature (Lee et al. 1996 [DIRS 100913]).

Lee et al. (1996 [DIRS 100913]) developed a model for steady-state and “quasi-transient” diffusive releases from waste packages into the invert. In this model, perforations in the package are assumed to be cylindrical in shape. The diffusion path consists of the approach to the opening of the perforation from the waste form side; the path through the cylindrical portion of the perforation, which is filled with corrosion products; and the path through the exit disk separating the perforation from the invert. The waste is assumed to be distributed uniformly inside the waste container. The package is approximated by an equivalent spherical configuration, and the underlying invert is represented by a spherical shell surrounding the package.

The model of Lee et al. (1996 [DIRS 100913]) is suitable for the late stages of package degradation when the waste form has become a mass of porous corrosion products. Although Lee et al. (1996 [DIRS 100913]) assumed the packages failed by localized corrosion, this model should be equally applicable to failure by general corrosion.

The assumption of Lee et al. (1996 [DIRS 100913]) that the waste (i.e., radionuclide source) is uniformly distributed inside the waste package restricts the applicability of the model and comparison to the in-package diffusion submodel to the times when the waste package has extensively corroded. The object of the in-package diffusion submodel is to provide more realism at earlier and intermediate times, when the waste cannot yet be considered a uniform porous medium. (In the in-package diffusion submodel, the dependence of the diffusive properties of the waste package on the extent of degradation is computed explicitly as a function of time; [Sections 6.3.4.3.5 and 6.5.2.2]. On the other hand, the fundamental assumption that diffusive releases are controlled by diffusion through breaches that are filled with porous corrosion products may be valid over much of the waste package lifetime, including early times, when stress corrosion cracks are the first breaches to appear. Lee et al. (1996 [DIRS 100913], p. 5-67) assume that the porosity of the perforations is $\phi_{CP} = 0.4$ and the volumetric water content is $\Phi = 10$ percent (so the water saturation in the perforations is a constant $S_w = \Phi / (100\phi_{CP}) = 0.25$). Based on data by Conca and Wright (1990 [DIRS 101582]; 1992 [DIRS 100436]), Lee et al. compute a diffusion coefficient, D ($\text{m}^2 \text{s}^{-1}$), for the porous corrosion products filling the perforations (Lee et al. 1996 [DIRS 100913], p. 5-67):

$$\log_{10} D = -12.255(\pm 0.0499) + 1.898(\pm 0.0464) \log_{10} \Phi, \quad (\text{Eq. 7.2.1.2-1})$$

where the numbers in parentheses are one standard deviation, and the constant term has been modified from Lee et al. to account for changing units on D from $\text{cm}^2 \text{s}^{-1}$ used by Lee et al. to $\text{m}^2 \text{s}^{-1}$. From the discussion in Section 6.3.4.1.1, it is likely that this equation, being based on

data by Conca and Wright (1990 [DIRS 101582]; 1992 [DIRS 100436]), should be written using $\log_{10}(\theta_w D)$ rather than $\log_{10} D$; however, this model validation comparison will use the equation as given by Lee et al., since not enough information is available to repeat their analysis.

For $\Phi = 10$ percent (the assumed volumetric water content of the perforations), Equation 7.2.1.2-1 gives $D = 4.4 \times 10^{-11} \text{ m}^2 \text{ s}^{-1}$. Lee et al. assume that the diffusion coefficient inside the waste package (as opposed to the perforations) is $10^{-9} \text{ m}^2 \text{ s}^{-1}$ (Lee et al. 1996 [DIRS 100913], p. 5-67). As a comparison, the self-diffusion coefficient for water is $2.299 \times 10^{-9} \text{ m}^2 \text{ s}^{-1}$ (Mills 1973 [DIRS 133392], Table III), and for actinides the free water diffusion coefficient in water ranges from $5.97 \times 10^{-10} \text{ m}^2 \text{ s}^{-1}$ (for Th) to $2.06 \times 10^{-9} \text{ m}^2 \text{ s}^{-1}$ (for Cs) (see Table 4.1-7). The value for D obtained from Equation 7.2.1.2-1 ($4.4 \times 10^{-11} \text{ m}^2 \text{ s}^{-1}$) accounts for porosity, saturation, and tortuosity, and thus is comparable to the values for $\phi S_w D_{si}$ obtained from Equation 6.3.4.3.5-2. For a water content of 10 percent, $\phi S_w D_{si}$ ranges from about $1.1 \times 10^{-11} \text{ m}^2 \text{ s}^{-1}$ (Th) to about $3.91 \times 10^{-11} \text{ m}^2 \text{ s}^{-1}$ (Cs), which compares favorably with the value used by Lee et al. (1996 [DIRS 100913], p. 5-67).

The in-package diffusion submodel provides a means for quantifying the uncertainty in diffusion coefficients for diffusion of radionuclides from within the waste form to the invert. Whereas other models consider only the times when the waste package is largely degraded, the in-package diffusion submodel presented here also considers earlier times, starting from the time of the initial waste package breach. The time period between initial breach and complete degradation of the internal components may span many thousands of years. Thus, the in-package diffusion submodel fills a major time gap in modeling diffusive releases from a waste package. In effect, it provides a rationale for interpolating between essentially a zero diffusion coefficient (due to the absence of water) when a waste package is first breached to a value at a time when porous corrosion products can be expected to fill the waste package with a degree of water saturation capable of transporting radionuclides. The in-package diffusion submodel is considered validated based on corroborating data for input parameters such as water adsorption isotherms and specific surface areas, and based on the agreement with two other waste package diffusion models in areas where these models apply.

7.2.2 Invert Diffusion Submodel—Temperature, Porosity, and Saturation Dependence

Level II validation is appropriate for the invert diffusion submodel as it is part of the mechanisms for radionuclide transport from waste package to the drift wall through the invert (see Section 7). In addition, the invert diffusion submodel has the following features:

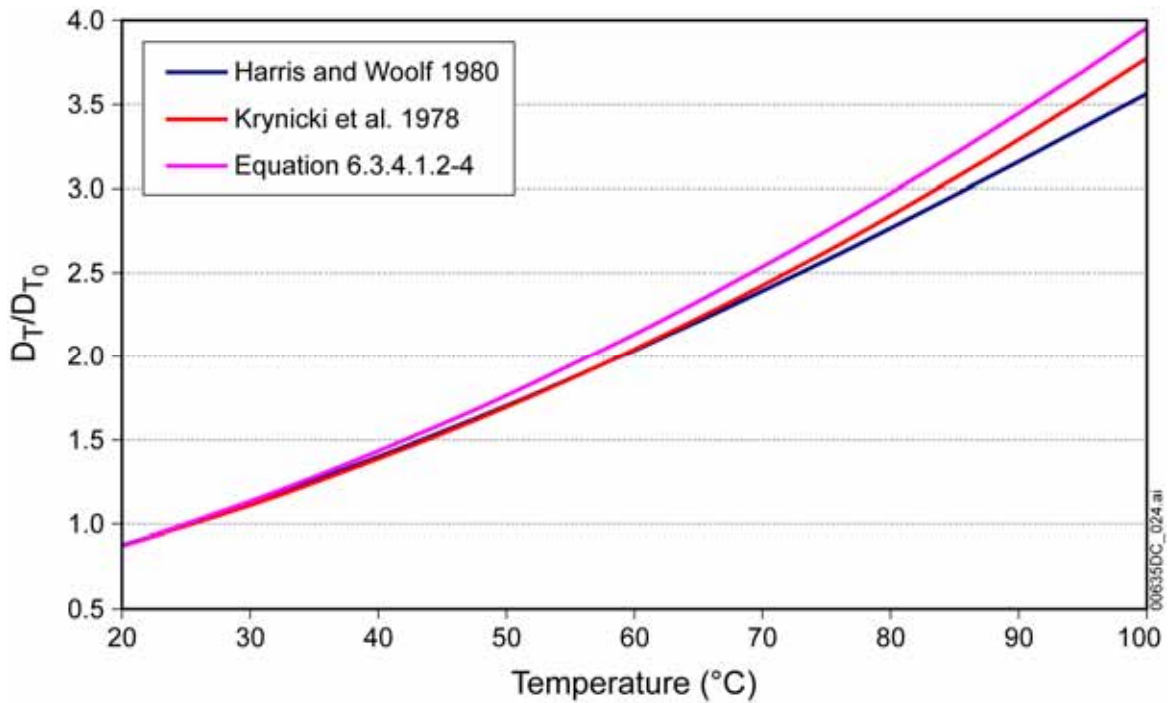
- Diffusive release from the engineered barrier system does not result in significant releases from the repository system. Under expected conditions, there is a small probability of waste package breaching, and only limited release at all is likely. Therefore, the diffusion properties of the invert that might affect this release are expected to play a small role in the estimate of performance of the system under these conditions. The invert diffusion coefficient is also expected to play a small role for disruptive conditions under which more significant breaching of the waste package might occur. In this case, transport through the invert would be dominated by advection, and diffusion would therefore provide only a minor contribution. Therefore, the

diffusion submodel is not expected to play a major role in the assessment of system performance.

- In addition to the above, the invert diffusion properties submodel is not extrapolated beyond the conditions and distances considered in the development of the model. The model applies only on the scale of the EBS and is not applied to larger scales, for example to the unsaturated zone rock.

The invert diffusion coefficient abstraction considers the free water diffusivity for radionuclides as an upper bound. The validation of each of these factors is considered in the following sections.

Section 6.3.4.1.2 describes modification of the diffusion coefficient due to temperature. The modification is based on established principles of diffusion in fluids; specifically, on the relationship among diffusivity, viscosity, and temperature (Cussler 1997 [DIRS 111468], p. 114). The relationship between temperature and viscosity of water is available in text books. Thus, it is straightforward to establish a direct relationship between diffusion coefficient and temperature. Validation of the dependency of diffusivity on temperature is provided by comparisons in Figure 7.2-9 with correlations fit to experimental measurements of the self-diffusion coefficient of water at various temperatures (Harris and Woolf 1980 [DIRS 177361], Equation 1; Krynicki et al. 1978 [DIRS 177360], Equation 13). The self-diffusion coefficient of water is used in these comparisons rather than the free water diffusion coefficients for the various radioelements that are used in the EBS transport model because more extensive data are available for the self-diffusion coefficient of water to make these comparisons over the full range of temperatures of interest. Figure 7.2-9 shows that Equation 6.3.4.1.2-4 agrees well with the correlations based on experimental measurements and provides an upper bound on the measured data.



Source: Harris and Woolf curve: Harris and Woolf 1980 [DIRS 177361], Equation 1; Krynicky et al. curve: Krynicky et al. 1978 [DIRS 177360], Equation 13

Figure 7.2-9. Comparison of Correlations for Self-Diffusion Coefficient of Water

Validation of the dependence of invert diffusion coefficient on porosity and saturation is provided by comparison with measured data obtained independently of the data used for model development. Data used for validation are obtained from diffusivity measurements for crushed tuff using electrical conductivity measurements (CRWMS M&O 2000 [DIRS 156680]) and from direct measurements of diffusivity between machined cubes of tuff (Hu et al. 2001 [DIRS 161623]).

Conca and Wright (1992 [DIRS 100436]) and Conca et al. (1993 [DIRS 170709]) obtained diffusion coefficients from electrical conductivity measurements for various granular materials, including tuff, with volumetric moisture content ranging from 0.5 percent to 66.3 percent. A statistical fit of the data (Conca and Wright 1992 [DIRS 100436], Figure 2; Conca et al. 1993 [DIRS 170709], Figure 2, Table 4.1-16) ranging from 1.5 percent to 66.3 percent volumetric moisture content, based on Archie's law, results in the model used in TSPA (Section 6.3.4.1.1 and Appendix G):

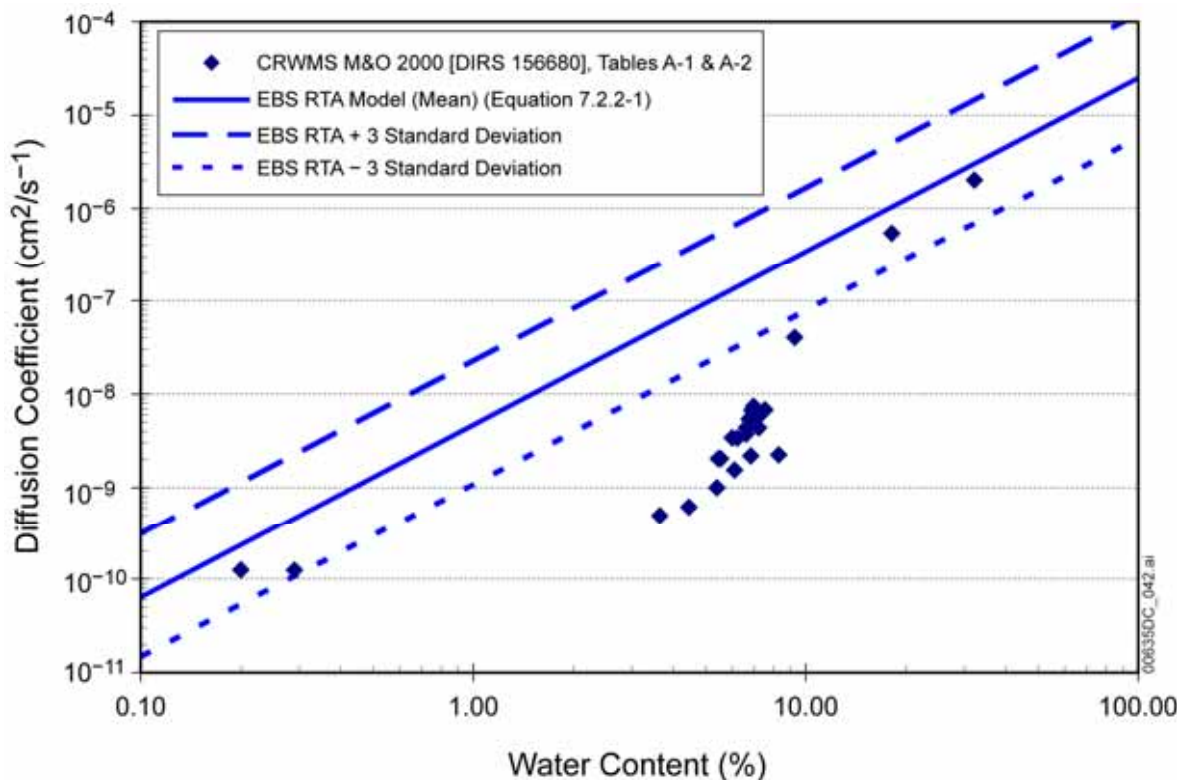
$$\begin{aligned}\theta_w D_I &= D_0 \phi^{1.863} S_w^{1.863} 10^{ND(\mu=0.033, \sigma=0.218)} \\ &= D_0 \theta_w^{1.863} 10^{ND(\mu=0.033, \sigma=0.218)}\end{aligned}\quad (\text{Eq. 7.2.2.-1})$$

where $\theta_w = \phi S_w$ is the volumetric moisture content (fraction: m^3 water m^{-3} rock), and ND represents a normal distribution with a mean, μ , of 0.033 and a standard deviation, σ , of 0.218. The object of this validation is to show that the diffusion coefficient given by Equation 7.2.2.-1 obtained from the electrical conductivity measurements of Conca and Wright (1992

[DIRS 100436]) and Conca et al. (1993 [DIRS 170709]) tends to overestimate the diffusivity of invert materials.

The diffusion coefficient has also been determined specifically for tuff, also using electrical conductivity measurements (CRWMS M&O 2000 [DIRS 156680], Tables A-1 and A-2). These data are listed in Table 7.2-1 and are plotted in Figure 7.2-10, along with the mean value and plus and minus three standard deviations from Equation 7.2.2.-1. This plot shows that the fit to the measured diffusion coefficient data (Equation 7.2.2.-1) overestimates the diffusion coefficient relative to *The Determination of Diffusion Coefficient of Invert Materials* (CRWMS M&O 2000 [DIRS 156680], Tables A-1 and A-2). This plot was created using Microsoft Excel (Appendix G, Worksheet: Validation, p. VII-10).

The electrical conductivity measurements by Conca and Wright (1992 [DIRS 100436]) and Conca et al. (1993 [DIRS 170709]) use conductivity as an analog for diffusivity. While the analog is known to be valid in fully saturated media, its application to unsaturated media, particularly at low moisture contents, is questionable due to the difficulty in preparing samples and in making reliable electrical contact between the electrical leads and samples. To avoid these problems, Hu et al. (2001 [DIRS 161623]) measured diffusive tracer concentrations in tuff cubes directly using laser ablation coupled with inductively coupled plasma-mass spectrometry (LA-ICP-MS), rather than relying on electrical analogs.



Source: CRWMS M&O 2000 [DIRS 156680]

Figure 7.2-10. Comparison of EBS Radionuclide Transport Abstraction Invert Diffusion Submodel (Equation 7.2.2.-1) with Measured Diffusion Coefficients for Tuff

Table 7.2-1 Diffusion Coefficient of Crushed Tuff Invert Materials

Sample	Volumetric Moisture Content (%)	Diffusion Coefficient (cm ² s ⁻¹)
1	32.13	2.02×10^{-6}
2	18.15	5.40×10^{-7}
3	9.26	4.05×10^{-8}
4	7.03	6.75×10^{-9}
5	6.97	7.45×10^{-9}
6	6.89	6.73×10^{-9}
7	6.75	5.42×10^{-9}
8	6.63	4.39×10^{-9}
9	6.63	3.76×10^{-9}
10	6.23	3.40×10^{-9}
11	6.00	3.43×10^{-9}
12	5.55	2.04×10^{-9}
13	5.46	2.04×10^{-9}
14	8.29	2.24×10^{-9}
15	7.54	6.81×10^{-9}
16	7.36	6.21×10^{-9}
17	7.22	4.38×10^{-9}
18	6.84	2.19×10^{-9}
19	6.11	1.55×10^{-9}
20	5.41	9.97×10^{-10}
21	4.45	6.19×10^{-10}
22	3.64	5.00×10^{-10}
23	0.29	1.24×10^{-10}
24	0.20	1.25×10^{-10}

Source: CRWMS M&O 2000 [DIRS 156680], Tables A-1 and A-2.

LA-ICP-MS has recently evolved as a powerful analytical tool for solid samples (Russo et al. 2000 [DIRS 155697]). It can simultaneously determine a large number of chemical elements with low detection limits. Laser ablation uses an intense burst of energy delivered by a short laser pulse to vaporize a minute sample (in the range of nanograms) from a small area. Several spot sizes can be selected (from 25 μm to 200 μm in diameter), allowing a choice of appropriate spot size for different applications. A smaller spot size will sample less solid material, leading to lower analytical precision, but allowing more heterogeneity to be observed. A single laser pulse reveals surface compositions, while multiple pulses allow compositions to be measured at various depths below the surface, with the crater depth proportional to the number of laser pulses applied. For example, two pulses reach about 4 μm into the tuff matrix (Hu et al. 2001 [DIRS 161623], p. 22), and 50 pulses ablates to a depth of about 35 μm (Hu et al. 2001 [DIRS 161623], Figure 6).

In the approach of Hu et al. (2001 [DIRS 161623]), a machined 1.5-cm tuff cube containing a tracer was placed in contact with a cube not containing the tracer, both under the same thermodynamic conditions. The tracer is allowed to diffuse from the tracer-containing cube to the other. Tracers were chosen based on their chemical similarity to radionuclides of interest.

The source cube was vacuum-saturated with a tracer solution mixture of NaBr, NaReO₄, CsBr, and RbBr; both Br⁻ and perrhenate (ReO₄⁻) act as non-sorbing tracers. The sink cube was also vacuum-saturated, but had no tracers. Source and sink cubes were separately placed inside a humidity chamber within an incubator maintained at 22°C until the cubes equilibrated to a constant weight (13 days). The cubes were then clamped together in the relative humidity (*RH*) chamber to start the diffusion test. After 87 days, the diffusion test was stopped by separating the source and sink cubes. The surface and depth distribution of the tracer was then mapped using LA-ICP-MS. The mapping was done on the interface, the far side face (opposite side from the interface), and along the side perpendicular to the interface.

Measurements along the outside surface of the sink cube indicated that a non-sorbing tracer (ReO₄⁻) diffused along the surface at a rate similar to its aqueous diffusion rate in bulk water (Hu et al. 2001 [DIRS 161623], pp. 21 and 22). This result was reasonable because the tuff cubes were located in the high-*RH* chamber, with the likely presence on the outside of the cube of a thick water film that behaves like bulk water. These measurements provided a bounding value for the diffusivity of the tracer, comparable to the diffusion coefficient for its analog, TcO₄⁻ of $1.48 \times 10^{-9} \text{ m}^2 \text{ s}^{-1}$ (Mills and Lobo 1989 [DIRS 138725], p. 105). In other words, in regions on the tuff samples that were saturated or at least had high water saturation, the direct diffusivity measurements agreed with theoretical predictions.

Hu et al. (2001 [DIRS 161623]) also measured tracer concentrations at greater depths into the cube by using the laser ablation technique to probe into the surface. They found that internal diffusion coefficients, at depths of 60 to 410 μm, were on the order of $10^{-16} \text{ m}^2 \text{ s}^{-1}$ (Hu et al. 2001 [DIRS 161623], p. 22). The measured volumetric water content of the tuff matrix was 8.9 percent (Hu et al. 2001 [DIRS 161623], p. 25). The mean diffusion coefficient predicted by the invert diffusion properties submodel (Equation 7.2.2.-1) would then be $2.6 \times 10^{-11} \text{ m}^2 \text{ s}^{-1}$. This is a factor of 10^5 larger than the measurement. Thus, the diffusion coefficient throughout most of a grain of crushed tuff is lower than that predicted by the invert diffusion properties submodel. This provides corroborating evidence that the invert diffusion properties submodel overestimates releases of radionuclides from the EBS. These data also show that the overestimation of diffusivities in the invert diffusion properties submodel may be excessive. However, insufficient data exist to reduce the uncertainty in this model, and, if this additional uncertainty were included in the invert diffusion submodel, estimated releases of radionuclides from the EBS would be reduced and no longer bounding. Because the model has a low impact on repository performance, the degree of uncertainty in this model is acceptable for the TSPA.

The study by Hu et al. (2001 [DIRS 161623]) was primarily a development of the technique for using LA-ICP-MS of microscale profiling of the distribution of diffusing tracers. However, in the process, some preliminary data were obtained that can be used to corroborate the electrical conductivity measurements of Conca and Wright (1992 [DIRS 100436]) and Conca et al. (1993 [DIRS 170709]).

Sections 7.2.1 and 7.2.2 have demonstrated that the component models of the EBS transport model meet Level II validation. Based on the validation results, the EBS transport model is adequate for its intended use.

7.2.3 Competitive Surface Complexation Model

Validation of the competitive surface complexation model (C-SCM) involves comparison with recent tabulations of K_{ds} measured in the laboratory (EPA 1999 [DIRS 170376]; EPA 2004 [DIRS 172215]). The EPA (1999 [DIRS 170376]; 2004 [DIRS 172215]) compiles K_{ds} for actinides (and other inorganic contaminants) measured on a large number of soils, rocks, and single mineral phases, and considers the general controls over sorption. This data set and critical analysis set some limits on the ranges of K_{ds} that might be expected and their functional dependencies on, for example, pH and P_{CO_2} . The comparison implicitly assumes that surface sites on exposed soil Fe(III) groups play a large role in determining overall soil K_{ds} at pH 7-9. (Exposed Al(III) groups should behave in a broadly similar fashion (Parks 1964 [DIRS 174361]) and are likewise considered collectively with Fe (III) sites).

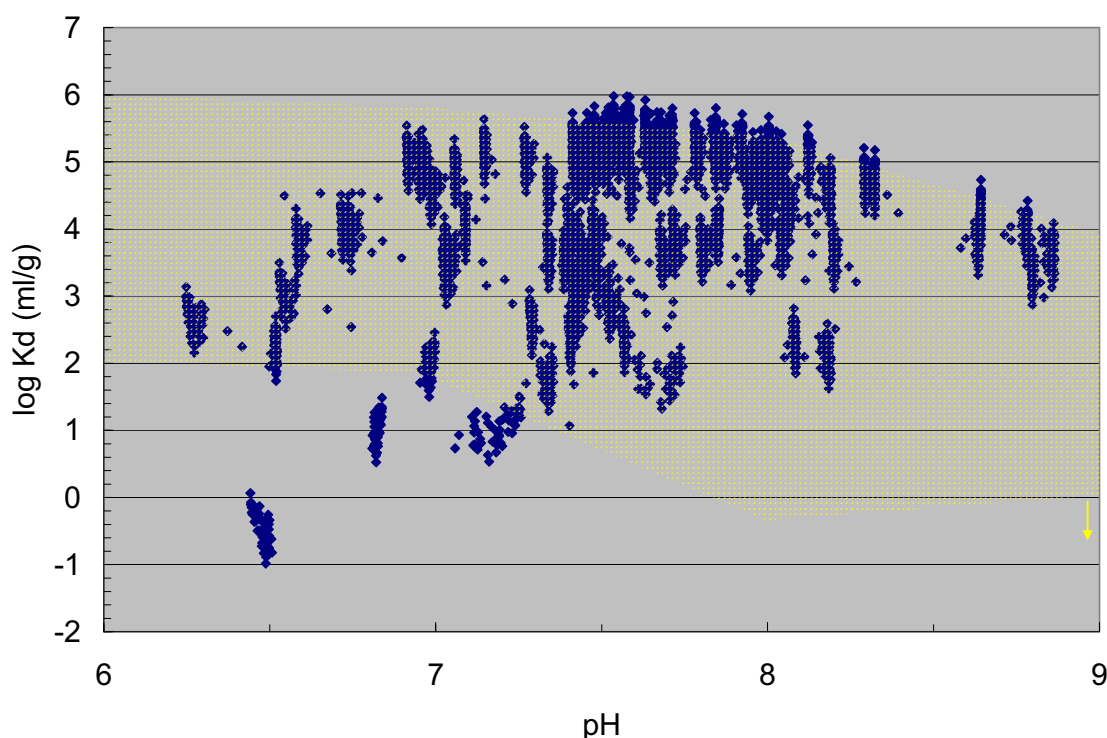
There are some obstacles to the comparison of the C-SCM and EPA compilation K_{ds} . The C-SCM predicts actinide K_{ds} only for iron oxyhydroxides, albeit for a wide range of available site densities. The EPA compilation typically provides K_{ds} for multi-mineralic soils that contain both clays and primary minerals (e.g., quartz, feldspars), as well as iron oxides and coatings and, possibly, organic matter. The iron oxide component of natural soils might be expected to dominate—and to be more easily resolvable—at pH 7 to 8, however. To begin with, quartz and feldspars tend to have relatively low surface areas and thus tend to be minor sorbers of actinides relative to clays and iron oxides. Typically, actinide sorption onto iron oxides is pH-dependent—maximal from pH 7 to 8, but lower at pH > 8 and pH < 7. At pH > 8, iron oxide surfaces become increasingly anionic, as do dissolved actinide complexes, causing adsorption to decrease. Plutonium, Uranium, Neptunium, and Americium all exchange onto clays. Clay exchange tends to be less pH-dependent and would be most clear in a soil containing both clays and iron oxides at pH values less than 7, where Fe oxide sorption is minimal. In other words, measured K_{ds} for a soil containing both clay and iron oxides (possibly including quartz and feldspar) should be larger at pH < 7 than what the C-SCM predicts for iron oxides. The actual difference would depend in a complex way on the iron content of the soil/rock considered in the latter reference and the degree to which it coated the primary minerals and clays. Adhesion of actinides to other soil functional groups (e.g., organics) might also lead to relatively high actinide uptake at pH values where iron oxide-actinide interaction is minimal.

The second difference between the two data sets is that, while the C-SCM considers competition with other surface species explicitly, the EPA compilation incorporates competition only implicitly and probably with less competition by surface-bound actinides. The EPA compilation K_{ds} are “snapshots” of actinide surface uptake in that any competition, for example, of sorbed Ca^{2+} for sorbed UO_2^{+2} , is not explicitly quantified. The bottoms-up approach of the C-SCM forces competition of actinides for surface sites at the outset. The inclusion of actinide (and Ni^{2+}) competition in the C-SCM might tend to lower the predicted K_{ds} relative to the EPA compilation. Any actual difference would depend in a complex fashion on the competing ions present in the EPA compilation K_{ds} and their respective binding constants. C-SCM K_{ds} were calculated for P_{CO_2} values ranging from 10^{-4} to 10^{-2} atm. Most soil K_{ds} are measured under ambient levels, $P_{CO_2} \sim 10^{-3.5}$ atm, which would tend to result in lower adsorption of those actinides that form carbonato complexes. The higher K_{ds} from the C-SCM are typically calculated when multiple extrema of the model are sampled (e.g., the highest surface areas, the

lowest P_{CO_2} values, the highest concentration of competing cations). When ranges closer to mean values are considered, the C-SCM K_d s are typically enveloped by the EPA soil K_d s. Lastly, although the EPA compilation considers sorption to pH values as low as 3, the comparison here will focus on the more repository relevant pH values of 6-9.

Uranium

EPA compilation U K_d s decrease from 10^2 to 10^6 ml g⁻¹ at pH 6 to <0.4 to 7,900 ml g⁻¹ at pH 9. The low end is for single mineral quartz substrates, the high end is for ferrihydrite (and kaolinite), which is probably more analogous to the C-SCM conditions. Some of the scatter in the EPA values comes from uncertainty in solution bicarbonate levels. The latter affect the formation of dissolved uranyl-carbonate species. Figure 7.2-11 shows the EPA compilation K_d range (from Table 5.17 in EPA 1999 [DIRS 170376]) as yellow shading. C-SCM K_d s are the blue diamonds. The pH < 7 EPA data might reflect exchange of uranyl onto clays (see above). A similar explanation might be applied to the other actinide sorption plots at these pH values as well, with the possible exception of thorium.



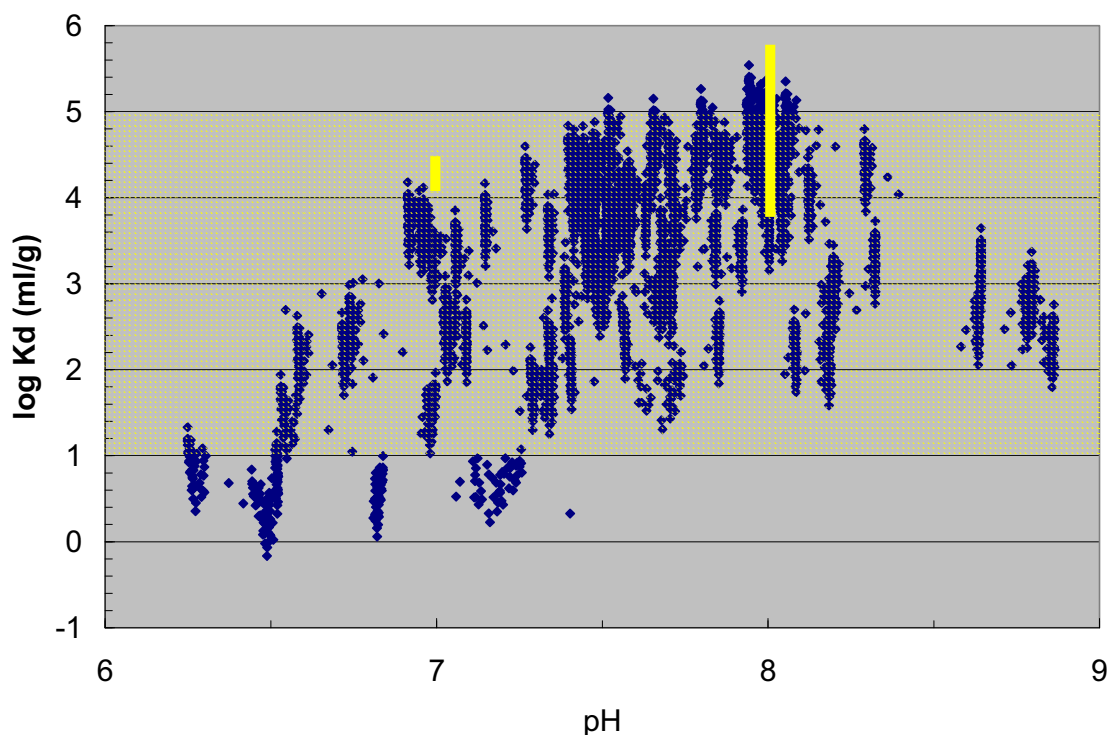
Source: EPA 1999 [DIRS 170376]

Figure 7.2-11. EPA U Soil K_d s (EPA 1999 [DIRS 170376]) and C-SCM Iron Oxide K_d s

From pH 7 to 9, the range of C-SCM predicted U K_d s tends to overlap the range of EPA soil U K_d s. Below pH 7, where clay contributions are presumed to raise the EPA data and the C-SCM predicts lower U K_d s, the datasets are less comparable.

Plutonium

There are very large uncertainties in plutonium sorption measurements (EPA 1999 [DIRS 170376]). Redox is often unmeasured and/or poorly controlled. Depending on the Pu valence state, solubilities may be exceeded in sorption experiments. Moreover, a number of minerals are able to shift the valence state of Pu during the sorption process. Although soil iron oxides are known to sorb Pu, the relationship between Fe content and Pu uptake is unclear (EPA 1999 [DIRS 170376]). The EPA review of literature Pu K_d s point to values between 10 and 10^5 ml g⁻¹. This range is compared with C-SCM K_d s in Figure 7.2-12. Figure 7.2-12 shows admittedly non-competitive sets of “iron oxide only” K_d s measured by Lu et al. (2000 [DIRS 166315]) and Sanchez et al. (1985 [DIRS 107213]). The Lu et al. (2000 [DIRS 166315], Table 2) values range from 4,900 to 170,000 ml g⁻¹ and were measured in J-13 and synthetic J-13 water having a pH ~8 and on colloidal hematite. Although the dissolved species present in J-13 were available to compete with actinides for surface sites, there was no competition among multiple actinides. Sanchez et al. (1985 [DIRS 107213]) measured Pu(IV) and Pu(V) sorption onto goethite, but did not report a gram specific surface area. Estimation of the latter (57 m² g⁻¹) would point to pH 7 K_d s of 13,000 to 32,000 ml g⁻¹. (The synthesis approach used by Sanchez et al. (1985 [DIRS 107213]) tends to produce surface areas of about 50 m² g⁻¹. The value 57 m² g⁻¹ was chosen because it would result in experimental ratios of 1.0 g L⁻¹.) A higher surface area would give lower K_d s and vice versa.



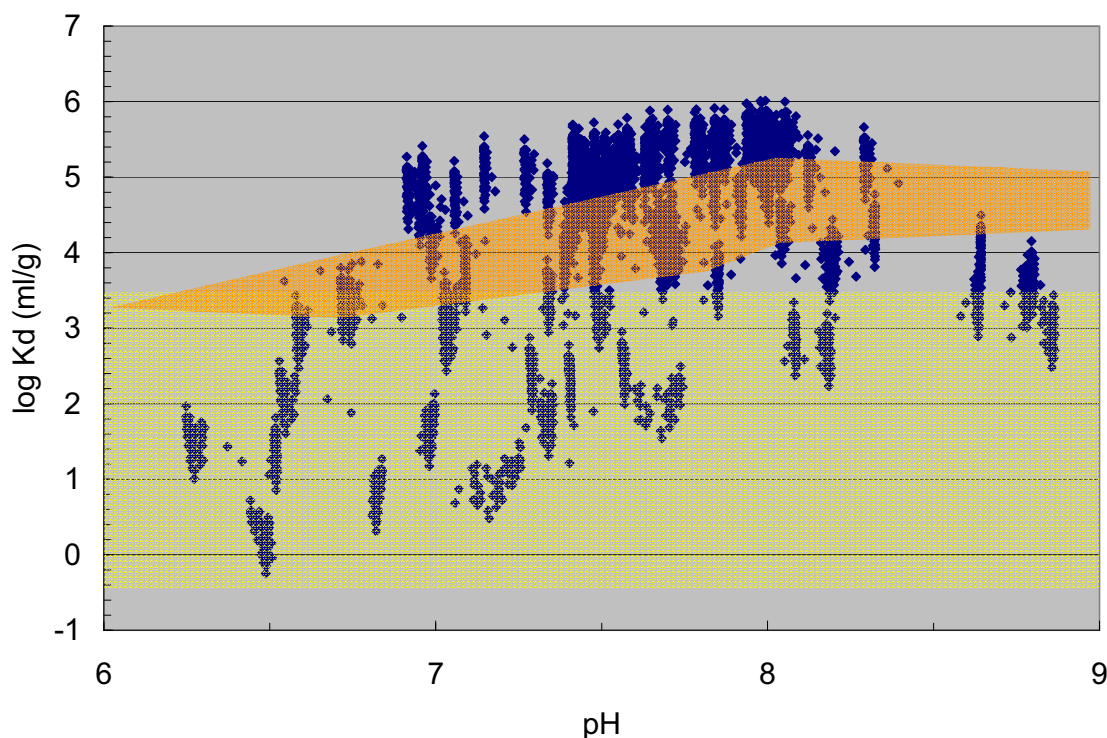
Sources: EPA 1999 [DIRS 170376]; Lu et al. 2000 [DIRS 166315]; Sanchez et al. [DIRS 107213]

NOTES: The yellow bar at pH 8 is the range of Pu K_d s measured on hematite colloids by Lu et al. (2000 [DIRS 166315]); the yellow bar at pH 7 shows estimated Pu K_d s from Sanchez et al. (1985 [DIRS 107213]).

Figure 7.2-12. EPA Pu Soil K_d s (EPA 1999) and C-SCM Iron Oxide K_d s

Neptunium

The EPA (2004 [DIRS 172215]) quotes Thibault et al. (1990 [DIRS 101161]), who report a range of 0.4 to 2575 ml g⁻¹ from a compilation of soil (sand, silt, clay only) Np K_d s. Figure 7.2-13 compares this range to the C-SCM predictions and to Jerden and Kropf (2007 [DIRS 181295]) K_d s for Np sorption on goethite. The Np K_d s predicted by the C-SCM appear to be at most a factor of ten higher than those measured by Jerden and Kropf (2007 [DIRS 181295]) on goethite. Part of this difference may arise from the fact that the C-SCM predicts sorption onto a mixture of ferrihydrite and goethite, and ferrihydrite has a surface area that is roughly five times that of goethite (in their mean values). The higher K_d s from the C-SCM are calculated when multiple extrema of the model are sampled (e.g., the highest surface areas, the lowest P_{CO_2} values, the highest concentration of competing cations). Sampling over the non-extrema of the model brings the predicted Np K_d s closer to measured values.



Sources: EPA 2004 [DIRS 170376]; Jerden and Kropf 2007 [DIRS 181295]

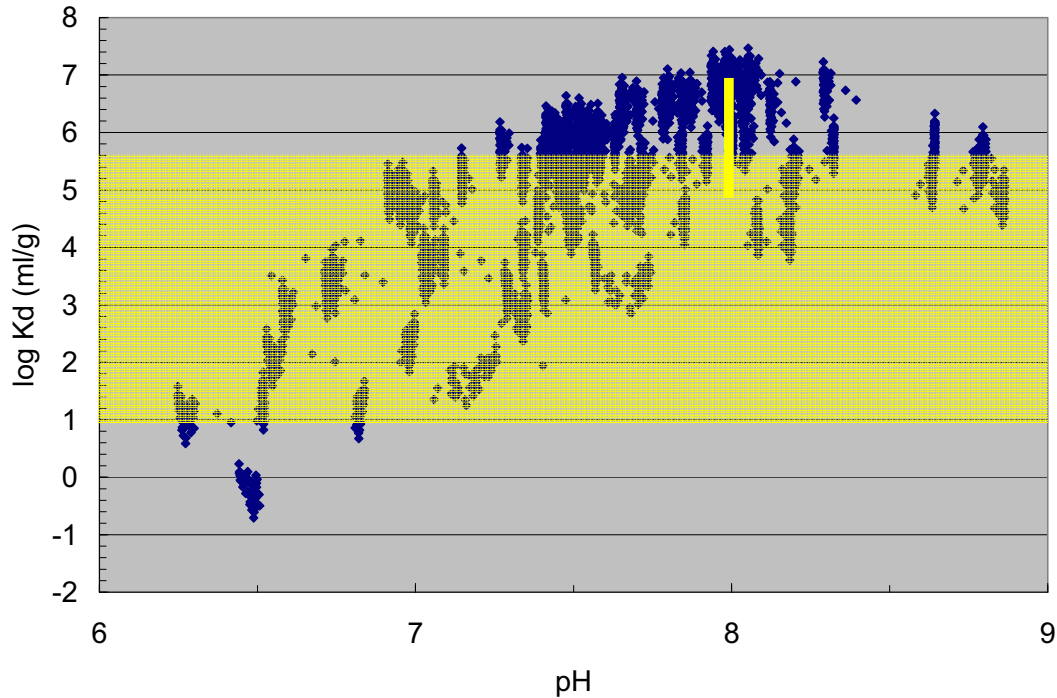
NOTE: The orange shaded area gives the range of Np K_d s measured on goethite by Jerden and Kropf (2007 [DIRS 181295]).

Figure 7.2-13. EPA Np Soil Kds (EPA 1999 [DIRS 170376]) (Yellow Shaded Area) and C-SCM Iron Oxide Kds

Americium and Thorium

The EPA (2004 [DIRS 172215]) quotes Thibault et al. (1990 [DIRS 101161]), who report a range of 8.2 to 400,000 ml g⁻¹ from a compilation of soil (sand, silt, clay only) Am K_d values and notes a clear correlation between soil K_d and soil Fe/Am oxide content. Figure 7.2-14 compares

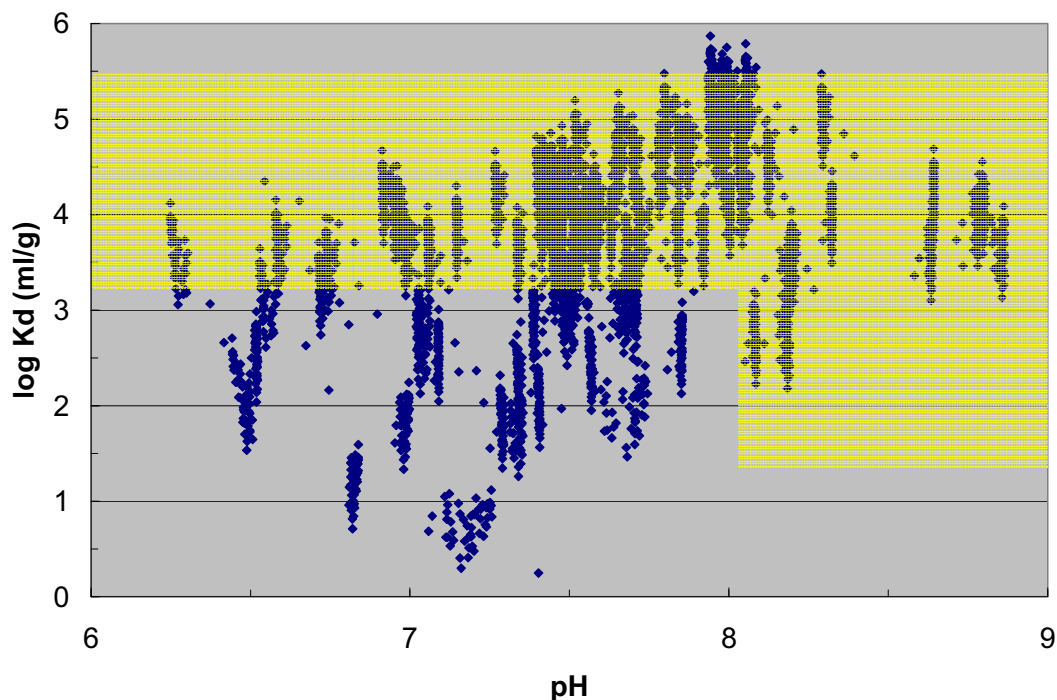
this range, the C-SCM results, and the hematite colloid Am K_{ds} of Lu et al. (2000 [DIRS 166315]). Figure 7.2-15 compares EPA (1999 [DIRS 170376]) and C-SCM thorium K_{ds} . The maximal Am K_{ds} predicted by the C-SCM appear to be roughly a factor of two higher than the maximal Am K_{ds} measured by Lu et al. (2000 [DIRS 166315]) on colloidal hematite. This is not a large difference compared to the range of C-SCM predicted K_{ds} at a given pH (3 – 4 orders of magnitude) and soil K_{ds} (4 – 5 orders of magnitude). The higher Am K_{ds} are calculated when multiple extrema of the model are sampled (e.g., the highest surface areas, the lowest P_{CO_2} values, the highest concentration of competing cations).



Sources: EPA 1999 [DIRS 170376]; Lu et al. [DIRS 166315]

NOTE: The yellow bar at pH 8 is the range of Am K_{ds} measured on hematite colloids by Lu et al. (2000 [DIRS 166315])

Figure 7.2-14. EPA Am Soil K_{ds} and C-SCM Iron Oxide K_{ds}



Source: EPA 1999 [DIRS 170376]

Figure 7.2-15. EPA Th Soil K_d s and C-SCM Iron Oxide K_d s

Summary

C-SCM predictions of actinide uptake are consistent with compilations of soil K_d s for the actinides considered. Soil K_d s for a given pH tend to vary by 2 to 4 orders of magnitude, while C-SCM predicted K_d s vary by 3 to 4 orders of magnitude for a given pH. The larger uncertainty for the C-SCM results is expected because it reflects the combination of effects due to uncertainty in various input parameters such as dissolved concentrations, sorption sites, and P_{CO_2} . The C-SCM occasionally predicts higher and lower values than are found in soils, or are measured in the lab. Advective transport of dissolved actinides will be under-predicted when estimated K_d s are higher than the true value, but colloidal transport will be over-predicted. When estimated K_d s are lower, colloidal transport will be under-predicted, but advective transport of dissolved actinides will be over-predicted. The overall comparison of results indicate that the K_d s computed from the C-SCM can be corroborated with the published values in the literature.

7.2.4 Results of Critical Review of the EBS Flow and Transport Models

A critical review of the EBS transport model was conducted as specified in the TWP (BSC 2006 [DIRS 177739], Section 2.2.3). This model validation approach is justified based on requirements of SCI-PRO-006, Section 6.3.2, where the critical review is listed as an appropriate method for model validation. The results of the critical review of the EBS transport model are presented in Appendix M.

7.3 EBS-UZ INTERFACE MODEL

The output of the invert domain feeds into the unsaturated zone through the EBS-UZ interface model. In the RTA, the invert is modeled as a single-continuum porous medium whereas the adjacent UZ is modeled as a dual continuum fracture-matrix medium. The model is described in detail in Section 6.5.2.6.

The mass flux from the invert flows into the top layer of the middle zone in the UZ. The portion of the advective flux from the invert that is attributable to the seepage flux (F_1) flows into the UZ fractures. The imbibition flux into the invert (F_7) flows out of the invert into the UZ matrix. The diffusive flux from the invert can go into both UZ continua based on the concentration gradient and effective diffusion coefficient. The diffusive area remains the same because they are overlapping continua. The advective flux flowing through the UZ fracture cells in the middle zone is given by the greater of the advective flux out of the invert and the steady state UZ fracture flux. The advective flux in the two outer zones is given by the steady state UZ flow in each continuum at the repository horizon; the drift shadow effects are ignored.

For the TSPA, a semi-infinite zero concentration boundary condition is used for the EBS-UZ interface. This is approximated by applying an effective zero-concentration boundary at approximately three drift diameters below the invert-UZ boundary into the UZ. By moving the zero concentration boundary some distance below the invert, a more realistic diffusive gradient through the invert is achieved.

The EBS-UZ interface model of the RTA provides input to the unsaturated zone radionuclide transport model in *Particle Tracking Model and Abstraction of Transport Processes* (SNL 2007 [DIRS 181006]). The appropriate level of confidence identified for unsaturated zone radionuclide transport is Level II. Therefore, Level II also represents appropriate level of confidence for the EBS-UZ interface model of the RTA.

Section 7.3.1 describes an alternative two-dimensional drift-scale dual continuum flow model developed using TOUGH2 V1.6 (2003 [DIRS 161491]), which is coupled with the transport model developed using T2R3D V1.4 (1999 [DIRS 146654]) that is used to compute the fracture-matrix flux partitioning at steady state. Results from this model (an independent mathematical model) are compared with the results of the EBS-UZ interface model using similar boundary conditions in order to validate the EBS-UZ interface model of the RTA. Section 7.3.1.8 compares the two interface models and discusses the applicability and suitability of the EBS-UZ interface model for TSPA transport modeling.

7.3.1 Description of Drift-Scale Dual Continuum Flow and Transport Model

A dual-continuum model to represent flow and transport through the invert to the UZ rock near the drift is developed for non-seeping drifts. The UZ rock is composed of fracture continuum and a matrix continuum while the invert is conceptualized to be composed of an intergranular continuum (which consists of the large pore spaces between invert grains) and an intragranular continuum (which consists of the small pore spaces inside the grains). Figure 7.3.1 shows the matrix/intragranular continuum, and there is a corresponding fracture/intergranular continuum at each point in space. The calculation uses a pseudo-3D representation in the y -direction for the

fracture and matrix continua. Each continuum is globally connected across all cells that have a common interface. At each point in space, the matrix/intragranular continuum is connected to the fracture/intergranular continuum. At the invert-rock boundary, global fracture-matrix connections are used between the intragranular porosity and the fractures as well as the intergranular porosity and the rock matrix. There is no seepage inside the drift.

The model domain is limited to a section of the Topopah Spring lower lithophysal unit, also denoted as the tsw35 model unit in the UZ flow and transport models (BSC 2005 [DIRS 175177], Section 6.1.5). This model unit was chosen because more than 80 percent of the waste emplacement area lies within this model unit (SNL 2007 [DIRS 179466]). The model developed is a two-dimensional symmetry model in which one-half of the cross section of the drift and the surrounding rock is represented. The two-dimensional domain extends from 17.5 m above the drift center to 47.5 m below the center of the drift, for a total vertical dimension of 65 m. The domain width is 40.5 m, which is half the distance between centers of waste emplacement drifts. The nodes shown in Figure 7.3.1 represent the centers of the elements, not the edges.

The cells are further divided into spatial zones given in the color coding of Figure 7.3.1a and b. These regions are (1) the general rock matrix excluding the drift shadow zone, (2) intragranular invert pore space excluding the cells at the top of the invert, (3) the intragranular pore space cells at the top of the invert, and (4) the rock matrix below the drift, designated as the drift shadow zone. Diversion of water by the waste emplacement drift leads to a zone of reduced water flow and saturation below the drift known as the drift shadow zone. The partitioning into drift shadow zone and other rock matrix was done to express the effects of reduced water saturation in the drift shadow zone on the effective diffusion coefficient in that zone. The invert is differentiated from the rock to represent the different properties and conditions in the invert, and the special cells at the top of the invert are distinguished because these cells are the cells used to release solutes into the system. Cells representing the air gap inside the drift above the invert are also given a separate designation. A parallel set of zones are also used for the fracture/intergranular continuum. Details concerning the grid development and structure are given in Appendix I.

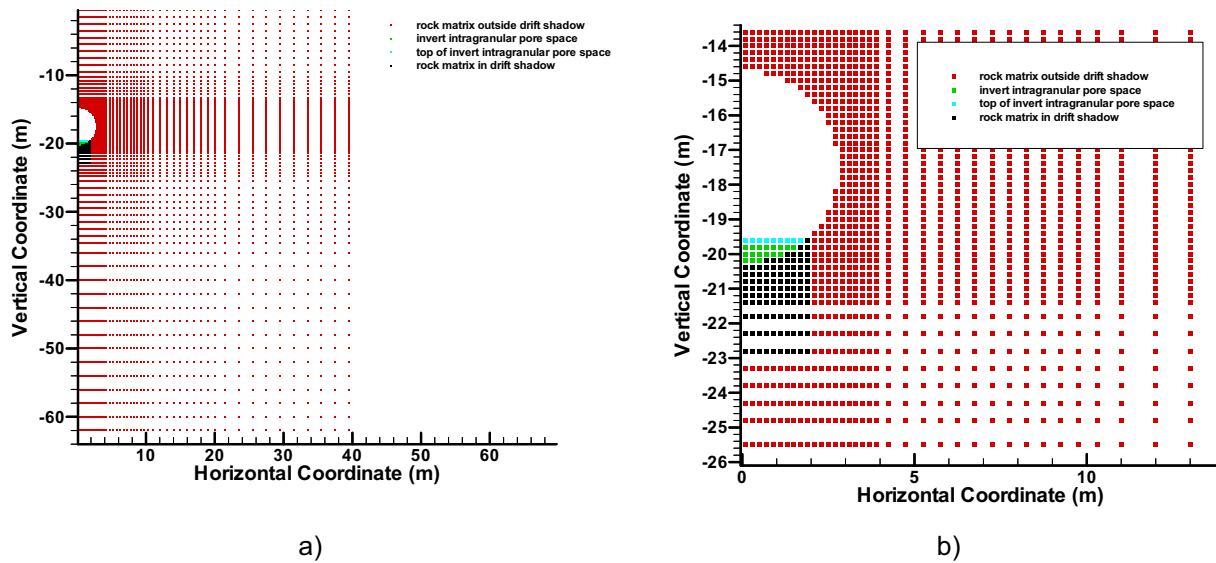


Figure 7.3-1. Domain used for the RTA Validation Calculation a) Full Domain b) Detail of the Domain Near the Waste Emplacement Drift

7.3.1.1 Conceptual Approach for Flow and Transport Processes

Flow is modeled using the traditional extension of Darcy's law for unsaturated conditions. In a dual-continuum, separate pressure and saturation conditions are used for the fracture/intergranular continuum and the matrix/intragranular continuum. Separate flow occurs in each continuum within its own global network, with local flow exchange between the continua. For mass transport, separate concentration conditions are used for the two continua, with global transport within each continuum and local exchange between the continua. Advective and diffusive transport processes are represented. Only non-sorbing, non-reactive solutes are evaluated. However, under steady-state solute mass flux conditions, linear equilibrium sorption processes will not affect the aqueous flux or concentration distributions. Hydrodynamic dispersion is neglected due to the minor effects this process has on transport in a dual-continuum system (*Particle Tracking Model and Abstraction of Transport Processes* (SNL 2007 [DIRS 181006], Section 4.1.2).

Flow distributions in the fracture continuum, are treated using the active fracture approach (Liu et al. 1998 [DIRS 105729]), which incorporates smaller-scale non-uniform flow within the fractures as a continuum property. The postulate is that only a subset of the total fracture population participates in the flow, therefore, flow is focused into a set of active fractures. This postulate affects the flow and transport behavior in the fractures as well as fracture-matrix exchange of both water and dissolved solutes. Connections between the rock matrix and fractures and the invert and the fractures are affected by the active fracture method because it fundamentally relates to the distribution of water flow in the fractures. The active fracture approach is not used for the intergranular continuum in the invert.

7.3.1.2 Parameterization for Flow

The fractured rock of the tsw35 is parameterized using the values given in DTN: LB0208UZDSCPMI.002 (BSC 2002 [DIRS 161243]). These consist of the permeability, porosity, capillary strength (van Genuchten α), pore-size distribution index (van Genuchten m), and residual saturation for both the fractures and matrix. This DTN also provides the active fracture parameter. The intragranular properties for the invert are also taken from the matrix properties of the tsw35 given in DTN: LB0208UZDSCPMI.002 (2002 [DIRS 161243]). The intergranular invert properties are the LTBM-2 average values taken from DTN: LB0208UZDSCPMI.002 (2002 [DIRS 161243]), except for the residual saturation, which was taken from an earlier version of DTN: LB0208UZDSCPMI.002 (2002 [DIRS 161243]) that was current when these calculations were carried out. The intergranular invert residual saturation is now specified to be 0.01, whereas the previously specified value, used in the calculations described here, was 0.15. Since this validation calculation, unlike TSPA compliance calculations, is merely intended to demonstrate that the EBS-UZ interface model gives similar results to an independently developed model, the use of a parameter value that is no longer current does not impact the validity of the comparison. The only important hydrological property of the air gap is the capillary strength as specified in the van Genuchten α parameter. By setting this parameter to a very high value, the air gap will divert all percolation flux around the drift. All other hydrological parameter values used for the air gap are simple placeholders and do not affect the behavior of the solution. Hydrological parameter values are summarized in Table 7.3-1.

Table 7.3-1. Hydrological Properties

Region	Porosity	Permeability (m ²)	van Genuchten α (Pa ⁻¹)	van Genuchten m	Residual Saturation
tsw35 matrix	0.131	4.48×10^{-18}	1.08×10^{-5}	0.216	0.12
tsw35 fracture*	0.0096	9.1×10^{-13}	1.02×10^{-4}	0.633	0.01
invert, intragranular	0.131	4.48×10^{-18}	1.08×10^{-5}	0.216	0.12
invert, intergranular	0.224	4.19×10^{-12}	1.781×10^{-2}	0.283	0.15 [‡]
air gap	1.0	1.0×10^{-12}	1.0×10^{10}	0.5	0.01

* The active fracture parameter for the rock fractures is 0.569.

‡ Value taken from a previous version of DTN: LB0208UZDSCPMI.002 (2002 [DIRS 161243]); currently accepted value is 0.01.

7.3.1.3 Parameterization for Transport

The only remaining parameter required for transport calculations, in addition to the parameters given for flow, are the diffusion coefficients. For the transport software used in this analysis, T2R3D V1.4 (1999 [DIRS 146654]), the effective diffusion coefficient in geologic or other porous materials is specified by a free-water diffusion times a tortuosity. The nominal free-water diffusion coefficient, D_0 , was taken to be $2.299 \times 10^{-9} \text{ m}^2 \text{ s}^{-1}$. Different correlations are used for assignment of diffusion coefficients in the invert and in the UZ rock.

Diffusion in the Rock

Diffusion coefficients for the rock matrix were assigned using the relationship reported in *Particle Tracking Model and Abstraction of Transport Processes* (SNL 2007 [DIRS 181006], p. 6-42):

$$\log(D_m) = -7.49 + 1.38\theta_m + 0.165\log(k_m), \quad (\text{Eq. 7.3.1.3-1})$$

where θ_m is the water content of the rock matrix and k_m is the effective permeability (m^2) of the rock matrix to water. The diffusion coefficient, D_m , is in units of $\text{m}^2 \text{s}^{-1}$.

The rock is divided into a “shadow zone” beneath the drift and the rock outside the matrix. The shadow zone was defined to be the area from the centerline to 1.9 m (one cell beyond the width of the invert) in the horizontal direction and from the elevation of the top of the invert (-19.6 m) to one drift radius below the lowest point on the drift (-23 m) in the vertical direction. The rock outside the shadow zone where significant transport would occur was defined to be the remaining rock in the region below the top of the invert (-19.6 m). Due to a lack of relevant data, Equation 7.3.1.3-1 was also used to determine diffusion coefficients in the rock fractures, where the water content and effective permeability of the rock fractures were used. Volume-weighted average values of water content and effective permeability were used for the fractures and rock matrix in both regions. Once the diffusion coefficient, D_m , was determined from Equation 7.3.1.3-1, the tortuosity, τ , was calculated as:

$$\tau = \frac{D_m}{D_0}. \quad (\text{Eq. 7.3.1.3-2})$$

Based on the average water content and effective permeability of both rock matrix and fractures, inside the drift shadow zone and outside the drift shadow zone, average tortuosity coefficients were derived and are summarized in Table 7.3-2.

Table 7.3-2. Tortuosity Coefficients for Diffusion in the Rock

Region	Average Water Content	Average Effective Permeability (m^2)	Tortuosity
tsw35 matrix in drift shadow	0.118	1.25×10^{-19}	0.0156
tsw35 fracture in drift shadow	0.000194	2.19×10^{-17}	0.0251
tsw35 matrix outside drift shadow	0.118	1.19×10^{-19}	0.0154
tsw35 fracture outside drift shadow	0.000273	7.29×10^{-17}	0.0306

Diffusion in the Invert

Radionuclide releases from drifts without seepage are expected to occur primarily through diffusion. Although some low levels of advection occur between the invert and the rock (from imbibition of water from the host rock into the invert and back to the host rock), the advective transport is small compared with diffusive transport when all water is diverted around the drift in

the no seepage case. Furthermore, differences in solute concentrations in the intergranular and intragranular porosities are expected to be small. Therefore, the diffusion coefficient for the invert is developed as an effective single continuum.

The diffusion coefficient correlation for the invert (based on Equation 6.3.4.1.1-22) is given as:

$$\phi_I S_{wI} D_I = D_0 \phi_I^{1.863} S_{wI}^{1.863} 10^{ND(\mu=0.033, \sigma=0.218)}, \quad (\text{Eq. 7.3.1.3-3})$$

where ϕ_I is the total porosity, and S_{wI} is the water saturation of the invert as an effective continuum. The tortuosity, $\tau = \frac{D_I}{D_0}$, is equal to:

$$\tau = \phi_I^{0.863} S_{wI}^{0.863} 10^{ND(\mu=0.033, \sigma=0.218)}. \quad (\text{Eq. 7.3.1.3-4})$$

The average value of the statistical parameter, $10^{ND(\mu=0.033, \sigma=0.218)}$, is used, which is $10^{0.033} = 1.078947$. Therefore,

$$\tau = 1.078947 \theta_I^{0.863}, \quad (\text{Eq. 7.3.1.3-5})$$

where $\theta_I = \phi_I S_{wI}$ is the invert water content, including both the intergranular and intragranular water. The bulk intragranular porosity, $\phi_{b,inter}$ (i.e., the intragranular pore volume divided by the bulk volume occupied by the invert), is given by:

$$\phi_{b,intra} = \phi_{intra} (1 - \phi_{inter}), \quad (\text{Eq. 7.3.1.3-6})$$

where ϕ_{intra} is the porosity of the intragranular pore space, 0.131 (i.e., the porosity of individual grains), and ϕ_{inter} is the intergranular porosity, 0.224 (which is a bulk porosity). The quantity $(1 - \phi_{inter})$ is the fraction of the bulk volume occupied by the intragranular material. The total water content of the invert is then:

$$\theta_I = \phi_{b,intra} S_{w,intra} + \phi_{inter} S_{w,inter}, \quad (\text{Eq. 7.3.1.3-7})$$

where $S_{w,intra}$ is the average intragranular water saturation, and $S_{w,inter}$ is the average intergranular water saturation. The resulting average water content was 0.1379 and the average tortuosity in the invert was found to be 0.1952.

Diffusion in the Air Gap

Because of the expected low water content of the air gap within the drift above the invert, the diffusion coefficient was set to $1.0 \times 10^{-20} \text{ m}^2 \text{ s}^{-1}$ and the tortuosity was set to 1.0×10^{-20} . These low values ensured that the diffusion of aqueous solutes was negligible in the air gap.

7.3.1.4 Flow Boundary Conditions

The flux into the boundary cell connected to the upper cells of the rock matrix is a fixed rate of $0.016955 \text{ mm yr}^{-1}$. The flux into the boundary cell connected to the rock fracture is a fixed $19.814 \text{ mm yr}^{-1}$. These values are considered representative of the glacial-transition mean climate in the tsw35 of the repository area. The specific values were taken from DTN: LB03023DSSCP9I.001 [DIRS 163044]). Details concerning the specific information taken from this DTN and the conversion of this information into flow injection rates used for the boundary cells is given in Appendix I. The side boundaries are symmetry, no-flow boundaries. The bottom boundary is also a no-flow boundary. To avoid the change in hydrologic conditions at the bottom of the model resulting from the no-flow condition, the two bottom boundary cells for the fractures and matrix were assigned very large volumes such that hydrological conditions in these cells remain essentially constant over the simulation period.

7.3.1.5 Transport Boundary Conditions

For solute transport, all external boundaries are no-flux boundaries. The nine cells at the top of the invert are used to inject solute at a constant rate. The total solute injection rate is $9 \times 10^{-13} \text{ kg s}^{-1}$. Details concerning the specific cells and solute injection rates, used for the top invert cells, are given in Appendix I. Because solute moves principally downward by advection in the UZ rock, solute ultimately finds its way into the two bottom boundary cells. Because these cells were assigned a very large volume, the solute concentration conditions in these cells are essentially constant over the simulation period.

7.3.1.6 Results of the Flow Calculation

Flow calculations were performed using TOUGH2 V1.6 (2003 [DIRS 161491]). The simulations were conducted for a time period of ten billion years to ensure that steady-state conditions were achieved. The saturation conditions in the rock matrix/intragranular pore space is shown in Figures 7.3-2a and b.

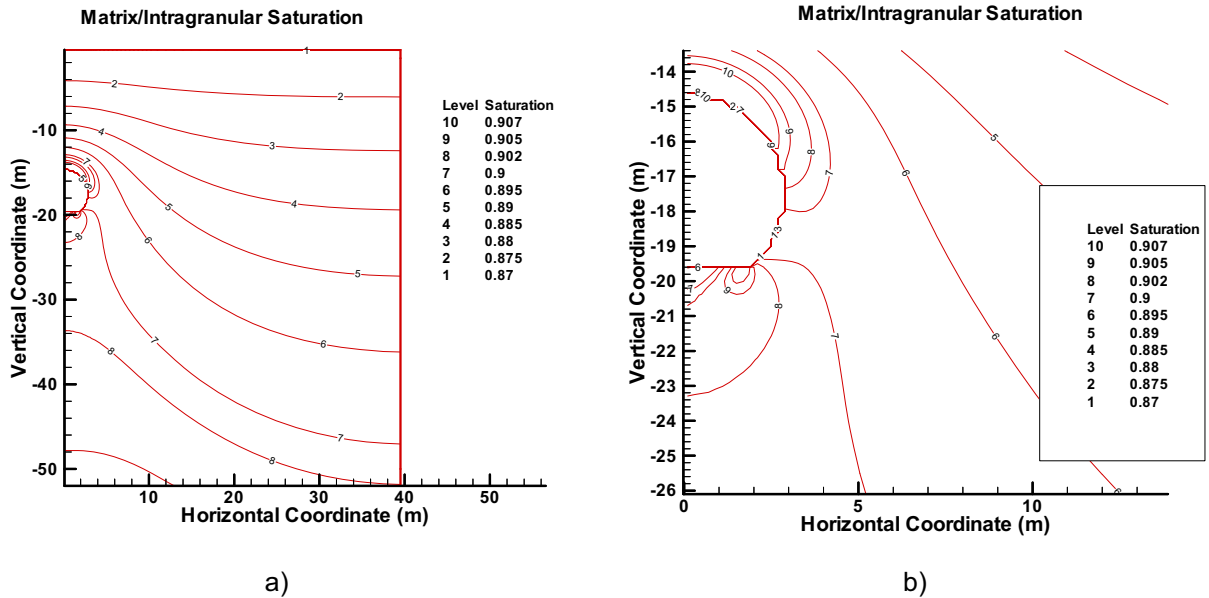


Figure 7.3-2. Matrix/Intragranular Water Saturations a) Saturation Contours Over Entire Domain; b) Saturation Contours Near the Drift

A general increase in matrix saturation with depth is a result of flow exchange between the fractures and the rock matrix. These figures also show a zone of enhanced saturation at the top of the drift where water is diverted around the drift by the capillary barrier of the air gap in the drift. Saturation contours below the drift are affected by the presence of the drift; however, saturation levels are not substantially smaller.

Fracture/intergranular saturations are shown in Figures 7.3-3a and b. Fracture saturations are more strongly affected by the flow pattern around the drift. High saturations are found at the top of the drift resulting from flow diversion around the drift. A more substantial drift shadow is found below the drift where water saturations are depressed. Intergranular water saturations in the invert are large compared with the fractures primarily because of the much larger residual saturation for the intergranular pore space (0.15) as compared with the fractures (0.01).

Water flux levels in the rock matrix/intragranular pore space are shown in Figure 7.3-4. The contours parallel those of water saturation in Figure 7.3-2; however, a zone of reduced vertical flux is found near the bottom of the drift and in the intragranular pore space.

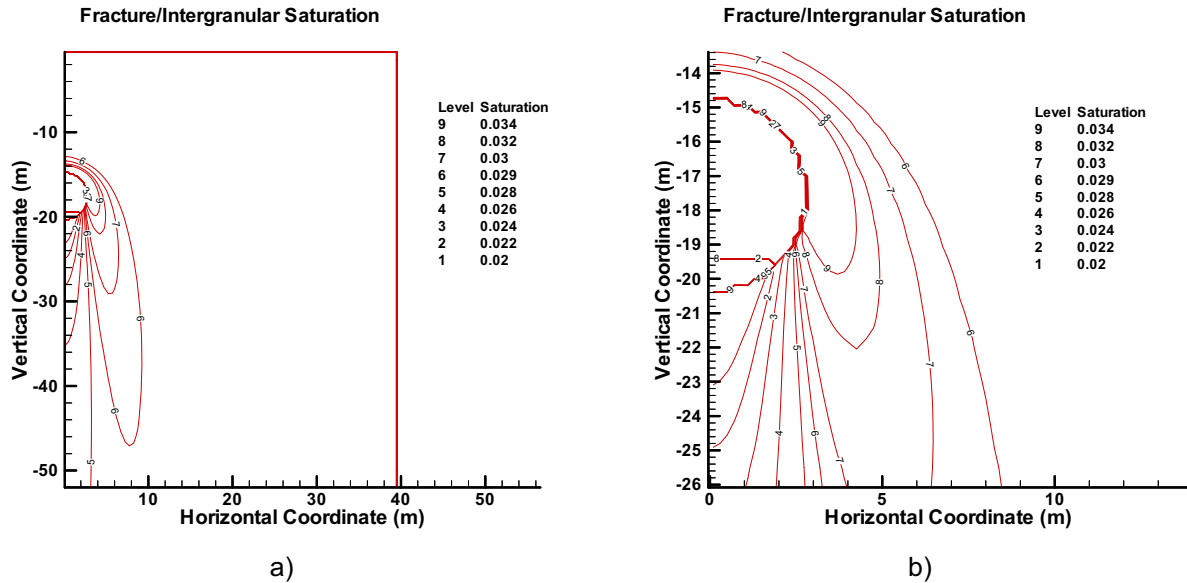


Figure 7.3-3. Fracture/Intergranular Water Saturations a) Saturation Contours Over Entire Domain; b) Saturation Contours Near the Drift

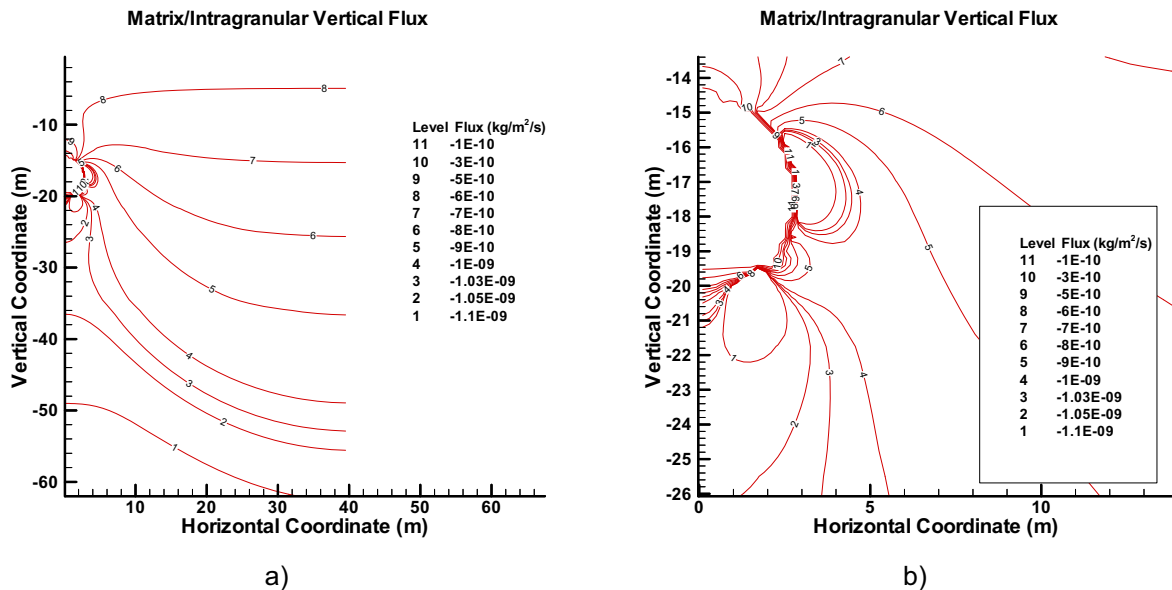


Figure 7.3-4. Matrix/Intragranular Water Flux a) Flux Contours Over Entire Domain; b) Flux Contours Near the Drift

Water flux levels in the fractures/intergranular pore space are shown in Figure 7.3-5. The contours parallel those of water saturation in Figure 7.3-3. As in the case of water saturations, a strong depression in the water flux is found below the drift, as well as enhanced flux moving from near the top of the drift along the right side of the drift. At the top of the drift the flux is reduced because a stagnation point in the flow field occurs at exactly the top of the drift.

The vertical flow rate from the invert to the rock was determined to be $-2.65 \times 10^{-10} \text{ kg s}^{-1}$, or $-0.00835 \text{ kg yr}^{-1}$ (by convention the negative sign indicates vertically downward flux). The associated vertical Darcy flux rate from the invert to the rock was found to be $-0.00184 \text{ mm yr}^{-1}$.

Details concerning the conduct of the flow calculations and post-processing of the results are given in Appendix I.

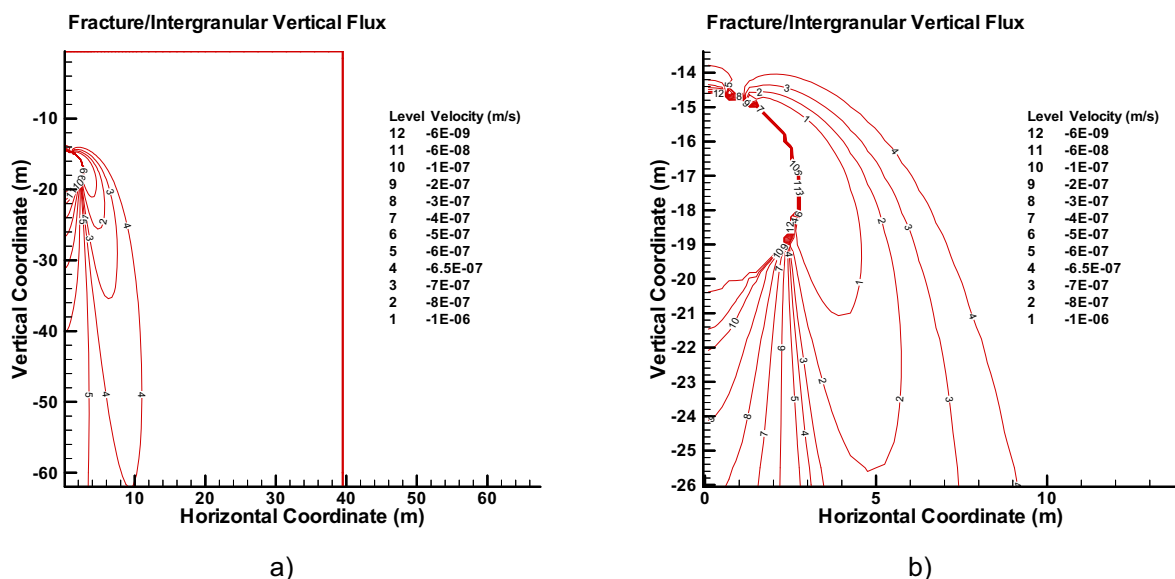


Figure 7.3-5. Fracture/Intergranular Water Flux a) Flux Contours Over Entire Domain; b) Flux Contours Near the Drift

7.3.1.7 Results of the Transport Calculation

Transport calculations were performed using T2R3D V1.4 (1999 [DIRS 146654]). The simulations were conducted for a time period of ten billion years to ensure that steady-state conditions were achieved. The solute concentrations in the rock matrix/intragranular pore space are shown in Figures 7.3-6a and b. The flow model output showed zero change in saturation for all cells in the model, to the five-place accuracy in the output, between the next-to-last time step at 2.74 billion years and the last time step at 10 billion years. Therefore, it can be concluded that steady state was achieved at or before 2.74 billion years. An approximate steady state suitable for this analysis may have been achieved at an earlier time, but finding out exactly when that occurred was not an objective of this work.

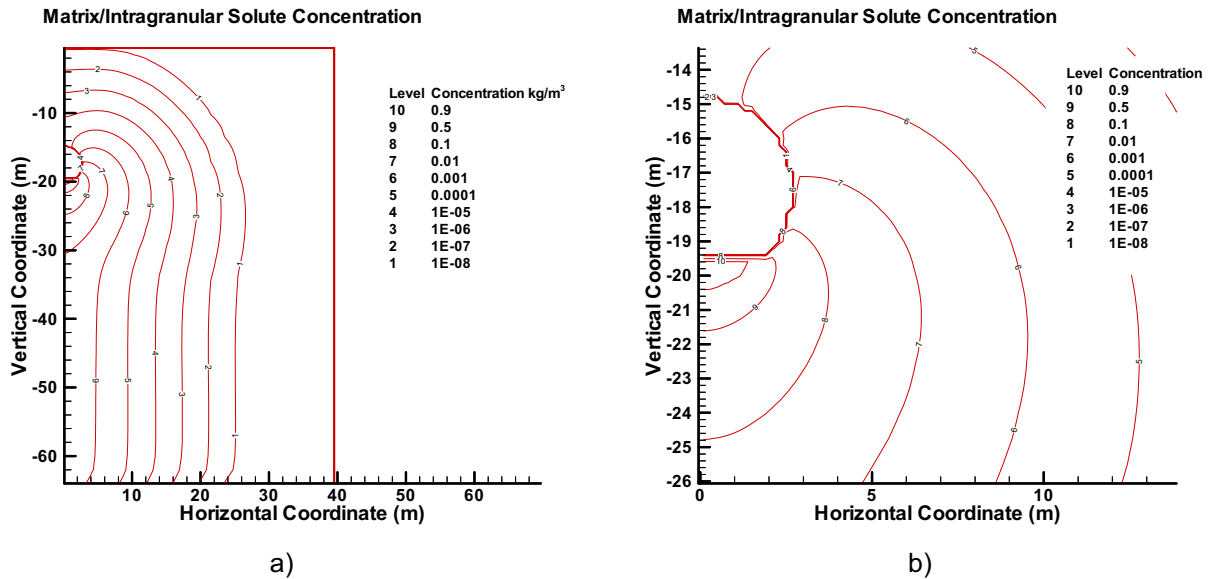


Figure 7.3-6. Matrix/Intragranular Solute Concentrations a) Concentration Contours Over Entire Domain; b) Concentration Contours Near the Drift

These figures show that diffusive transport in the rock matrix allows for a small amount of solute released at the top of the drift invert to migrate above the drift. Similarly, the advective transport process tends to keep concentrations low at locations horizontally displaced from the drift. The main solute concentration field lies beneath the drift.

Fracture/intergranular concentrations are shown in Figures 7.3-7a and b. Fracture concentrations display a similar pattern to the concentrations in the matrix. However, the solute concentration contours are slightly more restricted to the area around and beneath the drift and more elongated in the vertical direction than the solute concentration contours in the matrix.

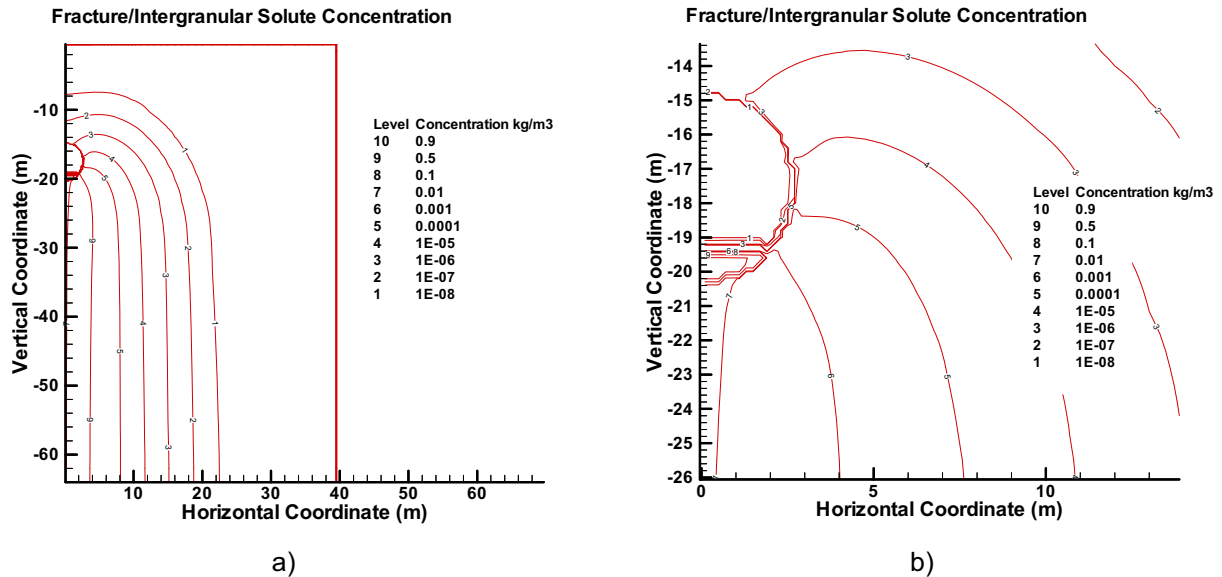


Figure 7.3-7. Fracture/Intergranular Solute Concentrations a) Concentration Contours Over Entire Domain. b) Concentration Contours Near the Drift

Solute flux in the matrix/intragranular pore space is shown in Figure 7.3-8a and b. Solute flux is shown to be upward at vertical coordinates above the top of the invert (at -19.6 m), and downward below this level. The upward movement is diffusive and is counter to the advective flow in the matrix. Most of the flux occurs in the zone below the invert.

Solute flux in the fracture/intergranular pore space is shown in Figure 7.3-9a and b. In this case solute flux is downward both above and below the level to the top of the invert. Solute that diffuses upwards in the rock matrix exchanges with the fractures and is transported downward by advection in the fractures. The peak solute flux contour emerges below the drift because of the preferential initial exchange of solute between the invert and rock in the rock matrix.

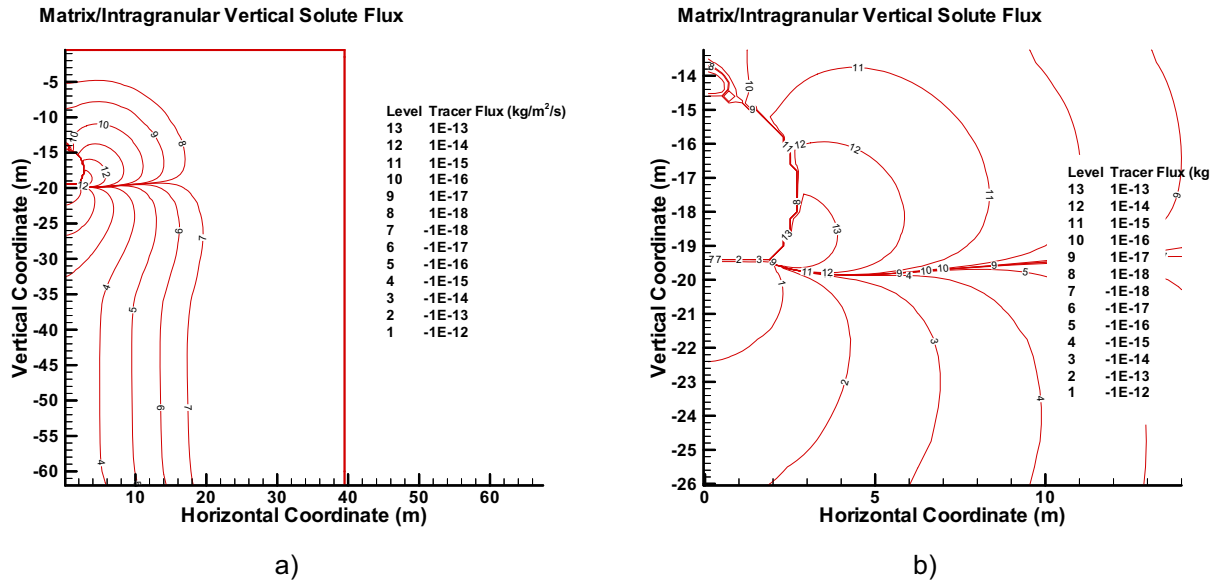


Figure 7.3-8. Matrix/Intragranular Solute Flux a) Solute Flux Contours Over Entire Domain; b) Solute Flux Contours Near the Drift

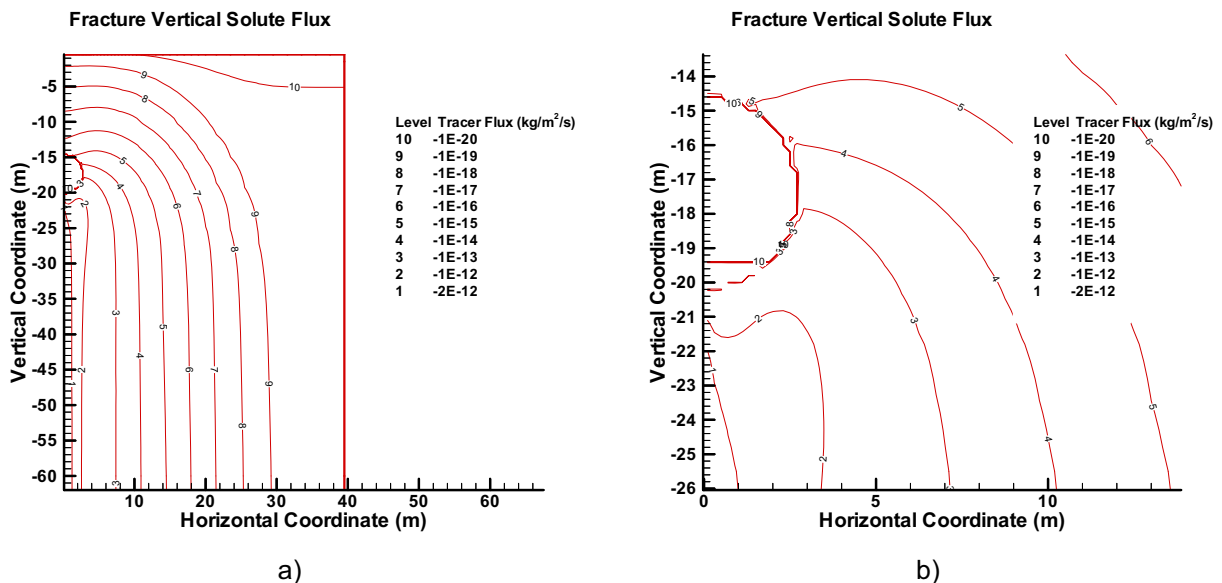


Figure 7.3-9. Fracture/Intergranular Solute Flux a) Solute Flux Contours Over Entire Domain; b) Solute Flux Contours Near the Drift

The steady-state solute mass flux between the invert and rock matrix and between the invert and rock fractures was computed. The solute mass flux ratio for mass flux into the fracture divided by mass flux into the matrix was found to be 0.0242. Therefore, solute is preferentially released to the rock matrix as compared to the fractures. This preferential release is caused by the much larger water content of the rock matrix as compared with the fractures beneath the invert. Details concerning the conduct of the transport calculations and post-processing of the results are given in Appendix I.

7.3.1.8 Comparison of Results from Drift-Scale Dual Continuum Model with Results from the Modified RTA

In order to compare the results from the drift-scale dual continuum transport model described above with the EBS-UZ interface model, the EBS transport model is modified to include similar boundary conditions and parameter values without changing the conceptual design or solution algorithm. Following are some of the major changes made to the EBS transport model using GoldSim V9.60.100 (2007 [DIRS 181903]):

1. Remove the connection of upstream waste form and corrosion products domains with the invert domain.
2. Set the reference diffusivity to $2.299 \times 10^{-9} \text{ m}^2 \text{ s}^{-1}$; set the invert tortuosity to 0.1952, matrix tortuosity to 0.0154, and fracture tortuosity to 0.0306.
3. Set the bulk water content of invert to 0.1379, matrix to 0.118, and fracture to 0.000273. Set the matrix porosity to 0.131 and fracture porosity to 0.0096, fracture frequency to 3.16 m^{-1} , active fracture parameter to 0.569, fracture percolation flux to $19.814 \text{ mm yr}^{-1}$, and matrix percolation flux to $0.016955 \text{ mm yr}^{-1}$. There is no drift-seepage flux. The only water flux through the invert is the imbibition flux equal to $0.00835 \text{ kg yr}^{-1}$ ($= 8.37 \times 10^{-6} \text{ m}^3 \text{ yr}^{-1}$).
4. Apply solute flux at the top of the invert at an injection rate of $9 \times 10^{-13} \text{ kg s}^{-1}$. This is achieved by changing the properties of the cell above the invert such that it becomes a negligibly thin cell and thus a uniform concentration at the top of the invert could be applied. For applying the solute flux, the radionuclide chosen is ^{99}Tc because it has no sorption and no solubility constraint in either domain. The mass flux for all other radionuclides is set to zero.

With above mentioned modifications, a deterministic calculation was performed with the EBS transport model. The ratio of the mass flux in the fracture to the mass flux in the matrix from the invert is found to be about 0.051 under steady state conditions. This value compares well with the value of 0.0242 calculated from the drift-scale dual continuum flow and transport model. The difference is likely due to the fact that in the EBS-UZ interface model the development of drift-shadow and its potential effect on changing the saturation state in the near-field UZ is ignored. Nevertheless, the comparison shows a similar qualitative and quantitative behavior between the two models, with the EBS-UZ interface model predicting a greater fraction of mass released to the UZ fractures compared to the matrix. This is reasonably bounding, since the radionuclides released from EBS would travel faster through the fractures without undergoing much retardation and radioactive decay. This would also slightly overestimate the mass flux at the UZ-SZ interface. The qualitative agreement in the results of the two models with slight over-prediction by the EBS-UZ interface model gives confidence that the EBS-UZ interface model is valid for use in the TSPA and meets the validation criteria mentioned in Section 7.

The above comparisons of the results of the two models and their comparative suitability for the TSPA have demonstrated that the EBS-UZ interface model meets Level II validation criteria. Based on the validation results, the EBS-UZ interface model is suitable for its intended use.

7.3.2 Results of Critical Review of the EBS-UZ Interface Model

A critical review of the EBS-UZ interface model was conducted as specified in the TWP (BSC 2006 [DIRS 177739], Section 2.2.3). This model validation approach is justified based on requirements of SCI-PRO-006, Section 6.3.2, where critical review is listed as an appropriate method for model validation. The results of the critical review of the EBS-UZ interface model are presented in Appendix M.

7.4 VALIDATION SUMMARY

The RTA has been validated by applying acceptance criteria based on an evaluation of the model's relative importance to the potential performance of the repository system. All validation requirements defined in the *Technical Work Plan for: Near-Field Environment: Engineered Barrier System: Radionuclide Transport Abstraction Model Report* (BSC 2006 [DIRS 177739], Sections 2.2.1, 2.2.2, and 2.2.3) have been fulfilled. Requirements for confidence building during model development have also been satisfied. The model development activities and post-development validation activities described establish the scientific bases for the RTA. Based on this, the RTA is considered to be sufficiently accurate and adequate for the intended purpose and to the level of confidence required by the model's relative importance to the performance of the proposed repository system.

INTENTIONALLY LEFT BLANK

8. CONCLUSIONS

This abstraction defines the conceptual model used to determine the rate of release of radionuclides from the Engineered Barrier System (EBS) to the unsaturated zone in the Total System Performance Assessment (TSPA) given the assumptions listed in Section 5. The Radionuclide Transport Abstraction (RTA) includes algorithms used in the TSPA for computing the flow of water and the transport of radionuclides through the EBS and specifies how parameters used in the model, are calculated or from what other models they are obtained. This model is reasonably bounding because it overestimates flow through the drip shield and into the waste package and transport out of the EBS. At the same time, wherever possible, it is realistic, not just bounding, within the appropriate range of uncertainty for TSPA calculations.

8.1 CONCEPTUAL MODEL SUMMARY

This section summarizes the conceptual model for transport of radionuclides from the EBS as modeled in the TSPA. Radionuclide transport out of the waste form and waste package, through the invert, and into the unsaturated zone is dependent on a complex series of events in the repository. After the waste packages are emplaced, radioactive decay of the waste will heat the drifts and locally perturb the normal percolation of water through the mountain. As the drifts cool, some of the water percolating through the mountain may drip into the drifts and subsequently contact some of the drip shields. Over time, the drip shield, waste package, and other components of the EBS are expected to degrade, leading to contact between the water and the waste form, resulting in the mobilization and transport of radionuclides through the EBS to the unsaturated zone. The primary transport medium through the EBS is anticipated to be water. Either a thin film of water or moving water is necessary for radionuclides to be transported out of the waste package and through the invert to the unsaturated zone.

A number of key factors will affect the mobilization and transport of radionuclides through the EBS, including barrier effectiveness and transport behavior:

- Performance of the drip shields
- Performance of the waste packages
- Protection provided by cladding
- Waste form degradation rates
- Entry and movement of water through waste packages
- Solubilities of radionuclides
- Transport of radionuclides through and out of the waste packages
- Transport of radionuclides through the invert below the waste packages
- Colloidal transport of radionuclides.

Once the drip shield is breached, water may contact the waste packages. Once a waste package is breached, water may enter the package as water vapor or as drips. If the cladding around spent fuel rods or the canister around a vitrified waste form is also breached, radionuclides may start to dissolve in the water. The concentration of each radionuclide mobilized from the waste form cannot exceed the radionuclide solubility limit, unless suspended colloids are included. Colloids are important for two reasons: they may potentially increase the release of radionuclides from the waste package, and they may potentially increase the transport velocity of radionuclides.

Radionuclides mobilized in water as dissolved species or in association with colloidal species may then be transported by advection and/or diffusion from the waste form, through the waste package, and out of breaches in the waste packages. Once outside the package, the radionuclides may be transported through the invert predominantly by diffusion, if water is not flowing through the invert, or by advection and diffusion, if water is flowing through the invert.

The conceptual model for flow of water through the EBS identifies eight key flow pathways. These pathways and their relationships are summarized in the following list and in Table 8.1-1. Sections 6.3.1.1, 6.3.2, 6.3.3, and 6.5.1.1 contain detailed technical discussions of the EBS flow abstraction portion of the RTA.

- **Total Dripping Flux**—This is the input flux or boundary condition; it is a time- and location-dependent input to this model provided in *Abstraction of Drift Seepage* (SNL 2007 [DIRS 181244]). Any condensation that may occur on the walls of the drift above the drip shield is added to the seepage flux, as described in *In-Drift Natural Convection and Condensation Model* (SNL 2007 [DIRS 181648], Section 8.3.1).
- **Through the Drip Shield to the Waste Package**—Flux through the drip shield is proportional to the ratio of the axial lengths of breaches in the drip shield to the total axial length of the drip shield, multiplied by a sampled factor that accounts for uncertainty in the fraction of the flux that is diverted by the drip shield. This flux-splitting submodel for the drip shield should only be applied when there is a time-varying failure of the drip shield.
- **Drip Shield to Invert (Diversion around the Drip Shield)**—Any seepage and wall condensation flux that does not go through the drip shield flows directly into the invert.
- **Through the Waste Package to the Waste Form**—Flux into the waste package is proportional to the product of the flux through the drip shield and the ratio of the lengths of breaches in the waste package to the total axial length of the waste package, multiplied by a sampled factor that accounts for uncertainty in the fraction of the flux that is diverted by the waste package. The number of corrosion patches in the waste package is calculated independently of the RTA by the WAPDEG code (SNL 2007 [DIRS 178871]).
- **Waste Package to Invert (Diversion around the Waste Package)**—Flow that does not go through the waste package is diverted directly to the invert.
- **Waste Package to Invert**—All of the flux from the waste package flows directly to the invert, independent of breach location on the waste package. The presence of the emplacement pallet, which maintains an air gap between the waste package and the invert and could potentially interfere with flow to the invert, is ignored in order to bound the water flow through this pathway.
- **Imbibition to Invert**—Water can be imbibed from the host rock matrix into the invert.
- **Invert to Unsaturated Zone**—All of the flux into the invert is released into the unsaturated zone.

Table 8.1-1. Summary of EBS Flow Abstraction

Flow Pathway, Pathway Flux	Flow Parameters	Data Sources and Notes
1. Total dripping flux (seepage + wall condensation), F_1	Total dripping flux is a function of fracture properties, rock properties, air and water properties, and the percolation flux.	<i>Abstraction of Drift Seepage</i> (SNL 2007 [DIRS 181244]) and <i>In-Drift Natural Convection and Condensation Model</i> (SNL 2007 [DIRS 181648]) provide time- and location-dependent values of total dripping flux.
2. Flux through the drip shield, F_2	L_{DS_Patch} is axial half-length of each Patch due to general corrosion of Ti. L_{DS} is axial length of the drip shield. N_{bDS} is number of corrosion patches of length L_{DS_Patch} in the drip shield. f'_{DS} is sampled uncertain parameter, DS_Flux_Uncertainty_a. $F_2 = \min[F_1 N_{bDS} L_{DS_Patch} f'_{DS} / L_{DS}, F_1]$	This flux splitting submodel for the drip shield should only be applied when there is a time-varying failure of the drip shield. For the seismic scenario class, the opening area is computed based on the drip shield damage fraction multiplied by the area of the drip shield.
3. Diversion around drip shield, F_3	$F_3 = F_1 - F_2$.	Continuity of liquid flux.
4. Flux into the waste package, F_4	L_{WP_Patch} is axial half-length of each patch due to general corrosion of Alloy 22. L_{WP} is axial length of the waste package. N_{bWP} is number of corrosion patches in the waste package. f'_{WP} is sampled uncertain parameter, WP_Flux_Uncertainty_a. $F_4 = \min[F_2 N_{bWP} L_{WP_Patch} f'_{WP} / L_{WP}, F_2]$	WAPDEG (SNL 2007 [DIRS 178871]) provides the number of patches and stress corrosion cracks on the waste package. No significant flow through stress corrosion cracks due to plugging (DTN: MO0706SPAFEPLA.001 [DIRS 181613], FEP Number 2.1.03.10.0A). Steady state flow through waste package (outflow = inflow in steady state; this is bounding for release).
5. Diversion around the waste package, F_5	$F_5 = F_2 - F_4$	Continuity of liquid flux.
6. Flux to the invert, F_6	$F_6 = F_5 + F_4 + F_3$ $= F_1$	All advective flux enters the invert. Only F_4 can transport radionuclides into the invert.
7. Imbibition flux from the host rock matrix into the invert, F_7	F_7 is an input to the EBS flow model.	Imbibition flux is provided by <i>Multiscale Thermohydrologic Model</i> calculations (SNL 2007 [DIRS 181383]).
8. Flux from the invert into to the unsaturated zone, F_8	$F_8 = F_6 + F_7$ $= F_1 + F_7$	Total dripping flux portion (F_1) of advective flux from the invert flows into the UZ fractures; imbibition flux (F_7) flows into the UZ matrix.

Output DTN: SN0703PAEBSRTA.001.

In the conceptual model of radionuclide transport through the EBS, the waste form is the source of all radionuclides in the repository system. Radionuclides can be transported downward, through corrosion products in the waste package, through the invert, and into the unsaturated zone. Transport can occur through advection when there is a liquid flux through the waste package, and by diffusion through any water present in the waste package. Diffusion can occur in a seep environment, when advective transport also takes place, as well as in a no-seep environment where no advective transport occurs; thin films of water are assumed to be present on all surfaces. If the only breaches in a waste package are stress corrosion cracks, advective transport does not occur, but diffusion of radionuclides out of the waste package can still take place. The concentration of each radionuclide during transport is limited by the sum of its solubility limit and the presence of any colloidal particles that may act as reversible or irreversible carriers for the radionuclide. The transport pathways and transport processes (advection or diffusion) are summarized in Table 8.1-2. Sections 6.3.4, 6.5.1.2, and 6.5.2 contain a detailed technical discussion of the EBS transport abstraction.

In the transport abstraction, the EBS is modeled as consisting of three computational domains. The first domain includes the waste form source (i.e., spent nuclear fuel (SNF) or high-level radioactive waste (HLW)) along with corrosion products from the degradation of steel components, such as high-level waste glass (HLWG) canisters and commercial spent nuclear fuel (CSNF) basket tubes, which are closely associated with the waste form. The second domain consists of corrosion products from the degradation of steel waste package internal components that are not included in the first domain. The third domain is the invert. The physical and chemical properties and conditions are uniform throughout each domain, as though the contents of the domain were thoroughly and continuously stirred.

Parameters that define the size of the two waste package domains, specifically the volumes and diffusive path lengths, are summarized in Table 8.2-1. Parameter values that are provided by other models are also identified there. The path length for diffusion through the invert is set to the average thickness of the invert, 0.934 m.

The mass of corrosion products is a function of time and depends on the corrosion rates of carbon steel and stainless steel, which are uncertain parameters with values that are sampled in TSPA. In a seep environment, the corrosion products and waste form degradation materials (or rind) are fully saturated with water. In a no-seep environment, the water saturation is based on the amount of water adsorbed onto iron oxide surfaces and waste form degradation materials, which is a function of the relative humidity. The RH is an input to the transport model that depends on time and location in the repository. Calculation of corrosion products mass and saturation is discussed in Section 6.5.2.2.

The diffusion coefficients in the corrosion products and waste form degradation rind are based on the species dependent free-water diffusion coefficients given in Table 4.1-7 (DTN: LB0702PAUZMTDF.001 [DIRS 180776], file *Readme.doc*, Table 8), modified for the porosity, time-dependent water saturation, and temperature.

The diffusion coefficient in the invert is also based on the species dependent free-water diffusion coefficients given in Table 4.1-7 (DTN: LB0702PAUZMTDF.001 [DIRS 180776], file *Readme.doc*, Table 8). The effects of porosity and time-dependent saturation in the invert are incorporated based on experimental data. The effect of temperature is also incorporated into the abstraction for the diffusion coefficient. The diffusion coefficient for colloids is computed using the Stokes-Einstein equation, Equation 6.3.4.4-1, as a function of temperature and colloid particle diameter (Section 6.3.4.4).

Sorption of radionuclides may occur on corrosion products in the waste package and on crushed tuff in the invert. Values for sorption distribution coefficients on corrosion products and on crushed tuff for all radionuclides of interest are determined in Sections 6.3.4.2 and 6.5.2.4.

Table 8.1-2. Summary of EBS Transport Abstraction

Transport Pathway	Transport Modes	Transport Parameters and Data Sources
1. Waste form and corrosion products domains	<p>Waste form domain: Diffusion and advection (when possible) through the waste form rind.</p> <p>Corrosion product domain: Diffusion through stress corrosion cracks (no advective transport through stress corrosion cracks). Diffusion and advection through corrosion products and corrosion patches.</p>	<p>No lateral or forward dispersion. Colloidal particles will transport radionuclides. Diffusive area for each stress corrosion crack is $7.7 \times 10^{-6} \text{ m}^2$ (Equation 8-16 and Section 6.3.3.2.2). Diffusion coefficient (all radionuclides):</p> <ul style="list-style-type: none"> • Species dependent free-water diffusion coefficients given in Table 4.1-7 (DTN: LB0702PAUZMTDF.001 [DIRS 180776], file <i>Readme.doc</i>, Table 8) • Modified for porosity and saturation (Section 6.3.4.3.5) • Temperature modification defined in Section 6.3.4.1.2; waste form temperature is provided by <i>Multiscale Thermohydrologic Model</i> calculations (SNL 2007 [DIRS 181383]) • Colloid diffusion coefficient computed as a function of waste form and corrosion product temperatures and sampled colloid particle diameter using Equation 6.3.4.4-1 (Section 6.3.4.4). <p>The cross-sectional area for radionuclide transport is dependent on the scenario class (Sections 6.5.2.1.1 and 6.5.2.1.2). Competitive sorption of radionuclides onto corrosion products; time-dependent mass of corrosion products available for sorption is calculated based on corrosion rates of carbon and stainless steels. See Section 6.5.2 for further details.</p>

Table 8.1-2. Summary of EBS Transport Abstraction (Continued)

Transport Pathway	Transport Modes	Transport Parameters and Data Sources
2. Invert	Diffusion and advection (F_6) from corrosion products domain into the invert.	<p>Liquid flux for advection = $F_6 = F_5$ (diverted by waste package) + F_4 (flux through waste package) + F_3 (diverted by drip shield).</p> <p>Diffusion coefficient (all radionuclides):</p> <ul style="list-style-type: none"> • Species dependent free-water diffusion coefficients given in Table 4.1-7 (DTN: LB0702PAUZMTDF.001 [DIRS 180776], file <i>Readme.doc</i>, Table 8) • Modified for porosity and saturation (Section 6.3.4.1) • Temperature modification defined in Section 6.3.4.1.2; invert temperature is provided by <i>Multiscale Thermohydrologic Model</i> calculations (SNL 2007 [DIRS 181383]) • Colloid diffusion coefficient computed as a function of invert temperature and sampled colloid particle diameter using Equation 6.3.4.4-1 (Section 6.3.4.4). <p>The cross-sectional area for radionuclide transport is the width of the invert times the waste package length. Transport of radionuclides is retarded by sorption onto crushed tuff in invert.</p> <p>See Section 6.5.2 for further details.</p>
3. Invert-UZ interface	Advection from the invert to UZ fractures (F_6) and UZ matrix (F_7); total flux is F_8 . Diffusion from the invert to UZ fractures and matrix.	The invert diffusion calculation uses radionuclide concentrations in the waste package corrosion products domain as the boundary condition at the top of the invert and a series of unsaturated zone computational cells below the invert that provide a gradient to a zero radionuclide concentration at some distance from the bottom of the invert (Section 6.5.2.6).

Output DTN: SN0703PAEBSRTA.001

8.2 MODEL OUTPUTS

Table 8.2-1 summarizes parameters that define the three-domain EBS transport abstraction, which is described in more detail in Section 6.5.2. These domains are comprised of:

- *The waste form.* In the case of CSNF waste packages, this consists of fuel rods, along with the corrosion products from the degradation of stainless steel fuel basket tube and borated stainless steel absorber plates; no credit is taken for fuel rod cladding as a barrier, and the presence of cladding, including the volume occupied by cladding, is ignored. In codisposal waste packages, the waste form is a composite of HLW glass and DOE spent nuclear fuel (DSNF); thus, there are two waste form subdomains. One subdomain consists of HLW glass and the corrosion products from the degradation of the stainless steel pour canisters that contain the HLW glass. The other subdomain consists of DSNF and the corrosion products from the degradation of stainless steel canisters and other associated steel components; as with CSNF, any fuel cladding is

neglected, and no credit is taken for the cladding as a barrier. Transport processes that occur in the waste form domain(s) are the dissolution of radionuclides and advection and diffusion to the corrosion products domain. Waste form colloids are generated from the alteration of HLW glass and carry radionuclides that are both reversibly and kinetically bound to the colloid.

- *Corrosion products inside the waste package.* These are the result of the corrosion of steel internal waste package components such as the guide assembly and transportation, aging, and disposal (TAD) canister (in CSNF waste packages); divider plate assemblies (in codisposal waste packages); and inner stainless steel vessel. The stationary iron-oxide-based corrosion products are strong sorbers, so sorption of radionuclides is modeled on the corrosion products. In addition, iron oxyhydroxide colloids (released from corrosion products) and groundwater colloids (from seepage water) are available in this domain. Both reversible and kinetic sorption is modeled on iron oxyhydroxide colloids but only reversible sorption is modeled on groundwater colloids. Precipitation and dissolution can also take place in this domain. Diffusion transports radionuclides into this domain from the waste form domain and from this domain to the invert domain.
- *Invert.* Advection and diffusion transport radionuclides into this domain from the corrosion products domain and from this domain to the unsaturated zone. Groundwater colloids are also available in this domain if there is any water flow. Reversible sorption of radionuclides is modeled on these colloids. Because the chemical environment of the invert may be different from the corrosion products domain, colloid stability may be affected and dissolution or precipitation of radionuclides may take place. The submodel for transport through the invert is summarized in transport pathway 3 of the transport abstraction summary, Table 8.1-2.

Transport is affected by the parameters that define the physicochemical environment, including the porosity and pore volume, water saturation, interfacial diffusive areas, diffusive path lengths, and diffusion coefficients. These diffusive transport parameters are discussed in Section 6.5.2.

Output from the RTA, including algorithms and parameters, is summarized in two output DTNs: SN0703PAEBSRTA.001, and SN0703PAEBSRTA.002.

Table 8.2-1. Parameters for EBS Transport Abstraction

Waste Type	Transport Properties	Seep Case	No-Seep Case
Waste Form Domain			
CSNF	Domain bulk volume, pore volume, and water volume	<p>Waste Form Domain consists of degradation products in fuel rods (SNF rind), fuel basket tubes (steel corrosion products), absorber plates (steel corrosion products) ; fuel rod cladding is treated as inert and its volume is neglected</p> <ul style="list-style-type: none"> • SNF rind volume (V_{rind}, function of time) and porosity (ϕ_{rind}) provided by <i>Cladding Degradation Summary for LA</i> (SNL 2007 [DIRS 180616], Tables 6-3 and 6-4) • Steel corrosion products (CP) mass from Equation 8-4, pore volume ($V_{\phi,CP}$) from Equation 8-7, bulk volume from Equation 8-8 • Total pore volume of CSNF Waste Form Domain, $V_{\phi,CSNF}$, given by Equation 8-13 • S_w = water saturation in domain = 1.0 • Domain water volume = total pore volume. 	<ul style="list-style-type: none"> • Domain characteristics (rind volume, corrosion products mass and volume, total pore volume) same as for Seep Case • $S_{w,rind}$ function of RH and sampled density and specific surface area of rind (Equation 8-12) • Rind water volume: $V_{w,rind} = S_{w,rind} \phi_{rind} V_{rind}$ • $S_{w,CP}$ function of RH, density, and sampled specific surface area of corrosion products (Equation 8-5) • Corrosion products water volume: $V_{w,CP} = S_{w,CP} V_{\phi,CP}$ • Domain water volume = $V_{w,CSNF} = V_{w,rind} + V_{w,CP}$
	Advection and diffusion	<p>Advective flux = volumetric flow rate through the waste package</p> <p>Diffusive area of Waste Form Domain:</p> <ul style="list-style-type: none"> • Set equal to surface area of a cylinder of radius $\frac{1}{2}$ of Diff_Path_Length_CSNF_1, length of fuel basket tubes; excluding ends • Fixed parameter: Diff_Area_CSNF_1. <p>Diffusive path length:</p> <ul style="list-style-type: none"> • Set equal to TAD canister inside radius • Fixed parameter: Diff_Path_Length_CSNF_1. <p>Diffusion coefficient in Waste Form Domain, D_{WF}:</p> <ul style="list-style-type: none"> • $\phi S_w D_{WF} = \phi^{1.3} S_w^2 D_i$ • ϕ = effective porosity of CSNF Waste Form Domain given by Equation 8-14 • S_w = water saturation in domain = 1.0 • D_i = free water diffusion coefficient. <p>(D_{WF} is an effective value that implicitly includes the effect of tortuosity in a porous medium).</p>	<ul style="list-style-type: none"> • No advective flux • Diffusive area same as for Seep Case • Diffusive path length same as for Seep Case <p>Diffusion coefficient in Waste Form Domain, D_{WF}:</p> <ul style="list-style-type: none"> • $\phi S_w D_{WF} = \phi^{1.3} S_w^2 D_i$ • Effective porosity ϕ of CSNF Waste Form Domain given by Equation 8-14, same as for Seep Case • Water saturation in Waste Form Domain: $S_w = \min[(V_{w,CSNF}/V_{\phi,CSNF}), 1.0]$ • D_i = free water diffusion coefficient • Modified for temperature. <p>(D_{WF} is an effective value that implicitly includes the effect of tortuosity in a porous medium).</p>

Table 8.2-1. Parameters for EBS Transport Abstraction (Continued)

Waste Type	Transport Properties	Seep Case	No-Seep Case
Waste Form Domain			
Codisposal	Domain bulk volume, pore volume, and water volume	<p>Waste Form Domain is divided into two subdomains: HLWG and DSNF Subdomains</p> <p><u>HLWG Subdomain:</u></p> <ul style="list-style-type: none"> Consists of degradation products of 5 stainless steel canisters and HLW glass contained therein Volume of HLWG degradation rind provided as function of time by <i>Defense HLW Glass Degradation Model</i> (BSC 2004 [DIRS 169988], Section 8.1, Eq. 54) Porosity of HLWG rind provided by <i>Defense HLW Glass Degradation Model</i> (BSC 2004 [DIRS 169988], Table 8-1) Steel corrosion products (CP) mass from Equation 8-4, pore volume ($V_{\phi,CP}$) from Equation 8-7, bulk volume from Equation 8-8 Total pore volume of HLWG Waste Form Subdomain, $V_{\phi,HLWG}$, given by Equation 8-13 S_w = water saturation in HLWG Waste Form Subdomain = 1.0. <p><u>DSNF Subdomain:</u></p> <ul style="list-style-type: none"> Consists of degradation products of standard stainless steel DSNF canister containing degraded DSNF (rind) Volume of DSNF rind, $V_{DSNF} = 1.0 \text{ m}^3$ (BSC 2004 [DIRS 172453], Section 8.1) Porosity of DSNF rind, $\phi_{DSNF} = 0.2$ Steel corrosion products (CP) mass from Equation 8-4, pore volume ($V_{\phi,CP}$) from Equation 8-7, bulk volume from Equation 8-8 Total pore volume of DSNF Waste Form Subdomain, $V_{\phi,DSNF}$, given by Equation 8-13 S_w = water saturation in DSNF = 1.0. 	<ul style="list-style-type: none"> No advective flux Diffusive area same as for Seep Case Diffusive path length same as for Seep Case <p><u>HLWG Subdomain:</u></p> <p>Diffusion coefficient in HLWG Waste Form Subdomain, D_{WF}:</p> <ul style="list-style-type: none"> $\phi S_w D_{WF} = \phi^{1.3} S_w^2 D_i$ Effective porosity ϕ of HLWG Waste Form Subdomain given by Equation 8-14, same as for Seep Case Water saturation in HLWG Waste Form Subdomain: $S_w = \min[(V_{w,HLWG}/V_{\phi,HLWG}), 1.0]$ Modified for temperature D_i = free water diffusion coefficient. <p><u>DSNF Subdomain:</u></p> <p>Diffusion coefficient in DSNF Waste Form Subdomain, D_{WF}:</p> <ul style="list-style-type: none"> $\phi S_w D_{WF} = \phi^{1.3} S_w^2 D_i$ Effective porosity ϕ of DSNF Waste Form Subdomain given by Equation 8-14, same as for Seep Case Water saturation in DSNF Waste Form Subdomain: $S_w = \min[(V_{w,DSNF}/V_{\phi,DSNF}), 1.0]$ Modified for temperature D_i = free water diffusion coefficient. <p>(D_{WF} is an effective value that implicitly includes the effect of tortuosity in a porous medium).</p>

Table 8.2-1. Parameters for EBS Transport Abstraction (Continued)

Waste Type	Transport Properties	Seep Case	No-Seep Case
Codisposal (continued)	Advection and diffusion (continued)	<p>Advective flux = volumetric flow rate through the waste package.</p> <p><u>HLWG Subdomain:</u></p> <p>Diffusive area:</p> <ul style="list-style-type: none"> • Diffusive area equal to surface area of cylinder with radius equal to 1/2 of Diff_Path_Length_CDSP_1a and length of inner vessel cavity of 5 DHLW/DOE SNF Long waste package, excluding ends • Fixed parameter: Diff_Area_CDSP_1a. <p>Diffusive path length:</p> <ul style="list-style-type: none"> • Set equal to the radius of inner vessel of 5 DHLW/DOE SNF Long waste package • Fixed parameter: Diff_Path_Length_CDSP_1a. <p>Diffusion coefficient in HLWG Waste Form Subdomain, D_{WF}:</p> <ul style="list-style-type: none"> • $\phi S_w D_{WF} = \phi^{1.3} S_w^2 D_i$ • ϕ = effective porosity of HLWG Waste Form Subdomain given by Equation 8-14 • S_w = water saturation = 1.0 • D_i = free water diffusion coefficient. <p>(D_{WF} is an effective value that implicitly includes the effect of tortuosity in a porous medium).</p>	
		<p><u>DSNF Subdomain:</u></p> <p>Diffusive area:</p> <ul style="list-style-type: none"> • Diffusive area set equal to the surface area of HLWG subdomain • Fixed parameter: Diff_Area_CDSP_1b. <p>Diffusive path length:</p> <ul style="list-style-type: none"> • Set equal to the diffusive path length in HLWG subdomain • Fixed parameter: Diff_Path_Length_CDSP_1b. <p>Diffusion coefficient in Waste Form Subdomain, D_{WF}:</p> <ul style="list-style-type: none"> • $\phi S_w D_{WF} = \phi S_w D_i$ • ϕ = effective porosity of DSNF Waste Form Subdomain given by Equation 8-14 • S_w = water saturation = 1.0 • D_i = free water diffusion coefficient. <p>(D_{WF} is an effective value that implicitly includes the effect of tortuosity in a porous medium).</p>	

Table 8.2-1. Parameters for EBS Transport Abstraction (Continued)

Waste Type	Transport Properties	Seep Case	No-Seep Case	
Corrosion Product Domain				
CSNF	Bulk volume and water volume	Pore volume of Corrosion Products Domain, V_{CP} : <ul style="list-style-type: none"> • Mass of corrosion products, m_{CP}, is function of time, Table 8.2-8, Equation 8-4 • Porosity $\phi_{CP} = 0.4$ • V_{CP} from Table 8.2-8, Equation 8-7. 	<ul style="list-style-type: none"> • Same as Seep Case 	
		Volume of water: <ul style="list-style-type: none"> • S_w = water saturation in corrosion products = 1.0 • Water volume = $V_{w,CP} = S_w V_{\phi_{CP}}$. 	Volume of water: <ul style="list-style-type: none"> • $S_{we,CP}$ = effective water saturation in Corrosion Products Domain from Equation 8-11 • Water volume = $S_{we,CP} V_{\phi_{CP}}$. 	
	Advection and Diffusion	Advective flux = volumetric flow rate through the waste package		<ul style="list-style-type: none"> • No advective flux
		Diffusive area: <ul style="list-style-type: none"> • Diffusive area, for the path excluding the outer barrier, is the surface area of a cylinder at the midpoint of the diffusive path, constant parameter: Diff_Area_CSNF_2 • Diffusive area for the path through the outer barrier of the waste package is taken to be the minimum of total area of all waste package breaches (scenario class dependent) and surface area of CSNF waste package given by the parameter: Diff_Area_CSNF_2_Max. 	<ul style="list-style-type: none"> • Same as Seep Case 	
		Diffusive path length: <ul style="list-style-type: none"> • Diffusive path excluding the outer barrier is given by the combined thickness of TAD canister and inner vessel, constant parameter: Diff_Path_Length_CSNF_2 • Diffusive path through the outer barrier is given by the thickness of the waste package outer barrier, constant parameter: Diff_Thick_OB_CSNF. 	<ul style="list-style-type: none"> • Same as Seep Case 	
		Diffusion coefficient in Corrosion Products Domain, D_{CP} : <ul style="list-style-type: none"> • $\phi_{CP} S_w D_{CP} = \phi_{CP}^{1.3} S_w^2 D_i$ • ϕ_{CP} = porosity of corrosion products = 0.4 • S_w = water saturation in corrosion products = 1.0 • D_i = free water diffusion coefficient. (D_{CP} is an effective value that implicitly includes the effect of tortuosity in a porous medium).	Diffusion coefficient in Corrosion Products Domain, D_{CP} : <ul style="list-style-type: none"> • $\phi_{CP} S_{we,CP} D_{CP} = \phi_{CP}^{1.3} S_{we,CP}^2 D_i$ • $S_{we,CP}$ = effective water saturation in corrosion products Table 8.2-8, Equation 8-11 • ϕ_{CP} = porosity of corrosion products = 0.4 • D_i = free water diffusion coefficient. (D_{CP} is an effective value that implicitly includes the effect of tortuosity in a porous medium).	

Table 8.2-1. Parameters for EBS Transport Abstraction (Continued)

Waste Type	Transport Properties	Seep Case	No-Seep Case
Codisposal	Bulk volume and water volume	Pore volume of Corrosion Products Domain, $V_{\phi_{CP}}$: <ul style="list-style-type: none"> Same as for CSNF Seep Case ϕ_{CP} = porosity of corrosion products = 0.4. 	<ul style="list-style-type: none"> Same as Seep Case
		Volume of water: <ul style="list-style-type: none"> S_w = water saturation in corrosion products = 1.0 Water volume = $S_w V_{\phi_{CP}}$. 	<ul style="list-style-type: none"> $S_{we,CP}$ = effective water saturation in corrosion products, Equation 8-11 Water volume = $S_{we,CP} V_{\phi_{CP}}$
	Advection and diffusion	Advective flux = volumetric flow rate through the waste package Diffusive area: <ul style="list-style-type: none"> Diffusive area, for the path excluding the outer barrier, is given by the surface area of a cylinder at the midpoint of the diffusive path, constant parameter: Diff_Area_CDSP_2 Diffusive area for the path through the outer barrier of the waste package is taken to be the minimum of total area of all waste package breaches (scenario class dependent) and surface area of co-disposal waste package given by the constant parameter: Diff_Area_CDSP_2_Max. Diffusive path length: <ul style="list-style-type: none"> Diffusive path excluding the outer barrier is given by the thickness of inner vessel, constant parameter: Diff_Path_Length_CDSP_2 Diffusive path through the outer barrier is given by the thickness of the waste package outer barrier, constant parameter: Diff_Thick_OB_CDSP. Diffusion coefficient in Corrosion Products Domain, D_{CP} : <ul style="list-style-type: none"> $\phi_{CP} S_w D_{CP} = \phi_{CP}^{1.3} S_w^2 D_i$ ϕ_{CP} = porosity of corrosion products = 0.4 S_w = water saturation = 1.0 D_i = free water diffusion coefficient. (D_{CP} is an effective value that implicitly includes the effect of tortuosity in a porous medium).	<ul style="list-style-type: none"> No advective flux Diffusive area same as for Seep Case Diffusive path length same as for Seep Case Diffusion coefficient in Corrosion Products Domain, D_{CP} : <ul style="list-style-type: none"> $_{CP} S_{we,CP} D_{CP} = \phi_{CP}^{1.3} S_{we,CP}^2 D_i$ $S_{we,CP}$ = effective water saturation in corrosion products, Equation 8-11 ϕ_{CP} = porosity of corrosion products = 0.4 D_i = free water diffusion coefficient. (D_{CP} is an effective value that implicitly includes the effect of tortuosity in a porous medium.)

Output DTN: SN0703PAEBSRTA.001

The ranges and distributions of radionuclide sorption distribution coefficients for sorption on devitrified unsaturated zone tuff given in DTNs: LA0408AM831341.001 [DIRS 171584] (file *UZ Kds.doc*, for all radionuclides of interest except for Se and Sn) and LB0701PAKDSESN.001 [DIRS 179299] (file *ReadMe.doc*, for Se and Sn) are assigned to K_d values on crushed tuff in the invert. Correlations, for sampling sorption distribution coefficient probability distributions for devitrified UZ tuff given in DTN: LB0701PAKDSESN.001 [DIRS 179299] (file *Sorption Correlation Table.xls*), are assigned to invert crushed tuff.

Invert hydrological properties are provided in DTN: MO0703PAHYTHRM.000 [DIRS 182093].

Radionuclide sorption site density data for goethite and HFO are summarized in Table 8.2-2. Parameters for the regression equations that provide sorption distribution coefficients in the competitive sorption model are given in Table 8.2-3.

Table 8.2-4 summarizes various sampled parameters to be used in the RTA, with the range and distribution of each parameter provided. Table 8.2-5 lists UZ fracture and matrix saturations and fluxes extracted from the UZ flow model output. A summary of fixed, single-value parameters to be used in the RTA is given in Table 8.2-6 (output DTN: SN0703PAEBSRTA.001). Equations used to compute various parameters in the RTA are shown in Table 8.2-8.

In Table 8.2-7, the impacts on model inputs of using preliminary design data are summarized. Because the TSPA calculations were started before the direct confirming data were available in the design interface documents (SNL 2007 [DIRS 179394], and SNL 2007 [DIRS 179567]), it was necessary to utilize preliminary values for the design of the EBS components to obtain the design-related parameters used as model inputs in the TSPA. The parameter values used in the TSPA, based on the preliminary design data, are compared in Table 8.2-7 with parameters derived from the final design data that is presented in the design interface documents (SNL 2007 [DIRS 179394], and SNL 2007 [DIRS 179567]).

Table 8.2-2. Sampled Parameter Ranges and Distributions Used for Kinetic Sorption on Stationary Corrosion Products

Input Name	Input Description	Range	Distribution
Goethite_Site_Density_a	Goethite site density; discrete distribution	Density (sites nm ⁻²)	Probability Level
		1.02	0.01786
		1.21	0.01786
		1.32	0.03571
		1.46	0.01786
		1.50	0.01786
		1.66	0.01786
		1.68	0.03571
		1.70	0.01786
		1.80	0.01786
		1.87	0.01786
		1.93	0.01786
		1.95	0.01786
		1.97	0.01786
		2.20	0.01786
		2.30	0.07143
		2.31	0.01786
		2.32	0.01786
		2.55	0.01786
		2.60	0.03571
		2.70	0.01786
		2.89	0.01786
		2.90	0.03571
		3.00	0.01786
		3.12	0.01786
		3.13	0.01786
		3.30	0.03571
		3.40	0.01786
		4.00	0.01786
		4.20	0.01786
		4.60	0.01786
		4.84	0.01786
		4.90	0.01786
5.00	0.01786		
5.53	0.01786		
6.15	0.01786		
6.30	0.01786		
6.31	0.03571		
6.60	0.01786		
7.00	0.05357		
7.20	0.01786		
7.40	0.01786		

Table 8.2-2. Sampled Parameter Ranges and Distributions Used for Kinetic Sorption on Stationary Corrosion Products (Continued)

Input Name	Input Description	Range	Distribution
Goethite_Site_Density_a (continued)		8.00	0.01786
		8.16	0.01786
		8.38	0.01786
		8.59	0.01778
HFO_Site_Density_a	HFO site density; discrete distribution	Density (sites nm ⁻²)	Probability Level
		0.56	0.05263
		1.13	0.10526
		1.47	0.05263
		1.58	0.05263
		1.69	0.10526
		1.81	0.05263
		2.03	0.10526
		2.26	0.26316
		2.60	0.05263
		2.71	0.05263
			4.00
	5.65	0.05265	

Output DTN: SN0703PAEBSRTA.001.

Table 8.2-3. Surface Complexation Sorption Coefficients for the Final Regression Models

No.	Parameter Name	Value (Dimensionless)
1	pH_Coeff_1 *	4.5342
2	pH_Coeff_2 *	0.6132
3	pH_Coeff_3 *	-0.3805
4	pH_Coeff_4 *	-0.0254
5	U_Sorb_Coeff_1	0.9727
6	U_Sorb_Coeff_2	-0.0837
7	U_Sorb_Coeff_3	1.0027
8	U_Sorb_Coeff_4	-0.3489
9	U_Sorb_Coeff_5	-0.0922
10	Pu_Sorb_Coeff_1	-2.0371
11	Pu_Sorb_Coeff_2	0.6036
12	Pu_Sorb_Coeff_3	0.9972
13	Pu_Sorb_Coeff_4	-0.9172
14	Pu_Sorb_Coeff_5	-0.0516
15	Pu_Sorb_Coeff_6	0.9500
16	Np_Sorb_Coeff_1	0.1561
17	Np_Sorb_Coeff_2	0.9789
18	Np_Sorb_Coeff_3	-1.1643

Table 8.2-3. Surface Complexation Sorption Coefficients for the Final Regression Models (Continued)

No.	Parameter Name	Value (dimensionless)
19	Np_Sorb_Coeff_4	-0.0671
20	Np_Sorb_Coeff_5	0.9784
21	Am_Sorb_Coeff_1	-3.2250
22	Am_Sorb_Coeff_2	1.019
23	Am_Sorb_Coeff_3	0.9754
24	Am_Sorb_Coeff_4	-1.4669
25	Am_Sorb_Coeff_5	-0.0887
26	Am_Sorb_Coeff_6	0.9423
27	Th_Sorb_Coeff_1	-0.3107
28	Th_Sorb_Coeff_2	0.0838
29	Th_Sorb_Coeff_3	1.0151
30	Th_Sorb_Coeff_4	-0.7201
31	Th_Sorb_Coeff_5	-0.0379
32	Th_Sorb_Coeff_6	0.8942
33	Ni_Sorb_Coeff_1	-5.0808
34	Ni_Sorb_Coeff_2	0.8026
35	Ni_Sorb_Coeff_3	0.9144
36	Ni_Sorb_Coeff_4	-1.6646
37	Ni_Sorb_Coeff_5	-0.1019
38	Ni_Sorb_Coeff_6	0.9478

* The pH for the corrosion products domain (Cell 2) is computed by applying the following equation:

$$\text{pH} = 4.5342 + 0.6132 \text{ pCO}_2 - 0.3805 \log_{10}[U] - 0.0254 (\log_{10}[U])^2 + E$$

where E is the error term (pH_Cell_2_Regression_Error) defined by a normal distribution with mean of zero and standard deviation of 0.32 truncated at ± 2 standard deviations.

Table 8.2-4. Sampled Model Inputs Used in the EBS Radionuclide Transport Abstraction

Input Name	Input Description	Range	Distribution
Invert_Diff_Coeff_Uncert_a	Invert diffusion coefficient uncertainty; Table 8.2-8, Equation 8-1	Range: $10^{\mu \pm 3\sigma}$ (dimensionless) Mean: $\mu = 0.033$; Std. Dev. $\sigma = 0.218$	10^{ND}
SS_Corrosion_Rate_a	Stainless steel corrosion rate (DTN: MO0409SPAACRWP.000 [DIRS 172059]); Spreadsheet <i>aqueous-316L.xls</i> , worksheet "freshwater," Columns C through G, Rows 59 through 64	$0.01 - 0.51 \mu\text{m yr}^{-1}$ Mean = $0.267 \mu\text{m yr}^{-1}$ Std. Dev. = $0.209 \mu\text{m yr}^{-1}$	Truncated Lognormal

Table 8.2-4. Sampled Model Inputs Used in the EBS Radionuclide Transport Abstraction (Continued)

Input Name	Input Description	Range	Distribution
CS_Corrosion_Rate_a	Carbon steel corrosion rate (DTN: MO0409SPAACRWP.000 [DIRS 172059]); Spreadsheet <i>aqueous-A516.xls</i> , worksheet "Freshwater," Column D, Rows 5 through 55	25 – 135 $\mu\text{m yr}^{-1}$ Mean = 78.5 $\mu\text{m yr}^{-1}$ Std. Dev. = 25.0 $\mu\text{m yr}^{-1}$	Truncated Lognormal
DS_Flux_Uncertainty_a	Drip shield flux splitting uncertainty factor	0 – 0.85 (dimensionless)	Uniform
WP_Flux_Uncertainty_a	Waste package flux splitting uncertainty factor	0 – 2.41 (dimensionless)	Uniform
Diameter_Colloid_a	Diameter of colloid particle	50 – 300 nm	Uniform
Goethite_SA_a	Specific surface area of goethite (FeOOH)	14.7 – 110 $\text{m}^2 \text{g}^{-1}$	Log-Normal (Truncated)
HFO_SA_a	Specific surface area of HFO	68 – 600 $\text{m}^2 \text{g}^{-1}$	Log-Normal (Truncated)
NiO_SA_a	Specific surface area of NiO	1 – 30 $\text{m}^2 \text{g}^{-1}$	Uniform
Cr2O3_SA_a	Specific surface area of Cr_2O_3	1 – 20 $\text{m}^2 \text{g}^{-1}$	Uniform
Relative_Abundance_Goethite_a	Mass fraction of iron oxides (goethite and HFO) that is goethite	0.45 – 0.80 (fraction)	Uniform
FHH_Isotherm_k_CP_a	FHH adsorption isotherm parameter k for corrosion products	1.048 – 1.370 (dimensionless)	Uniform
FHH_Isotherm_s_CP_a	FHH adsorption isotherm parameter s for corrosion products	1.525 – 1.852 (dimensionless)	Uniform
CSNF_Rind_SA_a	Specific surface area of CSNF rind	0.5 – 60 $\text{m}^2 \text{g}^{-1}$	Uniform
Density_CSNF_Rind_a	Density of CSNF rind	5,600 – 11,500 kg m^{-3}	Uniform
Porosity_Rind_CSNF_a	Porosity of CSNF rind (DTN: MO0411SPACLDDG.003 [DIRS 180755], Table 7-1)	0.05 – 0.3 (fraction)	Uniform
FHH_Isotherm_k_CSNF_Rind_a	FHH adsorption isotherm parameter k for CSNF rind	1.606 – 8.215 (dimensionless)	Uniform
FHH_Isotherm_s_CSNF_Rind_a	FHH adsorption isotherm parameter s for CSNF rind	1.656 – 3.038 (dimensionless)	Uniform
HLWG_Rind_SA_a	Specific surface area of HLWG rind	10 – 38 $\text{m}^2 \text{g}^{-1}$	Uniform
ff_group8_a	Unsaturated zone fracture frequency DTN: LA0701PANS02BR.003 [DIRS 180497]	Mean = $\exp(1.12) \text{m}^{-1}$ Std. Dev. = $\exp(0.724) \text{m}^{-1}$	Log-normal
Por_group8_a	Unsaturated zone fracture porosity DTN: LA0701PANS02BR.003 [DIRS 180497], Table 1	0 – 1 (fraction); $E(x) = 0.0105$; $\sigma(x) = 0.0031$	Beta
Gamma_AFM_a	Active fracture model gamma parameter DTN: LA0701PANS02BR.003 [DIRS 180497]	0.2 – 0.6	Uniform

Table 8.2-4. Sampled Model Inputs Used in the EBS Radionuclide Transport Abstraction (Continued)

Input Name	Input Description	Range	Distribution
EBS_UZ_Flux_Sat_PS1 EBS_UZ_Flux_Sat_PS2 EBS_UZ_Flux_Sat_PS3 EBS_UZ_Flux_Sat_PS4 EBS_UZ_Flux_Sat_PS5	Unsaturated zone fracture saturation DTN: LA0701PANS02BR.003 [DIRS 180497] This includes the average fracture and matrix percolation fluxes and saturations for both glacial transition and post-10,000 year periods. There are total of five Percolation Subregions.	Average values for the five percolation subregions based on the average of repository nodes in each Percolation Subregion.	2-D Table; see Table 8.2-5
Diff_Path_Length_Invert_Top_a	Diffusive path length from waste package outer corrosion barrier to mid-point of invert	0.30 – 1.24 m	Uniform

Output DTN: SN0703PAEBSRTA.001

NOTES: ND = Truncated normal distribution
 $E(x)$ = Expected value
 $\sigma(x)$ = Standard deviation
CDF = Cumulative distribution function.

Table 8.2-5. Unsaturated Zone Saturation and Flux Inputs Used in the EBS Radionuclide Transport Abstraction

Parameter: EBS_UZ_Flux_Sat_PS1				
	Fracture Saturation	Matrix Saturation	Fracture Flux	Matrix Flux
gt10	1.29E-02	9.14E-01	3.44E-01	3.32E-01
gt30	1.65E-02	9.34E-01	1.82E+00	4.81E-01
gt50	1.41E-02	9.00E-01	1.94E+00	4.25E-01
gt90	1.43E-02	8.85E-01	4.77E+00	5.86E-01
pk10	1.57E-02	9.66E-01	1.55E+00	7.14E-01
pk30	1.65E-02	9.32E-01	1.99E+00	4.66E-01
pk50	1.52E-02	9.23E-01	3.55E+00	5.39E-01
pk90	1.52E-02	9.02E-01	7.10E+00	7.01E-01
Parameter: EBS_UZ_Flux_Sat_PS2				
	Fracture Saturation	Matrix Saturation	Fracture Flux	Matrix Flux
gt10	1.69E-02	9.75E-01	2.81E+00	5.12E-01
gt30	2.17E-02	9.83E-01	1.11E+01	6.21E-01
gt50	1.61E-02	9.68E-01	1.21E+01	6.45E-01
gt90	1.82E-02	9.39E-01	3.29E+01	7.77E-01
pk10	2.23E-02	9.87E-01	1.27E+01	7.23E-01
pk30	2.25E-02	9.84E-01	1.35E+01	6.55E-01
pk50	1.79E-02	9.73E-01	2.41E+01	7.37E-01
pk90	1.87E-02	9.41E-01	3.81E+01	8.16E-01

Table 8.2-5. Unsaturated Zone Saturation and Flux Inputs Used in the EBS Radionuclide Transport Abstraction (Continued)

Parameter: EBS_UZ_Flux_Sat_PS3				
	Fracture Saturation	Matrix Saturation	Fracture Flux	Matrix Flux
gt10	2.06E-02	9.86E-01	9.10E+00	6.69E-01
gt30	2.50E-02	9.88E-01	2.43E+01	7.64E-01
gt50	1.86E-02	9.75E-01	3.28E+01	7.92E-01
gt90	2.09E-02	9.31E-01	6.96E+01	9.21E-01
pk10	2.51E-02	9.88E-01	2.18E+01	7.28E-01
pk30	2.76E-02	9.89E-01	3.67E+01	7.89E-01
pk50	2.03E-02	9.76E-01	5.15E+01	8.11E-01
pk90	2.06E-02	9.30E-01	6.34E+01	8.99E-01
Parameter: EBS_UZ_Flux_Sat_PS4				
	Fracture Saturation	Matrix Saturation	Fracture Flux	Matrix Flux
gt10	2.36E-02	9.87E-01	1.92E+01	7.25E-01
gt30	2.72E-02	9.88E-01	3.72E+01	7.99E-01
gt50	1.95E-02	9.70E-01	5.36E+01	8.14E-01
gt90	2.14E-02	9.14E-01	9.32E+01	9.77E-01
pk10	2.53E-02	9.87E-01	2.62E+01	7.34E-01
pk30	3.07E-02	9.88E-01	6.00E+01	8.12E-01
pk50	2.04E-02	9.70E-01	6.93E+01	8.24E-01
pk90	2.06E-02	9.11E-01	7.62E+01	9.20E-01
Parameter: EBS_UZ_Flux_Sat_PS5				
	Fracture Saturation	Matrix Saturation	Fracture Flux	Matrix Flux
gt10	2.52E-02	9.88E-01	2.81E+01	7.34E-01
gt30	2.82E-02	9.89E-01	4.51E+01	8.04E-01
gt50	1.95E-02	9.73E-01	6.68E+01	8.15E-01
gt90	2.16E-02	9.30E-01	1.09E+02	1.02E+00
pk10	2.55E-02	9.88E-01	2.95E+01	7.36E-01
pk30	3.21E-02	9.90E-01	7.48E+01	8.20E-01
pk50	2.03E-02	9.74E-01	8.11E+01	8.18E-01
pk90	2.05E-02	9.26E-01	8.49E+01	9.42E-01

NOTE: Flux values are given in mm/yr but are entered as dimensionless in database. The units are added later in the model.

Output DTN: SN0703PAEBSRTA.001, files *Repository Values for Saturation and Flux.doc*,
bin splits gt10.xls, *bin splits gt30.xls*, *bin splits gt50.xls*, *bin splits gt90.xls*,
bin splits pk10.xls, *bin splits pk30.xls*, *bin splits pk50.xls*, *bin splits pk90.xls*.

Table 8.2-6. Fixed Model Inputs Used in the EBS Radionuclide Transport Abstraction

Input Name	Input Description	Source or Developed in RTA	Value
Frac_CS_CDSP_1a	Fraction of total steel mass in codisposal waste package HLWG waste form subdomain that is carbon steel	Developed: Table 6.3-9	0 (fraction)
Frac_CS_CDSP_1b	Fraction of total steel mass in codisposal waste package DSNF waste form subdomain that is carbon steel	Developed: Table 6.3-9	0.25 (fraction)
Frac_CS_CDSP_2	Fraction of total steel mass in codisposal waste package corrosion products domain that is carbon steel	Developed: Table 6.3-9	0.31 (fraction)
Frac_CS_CSNF_1	Fraction of total steel mass in CSNF waste package waste form domain that is carbon steel	Developed: Table 6.3-8	0 (fraction)
Frac_CS_CSNF_2	Fraction of total steel mass in CSNF waste package corrosion products domain that is carbon steel	Developed: Table 6.3-8	0 (fraction)
Max_Thick_CS_CSNF_1	Maximum thickness of carbon steel waste package internal components in CSNF waste package waste form domain	Placeholder parameter; no carbon steel in CSNF waste package	0 mm
Max_Thick_CS_CSNF_2	Maximum thickness of carbon steel waste package internal components in CSNF waste package corrosion products domain	Placeholder parameter; no carbon steel in CSNF waste package	0 mm
Max_Thick_CS_CDSP_1a	Maximum thickness of carbon steel waste package internal components in CDSP waste package HLW glass subdomain	Placeholder parameter; no carbon steel in CDSP waste package HLW glass subdomain	0 mm
Max_Thick_CS_CDSP_1b	Maximum thickness of carbon steel waste package internal components in CDSP waste package DSNF subdomain	DOE 2003 [DIRS 164970], Fig. 13 (16" Carbon Steel Sleeve)	6.35 mm
Max_Thick_CS_CDSP_2	Maximum thickness of carbon steel waste package internal components in CDSP waste package corrosion products domain	SNL 2007 [DIRS 179567], Table 4-8 (Support Tube)	31.75 mm
Max_Thick_SS_CSNF_1	Maximum thickness of stainless steel waste package internal components in CSNF waste package waste form domain	SNL 2007 [DIRS 179394], Table 4-2 (Borated Stainless Steel Absorber Plates)	11.11 mm
Max_Thick_SS_CSNF_2	Maximum thickness of stainless steel waste package internal components in CSNF waste package corrosion products domain	SNL 2007 [DIRS 179394], Table 4-3 (Inner Vessel)	50.8 mm

Table 8.2-6. Fixed Model Inputs Used in the EBS Radionuclide Transport Abstraction (Continued)

Input Name	Input Description	Source or Developed in RTA	Value
Max_Thick_SS_CDSP_1a	Maximum thickness of stainless steel waste package internal components in CDSP waste package HLW glass subdomain	CRWMS M&O 2000 [DIRS 151743], Table 3 (HLW Glass Canister)	10.5 mm
Max_Thick_SS_CDSP_1b	Maximum thickness of stainless steel waste package internal components in CDSP waste package DSNF subdomain	DOE 2003 [DIRS 164970], Fig. 13	9.525 mm
Max_Thick_SS_CDSP_2	Maximum thickness of stainless steel waste package internal components in CDSP waste package corrosion products domain	CRWMS M&O 2000 [DIRS 151743], Table 3 (SNF Standard Canister)	50.8 mm
Mass_Steel_CSNF_1	Mass of steel in CSNF waste package waste form domain	Developed: Table 6.3-8	9,980 kg
Mass_Steel_CSNF_2	Mass of steel in CSNF waste package corrosion products domain	Developed: Table 6.3-8	24,700 kg
Mass_Steel_CDSP_1a	Mass of steel in CDSP waste package HLW glass subdomain	Developed: Table 6.3-9	3,800 kg
Mass_Steel_CDSP_1b	Mass of steel in CDSP waste package DSNF subdomain	Developed: Table 6.3-9	1,270 kg
Mass_Steel_CDSP_2	Mass of steel in CDSP waste package corrosion products domain	Developed: Table 6.3-9	18,900 kg
Density_Goethite	Density of goethite (FeOOH)	Lide 2000 [DIRS 162229], pp. 4-66	4,260 kg m ⁻³
Density_HFO	Density of HFO	Towe and Bradley 1967 [DIRS 155334], p. 386	3,960 kg m ⁻³
Density_Cr2O3	Density of Cr ₂ O ₃	Lide 2000 [DIRS 162229], pp. 4-54	5,220 kg m ⁻³
Density_NiO	Density of NiO	Lide 2000 [DIRS 162229], pp. 4-75	6,720 kg m ⁻³
Mass_Fract_Fe_CS	Mass fraction of iron in carbon steel	ASTM A 516/A 516M-90. 1991 [DIRS 117138]	0.98 kg kg ⁻¹
Mass_Fract_Ni_CS	Mass fraction of nickel in carbon steel	ASTM A 516/A 516M-90. 1991 [DIRS 117138]	0 kg kg ⁻¹
Mass_Fract_Cr_CS	Mass fraction of chromium in carbon steel	ASTM A 516/A 516M-90. 1991 [DIRS 117138]	0 kg kg ⁻¹
Mass_Fract_Fe_SS	Mass fraction of iron in stainless steel	DTN: MO0003RIB00076.000 [DIRS 153044]; balance*	0.65 kg kg ⁻¹
Mass_Fract_Ni_SS	Mass fraction of nickel in stainless steel	DTN: MO0003RIB00076.000 [DIRS 153044]; average*	0.12 kg kg ⁻¹
Mass_Fract_Cr_SS	Mass fraction of chromium in stainless steel	DTN: MO0003RIB00076.000 [DIRS 153044]; average*	0.17 kg kg ⁻¹

Table 8.2-6. Fixed Model Inputs Used in the EBS Radionuclide Transport Abstraction (Continued)

Input Name	Input Description	Source or Developed in RTA	Value
Atomic_Wt_Fe	Atomic weight of iron	Weast 1985 [DIRS 111561], p. B-102	0.055847 kg mol ⁻¹
Atomic_Wt_Ni	Atomic weight of nickel	Weast 1985 [DIRS 111561], p. B-118	0.05869 kg mol ⁻¹
Atomic_Wt_Cr	Atomic weight of chromium	Weast 1985 [DIRS 111561], p. B-88	0.051996 kg mol ⁻¹
Molec_Wt_Goethite	Molecular weight of goethite	Lide 2000 [DIRS 162229], pp. 4-66	0.088852 kg mol ⁻¹
Molec_Wt_HFO	Molecular weight of HFO	See Section 6.3.4.2.3.1	0.088852 kg mol ⁻¹
Molec_Wt_NiO	Molecular weight of NiO	Lide 2000 [DIRS 162229], pp. 4-75	0.074692 kg mol ⁻¹
Molec_Wt_Cr2O3	Molecular weight of Cr ₂ O ₃	Lide 2000 [DIRS 162229], pp. 4-54	0.151990 kg mol ⁻¹
Stoich_Cr_Cr2O3	Stoichiometric coefficient for conversion of Cr to Cr ₂ O ₃	Developed: Table 6.5-6	2 mol Cr (mol Cr ₂ O ₃) ⁻¹
Stoich_Fe_Goethite	Stoichiometric coefficient for conversion of Fe to goethite	Developed: Table 6.5-6	1 mol Fe (mol goethite) ⁻¹
Stoich_Fe_HFO	Stoichiometric coefficient for conversion of Fe to HFO	Developed: Table 6.5-6	1 mol Fe (mol HFO) ⁻¹
Stoich_Ni_NiO	Stoichiometric coefficient for conversion of Ni to NiO	Developed: Table 6.5-6	1 mol Ni (mol NiO) ⁻¹
Density_HLWG_Rind	Grain density of HLW glass rind	DTN: MO0502ANLGAMR1.016 ECN1 [DIRS 172830], Table 8-1	2,700 kg m ⁻³
FHH_Isotherm_k_HLWG	FHH adsorption isotherm parameter <i>k</i> for HLW glass	Ebert et al. 1991 [DIRS 111028], p. 134, Figure 1b	3.2 (dimensionless)
FHH_Isotherm_s_HLWG	FHH adsorption isotherm parameter <i>s</i> for HLW glass	Ebert et al. 1991 [DIRS 111028], p. 134, Figure 1b	1.5 (dimensionless)
Porosity_HLWG_Rind	Porosity of HLW glass rind	DTN: MO0502ANLGAMR1.016 ECN1 [DIRS 172830], Table 8-1	0.17 (fraction)
Monolayer_thickness	Thickness of monolayer of adsorbed water	Developed: Equation 6.3.4.3.2-4	0.283 nm
DS_Total_Length	Length of drip shield	SNL 2007 [DIRS 179354], Table 4-2, Parameter Number 07-01	5,805 mm
Porosity_CP	Porosity of corrosion products	Developed: Section 6.3.4.3.4	0.4 (fraction)
Width_Invert	Width of invert	Developed: Equation 6.5.2.3-1	4.70 m
Thick_Invert	Average thickness of invert (flow and diffusive path length)	Developed: Equation 6.5.2.3-5	0.934 m
Vert_Cross_Sect_Area_Invert	Vertical cross-sectional area of invert	Developed: Equation 6.5.2.3-2	4.39 m ²
Density_Water	Water density at 25°C	Weast 1985 [DIRS 111561]	997.0449 kg m ⁻³

Table 8.2-6. Fixed Model Inputs Used in the EBS Radionuclide Transport Abstraction (Continued)

Input Name	Input Description	Source or Developed in RTA	Value
Viscosity_Water	Water viscosity at 25°C	Lide 2000 [DIRS 162229]	$0.890 \times 10^{-3} \text{ Pa s}$ ($0.000890 \text{ kg m}^{-1} \text{ s}^{-1}$)
Intergranular_Porosity_Invert	Porosity of crushed tuff invert ballast	DTN: MO0703PAHYTHRM.000 [DIRS 182093]	0.224 (fraction)
Invert_Viscosity_Ref_Temp	Reference temperature for viscosity giving temperature dependence of invert diffusion coefficient	Reference temperature for free water diffusion coefficient (25°C)	298.15 K
Interface_Scale_Factor	Scale factor used in numerical approximation for computing mass flux distribution from single-continuum to dual-continuum medium	Developed: Section 6.5.2.5	1×10^{-6} (dimensionless)
Intragranular_Porosity_Invert	Porosity of TSw35 tuff rock matrix (used in dual-continuum invert alternative conceptual model)	DTN: MO0703PAHYTHRM.000 [DIRS 182093]	0.111 (fraction)
Fracture_Interface_Area	Unsaturated zone fracture interface area	DTN: LB0205REVUZPRP.001 [DIRS 159525], file <i>FRACTURE_PROPERTY.xls</i> , Row 20, Column R	$9.68 \text{ m}^2 \text{ m}^{-3}$
Fracture_Residual_Sat	Unsaturated zone fracture residual saturation	DTN: LB0207REVUZPRP.001 [DIRS 159526], file <i>faultprops_2002.xls</i> , worksheet "summary," Model Layer <i>tswf</i>	0.01 (fraction)
UZ_Matrix_Porosity	Unsaturated zone matrix porosity	Section 6.5.2.6	0.149 (fraction)
UZ_Matrix_Density	Unsaturated zone dry matrix density for TSw35 (stratigraphic unit Tptpl)	DTN: SN0404T0503102.011 [DIRS 169129], file <i>ReadMe.doc</i> , Table 7-10	$1,980 \text{ kg m}^{-3}$
Diff_Thick_OB_CDSP	Outer barrier thickness for CDSP waste package	Section 6.5.2.1.1.2	0.0302 m
Diff_Thick_OB_CSNF	Outer barrier thickness for CSNF waste package	Section 6.5.2.1.2	0.0301 m
Diff_Area_CSNF_1	Diffusive area of CSNF waste form	Section 6.5.2.1.1.1	12.5 m^2
Diff_Area_CSNF_2	Diffusive area of CSNF corrosion products for the path excluding the outer barrier	Section 6.5.2.1.1.2	29.9 m^2
Diff_Area_CSNF_2_Max	Maximum diffusive area of CSNF corrosion products for the path through the outer barrier	Section 6.5.2.1.1.2	33.1 m^2
Diff_Area_CDSP_1a	Diffusive area of HLWG waste form subdomain in codisposal waste package	Section 6.5.2.1.2	13.7 m^2

Table 8.2-6. Fixed Model Inputs Used in the EBS Radionuclide Transport Abstraction (Continued)

Input Name	Input Description	Source or Developed in RTA	Value
Diff_Area_CDSP_1b	Diffusive area of DSNF waste form subdomain in codisposal waste package	Section 6.5.2.1.2	13.7 m ²
Diff_Area_CDSP_2	Diffusive area of CDSP corrosion products for the path excluding the outer barrier	Section 6.5.2.1.2	29.7 m ²
Diff_Area_CDSP_2_Max	Maximum diffusive area of CDSP corrosion products for the path through the outer barrier	Section 6.5.2.1.2	32.6 m ²
Diff_Path_Length_CSNF_1	Diffusive path length through CSNF waste form domain in CSNF waste package	Section 6.5.2.1.1.1	0.819 m
Diff_Path_Length_CSNF_2	Diffusive path length through corrosion products domain in CSNF waste package	Section 6.5.2.1.1.2	0.0914 m
Diff_Path_Length_CDSP_2	Diffusive path length through corrosion products domain in codisposal waste package	Section 6.5.2.1.2	0.0508 m
Diff_Path_Length_CDSP_1a	Diffusive path length through HLWG subdomain in codisposal waste package	Section 6.5.2.1.2	0.941 m
Diff_Path_Length_CDSP_1b	Diffusive path length through DSNF waste form subdomain in codisposal waste package	Section 6.5.2.1.2	0.0730
WP_Total_Length_CSNF	Total length of CSNF waste package	Section 6.5.2.1.1.2	5.691 m
WP_Total_Length_CDSP	Total length of CDSP waste package	Section 6.5.2.1.2	5.145 m
DS_Patch_Area	Area of a drip shield patch for analysis of the flux splitting experiments	Section 6.5.1.1.1	7.214 × 10 ⁴ mm ²
DS_Total_Width	Width of unfolded drip shield	Figure 4.1-1	4,880 mm
Porosity_DSNF	DSNF porosity	Section 6.5.2.1.2	0.2 (dimensionless)
WP_Crack_Area	Area of a single crack on the waste package	Table 6.3-3	7.7 × 10 ⁻⁶ m ²
X_length_1	Width of cells to the left and right of the middle cells	Section 6.5.2.6	5.5 m
Z_length_1	Depth of first layer of matrix-fracture cells	Section 6.5.2.6	1.0274 m
Z_length_2	Depth of second layer of matrix-fracture cells	Section 6.5.2.6	2.0548 m
Z_length_3	Depth of third layer of matrix-fracture cells	Section 6.5.2.6	5 m
Z_length_4	Depth of fourth layer of matrix-fracture cells	Section 6.5.2.6	10 m

Table 8.2-6. Fixed Model Inputs Used in the EBS Radionuclide Transport Abstraction (Continued)

Input Name	Input Description	Source or Developed in RTA	Value
Diff_Free_Am	Free water diffusion coefficient for Am	DTN: LB0702PAUZMTDF.001 [DIRS 180776], file <i>Readme.doc</i> , Table 8	$9.49 \times 10^{-10} \text{ m}^2 \text{ s}^{-1}$
Diff_Free_C	Free water diffusion coefficient for C	DTN: LB0702PAUZMTDF.001 [DIRS 180776], file <i>Readme.doc</i> , Table 8	$1.18 \times 10^{-9} \text{ m}^2 \text{ s}^{-1}$
Diff_Free_Cl	Free water diffusion coefficient for Cl	DTN: LB0702PAUZMTDF.001 [DIRS 180776], file <i>Readme.doc</i> , Table 8	$2.03 \times 10^{-9} \text{ m}^2 \text{ s}^{-1}$
Diff_Free_Cm	Free water diffusion coefficient for Cm; not transported in EBS	Section 6.3.4	$0.0 \text{ m}^2 \text{ s}^{-1}$
Diff_Free_Cs	Free water diffusion coefficient for Cs	DTN: LB0702PAUZMTDF.001 [DIRS 180776], file <i>Readme.doc</i> , Table 8	$2.06 \times 10^{-9} \text{ m}^2 \text{ s}^{-1}$
Diff_Free_I	Free water diffusion coefficient for I	DTN: LB0702PAUZMTDF.001 [DIRS 180776], file <i>Readme.doc</i> , Table 8	$2.05 \times 10^{-9} \text{ m}^2 \text{ s}^{-1}$
Diff_Free_Np	Free water diffusion coefficient for Np	DTN: LB0702PAUZMTDF.001 [DIRS 180776], file <i>Readme.doc</i> , Table 8	$6.18 \times 10^{-10} \text{ m}^2 \text{ s}^{-1}$
Diff_Free_Pa	Free water diffusion coefficient for Pa	DTN: LB0702PAUZMTDF.001 [DIRS 180776], file <i>Readme.doc</i> , Table 8	$6.04 \times 10^{-10} \text{ m}^2 \text{ s}^{-1}$
Diff_Free_Pu	Free water diffusion coefficient for Pu	DTN: LB0702PAUZMTDF.001 [DIRS 180776], file <i>Readme.doc</i> , Table 8	$1.30 \times 10^{-9} \text{ m}^2 \text{ s}^{-1}$
Diff_Free_Pu241	Free water diffusion coefficient for ^{241}Pu ; not transported in EBS	Section 6.3.4	$0.0 \text{ m}^2 \text{ s}^{-1}$
Diff_Free_Ra	Free water diffusion coefficient for Ra	DTN: LB0702PAUZMTDF.001 [DIRS 180776], file <i>Readme.doc</i> , Table 8	$8.89 \times 10^{-10} \text{ m}^2 \text{ s}^{-1}$
Diff_Free_Se	Free water diffusion coefficient for Se	DTN: LB0702PAUZMTDF.001 [DIRS 180776], file <i>Readme.doc</i> , Table 8	$1.04 \times 10^{-9} \text{ m}^2 \text{ s}^{-1}$
Diff_Free_Sn	Free water diffusion coefficient for Sn	DTN: LB0702PAUZMTDF.001 [DIRS 180776], file <i>Readme.doc</i> , Table 8	$1.55 \times 10^{-9} \text{ m}^2 \text{ s}^{-1}$

Table 8.2-6. Fixed Model Inputs Used in the EBS Radionuclide Transport Abstraction (Continued)

Input Name	Input Description	Source or Developed in RTA	Value
Diff_Free_Sr	Free water diffusion coefficient for Sr	DTN: LB0702PAUZMTDF.001 [DIRS 180776], file <i>Readme.doc</i> , Table 8	$7.91 \times 10^{-10} \text{ m}^2 \text{ s}^{-1}$
Diff_Free_Tc	Free water diffusion coefficient for Tc	DTN: LB0702PAUZMTDF.001 [DIRS 180776], file <i>Readme.doc</i> , Table 8	$1.95 \times 10^{-9} \text{ m}^2 \text{ s}^{-1}$
Diff_Free_Th	Free water diffusion coefficient for Th	DTN: LB0702PAUZMTDF.001 [DIRS 180776], file <i>Readme.doc</i> , Table 8	$5.97 \times 10^{-10} \text{ m}^2 \text{ s}^{-1}$
Diff_Free_U	Free water diffusion coefficient for U	DTN: LB0702PAUZMTDF.001 [DIRS 180776], file <i>Readme.doc</i> , Table 8	$6.64 \times 10^{-10} \text{ m}^2 \text{ s}^{-1}$

* Computed using average mass fractions of components for which a range is specified; rounded to two digits.

Output DTN: SN0703PAEBSRTA.001

Table 8.2-7. Impact Assessment of Using Preliminary Design Data and Preliminary Calculated Model Inputs Based on Design Data in the EBS Radionuclide Transport Abstraction

Input Name	Input Description	Preliminary Value, Used in the TSPA	Final Design Value	Relative Difference ^a and Impact
Frac_CS_CDSP_1a	Fraction of total steel mass in codisposal waste package HLWG waste form subdomain that is carbon steel	0 (fraction)	0 (fraction)	Identical; no impact
Frac_CS_CDSP_1b	Fraction of total steel mass in codisposal waste package DSNF waste form subdomain that is carbon steel	0.25 (fraction)	0.25 (fraction)	Identical; no impact
Frac_CS_CDSP_2	Fraction of total steel mass in codisposal waste package corrosion products domain that is carbon steel	0.31 (fraction)	0.31 (fraction)	Identical; no impact
Frac_CS_CSNF_1	Fraction of total steel mass in CSNF waste package waste form domain that is carbon steel	0 (fraction)	0 (fraction)	Identical; no impact
Frac_CS_CSNF_2	Fraction of total steel mass in CSNF waste package corrosion products domain that is carbon steel	0 (fraction)	0 (fraction)	Identical; no impact

Table 8.2-7. Impact Assessment of Using Preliminary Design Data and Preliminary Calculated Model Inputs Based on Design Data in the EBS Radionuclide Transport Abstraction
(Continued)

Input Name	Input Description	Preliminary Value, Used in the TSPA	Final Design Value	Relative Difference^a and Impact
Max_Thick_CS_CSNF_1	Maximum thickness of carbon steel waste package internal components in CSNF waste package waste form domain	0 mm	0 mm	Identical; no impact
Max_Thick_CS_CSNF_2	Maximum thickness of carbon steel waste package internal components in CSNF waste package corrosion products domain	0 mm	0 mm	Identical; no impact
Max_Thick_CS_CDSP_1a	Maximum thickness of carbon steel waste package internal components in CDSP waste package HLW glass subdomain	0 mm	0 mm	Identical; no impact
Max_Thick_CS_CDSP_1b	Maximum thickness of carbon steel waste package internal components in CDSP waste package DSNF subdomain	6.35 mm	6.35 mm	Identical; no impact
Max_Thick_CS_CDSP_2	Maximum thickness of carbon steel waste package internal components in CDSP waste package corrosion products domain	31.75 mm	31.75 mm	Identical; no impact
Max_Thick_SS_CSNF_1	Maximum thickness of stainless steel waste package internal components in CSNF waste package waste form domain	11.11 mm	11.11 mm	Identical; no impact
Max_Thick_SS_CSNF_2	Maximum thickness of stainless steel waste package internal components in CSNF waste package corrosion products domain	50.8 mm	50.8 mm	Identical; no impact
Max_Thick_SS_CDSP_1a	Maximum thickness of stainless steel waste package internal components in CDSP waste package HLW glass subdomain	10.5 mm	10.5 mm	Identical; no impact
Max_Thick_SS_CDSP_1b	Maximum thickness of stainless steel waste package internal components in CDSP waste package DSNF subdomain	9.525 mm	9.525 mm	Identical; no impact

Table 8.2-7. Impact Assessment of Using Preliminary Design Data and Preliminary Calculated Model Inputs Based on Design Data in the EBS Radionuclide Transport Abstraction
(Continued)

Input Name	Input Description	Preliminary Value, Used in the TSPA	Final Design Value	Relative Difference ^a and Impact
Max_Thick_SS_CDSP_2	Maximum thickness of stainless steel waste package internal components in CDSP waste package corrosion products domain	50.8 mm	50.8 mm	Identical; no impact
Mass_Steel_CSNF_1	Mass of steel in CSNF waste package waste form domain CSNF-1	9,980 kg	9,990 kg	0.1 % Negligible impact
Mass_Steel_CSNF_2	Mass of steel in CSNF waste package corrosion products domain CSNF-2	24,700 kg	24,600 kg	-0.4 % Negligible impact
Mass_Steel_CDSP_1a	Mass of steel in CDSP waste package waste form domain CDSP-1a	3,800 kg	3,780 kg	-0.5 % Negligible impact
Mass_Steel_CDSP_1b	Mass of steel in CDSP waste package waste form domain CDSP-1b	1,270 kg	1,280 kg	0.8 % Negligible impact
Mass_Steel_CDSP_2	Mass of steel in CDSP waste package corrosion products domain CDSP-2	18,900 kg	18,900 kg	Identical; no impact
Width_Invert	Width of invert	4.70 m	4.70 m	Identical; no impact
Thick_Invert	Average thickness of invert (flow and diffusive path length)	0.934 m	0.934 m	Identical; no impact
Vert_Cross_Sect_Area_Invert	Vertical cross-sectional area of invert	4.39 m ²	4.39 m ²	Identical; no impact
Diff_Thick_OB_CDSP	Outer barrier thickness for CDSP waste package	0.0302 m	0.0302 m	Identical; no impact
Diff_Thick_OB_CSNF	Outer barrier thickness for CSNF waste package	0.0301 m	0.0301 m	Identical; no impact
Diff_Area_CSNF_1	Diffusive area of CSNF waste form	12.5 m ²	12.5 m ²	Identical; no impact
Diff_Area_CSNF_2	Diffusive area of CSNF corrosion products for the path excluding the outer barrier	29.9 m ²	29.9 m ²	Identical; no impact
Diff_Area_CSNF_2_Max	Maximum diffusive area of CSNF corrosion products for the path through the outer barrier	33.1 m ²	33.1 m ²	Identical; no impact
Diff_Area_CDSP_1a	Diffusive area of HLWG waste form subdomain in codisposal waste package	13.7 m ²	13.7 m ²	Identical; no impact
Diff_Area_CDSP_1b	Diffusive area of DSNF waste form subdomain in codisposal waste package	13.7 m ²	13.7 m ²	Identical; no impact

Table 8.2-7. Impact Assessment of Using Preliminary Design Data and Preliminary Calculated Model Inputs Based on Design Data in the EBS Radionuclide Transport Abstraction
(Continued)

Input Name	Input Description	Preliminary Value, Used in the TSPA	Final Design Value	Relative Difference ^a and Impact
Diff_Area_CDSP_2	Diffusive area of CDSP corrosion products for the path excluding the outer barrier	29.7 m ²	28.9 m ²	-2.8 % Negligible impact; overestimates diffusive releases
Diff_Area_CDSP_2_Max	Maximum diffusive area of CDSP corrosion products for the path through the outer barrier	32.6 m ²	32.6 m ²	Identical; no impact
Diff_Path_Length_CSNF_1	Diffusive path length through CSNF waste form domain in CSNF waste package	0.819 m	0.819 m	Identical; no impact
Diff_Path_Length_CSNF_2	Diffusive path length through corrosion products domain in CSNF waste package	0.0914 m	0.0914 m	Identical; no impact
Diff_Path_Length_CDSP_2	Diffusive path length through corrosion products domain in codisposal waste package	0.0508 m	0.0508 m	Identical; no impact
Diff_Path_Length_CDSP_1a	Diffusive path length through HLWG subdomain in codisposal waste package	0.941 m	0.941 m	Identical; no impact
Diff_Path_Length_CDSP_1b	Diffusive path length through DSNF waste form subdomain in codisposal waste package	0.0730	0.0730	Identical; no impact
WP_Total_Length_CSNF	Total length of CSNF waste package	5.691 m	5.691 m	Identical; no impact
WP_Total_Length_CDSP	Total length of CDSP waste package	5.145 m	5.145 m	Identical; no impact

^a Relative difference (%) = $100 \times (\text{Final} - \text{Preliminary})/\text{Final}$.

Output DTN: SN0703PAEBSRTA.001, file *Preliminary Design Impact Assessment.doc*

Table 8.2-8. Model Equation Inputs Used in the EBS Radionuclide Transport Abstraction

Input Description	Input Equation and Parameter Description
<p>Equation 8-1 Invert diffusion coefficient (Equation 6.3.4.1.1-22)</p>	$\phi S_w D_{il} = D_{wi} \phi^{1.863} S_w^{1.863} 10^{ND(\mu=0.033, \sigma=0.218)}$ <p> D_{il} = effective invert diffusion coefficient ($m^2 s^{-1}$) D_{wi} = free water diffusion coefficient ($m^2 s^{-1}$) ϕ = invert bulk porosity (fraction) S_w = invert water saturation (fraction) ND = truncated normal distribution (± 3 standard deviations from the mean) μ = mean σ = standard deviation (D_{il} is an effective value that includes the effects of tortuosity.) </p>
<p>Equation 8-2 Temperature modification for diffusion coefficient (Equation 6.3.4.1.2-4)</p>	$D_T = D_{T_0} \frac{T}{T_0} 10^{\left[\frac{1.3272(293.15-T_0) - 0.001053(T_0-293.15)^2}{T_0-168.15} \right] \left[\frac{1.3272(293.15-T) - 0.001053(T-293.15)^2}{T-168.15} \right]}$ <p> D_T = diffusion coefficient at temperature T ($m^2 s^{-1}$) D_{T_0} = diffusion coefficient at temperature T_0 ($m^2 s^{-1}$) T = temperature (K); valid range: $293.15 K \leq T \leq 373.15 K$ T_0 = reference temperature (K) (Invert_Viscosity_Ref_Temp) </p>
<p>Equation 8-3 <u>Number of monolayers of water vapor adsorbed onto surfaces of SNF or HLWG degradation rind or corrosion products</u> (Equation 6.3.4.3.2-3)</p>	$\theta_a = \left[\frac{-k}{\ln(RH)} \right]^{\frac{1}{s}}$ <p> θ_a = number of monolayers of water adsorbed on the surface [dimensionless] RH = relative humidity [fraction] k = empirical FHH isotherm fitting parameter [dimensionless] (FHH_Isotherm_k_Rind, FHH_Isotherm_k_HLWG, or FHH_Isotherm_k_CP) s = empirical FHH isotherm fitting parameter [dimensionless] (FHH_Isotherm_s_Rind, FHH_Isotherm_s_HLWG, or FHH_Isotherm_s_CP) </p>

Table 8.2-8. Model Equation Inputs Used in the EBS Radionuclide Transport Abstraction (Continued)

Input Description	Input Equation and Parameter Description
<p>Equation 8-4 Mass of corrosion products (Equations 6.5.2.2.1-1 to 6.5.2.2.1-4)</p>	$t_{LCS,n} = \frac{1000 t_{max,CS,n}}{2r_{CS}}$ $t_{LSS,n} = \frac{1000 t_{max,SS,n}}{2r_{SS}}$ $m_{CPm,CS,n}(t) = \begin{cases} \left(\frac{t-t_0}{t_{LCS,n}}\right) f_{CS} f_{GHFO} \omega_{CS,m} \frac{M_{CPm}}{\alpha_{CPm} M_m} m_{s,n}, & t-t_0 \leq t_{LCS,n} \\ f_{CS} f_{GHFO} \omega_{CS,m} \frac{M_{CPm}}{\alpha_{CPm} M_m} m_{s,n}, & t-t_0 > t_{LCS,n} \end{cases}$ $m_{CPm,SS,n}(t) = \begin{cases} \left(\frac{t-t_0}{t_{LSS,n}}\right) (1-f_{CS}) f_{GHFO} \omega_{SS,m} \frac{M_{CPm}}{\alpha_{CPm} M_m} m_{s,n}, & t-t_0 \leq t_{LSS,n} \\ (1-f_{CS}) f_{GHFO} \omega_{SS,m} \frac{M_{CPm}}{\alpha_{CPm} M_m} m_{s,n}, & t-t_0 > t_{LSS,n} \end{cases}$ $m_{CP,n} = \sum_{CPm} (m_{CPm,CS,n} + m_{CPm,SS,n})$ <p> $t_{LCS,n}$ = lifetime of carbon steel in domain n [yr] $t_{LSS,n}$ = lifetime of stainless steel in domain n [yr] r_{CS} = rate of corrosion of carbon steel [$\mu\text{m yr}^{-1}$] (CS_Corrosion_Rate) r_{SS} = rate of corrosion of stainless steel [$\mu\text{m yr}^{-1}$] (SS_Corrosion_Rate) $t_{max,CS,n}$ = maximum thickness of carbon steel in domain n [m] (Max_Thick_CS) $t_{max,SS,n}$ = maximum thickness of stainless steel in domain n [m] (Max_Thick_SS) $m_{CPm,n,CS}$ = mass of corrosion products CPm in domain n from corrosion of carbon steel [kg] $m_{CPm,n,SS}$ = mass of CPm in domain n from corrosion of stainless steel [kg] $m_{CP,n}$ = total mass of corrosion products in domain n [kg] t = time since waste package emplacement [yr] </p>

Table 8.2-8. Model Equation Inputs Used in the EBS Radionuclide Transport Abstraction (Continued)

Input Description	Input Equation and Parameter Description
<p>Equation 8-4 Mass of corrosion products (Equations 6.5.2.2.1-1 to 6.5.2.2.1-4) (Continued)</p>	<p>t_0 = time of waste package breach [yr]</p> <p>$f_{CS,n}$ = fraction of carbon steel in steel mass in domain n (remainder is stainless steel) [dimensionless]</p> <p>$m_{s,n}$ = total mass of steel in domain n [kg]</p> <p>$f_{GHFO} = \begin{cases} \omega_G, & \text{for goethite} \\ (1 - \omega_G), & \text{for HFO} \\ 1.0, & \text{for NiO and Cr}_2\text{O}_3 \end{cases}$</p> <p>$\omega_G$ = mass fraction of goethite in iron corrosion products [dimensionless]</p> <p>$\omega_{CS,m}$ = mass fraction of metal m in carbon steel [dimensionless]</p> <p>$\omega_{SS,m}$ = mass fraction of metal m in stainless steel [dimensionless]</p> <p>M_m = atomic weight of metal m [kg mol⁻¹]</p> <p>M_{CPm} = molecular weight of corrosion products from corrosion of metal m [kg mol⁻¹]</p> <p>α_{CPm} = stoichiometric coefficient for conversion of metal m to corrosion products from corrosion of metal m [mol m mol⁻¹ CPm]</p>
<p>Equation 8-5 Effective water saturation of corrosion products (Equation 6.5.2.2.1-6)</p>	<p>$S_{we,CPm,n}(RH) = \min \left[t_f \rho_{CPm} \bar{s}_{CPm,n} \left(\frac{1 - \phi_{CP}}{\phi_{CP}} \right) \theta_{CP,n}(RH), 1.0 \right]$</p> <p>$S_{we,CPm,n}$ = effective water saturation of corrosion products</p> <p>RH = relative humidity (fraction)</p> <p>t_f = thickness of monolayer of water [m] (Thick_Water)</p> <p>ρ_{CPm} = density of corrosion product CPm [kg m⁻³]</p> <p>$\bar{s}_{CPm,n}$ = specific surface area of corrosion products CPm in domain n (m² kg⁻¹)</p> <p>ϕ_{CP} = porosity of corrosion products [m³ void m⁻³ bulk vol.] (Porosity_CP)</p> <p>$\theta_{CP,n}$ = number of monolayers of water adsorbed on the surface of corrosion products in domain n [dimensionless]</p>
<p>Equation 8-6 Pore volume in each type of corrosion product in each domain (Equation 6.5.2.2.1-7)</p>	<p>$V_{\phi,CPm,n}(t) = \frac{[m_{CPm,CS,n}(t) + m_{CPm,SS,n}(t)] \left(\frac{\phi_{CP}}{1 - \phi_{CP}} \right)}{\rho_{CPm}}$</p> <p>$V_{\phi,CPm,n}$ = pore volume of corrosion product CPm in domain n [m³]</p> <p>t = time since waste package emplacement [yr]</p> <p>$m_{CPm,n,CS}$ = mass of corrosion products CPm in domain n from corrosion of carbon steel [kg]</p> <p>$m_{CPm,n,SS}$ = mass of corrosion products CPm in domain n from corrosion of stainless steel [kg]</p> <p>ρ_{CPm} = density of corrosion product CPm [kg m⁻³]</p>

Table 8.2-8. Model Equation Inputs Used in the EBS Radionuclide Transport Abstraction (Continued)

Input Description	Input Equation and Parameter Description
	ϕ_{CP} = porosity of corrosion products [m^3 void m^{-3} bulk vol.] (Porosity_CP)
Equation 8-7 Total pore volume in each domain (Equation 6.5.2.2.1-8)	$V_{\phi,CP,n}(t) = \left(\frac{\phi_{CP}}{1 - \phi_{CP}} \right) \sum_{CPm} \left[\frac{m_{CPm,CS,n}(t) + m_{CPm,SS,n}(t)}{\rho_{CPm}} \right]$ $V_{\phi,CP,n}$ = total pore volume of corrosion products in domain n [m^3] t = time since waste package emplacement [yr] $m_{CPm,n,CS}$ = mass of corrosion products CPm in domain n from corrosion of carbon steel [kg] $m_{CPm,n,SS}$ = mass of corrosion products CPm in domain n from corrosion of stainless steel [kg] ρ_{CPm} = density of corrosion product CPm [kg m^{-3}] ϕ_{CP} = porosity of corrosion products [m^3 void m^{-3} bulk vol.] (Porosity_CP)
Equation 8-8 Total bulk volume of corrosion products in each domain (Equation 6.5.2.2.1-8)	$V_{CP,n}(t) = \left(\frac{1}{1 - \phi_{CP}} \right) \sum_{CPm} \left[\frac{m_{CPm,CS,n}(t) + m_{CPm,SS,n}(t)}{\rho_{CPm}} \right]$ $V_{CP,n}$ = total bulk volume of corrosion products in domain n [m^3] t = time since waste package emplacement [yr] $m_{CPm,n,CS}$ = mass of corrosion products CPm in domain n from corrosion of carbon steel [kg] $m_{CPm,n,SS}$ = mass of corrosion products CPm in domain n from corrosion of stainless steel [kg] ρ_{CPm} = density of corrosion product CPm [kg m^{-3}] ϕ_{CP} = porosity of corrosion products [m^3 void m^{-3} bulk vol.] (Porosity_CP)
Equation 8-9 Water volume in each corrosion product in each domain (Equation 6.5.2.2.1-10)	$V_{w,CPm,n}(RH, t) = V_{\phi,CPm,n}(t) S_{we,CPm,n}(RH)$ $V_{w,CPm,n}$ = water volume in corrosion products CPm in domain n [m^3] RH = relative humidity (fraction) t = time since waste package emplacement [yr] $V_{\phi,CPm,n}$ = pore volume of corrosion product CPm in domain n [m^3] $S_{we,CPm,n}$ = effective water saturation of corrosion products
Equation 8-10 Total water volume in corrosion products domains (Equation 6.5.2.2.1-11)	$V_{w,CP,n}(RH, t) = \sum_{CPm} [V_{w,CPm,n}(RH, t)]$ $V_{w,CP,n}$ = total water volume in corrosion products in domain n [m^3] RH = relative humidity (fraction) t = time since waste package emplacement [yr] $V_{w,CPm,n}$ = water volume in corrosion products CPm in domain n [m^3]

Table 8.2-8. Model Equation Inputs Used in the EBS Radionuclide Transport Abstraction (Continued)

Input Description	Input Equation and Parameter Description
<p>Equation 8-11 Water saturation in corrosion products domains (Equation 6.5.2.2.1-12)</p>	$S_{we,CP,n}(RH) = \min \left[\frac{V_{w,CP,n}(RH,t)}{V_{\phi,CP,n}(t)}, 1.0 \right]$ <p>$S_{we,CP,n}$ = effective water saturation of corrosion products domain n [dimensionless]</p> <p>$S_{we,CPm,n}$ = effective water saturation of corrosion products CPm in domain n [dimensionless]</p> <p>$V_{w,CP,n}$ = total water volume in corrosion products in domain n [m³]</p> <p>$V_{\phi,CP,n}$ = total pore volume of corrosion products in domain n [m³]</p>
<p>Equation 8-12 Effective water saturation of SNF degradation rind (Equation 6.5.2.2.2-1)</p>	$S_{we,r,n}(RH) = \min \left[t_f \rho_r \bar{s}_{r,n} \left(\frac{1 - \phi_r}{\phi_r} \right) \theta_{r,n}(RH), 1.0 \right]$ <p>$S_{we,r,n}$ = effective water saturation of SNF degradation rind in domain n [dimensionless]</p> <p>RH = relative humidity (fraction)</p> <p>t_f = thickness of monolayer of water [m] (Thick_Water)</p> <p>ρ_r = density of SNF degradation rind [kg m⁻³]</p> <p>$\bar{s}_{r,n}$ = specific surface area of SNF degradation rind in domain n (m² kg⁻¹)</p> <p>ϕ_r = porosity of SNF degradation rind [m³ void m⁻³ bulk vol.] (Porosity_Rind_CS NF or Porosity_DS NF)</p> <p>$\theta_{r,n}$ = number of monolayers of water adsorbed on the surface of SNF degradation rind in domain n [dimensionless]</p>
<p>Equation 8-13 Total pore volume in SNF domain containing corrosion products (Equation 6.5.2.2.2-5)</p>	$V_{\phi,CSNF}(t) = \phi_{rind} V_{rind,CSNF}(t) + V_{\phi,CP,CSNF}(t)$ <p>$V_{\phi,CSNF}$ = total pore volume in SNF domain (CSNF or DS NF) containing corrosion products [m³]</p> <p>t = time since waste package emplacement [yr]</p> <p>ϕ_{rind} = porosity of SNF degradation rind [m³ void m⁻³ bulk vol.] (Porosity_Rind_CS NF or Porosity_DS NF)</p> <p>$V_{rind,CSNF}$ = total pore volume of SNF degradation rind in SNF domain (CSNF or DS NF) [m³]</p> <p>$V_{\phi,CP,CSNF}$ = total pore volume of corrosion products in SNF domain (CSNF or DS NF) containing corrosion products [m³]</p>

Table 8.2-8. Model Equation Inputs Used in the EBS Radionuclide Transport Abstraction (Continued)

Input Description	Input Equation and Parameter Description
<p>Equation 8-14 Effective porosity of SNF domain containing corrosion products (Equation 6.5.2.2.2-6)</p>	$\phi_{CSNF}(t) = \frac{V_{\phi,CSNF}(t)}{V_{rind,CSNF}(t) + V_{CP,CSNF}(t)}$ <p> ϕ_{CSNF} = porosity of SNF domain [m³ void m⁻³ bulk vol.] t = time since waste package emplacement [yr] $V_{\phi,CSNF}$ = total pore volume in SNF domain (CSNF or DSNF) containing corrosion products [m³] $V_{rind,CSNF}$ = total pore volume of SNF degradation rind in SNF domain (CSNF or DSNF) [m³] $V_{CP,CSNF}$ = total bulk volume of SNF degradation rind in SNF domain (CSNF or DSNF) [m³] </p>
<p>Equation 8-15 Colloid diffusion coefficient (Equation 6.3.4.4-1)</p>	$D_{coll} = \frac{kT}{3\pi\mu_w d_{coll}}$ <p> D_{coll} = diffusion coefficient for a colloid particle of diameter d_{coll} (m² s⁻¹) k = Boltzmann constant (1.3806503 × 10⁻²³ J K⁻¹; Lide 2000 [DIRS 162229], p. 1-8) T = absolute temperature of waste form, corrosion products, or invert (K) μ_w = viscosity of water at temperature T (Pa s) d_{coll} = diameter of the colloid particle (m) (Diameter_Colloid_a) </p>
<p>Equation 8-16 Total SCC opening area resulting from seismic damage (Equations 6.3.3.2.4-7 and 6.3.3.2.4-7)</p>	$A_{DS_SCC} = C \frac{\pi\sigma_{YS_DS}}{\sqrt{3} E_{DS}} \cdot A_{SD_DS}$ $A_{WP_SCC} = C \frac{\pi\sigma_{YS_WP}}{\sqrt{3} E_{WP}} \cdot A_{SD_WP}$ <p> A_{DS_SCC} = total SCC opening area per drip shield [m²] A_{WP_SCC} = total SCC opening area per waste package [m²] C = uncertainty factor [dimensionless] $\sigma_{YS_DS}, \sigma_{YS_WP}$ = yield strength [Pa] E_{DS}, E_{WP} = modulus of elasticity [Pa] </p>

Output DTN: SN0703PAEBSRTA.001

Input parameters for the dual-continuum invert alternative conceptual model are listed in Table 8.2-9. Equations for calculating the intergranular and intragranular diffusion coefficients are listed in Table 8.2-10.

Table 8.2-9. Invert Diffusion Coefficient Alternative Conceptual Model Parameters

Input Name	Input Description	Where Developed in RTA	Value
Invert_Geometry_Coef	Dimensionless geometry-dependent coefficient for intergranular-intragranular mass transfer coefficient	Section 6.6.3.1	8 - 21 (dimensionless) Uniform
Diff_Length_Inv_Inter_Intra	Characteristic length of the matrix structure	Section 6.6.3.1	5 mm
Crit_Moisture_Content_Intra	Critical moisture content of invert intragranular continuum	Section 6.6.4.1	0.089 (fraction)
Crit_Moisture_Content_Inter	Critical moisture content of invert intergranular continuum	Section 6.6.4.1	0.00932 – 0.0612 Uniform
Diff_Threshold_Invert	Threshold value of diffusion coefficient in intragranular invert continuum	Section 6.6.4.2	$1 \times 10^{-16} \text{ m}^2 \text{ s}^{-1}$
Sat_Diff_Coeff_Matrix	Diffusion coefficient in saturated UZ matrix	Section 6.6.4.2	$9.24 \times 10^{-11} \text{ m}^2 \text{ s}^{-1}$

Table 8.2-10. Model Equation Inputs Used in the EBS Radionuclide Transport Abstraction Invert Diffusion Coefficient Alternative Conceptual Model

Input Description	Input Equation and Parameter Description
<p>Equation 8-17 Invert intergranular continuum diffusion coefficient (Equation 6.6.4.2-3)</p>	$D_{inter} = 0.45D_0 \left(\frac{\theta}{100\phi_{inter}} \right) \left(\frac{\theta - \theta_C}{100\phi_I - \theta_C} \right), \quad \theta \geq \theta_C$ $D_{inter} = D_{limit}, \quad \theta < \theta_C$ <p> D_0 = free water diffusion coefficient ($\text{m}^2 \text{ s}^{-1}$) D_{inter} = invert intergranular continuum diffusion coefficient ($\text{m}^2 \text{ s}^{-1}$) ϕ_I = $\phi_{inter} + (1 - \phi_{inter})\phi_{intra}$ = bulk porosity of invert (fraction) ϕ_{inter} = invert intergranular continuum porosity (fraction) (Intergranular_Porosity_Invert) ϕ_{intra} = invert intragranular continuum porosity (fraction) (Intragranular_Porosity_Invert) θ = invert bulk moisture content (percent) θ_C = invert intergranular continuum critical moisture content (percent) (Crit_Moisture_Content_Inter) </p>

Table 8.2-10. Model Equation Inputs Used in the EBS Radionuclide Transport Abstraction Invert Diffusion Coefficient Alternative Conceptual Model (Continued)

Input Description	Input Equation and Parameter Description
<p>Equation 8-18 Invert intragranular continuum diffusion coefficient (Equations 6.6.4.2-5 and 6.6.4.2-6)</p>	$D_{intra} = D_{ms} \left(\frac{\theta_{intra}}{100\phi_{intra}} \right)^p, \quad \theta_{intra} \geq \theta_{min}$ $D_{intra} = D_{limit}, \quad \theta_{intra} < \theta_{min}$ <p> D_{intra} = invert intragranular continuum diffusion coefficient ($m^2 s^{-1}$) D_{ms} = tuff matrix saturated diffusion coefficient ($m^2 s^{-1}$) (Sat_Diff_Coeff_Matrix) D_{limit} = threshold value of diffusion coefficient in intragranular invert continuum ($m^2 s^{-1}$) (Diff_Threshold_Invert) θ_{intra} = invert intragranular continuum moisture content (percent) ϕ_{intra} = invert intragranular continuum porosity (fraction) (Intragranular_Porosity_Invert) $p = \frac{\log_{10} D_{limit} - \log_{10} D_{ms}}{\log_{10} \left(\frac{\theta_{min}}{100} \right) - \log_{10} \phi_{intra}}$ θ_{min} = critical moisture content of invert intragranular continuum (percent) (Crit_Moisture_Content_Intra) </p>

8.3 EVALUATION OF YUCCA MOUNTAIN REVIEW PLAN CRITERIA

This model report documents the abstraction model for the flow of liquid and transport of radionuclides through the EBS. This section provides responses to *Yucca Mountain Review Plan, Final Report* (NRC 2003 [DIRS 163274]) acceptance criteria applicable to this model report. Being conceptual in nature, it is not possible to evaluate quantitatively many of the *Yucca Mountain Review Plan, Final Report* (NRC 2003 [DIRS 163274]) acceptance criteria in Sections 4.2.1 and 4.2.2.

The relevance of this model report to *Yucca Mountain Review Plan, Final Report* (NRC 2003 [DIRS 163274], Section 2.2.1.3.3) criteria for “Quantity and Chemistry of Water Contacting Engineered Barriers and Waste Forms,” which are based on meeting the requirements of 10 CFR 63.114(a)–(c) and (e)–(g) [DIRS 178394], is as follows:

Acceptance Criterion 1—System Description and Model Integration are Adequate.

- (1) Total system performance assessment adequately incorporates important design features, physical phenomena, and couplings, and uses consistent and appropriate assumptions throughout the quantity and chemistry of water contacting engineered barriers and waste forms abstraction process.

Response: The EBS radionuclide transport abstraction incorporates important design features, physical phenomena, and couplings, and uses consistent assumptions throughout the evaluation of the quantity of water contacting engineered barriers and waste forms. Sections 6.3.2 and 6.3.3 describe the conceptual model for water flux through the EBS. Section 6.5.1 describes the mathematical description of the EBS flow model. These sections provide information on seepage, effectiveness of the EBS components and mechanisms for breach or failure of the drip shield and waste package. Important general technical information related to water flow through the EBS can also be found throughout Section 6. This criterion was addressed satisfactorily.

- (2) The abstraction of the quantity and chemistry of water contacting engineered barriers and waste forms uses assumptions, technical bases, data, and models, that are appropriate and consistent with other related U.S. Department of Energy abstractions. For example, the assumptions used for the quantity and chemistry of water contacting engineered barriers and waste forms are consistent with the abstractions of “Degradation of Engineered Barriers” (NRC 2003 [DIRS 163274], Section 2.2.1.3.1); “Mechanical Disruption of Engineered Barriers” (NRC 2003 [DIRS 163274], Section 2.2.1.3.2); “Radionuclide Release Rates and Solubility Limits” (Section 2.2.1.3.4); “Climate and Infiltration” (NRC 2003 [DIRS 163274], Section 2.2.1.3.5); and “Flow Paths in the Unsaturated Zone” (NRC 2003 [DIRS 163274], Section 2.2.1.3.6). The descriptions and technical bases provide transparent and traceable support for the abstraction of quantity and chemistry of water contacting engineered barriers and waste forms.

Response: The EBS radionuclide transport abstraction uses assumptions, technical bases, data, and models that are consistent with other related U.S. Department of Energy abstractions. Sections 6.3.2, 6.3.3, and 6.5.1 of this model report, provide descriptions and technical bases to support the quantity-related portion of the abstraction of quantity and chemistry of water contacting engineered barriers and waste forms. Section 5 provides assumptions that are relevant to the EBS flow model. This criterion was addressed satisfactorily.

- (3) Important design features, such as waste package design and material selection, drip shield, ground support, thermal loading strategy, and degradation processes, are considered during the determination of initial and boundary conditions for calculations of the quantity of water contacting engineered barriers and waste forms.

Response: Sections 6.3 and 6.5 provide the technical bases and details of model features for the EBS flow model. Section 6.3.2 describes drip shield design, effectiveness and breaching. Section 6.3.3 describes waste package design, breaching and impact of heat generation. Sections 6.3.3 and 6.5.2 provide invert model features. This criterion was addressed satisfactorily.

- (4) The U.S. Department of Energy reasonably accounts for the range of environmental conditions expected inside breached waste packages and in the engineered barrier environment surrounding the waste package. For example, the U.S. Department of Energy should provide a description and sufficient technical bases for its abstraction of changes in hydrologic properties in the near field, caused by coupled thermal-hydrologic mechanical-chemical processes.

Response: Spatial and temporal abstractions address physical couplings (thermal-hydrologic mechanical-chemical). Sections 6.3 and 6.5 provide descriptions of coupled effects for the flow model. These effects include heat generation inside the waste package and condensation on the drip shield surface. The seepage and imbibition fluxes are also the product of coupled thermal-hydrologic mechanical-chemical processes. This criterion was addressed satisfactorily.

- (5) Sufficient technical bases and justification are provided for the total system performance assessment assumptions and approximations for modeling coupled thermal-hydrologic-mechanical-chemical effects on seepage and flow, the waste package chemical environment, and the chemical environment for radionuclide release. The effects of distribution of flow on the amount of water contacting the engineered barriers and waste forms are consistently addressed, in all relevant abstractions.

Response: The technical bases and justification are provided for TSPA assumptions and approximations for modeling coupled thermal-hydrologic mechanical-chemical effects on flow and radionuclide release throughout Sections 5 and 6. The effects of distribution of flow on the amount of water contacting the engineered barriers and waste forms are consistently addressed in Sections 6.3 and 6.5. This criterion was addressed satisfactorily.

- (6) The expected ranges of environmental conditions within the waste package emplacement drifts, inside of breached waste packages, and contacting the waste forms and their evolution with time are identified.

Response: These are provided in Sections 6.3, 6.5 and 6.7. Examples include the effects of the drip shield on the quantity of water (Sections 6.3.2 and 6.5.1); conditions that promote corrosion of engineered barriers and degradation of waste forms (Sections 6.3 and 6.5); wet and dry cycles; and size and distribution of penetrations of engineered barriers. This criterion was addressed satisfactorily.

- (7) The model abstraction for quantity and chemistry of water contacting engineered barriers and waste forms is consistent with the detailed information on engineered barrier design and other engineered features. For example, consistency is demonstrated for: (i) dimensionality of the abstractions; (ii) various design features and site characteristics; and (iii) alternative conceptual approaches. Analyses are adequate to demonstrate that no deleterious effects are caused by design or site features that the U.S. Department of Energy does not take into account in this abstraction.

Response: The EBS radionuclide transport abstraction is consistent with detailed information on engineered barrier design and other engineered features. Analysis discussions in Section 6 demonstrate that no deleterious effects are caused by design or site features that are not taken into account in this abstraction. Section 6.7 provides a summary discussion on the capability of the engineered barriers. This criterion was addressed satisfactorily.

- (8) Adequate technical bases are provided, including activities such as independent modeling, laboratory or field data, or sensitivity studies, for inclusion

of any thermal-hydrologic-mechanical-chemical couplings and features, events, and processes.

Response: Technical bases are provided, including activities such as independent modeling, laboratory or field data, or sensitivity studies, for inclusion of any thermal-hydrologic-mechanical-chemical couplings and features, events, and processes. These are provided throughout Sections 6 and 7. This criterion was addressed satisfactorily.

- (9) Performance—affecting processes that have been observed in thermal-hydrologic tests and experiments are included into the performance assessment. For example, the U.S. Department of Energy either demonstrates that liquid water will not reflux into the underground facility or incorporates refluxing water into the performance assessment calculation, and bounds the potential adverse effects of alteration of the hydraulic pathway that result from refluxing water.

Response: Performance—affecting processes that have been observed in thermal-hydrologic tests and experiments are included primarily through the inputs (e.g., seepage values from *Abstraction of Drift Seepage* (SNL 2007 [DIRS 181244])), described in Section 6.3.2 of this model report, which are required to implement the EBS radionuclide transport abstraction. This criterion was addressed satisfactorily.

Acceptance Criterion 2—Data are Sufficient for Model Justification.

- (1) Geological, hydrological, and geochemical values used in the License Application are adequately justified. Adequate description of how the data were used, interpreted, and appropriately synthesized into the parameters is provided.

Response: The EBS radionuclide transport abstraction provides the technical justification for geological, hydrological, and geochemical values used. There is also a description of how the data were used, interpreted, and synthesized into associated parameter values. Throughout Section 6, the range, distribution and uncertainty of model data are discussed. Detailed description of data and technical justification of values used is provided throughout Sections 6.3 and 6.5. This criterion was addressed satisfactorily.

- (2) Sufficient data were collected on the characteristics of the natural system and engineered materials to establish initial and boundary conditions for conceptual models of thermal-hydrologic-mechanical-chemical coupled processes, that affect seepage and flow and the engineered barrier chemical environment.

Response: Data and sources of data are provided in Section 4.1 on the characteristics of the natural system and engineered materials needed to establish initial and boundary conditions for conceptual models of thermal-hydrologic-mechanical-chemical coupled processes that affect flow. Collection of input data used in this model report was done using acceptable techniques under the YMP quality assurance plan; specific techniques are provided in Sections 4.1.1 to 4.1.3. This criterion was addressed satisfactorily.

- (4) Sufficient information to formulate the conceptual approach(es) for analyzing water contact with the drip shield, engineered barriers, and waste forms is provided.

Response: Information required to formulate the conceptual approaches for analyzing water contact with the drip shield, engineered barriers, and waste forms is provided in Sections 6.3 and 6.5. Sections 6.3.2, 6.3.3 and 6.5.1 present the conceptual models used for water flux through the E B S, together with information on drip shield effectiveness, drip shield and waste package breaching, seepage and imbibition flux from the unsaturated zone matrix. This criterion was addressed satisfactorily.

Acceptance Criterion 3—Data Uncertainty Is Characterized and Propagated Through the Model Abstraction.

- (1) Models use parameter values, assumed ranges, probability distributions, and bounding assumptions that are technically defensible, reasonably account for uncertainties and variabilities, and do not result in an under representation of the risk estimate.

Response: The EBS radionuclide transport abstraction uses parameter values, assumed ranges, probability distributions, and bounding assumptions that account for uncertainties and variabilities, and that do not result in an under-representation of the risk estimate. Section 4.1 lists the data and parameters used, together with their sources. Section 8 provides a summary of the base case model inputs together with associated uncertainties. This criterion was addressed satisfactorily.

- (2) Parameter values, assumed ranges, probability distributions, and bounding assumptions used in the total system performance assessment calculations of quantity and chemistry of water contacting engineered barriers and waste forms are technically defensible and reasonable, based on data from the Yucca Mountain region (e.g., results from large block and drift-scale heater and niche tests), and a combination of techniques that may include laboratory experiments, field measurements, natural analog research, and process-level modeling studies.

Response: Parameter values, assumed ranges, probability distributions, and bounding assumptions used in the TSPA calculations of quantity of water contacting engineered barriers and waste forms are based on data from the Yucca Mountain region, laboratory experiments, field measurements, natural analog research, and process-level modeling studies. Section 4.1 lists the data and parameters used, together with their sources. Section 8 provides a summary of the base case model inputs together with associated uncertainties. This criterion was addressed satisfactorily.

- (3) Input values used in the total system performance assessment calculations of quantity and chemistry of water contacting engineered barriers (e.g., drip shield and waste package) are consistent with the initial and boundary conditions and the assumptions of the conceptual models and design concepts for the Yucca Mountain site. Correlations between input values are appropriately established in the U.S. Department of Energy total system performance assessment. Parameters used to define initial conditions, boundary conditions, and computational domain in sensitivity analyses involving coupled thermal-hydrologic-mechanical-chemical effects on seepage and flow, the waste package chemical environment, and the chemical

environment for radionuclide release, are consistent with available data. Reasonable or conservative ranges of parameters or functional relations are established.

Response: Input values used in the TSPA calculations of quantity of water contacting engineered barriers (e.g., drip shield and waste package) are consistent with the initial and boundary conditions and the assumptions of the conceptual models and design concepts for the Yucca Mountain site. Reasonable or conservative ranges of parameters or functional relations have been established. Section 4.1 lists the data and parameters used, together with their sources. Section 8 provides a summary of the base case model inputs together with associated uncertainties. This criterion was addressed satisfactorily.

- (4) Uncertainty is adequately represented in parameter development for conceptual models, process models, and alternative conceptual models considered in developing the abstraction of radionuclide release rates and solubility limits, either through sensitivity analyses or use of bounding analyses.

Response: Adequate representation of uncertainties in the characteristics of the natural system and engineered materials is provided in parameter development for conceptual models, process-level models, and alternative conceptual models. In some instances, uncertainty is constrained using conservative limits. Parameter development for the models described in this model report is provided throughout Sections 6.3, 6.4, 6.5 and 6.6. This criterion was addressed satisfactorily.

Acceptance Criterion 4—Model Uncertainty Is Characterized and Propagated Through the Model Abstraction.

- (1) Alternative modeling approaches of features, events, and processes are considered and are consistent with available data and current scientific understanding, and the results and limitations are appropriately considered in the abstraction.

Response: Alternative modeling approaches of features, events, and processes are considered in Sections 6.4 and 6.6 and are consistent with available data and current scientific understanding, and the results and limitations are considered. This criterion was addressed satisfactorily.

- (2) Alternative modeling approaches are considered and the selected modeling approach is consistent with available data and current scientific understanding. A description that includes a discussion of alternative modeling approaches not considered in the final analysis and the limitations and uncertainties of the chosen model is provided.

Response: Alternative modeling approaches are considered in Sections 6.4 and 6.6. The selected modeling approach is consistent with available data and current scientific understanding. A description that includes a discussion of alternative modeling approaches not considered in the final analysis and the limitations and uncertainties of the chosen model is provided. This criterion was addressed satisfactorily.

- (3) Consideration of conceptual model uncertainty is consistent with available site characterization data, laboratory experiments, field measurements, natural analog

information and process-level modeling studies; and the treatment of conceptual model uncertainty does not result in an under-representation of the risk estimate.

Response: Consideration of conceptual model uncertainty is consistent with available site characterization data, laboratory experiments, field measurements, natural analog information and process-level modeling studies. The fundamental relationships (e.g., mass balance and flow equations) upon which the EBS radionuclide transport abstraction is based, are well-established with a long history of use in the scientific community and as such are not subject to significant uncertainty. In addition, the alternative conceptual models have been screened out (Section 6.4), thereby increasing confidence in the selected conceptual model. Other sources of uncertainty involve modeling choices (e.g., assumptions, geometry) that, because of their conservative nature, effectively bound uncertainty. This treatment of conceptual model uncertainty does not result in an under-representation of the risk estimate. This criterion was addressed satisfactorily.

- (4) Adequate consideration is given to effects of thermal-hydrologic-mechanical-chemical coupled processes in the assessment of alternative conceptual models. These effects may include: (i) thermal-hydrologic effects on gas, water, and mineral chemistry; (ii) effects of microbial processes on the engineered barrier chemical environment and the chemical environment for radionuclide release; (iii) changes in water chemistry that may result from the release of corrosion products from the engineered barriers and interactions between engineered materials and groundwater; and (iv) changes in boundary conditions (e.g., drift shape and size) and hydrologic properties, relating to the response of the geomechanical system to thermal loading.

Response: Consideration is given in Sections 6.4 and 6.6 to effects of thermal-hydrologic-mechanical-chemical coupled processes in the assessment of alternative conceptual models. This criterion was addressed satisfactorily.

Acceptance Criterion 5—Model Abstraction Output Is Supported by Objective Comparisons.

- (1) The models implemented in this total system performance assessment abstraction provide results consistent with output from detailed process-level models and/or empirical observations (laboratory and field testings and/or natural analogs).

Response: The models implemented in this TSPA abstraction provide results consistent with output from detailed process-level models and/or empirical observations (laboratory testings). For example, Sections 6.5.1 and 7.1 provide comparison of the drip shield and waste package flux splitting models with breached drip shield and waste package experiments. This criterion was addressed satisfactorily.

- (2) Abstracted models for coupled thermal-hydrologic- mechanical-chemical effects on seepage and flow and the engineered barrier chemical environment, as well as on the chemical environment for radionuclide release, are based on the same assumptions and approximations demonstrated to be appropriate for process-level models or closely analogous natural or experimental systems. For example, abstractions of processes, such as thermally induced changes in hydrological properties, or estimated diversion

of percolation away from the drifts, are adequately justified by comparison to results of process-level modeling, that are consistent with direct observations and field studies.

Response: Abstracted models for coupled thermal-hydrologic mechanical-chemical effects on flow and radionuclide release are based on the same assumptions and approximations demonstrated to be appropriate for process-level models or closely analogous natural or experimental systems, as demonstrated throughout Sections 5 and 6. This criterion was addressed satisfactorily.

- (3) Accepted and well-documented procedures are used to construct and test the numerical models that simulate coupled thermal-hydrologic- mechanical-chemical effects on seepage and flow, engineered barrier chemical environment, and the chemical environment for radionuclide release. Analytical and numerical models are appropriately supported. Abstracted model results are compared with different mathematical models, to judge robustness of results.

Response: The EBS radionuclide transport abstraction uses accepted and well-documented procedures to construct and test the numerical models that simulate coupled thermal-hydrologic-mechanical-chemical effects on flow and radionuclide release, as provided throughout Sections 6 and 7. Technical support is presented for analytical and numerical models. This criterion was addressed satisfactorily.

The relevance of this model report to *Yucca Mountain Review Plan (Final Report)* criteria for “Radionuclide Release Rates and Solubility Limits” (NRC 2003 [DIRS 163274], Section 2.2.1.3.4), which are based on meeting the requirements of 10 CFR 63.114(a)–(c) and (e)–(g) [DIRS 178394], is as follows:

Acceptance Criterion 1—System Description and Model Integration Are Adequate.

- (1) Total system performance assessment adequately incorporates important design features, physical phenomena, and couplings, and uses consistent and appropriate assumptions throughout the radionuclide release rates and solubility limits abstraction process.

Response: Total system performance assessment adequately incorporates important design features, physical phenomena, and couplings, and uses consistent and appropriate assumptions throughout the radionuclide release rates and solubility limits abstraction process. Section 6.3.4 describes the conceptual model for EBS transport model. Sections 6.5.1 and 6.5.2 describe the mathematical description of the EBS transport model components. These sections provide information on diffusion, retardation, transport through stress corrosion cracks, and EBS-UZ boundary condition implementation. Important general technical information related to radionuclide transport through the EBS can also be found throughout Section 6. This criterion was addressed satisfactorily.

- (2) The abstraction of radionuclide release rates uses assumptions, technical bases, data, and models that are appropriate and consistent with other related U.S. Department of Energy abstractions. For example, the assumptions used for this model abstraction are

consistent with the abstractions of “Degradation of Engineered Barriers” (NRC 2003 [DIRS 163274], Section 2.2.1.3.1); “Mechanical Disruption of Engineered Barriers” (NRC 2003 [DIRS 163274], Section 2.2.1.3.2); “Quantity and Chemistry of Water Contacting Engineered Barriers and Waste Forms” (NRC 2003 [DIRS 163274], Section 2.2.1.3.3); “Climate and Infiltration” (NRC 2003 [DIRS 163274], Section 2.2.1.3.5); and “Flow Paths in the Unsaturated Zone” (NRC 2003 [DIRS 163274], Section 2.2.1.3.6). The descriptions and technical bases provide transparent and traceable support for the abstraction of radionuclide release rates.

Response: The EBS radionuclide transport abstraction uses assumptions, technical bases, data, and models consistent with other related U.S. Department of Energy abstractions. The descriptions and technical bases described in Sections 6.3.4, 6.5.1, and 6.5.2 provide support for the abstraction of radionuclide release rates. Section 5 provides assumptions that are relevant to the EBS transport model. This criterion was addressed satisfactorily.

- (3) The abstraction of radionuclide release rates provides sufficient, consistent design information on waste packages and engineered barrier systems. For example, inventory calculations and selected radionuclides are based on the detailed information provided on the distribution (both spatially and by compositional phase) of the radionuclide inventory, within the various types of high-level radioactive waste.

Response: The EBS radionuclide transport abstraction provides consistent design information on waste packages and engineered barrier systems (Section 4.1 and throughout Section 6). Selected radionuclides are based on the detailed information provided on the distribution (both spatially and by compositional phase) of the radionuclide inventory, within the various types of HLW. Input data on radionuclides are provided in Section 4.1 and 6. This criterion was addressed satisfactorily.

- (4) The U.S. Department of Energy reasonably accounts for the range of environmental conditions expected inside breached waste packages and in the engineered barrier environment surrounding the waste package. For example, the U.S. Department of Energy should provide a description and sufficient technical bases for its abstraction of changes in hydrologic properties in the near field, caused by coupled thermal-hydrologic-mechanical-chemical processes.

Response: The EBS radionuclide transport abstraction accounts for the range of environmental conditions expected inside breached waste packages and in the engineered barrier environment surrounding the waste package. Sections 6.3 and 6.5 describe provisions for thermal, chemical, and hydrologic conditions inside and surrounding the waste package. This criterion was addressed satisfactorily.

- (5) The description of process-level conceptual and mathematical models is sufficiently complete, with respect to thermal-hydrologic processes affecting radionuclide release from the emplacement drifts. For example, if the U.S. Department of Energy uncouples coupled processes, the demonstration that uncoupled model results bound predictions of fully coupled results is adequate.

Response: The description of process-level conceptual and mathematical models, with respect to thermal-hydrologic processes affecting radionuclide release from the emplacement drifts, is provided in Section 6.5. This criterion was addressed satisfactorily.

- (6) Technical bases for inclusion of any thermal-hydrologic-mechanical-chemical couplings and features, events, and processes in the radionuclide release rates and solubility Review Plan for Safety Analysis Report limits model abstraction are adequate. For example, technical bases may include activities, such as independent modeling, laboratory or field data, or sensitivity studies.

Response: Technical bases for inclusion of thermal-hydrologic-mechanical-chemical couplings and the disposition of features, events, and processes in the EBS radionuclide transport abstraction are summarized in Section 6.2. This criterion was addressed satisfactorily.

Acceptance Criterion 2—Data Are Sufficient for Model Justification.

- (1) Geological, hydrological, and geochemical values used in the License Application are adequately justified. Adequate description of how the data were used, interpreted, and appropriately synthesized into the parameters is provided.

Response: Technical justification for the geological, hydrological, and geochemical values used in the EBS radionuclide transport abstraction is provided. There is also a discussion of how the data are used, interpreted, and synthesized into associated parameters values. Throughout Section 6, the range, distribution and uncertainty of the model data are discussed. Detailed descriptions of data and technical justification of values used are provided throughout Sections 6.3 and 6.5. This criterion was addressed satisfactorily.

- (2) Sufficient data have been collected on the characteristics of the natural system and engineered materials to establish initial and boundary conditions for conceptual models and simulations of thermal-hydrologic-chemical coupled processes. For example, sufficient data should be provided on design features, such as the type, quantity, and reactivity of materials, that may affect radionuclide release for this abstraction.

Response: Section 4.1 provides data on characteristics of the natural system and engineered materials needed to establish initial and boundary conditions for the EBS radionuclide transport abstraction conceptual models and simulations of thermal-hydrologic-chemical coupled processes. This criterion was addressed satisfactorily.

- (4) The corrosion and radionuclide release testing program for high-level radioactive waste forms intended for disposal provides consistent, sufficient, and suitable data for the in-package and in-drift chemistry used in the abstraction of radionuclide release rates and solubility limits. For expected environmental conditions, the U.S. Department of Energy provides sufficient justification for the use of test results, not specifically collected from the Yucca Mountain site, for engineered barrier components, such as high-level radioactive waste forms, drip shield, and backfill.

Response: The corrosion and radionuclide release testing program for HLW forms intended for disposal provides data for the in-package and in-drift chemistry used in the EBS radionuclide transport abstraction (Section 4.1). For expected environmental conditions, the EBS radionuclide transport abstraction provides justification for the use of test results, not specifically collected from the Yucca Mountain site, for engineered barrier components, such as HLW forms and drip shield (Sections 6.3 and 6.5). This criterion was addressed satisfactorily.

Acceptance Criterion 3—Data Uncertainty Is Characterized and Propagated Through the Model Abstraction.

- (1) Models use parameter values, assumed ranges, probability distributions, and bounding assumptions that are technically defensible, reasonably account for uncertainties and variabilities, and do not result in an under representation of the risk estimate.

Response: The EBS radionuclide transport abstraction uses parameter values, assumed ranges, probability distributions, and/or bounding assumptions that account for uncertainties and variabilities, and that do not cause an under-representation of the risk estimate. Section 4.1 lists the data and parameters used, together with their sources. Section 8 provides a summary of the base case model inputs together with associated uncertainties. This criterion was addressed satisfactorily.

- (2) Parameter values, assumed ranges, probability distributions, and bounding assumptions used in the abstractions of radionuclide release rates and solubility limits in the total system performance assessment are technically defensible and reasonable based on data from the Yucca Mountain region, laboratory tests, and natural analogs. For example, parameter values, assumed ranges, probability distributions, and bounding assumptions adequately reflect the range of environmental conditions expected inside breached waste packages.

Response: Parameter values, assumed ranges, probability distributions, and bounding assumptions used in the abstractions of radionuclide release rates and solubility limits in the TSPA are based on data from the Yucca Mountain region, laboratory tests, and natural analogs. Parameter values, assumed ranges, probability distributions, and bounding assumptions reflect the range of environmental conditions expected inside breached waste packages. Section 4.1 lists the data and parameters used, together with their sources. Section 8 provides a summary of the base case model inputs together with associated uncertainties. This criterion was addressed satisfactorily.

- (3) DOE uses reasonable or conservative ranges of parameters or functional relations to determine effects of coupled thermal-hydrologic-chemical processes on radionuclide release. These values are consistent with the initial and boundary conditions and the assumptions for the conceptual models and design concepts for natural and engineered barriers at the Yucca Mountain site. If any correlations between the input values exist, they are adequately established in the total system performance assessment. For example, estimations are based on a thermal loading and ventilation strategy; engineered barrier system design (including drift liner, backfill, and drip-shield); and

natural system masses and fluxes that are consistent with those used in other abstractions.

Response: The EBS radionuclide transport abstraction uses reasonable or conservative ranges of parameters or functional relations to determine effects of coupled thermal-hydrologic-chemical processes on radionuclide release. These values are consistent with the initial and boundary conditions and the assumptions for the conceptual models and design concepts for natural and engineered barriers at the Yucca Mountain site. Section 4.1 lists the data and parameters used, together with their sources. Section 8 provides a summary of the base case model inputs together with associated uncertainties. This criterion was addressed satisfactorily.

- (4) Uncertainty is adequately represented in parameter development for conceptual models, process models, and alternative conceptual models considered in developing the abstraction of radionuclide release rates and solubility limits, either through sensitivity analyses or use of bounding analyses.

Response: Uncertainty is represented in parameter development for conceptual models, process models, and alternative conceptual models considered in developing the abstraction of radionuclide release rates and solubility limits. Parameter development for the models described in this model report is provided throughout Sections 6.3, 6.4, 6.5, and 6.6. This criterion was addressed satisfactorily.

- (5) Parameters used to describe flow through and out of the engineered barrier, sufficiently bound the effects of backfill, excavation-induced changes, and thermally induced mechanical changes that affect flow.

Response: The EBS radionuclide transport abstraction considers the uncertainties in the characteristics of the natural system and engineered materials, such as the type, quantity, and reactivity of material, in establishing initial and boundary conditions for conceptual models and simulations of thermal-hydrologic-chemical coupled processes that affect radionuclide release. Parameter development for the models described in this model report is provided throughout Sections 6.3, 6.4, 6.5, and 6.6. This criterion was addressed satisfactorily.

- (8) DOE adequately considers the uncertainties, in the characteristics of the natural system and engineered materials, such as the type, quantity, and reactivity of material, in establishing initial and boundary conditions for conceptual models and simulations of thermal-hydrologic-chemical coupled processes that affect radionuclide release.

Response: Parameters used to describe flow through and out of the engineered barrier bound, the effects of excavation-induced changes, and thermally induced mechanical changes that affect flow. This criterion was addressed satisfactorily.

Acceptance Criterion 4—Model Uncertainty Is Characterized and Propagated Through the Model Abstraction.

- (1) Alternative modeling approaches of features, events, and processes are considered and are consistent with available data and current scientific understanding, and the results and limitations are appropriately considered in the abstraction.

Response: Alternative modeling approaches of features, events, and processes are considered in Section 6.4 and are consistent with available data and current scientific understanding, and the results and limitations are considered. This criterion was addressed satisfactorily.

- (2) In considering alternative conceptual models for radionuclide release rates and solubility limits, DOE uses appropriate models, tests, and analyses that are sensitive to the processes modeled for both natural and engineering systems. Conceptual model uncertainties are adequately defined and documented, and effects on conclusions regarding performance are properly assessed. For example, in modeling flow and radionuclide release from the drifts, DOE represents significant discrete features, such as fault zones, separately, or demonstrates that their inclusion in the equivalent continuum model produces a conservative effect on calculated performance.

Response: In considering alternative conceptual models for radionuclide release rates and solubility limits (Sections 6.4. and 6.6), the EBS radionuclide transport abstraction uses models and analyses that are sensitive to the processes modeled for both natural and engineering systems. Conceptual model uncertainties are defined and documented, and effects on conclusions regarding performance are assessed. The fundamental relationships (e.g., mass balance and flow equations, upon which the EBS radionuclide transport abstraction is based), are well-established with a long history of use in the scientific community and as such are not subject to significant uncertainty. In addition, the alternative conceptual models have been screened out (Section 6.4), thereby increasing confidence in the selected conceptual model. Other sources of uncertainty involve modeling choices (e.g., assumptions, geometry) that, because of their conservative nature, effectively bound uncertainty. This criterion was addressed satisfactorily.

- (3) Consideration of conceptual model uncertainty is consistent with available site characterization data, laboratory experiments, field measurements, natural analog information and process-level modeling studies; and the treatment of conceptual model uncertainty does not result in an under-representation of the risk estimate.

Response: Consideration of conceptual model uncertainty is consistent with available site characterization data, laboratory experiments, field measurements, natural analog information, and process-level modeling studies. The treatment of conceptual model uncertainty does not result in an under-representation of the risk estimate, as discussed throughout Section 6. Parameter uncertainty is discussed throughout Section 6. This criterion was addressed satisfactorily.

- (4) The effects of thermal-hydrologic-chemical coupled processes that may occur in the natural setting, or from interactions with engineered materials, or their alteration products, on radionuclide release, are appropriately considered.

Response: The effects of thermal-hydrologic-chemical coupled processes that may occur in the natural setting or from interactions with engineered materials or their alteration products, on radionuclide release, are considered in Section 6. For example, the effect of corrosion products on the transport of radionuclides is provided in Sections 6.3.4, 6.5.1, and 6.5.2. This criterion was addressed satisfactorily.

Acceptance Criterion 5—Model Abstraction Output Is Supported by Objective Comparisons.

- (1) The models implemented in this total system performance assessment abstraction provide results consistent with output from detailed process-level models and/or empirical observations (laboratory and field testings and/or natural analogs).

Response: The models implemented in this TSPA abstraction provide results consistent with output from detailed process-level models and/or empirical observations (laboratory testings), as described in Sections 6.3, 6.5, and 7. Section 7 provides comparisons of models developed in this model report with other models and experimental results. This criterion was addressed satisfactorily.

- (3) DOE adopts well-documented procedures that have been accepted by the scientific community to construct and test the numerical models, used to simulate coupled thermal-hydrologic-chemical effects on radionuclide release. For example, DOE demonstrates that the numerical models used for high-level radioactive waste degradation and dissolution, and radionuclide release from the engineered barrier system, are adequate representations; include consideration of uncertainties; and are not likely to underestimate radiological exposures to the reasonably maximally exposed individual and releases of radionuclides into the accessible environment.

Response: The EBS radionuclide transport abstraction uses well-documented procedures in Section 6.5 that have been accepted by the scientific community to construct and test the numerical models used to simulate radionuclide release. The abstraction demonstrates that the numerical models used for radionuclide release from the EBS include consideration of uncertainties and are not likely to underestimate radiological exposures to the reasonably maximally exposed individual and releases of radionuclides into the accessible environment. This criterion was addressed satisfactorily.

8.4 RESTRICTIONS FOR SUBSEQUENT USE

This abstraction was developed specifically for application in the TSPA. Assumptions and approximations are made in order to integrate with and be consistent with other models and abstractions incorporated in the TSPA. Therefore, individual submodels should not be used independently outside of the TSPA framework. This abstraction must be reevaluated if any models that feed into it are modified.

9. INPUTS AND REFERENCES

The following is a list of references cited in this document. Column 1 represents the unique six-digit identifier numerical identifier (the Document Input Reference System number), which is placed in the text following the reference callout (e.g., BSC 2006 [DIRS 177739]). The purpose of these numbers is to assist in locating a specific reference. Within the reference list, multiple sources by the same author (e.g., SNL 2007) are sorted alphabetically by title.

9.1 DOCUMENTS CITED

- 173033 Ainsworth, C.C.; Pilon, J.L.; Gassman, P.L.; and Van Der Sluys, W.G. 1994. "Cobalt, Cadmium, and Lead Sorption to Hydrous Iron Oxide: Residence Time Effect." *Soil Science Society America Journal*, 58, 1615-1623. [Madison, Wisconsin]: Soil Science Society of America. TIC: 257037.
- 179663 Alonso, U. and Degueldre, C. 2003. "Modelling Americium Sorption onto Colloids: Effect of Redox Potential." *Colloids and Surfaces A: Physicochemical and Engineering Aspects*, 217, 55-62. [New York, New York]: Elsevier. TIC: 258859.
- 123665 Anderson, M.P. and Woessner, W.W. 1992. *Applied Groundwater Modeling, Simulation of Flow and Advective Transport*. San Diego, California: Academic Press. TIC: 103227.
- 168168 Appelo, C.A.J.; Van der Weiden, M.J.J.; Tournassat, C.; and Charlet, L. 2002. "Surface Complexation of Ferrous Iron and Carbonate on Ferrihydrite and the Mobilization of Arsenic." *Environmental Science & Technology*, 36, (14), 3096-3103. Washington, D.C.: American Chemical Society. TIC: 255581.
- 154430 Archie, G.E. 1942. "The Electrical Resistivity Log as an Aid in Determining Some Reservoir Characteristics." *Petroleum Development and Technology, Transactions of American Institute of Mining and Metallurgical Engineers*, 146, 54-62. New York, New York: American Institute of Mining and Metallurgical Engineers. TIC: 249687.
- 111464 Atkins, P.W. 1990. *Physical Chemistry*. 4th Edition. New York, New York: W.H. Freeman and Company. TIC: 245483.
- 178654 Axe, L. and Anderson, P.R. 1995. "Sr Diffusion and Reaction Within Fe Oxides: Evaluation of the Rate-Limiting Mechanism for Sorption." *Journal of Colloid and Interface Science*, 175, 157-165. [New York, New York]: Academic Press. TIC: 259021.
- 174739 Bachmann, J. and van der Ploeg, R.R. 2002. "A Review on Recent Developments in Soil Water Retention Theory: Interfacial Tension and Temperature Effects." *Journal of Plant Nutrition and Soil Science*, 165, 468-478. Weinheim, Germany: Wiley-VCH Verlag. TIC: 257579.

- 173887 Bachmann, J.; Horton, R.; Grant, S.A.; and van der Ploeg, R.R. 2002. "Temperature Dependence of Water Retention Curves for Wettable and Water-Repellent Soils." *Soil Science Society America Journal*, 66, 44-52. [Madison, Wisconsin]: Soil Science Society of America. TIC: 257501.
- 157860 Baes, C.F., Jr. and Mesmer, R.E. 1976. *The Hydrolysis of Cations*. Pages 1, 6, 7, 176, 177, 180, 181, 184-191. New York, New York: John Wiley & Sons. TIC: 217440.
- 170953 Baker, N.A. and Grisak, G.E. 2004. "Independent Model Validation Technical Review of the EBS-UZ Interface Sub-Model of the Radionuclide Transport Abstraction Model for the Yucca Mountain Project." Memo from N.A. Baker (INTERA) and G.E. Grisak (INTERA) to J. Schreiber and C. Howard, July 27, 2004. ACC: MOL.20040730.0182.
- 181308 Balistrieri, L.S. and Murray, J.W. 1981. "The Surface Chemistry of Goethite (α -FeOOH) in Major Ion Seawater." *American Journal of Science*, 281, (6), 788-806. New Haven, Connecticut: Yale University, Kline Geology Laboratory. TIC: [223995](#).
- 163015 Ball, J.W. and Nordstrom, D.K. 1998. "Critical Evaluation and Selection of Standard State Thermodynamic Properties for Chromium Metal and its Aqueous Ions, Hydrolysis Species, Oxides, and Hydroxides." *Journal of Chemical & Engineering Data*, 43, (6), 895-918. [Washington, D.C.]: American Chemical Society. TIC: 254015.
- 174702 Barney, G.S. 1984. "Radionuclide Sorption and Desorption Reactions with Interbed Materials from the Columbia River Basalt Formation." In *ACS Symposium Series 246*, Chapter 1 of *Geochemical Behavior of Disposed Radioactive Waste*. Barney, G.S.; Navartil, J.D.; and Schulz, W.W., eds. Washington, D.C.: American Chemical Society. TIC: 206845.
- 101379 Bear, J. 1988. *Dynamics of Fluids in Porous Media*. New York, New York: Dover Publications. TIC: 217568.
- 181190 Berry, J.A.; Brownsword, J.A.; Ilett, D.J.; Linklater, C.M.; Mason, C.; Tweed, C.J.; and Yui, M. 2002. "Effect of Redox Conditions on the Sorption of Plutonium onto Geological Materials." *Scientific Basis for Nuclear Waste Management XXV, Symposium Held November 26-29, 2001, Boston, Massachusetts*. McGrail, B.P. and Cragolino, G.A., eds. 713, 791-798. Warrendale, Pennsylvania: Materials Research Society. TIC: 248663.
- 154437 Bethke, C.M. and Brady, P.V. 2000. "How the Kd Approach Undermines Ground Water Cleanup." *Ground Water*, 38, (3), 435-443. Westerville, Ohio: National Ground Water Association. TIC: 249781.
- 103524 Bird, R.B.; Stewart, W.E.; and Lightfoot, E.N. 1960. *Transport Phenomena*. New York, New York: John Wiley & Sons. TIC: 208957.

- 173707 Boily, J.F.; Lützenkirchen, J.; Balmès, O.; Beattie, J.; and Sjöberg, S. 2001. "Modeling Proton Binding at the Goethite (α -FeOOH)-Water Interface." *Colloids and Surfaces A: Physicochemical and Engineering Aspects*, 179, 11-27. [New York, New York]: Elsevier. TIC: 257303.
- 154421 Brady, P.V.; Spalding, B.P.; Krupka, K.M.; Waters, R.D.; Zhang, P.; Borns, D.J.; and Brady, W.D. 1999. *Site Screening and Technical Guidance for Monitored Natural Attenuation at DOE Sites*. SAND99-0464. Albuquerque, New Mexico: Sandia National Laboratories. TIC: 249720.
- 161617 Briand, L.E.; Hirt, A.M.; and Wachs, I.E. 2001. "Quantitative Determination of the Number of Surface Active Sites and the Turnover Frequencies for Methanol Oxidation over Metal Oxide Catalysts: Application to Bulk Metal Molybdates and Pure Metal Oxide Catalysts." *Journal of Catalysis*, 202, ([2]), 268-278. [New York, New York]: Academic Press. TIC: 253845.
- 131479 Brown, R.L. and Richards, J.C. 1970. *Principles of Powder Mechanics, Essays on the Packing and Flow of Powders and Bulk Solids*. Pages 17-20. New York, New York: Pergamon Press. TIC: 245119.
- 154877 BSC (Bechtel SAIC Company) 2001. *User Manual (UM) for PHREEQC Version 2.3*. SDN: 10068-UM-2.3-00. Las Vegas, Nevada: Bechtel SAIC Company. ACC: MOL.20010525.0172.
- 158193 BSC 2002. *Test Plan for: Atlas Breached Waste Package Test and Drip Shield Experiments*. SITP-02-EBS-005 REV 00. Las Vegas, Nevada: Bechtel SAIC Company. ACC: MOL.20020314.0181.
- 163406 BSC 2003. *Atlas Breached Waste Package and Drip Shield Experiments: Breached Drip Shield Tests*. TDR-EBS-MD-000025 REV 00. Las Vegas, Nevada: Bechtel SAIC Company. ACC: DOC.20030619.0001.
- 168796 BSC 2003. *Risk Information to Support Prioritization of Performance Assessment Models*. TDR-WIS-PA-000009 REV 01 ICN 01 [Errata 001]. Las Vegas, Nevada: Bechtel SAIC Company. ACC: MOL.20021017.0045; DOC.20031014.0003.
- 170038 BSC 2004. *Analysis of Hydrologic Properties Data*. ANL-NBS-HS-000042 REV 00. Las Vegas, Nevada: Bechtel SAIC Company. ACC: DOC.20041005.0004; DOC.20050815.0003.
- 168030 BSC 2004. *Characterize Framework for Seismicity and Structural Deformation at Yucca Mountain, Nevada*. ANL-CRW-GS-000003 REV 00 [Errata 001]. Las Vegas, Nevada: Bechtel SAIC Company. ACC: MOL.20000510.0175; DOC.20040223.0007.

- 169987 BSC 2004. *CSNF Waste Form Degradation: Summary Abstraction*. ANL-EBS-MD-000015 REV 02. Las Vegas, Nevada: Bechtel SAIC Company. ACC: DOC.20040908.0001; DOC.20050620.0004.
- 169988 BSC 2004. *Defense HLW Glass Degradation Model*. ANL-EBS-MD-000016 REV 02. Las Vegas, Nevada: Bechtel SAIC Company. ACC: DOC.20041020.0015; DOC.20050922.0002.
- 168326 BSC 2004. *Design and Engineering, Drip Shield Connector Guide*. 000-M00-SSE0-02001-000-00A. Las Vegas, Nevada: Bechtel SAIC Company. ACC: ENG.20040309.0011.
- 172453 BSC 2004. *DSNF and Other Waste Form Degradation Abstraction*. ANL-WIS-MD-000004 REV 04. Las Vegas, Nevada: Bechtel SAIC Company. ACC: DOC.20041201.0007.
- 168138 BSC 2004. *Estimation of Mechanical Properties of Crushed Tuff for Use as Ballast Material in Emplacement Drifts*. 800-CYC-SSE0-00100-000-00A. Las Vegas, Nevada: Bechtel SAIC Company. ACC: ENG.20040309.0023; ENG.20050817.0009; ENG.20050829.0017.
- 166369 BSC 2004. *Repository Subsurface Emplacement Drifts Steel Invert Structure Plan & Elevation*. 800-SS0-SSE0-00101-000-00A. Las Vegas, Nevada: Bechtel SAIC Company. ACC: ENG.20040121.0004.
- 167652 BSC 2004. *Seepage Model for PA Including Drift Collapse*. MDL-NBS-HS-000002 REV 03. Las Vegas, Nevada: Bechtel SAIC Company. ACC: DOC.20040922.0008; DOC.20051205.0001.
- 169854 BSC 2004. *Thermal Conductivity of the Potential Repository Horizon*. MDL-NBS-GS-000005 REV 01. Las Vegas, Nevada: Bechtel SAIC Company. ACC: DOC.20040928.0006.
- 174152 BSC 2005. *21-PWR Site-Specific Canister/Basket Fuel Tube Assembly Detail Drawing [Sheet 7]*. 000-M00-HA00-00107-000-00B. Las Vegas, Nevada: Bechtel SAIC Company. ACC: ENG.20050613.0024.
- 173303 BSC 2005. *IED Interlocking Drip Shield and Emplacement Pallet [Sheet 1 of 1]*. 800-IED-WIS0-00401-000-00E. Las Vegas, Nevada: Bechtel SAIC Company. ACC: ENG.20050301.0007.
- 174695 BSC 2005. *Technical Management Review Board (TMRB) Decision Proposal*. TMRB-2005-028. Las Vegas, Nevada: Bechtel SAIC Company. ACC: MOL.20050330.0218.

- 177739 BSC 2006. *Technical Work Plan for: Near-Field Environment: Engineered Barrier System: Radionuclide Transport Abstraction Model Report*. TWP-MGR-PA-000020 REV 03. Las Vegas, Nevada: Bechtel SAIC Company. ACC: DOC.20060915.0005.
- 182365 BSC 2007. *5-DHLW/DOE SNF - Long Co-Disposal Waste Package Configuration*. 000-MW0-DS00-00202-000 REV 00C. Las Vegas, Nevada: Bechtel SAIC Company. ACC: ENG.20070719.0006.
- 180938 BSC 2007. *IED Subsurface Facilities Geographical Data*. 800-IED-WIS0-01801-000 REV 00B. Las Vegas, Nevada: Bechtel SAIC Company. ACC: ENG.20070716.0007.
- 179843 BSC 2007. *Interlocking Drip Shield Configuration*. 000-M00-SSE0-00101-000 REV 00C. Las Vegas, Nevada: Bechtel SAIC Company. ACC: ENG.20070409.0001.
- 179838 BSC 2007. *Interlocking Drip Shield Configuration*. 000-M00-SSE0-00102-000 REV 00C. Las Vegas, Nevada: Bechtel SAIC Company. ACC: ENG.20070409.0002.
- 180109 BSC 2007. *Q-List*. 000-30R-MGR0-00500-000-004. Las Vegas, Nevada: Bechtel SAIC Company.
- 180181 BSC 2007. *Repository Subsurface Emplacement Drifts Steel Invert Structure Plan & Elevation*. 800-SS0-SSE0-00201-000 REV 00B. Las Vegas, Nevada: Bechtel SAIC Company. ACC: ENG.20070327.0001.
- 180030 BSC 2007. *Repository Subsurface Emplacement Drifts Steel Invert Structure Section & Materials*. 800-SS0-SSE0-00202-000 REV 00B. Las Vegas, Nevada: Bechtel SAIC Company. ACC: ENG.20070327.0005.
- 173752 Buerge-Weirich, D.; Hari, R.; Xue, H.; Behra, P.; and Sigg, L. 2002. "Adsorption of Cu, Cd, and Ni on Goethite in the Presence of Natural Groundwater Ligands." *Environmental Science & Technology*, 36, (3), 328-336. [New York, New York]: American Chemical Society. TIC: 257348.
- 163817 Campbell, A.N. and Smith, N.O. 1951. *The Phase Rule and its Applications*. 9th Edition. New York, New York: Dover Publications. TIC: 254360.
- 100565 Campbell, G.S. 1985. *Soil Physics with BASIC Transport Models for Soil-Plant Systems*. Developments in Soil Science 14. Amsterdam, The Netherlands: Elsevier. TIC: 214477.
- 142788 Carlson, L. and Schwertmann, U. 1981. "Natural Ferrihydrites in Surface Deposits from Finland and Their Association with Silica." *Geochimica et Cosmochimica Acta*, 45, (3), 421-429. [New York, New York]: Pergamon Press. TIC: 247999.

- 179642 Carpenter Technology 2003. "Micro-Melt NeutroSorb PLUS Alloys" *Alloy Data*. Wyomissing, Pennsylvania: Carpenter Technology. Accessed August 16, 2006. TIC: 259154.
URL: <http://cartech.ides.com/datasheet.aspx?&E=232&CK289296&FMT=PRINT>
- 178656 Carruthers, J.D.; Payne, D.A.; Sing, K.S.W.; and Stryker, L.J. 1971. "Specific and Nonspecific Interactions in the Adsorption of Argon, Nitrogen, and Water Vapor on Oxides." *Journal of Colloid and Interface Science*, 36, (2), 205-216. [New York, New York]: Academic Press. TIC: 259022.
- 100968 Carslaw, H.S. and Jaeger, J.C. 1959. *Conduction of Heat in Solids*. 2nd Edition. Oxford, Great Britain: Oxford University Press. TIC: 206085.
- 174705 Chien, S.H. and Clayton, W.R. 1980. "Application of Elovich Equation to the Kinetics of Phosphate Release and Sorption in Soils." *Soil Science Society of America Journal*, 44, 265-268. [Madison, Wisconsin]: Soil Science Society of America. TIC: 257577.
- 161621 Choi, H. and Corapcioglu, M.Y. 1997. "Transport of a Non-volatile Contaminant in Unsaturated Porous Media in the Presence of Colloids." *Journal of Contaminant Hydrology*, 25, ([3-4]), 299-324. [New York, New York]: Elsevier. TIC: 253843.
- 173811 Christl, I. and Kretzschmar R. 1999. "Competitive Sorption of Copper and Lead at the Oxide-Water Interface: Implications for Surface Site Density." *Geochimica et Cosmochimica Acta*, 63, (19/20), 2929-2938. [New York, New York]: Pergamon. TIC: 257338.
- 173020 Christophi, C. and Axe, L. 2000. "Competition of Cd, Cu, and Pb Adsorption on Goethite." *Journal of Environmental Engineering*, 126, (1), 66-74. [Reston, Virginia]: American Society of Civil Engineers. TIC: 257038.
- 178655 Clausen, L. and Fabricius, I. 2000. "BET Measurements: Outgassing of Minerals." *Journal of Colloid and Interface Science*, 227, 7-15. [New York, New York]: Academic Press. TIC: 259023.
- 101582 Conca, J.L. and Wright, J. 1990. "Diffusion Coefficients in Gravel Under Unsaturated Conditions." *Water Resources Research*, 26, (5), 1055-1066. Washington, D.C.: American Geophysical Union. TIC: 237421.
- 100436 Conca, J.L. and Wright, J. 1992. "Diffusion and Flow in Gravel, Soil, and Whole Rock." *Applied Hydrogeology*, 1, 5-24. Hanover, Germany: Verlag Heinz Heise GmbH. TIC: 224081.

- 170709 Conca, J.L.; Apted, M.; and Arthur, R. 1993. "Aqueous Diffusion in Repository and Backfill Environments." *Scientific Basis for Nuclear Waste Management XVI, Symposium held November 30-December 4, 1992, Boston, Massachusetts*. Interrante, C.G. and Pabalan, R.T., eds. 294, 395-402. Pittsburgh, Pennsylvania: Materials Research Society. TIC: 208880.
- 174120 Constantz, J. 1991. "Comparison of Isothermal and Isobaric Water Retention Paths in Nonswelling Porous Materials." *Water Resources Research*, 27, (12), 3165-3170. [Washington, D.C.]: American Geophysical Union. TIC: 257437.
- 105761 Corapcioglu, M.Y. and Jiang, S. 1993. "Colloid-Facilitated Groundwater Contaminant Transport." *Water Resources Research*, 29, (7), 2215-2226. Washington, D.C.: American Geophysical Union. TIC: 222362.
- 167464 Corapcioglu, M.Y. and Wang, S. 1999. "Dual-Porosity Groundwater Contaminant Transport in the Presence of Colloids." *Water Resources Research*, 35, (11), 3261-3273. Washington, D.C.: American Geophysical Union. TIC: 255571.
- 178659 Cornejo, J. 1987. "Porosity Evolution of Thermally Treated Hydrous Ferric Oxide Gel." *Journal of Colloid and Interface Science*, 115, (1), 260-263. [New York, New York]: Academic Press. TIC: 259024.
- 178660 Cornejo, J.; Serna, C.J.; and Hermosín, M.C. 1984. "Nitrogen Adsorption on Synthetic Ferrihydrite." *Journal of Colloid and Interface Science*, 102, (1), 101-106. [New York, New York]: Academic Press. TIC: 259025.
- 173864 Cornell, R.M. and Giovanoli R. 1988. "The Influence of Copper on the Transformation of Ferrihydrite ($5\text{Fe}_2\text{O}_3 \cdot 9\text{H}_2\text{O}$) into Crystalline Products in Alkaline Media." *Polyhedron*, 7, (5), 385-391. [New York, New York]: Pergamon Press. TIC: 257362.
- 173037 Cornell, R.M. and Schwertmann, U. 2003. *The Iron Oxides, Structure, Properties, Reactions, Occurrences and Uses*. 2nd Edition. Weinheim, Germany: Wiley-VCH Verlagsgesellschaft. TIC: 257034.
- 173865 Cornell, R.M.; Schneider, W.; and Giovanoli R. 1989. "Phase Transformations in the Ferrihydrite/Cysteine System." *Polyhedron*, 8, (23), 2829-2836. [New York, New York]: Pergamon Press. TIC: 257364.
- 173030 Coughlin, B.R. and Stone, A.T. 1995. "Nonreversible Adsorption of Divalent Metal Ions (Mn^{II} , Co^{II} , Ni^{II} , Cu^{II} , and Pb^{II}) onto Goethite: Effects of Acidification, Fe^{II} Addition, and Picolinic Acid Addition." *Environmental Science Technology*, 29, (9), 2445-2455. [Washington, D.C.]: American Chemical Society. TIC: 257061.
- 132164 Coughtrey, P.J.; Jackson, D.; and Thorne, M.C. 1983. *Radionuclide Distribution and Transport in Terrestrial and Aquatic Ecosystems, A Critical Review of Data*. Six volumes. Rotterdam, The Netherlands: A.A. Balkema. TIC: 240299.

- 179616 Cromières, L.; Moulin, V.; Fourest, B.; Guillaumont, R.; and Giffaut, E. 1998. "Sorption of Thorium onto Hematite Colloids." *Radiochimica Acta*, 82, 249-255. München, Germany: R. Oldenbourg Verlag. TIC: 258879.
- 178662 Crosby, S.A.; Glasson, D.R.; Cuttler, A.H.; Butler, I.; Turner, D.R.; Whitfield, M.; and Millward, G.E. 1983. "Surface Areas and Porosities of Fe(III)- and Fe(II)-Derived Oxyhydroxides." *Environmental Science & Technology*, 17, (12), 709-713. [Washington, D.C.]: American Chemical Society. TIC: 257716.
- 102824 CRWMS M&O 1997. *Criticality Evaluation of Degraded Internal Configurations for the PWR AUCF WP Designs*. BBA000000-01717-0200-00056 REV 00. Las Vegas, Nevada: CRWMS M&O. ACC: MOL.19971231.0251.
- 151743 CRWMS M&O 2000. *Evaluation of Codisposal Viability for Th/U Oxide (Shippingport LWR) DOE-Owned Fuel*. TDR-EDC-NU-000005 REV 00. Las Vegas, Nevada: CRWMS M&O. ACC: MOL.20001023.0055.
- 156680 CRWMS M&O 2000. *The Determination of Diffusion Coefficient of Invert Materials*. TDR-EBS-MD-000002 REV 00. Las Vegas, Nevada: CRWMS M&O. ACC: MOL.20000124.0320.
- 151566 CRWMS M&O 2000. *WAPDEG Analysis of Waste Package and Drip Shield Degradation*. ANL-EBS-PA-000001 REV 00 ICN 01. Las Vegas, Nevada: CRWMS M&O. ACC: MOL.20001208.0063.
- 154071 CRWMS M&O 2001. *Colloid-Associated Radionuclide Concentration Limits: ANL*. ANL-EBS-MD-000020 REV 00 ICN 01. Las Vegas, Nevada: CRWMS M&O. ACC: MOL.20010216.0003.
- 111468 Cussler, E.L. 1997. *Diffusion: Mass Transfer in Fluid Systems*. 2nd Edition. Cambridge, United Kingdom: Cambridge University Press. TIC: 241150.
- 178666 Davies-Colley, R.J.; Nelson, P.O.; and Williamson, K.J. 1984. "Copper and Cadmium Uptake by Estuarine Sedimentary Phases." *Environmental Science & Technology*, 18, (7), 491-499. [New York, New York]: American Chemical Society. TIC: 259027.
- 182146 Davis III, J.A., 1978. *Adsorption of Trace Metals and Complexing Ligands at the Oxide/Water Interface*. Stanford, California: Stanford University. TIC: xxxxxx.
- 173743 Davis, A.P. and Upadhyaya, M. 1996. "Desorption of Cadmium from Goethite (α -FeOOH)." *Water Research*, 30, (8), 1894-1904. [New York, New York]: Pergamon. TIC: 257327.

- 143280 Davis, J.A. and Kent, D.B. 1990. "Surface Complexation Modeling in Aqueous Geochemistry." *Mineral-Water Interface Geochemistry*. Hochella, M.F., Jr. and White, A.F., eds. Reviews in Mineralogy Volume 23. Pages 177-260. Washington, D.C.: Mineralogical Society of America. TIC: 224085.
- 125591 Davis, J.A. and Leckie, J.O. 1978. "Surface Ionization and Complexation at the Oxide/Water Interface: II. Surface Properties of Amorphous Iron Oxyhydroxide and Adsorption of Metal Ions." *Journal of Colloid and Interface Science*, 67, (1), 90-107. Orlando, Florida: Academic Press. TIC: 223905.
- 154436 Davis, J.A.; Coston, J.A.; Kent, D.B.; and Fuller, C.C. 1998. "Application of the Surface Complexation Concept to Complex Mineral Assemblages." *Environmental Science & Technology*, 32, (19), 2820-2828. Washington, D.C.: American Chemical Society. TIC: 249656.
- 174069 Degueldre, C.; Ulrich, H.J.; and Silby, H. 1994. "Sorption of ²⁴¹Am onto Montmorillonite, Illite and Hematite Colloids." *Radiochimica Acta*, 65, 173-179. München, Germany: R. Oldenbourg Verlag. TIC: 257440.
- 171480 Dillmann, Ph.; Mazaudier, F.; and Hœrlé, S. 2004. "Advances in Understanding Atmospheric Corrosion of Iron. I. Rust Characterisation of Ancient Ferrous Artefacts Exposed to Indoor Atmospheric Corrosion." *Corrosion Science*, 46, 1401 - 1429. [New York, New York]: Elsevier. TIC: 256483.
- 164970 DOE (U.S. Department of Energy) 2003. *TMI Fuel Characteristics for Disposal Criticality Analysis*. DOE/SNF/REP-084, Rev. 0. Idaho Falls, Idaho: U.S. Department of Energy, Idaho Operations Office. ACC: MOL.20031013.0388.
- 181106 DOE 2007. *Requirements Document for: GoldSim v9.60*. Document ID: 10344-RD-9.60-00. Las Vegas, Nevada: U.S. Department of Energy, Office of Repository Development. ACC: MOL.20070416.0330.
- 102588 DOE 1992. *Characteristics of Potential Repository Wastes*. DOE/RW-0184-R1. Four volumes. Washington, D.C.: U.S. Department of Energy, Office of Civilian Radioactive Waste Management. ACC: HQO.19920827.0001; HQO.19920827.0002; HQO.19920827.0003; HQO.19920827.0004.
- 153849 DOE 2001. *Yucca Mountain Science and Engineering Report*. DOE/RW-0539. [Washington, D.C.]: U.S. Department of Energy, Office of Civilian Radioactive Waste Management. ACC: MOL.20010524.0272.
- 169875 DOE 2004. *Requirements Document for: GoldSim V8.02, Rev. No. 00*. Document ID: 10344-RD-8.02-00. Las Vegas, Nevada: U.S. Department of Energy, Office of Repository Development. ACC: MOL.20040623.0257.

- 169354 DOE 2004. *Source Term Estimates for DOE Spent Nuclear Fuels*. DOE/SNF/REP-078, Rev. 1. Three volumes. Idaho Falls, Idaho: U.S. Department of Energy, Idaho Operations Office. ACC: MOL.20040524.0451.
- 173019 Duc, M.; Lefevre, G.; Fedoroff, M.; Jeanjean, J.; Rouchaud, J.C.; Monteil-Rivera, F.; Dumonceau, J.; and Milonjic, S. 2003. "Sorption of Selenium Anionic Species on Apatites and Iron Oxides from Aqueous Solutions." *Journal of Environmental Radioactivity*, 70, 61-72. [New York, New York]: Elsevier. TIC: 257072.
- 105483 Dzombak, D.A. and Morel, F.M.M. 1990. *Surface Complexation Modeling, Hydrous Ferric Oxide*. New York, New York: John Wiley & Sons. TIC: 224089.
- 111028 Ebert, W.L.; Hoburg, R.F.; and Bates, J.K. 1991. "The Sorption of Water on Obsidian and a Nuclear Waste Glass." *Physics and Chemistry of Glasses*, 32, (4), 133-137. Sheffield, England: Society of Glass Technology. TIC: 246078.
- 173878 Eggleton, R.A. and Fitzpatrick, R.W. 1988. "New Data and a Revised Structural Model for Ferrihydrite." *Clays and Clay Minerals*, 36, (2), 111-124. [Aurora, Colorado]: Clay Minerals Society. TIC: 257392.
- 174704 Eick, M.J.; Peak, J.D.; Brady, P.V.; and Pesek, J.D. 1999. "Kinetics of Lead Adsorption/Desorption on Goethite: Residence Time Effect." *Soil Science*, 164, (1), 28-39. [Baltimore, Maryland]: Lippincott Williams & Wilkins. TIC: 257580.
- 170376 EPA (U.S. Environmental Protection Agency) 1999. *Review of Geochemistry and Available K_d Values for Cadmium, Cesium, Chromium, Lead, Plutonium, Radon, Strontium, Thorium, Tritium (3H), and Uranium*. Volume II of *Understanding Variation in Partition Coefficient, K_d Values*. EPA 402-R-99-004B. Washington, D.C.: U.S. Environmental Protection Agency, Office of Radiation and Indoor Air. ACC: MOL.20040628.0034.
- 147475 EPA 1999. *Understanding Variation in Partition Coefficient, K_d Values*. EPA 402-R-99-004A&B Two volumes. Washington, D.C.: U.S. Environmental Protection Agency. TIC: 249201.
- 172215 EPA 2004. "Review of Geochemistry and Available K_d Values for Americium, Arsenic, Curium, Iodine, Neptunium, Radium, and Technetium." Volume III of *Understanding the Variation in Partition Coefficient, K_d Values*. EPA 402-R-04-002C. Washington, D.C.: U.S. Environmental Protection Agency. ACC: MOL.20041102.0060.
- 154149 EPRI (Electric Power Research Institute) 2000. *Evaluation of the Candidate High-Level Radioactive Waste Repository at Yucca Mountain Using Total System Performance Assessment, Phase 5*. 1000802. Palo Alto, California: Electric Power Research Institute. TIC: 249555.

- 173708 Felmy, A.R. and Rustad J.R. 1998. "Molecular Statics Calculations of Proton Binding to Goethite Surfaces: Thermodynamic Modeling of the Surface Charging and Protonation of Goethite in Aqueous Solution." *Geochimica et Cosmochimica Acta*, 62, (1), 25-31. New York, New York: Pergamon. TIC: 257304.
- 173031 Fendorf, S.; Eick, M.J.; Grossl, P.; and Sparks, D.L. 1997. "Arsenate and Chromate Retention Mechanisms on Goethite. 1. Surface Structure." *Environmental Science & Technology*, 31, (2), 315-320. [Washington, D.C.]: American Chemical Society. TIC: 257062.
- 173034 Fendorf, S.E.; Li, G.; and Gunter, M.E. 1996. "Micromorphologies and Stabilities of Chromium (III) Surface Precipitates Elucidated by Scanning Force Microscopy." *Soil Science Society America Journal*, 60, 99-106. [Madison, Wisconsin]: Soil Science Society America. TIC: 257036.
- 174727 Ford, R.G.; Bertsch, P.M.; and Farley, K.J. 1997. "Changes in Transition and Heavy Metal Partitioning during Hydrous Iron Oxide Aging." *Environmental Science & Technology*, 31, (7), 2028-2033. [Washington, D.C.]: American Chemical Society. TIC: 257574.
- 101173 Freeze, R.A. and Cherry, J.A. 1979. *Groundwater*. Englewood Cliffs, New Jersey: Prentice-Hall. TIC: 217571.
- 108201 Fuger, J. 1992. "Thermodynamic Properties of Actinide Aqueous Species Relevant to Geochemical Problems." *Radiochimica Acta*, 58/59, (I), 81-91. München, Germany: R. Oldenbourg Verlag. TIC: 245944.
- 178306 Fuller, E.L., Jr. and Agron, P.A. 1976. "Sorption of Water, Carbon Dioxide and Nitrogen by Sol-Gel Thorium Oxide." *Journal of Colloid and Interface Science*, 57, (2), 193-200. [New York, New York]: Academic Press. TIC: 258818.
- 130407 Gabriel, U.; Gaudet, J.-P.; Spadini, L.; and Charlet, L. 1998. "Reactive Transport of Uranyl in a Goethite Column: An Experimental and Modelling Study." *Chemical Geology*, 151, p. 107-128. New York, New York: Elsevier. TIC: 246884.
- 178304 Gammage, R.B.; Fuller, E.L., Jr.; and Holmes, H.F. 1970. "Gravimetric Adsorption Studies of Thorium Oxide. V. Water Adsorption between 25 and 500°." *Journal of Physical Chemistry*, 74, (24), 4276-4280. [Easton, Pennsylvania]: American Chemical Society. TIC: 258816.
- 173750 Gao, Y. and Mucci, A. 2001. "Acid Base Reactions, Phosphate and Arsenate Complexation, and Their Competitive Adsorption at the Surface of Goethite in 0.7 M NaCl Solution." *Geochimica et Cosmochimica Acta*, 65, (14), 2361-2378. [New York, New York]: Pergamon. TIC: 257331.

- 167466 Gerke, H.H. and van Genuchten, M.Th. 1996. "Macroscopic Representation of Structural Geometry for Simulating Water and Solute Movement in Dual-Porosity Media." *Advances in Water Resources*, 19, (6), 343-357. [New York, New York]: Elsevier. TIC: 255572.
- 107880 Gertsch, R.E.; Fjeld, A.; Asbury, B.; and Ozdemir, L. 1993. *Construction Applications for TSw2 TBM Cuttings at Yucca Mountain*. Golden, Colorado: Colorado School of Mines. ACC: NNA.19940317.0013.
- 180108 Girvin, D.C.; Ames, L.L.; Schwab, A.P.; and McGarrah, J.E. 1991. "Neptunium Adsorption on Synthetic Amorphous Iron Oxyhydroxide." *Journal of Colloid and Interface Science*, 141, (1), 67-78. San Diego, California: Academic Press. TIC: 224097.
- 181727 GoldSim Technology Group 2007. *User's Guide, GoldSim Probabilistic Simulation Environment*. Version 9.60. Two volumes. Issaquah, Washington: GoldSim Technology Group. TIC: 259221.
- 166226 GoldSim Technology Group. 2003. *User's Guide, GoldSim Probabilistic Simulation Environment*. Version 8.01. Redmond, Washington: Golder Associates. TIC: 255170.
- 173751 Gräfe, M.; Nachttegaal, M.; and Sparks, D.L. 2004. "Formation of Metal-Arsenate Precipitates at the Goethite-Water Interface." *Environmental Science & Technology*, 38, (24), 6561-6570. [Washington, D.C.]: American Chemical Society. TIC: 257349.
- 174738 Grant, S.A. and Salehzadeh, A. 1996. "Calculation of Temperature Effects on Wetting Coefficients of Porous Solids and Their Capillary Pressure Functions." *Water Resources Research*, 32, (2), 261-270. Washington, D.C.: American Geophysical Union. TIC: 252291.
- 138541 Gray, D.E., ed. 1972. *American Institute of Physics Handbook*. 3rd Edition. New York, New York: McGraw-Hill Book Company. TIC: 247425.
- 153010 Gregg, S.J. and Sing, K.S.W. 1982. *Adsorption, Surface Area and Porosity*. 2nd Edition. 4th Printing 1997. San Diego, California: Academic Press. TIC: 249076.
- 101671 Grenthe, I.; Fuger, J.; Konings, R.J.M.; Lemire, R.J.; Muller, A.B.; Nguyen-Trung, C.; and Wanner, H. 1992. *Chemical Thermodynamics of Uranium*. Volume 1 of *Chemical Thermodynamics*. Wanner, H. and Forest, I., eds. Amsterdam, The Netherlands: North-Holland Publishing Company. TIC: 224074.
- 173032 Grossl, P.R.; Eick, M.; Sparks, D.L.; Goldberg, S.; and Ainsworth, C.C. 1997. "Arsenate and Chromate Retention Mechanisms on Goethite. 2. Kinetic Evaluation Using a Pressure-Jump Relaxation Technique." *Environmental Science & Technology*, 31, (2), 321-326. [Washington, D.C.]: American Chemical Society. TIC: 257083.

- 168382 Guillaumont, R.; Fanghänel, T.; Fuger, J.; Grenthe, I.; Neck, V.; Palmer, D.A.; and Rand, M.H. 2003. *Update on the Chemical Thermodynamics of Uranium, Neptunium, Plutonium, Americium and Technetium*. Mompean, F.J.; Illemassene, M.; Domenech-Orti, C.; and Ben Said, K., eds. *Chemical Thermodynamics 5*. Amsterdam, The Netherlands: Elsevier. TIC: 255230.
- 178669 Guzman, G.; Alcantara, E.; Barron, V.; and Torrent, J. 1994. "Phytoavailability of Phosphate Adsorbed on Ferrihydrite, Hematite, and Goethite." *Plant and Soil*, 159, 219-225. [Boston, Massachusetts]: Kluwer Academic Publishers. TIC: 259029.
- 179671 Haas, J.R.; Shock, E.L.; and Sassani, D.C. 1995. "Rare Earth Elements in Hydrothermal Systems: Estimates of Standard Partial Molal Thermodynamic Properties of Aqueous Complexes of the Rare Earth Elements at High Pressures and Temperatures." *Geochimica et Cosmochimica Acta*, 59, (21), 4329-4350. [New York, New York]: Pergamon. TIC: 232498.
- 173866 Hamzaoui, A.; Mgaidi, A.; Megriche, A.; and El Maaoui, M. 2002. "Kinetic Study of Goethite Formation from Ferrihydrite in Alkaline Medium." *Industrial & Engineering Chemistry Research*, 41, (21), 5226-5231. [Washington, D.C.]: American Chemical Society. TIC: 257379.
- 173742 Hansmann, D.D. and Anderson M.A. 1985. "Using Electrophoresis in Modeling Sulfate, Selenite, and Phosphate Absorption onto Goethite." *Environmental Science & Technology*, 19, (6), 544-551. [Washington, D.C.]: American Chemical Society. TIC: 257350.
- 174125 Haridasan, M. and Jensen, R.D. 1972. "Effect of Temperature on Pressure Head-Water Content Relationship and Conductivity of Two Soils." *Soil Science Society of America Proceedings*, 36, 703-708. Madison, Wisconsin: Soil Science Society of America. TIC: 257435.
- 178670 Harju, M.; Mäntylä, T.; Vähä-Heikkilä, K.; and Lehto, V-P. 2005. "Water Adsorption on Plasma Sprayed Transition Metal Oxides." *Applied Surface Science*, 249, 115-126. [New York, New York]: Elsevier. TIC: 259030.
- 177361 Harris, K.R. and Woolf, L.A. 1980. "Pressure and Temperature Dependence of the Self Diffusion Coefficient of Water and Oxygen-18 Water." *Journal of the Chemical Society, Faraday Transactions 1*, 76, 377-385. [London, England: Royal Society of Chemistry]. TIC: 258526.
- 174706 Havlin, J.L.; Westfall, D.G.; and Olsen, S.R. 1985. "Mathematical Models for Potassium Release Kinetics in Calcareous Soils." *Soil Science Society of America Journal*, 49, 371-376. [Madison, Wisconsin]: Soil Science Society of America. TIC: 257578.

- 179121 Hayes, K.F. and Katz, L.E. 1996. "Application of X-Ray Absorption Spectroscopy for Surface Complexation Modeling of Metal Ion Sorption." *Chapter 3 of Physics and Chemistry of Mineral Surfaces*. Brady, P.V., ed. CRC Series in Chemistry and Physics of Surfaces and Interfaces. Boca Raton, Florida: CRC Press. TIC: 259104.
- 173817 Hayes, K.F. and Leckie, J.O. 1987. "Modeling Ionic Strength Effects on Cation Adsorption at Hydrous Oxide/Solution Interfaces." *Journal of Colloid and Interface Science*, 115, (2), 564-572. [New York, New York]: Academic Press. TIC: 226460.
- 137246 Helgeson, H.C. 1969. "Thermodynamics of Hydrothermal Systems at Elevated Temperatures and Pressures." *American Journal of Science*, 267, (6), 729-804. New Haven, Connecticut: Scholarly Publications. TIC: 241817.
- 173023 Hiemstra, T. and Van Riemsdijk, W.H. 1996. "A Surface Structural Approach to Ion Adsorption: The Charge Distribution (CD) Model." *Journal of Colloid and Interface Science*, 179, 488-508. [New York, New York]: Academic Press. TIC: 257052.
- 173783 Hofmann, A.; Pelletier, M.; Michot, L.; Stradner, A.; Schurtenberger, P.; and Kretzschmar, R. 2004. "Characterization of the Pores in Hydrous Ferric Oxide Aggregates Formed by Freezing and Thawing." *Journal of Colloid and Interface Science*, 271, 163-173. [New York, New York]: Elsevier. TIC: 257504.
- 173711 Hofmann, A.; van Beinum, W.; Meeussen, J.C.L.; and Kretzschmar, R. 2005. "Sorption Kinetics of Strontium in Porous Hydrous Ferric Oxide Aggregates II. Comparison of Experimental Results and Model Predictions." *Journal of Colloid and Interface Science*, 283, 29-40. [New York, New York]: Elsevier. TIC: 257308.
- 154379 Holmes, H.F.; Fuller, E.L., Jr.; and Beh, R.A. 1974. "Adsorption of Argon, Nitrogen, and Water Vapor on Zirconium Oxide." *Journal of Colloid and Interface Science*, 47, (2), 365-371. [New York, New York]: Academic Press. TIC: 249666.
- 173754 Hongshao, Z. and Stanforth, R. 2001. "Competitive Adsorption of Phosphate and Arsenate on Goethite." *Environmental Science & Technology*, 35, (24), 4753-4757. [Washington, D.C.]: American Chemical Society. TIC: 257347.
- 174122 Hopmans, J.W. and Dane, J.H. 1986. "Temperature Dependence of Soil Hydraulic Properties." *Soil Science Society of America Journal*, 50, 4-9. Madison, Wisconsin: Soil Science Society of America. TIC: 257434.
- 161516 Howard, C.L. 2002. Breached Waste Package Test and Drip Shield Experiments. Scientific Notebook SN-M&O-SCI-043-V1. ACC: MOL.20021219.0022.
- 161522 Howard, C.L. 2002. Breached Waste Package Test and Drip Shield Experiments. Scientific Notebook SN-M&O-SCI-043-V2. ACC: MOL.20021219.0023.

- 106131 Hsi, C-K.D. and Langmuir, D. 1985. "Adsorption of Uranyl onto Ferric Oxyhydroxides: Application of the Surface Complexation Site-Binding Model." *Geochimica et Cosmochimica Acta*, 49, 1931-1941. New York, New York: Pergamon Press. TIC: 224090.
- 161623 Hu, Q.; Kneafsey, T.; Wang, J.S.Y.; Roberts, J.; and Carlson, S. 2001. *Summary Report on Phase I Feasibility Study of In-Drift Diffusion*. [LBNL-49063]. [Berkeley, California: Lawrence Berkeley National Laboratory]. ACC: MOL.20030225.0125.
- 147464 Hunter, K.A.; Hawke, D.J.; and Choo, L.K. 1988. "Equilibrium Adsorption of Thorium by Metal Oxides in Marine Electrolytes." *Geochimica et Cosmochimica Acta*, (52), 627-636. New York, New York: Pergamon Press. TIC: 237440.
- 170882 Ibrahim, S.A. and Salazar, W.R. 2000. "Physicochemical Speciation of Americium in Soils from Rocky Flats, Colorado, USA." *Journal of Radioanalytical and Nuclear Chemistry*, 243, (2), 347-351. Dordrecht, [The Netherlands]: Kluwer Academic Publishers. TIC: 256466.
- 179309 Icenhour, A.S.; Toth, L.M.; and Luo, H. 2004. "Water Sorption and Gamma Radiolysis Studies for Uranium Oxides." *Nuclear Technology*, 147, 258-268. [La Grange Park, Illinois: American Nuclear Society]. TIC: 259121.
- 146012 Iman, R.L. 1982. "Statistical Methods for Including Uncertainties Associated with the Geologic Isolation of Radioactive Waste Which Allow for a Comparison with Licensing Criteria." *Proceedings of the Symposium on Uncertainties Associated with the Regulation of the Geologic Disposal of High-Level Radioactive Waste, Gatlinburg, Tennessee, March 9-13, 1981*. Kocher, D.C., ed. NUREG/CP-0022. Pages 145-157. Washington, D.C.: U.S. Nuclear Regulatory Commission. TIC: 213069.
- 162328 Jenne, E.A. 1998. "Adsorption of Metals by Geomedia: Data Analysis, Modeling, Controlling Factors, and Related Issues." *Adsorption of Metals by Geomedia*. Jenne, E.A, ed. Pages 1-73. San Diego, California: Academic Press. TIC: 254037.
- 181295 Jerden, J.L.; Kropf, A.J. 2007. "Surface Complexation of Neptunium(V) with Goethite." *Materials Research Society (MRS)*. D.S. Dunn; C. Poinssot, B. Begg. 985, Warrendale, PA: Materials Research Society.
- 154381 Jurinak, J.J. 1964. "Interaction of Water with Iron and Titanium Oxide Surfaces: Goethite, Hematite, and Anatase." *Journal of Colloid Science*, 19, 477-487. [New York, New York: Academic Press]. TIC: 249667.
- 102010 Jury, W.A.; Gardner, W.R.; and Gardner, W.H. 1991. *Soil Physics*. 5th Edition. New York, New York: John Wiley & Sons. TIC: 241000.

- 178680 Kandori, K. and Ishikawa, T. 1991. "Selective Adsorption of Water on Amorphous Ferric Oxide Hydroxide." *Langmuir*, 7, (10), 2213-2218. [Washington, D.C.]: American Chemical Society. TIC: 259031.
- 106313 Keeney-Kennicutt, W.L. and Morse, J.W. 1985. "The Redox Chemistry of Pu(V)O_2^+ Interaction with Common Mineral Surfaces in Dilute Solutions and Seawater." *Geochimica et Cosmochimica Acta*, 49, ([12]), 2577-2588. New York, New York: Pergamon. TIC: 237000.
- 111470 Keller, G.V. and Frischknecht, F.C. 1966. *Electrical Methods in Geophysical Prospecting*. Volume 10 of *International Series in Electromagnetic Waves*. Cullen, A.L.; Fock, V.A.; and Wait, J.R., eds. New York, New York: Pergamon Press. TIC: 230941.
- 103282 Kersting, A.B.; Efurud, D.W.; Finnegan, D.L.; Rokop, D.J.; Smith, D.K.; and Thompson, J.L. 1999. "Migration of Plutonium in Ground Water at the Nevada Test Site." *Nature*, 397, ([6714]), 56-59. [London, England: Macmillan Journals]. TIC: 243597.
- 178830 Kittaka, S.; Fujinaga, R.; Morishige, K.; and Morimoto, T. 1984. "Adsorption of Water on the Surfaces of $\alpha\text{-HCrO}_2$ and Cr_2O_3 ." *Journal of Colloid and Interface Science*, 102, (2), 453-461. [New York, New York: Academic Press]. TIC: 259089.
- 178681 Kittaka, S.; Morishige, K.; Nishiyama, J.; and Morimoto, T. 1983. "The Effect of Surface Hydroxyls of Cr_2O_3 on the Adsorption of N_2 , Ar, Kr, and H_2O in Connection with the Two-Dimensional Condensation." *Journal of Colloid and Interface Science*, 91, (1), 117-124. [New York, New York]: Academic Press. TIC: 259032.
- 173784 Koch, C.J.W. and Møller, P.J. 1987. "Adsorption of Nitrogen and Water Vapour onto Goethite Surfaces." *Thermochimica Acta*, 114, 139-144. Amsterdam, The Netherlands: Elsevier. TIC: 257505.
- 177360 Krynicky, K.; Green, C.D.; and Sawyer, D.W. 1978. "Pressure and Temperature Dependence of Self-Diffusion in Water." *Structure and Motion in Molecular Liquids*. Faraday Discussions of the Chemical Society No. 66. Pages 199-208. London, England: Chemical Society, Faraday Division. TIC: 258527.
- 107760 Kügler, A. 1996. *Böhler Neutronit A976 Sheet and Plate for Nuclear Engineering*. Müzzschlag, Austria: Böhler Bleche GmbH. TIC: 240558.
- 181246 Kuroda, Y; Kittaka, S; Takahara, S; Yamaguchi, T; Bellissent-Funel, M-C 1999. "Characterization of the State of Two-Dimensionally Condensed Water on Hydroxylated Chromium(III) Oxide Surface through FT-IR, Quasielastic Neutron Scattering, and Dielectric Relaxation Measurements." *Journal of Physical Chemistry*, 103, 11064-11073. Washington, DC: American Chemical Society (ACS). TIC: 259462.

- 178682 Kuwabara, R.; Iwaki, T.; and Morimoto, T. 1987. "Dielectric Behavior of Adsorbed Water. 5. Measurement at Room Temperature on α -Fe₂O₃." *Langmuir*, 3, (6), 1059-1062. [Washington, D.C.]: American Chemical Society. TIC: 259033.
- 147523 La Flamme, B.D. and Murray, J.W. 1987. "Solid/Solution Interaction: The Effect of Carbonate Alkalinity on Adsorbed Thorium." *Geochimica et Cosmochimica Acta*, 51, 243-250. New York, New York: Pergamon Press. TIC: 237034.
- 125369 Langmuir, D. 1997. "The Use of Laboratory Adsorption Data and Models to Predict Radionuclide Releases from a Geological Repository: A Brief History." *Scientific Basis for Nuclear Waste Management XX, Symposium held December 2-6, 1996, Boston, Massachusetts*. Gray, W.J. and Triay, I.R., eds. 465, 769-780. Pittsburgh, Pennsylvania: Materials Research Society. TIC: 238884.
- 100051 Langmuir, D. 1997. *Aqueous Environmental Geochemistry*. Upper Saddle River, New Jersey: Prentice Hall. TIC: 237107.
- 178683 Larsen, O. and Postma, D. 2001. "Kinetics of Reductive Bulk Dissolution of Lepidocrocite, Ferrihydrite, and Goethite." *Geochimica et Cosmochimica Acta*, 65, (9), 1367-1379. [New York, New York]: Pergamon. TIC: 259034.
- 178303 LaVerne, J.A. and Tandon, L. 2003. "H₂ Production in the Radiolysis of Water on UO₂ and Other Oxides." *Journal of Physical Chemistry B*, 107, (49), 13623-13628. [Washington, D.C.]: American Chemical Society. TIC: 258815.
- 170765 LBNL (Lawrence Berkeley National Laboratory) 2002. *Users Manual (UM) for TOUGH Version 1.6*. Document Identifier: 10007-UM-1.6-00. Berkeley, [California]: Lawrence Berkeley National Laboratory. ACC: MOL.20020925.0042.
- 100913 Lee, J.H.; Chambré, P.L.; and Andrews, R.W. 1996. "Mathematical Models for Diffusive Mass Transfer from Waste Package Container with Multiple Perforations." *Proceedings of the 1996 International Conference on Deep Geological Disposal of Radioactive Waste, September 16-19, 1996, Winnipeg, Manitoba, Canada*. Pages 5-61-5-72. Toronto, Ontario, Canada: Canadian Nuclear Society. TIC: 233923.
- 154380 Lee, S. and Staehle, R.W. 1994. *Report to TRW on Contract No. DX 1456KP2L, Adsorption Studies of Water on Gold, Copper, Nickel and Iron Using the Quartz-Crystal Microbalance Technique*. [Minneapolis, Minnesota]: University of Minnesota. ACC: NNA.19940428.0129.
- 104943 Lee, S. and Staehle, R.W. 1997. "Adsorption of Water on Copper, Nickel, and Iron." *Corrosion*, 53, (1), 33-42. Houston, Texas: National Association of Corrosion Engineers. TIC: 244501.
- 168991 Leenaers, A.; Sannen, L.; Van den Berghe, S.; and Verwerft, M. 2003. "Oxidation of Spent UO₂ Fuel Stored in Moist Environment." *Journal of Nuclear Materials*, 317, ([2-3]), 226-233. [New York, New York]: Elsevier. TIC: 256014.

- 106580 Lemire, R.J. and Garisto, F. 1989. *The Solubility of U, Np, Pu, Th and Tc in a Geological Disposal Vault for Used Nuclear Fuel*. AECL-10009. Pinawa, Manitoba, Canada: Atomic Energy of Canada Limited. TIC: 213161.
- 179672 Lenhart, J.J. and Honeyman, B.D. 1999. "Uranium(VI) Sorption to Hematite in the Presence of Humic Acid." *Geochimica et Cosmochimica Acta*, 63, (19/20), 2891-2901. [New York, New York]: Pergamon. TIC: 258860.
- 178684 Leone, P.; Gennari, M.; Nègre, M.; and Boero, V. 2001. "Role of Ferrihydrite in Adsorption of Three Imidazolinone Herbicides." *Journal of Agricultural and Food Chemistry*, 49, (3), 1315-1320. [Washington, D.C.]: American Chemical Society. TIC: 259035.
- 178685 Liaw, B.J.; Cheng, D.S.; and Yang, B.L. 1989. "Oxidative Dehydrogenation of 1-Butene on Iron Oxyhydroxides and Hydrated Iron Oxides." *Journal of Catalysis*, 118, 312-326. [New York, New York]: Academic Press. TIC: 259036.
- 162229 Lide, D.R., ed. 2000. *CRC Handbook of Chemistry and Physics*. 81st Edition. Boca Raton, Florida: CRC Press. TIC: 253056.
- 160832 Lide, D.R., ed. 2002. *CRC Handbook of Chemistry and Physics*. 83rd Edition. Boca Raton, Florida: CRC Press. TIC: 253582.
- 161667 Litaor, M.I. and Ibrahim, S.A. 1996. "Plutonium Association with Selected Solid Phases in Soils of Rocky Flats, Colorado, Using Sequential Extraction Technique." *Journal of Environmental Quality*, 25, (5), 1144-1151. Madison, Wisconsin: American Society of Agronomy. TIC: 252783.
- 105729 Liu, H.H.; Doughty, C.; and Bodvarsson, G.S. 1998. "An Active Fracture Model for Unsaturated Flow and Transport in Fractured Rocks." *Water Resources Research*, 34, (10), 2633-2646. Washington, D.C.: American Geophysical Union. TIC: 243012.
- 173771 Lövgren, L.; Sjöberg, S.; and Schindler, P.W. 1990. "Acid/Base Reactions and Al(III) Complexation at the Surface of Goethite." *Geochimica et Cosmochimica Acta*, 54, 1301-1306. [New York, New York]: Pergamon Press. TIC: 257334.
- 174812 Low, M.J.D. 1960. "Kinetics of Chemisorption of Gases on Solids." *Chemical Reviews*, [60], ([3]), 267-312. [Washington, D.C.: American Chemical Society]. TIC: 257620.
- 166315 Lu, N.; Conca, J.; Parker, G.R.; Leonard, P.A.; Moore, B.; Strietelmeier, B.; and Triay, I.R. 2000. *Adsorption of Actinides onto Colloids as a Function of Time, Temperature, Ionic Strength, and Colloid Concentration, Waste Form Colloids Report for Yucca Mountain Program (Colloid Data Summary from 1999 to 2000 Research)*. LA-UR-00-5121. Los Alamos, New Mexico: Los Alamos National Laboratory. ACC: MOL.20031204.0108.

- 174714 Lu, N.; Cotter, C.R.; Kitten, H.D.; Bentley, J.; and Triay, I.R. 1998. "Reversibility of Sorption of Plutonium-239 onto Hematite and Goethite Colloids." *Radiochimica Acta*, 83, 167-173. München, Germany: R. Oldenbourg Verlag. TIC: 257572.
- 100946 Lu, N.; Triay, I.R.; Cotter, C.R.; Kitten, H.D.; and Bentley, J. 1998. *Reversibility of Sorption of Plutonium-239 onto Colloids of Hematite, Goethite, Smectite, and Silica*. LA-UR-98-3057. Los Alamos, New Mexico: Los Alamos National Laboratory. ACC: MOL.19981030.0202.
- 173757 Lützenkirchen, J.; Boily, J-F.; Lövgren, L.; and Sjöberg, S. 2002. "Limitations of the Potentiometric Titration Technique in Determining the Proton Active Site Density of Goethite Surfaces." *Geochimica et Cosmochimica Acta*, 66, (19), 3389-3396. [New York, New York]: Pergamon. TIC: 257328.
- 173758 Machesky, M.L.; Andrade, W.O.; and Rose, A.W. 1991. "Adsorption of Gold(III) and Gold(I)-Thiosulfate Anions by Goethite." *Geochimica et Cosmochimica Acta*, 55, 769-776. Elmsford, New York: Pergamon. TIC: 257329.
- 174725 Manning, B.A. and Burau, R.G. 1995. "Selenium Immobilization in Evaporation Pond Sediments by In Situ Precipitation of Ferric Oxyhydroxide." *Environmental Science & Technology*, 29, (10), 2639-2646. [Washington, D.C.]: American Chemical Society. TIC: 257575.
- 181188 Mariner, P.E. and Jackson, R.E. 1993. "Surface Complexation Model Prediction of Np and Pu Distribution Coefficients." *High Level Radioactive Waste Management, Proceedings of the Fourth Annual International Conference, Las Vegas, Nevada, April 26-30, 1993*. 2, 1539-1546. La Grange Park, Illinois: American Nuclear Society. TIC: 208542.
- 154383 Matsuda, T.; Taguchi, H.; and Nagao, M. 1992. "Energetic Properties of NiO Surface Examined by Heat-of-Adsorption Measurement." *Journal of Thermal Analysis*, 38, 1835-1845. Chichester, England: John Wiley & Sons. TIC: 249669.
- 181235 Mazeina, L; Navrotsky, A. 2007. "Enthalpy of Water Adsorption and Surface Enthalpy of Goethite (α -FeOOH) and Hematite (α -Fe₂O₃)." *Chemistry of Materials*, 19, 825-833. Washington, DC: American Chemical Society. TIC: 259461.
- 154382 McCafferty, E. and Zettlemoyer, A.C. 1970. "Entropy of Adsorption and the Mobility of Water Vapor on Alpha-Fe₃O₃." *Journal of Colloid and Interface Science*, 34, (3), 452-460. [New York, New York: Academic Press]. TIC: 249668.
- 154378 McCafferty, E. and Zettlemoyer, A.C. 1971. "Adsorption of Water Vapour on Alpha-Fe₂O₃." *Discussions of the Faraday Society*, 52, 239-263. [London, England: Gurney and Jackson]. TIC: 249665.

- 113270 McEachern, R.J. and Taylor, P. 1998. "A Review of the Oxidation of Uranium Dioxide at Temperatures Below 400°C." *Journal of Nuclear Material*, 254, 87-121. Amsterdam, The Netherlands: Elsevier. TIC: 246427.
- 100780 Meijer, A. 1990. *Yucca Mountain Project Far-Field Sorption Studies and Data Needs*. LA-11671-MS. Los Alamos, New Mexico: Los Alamos National Laboratory. ACC: MOL.19980508.1113.
- 173785 Micale, F.J.; Kiernan, D.; and Zettlemoyer, A.C. 1985. "Characterization of the Surface Properties of Iron Oxides." *Journal of Colloid and Interface Science*, 105, (2), 570-576. [New York, New York]: Academic Press. TIC: 257514.
- 179136 Micale, F.J.; Topic, M.; Cronan, C.L.; Leidheiser, H., Jr.; and Zettlemoyer, A.C. 1976. "Surface Properties of Ni(OH)₂ and NiO 1. Water Adsorption and Heat of Immersion of Ni(OH)₂." *Journal of Colloid and Interface Science*, 55, (3), 540-545. [New York, New York]: Academic Press. TIC: 259105.
- 139143 Millington, R.J. and Quirk, J.M. 1961. "Permeability of Porous Solids." *Transactions of the Faraday Society*, 57, (7), 1200-1207. Toronto, Canada: Royal Society of Chemistry. TIC: 246707.
- 133392 Mills, R. 1973. "Self-Diffusion in Normal and Heavy Water in the Range 1-45°." *Journal of Physical Chemistry*, 77, (5), 685-688. Washington, D.C.: American Chemical Society. TIC: 246404.
- 138725 Mills, R. and Lobo, V.M.M. 1989. *Self-Diffusion in Electrolyte Solutions, A Critical Examination of Data Compiled from the Literature*. Physical Sciences Data 36. Pages 314-319. New York, New York: Elsevier. TIC: 248026.
- 159327 Misawa, T.; Hashimoto, K.; and Shimodaira, S. 1974. "The Mechanism of Formation of Iron Oxide and Oxyhydroxides in Aqueous Solutions at Room Temperature." *Corrosion Science*, 14, 131-149. [New York, New York]: Pergamon Press. TIC: 212539.
- 173759 Missana, T.; García-Gutiérrez, M.; and Maffiotte, C. 2003. "Experimental and Modeling Study of the Uranium (VI) Sorption on Goethite." *Journal of Colloid and Interface Science*, 260, 291-301. [New York, New York]: Academic Press. TIC: 257330.
- 178686 Mitov, I.; Paneva, D.; and Kunev, B. 2002. "Comparative Study of the Thermal Decomposition of Iron Oxyhydroxides." *Thermochimica Acta*, 386, 179-188. [New York, New York]: Elsevier. TIC: 259037.
- 130419 Mohanty, S.; Cragolino, G.; Ahn, T.; Dunn, D.S.; Lichtner, P.C.; Manteufel, R.D.; and Sridhar, N. 1996. *Engineered Barrier System Performance Assessment Code: Ebspac Version 1.0B Technical Description and User's Manual*. CNWRA 96-011. San Antonio, Texas: Center for Nuclear Waste Regulatory Analyses. TIC: 233382.

- 151052 Morel, F.M.M. and Hering, J.G. 1993. *Principles and Applications of Aquatic Chemistry*. New York, New York: John Wiley & Sons. TIC: 248465.
- 162877 Morimoto, T.; Nagao, M.; and Tokuda, F. 1969. "The Relation Between the Amounts of Chemisorbed and Physisorbed Water on Metal Oxides." *The Journal of Physical Chemistry*, 73, (1), 243 -248. [Washington, D.C.]: American Chemical Society. TIC: 254165.
- 174703 Morse, J.W. and Choppin, G.R. 1986. "Laboratory Studies of Plutonium in Marine Systems." *Marine Chemistry*, 20, 73-89. Amsterdam, The Netherlands: Elsevier. TIC: 257581.
- 173760 Müller, B. and Sigg, L. 1992. "Adsorption of Lead(II) on the Goethite Surface: Voltammetric Evaluation of Surface Complexation Parameters." *Journal of Colloid and Interface Science*, 148, (2), 517-532. [New York, New York]: Academic Press. TIC: 257336.
- 179553 Murphy, R.J.; Lenhart, J.J.; and Honeyman, B.D. 1999. "The Sorption of Thorium (IV) and Uranium (VI) to Hematite in the Presence of Natural Organic Matter." *Colloids and Surfaces A: Physicochemical and Engineering Aspects*, 157, 47-62. Amsterdam, The Netherlands: Elsevier. TIC: 259627.
- 162878 Nagao, M.; Kumashiro, R.; Matsuda, T.; and Kuroda, Y. 1995. "Calorimetric Study of Water Two-Dimensionally Condensed on the Homogeneous Surface of a Solid." *Thermochimica Acta*, 253, ([1-2]), 221-233. [New York, New York]: Elsevier. TIC: 254099.
- 172676 Nakayama, S. and Sakamoto, Y. 1991. "Sorption of Neptunium on Naturally-Occurring Iron-Containing Minerals." *Radiochimica Acta*, 52/53, (1), 153-157. München, Germany: R. Oldenbourg Verlag. TIC: 238750.
- 174394 National Research Council 2000. *Natural Attenuation for Groundwater Remediation*. Washington, D.C.: National Academy Press. TIC: 257470.
- 173018 Naveau, A.; Monteil-Rivera, F.; Dumonceau, J.; and Boudesocque, S. 2005. "Sorption of Europium on a Goethite Surface: Influence of Background Electrolyte." *Journal of Contaminant Hydrology*, 77, 1-16. [New York, New York]: Elsevier. TIC: 257071.
- 174124 Nimmo, J.R. and Miller, E.E. 1986. "The Temperature Dependence of Isothermal Moisture vs. Potential Characteristics of Soils." *Soil Science Society of America Journal*, 50, 1105-1113. Madison, Wisconsin: Soil Science Society of America. TIC: 257436.
- 163274 NRC (U.S. Nuclear Regulatory Commission) 2003. *Yucca Mountain Review Plan, Final Report*. NUREG-1804, Rev. 2. Washington, D.C.: U.S. Nuclear Regulatory Commission, Office of Nuclear Material Safety and Safeguards. TIC: 254568.

- 167377 Nye, P.H. 1979. "Diffusion of Ions and Uncharged Solutes in Soils and Soil Clays." *Advances in Agronomy*, 31, 225-272. New York, New York: Academic Press. TIC: 255345.
- 178704 O'Reilly, S.E. and Hochella, M.F., Jr. 2003. "Lead Sorption Efficiencies of Natural and Synthetic Mn and Fe-Oxides." *Geochimica et Cosmochimica Acta*, 67, (23), 4471-4487. [New York, New York]: Elsevier. TIC: 259038.
- 159027 OECD (Organisation for Economic Co-operation and Development, Nuclear Energy Agency) 2001. *Chemical Thermodynamics of Neptunium and Plutonium*. Volume 4 of *Chemical Thermodynamics*. New York, New York: Elsevier. TIC: 209037.
- 154588 Olesen, T.; Moldrup, P.; and Gamst, J. 1999. "Solute Diffusion and Adsorption in Six Soils along a Soil Texture Gradient." *Soil Science Society of America Journal*, 63, (3), 519-524. Madison, Wisconsin: Soil Science Society of America. TIC: 249743.
- 155700 Olesen, T.; Moldrup, P.; Henriksen, K.; and Petersen, L.W. 1996. "Modeling Diffusion and Reaction in Soils: IV. New Models for Predicting Ion Diffusivity." *Soil Science*, 161, (10), 633-645. [Baltimore, Maryland: Williams & Wilkins]. TIC: 250477.
- 173799 Or, D. and Tuller, M. 1999. "Liquid Retention and Interfacial Area in Variability Saturated Porous Media: Upscaling from Single-Pore To Sample-Scale Model." *Water Resources Research*, 35, (12), 3591-3605. Washington, D.C.: American Geophysical Union. TIC: 257326.
- 179704 Östholms, E. 1995. "Thorium Sorption on Amorphous Silica." *Geochimica et Cosmochimica Acta*, 59, (7), 1235-1249. [New York, New York]: Pergamon. TIC: 258882.
- 178712 Paffett, M.T.; Kelly, D.; Joyce, S.A.; Morris, J.; and Veirs, K. 2003. "A Critical Examination of the Thermodynamics of Water Adsorption on Actinide Oxide Surfaces." *Journal of Nuclear Materials*, 322, 45-56. [New York, New York]: Elsevier. TIC: 259039.
- 174071 Painter, S.; Cvetkovic, V.; Pickett, D.; and Turner, D.R. 2002. "Significance of Kinetics for Sorption of Inorganic Colloids: Modeling and Experiment Interpretation Issues." *Environmental Science & Technology*, 36, (24), 5369-5375. [Washington, D.C.]: American Chemical Society. TIC: 257438.
- 159511 Parkhurst, D.L. and Appelo, C.A.J. 1999. *User's Guide to PHREEQC (Version 2)—A Computer Program for Speciation, Batch-Reaction, One-Dimensional Transport, and Inverse Geochemical Calculations*. Water-Resources Investigations Report 99-4259. Denver, Colorado: U.S. Geological Survey. TIC: 253046.

- 174361 Parks, G.A. 1964. "The Isoelectric Points of Solid Oxides, Solid Hydroxides, and Aqueous Hydroxo Complex Systems." [*Chemical Reviews*], [65], ([2]), 177-198. [Washington, D.C.: American Chemical Society]. TIC: 257467.
- 174707 Payne, T.E.; Davis, J.A.; and Waite, T.D. 1994. "Uranium Retention by Weathered Schists - The Role of Iron Minerals." *Radiochimica Acta*, 66/67, 297-303. München, Germany: R. Oldenbourg Verlag. TIC: 257571.
- 109941 Penman, H.L. 1940. "Gas and Vapor Movement in Soils I. The Diffusion of Vapours Through Porous Solids." *Journal of Agricultural Science*, 30, 437-462. Cambridge, England: The University Press. TIC: 236561.
- 179622 Pepper, S.E.; Hull, L.C.; Bottenus, B.V.; and Clark, S.B. 2006. "Adsorption of Lanthanum to Goethite in the Presence of Gluconate." *Radiochimica Acta*, 94, 229-237. München, Germany: Oldenbourg Wissenschaftsverlag. TIC: 258861.
- 104946 Perry, R.H. and Chilton, C.H., eds. 1973. *Chemical Engineers' Handbook*. 5th Edition. New York, New York: McGraw-Hill. TIC: 242591.
- 119529 Perry, R.H.; Chilton, C.H.; and Kirkpatrick, S.D., eds. 1963. *Chemical Engineers' Handbook*. 4th Edition. New York, New York: McGraw-Hill. TIC: 237828.
- 173762 Persson, P.; Nordin, J.; Rosenqvist, J.; Lövgren, L.; Öhman, L-O.; and Sjöberg, S. 1998. "Comparison of the Adsorption of o-Phthalate on Boehmite (γ -AlOOH), Aged (γ -Al₂O₃, and Goethite (α -Fe-OOH)." *Journal of Colloid and Interface Science*, 206, 252-266. [New York, New York]: Academic Press. TIC: 257283.
- 105743 Philip, J.R.; Knight, J.H.; and Waechter, R.T. 1989. "Unsaturated Seepage and Subterranean Holes: Conspectus, and Exclusion Problem for Circular Cylindrical Cavities." *Water Resources Research*, 25, (1), 16-28. Washington, D.C.: American Geophysical Union. TIC: 239117.
- 111477 Pirson, S.J. 1963. *Handbook of Well Log Analysis for Oil and Gas Formation Evaluation*. Englewood Cliffs, New Jersey: Prentice-Hall. TIC: 245393.
- 173714 Pivovarov, S. 1997. "Surface Structure and Site Density of the Oxide-Solution Interface." *Journal of Colloid and Interface Science*, 196, 321-323. [New York, New York]: Academic Press. TIC: 257309.
- 123115 Porter, L.K.; Kemper, W.D.; Jackson, R.D.; and Stewart, B.A. 1960. "Chloride Diffusion in Soils as Influenced by Moisture Content." *Soil Science Society of America Proceedings*, 24, (5), 460-463. Danville, Illinois: Soil Science Society of America. TIC: 246854.

- 174726 Powell, B.A.; Fjeld, R.A.; Kaplan, D.I.; Coates, J.T.; and Serkiz, S.M. 2005. "Pu(V)O₂⁺ Adsorption and Reduction by Synthetic Hematite and Goethite." *Environmental Science & Technology*, 39, (7), 2107-2114. [Washington, D.C.]: American Chemical Society. TIC: 257576.
- 100605 Pruess, K. 1983. *GMINC - A Mesh Generator for Flow Simulations in Fractured Reservoirs*. LBL-15227. Berkeley, California: Lawrence Berkeley Laboratory. ACC: NNA.19910307.0134.
- 179706 Quigley, M.S.; Honeyman, B.D.; and Santschi, P.H. 1996. "Thorium Sorption in the Marine Environment: Equilibrium Partitioning at the Hematite/Water Interface, Sorption/Desorption Kinetics and Particle Tracing." *Aquatic Geochemistry*, 1, 277-301. [Boston, Massachusetts]: Kluwer Academic Publishers. TIC: 258877.
- 173709 Randall, S.R.; Sherman, D.M.; Ragnardottir, K.V.; and Collins, C.R. 1999. "The Mechanism of Cadmium Surface Complexation on Iron Oxyhydroxide Minerals." *Geochimica et Cosmochimica Acta*, 63, (19/20), 2971-2987. [New York, New York]: Pergamon. TIC: 257307.
- 154434 Reardon, E.J. 1981. "Kd's — Can They be Used to Describe Reversible Ion Sorption Reactions in Contaminant Migration?" *Ground Water*, 19, (3), 279-286. Worthington, Ohio: Water Well Journal Publishing Company. TIC: 249726.
- 179246 Reimus, P.W.; Callahan, T.J.; Ware, S.D.; Haga, M.J.; and Counce, D.A. 2007. "Matrix Diffusion Coefficients in Volcanic Rocks at the Nevada Test Site: Influence of Matrix Porosity, Matrix Permeability, and Fracture Coating Minerals." *Journal of Contaminant Hydrology*, 93, 85-95. [New York, New York]: Elsevier. TIC: 259673.
- 163008 Reimus, P.W.; Ware, S.D.; Benedict, F.C.; Warren, R.G.; Humphrey, A.; Adams, A.; Wilson, B.; and Gonzales, D. 2002. *Diffusive and Advective Transport of ³H, ¹⁴C, and ⁹⁹Tc in Saturated, Fractured Volcanic Rocks from Pahute Mesa, Nevada*. LA-13891-MS. Los Alamos, New Mexico: Los Alamos National Laboratory. TIC: 253905.
- 173846 Rhoades, J.D. and Oster, J.D. 1986. "Solute Content." Chapter 42 of *Methods of Soil Analysis, Part 1 Physical and Mineralogical Methods*. Klute, A., ed. 2nd Edition. Madison, Wisconsin: Soil Science Society of America. TIC: 217566.
- 173835 Rhoades, J.D.; Raats, P.A.C.; and Prather, R.J. 1976. "Effects of Liquid-Phase Electrical Conductivity, Water Content, and Surface Conductivity on Bulk Soil Electrical Conductivity." *Soil Science Society America Journal*, 40, (5), 651-655. Madison, Wisconsin: Soil Science Society of America. TIC: 257324.
- 178725 Rice, D.W.; Phipps, P.B.P.; and Tremoureaux, R. 1980. "Atmospheric Corrosion of Nickel." *Journal of the Electrochemical Society*, 127, (3), 563-568. [New York, New York]: Electrochemical Society. TIC: 259040.

- 180019 Richter, A.; Brendler, V.; and Nebelung, C. 2005. "The Effect of Parameter Uncertainty on Blind Prediction of Np(V) Sorption onto Hematite Using the Diffuse Double Layer Model." *Radiochimica Acta*, 93, 527-531. München, Germany: Oldenbourg Wissenschaftsverlag. TIC: 258863.
- 179308 Ritchie, A.G. 1981. "A Review of the Rates of Reaction of Uranium with Oxygen and Water Vapour at Temperatures Up to 300°C." *Journal of Nuclear Materials*, 102, 170-182. [New York, New York]: North-Holland Publishing Company. TIC: 259118.
- 101710 Roberts, J.J. and Lin, W. 1997. "Electrical Properties of Partially Saturated Topopah Spring Tuff: Water Distribution as a Function of Saturation." *Water Resources Research*, 33, (4), 577-587. Washington, D.C.: American Geophysical Union. TIC: 239736.
- 173763 Robertson, A.P. and Leckie, J.O. 1997. "Cation Binding Predictions of Surface Complexation Models: Effects of pH, Ionic Strength, Cation Loading, Surface Complex, and Model Fit." *Journal of Colloid and Interface Science*, 188, 444-472. [New York, New York]: Academic Press. TIC: 257300.
- 173710 Rodda, D.P.; Johnson, B.B.; and Wells, J.D. 1996. "Modeling the Effect of Temperature on Adsorption of Lead(II) and Zinc(II) onto Goethite at Constant pH." *Journal of Colloid and Interface Science*, 184, 365-377. [New York, New York]: Academic Press. TIC: 257312.
- 171518 Roden, E.E. and Zachara, J.M. 1996. "Microbial Reduction of Crystalline Iron(III) Oxides: Influence of Oxide Surface Area and Potential for Cell Growth." *Environmental Science & Technology*, 30, (5), 1618-1628. Washington, D.C.: American Chemical Society. TIC: 256499.
- 174022 Romero E.; Gens, A.; and Lloret, A. 2001. "Temperature Effects on the Hydraulic Behaviour of an Unsaturated Clay." *Geotechnical and Geological Engineering*, 19, 311-332. Amsterdam, The Netherlands: Kluwer Academic Publishers. TIC: 257400.
- 168432 Runde, W.; Conradson, S.D.; Efurud, D.W.; Lu, N.P.; VanPelt, C.E.; and Tait, C.D. 2002. "Solubility and Sorption of Redox-Sensitive Radionuclides (Np, Pu) in J-13 Water from the Yucca Mountain Site: Comparison between Experiment and Theory." *Applied Geochemistry*, 17, (6), 837-853. New York, New York: Pergamon. TIC: 254046.
- 155697 Russo, R.E.; Mao, X.; Borisov, O.V.; and Liu, H. 2000. "Laser Ablation in Atomic Spectroscopy." *Encyclopedia of Analytical Chemistry*. Meyers, R.A., ed. Pages 9485-9506. Chichester, England: John Wiley & Sons. TIC: 250479.

- 173766 Rustad, J.R.; Felmy, A.R.; and Hay, B.P. 1996. "Molecular Statics Calculations of Proton Binding to Goethite Surfaces: A New Approach to Estimation of Stability Constants for Multisite Surface Complexation Models." *Geochimica et Cosmochimica Acta*, 60, (9), 1563-1576. [New York, New York]: Pergamon. TIC: 257333.
- 173812 Sahai, N. and Sverjensky D.A. 1997. "Evaluation of Internally Consistent Parameters for the Triple-Layer Model by the Systematic Analysis of Oxide Surface Titration Data." *Geochimica et Cosmochimica Acta*, 61, (14), 2801-2826. New York, New York: Pergamon. TIC: 257337.
- 107213 Sanchez, A.L.; Murray, J.W.; and Sibley, T.H. 1985. "The Adsorption of Plutonium IV and V on Goethite." *Geochimica et Cosmochimica Acta*, 49, (11), 2297-2307. New York, New York: Pergamon Press. TIC: 224091.
- 178727 Sani, R.K.; Peyton, B.M.; Amonette, J.E.; and Geesey, G.G. 2004. "Reduction of Uranium(VI) Under Sulfate-Reducing Conditions in the Presence of Fe(III)-(Hydr)oxides." *Geochimica et Cosmochimica Acta*, 68, (12), 2639-2648. [New York, New York]: Pergamon. TIC: 259041.
- 170923 Santschi, P.H.; Roberts, K.A.; and Guo, L. 2002. "Organic Nature of Colloidal Actinides Transported in Surface Water Environments." *Environmental Science & Technology*, 36, (17), 3711-3719. [Washington, D.C.]: American Chemical Society. TIC: 256463.
- 178732 Sauvé, S.; Martínez, C.E.; McBride, M.; and Hendershot, W. 2000. "Adsorption of Free Lead (Pb⁺) by Pedogenic Oxides, Ferrihydrite, and Leaf Compost." *Soil Science Society of America Journal*, [64, (2)], 595-599. [Madison, Wisconsin]: Soil Science Society of America. TIC: 259042.
- 173028 Schultz, M.F.; Benjamin, M.M.; and Ferguson, J.F. 1987. "Adsorption and Desorption of Metals on Ferrihydrite: Reversibility of the Reaction and Sorption Properties of the Regenerated Solid." *Environmental Science Technology*, 21, (9), 863-869. [Washington, D.C.]: American Chemical Society. TIC: 257057.
- 144629 Schwertmann, U. and Cornell, R.M. 1991. *Iron Oxides in the Laboratory: Preparation and Characterization*. New York, New York: VCH Publishers. TIC: 237942.
- 178734 Schwertmann, U.; Friedl, J.; and Kyek, A. 2004. "Formation and Properties of a Continuous Crystallinity Series of Synthetic Ferrihydrites (2- to 6-Line) and Their Relation to FeOOH Forms." *Clays and Clay Minerals*, 52, (2), 221-226. [Chantilly, Virginia: Clay Minerals Society]. TIC: 259043.

- 173863 Schwertmann, U.; Friedl, J.; Stanjek, H.; and Schulze, D.G. 2000. "The Effect of Al on Fe Oxides. XIX. Formation of Al-Substituted Hematite from Ferrihydrite at 25°C and pH 4 to 7." *Clays and Clay Minerals*, 48, (2), 159-172. [Aurora, Colorado]: Clay Minerals Society. TIC: 257393.
- 179307 Senanayake, S.D.; Rousseau, R.; Colegrave, D.; and Idriss, H. 2005. "The Reaction of Water on Polycrystalline UO₂: Pathways to Surface and Bulk Oxidation." *Journal of Nuclear Materials*, 342, 179-187. [New York, New York]: Elsevier. TIC: 259122.
- 173836 Shainberg, I.; Rhoades, J.D.; and Prather, R.J. 1980. "Effect of Exchangeable Sodium Percentage, Cation Exchange Capacity, and Soil Solution Concentration on Soil Electrical Conductivity." *Soil Science Society America Journal*, 44, (3), 469-473. Madison, Wisconsin: Soil Science Society of America. TIC: 257317.
- 167469 Šimuněk, J.; Jarvis, N.J.; van Genuchten, M.Th.; and Gardenas, A. 2003. "Review and Comparison of Models for Describing Non-Equilibrium and Preferential Flow and Transport in the Vadose Zone." *Journal of Hydrology*, 272, ([1-4]), 14-35. [New York, New York]: Elsevier. TIC: 255570.
- 161624 Singh, A.K.; Singh, H.; Singh, S.P.; and Sawhney, R.L. 2002. "Numerical Calculation of Psychrometric Properties on a Calculator." *Building and Environment*, 37, ([4]), 415-419. [New York, New York]: Elsevier. TIC: 253846.
- 181244 SNL (Sandia National Laboratories) 2007. *Abstraction of Drift Seepage*. MDL-NBS-HS-000019 REV 01 ADD 01. Las Vegas, Nevada: Sandia National Laboratories. ACC: DOC.20070807.0001.
- 177431 SNL 2007. *Atmospheric Dispersal and Deposition of Tephra from a Potential Volcanic Eruption at Yucca Mountain, Nevada*. MDL-MGR-GS-000002 REV 03. Las Vegas, Nevada: Sandia National Laboratories.
- 179545 SNL 2007. *Calibrated Unsaturated Zone Properties*. ANL-NBS-HS-000058 REV 00. Las Vegas, Nevada: Sandia National Laboratories. ACC: DOC.20070530.0013.
- 180616 SNL 2007. *Cladding Degradation Summary for LA*. ANL-WIS-MD-000021 REV 03 ADD 01. Las Vegas, Nevada: Sandia National Laboratories. ACC: DOC.20050815.0002; DOC.20070614.0002.
- 177430 SNL 2007. *Dike/Drift Interactions*. MDL-MGR-GS-000005 REV 02. Las Vegas, Nevada: Sandia National Laboratories.
- 177418 SNL 2007. *Dissolved Concentration Limits of Elements with Radioactive Isotopes*. ANL-WIS-MD-000010 REV 06. Las Vegas, Nevada: Sandia National Laboratory. ACC: DOC.20070918.0010.

- 177412 SNL 2007. *Engineered Barrier System: Physical and Chemical Environment*. ANL-EBS-MD-000033 REV 06. Las Vegas, Nevada: Sandia National Laboratories. ACC: DOC.20070907.0003.
- 180778 SNL 2007. *General Corrosion and Localized Corrosion of the Drip Shield*. ANL-EBS-MD-000004 REV 02 ADD 01. Las Vegas, Nevada: Sandia National Laboratories. ACC: DOC.20060427.0002; DOC.20070807.0004.
- 178519 SNL 2007. *General Corrosion and Localized Corrosion of Waste Package Outer Barrier*. ANL-EBS-MD-000003 REV 03. Las Vegas, Nevada: Sandia National Laboratories. ACC: DOC.20070730.0003; DOC.20070807.0007.
- 181165 SNL 2007. *Geochemistry Model Validation Report: Material Degradation and Release Model*. ANL-EBS-GS-000001 REV 02. Las Vegas, Nevada: Sandia National Laboratories.
- 181648 SNL 2007. *In-Drift Natural Convection and Condensation*. MDL-EBS-MD-000001 REV 00, AD 01. Las Vegas, Nevada: Sandia National Laboratories. ACC: DOC.20041025.0006; DOC.20050330.0001; DOC.20051122.0005; DOC.20070907.0004.
- 180506 SNL 2007. *In-Package Chemistry Abstraction*. ANL-EBS-MD-000037 REV 04 ADD 01. Las Vegas, Nevada: Sandia National Laboratories. ACC: DOC.20051130.0007; DOC.20070816.0004.
- 180472 SNL 2007. *Initial Radionuclides Inventory*. ANL-WIS-MD-000020 REV 01 ADD 01. Las Vegas, Nevada: Sandia National Laboratories. ACC: DOC.20050927.0005; DOC.20070801.0001.
- 181383 SNL 2007. *Multiscale Thermohydrologic Model*. ANL-EBS-MD-000049 REV 03 AD01. Las Vegas, Nevada: Sandia National Laboratories. ACC: DOC.20070831.0003..
- 177432 SNL 2007. *Number of Waste Packages Hit by Igneous Intrusion*. ANL-MGR-GS-000003 REV 03. Las Vegas, Nevada: Sandia National Laboratories.
- 181006 SNL 2007. *Particle Tracking Model and Abstraction of Transport Processes*. MDL-NBS-HS-000020 REV 02 ADD 01. Las Vegas, Nevada: Sandia National Laboratories. ACC: DOC.20050808.0006; DOC.20070823.0005.
- 177409 SNL 2007. *Qualification of Thermodynamic Data for Geochemical Modeling of Mineral-Water Interactions in Dilute Systems*. ANL-WIS-GS-000003 REV 01. Las Vegas, Nevada: Sandia National Laboratories. ACC: DOC.20070619.0007.
- 177424 SNL 2007. *Radionuclide Screening*. ANL-WIS-MD-000006 REV 02. Las Vegas, Nevada: Sandia National Laboratories. ACC: DOC.20070326.0003.

- 177396 SNL 2007. *Radionuclide Transport Models Under Ambient Conditions*. MDL-NBS-HS-000008 REV 02 ADD 01. Las Vegas, Nevada: Sandia National Laboratories. ACC: DOC.20041101.0002; DOC.20050823.0003; DOC.20070718.0003.
- 181650 SNL 2007. *Saturated Zone Flow and Transport Model Abstraction*. MDL-NBS-HS-000021 REV 03 AD 01. Las Vegas, Nevada: Sandia National Laboratories. ACC: DOC.20050808.0004; DOC.20070913.0002.
- 176828 SNL 2007. *Seismic Consequence Abstraction*. MDL-WIS-PA-000003 REV 03. Las Vegas, Nevada: Sandia National Laboratories.
- 181953 SNL 2007. *Stress Corrosion Cracking of Waste Package Outer Barrier and Drip Shield Materials*. ANL-EBS-MD-000005 REV 04. Las Vegas, Nevada: Sandia National Laboratories. ACC: DOC.20070913.0001.
- 179567 SNL 2007. *Total System Performance Assessment Data Input Package for Requirements Analysis for DOE SNF/HLW and Navy SNF Waste Package Overpack Physical Attributes Basis for Performance Assessment*. TDR-TDIP-ES-000009 REV 00. Las Vegas, Nevada: Sandia National Laboratories. ACC: DOC.20070921.0009.
- 179354 SNL 2007. *Total System Performance Assessment Data Input Package for Requirements Analysis for EBS In-Drift Configuration*. TDR-TDIP-ES-000010 REV 00. Las Vegas, Nevada: Sandia National Laboratories. ACC: DOC.20070921.0008.
- 179466 SNL 2007. *Total System Performance Assessment Data Input Package for Requirements Analysis for Subsurface Facilities*. TDR-TDIP-PA-000001 REV 00. Las Vegas, Nevada: Sandia National Laboratories. ACC: DOC.20070921.0007.
- 179394 SNL 2007. *Total System Performance Assessment Data Input Package for Requirements Analysis for TAD Canister and Related Waste Package Overpack Physical Attributes Basis for Performance Assessment*. TDR-TDIP-ES-000006 REV 00. Las Vegas, Nevada: Sandia National Laboratories. ACC: DOC.20070918.0005.
- 178871 SNL 2007. *Total System Performance Assessment Model /Analysis for the License Application*. MDL-WIS-PA-000005 REV 00. Las Vegas, Nevada: Sandia National Laboratories.
- 175177 SNL 2007. *UZ Flow Models and Submodels*. MDL-NBS-HS-000006 REV 03. Las Vegas, Nevada: Sandia National Laboratories. ACC: DOC.20070907.0001.
- 177423 SNL 2007. *Waste Form and In-Drift Colloids-Associated Radionuclide Concentrations: Abstraction and Summary*. MDL-EBS-PA-000004 REV 03. Las Vegas, Nevada: Sandia National Laboratories.
- 170588 So, H.B. and Nye, P.H. 1989. "The Effect of Bulk Density, Water Content and Soil Type on the Diffusion of Chloride in Soil." *Journal of Soil Science*, 40, ([4]), 743-749. [Oxford, England: Blackwell Scientific]. TIC: 255392.

- 100927 Southwell, C.R.; Bultman, J.D.; and Alexander, A.L. 1976. "Corrosion of Metals in Tropical Environments - Final Report of 16-Year Exposures." *Materials Performance*, 15, (7), 9-25. Houston, Texas: National Association of Corrosion Engineers. TIC: 224022.
- 127253 Sposito, G. 1984. *The Surface Chemistry of Soils*. New York, New York: Oxford University Press. TIC: 217687.
- 178302 Stakebake, J.L. 1971. "The Storage Behavior of Plutonium Metal, Alloys, and Oxide." *Journal of Nuclear Materials*, 38, 241-259. Amsterdam, [The Netherlands]: North-Holland Publishing. TIC: 258814.
- 178840 Stakebake, J.L. and Dringman, M.R. 1968. *Hygroscopicity of Plutonium Dioxide, with Errata*. RFP -1056. Golden, Colorado: U.S. Atomic Energy Commission. ACC: MOL.20070125.0049.
- 178305 Stakebake, J.L. and Steward, L.M. 1973. "Water Vapor Adsorption on Plutonium Dioxide." *Journal of Colloid and Interface Science*, 42, (2), 328-333. [New York, New York]: Academic Press. TIC: 258817.
- 141778 Stumm, W. 1992. *Chemistry of the Solid-Water Interface, Processes at the Mineral-Water and Particle-Water Interface in Natural Systems*. New York, New York: John Wiley & Sons. TIC: 237213.
- 181231 Stumm, W; Huang, CP; Jenkins, SR 1970. "Specific Chemical Interaction Affecting Stability of Dispersed Systems." *Croatia Chemical Acta*, 42, (2), 223-245. Zagreb, Croatia: Marulicev Trg. Order Requested
- 167756 Tada, H.; Paris, P.C.; and Irwin, G.R. 2000. *The Stress Analysis of Cracks Handbook*. 3rd Edition. New York, New York: American Society of Mechanical Engineers. TIC: 255547.
- 161625 Tamura, H.; Tanaka, A.; Mita, K.; and Furuichi, R. 1999. "Surface Hydroxyl Site Densities on Metal Oxides as a Measure for the Ion-Exchange Capacity." *Journal of Colloid and Interface Science*, 209, ([1]), 225-231. [New York, New York]: Academic Press. TIC: 253844.
- 101161 Thibault, D.H.; Sheppard, M.I.; and Smith, P.A. 1990. *A Critical Compilation and Review of Default Soil Solid/Liquid Partition Coefficients, K_d , for Use in Environmental Assessments*. AECL-10125. Pinawa, Manitoba, Canada: Atomic Energy of Canada Limited. TIC: 237236.
- 120496 Thiel, P.A. and Madey, T.E. 1987. "The Interaction of Water with Solid Surfaces: Fundamental Aspects." *Surface Science Reports*, 7, (6-8), 211-385. Amsterdam, The Netherlands: Elsevier. TIC: 246880.

- 178737 Tipping, E. 1981. "The Adsorption of Aquatic Humic Substances by Iron Oxides." *Geochimica et Cosmochimica Acta*, 45, 191-199. [New York, New York]: Pergamon Press. TIC: 239483.
- 144644 Tochiyama, O.; Endo, S.; and Inoue, Y. 1995. "Sorption of Neptunium(V) on Various Iron Oxides and Hydrous Iron Oxides." *Radiochimica Acta*, [68, (2), 105-111. München, Germany]: R. Oldenbourg Verlag. TIC: 238248.
- 155334 Towe, K.M. and Bradley, W.F. 1967. "Mineralogical Constitution of Colloidal 'Hydrous Ferric Oxides'." *Journal of Colloid and Interface Science*, 24, 384-392. [New York, New York: Academic Press]. TIC: 250230.
- 113425 Tripathi, V.S. 1984. *Uranium (VI) Transport Modeling: Geochemical Data and Submodels*. Ph.D. Thesis. Ann Arbor, Michigan: University Microfilms International. TIC: 224558.
- 173021 Trivedi, P.; Axe, L.; and Dyer, J. 2001. "Adsorption of Metal Ions onto Goethite: Single-Adsorbate and Competitive Systems." *Colloids and Surfaces*, 191, 107-121. [New York, New York]: Elsevier. TIC: 257088.
- 144697 Turner, D.R. 1995. *A Uniform Approach to Surface Complexation Modeling of Radionuclide Sorption*. CNWRA 95-001. San Antonio, Texas: Center for Nuclear Waste Regulatory Analyses. TIC: 236937.
- 179618 Turner, D.R. and Sassman, S.A. 1996. "Approaches to Sorption Modeling for High-Level Waste Performance Assessment." *Journal of Contaminant Hydrology*, 21, 311-332. [New York, New York]: Elsevier. TIC: 237447.
- 178740 Van Der Giessen, A.A. 1966. "The Structure of Iron (III) Oxide-Hydrate Gels." *Journal of Inorganic & Nuclear Chemistry*, 28, 2155-2159. [New York, New York]: Pergamon Press. TIC: 257713.
- 180973 van der Lee, J. and Lomenech, C. 2004. "Towards a Common Thermodynamic Database for Speciation Models." *Radiochimica Acta*, 92, 811-818. München, Germany: Oldenbourg Wissenschaftsverlag. TIC: 258878.
- 144702 Van Geen, A.; Robertson, A.P.; and Leckie, J.O. 1994. "Complexation of Carbonate Species at the Goethite Surface: Implications for Adsorption of Metal Ions in Natural Waters." *Geochimica et Cosmochimica Acta*, 58, (9), 2073-2086. New York, New York: Elsevier. TIC: 212000.
- 100610 van Genuchten, M.T. 1980. "A Closed-Form Equation for Predicting the Hydraulic Conductivity of Unsaturated Soils." *Soil Science Society of America Journal*, 44, (5), 892-898. Madison, Wisconsin: Soil Science Society of America. TIC: 217327.
- 159088 Venables, W.N. and Ripley, B.D. 2001. *Modern Applied Statistics with S-PLUS*. 3rd Edition. New York, New York: Springer-Verlag. TIC: 252781.

- 173017 Villalobos, M.; Trotz, M.A.; and Leckie, J.O. 2003. "Variability in Goethite Surface Site Density: Evidence from Proton and Carbonate Sorption." *Journal of Colloid and Interface Science*, 268, 273-287. [New York, New York]: Elsevier. TIC: 257076.
- 108746 Waite, T.O.; Davis, J.A.; Payne, T.E.; Waychunas, G.A.; and Xu, N. 1994. "Uranium(VI) Adsorption to Ferrihydrite: Application of a Surface Complexation Model." *Geochimica et Cosmochimica Acta*, 58, (24), 5465-5478. Oxford, England: Elsevier. TIC: 226322.
- 108285 Wan, J. and Tokunaga, T.K. 1997. "Film Straining on Colloids in Unsaturated Porous Media: Conceptual Model and Experimental Testing." *Environmental Science & Technology*, 31, (8), 2413-2420. [Washington, D.C.: American Chemical Society]. TIC: 234804.
- 124994 Wan, J. and Wilson, J.L. 1994. "Visualization of the Role of the Gas-Water Interface on the Fate and Transport of Colloids in Porous Media." *Water Resources Research*, 30, (1), 11-23. Washington, D.C.: American Geophysical Union. TIC: 246300.
- 181213 Wang, P. and Anderko, A. 1999. *Thermodynamic Modeling of Radionuclide Sorption*. San Antonio, Texas: Center for Nuclear Waste Regulatory Analyses. ACC: LLR.20070605.0159.
- 176816 Wang, P.; Anderko, A.; and Turner, D.R. 2001. "Thermodynamic Modeling of the Adsorption of Radionuclides on Selected Minerals. I: Cations." *Industrial & Engineering Chemistry Research*, 40, (20), 4428-4443. [Washington, D.C.]: American Chemical Society. TIC: 258274.
- 100611 Warren, J.E. and Root, P.J. 1963. "The Behavior of Naturally Fractured Reservoirs." *Society of Petroleum Engineers Journal*, 3, (3), 245-255. Dallas, Texas: Society of Petroleum Engineers. TIC: 233671.
- 173035 Watson, E.B. 1996. "Surface Enrichment and Trace-Element Uptake during Crystal Growth." *Geochimica et Cosmochimica Acta*, 60, (24), 5013-5020. Tarrytown, New York: Elsevier. TIC: 257077.
- 180093 Wazne, M.; Korfiatis, G.P.; and Meng, X. 2003. "Carbonate Effects on Hexavalent Uranium Adsorption by Iron Oxyhydroxide." *Environmental Science & Technology*, 37, (16), 3619-3624. [Washington, D.C.]: American Chemical Society. TIC: 258886.
- 100833 Weast, R.C. and Astle, M.J., eds. 1981. *CRC Handbook of Chemistry and Physics*. 62nd Edition. Boca Raton, Florida: CRC Press. TIC: 240722.
- 111561 Weast, R.C., ed. 1985. *CRC Handbook of Chemistry and Physics*. 66th Edition. Boca Raton, Florida: CRC Press. TIC: 216054.

- 178741 Weidler, P.G. 1997. "BET Sample Pretreatment of Synthetic Ferrihydrite and its Influence on the Determination of Surface Area and Porosity." *Journal of Porous Materials*, 4, 165-169. [Boston, Massachusetts]: Kluwer Academic Publishers. TIC: 259044.
- 181192 Westall, J.; Hohl, H. 1980. "A Comparison of Electrostatic Models for the Oxide/Solution Interface." *Advances in Colloid and Interface Science*, 12, (4), 265-294. Amsterdam, Netherlands: Elsevier Scientific. TIC: 259451.
- 181271 Westall, J.C. 1992. *FITEQL, A Computer Program for Determination of Chemical Equilibrium Constants from Experimental Data, with Addendum*. Report 82-02, Version 2.0. Corvallis, Oregon: Oregon State University, Department of Chemistry. TIC: 222339.
- 100835 Wolery, T.J. 1992. *EQ3/6, A Software Package for Geochemical Modeling of Aqueous Systems: Package Overview and Installation Guide (Version 7.0)*. UCRL-MA-110662 PT I. Livermore, California: Lawrence Livermore National Laboratory. TIC: 205087.
- 100836 Wolery, T.J. 1992. *EQ3NR, A Computer Program for Geochemical Aqueous Speciation-Solubility Calculations: Theoretical Manual, User's Guide, and Related Documentation (Version 7.0)*. UCRL-MA-110662 PT III. Livermore, California: Lawrence Livermore National Laboratory. ACC: MOL.19980717.0626.
- 100649 Wu, Y.S.; Ahlers, C.F.; Fraser, P.; Simmons, A.; and Pruess, K. 1996. *Software Qualification of Selected TOUGH2 Modules*. LBL-39490. Berkeley, California: Lawrence Berkeley National Laboratory. ACC: MOL.19970219.0104.
- 181191 Xu, Ying; Axe, Lisa; Yee, Nathan, Dyer, James A. 2006. "Bidentate Complexation Modeling of Heavy Metal Adsorption and Competition on Goethite." *Environmental Science and Technology*, 40, 2213-2218. Washington, D.C.: ACS. Copyright Requested
- 173713 Xue, Y. and Traina, S.J. 1996. "Cosolvent Effect on Goethite Surface Protonation." *Environmental Science & Technology*, 30, (11), 3161 - 3166. Washington, D.C.: American Chemical Society. TIC: 257272.
- 181240 Yao, Yung-Fang Yu 1965. "Adsorption of Polar Molecules on Metal Oxide Single Crystals." *Journal of Physical Chemistry*, 69, (11), 3930 - 3941. Washington, D.C.: American Chemical Society. TIC: 259463.
- 104441 YMP (Yucca Mountain Site Characterization Project) 1998. *Disposal Criticality Analysis Methodology Topical Report*. YMP/TR-004Q, Rev. 00. Las Vegas, Nevada: Yucca Mountain Site Characterization Office. ACC: MOL.19990210.0236.

- 105963 Zachara, J.M.; Girvin, D.C.; Schmidt, R.L.; and Resch, C.T. 1987. "Chromate Adsorption on Amorphous Iron Oxyhydroxide in the Presence of Major Groundwater Ions." *Environmental Science & Technology*, 21, (6), 589-594. Easton, Pennsylvania: American Chemical Society. TIC: 243613.
- 171238 Zarrabi, K.; McMillan, S.; Elkonz, S.; and Cizdziel, J. 2003. *Corrosion and Mass Transport Processes in Carbon Steel Miniature Waste Packages*. Document TR-03-003, Rev. 0. Task 34. Las Vegas, Nevada: University of Nevada, Las Vegas. ACC: MOL.20040202.0079.
- 181272 Zavarin, M. and Bruton, C.J. 2004. *A Non-Electrostatic Surface Complexation Approach to Modeling Radionuclide Migration at the Nevada Test Site: I. Iron Oxides and Calcite*. UCRL-TR-208673. Livermore, California: Lawrence Livermore National Laboratory. ACC: LLR.20070605.0144.

9.2 CODES, STANDARDS, REGULATIONS, AND PROCEDURES

- 180319 10 CFR 63. 2007. Energy: Disposal of High-Level Radioactive Wastes in a Geologic Repository at Yucca Mountain, Nevada. Internet Accessible.
- 178394 70 FR 53313. Implementation of a Dose Standard After 10,000 Years. Internet Accessible.
- 154085 ASM (American Society for Metals) 1979. *Properties and Selection: Nonferrous Alloys and Pure Metals*. Volume 2 of *Metals Handbook*. 9th Edition. Metals Park, Ohio: American Society for Metals. TIC: 209800.
- 179346 ASTM A 240/A 240M-06c. 2006. *Standard Specification for Chromium and Chromium-Nickel Stainless Steel Plate, Sheet, and Strip for Pressure Vessels and for General Applications*. West Conshohocken, Pennsylvania: American Society for Testing and Materials. TIC: 259153.
- 117138 ASTM A 516/A 516M-90. 1991. *Standard Specification for Pressure Vessel Plates, Carbon Steel, for Moderate-and Lower-Temperature Service*. West Conshohocken, Pennsylvania: American Society for Testing and Materials. TIC: 240032.
- 178058 ASTM A 887-89 (Reapproved 2004). 2004. *Standard Specification for Borated Stainless Steel Plate, Sheet, and Strip for Nuclear Application*. West Conshohocken, Pennsylvania: American Society for Testing and Materials. TIC: 258746.
- 181437 ASTM G 1-03. 2003. *Standard Practice for Preparing, Cleaning, and Evaluating Corrosion Test Specimens*. West Conshohocken, Pennsylvania: American Society for Testing and Materials. TIC: 259413.

9.3 SOURCE DATA, LISTED BY DATA TRACKING NUMBER

- 149232 LA0002SK831352.001. Total Colloidal Particles Concentration and Size Distribution in Groundwaters from the Nye County Early Warning Drilling Program. Submittal date: 02/24/2000.
- 150272 LA0004NL831352.001. Pu(IV) and Pu(V) Sorption on Hematite and Goethite Colloids with Natural and Synthetic J-13 Water (1997-98 Data). Submittal date: 04/04/2000.
- 171584 LA0408AM831341.001. Unsaturated Zone Distribution Coefficients (Kds) for U, Np, Pu, Am, Pa, Cs, Sr, Ra, and Th. Submittal date: 08/24/2004.
- 180497 LA0701PANS02BR.003. UZ Transport Parameters. Submittal date: 04/23/2007.
- 159525 LB0205REVUZPRP.001. Fracture Properties for UZ Model Layers Developed from Field Data. Submittal date: 05/14/2002.
- 159526 LB0207REVUZPRP.001. Revised UZ Fault Zone Fracture Properties. Submittal date: 07/30/2002.
- 159672 LB0207REVUZPRP.002. Matrix Properties for UZ Model Layers Developed from Field and Laboratory Data. Submittal date: 07/15/2002.
- 161243 LB0208UZDSCPMI.002. Drift-Scale Calibrated Property Sets: Mean Infiltration Data Summary. Submittal date: 08/26/2002.
- 163044 LB03023DSSCP9I.001. 3-D Site Scale UZ Flow Field Simulations for 9 Infiltration Scenarios. Submittal date: 02/28/2003.
- 178587 LB06123DPDUZFF.001. 3-D UZ Flow Fields for Present-Day Climate of 10th-, 30th-, 50th- and 90th -Percentile Infiltration Maps. Submittal date: 12/19/2006. TBV-7811
- 179066 LB07013DGTUZFF.001. 3-D UZ Flow Fields for Glacial Transition Climate of 10th-, 30th-, 50th-, and 90th-Percentile Infiltration Maps. Submittal date: 01/03/2007. TBV-7848
- 179299 LB0701PAKDSESN.001. Unsaturated Zone Sorption Coefficients for Selenium and Tin. Submittal date: 01/31/2007.
- 180776 LB0702PAUZMTDF.001. Unsaturated Zone Matrix Diffusion Coefficients. Submittal date: 05/10/2007.
- 179324 LB0702UZP10KFF.002. 3-D UZ Flow Fields for Post-10,000 Climate Infiltration Maps. Submittal date: 02/15/2007. TBV-7852

- 152621 LL000905312241.018. Data Associated with the Detection and Measurement of Colloids Recorded in Scientific Notebook 1644. Submittal date: 09/29/2000.
- 142910 LL991109751021.094. Data Associated with the Detection and Measurement of Colloids in Scientific Notebook SN 1644. Submittal date: 01/10/2000.
- 153044 MO0003RIB00076.000. Physical and Chemical Characteristics of Type 316N Grade. Submittal date: 03/14/2000.
- 151029 MO0006J13WTRCM.000. Recommended Mean Values of Major Constituents in J-13 Well Water. Submittal date: 06/07/2000.
- 163399 MO0207EBSATBWP.021. Atlas Breached Waste Package and Drip Shield Experiments: Initial Tests for Rough Drip Shield Surface. Submittal date: 07/31/2002.
- 163400 MO0207EBSATBWP.022. Atlas Breached Waste Package and Drip Shield Experiments: Initial Tests for Smooth Drip Shield Surface. Submittal date: 07/31/2002.
- 163402 MO0207EBSATBWP.023. Atlas Breached Waste Package and Drip Shield Experiments: Single Patch Q(Splash) and Q(Film) Tests on the Smooth Drip Shield Surface. Submittal date: 07/31/2002.
- 163401 MO0207EBSATBWP.024. Atlas Breached Waste Package and Drip Shield Experiments: Multiple Patch Tests for Smooth Drip Shield Surface. Submittal date: 07/31/2002.
- 163403 MO0207EBSATBWP.025. Atlas Breached Waste Package and Drip Shield Experiments: Bounding Flow Rate Tests on the Smooth Drip Shield Surface. Submittal date: 07/31/2002.
- 163404 MO0208EBSATBWP.027. Atlas Breached Waste Package and Drip Shield Experiments: Multiple Patch Tests on the Rough Drip Shield Surface. Submittal date: 08/13/2002.
- 163405 MO0208EBSATBWP.028. Atlas Breached Waste Package and Drip Shield Experiments: Bounding Flow Rate Tests on the Rough Drip Shield Surface. Submittal date: 08/13/2002.
- 162871 MO0302UCC034JC.003. Graphical X-Ray Diffractometer Data and Mineral Analysis of Filtered Solids from Effluent Solution During Miniature Waste Package Corrosion. Submittal date: 02/10/2003.
- 172059 MO0409SPAACRWP.000. Aqueous Corrosion Rates For Non-Waste Form Waste Package Materials. Submittal date: 09/16/2004.

- 180755 MO0411SPACLDDG.003. Updated TSPA-LA Parameters from Clad Degradation-Summary and Abstraction for LA, ANL-WIS-MD-000021 REV 03. Submittal date: 05/10/2007.
- 172830 MO0502ANLGAMR1.016. HLW Glass Degradation Model. Submittal date: 02/08/2005.
- 182278 MO0508SPAUZDIF.000. Verification of Dual Invert/Dual UZ Diffusive Flux Bifurcation. Submittal Date: 08/18/2005.
- 179645 MO0609SPAINOUT.002. PHREEQC Modeling Inputs and Outputs for Geochemistry Model Validation Report: External Accumulation Model. Submittal date: 09/27/2006.
- 180439 MO0701PACSNFCP.000. CSNF Colloid Parameters. Submittal date: 04/17/2007.
- 180440 MO0701PAIRONCO.000. Colloidal Iron Corrosion Products Parameters. Submittal date: 04/17/2007.
- 180392 MO0701PAKDSUNP.000. Colloidal KDS for U, NP, RA and SN. Submittal date: 04/17/2007.
- 180391 MO0701PASORPTN.000. Colloidal Sorption Coefficients for PU, AM, TH, CS, and PA. Submittal date: 04/17/2007.
- 179358 MO0702PADISCON.001. Dissolved Concentration Limits of Elements with Radioactive Isotopes. Submittal date: 02/15/2007.
- 181219 MO0702PAFLUORI.000. Fluoride Uncertainty Associated with Dissolved Concentration Limits. Submittal date: 06/01/2007.
- 180514 MO0702PASTRESS.002. Output DTN of Model Report, "Stress Corrosion Cracking of Waste Package Outer Barrier and Drip Shield Materials," ANL-EBS-MD-000005. Submittal date: 04/24/2007.
- 182093 MO0703PAHYTHRM.000. Hydrological and Thermal Properties of the Invert. Submittal date: 07/19/2007.
- 183148 MO0703PASDSTAT.001. Analyses for Seismic Damage Abstractions. Submittal date: 09/21/2007.
- 183156 MO0703PASEISDA.002. Seismic Damage Abstractions for TSPA Compliance Case. Submittal date: 09/21/2007.
- 181613 MO0706SPAFEPLA.001. FY 2007 LA FEP List and Screening. Submittal date: 06/20/2007.

- 168761 SN0310T0505503.004. Initial Radionuclide Inventories for TSPA-LA. Submittal date: 10/27/2003.
- 169129 SN0404T0503102.011. Thermal Conductivity of the Potential Repository Horizon Rev 3. Submittal date: 04/27/2004.
- 182215 SN0508T0507703.020. Calculations Supporting an Alternative Conceptual Model for Sorption of Pu onto In-Package Corrosion Products, for ANL-WIS-PA-000001 REV 02, EBS Radionuclide Transport Abstraction. Submittal Date: 08/11/2005.

9.4 OUTPUT DATA, LISTED BY DATA TRACKING NUMBER

SN0703PAEBSRTA.001. Inputs Used in the Engineered Barrier System (EBS) Radionuclide Transport Abstraction. Submittal date: 03/09/2007.

SN0703PAEBSRTA.002. Surface Complexation Modeling Results, Actinide Kd Abstractions and pH Abstraction. Submittal date: 03/13/2007.

9.5 SOFTWARE CODES

- 174650 GoldSim V. 8.02.500. 2005. WINDOWS 2000. STN: 10344-8.02-05.
- 181903 GoldSim V. 9.60.100. 2007. WIN 2000, 2003, XP. STN: 10344-9.60-01.
- 175698 PHREEQC V. 2.11. 2006. WINDOWS 2000. STN: 10068-2.11-00.
- 146654 T2R3D V. 1.4. 1999. UNIX, WINDOWS 95/98NT 4.0. STN: 10006-1.4-00.
- 161491 TOUGH2 V. 1.6. 2003. DOS Emulation (win95/98), SUN OS 5.5.1., OSF1 V4.0. STN: 10007-1.6-01.

APPENDIX A
NOTATION

APPENDIX A — NOTATION

Notation

Variable	Definition	Units	Where First Used
A	Cross-sectional area of diffusive or flow pathway	m ²	Eq. 6.3.4.1.1-4
A_f	Diffusive area of UZ fracture cell	m ²	Eq. 6.5.2.5-21
A_g	Surface area of crushed tuff granule	m ²	Section 6.6.3.1
A_I	Invert cross-sectional area (circle segment)	m ²	Eq. 6.5.2.3-2
A_I	Diffusive area of single-continuum invert cell	m ²	Eq. 6.5.1.2-51
A_{Is}	Intercepted flow area of a drift over the length of one waste package	m ²	Eq. 6.5.2.3-12
$A_{I/UZ}$	Diffusive area between invert and UZ cells	m ²	Eq. 6.5.2.3-4
A_m	Diffusive area of UZ matrix cell	m ²	Eq. 6.5.2.5-21
A_{mf}	Diffusive area normal to transport in the matrix/fracture domain	m ²	Eq. 6.5.1.2-52
$A_{SCC,DS}$	Total SCC opening area per drip shield	m ²	Eq. 6.3.3.2.4-7
$A_{SCC,WP}$	Total SCC opening area per waste package	m ²	Eq. 6.3.3.2.4-8
$A_{SD,DS}$	Seismically damaged area in drip shield	m ²	Eq. 6.3.3.2.4-7
$A_{SD,WP}$	Seismically damaged area in waste package	m ²	Eq. 6.3.3.2.4-8
A_{scc}	Cross-sectional area of stress corrosion crack	m ²	Eq. 6.3.3.2.2-2
$A_{scc,eff}$	Effective cross-sectional area of stress corrosion crack	m ²	Section 6.6.2
A_{UZ}	Projected area of UZ normal to vertical flux	m ²	Eq. 6.5.2.6-1
A_w	Cross-sectional area of water molecule	m ²	Eq. 6.3.4.3.2-4
a	Fitting parameter	m ⁻¹	Eq. 6.3.4.3.1-3
a	Constant in equation for binary diffusion coefficient	dimensionless	Eq. 6.6.2-9
a	Empirical parameter in Archie's law	dimensionless	Eq. 6.3.4.1.1-1
a	Slope of linear regression line	dimensionless	Section 6.3.4.6.1
a_g	Effective length of tuff granule matrix pore system	m	Section 6.6.3.1
a_0	Fitting parameter	Pa	Eq. 6.3.4.3.1-1
b	Maximum SCC width	m	Fig. 6.3-1; Eq. 6.3.3.2.2-1
b	Exponent in equation for binary diffusion coefficient	dimensionless	Eq. 6.6.2-9
b	Fitting parameter	Pa K ⁻¹	Eq. 6.3.4.3.1-1
b	Intercept of linear regression line	dimensionless	Section 6.3.4.6.1
b	Slope of the $\ln \psi$ versus $\ln \theta$ curve	dimensionless	Eq. 6.6.4.1-2

Notation (Continued)

Variable	Definition	Units	Where First Used
C_c	Substrate load in solution	g L^{-1}	Eq. 6.6.6.1-1
C_{cFeO}	Concentration of mobile iron oxyhydroxide (FeO) colloids	kg m^{-3}	Eq. 6.5.1.2-16
C_{cGW}	Concentration of mobile groundwater (GW) colloids	kg m^{-3}	Eq. 6.5.1.2-16
C_{cWF}	Concentration of mobile waste form colloids	kg m^{-3}	Eq. 6.5.1.2-16
C_i	Concentration of radionuclide species i	kg m^{-3}	Eq. 6.3.4.3.5-1
C_i^{embed}	Concentration of radionuclide species i embedded on waste form colloids	kg m^{-3}	Eq. 6.5.1.2-38
C_i^P	Concentration of parent of radionuclide species i	kg m^{-3}	Eq. 6.5.1.2-10
$C_i^{P,embed}$	Concentration of parent of radionuclide species i embedded on waste form colloids	kg m^{-3}	Eq. 6.5.1.2-38
C_{iA}, C_{iB}	Concentration of radionuclide species i in cells A and B	kg m^{-3}	Eq. 6.5.2.5-5
$C_{A/B}$	Concentration of radionuclide species i at the interface between cells A and B	kg m^{-3}	Eq. 6.5.2.5-5
C_{iCP}	Concentration of dissolved radionuclide species i in corrosion products domain or cell	kg m^{-3}	Eq. 6.6.3-1
C_{iI}	Concentration of radionuclide species i in the single-continuum invert cell	kg m^{-3}	Eq. 6.5.1.2-51
$C_{iI/UZ}$	Concentration of radionuclide species i at the interface between the invert and UZ cells	kg m^{-3}	Eq. 6.5.2.5-11
C_{if}	Concentration of radionuclide species i in the UZ fracture cell	kg m^{-3}	Eq. 6.5.1.2-53
C_{im}	Concentration of radionuclide species i in the UZ matrix cell	kg m^{-3}	Eq. 6.5.1.2-52
$C_{i,new}$	"New" input concentration of radionuclide species i	kg m^{-3}	Eq. 6.6.1.2.1-1
$C_{i,old}$	"Old" input concentration of radionuclide species i	kg m^{-3}	Eq. 6.6.1.2.1-1
C_{icFeO}	Concentration of radionuclide species i sorbed onto mobile iron oxyhydroxide (FeO) colloids	kg m^{-3}	Eq. 6.5.1.2-16
\hat{C}_{icFeO}	Concentration of radionuclide species i kinetically adsorbed onto mobile iron oxyhydroxide (FeO) colloids	kg m^{-3}	Eq. 6.5.1.2-30
\hat{C}_{icFeO}^P	Concentration of parent of radionuclide species i kinetically sorbed onto mobile iron oxyhydroxide (FeO) colloids	kg m^{-3}	Eq. 6.5.1.2-30
C_{icGW}	Concentration of radionuclide species i sorbed onto mobile groundwater (GW) colloids	kg m^{-3}	Eq. 6.5.1.2-16
\hat{C}_{iCP}	Concentration of radionuclide species i kinetically sorbed onto iron oxyhydroxide corrosion products	kg m^{-3}	Eq. 6.5.1.2-15
$C_{iCP/invint}$	Concentration of radionuclide species i at the interface between the corrosion products and invert cells	kg m^{-3}	Eq. 6.5.3.5-7
C_{icWF}	Concentration of radionuclide species i sorbed onto mobile waste form colloids	kg m^{-3}	Eq. 6.5.1.2-16
C_{iinter}	Concentration of dissolved radionuclide species i in invert intergranular continuum	kg m^{-3}	Eq. 6.6.3-2

Notation (Continued)

Variable	Definition	Units	Where First Used
$C_{i\text{intra}}$	Concentration of dissolved radionuclide species i in invert intragranular continuum	kg m^{-3}	Eq. 6.6.3-3
$C_{i\text{cFeO}}^P$	Concentration of parent of radionuclide species i sorbed onto mobile iron oxyhydroxide (FeOx) colloids	kg m^{-3}	Eq. 6.5.1.2-16
$C_{i\text{cGW}}^P$	Concentration of parent of radionuclide species i sorbed onto mobile (GW) colloids	kg m^{-3}	Eq. 6.5.1.2-16
$\hat{C}_{i\text{cP}}^P$	Concentration of parent of radionuclide species i kinetically sorbed onto stationary iron oxyhydroxide corrosion products	kg m^{-3}	Eq. 6.5.1.2-32
$C_{i\text{cWF}}^P$	Concentration of parent of radionuclide species i sorbed onto mobile waste form colloids	kg m^{-3}	Eq. 6.5.1.2-16
C_{SD}	Uncertainty factor for seismic damage	dimensionless	Eq. 6.3.3.2.4-5
C_{si}	Maximum concentration (solubility limit) of radionuclide species i	kg m^{-3}	Eq. 6.6.1.1.2-1
$C_{si,\text{new}}$	Maximum concentration (solubility limit) of radionuclide species i in "new" chemistry	kg m^{-3}	Eq. 6.6.1.2.2-9
$C_{si,\text{old}}$	Maximum concentration (solubility limit) of radionuclide species i in "old" chemistry	kg m^{-3}	Eq. 6.6.1.2.2-9
C_1, C_2	Integration constants	dimensionless	Eq. 6.6.2-14
c	Molar density	mol m^{-3}	Eq. 6.6.2-10
c	Thickness of wall in SCC model	m	Fig. 6.3-3; Eq. 6.3.3.2.2-1
c_i	Concentration of radionuclide species i	mol m^{-1}	Eq. 6.3.4.1.1-10
D	Diffusion coefficient	$\text{m}^2 \text{s}^{-1}$	Eq. 6.6.4.1-1
D_{AB}	Binary diffusion coefficient	$\text{m}^2 \text{s}^{-1}$	Eq. 6.6.2-9
D_B	Diffusion coefficient for Brownian motion	$\text{m}^2 \text{s}^{-1}$	Eq. 6.5.1.2-36
D_c	Colloid dispersion or diffusion coefficient	$\text{m}^2 \text{s}^{-1}$	Eq. 6.5.1.2-17
\hat{D}_c	Effective diffusive conductance of radionuclide species i	$\text{m}^3 \text{s}^{-1}$	Eq. 6.6.3.2-26
$D_{c_A/B}$	Interface diffusive conductance of radionuclide species i between cell A and cell B	$\text{m}^3 \text{s}^{-1}$	Eq. 6.5.2.5-6
$D_{c_B/C}$	Interface diffusive conductance of radionuclide species i between cell B and cell C	$\text{m}^3 \text{s}^{-1}$	Eq. 6.5.2.5-8
D_{coll}	Colloid diffusion coefficient	$\text{m}^2 \text{s}^{-1}$	Eq. 6.3.4.4-1
D_{CP}	Diffusion coefficient of radionuclide species i in corrosion products domain	$\text{m}^2 \text{s}^{-1}$	Eq. 6.6.3-1
\hat{D}_{CP}	Diffusive conductance of radionuclide species i in corrosion products cell	$\text{m}^3 \text{s}^{-1}$	Eq. 6.6.3.2-1
$\hat{D}_{CP/CP-int}$	Diffusive conductance of radionuclide species i between corrosion products cell and corrosion products interface cell	$\text{m}^3 \text{s}^{-1}$	Eq. 6.6.3.2-15
$\hat{D}_{CP-int/inter}$	Diffusive conductance of radionuclide species i between corrosion products interface cell and invert intergranular cell	$\text{m}^3 \text{s}^{-1}$	Eq. 6.6.3.2-16
$\hat{D}_{CP-int/intra}$	Diffusive conductance of radionuclide species i between corrosion products interface cell and invert intragranular cell	$\text{m}^3 \text{s}^{-1}$	Eq. 6.6.3.2-17

Notation (Continued)

Variable	Definition	Units	Where First Used
$\hat{D}_{CP/inter}$	Effective diffusive conductance of radionuclide species i between corrosion products cell and invert intergranular cell	$m^3 s^{-1}$	Eq. 6.6.3.2-8
$\hat{D}_{CP/intra}$	Effective diffusive conductance of radionuclide species i between corrosion products cell and invert intragranular cell	$m^3 s^{-1}$	Eq. 6.6.3.2-9
\mathbf{D}_{di}	Mechanical dispersivity tensor of radionuclide species i	$m^2 s^{-1}$	Eq. 6.5.1.2-6
$\hat{D}_{intra/inter}$	Effective diffusive conductance of radionuclide species i between intragranular and invert intergranular cells	$m^3 s^{-1}$	Eq. 6.6.3.2-10
D_f	Effective diffusion coefficient of radionuclide species i within the UZ fracture cell	$m^2 s^{-1}$	Eq. 6.5.2.5-14
\hat{D}_f	Diffusive conductance of radionuclide species i within the UZ fracture cell	$m^3 s^{-1}$	Eq. 6.5.2.5-14
\hat{D}_I	Diffusive conductance of radionuclide species i within the invert cell	$m^3 s^{-1}$	Eq. 6.5.2.5-13
D_{iI}	Effective diffusion coefficient of radionuclide species i within the invert cell	$m^2 s^{-1}$	Eq. 6.3.4.1.1-16
\hat{D}_{If}	Effective diffusive conductance of radionuclide species i between invert cell and UZ fracture cell	$m^3 s^{-1}$	Eq. 6.5.2.5-20
\hat{D}_{Im}	Effective diffusive conductance of radionuclide species i between invert cell and UZ matrix cell	$m^3 s^{-1}$	Eq. 6.5.2.5-20
$\hat{D}_{I/I-int}$	Diffusive conductance of radionuclide species i between the invert cell and the invert interface cell	$m^3 s^{-1}$	Eq. 6.5.2.5-27
$\hat{D}_{I-int/f}$	Diffusive conductance of radionuclide species i between the invert interface cell and the UZ fracture cell	$m^3 s^{-1}$	Eq. 6.5.2.5-28
$\hat{D}_{I-int/m}$	Diffusive conductance of radionuclide species i between the invert interface cell and the UZ matrix cell	$m^3 s^{-1}$	Eq. 6.5.2.5-29
D_i	Diffusion coefficient of radionuclide species i	$m^2 s^{-1}$	Eq. 6.3.4.1.1-10
\mathbf{D}_i	Hydrodynamic dispersion tensor of radionuclide species i	$m^2 s^{-1}$	Eq. 6.5.1.2-4
D_{ie}	Effective diffusion coefficient of the interface between two continua for radionuclide species i	$m^2 s^{-1}$	Eq. 6.5.1.2-24
D_{if}	Effective diffusion coefficient of radionuclide species i of the UZ fracture continuum	$m^2 s^{-1}$	Eq. 6.5.1.2-53
D_{im}	Effective diffusion coefficient of radionuclide species i of the UZ matrix continuum	$m^2 s^{-1}$	Eq. 6.5.1.2-52
D_{inter}	Diffusion coefficient of radionuclide species i for invert intergranular continuum	$m^2 s^{-1}$	Eq. 6.6.3-2
\hat{D}_{inter}	Diffusive conductance of radionuclide species i in invert intergranular cell	$m^3 s^{-1}$	Eq. 6.6.3.2-2
$\hat{D}_{inter/inter-int}$	Diffusive conductance of radionuclide species i between the invert intergranular cell and the invert intergranular interface cell	$m^3 s^{-1}$	Eq. 6.6.3.2-19
$\hat{D}_{intra-int/UZm}$	Diffusive conductance of radionuclide species i between the invert intergranular cell and the invert intragranular interface cell	$m^3 s^{-1}$	Eq. 6.6.3.2-21

Notation (Continued)

Variable	Definition	Units	Where First Used
$\hat{D}_{intra-int/UZf}$	Diffusive conductance of radionuclide species i between the invert intergranular cell and the UZ fracture cell	$m^3 s^{-1}$	Eq. 6.6.3.2-22
D_{intra}	Diffusion coefficient of radionuclide species i for invert intragranular continuum	$m^2 s^{-1}$	Eq. 6.6.3-3
\hat{D}_{intra}	Diffusive conductance of radionuclide species i in invert intragranular cell	$m^3 s^{-1}$	Eq. 6.6.3.2-3
$\hat{D}_{intra/intra-int}$	Diffusive conductance of radionuclide species i between the invert intragranular cell and the UZ matrix cell	$m^3 s^{-1}$	Eq. 6.6.3.2-20
$\hat{D}_{inter-int/UZm}$	Diffusive conductance of radionuclide species i between the invert intragranular cell and the invert intragranular interface cell	$m^3 s^{-1}$	Eq. 6.6.3.2-23
$\hat{D}_{inter-int/UZf}$	Diffusive conductance of radionuclide species i between the invert intragranular cell and the UZ fracture cell	$m^3 s^{-1}$	Eq. 6.6.3.2-24
D_m	Mean binary diffusion coefficient for water vapor and oxygen	$m^3 s^{-1}$	Eq. 6.6.2-10
\hat{D}_m	Diffusive conductance of radionuclide species i within the UZ matrix cell	$m^3 s^{-1}$	Eq. 6.5.2.5-13
\hat{D}_{mf}	Effective diffusive conductance of radionuclide species i between UZ fracture and matrix cells	$m^3 s^{-1}$	Eq. 6.5.2.5-22
D_{limit}	Diffusion coefficient measurement limit	$m^2 s^{-1}$	Eq. 6.6.4.2-5
D_{MD}	Mechanical dispersion coefficient	$m^2 s^{-1}$	Eq. 6.5.1.2-36
D_{mi}	Molecular diffusion coefficient of species i	$m^2 s^{-1}$	Eq. 6.5.1.2-6
D_{ms}	Diffusion coefficient for saturated tuff matrix	$m^2 s^{-1}$	Eq. 6.6.4.2-4
D_{si}	Effective diffusion coefficient	$m^2 s^{-1}$	Eq. 6.3.4.3.5-1
$D_{s,rind}$	Diffusion coefficient for CSNF degradation rind	$m^2 s^{-1}$	Eq. 6.3.4.6.1-5
D_T	Diffusion coefficient at temperature T	$m^2 s^{-1}$	Eq. 6.3.4.1.2-1
D_{T_0}	Diffusion coefficient at temperature T_0	$m^2 s^{-1}$	Eq. 6.3.4.1.2-1
D_{WF}	Diffusion coefficient in waste form domain	$m^2 s^{-1}$	Table 8.2-1
D_w	Diffusion coefficient of an ion in solution at infinite dilution	$m^2 s^{-1}$	Eq. 6.3.4.1.1-6
D_{wi}	Diffusion coefficient of i^{th} ion in dilute aqueous solution	$m^2 s^{-1}$	Eq. 6.3.4.1.1-10
d	Characteristic length of the tuff matrix structure	m	Eq. 6.5.1.2-24
d_{coll}	Diameter of colloid particle	m	Eq. 6.3.4.4-1
d_D	Diameter of drift	m	Eq. 6.5.2.6-1
d_g	Geometric particle diameter	mm	Eq. 6.6.4.1-3
E	Modulus of elasticity	Pa	Eq. 6.3.3.2.2-1
E_{DS}	Modulus of elasticity of drip shield material	Pa	Eq. 6.3.3.2.4-7

Notation (Continued)

Variable	Definition	Units	Where First Used
E_{WP}	Modulus of elasticity of waste package material	Pa	Eq. 6.3.3.2.4-8
$E(x)$	Expected value	mL g^{-1}	Table 8.2-4
F	Faraday constant	C mol^{-1}	Eq. 6.3.4.1.1.-6
F	Fraction of seepage flux onto drip shield or waste package that flows into a breach	dimensionless	Eq. 6.5.1.1.2.1-7
$F_{A/B}$, $F_{B/C}$	Diffusion rate across cell A and B interface and across cell B and C interface	kg s^{-1}	Eq. 6.5.2.5-4
F_{alt}	Radionuclide release rate from waste package in alternative patch geometry model	kg s^{-1}	Eq. 6.6.1.2.3-2
F_{iCP}	Diffusive flux of radionuclide species i in corrosion products cell	kg s^{-1}	Eq. 6.6.3.2-1
F_{if}	Diffusive fluxes of radionuclide species i within the UZ fracture cell	kg s^{-1}	Eq. 6.5.2.5-12
F_{il}	Diffusive fluxes of radionuclide species i within the invert cell	kg s^{-1}	Eq. 6.5.2.5-11
F_{iinter}	Diffusive flux of radionuclide species i in invert intergranular cell	kg s^{-1}	Eq. 6.6.3.2-2
F_{iintra}	Diffusive flux of radionuclide species i in invert intragranular cell	kg s^{-1}	Eq. 6.6.3.2-3
F_{im}	Diffusive fluxes of radionuclide species i within the UZ matrix cell	kg s^{-1}	Eq. 6.5.2.5-13
F_j	Volumetric flow rate or flux of water in flow path j ($j = 1$ to 8)	$\text{m}^3 \text{s}^{-1}$	Section 6.3.1.1; Table 6.3-1; Eq. 6.5.1.1-5
F_{pri}	Radionuclide release rate from waste package in primary patch geometry model	kg s	Eq. 6.6.1.2.3-1
F_R	Formation factor	dimensionless	Section 6.3.4.1.1
F_w	Volumetric flow rate of water	$\text{m}^3 \text{s}^{-1}$	Eq. 6.5.1.1-4
F_w^m	Volumetric flow rate of water across bounding surfaces in the EBS by mass transfer	$\text{m}^3 \text{s}^{-1}$	Eq. 6.5.1.1-4
f	Theoretical fraction of dripping flux falling between two points that flows into a drip shield breach	dimensionless	Section 6.5.1.1.2.1
$f_{A\ell}$	Theoretical fraction of dripping flux falling between Points A and $-\ell$ that flows into a drip shield breach	dimensionless	Eq. 6.5.1.1.2.1-2
f_{Am}	Conversion factor for americium species, as applied in GoldSim	dimensionless	Eq. 6.5.2.7.2-9
f_{A-}	Theoretical fraction of dripping flux falling at Point $y < y_A$ that flows into a drip shield breach	dimensionless	Section 6.5.1.1.2.1
$f_{C\ell}$	Theoretical fraction of dripping flux falling between Points C and $+\ell$ that flows into a drip shield breach	dimensionless	Eq. 6.5.1.1.2.1-5
f_c	Fraction of total kinetic sorption going to iron oxyhydroxide colloids	dimensionless	Eq. 6.5.2.7.2-12
f_{calc}	Calculated fraction of dripping flux that flows into a drip shield breach	dimensionless	Section 6.5.1.1.2.4
$f_{CS,n}$	Fraction of carbon steel in steel mass in domain n (remainder is stainless steel)	dimensionless	Eq. 6.5.2.2.1-4

Notation (Continued)

Variable	Definition	Units	Where First Used
f_{DS}	Uncertain drip shield flux splitting factor	dimensionless	Eq. 6.3.2.4-2
f'_{DS}	Sampled drip shield flux splitting factor that accounts for rivulet spread angle uncertainty	dimensionless	Table 6.3-1; Eq. 6.3.2.4-5
f_{D+}	Theoretical fraction of dripping flux falling at Point $y > y_D$ that flows into a drip shield breach	dimensionless	Section 6.5.1.1.2.1
f_{expt}	Experimentally measured fraction of dripping flux that flows into a drip shield breach	dimensionless	Section 6.5.1.1.2.4
f_{GHFO}	Placeholder variable, fraction of corrosion products as goethite or HFO	dimensionless	Eq. 6.5.2.2.1-4
f_{lB}	Theoretical fraction of dripping flux falling between Points $-l$ and B that flows into a drip shield breach	dimensionless	Eq. 6.5.1.1.2.1-3
f_{lD}	Theoretical fraction of dripping flux falling between Points $-l$ and D that flows into a drip shield breach	dimensionless	Eq. 6.5.1.1.2.1-6
f_{VD}	Model validation uncertain drip shield flux splitting factor	dimensionless	Eq. 7.1.1.1-1
f'_{VD}	Model validation sampled drip shield flux splitting factor that accounts for rivulet spread angle uncertainty	dimensionless	Eq. 7.1.1.1-3
f_{VW}	Model validation uncertain waste package flux splitting factor	dimensionless	Eq. 7.1.1.2-1
f'_{VW}	Model validation sampled waste package flux splitting factor that accounts for rivulet spread angle uncertainty	dimensionless	Eq. 7.1.1.2-3
f_{WP}	Uncertain waste package flux splitting factor	dimensionless	Eq. 6.3.3.2.5-1
f'_{WP}	Sampled waste package flux splitting factor	dimensionless	Table 6.3-1; Eq. 6.3.3.2-3
f_0	Theoretical fraction of dripping flux falling between Points B and C that flows into a drip shield breach	dimensionless	Eq. 6.5.1.1.2.1-4
G	Electrical conductance	S	Eq. 6.3.4.1.1-14
G_t	Conductance of bulk porous medium	S	Eq. 6.3.4.1.1-5
G_w	Conductance of water	S	Eq. 6.3.4.1.1-5
H_m	Absolute humidity of air	kg kg ⁻¹	Eq. 6.6.2-3
H_{mol}	Molal humidity of air	mol mol ⁻¹	Eq. 6.6.2-4
\mathbf{I}	Identity tensor	dimensionless	Eq. 6.5.1.2-6
I_s	Hydraulic head gradient in the invert	m m ⁻¹	Eq. 6.5.2.3-12
\mathbf{i}	Unit vector in the z-direction	dimensionless	Section 6.5.1.2
\mathbf{J}_{cB}	Mass flux of waste form colloids due to Brownian motion	kg m ⁻² s ⁻¹	Eq. 6.5.1.2-36
\mathbf{J}_{cMD}	Mass flux of waste form colloids due to mechanical dispersion	kg m ⁻² s ⁻¹	Eq. 6.5.1.2-36
\mathbf{J}_{cWF}	Mass flux of waste form colloids	kg m ⁻² s ⁻¹	Eq. 6.5.1.2-34
\mathbf{J}_i	Mass flux vector (mass specific discharge) of radionuclide species i	kg m ⁻² s ⁻¹	Eq. 6.5.1.2-1

Notation (Continued)

Variable	Definition	Units	Where First Used
J_{icFeO}	Total mass flux of mobile iron oxyhydroxide (FeO) colloids containing adsorbed radionuclide species i	$\text{kg m}^{-2} \text{s}^{-1}$	Eq. 6.5.1.2-16
$J_{icFeO}^{kinetic}$	Total mass flux of mobile iron oxyhydroxide (FeO) colloids containing kinetically sorbed radionuclide species i	$\text{kg m}^{-2} \text{s}^{-1}$	Eq. 6.5.1.2-30
J_{icGW}	Total mass flux of mobile GW colloids containing adsorbed radionuclide species i	$\text{kg m}^{-2} \text{s}^{-1}$	Eq. 6.5.1.2-16
J_{icWF}	Total mass flux of mobile waste form colloids containing adsorbed radionuclide species i	$\text{kg m}^{-2} \text{s}^{-1}$	Eq. 6.5.1.2-16
K	Solubility constant	dimensionless	Section 6.3.4.2.3
K_c	Distribution coefficient for the fast site	L g^{-1}	Eq. 6.6.6.1-1
K'_c	Distribution coefficient for the slow site	L g^{-1}	Eq. 6.6.6.1-2
K_d	Sorption distribution (or partition) coefficient	mL g^{-1}	Section 6.3.4.2
\bar{K}_d	Dimensionless distribution (or partition) coefficient of adsorbed radionuclide species i	dimensionless	Eq. 6.5.2.7.2-5
$K_{dc,Am,GW}$	Americium distribution coefficient for ground water colloids	$\text{m}^3 \text{kg}^{-1}$	Eq. 6.5.2.7.2-9
$K_{dc,Am,WF}$	Americium distribution coefficient for waste form colloids	$\text{m}^3 \text{kg}^{-1}$	Eq. 6.5.2.7.2-9
\bar{K}_{dic}	Dimensionless distribution (or partition) coefficient of colloids containing adsorbed radionuclide species i	dimensionless	Eq. 6.5.2.5-2
K_{dicFeO}	Sorption distribution (or partition) coefficient of iron oxyhydroxide colloids containing adsorbed radionuclide species i	mL g^{-1}	Eq. 6.5.1.2-16
K_{dicGW}	Sorption distribution (or partition) coefficient of groundwater colloids containing adsorbed radionuclide species i	mL g^{-1}	Eq. 6.5.1.2-16
K_{dicWF}	Sorption distribution (or partition) coefficient of waste form colloids containing adsorbed radionuclide species i	mL g^{-1}	Eq. 6.5.1.2-16
K_{dis}	Sorption distribution (or partition) coefficient of radionuclide species i	mL g^{-1}	Eq. 6.5.1.2-13
K_{dis}^p	Sorption distribution (or partition) coefficient of parent of radionuclide species i	mL g^{-1}	Eq. 6.5.1.2-13
K_{us}	Unsaturated hydraulic conductivity of invert	m s^{-1}	Eq. 6.5.2.3-12
k	Boltzmann constant	J K^{-1}	Eq. 6.3.4.4-1
k	Parameter in FHH adsorption isotherm	dimensionless	Eq. 6.3.4.3.2-1
k_{CP}	Parameter in FHH adsorption isotherm for steel corrosion products	dimensionless	Section 6.5.2.2.1
k_f	Forward rate constant for the fast site	hr^{-1}	Eq. 6.6.6.1-1
k_{HLWG}	Parameter in FHH adsorption isotherm for HLWG degradation rind	dimensionless	Eq. 6.3.4.6.1-1
k_{if}	Kinetic forward sorption rate constant for radionuclide species i	$\text{m}^3 \text{m}^{-2} \text{s}^{-1}$	Eq. 6.5.1.2-14

Notation (Continued)

Variable	Definition	Units	Where First Used
k_{ir}	Kinetic reverse sorption rate constant for radionuclide species i	$\text{m}^3 \text{m}^{-2} \text{s}^{-1}$	Eq. 6.5.1.2-14
k_m	Intrinsic permeability of saturated tuff matrix	m^2	Eq. 6.6.4.2-4
k_r	Reverse rate constant for the fast site	hr^{-1}	Eq. 6.6.6.1-1
k_{rind}	Parameter in FHH adsorption isotherm for CSNF degradation rind	dimensionless	Eq. 6.3.4.6.1-1
k_{rm}	Relative permeability of tuff matrix	dimensionless	Eq. 6.5.3.6-3
L	Length of porous medium	m	Eq. 6.3.4.1.1-4
L_A	Diffusive lengths from the cell centers to the cell interface within cell A	m	Eq. 6.5.2.5-5
L_B	Diffusive lengths from the cell centers to the cell interface within cell B	m	Eq. 6.5.2.5-5
L_{DS}	Axial length of drip shield	m	Table 6.3-1
L_{DS_Patch}	Axial half-length of each drip shield patch due to general corrosion	m	Table 6.3-1
L_f	Diffusive length within the UZ fracture cell	m	Eq. 6.5.2.5-12
L_I	Diffusive length within the invert cell	m	Eq. 6.5.2.5-11
L_{I-int}	Diffusive length of invert-to-UZ interface cell	m	Eq. 6.5.2.5-24
L_{inter}	Diffusive length within the invert intergranular cell	m	Eq. 6.6.3.2-2
L_{intra}	Diffusive length within the invert intragranular cell	m	Eq. 6.6.3.2-3
L_m	Diffusive length within the UZ matrix cell	m	Eq. 6.5.2.5-13
L_{UZ}	Diffusive length of the UZ fracture and matrix cells	m	Eq. 6.5.2.5-26
L_{WP}	Length of waste package	m	Table 6.3-1
L_{WP_Patch}	Axial half-length of each drip shield waste package due to general corrosion	m	Table 6.3-1
\bar{l}	Average ionic conductivity at infinite dilution	$\text{S m}^2 \text{equivalent}^{-1}$	Eq. 6.3.4.1.1-7
l_+^0, l_-^0	Cationic and anionic conductivity at infinite dilution	$\text{S m}^2 \text{equivalent}^{-1}$	Eq. 6.3.4.1.1-6
ℓ	One-half width of corrosion patch in drip shield	m	Eq. 6.3.2.4-2
ℓ_{WP}	One-half width of corrosion patch in waste package	m	Eq. 6.3.3.2.5-1
M_A, M_B	Molecular weights of components A and B	g mol^{-1}	Eq. 6.6.2-9
M_{CPm}	Molecular weight of corrosion product CPm	kg mol^{-1}	Eq. 6.5.2.2.1-3
M_{Cr}	Atomic weight of chromium	kg mol^{-1}	Eq. 6.5.2.2.1-4
M_{CrOx}	Molecular weight of Cr_2O_3	kg mol^{-1}	Eq. 6.5.2.2.1-4
M_{Fe}	Atomic weight of iron	kg mol^{-1}	Eq. 6.5.2.2.1-4
M_G	Molecular weight of goethite	kg mol^{-1}	Eq. 6.5.2.2.1-4

Notation (Continued)

Variable	Definition	Units	Where First Used
M_{HFO}	Molecular weight of HFO	kg mol ⁻¹	Eq. 6.5.2.2.1-4
M_m	Atomic weight of metal m in steel	kg mol ⁻¹	Eq. 6.5.2.2.1-4
M_{Ni}	Atomic weight of nickel	kg mol ⁻¹	Eq. 6.5.2.2.1-4
M_{NiO}	Molecular weight of NiO	kg mol ⁻¹	Eq. 6.5.2.2.1-4
M_w	Molecular weight of water	kg mol ⁻¹	Eq. 6.3.4.3.2-4
m	Exponent on porosity in Archie's law (cementation factor)	dimensionless	Eq. 6.3.4.1.1-1
m	Fitting parameter	dimensionless	Eq. 6.3.4.3.1-3
m	Van Genuchten m value	dimensionless	Eq. 6.5.2.3-14
m_{CP}	Mass of corrosion products inside waste package; function of time t	kg	Eq. 6.3.4.3.5-3
$m_{CPm,CS,CSN}$	Mass of corrosion product CPm in CSNF waste form domain from corrosion of carbon steel	kg	Eq. 6.5.2.2.2.1-4
$m_{CPm,CS,n}$	Mass of corrosion product CPm (goethite, HFO, NiO, and Cr ₂ O ₃) in each domain n from corrosion of carbon steel	kg	Eq. 6.5.2.2.1-3
$m_{CPm,SS,CSN}$	Mass of corrosion product CPm CSNF waste form domain from corrosion of stainless steel	kg	Eq. 6.5.2.2.2.1-4
$m_{CPm,SS,n}$	Mass of corrosion product CPm (goethite, HFO, NiO, and Cr ₂ O ₃) in each domain n from corrosion of stainless steel	kg	Eq. 6.5.2.2.1-3
$m_{CrOx,n,CS}$	mass of Cr ₂ O ₃ in domain n from corrosion of carbon steel	kg	Eq. 6.5.2.2.1-4
$m_{CrOx,n,SS}$	mass of Cr ₂ O ₃ in domain n from corrosion of stainless steel	kg	Eq. 6.5.2.2.1-4
m_{cGW}	Mass of ground water colloids in the corrosion products	kg	Eq. 6.5.2.7.2-9
m_{cWF}	Mass of waste form colloids in the corrosion products cell	kg	Eq. 6.5.2.7.2-9
$m_{G,n,CS}$	Mass of goethite in domain n from corrosion of carbon steel	kg	Eq. 6.5.2.2.1-4
$m_{G,n,SS}$	Mass of goethite in domain n from corrosion of stainless steel	kg	Eq. 6.5.2.2.1-4
$m_{HFO,n,CS}$	Mass of HFO in domain n from corrosion of carbon steel	kg	Eq. 6.5.2.2.1-4
$m_{HFO,n,SS}$	Mass of HFO in domain n from corrosion of stainless steel	kg	Eq. 6.5.2.2.1-4
$m_{NiO,n,CS}$	Mass of NiO in domain n from corrosion of carbon steel	kg	Eq. 6.5.2.2.1-4
$m_{NiO,n,SS}$	Mass of NiO in domain n from corrosion of stainless steel	kg	Eq. 6.5.2.2.1-4
m_i	Mass of radionuclide species i in waste package	kg	Eq. 6.6.1.1.1-2
\dot{m}_i	Rate of release of radionuclide species i into water in waste package	kg s ⁻¹	Eq. 6.6.1.1.1-1
$m_{s,n}$	Total mass of steel in domain n	kg	Eq. 6.5.2.2.1-4

Notation (Continued)

Variable	Definition	Units	Where First Used
m_w	Instantaneous total mass of water within the walls of a drift	kg	Eq. 6.5.1.1-1
N	Factor by which maximum fluoride concentration uncertainty is normalized for pH	dimensionless	Eq. 6.5.2.4.1-1
N_A	Avogadro's number	molecules mol ⁻¹	Eq. 6.3.4.2.3.1-1
N_A, N_C	Molar diffusive flux of water vapor (A) and oxygen (B)	mol m ⁻² s ⁻¹	Eq. 6.6.2-10
N_b	Number of breaches (corrosion patches) in drip shield	dimensionless	Eq. 6.3.2.4-2
N_{bDS}	Number of breaches (corrosion patches) in drip shield	dimensionless	Table 6.3-1
N_{bWP}	Number of breaches (corrosion patches) in waste package	dimensionless	Table 6.3-1
N_c	Number of breaches (corrosion patches) on crown of drip shield	dimensionless	Eq. 6.5.1.1.1-1
N_{cw_SCC}	Maximum number of through-wall radial cracks in closure-weld region	dimensionless	Eq. 6.3.3.2.3-1
ND	Normal distribution	dimensionless	Eq. 6.3.4.1.1-22
$N_{S,G}$	Sorption site density for goethite	sites nm ⁻²	Eq. 6.3.4.2.3.1-1
$N_{S,HFO}$	Sorption site density for HFO	sites nm ⁻²	Eq. 6.3.4.2.3.1-1
n	Fitting parameter	dimensionless	Eq. 6.3.4.3.1-3
n	Exponent on saturation or water content in power law dependence of diffusion coefficient (e.g., Archie's law)	dimensionless	Eq. 6.3.4.1.1-2
n	Number of standard deviations	dimensionless	Section 6.3.4.6.1
n	Time step number	dimensionless	Eq. 6.5.2.5-1
\mathbf{n}	Unit vector in the direction of the flow path	dimensionless	Eq. 6.5.1.2-5
n	Van Genuchten n value	dimensionless	Eq. 6.5.2.3-14
P	Pressure	Pa	Fig. 6.3-8
P_{CO_2}	Partial pressure of CO ₂	Pa	Section 6.3.4.2.3
P_{O_2}	Partial pressure of O ₂	Pa	Section 6.5.2.4.2
P_0	Vapor pressure of water	Pa	Fig. 6.3-8
p	Slope of the model function	dimensionless	Eq. 6.6.4.2-6
p	Total pressure	atm	Eq. 6.6.2-9
P_{cA}, P_{cB}	Critical pressure of components A and B	atm	Eq. 6.6.2-9
P_w	Partial pressure of water	Pa	Eq. 6.3.4.3.2-1
p_w^o	Vapor pressure of water	Pa	Eq. 6.3.4.3.2-1
$Q_{adv/diff}^{wfc}$	Total mass flux (combined advective and diffusive mass flux) of waste form colloids per unit bulk volume	kg m ⁻³ s ⁻¹	Eq. 6.5.2.5-10
Q_{cWF}	Net rate of waste form colloid capture on the solid surface	kg m ⁻³ s ⁻¹	Eq. 6.5.1.2-33

Notation (Continued)

Variable	Definition	Units	Where First Used
Q_{cWF}^{int}	Net rate of waste form colloid capture at the air-water interface	$\text{kg m}^{-3} \text{s}^{-1}$	Eq. 6.5.1.2-33
Q_{cWFfg}	Net rate of waste form colloid removal from suspension by means of physical filtering (pore clogging, sieving, and straining) and by gravitational settling	$\text{kg m}^{-3} \text{s}^{-1}$	Eq. 6.5.1.2-33
Q_{cWFmt}	Net rate of interface transfer of waste form colloidal mass between the continua in the dual continuum invert	$\text{kg m}^{-3} \text{s}^{-1}$	Eq. 6.5.1.2-33
Q_{cWFs}	Net rate of waste form colloid formation	$\text{kg m}^{-3} \text{s}^{-1}$	Eq. 6.5.1.2-33
Q_I	Volumetric discharge into the invert	$\text{m}^3 \text{s}^{-1}$	Eq. 6.5.2.3-12
Q_i^m	Net rate of various mass transfer process involving radionuclide species i	$\text{kg m}^{-3} \text{s}^{-1}$	Eq. 6.5.1.2-1
$Q_{iaq}^{kinetic}$	Rate of desorption from stationary iron oxyhydroxide corrosion products to solution	$\text{kg m}^{-3} \text{s}^{-1}$	Eq. 6.5.1.2-8
Q_{icc}	Net rate of sorption of radionuclide species i onto immobile colloid surfaces captured by the solid matrix	$\text{kg m}^{-3} \text{s}^{-1}$	Eq. 6.5.1.2-8
Q_{icc}^{int}	Net rate of sorption of radionuclide species i onto immobile colloid surfaces captured by the air-water interface	$\text{kg m}^{-3} \text{s}^{-1}$	Eq. 6.5.1.2-8
Q_{icm}^{embed}	Rate of mass conversion from dissolved state to embedded state onto waste form colloids for radionuclide species i	$\text{kg m}^{-3} \text{s}^{-1}$	Eq. 6.5.1.2-8
$Q_{icm}^{kinetic}$	Rate of kinetic sorption of radionuclide species i onto mobile colloid surfaces	$\text{kg m}^{-3} \text{s}^{-1}$	Eq. 6.5.1.2-8
Q_{icm}^{rev}	Net rate of reversible sorption of radionuclide species i onto mobile colloid surfaces	$\text{kg m}^{-3} \text{s}^{-1}$	Eq. 6.5.1.2-8
Q_{idp}	Rate of dissolution or precipitation of radionuclide species i	$\text{kg m}^{-3} \text{s}^{-1}$	Eq. 6.5.1.2-8
Q_{imt}	Net rate of interface transfer of dissolved mass between the continua in the dual continuum invert	$\text{kg m}^{-3} \text{s}^{-1}$	Eq. 6.5.1.2-8
$Q_{is}^{kinetic}$	Rate of kinetic sorption of radionuclide species i onto the solid matrix	$\text{kg m}^{-3} \text{s}^{-1}$	Eq. 6.5.1.2-8
Q_{is}^{rev}	Net rate of reversible sorption of radionuclide species i onto the solid matrix	$\text{kg m}^{-3} \text{s}^{-1}$	Eq. 6.5.1.2-8
Q_{wz}	Advective water flow per unit bulk volume	$\text{m}^3 \text{m}^{-3} \text{yr}^{-1}$	Eq. 6.5.2.5-3
q_i	Rate of diffusion of radionuclide species i	kg s^{-1}	Eq. 6.3.4.3.5-1
q_{in}	Rate of water flow into waste package	$\text{m}^3 \text{s}^{-1}$	Section 6.6.1.1.1
$q_{in,new}$	"New" rate of water flow into waste package	$\text{m}^3 \text{s}^{-1}$	Section 6.6.1.2.1
$q_{in,old}$	"Old" rate of water flow into waste package	$\text{m}^3 \text{s}^{-1}$	Section 6.6.1.2.1
q_{out}	Rate of water flow out of waste package	$\text{m}^3 \text{s}^{-1}$	Section 6.6.1.1.1
$q_{out,new}$	"New" rate of water flow out of waste package	$\text{m}^3 \text{s}^{-1}$	Section 6.6.1.2.1
q_{wz}	Scalar specific discharge (Darcy velocity) of water in the downward +z-direction	m s^{-1}	Eq. 6.5.1.2-47

Notation (Continued)

Variable	Definition	Units	Where First Used
q_w	Specific discharge vector (Darcy velocity) of water	m s^{-1}	Eq. 6.5.1.2-4
R	Radius of waste package	m	Eq. 6.3.3.2.3-1
R	Universal gas constant	$\text{J mol}^{-1} \text{K}^{-1}$	Eq. 6.3.4.1.1-6
R^{max}	Maximum ratio of dissolved concentration to the mean solubility	dimensionless	Eq. 6.5.2.4.1-3
R^2	Coefficient of determination	dimensionless	Figure 6.3-4
R_A	Particle radius	m	Table 4.1-9
R_b	Resistance of a porous medium in Rhoades et al. 1976 [DIRS 173835], Equation 11	Ω	Section 6.3.4.1.1
R_f	Retardation factor	dimensionless	Eq. 6.6.5-1
R_{fc}	^{243}Am conversion rate to kinetically sorbed to iron oxyhydroxide colloids	yr^{-1}	Eq. 6.5.2.7.2-1
R_{fcp}	^{243}Am conversion rate to kinetically sorbed to iron oxyhydroxide corrosion products	yr^{-1}	Eq. 6.5.2.7.2-1
R_{fi}	Retardation factor for radionuclide species i	dimensionless	Eq. 6.5.1.2-39
R_{fi}^p	Retardation factor for parent of radionuclide species i	dimensionless	Eq. 6.5.1.2-39
R_{rerp}	Reverse desorption rate for the $\text{lfc}p^{243}\text{Am}$ species	yr^{-1}	Eq. 6.5.2.7.2-25
RH	Relative humidity	kg kg^{-1}	Section 6.3.4.3.1
R_t	Resistance of a porous medium	Ω	Eq. 6.3.4.1.1-4
r_{CS}	Rate of corrosion of carbon steel	$\mu\text{m yr}^{-1}$	Eq. 6.5.2.2.1-1
r_D	Drift radius	m	Eq. 6.5.2.3-1
r_{Mi}^p	Ratio of the mass of radionuclide species i produced by decay of the parent species to the mass of the parent species lost by decay	kg kg^{-1}	Eq. 6.5.1.2-10
r_{SS}	Rate of corrosion of stainless steel	$\mu\text{m yr}^{-1}$	Eq. 6.5.2.2.1-2
r_s	Dissolution rate of the waste form	kg s^{-1}	Eq. 6.6.1.1.1-1
r_w	Rate of production of water by chemical reactions	kg s^{-1}	Eq. 6.5.1.1-1
S	Logarithm of actinide solubility	dimensionless	Eq. 6.5.2.4.1-1
S_{ef}	Effective UZ fracture saturation	$\text{m}^3 \text{m}^{-3}$	Eq. 6.5.2.6-2
S_w	Water saturation	$\text{m}^3 \text{m}^{-3}$	Eq. 6.3.4.1.1-2
$S_{we,CP}$	Effective water saturation within a corrosion patch or corrosion products	$\text{m}^3 \text{m}^{-3}$	Eq. 6.3.4.3.5-5
$S_{we,CP,n}$	Effective water saturation in all corrosion products CPm in domain n	$\text{m}^3 \text{m}^{-3}$	Eq. 6.5.2.2.1-12
$S_{we,CPm,n}$	Effective water saturation in corrosion products CPm in domain n	$\text{m}^3 \text{m}^{-3}$	Eq. 6.5.2.2.1-6
$S_{we,CSNF}$	Effective water saturation of CSNF waste form domain	$\text{m}^3 \text{m}^{-3}$	Eq. 6.5.2.2.2.1-8

Notation (Continued)

Variable	Definition	Units	Where First Used
$S_{we,DSNF}$	Effective water saturation of DSNF waste form subdomain	$m^3 m^{-3}$	Eq. 6.5.2.2.2.1-21
$S_{we,HLWG}$	Effective water saturation of HLWG waste form subdomain	$m^3 m^{-3}$	Eq. 6.5.2.2.2.1-16
$S_{we,rind}$	Effective water saturation of CSNF degradation rind	$m^3 m^{-3}$	Eq. 6.3.4.6.1-4
S_{w_CP}	Water saturation in corrosion products domain	$m^3 m^{-3}$	Eq. 6.6.3-1
S_{wf}	UZ fracture water saturation	$m^3 m^{-3}$	Eq. 6.5.2.6-2
S_{wfr}	UZ fracture residual water saturation	$m^3 m^{-3}$	Eq. 6.5.2.6-2
S_{w_inter}	Water saturation in invert intergranular continuum	$m^3 m^{-3}$	Eq. 6.6.3-2
S_{w_intra}	Water saturation in invert intragranular continuum	$m^3 m^{-3}$	Eq. 6.5.1.2-22
s	Exponent in FHH adsorption isotherm	dimensionless	Eq. 6.3.4.3.2-1
S_{CP}	Surface area of corrosion products	m^2	Eq. 6.3.4.3.5-3
\bar{s}_{cFeO}	Specific surface area of mobile iron oxyhydroxide colloids	$m^2 g^{-1}$	Eq. 6.5.1.2-20
\bar{s}_{CP}	Specific surface area of corrosion products	$m^2 kg^{-1}$	Eq. 6.3.4.3.5-3
$\bar{s}_{CPm,n}$	Specific surface area of corrosion products CPm in domain n	$m^2 kg^{-1}$	Eq. 6.5.2.2.1-6
\bar{s}_G	Specific surface area of goethite	$m^2 g^{-1}$	Eq. 6.3.4.2.3.1-1
$\bar{s}_{Goethite}$	Specific surface area of goethite	$m^2 g^{-1}$	Section 6.3.4.3
\bar{s}_{HFO}	Specific surface area of HFO	$m^2 g^{-1}$	Eq. 6.3.4.2.3.1-1
S_{HLWG}	Exponent in FHH adsorption isotherm for HLWG degradation rind	dimensionless	Eq. 6.3.4.6.2-1
\bar{s}_{HLWG}	Specific surface area of HLWG degradation rind	$m^2 kg^{-1}$	Eq. 6.3.4.6.2-2
S_{rind}	Exponent in FHH adsorption isotherm for CSNF degradation rind	dimensionless	Eq. 6.3.4.6.1-1
\bar{s}_{rind}	Specific surface area of CSNF degradation rind	$m^2 kg^{-1}$	Eq. 6.3.4.6.1-4
$\bar{s}_{rind,n}$	Specific surface area of degradation rind in domain n	$m^2 kg^{-1}$	Eq. 6.5.2.2.2.1-1
T	Temperature	K	Eq. 6.3.4.1.1-6
T^*	Transmission coefficient	dimensionless	Eq. 6.3.4.1.1-11
T_{cA}, T_{cB}	Critical temperatures of components A and B	K	Eq. 6.6.2-9
T_r	Reference temperature	K	Eq. 6.3.4.3.1-2
T_0	Reference temperature	K	Eq. 6.3.4.1.2-1
t	Remaining thickness of closure lid	m	Eq. 6.3.3.2.3-1
t	Time	s	Eq. 6.5.1.1-1
t_f	Thickness of a water monolayer	m	Eq. 6.3.4.3.2-4

Notation (Continued)

Variable	Definition	Units	Where First Used
t_{fill}	Time for a waste package to fill with water	s	Section 6.6.1.1
$t_{I,max}$	Maximum thickness of the invert	m	Eq. 6.5.2.3-1
\bar{t}_I	Average thickness of the invert	m	Eq. 6.5.2.5-5
t_i	Transport number for the i^{th} ion	dimensionless	Eq. 6.3.4.1.1-10
$t_{LCS,n}$	Lifetime of carbon steel in domain n	yr	Eq. 6.5.2.2.1-1
$t_{LSS,n}$	Lifetime of stainless steel in domain n	yr	Eq. 6.5.2.2.1-2
$t_{max,CS,n}$	Maximum thickness of carbon steel in domain n	m	Eq. 6.5.2.2.1-1
$t_{max,SS,n}$	Maximum thickness of stainless steel in domain n	m	Eq. 6.5.2.2.1-2
t_0	Time of first breach of the waste package	yr	Eq. 6.5.2.2.1-3
$t_{1/2,i}^P$	Half-life of parent of radionuclide species i	s	Eq. 6.5.1.2-11
V	Volume of water vapor adsorbed at water partial pressure p_w	$m^3 kg^{-1}$	Eq. 6.3.4.3.2-1
$V(t)$	Volume of water within a waste package at time t	m^3	Section 6.6.1.1
V_B	Volume of cell B	m^3	Eq. 6.5.2.5-4
V_b	Bulk volume of UZ matrix cell	$m^3 kg^{-1}$	Section 6.5.2.6
V_{CP}	Pore volume (water volume when fully saturated) of corrosion products	m^3	Eq. 6.3.4.3.5-3
$V_{CP,n}$	Bulk volume of corrosion products in domain n	m^3	Eq. 6.5.2.2.1-9
$V_{CP,CSNF}$	Bulk volume of steel corrosion products in CSNF waste form domain	m^3	Eq. 6.5.2.2.2.1-3
V_{CSNF}	Bulk volume of CSNF waste form domain	m^3	Eq. 6.5.2.2.2.1-3
V_{DSNF}	Bulk volume of DSNF waste form subdomain	m^3	Eq. 6.5.2.2.2.1-18
V_g	Volume of crushed tuff granule	m^3	Section 6.6.3.1
V_{HLWG}	Volume of HLWG degradation rind	m^3	Eq. 6.5.2.2.2.1-13
V_m	Volume of water adsorbed that provides one monolayer coverage on the surface	$m^3 kg^{-1}$	Eq. 6.3.4.3.2-1
V_{new}	Volume of "new" water in waste package	m^3	Section 6.6.1.2.2
V_{old}	Volume of "old" water in waste package	m^3	Section 6.6.1.2.1
V_p	Total volume of pore space in bulk invert	m^3	Eq. 6.5.1.2-27
V_{p_inter}	Intergranular pore space pore volume	m^3	Eq. 6.5.1.2-25
V_{p_intra}	Intragranular pore space pore volume	m^3	Eq. 6.5.1.2-26
V_{rind}	Volume of CSNF degradation rind	m^3	Eq. 6.5.2.1.1.1-1

Notation (Continued)

Variable	Definition	Units	Where First Used
$V_{rind,CSNF}$	Volume of CSNF degradation rind in CSNF waste form domain	m ³	Eq. 6.5.2.2.2.1-3
$V_{rind,DSNF}$	Volume of CSNF degradation rind in DSNF waste form subdomain	m ³	Eq. 6.5.2.2.2.1-17
$V_{rind,HLWG}$	Volume of HLWG degradation rind in HLWG waste form subdomain	m ³	Eq. 6.5.2.2.2.1-12
$V_{rind,n}$	Volume of degradation rind in domain n	m ³	Eq. 6.5.2.2.2.1-2
V_t	Bulk invert total volume	m ³	Eq. 6.5.1.2-25
V_{t_inter}	Intergranular pore space total volume	m ³	Eq. 6.5.1.2-28
V_{t_intra}	Intragranular pore space total volume	m ³	Eq. 6.5.1.2-29
V_{tub}	Volume of water that can be retained within a waste package before it overflows	m ³	Section 6.6.1.1
V_w	Volume of water in the corrosion products cell	m ³	Eq. 6.5.2.7.2-9
$V_{w,CP,CSNF}$	Volume of water in all corrosion products in CSNF waste form domain	m ³	Eq. 6.5.2.2.2.1-7
$V_{w,CP,DSNF}$	Volume of water in all corrosion products in DSNF waste form subdomain	m ³	Eq. 6.5.2.2.2.1-17
$V_{w,CP,HLWG}$	Volume of water in all corrosion products in HLWG waste form subdomain	m ³	Eq. 6.5.2.2.2.1-15
$V_{w,CP,n}$	Volume of water in all corrosion products in domain n	m ³	Eq. 6.5.2.2.1-11
$V_{w,CPm,n}$	Volume of water in corrosion products CPm in domain n	m ³	Eq. 6.5.2.2.1-11
$V_{w,CSNF}$	Volume of water in CSNF waste form domain	m ³	Eq. 6.5.2.2.2.1-7
$V_{w,HLWG}$	Volume of water in HLWG degradation rind	m ³	Eq. 6.5.2.2.2.1-15
V_{wI}	Volume of water in invert	m ³	Eq. 6.5.2.3-3
V_{w_inter}	Volume of water in invert intergranular pore space	m ³	Eq. 6.5.2.3-6
V_{w_intra}	Volume of water in invert intragranular pore space	m ³	Eq. 6.5.2.3-6
$V_{w,rind}$	Volume of water in CSNF degradation rind	m ³	Eq. 6.5.2.1.1.1-1
$V_{w,rind,CSNF}$	Volume of water in CSNF degradation rind in CSNF waste form domain	m ³	Eq. 6.5.2.2.2.1-7
$V_{w,rind,DSNF}$	Volume of water in DSNF degradation rind in DSNF waste form subdomain	m ³	Eq. 6.5.2.2.2.1-20
$V_{w,rind,HLWG}$	Volume of water in HLWG degradation rind in HLWG waste form subdomain	m ³	Eq. 6.5.2.2.2.1-15
$V_{w,rind,n}$	Volume of water in degradation rind in domain n	m ³	Eq. 6.5.2.2.2.1-2
$V_{\phi,CP,CSNF}$	Pore volume in corrosion products in CSNF waste form domain	m ³	Eq. 6.5.2.2.2.1-5

Notation (Continued)

Variable	Definition	Units	Where First Used
$V_{\phi,CP,DSNF}$	Pore volume in corrosion products in DSNF waste form subdomain	m^3	Eq. 6.5.2.2.2.1-20
$V_{\phi,CP,HLWG}$	Pore volume in corrosion products in HLWG waste form subdomain	m^3	Eq. 6.5.2.2.2.1-12
$V_{\phi,CP,n}$	Pore volume in all corrosion products in domain n	m^3	Eq. 6.5.2.2.1-8
$V_{\phi,CPm,n}$	Pore volume in corrosion products CPm in domain n	m^3	Eq. 6.5.2.2.1-7
$V_{\phi,CSNF}$	Pore volume in CSNF waste form domain	m^3	Eq. 6.5.2.2.2.1-5
$V_{\phi,HLWG}$	Pore volume in HLWG waste form subdomain	m^3	Eq. 6.5.2.2.2.1-12
\bar{v}	Average water velocity	$m\ yr^{-1}$	Eq. 6.6.5-1
v_c	Average contaminant front velocity	$m\ yr^{-1}$	Eq. 6.6.5-1-1
W_{DS}	Total unfolded width of drip shield	m	Eq. 6.5.1.1.1-7
w	Water content	percent	Figure 6.3-9
w_I	Width of top surface of invert	m	Eq. 6.5.2.3-1
W_{inter}	Volumetric ratio of the intergranular continuum volume to the total bulk invert volume	$m^3\ m^{-3}$	Eq. 6.5.1.2-23
W_w^m	Net mass flow rate of water across bounding surfaces by mass transfer	$kg\ s^{-1}$	Eq. 6.5.1.1-1
X	Linear variable in least squares fit	dimensionless	Eq. 6.3.4.1.1-19
x	Arc length from the crown of the drip shield down to a corrosion patch; One-dimensional coordinate or distance	m	Eq. 6.3.2.4-2 Figure 6.3-2
x_A	Mole fraction of water vapor (species A) in air	dimensionless	Eq. 6.6.2-8
x_{Ab}	Mole fraction of water vapor in the bulk drift air	dimensionless	Eq. 6.6.2-13
x_{As}	Mole fraction of water vapor at the inside surface of the outer corrosion barrier wall or closure lid	dimensionless	Eq. 6.6.2-13
Y	Linear variable in least squares fit	dimensionless	Eq. 6.3.4.1.1-19
y	Distance along drip shield crown	m	Section 6.5.1.1.2.1
y	Equation for line in linear regression	dimensionless	Section 6.3.4.6.1
y_A	Distance along drip shield crown from center of breach – farthest point to the left from which rivulets can enter breach	m	Eq. 6.5.1.1.2.1-1
y_B	Distance along drip shield crown from center of breach – farthest point to the left from which rivulets can enter top of breach	m	Eq. 6.5.1.1.2.1-1
y_C	Distance along drip shield crown from center of breach – farthest point to the right from which rivulets can enter top of breach	m	Eq. 6.5.1.1.2.1-1
y_D	Distance along drip shield crown from center of breach – farthest point to the right from which rivulets can enter breach	m	Eq. 6.5.1.1.2.1-1
z	One-dimensional coordinate or distance	m	Eq. 6.5.1.2-47
z_i	Charge valence of the i^{th} ion	dimensionless	Eq. 6.3.4.1.1-10

Notation (Continued)

Variable	Definition	Units	Where First Used
$z_{interface}$	Spatial location of the invert/UZ interface	m	Section 6.5.1.2
z^-, z^+	Spatial location on the upstream (-) and downstream (+) side of the invert/UZ interface	m	Eq. 6.5.1.2-54
z_+, z_-	Valence of cation and anion, respectively; magnitude only – no sign	dimensionless	Eq. 6.3.4.1.1-6
ΔC_i	Concentration difference	kg m ⁻³	Eq. 6.3.4.3.5-1
ΔF_w	Difference between volumetric flow rate into and out of the EBS	m ³ s ⁻¹	Eq. 6.5.1.1-4
Δt	Time to empty retained water in waste package	s	Eq. 6.6.1.2.3-2
Δt	Time step size from the n^{th} to the $(n+1)^{\text{th}}$ time	s or yr	Eq. 6.5.2.5-1
Δw_w	Difference between mass rate of flow into and out of the EBS	kg s ⁻¹	Eq. 6.5.1.1-1
Δx	Thickness or length of flow or diffusion path	m	Eq. 6.3.4.3.5-1
ΔY	Interquartile range	dimensionless	Appendix K
Δz	Thickness of the outer corrosion barrier wall or closure lid	m	Eq. 6.6.2-13
Θ	Cell constant	m ⁻¹	Eq. 6.3.4.1.1-14
Λ_i	Reaction term accounting for decay and ingrowth of species i	kg m ⁻³ s ⁻¹	Eq. 6.5.1.2-1
Λ_0	Equivalent electrolyte conductivity at infinite dilution	S m ² equivalent ⁻¹	Eq. 6.3.4.1.1-6
$\Lambda_{^{243}\text{Am}}$	Total effective conversion rate of ²⁴³ Am to ²³⁹ Pu or embedded or sorbed species	yr ⁻¹	Eq. 6.5.2.7.2-3
$\Lambda_{^{243}\text{Am},GS}$	Total effective conversion rate of ²⁴³ Am to ²³⁹ Pu or embedded or sorbed species, as applied in GoldSim	yr ⁻¹	Eq. 6.5.2.7.2-10
Ω	Colloid target flux out ratio	dimensionless	Eq. 6.5.2.4-7
Φ	Volumetric water content	percent	Eq. 7.2.1.2-1
α	Drip shield or waste package rivulet spread half angle	radian or degree	Eq. 6.3.2.4-2
α	First-order mass transfer coefficient	s ⁻¹	Eq. 6.5.1.2-22
α	Forward rate constant for the slow site	hr ⁻¹	Eq. 6.6.6.1-2
α	Van Genuchten air-entry parameter	bar ⁻¹	Eq. 6.5.2.3-14
α_{CPm}	Stoichiometric coefficient, number of moles of metal m in a mole of corrosion product CPm , when the corrosion products are represented as FeOOH, Cr ₂ O ₃ , and NiO	mol m mol ⁻¹ CPm	Eq. 6.5.2.2.1-4
β	Geometry-dependent factor in expression for dual-continuum invert interface mass transfer coefficient	dimensionless	Eq. 6.5.1.2-24
β	Reverse rate constant for the slow site	hr ⁻¹	Eq. 6.6.6.1-2
β	Volume fraction of “old” water in total water volume of waste package	m ³ m ⁻³	Eq. 6.6.1.2.1-2
β_0	Ratio of fitting parameters	K	Eq. 6.3.4.3.1-2
γ	UZ active fracture parameter	dimensionless	Section 6.5.2.6

Notation (Continued)

Variable	Definition	Units	Where First Used
γ_c	Colloid mass transfer coefficient	s^{-1}	Eq. 6.5.1.2-21
γ_d	Dissolved species mass transfer coefficient	s^{-1}	Eq. 6.5.1.2-21
δ	Stress corrosion crack gap width	m	Eq. 6.3.3.1-1
δ_i	Stress corrosion crack gap width, inner surface	m	Figure 6.3-3
δ_o	Stress corrosion crack gap width, outer surface	m	Figure 6.3-3
ε_1	Uncertainty term associated with uncertainty in logarithm of solubility product values described by normal distribution	dimensionless	Eq. 6.5.2.4.1-1
ε_2	Uncertainty term associated with variations in fluoride concentration	dimensionless	Eq. 6.5.2.4.1-1
ζ	Dimensionless surface-area-to-volume ratio	dimensionless	Section 6.6.3.1
η_T	Viscosity of water at temperature T	Pa s	Eq. 6.3.4.1.2-1
η_{T_0}	Viscosity of water at temperature T_0	Pa s	Eq. 6.3.4.1.2-1
η_{20}	Viscosity of water at temperature $T = 20^\circ\text{C}$	Pa s	Eq. 6.3.4.1.2-1
θ	Volumetric water content	percent	Eq. 6.3.4.1.1-16
θ_a	Number of monolayers of adsorbed water	dimensionless	Eq. 6.3.4.3.2-2
θ_C	Critical volumetric water content	percent	Eq. 6.6.4.2-2
$\theta_{CP,n}$	Number of monolayers of water adsorbed onto corrosion products in domain n	dimensionless	Eq. 6.5.2.2.1-6
θ_{HLWG}	Number of monolayers of water adsorbed onto HLWG degradation rind surface	dimensionless	Eq. 6.3.4.6.2-1
θ_{inter}	Intergranular water content	percent	Eq. 6.5.2.3-6
θ_{intra}	Water content of invert intragranular continuum	percent	Eq. 6.5.2.3-10
θ_{min}	Minimum volumetric water content for diffusivity to be greater than limiting diffusivity	percent	Eq. 6.6.4.2-5
θ_r	Residual water content	percent	Eq. 6.3.4.3.1-3
θ_{rind}	Number of monolayers of water adsorbed onto CSNF degradation rind surface	dimensionless	Eq. 6.3.4.6.1-1
θ_s	Saturated water content	percent	Eq. 6.3.4.3.1-3
θ_w	Water content	$m^3 m^{-3}$	Eq. 6.5.1.2-2
θ_{wf}	Water content of UZ fracture continuum	$m^3 m^{-3}$	Eq. 6.5.1.2-52
θ_{wm}	Water content of UZ matrix continuum	$m^3 m^{-3}$	Eq. 6.5.1.2-53
κ_a	Bulk soil or rock conductivity	$\Omega^{-1}m^{-1}$ or $S m^{-1}$	Eq. 6.3.4.1.1-11
κ_s	Electrical conductivity of the solution	$\Omega^{-1}m^{-1}$ or mho/m	Eq. 6.3.4.1.1-11
κ_w	Electrical conductivity of the solution	$\Omega^{-1}m^{-1}$ or $S m^{-1}$	Eq. 6.3.4.1.1-10

Notation (Continued)

Variable	Definition	Units	Where First Used
λ_i	Radioactive decay constant for species i	s^{-1} or yr^{-1}	Eq. 6.5.1.2-10
λ_i^p	Radioactive decay constant for parent of species i	s^{-1} or yr^{-1}	Eq. 6.5.1.2-10
λ_i^{embed}	First order rate constant for mass conversion from dissolved state to embedded state onto waste form colloids for radionuclide species i	s^{-1} or yr^{-1}	Eq. 6.5.1.2-9
$\lambda_{T,Am}$	Total kinetic reaction rate in the corrosion products domain, or kinetic conversion rate	yr^{-1}	Eq. 6.5.2.7.2-11
$\lambda_{243 Am}$	^{243}Am conversion rate to ^{239}Pu	yr^{-1}	Eq. 6.5.2.7.2-1
$\lambda_{243 Am}^{embed}$	^{243}Am conversion rate to embedded on waste form colloids	yr^{-1}	Eq. 6.5.2.7.2-1
μ	Mean value	dimensionless	Eq. 6.3.4.1.1-22
μ_w	Water viscosity	Pa s	Eq. 6.3.4.4-1
$V_{Ic^{243} Am}$	Stoichiometric coefficient for conversion of ^{243}Am to ^{243}Am species embedded on waste form colloids	$mol mol^{-1} ^{243}Am$	Eq. 6.5.2.7.2-2
$V_{Ifcp^{243} Am}$	Stoichiometric coefficient for conversion of ^{243}Am to ^{243}Am species kinetically sorbed to iron oxyhydroxide corrosion products	$mol mol^{-1} ^{243}Am$	Eq. 6.5.2.7.2-2
$V_{If^{243} Am}$	Stoichiometric coefficient for conversion of ^{243}Am to ^{243}Am species kinetically sorbed to iron oxyhydroxide colloids	$mol mol^{-1} ^{243}Am$	Eq. 6.5.2.7.2-2
$V_{239 Pu}$	Stoichiometric coefficient for conversion of ^{243}Am to ^{239}Pu	$mol mol^{-1} ^{243}Am$	Eq. 6.5.2.7.2-2
ρ_b	Dry bulk density of the stationary solid matrix	$kg m^{-3}$	Eq. 6.5.1.2-13
ρ_{CPm}	Density of corrosion product CPm	$kg m^{-3}$	Eq. 6.5.2.2.1-6
ρ_{HLWG}	Density of HLWG degradation rind	$kg m^{-3}$	Eq. 6.3.4.6.2-2
$\rho_{Ifcp^{243} Am}$	Effective conversion rate for the $Ifcp^{243} Am$ species	yr^{-1}	Eq. 6.5.2.7.2-25
ρ_i	Mass concentration of radionuclide species i	$kg m^{-3}$	Eq. 6.5.1.2-1
ρ_{rind}	Density of CSNF degradation rind	$kg m^{-3}$	Eq. 6.3.4.6.1-4
ρ_{SCC}	SCC density (max and min): number of through-wall SCCs per unit seismically damaged area	m^{-2}	Eq. 6.3.3.2.4-1
ρ_{SCCA}	SCC opening area density (max and min): crack opening area per unit seismically damaged area	m^{-2}	Eq. 6.3.3.2.4-3
ρ_s	Electrical resistivity of a porous medium	Ωm	Eq. 6.3.4.1.1-1
ρ_t	Bulk resistivity of a partially saturated porous medium	Ωm	Eq. 6.3.4.1.1-2
ρ_w	Density of water	$kg m^{-3}$	Eq. 6.3.4.3.2-4
ρ_w^e	Electrical resistivity of liquid water	Ωm	Eq. 6.3.4.1.1-1
$\rho_{234 Am}$	Total or effective ^{243}Am conversion rate	yr^{-1}	Eq. 6.5.2.7.2-1
σ	Standard deviation	dimensionless	Eq. 6.3.4.1.1-22

Notation (Continued)

Variable	Definition	Units	Where First Used
σ	Residual tensile stress	Pa	Eq. 6.3.3.2.2-1
$\sigma(x)$	Standard deviation of the K_d distribution	mL g^{-1}	Table 6.6-4
σ_a	Standard deviation of the slope of linear regression line	dimensionless	Section 6.3.4.6.1
σ_b	Standard deviation of the intercept of linear regression line	dimensionless	Section 6.3.4.6.1
σ_g	Standard deviation of the pore size	mm	Eq. 6.6.4.1-4
σ_s	Sample standard deviation	dimensionless	Section 7.3.1.2
σ_{YS}	Yield strength	Pa	Section 6.3.3.2.2; Eq. 6.3.3.2.4-3
σ_{YS_DS}	Yield strength of drip shield material	Pa	Eq. 6.3.3.2.4-7
σ_{YS_WP}	Yield strength of waste package material	Pa	Eq. 6.3.3.2.4-8
ϕ	Porosity	$\text{m}^3 \text{m}^{-3}$	Eq. 6.3.4.1.1-1
ϕ_{CP}	Porosity of corrosion products	$\text{m}^3 \text{m}^{-3}$	Eq. 6.3.4.3.5-3
ϕ_{CSNF}	Porosity of CSNF waste form domain	$\text{m}^3 \text{m}^{-3}$	Eq. 6.5.2.2.2.1-6
ϕ_{DSNF}	Porosity of DSNF degradation rind	$\text{m}^3 \text{m}^{-3}$	Eq. 6.5.2.2.2.1-17
ϕ_{HLWG}	Porosity of HLWG degradation rind	kg m^{-3}	Eq. 6.3.4.6.2-2
ϕ_I	Bulk porosity of invert	$\text{m}^3 \text{m}^{-3}$	Eq. 6.5.1.2-27
ϕ_{inter}	Porosity of invert intergranular continuum	$\text{m}^3 \text{m}^{-3}$	Eq. 6.5.2.3-10
ϕ_{intra}	Porosity of invert intragranular continuum	$\text{m}^3 \text{m}^{-3}$	Eq. 6.5.1.2-22
ϕ_m	Porosity of saturated tuff matrix	$\text{m}^3 \text{m}^{-3}$	Eq. 6.6.4.2-4
ϕ_{rind}	Porosity of CSNF waste form degradation rind	$\text{m}^3 \text{m}^{-3}$	Table 6.3-11
ϕ_{scc}	Porosity of SCCs	$\text{m}^3 \text{m}^{-3}$	Section 6.6.2
$\phi_{T,DSNF}$	Porosity of DSNF waste form subdomain	$\text{m}^3 \text{m}^{-3}$	Eq. 6.5.2.2.2.1-19
$\phi_{T,HLWG}$	Porosity of HLWG waste form subdomain	$\text{m}^3 \text{m}^{-3}$	Eq. 6.5.2.2.2.1-14
ψ	Capillary pressure	Pa	Eq. 6.3.4.3.1-1
ψ	Moisture potential	J kg^{-1}	Eq. 6.6.4.1-2
ψ_e	Air-entry moisture potential	J kg^{-1}	Eq. 6.6.4.1-2
ψ_{es}	Air-entry moisture potential at a bulk density of $1,300 \text{ kg m}^{-3}$	J kg^{-1}	Eq. 6.6.4.1-3
ψ_{T_r}	Capillary pressure at reference temperature T_r	Pa	Eq. 6.3.4.3.1-2
$\omega_{CS,Cr}$	Mass fraction of chromium in carbon steel	dimensionless	Eq. 6.5.2.2.1-3
$\omega_{CS,Fe}$	Mass fraction of iron in carbon steel	dimensionless	Eq. 6.5.2.2.1-3

Notation (Continued)

Variable	Definition	Units	Where First Used
$\omega_{CS,m}$	Mass fraction of metal m in carbon steel	dimensionless	Eq. 6.5.2.2.1-3
$\omega_{CS,Ni}$	Mass fraction of nickel in carbon steel	dimensionless	Eq. 6.5.2.2.1-3
ω_G	Mass fraction of corrosion products as goethite	dimensionless	Eq. 6.3.4.2.3.1-1
ω_i	Mass fraction of radionuclide species i released per unit mass of waste form	kg kg ⁻¹	Eq. 6.6.1.1.1-1
$\omega_{SS,Cr}$	Mass fraction of chromium in stainless steel	dimensionless	Eq. 6.5.2.2.1-4
$\omega_{SS,Fe}$	Mass fraction of iron in stainless steel	dimensionless	Eq. 6.5.2.2.1-4
$\omega_{SS,m}$	Mass fraction of metal n in stainless steel	dimensionless	Eq. 6.5.2.2.1-4
$\omega_{SS,Ni}$	Mass fraction of nickel in stainless steel	dimensionless	Eq. 6.5.2.2.1-4
∇	Del operator: $\mathbf{i} \frac{\partial}{\partial x} + \mathbf{j} \frac{\partial}{\partial y} + \mathbf{k} \frac{\partial}{\partial z}$, where \mathbf{i} , \mathbf{j} , and \mathbf{k} are unit vectors in the x-, y-, and z-directions, respectively	m ⁻¹	Eq. 6.5.1.2-1

APPENDIX B

IMPLEMENTATION OF RADIONUCLIDE SORPTION ONTO COLLOIDAL AND STATIONARY PHASES WITH FINITE DIFFERENCE SOLUTION

IMPLEMENTATION OF RADIONUCLIDE SORPTION ONTO COLLOIDAL AND STATIONARY PHASES WITH FINITE DIFFERENCE SOLUTION

CONCEPTUAL MODEL

The colloid transport model accounts for kinetic sorption onto the iron oxyhydroxide (designated FeO) mobile colloids and the immobile FeO corrosion products, together with reversible sorption onto both waste form (WF) and groundwater (GW) colloids within the corrosion product domain of the engineered barrier system. The radionuclides that experience kinetic sorption are the plutonium and americium isotopes. Since the material balance equations are written as a mass balance, the equations are valid for any solute species. Certain system parameters, such as solubility, decay rate, and distribution coefficients, will be dependent on the species. In this appendix, the species used for subsequent analysis and discussion is plutonium. The analysis and discussion is appropriate for all kinetic sorption species.

FINITE DIFFERENCE SOLUTION OF TRANSPORT EQUATIONS

Consider a finite difference approximation of the governing mass balance equations. Several modeling assumptions are made to render the subsequent analysis and numerical solutions tractable. Simplifying assumptions include:

- No radionuclide in-growth
- No precipitation
- The reverse kinetic sorption rate is a multiple of the forward kinetic sorption rate
- A 3-cell finite difference grid
- Cell 1 represents waste form cell with concentration maintained at constant solubility
- Cell 2 represent the corrosion product domain
- Cell 3 represents a downstream zero concentration boundary
- Waste form colloids originate in cell 1
- Ground water and FeO colloids originate in cell 2
- No upstream diffusion of groundwater or FeO colloids to cell 1
- Constant values for all equilibrium distribution coefficients, water contents, advective water flux, and waste form solubility.

Since cells one and three represent boundary conditions, this discretization is a zero-dimensional or single cell representation of the processes. Let the time step length be denoted Δt . Let superscript n denote the n^{th} time step, for example $c_{Pu_{aq}}^n$, denotes the aqueous concentration at

the n^{th} time step. The discretization uses a first order backward difference approximation for the time derivative and the advective transport term. The diffusive flux uses a second order approximation. This discretization is consistent with GoldSim (GoldSim V. 9.60.100 2007 [DIRS 181903]). In this model, advection and diffusion of dissolved mass and equilibrium sorbed mass to the waste form colloids occur at the left boundary (cell 1 to cell 2 boundary). At the right boundary (cell 2 to cell 3 boundary), advection and diffusion of both dissolved mass and all colloid sorbed mass occur. Although the water content is time-independent, it may vary spatially. If the discretization is fully implicit in concentrations, then the discrete mass balance approximation for the dissolved and equilibrium sorbed mass within cell 2, in units of mass per unit water volume per unit time, is:

$$\begin{aligned} \bar{K}_1 \frac{c_{Pu_aq}^{n+1} - c_{Pu_aq}^n}{\Delta t} = & \bar{Q}\bar{K}_3 c_s - \bar{Q}\bar{K}_1 c_{Pu_aq}^{n+1} - \bar{D}_{left_aq} (c_{Pu_aq}^{n+1} - c_s) - \bar{D}_{right_aq} c_{Pu_aq}^{n+1} \\ & - \bar{D}_{left_col} \bar{K}_{d_WF_col} (c_{Pu_aq}^{n+1} - c_s) - \bar{D}_{right_col} \bar{K}_2 c_{Pu_aq}^{n+1} \\ & - (r_{f_cp} + r_{f_col} + \lambda \bar{K}_1) c_{Pu_aq}^{n+1} + r_{r_cp} \hat{c}_{Pu_cp}^{n+1}. \end{aligned} \quad (\text{Eq. B-1})$$

where

- c_{Pu_aq} = concentration of Pu in aqueous solution
- \hat{c}_{Pu_cp} = concentration of Pu in the stationary FeO corrosion product state due to kinetic sorption
- \hat{c}_{Pu_col} = concentration of Pu in the FeO colloid state due to kinetic sorption
- c_s = Pu concentration at solubility limit, assumed to be constant.

The equilibrium sorption to the waste form and groundwater colloids are determined by parameters:

- $\bar{K}_{d_WF_col}$ = dimensionless distribution coefficient for waste form colloids
- $\bar{K}_{d_GW_col}$ = dimensionless distribution coefficient for groundwater colloids.

Equation B-1 uses the compact notation:

$$\begin{aligned} \bar{K}_1 &= 1 + \bar{K}_{d_WF_col} + \bar{K}_{d_GW_col} \\ \bar{K}_2 &= \bar{K}_{d_WF_col} + \bar{K}_{d_GW_col} \\ \bar{K}_3 &= 1 + \bar{K}_{d_WF_col}. \end{aligned}$$

The dimensionless distribution coefficients are given by:

$$\bar{K}_{d_WF_col} = c_{WF_col} K_{d_WF_col}$$

$$\bar{K}_{d_GW_col} = c_{GW_col} K_{d_GW_col}$$

where

- c_{WF_col} = waste form colloid concentration in the water
- c_{GW_col} = groundwater colloid concentration in the water
- $K_{d_WF_col}$ = waste form colloid equilibrium distribution coefficient
- $K_{d_GW_col}$ = groundwater colloid equilibrium distribution coefficient.

The kinetic sorption model is given by:

$$r_{f_cp} = \hat{S}_{FeO_cp} c_{FeO_cp} k$$

$$r_{f_col} = \hat{S}_{FeO_col} c_{FeO_col} k$$

$$r_{r_cp} = 0.001 r_{f_cp}$$

where

- r_{f_cp} = forward kinetic sorption rate to the FeO corrosion products
- r_{r_cp} = reverse kinetic desorption rate from the FeO corrosion products
- r_{f_col} = forward kinetic sorption rate to the FeO colloids

and

- \hat{S}_{FeO_cp} = specific surface area of FeO corrosion products
- \hat{S}_{FeO_col} = specific surface area of FeO colloids
- c_{FeO_cp} = concentration of FeO corrosion products in water
- c_{FeO_col} = concentration of FeO colloids in water
- k = kinetic sorption rate constant.

The advective transport rate constant is:

$$\bar{Q} = \text{water rate constant [volumetric water flux/volume water in cell].}$$

The diffusive rate constants subscript left or right refers to the left or right diffusive boundaries, while the subscript *aq* or *col* refers to diffusion of the dissolved mass or colloid mass, respectively. The diffusive interface terms are determined by the harmonic average, denoted *H*, of $\frac{\theta DA}{2L}$ with respect to water volume:

$$\bar{D} = \frac{H\left(\frac{\theta DA}{2L}\right)}{V_{water}},$$

where

- θ = cell water content
- D = effective aqueous or colloid diffusivity
- A = cell diffusive area in the direction of transport
- L = diffusive half length from cell center to cell boundary
- V_{water} = cell water volume.

The discretization of the mass balance for kinetically sorbed Pu mass on the stationary FeO corrosion products is:

$$\frac{\hat{c}_{Pu_cp}^{n+1} - \hat{c}_{Pu_cp}^n}{\Delta t} = -r_{r_cp} \hat{c}_{Pu_cp}^{n+1} - \lambda \hat{c}_{Pu_cp}^{n+1} + r_{f_cp} c_{Pu_aq}^{n+1} \quad (\text{Eq. B-2})$$

and for kinetically sorbed Pu mass on the mobile FeO colloids:

$$\frac{\hat{c}_{Pu_col}^{n+1} - \hat{c}_{Pu_col}^n}{\Delta t} = -\bar{Q} \hat{c}_{Pu_col}^{n+1} - \bar{D}_{right_col} \hat{c}_{Pu_col}^{n+1} - \lambda \hat{c}_{Pu_col}^{n+1} + r_{f_col} c_{Pu_aq}^{n+1}. \quad (\text{Eq. B-3})$$

The mass balance equation, Equation B-1, for the dissolved and equilibrium sorbed mass is written in the form of a first order difference equation:

$$c_{Pu_aq}^{n+1} = a_1 c_{Pu_aq}^n + a_2 \hat{c}_{Pu_cp}^{n+1} + a_3. \quad (\text{Eq. B-4})$$

The coefficients in Equation B-4 are determined by defining:

$$\Lambda = \bar{K}_1 + (\bar{D}_{right_aq} + \bar{D}_{left_aq} + \bar{D}_{right_col} \bar{K}_2 + \bar{D}_{left_col} \bar{K}_{d_WF_col} + \bar{Q} \bar{K}_1 + r_{f_cp} + r_{f_col} + \lambda \bar{K}_1) \Delta t,$$

then

$$a_1 = \frac{\bar{K}_1}{\Lambda} \quad (\text{Eq. B-5})$$

$$a_2 = \frac{r_{r_cp} \Delta t}{\Lambda} \quad (\text{Eq. B-6})$$

$$a_3 = \frac{c_s (\bar{Q} \bar{K}_3 + \bar{D}_{left_aq} + \bar{D}_{left_col} \bar{K}_{d_WF_col}) \Delta t}{\Lambda} \quad (\text{Eq. B-7})$$

The mass balance equation, Equation B-2, for the kinetically sorbed mass to the corrosion products is written as:

$$\hat{c}_{Pu_cp}^{n+1} = b_1 \hat{c}_{Pu_cp}^n + b_2 c_{Pu_aq}^{n+1} \quad (\text{Eq. B-8})$$

where

$$b_1 = \frac{1}{1 + (r_{r_cp} + \lambda) \Delta t} \quad (\text{Eq. B-9})$$

$$b_2 = \frac{r_{f_cp} \Delta t}{1 + (r_{r_cp} + \lambda) \Delta t}. \quad (\text{Eq. B-10})$$

The mass balance equation, Equation B-3, for the kinetically sorbed mass to the FeO colloids is written as:

$$\hat{c}_{Pu_col}^{n+1} = e_1 \hat{c}_{Pu_col}^n + e_2 c_{Pu_aq}^{n+1} \quad (\text{Eq. B-11})$$

where

$$e_1 = \frac{1}{1 + (\bar{D}_{right_col} + \bar{Q} + \lambda) \Delta t} \quad (\text{Eq. B-12})$$

$$e_2 = \frac{r_{f_col} \Delta t}{1 + (\bar{D}_{right_col} + \bar{Q} + \lambda) \Delta t}. \quad (\text{Eq. B-13})$$

The mass balance equation for the dissolved mass, Equation B-4, and the mass balance equation for the kinetically sorbed mass on the corrosion products, Equation B-8, are coupled by the reverse kinetic sorption term. In order to compute a solution of Equation B-4 for $c_{Pu_aq}^{n+1}$, Equation B-8 is used to eliminate the dependence of $\hat{c}_{Pu_cp}^{n+1}$ in Equation B-4. This results in the equation:

$$c_{Pu_aq}^{n+1} = \tilde{a}_1 c_{Pu_aq}^n + \tilde{a}_2 \hat{c}_{Pu_cp}^n + \tilde{a}_3. \quad (\text{Eq. B-14})$$

where

$$\tilde{a}_1 = \frac{a_1}{1 - a_2 b_2} \quad (\text{Eq. B-15})$$

$$\tilde{a}_2 = \frac{a_2 b_1}{1 - a_2 b_2} \quad (\text{Eq. B-16})$$

$$\tilde{a}_3 = \frac{a_3}{1 - a_2 b_2}. \quad (\text{Eq. B-17})$$

If concentrations are known at time level n , then Equation B-14 is solved for the dissolved concentration at time level $n+1$, $c_{Pu_aq}^{n+1}$. Once $c_{Pu_aq}^{n+1}$ is known, Equation B-8 yields $\hat{c}_{Pu_cp}^{n+1}$, and Equation B-11 yields $\hat{c}_{Pu_col}^{n+1}$.

SAMPLE CALCULATION WITH REPRESENTATIVE PARAMETERS

A sample calculation is performed to demonstrate the solution technique and illustrate the types of behavior that might be expected in this model. Parameter values used in this sample calculation are shown on Table B-1. The spatial discretization represents the three cells with radial geometry. The diffusive path lengths, diffusive areas, and cell volumes are determined from this cell geometry. The radial distances to the outer boundary of each cell and the cylindrical length of each cell is shown on Table B-1 (cylindrical length of cell 3 is equal to that of cell 2). For this set of parameters, the kinetic reactive rates, advective rate, diffusive rates, decay rate, and the dimensionless colloid distribution coefficients are:

$$r_{f_cp} = 3.566 \times 10^7 \text{ yr}^{-1}$$

$$r_{f_col} = 0.2600 \text{ yr}^{-1}$$

$$r_{r_cp} = 0.001 r_{f_cp}$$

$$\bar{Q} = 0.09145 \text{ yr}^{-1}$$

$$\bar{D}_{left_aq} = 0.3315 \text{ yr}^{-1}$$

$$\bar{D}_{right_aq} = 0.5315 \text{ yr}^{-1}$$

$$\bar{D}_{left_col} = \bar{D}_{left_aq} / 100$$

$$\bar{D}_{right_col} = \bar{D}_{right_aq} / 100$$

$$\lambda = 2.9 \times 10^{-5} \text{ yr}^{-1}$$

$$\bar{K}_{d_WF_col} = 0.025$$

$$\bar{K}_{d_GW_col} = 0.01$$

The simulation for the mixing cell (cell 2) concentrations over a 2,000-year time interval is shown on Figure B-1. The dominant rate constant, by several orders of magnitude, is the kinetic forward rate constant to the corrosion products, $r_{f_cp} = 3/566 \times 10^7 \text{ yr}^{-1}$. However, this large rate is mitigated by the reverse or desorption rate $r_{r_cp} = 0.001r_{f_cp}$ from the corrosion products. The large kinetic forward rate is a result of the large mass of corrosion products. For this simulation, the amount of corrosion product mass is representative of the total mass of corrosion products in a waste package, and all the corrosion products are available at initial time. In the TSPA-LA abstraction model, the corrosion product mass is time dependent and a function of the corrosion rates for the carbon and stainless steel (see Section 6.5.2.2).

A calculation with no advective transport is reported on Figure B-2. For this calculation, the advective flux rate is set to zero and the dryer environment is represented by assuming the water saturation in each cell is one half of the water saturation for the advective case. The FeO colloid concentration is approximately one order of magnitude greater, while the dissolved and corrosion product concentration decrease slightly. Thus, for diffusion only (zero advection), a proportionally higher transport due to the FeO colloids is predicted.

The qualitative behavior of the concentrations on Figure B-1 shows the concentrations approach limiting values or steady state values. These steady state values are determined by assuming the time-dependent concentrations have converged to the steady state values in Equation B-4, B-8, and B-11. This results in the linear system:

$$c_{Pu_aq}^{ss} = a_1 c_{Pu_aq}^{ss} + a_2 \hat{c}_{Pu_cp}^{ss} + a_3 \quad (\text{Eq. B-18})$$

$$\hat{c}_{Pu_cp}^{ss} = b_1 \hat{c}_{Pu_cp}^{ss} + b_2 c_{Pu_aq}^{ss} \quad (\text{Eq. B-19})$$

$$\hat{c}_{Pu_col}^{ss1} = e_1 \hat{c}_{Pu_col}^{ss} + e_2 c_{Pu_aq}^{ss}, \quad (\text{Eq. B-20})$$

where the superscript *ss* denotes steady state values. The solution of this system of equations gives the steady state values:

$$c_{Pu_aq}^{ss} = \frac{a_3(1-b_1)}{(1-a_1)(1-b_1)-a_2b_2} \quad (\text{Eq. B-21})$$

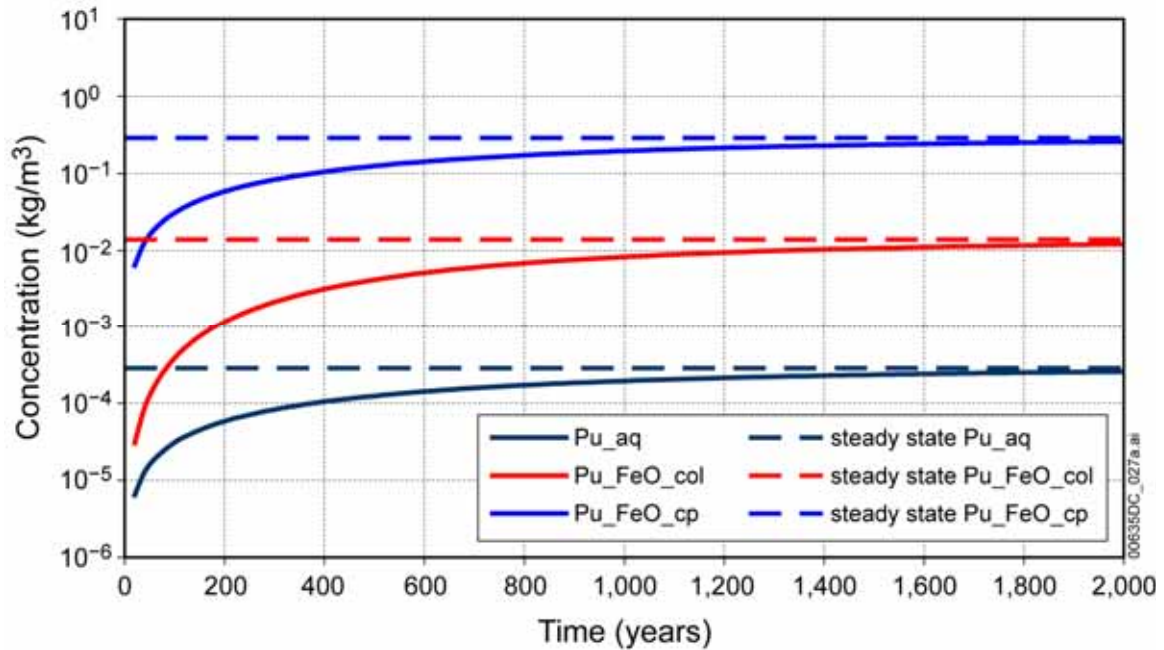
$$c_{Pu_cp}^{ss} = \frac{b_2}{1-b_1} c_{Pu_aq}^{ss} \quad (\text{Eq. B-22})$$

$$c_{Pu_col}^{ss} = \frac{e_2}{1-e_1} c_{Pu_aq}^{ss}. \quad (\text{Eq. B-23})$$

These steady state values are shown on Figure B-1 at 2,000 year. The steady state concentrations are reached in approximately 1,500 to 2,000 years.

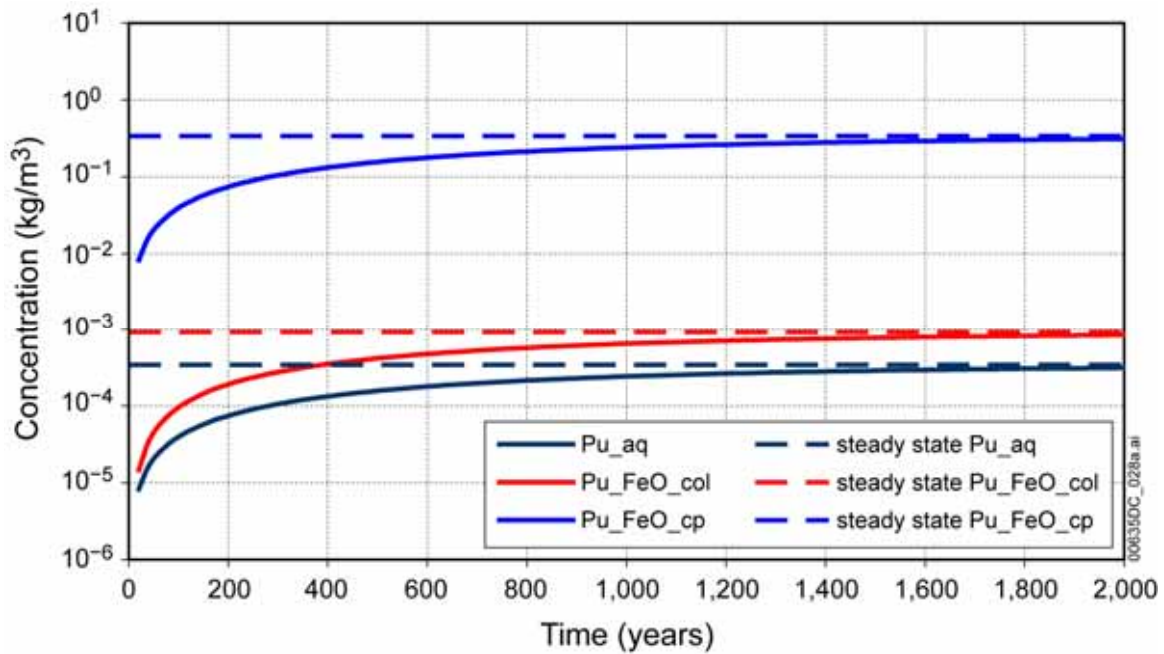
Table B-1. Representative Parameter Values for Sample Calculation

Parameter	Value	Units	Description
c_s	1.0	mg L ⁻¹	Solubility
θ_1	0.3	dimensionless	Water content of Cell 1
θ_2	0.4	dimensionless	Water content of Cell 2
θ_3	0.3	dimensionless	Water content of Cell 3
Q	0.1	m ³ yr ⁻¹	Volumetric water flux
$K_{d_WF_col}$	10 ⁵	mL g ⁻¹	Waste form colloids distribution coefficient
$K_{d_GW_col}$	10 ⁵	mL g ⁻¹	Groundwater colloids distribution coefficient
\hat{S}_{FeO_col}	130	m ² g ⁻¹	Specific surface area of FeO colloids
\hat{S}_{FeO_cp}	130	m ² g ⁻¹	Specific surface area of FeO corrosion products
c_{FeO_col}	0.1	mg L ⁻¹	Concentration of FeO colloids
$mass_{FeO_cp}$	15000	Kg	mass of FeO corrosion products
c_{WF_col}	0.25	mg L ⁻¹	Concentration of waste form colloids
c_{GW_col}	0.1	mg L ⁻¹	Concentration of groundwater colloids
k	0.02	m yr ⁻¹	Forward kinetic sorption rate constant
V_{water}	1.093	m ³	Water volume
A_1	12.48	m ²	Diffusive area Cell 1
A_2	29.88	m ²	Diffusive area Cell 2
A_3	102.1	m ²	Diffusive area Cell 3
L_1	0.4095	m	Half-length of Cell 1 diffusive path
L_2	0.04575	m	Half-length of Cell 2 diffusive path
L_3	2.045	m	Half-length of Cell 3 diffusive path
D_{aq}	1.3 × 10 ⁻⁹	m ² s ⁻¹	Aqueous diffusivity
D_{col}	1.3 × 10 ⁻¹¹	m ² s ⁻¹	Colloid diffusivity
λ	2.9 × 10 ⁻⁵	yr ⁻¹	Radionuclide decay rate
Δt	20	yr	Time step size



Source: Output DTN: SN0703PAEBSRTA.001, file *Transport_Calc_Appendix_B.xls*, worksheet "advection"

Figure B-1. Concentrations with Respect to Water Volume, Advection Case



Source: Output DTN: SN0703PAEBSRTA.001, file *Transport_Calc_Appendix_B.xls*, worksheet "no_advection"

Figure B-2. Concentrations with Respect to Water Volume, No Advection Case

BOUNDARY FLUXES

The plutonium mass exiting the corrosion product domain (cell 2) is expected to be proportioned such that the mass of plutonium, sorbed onto the colloids is some fraction of the total mass of plutonium exiting the system (see Section 6.5.2.4.6). Observations in nature, such as the transport of plutonium from the Benham test site (Kersting et al. 1999 [DIRS 103282]), suggest that this fraction is about 95 percent. This is expressed as:

$$\Omega = 0.95, \quad (\text{Eq. B-24})$$

where Ω denotes the ratio of the colloid flux out of the corrosion product domain to the total flux out. The kinetic rate constant for conversion of mass kinetically sorbed to the corrosion products and FeO colloids is considered a fitting parameter, which is determined so that a specified flux out ratio, Ω , is honored. In order to obtain this result, the assumption is made that the steady state concentration values are attained.

The right or downstream boundary flux has contributions from advection and diffusion of Plutonium in solution and waste form and groundwater colloids together with advection and diffusion of plutonium kinetically sorbed onto the FeO colloids. There is no advective or diffusive flux associated with the immobile corrosion products. The mass flux rates (kg yr^{-1}) at the right boundary assuming zero downstream concentrations are:

$$\begin{aligned} \text{Advective Pu}_{\text{aq}} \text{ (kg yr}^{-1}\text{)} &= \bar{Q} V_{\text{water}} c_{\text{Pu}_{\text{aq}}}^{\text{SS}} \\ \text{Diffusive Pu}_{\text{aq}} \text{ (kg yr}^{-1}\text{)} &= \bar{D}_{\text{right}_{\text{aq}}} V_{\text{water}} c_{\text{Pu}_{\text{aq}}}^{\text{SS}} \\ \text{Advective kinetic Pu}_{\text{FeO}_{\text{c}}} \text{ (kg yr}^{-1}\text{)} &= \bar{Q} V_{\text{water}} \hat{c}_{\text{Pu}_{\text{col}}}^{\text{SS}} \\ \text{Diffusive kinetic Pu}_{\text{FeO}_{\text{c}}} \text{ (kg yr}^{-1}\text{)} &= \bar{D}_{\text{right}_{\text{col}}} V_{\text{water}} \hat{c}_{\text{Pu}_{\text{col}}}^{\text{SS}} \\ \text{Advective Pu}_{\text{WF}_{\text{c}}} \text{ (kg yr}^{-1}\text{)} &= \bar{Q} V_{\text{water}} \bar{K}_{\text{d}_{\text{WF}_{\text{c}}}} c_{\text{Pu}_{\text{aq}}}^{\text{SS}} \\ \text{Diffusive Pu}_{\text{WF}_{\text{c}}} \text{ (kg yr}^{-1}\text{)} &= \bar{D}_{\text{right}_{\text{col}}} V_{\text{water}} \bar{K}_{\text{d}_{\text{WF}_{\text{c}}}} c_{\text{Pu}_{\text{aq}}}^{\text{SS}} \\ \text{Advective Pu}_{\text{GW}_{\text{c}}} \text{ (kg yr}^{-1}\text{)} &= \bar{Q} V_{\text{water}} \bar{K}_{\text{d}_{\text{GW}_{\text{c}}}} c_{\text{Pu}_{\text{aq}}}^{\text{SS}} \\ \text{Diffusive Pu}_{\text{GW}_{\text{c}}} \text{ (kg yr}^{-1}\text{)} &= \bar{D}_{\text{right}_{\text{col}}} V_{\text{water}} \bar{K}_{\text{d}_{\text{GW}_{\text{c}}}} c_{\text{Pu}_{\text{aq}}}^{\text{SS}} \end{aligned}$$

The condition discussed in Equation B-24 considers the ratio of the colloid mass to total mass flux out the right boundary. The right boundary colloidal flux, $F_{\text{right}_{\text{colloid}}}$, due to both reversibly and kinetically sorbed Pu is:

$$\begin{aligned} F_{\text{right}_{\text{colloid}}} &= \bar{Q} V_{\text{water}} c_{\text{Pu}_{\text{aq}}}^{\text{SS}} + \bar{Q} V_{\text{water}} \hat{c}_{\text{Pu}_{\text{col}}}^{\text{SS}} + \bar{Q} V_{\text{water}} \bar{K}_{\text{d}_{\text{WF}_{\text{c}}}} c_{\text{Pu}_{\text{aq}}}^{\text{SS}} \\ &+ \bar{Q} V_{\text{water}} \bar{K}_{\text{d}_{\text{GW}_{\text{c}}}} c_{\text{Pu}_{\text{aq}}}^{\text{SS}} + \bar{D}_{\text{right}_{\text{col}}} V_{\text{water}} \bar{K}_{\text{d}_{\text{FeO}_{\text{c}}}} c_{\text{Pu}_{\text{aq}}}^{\text{SS}} \end{aligned}$$

$$\begin{aligned}
 & + \bar{D}_{right_col} V_{water} \hat{c}_{Pu_col}^{ss} + \bar{D}_{right_col} V_{water} \bar{K}_{d_WF_c} c_{Pu_aq}^{ss} \\
 & + \bar{D}_{right_col} V_{water} \bar{K}_{d_GW_c} c_{Pu_aq}^{ss} .
 \end{aligned} \tag{Eq. B-25}$$

The total Pu flux at the right boundary is:

$$F_{right_total} = F_{right_colloid} + \bar{Q} V_{water} c_{Pu_aq}^{ss} + \bar{D}_{right_aq} V_{water} c_{Pu_aq}^{ss} . \tag{Eq. B-26}$$

The right boundary ratio of colloid flux out to total flux out is:

$$\Omega = \frac{F_{right_colloid}}{F_{right_total}} . \tag{Eq. B-27}$$

Then

$$\Omega = \frac{\frac{\hat{c}_{Pu_col}^{ss}}{c_{Pu_aq}^{ss}} + \bar{K}_2}{\frac{\hat{c}_{Pu_col}^{ss}}{c_{Pu_aq}^{ss}} + \bar{K}_2 + \frac{\bar{Q} + \bar{D}_{right_aq}}{\bar{Q} + \bar{D}_{right_col}}} . \tag{Eq. B-28}$$

From Equation B-23 and Equation B-11:

$$\frac{c_{Pu_col}^{ss}}{c_{Pu_aq}^{ss}} = \frac{e_2}{1 - e_1} = \frac{r_{f_col}}{\bar{Q} + \bar{D}_{right_col} + \lambda} . \tag{Eq. B-29}$$

Substitution of Equation B-29 into Equation B-28 gives:

$$\Omega = \frac{r_{f_col} + p_1}{r_{f_col} + p_2} \tag{Eq. B-30}$$

where

$$p_1 = \bar{K}_2 (\bar{Q} + \bar{D}_{right_col} + \lambda) \tag{Eq. B-31}$$

$$p_2 = p_1 + (\bar{Q} + \bar{D}_{right_col} + \lambda) \frac{\bar{Q} + \bar{D}_{right_aq}}{\bar{Q} + \bar{D}_{right_col}} . \tag{Eq. B-32}$$

Note the limiting flux out ratio Ω satisfies the inequalities:

$$0 < \frac{\bar{K}_2}{\bar{K}_2 + \frac{\bar{Q} + \bar{D}_{right_aq}}{\bar{Q} + \bar{D}_{right_col}}} < \Omega < 1, \quad (\text{Eq. B-33})$$

where the lower bound on Ω is obtained when $r_{f_col} = 0$. Qualitatively, if the advective, diffusive, and decay rates dominate the reactive rate constant r_{f_col} , then Ω is close to the minimum value. However, if the reactive rate constant dominates, then Ω is close to one.

The limiting flux out ratio for Table B-1 parameter values ($k = 2 \text{ cm yr}^{-1}$) is $\Omega = 0.297$; in other words, about 29.7 percent of the total plutonium mass exiting the cell is sorbed onto colloids.

The kinetic sorption rate to colloids was defined previously as:

$$r_{f_col} = \hat{S}_{FeO_col} c_{FeO_col} k, \quad (\text{Eq. B-34})$$

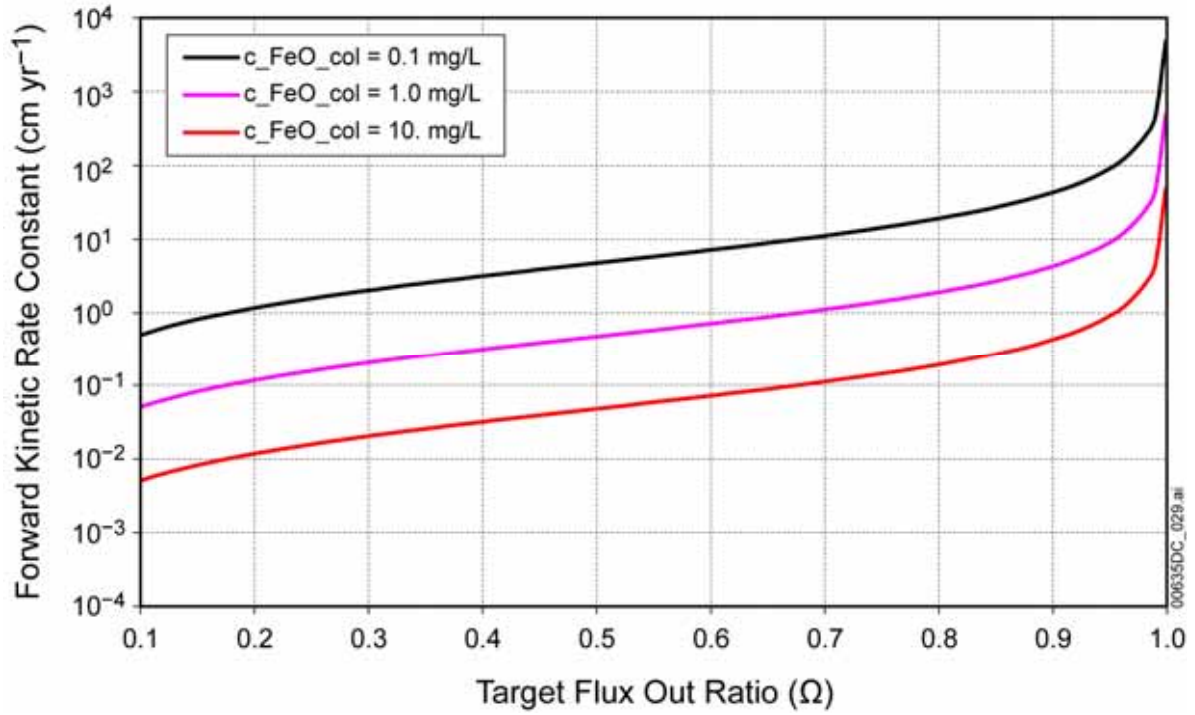
where

k	=	kinetic sorption rate constant
\hat{S}_{FeO_col}	=	specific surface area of FeO colloids
c_{FeO_col}	=	concentration of FeO colloid in water.

Now consider the kinetic reaction rate k a fitting parameter to match a specified flux out ratio Ω . Then the solution of Equation B-30 for k is:

$$k = \frac{p_2 \Omega - p_1}{(1 - \Omega) \hat{S}_{FeO_col} c_{FeO_col}}. \quad (\text{Eq. B-35})$$

The result in Equation B-35 provides the fitting parameter, k , given a target flux out ratio Ω . From the parameter values in Table B-1 and with $\Omega = 0.95$, the kinetic linear reaction rate is determined from Equation B-35 as $k = 91.05 \text{ cm yr}^{-1}$. The fitting parameter curve is shown on Figure B-3 for a family of FeO colloid concentrations. From Equation B-35 it follows that the kinetic rate k depends inversely on the FeO colloid concentration. Therefore, on Figure B-3 as the FeO colloid concentration is increased an order of magnitude, the fitting curve is reduced an order of magnitude.



Source: Output DTN: SN0703PAEBSRTA.001, file *flux_out_ratio.xls*

Figure B-3. Kinetic Sorption Reaction Rate as a Function of Colloid to Total Flux Out Ratio, Ω

INTENTIONALLY LEFT BLANK

APPENDIX C

MICROSOFT EXCEL SPREADSHEET “FLUX SPLIT DRIP SHIELD MODEL”

MICROSOFT EXCEL SPREADSHEET “FLUX SPLIT DRIP SHIELD MODEL” SPREADSHEET “FLUX SPLIT DRIP SHIELD MODEL” WORKSHEET “F CALCULATIONS”

Breach Flow Fraction Calculation using Smooth Drip Shield Data, On-Crown Tests														
Source Data							Calculated results							
DTN: MO0207EBSATBWP.023														
For $\alpha = 8.8708$ degrees														
Drip Location (Test Description)	Breach No.	g , Drip Location Relative to Breach Center (cm)	z , Vertical Distance from Crown (drip) to Top of Breach (cm)	l , Patch half-width (cm)	Drip Flux (g)	Flow into Breach (g)	f_{exp}	f_{mod}	Model Case #	Y_a	Y_b	Y_c	Y_d	Fraction Case #
8 cm right of Patch 4 centerline (Q(film) Test)	4	8	136.5	13.5	178.2	22.02	0.2471	21.3040	2	-39.0180	-7.8040	7.8040	39.0180	5
Patch 5 centerline (Q(film) Test)	5	0	86	13.5	163.74	21.12	0.2580	13.4223	1	-31.1363	-0.0777	0.0777	31.1363	4
4 cm left of Patch 5 centerline (Q(film) Test)	5	-4	86	13.5	133.79	9.1	0.1360	13.4223	1	-31.1363	-0.0777	0.0777	31.1363	3
Patch 4 centerline (Q(film) Test)	4	0	136.5	13.5	188.63	22.25	0.2359	21.3040	2	-39.0180	-7.8040	7.8040	39.0180	4
27 cm right of DS center (Multiple Patch Test)	5	-27	86	13.5	276.14	4.49	0.0325	13.4223	1	-31.1363	-0.0777	0.0777	31.1363	2
27 cm left of DS center (Multiple patch test)	4	27	136.5	13.5	276.83	2.63	0.0190	21.3040	2	-39.0180	-7.8040	7.8040	39.0180	6
81 cm left of DS center (Multiple Patch Test)	4	-27	136.5	13.5	226.22	3.45	0.0305	21.3040	2	-39.0180	-7.8040	7.8040	39.0180	2
81 cm right of DS center (Multiple Patch Test)	5	27	86	13.5	221.12	3.54	0.0320	13.4223	1	-31.1363	-0.0777	0.0777	31.1363	6
54 cm left of DS center (High Flow Rate Test)	4	0	136.5	13.5	337.72	46.41	0.2748	21.3040	2	-39.0180	-7.8040	7.8040	39.0180	4
54 cm left of DS center (Low Flow Rate Test)	4	0	136.5	13.5	88.89	7.88	0.1773	21.3040	2	-39.0180	-7.8040	7.8040	39.0180	4
27 cm left of DS center (High Flow Rate Test)	4	27	136.5	13.5	332.69	3.35	0.0201	21.3040	2	-39.0180	-7.8040	7.8040	39.0180	6
27 cm left of DS center (Low Flow Rate Test)	4	27	136.5	13.5	100.95	0.65	0.0129	21.3040	2	-39.0180	-7.8040	7.8040	39.0180	6
27 cm right of DS center (High Flow Rate Test)	5	-27	86	13.5	378.73	2.45	0.0129	13.4223	1	-31.1363	-0.0777	0.0777	31.1363	2
27 cm right of DS center (Low Flow Rate Test)	5	-27	86	13.5	137.72	4.45	0.0646	13.4223	1	-31.1363	-0.0777	0.0777	31.1363	2
DTN: MO0207EBSATBWP.024														
DTN: MO0207EBSATBWP.025														

Source: DTN: MO0207EBSATBWP.023 [DIRS 163402]; DTN: MO0207EBSATBWP.024 [DIRS 163401]; DTN: MO0207EBSATBWP.025 [DIRS 163403]. Output DTN: SN0703PAEBSRTA.001, file *Flux Split Drip Shield Model.xls*, worksheet “f calculations”

Figure C-1. Calculation of Experimental Breach Flow Fractions and Model Flow Fractions for Mean Minus One Standard Deviation Rivulet Spread Angle

The purpose of this spreadsheet is to develop the drip shield flux-splitting submodel using experimental data from the breached drip shield experiments. The data are analyzed to estimate an average and range of the rivulet spread angle, α . The disparity between measured fraction of dripping flux that enters a breach and the fraction calculated using the model (with the measured range of the rivulet spread angle) is then used to establish a range of uncertainty in the model.

All descriptions for this worksheet (Figures C-1 to C-4) pertain to Rows 9–22. Equations in spreadsheet format are illustrated using Row 9.

Column B: Drip location as indicated for each test in the designated DTN (Figure C-1).

Column C: Breach or patch number most pertinent to this particular test, for which flow is analyzed in this row of the spreadsheet.

Column D: Drip location, y , relative to the center of the breach listed in Column C.

Column E: Distance along the drip shield curved surface, x , from the drip shield crown to the top of the breach.

Column F: Half-width, ℓ , of the breach (13.5 cm), same for all breaches.

Column G: Measured mass of water, F_1 , dripped onto the drip shield during the test. It is assumed that half of the water that dripped onto the drip shield, $F_1/2$, flowed down the side that contained the breach.

Column H: Measured mass of water, F_2 , that flowed into the breach during the test.

Column I: Fraction of water dripped onto the drip shield that flowed into the breach:

$$f_{\text{expt}} = \frac{F_2}{F_1/2} = \frac{2F_2}{F_1}.$$

$$I9=H9*2/G9$$

Column J: $x \tan \alpha$, where x is from Column E, and α is the spread angle. For Columns J-X, the value used for α is 8.8708° (Cell $\$M\7), which is one standard deviation less than the mean measured spread angle for these tests (see Worksheet “Spread angles”).

$$J9=\$E9*\text{TAN}(\text{RADIANS}(\$M\$7))$$

Column K: Case number as described in Sections 6.5.1.1.2.1 and 6.5.1.1.2.2. For Case 1, $\ell > x \tan \alpha$; for Case 2, $\ell < x \tan \alpha$; x is from Column E, and the half-width of the breach, ℓ , is from Column F.

$$K9=\text{IF}(\$F9>J9,1,2)$$

Column L: Value of y_A (Point A) as described in Sections 6.5.1.1.2.1 and 6.5.1.1.2.2, corresponding to the leftmost point from which the edge of the fan from the rivulet can enter the left side of the breach:

$$y_A = -\ell - (x + 2\ell) \tan \alpha$$

$$L9=-\$F9-(\$E9+2*\$F9)*\text{TAN}(\text{RADIANS}(\$M\$7))$$

Column M: Value of y_B (Point B) as described in Sections 6.5.1.1.2.1 and 6.5.1.1.2.2, corresponding to the leftmost point from which rivulets will enter the top edge of the breach. The value of y_B depends on the Model Case number (Column K):

$$y_B = -\ell + x \tan \alpha \quad \text{Case 1.}$$

$$y_B = \ell - x \tan \alpha \quad \text{Case 2.}$$

$$M9=IF(K9=1,(-\$F9+\$E9*TAN(RADIANS(\$M\$7))), \\ (\$F9-\$E9*TAN(RADIANS(\$M\$7))))$$

Column N: Value of y_C (Point C) as described in Sections 6.5.1.1.2.1 and 6.5.1.1.2.2, corresponding to the rightmost point from which rivulets will enter the top edge of the breach. The value of y_C depends on the Model Case number (Column K):

$$y_C = \ell - x \tan \alpha \quad \text{Case 1.}$$

$$y_C = -\ell + x \tan \alpha \quad \text{Case 2.}$$

$$N9=IF(K9=1,(\$F9-\$E9*TAN(RADIANS(\$M\$7))), \\ (-\$F9+\$E9*TAN(RADIANS(\$M\$7))))$$

Column O: Value of y_D (Point D) as described in Sections 6.5.1.1.2.1 and 6.5.1.1.2.2, corresponding to the rightmost point from which the edge of the fan from the rivulet can enter the right side of the breach:

$$y_D = \ell + (x + 2\ell) \tan \alpha$$

$$O9=\$F9+(\$E9+2*\$F9)*TAN(RADIANS(\$M\$7))$$

Column P: Determines which region (designated as Fraction Case #) along the crown where the drip is located:

1. $y \leq y_A$
2. $y_A < y \leq -\ell$
3. $-\ell < y < y_B$
4. $y_B \leq y \leq y_C$
5. $y_C < y < \ell$
6. $\ell \leq y < y_D$
7. $y \geq y_D$

$$P9=IF(D9<=L9,1,IF(D9<=-F9,2,IF(D9<M9,3, \\ IF(D9<=N9,4,IF(D9<F9,5,IF(D9<O9,6,IF(D9>=O9,7))))))$$

	I	J	K	L	M	N	O	P	Q	R	S	T	U	V	W	X
1	Crown Tests															
2																
3																
4	The spread angles are the mean, 1-sigma, and 1+sigma, calculated on the "Spread Angles" sheet			This cell performs a conditional test, comparing y to Ya, Yb, Yc, Yd, and I to determine which case applies					This cell is the I value determined by the appropriate case of the 7							
5																
6																
7	For $\alpha = 8.8708$ degrees															
8	f_{expt}	$f_{tan(\alpha)}$	Model Case #	Y_a	Y_b	Y_c	Y_d	Fraction Case #	f_{calc}	f_1	f_2	f_3	f_4	f_5	f_6	f_7
9	0.2471	21.3040	2	-39.0180	-7.8040	7.8040	39.0180	5	0.6291	0.0000	0.9213	1.0046	0.6337	0.6291	0.6078	0.0000
10	0.2580	13.4223	1	-31.1363	-0.0777	0.0777	31.1363	4	1.0000	0.0000	0.8827	1.0029	1.0000	1.0029	0.8827	0.0000
11	0.1360	13.4223	1	-31.1363	-0.0777	0.0777	31.1363	3	0.8539	0.0000	0.7693	0.8539	1.0000	1.1519	0.9961	0.0000
12	0.2359	21.3040	2	-39.0180	-7.8040	7.8040	39.0180	4	0.6337	0.0000	0.7645	0.8168	0.6337	0.8168	0.7645	0.0000
13	0.0325	13.4223	1	-31.1363	-0.0777	0.0777	31.1363	2	0.1173	0.0000	0.1173	-0.0029	1.0000	2.0087	1.6482	0.0000
14	0.0190	21.3040	2	-39.0180	-7.8040	7.8040	39.0180	6	0.2355	0.0000	1.2936	1.4505	0.6337	0.1832	0.2355	0.0000
15	0.0305	21.3040	2	-39.0180	-7.8040	7.8040	39.0180	2	0.2355	0.0000	0.2355	0.1832	0.6337	1.4505	1.2936	0.0000
16	0.0320	13.4223	1	-31.1363	-0.0777	0.0777	31.1363	6	0.1173	0.0000	1.6482	2.0087	1.0000	-0.0029	0.1173	0.0000
17	0.2748	21.3040	2	-39.0180	-7.8040	7.8040	39.0180	4	0.6337	0.0000	0.7645	0.8168	0.6337	0.8168	0.7645	0.0000
18	0.1773	21.3040	2	-39.0180	-7.8040	7.8040	39.0180	4	0.6337	0.0000	0.7645	0.8168	0.6337	0.8168	0.7645	0.0000
19	0.0201	21.3040	2	-39.0180	-7.8040	7.8040	39.0180	6	0.2355	0.0000	1.2936	1.4505	0.6337	0.1832	0.2355	0.0000
20	0.0129	21.3040	2	-39.0180	-7.8040	7.8040	39.0180	6	0.2355	0.0000	1.2936	1.4505	0.6337	0.1832	0.2355	0.0000
21	0.0129	13.4223	1	-31.1363	-0.0777	0.0777	31.1363	2	0.1173	0.0000	0.1173	-0.0029	1.0000	2.0087	1.6482	0.0000
22	0.0646	13.4223	1	-31.1363	-0.0777	0.0777	31.1363	2	0.1173	0.0000	0.1173	-0.0029	1.0000	2.0087	1.6482	0.0000
23																

Source: Output DTN: SN0703PAEBSRTA.001, file *Flux Split Drip Shield Model.xls*, worksheet "f calculations"

Figure C-2. Calculation of Model Flow Fractions for Mean Minus One Standard Deviation Rivulet Spread Angle

Columns R through X (Figure C-2) compute the fraction of dripping flux f_{calc} that is predicted to flow into a breach, assuming the drip location is within each of seven regions along the crown. Although f_{calc} is computed for all seven regions, it is valid in only one of the regions. The correct valid region is determined in Column P (Fraction Case #), and the appropriate value from Columns R through X is entered in Column Q.

Column Q: f_{calc} is the fraction of dripping flux onto the drip shield that is predicted by the drip shield flux-splitting submodel, Equations 6.5.1.1.2-2 through 6.5.1.1.2-6 or 6.5.1.1.2-19 through 6.5.1.1.2-23, for Cases 1 and 2, respectively. f_{calc} is intended to be compared with f_{expt} (Column I). The value of f_{calc} is selected from Columns R through X, depending on the appropriate Fraction Case # (Column P).

$$Q9=IF(P9=1,R9,IF(P9=2,S9,IF(P9=3,T9,IF(P9=4,U9,IF(P9=5,V9,IF(P9=6,W9,IF(P9=7,X9))))))$$

Column R: Value of f_{calc} in region 1 ($y \leq y_A$), where $f_{calc} = 0$.

$$R9=0$$

Column S: Value of f_{calc} in region 2 ($y_A < y \leq -\ell$):

$$f_{calc} = \frac{y + \ell + (x + 2\ell) \tan \alpha}{2(x + 2\ell) \tan \alpha}$$

$$S9=(D9+F9+(E9+2*F9)*TAN(RADIANS(M7)))/(2*(E9+2*F9)*TAN(RADIANS(M7)))$$

Column T: Value of f_{calc} in region 3 ($-\ell < y < y_B$):

$$f_{calc} = \frac{y + \ell + x \tan \alpha}{2x \tan \alpha}$$

$$T9=(D9+F9+E9*TAN(RADIANS(M7)))/(2*E9*TAN(RADIANS(M7)))$$

Column U: Value of f_{calc} in region 4 ($y_B \leq y \leq y_C$):

$$f_{calc} = \frac{2\ell}{2x \tan \alpha}$$

$$U9=IF(K9=1,1,(2*$F9/(2*$E9*TAN(RADIANS(M7))))))$$

Column V: Value of f_{calc} in region 5 ($y_C < y < \ell$):

$$f_{calc} = \frac{-y + \ell + x \tan \alpha}{2x \tan \alpha}$$

$$V9=(-D9+F9+E9*TAN(RADIANS(M7)))/(2*E9*TAN(RADIANS(M7)))$$

Column W: Value of f_{calc} in region 6 ($\ell \leq y < y_D$):

$$f_{calc} = \frac{-y + \ell + (x + 2\ell) \tan \alpha}{2(x + 2\ell) \tan \alpha}$$

$$W9=(-D9+F9+(E9+2*F9)*TAN(RADIANS(M7)))/(2*(E9+2*F9)*TAN(RADIANS(M7)))$$

Column X: Value of f_{calc} in region 7 ($y \geq y_D$) where $f_{calc} = 0$:

$$X9=0$$

	Y	Z	AA	AB	AC	AD	AE	AF	AG	AH	AI	AJ	AK	AL	AM
1															
2															
3															
4															
5															
6															
7	For $\alpha = 13.1527$ degrees														
8	$E \cdot \tan(\alpha_j)$	Mode Case #	Y_a	Y_b	Y_c	Y_d	Fractio n Case #	f_{total}	f_1	f_2	f_3	f_4	f_5	f_6	f_7
9	31.8968	2	-51.7061	-18.3968	18.3968	51.7061	4	0.4232	0.0000	0.7814	0.8370	0.4232	0.5862	0.5720	0.0000
10	20.0962	2	-39.9054	-6.5962	6.5962	39.9054	4	0.6718	0.0000	0.7556	0.8359	0.6718	0.8359	0.7556	0.0000
11	20.0962	2	-39.9054	-6.5962	6.5962	39.9054	2	0.6799	0.0000	0.6799	0.7364	0.6718	0.9354	0.8314	0.0000
12	31.8968	2	-51.7061	-18.3968	18.3968	51.7061	4	0.4232	0.0000	0.6767	0.7116	0.4232	0.7116	0.6767	0.0000
13	20.0962	2	-39.9054	-6.5962	6.5962	39.9054	2	0.2444	0.0000	0.2444	0.1641	0.6718	1.5077	1.2669	0.0000
14	31.8968	2	-51.7061	-18.3968	18.3968	51.7061	6	0.3233	0.0000	1.0300	1.1349	0.4232	0.2884	0.3233	0.0000
15	31.8968	2	-51.7061	-18.3968	18.3968	51.7061	2	0.3233	0.0000	0.3233	0.2884	0.4232	1.1349	1.0300	0.0000
16	20.0962	2	-39.9054	-6.5962	6.5962	39.9054	6	0.2444	0.0000	1.2669	1.5077	0.6718	0.1641	0.2444	0.0000
17	31.8968	2	-51.7061	-18.3968	18.3968	51.7061	4	0.4232	0.0000	0.6767	0.7116	0.4232	0.7116	0.6767	0.0000
18	31.8968	2	-51.7061	-18.3968	18.3968	51.7061	4	0.4232	0.0000	0.6767	0.7116	0.4232	0.7116	0.6767	0.0000
19	31.8968	2	-51.7061	-18.3968	18.3968	51.7061	6	0.3233	0.0000	1.0300	1.1349	0.4232	0.2884	0.3233	0.0000
20	31.8968	2	-51.7061	-18.3968	18.3968	51.7061	6	0.3233	0.0000	1.0300	1.1349	0.4232	0.2884	0.3233	0.0000
21	20.0962	2	-39.9054	-6.5962	6.5962	39.9054	2	0.2444	0.0000	0.2444	0.1641	0.6718	1.5077	1.2669	0.0000
22	20.0962	2	-39.9054	-6.5962	6.5962	39.9054	2	0.2444	0.0000	0.2444	0.1641	0.6718	1.5077	1.2669	0.0000

Source: Output DTN: SN0703PAEBSRTA.001, file *Flux Split Drip Shield Model.xls*, worksheet "f calculations"

Figure C-3. Calculation of Model Flow Fractions for Mean Rivulet Spread Angle

Columns Y through AM (Figure C-3) repeat the calculations performed in Columns J through X using the mean rivulet spread angle of $\alpha = 13.1527^\circ$ (Cell \$AB\$7). For Row 9, the spreadsheet equations are as follows:

$$Y9 = \$E9 * \text{TAN}(\text{RADIANS}(\$AB\$7))$$

$$Z9 = \text{IF}(\$F9 > Y9, 1, 2)$$

$$AA9 = -\$F9 - (\$E9 + 2 * \$F9) * \text{TAN}(\text{RADIANS}(\$AB\$7))$$

$$AB9 = \text{IF}(Z9 = 1, (-\$F9 + \$E9 * \text{TAN}(\text{RADIANS}(\$AB\$7))), (\$F9 - \$E9 * \text{TAN}(\text{RADIANS}(\$AB\$7))))$$

$$AC9 = \text{IF}(Z9 = 1, (\$F9 - \$E9 * \text{TAN}(\text{RADIANS}(\$AC\$7))), (-\$F9 + \$E9 * \text{TAN}(\text{RADIANS}(\$AB\$7))))$$

$$AD9 = \$F9 + (\$E9 + 2 * \$F9) * \text{TAN}(\text{RADIANS}(\$AB\$7))$$

$$AE9 = \text{IF}(D9 \leq AA9, 1, \text{IF}(D9 < -U9, 2, \text{IF}(D9 < AB9, 3, \text{IF}(D9 \leq AC9, 4, \text{IF}(D9 < U9, 5, \text{IF}(D9 < AD9, 6, \text{IF}(D9 \geq AD9, 7))))))$$

AF9=IF(AE9=1,AG9,IF(AE9=2,AH9,IF(AE9=3,AI9,IF(AE9=4,AJ9,IF(AE9=5,AK9,IF(AE9=6,AL9,IF(AE9=7,AM9))))))

AG9=0

AH9=(D9+F9+(E9+2*F9)*TAN(RADIANS(\$AB\$7)))/
(2*(E9+2*F9)*TAN(RADIANS(\$AB\$7)))

AI9=(D9+F9+E9*TAN(RADIANS(\$AB\$7)))/(2*E9*TAN(RADIANS(\$AB\$7)))

AJ9=IF(Z9=1,1,(2*\$F9/(2*\$E9*TAN(RADIANS(\$AB\$7)))))

AK9=(-D9+F9+E9*TAN(RADIANS(\$AB\$7)))/(2*E9*TAN(RADIANS(\$AB\$7)))

AL9=(-D9+F9+(E9+2*F9)*TAN(RADIANS(\$AB\$7))/
(2*(E9+2*F9)*TAN(RADIANS(\$AB\$7)))

AM9=0

Columns AN through BB (Figure C-1) repeat the calculations performed in Columns J through X using a rivulet spread angle of $\alpha = 17.2903^\circ$ (Cell \$AQ\$7), which is one standard deviation greater than the mean rivulet spread angle. For Row 9, the spreadsheet equations are as follows:

AN9=\$E9*TAN(RADIANS(\$AQ\$7))

AO9=IF(\$F9>AN9,1,2)

AP9=-\$F9-(\$E9+2*\$F9)*TAN(RADIANS(\$AQ\$7))

AQ9=IF(AO9=1,(-\$F9+\$E9*TAN(RADIANS(\$AQ\$7))),(\$F9-\$E9*TAN(RADIANS(\$AQ\$7))))

AR9=IF(AO9=1,(\$F9-\$E9*TAN(RADIANS(\$AQ\$7))),
(-\$F9+\$E9*TAN(RADIANS(\$AQ\$7))))

AS9=\$F9+(\$E9+2*\$F9)*TAN(RADIANS(\$AQ\$7))

AT9=IF(AH9<=AP9,1,IF(AH9<=-AJ9,2,IF(AH9<AQ9,3,IF(AH9<=AR9,4,
IF(AH9<AJ9,5,IF(AH9<AS9,6,IF(AH9>=AS9,7))))))

AU9=IF(AT9=1,AV9,IF(AT9=2,AW9,IF(AT9=3,AX9,IF(AT9=4,AY9,IF(AT9=5,AZ9,IF
(AT9=6,BA9,IF(AT9=7,BB9))))))

AV9=0

AW9=(D9+F9+(E9+2*F9)*TAN(RADIANS(\$AQ\$7)))/
(2*(E9+2*F9)*TAN(RADIANS(\$AQ\$7)))

AX9=(D9+F9+E9*TAN(RADIANS(\$AQ\$7)))/(2*E9*TAN(RADIANS(\$AQ\$7)))

AY9=IF(AO9=1,1,(2*\$F9/(2*\$E9*TAN(RADIANS(\$AQ\$7)))))

AZ9=(-D9+F9+E9*TAN(RADIANS(\$AQ\$7)))/(2*E9*TAN(RADIANS(\$AQ\$7)))

BA9=(-D9+F9+(E9+2*F9)*TAN(RADIANS(\$AQ\$7))/
(2*(E9+2*F9)*TAN(RADIANS(\$AQ\$7)))

BB9=0

	AN	AO	AP	AQ	AR	AS	AT	AU	AV	AW	AX	AY	AZ	BA	BB
1															
2															
3															
4															
5															
6															
7	For $\alpha = #####$ degrees														
8	$x \cdot \tan(\alpha)$	Mode / Case #	Ya	Yb	Yc	Yd	Fracti on Case #	f _{total}	f1	f2	f3	f4	f5	f6	f7
9	42.4896	2	-64.3942	-28.9896	28.9896	64.3942	4	0.3177	0.0000	0.7112	0.7530	0.3177	0.5647	0.5540	0.0000
10	26.7700	2	-48.6746	-13.2700	13.2700	48.6746	4	0.5043	0.0000	0.6919	0.7521	0.5043	0.7521	0.6919	0.0000
11	26.7700	2	-48.6746	-13.2700	13.2700	48.6746	4	0.5043	0.0000	0.6350	0.6774	0.5043	0.8269	0.7488	0.0000
12	42.4896	2	-64.3942	-28.9896	28.9896	64.3942	4	0.3177	0.0000	0.6326	0.6589	0.3177	0.6589	0.6326	0.0000
13	26.7700	2	-48.6746	-13.2700	13.2700	48.6746	4	0.5043	0.0000	0.3081	0.2479	0.5043	1.2564	1.0757	0.0000
14	42.4896	2	-64.3942	-28.9896	28.9896	64.3942	4	0.3177	0.0000	0.8979	0.9766	0.3177	0.3411	0.3674	0.0000
15	42.4896	2	-64.3942	-28.9896	28.9896	64.3942	4	0.3177	0.0000	0.3674	0.3411	0.3177	0.9766	0.8979	0.0000
16	26.7700	2	-48.6746	-13.2700	13.2700	48.6746	4	0.5043	0.0000	1.0757	1.2564	0.5043	0.2479	0.3081	0.0000
17	42.4896	2	-64.3942	-28.9896	28.9896	64.3942	4	0.3177	0.0000	0.6326	0.6589	0.3177	0.6589	0.6326	0.0000
18	42.4896	2	-64.3942	-28.9896	28.9896	64.3942	4	0.3177	0.0000	0.6326	0.6589	0.3177	0.6589	0.6326	0.0000
19	42.4896	2	-64.3942	-28.9896	28.9896	64.3942	4	0.3177	0.0000	0.8979	0.9766	0.3177	0.3411	0.3674	0.0000
20	42.4896	2	-64.3942	-28.9896	28.9896	64.3942	4	0.3177	0.0000	0.8979	0.9766	0.3177	0.3411	0.3674	0.0000
21	26.7700	2	-48.6746	-13.2700	13.2700	48.6746	4	0.5043	0.0000	0.3081	0.2479	0.5043	1.2564	1.0757	0.0000
22	26.7700	2	-48.6746	-13.2700	13.2700	48.6746	4	0.5043	0.0000	0.3081	0.2479	0.5043	1.2564	1.0757	0.0000

Source: Output DTN: SN0703PAEBSRTA.001, file *Flux Split Drip Shield Model.xls*, worksheet "f calculations"

Figure C-4. Calculation of Model Flow Fractions for Mean Plus One Standard Deviation Rivulet Spread Angle

Rivulet spread measurements are listed in Column D, Rows 6-31 (Figure C-5), for 26 tests described in the indicated DTNs. The sketch to the right shows the relationships between measured rivulet spread ("1/2 spread") and the "1/2 spread angle," α . The average, μ_r , of the 26 spread measurements (Cell D33) is 20.096 cm, with a standard deviation, σ , of 6.674 cm. The uncertainty in the spread angle is incorporated into the drip shield flux-splitting submodel by assigning a range for the rivulet spread of $\mu_r \pm 1\sigma$, with one standard deviation being reasonably representative of the spread observed in the measured spread angles. The mean rivulet spread and $\mu_r \pm 1\sigma$ are shown in Cells K6-K8. The rivulet spread is converted to spread angle in Cells L6-L8 using the relation shown on the sketch that defines α :

$$\alpha = \tan^{-1}\left(\frac{w_r}{x}\right),$$

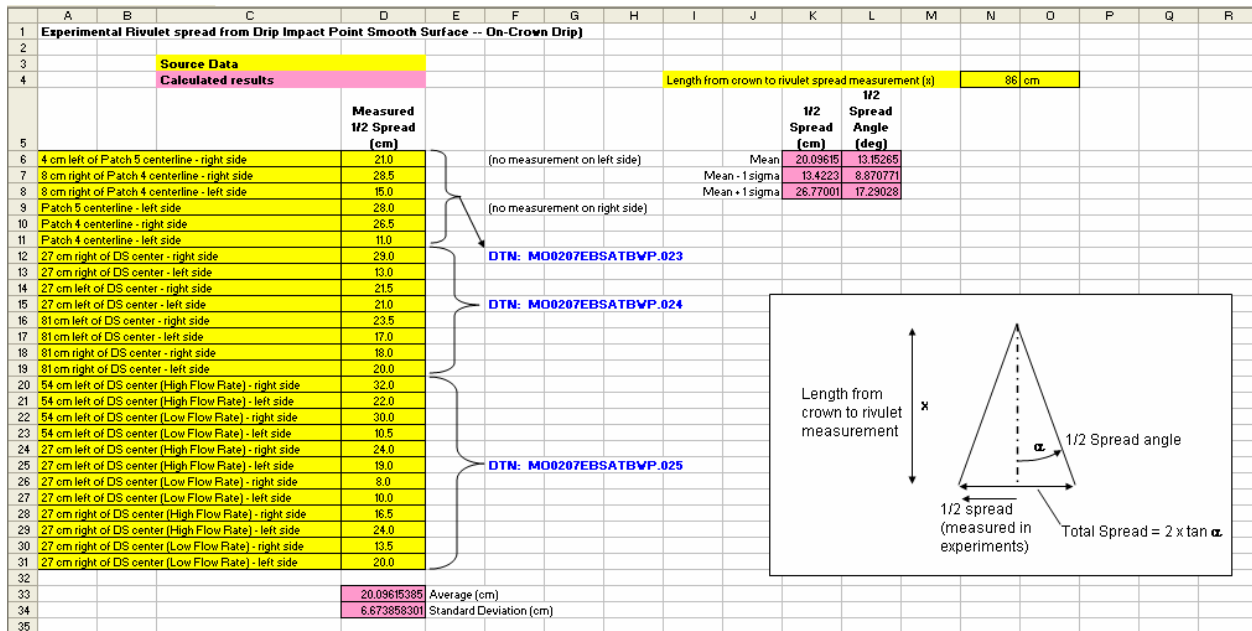
where w_r is the rivulet “1/2 spread” (cm), and x is the distance from the crown to the spread measurement location (cm). The Microsoft Excel equation for the mean spread angle is:

$$L6=DEGREES(ATAN(K6/(\$N\$4)))$$

where $\$N\$4 = x = 86$ cm for these tests. The Microsoft Excel function ATAN returns a value in radians, which must be converted to degrees using the DEGREES function.

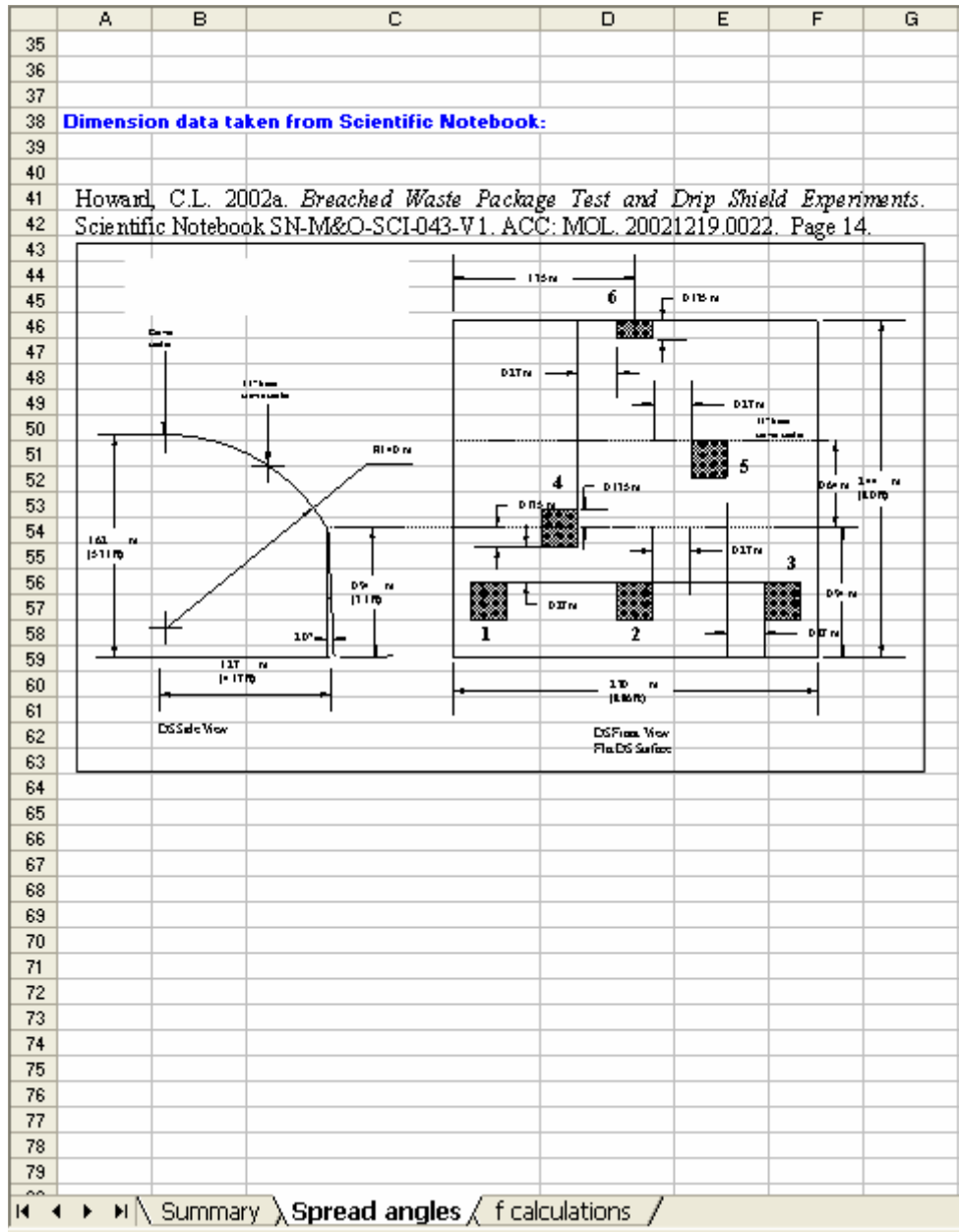
Also included in this worksheet is a sketch (Figure C-6) showing the dimensions and locations of breaches in the drip shield mockup used in the experiments. The sketch appears in the scientific notebook from the experiments (Howard 2002 [DIRS 161516], p. 14), and is also shown on Figure 4.1-1, Section 4.1.1.

SPREADSHEET “FLUX SPLIT DRIP SHIELD MODEL” WORKSHEET “SPREAD ANGLES”



Source:DTN: MO0207EBSATBWP.023 [DIRS 163402]; DTN: MO0207EBSATBWP.024 [DIRS 163401];
 DTN: MO0207EBSATBWP.025 [DIRS 163403]. Output DTN: SN0703PAEBSRTA.001, file *Flux Split Drip Shield Model.xls*, worksheet “Spread angles.”

Figure C-5. Calculation of Rivulet Spread Angle



Source: Howard 2002 [DIRS 161516], p. 14. Output DTN: SN0703PAEBSRTA.001, file *Flux Split Drip Shield Model.xls*, worksheet "Spread angles."

Figure C-6. Dimensions and Locations of Breaches in Drip Shield Mockup Used in Breached Drip Shield Experiments

SPREADSHEET “FLUX SPLIT DRIP SHIELD MODEL” WORKSHEET “SUMMARY”

	A	B	C	D	E	F	G	H	I	J	K
1											
2		Drip Shield Model: Comparison of Measured and Modeled Fraction of Drip Seepage Flowing into a Breach									
3											
4											
5											
6		This spreadsheet compares results from the "Atlas Breached Waste Package and Drip Shield Experiments: Breached Drip Shield Tests" (documented in TDR-EBS-MD-000025-00 REV 00) with the model developed in the "EBS Radionuclide Transport Abstraction" (ANL-WIS-PA-0000001 REV 02). Test data are taken directly from the TDMS for this comparison.									
7											
8		<u>Methodology:</u>									
9		1. Spreading angles are calculated from the test data in the sheet titled <u>Spread angles</u>									
10		2. Given spread angle and test geometry, seepage fractions are calculated for both the test data and the model in the worksheet <u>f calculations</u> :									
11			a. Geometric data for each measurement (x,y,l) and the spread angle are used to determine which of 7 cases the measurement corresponds to								
12			b. For each test result the appropriate case model is applied to calculate the seepage flow fraction f								
13		3. The seepage fractions calculated from both the test and model are listed and compared in the two tables listed below in this <u>Summary</u> worksheet									
14											
15		<u>Notes:</u>									
16		Source data DTNs are noted where source data is used									
17		Model equations are provided on the calculational sheets									
18		Data in tables below is linked directly to the calculational worksheets									
19											

Source: BSC 2003 [DIRS 163406]. Output DTN: SN0703PAEBSRTA.001, file *Flux Split Drip Shield Model.xls*, worksheet "Summary."

Figure C-7. Summary of Drip Shield Flux-Splitting Submodel

This worksheet, beginning with Figure C-7, summarizes the calculations in worksheets "Spread angles" and "f calculations."

The first table (Figure C-8), "Measured Breach Flow Fractions and Calculated Breach Flow Fractions," Rows 25-43, Columns B-I, is identical to Table 6.5-2. Columns B-E are identical to the same respective columns described earlier for worksheet "f calculations." Column F is identical to Column I in worksheet "f calculations." Columns G-I summarize the calculated fraction of the dripping flux that the flux-splitting submodel predicts should flow into the breach, for the minimum, mean, and maximum spread angles. The minimum spread angle is specified to be one standard deviation less than the mean of the measured spread angles. The maximum spread angle is specified to be one standard deviation greater than the mean of the measured spread angles. Column G is identical to Column Q of worksheet "f calculations." Column H is identical to Column AF of worksheet "f calculations." Column I is identical to Column AU of worksheet "f calculations."

Rows 39-43, Columns F-I, show the results of Microsoft Excel functions "AVERAGE," "STDEVA," "MEDIAN," "MIN", and "MAX," respectively, as applied to Rows 25-38.

	A	B	C	D	E	F	G	H	I
19									
20		Measured Breach Flow Fractions and Calculated Breach Flow Fractions							
21									
22		Drip Location (Test Description)	Breach No.	y, Drip Location Relative to Breach Center (cm)	z, Vertical Distance from Crown (drip) to Top of Breach (cm)	f_{exp}	f_{calc}		
23	α (deg)						α (deg)	α (deg)	
24							8.87	13.15	17.29
25		8 cm right of Patch 4 centerline [Q(film) Test]	4	8	136.5	0.2471	0.6291	0.4232	0.3177
26		Patch 5 centerline [Q(film) Test]	5	0	86.0	0.2580	1.0000	0.6718	0.5043
27		4 cm left of Patch 5 centerline [Q(film) Test]	5	-4	86.0	0.1360	0.8539	0.6799	0.5043
28		Patch 4 centerline [Q(film) Test]	4	0	136.5	0.2359	0.6337	0.4232	0.3177
29		27 cm right of DS center [Multiple Patch Test]	5	-27	86.0	0.0325	0.1173	0.2444	0.5043
30		27 cm left of DS center [Multiple patch test]	4	27	136.5	0.0190	0.2355	0.3233	0.3177
31		81 cm left of DS center [Multiple Patch Test]	4	-27	136.5	0.0305	0.2355	0.3233	0.3177
32		81 cm right of DS center [Multiple Patch Test]	5	27	86.0	0.0320	0.1173	0.2444	0.5043
33		54 cm left of DS center [High Flow Rate Test]	4	0	136.5	0.2748	0.6337	0.4232	0.3177
34		54 cm left of DS center [Low Flow Rate Test]	4	0	136.5	0.1773	0.6337	0.4232	0.3177
35		27 cm left of DS center [High Flow Rate Test]	4	27	136.5	0.0201	0.2355	0.3233	0.3177
36		27 cm left of DS center [Low Flow Rate Test]	4	27	136.5	0.0129	0.2355	0.3233	0.3177
37		27 cm right of DS center [High Flow Rate Test]	5	-27	86.0	0.0129	0.1173	0.2444	0.5043
38		27 cm right of DS center [Low Flow Rate Test]	5	-27	86.0	0.0646	0.1173	0.2444	0.5043
39		Mean				0.1110	0.4139	0.3797	0.3977
40		Std. Dev.				0.1055	0.3048	0.1438	0.0958
41		Median				0.0486	0.2355	0.3233	0.3177
42		Minimum				0.0129	0.1173	0.2444	0.3177
43		Maximum				0.2748	1.0000	0.6799	0.5043
44									

Source: Output DTN: SN0703PAEBSRTA.001, file *Flux Split Drip Shield Model.xls*, worksheet "Summary."

Figure C-8. Summary of Drip Shield Flux-Splitting Submodel

The second table (Figure C-9), "Comparison of Measured and Calculated Breach Flows," is identical to Table 6.5-3. Column K is again the drip location. Column L is the fraction of dripping flux that flowed into a breach as measured experimentally; this is identical to Column F of the preceding table, or Column I in worksheet "f calculations." The next three columns (M-O) show the difference between the predicted breach flow fraction, f_{calc} , and the measured fraction, f_{expt} , for the minimum, mean, and maximum rivulet spread angle. Columns P-R show the ratio f_{calc} / f_{expt} for the minimum, mean, and maximum rivulet spread angle.

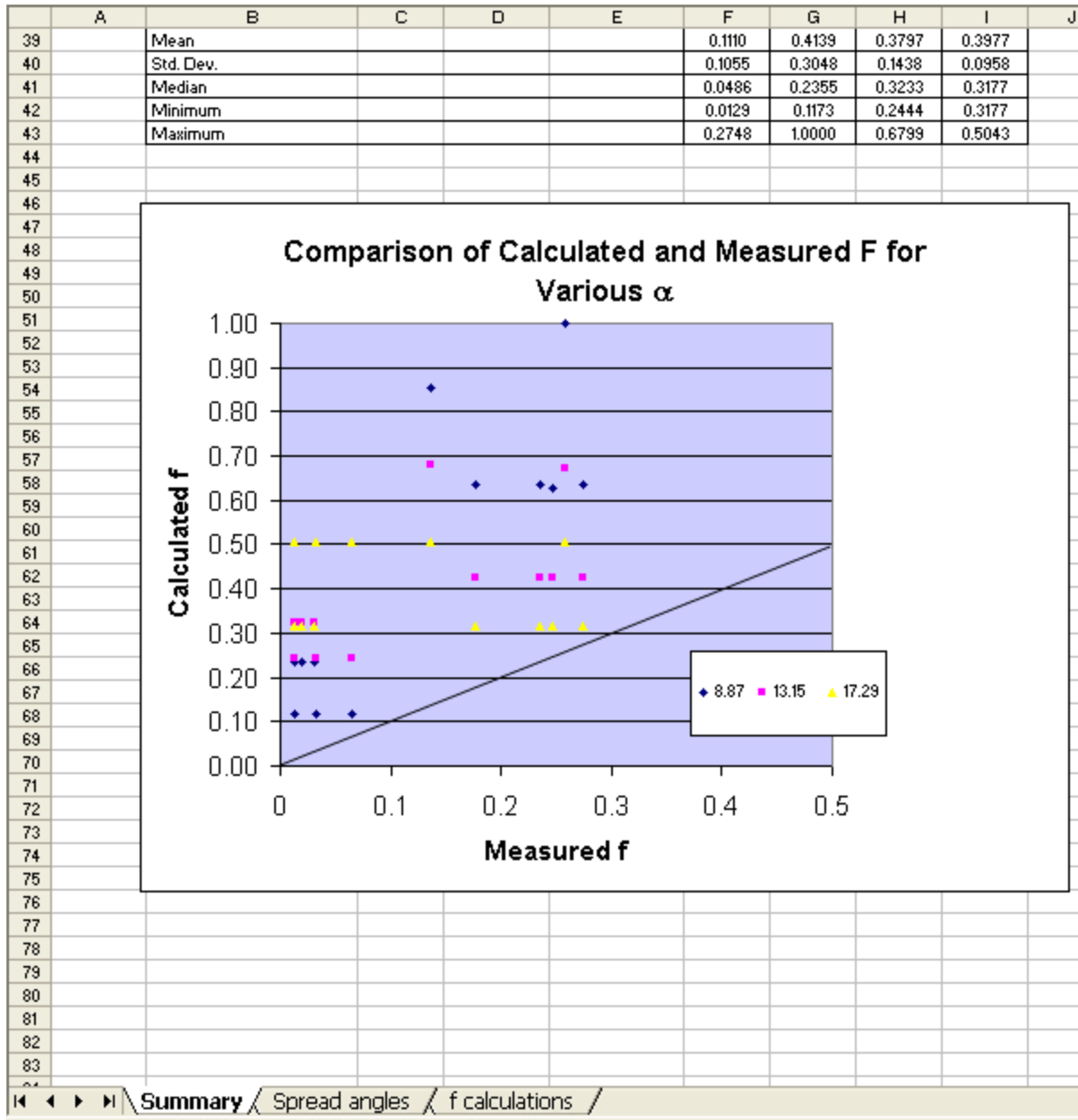
Rows 39-43, Columns L-R, show the results of Microsoft Excel functions "AVERAGE," "STDEVA," "MEDIAN," "MIN," and "MAX," respectively, as applied to Rows 25-38.

	J	K	L	M	N	O	P	Q	R
19									
20									
21		Comparison of Measured and Calculated Breach Flows							
22		Drip Location (Test Description)	f_{expt}	$f_{calc} - f_{expt}$			$f_{calc} \setminus f_{expt}$		
23	α (deg)			α (deg)	α (deg)	α (deg)	α (deg)	α (deg)	
24	8.87			13.15	17.29	8.87	13.15	17.29	
25		8 cm right of Patch 4 centerline [Q(film) Test]	0.2471	0.3819	0.1761	0.0706	2.5455	1.7126	1.2856
26		Patch 5 centerline [Q(film) Test]	0.2580	0.7420	0.4138	0.2463	3.8764	2.6041	1.9549
27		4 cm left of Patch 5 centerline [Q(film) Test]	0.1360	0.7179	0.5439	0.3683	6.2770	4.9979	3.7071
28		Patch 4 centerline [Q(film) Test]	0.2359	0.3978	0.1873	0.0818	2.6861	1.7941	1.3468
29		27 cm right of DS center [Multiple Patch Test]	0.0325	0.0847	0.2119	0.4718	3.6060	7.5145	15.5074
30		27 cm left of DS center [Multiple patch test]	0.0190	0.2165	0.3043	0.2987	12.3932	17.0164	16.7216
31		81 cm left of DS center [Multiple Patch Test]	0.0305	0.2050	0.2928	0.2872	7.7203	10.6004	10.4168
32		81 cm right of DS center [Multiple Patch Test]	0.0320	0.0852	0.2124	0.4723	3.6624	7.6321	15.7500
33		54 cm left of DS center [High Flow Rate Test]	0.2748	0.3588	0.1484	0.0429	2.3056	1.5399	1.1560
34		54 cm left of DS center [Low Flow Rate Test]	0.1773	0.4564	0.2459	0.1404	3.5741	2.3872	1.7920
35		27 cm left of DS center [High Flow Rate Test]	0.0201	0.2153	0.3032	0.2976	11.6928	16.0548	15.7767
36		27 cm left of DS center [Low Flow Rate Test]	0.0129	0.2226	0.3104	0.3048	18.2860	25.1075	24.6725
37		27 cm right of DS center [High Flow Rate Test]	0.0129	0.1043	0.2314	0.4914	9.0637	18.8879	38.9779
38		27 cm right of DS center [Low Flow Rate Test]	0.0646	0.0526	0.1797	0.4397	1.8146	3.7814	7.8035
39		Mean	0.1110	0.3029	0.2687	0.2867	6.3931	8.6879	11.2049
40		Std. Dev.	0.1055	0.2210	0.1065	0.1550	4.8845	7.6717	11.0326
41		Median	0.0486	0.2195	0.2387	0.2982	3.7694	6.2562	9.1102
42		Minimum	0.0129	0.0526	0.1484	0.0429	1.8146	1.5399	1.1560
43		Maximum	0.2748	0.7420	0.5439	0.4914	18.2860	25.1075	38.9779

Source: Output DTN: SN0703PAEBSRTA.001, file *Flux Split Drip Shield Model.xls*, worksheet "Summary."

Figure C-9. Summary of Drip Shield Flux-Splitting Submodel Comparing Measured and Calculated Breach Flows

Finally, a plot in worksheet "Summary" (Figure C-10) compares the calculated f_{calc} with the measured f_{expt} (Column F) for the minimum, mean, and maximum spread angles (Columns G, H, and I, respectively); the f_{expt} and f_{calc} values that are plotted on Figure C-10 are shown on Figure C-8. The diagonal line in the plot represents $f_{calc} = f_{expt}$. All values of f_{calc} lie above the line $f_{calc} = f_{expt}$, indicating that the drip shield flux-splitting submodel overestimates the flow into breaches.



Source: Output DTN: SN0703PAEBSRTA.001, file *Flux Split Drip Shield Model.xls*, worksheet "Summary."

Figure C-10. Comparison of Calculated and Measured Breach Flow Fractions for Drip Shield Flux-Splitting Submodel for Minimum (8.87°), Mean (13.15°), and Maximum (17.29°) Rivulet Spread Angles

APPENDIX D

MICROSOFT EXCEL SPREADSHEET “FLUX SPLIT WASTE PACKAGE MODEL”

MICROSOFT EXCEL SPREADSHEET “FLUX SPLIT WASTE PACKAGE MODEL” SPREADSHEET “FLUX SPLIT WASTE PACKAGE MODEL”–WORKSHEET “F CALCULATIONS”

Breach Flow Fraction Calculation using Smooth Drip Shield Data, Off-Crown Tests													
Single Patch Tests (DTN: MO0207EBSATBWP.023)										Source Data		The Model Case depends on whether the breach is wider (case 1) or narrower (case 2) than the spread at the breach. So the patch width is compared to $x \tan(\alpha)$.	
										Calculated results			
Test Type	Test Date	Drip Location (Test Description)		Breach No.	Location of Drip Relative to DS Centerline (cm)	Location of Breach Relative to DS Centerline (cm)	y, Drip Location Relative to Breach Center (cm)	z, Vertical Distance from Drip to Top of Breach (cm)	l, Patch half-width (cm)	Drip Flux (g)	Flow into Breach (g)	f_{gpc}	$x \tan(\alpha)$
Q(splash)	5/17/2002	P5, 17.5 cm left of center, 33°		4			-17.5	50.5	13.5	89.77	0	0.0000	4.8659
Q(splash)	5/20/2002	P4, center, 33°		4			0.0	50.5	13.5	137.21	109.84	0.8005	4.8659
Q(splash)	5/20/2002	P4, 17.5 cm right of center, 33°		4			17.5	50.5	13.5	131.42	8.96	0.0682	4.8659
Q(splash)	5/21/2002	P4, 17.5 cm right of center, 16.5°		4			17.5	93.5	13.5	150.76	1.79	0.0119	9.0092
Q(splash)	5/21/2002	P4, centerline, 16.5°		4			0.0	93.5	13.5	139.9	84.35	0.6029	9.0092
Q(splash)	5/21/2002	P5, 17.5 cm left of center, 16.5°		5			-17.5	43	13.5	187.5	2.66	0.0142	4.1432
Q(splash)	5/21/2002	P5, 35.5 cm left of center, 16.5°		4			18.5	93.5	13.5	142.28	0.22	0.0015	9.0092
Q(splash)	5/22/2002	P5, centerline, 16.5°		5			0.0	43	13.5	124.74	90.56	0.7260	4.1432
Q(splash)	5/22/2002	P6, 36.5 cm left of center, between crown and 16.5°		4			17.5	115	13.5	129.27	6.63	0.0513	11.0808
Q(film)	5/31/2002	P4, 8 cm right of center, 16.5°		4			8.0	93.5	13.5	172.38	92.53	0.5368	9.0092
Q(film)	5/31/2002	P2, center, 16.5°		4			54.0	93.5	13.5	242.49	151.66	0.6254	9.0092
Q(film)	5/31/2002	P2, 15 cm right of center, 16.5°		5			-39.0	43	13.5	177.22	0.39	0.0022	4.1432
Q(film)	5/31/2002	P5, 4 cm left of center, 16.5°		5			-4.0	43	13.5	173.17	184.54	1.0657	4.1432
Q(film)	6/1/2002	P4, 8 cm right of center, 16.5°		4			8.0	93.5	13.5	137.44	107.39	0.7813	9.0092
Bounding	6/18/2002	54 cm left of DS center, 16.5°		4	-54	-54	0.0	93.5	13.5	353.43	169.77	0.4803	9.0092
Bounding	6/19/2002	54 cm left of DS center, 16.5°		4	-54	-54	0.0	93.5	13.5	107.01	84.55	0.7901	9.0092
Bounding	6/16/2002	27 cm left of DS center, 16.5°		5	-27	54	-81.0	43	13.5	121.76	0.58	0.0048	4.1432
Bounding	6/20/2002	27 cm left of DS center, 16.5°		5	-27	54	-81.0	43	13.5	370.41	1.15	0.0031	4.1432
Bounding	6/20/2002	27 cm right of DS center, 16.5°		5	27	54	-27.0	43	13.5	339.74	4.24	0.0125	4.1432
Bounding	6/20/2002	27 cm right of DS center, 16.5°		5	27	54	-27.0	43	13.5	95.41	0.78	0.0082	4.1432
Bounding	6/20/2002	27 cm left of DS center, 33°		4	-27	-54	27.0	50.5	13.5	367.11	0.96	0.0026	4.8659
Bounding	6/20/2002	27 cm right of DS center, 33°		4	27	-54	81.0	50.5	13.5	317.6	0.62	0.0020	4.8659
Bounding	6/20/2002	54 cm left of DS center, 33°		4	-54	-54	0.0	50.5	13.5	328.85	186.85	0.5682	4.8659
Bounding	6/21/2002	54 cm left of DS center, 33°		4	-54	-54	0.0	50.5	13.5	101.13	83.1	0.8217	4.8659
Bounding	6/24/2002	27 cm left of DS center, 33°		4	-27	-54	27.0	50.5	13.5	96.21	1.18	0.0123	4.8659
Bounding	6/24/2002	27 cm right of DS center, 33°		4	27	-54	81.0	50.5	13.5	95.75	0	0.0000	4.8659

Source:DTN: MO0207EBSATBWP.023 [DIRS 163402]; DTN: MO0207EBSATBWP.025 [DIRS 163403]. Output DTN: SN0703PAEBSRTA.001, file *Flux Split Waste Package Model.xls*, worksheet “f calculations.”

Figure D-1. Calculation of Experimental Breach Flow Fractions and Model Flow Fractions for Mean Minus One Standard Deviation Rivulet Spread Angle

The purpose of this spreadsheet is to develop the waste package flux-splitting submodel using experimental data from the breached drip shield experiments. The data are analyzed to estimate an average and range of the rivulet spread angle, α . The disparity between measured fraction of dripping flux that enters a breach and the fraction calculated using the model (with the measured range of the rivulet spread angle) is then used to establish a range of uncertainty in the model. Whereas the drip shield submodel is based on data from on-crown drip locations, the waste package submodel uses off-crown drip data, for which the drip location is some distance away from the crown of the drip shield mockup.

All descriptions for this worksheet pertain to Rows 9-34. Equations in spreadsheet format are illustrated using Row 9.

Column B: Test type. The first three columns (B-D) help identify uniquely, each test as described in the designated DTN.

Column C: Test date.

Column D: Drip location as indicated for each test in the designated DTN.

Column E: Breach or patch number most pertinent to this particular test, for which flow is analyzed in this row of the spreadsheet.

Column F: Drip location relative to drip shield center. Applies only to Bounding tests, further defining the drip location as specified in the DTN.

Column G: Breach location relative to drip shield center. Applies only to Bounding tests, further defining the breach location as specified in the DTN.

Column H: Drip location, y , relative to the center of the breach listed in Column E.

Column I: Vertical distance, x , from the drip location to the top of the breach.

Column J: Half-width, ℓ , of the breach—13.5 cm, same for all breaches.

Column K: Measured mass of water, F_1 , dripped onto the drip shield during the test. For the on-crown drips, it is assumed that half of the water that dripped onto the drip shield, $F_1/2$, flowed down the side that contained the breach. For these off-crown tests, the full dripping flux is assumed to flow down the side where the drip is located.

Column L: Measured mass of water, F_2 , that flowed into the breach during the test.

Column M: Fraction of water dripped onto the drip shield that flowed into the breach:

$$f_{expt} = \frac{F_2}{F_1}.$$

$$M9=L9/K9$$

Columns N through AB perform calculations that result in f_{calc} , the fraction of dripping flux that is predicted by the model to flow into a breach.

Column N: $x \tan \alpha$, where x is from Column I, and α is the spread angle. For Columns N-AB, the value used for α is 5.5037° (Cell \$Q\$7), which is one standard deviation less than the mean measured spread angle for these tests (see Worksheet “Spread angles”).

$$N9=\$I9*\text{TAN}(\text{RADIANS}(\$Q\$7))$$

Column O: Case number as described in Sections 6.5.1.1.2.1 and 6.5.1.1.2.2. For Case 1, $\ell > x \tan \alpha$; for Case 2, $\ell < x \tan \alpha$; x is from Column I, and the half-width of the breach, ℓ , is from Column J.

$$O9=IF(\$J9>N9,1,2)$$

Column P: Value of y_A (Point A) as described in Sections 6.5.1.1.2.1 and 6.5.1.1.2.2, corresponding to the leftmost point from which the edge of the fan from the rivulet can enter the left side of the breach:

$$y_A = -\ell - (x + 2\ell) \tan \alpha$$

$$P9=-\$J9-(\$I9+2*\$J9)*TAN(RADIANS(\$Q\$7))$$

Column Q: Value of y_B (Point B) as described in Sections 6.5.1.1.2.1 and 6.5.1.1.2.2, corresponding to the leftmost point from which rivulets will enter the top edge of the breach. The value of y_B depends on the Model Case number (Column O):

$$y_B = -\ell + x \tan \alpha \quad \text{Case 1.}$$

$$y_B = \ell - x \tan \alpha \quad \text{Case 2.}$$

$$Q9=IF(O9=1,(-\$J9+\$I9*TAN(RADIANS(\$Q\$7))),$$

$$(\$J9-\$I9*TAN(RADIANS(\$Q\$7))))$$

Column R: Value of y_C (Point C) as described in Sections 6.5.1.1.2.1 and 6.5.1.1.2.2, corresponding to the rightmost point from which rivulets will enter the top edge of the breach. The value of y_C depends on the Model Case number (Column O):

$$y_C = \ell - x \tan \alpha \quad \text{Case 1.}$$

$$y_C = -\ell + x \tan \alpha \quad \text{Case 2.}$$

$$R9=IF(O9=1,(\$J9-\$I9*TAN(RADIANS(\$Q\$7))),$$

$$(-\$J9+\$I9*TAN(RADIANS(\$Q\$7))))$$

Column S: Value of y_D (Point D) as described in Sections 6.5.1.1.2.1 and 6.5.1.1.2.2, corresponding to the rightmost point from which the edge of the fan from the rivulet can enter the right side of the breach:

$$y_D = \ell + (x + 2\ell) \tan \alpha$$

$$S9=\$J9+(\$I9+2*\$J9)*TAN(RADIANS(\$Q\$7))$$

Column T: Determines which region (designated as Fraction Case #) along the drip shield relative to the center of the breach where the drip is located:

1. $y \leq y_A$
2. $y_A < y \leq -l$
3. $-l < y < y_B$
4. $y_B \leq y \leq y_C$
5. $y_C < y < l$
6. $l \leq y < y_D$
7. $y \geq y_D$

T9=IF(\$H9<=P9,1,IF(\$H9<=-\$J9,2,IF(\$H9<Q9,3,IF(\$H9<=R9,4,IF(\$H9<\$J9,5,IF(\$H9<S9,6,IF(\$H9>=S9,7))))))

	N	O	P	Q	R	S	T	U	V	W	X	Y	Z	AA	AB
1															
2															
3															
4															
5															
6															
7															
			For $\alpha = 5.5037$ degrees												
8															
9															
10															
11															
12															
13															
14															
15															
16															
17															
18															
19															
20															
21															
22															
23															
24															
25															
26															
27															
28															
29															
30															
31															
32															
33															
34															

Source: Output DTN: SN0703PAEBSRТА.001, file Flux Split Waste Package Model.xls, worksheet "f calculations."

Figure D-2. Calculation of Model Flow Fractions for Mean Minus One Standard Deviation Rivulet Spread Angle

Columns V though AB compute the fraction of dripping flux f_{calc} that is predicted to flow into a breach, assuming the drip location is within each of seven regions listed above under Column T.

Although f_{calc} is computed for all seven regions, it is valid in only one of the regions. The correct valid region is determined in Column T (Fraction Case #), and the appropriate value from Columns V–AB is entered in Column U.

Column U: f_{calc} is the fraction of dripping flux onto the drip shield that is predicted by the drip shield flux-splitting submodel, Equations 6.5.1.1.2-2 through 6.5.1.1.2-6 or 6.5.1.1.2-19 through 6.5.1.1.2-23, for Cases 1 and 2, respectively. f_{calc} is intended to be compared with f_{expt} (Column M). The value of f_{calc} is selected from Columns V through AB, depending on the appropriate Fraction Case # (Column T).

$$U9 = \text{IF}(T9=1, V9, \text{IF}(T9=2, W9, \text{IF}(T9=3, X9, \text{IF}(T9=4, Y9, \text{IF}(T9=5, Z9, \text{IF}(T9=6, AA9, \text{IF}(T9=7, AB9)))))))$$

Column V: Value of f_{calc} in region 1 ($y \leq y_A$), where $f_{calc} = 0$.

$$V9=0$$

Column W: Value of f_{calc} in region 2 ($y_A < y \leq -\ell$):

$$f_{calc} = \frac{y + \ell + (x + 2\ell) \tan \alpha}{2(x + 2\ell) \tan \alpha}$$

$$W9 = \frac{(H9 + J9 + (I9 + 2 * J9) * \text{TAN}(\text{RADIANS}(\$Q\$7)))}{(2 * (I9 + 2 * J9) * \text{TAN}(\text{RADIANS}(\$Q\$7)))}$$

Column X: Value of f_{calc} in region 3 ($-\ell < y < y_B$):

$$f_{calc} = \frac{y + \ell + x \tan \alpha}{2x \tan \alpha}$$

$$X9 = \frac{(H9 + J9 + I9 * \text{TAN}(\text{RADIANS}(\$Q\$7)))}{(2 * I9 * \text{TAN}(\text{RADIANS}(\$Q\$7)))}$$

Column Y: Value of f_{calc} in region 4 ($y_B \leq y \leq y_C$):

$$f_{calc} = \frac{2\ell}{2x \tan \alpha}$$

$$Y9 = \text{IF}(O9=1, 1, (2 * \$J9 / (2 * \$I9 * \text{TAN}(\text{RADIANS}(\$Q\$7))))))$$

Column Z: Value of f_{calc} in region 5 ($y_C < y < \ell$):

$$f_{calc} = \frac{-y + \ell + x \tan \alpha}{2x \tan \alpha}$$

$$Z9 = \frac{(-H9 + J9 + I9 * \text{TAN}(\text{RADIANS}(\$Q\$7)))}{(2 * I9 * \text{TAN}(\text{RADIANS}(\$Q\$7)))}$$

Column AA: Value of f_{calc} in region 6 ($\ell \leq y < y_D$):

$$f_{calc} = \frac{-y + \ell + (x + 2\ell) \tan \alpha}{2(x + 2\ell) \tan \alpha}$$

$$AA9 = \frac{(-H9 + J9 + I9 * \text{TAN}(\text{RADIANS}(\$Q\$7)))}{(2 * I9 * \text{TAN}(\text{RADIANS}(AA9\$Q\$7)))}$$

Column AB: Value of f_{calc} in region 7 ($y \geq y_D$) where $f_{calc} = 0$:

$$AB9 = 0$$

	AC	AD	AE	AF	AG	AH	AI	AJ	AK	AL	AM	AN	AO	AP	AQ
1															
2															
3															
4															
5															
6															
7	For $\alpha = 13.7326$ degrees														
8	$x * \tan(\alpha)$	Model Case #	Ya	Yb	Yc	Yd	Fraction Case #	f_{calc}	f1	f2	f3	f4	f5	f6	f7
9	12.3410	1	-32.4391	-1.1590	1.1590	32.4391	2	0.3944	0.0000	0.3944	0.3379	1.0000	1.7560	1.3184	0.0000
10	12.3410	1	-32.4391	-1.1590	1.1590	32.4391	4	1.0000	0.0000	0.8564	1.0470	1.0000	1.0470	0.8564	0.0000
11	12.3410	1	-32.4391	-1.1590	1.1590	32.4391	6	0.3944	0.0000	1.3184	1.7560	1.0000	0.3379	0.3944	0.0000
12	22.8491	2	-42.9473	-9.3491	9.3491	42.9473	6	0.4321	0.0000	1.0264	1.1784	0.5908	0.4125	0.4321	0.0000
13	22.8491	2	-42.9473	-9.3491	9.3491	42.9473	4	0.5908	0.0000	0.7292	0.7954	0.5908	0.7954	0.7292	0.0000
14	10.5082	1	-30.6063	-2.9918	2.9918	30.6063	2	0.3831	0.0000	0.3831	0.3097	1.0000	1.9750	1.4061	0.0000
15	22.8491	2	-42.9473	-9.3491	9.3491	42.9473	6	0.4151	0.0000	1.0433	1.2002	0.5908	0.3906	0.4151	0.0000
16	10.5082	1	-30.6063	-2.9918	2.9918	30.6063	4	1.0000	0.0000	0.8946	1.1424	1.0000	1.1424	0.8946	0.0000
17	28.1032	2	-48.2014	-14.6032	14.6032	48.2014	6	0.4424	0.0000	0.9467	1.0515	0.4804	0.4288	0.4424	0.0000
18	22.8491	2	-42.9473	-9.3491	9.3491	42.9473	4	0.5908	0.0000	0.8651	0.9705	0.5908	0.6204	0.5934	0.0000
19	22.8491	2	-42.9473	-9.3491	9.3491	42.9473	7	0.0000	0.0000	1.6461	1.9771	0.5908	-0.3862	-0.1877	0.0000
20	10.5082	1	-30.6063	-2.9918	2.9918	30.6063	1	0.0000	0.0000	-0.2453	-0.7133	1.0000	2.9981	2.0345	0.0000
21	10.5082	1	-30.6063	-2.9918	2.9918	30.6063	3	0.9520	0.0000	0.7777	0.9520	1.0000	1.3327	1.0115	0.0000
22	22.8491	2	-42.9473	-9.3491	9.3491	42.9473	4	0.5908	0.0000	0.8651	0.9705	0.5908	0.6204	0.5934	0.0000
23	22.8491	2	-42.9473	-9.3491	9.3491	42.9473	4	0.5908	0.0000	0.7292	0.7954	0.5908	0.7954	0.7292	0.0000
24	22.8491	2	-42.9473	-9.3491	9.3491	42.9473	4	0.5908	0.0000	0.7292	0.7954	0.5908	0.7954	0.7292	0.0000
25	10.5082	1	-30.6063	-2.9918	2.9918	30.6063	1	0.0000	0.0000	-1.4730	-2.7118	1.0000	4.9965	3.2621	0.0000
26	10.5082	1	-30.6063	-2.9918	2.9918	30.6063	1	0.0000	0.0000	-1.4730	-2.7118	1.0000	4.9965	3.2621	0.0000
27	10.5082	1	-30.6063	-2.9918	2.9918	30.6063	2	0.1054	0.0000	0.1054	-0.1424	1.0000	2.4271	1.6838	0.0000
28	10.5082	1	-30.6063	-2.9918	2.9918	30.6063	2	0.1054	0.0000	0.1054	-0.1424	1.0000	2.4271	1.6838	0.0000
29	12.3410	1	-32.4391	-1.1590	1.1590	32.4391	6	0.1436	0.0000	1.5692	2.1409	1.0000	-0.0470	0.1436	0.0000
30	12.3410	1	-32.4391	-1.1590	1.1590	32.4391	7	0.0000	0.0000	2.9948	4.3287	1.0000	-2.2348	-1.2820	0.0000
31	12.3410	1	-32.4391	-1.1590	1.1590	32.4391	4	1.0000	0.0000	0.8564	1.0470	1.0000	1.0470	0.8564	0.0000
32	12.3410	1	-32.4391	-1.1590	1.1590	32.4391	4	1.0000	0.0000	0.8564	1.0470	1.0000	1.0470	0.8564	0.0000
33	12.3410	1	-32.4391	-1.1590	1.1590	32.4391	6	0.1436	0.0000	1.5692	2.1409	1.0000	-0.0470	0.1436	0.0000
34	12.3410	1	-32.4391	-1.1590	1.1590	32.4391	7	0.0000	0.0000	2.9948	4.3287	1.0000	-2.2348	-1.2820	0.0000

Source: Output DTN: SN0703PAEBSRTA.001, file *Flux Split Waste Package Model.xls*, worksheet "f calculations."

Figure D-3. Calculation of Model Flow Fractions for Mean Rivulet Spread Angle

Columns AC through AQ repeat the calculations done in Columns N through AB using the mean rivulet spread angle of $\alpha = 13.7326^\circ$ (Cell \$AF\$7). For Row 9, the spreadsheet equations are as follows:

$$AC9 = I9 * \text{TAN}(\text{RADIANS}(\$AF\$7))$$

$$AD9=IF(\$J9>AC9,1,2)$$

$$AE9=-\$J9-(\$I9+2*\$J9)*TAN(RADIANS(\$AF\$7))$$

$$AF9=IF(AD9=1,(-\$J9+\$I9*TAN(RADIANS(\$AF\$7))),(\$J9-\$I9*TAN(RADIANS(\$AF\$7))))$$

$$AG9=IF(AD9=1,(\$J9-\$I9*TAN(RADIANS(\$AF\$7))),(-\$J9+\$I9*TAN(RADIANS(\$AF\$7))))$$

$$AH9=\$J9+(\$I9+2*\$J9)*TAN(RADIANS(\$AF\$7))$$

$$AI9=IF(\$H9<=AE9,1,IF(\$H9<=-\$J9,2,IF(\$H9<AF9,3,IF(\$H9<=AG9,4,IF(\$H9<\$J9,5,IF(\$H9<AH9,6,IF(\$H9>=AH9,7))))))$$

$$AJ9=IF(AI9=1,AK9,IF(AI9=2,AL9,IF(AI9=3,AM9,IF(AI9=4,AN9,IF(AI9=5,AO9,IF(AI9=6,AP9,IF(AI9=7,AQ9))))))$$

$$AK9=0$$

$$AL9=(H9+J9+(I9+2*J9)*TAN(RADIANS(\$AF\$7)))/(2*(I9+2*J9)*TAN(RADIANS(\$AF\$7)))$$

$$AM9=(H9+J9+I9*TAN(RADIANS(\$AF\$7)))/(2*I9*TAN(RADIANS(\$AF\$7)))$$

$$AN9=IF(AD9=1,1,(2*\$J9/(2*\$I9*TAN(RADIANS(\$AF\$7))))$$

$$AO9=(-H9+J9+I9*TAN(RADIANS(\$AF\$7)))/(2*I9*TAN(RADIANS(\$AF\$7)))$$

$$AP9=(-H9+J9+(I9+2*J9)*TAN(RADIANS(\$AF\$7)))/(2*(I9+2*J9)*TAN(RADIANS(\$AF\$7)))$$

$$AQ9=0$$

Columns AR though BF (next page) repeat the calculations done in Columns N though AB using a rivulet spread angle of $\alpha = 21.9614^\circ$ (Cell \$AU\$7), which is one standard deviation greater than the mean rivulet spread angle. For Row 9, the spreadsheet equations are as follows:

$$AR9=\$I9*TAN(RADIANS(\$AU\$7))$$

$$AS9=IF(\$J9>AR9,1,2)$$

$$AT9=-\$J9-(\$I9+2*\$J9)*TAN(RADIANS(\$AU\$7))$$

$$AU9=IF(AS9=1,(-\$J9+\$I9*TAN(RADIANS(\$AU\$7))),(\$J9-\$I9*TAN(RADIANS(\$AU\$7))))$$

$$AV9=IF(AS9=1,(-\$J9+\$I9*TAN(RADIANS(\$AU\$7))),(\$J9-\$I9*TAN(RADIANS(\$AU\$7))))$$

$$AW9=\$J9+(\$I9+2*\$J9)*TAN(RADIANS(\$AU\$7))$$

$$AX9=IF(\$H9<=AT9,1,IF(\$H9<=-\$J9,2,IF(\$H9<AU9,3,IF(\$H9<=AV9,4,IF(\$H9<\$J9,5,IF(\$H9<AW9,6,IF(\$H9>=AW9,7))))))$$

$$AY9=IF(AX9=1,AZ9,IF(AX9=2,BA9,IF(AX9=3,BB9,IF(AX9=4,BC9,IF(AX9=5,BD9,IF(AX9=6,BE9,IF(AX9=7,BF9))))))$$

$$AZ9=0$$

$$BA9=(H9+J9+(I9+2*J9)*TAN(RADIANS(AU7)))/(2*(I9+2*J9)*TAN(RADIANS(AU7)))$$

$$BB9=(H9+J9+I9*TAN(RADIANS(AU7)))/(2*I9*TAN(RADIANS(AU7)))$$

$$BC9=IF(AS9=1,1,(2*$J9/(2*$I9*TAN(RADIANS(AU7))))$$

$$BD9=(-H9+J9+I9*TAN(RADIANS(AU7)))/(2*I9*TAN(RADIANS(AU7)))$$

$$BE9=(-H9+J9+(I9+2*J9)*TAN(RADIANS(AU7)))/(2*(I9+2*J9)*TAN(RADIANS(AU7)))$$

$$BF9=0$$

	AR	AS	AT	AU	AV	AW	AX	AY	AZ	BA	BB	BC	BD	BE	BF
1															
2															
3															
4															
5															
6															
7	For $\alpha = 21.9614$ degrees														
8	$X^*tan(\alpha)$	Model Case #	Ya	Yb	Yc	Yd	Fraction Case #	f_{calc}	f1	f2	f3	f4	f5	f6	f7
9	20.3638	2	-44.7513	-6.8638	6.8638	44.7513	2	0.4360	0.0000	0.4360	0.4018	0.6629	1.2612	0.9960	0.0000
10	20.3638	2	-44.7513	-6.8638	6.8638	44.7513	4	0.6629	0.0000	0.7160	0.8315	0.6629	0.8315	0.7160	0.0000
11	20.3638	2	-44.7513	-6.8638	6.8638	44.7513	6	0.4360	0.0000	0.9960	1.2612	0.6629	0.4018	0.4360	0.0000
12	37.7032	2	-62.0907	-24.2032	24.2032	62.0907	4	0.3581	0.0000	0.8190	0.9111	0.3581	0.4470	0.4588	0.0000
13	37.7032	2	-62.0907	-24.2032	24.2032	62.0907	4	0.3581	0.0000	0.6389	0.6790	0.3581	0.6790	0.6389	0.0000
14	17.3394	2	-41.7270	-3.8394	3.8394	41.7270	2	0.4291	0.0000	0.4291	0.3847	0.7786	1.3939	1.0491	0.0000
15	37.7032	2	-62.0907	-24.2032	24.2032	62.0907	4	0.3581	0.0000	0.8293	0.9244	0.3581	0.4337	0.4485	0.0000
16	17.3394	2	-41.7270	-3.8394	3.8394	41.7270	4	0.7786	0.0000	0.7391	0.8893	0.7786	0.8893	0.7391	0.0000
17	46.3729	2	-70.7605	-32.8729	32.8729	70.7605	4	0.2911	0.0000	0.7707	0.8342	0.2911	0.4569	0.4651	0.0000
18	37.7032	2	-62.0907	-24.2032	24.2032	62.0907	4	0.3581	0.0000	0.7212	0.7851	0.3581	0.5729	0.5666	0.0000
19	37.7032	2	-62.0907	-24.2032	24.2032	62.0907	6	0.0833	0.0000	1.1946	1.3951	0.3581	-0.0371	0.0833	0.0000
20	17.3394	2	-41.7270	-3.8394	3.8394	41.7270	2	0.0483	0.0000	0.0483	-0.2353	0.7786	2.0139	1.4300	0.0000
21	17.3394	2	-41.7270	-3.8394	3.8394	41.7270	3	0.7739	0.0000	0.6683	0.7739	0.7786	1.0046	0.8100	0.0000
22	37.7032	2	-62.0907	-24.2032	24.2032	62.0907	4	0.3581	0.0000	0.7212	0.7851	0.3581	0.5729	0.5666	0.0000
23	37.7032	2	-62.0907	-24.2032	24.2032	62.0907	4	0.3581	0.0000	0.6389	0.6790	0.3581	0.6790	0.6389	0.0000
24	37.7032	2	-62.0907	-24.2032	24.2032	62.0907	4	0.3581	0.0000	0.6389	0.6790	0.3581	0.6790	0.6389	0.0000
25	17.3394	2	-41.7270	-3.8394	3.8394	41.7270	1	0.0000	0.0000	-0.6957	-1.4464	0.7786	3.2250	2.1739	0.0000
26	17.3394	2	-41.7270	-3.8394	3.8394	41.7270	1	0.0000	0.0000	-0.6957	-1.4464	0.7786	3.2250	2.1739	0.0000
27	17.3394	2	-41.7270	-3.8394	3.8394	41.7270	2	0.2609	0.0000	0.2609	0.1107	0.7786	1.6679	1.2174	0.0000
28	17.3394	2	-41.7270	-3.8394	3.8394	41.7270	2	0.2609	0.0000	0.2609	0.1107	0.7786	1.6679	1.2174	0.0000
29	20.3638	2	-44.7513	-6.8638	6.8638	44.7513	6	0.2840	0.0000	1.1480	1.4944	0.6629	0.1685	0.2840	0.0000
30	20.3638	2	-44.7513	-6.8638	6.8638	44.7513	7	0.0000	0.0000	2.0119	2.8203	0.6629	-1.1574	-0.5800	0.0000
31	20.3638	2	-44.7513	-6.8638	6.8638	44.7513	4	0.6629	0.0000	0.7160	0.8315	0.6629	0.8315	0.7160	0.0000
32	20.3638	2	-44.7513	-6.8638	6.8638	44.7513	4	0.6629	0.0000	0.7160	0.8315	0.6629	0.8315	0.7160	0.0000
33	20.3638	2	-44.7513	-6.8638	6.8638	44.7513	6	0.2840	0.0000	1.1480	1.4944	0.6629	0.1685	0.2840	0.0000
34	20.3638	2	-44.7513	-6.8638	6.8638	44.7513	7	0.0000	0.0000	2.0119	2.8203	0.6629	-1.1574	-0.5800	0.0000

Source: Output DTN: SN0703PAEBSRTA.001, file *Flux Split Waste Package Model.xls*, worksheet "f calculations."

Figure D-4. Calculation of Model Flow Fractions for Mean Plus One Standard Deviation Rivulet Spread Angle

SPREADSHEET “FLUX SPLIT WASTE PACKAGE MODEL”–WORKSHEET “SPREAD ANGLES”

	A	B	C	D	E	F	G	H	I	J	K
1	Rivulet spread measurements for WP model: Drips at 16.5° and 33°, measurements at 33° and transition Smooth Drip Shield)										
2											
3					Source Data						
4					Calculated results						
5											
6					Rivulet Spread Measurements						
7					At 33°			At Transition			
8								x (distance from drop, cm)			
		Q(film) (DTN: MO0207EBSATBWP.023)	Drop Location	x (distance from drop, cm)	Right (cm)	Left (cm)			Right (cm)	Left (cm)	
9		5/31/2002	P4, 8 cm right of center, 16.5°	16.5°	43	5.5	3.5	107.0	13.5		
10		5/31/2002	P2, center, 16.5°	16.5°	43	7.5	4.5	107.0	19.5	22.0	
11		5/31/2002	P2, 15 cm right of center, 16.5°	16.5°	43	11.5	9.0	107.0	18.0	15.0	
12		5/31/2002	P5, 4 cm left of center, 16.5°	16.5°	43	8.5	8.5	107.0			
13											
14					Bounding (DTN: MO0207EBSATBWP.025)						
15		6/18/2002	54 cm left of DS center, 16.5°	16.5°	43	31.0	46.0	107.0	35.0	46.0	
16		6/19/2002	54 cm left of DS center, 16.5°	16.5°	43	8.5	10.0	107.0	19.0	27.0	
17		6/16/2002	27 cm left of DS center, 16.5°	16.5°	43	6.0	8.0	107.0	17.0	16.0	
18		6/20/2002	27 cm left of DS center, 16.5°	16.5°	43	18.0	24.0	107.0	22.0	19.0	
19		6/20/2002	27 cm right of DS center, 16.5°	16.5°	43	13.0	27.0	107.0	14.0	23.0	
20		6/20/2002	27 cm right of DS center, 16.5°	16.5°	43	12.0	17.0	107.0	16.0	19.0	
21		6/20/2002	27 cm left of DS center, 33°	33°				64.0	11.0	17.0	
22		6/20/2002	27 cm right of DS center, 33°	33°				64.0	15.0	17.0	
23		6/20/2002	54 cm left of DS center, 33°	33°				64.0	17.0	17.0	
24		6/24/2002	27 cm left of DS center, 33°	33°				64.0	9.0	9.5	
25		6/24/2002	27 cm right of DS center, 33°	33°				64.0	8.5	10.0	
26											

Source: DTN: MO0207EBSATBWP.023 [DIRS 163402]; DTN: MO0207EBSATBWP.025 [DIRS 163403]. Output DTN: SN0703PAEBSRTA.001, file *Flux Split Waste Package Model.xls*, worksheet “Spread angles.”

Figure D-5. Calculation of Rivulet Spread Angle

In this worksheet, the mean and range of the rivulet spread angle α is determined from spread measurements. The drip locations are off-crown, at the 16.5° and 33° positions on the drip shield mockup. These angles are the angular distances from the crown about the center of curvature of the drip shield; thus, the crown is at 0°, and the transition from the curved top surface to the vertical side of the drip shield is located about 60° from vertical. The actual distance (arc length) from the crown to the 16.5° line is 43 cm; from the crown to the 33° line the distance is 86 cm; and from the crown to the transition line the distance is 150 cm. The distance x from the drip location to the spread measurement location (the 33° line or the transition line) is shown in Columns E and H, respectively.

Columns B and C identify the pertinent tests as described in the designated DTNs. In each test, the spread of rivulets to the right and to the left of the drip location was measured. The spread distance measured at the 33° line is listed in Columns F and G. The spread distance measured at the transition line is listed in Columns I and J. For drips at the 33° location, no rivulet spread was measured, although splattering upslope may have resulted in some rivulets appearing at the drip location.

In Column R (Figures D-7 and D-8), the mean spread angle and standard deviation are shown for comparison for three groups of data—drip location at 16.5° measured at 33°, drip location at 16.5° measured at the transition line, and drip location at 33° measured at the transition line. The statistics for all measurements are computed in Column U. The mean rivulet spread angle (Cell U19) and the bounds on the range for spread angle, as defined by the mean minus one standard deviation (Cell U21) and the mean plus one standard deviation (Cell U22), are used in Worksheet “f calculations” as the basis of the waste package flux-splitting submodel to compute the predicted fraction of dripping flux that flows into a breach, f_{calc} , with one standard deviation being reasonably representative of the spread observed in the measured spread angles.

	L	M	N	O	P	Q	R	S	T	U
29										
30										
31		13.5	107	7.1909						
32		19.5	107	10.3284						
33		18.0	107	9.5491						
34		22.0	107	11.6185						
35		15.0	107	7.9801						
36		35.0	107	18.1131						
37		19.0	107	10.0691						
38		17.0	107	9.0276						
39		22.0	107	11.6185						
40		14.0	107	7.4543						
41		16.0	107	8.5046						
42		46.0	107	23.2632						
43		27.0	107	14.1622						
44		16.0	107	8.5046						
45		19.0	107	10.0691						
46		23.0	107	12.1313						
47		19.0	107	10.0691						
48										
49										
50		11.0	64	9.7524						
51		15.0	64	13.1906						
52		17.0	64	14.8757						
53		9.0	64	8.0047						
54		8.5	64	7.5653						
55		17.0	64	14.8757						
56		17.0	64	14.8757						
57		17.0	64	14.8757						
58		9.5	64	8.4432						
59		10.0	64	8.8807						

Drip at 16.5°.	
Spread Angle	
No. of mea	17
Mean	11.1561
Std. Dev.	4.110299

Drip at 33°.	
Spread Angle	
No. of mea	10
Mean	11.5340
Std. Dev.	3.255512

Source: Output DTN: SN0703PAEBSRTA.001, file *Flux Split Waste Package Model.xls*, worksheet “Spread angles.”

Figure D-8. Calculation of Rivulet Spread Angles

SPREADSHEET “FLUX SPLIT WASTE PACKAGE MODEL”–WORKSHEET “SUMMARY”

	A	B	C	D	E	F	G	H	I	J	K
1											
2											
3											
4		Waste Package Model: Comparison of Measured and Modeled Fraction of Drip Seepage Flowing into a Breach									
5											
6		This spreadsheet compares results from the "Atlas Breached Waste Package and Drip Shield Experiments: Breached Drip Shield Tests" (documented in TDR-EBS-MD-000025-00 REV 00) with the model developed in the "EBS Radionuclide Transport Abstraction" (ANL-WIS-PA-0000001 REV 02). Test data are taken directly from the TDMS for this comparison.									
7											
8		<u>Methodology:</u>									
9		1. Spreading angles are calculated from the test data in the sheet titled <u>Spread angles</u>									
10		2. Given spread angle and test geometry, seepage fractions are calculated for both the test data and the model in the worksheet <u>f calculations</u> :									
11			a. Geometric data for each measurement (x,y,l) and the spread angle are used to determine which of 7 cases the measurement corresponds to								
12			b. For each test result the appropriate case model is applied to calculate the seepage flow fraction f								
13		3. The seepage fractions calculated from both the test and model are listed and compared in the two tables listed below in this <u>Summary</u> worksheet									
14		<u>Notes:</u>									
15		Source data DTNs are noted where source data is used									
16		Model equations are provided on the calculational sheets									
17		Data in tables below is linked directly to the calculational worksheets									
18											
19											

Source: BSC 2003 [DIRS 163406]. Output DTN: SN0703PAEBSRTA.001, file *Flux Split Waste Package Model.xls*, worksheet “Summary.”

Figure D-9. Summary of Waste Package Flux-Splitting Submodel

This worksheet, beginning with Figure D-9, summarizes the calculations in Worksheets “Spread angles” and “f calculations.”

In the first table (Figure D-10), “Measured Breach Flow Fractions and Calculated Breach Flow Fractions,” Columns B, C, D, and E are identical to Columns D, E, H, and I described earlier for Worksheet “f calculations.” Column F (f_{expt}) is identical to Column M in Worksheet “f calculations.” Columns G–I summarize the calculated fraction of the dripping flux that the flux-splitting submodel predicts should flow into the breach, for the minimum, mean, and maximum spread angles. The minimum spread angle is specified to be one standard deviation less than the mean of the measured spread angles. The maximum spread angle is specified to be one standard deviation greater than the mean of the measured spread angles. Column G is identical to Column U of Worksheet “f calculations.” Column H is identical to Column AJ of Worksheet “f calculations.” Column I is identical to Column AY of Worksheet “f calculations.”

Rows 50–54, Columns F–I, show the results of Microsoft Excel functions “AVERAGE,” “STDEVA,” “MEDIAN,” “MIN,” and “MAX,” respectively, as applied to Rows 25–49.

	A	B	C	D	E	F	G	H	I
19									
20	Measured Branch Flux Fractions and Calculated Branch Flux Fractions								
21									
22				y, Drip Location Relative to Branch Center (cm)	x, Vertical Distance from Drip to Top of Branch (cm)		f_{calc}		
23							α (deg)	ε (deg)	κ (deg)
24		Drip Location (Text Description)	Breach No.			f_{meas}	5.50	13.73	21.96
25		P5, 17.5 cm left of center, 33'	4	-17.5	50.5	0.0000	0.2322	0.3944	0.4360
26		P4, center, 33'	4	0	50.5	0.8005	1.0000	1.0000	0.6629
27		P4, 17.5 cm right of center, 33'	4	17.5	50.5	0.0682	0.2322	0.3944	0.4360
28		P4, 17.5 cm right of center, 16.5'	4	17.5	93.5	0.0119	0.3277	0.4321	0.3581
29		P4, centerline, 16.5'	4	0	93.5	0.6029	1.0000	0.5908	0.3581
30		P5, 17.5 cm left of center, 16.5'	5	-17.5	43.0	0.0142	0.2035	0.3831	0.4291
31		P6, 35.5 cm left of center, 16.5'	4	18.5	93.5	0.0015	0.2847	0.4151	0.3581
32		P5, centerline, 16.5'	5	0	43.0	0.7260	1.0000	1.0000	0.7786
33		P6, 35.5 cm left of center, between crane and 16.5'	4	17.5	115.0	0.0513	0.3538	0.4424	0.2911
34		P4, 8 cm right of center, 16.5'	4	8	93.5	0.5368	0.8052	0.5908	0.3581
35		P2, 15 cm right of center, 16.5'	5	-39	43.0	0.0022	0.0000	0.0000	0.0483
36		P5, 4 cm left of center, 16.5'	5	-4	43.0	1.0657	1.0000	0.9520	0.7739
37		P4, 8 cm right of center, 16.5'	4	8	93.5	0.7813	0.8052	0.5908	0.3581
38		S4 cm left of DS center, 16.5'	4	0	93.5	0.4803	1.0000	0.5908	0.3581
39		S4 cm left of DS center, 16.5'	4	0	93.5	0.7901	1.0000	0.5908	0.3581
40		T7 cm left of DS center, 16.5'	5	-81	43.0	0.0048	0.0000	0.0000	0.0000
41		T7 cm left of DS center, 16.5'	5	-81	43.0	0.0031	0.0000	0.0000	0.0000
42		T7 cm right of DS center, 16.5'	5	-27	43.0	0.0125	0.0000	0.1054	0.2609
43		T7 cm right of DS center, 16.5'	5	-27	43.0	0.0082	0.0000	0.1054	0.2609
44		T7 cm left of DS center, 33'	4	27	50.5	0.0026	0.0000	0.1436	0.2840
45		T7 cm right of DS center, 33'	4	81	50.5	0.0020	0.0000	0.0000	0.0000
46		S4 cm left of DS center, 33'	4	0	50.5	0.5682	1.0000	1.0000	0.6629
47		S4 cm left of DS center, 33'	4	0	50.5	0.8217	1.0000	1.0000	0.6629
48		T7 cm left of DS center, 33'	4	27	50.5	0.0123	0.0000	0.1436	0.2840
49		T7 cm right of DS center, 33'	4	81	50.5	0.0000	0.0000	0.0000	0.0000
50		Mean				0.2947	0.4498	0.4346	0.3511
51		Std. Dev.				0.3683	0.4426	0.3539	0.2316
52		Median				0.0142	0.2847	0.4151	0.3581
53		Minimum				0.0000	0.0000	0.0000	0.0000
54		Maximum				1.0657	1.0000	1.0000	0.7786
55	Summary / Spread angles / f calculations /								

Source: Output DTN: SN0703PAEBSRTA.001, file *Flux Split Waste Package Model.xls*, worksheet "Summary."

Figure D-10. Summary of Waste Package Flux-Splitting Submodel

In the second table (Figure D-11), "Comparison of Measured and Calculated Breach Flows," Column K is again the drip location. Column L is the fraction of dripping flux (f_{expt}) that flowed into a breach as measured experimentally; this is identical to Column F of the preceding table, or Column M in Worksheet "f calculations." The next three columns (M-O) show the difference between the predicted breach flow fraction, f_{calc} , and the measured fraction, f_{expt} , for the minimum, mean, and maximum rivulet spread angle. Columns P-R show the ratio f_{calc} / f_{expt} for the minimum, mean, and maximum rivulet spread angle.

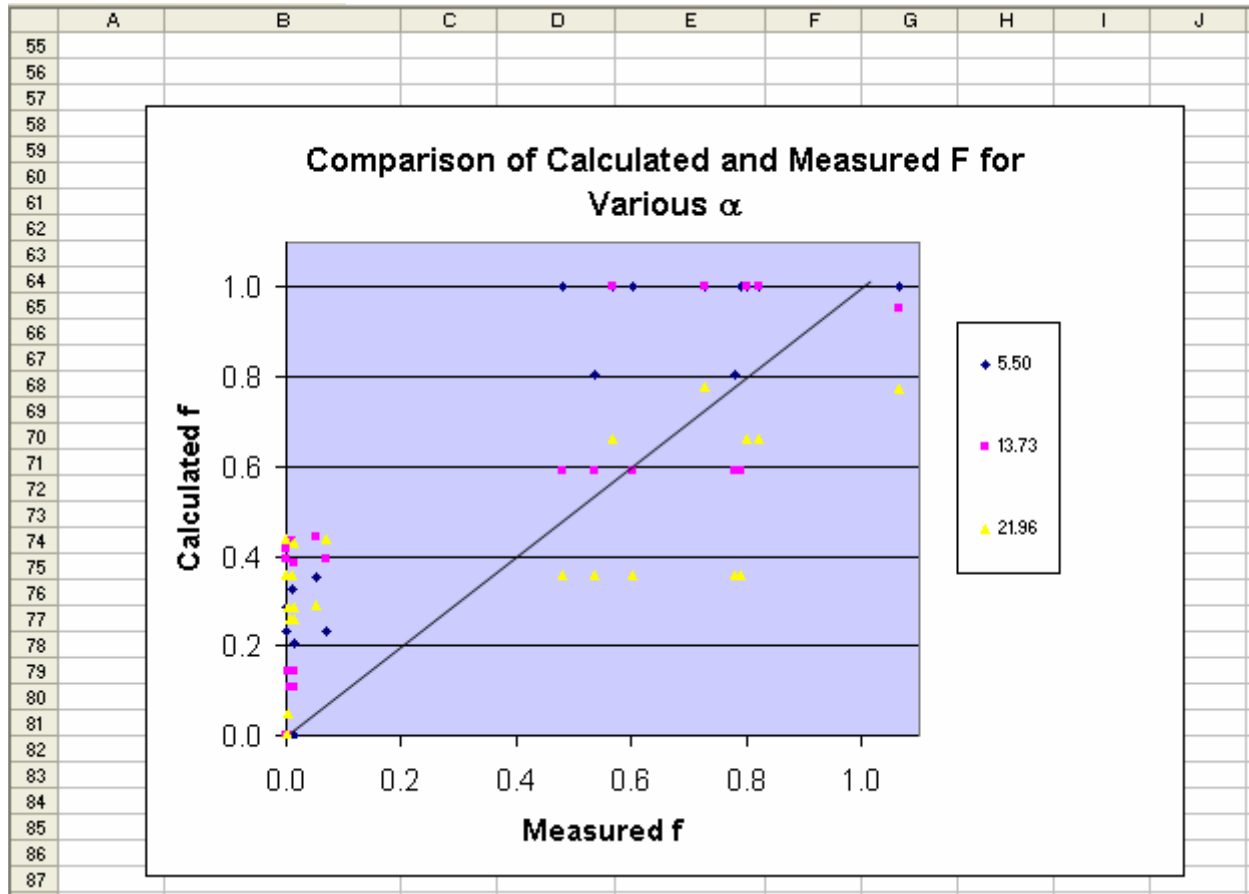
Rows 50-54, Columns L-R, show the results of Microsoft Excel functions “AVERAGE,” “STDEVA,” “MEDIAN,” “MIN,” and “MAX,” respectively, as applied to Rows 25-49.

	J	K	L	M	N	O	P	Q	R
19									
20		Comparison of Measured and Calculated Breach Flow							
21									
22				<i>f_{calc} - f_{meas}</i>			<i>f_{calc} / f_{meas}</i>		
23				<i>σ (deg)</i>	<i>σ (deg)</i>	<i>σ (deg)</i>	<i>σ (deg)</i>	<i>σ (deg)</i>	<i>σ (deg)</i>
24		Drip Location (Text Description)	<i>f_{meas}</i>	5.50	13.73	21.96	5.50	13.73	21.96
25		P5, 17.5 cm left of center, 33°	0.0000	0.2322	0.3944	0.4360			
26		P4, center, 33°	0.8005	0.1995	0.1995	-0.1376	1.2492	1.2492	0.8281
27		P4, 17.5 cm right of center, 33°	0.0682	0.1640	0.3262	0.3678	3.4054	5.7848	6.3950
28		P4, 17.5 cm right of center, 16.5°	0.0119	0.2159	0.4202	0.3462	27.6039	36.3914	30.1570
29		P4, centerline, 16.5°	0.6029	0.2971	-0.0121	-0.2449	1.6586	0.9799	0.5939
30		P5, 17.5 cm left of center, 16.5°	0.0142	0.1893	0.3689	0.4150	14.3428	27.0031	30.2499
31		P6, 36.5 cm left of center, 16.5°	0.0015	0.2831	0.4136	0.3565	184.1115	268.4581	231.5671
32		P5, centerline, 16.5°	0.7260	0.2740	0.2740	0.0526	1.3774	1.3774	1.0724
33		P6, 36.5 cm left of center, between crown and 16.5°	0.0512	0.3025	0.3911	0.2398	6.8988	8.6251	5.6761
34		P4, 8 cm right of center, 16.5°	0.5368	0.2685	0.0541	-0.1787	1.5001	1.1007	0.6671
35		P2, 15 cm right of center, 16.5°	0.0022	-0.0022	-0.0022	0.0461	0.0000	0.0000	21.9501
36		P5, 4 cm left of center, 16.5°	1.0657	-0.0657	-0.1136	-0.2917	0.9384	0.8934	0.7263
37		P4, 8 cm right of center, 16.5°	0.7812	0.0240	-0.1905	-0.4232	1.0307	0.7562	0.4583
38		54 cm left of DS center, 16.5°	0.4802	0.5197	0.1105	-0.1223	2.0818	1.2300	0.7454
39		54 cm left of DS center, 16.5°	0.7901	0.2099	-0.1993	-0.4321	1.2656	0.7478	0.4532
40		27 cm left of DS center, 16.5°	0.0048	-0.0048	-0.0048	-0.0048	0.0000	0.0000	0.0000
41		27 cm left of DS center, 16.5°	0.0031	-0.0031	-0.0031	-0.0031	0.0000	0.0000	0.0000
42		27 cm right of DS center, 16.5°	0.0125	-0.0125	0.0929	0.2484	0.0000	8.4461	20.9026
43		27 cm right of DS center, 16.5°	0.0082	-0.0082	0.0972	0.2527	0.0000	12.8936	31.9094
44		27 cm left of DS center, 33°	0.0026	-0.0026	0.1410	0.2814	0.0000	54.9116	108.6068
45		27 cm right of DS center, 33°	0.0020	-0.0020	-0.0020	-0.0020	0.0000	0.0000	0.0000
46		54 cm left of DS center, 33°	0.5682	0.4318	0.4318	0.0948	1.7600	1.7600	1.1668
47		54 cm left of DS center, 33°	0.8217	0.1783	0.1783	-0.1588	1.2170	1.2170	0.8068
48		27 cm left of DS center, 33°	0.0123	-0.0123	0.1313	0.2717	0.0000	11.7079	23.1564
49		27 cm right of DS center, 33°	0.0000	0.0000	0.0000	0.0000			
50		Mean	0.2947	0.1551	0.1399	0.0564	10.8887	19.3710	22.5256
51		Std. Dev.	0.3682	0.1670	0.1938	0.2596	38.2681	56.0050	51.4010
52		Median	0.0142	0.1783	0.1105	0.0461	1.2492	1.2492	1.0724
53		Minimum	0.0000	-0.0657	-0.1993	-0.4321	0.0000	0.0000	0.0000
54		Maximum	1.0657	0.5197	0.4318	0.4360	184.1115	268.4581	231.5671
55									

Source: Output DTN: SN0703PAEBSRTA.001, file *Flux Split Waste Package Model.xls*, worksheet “Summary.”

Figure D-11. Summary of Waste Package Flux-Splitting Submodel Comparing Measured and Calculated Breach Flows

Lastly, a plot in Worksheet “Summary” (Figure D-12) compares the calculated f_{calc} with the measured f_{expt} for the minimum, mean, and maximum spread angles; the f_{expt} and f_{calc} values that are plotted on Figure D-12 are shown in Figure D-10. The diagonal line in the plot represents $f_{calc} = f_{expt}$. Most values of f_{calc} lie above the line $f_{calc} = f_{expt}$, indicating that the waste package flux-splitting submodel tends to overestimate the flow into breaches.



Source: Output DTN: SN0703PAEBSRTA.001, file *Flux Split Waste Package Model.xls*, worksheet “Summary.”

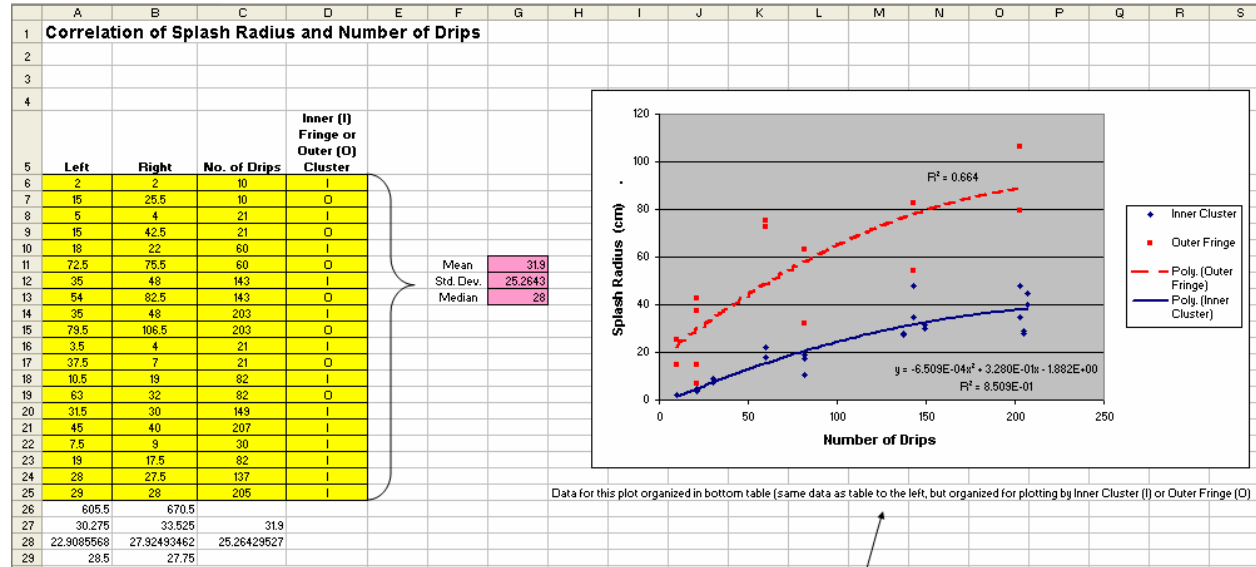
Figure D-12. Comparison of Calculated and Measured Breach Flow Fractions for Waste Package Flux-Splitting Submodel for Minimum (5.50°), Mean (13.73°), and Maximum (21.96°) Rivulet Spread Angles

APPENDIX E

MICROSOFT EXCEL SPREADSHEET “FLUX SPLITTING VALIDATION”

MICROSOFT EXCEL SPREADSHEET “FLUX SPLITTING VALIDATION”

SPREADSHEET “FLUX SPLITTING VALIDATION”–WORKSHEET “SPLASH RAD VS NUMBER”



Source: Output DTN: SN0703PAEBSRTA.001, file *Flux Splitting Validation.xls*, worksheet “Splash Rad vs Number.”

Figure E-1. Effect of Number of Drips on Splash Radius

In this worksheet (Figures E-1 to E-3), the effect of the number of drips on the splash radius is analyzed using data from dripping on the crown in the rough drip shield tests. This analysis is used for validation of the drip shield flux-splitting submodel. The splash distance or radius (cm) to the left and to the right of the drip location are listed in Columns A and B, respectively. The number of drips in each test is given in Column C. The type of measurement—inner cluster (I) or outer fringe (O)—is indicated in Column D. These data and the DTN from which they were obtained (MO0207EBSATBWP.021 [DIRS 163399]) are also presented in Table 7.1-1. In Row 26, the sum of the splash radii is shown. Rows 27, 28, and 29 give the mean, standard deviation, and median for each column. The mean, standard deviation, and median for all 40 splash radius measurements are listed in Column G, Rows 11, 12, and 13, respectively.

The plot to the right in Figure E-1, which is reproduced as Figure 7.1-1, shows the dependence of splash radius on the number of drips. As indicated beneath the figure, the data are the same as in the table, but organized by type of measurement farther down in this worksheet. The Trendline tool in Microsoft Excel is used to fit a quadratic curve to the inner cluster and outer fringe data. The correlation coefficient is shown for each curve, and the correlation equation is shown for the inner cluster curve. A second degree polynomial was chosen for the Trendline in order to display the expected behavior—the splash radius should increase with the number of drips, but eventually reach a maximum. A functional form such as $y = y_{\max} (1 - e^{-ax})$ may be more appropriate, but because this is nonlinear in the fitting parameter a , a simple linear least squares fit using Trendline is not possible. Since the object is simply to demonstrate a correlation, a more accurate fit to the data is not necessary.

On Figure E-2, the experimental data from the top of the worksheet are reorganized by type of measurement and, in Figure E-3, all left and right measurements are consolidated for plotting in the plot at the top of the worksheet (shown in Figure E-1).

	A	B	C	D	E	F	G	H	I	J	K	L	M
25	29	28	205	I									
26	605.5	670.5											
27	30.275	33.525	31.9										
28	22.9085568	27.92493462	25.26429527										
29	28.5	27.75											
30	<i>Inner Cluster Data Only (from table at top of sheet)</i>												
				Inner (I) Fringe or Outer (O) Cluster									
31	Left	Right	No. of Drips										
32	2	2	10	I									
33	5	4	21	I									
34	18	22	60	I									
35	35	48	143	I									
36	35	48	203	I									
37	3.5	4	21	I									
38	10.5	19	82	I									
39	31.5	30	149	I									
40	45	40	207	I									
41	7.5	9	30	I									
42	19	17.5	82	I									
43	28	27.5	137	I									
44	29	28	205	I									
45													
46													
47	<i>Outer Cluster Data Only (from table at top of sheet)</i>												
				Inner Fringe (I) or Outer (O) Cluster									
48	Left	Right	No. of Drips										
49	15	25.5	10	O									
50	15	42.5	21	O									
51	72.5	75.5	60	O									
52	54	82.5	143	O									
53	79.5	106.5	203	O									
54	37.5	7	21	O									

Source: Output DTN: SN0703PAEBSRTA.001, file *Flux Splitting Validation.xls*, worksheet "Splash Rad vs Number."

Figure E-2. Effect of Number of Drips on Splash Radius; Data Organized by Type of Measurement

	A	B	C	D	E	F	G	H	I	J	K	L	M
56													
57													
58													
59													
60													
61													
62													
63													
64													
65													
66													
67													
68													
69													
70													
71													
72													
73													
74													
75													
76													
77													
78													
79													
80													
81													
82													
83													
84													
85													
86													
87													
88													
89													
90													
91													
92													

Source: Output DTN: SN0703PAEBSRTA.001, file *Flux Splitting Validation.xls*, worksheet "Splash Rad vs Number."

Figure E-3. Effect of Number of Drips on Splash Radius; All Left and Right Measurements Are Consolidated

SPREADSHEET "FLUX SPLITTING VALIDATION"–WORKSHEET "SPLASH RADIUS"

For validation of the drip shield and waste package flux-splitting submodels, splash radius data are analyzed for measurements on the rough drip shield surface, with dripping on the crown and at off-crown locations. Data for crown drip locations are used for the drip shield submodel validation, and off-crown drip locations are used for the waste package submodel validation. The statistics (mean, standard deviation, median, mean plus one standard deviation, and mean minus one standard deviation) are shown in Column I, Rows 19–23 for crown drip locations, and in Rows 37-41 for off-crown locations. The data actually used in the model validation are the minimum and maximum values for more than 20 drips, Cells H11 and I9, respectively, for crown locations, and Cells H31 and I36, respectively, for off-crown locations.

	A	B	C	D	E	F	G	H	I	J	K	L	M	N
1	Splash Radius Determination, Rough Drip Shield Surface, Dripping on Crown													
2														
3	Source Data													
4	Calculated results													
5							# Drips	Left (cm)	Right (cm)					
6	Splash Radius Test #1 - Rough DS Surface - Crown						10	2.0	2.0					
7							21	5.0	4.0					
8							60	18.0	22.0					
9							143	35.0	48.0					
10							203	35.0	48.0					
11	Splash Radius Test #2 - Rough DS Surface - Crown						21	3.5	4.0					
12							82	10.5	19.0					
13							149	31.5	30.0					
14							207	45.0	40.0					
15	Splash Radius Test #3 - Rough DS Surface - Crown						30	7.5	9.0					
16							82	19.0	17.5					
17							137	28.0	27.5					
18							205	29.0	28.0					
19								Mean	21.8					
20								Std. Dev.	14.8228					
21								Median	20.5					
22								Mean-SD	7.023354					
23								Mean+SD	36.66895					
24														
25														
26	Splash Radius Determination, Rough Drip Shield Surface, Dripping off Crown													
27														
28	Source Data													
29	Calculated results													
30							# Drips	Left (cm)	Right (cm)					
31	Splash Radius Test #4 - Rough DS Surface - 33 degrees						31	3	3.5					
32							82	5.5	6					
33							158	6.5	6.5					
34	Splash Radius Test #5 - Rough DS Surface - 16.5 degrees						22	9	10					
35							82	13	14.5					
36							156	14	15					
37								Mean	8.875					
38								Std. Dev.	4.349112					
39								Median	7.75					
40								Mean-SD	4.525888					
41								Mean+SD	13.22411					
42														
◀ ▶ 🔍 Splash Rad vs Number \ Splash Radius / Rough DS / Rough off crown WP model / ◀ ▶														

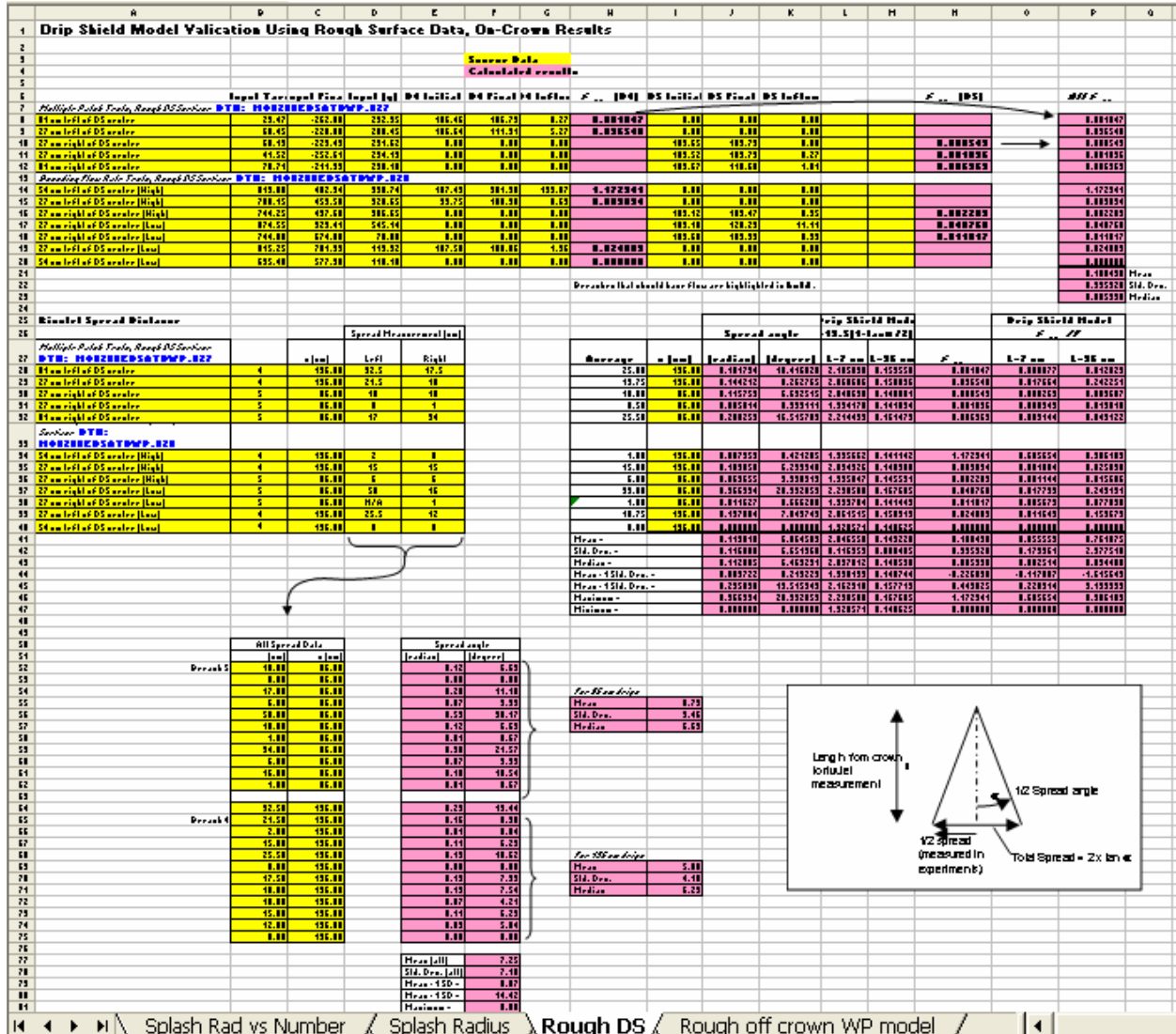
DTN: MO0207EBSATBWP.021

Source:DTN: MO0207EBSATBWP.021 [DIRS 163399]. Output DTN: SN0703PAEBSRTA.001, file *Flux Splitting Validation.xls*, worksheet "Splash Radius."

Figure E-4. Splash Radius Determination

SPREADSHEET “FLUX SPLITTING VALIDATION”–WORKSHEET “ROUGH DS”

This worksheet provides calculations for validation of the drip shield flux-splitting submodel based on data from rough drip shield surface tests. An overall view of the worksheet is shown in Figure E-5 to show the layout of the worksheet, and individual tables are then presented more legibly and described in detail on following pages.



Source:DTN: MO0208EBSATBWP.027 [DIRS 163404]; DTN: MO0208EBSATBWP.028 [DIRS 163405]. Output DTN: SN0703PAEBSRTA.001, file Flux Splitting Validation.xls, worksheet “Rough DS.”

Figure E-5. Worksheet Overview

	A	B	C	D	E	F	G	H
1	Drip Shield Model Valication Using Rough Surface Data, On-Crown Results							
2								
3						Source Data		
4						Calculated results		
5								
6		Input Tare	Input Final	Input (g)	B4 Initial	B4 Final	B4 Inflow	f_{expt} (B4)
7	<i>Multiple Patch Tests, Rough DS Surface</i> DTN: MO0208EBSATBWP.027							
8	81 cm left of DS center	29.47	-262.88	292.35	106.46	106.73	0.27	0.001847
9	27 cm left of DS center	68.45	-220.00	288.45	106.64	111.91	5.27	0.036540
10	27 cm right of DS center	68.19	-223.43	291.62	0.00	0.00	0.00	
11	27 cm right of DS center	41.52	-252.61	294.13	0.00	0.00	0.00	
12	81 cm right of DS center	78.71	-211.39	290.10	0.00	0.00	0.00	
13	<i>Bounding Flow Rate Tests, Rough DS Surface</i> DTN: MO0208EBSATBWP.028							
14	54 cm left of DS center (High)	813.08	482.34	330.74	107.43	301.30	193.87	1.172341
15	27 cm left of DS center (High)	788.15	459.50	328.65	99.75	100.38	0.63	0.003834
16	27 cm right of DS center (High)	744.25	437.60	306.65	0.00	0.00	0.00	
17	27 cm right of DS center (Low)	874.55	329.41	545.14	0.00	0.00	0.00	
18	27 cm right of DS center (Low)	744.80	674.00	70.80	0.00	0.00	0.00	
19	27 cm left of DS center (Low)	815.25	701.93	113.32	107.50	108.86	1.36	0.024003
20	54 cm left of DS center (Low)	695.48	577.38	118.10	0.00	0.00	0.00	0.000000
21								
22								Breaches that sho
23								

Source:DTN: MO0208EBSATBWP.027 [DIRS 163404]; DTN: MO0208EBSATBWP.028 [DIRS 163405]. Output DTN: SN0703PAEBSRTA.001, file *Flux Splitting Validation.xls*, worksheet "Rough DS."

Figure E-6. Calculation of Experimental Breach Flow Fractions

	H	I	J	K	L	M	N	O	P	Q	
1											
2											
3											
4											
5											
6	f_{expt} (B4)	B5 Initial	B5 Final	B5 Inflow			f_{expt} (B5)		$All f_{\text{expt}}$		
7											
8	0.001847	0.00	0.00	0.00					0.001847		
9	0.036540	0.00	0.00	0.00					0.036540		
10		109.65	109.73	0.08			0.000549		0.000549		
11		109.52	109.79	0.27			0.001836		0.001836		
12		109.67	110.68	1.01			0.006963		0.006963		
13											
14	1.172341	0.00	0.00	0.00					1.172341		
15	0.003834	0.00	0.00	0.00					0.003834		
16		109.12	109.47	0.35			0.002283		0.002283		
17		109.18	120.29	11.11			0.040760		0.040760		
18		109.60	109.99	0.39			0.011017		0.011017		
19	0.024003	0.00	0.00	0.00					0.024003		
20	0.000000	0.00	0.00	0.00					0.000000		
21									0.108498	Mean	
22	Breaches that should have flow are highlighted in bold .									0.335328	Std. Dev.
23									0.005398	Median	

Source: Output DTN: SN0703PAEBSRTA.001, file *Flux Splitting Validation.xls*, worksheet "Rough DS."

Figure E-7. Summary of Experimental Breach Flow Fractions

Tests are identified in Figure E-6 in Column A. Columns B and C are raw data—the initial and final water mass in the input water container. Column D is the difference between Columns B and C (e.g., $D8=B8-C8$), giving the mass of water dripped onto the drip shield. Columns E and F are the initial and final masses of water in the Breach B4 collection vessel. The difference, in Column G (e.g., $G8=F8-E8$), is the mass of water that flowed into B4. In Column H (Figure E-7), the fraction of the dripping flux that flowed into B4, f_{expt} (B4), is calculated for tests in which the flow into B4 was greater than zero (e.g., $H8=2*G8/D8$). Because the dripping was onto the crown, it is assumed that only half of the total input (i.e., $D8/2$) flowed down the side of the drip shield where B4 was located.

Columns I and J are the initial and final masses of water in the Breach B5 collection vessel. The difference, in Column K (e.g., $K8=J8-I8$), is the mass of water that flowed into B5. In Column N, the fraction of the dripping flux that flowed into B5, f_{expt} (B5), is calculated for tests in which the flow into B5 was greater than zero (e.g., $N10=2*K10/D10$). Because the drip location was the crown, it is assumed that only half of the total input (i.e., $D10/2$) flowed down the side of the drip shield where B5 was located.

The input water mass and flows into Breaches B4 and B5 are summarized in Table 7.1-3.

In Column P, all values of f_{expt} are consolidated. The mean, standard deviation, and median for the 12 data values are given in Rows 21, 22, and 23, respectively. The values of f_{expt} are listed in Table 7.1-4.

Rivulet Spread Distance					Spread Measurement (cm)				Spread angle			
Multiple Patch Tests, Rough DS Surface DTN: MO0208EBSATBWP.027					x (cm)	Left	Right	Average	x (cm)	(radian)	(degree)	
28	81 cm left of DS center	4	136.00	32.5	17.5	25.00	136.00	0.181734	10.416028			
29	27 cm left of DS center	4	136.00	21.5	18	19.75	136.00	0.144212	8.262765			
30	27 cm right of DS center	5	86.00	10	10	10.00	86.00	0.115759	6.632515			
31	27 cm right of DS center	5	86.00	0	1	0.50	86.00	0.005814	0.333111			
32	81 cm right of DS center	5	86.00	17	34	25.50	86.00	0.288253	16.515703			
Bounding Flow Rate Tests, Rough DS Surface DTN: MO0208EBSATBWP.028												
34	54 cm left of DS center (High)	4	136.00	2	0	1.00	136.00	0.007353	0.421295			
35	27 cm left of DS center (High)	4	136.00	15	15	15.00	136.00	0.109850	6.293948			
36	27 cm right of DS center (High)	5	86.00	6	6	6.00	86.00	0.069655	3.990913			
37	27 cm right of DS center (Low)	5	86.00	50	16	33.00	86.00	0.366394	20.992853			
38	27 cm right of DS center (Low)	5	86.00	N/A	1	1.00	86.00	0.011627	0.666200			
39	27 cm left of DS center (Low)	4	136.00	25.5	12	18.75	136.00	0.137004	7.849749			
40	54 cm left of DS center (Low)	4	136.00	0	0	0.00	136.00	0.000000	0.000000			
41								Mean =	0.119810	6.864589		
42								Std. Dev. =	0.116088	6.651360		
43								Median =	0.112805	6.463231		
44								Mean - 1 Std. Dev. =	0.003722	0.213229		
45								Mean + 1 Std. Dev. =	0.235698	13.515949		
46								Maximum =	0.366394	20.992853		
47								Minimum =	0.000000	0.000000		
48												
49												
50			All Spread Data					Spread angle				

Source:DTN: MO0208EBSATBWP.027 [DIRS 163404]; DTN: MO0208EBSATBWP.028 [DIRS 163405]. Output DTN: SN0703PAEBSRTA.001, file Flux Splitting Validation.xls, worksheet "Rough DS."

Figure E-8. Rivulet Spread Distances

Rivulet spread distances for each test are listed in Figure E-8, Columns D and E, Rows 28-40, for drips originating on the crown of the rough drip shield surface. The spread data are reorganized

in Column B, starting in Row 52 (see Figure E-9). All spread data measured 86 cm from the drip location are listed first, followed by all data measured 136 cm from the drip location. The corresponding x -distance is listed in Column C, starting in Row 52. In Column E, the spread distances, w_r , are converted to spread angles using the formula:

$$\alpha = \tan^{-1}\left(\frac{w_r}{x}\right).$$

In Cell E52, for example, the Microsoft Excel equation is: `E52=ATAN(B52/C52)`. The result is the spread angle in radians, which is converted to degrees in Column F (e.g., `F52=DEGREES(E52)`). The mean spread angle for 86-cm drips is given in Cell I55 (`I55=AVERAGE(F52:F63)`) and for 136-cm drips in Cell I69 (`I69=AVERAGE(F65:F75)`). Statistics are computed for all individual spread angle data in Column F, Rows 77-82:

$$F77=AVERAGE(F52:F75)$$

$$F78=STDEVA(F52:F75)$$

$$F79=F77-F78$$

$$F80=F77+F78$$

$$F81=MIN(F52:F75)$$

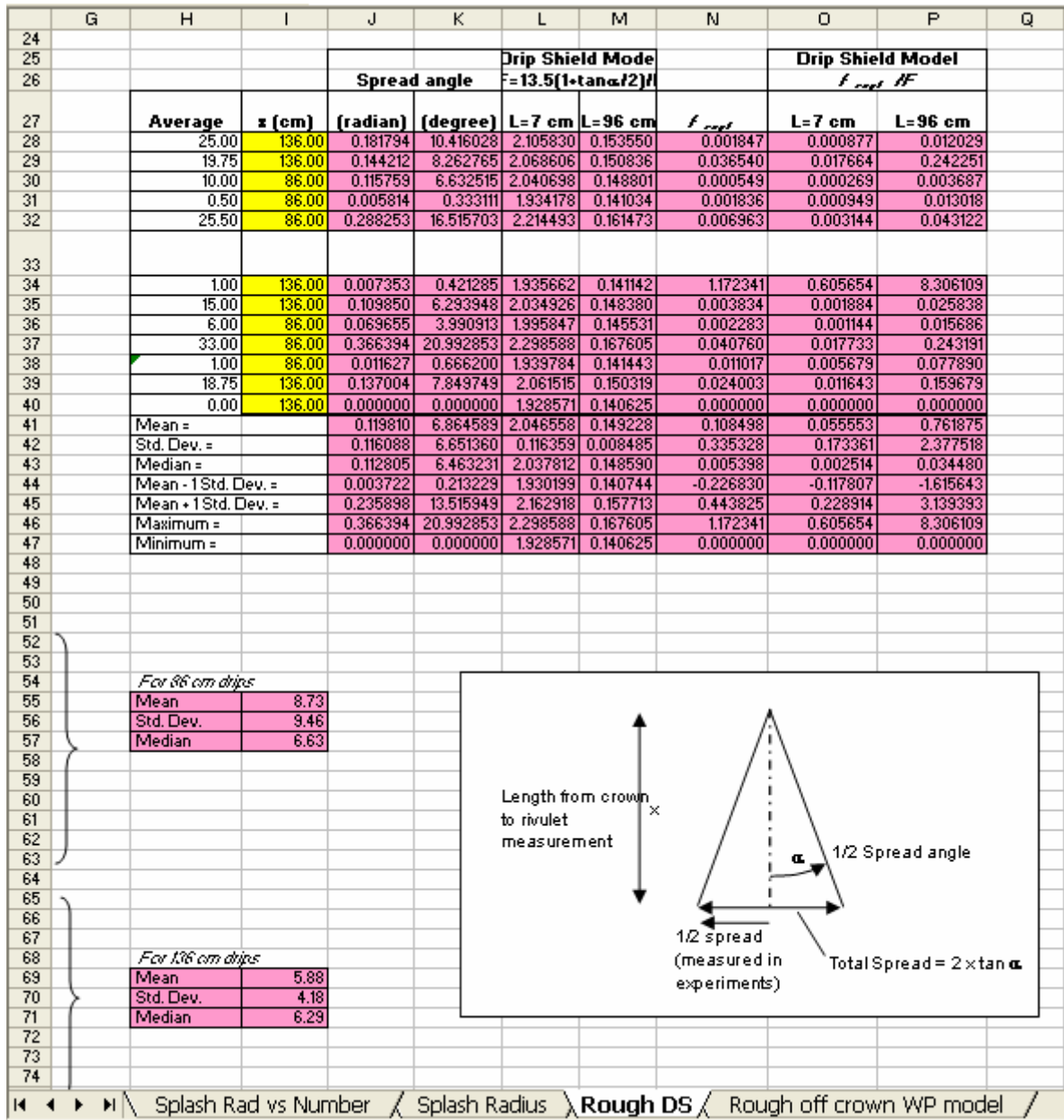
$$F82=MAX(F52:F75)$$

As shown in F79 and F80, the range for the spread angle is zero (rounding down) to 14.4°.

	A	B	C	D	E	F	G	H	I	J	K
40	54 cm left of DS center (Low)	4	136.00	0	0			0.00	136.00	0.000000	0.000000
41								Mean =	0.119810	6.864589	
42								Std. Dev. =	0.116088	6.651360	
43								Median =	0.112805	6.463231	
44								Mean + 1 Std. Dev. =	0.003722	0.213229	
45								Mean - 1 Std. Dev. =	0.235838	13.515949	
46								Maximum =	0.366394	20.932853	
47								Minimum =	0.000000	0.000000	
48											
49											
50											
51		All Spread Data		Spread angle							
52		Breach 5	(cm)	z (cm)	(radian)	(degree)					
53			10.00	96.00	0.12	6.63					
54			0.00	96.00	0.00	0.00					
55			17.00	96.00	0.20	11.18					
56			6.00	96.00	0.07	3.99					
57			50.00	96.00	0.53	30.17					
58			10.00	96.00	0.12	6.63					
59			1.00	96.00	0.01	0.67					
60			34.00	96.00	0.38	21.57					
61			6.00	96.00	0.07	3.99					
62			16.00	96.00	0.18	10.54					
63			1.00	96.00	0.01	0.67					
64			32.50	136.00	0.23	13.44					
65		Breach 4	21.50	136.00	0.16	8.98					
66			2.00	136.00	0.01	0.84					
67			15.00	136.00	0.11	6.29					
68			25.50	136.00	0.19	10.62					
69			0.00	136.00	0.00	0.00					
70			17.50	136.00	0.13	7.33					
71			18.00	136.00	0.13	7.54					
72			10.00	136.00	0.07	4.21					
73			15.00	136.00	0.11	6.29					
74			12.00	136.00	0.09	5.04					
75			0.00	136.00	0.00	0.00					
76											
77					Mean (all)	7.25					
78					Std. Dev. (all)	7.18					
79					Mean - 1SD =	0.07					
80					Mean + 1SD =	14.42					
81					Maximum =	0.00					
82					Minimum =	-30.17					
83											
84											

Source: Output DTN: SN0703PAEBSRTA.001, file Flux Splitting Validation.xls, worksheet "Rough DS."

Figure E-9. Rivulet Spread Data Reorganized



Source: Output DTN: SN0703PAEBSRTA.001, file Flux Splitting Validation.xls, worksheet "Rough DS."

Figure E-10. Calculation of Rivulet Spread Angles

In Column H, Rows 28-40 (see Figure E-10), the average rivulet spread is computed for each experiment (e.g., H28=(D28+E28)/2). Column I is the distance from the crown to the point where the rivulet spread was measured (identical to Column C). The spread angle is computed in Column J, Rows 28-40, (e.g., J28=ATAN(H28/I28)). In Column K, Rows 28-40, the

average spread angle in radians is converted to degrees (e.g., $K28=DEGREES(J28)$). In Worksheet “Splash Rad vs Number,” the minimum splash radius for tests using 20 or more drips was 3.5 cm, for a total splash distance of 7 cm. This is used as the effective drip shield length in Column L, where f_{calc} is obtained using the formula

$$\begin{aligned} f_{calc} &= \frac{\ell}{L} \left(1 + \frac{\tan \alpha}{2} \right) \\ &= \frac{13.5}{7} \left(1 + \frac{\tan \alpha}{2} \right) \end{aligned}$$

$$L28=13.5*(1+\text{TAN}(J28)/2)/7$$

The maximum splash radius tests using 20 or more drips was 48 cm in Worksheet “Splash Rad vs. Number,” giving a total splash distance of 96 cm. This is used as the effective drip shield length in Column M:

$$\begin{aligned} f_{calc} &= \frac{\ell}{L} \left(1 + \frac{\tan \alpha}{2} \right) \\ &= \frac{13.5}{96} \left(1 + \frac{\tan \alpha}{2} \right) \end{aligned}$$

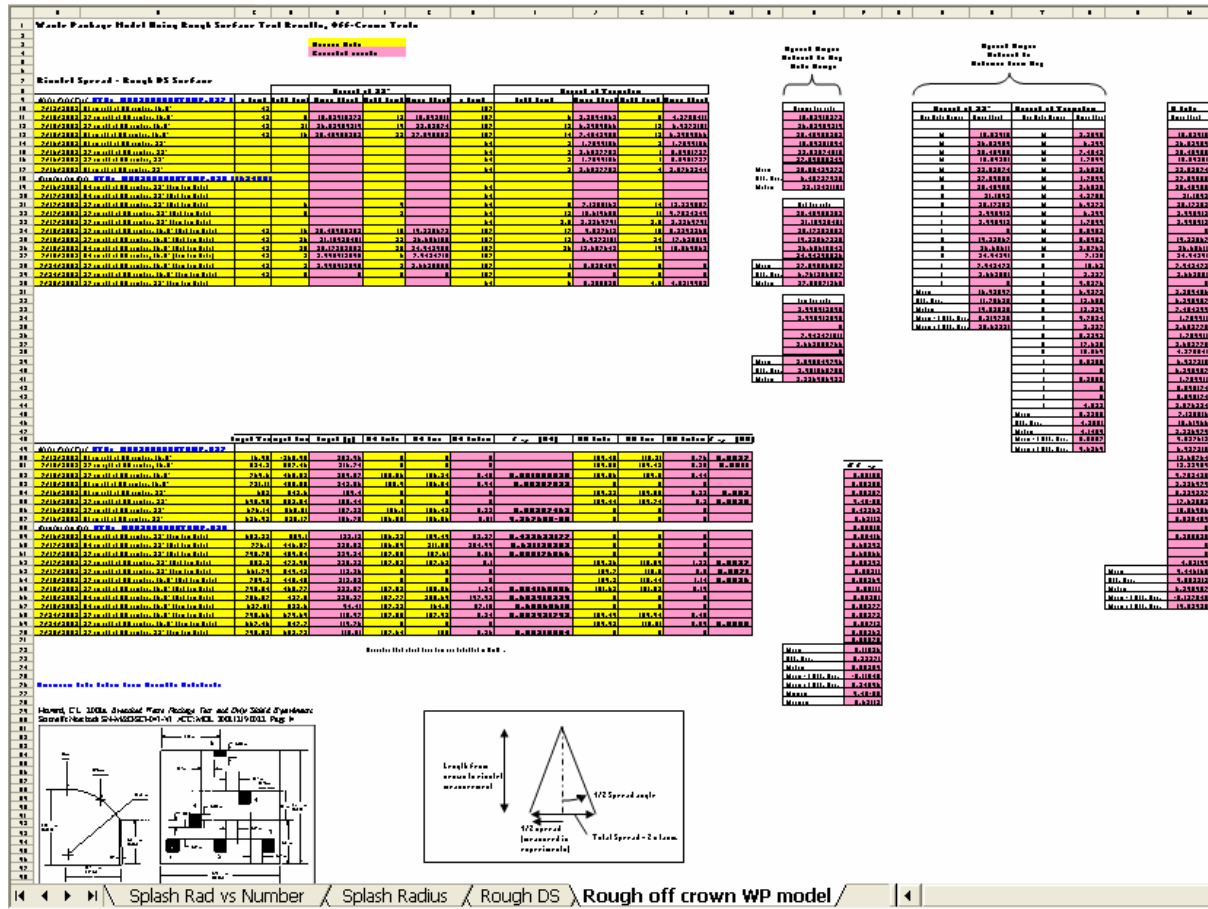
$$M28=13.5*(1+\text{TAN}(J28)/2)/96$$

The values of f_{calc} in Columns L and M are similar to F/f_{VD} in Table 7.1-5, the only difference being the values used for spread angle. Table 7.1-5 uses the rounded values for spread angle obtained from Figure E-9, zero to 14.4°, whereas in Columns L and M in Figure E-10, f_{calc} is calculated from a different average spread angle. As shown in the statistics (Rows 46–47), f_{calc} or F/f_{VD} ranges from 0.141 to 2.30, based on minimum and maximum average spread angles. Using the mean plus or minus one standard deviation for the spread angle, f_{calc} ranges from 0.141 to 2.16 (Rows 44-45, Columns L and M), close to the values reported in Table 7.1-5 (0.141 to 2.17).

In Column N, Rows 28–40, the values of f_{expt} are transferred from Column P, Rows 8–20. In Column O, the ratio f_{expt}/f_{calc} is computed (e.g., $O28=N28/L28$) for the minimum effective drip shield length of 7 cm. In Column P, the ratio f_{expt}/f_{calc} is computed (e.g., $P28=N28/M28$) for the maximum effective drip shield length of 96 cm. This ratio is identical to the uncertainty factor f_{VD} in Equation 7.1.1.1-2. As shown in the statistics (Rows 46–47), F/f_{VD} for the experimental data ranges from 0.0 to 8.306.

SPREADSHEET “FLUX SPLITTING VALIDATION”–WORKSHEET “ROUGH OFF CROWN WP MODEL”

This worksheet provides calculations for validation of the waste package flux-splitting submodel based on data from the rough drip shield surface tests. An overall view of the worksheet is shown on Figure E-11, and individual tables are then described in detail.



Source: Output DTN: SN0703PAEBSRTA.001, file *Flux Splitting Validation.xls*, worksheet “Rough off crown WP model.”

Figure E-11. Worksheet Overview

	A	B	C	D	E	F	G	H	I	J	K	L
1	Waste Package Model Using Rough Surface Test Results, Off-Crown Tests											
2												
3												
4												
5												
6												
7	Rivulet Spread - Rough DS Surface											
8												
9	Multiple Patch Test DTN: MO0208EBSATBWP.027											
10												
11												
12												
13												
14												
15												
16												
17												
18	Bounding Flow Rate DTN: MO0208EBSATBWP.028											
19												
20												
21												
22												
23												
24												
25												
26												
27												
28												
29												
30												
31												

Source:DTN: MO0208EBSATBWP.027 [DIRS 163404]; DTN: MO0208EBSATBWP.028 [DIRS 163405]. Output DTN: SN0703PAEBSRTA.001, file *Flux Splitting Validation.xls*, worksheet "Rough off crown WP model."

Figure E-12. Calculation of Rivulet Spread Angles

In Figure E-12, Columns A and B, Rows 10–30, identify the tests reported in indicated DTNs. In Columns C and H, the value of x , the distance from the drip location to the measurement point, is listed. Rivulet spread measured to the left and right of the drip location is shown in Columns D and F, respectively, for measurements at the 33° line. Measurements at the transition line are listed in Columns I and K. Portions of this table are reproduced in Table 7.1-8.

The spread distance, w_r , is converted to spread angle, α , in Columns E, G, J, and L:

$$\alpha = \tan^{-1}\left(\frac{w_r}{x}\right).$$

An example of the Microsoft Excel equation used for this calculation is:

$$E11=DEGREES(ATAN(D11/C11))$$

where the DEGREES function converts the result of the inverse tangent function ATAN from radians to degrees.

In Figure E-13, Column O, Rows 11–38, the spread angles measured at the 33° line are ordered by drip rate. The “nominal” drip rate is that used in the Multiple Patch tests, and the high and low drip rates were used in the Bounding Flow Rate tests. The mean, standard deviation, and median are computed for each of the three drip rates.

In Column S, the spread angles from Column O are repeated, and statistics (mean, standard deviation, median, and mean plus or minus one standard deviation) are computed for the entire set in Rows 31–35. The drip rate is indicated in Column R, where “M” indicates the nominal drip rate.

In Column U, the spread angles from Columns J and L are consolidated for measurements at the transition line. The drip rate used in each test is indicated in Column T. (The values in this column are currently incorrect, since they are just copies of the incorrect results in Column L and incorrectly recalculated values from Column J, where the actual Column J values are correct.)

All 50 spread angle measurements are compiled in Column W, with statistics (mean, standard deviation, median, and mean plus or minus one standard deviation) computed for the entire set in Rows 63-67 (Figure E-14). The mean plus or minus one standard deviation are used as the spread angle range in Section 7.1.1.2 for determination of the uncertainty in the waste package flux splitting-submodel validation.

	M	N	O	P	Q	R	S	T	U	V	W
1											
2											
3											
4											
5											
6											
7											
8											
9											
10											
11											
12											
13											
14											
15											
16											
17											
18											
19											
20											
21											
22											
23											
24											
25											
26											
27											
28											
29											
30											
31											
32											
33											
34											
35											
36											
37											
38											
39											
40											
41											
42											
43											
44											
45											
46											
47											
48											
49											
50											
51											
52											
53											

Source: Output DTN: SN0703PAEBSRTA.001, file Flux Splitting Validation.xls, worksheet "Rough off crown WP model."

Figure E-13. Additional Calculations of Rivulet Spread Angles

	S	T	U	V	W
45		Mean	5.23878		7.12501635
46		Std. Dev.	4.38812		10.6196553
47		Median	4.14892		2.23697906
48		Mean - 1 Std. Dev.	0.85066		9.02761295
49		Mean + 1 Std. Dev.	9.6269		6.92721813
50					13.6576425
51					12.3390873
52					9.75242494
53					2.23697906
54					5.3392368
55					17.6280194
56					10.0690627
57					0.53545899
58					0
59					5.35582504
60					0
61					0
62					4.02199018
63				Mean	9.4461677
64				Std. Dev.	9.58321235
65				Median	6.39895663
66				Mean - 1 Std. Dev.	-0.1370447
67				Mean + 1 Std. Dev.	19.02938

Source: Output DTN: SN0703PAEBSRTA.001, file *Flux Splitting Validation.xls*, worksheet "Rough off crown WP model."

Figure E-14. Statistics of Rivulet Spread Angles

	A	B	C	D	E	F	G	H	I
47									
48			Input Tare	Input Final	Input (g)	B4 Initial	B4 Final	B4 Inflow	f_{expt} (B4)
49	<i>Multiple Patch Test</i> DTN: MO0208EBSATBWP.027								
50	7/12/2002	81 cm right of DS center, 16.5'	16.98	-265.98	282.96	0	0	0	
51	7/15/2002	27 cm right of DS center, 16.5'	824.2	507.46	316.74	0	0	0	
52	7/15/2002	27 cm left of DS center, 16.5'	769.6	460.03	309.57	105.86	106.34	0.48	0.001550538
53	7/15/2002	81 cm left of DS center, 16.5'	731.11	488.55	242.56	105.9	106.84	0.34	0.00387533
54	7/16/2002	81 cm right of DS center, 33'	652	542.6	109.4	0	0	0	
55	7/16/2002	27 cm right of DS center, 33'	690.98	582.54	108.44	0	0	0	
56	7/16/2002	27 cm left of DS center, 33'	676.14	568.81	107.33	106.1	106.43	0.33	0.00307463
57	7/16/2002	81 cm left of DS center, 33'	636.92	530.17	106.75	106.05	106.06	0.01	9.36768E-05
58	<i>Bounding Flow Rate</i> DTN: MO0208EBSATBWP.028								
59	7/16/2002	54 cm left of DS center, 33' (Low Flow Rate)	682.23	559.1	123.13	106.22	159.49	53.27	0.432632177
60	7/17/2002	54 cm left of DS center, 33' (High Flow Rate)	776.1	446.07	330.03	106.09	311.08	204.99	0.621125352
61	7/17/2002	27 cm left of DS center, 33' (High Flow Rate)	798.78	459.54	339.24	107.55	107.61	0.06	0.000176866
62	7/17/2002	27 cm right of DS center, 33' (High Flow Rate)	803.2	472.98	330.22	107.52	107.62	0.1	
63	7/17/2002	27 cm right of DS center, 33' (Low Flow Rate)	661.79	549.43	112.36	0	0	0	
64	7/18/2002	27 cm right of DS center, 16.5' (High Flow Rate)	759.3	445.48	313.82	0	0	0	
65	7/18/2002	27 cm left of DS center, 16.5' (High Flow Rate)	790.84	468.77	322.07	107.52	108.86	1.34	0.004160586
66	7/18/2002	54 cm left of DS center, 16.5' (High Flow Rate)	756.07	427.8	328.27	107.77	305.69	197.32	0.602918329
67	7/18/2002	54 cm left of DS center, 16.5' (Low Flow Rate)	627.01	532.6	94.41	107.32	164.5	57.18	0.60565618
68	7/24/2002	27 cm left of DS center, 16.5' (Low Flow Rate)	795.66	679.69	115.97	107.58	107.92	0.34	0.002931793
69	7/24/2002	27 cm right of DS center, 16.5' (Low Flow Rate)	667.46	547.7	119.76	0	0	0	
70	7/25/2002	27 cm left of DS center, 33' (Low Flow Rate)	798.53	682.72	115.81	107.64	108	0.36	0.00310854
71									
72						Breaches that should have flow are highlighted in bold.			

Source: DTN: MO0208EBSATBWP.027 [DIRS 163404]; DTN: MO0208EBSATBWP.028 [DIRS 163405]. Output DTN: SN0703PAEBSRTA.001, file *Flux Splitting Validation.xls*, worksheet "Rough off crown WP model."

Figure E-15. Calculation of Experimental Breach Flow Fractions

For the tests identified in Columns A and B, Rows 50–70 (Figure E-15), the initial and final water mass in the input water container are listed in Columns C and D, and the amount of water dripped onto the drip shield is calculated in Column E (e.g., E50=C50-D50). The initial and final mass of water in the Breach B4 collection vessel is listed in Columns F and G, respectively, and the amount of water collected from flow into Breach B4 is calculated in Column H (e.g., H52=G52-F52). The fraction of water dripped onto the drip shield that flowed into Breach B4, f_{expt} (B4), is computed in Column I for the tests in which the inflow was greater than zero (e.g., I52=H52/E52).

	J	K	L	M	N	O	P
47							
48	B5 Initial	B5 Final	B5 Inflow	f_{expt} (B5)			
49							
50	109.45	110.21	0.76	0.00268589			
51	109.08	109.43	0.35	0.00110501			<i>All f_{expt}</i>
52	109.06	109.5	0.44				0.001550538
53	0	0	0				0.00387533
54	109.33	109.55	0.22	0.00201097			0.00307463
55	109.44	109.74	0.3	0.00276651			9.36768E-05
56	0	0	0				0.432632177
57	0	0	0				0.621125352
58							0.000176866
59	0	0	0				0.004160586
60	0	0	0				0.602918329
61	0	0	0				0.60565618
62	109.36	110.59	1.23	0.00372479			0.002931793
63	109.7	110.5	0.8	0.00711997			0.00310854
64	109.3	110.44	1.14	0.00363266			0.002685892
65	101.63	101.82	0.19				0.001105007
66	0	0	0				0.002010969
67	0	0	0				0.002766507
68	109.49	109.94	0.45				0.00372479
69	109.92	110.01	0.09	0.0007515			0.007119972
70	0	0	0				0.003632656
71							0.000751503
72						Mean	0.115255065
73						Std. Dev.	0.233709623
74						Median	0.003091585
75						Mean - 1 Std. Dev.	-0.11845456
76						Mean + 1 Std. Dev.	0.348964688
77						Minimum	9.36768E-05
78						Maximum	0.621125352

Source: Output DTN: SN0703PAEBSRTA.001, file *Flux Splitting Validation.xls*, worksheet "Rough off crown WP model."

Figure E-16. Summary of Experimental Breach Flow Fractions

The initial and final mass of water in the Breach B5 collection vessel is listed in Figure E-16, Columns I and J, respectively, and the amount of water collected from flow into Breach B5 is calculated in Column L (e.g., L50=K50-J50). The fraction of water dripped onto the drip shield that flowed into Breach B5, f_{expt} (B5), is computed in Column M for the tests in which the inflow was greater than zero (e.g., M50=L50/E50).

The 20 values of f_{expt} are compiled in Column P, with statistics (mean, standard deviation, median, and mean plus or minus one standard deviation) presented in Rows 73-76.

The input water, breach inflows, and f_{expt} for each breach are reproduced in Table 7.1-10.

APPENDIX F

ANALYSIS OF STAINLESS STEEL AND CARBON STEEL CORROSION RATES USING BAYESIAN UPDATING METHODOLOGY

ANALYSIS OF STAINLESS STEEL AND CARBON STEEL CORROSION RATES USING BAYESIAN UPDATING METHODOLOGY

R. L. Iman
Southwest Technology Consultants

Bayesian Updating. As will be demonstrated, the uncertainty in the Stainless Steel Type 316 (hereafter referred to as 316 SS) and Carbon Steel Type A 516 (hereafter referred to as A 516 CS) corrosion rate data (in units of $\mu\text{m yr}^{-1}$) is characterized by lognormal distributions. It is well known that if the random variable Y has a lognormal distribution, then $\ln(Y)$ has a normal distribution, which is a key to the Bayesian updating methodology for lognormal distributions, as will be explained. In way of review, if the random variable X has a normal distribution with mean μ_X and standard deviation σ_X , then:

$$Y = e^X \quad (\text{Eq. F-1})$$

has a lognormal distribution with μ_X as its location parameter and σ_X as its scale parameter. These two parameters are not the mean and standard deviation for the lognormal distribution, rather the mean of the lognormal is given as:

$$\mu_Y = e^{\mu_X + \sigma_X^2/2}, \quad (\text{Eq. F-2})$$

and its variance is given as:

$$\sigma_Y^2 = e^{2\mu_X + \sigma_X^2} (e^{\sigma_X^2} - 1). \quad (\text{Eq. F-3})$$

Thus, the mean and the variance of the lognormal both involve the parameters μ_X and σ_X of the normal distribution.

The median of the lognormal is given as:

$$Y_{0.5} = e^{\mu_X} \quad (\text{Eq. F-4})$$

The uncertainty in the 316 SS and A 516 CS data can be characterized with lognormal distributions if the respective logs of the sample data have a normal distribution. Figures F-1 and F-2 give the graphical results (Iman 1982 [DIRS 146012]) of the Lilliefors tests for normality of the natural logs of the 316 SS and A 516 CS, respectively. If the red empirical distribution functions (EDFs) in these graphs remain within the dashed bounds, then the assumption of normality for sample data is reasonable, which is the case in both figures.

Attention is now directed toward the normal distribution (i.e., the natural logs for the 316 SS and A 516 CS corrosion rates) and the lognormal distribution is omitted from the discussion until later. The mean corrosion rate m is unknown, but it is assumed that m is the mean of a normal distribution with a known standard deviation h . Moreover, it is assumed that m itself has a

normal distribution. In particular, the prior distribution for m is normal with mean m_0 and standard deviation h_0 , that is $m \sim N(m_0, h_0)$.

The prior distribution for 316 SS uses $m_0 = -1$ and $h_0 = 1$. From Equations F-2 and F-3, the prior mean and standard deviation of the corresponding lognormal distribution are 0.607 and 0.795.

The prior distribution for A 516 CS uses $m_0 = 4.5$ and $h_0 = 0.5$. Again, using Equations F-2 and F-3, the prior mean and standard deviation of the corresponding lognormal distribution are 102.003 and 54.361.

Professional judgment was used to determine the values of the prior distributions for both 316 SS and A 516 CS. The analyst has considerable freedom in selecting the parameters of the prior distribution as will be demonstrated.

Whenever possible, Bayesian updating utilizes certain “conjugate pairs” of distributions to make the mathematics more tractable. For example, a normal-normal conjugate pair means that a normal distribution for the prior produces a normal distribution for the posterior distribution.

The sample mean for the $n = 16$ sample observations for the 316 SS is $\bar{x} = -1.577$ with a standard deviation $s = 0.671$.

The posterior mean is a weighted average of the prior mean and the sample mean. These weights are determined by the prior precision, the sample precision and the posterior precision, which are defined as follows for the 316 SS Bayesian analysis:

$$\text{Prior precision} = c_0 = 1/h_0^2 = 1/1^2 = 1 \quad (\text{Eq. F-5})$$

$$\text{Sample precision} = c = n/s^2 = 16/0.671^2 = 35.518 \quad (\text{Eq. F-6})$$

$$\text{Posterior precision} = c_1 = c_0 + c = 1 + 35.518 = 36.518 \quad (\text{Eq. F-7})$$

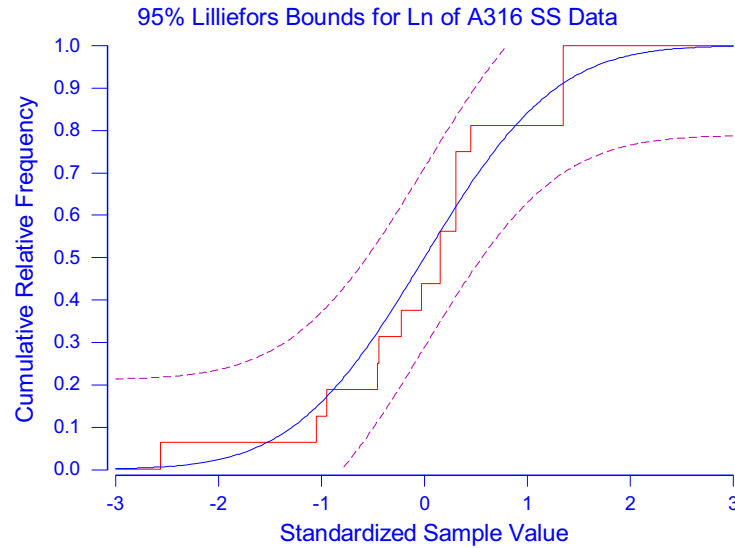


Figure F-1. Lilliefors Test for Normality for the 316 SS Data

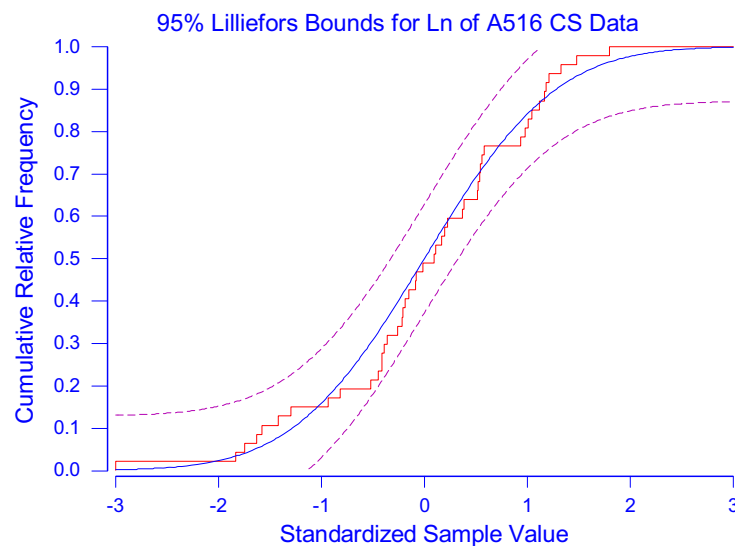


Figure F-2. Lilliefors Test for Normality for the A 516 CS Data

The posterior mean of the normal distribution is given as:

$$m_1 = \left(\frac{c_0}{c_1} \right) m_0 + \left(\frac{c}{c_1} \right) \bar{x} = \left(\frac{1}{36.518} \right) (-1) + \left(\frac{35.518}{36.518} \right) (-1.577) = -1.561 \quad (\text{Eq. F-8})$$

Note that the weight for m_0 is $1/36.518 = 0.027$ and the weight for \bar{x} is $35.518/36.518 = 0.973$. Or, the prior has a weight of 2.7 percent and the sample data have a weight of 97.3 percent. Thus, the sample data dominate the posterior distribution.

The posterior standard deviation of the normal distribution is given as:

$$\sqrt{s^2 + \frac{1}{c_1}} = \sqrt{0.671^2 + \frac{1}{36.518}} = 0.691 \quad (\text{Eq. F-9})$$

Now to return to the lognormal distribution, the posterior mean of the lognormal is found from Equations F-2, F-8, and F-9 as follows:

$$e^{\mu + \sigma^2/2} = e^{-1.561 + 0.691^2/2} = 0.267 \quad (\text{Eq. F-10})$$

The posterior standard deviation of the lognormal is found from Equations F-3, F-8, and F-9 as follows:

$$\sqrt{e^{2\mu + \sigma^2} (e^{\sigma^2} - 1)} = \sqrt{e^{2(-1.561) + 0.691^2} (e^{0.691^2} - 1)} = 0.209 \quad (\text{Eq. F-11})$$

Likewise, the posterior median of the lognormal is found from Equations F-4 and F-8 as follows:

$$e^{\mu} = e^{-1.561} = 0.210 \quad (\text{Eq. F-12})$$

As a check on these calculations, 1,000 random samples were obtained from a normal distribution with $\mu = -1.561$ and $\sigma = 0.691$. These values were exponentiated as in Equation F-1 to produce a lognormal distribution. Then, an additional 1,000 random samples were obtained directly from a lognormal distribution using $\mu = -1.561$ as a location parameter and $\sigma = 0.691$ as a scale parameter. The summary statistics for those two simulations are compared to the Bayesian analysis in Table F-1.

Table F-1. Comparison of Two Simulations with Bayesian Analysis for 316 SS Corrosion Rates

	Mean	Median	St. Dev.
Normal simulation, $Y = \exp(X)$	0.262	0.213	0.192
Lognormal simulation	0.268	0.208	0.216
Bayesian Posterior Parameters	0.267	0.210	0.209

This summary makes it clear that the simulation results are in excellent agreement with the posterior Bayesian parameters.

The comment was made earlier that the analyst has considerable freedom in selecting the parameters of the prior distribution of the logs, which were $m_0 = -1$ and $h_0 = 1$ for 316 SS corrosion rates. From Equations F-2 and F-3, these prior values produce a mean of 0.607 and a standard deviation of 0.795 for the lognormal distribution. These prior values differ considerably from the posterior mean 0.267 and standard deviation 0.209. The reason for this lies in the weights that were used in Equation F-8. That is to say, if the prior mean m_0 is known with great precision (h_0 is small), then the prior precision increases as seen in Equation F-5. For

example, if h_0 had been selected as 0.5, then the weights in Equation F-8 would have been 10.1 percent for the prior and 89.9 percent for the sample.

It was desired to truncate the posterior lognormal distribution at 0.01 and 0.51, which were regarded as physically reasonable limits for 316 SS corrosion rates. The quantiles corresponding to these truncation points for a lognormal distribution with location parameter $\mu = -1.561$ and scale parameter $\sigma = 0.691$ are as follows:

$$P(CR_{316 SS} < 0.01) = 0.000005 \quad \text{and} \quad P(CR_{316 SS} < 0.51) = 0.900533.$$

Thus, the truncation value of 0.01 is in the very extreme lower tail of the posterior lognormal distribution while the value of 0.51 is at the 90th percentile. The desired truncation values can be expressed probabilistically as:

$$P(CR_{316 SS} < 0.01) = 0 \quad \text{and} \quad P(CR_{316 SS} < 0.51) = 1.$$

Combining these two probabilistic statements yields the following truncation rules:

If $CR_{316 SS} < 0.01$, then the cumulative probability is 0.

If $CR_{316 SS} > 0.51$, then the cumulative probability is 1.

If $0.01 < CR_{316 SS} < 0.51$, then the cumulative probability is found through interpolation as:

$$\frac{P(Y \leq CR_{316 SS}) - 0.000005}{0.900533 - 0.000005}, \quad (\text{Eq. F-13})$$

where Y is the random variable representing the posterior lognormal distribution. That is, find $P(Y < CR_{316 SS})$ for the lognormal distribution with location parameter $\mu = -1.561$ and scale parameter $\sigma = 0.691$ (or a mean of 0.267 and a standard deviation of 0.209) and substitute this probability into Equation F-13 to find the corresponding cumulative probability for the truncated lognormal distribution.

The truncated distribution is in the form of a look up table Columns I and K of Excel file *Bayesian Updating Short Term Fresh Water Corrosion Rate - 3-6-2007.xls* (DTN: SN0703PAEBSRTA.001, Worksheet "A316 SS Short Term Fresh Water"), which provides the Bayesian updating calculations.

The Bayesian analysis for 316 SS also provides the following standard deviation for the mean m_1 of the posterior normal distribution:

$$h_1 = \frac{1}{\sqrt{c_1}} = \frac{1}{\sqrt{36.518}} = 0.165 \quad (\text{Eq. F-14})$$

Thus, the uncertainty in the mean of the posterior normal distribution can be characterized as a cumulative distribution function (CDF). Since the median of a lognormal distribution is found as $\exp(m_1)$ (see Equation F-4), the uncertainty distribution for m_1 becomes an uncertainty distribution for the median of the lognormal through this simple transformation. This CDF is also given in Excel file *Bayesian Updating Short Term Fresh Water Corrosion Rate - 3-6-2007.xls* (DTN: SN0703PAEBSRTA.001, file).

The corresponding Bayesian analysis for A 516 CS is summarized as follows:

As mentioned previously, the prior distribution for the logs of A 516 CS has $m_0 = 4.5$ and $h_0 = 0.5$ with the mean and standard deviation of the corresponding lognormal distribution being 102.003 and 54.361. The sample mean for the $n = 47$ sample observations for the A 516 CS corrosion rates is $\bar{x} = 4.314$ with a standard deviation $s = 0.308$.

The prior, sample and posterior precisions for A 516 CS are:

$$\text{Prior precision} = c_0 = 1/h_0^2 = 1/0.5^2 = 4 \quad (\text{Eq. F-15})$$

$$\text{Sample precision} = c = n/s^2 = 47/0.308^2 = 495.058 \quad (\text{Eq. F-16})$$

$$\text{Posterior precision} = c_1 = c_0 + c = 4 + 495.058 = 499.058 \quad (\text{Eq. F-17})$$

The posterior mean of the normal distribution is given as:

$$m_1 = \left(\frac{c_0}{c_1}\right)m_0 + \left(\frac{c}{c_1}\right)\bar{x} = \left(\frac{1}{499.058}\right)(4.5) + \left(\frac{495.058}{499.058}\right)(4.314) = 4.315 \quad (\text{Eq. F-18})$$

The weight for m_0 is $1/499.058 = 0.002$ and the weight for \bar{x} is $495.058/499.058 = 0.998$. Or, the prior has a weight of 0.2 percent and the sample data have a weight of 99.8 percent. Unlike the previous example where $n = 16$, the A 516 CS has $n = 47$, which when combined with the decrease in the standard deviation, gives more weight to the sample. Thus, the sample data again dominate the posterior distribution.

The posterior standard deviation of the normal distribution is given as:

$$\sqrt{s^2 + \frac{1}{c_1}} = \sqrt{0.308^2 + \frac{1}{499.058}} = 0.311 \quad (\text{Eq. F-19})$$

The posterior mean of the lognormal is:

$$e^{\mu + \sigma^2/2} = e^{4.315 + 0.311^2/2} = 78.521 \quad (\text{Eq. F-20})$$

The posterior standard deviation of the lognormal is:

$$\sqrt{e^{2\mu+\sigma^2} (e^{\sigma^2} - 1)} = \sqrt{e^{2(4.315)+0.311^2} (e^{0.311^2} - 1)} = 25.022. \quad (\text{Eq. F-21})$$

Likewise, the posterior median of the lognormal is found from Equations F-4 and F-18 as follows:

$$e^\mu = e^{4.315} = 74.814. \quad (\text{Eq. F-22})$$

As before, 1,000 random samples were obtained from a normal distribution with $\mu = 4.315$ and $\sigma = 0.311$. These values were exponentiated as in Equation F-1 to produce a lognormal distribution. Then, an additional 1,000 random samples were obtained directly from a lognormal distribution using $\mu = 4.315$ as a location parameter and $\sigma = 0.311$ as a scale parameter. The summary statistics for those two simulations are compare to the Bayesian analysis in Table F-2.

Table F-2. Comparison of Two Simulations with Bayesian Analysis for A 516 CS Corrosion Rates

	Mean	Median	St. Dev.
Normal simulation, $Y = \exp(X)$	78.914	74.303	26.102
Lognormal simulation	78.980	75.766	25.781
Bayesian Posterior Parameters	78.521	74.814	25.022

The simulation results are in excellent agreement with the posterior Bayesian parameters.

It was also desired to truncate the posterior lognormal distribution at 25 and 135, which were regarded as physically reasonable limits for A 516 CS corrosion rates. The quantiles corresponding to these truncation points for a lognormal distribution with location parameter $\mu = 4.315$ and scale parameter $\sigma = 0.045$ are as follows:

$$P(CR_{A\ 516\ CS} < 25) = 0.000212 \quad \text{and} \quad P(CR_{A\ 516\ CS} < 135) = 0.971151.$$

Thus, the truncation value of 25 is in the very extreme lower tail of the posterior lognormal distribution, while the value of 135 is at the 97th percentile. The desired truncations values are expressed probabilistically as:

$$P(CR_{A\ 516\ CS} < 25) = 0 \quad \text{and} \quad P(CR_{A\ 516\ CS} < 135) = 1.$$

Combining these two probabilistic states yields the following truncation rules:

If $CR_{A516CS} < 25$, then the cumulative probability is 0.

If $CR_{A516CS} > 125$, then the cumulative probability is 1.

If $25 < CR_{A516CS} < 135$, then the cumulative probability is found through interpolation as:

$$\frac{P(Y \leq CR_{A516CS}) - 0.000212}{0.901151 - 0.000212}, \quad (\text{Eq. F-23})$$

where Y is the random variable representing the posterior lognormal distribution. That is, find $P(Y < CR_{A516CS})$ for the lognormal distribution with location parameter $\mu = 4.315$ and scale parameter $\sigma = 0.331$ (or a mean of 78.521 and a standard deviation of 25.022) and substitute this probability into Equation F-23 to find the corresponding cumulative probability for the truncated lognormal distribution.

The truncated distribution is in the form of a lookup table Columns I and K of Excel file *Bayesian Updating Short Term Fresh Water Corrosion Rate - 3-6-2007.xls* (DTN: SN0703PAEBSRTA.001, Worksheet “A516 CS 60 & 90 Degrees”) that provides the Bayesian updating calculations.

The Bayesian analysis also provides the following standard deviation for the mean m_1 of the posterior normal distribution:

$$h_1 = \frac{1}{\sqrt{c_1}} = \frac{1}{\sqrt{499.058}} = 0.045 \quad (\text{Eq. F-24})$$

Thus, the uncertainty in the mean of the posterior normal distribution can be characterized as a CDF. Since the median of a lognormal distribution is found as $\exp(m_1)$ (see Equation F-4), the uncertainty distribution for m_1 becomes an uncertainty distribution for the median of the lognormal through this simple transformation. This CDF is also given in the Excel file in DTN: SN0703PAEBSRTA.001, file *Bayesian Updating Short Term Fresh Water Corrosion Rate - 3-6-2007.xls*, Worksheet “A516 CS 60 & 90 Degrees”.

APPENDIX G

MICROSOFT EXCEL SPREADSHEET “INVERT DIFFUSION COEFFICIENT”

MICROSOFT EXCEL SPREADSHEET “INVERT DIFFUSION COEFFICIENT”

SPREADSHEET “INVERT DIFFUSION COEFFICIENT” WORKSHEET “MODEL”

The purpose of this spreadsheet is to perform a statistical analysis of the dependence of effective invert diffusion coefficients, D_I ($\text{m}^2 \text{s}^{-1}$), on volumetric moisture content, θ (percent, $100 \text{ m}^3 \text{ water m}^{-3} \text{ bulk volume}$), as described in Section 6.3.4.1.1. The diffusion data are fit to an equation of the form:

$$\phi S_w D_I = D_0 \left(\frac{\theta}{100} \right)^n, \quad (\text{Eq. G-1})$$

where ϕ is the porosity ($\text{m}^3 \text{ void volume m}^{-3} \text{ bulk volume}$), S_w is the water saturation ($\text{m}^3 \text{ water m}^{-3} \text{ void volume}$) ($100\phi S_w = \theta$), D_0 is the self-diffusion coefficient of water ($2.299 \times 10^{-9} \text{ m}^2 \text{ s}^{-1}$) (Mills 1973 [DIRS 133392], Table III), and the fitting parameter is the exponent, n . To perform a least squares fit of the data, this equation is linearized in terms of n :

$$\log_{10} \left(\frac{\phi S_w D_I}{D_0} \right) = n \log_{10} \left(\frac{\theta}{100} \right). \quad (\text{Eq. G-2})$$

Column A, Rows 1 through 125, of the spreadsheet, shown on Figures G-1 through G-4, contains the moisture content values, θ (percent) (Conca and Wright 1992 [DIRS 100436]; Conca et al. 1993 [DIRS 170709]), that are listed in Table 4.1-16. The corresponding diffusion coefficient values ($\phi S_w D_I$) listed in Table 4.1-16 are in Column B, Rows 1 through 125 (where they are labeled D , which represents the effective diffusion coefficient, $\phi S_w D_I$, used in Section 6.3.4.1.1). In Column C, the quantity $\theta/100$ is computed (e.g., C3=A3/100], and $\phi S_w D_I / D_0$ is computed in Column D (e.g., D3=B3/0.00002299). The log term on the right-hand side of Equation G-2, containing the moisture content, is computed Column E (e.g., E3=LOG10(A3)-2). In Column F, the left-hand side of Equation G-2 is calculated (e.g., F3=LOG10(D3)).

The least squares fit of the data is done using the Microsoft Excel Trendline tool. In Figure G-5, the results in Column F are plotted on the y -axis against the corresponding values in Column E on the x -axis in the plot located between Rows 132 and 154 of the worksheet. The type of regression is linear. The Trendline features, “Set intercept = 0,” “Display equation on chart,” and “Display R-squared value on chart” are clicked on. In particular, the “Set intercept = 0” feature results in a fit to Equation G-2, in which the intercept is constrained to be zero.

As shown on the charts, the fitting parameter, n , has a value of 1.863. The correlation coefficient, R^2 , is 0.915, indicating a strong correlation between the diffusion coefficient and the volumetric moisture content. The equation resulting from the regression is:

$$\phi S_w D_I = D_0 \left(\frac{\theta}{100} \right)^{1.863}, \quad (\text{Eq. G-3})$$

In Column G, the error, or deviation of each data point from the fitted equation, is calculated (e.g., G3=F3-1.862899*E3); i.e., for data point i , the calculation in Column G is the deviation ε_i

$$\varepsilon_i = \log_{10}\left(\frac{\phi S_w D_i}{D_0}\right) - 1.863 \log_{10}\left(\frac{\theta}{100}\right). \quad (\text{Eq. G-4})$$

In Cell G128, the average of the 125 values of ε_i is computed: G128=AVERAGE(G3:G127). The standard deviation of the ε_i , Cell G129 is computed: G129=STDEV(G3:G127).

	A	B	C	D	E	F	G
1	Water Content, θ	Diffusion Coefficient, D					Error = [$\log_{10}(D/D_0)$
2	(%)	(cm^2/s)	$\theta/100$	D/D_0	$\log_{10}\theta - 2$	$\log_{10}(D/D_0)$	- 1.863 ($\log_{10}\theta - 2$)]
3	1.50	1.39E-08	0.0150	6.046E-04	-1.824	-3.219	0.1792
4	1.70	6.60E-09	0.0170	2.871E-04	-1.770	-3.542	-0.2455
5	1.90	8.60E-09	0.0190	3.741E-04	-1.721	-3.427	-0.2205
6	2.17	2.77E-08	0.0217	1.205E-03	-1.664	-2.919	0.1799
7	2.20	3.63E-08	0.0220	1.579E-03	-1.658	-2.802	0.2863
8	2.29	1.09E-08	0.0229	4.741E-04	-1.640	-3.324	-0.2687
9	2.50	2.50E-08	0.0250	1.087E-03	-1.602	-2.964	0.0209
10	3.10	3.30E-08	0.0310	1.435E-03	-1.509	-2.843	-0.0326
11	3.14	3.06E-08	0.0314	1.331E-03	-1.503	-2.876	-0.0757
12	3.20	1.35E-08	0.0320	5.872E-04	-1.495	-3.231	-0.4465
13	3.27	2.79E-08	0.0327	1.214E-03	-1.485	-2.916	-0.1487
14	3.33	6.35E-08	0.0333	2.762E-03	-1.478	-2.559	0.1938
15	3.34	2.60E-08	0.0334	1.131E-03	-1.476	-2.947	-0.1965
16	3.57	3.37E-08	0.0357	1.466E-03	-1.447	-2.834	-0.1377
17	3.70	3.70E-08	0.0370	1.609E-03	-1.432	-2.793	-0.1260
18	3.70	6.60E-08	0.0370	2.871E-03	-1.432	-2.542	0.1253
19	4.00	5.22E-08	0.0400	2.271E-03	-1.398	-2.644	-0.0396
20	4.20	5.94E-08	0.0420	2.584E-03	-1.377	-2.588	-0.0230
21	4.60	6.21E-08	0.0460	2.701E-03	-1.337	-2.568	-0.0773
22	4.90	7.20E-08	0.0490	3.132E-03	-1.310	-2.504	-0.0642
23	5.10	1.32E-07	0.0510	5.742E-03	-1.292	-2.241	0.1667
24	5.30	2.40E-08	0.0530	1.044E-03	-1.276	-2.981	-0.6048
25	5.40	7.60E-08	0.0540	3.306E-03	-1.268	-2.481	-0.1193
26	5.51	7.68E-08	0.0551	3.341E-03	-1.259	-2.476	-0.1311
27	5.83	1.23E-07	0.0583	5.350E-03	-1.234	-2.272	0.0278
28	5.90	9.30E-08	0.0590	4.045E-03	-1.229	-2.393	-0.1033
29	6.00	8.92E-08	0.0600	3.880E-03	-1.222	-2.411	-0.1350
30	6.30	1.06E-07	0.0630	4.611E-03	-1.201	-2.336	-0.0995
31	6.90	6.00E-08	0.0690	2.610E-03	-1.161	-2.583	-0.4203
32	6.93	1.50E-07	0.0693	6.525E-03	-1.159	-2.185	-0.0259

Source: Output DTN: SN0703PAEBSRTA.001, file *Invert Diffusion Coefficient.xls*, worksheet "Model."

Figure G-1. Invert Diffusion Coefficient Input Data (Water Content 1.50% to 6.93%)

	A	B	C	D	E	F	G
33	7.30	1.60E-07	0.0730	6.960E-03	-1.137	-2.157	-0.0399
34	7.40	2.50E-07	0.0740	1.087E-02	-1.131	-1.964	0.1429
35	7.60	2.60E-07	0.0760	1.131E-02	-1.119	-1.947	0.1384
36	7.60	1.10E-07	0.0760	4.785E-03	-1.119	-2.320	-0.2352
37	7.60	2.69E-07	0.0760	1.170E-02	-1.119	-1.932	0.1531
38	7.70	1.10E-07	0.0770	4.785E-03	-1.114	-2.320	-0.2458
39	8.00	1.98E-07	0.0800	8.612E-03	-1.097	-2.065	-0.0214
40	8.10	1.70E-07	0.0810	7.395E-03	-1.092	-2.131	-0.0977
41	8.32	4.10E-07	0.0832	1.783E-02	-1.080	-1.749	0.2629
42	8.35	2.15E-07	0.0835	9.352E-03	-1.078	-2.029	-0.0203
43	8.60	3.20E-07	0.0860	1.392E-02	-1.066	-1.856	0.1285
44	8.80	2.30E-07	0.0880	1.000E-02	-1.056	-2.000	-0.0335
45	9.24	2.55E-07	0.0924	1.109E-02	-1.034	-1.955	-0.0282
46	9.24	2.55E-07	0.0924	1.109E-02	-1.034	-1.955	-0.0282
47	9.56	3.00E-07	0.0956	1.305E-02	-1.020	-1.884	0.0149
48	9.64	3.07E-07	0.0964	1.335E-02	-1.016	-1.874	0.0182
49	9.75	3.20E-07	0.0975	1.392E-02	-1.011	-1.856	0.0270
50	10.10	3.51E-07	0.1010	1.527E-02	-0.996	-1.816	0.0386
51	10.10	3.62E-07	0.1010	1.575E-02	-0.996	-1.803	0.0520
52	10.20	3.54E-07	0.1020	1.540E-02	-0.991	-1.813	0.0343
53	10.20	3.30E-07	0.1020	1.435E-02	-0.991	-1.843	0.0039
54	10.30	3.34E-07	0.1030	1.453E-02	-0.987	-1.838	0.0012
55	10.30	2.10E-07	0.1030	9.134E-03	-0.987	-2.039	-0.2003
56	10.40	3.40E-07	0.1040	1.479E-02	-0.983	-1.830	0.0011
57	10.90	3.62E-07	0.1090	1.575E-02	-0.963	-1.803	-0.0097
58	11.10	3.72E-07	0.1110	1.618E-02	-0.955	-1.791	-0.0125
59	11.10	4.22E-07	0.1110	1.836E-02	-0.955	-1.736	0.0422
60	11.10	4.27E-07	0.1110	1.857E-02	-0.955	-1.731	0.0474
61	11.20	4.19E-07	0.1120	1.823E-02	-0.951	-1.739	0.0319
62	11.20	5.48E-07	0.1120	2.384E-02	-0.951	-1.623	0.1485
63	11.40	4.27E-07	0.1140	1.857E-02	-0.943	-1.731	0.0258
64	11.40	4.12E-07	0.1140	1.792E-02	-0.943	-1.747	0.0102
65	11.60	5.40E-07	0.1160	2.349E-02	-0.936	-1.629	0.1137

Source: Output DTN: SN0703PAEBSRTA.001, file *Invert Diffusion Coefficient.xls*, worksheet "Model."

Figure G-2. Invert Diffusion Coefficient Input Data (Water Content 7.30% to 11.60%)

	A	B	C	D	E	F	G
65	11.60	5.40E-07	0.1160	2.349E-02	-0.936	-1.629	0.1137
66	11.70	2.60E-07	0.1170	1.131E-02	-0.932	-1.947	-0.2107
67	11.80	4.80E-07	0.1180	2.088E-02	-0.928	-1.680	0.0487
68	12.00	2.40E-07	0.1200	1.044E-02	-0.921	-1.981	-0.2659
69	12.00	4.47E-07	0.1200	1.944E-02	-0.921	-1.711	0.0042
70	12.20	4.09E-07	0.1220	1.779E-02	-0.914	-1.750	-0.0478
71	12.30	5.05E-07	0.1230	2.197E-02	-0.910	-1.658	0.0372
72	12.30	4.40E-07	0.1230	1.914E-02	-0.910	-1.718	-0.0227
73	12.30	3.60E-07	0.1230	1.566E-02	-0.910	-1.805	-0.1098
74	12.30	4.50E-07	0.1230	1.957E-02	-0.910	-1.708	-0.0129
75	12.50	2.90E-07	0.1250	1.261E-02	-0.903	-1.899	-0.2168
76	12.70	4.37E-07	0.1270	1.901E-02	-0.896	-1.721	-0.0515
77	12.70	4.90E-07	0.1270	2.131E-02	-0.896	-1.671	-0.0018
78	12.70	5.32E-07	0.1270	2.314E-02	-0.896	-1.636	0.0339
79	13.10	4.77E-07	0.1310	2.075E-02	-0.883	-1.683	-0.0386
80	13.90	5.39E-07	0.1390	2.344E-02	-0.857	-1.630	-0.0335
81	13.90	7.80E-07	0.1390	3.393E-02	-0.857	-1.469	0.1270
82	14.10	5.12E-07	0.1410	2.227E-02	-0.851	-1.652	-0.0674
83	14.20	5.52E-07	0.1420	2.401E-02	-0.848	-1.620	-0.0404
84	14.40	4.50E-07	0.1440	1.957E-02	-0.842	-1.708	-0.1404
85	14.40	5.20E-07	0.1440	2.262E-02	-0.842	-1.646	-0.0776
86	14.40	4.50E-07	0.1440	1.957E-02	-0.842	-1.708	-0.1404
87	14.60	6.82E-07	0.1460	2.967E-02	-0.836	-1.528	0.0290
88	14.70	9.00E-07	0.1470	3.915E-02	-0.833	-1.407	0.1439
89	14.80	6.54E-07	0.1480	2.845E-02	-0.830	-1.546	-0.0002
90	16.00	1.47E-06	0.1600	6.394E-02	-0.796	-1.194	0.2884
91	16.10	6.82E-07	0.1610	2.967E-02	-0.793	-1.528	-0.0502
92	16.50	5.45E-07	0.1650	2.371E-02	-0.783	-1.625	-0.1674
93	16.70	6.60E-07	0.1670	2.871E-02	-0.777	-1.542	-0.0940
94	17.00	1.20E-06	0.1700	5.220E-02	-0.770	-1.282	0.1512
95	17.10	8.20E-07	0.1710	3.567E-02	-0.767	-1.448	-0.0189
96	17.30	1.76E-06	0.1730	7.656E-02	-0.762	-1.116	0.3034
97	17.50	1.10E-06	0.1750	4.785E-02	-0.757	-1.320	0.0900

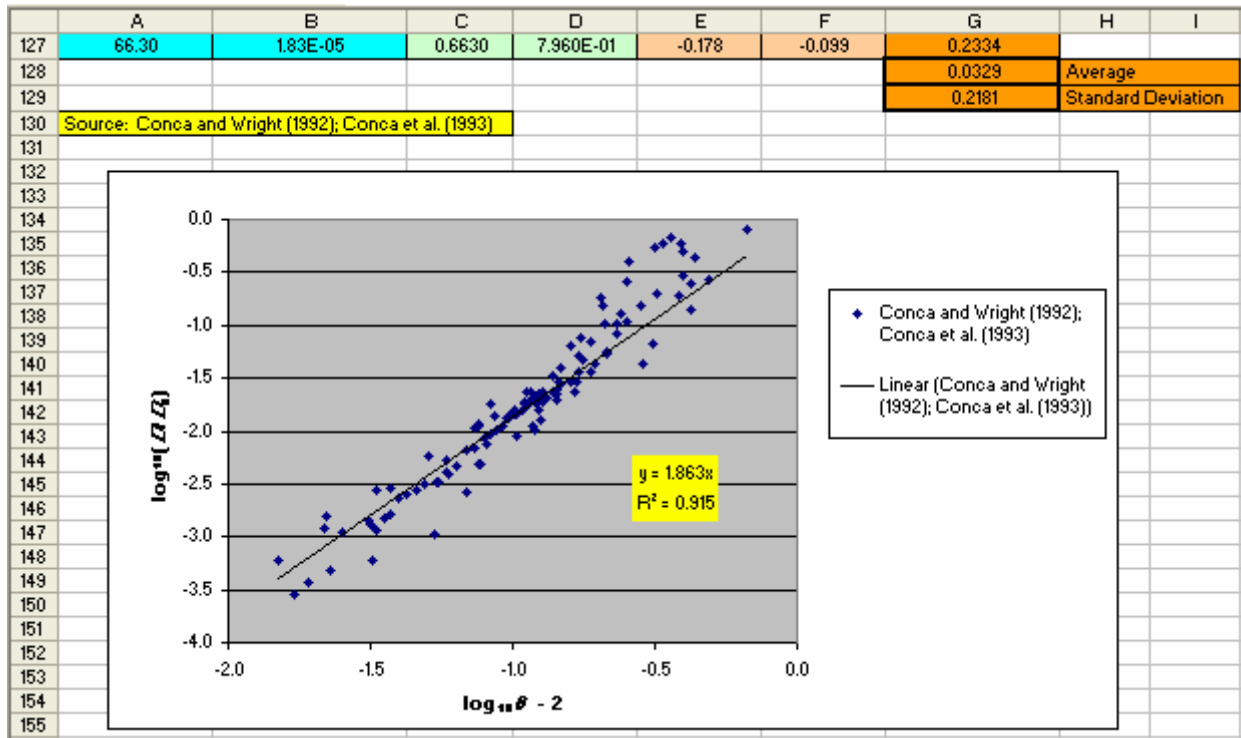
Source: Output DTN: SN0703PAEBSRTA.001, file *Invert Diffusion Coefficient.xls*, worksheet "Model."

Figure G-3. Invert Diffusion Coefficient Input Data (Water Content 11.60% to 17.50%)

	A	B	C	D	E	F	G	H	I
97	17.50	1.10E-06	0.1750	4.785E-02	-0.757	-1.320	0.0900		
98	18.80	1.60E-06	0.1880	6.960E-02	-0.726	-1.157	0.1948		
99	18.90	8.19E-07	0.1890	3.562E-02	-0.724	-1.448	-0.1004		
100	19.40	9.89E-07	0.1940	4.302E-02	-0.712	-1.366	-0.0396		
101	20.40	4.19E-06	0.2040	1.823E-01	-0.690	-0.739	0.5468		
102	20.80	3.58E-06	0.2080	1.557E-01	-0.682	-0.808	0.4627		
103	21.00	2.34E-06	0.2100	1.018E-01	-0.678	-0.992	0.2703		
104	21.50	1.23E-06	0.2150	5.350E-02	-0.668	-1.272	-0.0280		
105	21.60	1.29E-06	0.2160	5.611E-02	-0.666	-1.251	-0.0111		
106	23.10	2.40E-06	0.2310	1.044E-01	-0.636	-0.981	0.2042		
107	23.10	1.90E-06	0.2310	8.264E-02	-0.636	-1.083	0.1027		
108	24.00	2.90E-06	0.2400	1.261E-01	-0.620	-0.899	0.2555		
109	25.30	5.82E-06	0.2530	2.532E-01	-0.597	-0.597	0.5153		
110	25.40	2.50E-06	0.2540	1.087E-01	-0.595	-0.964	0.1451		
111	25.70	9.26E-06	0.2570	4.028E-01	-0.590	-0.395	0.7043		
112	28.20	3.50E-06	0.2820	1.522E-01	-0.550	-0.817	0.2067		
113	28.50	1.00E-06	0.2850	4.350E-02	-0.545	-1.362	-0.3460		
114	30.90	1.51E-06	0.3090	6.568E-02	-0.510	-1.183	-0.2324		
115	31.70	1.23E-05	0.3170	5.350E-01	-0.499	-0.272	0.6578		
116	32.30	4.60E-06	0.3230	2.001E-01	-0.491	-0.699	0.2155		
117	33.80	1.34E-05	0.3380	5.829E-01	-0.471	-0.234	0.6431		
118	35.80	1.57E-05	0.3580	6.829E-01	-0.446	-0.166	0.6654		
119	38.50	4.33E-06	0.3850	1.883E-01	-0.415	-0.725	0.0472		
120	39.30	1.36E-05	0.3930	5.916E-01	-0.406	-0.228	0.5276		
121	39.50	1.13E-05	0.3950	4.915E-01	-0.403	-0.308	0.4430		
122	40.00	6.90E-06	0.4000	3.001E-01	-0.398	-0.523	0.2186		
123	42.00	5.80E-06	0.4200	2.523E-01	-0.377	-0.598	0.1037		
124	42.50	3.22E-06	0.4250	1.401E-01	-0.372	-0.854	-0.1614		
125	43.40	1.02E-05	0.4340	4.437E-01	-0.363	-0.353	0.3224		
126	49.00	6.09E-06	0.4900	2.649E-01	-0.310	-0.577	0.0002		
127	66.30	1.83E-05	0.6630	7.960E-01	-0.178	-0.099	0.2334		
128							0.0329	Average	
129							0.2181	Standard Deviation	

Source: Output DTN: SN0703PAEBSRTA.001, file *Invert Diffusion Coefficient.xls*, worksheet "Model."

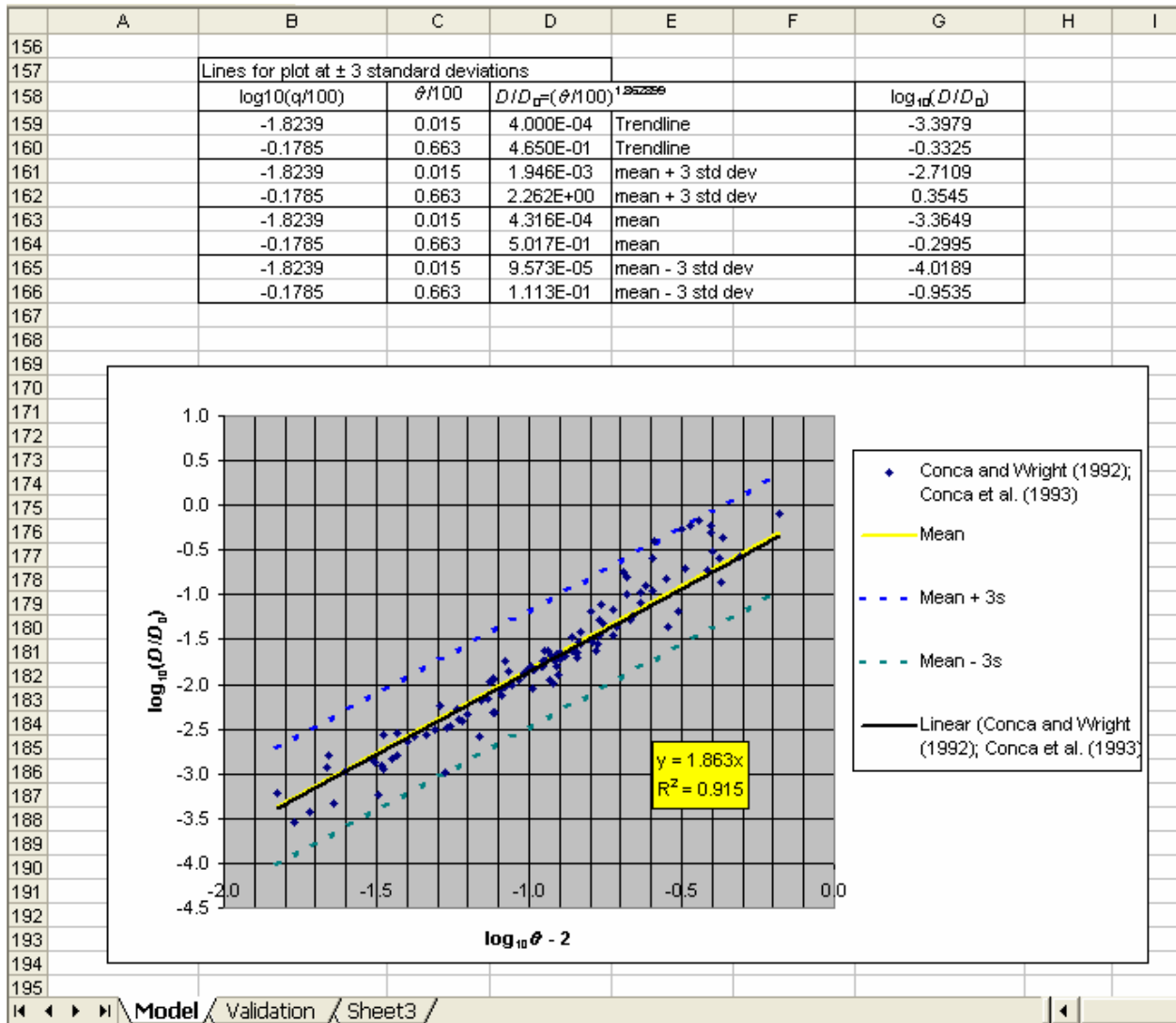
Figure G-4. Invert Diffusion Coefficient Input Data (Water Content 17.50% to 66.30%)



Source: Conca and Wright 1992 [DIRS 100436]; Conca et al. 1993 [DIRS 170709]. Output DTN: SN0703PAEBSRTA.001, file *Invert Diffusion Coefficient.xls*, worksheet "Model."

Figure G-5. Plot of Fitted Invert Diffusion Coefficient Data

In the plot in Figure G-6 between Rows 169 and 191, the lines for the mean and for the mean plus or minus three standard deviations are added to the plot shown earlier. The lines are drawn over the range of the data, i.e., for $\theta/100$ from 0.015 to 0.663 (Column C, Rows 159 to 166). The y -values for the Trendline fit are computed as $\phi S_w D_I / D_0 = (\theta/100)^{1.863}$ (e.g., D159=(C159^1.863)), and the values plotted are $\log_{10}(\phi S_w D_I / D_0)$ (e.g., G159=LOG10(D159)). For the mean curve, the y -values are computed as $\phi S_w D_I / D_0 = (\theta/100)^{1.863} 10^{0.033}$ (e.g., D163=(C163^1.863)*10^(0.033)), and the values plotted are again $\log_{10}(\phi S_w D_I / D_0)$ (e.g., G163=LOG10(D163)). For the mean plus three standard deviations curve, the y -values are computed as $\phi S_w D_I / D_0 = (\theta/100)^{1.863} 10^{0.033+3(0.218)}$ (e.g., G161=(C161^1.863)*10^(0.033+3*0.218)), and the values plotted are again $\log_{10}(\phi S_w D_I / D_0)$ (e.g., G161=LOG10(D161)). The mean minus three standard deviations curve is done similarly. This plot is shown as Figure 6.3-4 in Section 6.3.4.1.1.



Source: Conca and Wright 1992 [DIRS 100436]; Conca et al. 1993 [DIRS 170709]. Output DTN: SN0703PAEBSRTA.001, file *Invert Diffusion Coefficient.xls*, worksheet "Model."

Figure G-6. Plotted Results of Invert Diffusion Coefficient Data, Showing Uncertainty Range as Mean ±3 Standard Deviations

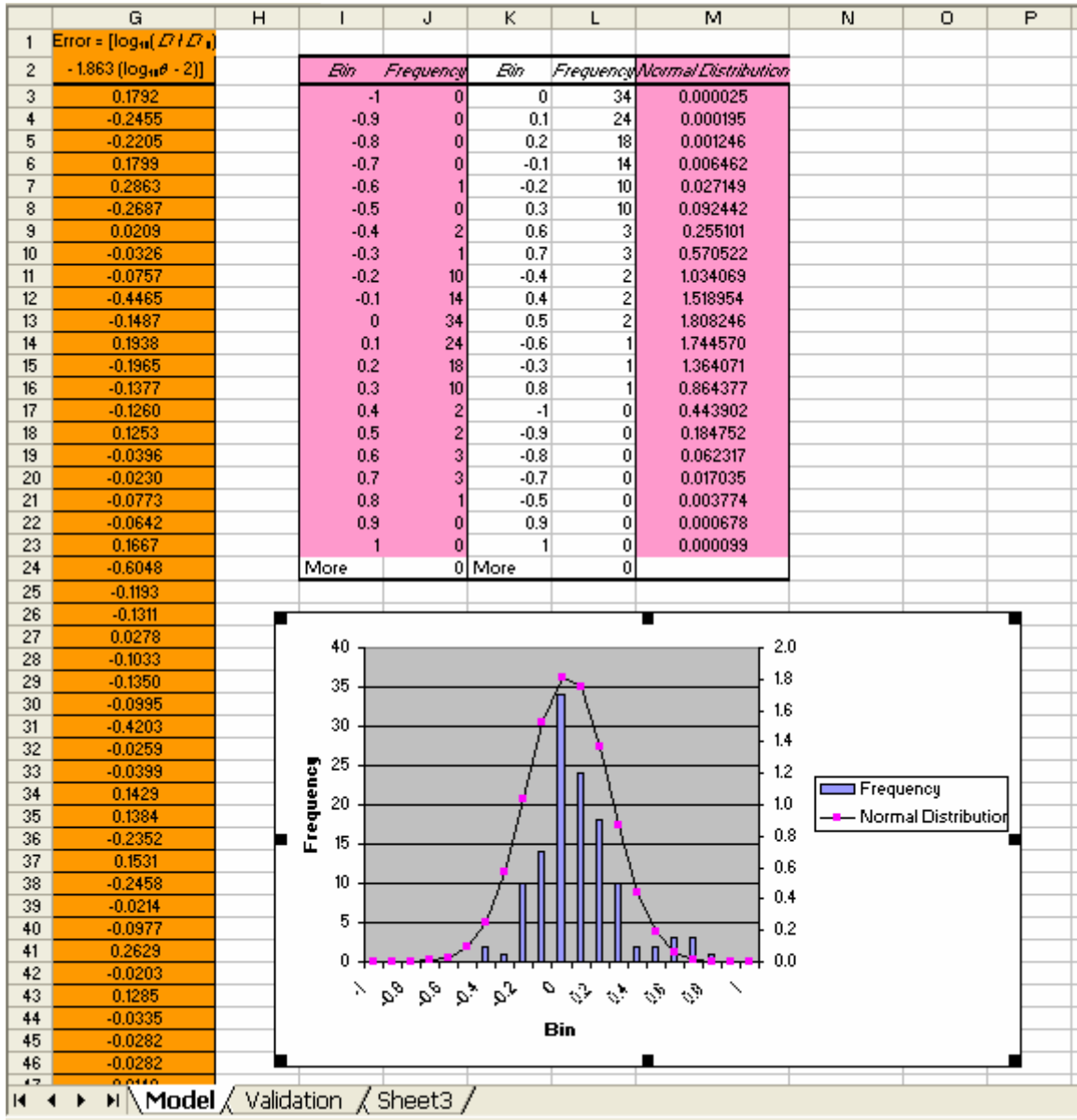
The data are further analyzed on Figure G-7 to demonstrate that the deviations approximately follow a normal distribution. Under the Microsoft Excel menu item Tools, Data Analysis... is clicked, and Histogram is selected under Analysis Tools. In the Histogram window, the error data (Column G, Rows 3 to 127) are entered for the Intput Range. For the Bin Range, Column I, Rows 3 to 22, is entered. The frequency distribution is output in Column J, Rows 3 to 22. For comparison, a theoretical normal distribution is computed over the same range in Column M:

$$f(x; \mu, \sigma) = \frac{1}{\sigma\sqrt{2\pi}} e^{-(x-\mu)^2 / 2\sigma^2}, \tag{Eq. G-5}$$

where x is the bin value, the mean $\mu \approx 0.033$, and the standard deviation $\sigma \approx 0.218$.

The Microsoft Excel formula is (for Cell M3, for example):

$$M3=EXP(-((I3-0.0329438386573088)^2)/(2*0.218121819319092^2))/(0.218121819319092*(2*PI())^0.5)$$

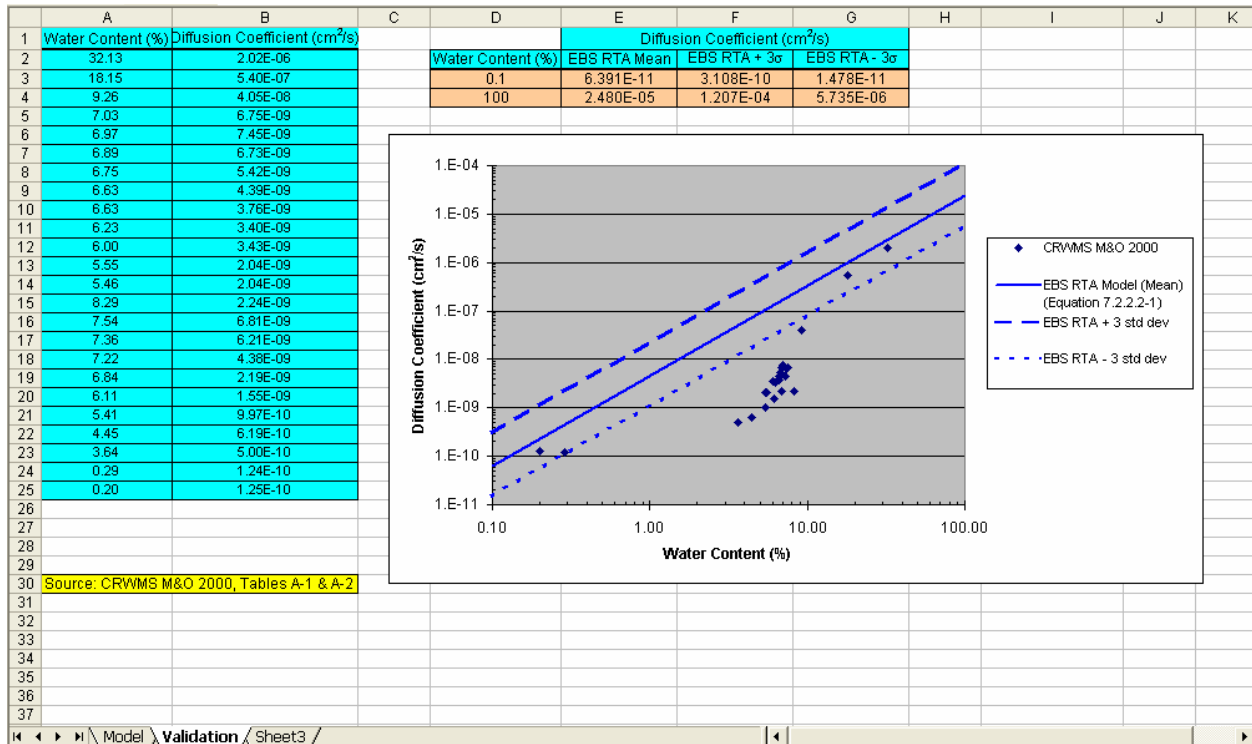


Source: Output DTN: SN0703PAEBSRTA.001, file *Invert Diffusion Coefficient.xls*, worksheet "Model."

Figure G-7. Further Analysis of Invert Diffusion Coefficient Data

SPREADSHEET “INVERT DIFFUSION COEFFICIENT” WORKSHEET “VALIDATION”

In this worksheet (Figure G-8), diffusion coefficient data (Column B) from Tables A-1 and A-2 of *The Determination of Diffusion Coefficient of Invert Materials* (CRWMS M&O 2000 [DIRS 156680]) are plotted against water content (Column A), along with the results of the analysis in Worksheet “Model.” The purpose of this worksheet is partially to validate the diffusion coefficient submodel by showing that the model overestimates the value of the invert diffusion coefficient, thereby overestimating diffusive releases of radionuclides through the invert. The model curve fit (Equation 6.3.4.1.1-22), also shown on p. G-7 and on Figure 6.3-4 in Section 6.3.4.1.1, is reproduced in Columns D-G, Rows 3 and 4, and plotted on Figure G-8.



Source: CRWMS M&O 2000 [DIRS 156680], Tables A-1 and A-2. Output DTN: SN0703PAEBSRTA.001, file *Invert Diffusion Coefficient.xls*, worksheet “Validation.”

Figure G-8. Validation of Invert Diffusion Coefficient Data

INTENTIONALLY LEFT BLANK

APPENDIX H

QUALIFICATION OF DIFFUSION COEFFICIENT DATA

QUALIFICATION OF DIFFUSION COEFFICIENT DATA

DESCRIPTION OF DATA TO BE QUALIFIED

The data reported in Conca and Wright (1992 [DIRS 100436]) and Conca et al. (1993 [DIRS 170709]) consist of measured diffusion coefficients of unsaturated soil, gravel, bentonite, rock, and crushed tuff from Yucca Mountain, over a broad range of water contents. These data have been collected and analyzed using standard scientific practices. The diffusivity data for various granular media at volumetric moisture contents ranging between 1.5% and 66.3% are given in Section 4.1.2, Table 4.1-16. These measured data have been used to analyze the dependence of the diffusion coefficient on volumetric moisture content for a variety of granular materials (Section 6.3.4.1.1). These data are qualified in accordance with the data qualification plan included in this appendix.

CORROBORATING DATA

The diffusion coefficient data for crushed tuff materials from *The Determination of Diffusion Coefficient of Invert Materials* (CRWMS M&O 2000 [DIRS 156680]) are used to qualify the data reported by Conca and Wright (1992 [DIRS 100436]) and Conca et al. (1993 [DIRS 170709]). The diffusion coefficient data found in *The Determination of Diffusion Coefficient of Invert Materials* (CRWMS M&O 2000 [DIRS 156680]) were collected in the DOE Atlas Facility. The tests were performed by the EBS Testing Department under YMP-approved procedures using the Unsaturated Flow Apparatus. The Unsaturated Flow Apparatus method is reported to be an accurate and fast indirect method of determining diffusion coefficients in porous media (Conca and Wright 1992 [DIRS 100436], p. 7). The method uses measurements of electrical conductivity, at specified volumetric moisture content, which is converted to diffusion coefficient. *The Determination of Diffusion Coefficient of Invert Materials* (CRWMS M&O 2000 [DIRS 156680]) reports that the error on the reported data is within $\pm 7\%$. The reported data are shown in Table H-1.

DATA EVALUATION CRITERIA

The diffusion coefficient data from Conca and Wright (1992 [DIRS 100436]) and Conca et al. (1993 [DIRS 170709]) will be considered qualified if they are within one order of magnitude of the values reported in *The Determination of Diffusion Coefficient of Invert Materials* (CRWMS M&O 2000 [DIRS 156680]); or if greater differences are observed, they result in more conservative results with regard to radionuclide releases.

COMPARISON OF THE DIFFUSION COEFFICIENT DATA IN CONCA AND WRIGHT (1992 [DIRS 100436]) AND CONCA ET AL. (1993 [DIRS 170709]) TO CRWMS M&O (2000 [DIRS 156680])

The data reported by Conca and Wright (1992 [DIRS 100436]) and Conca et al. (1993 [DIRS 170709]) (shown in Section 4.1.2, Table 4.1-16) consist of diffusion coefficient data for the range of 1.5% to 66.3% volumetric moisture content. The data from *The Determination of Diffusion Coefficient of Invert Materials* (CRWMS M&O 2000 [DIRS 156680]) ranges between 0.2% and 32.13%. Figure H-1 shows a plot of moisture content versus diffusion coefficient for data from both sources. The figure shows that overall the Conca and Wright

(1992 [DIRS 100436]) and Conca et al. (1993 [DIRS 170709]) data have higher diffusion coefficient values over the measured range of water content. The differences are highest at low water content. At water content values below 10%, the Conca and Wright (1992 [DIRS 100436]) and Conca et al. (1993 [DIRS 170709]) diffusion coefficient values are higher by as much as two orders of magnitude. For water content values above 10%, the Conca and Wright (1992 [DIRS 100436]) and Conca et al. (1993 [DIRS 170709]) diffusion coefficient data show higher but comparable values.

The differences in diffusion coefficient at low water content values can be partly attributed to the measurement technique. As discussed in Section 6 of *The Determination of Diffusion Coefficient of Invert Materials* (CRWMS M&O 2000 [DIRS 156680]), errors in measurement are higher at low diffusion coefficient values. Conca and Wright (1992 [DIRS 100436], p. 10) also reported that, at low water content, reductions in water content result in sharp declines in the measured diffusion coefficient as surface films become thin and discontinuous, and pendular water elements become small. Measurement differences could also be attributed to the different porous medium samples used. The Conca and Wright (1992 [DIRS 100436]) and Conca et al. (1993 [DIRS 170709]) data include various material samples whereas the determination report (CRWMS M&O 2000 [DIRS 156680]) data are for crushed tuff only. The data from both sources show some scatter. The diffusion coefficient data of Conca and Wright (1992 [DIRS 100436]) and Conca et al. (1993 [DIRS 170709]) are thus comparable to those of the determination report (CRWMS M&O 2000 [DIRS 156680]) for volumetric water content values above 10%. For low volumetric water content values, the differences are greater. However, the higher diffusion coefficient values of Conca and Wright (1992 [DIRS 100436]) and Conca et al. (1993 [DIRS 170709]) will result in predicted radionuclide releases being higher.

The Conca and Wright (1992 [DIRS 100436]) data have been published in a peer-reviewed journal (*Applied Hydrogeology*), and thus have undergone strict review. The data are shown plotted on Figure 2 of Conca and Wright (1992 [DIRS 100436]).

The Conca et al. (1993 [DIRS 170709]) data have been published in the proceedings of the *Scientific Basis for Nuclear Waste Management XVI Symposium* held November 30 to December 4, 1992. This symposium was organized by the Materials Research Society, which was formed in 1973. The most recent *Scientific Basis for Nuclear Waste Management XVI Symposium* is XXVII, the proceedings of which were published in 2004. Papers published in the proceedings undergo peer review prior to publication and must be presented at the meeting in order to be published.

SUMMARY OF QUALIFICATION

The diffusion coefficient data of Conca and Wright (1992 [DIRS 100436]) and Conca et al. (1993 [DIRS 170709]) have been evaluated in the context of their use in radionuclide transport modeling, and are considered qualified for use within this report per LP-SIII.2Q-BSC, *Qualification of Unqualified Data*, Attachment 3, on the basis of:

- Availability of corroborating data—The corroborating data are YMP-generated data using the same measurement technique.

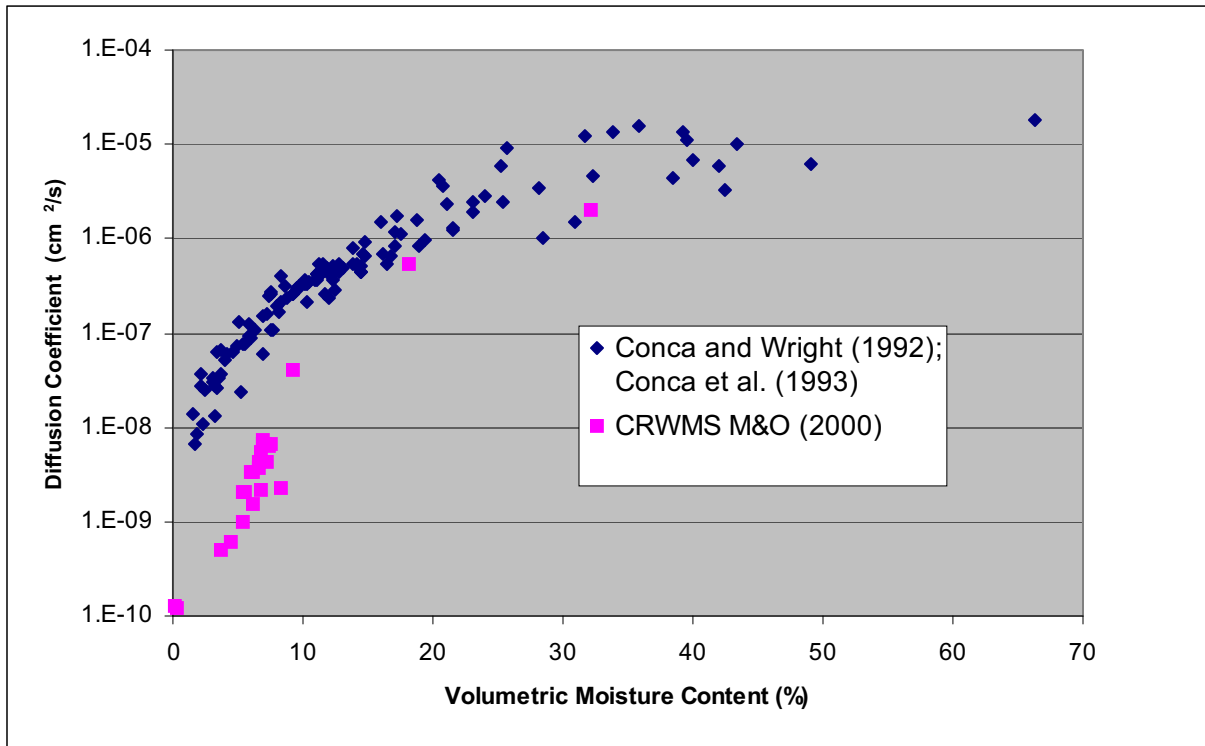
- Reliability of data sources—The data are published in a peer-reviewed journal and in a peer-reviewed symposium proceedings.
- Data demonstrate properties of interest—The published data, diffusion coefficients in crushed rock, are the data required for the model of transport in the invert.

The above comparison of the diffusion coefficient data by Conca and Wright (1992 [DIRS 100436]) and Conca et al. (1993 [DIRS 170709]), with the corroborating data from CRWMS M&O 2000 [DIRS 156680], shows that the data evaluation criteria have been met. The data to be qualified are within one order of magnitude of the values in the corroborating source for volumetric water content values above 10% (Figure H-1). The differences between the two data sets are greater than one order of magnitude below 10%; however, the higher diffusion coefficient values of Conca and Wright (1992 [DIRS 100436]) and Conca et al. (1993 [DIRS 170709]) will result in predicted radionuclide releases being higher. Therefore, the Conca and Wright (1992 [DIRS 100436]) and Conca et al. (1993 [DIRS 170709]) diffusion coefficient data shown in Table 4.1-16 are judged to be qualified for use in this report. Use of these data in other applications would require a comparable evaluation for that specific use.

Table H-1. Diffusion Coefficient of Crushed Tuff Invert Materials

Sample	Volumetric Moisture Content (%)	Diffusion Coefficient ($\text{cm}^2 \text{s}^{-1}$)
1	32.13	2.02×10^{-6}
2	18.15	5.40×10^{-7}
3	9.26	4.05×10^{-8}
4	7.03	6.75×10^{-9}
5	6.97	7.45×10^{-9}
6	6.89	6.73×10^{-9}
7	6.75	5.42×10^{-9}
8	6.63	4.39×10^{-9}
9	6.63	3.76×10^{-9}
10	6.23	3.40×10^{-9}
11	6.00	3.43×10^{-9}
12	5.55	2.04×10^{-9}
13	5.46	2.04×10^{-9}
14	8.29	2.24×10^{-9}
15	7.54	6.81×10^{-9}
16	7.36	6.21×10^{-9}
17	7.22	4.38×10^{-9}
18	6.84	2.19×10^{-9}
19	6.11	1.55×10^{-9}
20	5.41	9.97×10^{-10}
21	4.45	6.19×10^{-10}
22	3.64	5.00×10^{-10}
23	0.29	1.24×10^{-10}
24	0.20	1.25×10^{-10}

Source: CRWMS M&O 2000 [DIRS 156680].



Source: Conca and Wright 1992 [DIRS 100436]; Conca et al. 1993 [DIRS 170709]; CRWMS M&O 2000 [DIRS 156680].

Figure H-1. Comparison of Diffusion Coefficients

DATA QUALIFICATION PLAN

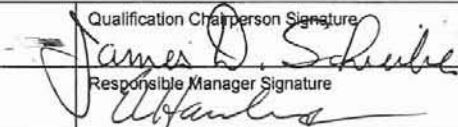
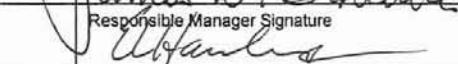
A facsimile of the data qualification plan developed for the above qualification effort is provided on Figure H-2. The original is included in the records package for this model report.

BSC

Data Qualification Plan

QA: QA
Page 1 of 1

Complete only applicable items.

Section I. Organizational Information		
Qualification Title QUALIFICATION OF DIFFUSION COEFFICIENT DATA		
Requesting Organization Near-Field Environment and Transport		
Section II. Process Planning Requirements		
1. List of Unqualified Data to be Evaluated Diffusion coefficient data reported in Conca and Wright (1992 [DIRS 100436]) and Conca et al. (1993 [DIRS 170709]). These data are shown on Table 4.1-17 of this report.		
2. Type of Data Qualification Method(s) [Including rationale for selection of method(s) (Attachment 3) and qualification attributes (Attachment 4)] Qualification method, from Attachment 3 of LP-SIII.2Q-BSC, REV 0 ICN 0: Corroborating Data. The diffusion coefficient data for crushed tuff materials from the Determination of Diffusion Coefficient of Invert Materials (CRWMS M&O 2000 [DIRS 156680]) are used to qualify the data reported by Conca and Wright (1992 [DIRS 100436]) and Conca et al. (1993 [DIRS 170709]). Attributes used from Attachment 4: (3) The extent to which the data demonstrate the properties of interest, (8) Prior peer or other professional review of the data and their results; and (10) Extent and quality of corroborating data.		
3. Data Qualification Team and Additional Support Staff Required Chairperson: James Schreiber, Sandia National Laboratories Technically competent individual: Teklu Hadgu, Sandia National Laboratories		
4. Data Evaluation Criteria The diffusion coefficient data from Conca and Wright (1992 [DIRS 100436]) and Conca et al. (1993 [DIRS 170709]) will be considered qualified if they are within one order of magnitude of the values reported in CRWMS M&O 2000 [DIRS 156680]; or if greater differences are observed, they result in more conservative results with regard to radionuclide releases.		
5. Identification of Procedures Used LP-SIII.2Q-BSC, Qualification of Unqualified Data LP-SIII.10Q-BSC, Models		
Section III. Approval		
Qualification Chairperson Printed Name James Schreiber	Qualification Chairperson Signature 	Date 8/24/05
Responsible Manager Printed Name Ernest Hardin	Responsible Manager Signature 	Date 8/24/05

LP-SIII.2Q-BSC

FORM NO. LSIII2-1 (Rev. 01/19/2005)

Figure H-2. Data Qualification Plan

INTENTIONALLY LEFT BLANK

APPENDIX I
EBS-UZ VALIDATION TOUGH2 CALCULATIONS – SETUP, EXECUTION, AND
POST-PROCESSING OF OUTPUT

EBS-UZ VALIDATION TOUGH2 CALCULATIONS – SETUP, EXECUTION, AND POST-PROCESSING OF OUTPUT

This appendix describes the grid development and calculations performed for validation of the EBS-UZ interface model presented in Section 7.3.1.

I.1. DEVELOPMENT OF THE GRID

This is a two-dimensional symmetry model in which one-half of the cross section of the drift and the surrounding rock are represented (see Figure 7.3-1). The vertical direction is designated by the coordinate “z”, and is positive upward, with zero at the top of the domain. Hence all values of “z” within the domain are negative. The horizontal direction is designated by the coordinate “x”, starting at 0 at the left-hand boundary and increasing to the right. The two-dimensional domain lies entirely within the tsw35 model unit and goes from 17.5 m above the drift center to 47.5 m below the center of the drift, for a total vertical dimension of 65 m. The domain width is 40.5 m, which is half the distance between centers of waste emplacement drifts (SNL 2007 [DIRS 179466], Table 4-1, Parameter No. 01-04). The calculation uses a two-dimensional grid with a pseudo-3D representation in the y-direction of the fracture and matrix continua. This requires specifying the cell thicknesses such that the area per unit volume for the tsw35 unit, $9.68 \text{ m}^2 \text{ m}^{-3}$ (BSC 2004 [DIRS 170038], Table 6-5) is achieved (i.e., this sets the y-dimension of the fracture and matrix continua to $(9.68 \text{ m}^2 \text{ m}^{-3})$, or 0.1033060 m).

Finer gridding (0.2 m) is used around the location of the drift. This finer-grid zone extends to 4 m from the left-hand boundary and 8 m across the drift vertically such that there is a minimum of 1.25 m of finer gridding around the entire boundary of a 2.75-m-diameter drift centered at the left-hand boundary and a vertical position of -17.5 m. The grid coarsens moving away from the drift, with maximum grid sizes of 2 m at the far right-hand and bottom boundaries.

The grid is produced using the command on the DEC alpha workstation “beagle”,

```
/usr/users/ysw/tough2_v16.dir/eos9_v16.dir/t2eos9v16.exe_medium
```

with the input file, /usr/users/house/DM/FINAL/mesh, given as follows.

```
TOUGH2 input file for generating 3D mesh
MESHMAKER -----*-----2-----*-----3-----*-----4-----*-----5-----*-----6-----*-----7-----*-----8
XYZ
NX      20 0.2000000
NX      13 0.5000000
NX      10 1.0000000
NX      10 2.0000000
NY       2 0.1033060
NZ       1 1.000E-10
NZ      10 1.0000000
NZ       7 0.5000000
NZ      40 0.2000000
NZ       7 0.5000000
NZ      10 1.0000000
NZ      15 2.0000000
NZ       1 1.000E-10

ENDFI ---1-----*-----2-----*-----3-----*-----4-----*-----5-----*-----6-----*-----7-----*-----8
```

The file “MESH” is created containing the basic numerical grid. This file is renamed for subsequent processing to “mesh.mes”. This file is first modified using AddBound V1.0 to generate a single boundary cell at the top of the model, denoted TOP 1, which replaces the thin (1.000E-10 m) elements in the basic grid.

This is performed using the following command on the workstation “hydra,”

```
hydra.lbl.gov 239> xAddBound

Add Boundary Element
*****

Input MESH file           : ?
mesh.mes
Output MESH file         : ?
mesht.mes
Boundary element name (AAAI) : ?
TOP 1
Boundary rock type name (A5) : ?
MSRCE
Boundary element volume   : ?
40.
Nodal distance to boundary element : ?
1.E-10
Xmin                       : ?
-1.
Xmax                       : ?
41.
Ymin                       : ?
-1.
Ymax                       : ?
1.
Zmin                       : ?
-0.25
Zmax                       : ?
0.25
```

Similarly, a single cell, denoted BOT 1, for the bottom boundary replaces the narrow elements at the bottom of the model. This was created using the following command,

```
hydra.lbl.gov 244> xAddBound

Add Boundary Element
*****

Input MESH file           : ?
mesht.mes
Output MESH file         : ?
meshtb.mes
Boundary element name (AAAI) : ?
BOT 1
Boundary rock type name (A5) : ?
MSINK
Boundary element volume   : ?
40.
Nodal distance to boundary element : ?
1.E-10
Xmin                       : ?
-1.
Xmax                       : ?
41.
Ymin                       : ?
-1.
```


Ymax	:	?
1.		
Zmin	:	?
-65.5		
Zmax	:	?
-64.5		

The file “meshtb.mes” was edited using Microsoft Word on a PC to add boundary cells “TOP 2” and “BOT 2”. These are needed to provide source and sink cells for the fracture continuum using TOP 1 and BOT 1 for the matrix continuum. Therefore, the cells TOP 1 and BOT 1 connected to cells with a “2” in the third character (the designation for fracture cells) were changed to TOP 2 and BOT 2. The BOT 1 and BOT 2 cells were expanded to a volume of 10^{50} m³ such that water and tracer entering these cells would represent a constant reservoir for water content and tracer concentration. The edited file was named “meshtbe.mes”.

The CONNE records for the fracture-matrix connections were edited so that the direction designation of “2” in column 30 were changed to -10 (columns 28 through 30). This invokes the active fracture formulation for fracture-matrix interaction. The connection distances between the fracture node and the interface between nodes was set to zero for columns 41 through 50 of the same records now having -10 in columns 28 through 30. The connection distance between the matrix node and the interface between nodes is set in columns 31 through 40. This distance is assigned the fracture spacing divided by 8, as given in the Warren and Root solution (Warren and Root 1963 [DIRS 100611]; Pruess 1983 [DIRS 100605], Table 1). The fracture spacing in the tsw35 is equal to the inverse of the fracture frequency, 3.16 m^{-1} , or 0.316 m. The distance of the matrix node to the interface between nodes is then $0.316/8$, or 0.0396 m.

The mesh file was then copied into Microsoft Excel to identify the nodes inside the drift, invert, the zone below the invert in the rock, and the connections between the invert and the rock.

The ELEME records were edited in the file “ELEME grid processing.xls” to distinguish several rock types. Two types to be distinguished are the fracture and matrix rock types. Cells with a “1” in the third character of the element name are designated as matrix by putting a “1” in column 20 of the element record. Cells with a “2” in the third character of the element name are designated as fracture by putting a “2” in column 20 of the element record. The elements are further distinguished between inside the drift in the air gap and inside the drift in the invert. The drift diameter is 5.5 m (SNL 2007 [DIRS 179466], Table 4-1, Parameter No. 01-04). The elements inside the drift are identified as nodes within 2.75 m of the point (0-17.5), which is the center of the drift. All nodes within the drift are in the air gap if z is greater than -19.6 m. The nodes within the drift with z less than or equal to -19.6 m are in the invert. The maximum invert depth used in this calculation is 0.8636 m (BSC 2004, [DIRS 166369]). The current invert design calls for a maximum depth of 1.32 m (4 ft 4 in.), as specified in *Total System Performance Assessment Data Input Package for Requirements Analysis for Engineered Barrier System In-Drift Configuration* (SNL 2007 [DIRS 179354], Table 4-1, Parameter No. 01-13A). The use of the outdated value for invert depth is suitable for this calculation, since the objective is simply to compare the results with those of the EBS-UZ interface model using the same input parameters. Given the 0.2 m vertical grid dimension, the closest approximation that can be made in the model is a maximum invert thickness of 0.8 m. For each zone, the nodes are further distinguished between fracture and matrix. The top of the invert are source zone nodes, and thus these are further distinguished.

Finally, nodes in the rock beneath the invert between vertical coordinates of -19.6 m and -23 m, and between horizontal coordinates of 0 and 1.9 m are given special designations because of the reduced flow and saturation in this region, known as the drift shadow.

The following gives the rock types assigned to each of these regions, which is given in column 20 of each of the element records:

1. rock matrix outside of drift shadow
2. rock fractures outside of drift shadow
3. air gap connected to rock matrix
4. air gap connected to rock fracture
5. intragranular invert (below top of invert cells)
6. intergranular invert (below top of invert cells)
7. intragranular invert top cells
8. intergranular invert top cells
9. rock matrix in drift shadow
10. rock fractures in drift shadow.

The CONNE records were edited in the file “CONNE grid processing.xls” to add global connections between the invert and the rock. These connections are added because the relationship of connections between the invert and the rock are not organized into a one-to-one relationship between intergranular pore space and rock fractures and between intragranular pore space and rock matrix. Therefore, intragranular and intergranular pore spaces are connected to both rock matrix and rock fractures. The connections to the rock fractures are treated as active fracture connections to limit the strength of these connections because connections between fracture water and invert material is expected to be limited at least as much as between fracture water and rock matrix. The edited ELEME and CONNE records were then combined into the text file “meshtberg.mes”.

Figures 7.3-1a and 7.3-1b in Section 7.3.1 provide a representation of the grid structure and were produced using Tecplot V7.0. The ELEME records from the file “meshtberg.mes” were copied and pasted into Microsoft Excel 2000 as text in the file “Grid plot.xls”. The text records were then converted into column data using the command “Text to Columns”. The last three columns of each ELEME record are the *x*-, *y*-, and *z*-coordinates (in meters) of the cell. The conditional statement “=IF(MID(A3,3,1)、“1”,1,2)” was put into cell “G2” and returns a value of 1 for matrix/intragranular media (where the third character of the element name is 1) or a value of 2 for fracture/intergranular media (where the third character of the element name is 2). This was then copied down to cell “G9435” to evaluate each row. The columns “A” through “G” are copied and pasted (as values) into columns “I” through “O” and then sorted in ascending order using the “Sort” command on column “Y”, then by column “N” in descending order. This splits the matrix/intragranular rows from the fracture/intergranular rows. The matrix/intragranular component was copied into a separate worksheet called “Matrix” and the fracture/intergranular component was copied into a separate worksheet called “Fracture” in the file “Grid plot.xls”. The horizontal (*X*) and vertical (*Z*) coordinates and rock type (types 1, 3, 5, 7, and 9 for the “Matrix” worksheet and 2, 4, 6, 8, and 10 for the “Fracture” worksheet) were copied into sets of three columns for each rock type and then copied into text files rt1.txt through rt10.txt. The files were read into Tecplot using the “Load DataFile(s)” command to generate the 2D scatter plots. The

output files from these contour plots are “matrix plot.lay” and “matrix plot.plt” for the matrix grids and “fracture plot.lay” and “fracture plot.plt” for the fracture grids. The files with the extension “lay” are text files containing the plot layout information and the file name containing the plot data. The file with the extension “plt” is a binary format file with the plot data.

I.2. WATER AND TRACER INJECTION RATES

Flow rates were taken from percolation flux rates in the tsw35. Computed fluxes are given in LB03023DSSCP9I.001 (2003 [DIRS 163044]). Representative fracture and matrix fluxes were taken from cell pairs F014Dh48 to F014Eh48 and M014Dh48 to M014Eh48. The following information is available in the file “glaq_mA.out”:

Table I.2-1. Hydrologic Conditions at F014Dh48 and M014Dh48

ELEM.	INDEX	PRES (Pa)	S(liq)	PCAP (Pa)	K(rel)	DIFFUS. (m ² s ⁻¹)	DL (kg m ⁻³)
F014Dh48	102743	5.8410E+04	1.6874E-02	-3.3590E+04	9.4051E-06	8.1238E-08	9.9716E+02
M014Dh48	102744	-2.8645E+04	8.4850E-01	-1.2065E+05	1.1010E-02	4.3616E-10	9.9716E+02

Table I.2-2. Flux Between Neighboring Vertical Elements

ELEM1	ELEM2	INDEX	FLO(LIQ.) (kg s ⁻¹)
F014Eh48	F014Dh48	102859	8.2142E-03
M014Eh48	M014Dh48	102860	7.0287E-06

The connection area is also needed to compute the flux, which is given in the file “mesh_2kb.dkm”,

Table I.2-3. Connection Areas for Vertical Connections

ELEME1	ELEME2	ISOT	DISTANCE1 (m)	DISTANCE2 (m)	AREA (m ²)
F014Eh48	F014Dh48	3	2.500E+00	2.500E+00	1.312E+04
M014Eh48	M014Dh48	3	2.500E+00	2.500E+00	1.312E+04

From this information, the percolation flux in the fractures is computed to be 19.814 mm yr⁻¹ and in the matrix, 0.016955 mm yr⁻¹. The TOUGH2 V1.6 (2003 [DIRS 161491]) input file requires the flux to be given in kg s⁻¹ for each of the top boundary cells, one connected to the fracture continuum and one connected to the matrix continuum. The area of each top cell is 40.5 m × 0.103306 m = 4.183893 m². The density of water used in the calculation is 999.213 kg m⁻³. Therefore, the mass flux into “TOP 1” connected to the rock matrix is 2.2460e-9 kg s⁻¹ and the mass flux into “TOP 2” connected to the fractures is 2.6250e-6 kg s⁻¹. These are the values shown in the “GENER” records for the flow input.

The solute is injected into the nine cells along the top of the invert, BE1 1 through BE1 9, that represent the intragranular porosity. Each cell receives a fixed solute mass injection rate of $1.0 \times 10^{-13} \text{ kg s}^{-1}$.

I.3. CONDUCT OF THE FLOW AND TRANSPORT CALCULATIONS

The input file for the flow calculation was prepared according to the discussion given in Attachment B of LBNL (2002, [DIRS 170765]). The input file along with the grid file renamed “MESH” were put into the directory on the DEC alpha computer “beagle” at Lawrence Berkeley National Laboratory. The flow field was computed with the software TOUGH2 V1.6 (2003 [DIRS 161491]) using the following command:

```
/usr/users/ysw/tough2_v16.dir/eos9_v16.dir/t2eos9v16.exe_medium
```

The input and output files were in the directory /usr/users/house/DM/FINAL. The input file name was “flow” and the output file name was “flow.out”.

To perform a transport calculation, a second flow calculation was performed to generate the “flow9.dat” file used by the transport software T2R3D V1.4 (1999, [DIRS 146654]). The “flow9.dat” file is generated by setting a switch from “0” to “1” in the 33rd column of the first record under “PARAM” in the input file. To reduce the volume of output for the “flow9.dat” file, the specified output times was reduced to just one time at the end of the simulation period, skipping the intermediate output times generated in the “flow.out” file. The modified input file was named “flow9” and the output file was named “flow9.dat”. The computation of the “flow9.dat” output file was performed using the same program execution command given above.

Once the “flow9.dat” file was generated, a transport calculation could be performed. The input file for the transport calculation uses many of the same records as in the flow input file. The additional records needed in the transport input file are described in Section 5.3 of Wu et al. (1996, [DIRS 100649]). The transport input file was named “trans2” and the output file was named “trans2.out”.

The transport calculation was performed with the software T2R3D V1.4 (1999, [DIRS 146654]) on the DEC alpha computer “beagle” using the following command:

```
/usr/users/ysw/t2r3dv14.dir/t2r3d_dc.exe
```

I.4. POST-PROCESSING OF THE FLOW AND TRANSPORT OUTPUT

Post-Processing the Flow Output

The flow output in the file “flow.out” was post-processed to produce Figures 7.3-2 through 7.3-5, shown in Section 7.3.1.6, as well as to determine average saturation and average effective permeabilities used to evaluate diffusion coefficients, as discussed in Section 7.3.1.3.

Average Saturations and Relative Permeabilities for Computing Diffusion Coefficients

The final output of the flow calculation recorded in the file “flow.out” follows the declaration “THE TIME IS 0.36525E+13 DAYS “, which corresponds to 10 billion years. The recorded cell hydrologic conditions follow with records that begin with an element name (e.g., A21 1). These were copied from “flow.out” and pasted as text into the file “analysis of diffusion.xls”. The records were recorded as a single text cell per line and are then sorted using the “Sort” command in Excel to separate the intermediate header information present in the copied text. This header information was deleted, except for the first header. Then the text records were converted to columns using the “Text to Columns” Excel command. The ELEM records from “meshtberg.xls” were copied and pasted into cells to the right of the flow output and are similarly converted to column data. The 9,438 element names from the flow output in column “A” are in the same order as the element names in the ELEM records. The rock type and cell volumes from columns “K” and “L” were copied into columns “R” and “S”. Liquid saturations and relative permeabilities from columns “D” and “F” were copied into columns “T” and “U” and the z (vertical) coordinates from column “O” were copied into column “V”. Then columns “R” through “V” were sorted using the Excel “Sort” command in ascending order based on column “R”. The various rock types were used to separate the drift shadow region from the other rock region and the invert. Volume-weighted averages for saturation and relative permeability were computed for rock type 9 (matrix in drift shadow) and rock type 10 (fractures in drift shadow), as shown in the file “analysis of diffusion.xls”. Volume-weighted averages for rock matrix and fractures outside the drift shadow, rock types 1 and 2, respectively, were restricted to elevations below the top of the invert, which is at -19.6 m. For the invert, volume-weighted average saturations were computed for the intragranular porosity, rock types 5 and 7, and for the intergranular porosity, rock types 6 and 8.

Saturation Information for Contour Plots

The same process as described above for the analysis of diffusion was used to put the flow output hydrologic conditions by cell with the grid element information into the Excel spreadsheet “saturations.xls”. The conditional statement “=IF(MID(A3,3,1)、“1”,1,2)” was put into cell “I3” and returns a value of 1 for matrix/intragranular media (where the third character of the element name is 1) or a value of 2 for fracture/intergranular media (where the third character of the element name is 2). This was then copied down to cell “I9436” to evaluate each row. The columns “A” through “O” are copied and pasted (as values) into columns “Q” through “AF” and then sorted in ascending order using the “Sort” command on column “Y”. This splits the matrix/intragranular rows from the fracture/intergranular rows. The matrix/intragranular component was copied into a separate worksheet called “Matrix” and the fracture/intergranular component was copied into a separate worksheet called “Fractures” in the file “saturations.xls”. In each of these worksheets, the horizontal coordinate (X) from column “N” was copied into column “R” and the vertical coordinate (Z) from column “P” was copied into column “S” and the liquid saturation from column from column “D” was copied into column “T”. Then columns “R” through “T” were sorted using the “Sort” command first on “S” in descending order and then by column “R” in ascending order. These three columns were then copied into text files “matrixsat.txt” and “fracturesat.txt” to be read into Tecplot V7.0. The two rows of header information at the top of each of these text files are needed by Tecplot to generate contour plots. The files were read into Tecplot using the “Load DataFile(s)” command to generate the 2D

contour plots. The output files from these contour plots are “matrixsat.lay” and “matrixsat.plt” for the matrix saturations and “fracturesat.lay” and “fracturesat.plt” for the fracture saturations. The files with the extension “lay” are text files containing the plot layout information and the file name containing the plot data. The file with the extension “plt” is a binary format file with the plot data.

Water Flux Information for Contour Plots

The flux and velocity information from the output file “flow.out” was copied as text into the Excel file “fluxes.xls”. This is the information following the cell by cell hydrological conditions in the “flow.out” file where each row identifies a pair of cells that are connected in the model. There are 23,539 cell pairs. Column “A” in the “fluxes.xls” file is sorted using the Excel “Sort” command to separate the intermediate header information, which is deleted except for the first header. The columns were then re-sorted back into the original order by sorting on column “C” in ascending order. The text was then split into column data using the “Text to Columns” command. The corresponding connection information from the CONNE records of the file “meshtberg.mes” was copied and pasted as text into columns to the right of the flow output in “fluxes.xls”. The CONNE text cells were then split into column data using the “Text to Columns” command. The cell pairs for the flow and CONNE information are in the same order. All columns from the “Flow Output” worksheet were copied into the “Vertical fluxes” worksheet. The data were first sorted by column “M” in descending order using the Excel “Sort” command to separate the vertical, horizontal, and fracture-matrix connections. Vertical connections have a value of “3”, horizontal connections have a value of “1”, and local fracture-matrix connections have a value of “-10” in column “M”. The horizontal and fracture-matrix connections were then deleted. All columns were then sorted by column “C” in ascending order using the Excel “Sort” command. The connections with “TOP” cells and with “BOT” cells were sorted for all columns, sorting by column “A” in descending order, and these connections were deleted. The columns were re-sorted into order using column “C”. Finally, the global fracture-matrix connections between the invert and the rock, which are the only remaining connections with different third characters in the element names (e.g., “BH2 1” and “BI1 1”), were deleted. Data from the ELEME records of the file “meshtberg.mes” were copied and pasted as text into columns to the right of the existing information in the worksheet “Vertical fluxes” of the file “fluxes.xls”. This information was then converted from text to column information using the “Text to Columns” command in Excel. The rows with elements beginning with “CK” were sorted out in descending order by column “S” and were deleted (because these elements no longer appear in column “A”). The elements were then re-sorted back into the original order. Thus, the elements of column “A”, “K”, and “S” now match. To separate the fracture/intergranular and matrix/intragranular components, the conditional statement, “=IF(MID(A3,3,1)、“1”,1,2)” was put into cell “Y3” and returns a value of 1 for matrix/intragranular media (where the third character of the element name is 1) or a value of 2 for fracture/intergranular media (where the third character of the element name is 2). This was then copied down to cell “Y9330” to evaluate each row. Column “Y” was then copied and pasted into column “Z” as values, and column “Y” was deleted. All columns were then sorted on column “Z” in ascending order. Matrix/intragranular information was copied into a separate worksheet labeled “Matrix” and fracture/intergranular information was copied into a separate worksheet labeled “Fracture. For both “Matrix” and “Fracture” worksheets, the horizontal coordinate (X) from column “V” was copied into column “AE”, the vertical coordinate (Z) from

column "X" was copied into column "AF", and the flux was computed from the expressing "=D3/P3" in cell "AG3", which was then copied down to cell "AG9330". Columns "AE", "AF", and "AG" were copied and pasted as values into columns "AI", "AJ", and "AK" and these columns were sorted first in descending order by column "AJ" and then by column "AI" in ascending order. These three columns were then copied into text files "matrixflux.txt" and "fractureflux.txt" to be read into Tecplot V7.0. The two rows of header information at the top of each of these text files is needed by Tecplot to generate contour plots. The files were read into Tecplot using the "Load DataFile(s)" command to generate the 2D contour plots. The output files from these contour plots are "matrixflux.lay" and "matrixflux.plt" for the matrix fluxes and "fractureflux.lay" and "fractureflux.plt" for the fracture fluxes. The files with the extension "lay" are text files containing the plot layout information and the file name containing the plot data. The file with the extension "plt" is a binary format file with the plot data.

Vertical Water Flux between the Invert and the Rock

The flux and velocity information from the output file "flow.out" was copied as text into the Excel file "analysis of flow out of the invert.xls". This is the information following the cell by cell saturation and relative permeability conditions in the "flow.out" file for the final output at a time of 0.36525E+13 days, where each row identifies a pair of cells that are connected in the model. There are 23,539 cell pairs. Column "A" in the "analysis of flow out of the invert.xls" file is sorted using the Excel "Sort" command to separate the intermediate header information, which is deleted except for the first header. The text was then split into column data using the "Text to Columns" command. The columns were then re-sorted back into the original order by sorting on column "C" in ascending order. A new column "A" was then created by the "Insert" "Columns" command and the cell name pairs for each row were concatenated into a single name. The cell pairs representing the connections from the invert to the rock were copied from the file "CONNE grid processing.xls", which are given in columns "L" and "M" of the worksheet "Add global connections". These cell pairs were then concatenated into a single name in column "N". The invert-rock connections from column "A" were then identified using the "MATCH" command in cell "O3", "=MATCH(N3,A\$3:A\$23541,0)", which was copied down to cell "O54" to find all of the connections. In cell "P3", the corresponding flow rate through the connection was identified using the command "=INDEX(E\$3:E\$23541,O3)", which was copied down to cell "P54" to identify all of the cumulative fluxes. In cell "Q3", the command "=MID(M3,3,1)" was used to identify if the downstream cell was fracture ("1") or matrix ("2"), which was copied down to cell "Q54" to distinguish all of the connection types. The conditional statement "=IF(Q3="1",1,2)" was entered into cell "R3" to provide numerical values for fracture or matrix for sorting purposes. This was then copied down to cell "R54". Columns "A" through "K" from the worksheet "Add global connections" in the file "CONNE grid processing.xls" were copied into the same columns of the worksheet "From CONNE - add global con" of the file "analysis of flow out of the invert.xls". Columns "A" and "B" were concatenated into Column "L" and Columns "J" and "K" were concatenated into Column "M". The statement "=MATCH(M2,L\$2:L\$23540,0)" was put into cell "N2" to identify the connections between the invert and the rock in the CONNE records. Cell "N2" was copied down to cell "N53". In cell "O2" the corresponding direction cosine was identified using the command "=INDEX(G\$2:G\$23540,N2)". Cell "O2" was copied down to cell "O53". A direction cosine of "1" indicates a vertical connection and a value of "0" indicates a horizontal connection. Cells "O2" through "O53" in the worksheet "From CONNE - add global con" of the file "analysis of

flow out of the invert.xls” were copied and pasted as values into cells “V3” through “V54” of the worksheet “Flow output” of the same file. In the worksheet “Flow output”, columns “L” and “M” were copied into columns “T” and “U”. Column “R” was copied and pasted as values into column “W” and column “P” was copied and pasted as values into column “X”. Columns “T” through “X” were then sorted first by column “V” in descending order, then by column “W” in ascending order and then by column “X” in ascending order. The statement “=IF(X3<0,X3,0)” was put into cell “Y3” to determine if the vertical flow was going from the invert into the rock (i.e., that the flow rate was negative). This was copied down to cell “Y38”, which is the last of the vertical connections. The connection areas for the vertical flow rates were taken from the CONNE records and are a fixed value of 0.2066 m² in cells “Z3” through “Z24”. The total vertical flow rate out of the invert was evaluated in cell “AA3” with the statement “=SUM(Y3:Y24)”. The total flow connection area was evaluated in cell “AB3” with the statement “=SUM(Z3:Z24)”. The density of water in the simulation is given in cell “AC3”, which was taken from the file “flow.out”. The vertical Darcy flux from the invert to the rock, in m s⁻¹, was evaluated in cell “AD3” with the statement “=AA3/(AB3*AC3)”. The vertical Darcy flux from the invert to the rock, in mm yr⁻¹, was evaluated in cell “AE3” with the statement “=AD3*1000*86400*365.25”.

Post-Processing the Transport Output

The transport output in the file “trans2.out” was post-processed to produce Figures 7.3-6 through 7.3-9 shown in Section 7.3.1.7, as well as to determine the mass flux ratio for solute transport from the invert to the rock matrix and from the invert to the fractures, as discussed in Section 7.3.1.7.

Ratio of Solute Flux between the Invert and the Rock Matrix to the Invert and the Fractures

The flux and velocity information from the output file “trans2.out” was copied as text into the Excel file “analysis of releases to fractures and matrix2.xls”. This is the information following the cell-by-cell saturation and solute concentration conditions in the “trans2.out” file for the final output at a time of 0.36525E+13 days, where each row identifies a pair of cells that are connected in the model. There are 23,539 cell pairs. Column “A” in the “analysis of releases to fractures and matrix2.xls” file is sorted using the Excel “Sort” command to separate the intermediate header information, which is deleted except for the first header. The text was then split into column data using the “Text to Columns” command. The columns were then re-sorted back into the original order by sorting on column “C” in ascending order. A new column “A” was then created by the “Insert” “Columns” command and the cell name pairs for each row were concatenated into a single name. The cell pairs representing the connections from the invert to the rock were copied from the file “CONNE grid processing.xls”, which are given in columns “J” and “K” of the worksheet “Add global connections”. These cell pairs were then concatenated into a single name in column L. The invert-rock connections from column “A” were then identified using the “MATCH” command in cell M3, “=MATCH(L3,A\$3:A\$23541,0)”, which was copied down to cell “M54” to find all of the connections. In cell “N3”, the corresponding cumulative tracer flux through the connection was identified using the command “=INDEX(H\$3:H\$23541,M3)”, which was copied down to cell “N54” to identify all of the cumulative fluxes. In cell “O3”, the command “=MID(K3,3,1)” was used to identify if the downstream cell was fracture (“1”) or matrix (“2”), which was copied down to cell “O54” to

distinguish all of the connection types. The conditional statement “=IF(O3=“1”,1,2)” was entered into cell “P3” to provide numerical values for fracture or matrix for sorting purposes. This was then copied down to cell “P54”. Columns “N” and “P3” were copied and pasted as values into columns “S” and “T”. Columns “S” and “T” were then sorted by column “T” in ascending order. The cumulative solute mass flux from the invert to the rock matrix was determined using the expression “=SUM(S3:S28)” in cell “W3” and the cumulative solute mass flux from the invert to the fractures was determined using the expression “=SUM(S29:S54)” in cell “W4”. The flux ratio was evaluated using the expression “=W4/W3”, in cell “W5”.

Concentration Information for Contour Plots

The same process as described above for the analysis of diffusion was used to put the transport output concentration conditions by cell with the grid element information into the Excel spreadsheet “concentrations2.xls”. The conditional statement “=IF(MID(A3,3,1)=“1”,1,2)” was put into cell “N3” and returns a value of 1 for matrix/intragranular media (where the third character of the element name is 1) or a value of 2 for fracture/intergranular media (where the third character of the element name is 2). This was then copied down to cell “N9436” to evaluate each row. The columns “A” through “N” are copied and pasted (as values) into columns “P” through “AC” and then sorted in ascending order using the “Sort” command on column “AC”. This splits the matrix/intragranular rows from the fracture/intergranular rows. The matrix/intragranular component was copied into a separate worksheet called “Matrix” and the fracture/intergranular component was copied into a separate worksheet called “Fracture” in the file “concentrations.xls”. In each of these worksheets, the horizontal coordinate (X) from column “K” was copied into column “O” and the vertical coordinate (Z) from column “M” was copied into column “P” and the solute concentration from column from column “F” was copied into column “Q”. Then columns “O” through “Q” were sorted using the “Sort” command first on “P” in descending order and then by column “O” in ascending order. These three columns were then copied into text files “matrixcon2.txt” and “fracturecon2.txt” to be read into Tecplot V7.0. The two rows of header information at the top of each of these text files are needed by Tecplot to generate contour plots. The files were read into Tecplot using the “Load DataFile(s)” command to generate the 2D contour plots. The output files from these contour plots are “matrixcon2.lay” and “matrixcon2.plt” for the matrix saturations and “fracturecon2.lay” and “fracturecon2.plt” for the fracture saturations. The files with the extension “lay” are text files containing the plot layout information and the file name containing the plot data. The file with the extension “plt” is a binary format file with the plot data.

Solute Mass Flux Information for Contour Plots

The solute mass flux information from the output file “trans2.out” was copied as text into the Excel file “solute flux2.xls”. This is the information following the cell-by-cell concentrations in the “trans2.out” file where each row identifies a pair of cells that are connected in the model. There are 23,539 cell pairs. Column “A” in the “solute flux2.xls” file is sorted using the Excel “Sort” command to separate the intermediate header information, which is deleted except for the first header. The columns were then re-sorted back into the original order by sorting on column “C” in ascending order. The text was then split into column data using the “Text to Columns” command. The corresponding connection information from the CONNE records of the file “meshtberg.mes” was copied and pasted as text into columns to the right of the flow output in

“solute flux2.xls”. The CONNE text cells were then split into column data using the “Text to Columns” command. The cell pairs for the flow and CONNE information are in the same order. All columns from the “Transport Output” worksheet were copied into the “Vertical fluxes” worksheet. The data were first sorted by column “K” in descending order using the Excel “Sort” command to separate the vertical, horizontal, and fracture-matrix connections. Vertical connections have a value of “3”, horizontal connections have a value of “1”, and local fracture-matrix connections have a value of “-10” in column “K”. The horizontal and fracture-matrix connections were then deleted. All columns were then sorted by column “C” in ascending order using the Excel “Sort” command. The connections with “TOP” cells and with “BOT” cells were sorted for all columns, sorting by column “A” in descending order, and these connections were deleted. The columns were re-sorted into order using column “C”. Finally, the global fracture-matrix connections between the invert and the rock, which are the only remaining connections with different third characters in the element names (e.g., “BH2 1” and “BI1 1”), were deleted. Data from the ELEME records of the file “meshtberg.mes” was copied and pasted as text into columns to the right of the existing information in the worksheet “Vertical fluxes” of the file “solute flux2.xls”. This information was then converted from text to column information using the “Text to Columns” command in Excel. The rows with elements beginning with “CK” were sorted out in descending order by column “S” and were deleted (because these elements no longer appear in column “A”). The elements were then re-sorted back into the original order. Thus, the elements of columns “A”, “I”, and “Q” now match. To separate the fracture/intergranular and matrix/intragranular components, the conditional statement, “=IF(MID(A3,3,1)、“1”,1,2)” was put into cell “W3” and returns a value of 1 for matrix/intragranular media (where the third character of the element name is 1) or a value of 2 for fracture/intergranular media (where the third character of the element name is 2). This was then copied down to cell “Y9330” to evaluate each row. Column “W” was then copied and pasted into column “W” as values. All columns were then sorted on column “W” in ascending order. Matrix/intragranular information was copied into a separate worksheet labeled “Matrix” and fracture/intergranular information was copied into a separate worksheet labeled “Fracture”. For both “Matrix” and “Fracture” worksheets, the horizontal coordinate (X) from column “T” was copied into column “X”, the vertical coordinate (Z) from column “V” was copied into column “Y”, and the solute mass flux was computed from the expression “=F3/N3” in cell “Z3”, which was then copied down to cell “ZG9330”. Columns “X”, “Y”, and “Z” were copied and pasted as values into columns “AB”, “AC”, and “AD” and these columns were sorted first in descending order by column “AC” and then by column “AB” in ascending order. These three columns were then copied into text files “matrixflux2.txt” and “fractureflux2.txt” to be read into Tecplot V7.0. The two rows of header information at the top of each of these text files is needed by Tecplot to generate contour plots. The files were read into Tecplot using the “Load DataFile(s)” command to generate the 2D contour plots. The output files from these contour plots are “matrixflux2.lay” and “matrixflux2.plt” for the matrix fluxes and “fractureflux2.lay” and “fractureflux2.plt” for the fracture fluxes. The files with the extension “lay” are text files containing the plot layout information and the file name containing the plot data. The file with the extension “plt” is a binary format file with the plot data.

APPENDIX J

QUALIFICATION OF THERMODYNAMIC DATA FOR GEOCHEMICAL MODELING OF ADSORPTION OF RADIONUCLIDES BY STATIONARY CORROSION PRODUCTS AND CORROSION PRODUCT COLLOIDS

QUALIFICATION OF THERMODYNAMIC DATA FOR GEOCHEMICAL MODELING OF ADSORPTION OF RADIONUCLIDES BY STATIONARY CORROSION PRODUCTS AND CORROSION PRODUCT COLLOIDS

J.1. PURPOSE

The purpose of this analysis report appendix is to qualify the thermochemical database of surface complexation constants used in calculations of radionuclide sorption by stationary corrosion products and corrosion product colloids. The surface complexation calculations were carried out using PHREEQC V2.11 (2006 [DIRS 175698]), a qualified thermodynamic speciation and solubility code to develop the empirical K_d competitive sorption model documented in Section 6.5.2.4.

A number of simplifying assumptions or decisions were made due to the definition of the scope of this work. In particular, it was assumed that for a database of thermochemical constants for use in calculation of competitive sorption in support of performance assessment calculations:

1. Internal self-consistency of the set of reaction constants was more important than accuracy of individual values or stoichiometry of surface complexes. The largest possible self-consistent network of reaction constants would be used as a base and missing data would be filled in by the use of analogs rather than the use of Linear Free Energy Relations. Available sorption data would not be remodeled to obtain the best set of parameters even if a particular surface species had been identified by spectroscopic studies.
2. An abstraction is desired. It is assumed that the actual uncertainty in the predicted radionuclide sorption can be bounded by the use of a large number of calculations over a range of pH and f_{CO_2} using a simple (1-site) model of the sorbent.

J.2. QUALITY ASSURANCE

The quality assurance program used for development of this activity and document is discussed in *Technical Work Plan for Near-Field Environment: Engineered Barrier System: Radionuclide Transport Abstraction Model Report* (BSC 2007 [DIRS 177739]). In accordance with the TWP, this appendix supports development of a surface complexation model of reversible radionuclide sorption documented in Section 6.5.2.4. Specifically, the information provided by this appendix is input data for calculations to investigate the range of radionuclide K_d s calculated from a surface complexation model over a range of f_{CO_2} and pH.

J.3. SOFTWARE

Off-the-shelf commercial software, including Microsoft Word and Microsoft Excel, were used to carry out this work. This software is exempt from qualification per IT-PRO-0011, Section 2.1. Spreadsheets were verified by hand calculations and included in the output DTNs submitted to the TDMS. The work was conducted using project standard desktop computers.

J.4. INPUTS

This appendix describes an initial set of surface complexation constants used in sensitivity calculations in a surface complexation sorption model for performance assessment. The data set includes surface complexation constant for the following radionuclides and valence states: Np(VI), Np(V), Np(IV), Pu(VI), Pu(V), Pu(IV), Am(III), Th(IV), U(VI), and U(IV) describing sorption onto either HFO or goethite. These are the predominant valence states of neptunium, plutonium, americium, thorium, and uranium expected in oxidizing natural waters and at Yucca Mountain.

Data described in this report is all obtained from published literature. A literature search was conducted using combinations of the keywords:

“Surface complexation” OR “surface complexation constants” OR SCM OR DLM OR “diffuse layer model” OR “double layer model”

AND

Goethite OR “hydrous ferric oxide” OR ferrihydrite OR “iron oxide” OR hematite OR HFO OR “iron oxyhydroxide”

AND one of the following:

Uranium OR uranyl OR uranium(IV) OR uranium(V) OR uranium(VI) OR U(VI)O₂ , OR U(V)O₂ OR U(VI) OR U(V) or U(IV) or using Arabic numeral like 6+, 4+

Neptunium OR Neptunium(VI) OR Neptunium(V) OR neptunyl OR Np(V)O₂ OR Np(VI)O₂ OR Np(IV) OR Np(VI) OR Np(V) or using Arabic numeral like 6+, 4+

Plutonium OR plutonium(VI) OR plutonium(V) OR plutonium(IV) OR plutonyl OR Pu(V)O₂ or Pu(VI)O₂ OR Pu(IV) OR Pu(V) OR Pu(VI) or using Arabic numeral like 6+, 4+

Americium OR Am(III) OR Am³⁺

Europium OR Eu(III) OR Eu³⁺

Thorium OR Th(IV) OR Th⁴⁺

The following databases and years were searched: BIOSIS®(2002); Engineering Index® (1969 -) Inspec® (1898 -); ISI Proceedings® (1990 -); and ISI SciSearch® (1945 -).

Approximately 250 references were located by this search; a subset of approximately 50 references was selected for detailed review.

J.5. ASSUMPTIONS

Surface complexation modeling approach

Detailed descriptions of Surface Complexation Models (SCMs) have been given elsewhere and will not be repeated here (see for example Dzombak and Morel (1990 [DIRS 105483]) and Davis and Kent 1990 [DIRS 143280]). The main assumptions of SCMs, particularly those that distinguish them from the use of an isotherm or K_d model, are:

1. Sorption involves the production of surface species by the formation of electrostatic and specific chemical bonds between the sorbate (e.g., UO_2^{2+}) and the sorbent (i.e., goethite, $\alpha\text{-FeOOH}$). These reactions are governed by thermodynamic equilibrium similar to those used to describe homogeneous chemical reaction between metals or radionuclides and hydroxide ions in solutions.
2. Deviations from ideal thermodynamic behavior of solution species can be described by the Davies or Debye Hückel activity coefficient models and the non-ideal behavior of the surface species can be attributed to the effects of electrical surface potential.
3. Changes in the amount of sorption due to changes in the composition of the solution (e.g., pH, concentrations of complexing ligands, and competing ions) can be predicted by a solution of a set of simultaneous equations based on laws of mass action (equilibrium constants) and mass balance (see, for example, Morel and Hering 1993 [DIRS 151052]) for the chemical species in the system.

Temperature and ionic strength effects on sorption

1. Calculations of radionuclide surface complexation carried out assuming a temperature of 25°C will give low estimates of sorption. It has been suggested that sorption of metals onto goethite is an endothermic process and therefore, the degree of sorption will increase at the higher temperatures possible in the waste package environment. This is based on observations that site densities and sorption equilibrium constants for sorption of transition metals onto goethite increase with temperature (cited in Trivedi et al. 2001 [DIRS 173021]).
2. The thermochemical database listed in this appendix mixes constant derived from the model using the Davies approximation for activity coefficients and the B-dot activity coefficient model. Differences between speciation calculated with the Davies and B-dot activity models are assumed to be negligible over the range of ionic strengths considered in the sorption calculations.

Use of single-site sorption model for calculations.

The single-site diffuse layer model has been used as the basis of these databases instead of the more complex generalized (2-site) diffuse layer model (Dzombak and Morel 1990 [DIRS 105483]) or triple-layer model (Davis and Kent 1990 [DIRS 143280]). In doing so, we have adopted the recommendations of Turner and Sassman (1996 [DIRS 179618]) and Wang et al. (2001 [DIRS 176816]) to use the single-site model even though the PHREEQC model allows

for use of a 2-site model. The choice of a single-site vs 2-site model is based on the assumptions that:

1. The corrosion products in the waste package will likely be a mixture of different iron oxyhydroxides (i.e., goethite, hematite, and ferrihydrite)
2. Estimates of the proportion of the components in the mixture are highly uncertain due to lack of data for corrosion and phase transformation kinetics
3. Wide ranges of site densities and site energies for each iron oxyhydroxide have been reported in the literature, thus, attempts to describe sorption onto corrosion products using a complex multi-site model will necessarily be highly uncertain.

A single self-consistent network for sorption of all the requested radionuclide species onto either goethite or HFO does not exist. Therefore, the largest self-consistent network was identified and additional data were used to fill in the gaps. Based on the above considerations, the compilations of Wang et al. (2001 [DIRS 176816]) and Turner and Sassman (1996 [DIRS 179618]) are the best reaction network upon which to base the set of surface complexation constants. These authors fit experimental data from several sources to a single-site Double Layer Model (DLM) using a standard set of acidity constants for goethite. Table J-2 contains the recommended constants obtained from Wang et al. (2001 [DIRS 176816]) and Turner and Sassman (1996 [DIRS 179618]) with supplementary constants obtained from other sources. Information about the sources of all the constants is contained in Section J.6.

J.6. SCIENTIFIC ANALYSIS

J.6.1 OVERVIEW OF ALTERNATIVE SORPTION MODELS

Two complementary approaches to describe interactions between radionuclides and geomeedia have emerged in the last three decades. The ‘empirical approach’ involves measurements of radionuclide distribution or sorption coefficients (K_d s or R_d s) in site-specific water rock systems using synthetic or natural groundwaters and crushed rock samples and 2) mechanistic-based approaches in which radionuclide thermodynamic surface or sorption complexation constants are obtained for simple electrolyte solutions with pure mineral phases. The approaches should be viewed as complementary; each fulfills a different need. For any application, the acceptable model for solute/rock interactions is the one that is sufficiently robust with respect to required ranges of solution and substrate compositions, ionic strength, solute/solid ratios, and observational time frames.

This appendix describes the thermochemical database of surface complexation constants to be used in calculations of radionuclide sorption by stationary corrosion products and corrosion product colloids. The surface complexation calculations will be carried out using PHREEQC V2.11 (2006 [DIRS 175698]), a qualified thermodynamic speciation and solubility code to develop the empirical K_d competitive sorption model documented in Section 6.5.2.4.

The different approaches to describing sorption can be discussed in order of increasing complexity and robustness:

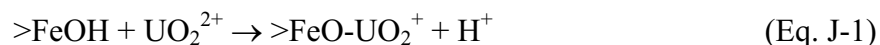
1. Linear Sorption (K_d or R_d)
2. Non-linear Sorption (Freundlich and other isotherms)
3. Constant-Charge (ion-exchange) Model
4. Constant-Capacitance Model
5. Diffuse Layer Model
6. Triple-Layer model (TLM)

These models differ with respect to the nature of the “conditional” and “intrinsic” constants that each requires. “Conditional” constants are valid for specific experimental conditions; “intrinsic” constants are valid over a wide range of conditions.

The simplest model (linear sorption or K_d) is widely used in contaminant transport models, and K_d values are relatively easy to obtain using batch sorption methods. The K_d model requires a single distribution constant that is conditional with respect to a large number of variables. Thus, even if a batch K_d experiment is carefully carried out to avoid introduction of extraneous effects such as precipitation, the K_d value that is obtained is valid only for the particular conditions of the experiment. The radionuclide concentration, pH, major and minor element composition, sorbent mineralogy, particle size and solid-surface-area/solution volume ratio must be specified for each K_d value.

The Triple-Layer Model (TLM) (Davis and Leckie 1978 [DIRS 125591]) is one of the most complex model surface complexation models (SCM). These models describe sorption within a framework similar to that used to describe associations between metals and ligands in solutions (Davis and Kent 1990 [DIRS 143280]; Stumm 1992 [DIRS 141778]). Reactions involving surface sites and solution species are postulated based on experimental data and theoretical principles. Mass/charge balance and mass action laws are used to predict sorption as a function of solution chemistry. Different surface complexation models incorporate different assumptions about the nature of the solid-solution interface. These include the number of distinct surface planes where cations and anions can attach (double layer vs. triple layer) and the relations between surface charge, electrical capacitance, and activity coefficients of surface species.

The TLM includes an inner plane (0 plane), an outer plane (β plane), and a diffuse layer that extends from the β plane to the bulk solutions. The sorption of uranium at the β plane of an iron oxyhydroxide surface (represented as $>\text{FeOH}$) can be represented by a surface reaction in a TLM as:



The mass action law for the reaction using the TLM is:

$$\beta^{\text{UO}_2^+} = \frac{\{>\text{FeO-UO}_2^+\} a_{\text{H}^+} \frac{\exp[e\psi_\beta - e\psi_0]}{kT}}{\{>\text{FeOH}\} a_{\text{UO}_2^{2+}}} \quad (\text{Eq. J-2})$$

where $\beta^{UO_2^+}$ is the intrinsic surface complexation constant for the uranyl cation; $\{\text{FeOH}\}$ and $\{\text{FeO-UO}_2^+\}$ are the concentrations of the uncomplexed and complexed surface sites, respectively; a_{H^+} and $a_{UO_2^{2+}}$ are activities of the aqueous species; ψ_β and ψ_0 are the electrical potentials for the outer (β) and inner (0) surface planes; and k , T , and e are the Boltzmann constant, absolute temperature, and the fundamental charge, respectively. The exponential term provides the activity coefficients for the surface sites.

In the above example, the uranyl ion is bound to the outer β surface plane (actually, most recent studies suggest it is bound to the inner plane). In natural waters, other surface reactions will be occurring simultaneously. These include protonation and deprotonation of the FeOH site at the inner 0 plane and complexation of other cations and anions to either the inner or outer surface planes. Expressions similar to Equation J-1 above can be written for each of these reactions. For more details about the properties of the electrical double layer, methods to calculate surface speciation, and alternative models for activity coefficients for surface sites, the reader should refer to the references cited above and other works cited therein.

The TLM contains eight adjustable constants that are valid over the ranges of pH, ionic strength, solution composition, specific areas, and site densities of the experiments used to extract the constants. The surface-complexation constants, however, must be determined for each sorbent of interest and should not be extrapolated outside of the original experimental conditions. Although the TLM constants are valid under a wider range of conditions than are K_d s, considerably more experimental data must be gathered to obtain the seven adjustable parameters. On the other hand, an important advantage of surface complexation constant models is that they provide a structured way to examine experimental data obtained in batch sorption studies. Application of such models may ensure that extraneous effects have not been introduced into the sorption experiment and that a valid sorption ratio has been obtained.

J.6.2 CRITERIA FOR SELECTION OF RECOMMENDED SURFACE COMPLEXATION CONSTANTS

It is important that compilations of thermodynamic data be *internally self consistent*. All equilibrium constants used in speciation calculations are “conditional” constants; they are dependent on the values of other constants or variables used either to extract them from experimental data or to estimate them from correlation techniques such as linear free-energy relations. Each of the SCMs reviewed in this data survey use different relationships between charge and surface potential, different assumed site densities, and in some cases different standard state conventions in deriving their sorption equilibrium constants. Thus, the surface acidity constants and sorption parameters are appropriate only within a given model; parameters from different models should not be mixed, because the resultant errors and uncertainties in K_d s calculated from simulations employing mixed parameters are difficult if not impossible to predict.

Ideally, the process of compiling an internally self consistent database consists of several steps: 1) compilation of process values such as equilibrium constants for reactions involving the element of interest, 2) extrapolation of equilibrium constants to reference conditions (usually zero ionic strength and 25°C), and 3) calculation of property values such as free energies of

formation of the products through reaction networks. Surface complexation constants will be obtained through fits of sorption isotherm data (sorption as a function of sorbate concentration) or sorption envelope data (sorption as a function of pH). Calculated thermodynamic constants from different experimental studies may be incompatible if different reference states or reaction networks are used. In addition, the constants are dependent on the methods of ionic strength correction and the values used for auxiliary species such as OH^- or SO_4^{2-} .

Often, alternative models for the stoichiometry provide adequate fits to the experimental data. Several researchers have illustrated the dependence and non-unique nature of the “intrinsic” binding constants by fitting similar sorption edges to a variety of models (Westall and Hohl 1980 [DIRS 181192]; Turner 1995 [DIRS 144697]). Robertson and Leckie 1997 [DIRS 173763]) systematically examined the effects of SCM model choice on cation-binding predictions when pH, ionic strength, cation loading, and proposed surface complex stoichiometry were varied. Although different models can be used to obtain comparable fits to the same experimental data set, the stoichiometry of the proposed surface complex will vary considerably between the models. Where possible, the chosen fits should be constrained by spectroscopic or molecular modeling studies and stoichiometries that fit a wide range of experimental data should be selected (Hayes and Katz 1996 [DIRS 179121]).

The approach taken in this compilation was to compile the largest internally self-consistent network of constants. To achieve this goal, one compromise that had to be accepted was that the existence of all recommended species could not be independently verified by experimental techniques to exist. A single self-consistent network for sorption of all the requested radionuclide species onto either goethite or HFO does not exist. Therefore, the largest self-consistent network was identified and additional data were used to fill in the gaps. Based on the above considerations, the compilations of Wang et al. (2001 [DIRS 176816]) and Turner and Sassman (1996 [DIRS 179618]) comprise the best reaction network upon which to base the set of surface complexation constants. These authors fit experimental data from several sources to a single site Diffuse Layer Model (DLM) using a standard set of acidity constants for goethite. The additional data were based on oxidation state analogs or using analogous data on other ferric oxyhydroxide substrate.

J.6.2.1 SELECTION OF DIFFUSE LAYER MODEL FOR THERMOCHEMICAL DATA BASE IN PA CALCULATIONS

The Diffuse Layer model was qualified for use in the performance assessment calculations based on its widespread use and acceptability in peer-reviewed literature and qualified research groups. Data selection criteria were based on widespread use of work by the cited author and evidence of standard knowledge and compatibility with the single-site diffuse layer model, as discussed below.

The Diffuse Layer Model (Stumm et al. 1970 [DIRS 181231]) has been used to model metal and radionuclide sorption by many research groups (Langmuir 1997 [DIRS 125369]; Jenne 1988 [DIRS 162328]; Dzombak and Morel 1990 [DIRS 105483], and EPA 1999 [DIRS 147475]). The generalized two-layer model developed by Dzombak and Morel (1990 [DIRS 105483]) and is used in the PHREEQC computer code for an extension of the Diffuse Layer Model to obtain better fits of sorption data at moderate to high sorbate/sorbent ratios. This is accomplished by

including two site types (weak site and strong site) for binding of surface species. This allows for differentiating strongly binding solutes from weakly binding solutes, however, the number of strong sites is very limited (ratio of weak to strong sites = 100:1 for HFO), and limitations of the charge distribution in the Gouy Chapman model as discussed below.

J.6.2.2 LIMITATIONS OF THE DIFFUSE LAYER MODEL

The various SCMs differ in assumptions made about the description of the interlayer region, specifically, the location of the sorbed species with respect to the surface and the equations used to calculate the relationship between electrical potential and charge from the surface to the solution. In the DLM (Stumm et al. 1970 [DIRS 181231]), only one sorption plane is allowed (the 0 plane), i.e., all sorbing species are assumed be located at the same distance from the surface. The relationship between charge and surface potential is described by the Stern-Grahame modification of the Gouy-Chapman diffuse layer model for symmetrical electrolytes. This model describes the surface charge density solely as a function of distance from the surface, the electrolyte concentration (or ionic strength of the bulk solution), electrolyte valence, and the electrical potential at the surface. The model is most accurate at low ionic strength. Most measurements have been made at ionic strengths of 1 M or less. The dependence of the charge relations solely on the ionic strength of the solution and not the identity of the solutes is an important limitation.

Experimental and spectroscopic data suggest that multiple planes of sorption exist (Hayes and Katz 1996 [DIRS 179121]). The distribution of different solutes (and their charges) at these different sorption planes will affect the relationship between surface charge density and electrical potential in ways not described by the simple Gouy-Chapman model. This charge distribution affects the sorption affinity of the solutes, the shapes of their sorption envelopes and sorption isotherms, and ultimately calculated K_d s.

An important limitation of the single plane for sorption in the DLM is that it can distinguish between strongly sorbing and weakly sorbing surface species only by varying the value of the sorption equilibrium constant. Although the DLM can be used to model sorption under the same ionic strength used for the model calibration experiments, it may not be able to account for the competitive effects of background electrolytes (such as Na and Cl) with weakly sorbing species (such as Ca and Mg) and the resultant effect on the competition between weakly and strongly sorbing cations.

Hayes and Katz (1996 [DIRS 179121]) compared the ability of the NEM (Non-Electrostatic Model), DLM and several versions of the TLM to fit divalent cation sorption data over a range of ionic strengths, metal concentrations and surface coverages. They found that while all models provided adequate fits for sorption envelopes to single sets of calibration data (i.e., at a given ionic strength or surface loading) the DLM and NEM were less successful than the TLM in modeling sorption for conditions outside of the narrow range of their calibration data sets. In particular, the use of a continuum of site types allows the TLM accurately to predict sorption over a wide range of site coverages using surface complexes that were consistent with X-ray adsorption spectroscopy data.

The relative importance of different surface species depends on the extent of surface coverage. Hayes and Katz (1996 [DIRS 179121]) compared the ability of monodentate vs. multidentate species in explaining sorption at low to moderate (0.1 – 10 percent) and moderate to high (10 percent – 100 percent) surface coverages. At moderate to low surface coverages, monodentate species predominate for strongly sorbing species and at all surface coverages for weakly sorbing species. They found that modeling with monodentate reactions alone lead to underprediction of sorption at higher (>10 percent) coverage.

The inability of DLM to predict sorption over a range of ionic strengths is due to the fact that the background electrolyte does not form surface complexes; i.e., no competition exists between the background electrolyte and the sorbing species. The only effect of ionic strength in the DLM on sorption is through the change in the diffuse layer charge through the Gouy Chapman relationship. This effect is second order compared to the direct competition possible in the Triple Layer Model. In the TLM, the background electrolyte will compete directly with sorbed species at the outer sorption (β) layer.

Hayes and Katz (1996 [DIRS 179121]) found that the DLM would under-predict sorption at some coverages and over predict at others and that addition of other multinuclear species did not improve the fits consistently over ranges of surface coverages and pH. However they also note that although the TLM was more robust than the DLM, it still failed to predict sorption at high (>12%) surface coverage without addition of multinuclear (polymeric) species and/or surface precipitation reactions. Appelo et al. (2002 [DIRS 168168]) compared the fit of TLM and DLM in their compilation of SCM parameters for carbonate sorption onto iron oxyhydroxides. They found that the fit of experimental data to the TLM was better and attributed it to the ability of the TLM to distribute the surface charge over two electrical double layers (α and β) compared to the single electrical double layer of the DLM. In general, at higher concentrations of sorbed species, steric and electrical potential effects may become more pronounced (i.e., the number of available surface sites decreases, and the surface charge changes). This may be important for large dioxy-actinide complexes (e.g., PuO_2^+ , UO_2^{2+} , etc.) or highly charged reduced species (Th^{4+} , Am^{3+}). In the case of carbonate sorption by goethite, Appelo et al. (2002 [DIRS 168168]) were able to improve the fit by introducing an additional divalent surface species. However, such modifications substantially increase the number of fitting parameters and experimental data requirements.

J.6.3 SORPTIVE COMPETITION

It is important to estimate how well the SCM parameters, obtained from single solute studies, will predict sorption using a single-site DLM when spectroscopic or speciation studies suggest that both inner sphere and outer sphere complexes exist in the system with mixtures of radionuclides and other solutes. Although this question is best addressed with speciation calculations, review of the literature suggests competition among radionuclides and the resultant K_d s will depend on the number of available sorption sites and concentrations of sorbates in solution. Thus, the ability of sorption parameters to predict the effects of competition depends on the available surface sites in both the systems used to calibrate the single-solute sorption models and the multi-solute system of interest, as well as the speciation model used in the calculations.

In some experimental studies of metal sorption by hydrous ferric oxides, little competition was observed among competing solutes because of the large number of sorption sites (in studies reviewed by Xu et al. 2006 [DIRS 181191], p. 2216; and Trivedi et al. 2001 [DIRS 173021]), whereas for studies with hematite or goethite, competitive effects were seen because of the relatively few number of sites. In a study of competitive sorption of Ni, Zn and Ca by goethite where the ratio of weak to strong sites was 100:1, Trivedi et al. (2001 [DIRS 173021]), found that a single-site Langmuir model provided a good description of sorptive competition of Ni and Zn exclusively onto one high affinity site while Ca sorption exclusively occurred at another weak affinity site.

As discussed above, the single-site DLM is less likely to be successful in predicting sorptive competition than the TLM because of its inability to distinguish between inner-sphere and outer-sphere complexes. A few researchers have been able to successfully model multi-solute sorption using surface complexation constants obtained in single sorbate studies. Xu et al. (2006 [DIRS 181191]) used single sorbate constants obtained with a TLM to successfully model competitive sorption of Ni and Zn by goethite over a wide range of solute concentrations at a neutral pH. Christl and Kretzschmar (1999 [DIRS 173811]) were able to reproduce sorptive competition between copper and lead onto hematite with a basic 2-pK Stern model or a TLM only if they used a specific site density of 5 – 10 sites nm⁻². Many other attempts to predict sorptive competition have been less successful (see review by Xu et al. 2006 [DIRS 181191]).

Accuracy of prediction of competitive sorption among radionuclides will depend on the choice of site density and specific surface area. Surface site densities of different iron oxyhydroxides studied in this review vary widely. Measured specific surface area of goethite ranges from 14.7 -110 m² g⁻¹ (Section 6.3.4.3.3). Site densities of goethite listed in Table 6.3-5 range from 1.02 – 8.59 sites nm⁻². Thus, the uncertainty in the predicted K_d s for multi-sorbate systems will be hard to quantify.

J.6.4 OTHER UNCERTAINTIES IN SURFACE COMPLEXATION CONSTANTS

J.6.4.1 Activity Coefficient Model

The database of Wang and Anderko (1999 [DIRS 181213]) and Wang et al. (2001 [DIRS 176816]), which was used as the source of constants for Np(V), Pu(V), and Pu(IV), used a version of FITEQL (Westall 1992 [DIRS 181271]), that used a modified version of the B-dot model of Helgeson (1969 [DIRS 137246]) for calculation of activity coefficients of aqueous species. Other data sources (e.g., Turner and Sassman 1996 [DIRS 179618]; Dzombak and Morel 1990 [DIRS 105483]) and the PHREEQC code (2006 [DIRS 175698]) used in the TSPA sorption calculations described in the TWP use the Davies equation in PHREEQC. The B-dot equation is valid over a wider range of ionic strengths (up to 3 molal) and temperature (up to 300°C) than the Davies equation (Wang et al. 2001 [DIRS 176816]). The ionic strength could exceed 3 molal in the TSPA model, but at that point, the solubility models are not valid, and alternative concentration limits are applied. At such high dissolved concentrations, the calculated K_d becomes very small. This difference in the activity coefficient models in the various sources of data and the PHREEQC code introduces some inconsistency and some uncertainty into sorption calculations using this database. Other constants were derived using the Specific Interaction Theory (SIT) Model (see Table J-2).

Wang and Anderko (1999 [DIRS 181213]) describe the modifications to the FITEQL code that were made to incorporate the B-dot equation and evaluated the potential effect on the calculated surface complexation constants. They found that at the ionic strengths found in most sorption experiments (10^{-3} to 10^{-1} M) differences in binding constants (as $\log K$), calculated using the B-dot versions, differed by 10^{-3} – 10^{-2} and were always smaller than standard deviations for the estimated binding constants in tested cases. Deviations from the constants calculated with the Davies equation were not evaluated but are assumed to be of similar magnitude. The increased accuracy from evaluating deviations from the Davies constants would be small. Ionic strength effects on sorption are less well modeled than ionic strength effects on pairing of dissolved ions.

J.6.4.2 Estimated Uncertainty in Model Fits

Binding constants for Pu(V), Pu(IV), and Np(V) taken from Wang et al. (2001 [DIRS 176816]) were obtained from weighted averages of several data sets using the method described by Dzombak and Morel (1990 [DIRS 105483]). The standard deviations of the constants were assigned equal to the largest σ from the individual data regressions and ranged from 0.03 to 1.0 (in $\log K$ units). Uncertainties in the binding constants for surface acidity and the uranium surface complexes were expressed as 95 percent deviations (about 2σ) for the weighted averages and ranged from 0.08 to 0.22 (K_2 , K_1) and 0.45 to 0.83 (uranyl surface complexes) $\log K$ units. Uncertainties in the thorium constants ranged from 0.1 to 1.0 $\log K$ units.

J.6.4.3 Aqueous Speciation Model

Wang et al. (2001 [DIRS 176816]) took the equilibrium constants for aqueous species from the Data0.com.V8.R6 file of the EQ3/6 thermodynamic database for Pu(V), Pu(IV), and Np(V) (Wolery 1992 [DIRS 100835], Wolery 1992 [DIRS 100836]). Sources for other aqueous species are described in Table J-2. Several differences between this speciation model and the one used in PHREEQC may introduce inconsistency into the calculations. In addition, differences from the more recent versions of Data0 may introduce inconsistencies between the results of the sorption calculations and the solubility calculation carried for the RTA and EBS. Some of these are discussed below in more detail.

J.6.4.4 Carbonate Complexes

The radioactive elements of interest in this database form strong aqueous carbonato-complexes. Different studies reviewed for this database included the effects of carbonate in different ways leading to another source of inconsistency in this set of SCM constants and uncertainty in calculations that use them. In some of these sorption experiments used to obtain surface complexation constants, CO_2 was not present (Turner and Sassman 1996 [DIRS 179618]). In other cases, CO_2 may have been present but neither aqueous nor adsorbed carbonate species were included in the model. For example, Wang et al. (2001 [DIRS 176816]) did not include PuO_2^+ -carbonato complexes in their aqueous model or in their surface complexes; even they used data from the experiments of Sanchez et al. (1985 DIRS 107213), which were conducted under atmospheric conditions. On the other hand, Wang et al. (2001 [DIRS 176816]) modeled NpO_2^+ speciation and sorption by iron oxyhydroxides assuming the presence of aqueous carbonate complexes. They included NpO_2 -carbonates in their aqueous model but did not include a sorbing NpO_2 -carbonato species. Their model of NpO_2^+ sorption by hydrargillite

matched the experimental data showing lower sorption at higher carbonate levels and they concluded “sorption behavior in the presence of CO₂ can be predicted using DLM without the inclusion of carbonate-containing surface complexes”. In contrast, Turner and Sassman (1996 [DIRS 179618]) included three UO₂-carbonato surface species in their model for U(VI)-CO₂ system.

Neither Wang et al. (2001 [DIRS 176816]) nor Turner and Sassman (1996 [DIRS 179618]) included sorption of CO₂ in their models and argued that at atmospheric P_{CO_2} , it would be insignificant. A number of researchers have shown that CO₂ does adsorb to iron oxyhydroxide, effectively competing with metals for sorption sites (Appelo et al. 2002 [DIRS 168168]; Van Geen et al. 1994 [DIRS 144702]). At the higher f_{CO_2} to be modeled in TSPA, such competition may be significant. However, including CO₂ sorption in the suite of reactions introduces additional uncertainty in the calculations because this reaction was not included when the binding constants for the radioelements were obtained from experimental data.

J.6.4.5 Use of Constants from 1-Site Model in 2-Site Calculations or Vice Versa

Although the SCM constants for U(VI) Turner and Sassman (1996 [DIRS 179618]) and Pu(IV), Pu(V) and NpO₂⁺ were fit with single-site DLMs, several of the other species were fit with 2-site DLMs in their source document. Because the data were not refit to a 1-site model for this study, it was necessary to mix surface complexation constants from single-site and two-site models in the database. There are several alternative ways to do this, as described in Table J-1. Each will introduce a different amount of uncertainty in the K_d calculations that use this database.

Table J-1. Possible Effects on Calculated K_d s of Alternative Ways to Mix SCM Constants from Single-Site and 2-Site Models

Approach	Effect
Use K_d s for single-site K , use total number sites = number of high energy sites	Will correspond to K_d (linear) region of isotherm and underestimate K_d at high loadings; i.e., total sorption capacity is truncated
Use K_d s for single-site K ; use total number of sites	Will correspond to K_d at low loadings and overestimate K_d at high loadings
Use mix of single- and 2-site models depending in calculation on what is available	Will be accurate for single solutes individually but lead to inconsistency in competition among solutes. Values for sorption constants for single-site models typically lie between values for weak site and strong site constants used in the 2-site models. So, even if solutes with a single site are assumed to bind to strong sites, they will be displaced by solutes from 2-site models (since they will have higher K). The solutes with single site will have no place to go and their K_d s will be underestimated.
Use 2-site model, set $K_d = K_w$ for those solutes with only one K , honor K_d/K_w ratio from Section 6.5.2.4.	Solutes with single K will not have many slots on strong sites but will have access to weak sites. K_d s for solutes with single K will be underestimated but not as much as in other cases.

The extent of uncertainty introduced by each of these approaches could be estimated by PHREEQC calculation.

J.6.5 SELECTION OF SURFACE COMPLEXATION CONSTANTS

In this section, the sources of data and uncertainties for the recommended surface complexation constants in Table J-2 are described. Alternative values and models that were considered are listed in Table J-3.

J.6.5.1 Goethite Properties

The properties of the sorbent assumed in this database are based on the model iron oxyhydroxide used in calculations by Turner and Sassman (1996 [DIRS 179618]). They assumed a model goethite based on studies by Balistrieri and Murray (1981 [DIRS 181308]) with a specific surface area of $50 \text{ m}^2 \text{ g}^{-1}$ and a single-site Diffuse Layer model with site density of 2.31 sites nm^{-2} following the recommendations of Dzombak and Morel (1990 [DIRS 105483]) and Davis and Kent (1990 [DIRS 143280]). The acidity constants were based on studies by Balistrieri and Murray (1981 [DIRS 181308]), where $\log K_+ = 7.35 \pm 0.11$ and $\log K_- = -9.17 \pm 0.08$.

J.6.5.2 Uranium

The U(VI) model is based on Turner and Sassman (1996 [DIRS 179618]) who fit multiple models to data from Tripathi (1984 [DIRS 113425]) and Hsi and Langmuir (1985 [DIRS 106131]) using the FITEQL V2 code (Westall 1992 [DIRS 181271]). The aqueous species model is based on the compilation by Grenthe et al. 1992 [DIRS 101671]; the Davies model was used to calculate activity coefficients. The estimated binding constants were based on weighted averages of multiple data sets following the procedure of Dzombak and Morel (1990 [DIRS 105483]) relying on the standard deviations of the fits calculated by the FITEQL V2 code. Data sets for the experiments where CO_2 was present and under CO_2 -free conditions led to different sets of recommended surface species. The species $\text{FeOH-UO}_2(\text{OH})_4^{2-}$ was used with some success to fit the data of Tripathi (1984 [DIRS 113425]) for CO_2 -free system (95 percent confidence interval = $\pm 0.64 \log K$) and systems where CO_2 was present (95 percent confidence interval = ± 0.83) and can be used over the range of f_{CO_2} in the TSPA calculations. The value recommended in Table J-2 is from the system where CO_2 was present. A better fit to the system where CO_2 is present is obtained, however, using the combination of the three species $\text{FeOH}_2-\text{UO}_2(\text{CO}_3)_2^-$, $\text{FeOH}_2-\text{UO}_2(\text{CO}_3)_3^{-3}$, and $\text{FeOH}_2-(\text{UO}_2)_2\text{CO}_3(\text{OH})_3$.

DLM data for U(IV) were not found in the literature review; the constant from Th(IV) or Pu(IV) could be used in initial calculations.

J.6.5.3 Plutonium

The Pu(V) and Pu(IV) models are taken from the work of Wang et al. (2001 [DIRS 176816]). The properties of the sorbent and the thermodynamic data for aqueous species are consistent with Turner and Sassman (1996 [DIRS 179618]) except the former use a B-dot model instead of a Davies model for activity coefficients. As mentioned above, Wang et al. (2001 [DIRS 176816]) fit the data without including either aqueous or adsorbed PuO_2^+ -carbonato complexes. Zavarin and Bruton (2004 [DIRS 181272]) included the suite of aqueous carbonato complexes from *Chemical Thermodynamics of Neptunium and Plutonium*. Volume 4 of *Chemical Thermodynamics* (OECD 2001 [DIRS 159027]), but had no adsorbed carbonato complexes in

the NEM that they fit to the same data set of Sanchez et al. (1985 [DIRS 107213]). Although there is evidence that aqueous PuO_2^+ -carbonato complexes exist and other researchers have included the adsorbed species in their fits as shown in Table J-3 below (Berry et al. 2002 [DIRS 181190]), we have decided to use the constants and speciation of Wang et al. (2001 [DIRS 176816]) to maintain consistency.

Wang et al. (2001 [DIRS 176816]) did not obtain single site DLM constants for Pu(III) and Pu(VI) from the data of Sanchez et al. (1985 [DIRS 107213]). Using the analog data for U(VI) and letting the aqueous speciation and solubility control the amount of Pu(VI) available is recommended in this database. Using the data for La(III) is recommended for Pu(III) for sorption onto goethite. Alternatively, it is possible to estimate the binding constants using a linear-free energy relationship (LFER), as discussed below. Alternatively, constants for HFO obtained from a LFER by Mariner and Jackson (1993 [DIRS 181188]) could be used.

J.6.5.4 Neptunium

Binding constants for Np(V) were obtained from Wang et al. (2001 [DIRS 176816]) who fit constants from the datasets of Nakayama and Sakamoto (1991 [DIRS 172676]) and Tochiyama et al. (1995 [DIRS 144644]). They modeled NpO_2^+ speciation and sorption by iron oxyhydroxides assuming the presence of aqueous carbonate complexes but did not include a sorbing NpO_2 -carbonato species. Their model of NpO_2^+ sorption by hydrargillite matched the experimental data showing lower sorption at higher carbonate levels, and they concluded “sorption behavior in the presence of CO_2 can be predicted using DLM without the inclusion of carbonate-containing surface complexes.”

Single-site DLM binding constants for Np(IV) and Np(III) were not available; therefore, the constants for Th(IV) or Pu(IV) and La(III), respectively, should be used in the calculations. Alternatively, the constants for HFO obtained from LFER by Mariner and Jackson (1993 [DIRS 181188]) could be used.

J.6.5.5 Americium

Single-site DLM binding constants were not found for Am(III). The Am(III) model in this database is based on a 2-site DLM for La(III) (Pepper 2006 [DIRS 179622]); only the weak site is used because it dominates above pH of 5.5. The same model could be used for Np(III) and Pu(III) to maintain internal consistency. The uncertainties associated with use of binding constants from a 2-site model in the 1-site model are discussed in Section J.6.4.5. Alternatively the single-site DLM of Naveau et al. (2005 [DIRS 173018]) for Eu(III) sorption by goethite can be used; however, they use a different set of surface acidity constants ($\log K_+ = 6.53$; $\log K_- = -7.54$). Alternatively, a set of constants for Am(III) could be obtained with a LFER as discussed below.

J.6.5.6 Thorium

A single-site DLM was not available for sorption of thorium by goethite. The single-site DLM constants in Table J-2 are taken from the thorium model of Cromières et al. (1998 [DIRS 179616]) for studies of thorium sorption by hematite in low CO_2 (10^{-5} M) systems. The SCM constants are consistent with hydrolysis constants from Baes and Mesmer (1976

[DIRS 157860]) and the Specific Interaction Theory for activity coefficients. A single-site model was fit by Cromières et al. (1998 [DIRS 179616]) because the surface coverage was very low in the experiments. This model is similar to other models using hematite with the Triple-Layer Model, as shown in Table J-3. In thorium sorption studies at higher CO₂ levels, Murphy et al. (1999 [DIRS 179553]) thorium-carbonate complexes dominated the speciation in solution but there were no adsorbed thorium-carbonate complexes in the single-site TLM fit to the data. Other studies using the TLM included carbonate complexes and a Th-SO₄ complex and are described in Table J-3.

J.6.5.7 Nickel

Binding constants for Ni(II) are taken from Dzombak and Morel (1990 [DIRS 105483]). They assumed a ferrihydrite sorbent with 2.31 sites nm⁻² in a 2-site DLM. The weak site constant was obtained by a linear free-energy relationship (their Table 10.5). The uncertainties associated with use of binding constants from a 2-site model in the 1-site model are discussed in Section J.6.4.5

J.6.5.8 Carbonate

Sorption of carbonate is considered explicitly in the calculations using complexation constants from Appelo et al. (2006 [DIRS 168168]). These constants were obtained from fits of carbonate sorption data of Zachara et al. (1987, DIRS 105963) onto ferrihydrite using substrate properties proposed by Dzombak and Morel (1990 [DIRS 105483]). Attempts to apply these constants in a DLM to predict sorption of CO₂ by goethite (Villalobos et al. 2003 [DIRS 173017]) were only partly successful; the pH sorption envelope was shifted by one pH unit to acid conditions. The model overpredicts sorption by about 33 percent at pH = 3 and under predicts it by about 33 percent at pH = 8. An alternative DLM using a doubly charged carbonate surface complex and adjusted surface acidity constants (K_{a1} and K_{a2}) was more successful in matching the data). As discussed in Section J.6.4.4 above, inclusion of a separate sorption reaction for carbonate will introduce inconsistency into the databases and uncertainty into the surface complexation calculations because several of the actinide SCM constants were derived without including a similar reaction in systems where CO₂ was present.

Table J-2. Summary of Surface Complexation Constants

Ref	Solid	Model/# of Sites	N_s sites nm ⁻²	Surface acidity constants: log K^+ log i^-	Surface species	Aqueous model	Activity coefficient model	Comments
Np(V)O₂⁺								
Wang et al. (2001 [DIRS 176816])	goethite	DLM/1	2.31	Turner and Sassman (1996 [DIRS 179618]) 7.35 -9.17	XOH-NpO ₂ ⁺ XO-NpO ₂ OH-	Fuger (1992 [DIRS 108201])	B-dot	
Pu(IV)								
Wang et al. (2001 [DIRS 176816])	goethite	DLM/1	2.31	Turner and Sassman (1996 [DIRS 179618]) 7.35 -9.17	XO-Pu ³⁺ XO-PuOH ²⁺ XO-Pu(OH) ₃	Fuger (1992 [DIRS 108201])	B-dot	Based on data from Sanchez et al. (1985 [DIRS 107213])
Pu(V)O₂⁺								
Wang et al. (2001 [DIRS 176816])	goethite	DLM/1	2.31	Turner and Sassman (1996 [DIRS 179618]) 7.35 -9.17	XOH-PuO ₂ ⁺ XO-PuO ₂ XO-PuO ₂ OH-	Fuger (1992 [DIRS 108201])	B-dot	Based on data from Sanchez et al. (1985 [DIRS 107213])
U(VI) – use for Pu(VI), Np(VI) also								
Turner and Sassman (1996 [DIRS 179618])	goethite	DLM/1	2.31	7.35 -9.17	XOH- UO ₂ (OH) ₄ ²⁻ XOH ₂ - UO ₂ (CO ₃) ₂ ⁻ XOH ₂ - UO ₂ (CO ₃) ₃ ⁻³ XOH ₂ - (UO ₂) ₂ CO ₃ (OH) ₃	Grenthe et al. (1992 [DIRS 101671])	Davies	Multiple fits to data of Tripathi (1983 [DIRS 113425]) and His and Langmuir (1985 [DIRS 106131]) possible, no spectra; no CO ₂ sorption; fit to data of Tripathi stressed for CO ₂ -free system (p. 321); 4 species needed for CO ₂ system

Table J-2. Summary of Surface Complexation Constants (Continued)

Ref	Solid	Model/# of Sites	N _s sites nm ⁻²	Surface acidity constants: log K ⁺ log i ⁻	Surface species	Aqueous model	Activity coefficient model	Comments
Th(IV) – use for U(IV) also								
Cromières et al. (1998 [DIRS 179616])	hematite	DLM/1	1.22 From 38.4 μeq/g; SA = 19 m ² g ⁻¹	Own work in previous publications; 0.01M NaCl 7.4 -8.1	FeOH-Th ⁴⁺ FeO-Th(OH) ₂ ⁺ FeO-Th(OH) ₄ ⁻	Baes and Mesmer (1976 [DIRS 157860])	SIT	Two sets of K _s ; depend on aqueous model; B&M preferred; low CO ₂ system
Analogous for Am(III) – use for Pu(III), Np(III) also								
Pepper et al. (2006 [DIRS 179622]) La(III)	goethite	DLM/2	1.78 w/s = 40	Turner and Sassman (1996 [DIRS 179618])	(s)FeO-La ²⁺ (w)FeO-LaOH ⁺	Haas et al. (1995 [DIRS 179671])	FITEQL	Suggested model assuming weak site dominates above pH=5
Naveau et al. (2005 [DIRS 173018]) Eu(III)	goethite	DLM/1	1.8	Own model 6.53 -7.54	X-OHEu ³⁺ X-OEu(OH) ₂	JCHESS/ FITEQL3.2	JCHESS	Alternate model; Eu(III); Non electrolyte model differs from models with background NaCl, NaNO ₃ , KNO ₃ ; low CO ₂
Ni(II)								
Dzombak and Morel (1990 [DIRS 105483])	ferrhydrite	DLM/2	2.25 SA = 600 m ² g ⁻¹	From Dzombak and Morel (1990 [DIRS 105483]) 7.29, -8.93	(s)FeO-Ni ⁺ (w)FeO-Ni ⁺⁺	Baes and Mesmer (1976 [DIRS 157860])	Davies	K ₂ Estimated by LFER (Table 10.5, Dzombak and Morel 1990 [DIRS 105483])
Carbonate								
Appelo et al. (2002 [DIRS 168168])	ferrhydrite	DLM/1	2.25 SA = 600 m ² g ⁻¹	From Dzombak and Morel (1990 [DIRS 105483]) 7.29, -8.93	Hfo_wOCO ₂ ⁻ Hfo_wOCO ₂ H	PHREEQC-2	Debye Hückel model in PHREEQC-2	Assume CO ₂ binds only to weak site of Dzombak and Morel (1990 [DIRS 105483]) 2-site model

Table J-3. Summary of Surface Speciation Models Reviewed

Ref	Solid	Model/ # of Sites	N _s sites nm ⁻²	Surface acidity	Surface species	Aqueous model	Activity coefficient model	Comments
Np(V)O ₂ ⁺								
Wang (2001 [DIRS 176816])	goethite	DLM/1	2.31	Turner and Sassman (1996 [DIRS 179618])	XOH-NpO ₂ ⁺ XO-NpO ₂ OH-	Fuger (1992 [DIRS 108201])	B-dot	
Wang (2001 [DIRS 176816])	ferrihydroxide	DLM/1	2.31	Turner and Sassman (1996 [DIRS 179618])	XO-NpO ₂	Fuger (1992 [DIRS 108201])	B-dot	
Richter (2005 [DIRS 180019])	hematite	DLM/1	12.05	Averages from multiple data sets	FeONpO ₂ FeONpO ₂ (O ₂ COH) ₂ ²⁻	Guillaumont et al. (2003 [DIRS 168382])	Davies	Need ternary carbonate complex
Zavarin (2004 [DIRS 181272])	goethite	NEM/1	2.31	Dzombak and Morel (1990 [DIRS 105483])	FeOHNpO ₂ ⁺ FeOHNpO ₃ ⁻	GEMBOCHS	Davies	Single site NEM using FITEQL and visual acceptance criteria
Mariner and Jackson (1993 [DIRS 181188])	HFO	DLM/2 or 1	2.31 w/s = 40	Dzombak and Morel (1990 [DIRS 105483])	SOHNpO ₂ (OH)	Lemire and Garisto (1989 [DIRS 106580]) AECL	MINTEQA	1 site for Np(V) used; Np data from Girvin et al. (1991 [DIRS 180108])
Np(IV)								
Mariner and Jackson (1993 [DIRS 181188])	HFO	DLM/2 or 1	2.31 w/s = 40	Dzombak and Morel (1990 [DIRS 105483])	SONp ³⁺ SONpOH ²⁺ SONp(OH) ₃ SONp(OH) ₄ ⁻	Lemire and Garisto (1989 [DIRS 106580]) AECL	MINTEQA	1 site for Np(IV) used; Pu data from Sanchez et al. (1985 [DIRS 107213]) fitted with FITEQL with sorption edge shifted 0.56 pH units based on diff with K ₁₁

Table J-3. Summary of Surface Speciation Models Reviewed (Continued)

Ref	Solid	Model/ # of Sites	N_s sites nm^{-2}	Surface acidity	Surface species	Aqueous model	Activity coefficient model	Comments
Np(III)								
Mariner and Jackson (1993 [DIRS 181188])	HFO	DLM/2 or 1	2.31 w/s = 40	Dzombak and Morel (1990 [DIRS 105483])	SONp^{2+}	Lemire and Garisto (1989 [DIRS 106580]) AECL	MINTEQ2A	1 strong site for Np(III) used; LFER for strong site.
Pu(IV)								
Wang et al. (2001 [DIRS 176816])	goethite	DLM/1	2.31	Turner and Sassman (1996 [DIRS 179618])	XO-Pu^{3+} XO-PuOH^{2+} XO-Pu(OH)_3	Fuger (1992 [DIRS 108201])	B-dot	Based on data from Sanchez et al. (1985 [DIRS 107213])
Mariner and Jackson (1993 [DIRS 181188])	HFO	DLM/2 or 1	2.31 w/s = 40	Dzombak and Morel (1990 [DIRS 105483])	SOPu^{3+} SOPuOH^{2+} SOPu(OH)_3 SOPu(OH)_4	Lemire and Garisto (1989 [DIRS 106580]) AECL	MINTEQ2A	1 site for Pu(IV) used; data from Sanchez et al. (1985 [DIRS 107213]) fitted with FITEQL
Zavarin (2004 [DIRS 181272])	goethite	NEM/1	2.31	Dzombak and Morel (1990 [DIRS 105483])	FeOHPuO_2^{2+} FeOHPuO_2	GEMBOCHS	Davies	Single site NEM using FITEQL and visual acceptance criteria
Pu(III)								
Mariner and Jackson (1993 [DIRS 181188])	HFO	DLM/2 or 1	2.31 w/s = 40	Dzombak and Morel (1990 [DIRS 105483])	SOPu^{2+}	Lemire and Garisto (1989 [DIRS 106580]) AECL	MINTEQ2A	1 strong site for Pu(III) used; LFER for strong site in D&M for cation assumed(?)

Table J-3. Summary of Surface Speciation Models Reviewed (Continued)

Ref	Solid	Model/ # of Sites	N_s sites nm^{-2}	Surface acidity	Surface species	Aqueous model	Activity coefficient model	Comments
Pu(V)O₂⁺								
Wang et al. (2001 [DIRS 176816])	goethite	DLM/1	2.31	Turner and Sassman (1996 [DIRS 179618])	XOH-PuO ₂ ⁺ XO-PuO ₂ XO-PuO ₂ OH ⁻	Fuger (1992 [DIRS 108201])	B-dot	Based on data from Sanchez et al. (1985 [DIRS 107213])
Zavarin (2004 [DIRS 181272])	goethite	NEM/1	2.31	Dzombak and Morel (1990 [DIRS 105483])	FeOHPuO ₂ ⁺ FeOHPuO ₃ ⁻	GEMBOCHS	Davies	Single site NEM using FITEQL and visual acceptance criteria
U(VI)								
Waite et al. (1994 [DIRS 108746])	ferrihydroxide	DLM/2	Total = 0.875 mol mol ⁻¹ Fe Fe _s = 1.8 mmol mol ⁻¹ Fe	Davis (1978 [DIRS 182146])	Fe _s O ₂ -UO ₂ Fe _w O ₂ -UO ₂ Fe _s O ₂ ⁻ UO ₂ CO ₃ ²⁻ Fe _w O ₂ ⁻ UO ₂ CO ₃ ²⁻	Grethe et al. (1992 [DIRS 101671]); Tripathi (1984 [DIRS 113425])	Davies	Includes Fe-CO ₃ H and Fe-CO ₃ ⁻ surface species
Turner and Sassman (1996 [DIRS 179618])	goethite	DLM/1	2.31	Turner and Sassman (1996 [DIRS 179618])	Simplest: XOH- UO ₂ (OH) ₂ XOH - UO ₂ CO ₃ Consistent: XOH- UO ₂ (OH) ₄ ²⁻ XOH ₂ - UO ₂ (CO ₃) ₂ ⁻ XOH ₂ - UO ₂ (CO ₃) ₃ ⁻³ XOH ₂ - (UO ₂) ₂ CO ₃ (OH) ₃	Grethe et al. (1992 [DIRS 101671])	Davies	Multiple fits possible, choice based on parsimony; no spectra; no CO ₂ sorption; fit to data of Tripathi stressed for CO ₂ free system (p. 321); 4 species needed for CO ₂ system

Table J-3. Summary of Surface Speciation Models Reviewed (Continued)

Ref	Solid	Model/ # of Sites	N_s sites nm^{-2}	Surface acidity	Surface species	Aqueous model	Activity coefficient model	Comments
Wazne et al. (2003 [DIRS 180093])	ferrhydrite	DLM/1	Total = 0.875 mol/mol Fe	Waite et al. (1994 [DIRS 108746])	SO- UO_2^+ SO- UO_2CO_3^- SO- $\text{UO}_2(\text{CO}_3)_2^{3-}$	MINTEQA2, Grenthe et al. (1992 [DIRS 101671]), Waite et al. (1994 [DIRS 108746]), Tripathi (1984 [DIRS 113425])	Davies	Species supported by zeta, FTIR; carbonate sorption
Lenhart and Honeyman (1999 [DIRS 179672])	hematite	TLM/2	2.31 $\text{Fe}_w/\text{Fe}_s = 325$	Waite et al. (1994 [DIRS 108746])	See Waite	Grenthe et al. (1992 [DIRS 101671])	Davies	TLM model
Van der Lee and Lomenech (2004 [DIRS 180973])	goethite	DLM/1	1.56	Own constants	(Fe-O) $_2\text{UO}_2$	Grenthe et al. (1992 [DIRS 101671])	CHES	Others SCMs available; no CO_2
Missana et al. (2003 [DIRS 173759]) JCIS	goethite	DLM/1	2.2	Own constants	1. FeO- UO_2^+ FeO- UO_2OH or 2. (Fe-O) $_2\text{UO}_2$	Grenthe et al. (1992 [DIRS 101671])	CHES	Model 1 works best; no CO_2 ; NEM did not work as well.
Th(IV)								
Murphy et al. (1999 [DIRS 179553])	hematite	TLM/1	2.31	Own data	FeOH- Th^{4+}	Baes and Mesmer (1976 [DIRS 157860]); Östholts (1995 [DIRS 179704])	Davies	TLM model CO_2 sorbs;
Cromières et al. (1998 [DIRS 179616])	hematite	DLM/1	38.4 $\mu\text{eq/g}$; SA = 19 $\text{m}^2 \text{g}^{-1}$	Own work in previous publications	FeOH- Th^{4+} FeO- $\text{Th}(\text{OH})_2^+$ FeO- $\text{Th}(\text{OH})_4^-$	Baes and Mesmer (1976 [DIRS 157860])	SIT	Two sets of Ks; depend on aqueous model; B&M preferred; low CO_2 system

Table J-3. Summary of Surface Speciation Models Reviewed (Continued)

Ref	Solid	Model/ # of Sites	N _s sites nm ⁻²	Surface acidity	Surface species	Aqueous model	Activity coefficient model	Comments
La Flamme and Murray (1987 [DIRS 147523])	goethite	TLM/1	See reference	See reference	5 hydrolyzed species; ternary Th carbonate complexes?	See reference	See reference	TLM model; CO ₂ sorbs; low solids concentration
Hunter et al. (1988 [DIRS 147464])	goethite	TLM/1	See reference	See reference	FeO ⁻ Th(OH) ₂ ²⁺ FeO ⁻ Th(OH) ₃ ⁺ FeO ⁻ Th(OH) ₄	Baes and Mesmer (1976 [DIRS 157860])	See reference	TLM model Possible importance of Th-SO ₄ pair; other surface species at pH>6?
Quigley et al. (1996 [DIRS 179706])	hematite	TLM/1	See reference	Own work	FeO-Th ³⁺	Baes and Mesmer (1976 [DIRS 157860]); Østhols (1995 [DIRS 179704])	Davies	TLM model Couldn't fit pH >3; CO ₂ sorbed; irreversible sorption?
Am(III)								
Degueldre et al. (1994 [DIRS 174069])	hematite	NES/1	3 sites nm ⁻²	NA	Multiple ternary	See reference	NA?	NES model; calculates K _p
Naveau et al. (2005 [DIRS 173018]) Eu(III)	goethite	DLM/1	1.8 sites nm ⁻²	Own model	X-OHEu ³⁺ X-OEu(OH) ₂	JCHESS/ FITEQL3.2	JCHESS	Eu(III); Non electrolyte model differs from models with background NaCl, NaNO ₃ , KNO ₃ ; low CO ₂

Table J-3. Summary of Surface Speciation Models Reviewed (Continued)

Ref	Solid	Model/ # of Sites	N_s sites nm^{-2}	Surface acidity	Surface species	Aqueous model	Activity coefficient model	Comments
Pepper et al. (2006 [DIRS 179622]) La(III)	goethite	DLM/2	1.78 sites nm^{-2} w/s = 40	Turner and Sassman (1996 [DIRS 179618])	(s)FeO-La ²⁺ (w)FeO-LaOH ⁺	Haas et al. (1995 [DIRS 179671])	FITEQL	La(III)
Alonso and Degueldre (2003 [DIRS 179663])	FeOOH	NES	3 sites nm^{-2}	See reference	FeO-Am ²⁺ FeO-AmOH ⁺	See reference	none	Has correlation between SCM and hydrolysis

NOTE: "w/s" = ratio of weak/strong sites

J.7. CONCLUSIONS

The set of constants provided in this appendix are good for a first set of sensitivity analysis calculations but may suffer from the use of analog elements used to maximize internal self-consistency. Errors in the calculated speciation from mixing values from different reaction networks in this set of constants are difficult to estimate without making ad hoc assumptions.

Alternative approaches may improve model performance. The first step would be to calculate a new set of LFERs based on Hard-Soft Acid-Base Theory (HSAB) for a single-site model for sorption of monodentate complexes onto goethite by combining data from different ferric iron substrates:

1. Plot $\log K_{DLM} + \log K_2$ vs $\log K_{11}$ for Eu^{3+} , La^{3+} , Cr^{3+} , Am^{3+} to obtain regression line and calculate values for Np^{3+} and Pu^{3+} for goethite.
2. Plot $\log K_{DLM} + \log K_{2a}$ vs $\log K_{11}$ for Th^{4+} , Pu^{4+} , to obtain regression line and calculate values for U^{4+} onto goethite.
3. Plot $\log K_{DLM} + \log K_{2a}$ vs $\log K_{11}$ for divalent cations (Hg, Cu, Zn, Ni, Cd, Ag) listed in Dzombak and Morel (1990 [DIRS 105483], Table 10.5) that fit best along the LFER, to obtain regression line and calculate values for Np(VI)O_2^{2+} , Pu(VI)O_2^{2+} onto goethite.

Alternative models might also benefit from a refined set of constants that include sorption of ternary surface actinide-carbonato complexes. It may also help to use smaller reaction networks using 2-site DLMS to consider competition under conditions with higher P_{CO_2} than the CO_2 -free or low P_{CO_2} conditions used in many of the cited studies from which the constants recommended in Table 4.1-17 were obtained.

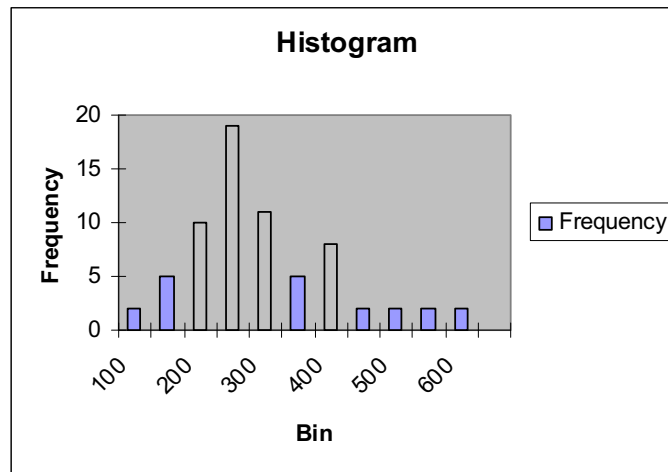
APPENDIX K

SPECIFIC SURFACE AREA DISTRIBUTIONS FOR HFO AND GOETHITE

SPECIFIC SURFACE AREA DISTRIBUTIONS FOR HFO AND GOETHITE

HFO SURFACE AREA

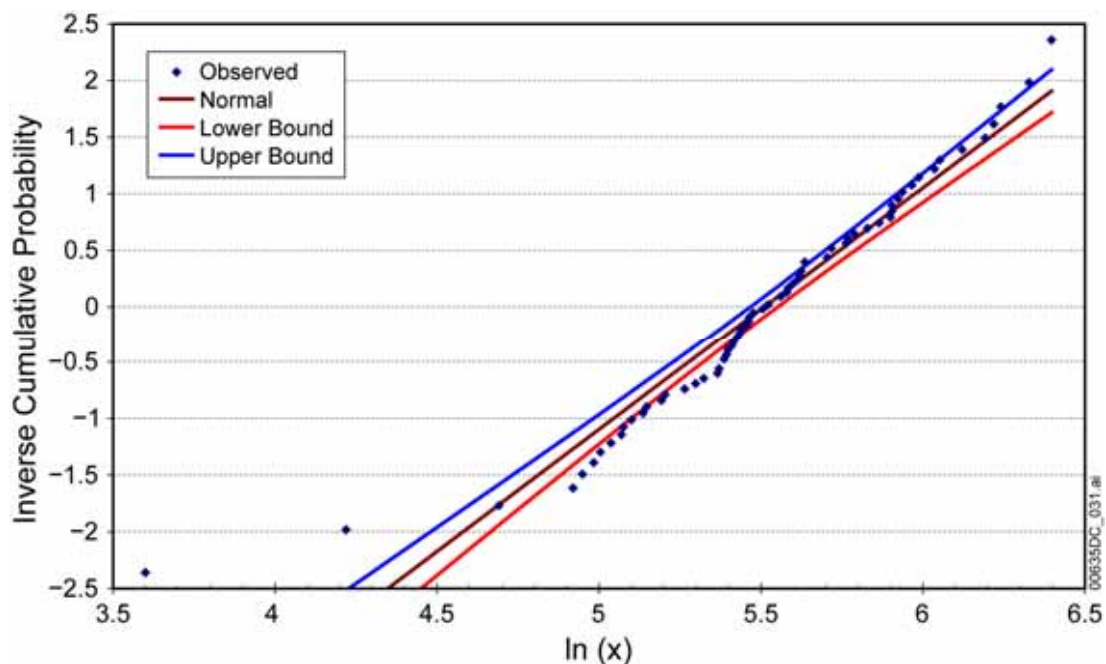
The tabulated data contained in Table 4.1-14 and reappearing in Excel file *HFO_Sp_Surf_Area_Analysis 7-12-2007.xls* (DTN: SN0703PAEBSRTA.001) is analyzed. Initial inspection of the histogram (Figure K-1) leads to a lognormal distribution as a good candidate for a distribution fit for the data.



Source: Output DTN: SN0703PAEBSRTA.001, file *HFO_Sp_Surf_Area_Analysis 7-12-2007.xls*, worksheet "fit".

Figure K-1. Histogram of HFO Specific Surface Area Data

Thus the data set was transformed to natural log space, and a Ryan-Joiner test for normality was performed. The normality test failed, so a Normality Plot with confidence bands was constructed to find suspected outliers.



Source: Output DTN: SN0703PAEBSRTA.001, file *HFO_Sp_Surf_Area_Analysis 7-12-2007.xls*, worksheet "plot".

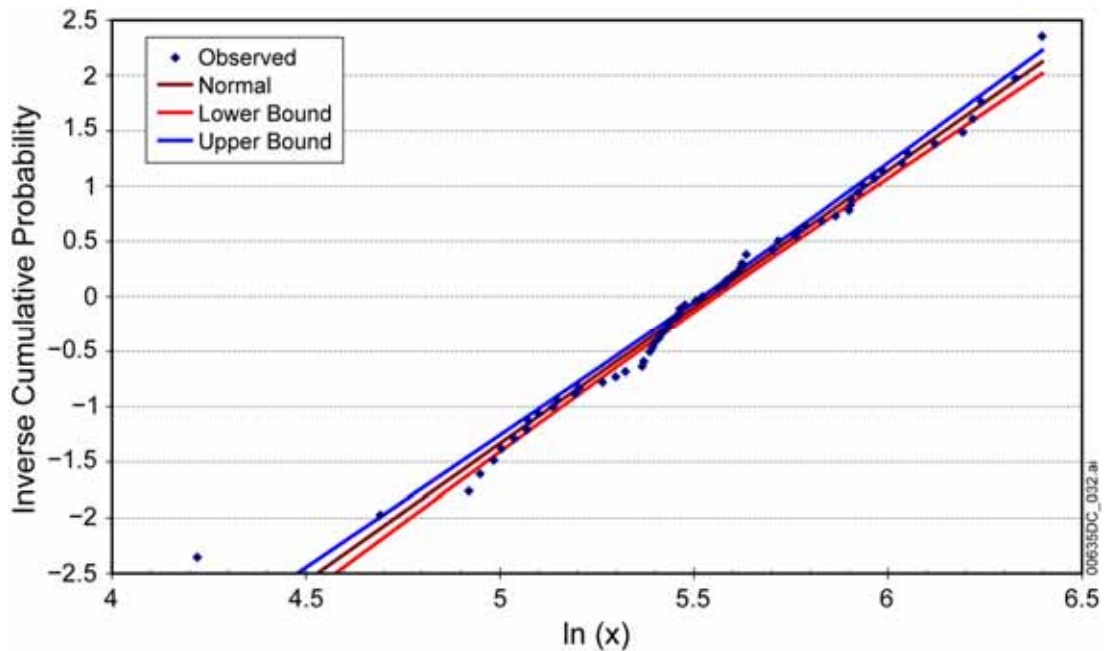
Figure K-2. Normality Plot of HFO Specific Surface Area Data

The model parameters (mean and standard deviation) were estimated as shown in Table K-1 in natural log space using the method of Least Squared error Estimation by means of the Excel "Solver" tool for later comparison.

Table K-1. HFO Specific Surface Area Statistical Parameters

Parameter	Natural Log Space	Real Space
Mean	5.532	274.1
Standard Deviation	0.404	115.4

Visual inspection of the data suggested that the lower two values may be outliers. An Outlier Test was performed on the entire dataset. For this, the interquartile range, ΔY (the range between the first quartile and the third quartile), of the dataset was obtained. It was found that all except two data points fall within the $1.5\Delta Y$ of the nearest quartile. One of the two outlier data points fell more than $3\Delta Y$ from the nearest quartile and was classified as an "extreme outlier," while the other data point was classified as a "mild outlier." The extreme outlier was removed from the data set, and the normality test was performed again for the remaining data.



Source: Output DTN: SN0703PAEBSRTA.001, file *HFO_Sp_Surf_Area_Analysis 7-12-2007.xls*, worksheet "rplot".

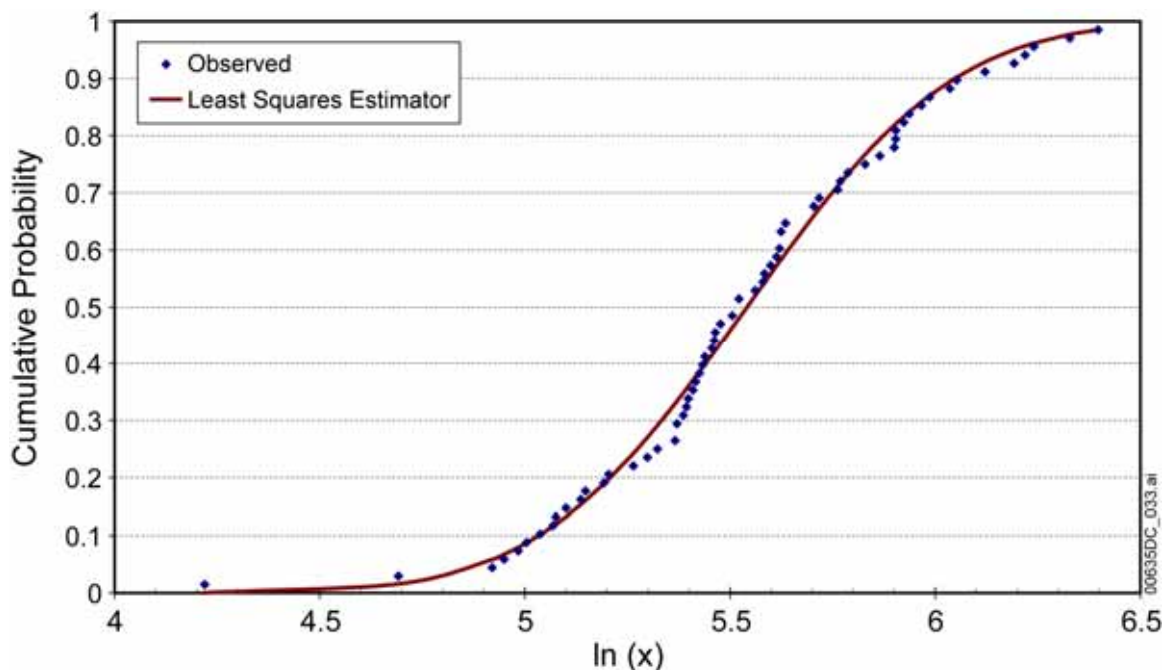
Figure K-3. Normality Plot of HFO Specific Surface Area Data with Extreme Outlier Removed

The remaining data were shown not to deviate significantly from the normality assumption. As shown on Figure K-3, eliminating the extreme outlier resulted in tighter confidence bands and inclusion of more observations within the band limits. The model parameters (mean and standard deviation) were then estimated in natural log space using the method of Least Squared error Estimation by means of the Excel "Solver" tool and are shown in Table K-2.

Table K-2. HFO Specific Surface Area Statistical Parameters with Extreme Outlier Removed

Parameter	Natural Log Space	Real Space
Mean	5.541	275.6
Standard Deviation	0.396	113.4

A plot of the observations and fitted distribution with $R^2 = 0.981$ is shown on Figure K-4.



Source: Output DTN: SN0703PAEBSRTA.001, file *HFO_Sp_Surf_Area_Analysis 7-12-2007.xls*, worksheets "fit" and "plot."

Figure K-4. Lognormal Fitted Distribution of HFO Specific Surface Area Data

Conclusion:

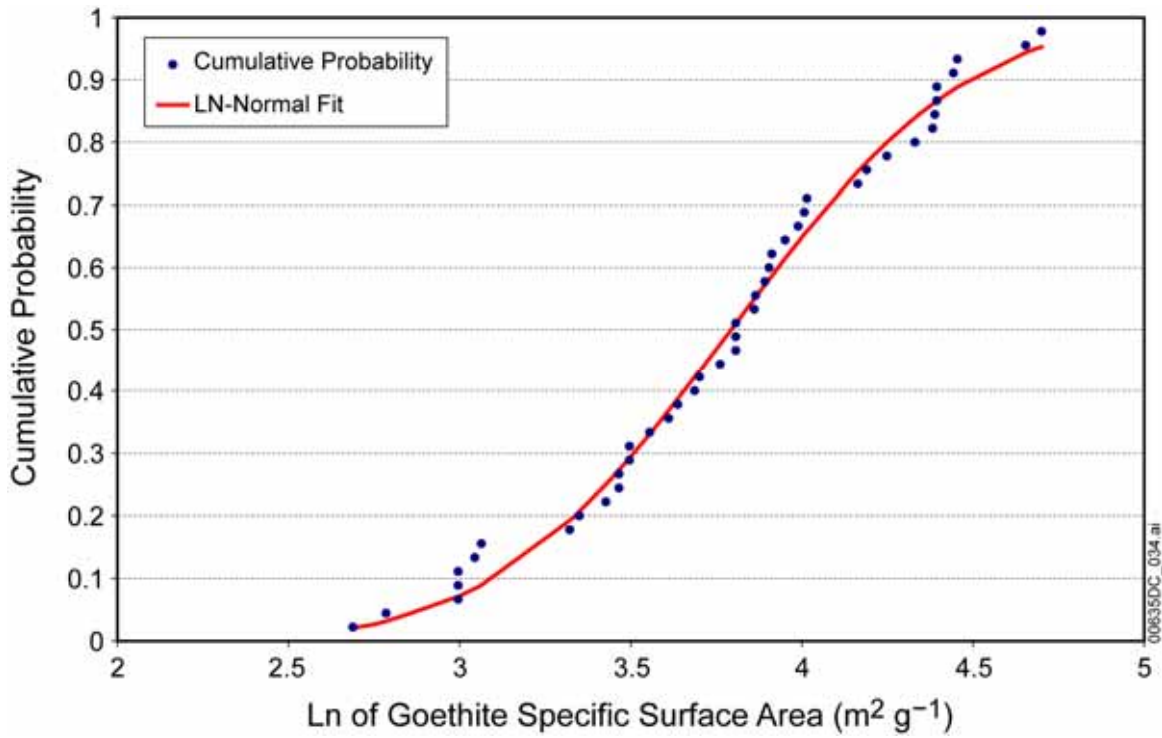
Although it appears that the model parameters had not changed significantly, they were changed enough to challenge the appropriateness of the distribution fit. This study closes with the recommendation of eliminating the lowest value from the data set, since it has qualified as an extreme outlier when compared to the rest of the data set.

GOETHITE SURFACE AREA

The tabulated data for goethite-specific surface area contained in Table 4.1-12 were observed to fit a lognormal distribution in DTN: SN0703PAEBSRTA.001, Excel file *Goethite Specific Surface Area 7-12-2007.xls*. Statistical parameters for the fit are shown in Table K-3. The lognormal fit to the data, with $R^2 = 0.996$, is shown on Figure K-5. The data were fit to a lognormal distribution by using the Excel "Solver" tool to minimize the sum of squared residuals (i.e., the square of the difference between the fitted curve and the measured value).

Table K-3. Goethite Specific Surface Area Statistical Parameters

Parameter	Natural Log Space	Real Space
Mean	3.793	51.42
Standard Deviation	0.543	30.09



Source: Output DTN: SN0703PAEBSRTA.001, file *Goethite specific surface area 7-12-2007.xls*.

Figure K-5. Lognormal Fitted Distribution of Goethite Specific Surface Area Data

INTENTIONALLY LEFT BLANK

APPENDIX L

REPRESENTATION OF RADIAL DIFFUSIVE TRANSPORT USING CARTESIAN GRID GEOMETRY

REPRESENTATION OF RADIAL DIFFUSIVE TRANSPORT USING CARTESIAN GRID GEOMETRY

Within the EBS, the waste form and corrosion products spatial domains are conceptualized using radial geometry. In order to show how the radial transport is captured by Cartesian geometry, it is necessary to demonstrate how to describe the diffusive areas and diffusive path lengths that determine the diffusive transport. With this objective in mind, a simple diffusive transport model is developed with finite difference discretization. The diffusive areas and path lengths are described and a computational solution is obtained that allows comparison with a known analytical solution.

Consider diffusive mass transport with diffusivity D in a region described by cylindrical coordinates (r, θ, z) with $0 \leq r \leq a$, $0 \leq \theta < 2\pi$, and $0 \leq z \leq L$. Assume initial and boundary conditions are such that there is symmetry in θ and that no diffusion occurs in the z -direction. The cylinder in the z -direction acts like an infinite cylindrical region or for a finite cylinder we assume there are no end effects. The one-dimensional radial diffusive transport in this cylindrical region is described by:

$$\frac{\partial c}{\partial t} = D \nabla^2 c = \frac{D}{r} \frac{\partial}{\partial r} \left(r \frac{\partial c}{\partial r} \right), \text{ for } 0 \leq r \leq a. \quad (\text{Eq. L-1})$$

A cell-centered finite difference discretization of the radial diffusion equation, Equation L-1, is considered. A discretization, which is first-order backward in time for the time derivative and second-order implicit for the spatial derivatives, is consistent with the discretization in the TSPA GoldSim model. The finite difference approximation is:

$$\frac{c_j^{n+1} - c_j^n}{\Delta t} = \frac{D}{r_j \Delta r_j} \left[r_{j+1/2} \left(\frac{c_{j+1}^{n+1} - c_j^{n+1}}{\Delta r_{j+1/2}} \right) - r_{j-1/2} \left(\frac{c_j^{n+1} - c_{j-1}^{n+1}}{\Delta r_{j-1/2}} \right) \right], \quad (\text{Eq. L-2})$$

where

- n = time index
- j = cell or spatial index
- r_j = center of cell j
- Δr_j = length of cell j
- $r_{j\pm 1/2}$ = interface location between cell j and cells $j \pm 1$
- $\Delta r_{j\pm 1/2}$ = radial length from center of cell j to center of cells $j \pm 1$.

If the diffusive flux terms in Equation L-2 are multiplied and divided by the constant factor $2\pi L$, then the discretized Equation L-2 is:

$$\frac{c_j^{n+1} - c_j^n}{\Delta t} = \frac{D}{2\pi L r_j \Delta r_j} \left[2\pi L r_{j+1/2} \left(\frac{c_{j+1}^{n+1} - c_j^{n+1}}{\Delta r_{j+1/2}} \right) - 2\pi L r_{j-1/2} \left(\frac{c_j^{n+1} - c_{j-1}^{n+1}}{\Delta r_{j-1/2}} \right) \right]. \quad (\text{Eq. L-3})$$

The term in the denominator is the volume of the j -cell:

$$\begin{aligned} V_j &= \pi (r_{j+1/2}^2 - r_{j-1/2}^2) L \\ &= \pi L (r_{j+1/2} + r_{j-1/2}) (r_{j+1/2} - r_{j-1/2}) \\ &= 2\pi L \frac{r_{j+1/2} + r_{j-1/2}}{2} \Delta r_j \\ &= 2\pi L r_j \Delta r_j \\ &= A_j \Delta r_j, \end{aligned} \quad (\text{Eq. L-4})$$

where the diffusive area of cell j is:

$$A_j = 2\pi L r_j. \quad (\text{Eq. L-5})$$

Define the diffusive area between cells as:

$$A_{j\pm 1/2} = 2\pi L r_{j\pm 1/2}. \quad (\text{Eq. L-6})$$

The discretized Equation L-3 is written as:

$$\frac{c_j^{n+1} - c_j^n}{\Delta t} = \frac{D}{A_j \Delta r_j} \left[A_{j+1/2} \left(\frac{c_{j+1}^{n+1} - c_j^{n+1}}{\Delta r_{j+1/2}} \right) - A_{j-1/2} \left(\frac{c_j^{n+1} - c_{j-1}^{n+1}}{\Delta r_{j-1/2}} \right) \right]. \quad (\text{Eq. L-7})$$

From Equation L-7, the diffusive flux across the $j + 1/2$ interface is:

$$F_{j+1/2}^{n+1} = D \frac{A_{j+1/2}}{\Delta r_{j+1/2}} (c_{j+1}^{n+1} - c_j^{n+1}). \quad (\text{Eq. L-8})$$

The continuity of the diffusive flux across the cell interfaces requires the evaluation of the interface terms $\frac{A_{j\pm 1/2}}{\Delta r_{j\pm 1/2}}$ as the harmonic average of the adjacent cell terms:

$$\frac{A_{j\pm 1/2}}{\Delta r_{j\pm 1/2}} = \frac{2}{\frac{\Delta r_j}{A_j} + \frac{\Delta r_{j\pm 1}}{A_{j\pm 1}}}. \quad (\text{Eq. L-9})$$

The one-dimensional diffusion equation in Cartesian space with diffusive area a function of the Cartesian variable x is:

$$A(x) \frac{\partial c}{\partial t} = D \frac{\partial}{\partial x} \left(A(x) \frac{\partial c}{\partial x} \right) \quad (\text{Eq. L-10})$$

on the interval $0 \leq x \leq a$. A discretization of the diffusion equation in Cartesian coordinates consistent with that used in the radial form of the transport equation, i.e., first-order backward in time and second-order implicit in space, is:

$$\frac{c_j^{n+1} - c_j^n}{\Delta t} = \frac{D}{A_j \Delta x_j} \left[\frac{A_{j+1/2}}{\Delta x_{j+1/2}} (c_{j+1}^{n+1} - c_j^{n+1}) - \frac{A_{j-1/2}}{\Delta x_{j-1/2}} (c_j^{n+1} - c_{j-1}^{n+1}) \right], \quad (\text{Eq. L-11})$$

where

- n = time index
- j = cell or spatial index
- x_j = center of cell j
- Δx_j = length of cell j
- $x_{j\pm 1/2}$ = interface location between cell j and cells $j \pm 1$
- $\Delta x_{j\pm 1/2}$ = length from center of cell j to center of cells $j \pm 1$.

Now define the diffusive area in cell j as:

$$A_j = 2\pi L x_j. \quad (\text{Eq. L-12})$$

If the Cartesian independent variable x is identified with the radial variable r , then the discretization in Cartesian coordinates, Equation L-11, is the same as the radial discretized Equation L-7. If $x = r$ the diffusive lengths in the Cartesian grid are the same as the diffusive lengths in the radial grid. The diffusive area given by Equation L-12 is identical to the radial diffusive area as given by Equation L-5. Also, the cell lengths are identical, $\Delta x_j = \Delta r_j$, and consequently, the Cartesian volume of cell j is $V_j = A_j \Delta x_j$. This is equal to the cell volume for the radial grid given in Equation L-4. Thus, the radial and Cartesian volumes for the cells are the same. Therefore, the Cartesian formulation is identical to the radial formulation if the diffusive areas and lengths are defined appropriately.

A computational example demonstrates the solution of the radial diffusion equation with appropriate Cartesian diffusive areas and lengths. Consider the solution of the radial diffusion equation, Equation L-1, with boundary conditions:

$$c(a,t) = c_a \text{ and } \frac{\partial c}{\partial r}(0,t) = 0, \quad 0 \leq t \leq T, \quad (\text{Eq. L-13})$$

and initial condition

$$c(r,0) = 0, \quad 0 \leq r \leq a. \quad (\text{Eq. L-14})$$

This boundary value problem has an analytic solution given by Carslaw and Jaeger (1959 [DIRS 100968], p. 199, Eq. 10):

$$c(r,t) = c_a \left[1 - 2 \sum_{n=1}^{\infty} \exp\left(-\frac{\beta_n^2 Dt}{a^2}\right) \frac{J_0(r\beta_n/a)}{\beta_n J_1(\beta_n)} \right], \quad (\text{Eq. L-15})$$

where $\beta_n, n = 1, 2, \dots$ are the roots of:

$$J_0(\beta) = 0. \quad (\text{Eq. L-16})$$

A uniform grid of size h for the spatial discretization of the radial geometry determines the radial cell centers as:

$$\begin{aligned} r_1 &= \frac{h}{2} \\ r_{j+1} &= r_j + h, \quad j = 1, \dots, N+1. \end{aligned} \quad (\text{Eq. L-17})$$

The spatial discretization contains N interior cells to the region $0 \leq r < a$. The boundary cell, cell index, $N+1$, is determined so that the cell center is located at the boundary $r = a$, which allows the boundary condition at $r = a$ to be honored. With this spatial discretization the uniform cell length is:

$$h = \frac{a}{N+1/2}. \quad (\text{Eq. L-18})$$

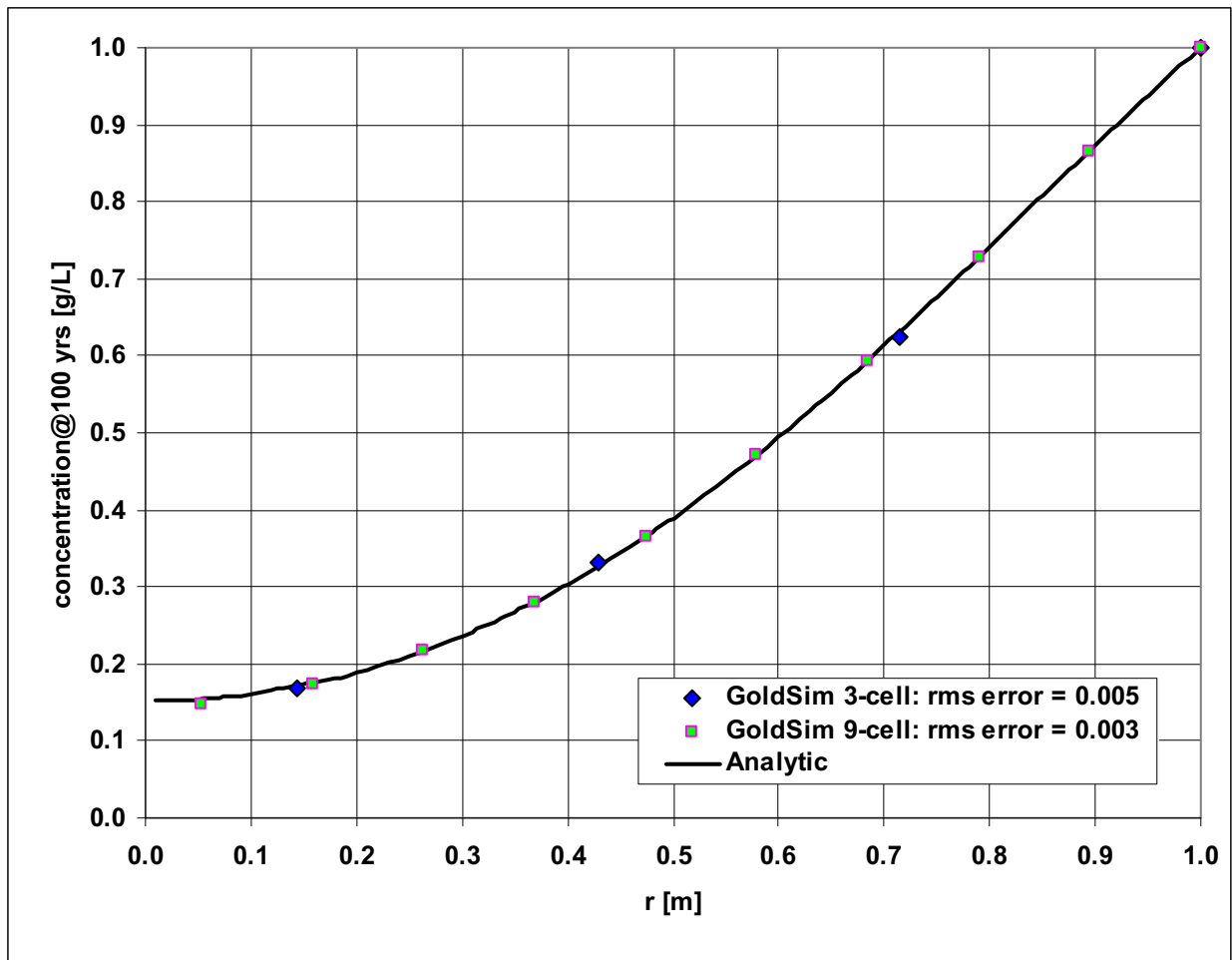
Solutions of the finite difference equation, Equation L-11, with diffusive areas determined by Equation L-12, and satisfying the initial and boundary conditions, are calculated with parameters:

$$\begin{aligned} D &= 0.001 \text{ [m}^2 \text{ yr}^{-1}\text{]} \\ a &= 1.0 \text{ [m]} \\ T &= 100 \text{ [yr]} \end{aligned}$$

$$\Delta t = 0.1 \text{ [yr]}$$

$$c_a = 1.0 \text{ [g m}^{-3}\text{]},$$

and with spatial grid refinement ($N = 3, 9$). GoldSim V. 9.60.100 (2007 [DIRS 181903]) was used to compute the finite difference solutions. The two GoldSim solutions and the analytic solution are shown on Figure L-1. The results show good agreement for the radial diffusion between the finite difference solution and the analytic solution. Convergence with respect to the spatial discretization of the finite difference solution to the analytic solution can be seen in the values for the root mean square error of the approximations on Figure L-1.



Source: Output DTN: SN0703PAEBSRTA.001.

Figure L-1. Radial Diffusion

INTENTIONALLY LEFT BLANK

APPENDIX M

**CRITICAL REVIEW OF THE EBS FLOW MODEL, EBS TRANSPORT MODEL AND
EBS-UZ INTERFACE MODEL**

CRITICAL REVIEW OF THE EBS FLOW MODEL, EBS TRANSPORT MODEL AND EBS-UZ INTERFACE MODEL

M.1 Results of Critical Review of the EBS Flow, Transport, and EBS-UZ Interface Models

A critical review of the EBS flow and transport models and the EBS-UZ interface model was conducted as specified in the TWP (BSC 2006 [DIRS 177739], Section 2.2.3). This model validation approach is justified based on requirements of SCI-PRO-006, Section 6.3.2, where the critical review is listed as an appropriate method for model validation. The results of the critical review of the EBS flow and transport models and EBS-UZ interface are presented in a letter (a facsimile follows).

August 19, 2007

Mr. Jerry McNeish
Bechtel SAIC Company, LLC
Las Vegas, NV

Dear Mr. McNeish:

CRITICAL REVIEW OF ANL-WIS-PA-000001 REV 03F

In this letter, I am documenting my critical review of the referenced document consistent with the procedure *Models* (SCI-PRO-006 REV 5, August 14, 2007) and the BSC *Technical Work Plan for: Near Field Environment: Engineered Barrier System: Radionuclide Transport Abstraction Model Report* (TWP-MGR-PA-000020 REV 3, September 2006).

To confirm the selection of me to do this critical review, I have a Ph.D. in Physical Chemistry and have worked for over 30 years in various aspects of the materials science associated with long-term disposal of high-level wastes. This experience ranges from the development of materials for immobilization of these wastes to the development of the dissolution model for silicate-based glasses. I have not been involved with the development of performance assessment models for use on the Yucca Mountain Project; I am the author of the *Defense HLW Glass Degradation Model* (ANL-ANS-MD-000016). I have been involved with the review of models under the Regulatory Integration Team activities in 2004.

Although I have reviewed the entire document and have comments, I will limit my comments and assessment here to those areas covered in an email from James Schreiber dated 16-August-2007, "RTA model changes – summary."

FLOW MODEL

No changes were made from the previous version of the Radionuclide Transport Abstraction (RTA); no comments shown here.

TRANSPORT MODEL

TWP Task 1.2.1 to develop the temperature dependence of diffusivity in the invert (RTA Sections 6.3.4.1.2 and 7.2.2)

Comments: The temperature dependence has been appropriately incorporated in the calculation of the diffusivity in the invert. This temperature dependence is appropriately validated in Section 7.2.2.

Telephone (509) 376 0677 ■ Email denis.strachan@pnl.gov ■ Fax (509) 376 3108

Mr. Jerry McNeish
August 19, 2007
Page {PAGE}

TWP Task 1.2.2 to revise the calculation of colloid diffusivity (RTA Section 6.3.4.4)

Comments: The revised section is adequate for its intended use.

TWP Task 1.2.3 to revise TSPA implementation of EBS discretization (1-cell vs 2-cell waste package) (throughout, but especially RTA Section 6.5.2); corrosion products water saturation submodel revised as a consequence of redefining the cell contents (RTA Sections 6.3.4.3, 6.5.2.2, and 7.2.1). The other part of the TWP to refine the EBS discretization was deferred.

Comments: Discretization is used to make the mathematics tractable in GoldSim where finite differences are used to solve the differential equations. It requires that the waste package be divided into two domains – a waste form corrosion products domain and a steel corrosion products domain for CSNF and a HLW glass corrosion products domain (sub-domain), DOE SNF corrosion products domain (sub-domain), and steel corrosion products domain for the co-disposal waste package. This discretization is appropriately applied and validated in Section 7.2.1.

TWP Task 1.2.4 to update design information provisionally (RTA Section 4.1.3 and throughout)

Comments: This update has been appropriately carried out.

TWP Task 1.2.6 to verify included FEPs that have been completed with no change to the RTA (Task not completed for this version of the RTA)

TWP Task 1.2.8 to develop corrosion products radionuclide sorption models (RTA Sections 6.3.4.2, 6.5.2.4, and 7.2.3); alternative models from the previous RTA version are retained as alternative conceptual models (RTA Sections 6.6.5 and 6.6.6)

Comments: Transport of radionuclides through the EBS are controlled by the sorption on and desorption from crushed Tuff and waste package corrosion products. In this model, corrosion products consist only of Fe-bearing oxides and oxyhydroxides and, separately, NiO and Cr₂O₃. The sorption and desorption occurs in this model only on the Fe-bearing corrosion products. Two assumptions of note are made – sorption and desorption are for single dissolved species only and the corrosion product of the steel contains only Fe. In the former, no competition for sorption sites is considered either by radionuclides or other dissolved constituents in the migrating water. In the latter, the Ni and Cr in the steel are segregated to NiO and Cr₂O₃. Given the paucity of data on these solid solutions, the model is appropriately developed (Sections 6.3.4.2 and 6.5.2.4) and validated (Section 7.2.3) for the present state of knowledge.

No comments on the retention of the alternative models from the previous version of the RTA.

TWP Task 1.2.9 to develop a waste form rind saturation model (RTA Sections 6.3.4.6, 6.5.2.2, and 7.2.1)

Mr. Jerry McNeish
August 19, 2007
Page {PAGE}

Comments: Overall, the model has been incorporated properly and adequately validated in Section 7.

TWP Task 1.2.10 to develop bounding analyses for the reactive gas flux into the waste package (RTA Section 6.6.2; most of the bounding analyses were delayed to PMA).

Comments: As an initial bounding case, the case presented is adequate for the intended purpose.

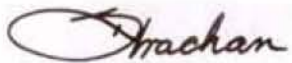
EBS-UZ Interface Model

TWP Task 1.2.5 to revise the EBS-UZ interface model (RTA Sections 6.5.2.6 and 7.3).

Comments: The interface model is adequate for the intended purpose.

If you have questions concerning my comments shown above, please contact me.

Sincerely,



Denis Strachan

M.2 Results of Critical Review of the EBS Flow and Transport Models

A critical review of the EBS flow and transport models was conducted as specified in the TWP (BSC 2006 [DIRS 177739], Section 2.2.3). This model validation approach is justified based on requirements of SCI-PRO-006, Section 6.3.2, where the critical review is listed as an appropriate method for model validation. The results of the critical review of the EBS flow and transport models are presented in a memo (a facsimile follows; “independent model validation review” is now referred to as a “critical review” in SCI-PRO-006).



Interoffice Memorandum

QA: QA

To: James D. Schreiber, Ernest Hardin **No.:** 0801056250
From: James A. Blink *JAB* **Date:** 16 Aug 05
Re: Independent Model Validation Review of ANL-WIS-PA-000001 Rev 2 **CC:** W. J. Duffy, E. F. Loros, Roberta Stambaugh

This IOM was included in draft form in the 2.14 review of the subject AMR. It was finalized prior to final checking.

I have completed the independent model validation review of the “*Engineered Barrier System Radionuclide Transport Abstraction*” AMR, ANL-WIS-PA-000001 Rev 2.

This review was conducted in accordance with “*Technical Work Plan for: Near-Field Environment and Transport: Engineered Barrier System: Radionuclide Transport Abstraction Model Report Integration*”, TWP-MGR-PA-000020 Rev 1.

REVIEWER QUALIFICATIONS:

I have met the qualification requirements to do this review, as established by Section 2.2.4 of the cited TWP, as follows:

- “Reviewer shall not have contributed to the development of model assumptions, parameters, or implementing algorithms.” I was not on the author team and have not had a management relationship with that team for the past three years.
- “Reviewer shall have an appropriate technical background (i.e., advanced degree in an appropriate technical field) and demonstrated expertise in fluid flow and transport of radionuclides in porous media.” I have a B.S. in Engineering Science from the University of Nevada, Reno; an M.S. in Nuclear Engineering from the Georgia Institute of Technology, and a Ph.D. in Engineering from the University of California – Davis. In addition to a variety of courses in physics and engineering that are pertinent to this subject, my nuclear engineering coursework included formal training in neutron transport, which uses the same mathematical methods as this AMR. Further, I have over 33 years of engineering experience in the U.S. Army and at Lawrence Livermore National Laboratory. That experience includes over 15 years of experience on the Yucca Mountain Project in a variety of technical areas, including the Engineered Barrier System and Design Basis

0801056250

Page 2

Models. My education and experience are included in records submitted to the Record Information System by Lawrence Livermore National Laboratory.

REVIEW REQUIREMENTS:

The TWP requires me, as the independent model validation technical reviewer, to do the following:

- “Review the validation criteria in this TWP.” I have reviewed those criteria, which are listed below.
- “Review relevant sections of the RTA report and meet with the document author and representatives from TSPA organization in order to obtain a full understanding of the model(s) and TSPA implementation.” I have read the entire report in detail, with the exception of the spreadsheet details listed in Appendices A, C, D, E, F, and G. I have had a number of discussions with the author (J. Schreiber) and the TSPA Analyst (S. Mehta). The author was also an appropriate TSPA-implementation point of contact for this AMR because the implementation was controlled using one or more Parameter Entry Forms accepted by the author, the TSPA implementing analyst and the TSPA Inputs Manager.
- “Assess whether or not the model(s) as documented in the RTA report meet the validation criteria.” My assessment is documented below in this memorandum.
- “Assess whether or not the model(s) are adequate for their intended use, meet with the author to resolve comments, and recommend actions, as appropriate, to resolve any inadequacies found as part of the review.” My assessment is documented below in this memorandum.
- “Document this review process as a memo to be included in the records package for the RTA report.” My review is documented in this memorandum.

REVIEW CRITERIA:

The TWP specifies the following validation criteria for the EBS Flow Model and the EBS Transport Model: “Criteria ... are as follows. Each shall be confirmed by the independent model validation technical reviewer.”

- “The approach and algorithms described in the document and provided to TSPA capture all known flow pathways into and from the EBS components.” [Flow Model]
- “The approach and algorithms described in the document and provided to TSPA address all known modes of radionuclide transport within and from the EBS components.” [Transport Model]
- “Modeling assumptions are clearly defined, discussed, and justified as appropriate for the intended use of the model.” [Both models]

0801056250

Page 3

- “Uncertainties in parameters, processes, and assumptions are sufficiently described, and impacts of these uncertainties discussed.” [Both models]
- “The overall technical credibility of the approach, including assumptions, parameters, equations, and the TSPA implementation, are sufficient for the model’s intended use.” [Both models]

The TWP also includes a separate criterion for the EBS-UZ Interface Model, which was reviewed by another reviewer in Revision 01 of the AMR. I have read the memorandum of that review which was included in the draft of Revision 02, and concur with it. In addition, my review of the Flow Model includes its lower boundary condition, which is described as the EBS-UZ Interface Model in the AMR and TWP.

CONCEPTUAL MODEL:

Based on the discussion below, I conclude that the conceptual models for EBS Flow, EBS Transport, and the EBS-UZ Interface are technically credible, are appropriate for their intended TSPA use, and that they capture the known flow pathways and transport modes.

Sections 6.1.2 and 6.7.1 state that this AMR applies only to the nominal scenario class, and it cites igneous and seismic AMRs to be used for the igneous and seismic scenario classes. It then discusses how those AMRs calculate EBS Flow and Transport, as follows: The igneous eruption modeling case results in waste being moved by the event to the mountain surface, making the EBS flow and transport models non-relevant. The igneous intrusion modeling case destroys the drip shield and waste packages in the affected repository area and makes the radionuclides available for transport into the UZ as calculated by the cited Dike/Drift Interactions AMR. The (low-probability) seismic scenario class also has two modeling cases: mechanical damage failure of waste packages and later failure of waste packages due to corrosion (primarily stress corrosion cracking due to seismically-induced stresses). Section 6.1.2 cites the Seismic Consequence Abstraction AMR and the Characterize Framework for Seismicity and Structural Deformation at Yucca Mountain, Nevada AMRs for these modeling cases. Section 6.5.3.1.1.2 discusses the WP breach area and its influence on the flow model for each scenario class and modeling case:

- Nominal scenario class with no early failures modeling case: The breach area comes from the cited WAPDEG Analysis of Waste Package and Drip Shield Degradation AMR. However, Section 7.1.1 notes that no waste packages fail due to general corrosion within 10,000 years. Beyond 10,000 yr, if the TSPA-LA model were to be extended, the drip shield general corrosion is modeled as a single patch, and the EBS Flow model would then become dripping from the drift crown onto the waste package crown
- Nominal scenario class early failure modeling case: The entire waste package surface area is breached (WAPDEG Analysis of Waste Package and Drip Shield Degradation AMR),

0801056250

Page 4

and conservatively unfolds onto the invert for diffusive transport calculation purposes. However, Section 7.1.1 notes that no drip shields fail within 10,000 years and hence the waste package breach area receives no seepage flux that can drive advection.

- Igneous intrusion modeling case: The entire waste package area is breached and there is no cladding protection. Transport begins at the top of the invert.
- Seismic ground motion modeling case: The cited Seismic Consequence Abstraction AMR calculates the breach area, and transport is sequentially through the waste package plan area (diameter times length) and then the breached area of the outer shell.
- Seismic localized corrosion modeling case: The breach area is calculated by the cited AMR (General Corrosion and Localized Corrosion of Waste Package Outer Barrier). The drip shield also is breached by stress corrosion cracking. However, the drip shield cracks are too small to support advective flux and no seepage is received by the waste package breaches.

The conceptual models for EBS Flow, EBS Transport, and the EBS/UZ Interface are discussed in Sections 1, 6.3, 6.5, and 7, and Appendix B. Section 8.1 (in the Conclusions chapter) provides a succinct summary of the conceptual models. These models are briefly summarized below, including notation of conservatism used to simplify the models.

The Flow Model is based on conservation of mass for the TSPA nominal scenario class. Three potential sources of moisture to the EBS (which is defined by the perimeter of the excavated emplacement drifts) were identified (seepage, condensation, and flow from the rock to the invert). One significant sink for water leaving the emplacement drifts was identified (flow into the UZ). The minor sink by evaporation and movement of vapor from the EBS into the rock or longitudinally into the mains was conservatively neglected.

Within the EBS, the movement of water is calculated along potential pathways. The analysis included diversion by the drip shield and flow through breaches in the drip shield. Condensation under the drip shield was excluded as a FEP in the EBS FEP AMR. Water moving through the breaches in the drip shield could be diverted by the waste package or enter the waste package through breaches. The invert receives water from these three sources (drip shield diversion, waste package diversion, and flow through waste package), as well as receiving water from the UZ.

Conservatism is used in the EBS Flow model as follows:

- All seepage (and in-drift condensation) is assumed to be from the crown (with the largest probability of reaching breaches). Dripping outboard of the drip shield and film flow down the drift wall are conservatively ignored (their flux is part of the conservatively consolidated crown seepage).
- All flow through the drip shield breaches is assumed to drip on the waste package crown. Dripping outboard of the waste package and film flow down the underside of the drip

0801056250

Page 5

shield are conservatively ignored (their flux is part of the conservatively consolidated dripping on the waste package crown).

- All flow into the waste package is assumed to contact the waste form and then move through the corrosion products to an exit breach from the waste package
- No seepage liquid evaporates after it enters the drift
- The exit breach from the waste package is assumed to be in direct contact with the invert
- Flow through the invert is assumed to be through the tuff ballast, with the oxidized steel components not being contacted; this reduces the sorption in the invert

The neglect of condensation on the underside of the drip shield is non-conservative, but the AMR states in Sections 6.3.3.2, 6.3.3.3 and 6.7.1 that a cited FEP AMR justifies its neglect based on low consequence.

The EBS Transport conceptual model includes all the significant processes that contribute either positively or negatively to radionuclide transport. These are advective transport in solution, diffusive transport in solution, reversible and irreversible sorption on immobile solids, reversible and irreversible sorption on colloids, and both advective and diffusive movement of colloids. The implemented numerical model conservatively neglects reversible sorption on immobile solids.

Conservatism is used in the EBS Transport model as follows:

- Lateral and longitudinal dispersion are neglected (Section 6.3.1.2) which results in somewhat more focused transport than the real situation. However, the effect is justified as being small because the EBS is such a small part of the overall transport path.
- Advective flux into the UZ just below the invert is the greater of the steady state UZ flux and F_8 . At locations with flow focusing, the (higher) focused flow will be used for transport calculation, and at locations with flow defocusing, the steady state (no flow defocusing) value will be used. The overall result is more flow from the EBS into the UZ than enters the EBS from the UZ, which will conservatively increase radionuclide release from the EBS.
- Reversible sorption of radionuclides onto stationary corrosion products is neglected (Sections 1, 6.3.4.2.3, 6.5.1.2, and Appendix B).
- Physical filtering and gravitational settling of colloids during transport is neglected (Section 6.5.1.2).
- For waste packages with early failures, the diffusion cross sectional area between the corrosion products domain and the invert domain is the entire waste package surface area.
- No sorption on oxidized iron components of the invert is calculated.
- A continuous path of water film is assumed within the waste package and invert when the temperature is below 100°C, allowing diffusion from shortly after the waste package breaches.
- Reduction in diffusion effectiveness due to discontinuous intergranular films at low humidity in the invert is not included in the model.

0801056250

Page 6

The EBS/UZ Interface model has two key features. The first is that the location of zero-concentration sink is significantly (about three drift diameters) below the bottom of the invert and extends laterally one drift diameter on each side (the domain of the interface model is three drift diameters wide and about three high). Second, the invert is a single (equivalent) continuum that couples to the dual fracture-matrix continuum of the UZ. Diffusion from the invert independently enters both UZ continua below the drift and can also diffuse, in the UZ, both between continua and laterally. Advective flux in the invert has two distinct sources, seepage from above (including the flux which transits a breached waste package) and percolation from the drift wall. The percolation flux into the invert exits the invert into the UZ matrix, and the seepage flux into the invert exits the invert into the UZ fractures.

The EBS/UZ Interface model uses the same properties as the UZ transport model and results in a radionuclide flux into the UZ at the bottom of the invert. That flux is the time-dependent boundary condition for the UZ transport model.

The EBS/UZ Interface model conservatively ignores the drift shadow effect, in which advective fluxes below the drift are expected to be less than those in the pillars between the drifts.

NUMERICAL MODEL:

Based on the discussion below, I conclude that the numerical implementation of the conceptual models for EBS Flow, EBS Transport, and the EBS-UZ Interface are technically credible, are appropriate for their intended TSPA use, and that they capture the known flow pathways and transport modes.

The conceptual models for EBS Flow, EBS Transport, and the EBS/UZ Interface are implemented in numerical models. Because these models will be run as part of the TSPA-LA runs (using TSPA software), the EBS Radionuclide Transport Abstraction AMRs develops the equations and the input parameters for those equations, and provides them to TSPA. The numerical implementation to be used by TSPA is discussed in Sections 6.5.1 and 6.5.3.

The development of the equations of flow through breaches in the waste package and drip shield in Section 6.5.1.1 is rigorous and clear. The development of the transport equations in Section 6.5.1.2 is extremely thorough and easy to follow. The derivation is supplemented by additional equation development in Appendix B, to produce models that were used to verify the accuracy of the base case derivation; readers seeking additional explanation of the development in Section 6.5.1.2 can find that information in Appendix B. Section 6.5.3 is a step-by-step prescription for implanting the numerical model in TSPA. Equation B-72 is also directly used by TSPA, using input parameters from controlled sources or calculated within the TSPA model.

0801056250

Page 7

Dimensional units are provided throughout the AMR for each symbol in each equation, and Section 6.5.1.3 is a comprehensive listing of the symbols used throughout the report. The authors did an excellent job of remaining consistent in their choice of symbols, and they avoided reader confusion by not reusing symbols to represent different quantities in different sections of the AMR.

Section 8.2 (in the Conclusions chapter) includes a succinct summary of the equations to be implemented in TSPA.

PARAMETERS USED IN NUMERICAL MODEL:

Based on the discussion below, I conclude that the numerical parameters developed for the numerical models for EBS Flow, EBS Transport, and the EBS-UZ Interface are technically credible and are appropriate for their intended TSPA use.

Section 6.5.2 provides an overview of the parameters to be used in the models, and the parameters are listed in Section 8.2 (in the Conclusions chapter).

The EBS Flow model parameters are based on experimental data that are analyzed in the AMR (Sections 6.5.1.1.2 and 7.1.1, and Appendices C, D, and E). The diffusion coefficient data are developed in Sections 6.3.4.1, 6.3.4.3, 6.5.2.1, and 6.5.2.4, and in Appendices G and H. The sorption parameters for the EBS Transport model are discussed in Sections 6.3.4.2, 6.5.2.3, and 6.5.3.2, through 6.5.3.4, and Appendix J.

The carbon steel corrosion rates used in developing the characteristics of the corrosion products domain are taken from 1 yr data, and are applied as if the corrosion of the stainless steel inner vessel or the waste package internal components is from one side only. Carbon steel corrosion rates are known to decrease until an equilibrium oxide thickness is reached (signifying a nominal equilibrium between periodic flaking of oxide and additional oxide layer formation at the interface with the base metal. The equilibrium oxide thickness depends on a number of difficult-to-quantify parameters, including the stress state of the component and the frequency and intensity of seismic events. It is possible that the overall average corrosion rate for the time to completely corrode the carbon steel components is lower than that used in this AMR. The influence of a lower corrosion rate is the following:

- For failed cladding, the early release of iodine and technetium will be prior to significant carbon steel corrosion for both the AMR's corrosion rate or a lower corrosion rate. There will be a low amount of corroded surface area and hence a low volume of adsorbed water (which may or may not be sufficient to form a thin continuous film and thus may or may not lead to diffusion). There will then be a high concentration of the radionuclide source and rapid diffusion of these radionuclides (assuming the concentration gradient factor is

more important than other diffusion factors, and that there is a continuous water film pathway for diffusion).

- For intact cladding, the failure time of the cladding will likely be much later than the corrosion time of the carbon steel, and there will be little effect on diffusion of fast-release of iodine and technetium.
- For failed cladding, the release of plutonium and americium will be slow because of the slow dissolution rate of the SNF matrix. The carbon steel corrosion rate will almost certainly be faster than the SNF matrix dissolution rate. Prior to full corrosion of the carbon steel, there are competing effects of different corrosion rates. Slower corrosion of the carbon steel leads to less surface area, less water volume, higher source concentrations, and faster diffusion (assuming the concentration factor is more important than other diffusion factors), just as for iodine and technetium. Slower corrosion of the carbon steel also leads to less irreversible sorption of the plutonium and americium, which results in less colloidal transport but also less removal onto the fixed corrosion products. Eventually, the carbon steel corrosion will be complete, and the remainder of the plutonium and americium releases will be unaffected by the prior corrosion rates.
- For TSPA, the effect will not be noticeable with respect to meeting the regulatory dose limits because of the small fraction of failed cladding and the small number of waste packages that fail during the 10,000-year TSPA calculation.

Transport requires a number of parameters in the following areas:

- The saturation in all three domains is 100%, except for the CSNF Corrosion Product (CP) domain in regions of no seepage. The saturation is calculated from relative humidity for that situation, and the humidity is an input from another AMR.
- Release of radionuclides from the waste form into the aqueous phase is calculated based on input from other AMRs, including solubility and WF degradation rate. The concentration of the radionuclides in the Waste Form (WF) domain is based on the amount of water in that domain, which is calculated from on the CSNF rind volume and porosity, HLW rind volume and porosity, and 1 m³ of DSNF volume with porosity of 20% (all from other AMRs).
- WF colloids are generated in the WF domain, based on another AMR, and include embedded radionuclides.
- The water content of the CP domain is calculated as a function of time based on the corrosion of the iron-based materials (see above) and the resulting surface area (uniform distribution of 1.0 – 22 m²/g to account for uncertainty).
- FeOx colloids are generated in the CP domain based on another AMR. Groundwater colloids enter the transport model at the CP domain.
- Dissolved radionuclides advect from the WF domain to the CP domain based on aqueous concentration and on flow rate. For CDSP waste packages, the advection is sequentially from the HLW WF subdomain to the DSNF WF subdomain, and then to the CP domain. For CSNF waste packages, the advection is from the WF domain to the CP domain.

Dissolved radionuclides diffuse through the same pathways, based on concentrations, diffusion coefficients, path lengths, and diffusion areas. These parameters are provided in Section 8 of the AMR, with some being single valued and others being distributions.

- In the CP domain, radionuclides can irreversibly sorb onto stationary FeOx, can irreversibly and reversibly sorb onto FeOX and waste form colloids, and can reversibly sorb onto groundwater colloids. The reversible Kd values are taken from another AMR's DTN and are listed in Table 6.3-11, with smectite being representative of both waste form and groundwater colloids. Table 6.3-11 includes 100x reductions in the Kds for Pu and Am on FeOx to be compatible with the mechanistic sorption model in another AMR. The irreversible reaction rates are a range taken from another AMR's DTN for locations without seepage. In seepage locations, the flux-out ratio is sampled from 90 to 99% based on another AMR, and the irreversible reaction rate is calculated from an expression derived in this AMR, using parameters available in TSPA from this AMR or other AMRs. Eq. B-72 in this AMR defines the parameters; those from this AMR are listed in Section 8.
- FeOx, WF, and groundwater colloids advect and diffuse from the CP domain to the Invert domain, with the colloid diffusion coefficient being 100x smaller than the aqueous diffusion coefficient.
- Dissolved radionuclides and WF and FeOx colloids advect and diffuse from the CP domain to the invert domain, with no credit taken for path length between the edge of the waste package breach and the top of the invert. Diffusion out of the corrosion products uses a sampled path length between the outer barrier thickness and the waste package radius, with the diffusion area depending on the scenario class and modeling case, as described under "conceptual model" above. The aqueous diffusion coefficient in the Invert domain is calculated (based on experimental data) from the water content and temperature (both obtained from another AMR), and includes a normal distribution for uncertainty that is truncated at ± 3 standard deviations.
- The Invert domain is modeled as a rectangular cross section that is 1 WP long. The cross section width is the same as the actual invert top surface, and the depth is that which preserves the overall volume of the invert. The small (10 cm) axial gap between waste packages does not contribute radionuclide transport in the invert, for this model.
- The invert is modeled as a single continuum with a thin interface zone at its lower surface. The interface zone is the starting point for diffusion and advection into the two continua of the UZ, which is assumed to be at zero concentration about three drift diameters below the invert.
- The near field of the UZ is modeled as three columns of cells, with each column being one drift diameter wide. (The middle column is as wide as the drift diameter, rather than the rectangular width of the invert domain, to facilitate linkage to the domain for the seepage flux.) Advective transport of the seepage plus condensation flux (F_6) in the invert moves into the fracture continuum of the middle column. Advective transport of the water that directly enters the invert from the UZ (F_7) moves into the matrix continuum of the middle column. Diffusive transport from the invert interface zone moves radionuclides and

0801056250

Page 10

colloids into both continua of the middle column. Within the three columns of four zones in the EBS/UZ boundary model domain, advection is calculated vertically in both continua, and diffusion is calculated between adjacent vertical and horizontal matrix zones and between matrix and fracture continua in each zone. All three columns of zones (in both continua) end in a single zero-concentration collector cell.

- The TSPA model calculates the transport through the coupled WF, CP, Invert, and UZ boundary domains to the collector cell in a self-consistent manner, using the parameters from this AMR and other AMRs. The resulting time-dependent radionuclide fluxes into the UZ from the invert interface zone are the starting point for the UZ transport model.

ALTERNATIVE CONCEPTUAL AND NUMERICAL MODELS:

The AMR includes a number of alternative conceptual models, for the purpose of evaluating whether the base model is adequate for TSPA. These models are well described and justify use of the base model in the TSPA.

The alternative models include the following:

- Treatment of the water flow through the waste package as a bathtub conceptual model rather than a steady state flow model. Variations of this alternative model include changing the inflow rate, changing the inflow chemistry, and changing the corrosion patch geometry (formation of a draining patch after the waste package “bathtub” fills).
- Limiting water vapor and oxygen diffusion rates into the waste package. These scoping calculations uses an atmospheric pressure at sea level; however, this inaccuracy does not affect the conclusion of the alternative model.
- Treating the invert as a dual continuum with intragranular and intergranular porosities.
- Single and dual continuum invert diffusion coefficients. The single continuum alternative diffusion coefficient was modeled as decreasing more rapidly than the base case as saturation decreases, at the dry end of the saturation spectrum.
- Reversible sorption onto corrosion products within the waste package.
- Slow desorption of irreversibly sorbed radionuclides.

MODEL VALIDATION AND MODEL TESTING RESULTS IN THE AMR:

Based on the discussion below, I conclude that the model validation activities and model testing of the numerical models for EBS Flow, EBS Transport, and the EBS-UZ Interface are technically credible and support the use of these models in TSPA. All of the comparisons with alternative data sources and models described below had reasonable results.

Flow Through Breaches in the WP and DS:

For the EBS Flow model, four series of tests were performed on a full-scale mock-up of one side of a drip shield. Two of the series of tests were configured to represent dripping from the drift crown onto the drip shield crown, and the other two tests were configured to represent dripping from the drip shield [or drift wall] onto the waste package crown. For each pair of test series, the initial tests were done with smooth mock-up surfaces, and the data were used to predict the splitting of flow between the outside of the drip shield and through the breaches. Then, the tests were repeated with a rough mock-up surface, and the results were compared to the smooth surface results as a means of model validation. The fraction of water through the breaches is expressed as a fraction of half the dripping water, since there is equal probability of dripping down either side of the crown of a full drip shield or waste package. Therefore, the results can conceivably range between 0 and 200%. The test results (rounded to integers for values >1%) were the following:

- Smooth drip shield test: Range 1% to 28%, Mean 11%, Median 5%
- Rough drip shield test: Range 0% to 117%, Mean 11%, Median 0.5%
- Smooth WP test: Range 0% to 107%, Mean 30%, Median 1%
- Rough WP test: Range 0.01% to 62%, Mean 12%, Median 0.3%

The values in these results were compared to a geometric prediction and to develop a multiplier range on that prediction (including the incorporation of uncertainty into the multiplier range). The actual values of the test results shown above are dependent on the selected combinations of drip and breach locations; however, the similarity and differences of the smooth and rough surface results are a combination of validation (repeatability), adequate statistics, and physical differences due to the surface texture itself. The experimental results are difficult to use to directly predict the splitting of flow because the initial drip splashing results in a distributed source of rivulets, because the flow is in rivulets with a variety of angles from the most downward, and because the experiment ends with a portion of the drip still on the surface as small mini-droplets which have neither run-off nor gone through breaches.

The model for the fraction entering breaches is a uniform distribution from zero to the computed maximum (but limited to no more than 100% of the total, both sides, source). The computed maximum is based on three multiplicative factors. The first factor is the geometric area fraction of the breach(es) length divided by the actual component length. The second factor, which normalizes the measured data, is based on three measured ranges for the smooth surface data for the component (drip shield or waste package). These three measured ranges are reduced to single values that result in a maximum multiplicative factor. The mean of the experimental breach fraction results (the first measured range) is used since it is larger than the median (it has a theoretical maximum of 200% of the single side source). The *minimum* of the measured rivulet spread angle (the second measured range) is used as it appears in the denominator of the multiplicative factor. The diameter of the inner cluster of splash mini-droplets is the third

0801056250

Page 12

measured range; the maximum was used and was the source of the “effective component (DS or WP) length”. The final factor in the calculation depends on the rivulet-spread angle, and it is independently maximized by using the *maximum* of the measured angle, even though the minimum of that angle was used in the second factor. The inconsistency in selection of the measured angle adds conservatism to the results as the maximizing end of the range is different in the second and third factors.

The net result passed to TSPA is the following:

- For the drip shield, breach flow is sampled between 0 and 85% of the source multiplied by one-half of the geometric fraction of the breach length divided by the drip shield segment length (the one-half factor accounts for only half the source flow going toward the breach side of the drip shield).
- For the waste package, breach flow is sampled between 0 and 241% of the source multiplied by the one-half of the geometric fraction of the breach length.
- In both cases, any sampled breach flow larger than the source is reduced to 100% of the source.

The drip shield multiplier maximum is somewhat less than the nominal expected maximum of 100%, reflecting the combination of the experimental issues (such as remaining liquid on the surface) and the choice of maximizing measured factors in the development of the multiplier. The waste package multiplier maximum is greater than 100%, reflecting the dominance of the conservatisms in the data reduction and the lesser effect of the remaining liquid issue when some of the drips are onto the sloping side surfaces.

The analysis of the rough surface (validation) experimental data resulted in maximum multipliers of 77% for the drip shield and 30% for the waste package. The drip shield breach flow model results are similar for the two surface textures, but the waste package breach flow results are much lower for the rough surface used in the validation tests. Since the TSPA model will use the larger values in both the DS and WP cases, the data selection for the TSPA is conservative (larger breach flow leads to more radionuclide transport).

Transport Model:

The EBS/UZ boundary condition involves bifurcation from a single continuum into a dual continuum. Two approaches were developed for this situation. The first is rigorous but difficult to implement efficiently. The second uses a thin interface layer at the base of the single continuum and is computationally efficient. Section 6.6.4.4 presents a test of the two methods for a simplified situation. Figures 6.6-4 and 6.6-5 present the results, which show that the two methods are in close agreement and that the GoldSim software implementation of the interface-layer method in TSPA matches a spreadsheet implementation of the same method. In addition, an alternative

0801056250

Page 13

model from the Drift-Scale Radionuclide Transport AMR (the fracture-matrix partitioning model) was compared to the results from this AMR.

For in-package diffusion, Section 7.2.1 compares the results with two published alternative models, including one developed by the Electric Power Research Institute. Section 7.2.2 compares the electrical analog tuff diffusion experimental results to results from direct measurements of diffusivity between machined cubes of tuff.

Finally, in Appendices B and F, the differential equations from the base case model were converted into a finite difference model and implemented in a spreadsheet program (with some simplifications compared to the base case model). The resulting model was exercised using reasonable input parameter values, and the results were analyzed in terms of the fraction of the release carried by irreversible sorption on colloids, and also of the temporal behavior of the modeled system.

CONCLUSION:

Based on the information above, I conclude that

- The approach and algorithms described in the document and provided to TSPA capture all known flow pathways into and from the EBS components.
- The approach and algorithms described in the document and provided to TSPA address all known modes of radionuclide transport within and from the EBS components.
- Modeling assumptions are clearly defined, discussed, and justified as appropriate for the intended use of the three models. Major assumptions are documented in Section 5 of the AMR, and the text discusses other assumptions as they occur.
- Uncertainties in parameters, processes, and assumptions are sufficiently described, and impacts of these uncertainties discussed. The organization of Section 8 of the AMR into single-value parameters and sampled parameters makes the treatment of uncertainty easy to follow.
- The overall technical credibility of the approach, including assumptions, parameters, equations, and the TSPA implementation, are sufficient for the model's intended use.

M.3 Results of Critical Review of the EBS-UZ Interface Model

A critical review of the EBS-UZ interface model was conducted as specified in the TWP (BSC 2006 [DIRS 177739], Section 2.2.3). This model validation approach is justified based on requirements of SCI-PRO-006, Section 6.3.2, where critical review is listed as an appropriate method for model validation. The results of the critical review of the EBS-UZ interface model are presented in a memo (Baker and Grisak 2004 [DIRS 170953]) (a verbatim copy follows; "independent model validation technical review" is now referred to as a "critical review" in SCI-PRO-006).

MEMO

Date: July 27, 2004

To: James Schreiber and Cliff Howard, Yucca Mountain Project

Cc:

From: Noreen A. Baker, Gerald E. Grisak, INTERA Inc., Austin, Texas

RE: Independent Model Validation Technical Review of the EBS-UZ Interface Sub-Model of the Radionuclide Transport Abstraction Model for the Yucca Mountain Project

Pursuant to your request to perform an independent model validation technical review of three sub-models of the Engineered Barrier System (EBS) Radionuclide Transport Abstraction (RTA) model as documented in ANL-WIS-PA-000001 Rev 01K, we have performed and documented the review consistent with the requirements of the Technical Work Plan TWP-MGR-PA-000020 Rev 00. We reviewed the EBS-UZ interface sub-model of the EBS RTA report, and the results of the review are provided in this memo.

Review Qualifications

Section 2.2.4 of the Technical Work Plan TWP-MGR-PA-000020 Rev 00 describes the qualifications and responsibilities of the independent model validation technical reviewer. We are qualified to perform the work described for the following reasons. (1) we have not contributed to the development of the model assumptions, parameters, or implementing algorithms documented in ANL-WIS-PA-000001 Rev 01K, (2) Noreen A. Baker has a BS and MS degree in Geology with specialties in Engineering Geology and Hydrogeology, respectively, with more than ten years of professional experience modeling fluid flow and transport in geologic media (3) G. E. Grisak has BS (Geology) and MS (Hydrogeology) degrees, and over 30 years experience evaluating and modeling fluid flow and transport in geologic media, including several publications on fracture/matrix flow and transport, (3) Both N. A. Baker and G. E. Grisak are licensed Professional Geoscientists in the State of Texas. More detailed information regarding credentials can be found in the resumes attached.

MEMO (Continued)**Appropriateness and Adequacy of the EBS-UZ Interface Sub-Model Conceptual Model**

Discussion of the EBS-UZ interface sub-model is provided in Section 6.5.2.6. Discussion of the EBS-UZ interface sub-model is provided in Section 6.5.2.6. In the EBS-UZ interface sub-model, the near-field UZ is modeled as a dual continuum of overlapping UZ-matrix and UZ-fracture media. This approach is consistent with current technical approaches to modeling flow and transport in fractured geologic media (Liu et al. 1998; Nitao 1991). The matrix and fracture continua are represented by a two dimensional vertical array of cells oriented parallel to a cross section of a drift and located immediately beneath a drift. The array consists of three vertical zones, with each zone containing both a fracture cell and a matrix cell. The vertical zones are four layers deep in the vertical direction. The invert is in direct communication with the center zone of UZ matrix/fracture cells. A semi-infinite zero concentration boundary condition at the EBS-UZ interface is approximated by setting a zero concentration boundary at a distance of 3 drift diameters below the invert-UZ boundary.

The mass flux from the invert flows into the top layer of the middle zone in the UZ. The mass flux from the invert is routed to both the fracture cell and the matrix cell in the center zone beneath the invert, with the advective flux routed to the fracture and matrix cells in a manner that is consistent with physical reality. That is, the advective flux coming out of the invert, which is attributable to the dripping flux is routed to the fracture cell in the middle zone, while the imbibition flux is routed to the matrix. The diffusive flux is allowed to enter both the matrix and the fracture cells. The advective flux in the fractures is taken as the larger of the steady-state advective flux in the fractures and the advective flux out of the invert.

The mass flux that enters the center zone cells in the UZ below the invert is then transported by advection and diffusion throughout the modeled area. The advective flux in the two outer zones is given by the steady state UZ flow in the fractures and the matrix at the repository horizon. Advection occurs downward only, from the fracture cell of one layer to the fracture cell of the underlying layer in the same zone, and from the matrix cell of one layer to the matrix cell of the underlying layer in the same zone. Advection does not occur across zones. The fracture and matrix cells of each zone interact via diffusion. The entire modeled area interacts through the matrix cells via diffusion, with the matrix cells of one zone interacting via diffusion with the matrix cells of adjacent zones, and the matrix cells of one layer in a zone interacting with adjacent overlying and underlying matrix cells in the same zone.

The conceptual model of how the EBS and UZ interface is well captured by the EBS-UZ interface model. The conceptual model recognizes the physical reality by considering both an advective and diffusive flux and by treating the UZ as a dual-permeability medium with both fracture and matrix continua. This modeling approach is consistent with the manner in which dual-permeability continua are modeled (Pruess 2003). The conceptual model is appropriate for describing the interconnection between the EBS and the UZ because it considers the important components of mass flux out of the EBS and it conserves all the mass flux from the EBS and transfers it to the UZ. The mass transfer to the UZ also captures temporal variations, which may be due to variable radionuclide concentrations in the waste, production of corrosion products, or varying water flux through the EBS. The mass is distributed to the fractures and the matrix in the EBS-UZ interface sub-model in a

MEMO (Continued)

manner that is conceptually logical. The mass is finally gathered from the EBS-UZ interface sub-model into a collector cell for delivery to the UZ transport model. The delivery from the collector cell to the UZ transport model retains the relative fractions of mass in the fractures and the matrix that is determined within the EBS-UZ interface sub-model.

Appropriateness of the Mathematical Representation of the EBS-UZ Interface Sub-Model

The EBS-UZ interface sub-model represents the UZ immediately below the invert as a dual continuum of UZ matrix and UZ fracture media. The dual permeability modeling approach is an appropriate way to model transport in fractured media. Mass is tracked and accounted for in the model in both fracture and matrix cells and the fracture and matrix cells have physical dimensions which adequately approximate the physical hydrogeologic system. The mathematical formulation of the dual permeability modeling approach is described in *Particle Tracking Model and Abstraction of Transport Processes* (BSC 2003w).

EBS-UZ Interface Sub-Model Assumptions and Boundary Conditions

The EBS-UZ sub-model assumptions and comments are provided below.

Assumptions/Boundary Condition	Comments
1. A semi-infinite zero concentration boundary condition is used for the EBS-UZ interface. The boundary condition is set at a distance of 3 drift diameters below the invert-UZ boundary.	We agree with the boundary condition and with the manner in which it is implemented. Placing the boundary condition at the interface would result in an unrealistically high diffusive flux from the invert to the UZ.
2. With respect to the advective flux in the outer two zones of cells, drift shadow effects are ignored.	We agree with the assumption. Drift shadow effects would increase the advective flux in the two outer zones and result in dilution of radionuclide concentrations entering the UZ immediately below the invert.

Evaluation of Model Validation

Documentation of the model validation is presented in Section 7.3.1. The EBS-UZ sub-model is validated by comparison with an alternative mathematical model developed for a closely comparable description of the EBS-UZ interface. The alternative model used for the comparison is the fracture-matrix partitioning model described in *Drift-Scale Radionuclide Transport* (BSC 2004m). The primary validation criterion is corroboration of the model results with an alternative mathematical model, as described in TWP-MGR-PA-000020 Rev 00. This is a common approach to model validation where site specific or generic field or laboratory data or experiments do not adequately capture the processes involved. The EBS-UZ interface sub-model involves coupling the porous medium invert to the dual-permeability UZ with a numerical solution of a discretized model. In the fracture-matrix partitioning model, the coupling is accomplished by formulating the problem as a partial differential equation for concentration and deriving an analytical solution to the problem. In order to compare the two models, all sampled and time-varying parameters in the EBS-UZ interface sub-model are made consistent with the parameters used in the fracture-matrix partitioning model. Additionally, other changes to the EBS-UZ interface sub-model were made to more closely approximate

MEMO (Continued)

conditions in the fracture-matrix partitioning model. The EBS-UZ interface sub-model was also run using an alternative conceptualization for the invert as a dual continuum. The results of the CDFs of the fraction released to fractures are then compared. This is a technically reasonable and appropriate approach to model validation.

Evaluation of Model Validation Criteria

In Section 2.2.4 of Technical Work Plan TWP-MGR-PA-000020 Rev 00, provides validation criteria for the EBS-UZ interface sub-model. The table below provides our assessment of these criteria.

Criteria	Criteria met?	Response
1. The results of the UBS-UZ interface sub-model shall show qualitative agreement with the results of the fracture-matrix partitioning model.	Yes	The two models display similar qualitative results, and in addition are reasonably similar quantitatively, in that the results of the EBS-UZ interface sub-model fall within the shadow of the error bars of the low, mean and high infiltration cases of the fracture-matrix partitioning model.
2. The report shall document equivalent trends and correlations between input parameter variation and predicted results	Yes	Equivalent trends and correlations between input parameter variations and predicted results are visually obvious on the graphical comparison between the two methods. Either the single or dual continuum representation of the invert by the EBS-UZ interface sub-model is adequate.
3. Identification of differences between model results.	Yes	Differences between model results and the reasons for the differences are provided in section 7.3.1.2
4. Demonstrate that the EBS-UZ interface sub-model does not underestimate radionuclide transport from the EBS to the UZ.	Yes	The suitability and applicability of the EBS-UZ interface sub-model is discussed and justified in Section 7.3.1.3. The sub-model is suitable for its intended use.

Conclusions

The EBS-UZ interface sub-model documented in report ANL-WIS-PA-000001 Rev 01K incorporates all the significant aspects contributing to mass flux from the invert to the UZ. The sub-model is validated against an alternative model developed for similar purposes and the results are comparable. The advective flux is the primary uncertainty in the mass flux to the fractures, and this uncertainty has been adequately and realistically bounded by the low, mean and high infiltration cases used in the fracture-matrix partitioning model in the validation comparison. It is our professional judgment that the EBS flow sub-model is appropriate for use in the Radionuclide Transport Abstraction.

MEMO (Continued)

References

Liu, H.H., C. Doughty and G.S. Bodvarsson 1998, "An active fracture model for unsaturated flow and transport in fractured rock," *Water Resources Research*, vol. 34, no. 10, pages 2633-2646.

Nitao, J.J. 1991, "Theory of matrix and fracture flow regimes in unsaturated, fractured media," *Proc., Second International High Level Radioactive Waste Management Conference*, Las Vegas, NV, April 29-May 3, 1991.

Pruess, K. (editor) 2003, *Proceedings, TOUGH Symposium 2003*, Lawrence Berkeley National Laboratory, CA, May 12-14.